INNOVATIVE NONDESTRUCTIVE TESTING (NDT) FOR CONDITION ASSESSMNET OF LONGITUDINAL JOINTS IN ASPHALT PAVEMENTS

by

Zhiyong Jiang

A thesis

presented to the University of Waterloo

in fulfillment of the

thesis requirement for the degree of

Master of Applied Science

in

Civil Engineering

Waterloo, Ontario, Canada, 2007

I hereby declare that I am the sole author of this thesis. This is a true copy of the thesis, including any required final revisions, as accepted by my examiners.

I understand that my thesis may be made electronically available to the public.

ABSTRACT

The failure of longitudinal construction joints is one of the critical factors causing accelerated pavement deterioration. Poor-quality longitudinal construction joints are often characterized by a difference in elevation between adjacent lanes or by unraveling of the hot mix asphalt (HMA). Current wave-based non-destructive testing (NDT) methods are efficient and economical for the evaluation of material properties. In this thesis, an innovative surface wave testing technique for condition assessment of longitudinal construction joints in asphalt pavements is presented. This method enables reduction of the number of cores required for large-strain testing and provision of a more uniform quality assessment of longitudinal joints as well as the relative condition of the asphalt pavements. The technical development is based on a theoretical study of the wave attenuation mechanisms and on the reported deficiencies in current seismic wave-based methods.

Traditionally, the use of ultrasonic testing to determine small-strain elastic property for asphalt concrete was uniquely based on the measurement of wave velocity. However, isolated use of wave velocity does not provide complete information of the materials strength because of the different variables that affect the strength-velocity relationship. Therefore, it is necessary to complement velocity data with independent information such as the change in attenuation and frequency content of the propagating pulse.

The existing deficiencies in current seismic wave-based methods were addressed to improve reliability, accuracy and consistency for asphalt concrete material characterization in the laboratory and in the field. Refined and improved signal processing techniques were used to overcome the shortcomings in the existing wave-based methods that contribute to uncertainties in the interpretation of test results. To capture more information from a wave, the signal was analyzed in the time and frequency domains. The basic analyses included a simple method such as peak to peak amplitude of the first cycle of arriving wave, and complex methods such as maximum magnitude and area of corresponding frequency spectrum through Fourier transform. A novel approach

based on wavelet transform of the signal was presented, which provides an alternative method to determine wave characteristics.

Material characterization tests (experiment Phase I) were carried out to study the relationship between the wave characteristics obtained from UPV test and the quality of the asphalt concrete specimens prepared in the laboratory. The specimens were identical in terms of aggregate and asphalt binder ratio, but varying in volumetric properties produced by different compaction efforts. The specimen quality was determined using two methods: 1) the traditional method using density measurement and 2) an innovative approach using dynamic modulus which is recommended by the Federal Highway Administration (FHWA) for use as a fundamental material property for characterizing Superpave mixes (Witczak, et al., 2002; Bonaquist et al., 2003; Christensen et al., 2004). The measured wave characteristics showed excellent correlations ($R^2 > 0.9$) with the fundamental properties of the mix. The results revealed that the wave amplitude parameters as the condition index have the potential to provide a reliable assessment of the quality of HMA mixtures. The finding is very critical to moving the technology forward in the right direction, and form an important basis for the experiment Phase II.

Experiment Phase II investigated the feasibility and effectiveness of using the wave characteristics identified in experiment Phase I to assess the condition of longitudinal construction joints. Particular attention was given to examining the sensitivity of the wave-based technique to different types of construction joints. For this purpose, three types of construction joints (good, fair and poor) were fabricated in the laboratory and identified using the wave-based technique. The research was intended to develop a suitable test procedure for condition assessment the longitudinal joints in asphalt pavement in the field. The data from experiment Phase II revealed that the wave-based technique enables assessment of not only the quality of different types of longitudinal construction joints but also the relative condition of asphalt pavements.

ACKNOWLEDGEMENTS

I would like to offer my sincerest appreciation to my supervisors: Prof. Joseph Ponniah and Prof. Giovanni Cascante of University of Waterloo.

Prof. Joseph Ponniah recommended the subject of this thesis and has been an indispensable source of suggestions with his valuable time, attention and patience. I am very thankful for all the assistance and excellent supervising he has given me.

Prof. Giovanni Cascante introduced me to the field of ultrasonic testing of materials. He has been a valuable guide during this research and review of this thesis, with his valuable time and expertise. I am very grateful for all the support and guidance he has given me.

Prof. Joseph Ponniah and Prof. Giovanni Cascante also gave me the opportunity to work with them on other projects and shared their experiences with me in different fields. The income generated form this has been the main source of financial support for my study.

Prof. Carl Hass and Prof. William K. Annable read this work when it was a draft. Their suggestions strongly influenced this final text.

My gratitude is extended to all the members in our NDT group and in the CPATT lab with whom I have worked. Special thanks to Jodi Norris who provided the material for the fabrication of the HMA slabs in this research. My sincere appreciation is also expressed to Yanjun Yang who shared with me his time and space.

Last but not least, I would like to thank my parents and fiancee for their continuous encouragement, support and love which enabled me to come through the difficult times; without them, my graduate studies would not have been successful.

TABLE OF CONTENTS

LIST OF TABLES

LIST OF FIGURES

CHAPTER 1
INTRODUCTION

1.1 Background

One of the major challenges facing pavement engineers and researchers is the development of non-destructive test (NDT) methods for the in-situ condition assessment of pavement structures. An efficient quality control and acceptance procedure is important to prevent premature pavement failures. The effects are costly in terms of additional maintenance and early rehabilitation costs. One of the critical sources causing accelerated pavement deterioration is the failure of longitudinal construction joints. Poor-quality longitudinal construction joints are often characterized by a difference in elevation between adjacent lanes or by raveling of the hot mix asphalt (HMA). Construction joint failures also permit the intrusion of water causing further deterioration.

Traditionally, the quality of construction joints is evaluated in terms of achieving adequate density at the joints between adjacent and paving lanes. This evaluation is done by comparing the in-place density obtained through pavement cores at five locations across the longitudinal joint of the pavement (typically at the centerline, 150 mm, and 450 mm on either side of the centerline). In general, it is assumed that good compaction at joints would lead to good performance. Asphalt density is believed to be a good performance indicator of the construction of longitudinal joints. However, this assumption needs validation.

Recent developments in quality control and quality assurance testing program for asphalt pavements identified the need for the use of fundamental material properties for assessing the HMA mix quality in addition to volumetric design properties such as density, void ratio, asphalt content, and so forth. The quality of asphalt concrete materials is often characterized by material properties such as dynamic modulus determined on the basis of the simple performance tests (SPT) recommended by the Federal Highway Administration (FHWA) (Witczak et al., 2002; Bonaquist et al., 2003; Christensen and

Bonaquist, 2004). The dynamic modulus (*E*) test is the oldest test recently modified for use as a part of simple performance tests for the evaluation of the long term performance of asphalt concrete mixture. Therefore, it is felt important that the parameters selected for use in the proposed NDT tests for the in-situ condition assessment of the longitudinal joints should be closely correlated to the mix properties such as dynamic modulus values determined in the laboratory using SPT.

1.2 The Need for Developing an innovative NDT Method

Highway transportation agencies are actively searching for innovative NDT methods for in-situ condition assessment of pavement structures because of the physical and economical constraints of destructive testing. Current density measurements are destructive and time consuming. This creates a need for a simple non-destructive test (NDT) that will be suitable for evaluating not only the quality of longitudinal construction joints but also the relative condition according to the HMA mix design material properties. NDT will reduce the number of cores as well. NDT methods are commonly used for material characterization (concrete, earth, steel, pavements, and wooden structures), flaw and crack detection (sewer systems, tunnel linings), and detection of underground anomalies (mining, detection of unexploded ordnances) and have been successfully used for the location of underground voids (Phillips et al. 2000, 2001, 2002, 2003).

Common wave-based methods such as ultrasonic pulse velocity (UPV), impact echo, and spectral analysis of surface waves (SASW) have gained increased use for material property evaluation for decades. However, there are some limitations in each of these methods. For example, the UPV method is one of the most widespread wave-based methods in NDT. Yet, its potential for assessing the quality of materials is limited because it is only based on measurement of wave velocity. Other important wave characteristics such as amplitude only received little attention. Since different variables can affect the strength - wave velocity relationship, wave velocity alone becomes less reliable for provision of complete information of the material strength. This may be the reason why poor correlation was observed between the wave propagation parameters

determined from the standard pulse velocity test method (ASTM C597) and the field rutting reported in FHWA, NCHRP Report 465 (Witczak et al, 2002). This limitation entails improved techniques for processing the output pulse signals such as the spectral analysis of attenuation to complement the strength-velocity data. Improvement in signal processing through innovation will enhance the utilization of wave-based techniques in highway applications in the future.

1.3 Objectives and Scope of the Research

The main objective of this research is to develop a simple and efficient non-destructive test method for the condition assessment of longitudinal construction joints in asphalt pavements. As a first step, the most promising non-destructive technique (transmission coefficient as described later) in conjunction with suitable static destructive tests will be explored in the laboratory for a comprehensive evaluation of pavement condition. The relationship between good compaction (typically equivalent to 100 gyrations) at joints and good bonding between the two adjacent lanes will be evaluated with a laboratory experimental program. Based on these test results, the most suitable NDT method will be recommended for testing in the field.

The scope of this research involved the following tasks:

- Understanding the propagation of ultrasonic wave in a material, with particular attention to the wave attenuation.
- Reviewing the literature and studying the recent developments of wave-based NDT methods and Superpave (Superior Pavement Performance) test methods for material characterization. Analyzing the limitations and advantages of the NDT techniques and developing an improved UPV-based technique with complementary use of wave characteristics for material characterization tests.
- Performing material characterization tests (Phase I) using laboratory-fabricated cylindrical specimens. The UPV tests in conjunction with the standard dynamic modulus tests (Superpave tests) were explored in the laboratory for a comprehensive evaluation of material quality. Examining the relationship among

the different parameters such density, dynamic modulus values and the wave attenuation measured in terms of signal amplitude and frequency content.

- ❖ Conducting laboratory experiments using fabricated pavement slabs to investigate the feasibility and effectiveness of using the wave characteristics identified in the experiments of Phase I to assess the condition of longitudinal construction joints.
- ❖ Investigating the complementary use of condition indices determined from the laboratory experiments, and developing a test procedure suitable for condition assessment of the longitudinal construction joints in the pavement slab prepared in the laboratory as well as the joints in asphalt pavements in the field.

1.4 Research Significance

The development of ultrasonic testing techniques for inhomogeneous, high damping construction materials such as asphalt concrete has made little progress in comparison to the progress made in the development of techniques for relatively homogeneous materials such as metals and ceramics. There has been ongoing research on the use of ultrasonic testing for bituminous materials, but no standard wave-based test protocol is available for condition assessment of asphalt concrete. The ultrasonic inspection of asphalt concrete is difficult because the composite characteristics of the materials result in scattering of waves and limit the penetration of waves into the object being investigated (Carino and Sansalone, 1988).

It is felt that further refinement of signal processing techniques involved in different NDT methods through research will help overcome the existing limitations in the use of seismic based NDT techniques and make it suitable for routine application in the condition assessment of asphalt pavements.

Traditionally, ultrasonic velocity measurements are used to assess material quality. The underlying principle is that the velocity of wave propagation depends on the elastic modulus, density, and Poisson's ratio of the medium concerned. In practice, however, the velocity-strength relationship is affected by the combined effect of aggregate size, air void, and moisture condition which can cause some degree of variability in the results.

Moreover, observations indicate that ultrasonic pulse velocity is not sensitive to the level of damage until nearly 80% of ultimate strength is reached (Suaris et al, 1987; Daponte, 1995). Therefore, traditional ultrasonic pulse method is not sufficient for condition assessment of asphalt concrete. It is necessary to complement velocity data with independent information such as the change in attenuation and frequency content of the propagating pulse. The attenuation characteristics of a medium are obtained from the frequency domain analysis of the data (Fourier analysis). This involves additional signal processing techniques to determine these wave attenuation parameters. However, these parameters are more sensitive than wave velocity in the detection of system flaws (Suaris et al, 1987; Daponte, 1995). In order to explore the use of additional wave characteristics, more extensive research and effort are required to improve signal processing techniques. It is expected that this study would contribute to increasing the reliability and consistency of NDT measurements which eventually will play an important role in taking the existing technology to the next level.

The findings of this research show excellent correlations ($R^2 > 0.9$) between the fundamental properties of the mix and the wave characteristics. Furthermore, the results show that wave attenuation parameters are effective in distinguishing between the poor and good construction joints of asphalt slabs fabricated in the laboratory. The proposed technique has the potential for development by further research into a more complete method suitable for field implementation.

1.5 Thesis Organization

The first chapter of the thesis gives the general outline of the existing problem, the need for further investigation and objectives of the study.

Chapter 2 begins with a theoretical background mainly on the theory of wave propagation related to elasticity the material. The characteristics of propagation of surface waves and body waves are illustrated. Basic wave equations are stated. The physical phenomena of wave propagation including wave reflection, refraction, mode conversion and superposition are discussed.

Chapter 3 provides the basic principles of associated signal processing techniques which allow for characterization of material properties in the subsequent research. The signal processing techniques mainly includes Fourier transform, windowing technique, short time Fourier transform, and wavelet transform.

Chapter 4 provides a review of wave-based NDT methods commonly employed to evaluate internal conditions of a structure. The testing procedures and associated computation process are described. The limitations and advantages with each test are discussed. This chapter provides information for the design of the experimental program of this research.

Chapter 5 provides the details of the experimental program of Phase 1. The description of tests involved in Phase 1 and their testing procedures are presented, with a particular attention to the Ultrasonic Pulse Velocity measurements. The instrumentation requirements for the ultrasonic testing are highlighted. The analyses and discussions of the experimental results of Phase 1 are presented. The most suitable condition indices were selected from wave characteristics for assessing the mix integrity. The information provided in this chapter forms an important basis for the design of the experiments of Phase 2.

Chapter 6 describes in detail the experimental program of Phase 2, focusing on fabrication of HMA slabs and application of the condition indices identified in the experiments Phase 1. This chapter concludes with the analysis and discussion of the experimental results for the slabs.

Finally, the main conclusions and recommendations of this research are summarized in Chapter 7.

CHAPTER 2
THEORY OF WAVE PROPAGATION

2.1 Background

Mechanical waves are generated by particle oscillation in a solid, liquid, or gas. No mechanical wave is able to propagate in vacuum because no particle oscillation occurs. The wave propagation depends on the elasticity of the material which acts as a restoring force returning each oscillating particle to its original position and starting its neighborhood particles oscillating. Individual particles will not move to another place; they only oscillate back and forth a distance from the equilibrium position. This distance of oscillation is defined as the amplitude of the wave.

Human beings are able to detect sound waves of a certain frequency range, roughly from 16 Hz to 20 kHz, known as the audible range. Sound waves below 16 Hz are considered subsonic; and those above 20 kHz are above the ability of human hearing and hence called ultrasonic (Hellier et al., 2001).

2.2 Modes of Propagation

In general, stresses and strains created by a transient disturbance on a half-space propagate as two types of waves: body and surface waves. Body waves consist of compression and shear waves which propagate radially outward from the source. The two major types of surface waves are Rayleigh and Love waves. In contrast to body waves, surface waves are confined to the near surface and are similar to waves propagating on the surface of water. Wave propagation modes are usually described in terms of the direction of particle motion in relation to the direction of propagation (Hellier et al., 2001).

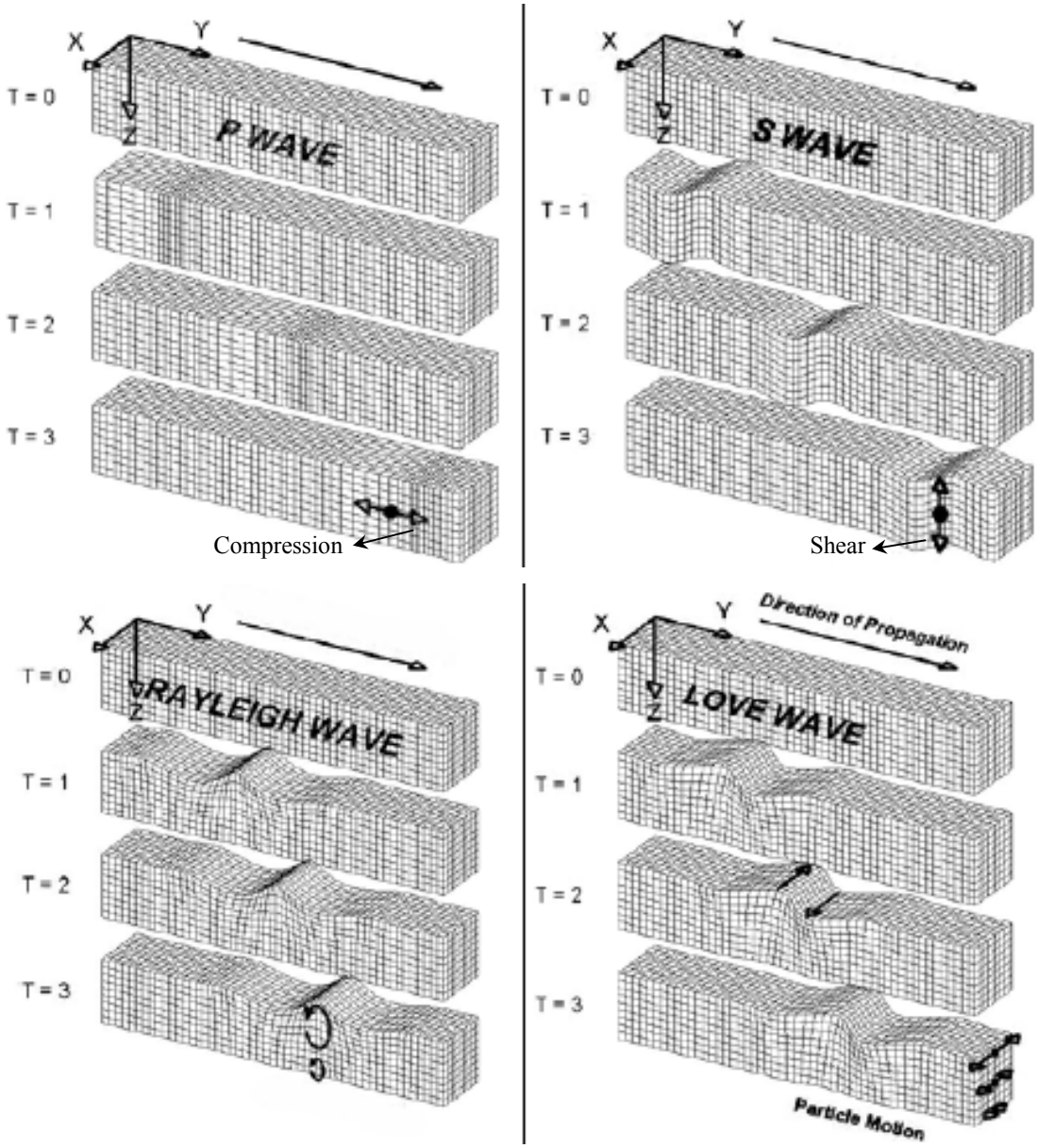

Figure 2.1: Propagation of body waves: P-waves and S-waves; and propagation of surface waves: Rayleigh waves and Love waves (Strobbia, 2003)

2.2.1 Compression wave (P-wave)

Compression wave is an oscillation mode propagating away from the source by successive compressive and dilative motions. It is also called longitudinal waves because it travels with particle motions (elongation and compression) parallel to the direction of propagation, as illustrated in Figure 2.1. Compression waves exist in solid, liquid and gas because the three substances can provide resistance forces to prevent the particles from being compressed and dilated. In solids, this force is attributed to the elastic properties of the medium (Young's modulus of elasticity). Compression waves are the fastest among other modes, hence they are also known as primary wave or P-wave.

2.2.2 Shear wave (S-wave)

Because solids also possess shear rigidity, another type of propagation mode is possible, which is known as shear wave. Shear waves propagate with particle motion normal to the direction of propagation, and thus they are also called a transverse waves (Figure 2.1). In contrast to the P-wave propagation, volume of an element does not change during the S-wave propagation. Since shear waves travel at a lower speed than P-waves, they are also called secondary waves or S-waves.

Wave velocity (group velocity)

Wave velocity is the speed of a wave propagating in a medium. It is indicative of material properties, such as stiffness, elasticity and density. Each material permits a distinct velocity of a wave. Measurement of wave velocity is, thus, a major step in material characterization using wave-based methods.

Factors affecting velocity

A wave travels at a characteristic velocity in a given medium. It travels fastest in solids, slower in liquids, and slowest in gases. The wave velocity is governed by two dominant factors which are the density and the elasticity of the material. This principle can be explained logically using a ball and a spring (Hellier et al., 2001). The ball represents a particle making up the material, and so its weight represents the material density. These balls are held together by springs which represent the elasticity or stiffness of the material.

For balls of given weight, stronger springs are faster to transmit the motion. Likewise, for springs of given strength, balls of lighter weight will take up the vibration faster. Thus, wave velocity is directly proportional to material elasticity and inversely proportional to material density. For a given material, P-wave velocity is controlled by the Young's modulus, while S-wave velocity is controlled by the shear modulus. Because the Young's modulus is higher than the shear modulus for a given material, P-waves always travel faster than S-waves.

In addition to density and elasticity, there is another factor affecting velocity, known as Poisson's ratio. The Poisson's ratio (ν) is expressed as:

$$\nu = -\frac{\varepsilon_{transverse}}{\varepsilon_{longitudinal}} \tag{2.1}$$

where $\varepsilon_{transverse}$ is the transverse contraction strain of a material being stretched and $\varepsilon_{longitudinal}$ is the longitudinal extension strain. When a material is stretched, it contracts in the cross section as illustrated in Figure 2.2. Any contraction displacement is considered negative, while the extension displacement is considered positive. There is a minus sign in front of the Poisson's ratio expression, thus resulting in a positive Poisson's ratio for normal materials. The Poisson's ratio of elastic materials falls between 0 (compressible materials) and 0.5 (incompressible materials). The Poisson's ratio that exceeds 0.5 represents a material dilated under loading.

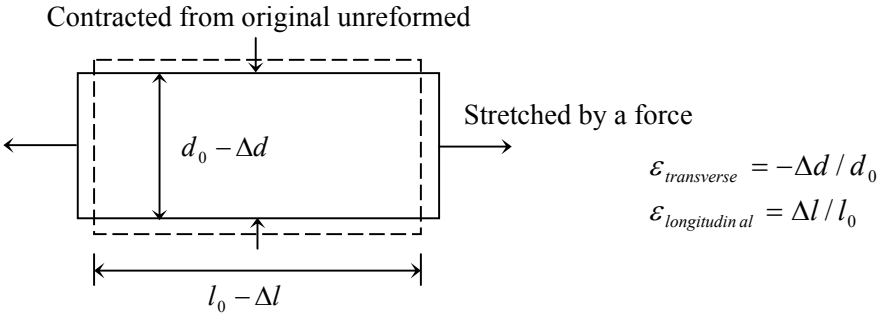

Figure 2.2: Poisson's ratio concept (length l_0 and diameter d_0 are initial dimensions.)

Wave equations

Wave propagation in isotropic infinite elastic solid satisfies Newton's second law (force is a product of mass and acceleration). The acceleration and force can be represented by partial derivatives of displacement and stress respectively. In the Cartesian coordinate system x(x_1, x_2, x_3) as shown in Figure 2.3, the following three equations are obtained (Buirks, 1991).

$$\rho \frac{\partial^2 u_1}{\partial t^2} = \frac{\partial \sigma_{11}}{\partial x_1} + \frac{\partial \sigma_{12}}{\partial x_2} + \frac{\partial \sigma_{13}}{\partial x_3} \tag{2.2}$$

$$\rho \frac{\partial^2 u_2}{\partial t^2} = \frac{\partial \sigma_{21}}{\partial x_1} + \frac{\partial \sigma_{22}}{\partial x_2} + \frac{\partial \sigma_{23}}{\partial x_3} \tag{2.3}$$

$$\rho \frac{\partial^2 u_3}{\partial t^2} = \frac{\partial \sigma_{31}}{\partial x_1} + \frac{\partial \sigma_{32}}{\partial x_2} + \frac{\partial \sigma_{33}}{\partial x_3} \tag{2.4}$$

where u(u_1, u_2, u_3) are the displacements of a point in the three coordinates x(x_1, x_2, x_3) respectively, t is time, and σ_{11}, σ_{12},… σ_{33} are stress components on the cube (Figure 2.3).

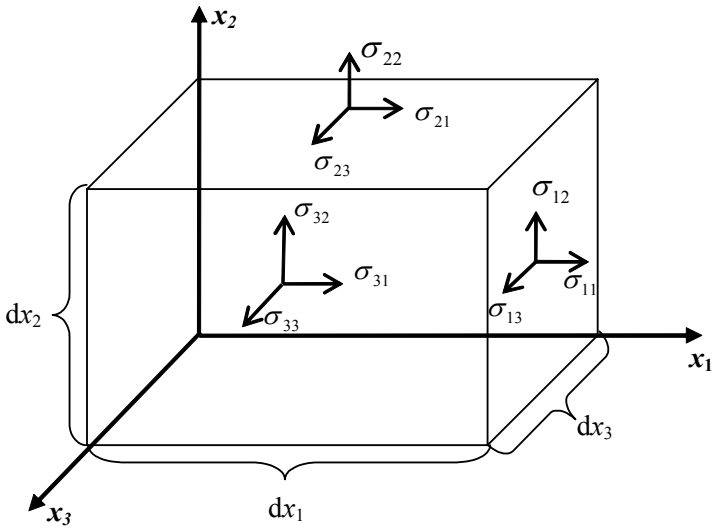

Figure 2.3: An element in an elastic, isotropic, and homogeneous solid

Hook's law states that the stresses acting on an elementary volume can be expressed as a linear combination of strains. As results, the stress components in Equation 2.2 to 2.4 can be rewritten in terms of strain and elastic constants as:

$$\sigma_{11} = \lambda\Delta + 2\mu\varepsilon_{11} \qquad \sigma_{22} = \lambda\Delta + 2\mu\varepsilon_{22} \qquad \sigma_{33} = \lambda\Delta + 2\mu\varepsilon_{33} \tag{2.5}$$

$$\sigma_{12} = \mu\varepsilon_{12} \qquad \sigma_{23} = \mu\varepsilon_{23} \qquad \sigma_{13} = \mu\varepsilon_{13} \tag{2.6}$$

where λ is the Lamé's elastic constant, μ is the shear modulus, and $\Delta = \varepsilon_{11} + \varepsilon_{22} + \varepsilon_{33}$ the change in volume of the element. Based on strain-displacement relationship, the six components of strain are given by:

$$\varepsilon_{11} = \frac{\partial u_1}{\partial x_1} \qquad \varepsilon_{22} = \frac{\partial u_2}{\partial x_2} \qquad \varepsilon_{33} = \frac{\partial u_3}{\partial x_3} \tag{2.7}$$

$$\varepsilon_{12} = \frac{\partial u_1}{\partial x_2} + \frac{\partial u_2}{\partial x_1} \qquad \varepsilon_{23} = \frac{\partial u_2}{\partial x_3} + \frac{\partial u_3}{\partial x_2} \qquad \varepsilon_{13} = \frac{\partial u_1}{\partial x_3} + \frac{\partial u_3}{\partial x_1} \tag{2.8}$$

According to the Equations 2.5 to 2.8, the wave Equations 2.2 to 2.4 can be rewritten by using displacements as:

$$\rho\frac{\partial^2 u_1}{\partial t^2} = (\lambda+\mu)\frac{\partial}{\partial x_1}\left(\frac{\partial u_1}{\partial x_1} + \frac{\partial u_2}{\partial x_2} + \frac{\partial u_3}{\partial x_3}\right) + \mu\nabla^2 u_1 \tag{2.9}$$

$$\rho\frac{\partial^2 u_2}{\partial t^2} = (\lambda+\mu)\frac{\partial}{\partial x_2}\left(\frac{\partial u_1}{\partial x_1} + \frac{\partial u_2}{\partial x_2} + \frac{\partial u_3}{\partial x_3}\right) + \mu\nabla^2 u_2 \tag{2.10}$$

$$\rho\frac{\partial^2 u_3}{\partial t^2} = (\lambda+\mu)\frac{\partial}{\partial x_3}\left(\frac{\partial u_1}{\partial x_1} + \frac{\partial u_2}{\partial x_2} + \frac{\partial u_3}{\partial x_3}\right) + \mu\nabla^2 u_3 \tag{2.11}$$

Equations 2.9 to 2.11 are the most general form of the wave equation and are known as the displacement equations of motion. These equations can be reduced to a vector form as:

$$\rho \frac{\partial^2 \mathrm{u}}{\partial t^2} = (\lambda + \mu)\nabla(\nabla \cdot \mathrm{u}) + \mu \nabla^2 \mathrm{u} \tag{2.12}$$

where ∇ is the vector operator

$$\nabla = \left(\frac{\partial}{\partial x_1}, \frac{\partial}{\partial x_2}, \frac{\partial}{\partial x_3} \right) \tag{2.13}$$

And ∇^2 is the scalar operator

$$\nabla^2 = \left(\frac{\partial^2}{\partial x_1^2} + \frac{\partial^2}{\partial x_2^2} + \frac{\partial^2}{\partial x_3^2} \right) \tag{2.14}$$

The Lamé's elastic constant and shear modulus can be expressed in terms of Young's modulus (E) and Poisson's ratio (v) as:

$$\lambda = \frac{E\,v}{(1+v)(1-2v)} \tag{2.15}$$

$$\mu = \frac{E}{2(1+v)} \tag{2.16}$$

Because solving the Equation 2.12 is difficult, it is necessary to assume a form of solution. Based on the assumption that the wavefront is an infinite plane normal to the traveling direction, a solution is obtained as:

$$\mathrm{u} = Ae^{i(kx_1 - \omega x)} + Be^{i(kx_1 + \omega x)} \tag{2.17}$$

where k is the wave number which is a ratio of 2π to wave length; ω represents the angular frequency; the term $Ae^{i(kx_1-\omega x)}$ represents a wave traveling in the positive x_1 direction with amplitude A; and $Be^{i(kx_1+\omega x)}$ represents a wave traveling in the opposite direction with amplitude B. By differentiating Equation 2.17 and substituting into Equation 2.12, two possible solutions are obtained:

$$\alpha = \sqrt{\frac{\lambda + 2\mu}{\rho}} \tag{2.18}$$

$$\beta = \sqrt{\frac{\mu}{\rho}} \tag{2.19}$$

Substitution of Equations 2.15 and 2.16 into these two solutions respectably yields the following expressions:

$$\sqrt{\frac{\lambda + 2\mu}{\rho}} = \sqrt{\frac{E(1-\nu)}{\rho(1+\nu)(1-2\nu)}} = V_P \tag{2.20}$$

$$\sqrt{\frac{\mu}{\rho}} = \sqrt{\frac{E}{2\rho(1+\nu)}} = V_S \tag{2.21}$$

Equations 2.20 and 2.21 are known as the velocity of compression waves (V_P) and the velocity of shear waves (V_S) in an infinite elastic isotropic medium. Equations 2.20 and 2.21 are often used in ultrasonic testing to characterize material properties, E and ν, from the measured wave velocity and density of the material. This will be discussed in detail in Chapter 3.

2.2.3 Lamb waves

In a slab, P-wave and S-waves interact with two parallel boundary surfaces generating Lamb waves. This phenomenon was first studied by Lamb (1917). He proposed two types of waves that are able to exist in a plate; one is symmetric mode (also known as longitudinal or extensional), and the other anti-symmetric (also called flexural or bending). Later, it was found that the Lamb wave motion followed a Rayleigh-Lamb-frequency equation (Viktorov, 1967):

$$\frac{\tanh(\beta h)}{\tanh(\alpha h)} = \left[\frac{4\alpha\beta k^2}{(k^2+\beta^2)} \right]^{\pm 1} \tag{2.22}$$

where $\alpha^2 = k^2 - (\omega / V_P)^2$ and $\beta^2 = k^2 - (\omega / V_S)^2$, V_P and V_S are the P-wave and S-wave velocities, h is half the thickness of the plate, ω is the circular frequency, and k is the wave number. The exponents +1 and -1 represent the solutions for symmetric and anti-symmetric lamb modes, respectively (Viktorov, 1967; Krautkramer and Krautkramer, 1990; Graff, 1991). Each mode has a characteristic dispersion curve. By using MathCAD®, an example of lamb mode dispersion curves in a HMA slab was obtained, as shown in Figure 2.4. Fundamental Lamb modes are present at frequencies below 40 kHz and behave analogous to Rayleigh wave modes for frequencies higher than 40 kHz.

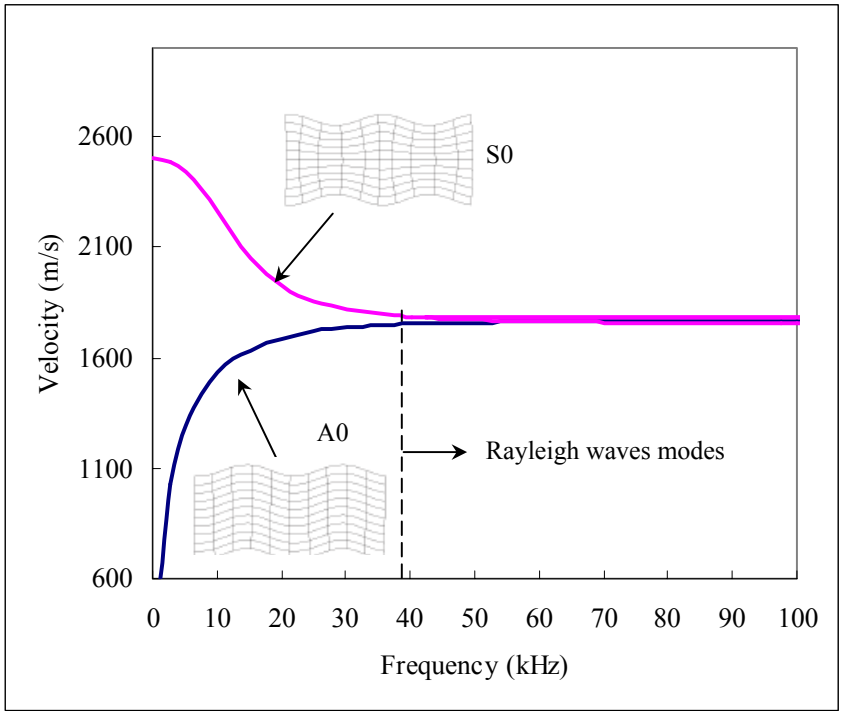

Figure 2.4: Dispersion curves of two Lamb wave modes for a HMA slab (80mm thickness, V_P = 3913m/s, V_P = 1830m/s) (S0: Symmetric fundamental mode; A0: Anti-symmetric fundamental mode)

2.2.4 Rayleigh wave (R-wave)

A surface wave is usually referred to as Rayleigh waves (R-wave). Rayleigh waves were first studied by John William Strutt, Lord Rayleigh (1885). They travel along the surface with the particle motion in a form of retrograde ellipse with the major axis of the ellipse perpendicular to the direction of propagation (Figure 2.1). This particle motion results from the combined effect of its vertical and horizontal displacements as shown in Figure 2.5 (Richart et al., 1970). The particle motion exhibits exponential decrease as increasing depth. R-waves penetrate to a shallow depth of approximately one wavelength. However, a penetration depth of roughly one-third their wavelength has been measured to be effective for material characterization (Stokoe and Nazarian 1983; Hevin, 1998). This is because its amplitude of motion experiences exponential attenuation with depth. At a depth of approximately one and a half times the wavelength, the vertical amplitude

reduces to approximately 10% of the original amplitude at the surface of the medium (Baker et al., 1995).

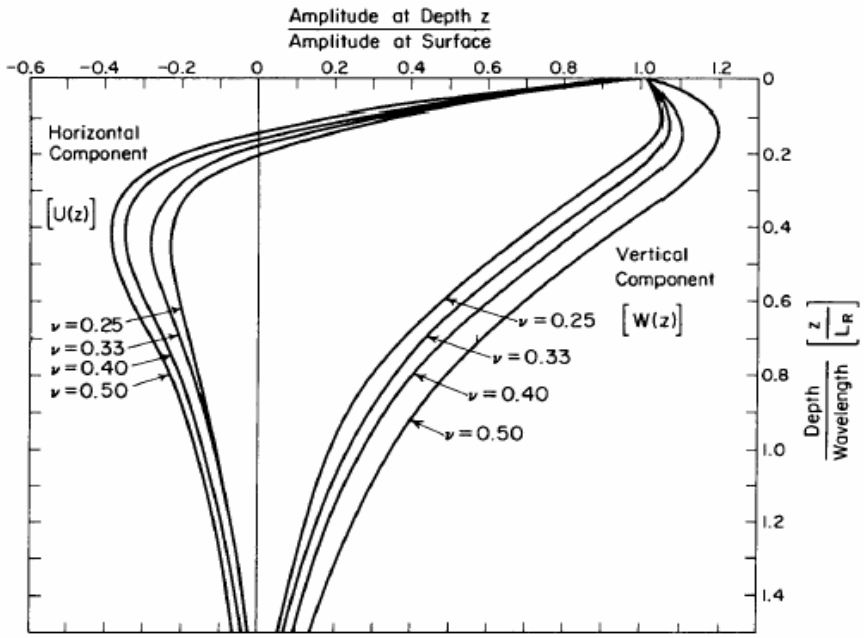

Figure 2.5: R-wave horizontal and vertical displacements with normalized depth (Richart et al., 1970)

In a homogeneous half-space, R-wave velocity (V_R) is constant and is independent of frequency (Nazarian et al., 1984). Thus, each frequency (f) is corresponding to a certain wavelength (L_R) through the relationship:

$$V_R = fL_R \tag{2.23}$$

However, in a layered medium with different material properties at different depths, R-wave velocity varies with wavelength (or frequency). The phenomenon associated with different wavelengths propagating at different velocities is known as dispersion. Short wavelengths (or high frequencies) sample the near surface, and the wave velocity depends on the surface material only. Long wavelengths (or low frequencies) allow for deeper investigations, and the wave velocity is strongly affected by the material

properties of the layers involved. The dispersion phenomenon is utilized in spectral analysis of surface waves (SASW) technique to evaluate elastic moduli and layer thickness of layered systems, such as pavement.

In a homogeneous medium, the R-wave velocity (V_R) is related to S-wave velocity (V_s) through the ratio of S-wave velocity to P-wave velocity (V_S/V_P) as:

$$-4s^2\sqrt{s^2-n^2}\sqrt{s^2-1}+(1-2s^2)^2=0 \qquad (2.24)$$

where s is the ratio V_S/V_R and n is V_S/V_P.

A solution to this equation indicating the R-wave velocity was found by Lord Rayleigh (1885). According to the equation, the R-wave velocity is nearly 10 percent slower than the S-wave velocity. Later, the relationship between V_R and V_s can be approximated in terms of Poisson's ratio (Achenbach, 1973):

$$V_R=\frac{0.862+1.14\nu}{1+\nu}V_S \qquad (2.25)$$

Although the V_R/V_s ratio is in direct proportion to the Poisson's ratio, the variation of this velocity ratio is not significant. Since the Poisson's ratio falls between 0 and 0.5 which gives V_R = 0.86 to 0.95V_S according to Equation 2.25. Thus, for practical purposes, the equation $V_R = 0.9V_s$ has less than 5 percent error (Nazarian et al., 1999).

2.2.5 Love wave (L-wave)

Love waves were first mathematically studied by A.E.H. Love (1911). They are the fastest surface waves. Love waves are confined to a horizontal plane with the particle motion perpendicular to the direction of propagation (Figure 2.1). However, this type of surface wave cannot be generated unless low-velocity layers overlie higher-velocity layers, because the waves are generated by total multiple reflections between the top and

bottom surfaces of the low-velocity layer. Therefore, Love waves do not exist in pavements (Baker et al., 1995).

Figure 2.6 illustrates the propagation of body and surface waves away from an impulse source at the surface of a homogenous half-space. Approximately 67 percent of the introduced energy from the source is carried by Rayleigh waves (Miller et al., 1955; Richard et at., 1970). Of the remaining energy, 26 percent propagates as compression waves and 7 percent as shear waves. Thus, larger amplitudes are found in Rayleigh waves than in body waves on the surface.

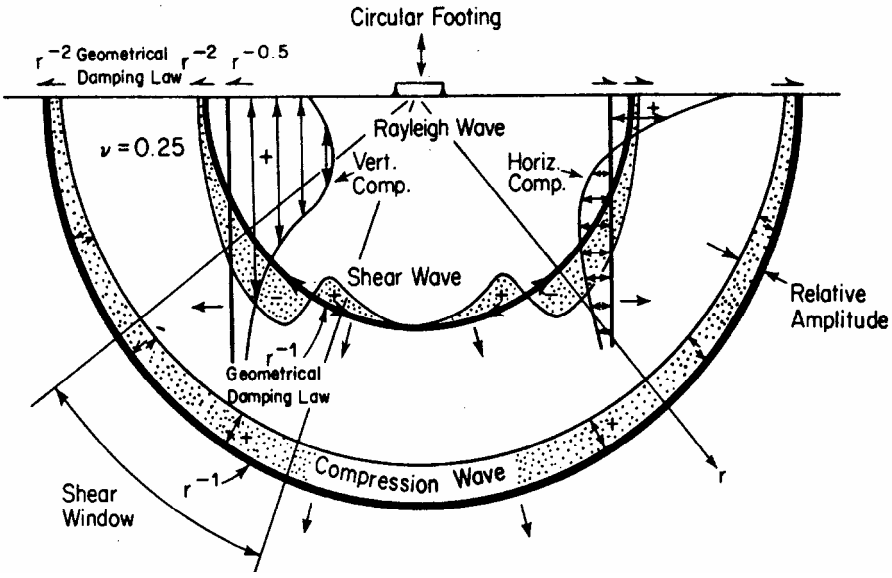

Figure 2.6: Distribution of seismic waves from a circular footing on a homogeneous, isotropic, elastic half-space (Richard et al., 1970)

2.3 Physical Phenomena of Wave Propagation

Wave-based methods are analytical methods used to nondestructively evaluate material properties. The theoretical stresses and displacements are analyzed to predict the long-term structural performance. Because of the complex nature of seismic wave propagation in civil engineering constructions, most analytical models assume that there are no additional boundaries or interfaces in a layered half-space where seismic waves propagate (Sheu at al., 1988). In other words, reflected waves from discontinuities such as edges, joints, or cracks, although known to occur in pavements, are not included in the analytical models. However, the existence of these reflected waves in a real system is inevitable. Thus, it is essential to investigate their impact on test results so that an appropriate approach adjusting the test procedure can be developed to minimize the adverse effect of the reflections.

Wave-based NDT methods basically consists of three steps: (1) send an impulse into a medium being investigated; (2) observe and record the signals from the medium by appropriate devices; and (3) extract information about the unknown properties of the medium by analyzing the signals. These methods are based on monitoring the propagation of different types of waves interacting with a volume of material between the transducers. The waves are modified by the material morphology and parameters including elasticity, density, texture, and boundary conditions (e.g. surfaces, edges, curvatures) (Vary A., 1991). For example, the most widely used Impact Echo (IE) technique is based on measurement of reflection and refraction of body waves, while the spectral analysis of surface waves (SASW) method is based on the dispersion properties of surface waves in a layered medium. Therefore, a good understanding of wave propagation in a layered medium is essential.

2.3.1 Acoustic impedance of materials

When a traveling wave strikes a boundary between two different media 1 and 2, a portion of the incident wave in media 1 is reflected back and the remainder is transmitted through media 2. The amounts of wave energy transmitted and reflected are governed by the acoustic properties of the two media. For each material, the reflectivity at an interface can

be quantified by a factor, known as "acoustic impedance" (Z), given by the product of density (ρ) and velocity (V) of ultrasound for that material as follows (Krautkramer and Krautkramer, 1990; Hellier et al., 2001):

$$Z = \rho \cdot V \tag{2.26}$$

Typical acoustic impedance values for various construction materials are listed in Table 1 (Garbacz, 2003). The transmission coefficient for normal incidence at an interface between two materials 1 and 2 is defined by (Kramer, 1996):

$$TC = \frac{2}{1 + \frac{Z_1}{Z_2}} \tag{2.27}$$

where Z_1 and Z_2 represent the acoustic impedance of the media 1 and 2 respectively.

Table 1: Acoustic impedance of common construction materials (Garbacz, 2003)

Material	Acoustic impedance (kg/m^2s)
Air	$4.1 \cdot 10^{-1}$
Water	$1.5 \cdot 10^{6}$
Soil	$(1 \text{ to } 3) \cdot 10^{6}$
Bitumen	$1 \cdot 10^{6}$
Asphalt	$5 \cdot 10^{6}$
Concrete	$(8 \text{ to } 10) \cdot 10^{6}$
Granite	$(15 \text{ to } 17) \cdot 10^{6}$
Steel	$4.6 \cdot 10^{7}$

2.3.2 Reflection

When a wave is introduced obliquely to an interface, part of the wave energy is reflected and the other transmitted (refracted). The directions of the waves reflected follow the general law stating that the angles of incidence (θ_i) and reflection (θ_r) are identical for a same type of wave in the same material, as shown in Figure 2.7 (Krautkramer and Krautkramer, 1990; Hellier et al., 2001). This law is known as Snell's law.

As described in the previous section, the reflectivity at an interface is governed by the acoustic impedance values of the materials separated by the interface. If on one side there is metal and on the other air, the reflection is nearly 100% because the acoustic impedance of metal is significantly larger than that of air (Table 1). Even at a metal-to-water interface, most of the energy will be reflected for the same reason. Interfaces inside an object can be its grain boundaries and discontinuities (e.g. cracks and voids). Interpretation of the waves reflected from these interfaces enables determination of the microstructural properties of the object.

2.3.3 Refraction

When an oblique wave encounters an interface between two different materials, part of the wave energy passes through and propagates in a new direction. This phenomenon is known as refraction. The angle of refraction is related to the angle of incidence and to the wave velocities of the two materials through Snell's law (Figure 2.7):

$$\frac{\sin\theta_i}{V_1} = \frac{\sin\theta_R}{V_2} \tag{2.28}$$

where θ_i° is the angle of incidence, θ_R° is the angle of refraction, V_1 and V_2 are the wave velocities in media 1 and 2 respectively.

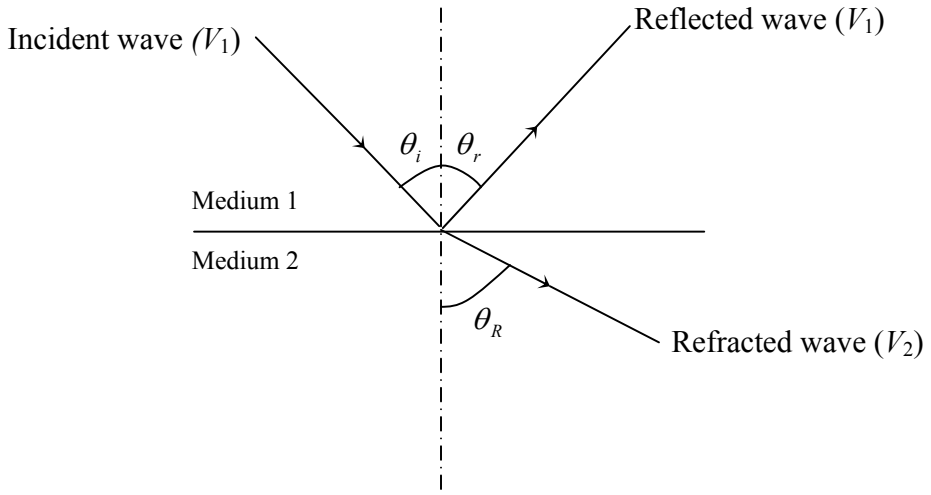

Figure 2.7: Snell's law for wave reflection and refraction (Hellier et al., 2001)

2.3.4 Mode conversion

When waves propagate from one medium to another, mode conversion occurs at the interface. Mode conversion is defined as the transformation of one wave type into another. For example, if a longitudinal wave obliquely strikes a plane interface, it can start a particle vibration in two directions: longitudinal and transverse. These two directions of vibration produce longitudinal (P) and transverse waves (S) at the vicinity of the interface. As a result, reflection and refraction of these two types of waves can occur, as illustrated in Figure 2.8.

The velocities and directions of the waves are governed by Snell's law, expressed as:

$$\frac{\sin\theta_{iP}}{V_{P1}} = \frac{\sin\theta_{rP}}{V_{P1}} = \frac{\sin\theta_{rS}}{V_{S1}} = \frac{\sin\theta_{RP}}{V_{S2}} = \frac{\sin\theta_{RS}}{V_{s2}} \tag{2.29}$$

where V_{P1} and V_{S1} represent the compression and shear wave velocities in medium 1, and V_{P2} and V_{S2} in medium 2. θ_{iP}, θ_{rP}, θ_{rS}, θ_{RP}, and θ_{RS} represent the angles (Figure 2.8). The subscript label *i* indicates incident, r reflection, R refraction, P P-waves, and S S-waves.

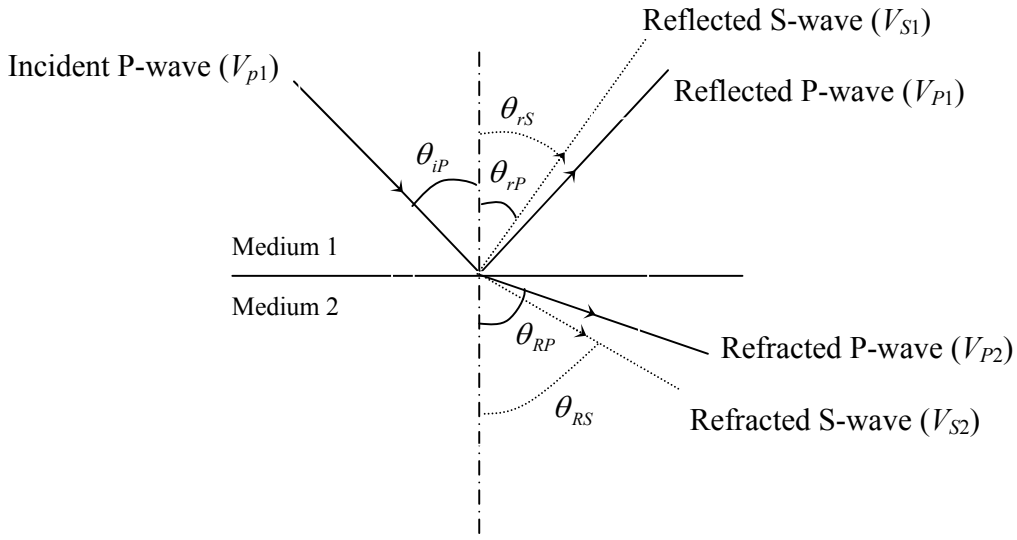

Figure 2.8: Mode conversion concept (Hellier et al., 2001)

Mode conversion can also arise when an oblique shear wave strikes an interface. The reflected angle of shear wave is again equal to the incident angle. In addition, a mode converted compression wave develops at the interface and is reflected at an angle determined by Snell's law.

The complex mode conversion phenomenon enables different types of waves to propagate at different velocities and in different directions. This phenomenon can cause uncertainty in wave analysis and signal interpretation. The solution of increasing the angle of incidence to eliminate the adverse effect has been used since 1947 (Hellier et al., 2001).

2.3.5 Superposition of waves

Waves traveling along the same path tend to overlap each other to produce a new wave. Their amplitudes corresponding to the same position of arrival are added. The sum reaches its maximum when there is no phase difference (Figure 2.9a), and gives its minimum when there is a π phase difference (Figure 2.9c). Figure 2.9b shows that superposition of two identical signals with phase differences between π/2 and zero produces amplitude between zero and double.

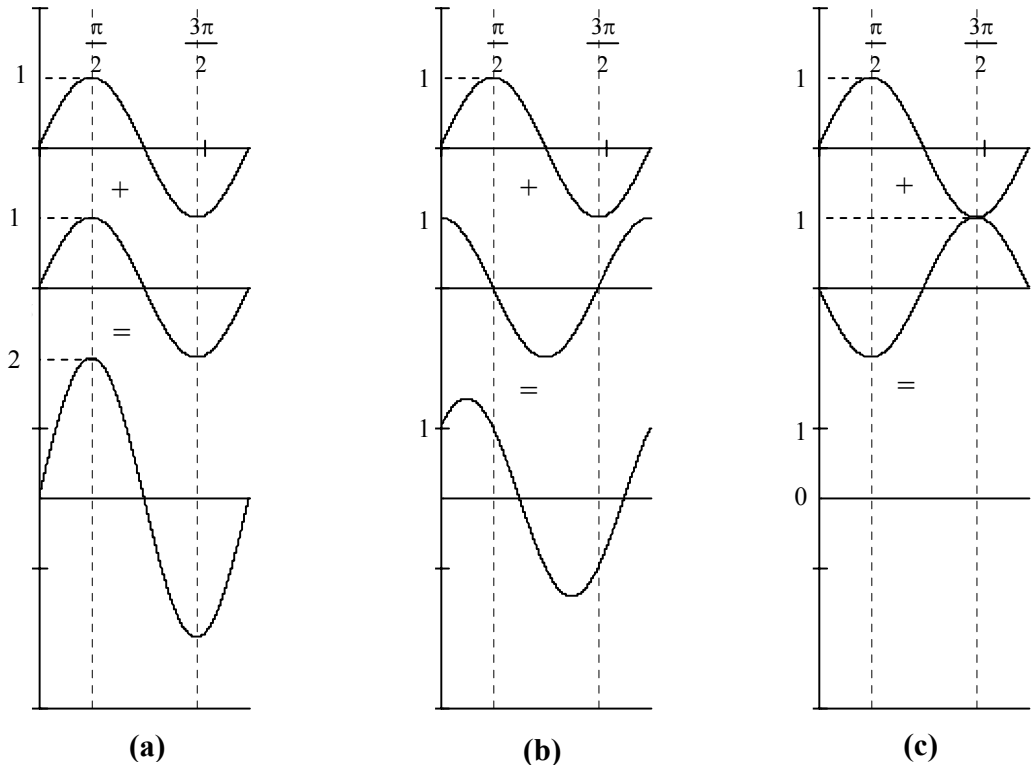

Figure 2.9: Superposition of two signals with identical amplitude – (a) identical in phase, (b) with π/2 phase difference, and (c) with π phase difference.

Stacking (averaging) can be described as another example of wave combination used to reduce noise in signals. In the operation, a series of signal traces are captured individually; and then the signal elements in the different traces are added and averaged to obtain a single average signal. Since noise is assumed to have a zero mean, the random noise component would be canceled out by algebraically adding multiple received traces

2.4 Wave Attenuation

Attenuation is the gradual loss of wave energy as a function of time and distance. It has been observed to be dependent on the porosity of materials (Generazio et al., 1988; Winkler and Murphy 1995), grain size (Winkler, 1983; Prasad and Meissner, 1992), and saturation levels (Tittmann et al., 1980; Prasad and Meissner, 1992; Velea et al., 2000). Thus, evaluation of attenuation enables characterization of the microstructural properties of a material.

Attenuation occurs as a result of three basic causes (Blitz and Simpson, 1996; Owino and Jacobs, 1999):

- deviation of energy from the parallel wave beam by reflection, refraction, mode conversion, and scattering;
- absorption, a conversion of part of the wave energy into heat; and
- wavefront spread.

As described in the foregoing section, wave reflection, refraction and mode conversion are caused by discontinuities within the object under test. Combination of scattering and absorption is called material attenuation (Krautkramer and Krautkramer, 1990; Owino and Jacobs, 1999). Wavefront spread leads to loss of wave energy in the far field, referred to as geometric attenuation.

2.4.1 Material attenuation

Material attenuation consists of scattering and absorption (Krautkramer and Krautkramer, 1990; Owino and Jacobs, 1999). Scattering losses depend on the acoustic impedance change at the interfaces (or scatterers), as well as on the number, distribution and sizes of these scatterers in an inhomogeneous material. Attenuation induced by scattering can be described in term of the transmission coefficient (TC) for a wave incident normally at an interface (Kramer, 1996):

$$\frac{A_2}{A_1} = TC \tag{2.30}$$

where A_1 and A_2 represent the wave amplitudes in media 1 and 2 separated by the interface; *TC* is the transmission coefficient (Equation 2.27).

Absorption losses are associated with intrinsic dissipation by the relative motions at the particles and interfaces. Absorption decreases the wave amplitude exponentially as a function of distance, expressed as (Aki and Richards, 1990):

$$A_2 = A_1 \cdot e^{-\alpha \cdot (x_2 - x_1)} \tag{2.31}$$

where α is the absorption coefficient of the material and has units of neper/m; A_1 and A_2 represent the wave amplitudes at distances x_1 and x_2 from the acoustic source respectively. The absorption coefficient (α) is a measure of the fractional loss of energy per unit distance and depends on the type of material. The absorption coefficient increases with frequency, thus high frequencies (small wavelengths) attenuate faster than low frequencies. Wave amplitude also decreases because of reflection, refraction, mode conversions, and diffraction at interfaces and anomalies.

Alternatively, material attenuation can be quantified by damping ratio. Damping ratio (D) is a measure of amplitude reduction per cycle of oscillation, and it is defined as:

$$D = \frac{V_R}{2\pi f \Delta x} \ln\left(\frac{A_1}{A_2}\right) \tag{2.32}$$

where V_R is the Rayleigh wave velocity, f frequency, Δx the distance between the two measurements, and A signal amplitude, while the subscripts denote the receiver locations. The calculation of damping ratio will be discussed in more detail in Chapter 6.

Scattering

The phenomenon of reflection becomes very complicated in inhomogeneous materials containing grain boundaries which are randomly oriented to the wave beam. In addition, there is a significant acoustic impedance contrast at these boundaries because the materials that meet at these interfaces are different in density and wave velocity. As a result, the wave is reflected in random directions, which is known as scattering. In a material with very fine grains, waves can pass through with less scattering. However, when the grain sizes are comparable to the wavelength, the scatter can be significant. For example in asphalt concrete mixtures, scattering of waves higher than 100kHz is significant because of the effects of aggregates and the presence of discontinuities such as cracks, laminations and air voids. Asphalt concrete mixtures are composed of a complex network of aggregates held with asphalt binder, considering a typical acoustic speed of 4000 m/s. The boundaries of these aggregates are randomly oriented to the wave beam. In addition, the aggregates may have a diameter up to 25mm. When the wavelength is comparable to the size of the aggregates, the waves will be reflected in random directions (scattered) from these interfaces. The dependence on the grain dimension also allows for the estimation of grain size from attenuation analysis (Krautkramer and Krautkramer, 1990; Hellier et al., 2001).

Discontinuities in an asphalt concrete are mostly in the form of air voids and cracks. The percentage and size of air voids in a given asphalt concrete mixture vary with compaction levels. For a wave incident at an aggregate-to-air interface, the reflection is almost 100% because of the extreme impedance mismatch between air and aggregate. In the case of discontinuities filled with water, such as water-filled cracks, up to approximately 60% of the energy can be reflected dependant on the type of asphalt concrete mixture. Reflections will also be affected by the geometry of the discontinuities (Gallan, 1990). For example, the reflections at a smooth interface are quit uniform, while at an irregular interface, the reflections can be completely scattered. As the wavelength increases to an extent from 100 to 1000 times the scatterer dimensions, the effect of scattering may become insignificant which appears as reduction in attenuation (Huntingdon, 1940).

Absorption

Absorption is referred to as the part wave energy directly converted into heat. Absorption of ultrasound in solids is attributable to a number of causes. Wave propagation in a solid is based on the particle oscillation. The relative motion of these particles causes friction and absorbs some of the energy. In general, a slow oscillation (low frequency) causes less energy loss than does a rapid oscillation (high frequency), and therefore low frequency is able to penetrate deeper into the material. Both absorption and scattering increase with frequency, but absorption increases at a slower rate (Krautkramer and Krautkramer, 1990).

Absorption may also be caused by the presence of microstructural flaws in a material. These small details may absorb some of the wave energy transmitted through the material. Their existence can adversely affect the rigidity and elasticity of the material (Blitz and Simpson, 1996).

2.4.2 Geometric attenuation

As a wave propagates away from its source, the wavefront spreads out over an increasing area. This behavior leads to a decay in the wave amplitude, known as geometric attenuation. Geometric attenuation is based on the principle of energy conservation stating that the energy remains constant in the wavefront, irrespective of distance. Since the energy is distributed on an increasing wavefront surface. With geometric attenuation, the ratio of two amplitudes at distances x_1 and x_2 obeys the relation:

$$\frac{A_2}{A_1} = \left(\frac{x_1}{x_2} \right)^{-\beta} \tag{2.33}$$

where the exponent β is the geometric attenuation coefficient governed by the shape of wavefront. Rayleigh waves propagate away from the source with cylindrical wavefronts, for which β is equal to 0.5 (Figure 2.6); the amplitude decreases in proportion to the square root of the distance from the source. Body waves propagate with spherical

wavefronts, for which β is equal to 1.0 (Figure 2.6); the amplitude decreases in proportion to the distance. However, as shown in Figure 2.6, because body wave energy leaks into the free space (Richard et al., 1970), the body waves at the free surface exhibit a decrease of amplitude proportional to the square of distance (β = 2 at the surface). An impact on the surface imparts most of its energy (approximately 67%) as surface waves. Therefore, Rayleigh waves are virtually dominant events at great distance from the source.

When comparing geometric attenuation and material attenuation, both types increase with propagation distance from the source. However, material attenuation is smaller than geometric attenuation, and it can be as low as one percent of the decay caused by geometric spreading in a spherical wavefront (Aki and Richards, 1990). The combination of geometric and material attenuations can be described as:

$$\frac{A_2}{A_1} = \left(\frac{x_1}{x_2} \right)^{-\beta} e^{-\alpha \cdot (x_2 - x_1)} \tag{2.34}$$

2.5 Summary

This chapter provides a review of seismic wave theory, including body waves (P and S-waves) and surface waves (Rayleigh, Love and Lamb waves). Wave equations have been summarized to describe the concepts of wave velocities for P-waves, S-waves and R-waves. The relationship between wave velocity and material elasticity is introduced. In addition, the physical properties of wave propagation including wave reflection, refraction, mode conversion and superposition are discussed. The mechanics of attenuation is presented. Information from the areas provides the basis for wave analysis and interpretation.

CHAPTER 3
SIGNAL PROCESSING TECHNIQUES

3.1 Introduction

Seismic wave signals measured from nondestructive tests (NDT) are analyzed using different signal processing techniques. In wave-based NDT investigations, surface displacements are commonly recorded in time domain. Time domain analysis is straightforward and the results can be examined visually for preliminary assessment of the medium through which the waves travel. In addition, the analysis in the frequency domain provides information on wave energy and phase distributions as a function of frequency. This chapter provides an overview of several signal processing techniques used in this study.

3.2 Time Domain Analysis

A typical time history of a recorded signal is illustrated in Figure 3.1. The amplitude is referred to as the distance from the mean position of the signal (Figure 3.1). In addition to the variation of the signal amplitude with time, other information includes the first arrival of the signal, subsequent wave reflections, and scatterings. This information permits determination of wave velocities, and hence, depths to reflecting interfaces, medium thickness, as well as the elastic profiles of the medium.

3.2.1 Stacking

The presence of noise in a signal can lead to an inaccurate determination of the arrival time and hence an erroneous estimation of wave velocity. Signal stacking or averaging is a common approach to eliminate random noise in a signal. Stacking is the simple operation of evaluating the average of the signal at every discrete measurement in time. This method works if the noise has zero mean; whereas, the real signal is repeatable and not affected by averaging. The random noise component is canceled out by algebraically adding multiple signals, and thus the real signal measurement is enhanced (signal-to-noise ratio). Stacking of 35 to 100 signals is sufficient to obtain clear measurements (De

Alba and Baldwin, 1991; Nakagawa et al., 1996). Figure 3.2 shows the effect of stacking 8 to 256 signals on the signal quality. After stacking 256 signals, the output signal is more clearly defined and its first arrival is well recognized. Signal stacking requires a repeatable signal. Thus, it is necessary to use ultrasonic transducers of high consistency, and synchronize with the signal the triggering of the recording device to eliminate random time shifting.

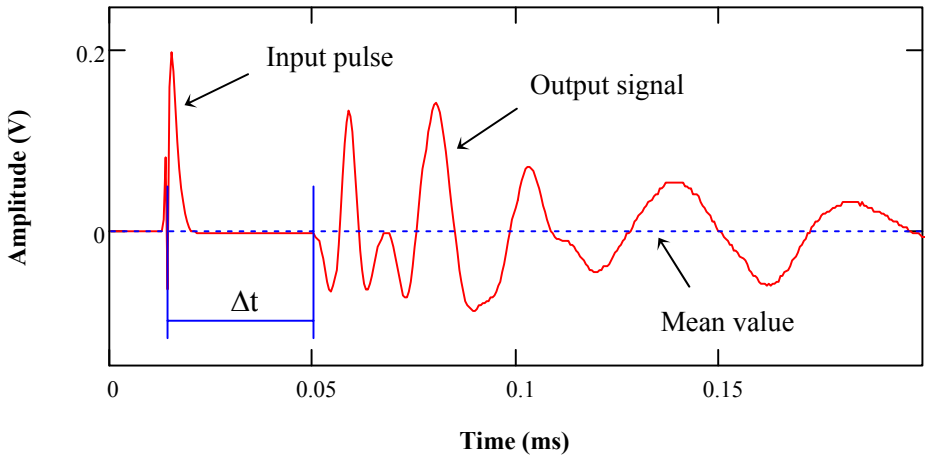

Figure 3.1: Typical input pulse and the output signal in time domain

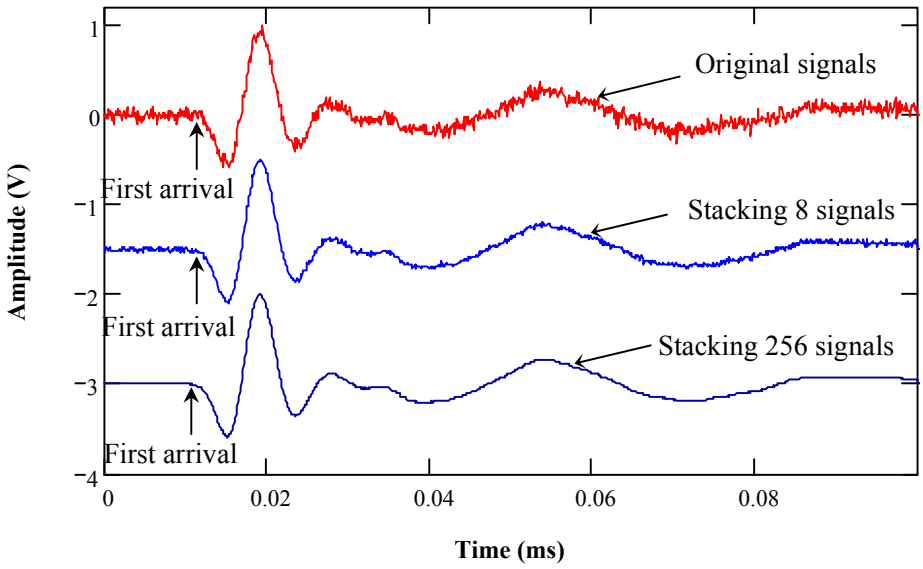

Figure 3.2: Noise control in time domain by signal stacking

3.3 Frequency Domain Analysis

The frequency domain analysis or spectral analysis is a common signal processing technique. A signal is translated from the time domain to the frequency domain by performing the Fourier transform. However, the Fourier transform provides an average of the frequency content over the complete duration of the signal. The evolution of the frequency components over time is not evaluated with the Fourier transform. The following sections describe different techniques such as the short-time Fourier transform and wavelet transform, which are used to estimate the evolution of frequency content as a function of time.

3.3.1 Fourier Transform

Fourier transform is one of the most conventional signal processing tools used by scientists and engineers. By means of Fourier transform, a signal is decomposed into sinusoidal functions of various amplitudes and frequencies. Thus, the signal is represented as a superposition of a series of sine and cosine functions. This representation enables examination of the frequency content of a given time domain signal, as illustrated in Figure 3.3. The Fourier transform of the signal can be reversed back into time domain by performing the inverse Fourier transform. The two transforms are given by the following relationships:

$$X(\omega) = \int_{-\infty}^{\infty} x(t) \cdot e^{-j \cdot \omega \cdot t} dt \tag{3.1}$$

$$x(t) = \frac{1}{2\pi} \int_{-\infty}^{\infty} X(\omega) \cdot e^{j \cdot \omega \cdot t} d\omega \tag{3.2}$$

where ω is angular frequency, t is time, and j denotes the imaginary component of complex numbers. The expression 3.1 is known as the continuous Fourier transform which identifies the similarities between the signal $x(t)$ and complex sinusoidal

functions. The expression 3.2 is called the inverse Fourier transform. The above two formulas can be rewritten as a function of frequency ($\frac{\omega}{2\pi}$) as:

$$X(f) = \int_{-\infty}^{\infty} x(t) \cdot e^{-j \cdot 2\pi f \cdot t} dt \tag{3.3}$$

$$x(t) = \int_{-\infty}^{\infty} X(f) \cdot e^{j \cdot 2\pi f \cdot t} df \tag{3.4}$$

Equations (3.1) to (3.4) are all in continuous form. However, digital signals recorded at discrete points are Fourier transform and inverse Fourier transform using the discrete representation of Equations (3.3) and (3.4) which are given by:

$$X(k \cdot \Delta f) = \Delta t \sum_{n=0}^{N-1} x(n \cdot \Delta t) \cdot e^{-j \cdot \left(k \frac{2\pi}{N} n \right)} \qquad (k = 0, 1 \ldots \text{N-1}) \tag{3.5}$$

$$x(n \cdot \Delta t) = \frac{1}{N \cdot \Delta t} \sum_{k=0}^{N-1} X(k \cdot \Delta f) \cdot e^{j \cdot \left(k \frac{2\pi}{N} n \right)} \qquad (n = 0, 1 \ldots \text{N-1}) \tag{3.6}$$

where N is the total number of sampled points of the time domain signal, k and n are integer counters, Δf is the frequency interval and Δt is the sampling interval in time. Δf is related to Δt through the relationship:

$$\Delta f = \frac{1}{N \cdot \Delta t} \tag{3.7}$$

The discrete Fourier transform of the signal can be represented by a set of complex numbers, expressed as:

$$X(f_n) = \mathrm{Re}[X(f_n)] + j \cdot \mathrm{Im}[X(f_n)] \qquad (n = 0, 1 \ldots \mathrm{N\text{-}1}) \tag{3.8}$$

where $f_n = n \cdot \Delta f$, Re[] and Im[] are the real and imaginary components, respectively. The functions of amplitude ($A(f_n)$) and phase ($\Phi(f_n)$) for each complex number are defined as:

$$A(f_n) = \sqrt{\{\mathrm{Re}[X(f_n)]\}^2 + \{\mathrm{Im}[X(f_n)]\}^2} \tag{3.9}$$

$$\Phi(f_n) = \tan^{-1}\left\{\frac{\mathrm{Im}[X(f_n)]}{\mathrm{Re}[X(f_n)]}\right\} \tag{3.10}$$

Accordingly, a time signal represented by a summation of a series of harmonically related sinusoidal functions can be expressed as:

$$x(t) = A_0 + \sum_{n}^{N-1} A(f_n) \cdot \sin[2\pi f_n t + \Phi(f_n)] \tag{3.11}$$

where $x(t)$ is the time signal function, A_0 is the offset of the signal also called the DC component.

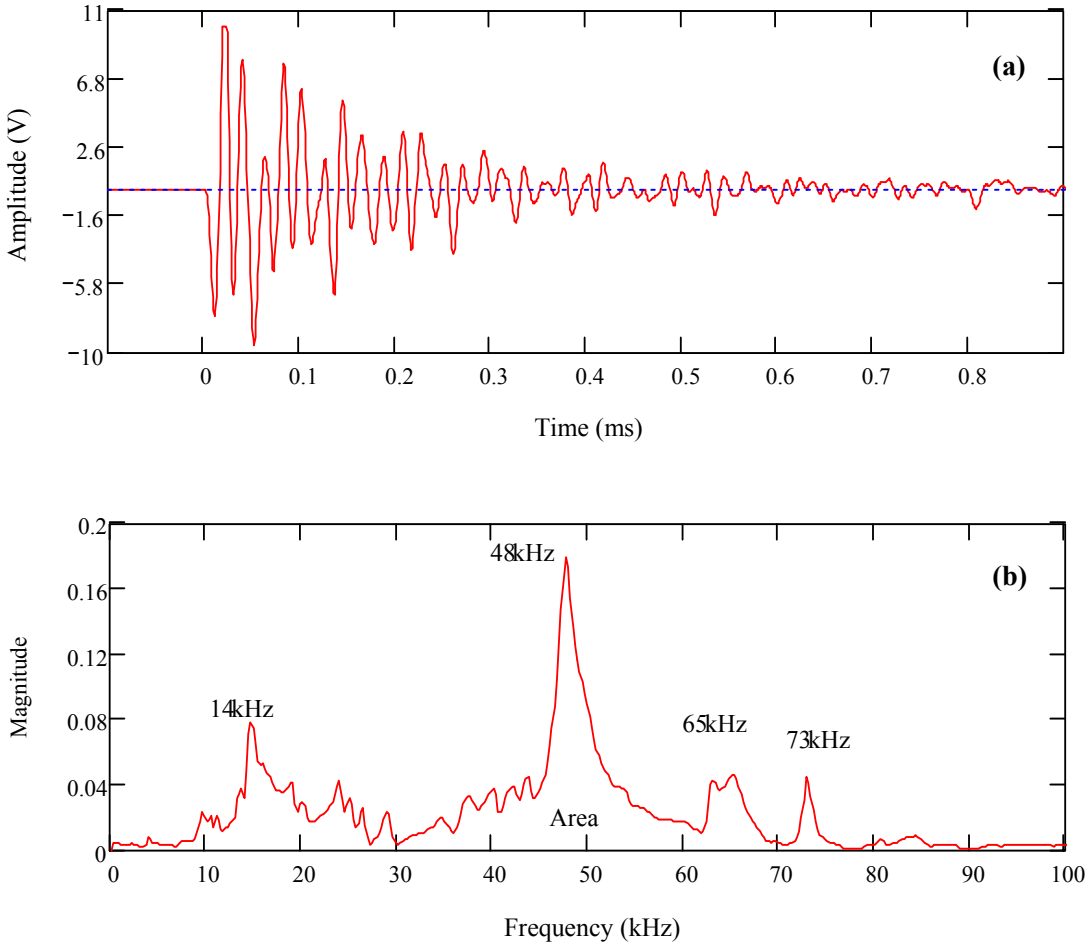

Figure 3.3: (a) Typical time signal and (b) corresponding Fourier transform

The main deficiency of Fourier transform is that it fails to indicate clearly a signal's frequency distribution over time. This deficiency can be overcome by performing a windowed Fourier transform.

Windowing

Windowing consists of isolating a given portion of the signal by multiplying a time window function and then performing Fourier transform on the isolated portion of the signal. There are several types of windows commonly used in signal processing, including rectangular, triangular, Hanning, and Hamming windows (Brook and Wynne,

1991; Baziw, 1993; Porat, 1997). The windowing operation is illustrated in Figure 3.4. The time window function used in this study is given by:

$$w(t,\omega)=\begin{cases}10\left|\cos(\omega\cdot t)^{10}-1\right| & 0\le t\le\dfrac{\pi}{\omega}\\ 0 \quad \text{otherwise}\end{cases} \tag{3.12}$$

where $w(t,\omega)$ represents time window as a function of time t and angular frequency ω that is equal to $2\pi f$.

The windowing technique is capable of reducing signal noise and scattering effects. In addition, it allows the frequency domain analysis of a specific section of the time signal rather than processing of the entire signal at once.

A parameter known as the peak-to-peak (PTP) amplitude of the first arrival is also identified (Figure 3.4). It measures the difference between the positive and the negative peak values of the first arrival of the signal. The PTP amplitude is indicative of wave energy. The maximum spectral amplitude and area of the frequency spectrum are also used as indicators of wave energy. The maximum spectral amplitude represents the peak value of the frequency spectrum, while the spectrum area (A_S) can be mathematically expressed as:

$$A_S=\int_0^{+\infty} FW(f)df \tag{3.13}$$

where $FW(f)$ is the Fourier representation of the windowed signal.

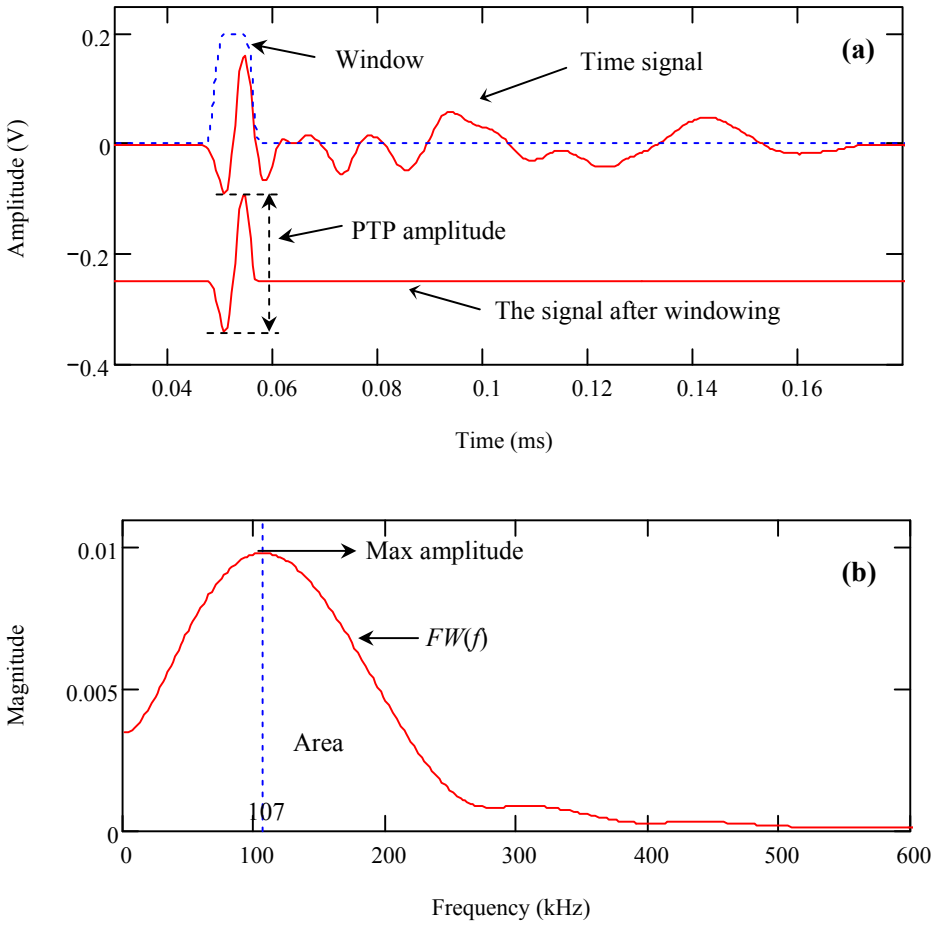

Figure 3.4: (a) Typical time windowing of the first arrival and (b) the corresponding Fourier transform

3.3.2 Shot Time Fourier Transform (STFT)

The use of time window forms a basis for the shot time Fourier transform (STFT). The concept of STFT was introduced by Dennis Gabor (1946). The STFT allows the evaluation of the time dependent behavior of the different frequencies in a signal. Its concept is illustrated in the Figures 3.5. The time signal function $x(t)$ is multiplied by a window function w(t), followed by computing Fourier transform. This process provides the frequency domain representation of the windowed signal. As the window is shifted along the time signal, the Fourier spectra are computed. Eventually, a contour plot is obtained, which shows the variation in frequency content of the signal with time.

The STFT can be mathematically defined as:

$$STFT(b,f) = \int_{-\infty}^{\infty} x(t) \cdot \psi(t-b) \cdot e^{-j \cdot 2\pi f \cdot (t-b)} dt \tag{3.14}$$

where f is the frequency, $x(t)$ is the time signal, $\psi(t)$ represents a window function which is time-shifted according to parameter b and frequency-modulated by $e^{-j \cdot \omega \cdot (t-b)}$. The width of the window applied determines the resolution in frequency domain through the relationship:

$$\Delta f = \frac{1}{N_w \cdot \Delta t} \tag{3.15}$$

where Δf and Δt are the frequency and time resolutions respectively, while N_w is the number of points in the time window, which is fixed for the different frequencies in the signal. The expression 3.15 indicates a trade-off in selecting the time and frequency resolution. A short-time duration window has a good resolution in time, but it is only suitable for capturing the spectral information in a relatively high frequency range (Figure 3.6). For a low frequency, a window of correspondingly large width is necessary, but information regarding high frequencies is lost because of the low time resolution.

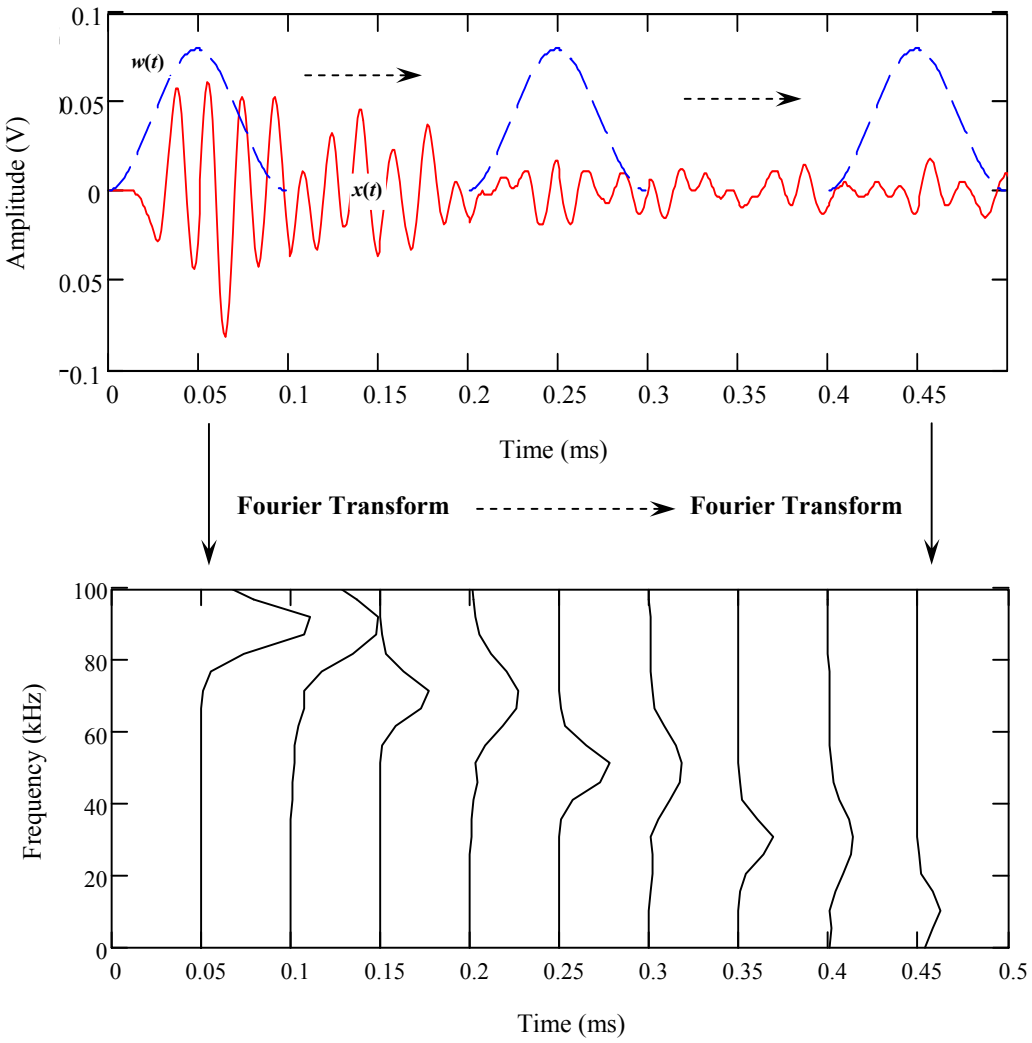

Figure 3.5: Short Time Fourier Transform Concept

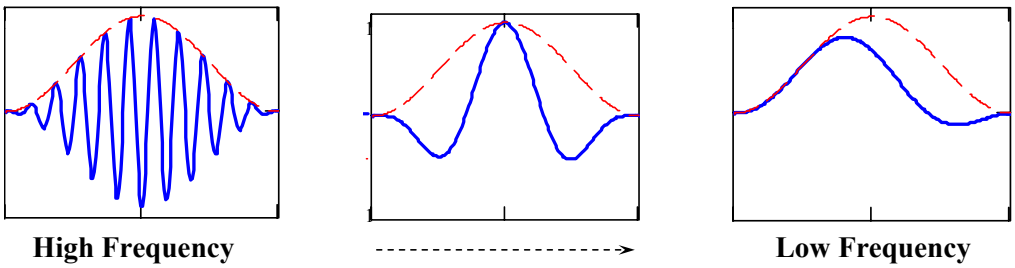

Figure 3.6: Effect of fixed window size on the frequency content of the STFT

3.3.3 Wavelet Transform (*WT*)

The Wavelet transform (*WT*) can be considered an improvement to the STFT. It overcomes the drawback of STFT where the frequency resolution and the time resolution cannot be enhanced simultaneously. The *WT* compares the similarities between the time signal and a window of variable size as it is time shifted along the signal. The *WT* is given by:

$$WT(a,b) = \frac{1}{\sqrt{|a|}} \int_{-\infty}^{\infty} x(t) \cdot \psi^*(\frac{t-b}{a}) dt \tag{3.16}$$

where $x(t)$ is the time signal; $\psi(t)$ represents the window known as mother wavelet; parameter b is used to time shift the window $\psi(t)$; parameter a is used to define the center frequency of $\psi(t)$; the star denotes the complex conjugate; and the coefficient $\frac{1}{\sqrt{|a|}}$ ensures the same energy for all dilated versions of $\psi(t)$ used to measure the time signal.

For practical applications, the wavelet transform (Equation 3.16) is computed in discrete form, given by:

$$W_{k,m} = \frac{1}{\sqrt{k}} \sum_{n=0}^{N-1} x_n \cdot \psi^*(\frac{n-m}{k}) \tag{3.17}$$

where x_n represents the discrete-time signal over a time period given by $N \cdot \Delta t$, Δt is the time sampling interval, k is an integer counter giving the center frequency of the wavelet $f_0 = \frac{1}{2k\Delta t}$, and m is an integer counter giving a shift time $m \cdot \Delta t$.

For the inverse *WT* to exist, the mother wavelet has to satisfy the following condition, known as the admissibility condition:

$$C_\psi = \int_{-\infty}^{\infty} \frac{|\psi(\omega)|^2}{|\omega|} d\omega < \infty \tag{3.18}$$

where ω is the angular frequency and $\psi(\omega)$ is the Fourier transform of the wavelet $\psi(t)$. $\psi(t)$ must further satisfy the following condition:

$$\int_{-\infty}^{\infty} \psi(t)\, dt = 0 \tag{3.19}$$

Equation 3.18 indicates that mother wavelet must have a zero mean. Then the original of $x(t)$ can be reconstructed by:

$$x(t) = \frac{1}{C_\psi} \int_{-\infty}^{\infty} \int_{-\infty}^{\infty} \frac{1}{a^2} WT(a,b) \cdot \psi(\frac{t-b}{a}) da\, db \tag{3.20}$$

Several types of wavelets are available for wavelet transform implementation (Qian, 2002). A common choice for seismic wave analysis is the Morlet wavelet, which is also used in this study to simulate the output of an ultrasonic transmitter. The Morlet function $\psi(t)$ is expressed as:

$$\psi(\frac{t-b}{a}) = e^{-j\cdot\frac{\pi(t-b)}{a}} \cdot e^{-\frac{(t-b)^2}{a^2}} \tag{3.21}$$

where j is the imaginary unit, the parameters a and b control the center frequency and time position of the wavelet, respectively. An example of Morlet wavelet is illustrated in Figure 3.7a in MathCAD file, where a_1 = 0.01 milliseconds result in a center frequency f_0 = 1/(2a_1) = 50 kHz, a_2 = 0.02 milliseconds result in f_0 = 1/(2a_2) = 25 kHz, and b = 0.05 milliseconds correspond to the time shift. The wavelet transform peaks at b = 0.096

milliseconds representing the time when the Morlet wavelet arrives at the receiver, as shown in Figure 3.7b.

Defined parameters for Morlet function with center frequency (f_0) defined by parameter "a":

$i := 1 .. 2^{10}$ $\Delta t := 0.001$ $t_i := i \cdot \Delta t$ (in millisecond) $\Delta f := 1\text{kHz}$

$a := (0.01 \quad 0.02)^T$ $b := 0.05$

Define Morlet function:

$$\text{Morlet}(a, b) := e^{-j \cdot \frac{\pi}{a} \cdot (b - t_i)} \cdot e^{-1 \cdot \left(\frac{b - t_i}{a}\right)^2}$$

Fourier transform of the Morlet:

FF := CFFT(Morlet)

$a_1 = 10\ \mu s$
($f_0 = 50$ kHz)

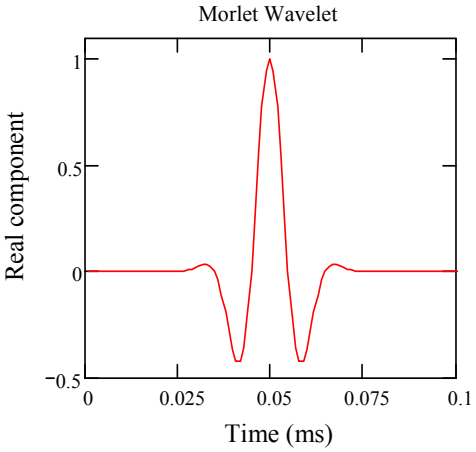

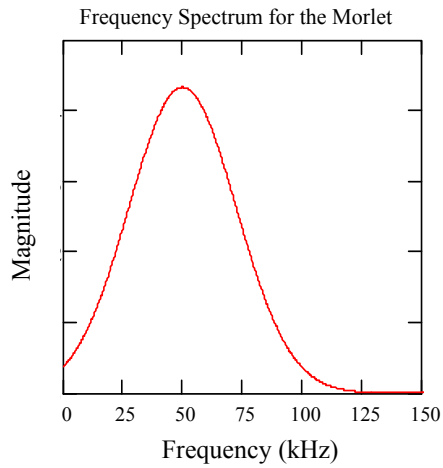

$a_2 = 20\ \mu s$
($f_0 = 25$ kHz)

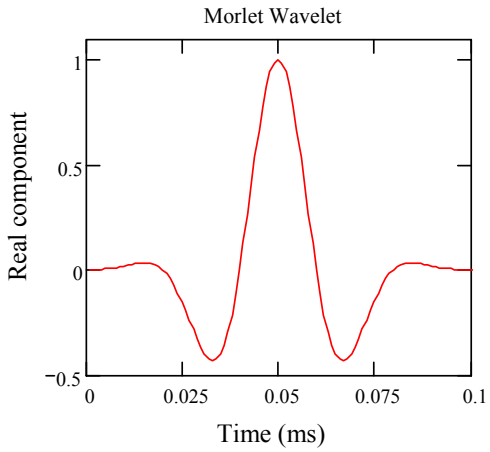

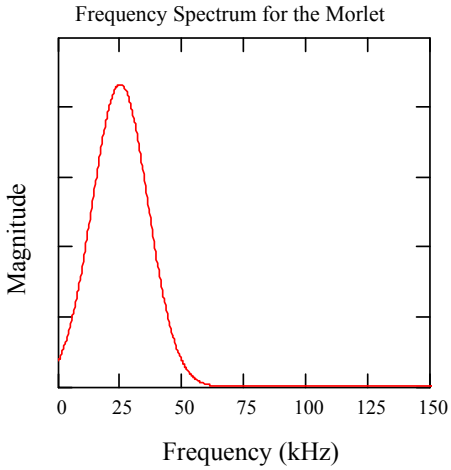

Figure 3.7 (a): A MathCAD file to illustrate a Morlet function

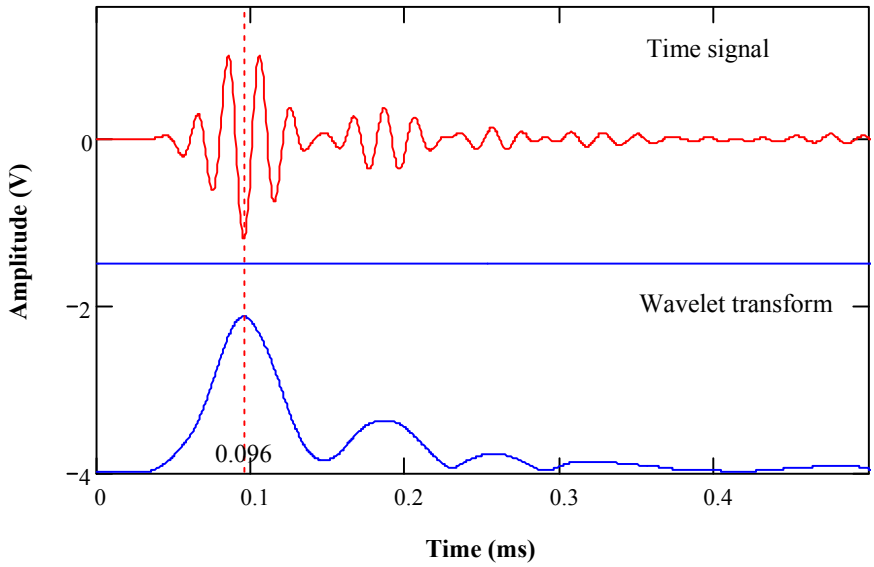

Figure 3.7 (b): Illustration of wavelet transform using Morlet wavelet (f_0 = 50 kHz)

Mallat's pyramid algorithm

Mallat's pyramid algorithm (Mallat, 1998) enables the detailed representation of the frequency content of a signal over time. In the discrete wavelet transform, Mallat's algorithm is used to decompose an arbitrary signal function into its components, as illustrated in Figure 3.8. Each component is called a level starting from level -1 and onwards. The summation of all the wavelet levels reconstructs the original signal. The number of levels is determined by the number of sampling points contained in the signal. If there are a number of points equal to $N = 2^n$ in the signal, there are $(n + 1)$ levels in the wavelet transform. The increase in the number of levels enhances the resolution in frequency. The shape of each wavelet component depends on the selection of the mother wavelet.

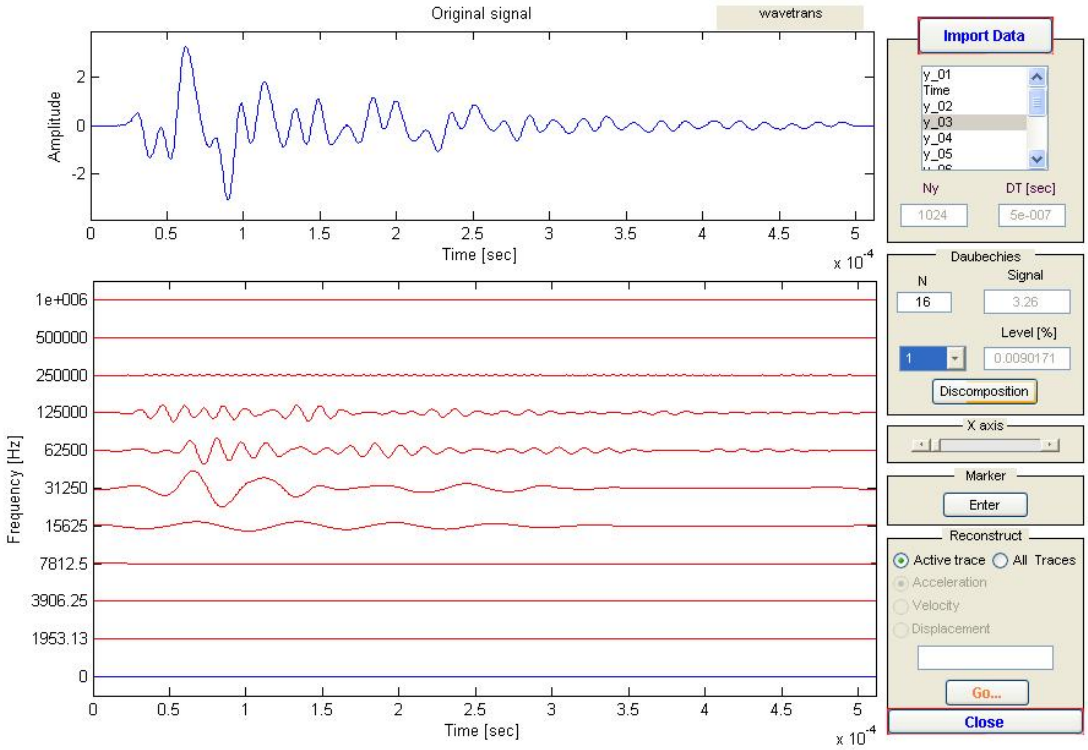

Figure 3.8: Decomposition of a signal into its wavelet components (Tallavo, 2007)

The *WT* decomposition of a signal *f*(*x*) can be mathematically expressed as:

$$f(x) = a_0\phi(x) + a_1 WT(x) + \begin{bmatrix} a_2 & a_3 \end{bmatrix}\begin{bmatrix} WT(2x) \\ WT(2x-1) \end{bmatrix} + \begin{bmatrix} a_4 & a_5 & a_2 & a_7 \end{bmatrix}\begin{bmatrix} WT(4x) \\ WT(4x-1) \\ WT(4x-2) \\ WT(4x-3) \end{bmatrix} +$$

$$+ \ldots + a_{2^j+k} WT(2^j x - k) + \ldots \qquad (3.22)$$

where $a_0 \ldots a_{2^j+k}$ are coefficients defining the amplitudes of the corresponding wavelets $WT()$, $j = 0 \ldots \infty$, $k = -\infty \ldots + \infty$, $\phi(x)$ is a scaling function, and $a_0\phi(x)$ can be visualized as a constant or static component. Note that each wavelet has a zero mean. Accordingly, a signal with a non-zero mean cannot be represented solely by a combination of these wavelets without addition of a static component.

Table 3.1: Comparison between levels and frequency

Level #	Number of coefficients	Number of wavelets	Description	Spacing between wavelets	Central frequency Hz
-1	1	None	$\phi(x)$	N/A	N/A
0	1	1	$WT(x)$	1024	1/T
1	2	2	$WT(2x-k)$	512	2/T
2	4	4	$WT(4x-k)$	256	4/T
3	8	8	$WT(8x-k)$	128	8/T
4	16	16	$WT(16x-k)$	64	16/T
5	32	32	$WT(32x-k)$	32	32/T
6	64	64	$WT(64x-k)$	16	64/T
7	128	128	$WT(128x-k)$	8	128/T
8	256	256	$WT(256x-k)$	4	256/T
9	512	512	$WT(512x-k)$	2	512/T

Note: T represents the time span of the signal being decomposed, in second.

$WT(x)$ is a dilated version of $WT(2x)$ that itself is a dilated version of $WT(4x)$, and so on. It is indicated that higher levels in the transform capture finer detail or higher frequency components in the signal. In Figure 3.8, the signal is decomposed into 11 wavelet levels. Most of the wave energy propagates at frequencies between 15,625Hz and 125,000Hz as indicated by their relatively high amplitudes. A wavelet level represents a frequency range. The comparison between 11 levels and the corresponding central frequencies for an arbitrary signal of $2^{10} = 1024$ sampling points is shown in Table 3.1. For example, at level 5 (the 7^{th} level), there are $2^5 = 32$ wavelets. In other words, the frequency range is centered at 32 cycles in T sec., which is a frequency of 32/T Hz.

Equation 3.22 identifies that an arbitrary signal with 2^n sampling points is approximated using 2^n coefficients. Then, the operation of decomposition for a signal f with 2^n points can be conceptually illustrated in Figure 3.9a. The original signal goes through a high-pass filter H and a low-pass filter L respectively. The outputs of H and L are

downsampled by 2 ($\downarrow 2$) to obtain, respectively, 2^{n-1} coefficients for wavelet level$_{n+1}$ and the coarser approximation (CA) of the signal defined by another 2^{n-1} coefficients. This process repeats itself recursively until the last coefficients are obtained for the 2nd level (level 0) and for $\phi(x)$ that is level -1 (Table 3.1).

The reconstruction of the original signal, known as inverse discrete wavelet transform, is achieved by iteratively upsampling each level through inserting zeros between sampling points, followed by passing through the corresponding *L* and *H*, as illustrated in Figure 3.9b. The operations of signal decomposition and reconstruction are implemented using MATLAB®.

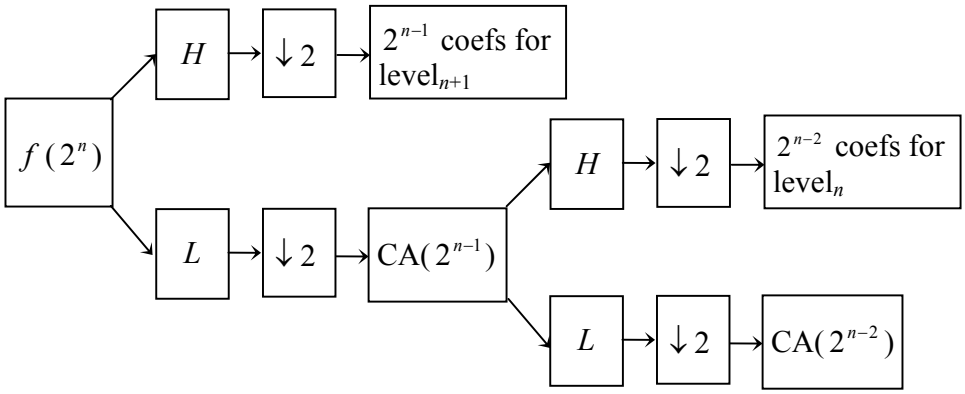

(a)

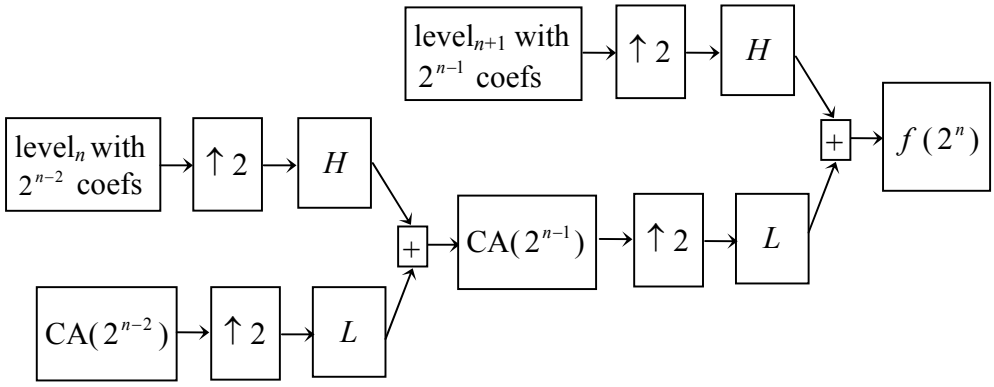

(b)

Figure 3.9: (a) Discrete wavelet transform and (b) Inverse discrete wavelet transform (Qian, 2002)

The frequency content of the signal is obtained by using the wavelet transform based on Mallat's algorithm (Equation 3.22), as shown in Figures 3.10a and 3.10b. The vertical axis in "scales" is equivalent to the "Spacing between wavelets" in Table 3.1 and is indicative of frequencies. For example, the dominant frequency is 22.2 kHz at the scale 70 (Figure 3.10b). The frequency decreases as the scale number increases.

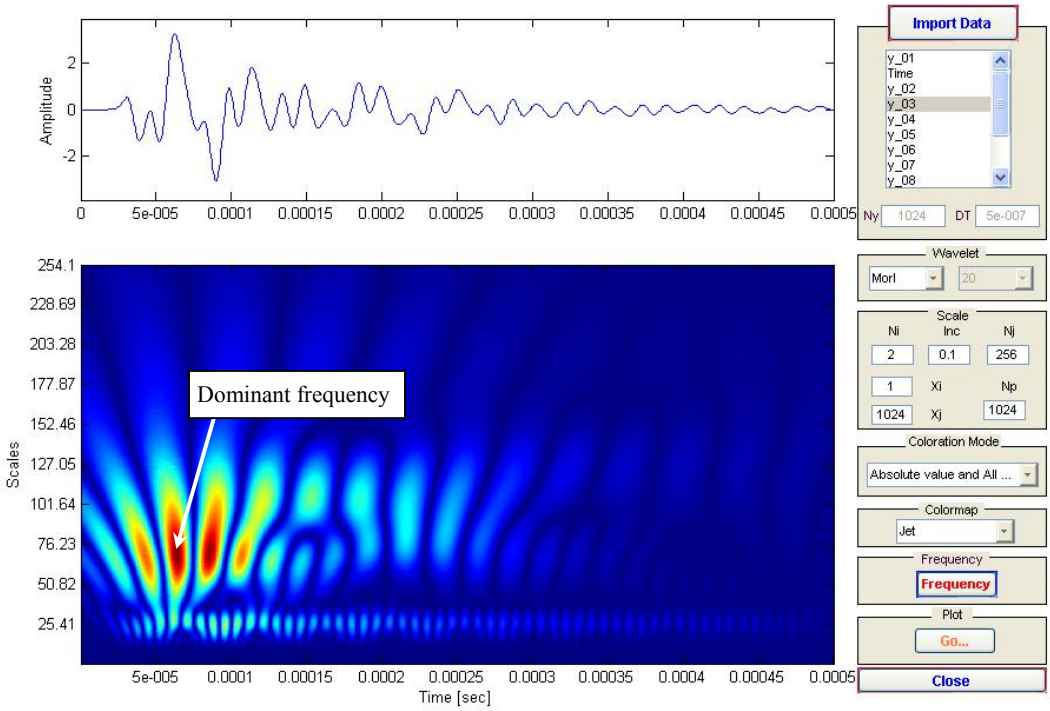

Figure 3.10 (a): Wavelet representation of a signal based on Mallat's algorithm (Tallavo, 2007)

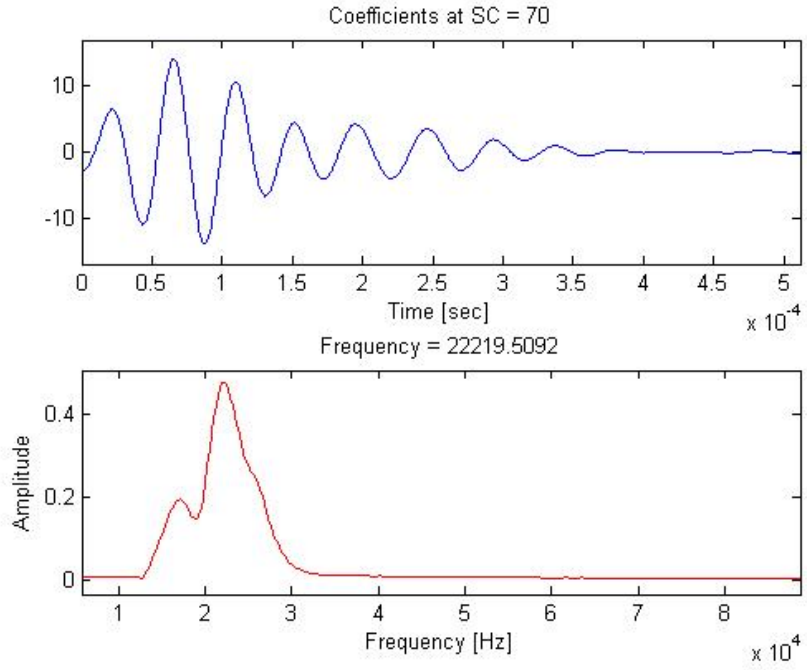

Figure 3.10 (b): Frequency content at scale 70 (Tallavo, 2007)

3.4 Summary

This chapter provides an introduction to the signal processing technique for analysis of signals in the time and frequency domains, including Fourier transform, windowing technique, short time Fourier transform, and wavelet transform. Understanding these techniques is crucial to material characterization using the wave-based testing methods.

CHAPTER 4
ULTRASONIC TESTING METHODS

4.1 Introduction

Most of the current NDT methods were invented in the late 1930s, after the first experiments using quartz transducers to create ultrasonic vibrations in materials by S.Y.Sokolov (1929) in Russia. With the rapid advancement of computer techniques for digital data acquisition and signal processing in the early 80's, significant improvements were made in seismic techniques that were previously impractical. Over the years, various NDT methods have been developed and applied in engineering with different degree of success (Nazarian et al., 2004; Nazarian et al., 1986; Phillips et al., 2000; Phillips et al., 2001; Phillips et al., 2004). Almost all the ultrasonic testing methods developed are based on monitoring wave propagation properties that are a function of the elastic properties and fracture pattern of the medium.

Wave-based methods are often employed to evaluate internal conditions and elastic properties of materials; which are not economically measured with traditional destructive methods. Four common techniques used in ultrasonic wave testing are Ultrasonic Pulse Velocity (UPV), Impact Echo (IE), Spectral Analysis of Surface Waves (SASW), and Fourier transmission coefficient (FTC).

4.2 Ultrasonic Pulse Velocity (UPV)

The UPV method is the oldest and most popular ultrasonic method used for the evaluation of construction materials such as concrete and rock. The application of the ultrasonic pulse velocity through concrete began in the early 1950's. The UPV method was later standardized for determination of pulse velocity through concrete (ASTM C597, 1967), and for laboratory determination of pulse velocities and ultrasonic elastic constants of rock (ASTM D2845, 1969). Other standards include BSI 98/105795 DC for determining the ultrasonic velocity of concrete, and ACI 228.2R for NDE applications. However, the successful application of these techniques to viscoelastic materials such as

asphalt concrete are still limited (Moorer et al., 1978; Smith et al., 1985; Rose et al., 1987; Rose et at., 1988).

4.2.1 Use of UPV test

The UPV method relies on the measurement of wave velocities through a test object. Wave velocities are indicative of elastic moduli that are in turn indicative of compressive strength of the material. Thus, it is theoretically possible to relate the wave velocities to the strength of the material (Chapter 2).

Measurements are performed by allowing ultrasonic stress waves to interact with a volume of material between the transducers. The waves are modified by the material morphology and parameters including elastic moduli, density, reflection and attenuation, texture, microstructure, and boundary conditions (surfaces, edges, curvatures, etc.) (Vary, 1991). The UPV test setup is illustrated in Figure 4.1. Two piezoelectric crystal transducers, one for pulse generation and the other for pulse detection, are placed in line with each other and on opposite ends of a specimen. The transmitting transducer converts a pulse of electric energy into a pulse of acoustic wave energy. The transducers are attached to the specimen with a coupling material such as vacuum grease. When the energy propagates through the specimen and reaches the receiver, it is converted back into an electric pulse; which is then displayed in an oscilloscope. The travel time of the wave through the specimen is measured and used to calculate the corresponding wave velocity, since the length of the specimen is known. Alternatively, given the wave velocity of a material, the travel time can be used to determine the thickness of a test object or the depth to a flaw. The measured signals are stored in a computer for further signal processing.

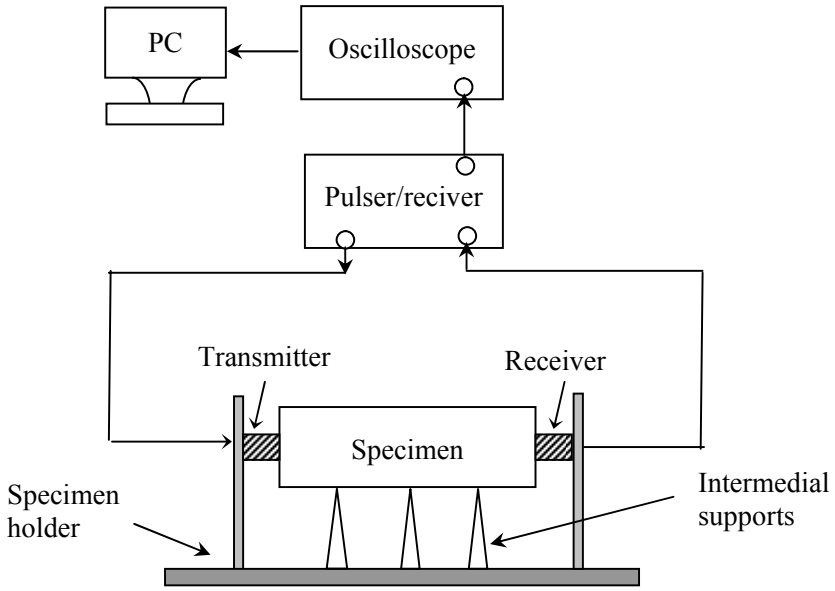

Figure 4.1: Schematic test setup for UPV method

P- and S-wave velocities in ultrasonic testing are determined as the length of the specimen (L) divided by the travel time (t):

$$V_P \text{ or } V_S = \frac{L}{t} \tag{4.1}$$

Wave velocity is directly proportional to material stiffness and inversely proportional to material density (Chapter 2). Equations 2.20 and 2.21 can be used to compute the Poisson's ratio (ν) and the Young's modulus (E) of the medium as:

$$\nu = \frac{0.5(V_P / V_S)^2 - 1}{(V_P / V_S)^2 - 1} \tag{4.2}$$

$$E = \frac{\rho(1+\nu)(1-2\nu)V_P^2}{1-\nu} = \frac{\rho V_S^2 (3V_P^2 - 4V_S^2)}{(V_P^2 - V_S^2)} \tag{4.3}$$

If a specimen is restricted from lateral deformation, the axial stress-to-strain ratio defines the constrained modulus (M). The constrained (M) and shear modulus (G) are given by:

$$M = \rho V_P^2 \tag{4.4}$$

$$G = \rho V_S^2 \tag{4.5}$$

Other applications of UPV method include detection of flaws and voids. The presence of a void in a medium delays the arrival of waves and thus results in lower wave velocities. If a honeycomb structure is present, wave velocities may remain unchanged, but the high frequency components of the signal are attenuated. For large voids, a complete loss of wave arrival may occur (McMaster, 1963; Olson, 2004). On the other hand, the signal amplitude also becomes small in a flawed object because the wave energy is attenuated by the reflection and/or scattering. In the UPV method, access to two surfaces of a test object is required and the distance between the transducers must be known. Depending on the locations of the transmitter and the receiver, three UPV test methods are possible: direct transmission, semi-direct transmission, and indirect transmission, as shown in Figure 4.2.

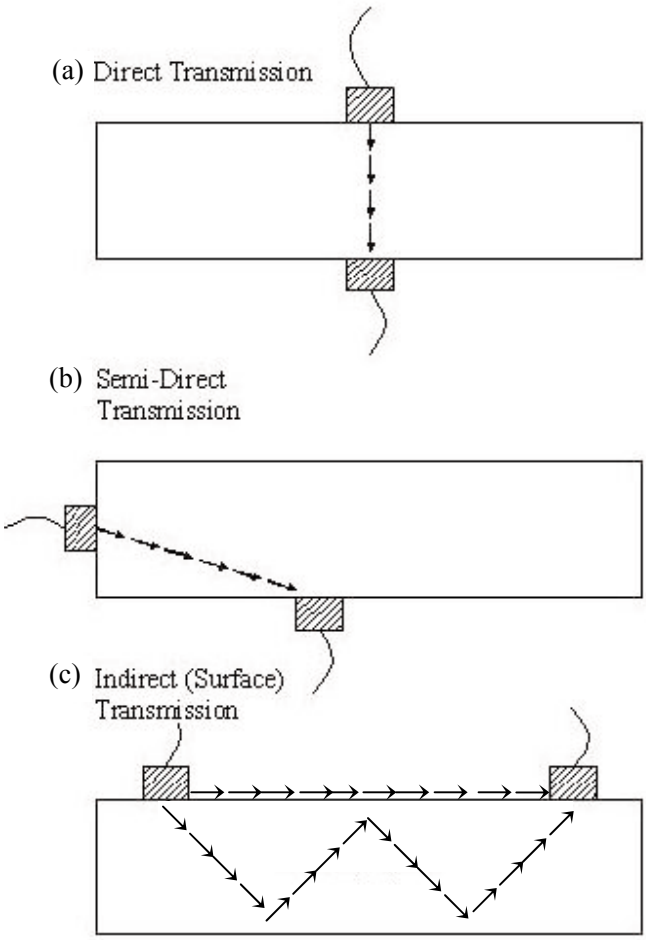

Figure 4.2: UPV test methods (Olson, 2004)

4.2.2 Limitations of UPV Test

Three principle limitations of the UPV method are:

1. Wave velocity is correlated to the Young's Modulus and hence the compressive strength of the test material. In practice, however, the relationship between ultrasonic pulse velocity and material strength for some composite materials (e.g. concrete) is complex (Popovics, 1969; Malhotra et al., 1980; Sturrup et al., 1984; Schickert, 1984; Popovics et al., 1990; Galan, 1990; Popovics and Popovics, 1992; Popovics and Rose, 1994). The reason is two fold. Firstly, the theoretical relationship (Equation 4.3)

works on the assumption that the materials tested at small-strain level (< 10^{-5}%) exhibit isotropic linear elastic properties. However, concrete or asphalt concrete has none of these properties (Rose, 1985; Popovics and Popovics, 1992; COST 333, 1999). The relationship between Young's modulus and strength for composite materials has been obtained empirically by curve fitting with a relatively low correlation (Popovics and Popovics, 1992). Secondly, there are other variables in composite materials affecting the wave velocities; or variables affecting the strength that may not have a significant effect on the wave velocity and vice versa (Popovics et al., 1990; Popovics and Popovics, 1992; Popovics and Rose, 1994). There is experimental evidence showing that while a significant decrease was observed in material strength with increase in porosity, almost no change was observed in wave velocity (Popovics, 1969). Experiments by Schickert (1984) also demonstrated the insensitivity of the pulse velocity to the presence of an opening cut in a slab. However, compared with strength, the pulse velocity was shown to be sensitive to changes of other factors such as moisture content, aggregate content, aggregate type, and maximum particle size of the mixture (Sturrup et al., 1984; Popovics and Popovics, 1992). Therefore, ultrasonic pulse velocity alone is not sufficient for condition and strength assessment of composite materials.

2. The common use of low frequencies (20 – 150 kHz) leads to a low axial resolution of waves. Low frequency measurements have been demonstrated to be insensitive to small voids and micro-cracking that are smaller than the signal wavelength (Suaris et al., 1987). However, the effect of increased attenuation and scattered noise must be compensated for when high frequencies are used.
3. The UPV method for concrete operates on the assumption that the wave velocities are frequency independent (ASTM, 1988). However, the wave velocity increases significantly (about 20%) as frequency increases from 25kHz to 2.25MHz (Popovics and Rose, 1994).

4.3 Impact-Echo (IE)

The IE method was a technique researched and developed at the national Institute of Standards and Technology (NIST) in the early to mid 1980's (Sansalone and Carino, 1986). This method was later standardized as a method for measuring the P-wave speed and the thickness of concrete plates using the Impact-Echo method (ASTM C1383-98a). The IE method has been successfully employed to locate voids, cracks, delaminations, and other damage in concrete, wood, stone, and masonry structures (Carino, 1984; Sansalone and Carino, 1986; Carino et al., 1986; Sansalone and Carino, 1988; Sansalone and Carino, 1989; Ghorbanpoor et al., 1992; Jaeger et al., 1996; Lin, 1996; Abraham and Philippe, 2002).

The basic principle of the IE method is shown in Figure 4.3. A short-duration mechanical impact by a hammer or impactor introduces into a medium a stress pulse that propagates radially outward from the source as compression (P) and shear (S) waves. Additionally, at the surface, Rayleigh waves propagate along the surface in a shallow zone (Figure 4.3a). The P- and S-waves reflect back and forth between the top surface and internal defects or the bottom of the test member. The multiple wave reflections arriving at the surface produce periodic displacements which are detected by a receiver adjacent to the impact source (Figure 4.3b). The recorded time-domain displacement waveform is transformed into frequency-domain for further interpretation of the test data. The single large peak at a frequency spectrum (Figure 4.3b) results from the multiple wave reflections from a reflector or the bottom boundary of the object. This dominant frequency is known as resonant frequency. The fundamental relationship to interpret the frequency spectrum in IE method is:

$$h = \frac{V_P}{2f} \tag{4.6}$$

where h is the distance to a reflecting interface, V_p is the compression wave velocity , and f is the frequency of P-wave reflections.

(a) Stress waves introduced by an impact

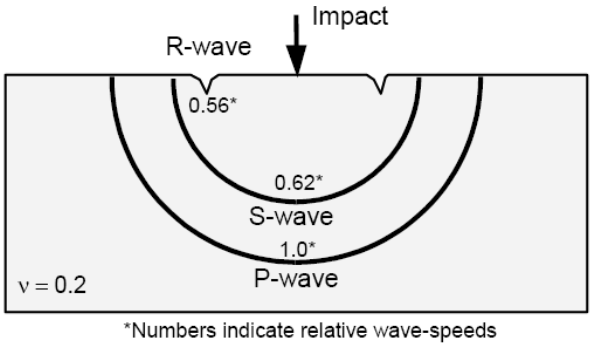

(b) IE method application

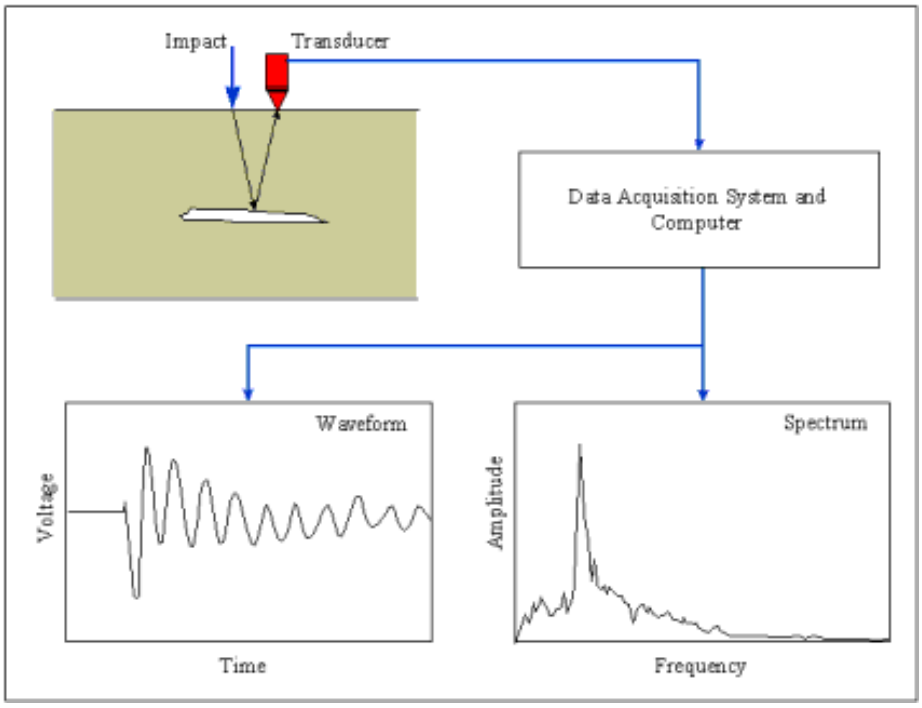

Figure 4.3: Principle of the IE method (Sansalone and Streett, 1997)

An advantage of the IE method is that access to only one surface of the object is required. This method is able to generate low frequency stress waves by a small hammer or steel ball to measure a thickness of up to several meters. However, a significant limitation of the IE method is that small details such as small voids and micro-cracks in inhomogeneous materials are not easy to detect because the relatively low frequency

range is commonly used (Popovics and Rose, 1994). Use of high frequencies (typically above 100 kHz) produced by a short duration impact, on the other hand, limits the investigation to relatively thin masonry structures because of the scattering of the high frequency stress waves.

4.4 Spectral Analysis of Surface Waves (SASW) Method

The SASW method was first introduced by Heisey et al. in 1982. Today it is commonly used as an in-situ seismic technique for determination of shear modulus profile and layer thicknesses in a layered medium. This method is based on the dispersion of the surface waves in a layered medium, that is, surface wave velocities vary with frequency or wavelength. The experimental dispersion curve is computed first, and then through an inversion process of the dispersion curve, the corresponding shear wave velocity profile, elastic moduli, and layer thicknesses are computed.

Surface waves attenuate much slower than body waves. In addition, surface waves (R-waves) carry 67% of the total energy generated by a surface impact, while body waves (P- and S-waves) only carry 33%. These properties of surface waves allow SASW measurements to cover a large testing area. The SASW method is able to accurately predict the thickness and stiffness of the surface layer in a pavement with an error less than 5% (Olson, 2004; Sheu and Rix et al., 1988; Sheu and Stokoe et al., 1988; Roesset et al., 1990; Akhalghi and Cogill, 1994). In addition, the SASW method has been used to detect the presence of moisture in the subgrade and aging of an asphalt concrete layer (Gucunski and Woods, 1992).

The SASW investigation commonly involves three steps (Nazarian et al., 1983; Nazarian, 1984; Hiltunen, 1988; Gucunski, 1991): 1) data collection in the field, 2) construction of a dispersion curve, and 3) inversion of the dispersion curve. The inversion process involves construction of a theoretical dispersion curve by assuming a shear wave velocity profile, and match of the theoretical with the experimental dispersion curves by iteratively adjusting the shear wave velocity profile. Once the pre-established threshold for the match is passed, a shear wave velocity profile is obtained. A computer-based

linearized iterative least squares algorithm has been used widely to compare the theoretical and experimental dispersion curves (e.g. Horike, 1985; Herrmann and Al-Eqabi, 1991; Lai, 1998; Foti, 2000).

The experimental arrangement is illustrated in Figure 4.4. Waves with various frequencies are transmitted to the medium by a mechanical impact (e.g. an impulsive hammer) on the ground surface. The propagation of the waves is monitored by an array of receivers on the surface. The receiver spacing depends on several factors (Nazarian et al., 1983): the wave velocity in the test medium, the expected investigation depth, the frequency range used; the attenuation properties of the medium, and the instrumental sensitivity. In general, short receiver spacings are used for shallow measurement, while long spacings are used for deep measurement. In addition, seismic waves must travel a minimum distance from the source before becoming fully formed (near-field effects). Conversely, low signal-to-noise ratios can be present at large distances from the source, relative to the wavelength (far-field effects). A number of criteria that relate receiver spacing to wavelength have been proposed (e.g. Lysmer, 1965; Sanchez-Salinero et al., 1987; Sheu et al., 1988; Roesset et al., 1989; Gucunski, 1991). One commonly accepted is expressed as (Heisey et al., 1982):

$$\frac{\lambda_R}{3} < x < 2\lambda_R \tag{4.7}$$

where λ_R denotes wavelength of R-wave, and x represents the receiver spacing that is commonly selected as equal to the distance between the source and the first receiver.

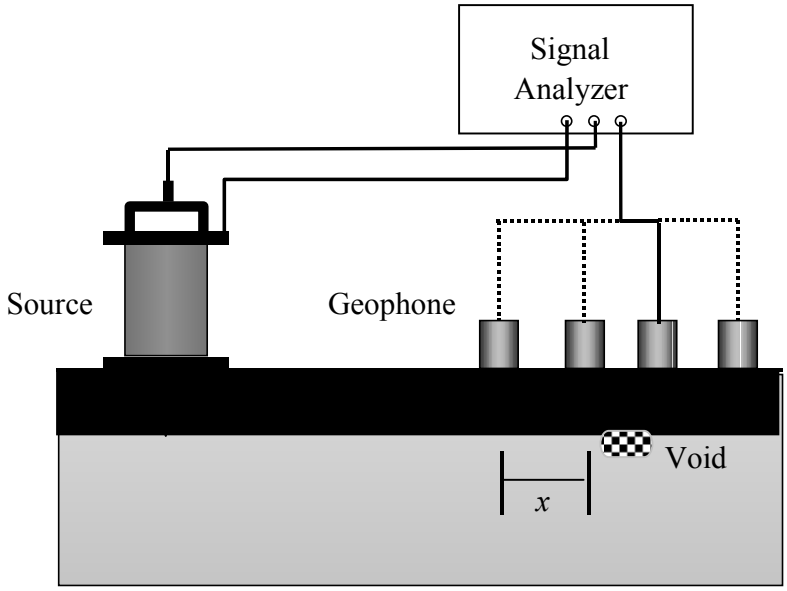

Figure 4.4: Test setup for SASW method

A Fourier spectral analyzer is used to process signals in the field. The phase difference beween the measured signals in obtained from the phase of the cross-power spectrum (CPS) of the two receivers. The CPS is expressed as:

$$CPS(f) = Y_1(f)Y_2(f)^* = A_1(f)A_2(f)e^{j\cdot\Delta\varphi(f)} \tag{4.8}$$

where $Y_1(f)$ and $Y_2(f)$ are the Fourier transforms of the two signals, * denotes the complex conjugate, $A_1(f)$ and $A_2(f)$ are spectral amplitudes, j is the imaginary unit, and $\Delta\varphi = \varphi_2 - \varphi_1$ denote the phase differences as a function of frequency.

The wavelength λ_R can be obtained as a function of frequency and as a function of the receiver spacing (x) as:

$$\lambda_R(f) = \frac{x \cdot 2\pi}{\Delta\varphi(f)} \tag{4.9}$$

Thus, the surface wave velocity V_R or phase velocity for a given frequency f is:

$$V_R(f) = \lambda_R(f) \cdot f \tag{4.10}$$

Care should be taken to select an appropriate frequency range of analysis to ensure that reliable information is obtained for construction of the dispersion curve. The coherence function is used to evaluate the quality of linear correlation between two signals. If coherence is smaller than 0.9, the measured data should not be considered reliable (Nazarian and Stokoe, 1986). A coherence value of 1 indicates perfect linear correlation between the two signals. The coherence function (γ_{12}) can be expressed as:

$$\gamma_{12}^2 = \frac{G_{12} \cdot G_{12}^*}{G_{11} \cdot G_{22}} \tag{4.11}$$

where G_{12} is the CPS as described in Equation 4.8, $G_{11} = Y_1(f)Y_1(f)^*$ is known as the auto power spectrum (APS) of signal 1, and $G_{22} = Y_2(f)Y_2(f)^*$ is the APS of signal 2.

A surface impact simultaneously generates surface waves and body waves in all directions. If there exist surface discontinuities or boundaries, some surface and body waves will be reflected and reach the receivers. Some body waves reach the receivers either directly from the source or through reflections from the bottom of the surface layer. All these waves contaminate the direct surface waves, thus leading to fluctuations or abrupt changes in the phase velocity profile and the dispersion curve as well (Jones, 1962; Vidale, 1964; Ullidtz, 1987; Sheu and Stokoe et al., 1988; Martincek, 1994). This problem may be overcome by proper adjustment of the source-receiver geometry (Sheu and Stokoe et al., 1988). On the other hand, the source-receiver geometry determines the measurable depth in the test. The elastic modulus profiles are computed from the wave velocities. However, these relationships for inhomogeneous, high dispersive materials such as asphalt concrete are not unique.

4.5 Fourier Transmission Coefficient (FTC)

Fourier transmission coefficient (FTC) method is an improved SASW measurement for the determination of the depth of a surface-breaking crack. This method allows the removal of unknown characteristics of the receiver, the wave source and the coupling (Popovics et al., 2000; Song et al., 2003; Yang, 2007). This method requires two sources and two receivers placed along a line at both sides of a surface defect as shown in Figure 4.5. The two sources are placed at locations A and E. First, the surface waves generated at location A are recorded by a receiver at location B as a signal f_{AB} and subsequently recorded at location D as f_{AD} across the crack. The process is repeated by generating surface waves at location E and receiving f_{ED} and f_{EB} at locations D and B respectively (Figure 4.5). These four received time signals can be expressed in frequency domain as:

$$F_{AB} = S_A C_A M_{AB} C_B R_B \tag{4.12}$$

$$F_{AD} = S_A C_A M_{AB} M_{BD} C_D R_D \tag{4.13}$$

$$F_{ED} = S_E C_E M_{ED} C_D R_D \tag{4.14}$$

$$F_{EB} = S_E C_E M_{ED} M_{DB} C_B R_B \tag{4.15}$$

where F_{AC}, F_{AB}, F_{DB} and F_{DC} are the Fourier transforms of the time signals f_{AC}, f_{AB}, f_{DB} and f_{DC}; the first subscript denotes the source location, generically labeled as "*i*" in the following discussion, whereas the second subscript is the receiver location, labeled as "*j*". S_i represents the source transfer function at locations *i*; C_i and C_j are the coupling transfer functions at locations *i* and *j*; M_{ij} is the transfer functions of the medium between locations *i* and *j*; and R_j is the receiver transfer function. The terms M_{BD} and M_{DB} can be considered equal because they indicate the same wave path and the same geometric attenuation. Accordingly, the signal transmission between locations B and D can be expressed as (Popovics et al., 2000):

$$FTC = \sqrt{\frac{F_{AD} \cdot F_{EB}}{F_{AB} \cdot F_{ED}}} = M_{BD} \tag{4.16}$$

The FTC is actually an amplitude ratio between measurements near the source and far from the source. It is indicative of wave attenuation for each frequency component transmitted through the crack. In ideal situations where the medium is intact, there is a total transmission of energy and the FTC = 1. *FTC* falls between 0 (complete attenuation) and 1 (complete transmission).

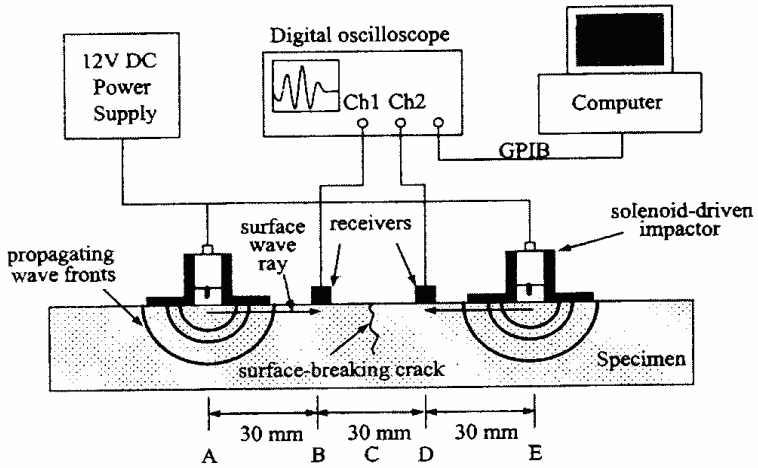

Figure 4.5: Test set up for the measurement of Transmission Coefficient (TC) (Song et al., 2003)

The FTC technique has the advantage that the wave velocity of the material is not required in advance and that the results are independent of the type of source, receiver, and coupling between the medium and the transducers. The main limitation of this technique is that surface waves detected at the near receiver are less affected by geometric attenuation than the signals at the far receiver. In addition, surface waves at the near receiver are also less affected by the reflected P-waves from the bottom of the slab. Besides, reflected waves from the surface crack could also interact with surface waves at the two receiver locations. The superposition of the reflected waves amplifies or reduces

signal amplitudes. Care should be taken to select appropriate source-receiver spacing as well as the distance between the receiver location and the crack concerned.

4.6 Summary

The NDT techniques of ultrasonic pulse velocity (UPV), impact echo (IE), spectral analysis of surface waves (SASW), and Fourier transmission coefficient (FTC) are reviewed in this chapter. The main advantages and limitations of these techniques are summarized in Table 4.1.

Table 4.1: Literature summary of the NDT techniques

Technique	Brief description	Advantages	Limitations
Ultrasonic pulse velocity (UPV)	Wave velocities are measured to assess material strength or stiffness with simple equations. Wave velocities can be used to indicate presence of flaws as well.	Easy to perform and mathematically simple.	The velocity-strength relationship for some composite materials needs validation. Commonly used low frequencies are not sensitive to small flaws.
Impact echo (IE)	The spectral analysis of multiple wave reflections enables detection of location and extent of flaws.	Low frequency waves used enable sampling up to several meters deep.	Only large flaws and material boundaries are accurately assessable with the low frequency wave used.
Spectral analysis of surface waves (SASW)	Dispersion curves of Rayleigh waves are developed to determine the shear modulus profile and layer thickness in a layered medium.	Use of surface waves enables testing of a large distance.	Boundary reflections from and direct body waves could adversely affect measurements of surface wave velocity and the dispersion curve.
Fourier transmission coefficient (FTC)	The FTC is a transmission ratio of surface waves through a crack. It indicates wave attenuation through the creak.	The wave velocity of the material is not required in advance. The results are independent of type of source, receiver, and coupling condition.	Interference of reflections from boundaries could cause erroneous amplitude measurements. A time window is required for isolated analysis of the surface wave portion.

CHAPTER 5
QUALITY ASSESSMENT OF HMA MIX CYLINDRICAL SPECIMEN TESTS: PHASE I

5.1 Introduction

The analytical investigation described in the previous chapter provides a basis for the design of suitable experimental program for the development of an innovative non destructive test procedure for condition assessment of longitudinal joints in asphalt pavements. A carefully planned laboratory study is necessary prior to testing in the field to develop an effective testing protocol suitable for field evaluation. The main objective of the laboratory experimental program was to evaluate the effectiveness of the proposed complimentary non-destructive testing methodology for assessing the condition of longitudinal joints in asphalt layers.

The experimental program consisted of two phases. Phase I mainly focused on studying the relationship between the wave characteristics obtained from UPV test and the quality of the asphalt concrete specimens prepared in the laboratory. Traditionally, the quality of asphalt concrete mix placed in the field is assessed in terms of percent compaction achieved in the field as compared to the density of the design mix obtained in the laboratory. Pavement experts agree that the percent compaction is necessary but not sufficient to ensure good quality. This agreement is because the quality of mix particularly in terms of durability and resistance to fatigue cracking and thermal cracking depends on good bonding between the asphalt binder and the aggregates. The bonding at the asphalt-aggregate interface relies on the adhesive binder properties and the binder-aggregate interface conditions in addition to good compaction. Therefore, a fundamental mix property that is sensitive to the asphalt-aggregate interaction within the mix is needed to ensure good quality mix. In this study, the specimen quality was determined using two methods: 1) the traditional method using density measurement and 2) an innovative approach using dynamic modulus which is recommended by the Federal Highway Administration (FHWA) for use as a fundamental material property for

characterizing Superpave mixes (Witczak, et al., 2002; Bonaquist et al., 2003; Christensen et al., 2004).

The experiments of Phase II (Chapter 6) focus on developing suitable test procedures for assessing the condition of longitudinal construction joints in asphalt pavements in the field based on the wave characteristics identified in the experiments of Phase I.

The following sections provide a detailed description of the approach used in the experimental program of Phase I. As well, the analyses of the experimental results are presented after description of each test.

5.2 Instrumentation

As a first step, it is important to select the appropriate sensors required for NDT testing in the laboratory. The assemblies of instrumentation and specimens used in the ultrasonic measurements are summarized in Table 5.1

5.2.1 Description of data acquisition system used in UPV tests

HMA mixtures exhibit large damping and heterogeneity. These characteristics entail a sufficiently high amplitude of signal output for detection of transmitted waves. In addition, precise detection of transmitted wave arrivals is needed to avoid erroneous velocity measurements. Therefore, it is necessary to select a suitable pulse transmitter device and data acquisition system capable of providing large amplitude motions, amplified received signals, and enhanced signal-to-noise ratio. For testing of HMA cylindrical specimens in this study, the transmitter and the data acquisition system were selected to meet the all these requirements for testing. The system included a pair of piezoelectric transducers (Panametrics V102, 1 in. diameter, 1MHz), a corresponding pulser/receiver (Panametrics 5052PR), a digital oscilloscope (HP 54610B), and a desktop computer. These devices are described in detail as follows.

Table 5.1: Assemblies of ultrasonic instrumentation and specimens

Phase	Specimen	Transmitter	Receiver	Purpose
I	PVC blocks; Steel blocks; Group A HMA (cylindrical)	1MHz (Panametrics V102)	1MHz (Panametrics V102)	To calibrate the test system.
	Group B HMA (cylindrical)	1MHz (Panametrics V102)	1MHz (Panametrics V102)	To determine wave attributes, e.g. attenuation and velocity.
II	Slab 1 (roller compaction)	1MHz (Panametrics V102)	50kHz (PCB353B65)	To estimate wave velocities; and determine wave attenuation due to a joint.
	Slab 2 (Traditional manual compaction using hand-held hammer)	50kHz (Pundit)	50kHz (PCB353B65)	Same as in slab 1
		50kHz (Pundit)	100kHz (PCB353A60)	To see the real frequency response of the slab (below 60kHz).
	Slab 3 (Improved manual compaction)	50kHz (Pundit)	50kHz (PCB353B65)	Same as in slab 1

Piezoelectric transducers

A piezoelectric transmitter generates a stress pulse when the piezoelectric crystal is deformed under the effect of an electric charge. A piezoelectric receiver produces electric energy when the crystal is deformed by a mechanical pressure. The compression (P) wave transducers used in this study are based on a typical deformation mode of thickness-expansion as illustrated in Figure 5.1. Since P-waves are the fastest traveling waves, use of P-wave transducers to generate and receive a P-wave allows a unique initial arrival to be identified.

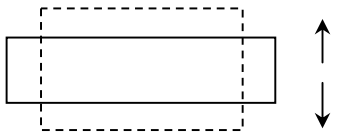

Compression motion

Figure 5.1: A basic deformation of a piezoelectric element (Hellier et al, 2001)

On the other hand, the traditional use of low frequencies (typically 50 kHz) in ultrasonic testing of concrete makes the test method insensitive to small details which are orders of magnitude smaller than the wavelength. Thus, for testing of HMA specimens in this study, a relatively high frequency is used by means of the 1MHz P-wave transducers to improve the sensitivity.

The signal waveform and frequency response of the 1MHz transducers are provided by the manufacturer, as illustrated in Figure 5.2. The center frequency is 0.92MHz and the transducer bandwidth typically measured at -6db level from the maximum amplitude is from 0.397 to 1.44 MHz, representing the effective frequency range of the pulse generated by the transducer.

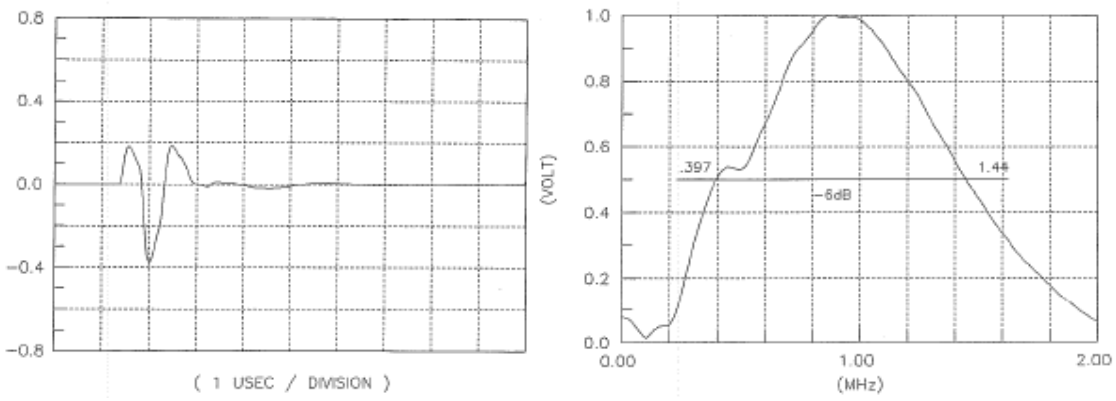

(a) **(b)**

Figure 5.2: (a) Signal waveform and (b) frequency response of the 1MHz transducers

Pulser/receiver

Figure 5.3 shows the front panel of the pulser/receiver used in this study. The pulser/receiver setting described in the following sections were used throughout the testing of HMA specimens.

Figure 5.3: The front panel of the pulser/receiver model 5052PR

Rep. Rate control

This switch enables alteration of the internal pulse repetition rate from 200 to 5000Hz. In general, the repetition rate of the pulse sent should be sufficiently low so that the waves generated by the previous pulse do not contaminate the waves generated by the following pulse. In this study, the minimum repetition rate 200Hz was used.

Energy control

This control provides four levels of excitation amplitude for a given transmitter. The output energy and its corresponding pulse amplitude are summarized in Table 5.2. In order to compensate for attenuation of wave energy through a high damping HMA specimen, energy "4" setting was used which is the maximum power available.

Table 5.2: Energy control specification of the pulser/receiver (Panametrics, 1984)

Energy setting	Damping resistance (ohms)	Available pulse energy (ujoules)	Pulse amplitude (volts)
1	50	14	140
2	100	36	200
3	100	58	200
3	250	58	240
4	500	94	270

Attenuation control

This control consists of a course and a fine attenuation switches. They allow the received signals to be attenuated to a maximum of 68dB in 2db increments. Zero attenuation was selected to produce the maximum possible signal amplitude in testing of asphalt concrete.

H. P. Filter control

This control allows passage of either a complete bandwidth of an original signal or just the high frequency components above the set cut-off frequency. In other words, it is used to remove the unwanted low frequency components. The cut-off frequency should be always set below the center frequency of the transducer. Since analysis of complete bandwidth signals was expected in this study, the setting should be adjusted to position "out".

Damping control

This control allows selection of an optimum damping resistance applied on a given transducer to achieve an optimum waveform. The control setting and the corresponding damping resistance are illustrated in Figure 5.4. This control setting is recommended to be in position "4" for common application (Panametrics, 1984).

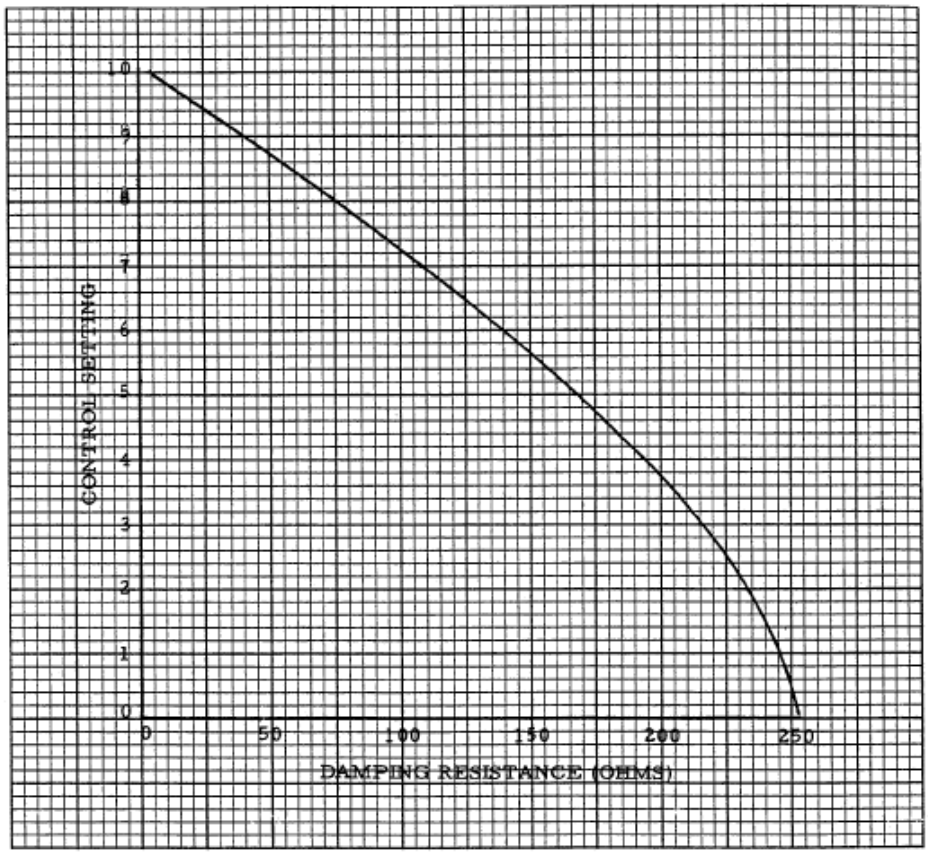

Figure 5.4: Damping control setting versus damping resistance (Panametrics, 1984)

Gain control

Gain control is functionally similar to attenuation control. The difference is that increasing gain level allows amplification of signals while increasing attenuation leads to decrease in signal amplitude. For application in asphalt concrete material, "40db" was selected corresponding to an amplification of 100 times.

T/R and RCVR connectors coupled with mode switch 1 and 2

When the mode switch is in position 1, only one transducer is needed and it is connected to the T/R connector. In this case, the transducer functions as both the transmitter and receiver. This setting is especially applicable to pulse-echo operation. When mode switch is in position 2, two transducers are needed and are respectively connected to T/R connector as the transmitter and to RCVR connector as the receiver. This setting is especially applicable to UPV operation.

Oscilloscope and computer

An oscilloscope allows the received electrical energy to be displayed as a digital signal waveform from which the travel times of waves through a given distance are measurable. In this study, the resolution for the travel time measurements in the oscilloscope was $0.2\,\mu s$. In addition, a sampling interval of $0.5\,\mu s$ was applied for measurement of a full length signal of 1,024 sampling points.

Besides, clear recognition of wave arrivals permits high accuracy evaluation of wave velocities. This goal is achievable by performing stacking in the oscilloscope. In this study, a series of 256 transient signals were stacked in the oscilloscope with the internal software to produce a single resultant signal with cancellation of noise. This stacked signal was stored in a computer for further analysis and study of the signal in frequency domain, for instance, using MathCAD and MATLAB software.

5.3 HMA Quality Assessment Using Wave Characteristics – Phase I

The goal of the experiments in Phase I is to determine the wave characteristics that are sensitive to the quality of the mix. For this purpose, HMA mixtures were compacted using the Superpave gyratory compactor at varying gyrations to produce specimens of different volumetric properties. It has been shown in the literature that the percent compaction increases with the number of gyrations for a given mixture and so the quality of the specimen (Nazarian and Stokoe, 1986). The correlations among wave characteristics, density, and the number of gyrations were examined in the experiments of Phase I. Based on these results, the potential correlations between the fundamental properties (e.g. the dynamic modulus) and the wave characteristics were explored for the selection of the most suitable parameter for assessing the mix integrity. The experimental design in Phase I involved five steps:

1. Sample preparation.
2. Calibration of newly purchased sensors to account for the delay time during wave transmission as well as to assess the reliability of the measurements.
3. Ultrasonic Pulse Velocity (UPV) testing of the asphalt concrete samples prepared in the laboratory. Selection of efficient signal processing techniques for characterizing output signals that could be used for condition assessment of asphalt concrete mixes.
4. Bulk density measurements of the asphalt concrete mixes prepared in the laboratory. Determination of dynamic modulus values of the asphalt concrete mixes based on Superpave testing protocol.
5. Examination of potential correlation between the dynamic modulus and the wave characteristics for identification of parameters suitable for condition assessment of asphalt mixes.

5.3.1 Preparation of asphalt concrete specimens

A plant mix (Superpave 19.5 mm) from Hwy 26 in southern Ontario was used to prepare samples required for testing. This mix is equivalent to the heavy duty binder mix commonly used in southern Ontario. The gradation of the batched aggregate was mixed according to the Job Mix Formula using 4.6% asphalt cement, as illustrated in Figure 5.5.

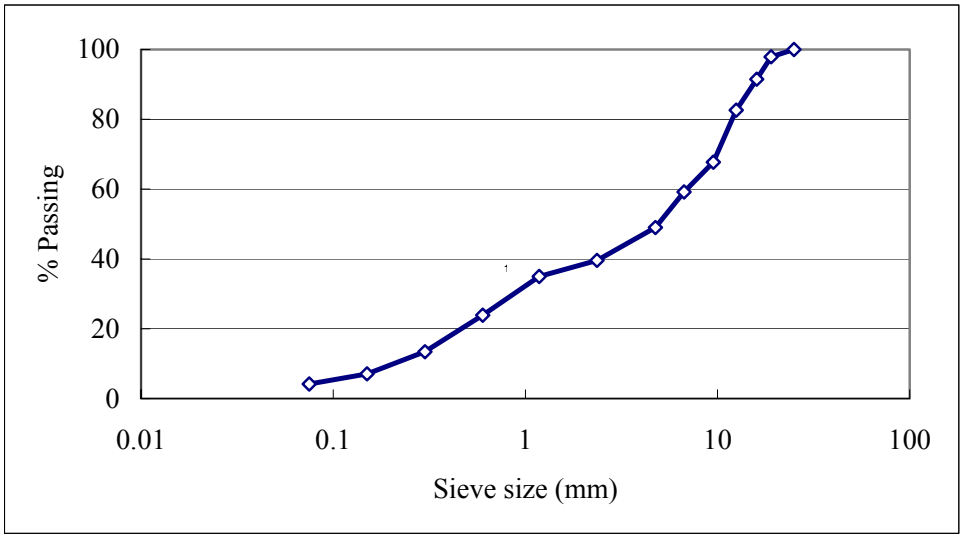

Figure 5.5: Aggregate gradation curve of SP 19 HMA mix

Two groups of HMA cylindrical specimens (Group A and Group B) were prepared in this study. Group A samples are used for calibration of the UPV test system. They are identical in terms of material type and compaction but different in lengths varying from 50 mm to 200 mm. Group B samples were used for the establishment of relationship between wave characteristics and the material quality compacted at different gyration levels varying from 40 to 140. The purpose of the different gyrations was to force the air void values to have a wide spread to check for correlation with wave characteristics and with the material quality as well. The following procedure was used for the preparation of cylindrical specimens in the laboratory.

1. A sufficient amount of loose material, in conjunction with the mixing bowl, was heated up to 160^{o}C in an oven for at least 4 hours. The designed compaction temperature for the material was at least 138^{o}C. The purpose of heating the sampling up to 160^{o}C was to compensate for the loss of temperature during material preparation and transfer to the gyratory mold.
2. The hot material was thoroughly mixed using a mixer (Figure 5.6a), followed by placing the bowl assembly back in the oven and heating to a temperature 160^{o}C.

3. A 150 mm specimen mold was heated to 160^{o}C and a paper disk was placed on the bottom of the mold, followed by placing the heated material into the mold thoroughly. In order to have a specimen with sufficient length for sawing, the mold was filled up to the top. The material was leveled in the mold, followed by placing another paper disk on the top.
4. The mold assembly was placed at the centre of the turntable. A temperature gun was used to ensure that the temperature of the mix in the mold assembly meets the required compaction temperature of 138 ^{o}C $\pm$ 2 ^{o}C.
5. During compaction, a vertical pressure of 600kPa $\pm$ 18kPa was applied to the material while the mold assembly was kept at a gyratory angle of 1.25^{o} $\pm$ 0.02^{o}. Different numbers of gyrations were selected to achieve different levels of compaction producing different quality mixes for Group B samples as described in step 8.
6. The mold was removed once the compaction is completed at the predetermined gyrations and allowed to cool. The compacted specimen was extracted from the mold using the extrusion jack (Figure 5.6b). The compacted specimen was approximately 210mm in height and 150mm in diameter. Care was taken while removing the paper disks and placing the specimen on a flat surface.
7. Steps 1 to 6 were repeated until sufficient amount of specimens at the designed number of gyrations were completed.
8. Each specimen was allowed to cool at room temperature before coring and sawing. As aforementioned, the specimens were divided into Group A and Group B, as shown in Figures 5.7a and 5.7b. Group A specimens consists of six cylindrical specimens of varying lengths from 50, 75, 90, 120, 155, 200 mm. Group A specimens were produced by sawing the original 210 mm specimens compacted at 100 gyrations. Group B specimens included six cylindrical specimens compacted at various gyration levels staring from 40, 60, 80, 100, 120, and 140. The Group B specimens of 100 mm diameter were cored from the center of the 150 mm diameter gyratory compacted cylindrical samples. The ends of the specimens were sawed to provide smooth surfaces perpendicular to the axis of specimens. The average height of Group B specimens was 150mm (Figure 5.7b).

(a) Mixing machine

(b) Superpave Gyratory Compactor

Figure 5.6: Specimen preparation machines

Figure 5.7 (a): Group A specimens for calibration purpose

Figure 5.7 (b): Group B specimen preparation

5.3.2 Calibration of UPV test system

The calibration was achieved by testing standard specimens such as stainless steel and PVC with known pulse velocity. For the purpose of this study, UPV method was selected as the nondestructive testing of cylindrical specimens because it is more effective and suitable for measurements of wave velocities and attenuations when two sides of a test object are accessible (Krautkramer and Krautkramer, 1990).

The experimental setup for UPV testing of a cylindrical specimen is illustrated in Figure 5.8. The instrumentation used in the study consisted of a data acquisition system (section 5.2) and a load cell system.

The contact pressure on the transducer affects the signal amplitude significantly. In order to improve consistency of tests, a constant pressure needs to be maintained on the transducers during all tests. A consistent pressure was obtained using a load cell system which consists of a multimeter (HP 34401 A), a power supply (HP 3620 A), and a load cell (type 20210-100, capacity 100 lb) attached on a frame (Figure 5.8). In this study, a constant pressure of 40 lbs was used and was monitored by the multimeter. The pressure

higher than 40 lbs may limit the transducer sensitivity and even cause damages (Naik and Malhorta, 1991).

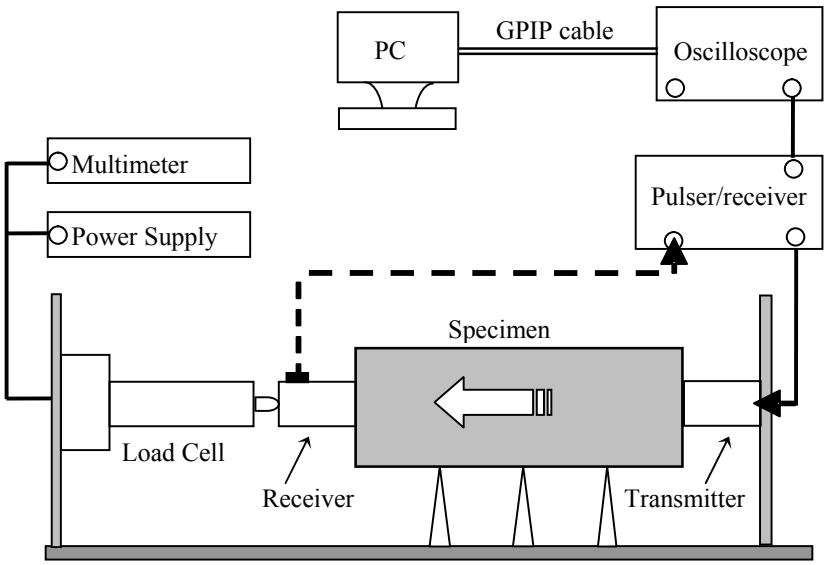

Figure 5.8: UPV testing of a specimen

Coupling technique

The proper contact between the transducer and the specimen surface is critical to minimize variation of impact event or receiver coupling and ensure reliable measurement of wave characteristics. If a transducer is directly pressed on to a test surface, air gaps are formed inevitably because of the surface roughness or irregularities. Since transmission of wave energy at a transducer-to-air interface is almost impossible, the energy allowed to transmit through the contact points between the transducer and the test surface is limited. The ultrasonic measurements will thus become unreliable. In addition, direct contact leads to wear of the transducer, thus adversely affecting economics of measurements. Therefore, it is necessary to prepare a flat and smooth test surface by either sawing or grinding, and employ a medium to fill the air gaps. The medium is known as a couplant. Several materials are commonly used as couplants: water, kerosene, oil, grease, glycerin, petroleum jelly (Krautkramer and Krautkramer, 1990; Hellier et al., 2001). In order to maximize energy transmission, silicone high vacuum grease was used in this study. It was found that the received signal slowly reached its maximum amplitude

as the grease was squeezed out around the transducer by the contact pressure. Therefore, it is preferable to wait for at least 5 minutes before the signal amplitude is measured and recorded. In this study, a coupling setting time of 5 minutes was maintained through out the UPV testings. It was also suggested that for wave velocity measurements, the couplant covering the transducer surface should be as thin as possible (Leong et al., 2004). Increasing the couplant thickness adds to the wave propagation distance, and hence, the travel time. Additionally, in order to have a uniform test result, the amount of couplant applied should be consistent throughout the ultrasonic tests.

Calibration procedure

A typical wave velocity should be constant for the same material, regardless of the dimension of the material. However, in reality, the measured P-wave velocities vary with specimen lengths because of the delay time produced by the transducer characteristics and peripheral electronic equipment used (ASTM D2845-95, Leong et al., 2004). This time delay varies with the type of material to be tested because different materials exhibit various degree of impedance mismatch with the transducers causing erroneous travel time measurement of waves from one end to the other. It is therefore important to calibrate the transducers before UPV testing of any material.

An important step in the calibration is the determination of wave travel time. The travel time (Δt) of a P-wave through a test object is measured as the interval between the pulse and the first rise or fall (arrival) of the time signal, as shown in Figure 5.9. Although the error in determination of the travel times is small ($< 1\ \mu s$), it has significant impact on the accuracy of the wave velocity measurements. The error is caused by the resolution used in identification of wave arrival times, operator's ability to identify the arrival times, and system delay. In this study, the resolution in identification of the arrival times is $0.2\ \mu s$. The calibration of the test system consists of determination of the system delay, followed by subtraction of the delay from the measured travel times. In this study, the system delay was determined by two methods: face-to-face testing of transducers (ASTM D2845-95); and determination of wave travel times for different specimen lengths. In the first method, a transmitter and a receiver were placed in direct contact with each other. The measured

travel time represented the system delay. The second method required the use of standard test blocks (i.e. PVC and Steel blocks) and HMA specimens (group A specimens), as illustrated in Figures 5.10 and 5.7a. The relationship between the measured travel times and the various lengths was examined based on linear regression analysis. The 'y' intercept of the line represents the system delay and the slope gives the P-wave velocity, as will be described in the following section.

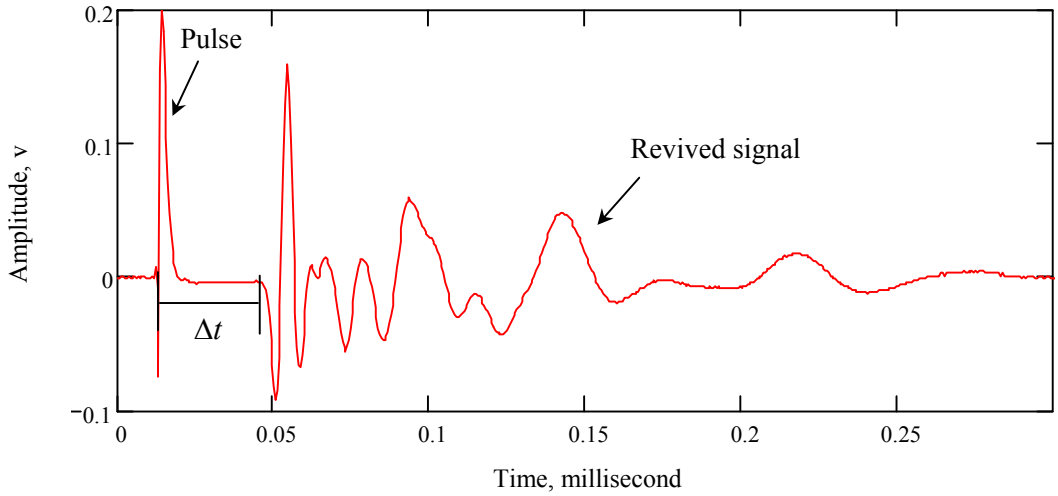

Figure 5.9: Determination of travel time and PTP amplitude from a time signal

Figure 5.10: PVC and steel standard test blocks for calibration

Calibration Test Results

The results of the calibration tests are summarized in Tables 5.3a to 5.3c. As expected, the measured P-wave velocities vary with specimen lengths. This result is attributable to the inherent time delay. For HMA specimens, the standard deviation observed for wave velocities before calibration is $\pm 80 m/s$ (Table 5.6 c).

Table 5.3 (a): Comparison of P-wave velocities of PVC before and after calibration

P-Wave Velocity of PVC (before calibration)				**P-Wave Velocity of PVC (after calibration)**		
Length (m)	**Travel time (μs)**	**V_p (m/s)**	**Difference (%)**	**Calibrated travel time (μs)**	**V_p (m/s)**	**Difference (%)**
0.2009	87.0	2309	0.2	86.9	2313	0.1
0.1503	65.3	2303	0.1	65.1	2307	0.2
0.1011	43.8	2306	0.1	43.7	2313	0.1
0.0510	22.2	2299	0.2	22.1	2312	0.1
Average, μ		**2304**	**0.1**	**Average, μ**	**2311**	**0.1**
Standard Deviation (STDV), σ		**4.2**		**STDV, σ**	**2.7**	
Variation, σ / μ		**0.2%**		**Variation, σ / μ**	**0.1%**	

Table 5.3 (b): Comparison of P-wave velocities of steel before and after calibration

P-Wave Velocity of Steel (before calibration)				**P-Wave Velocity of Steel (after calibration)**		
Length (m)	**Travel time (μs)**	**V_p (m/s)**	**Difference (%)**	**Calibrated travel time (μs)**	**V_p (m/s)**	**Difference (%)**
0.1986	34.8	5707	0.9	34.5	5753	0.0
0.1580	27.7	5696	0.7	27.5	5754	0.0
0.1239	21.8	5683	0.4	21.5	5758	0.1
0.0988	17.5	5652	0.1	17.2	5745	0.2
0.0734	13.1	5612	0.8	12.8	5735	0.3
0.0493	8.8	5596	1.1	8.5	5780	0.5
Average, μ		**5658**	**0.7**	**Average, μ**	**5754**	**0.2**
Standard Deviation (STDV), σ		**45.8**		**STDV, σ**	**15.2**	
Variation, σ / μ		**0.8%**		**Variation, σ / μ**	**0.3%**	

Table 5.3 (c): Comparison of P-wave velocities of HMA before and after calibration

P-Wave Velocity of HMA SP19 (before calibration)				P-Wave Velocity of HMA SP19 (after calibration)		
Length (m)	**Travel time (μs)**	**V_p (m/s)**	**Difference (%)**	**Calibrated travel time (μs)**	**V_p (m/s)**	**Difference (%)**
0.2028	48.0	4225	2.3	48.8	4156	0.4
0.1558	36.1	4316	0.2	36.9	4222	1.2
0.1191	28.0	4254	1.6	28.8	4135	0.9
0.0917	20.9	4392	1.5	21.7	4230	1.4
0.0763	17.6	4325	0.0	18.4	4138	0.8
0.0524	11.8	4437	2.6	12.6	4156	0.4
Average, μ		**4325**	**1.4**	**Average, μ**	**4173**	**0.9**
Standard Deviation (STDV), σ		**80.3**		**STDV, σ**	**42.2**	
Variation, σ / μ		**1.9%**		**Variation, σ / μ**	**1.0%**	

The face-to-face method gave a system delay of 0.236 μs . From the second method as aforementioned, a linear relationship between the measured travel times and the various lengths in each specimen group was obtained, as illustrated in Figure 5.11. Strong correlations ($R^2 \sim 1$) between the wave travel times and specimen lengths for the three materials were observed. The time delay is given by the 'y' intercepts which varies with the type of material used as described previously. For example, the estimated intercept value of - 0.7998 μs for HMA 19 mix is considered the system delay for this mix which is different from 0.236 μs estimated from fact-to-face testing. After subtraction of the system delay, the standard deviation for the P-Wave velocity is almost reduced by 50% as seen in Table 5.3c.

Alternatively, the P-wave velocity for each group of specimens was computed using the corresponding slope of the travel times – specimen lengths plots (Figure 5.11). The results are summarized in Table 5.4 showing that the velocities given by the slopes agree well with the average velocities obtained after calibration of the system delay (Table 5.4).

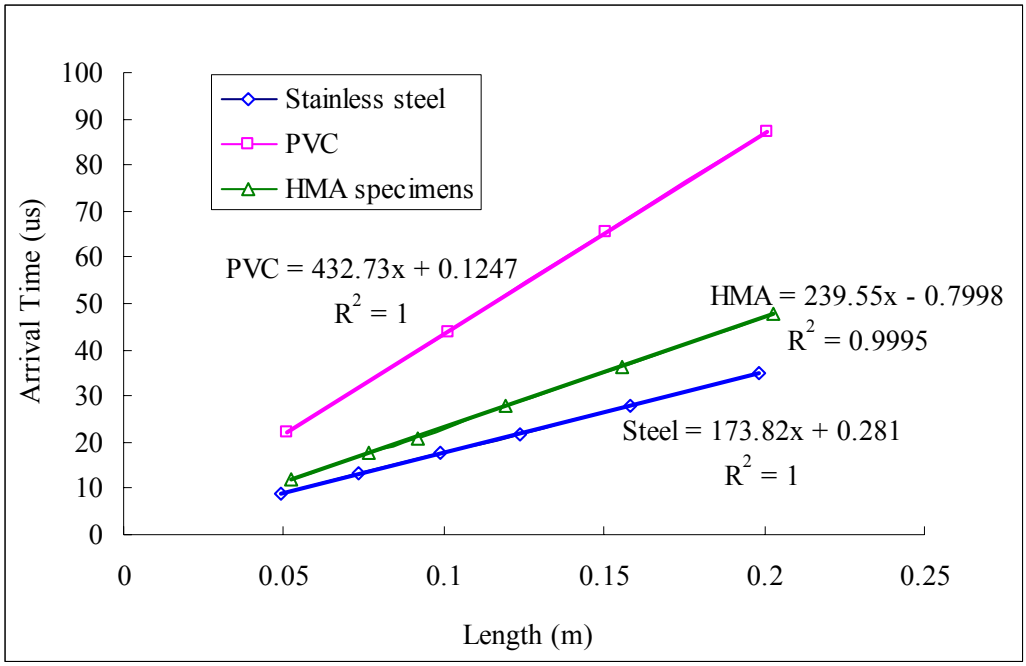

Figure 5.11: P-wave calibration using 1MHz transducer

Table 5.4: Results of V_P calculated using the slopes of time-length plots (Figure 5.11)

Material	**System delay (μs)**	**Observed P-wave velocity (m/s)**	**Typical P-wave velocity (m/s)** (ASTM E494 – 95)
Transducers (face-to-face)	0.236	N/A	N/A
Standard PVC	0.1247	$\frac{1}{432.73\times10^{-6}} = 2310.9$	2300
Standard Steel	0.281	$\frac{1}{173.82\times10^{-6}} = 5753.1$	5790
HMA SP19	- 0.7998	$\frac{1}{239.55\times10^{-6}} = 4174.5$	N/A

5.3.3 Material characterization using UPV testing

Group B specimens at different gyration levels were the specimens of interest in this step. The actual instrumentation setup for the UPV testing is illustrated in Figure 5.12. Repeated pulses from the pulser/receiver were transmitted into one side of a specimen by a transducer. These pulses propagating through the specimen were affected by the elastic properties and internal flaws before being received by the receiver on the opposite side of the specimen. The travel time of P-wave was measured and used to compute P-wave velocity and moduli of elasticity of the specimen. The signal waveform displayed in the oscilloscope was further processed and analyzed in both time and frequency domain to measure wave attenuation parameters.

Figure 5.12: Ultrasonic pulse velocity (UPV) test setup

Wave characteristics obtained in time domain

Each measured travel time was calibrated by subtracting the system delay associated with the HMA material. The P-wave velocity for each specimen was calculated as the specimen thickness divided by the corresponding calibrated travel time. The moduli of elasticity for each specimen, i.e. Constrained and Young's moduli, were then calculated based on the corresponding P-wave velocity, measured specific density and the Poisson's

ratio which was assumed to be 0.313 based on the predetermined S-wave velocity. Comparison of the P-wave velocities or elastic moduli of the six specimens will provide a basis for evaluation the condition of the specimens tested.

Another measurable variable is known as the peak-to-peak (PTP) amplitude of the first arrival (Chapter 3). It was measured as the difference between the positive and the negative peak values of the first arrival of the signal. The PTP amplitude could be used as an indicator of the quality of the specimen. The higher the PTP value the better the quality of the mix used in the specimen.

Wave characteristics obtained in frequency domain

The recorded time domain signals were Fourier transformed into frequency domain for the assessment of the frequency content of the entire signals (Chapter 3). In a direct travel time signal record, a wave traveling along the stiffest and shortest possible part inside a specimen appear as the first arriving wave. Following the first arrival are considerable ultrasonic scatterings and reflections from boundaries, as illustrated in Figure 5.13a. In order to eliminate the unwanted waves, the contribution of only the first arriving wave was isolated by a time window (Equation 3.12) of suitable width and Fourier transformed into frequency domain (Figures 5.13a and 5.13c). The Fourier representation of the windowed portion allows for determination of maximum amplitude and area of the frequency spectrum which are two additional indicators of wave energy (Chapter 3).

Results and discussion

The received time signals for Group B specimens are shown in Figure 5.13a. The wave travel time Δt in each signal was measured to calculate the P-wave velocity for the corresponding specimen.

The amplitude of the frequency contents of the full signals from six specimens is shown in Figure 5.13b. Almost zero amplitude is observed at frequencies beyond 200 kHz. This confirms that high frequency components have been attenuated when traveling though a medium made of complex network of aggregates and air voids (Chapter 2).

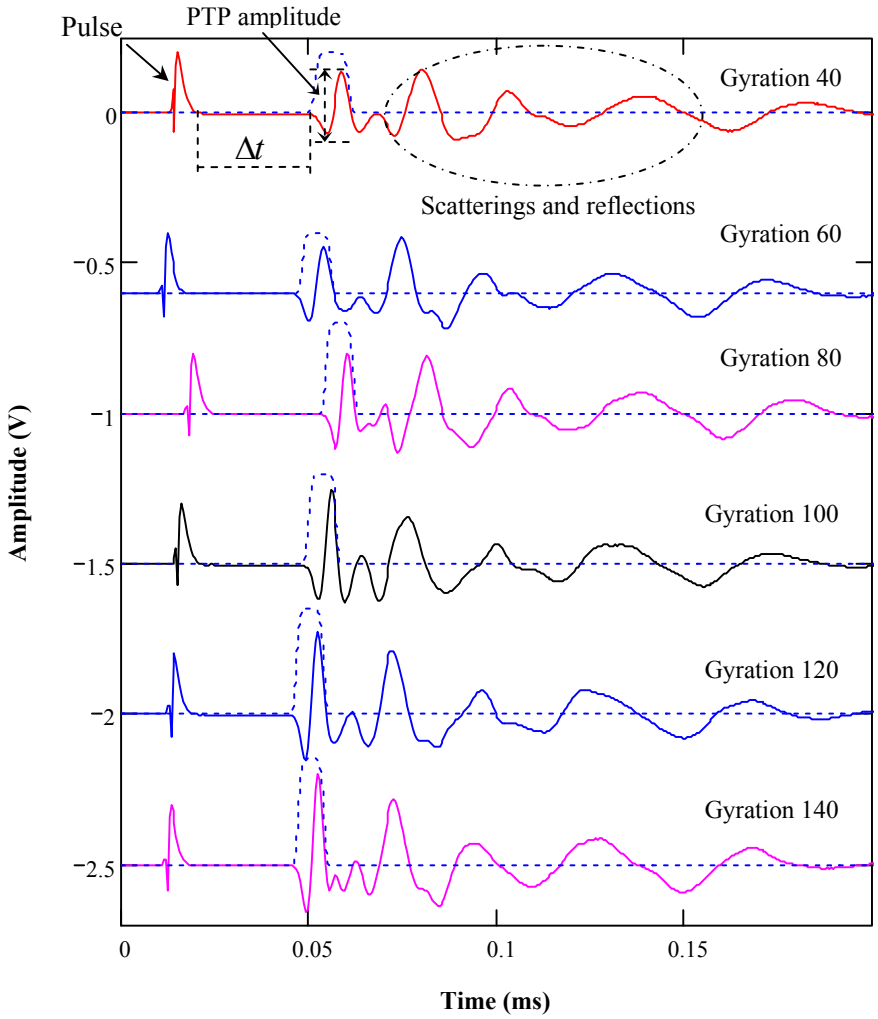

Figure 5.13 (a): Received time signals for the specimens at the six gyration levels

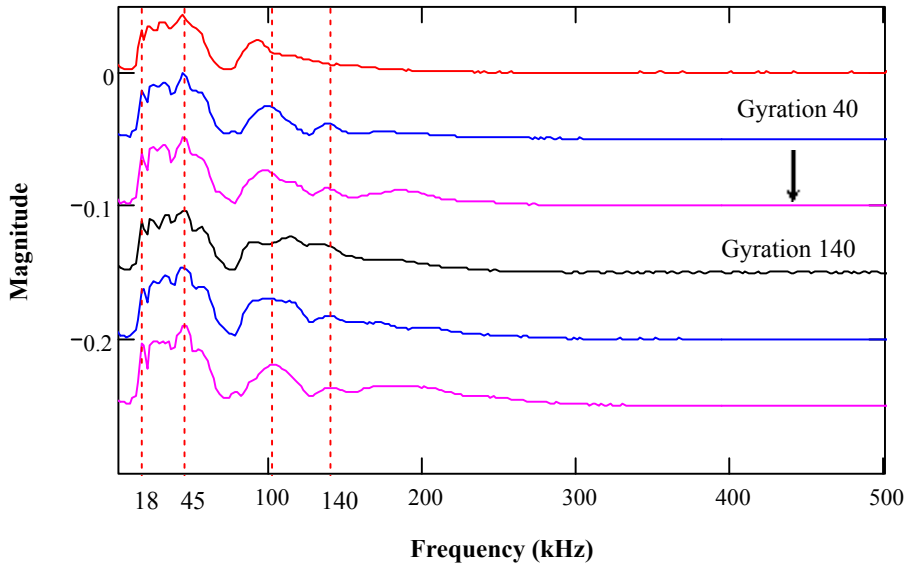

Figure 5.13 (b): Frequency spectra of the full signals for the specimens at the six gyration levels

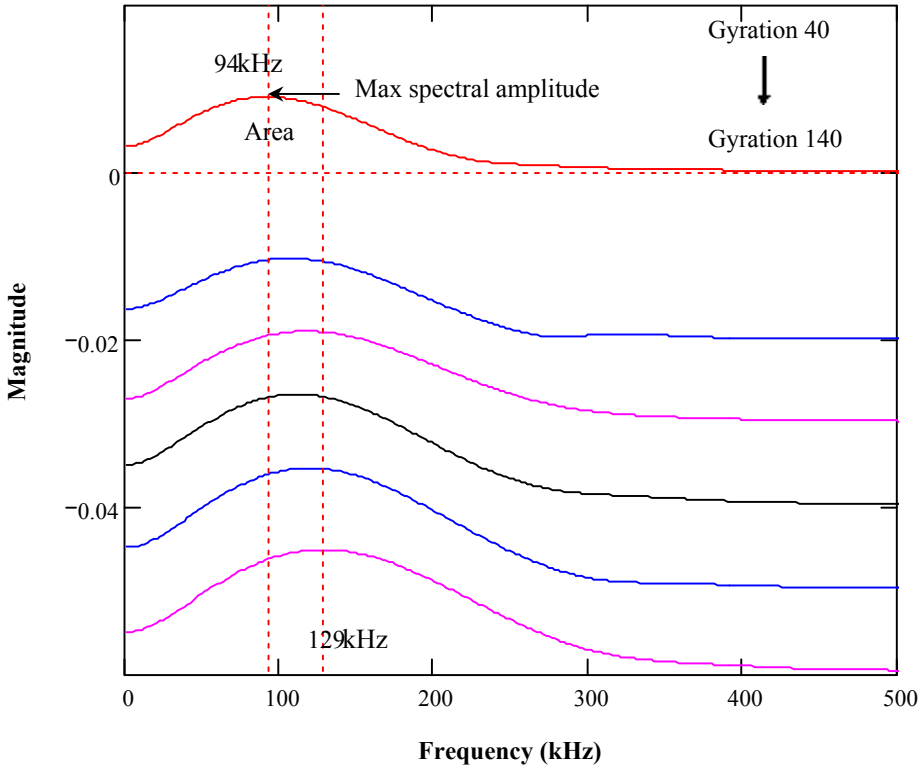

Figure 5.13 (c): Frequency spectra of the windowed signals

Relationship between wave characteristics and gyration levels

Five wave characteristics: wave velocity, peak to peak amplitude in time domain, dominant frequencies of the first arrivals, maximum magnitude, and areas of frequency spectra for the first arrivals (Figure 5.13c) were used to evaluate the quality of the mix. The geometric attenuation is proportional to the specimen length. In this case, although attempts were made to prepare specimens of equal lengths, small differences in the specimen lengths were noticed because of errors associated with saw cutting. Therefore, geometric attenuation had been calibrated to specimen length to ensure that observed difference in attenuation for different specimens is only attributed to the material properties of the medium through which the wave traveled. Hence, the material attenuation/damping can be considered the only factor causing the change in amplitude of the first arrivals.

As a first step, the relationships between wave characteristics and gyration levels were examined and the results are shown in Figure 5.14. The results indicate strong correlations ($R^2 = 0.99$) between the number of gyrations and the wave characteristics in terms of peak to peak amplitude, the spectral area, and the magnitude. This observation strongly supports the concept that seismic wave technique has the potential for assessing the integrity of the HMA material in terms of their wave characteristics. The observed velocities are almost the same for all the specimens (Figure 5.14). This appears to support the previous findings that the wave velocity of seismic waves may not be adequate enough to assess the quality of different HMA mixtures (Malhotra and Carette, 1980; Schickert, 1984; Sturrup et al., 1984; Galan, 1990; Krautkramer and Krautkramer, 1990; Popovics and Popovics, 1990; Popovics and Popovics, 1992; Popovics and Rose, 1994; Witczak et al., 2002).

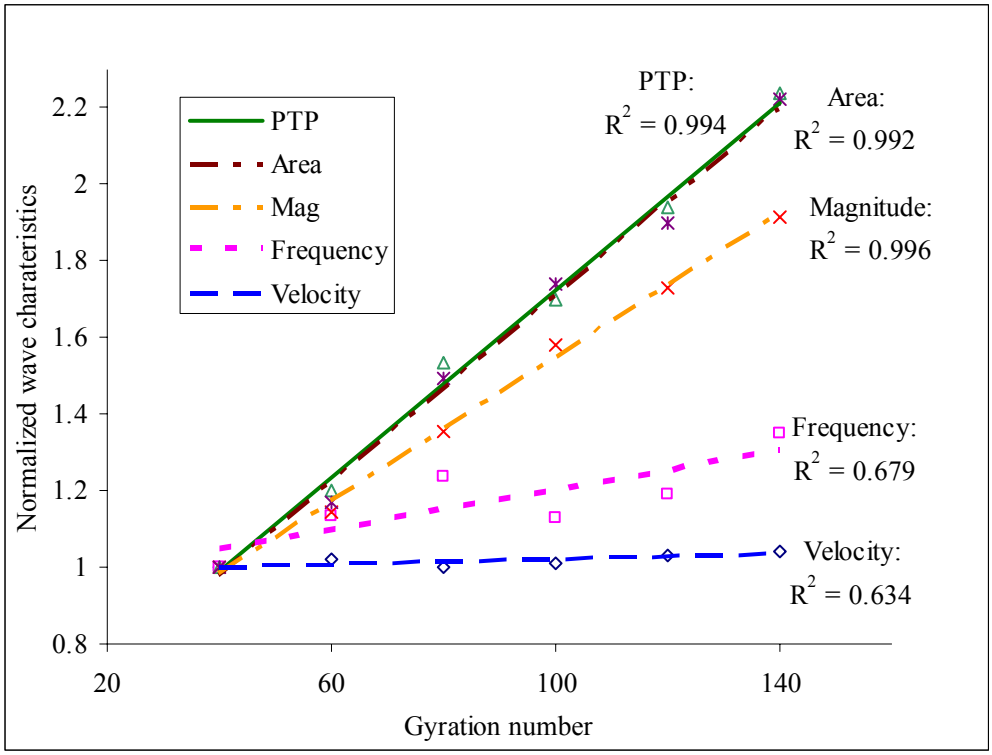

Figure 5.14: Wave characteristics vs. gyration number

(Note: velocity is normalized to 4318m/s, frequency to 93.75 kHz, magnitude to 0.096, spectral area to 1.435, and PTP to 1.2**)**

Compared to the other wave characteristics, the dominant frequencies of the first arriving waves showed a moderate correlation with the number of gyrations (Figure 5.14). It is implied that frequency content may not be sensitive to evaluating the mix quality determine in terms gyration. However, this may be useful for evaluating a specific type of pavement failure, such as permanent deformation due to creep, as discussed later. For the purpose of assessing the general pavement condition, any one of the three characteristics, peak to peak to amplitude, the spectral area, and the magnitude of frequency spectrum will be adequate. The selection of a suitable parameter from the three wave characteristics will depend on which one will be efficient to measure in the field in terms of computation time and equipment without compromising the accuracy. The peak to peak amplitude (PTP) is seemingly more suitable for field application as it can be monitored and measured in time domain on site without extensive mathematical computation.

The constraint elastic modulus (M) has been used in seismic wave analysis. It was computed from the wave velocity ($M = \rho \cdot V_P^2$) for the mixes compacted with different gyrations. The relationship of this parameter with gyrations is shown in Figure 5.15. The correlation of the constraint modulus with gyration levels is 0.75. This correlation is slightly better than the correlation observed for the velocity but not as strong as observed for the other wave characteristics. The slight improvement in comparison to velocity is probably attributed to the effect of density used in the equation to calculate M which increases with the number of gyrations.

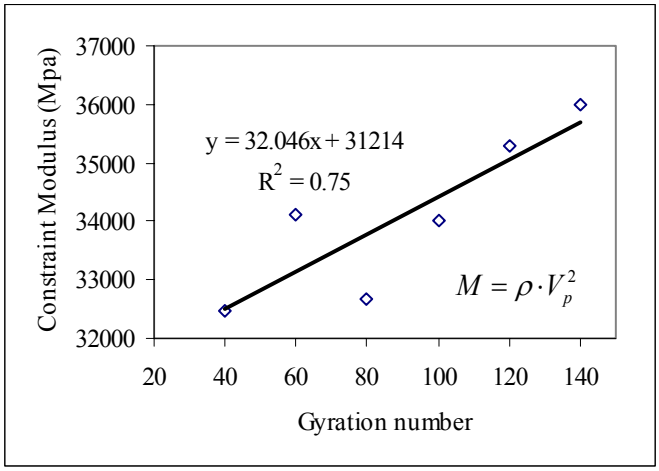

Figure 5.15: Constraint modulus (M) vs. gyration levels

In summary, wave characteristics are sensitive to the number of gyrations that are a measure of mix quality. This is because as the number of gyrations increases the inter-particle contacts and bonding strength increases, producing a stiffer specimen. It is expected that the wave attenuation is minimized if there is a good bonding at the aggregate-asphalt interface to ensure continuous medium for waves traveling. This is a useful and important finding because it demonstrates that wave characteristics can be used as quality indicators of asphaltic concrete mix. However, this needs further validation by studying the relationship of wave characteristics with a fundamental property such as dynamic modulus that is an objective and reliable measure of the mix quality. The relationship between the wave characteristic and density that is commonly

used to measure quality was also examined. Associated data processing for computation of wave characteristics is presented in Appendix A.

5.3.4 Relationship between wave characteristics and mix quality

Group B specimens were used to determine the potential correlation between the wave characteristics and mix quality that is measured in terms of density and dynamic modulus. The following sections describe the procedures used to determine the bulk density and dynamic modulus of HMA.

Bulk density measurements

After coring and sawing, group B specimens were allowed to dry overnight to a constant temperature in the oven at 52 $\pm$ 3^{o}C, followed by cooling down to room temperature at 25 $\pm$ 5^{o}C. The bulk densities of the specimens were measured using the following equation (ASTM D2726):

$$Bulk\ \ specific\ \ gravity = \frac{A}{B - C} \tag{5.1}$$

where A is the mass in grams of the dry specimen in air, B is the mass in grams of the surface-dry specimen in air, and C is the mass in grams of the specimen in water. This method was considered suitable because the specimen surfaces were polished.

Relationship between bulk densities and gyration levels

The bulk densities obtained from Group B specimens at the different gyration levels are tabulated in Table 5.5. The correlation between specimen densities and the gyration levels is illustrated in Figure 5.16. A moderate correlation (R^2 = 0.79) was observed. In some cases, lower gyrations (e.g. at 100 and 120) produced a higher density than the value obtained at higher gyrations (e.g. at 140) for the same mix (Figure 5.16). This unusual result could be attributed to aggregate segregation while sampling from different batches and temperature drop during compaction. This condition typically occurs in the field during placement of mix. Hence, density is not always a good indicator of

workmanship. It is implied that a suitable parameter in addition to the density is needed for quality assurance of HMA mixes. Consequently, dynamic modulus test was recommended by FWHA for use as a performance based test to assess the quality of asphalt concrete mix.

Table 5.5: Density measurements of group B specimens

Gyration	Mass of Dry Specimen in Air, A, g	Mass of Saturated Surface Dry Specimen in Air, B, g	Mass of Specimen in Water, C, g	Bulk Specific Gravity = A/ (B-C)	Density kg/m^3
40	2742.0	2746.4	1623.3	2.442	2434.2
60	2737.0	2741.4	1630.2	2.463	2455.7
80	2730.0	2733.3	1623.3	2.459	2452.1
100	2672.6	2676.8	1606.1	2.496	2488.6
120	2631.5	2633.4	1582.9	2.505	2497.4
140	2739.0	2742.1	1641.5	2.489	2481.2

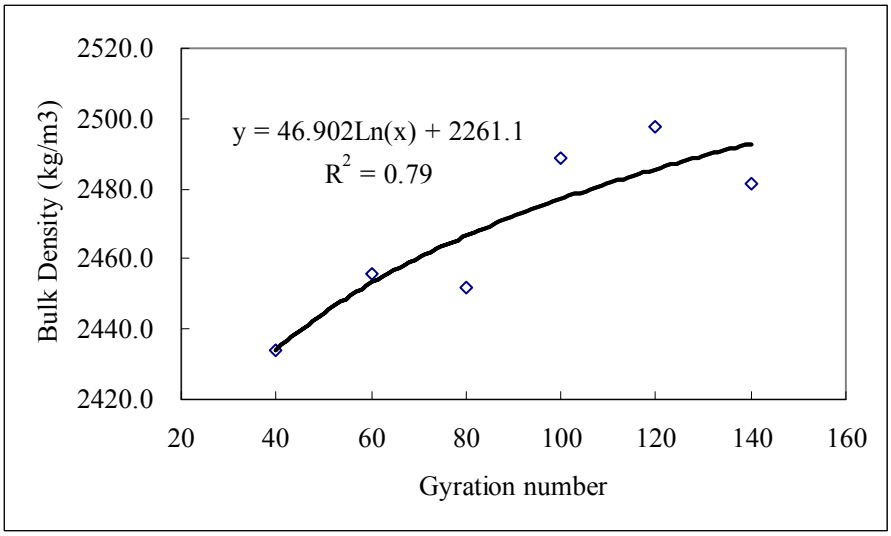

Figure 5.16: Specimen density vs. gyration levels

Dynamic modulus test

The dynamic modulus test is a part of Superpave test protocols based on Simple Performance Tests (SPT) that include the use of dynamic modulus values as a performance criterion of the asphalt mix. This test is expected to identify inferior HMA

mixtures (i.e., must determine a mix's relative susceptibility to excessive distortion or fracture or both under defined conditions) and not necessarily predict the entire performance history.

The dynamic modulus test is the oldest and one of the best compression tests for Hot Mix Asphalt (HMA) characterization because of its ability to provide reliable, full characterization of the mix over a wide range of temperatures and cyclic loading frequencies (Witczak et al., 2002). This test method was standardized for dynamic modulus testing of asphalt concrete mixtures (ASTM D3497, 1979). The dynamic modulus test applies a sinusoidal (harversine) axial compressive stress to an asphalt concrete specimen at a given temperature and loading frequency. Measurements of the applied stress and the resulting recoverable axial strain response of the specimen allow for calculation of the dynamic modulus. The values of dynamic modulus can be utilized as a measure of asphalt concrete mix quality.

The loading frequencies and the test temperatures depend on the purpose of the test. For example, the procedure uses a sinusoidal (haversine) compressive axle load for a duration of 0.1 seconds with a rest period of 0.9 seconds at a single test temperature at which the mix is susceptible to permanent deformation in the field. The test temperatures are selected by the designer based on measurements of seasonal temperatures through out the year for specific site conditions. In addition, an effective pavement temperature and a design loading frequency are selected by the designer for assessing the fatigue cracking resistance of the asphalt concrete mix. The effective pavement temperature in this case covers approximately the temperature range of 4 ^{o}C to 21 ^{o}C and the design frequency covers the range between 5 to 25 Hz.

The relationship between stress and strain for a linear viscoelastic material is defined by a complex number known as the complex modulus (E^*). The real and imaginary components of the complex modulus are given by:

$$E^* = E' + iE'' \tag{5.2}$$

where E' is the storage or elastic component that contributes to recovery of deformation; while E'' is the loss or viscous component that contributes to permanent deformation. The strain ε_o lags behind the stress σ_o by an angle, known as the phase angle (N) indicating the viscous properties of the material. For a pure elastic material, N = 0, and the complex modulus E^* is equal to the absolute value or dynamic modulus. For a pure viscous material, N = 90^o.

The magnitude of the dynamic modulus (| E^*|) is calculated as the maximum stress (σ_o) divided by the recoverable axial strain (ε_o):

$$\left|E^*\right| = \frac{\sigma_o}{\varepsilon_o} \tag{5.3}$$

For the dynamic modulus testing, six mounting studs were attached to each specimen in Group B with epoxy cement using suitable alignment and spacing fixture, as shown in Figure 5.17. The finished stud arrays should be 120^{o}C apart. These stud arrays were intended for mounting of the linear variable differential transformers (LVDT) to monitor the axial deformation of the specimen under cyclic loading.

Figure 5.17: Specimens for dynamic modulus test

The dynamic modulus tests were conducted using the Interlaken integrated asphalt test system as shown in Figure 5.18. The test system is fully controllable by a computer using the UniTest software. The dynamic modulus tests were carried out at loading frequencies in sequence 25, 10, 5, 1.0, 0.5, and 0.1Hz at each selected temperature. The number of cycles corresponding to each loading frequency is summarized in Table 5.6. The axial load was applied to the specimen via a loading ram (Figure 5.6). The applied load was measured by an electronic load cell connected to the specimen cap, while the resulting recoverable axial strain response of the specimen was monitored by the LVDTs mounted on the specimen. These LVDTs allow for determination of dynamic behavior of the specimen during cyclic loading. The dynamic modulus was automatically calculated by the Software as the output.

Figure 5.18: Dynamic modulus test setup

Table 5.6: Number of Cycles for the Test Sequence (ASTM D3497)

Loading Frequency (Hz)	Number of Loading Cycles
25	200
10	200
5	100
1	20
0.5	15
0.1	15

Relationship between Dynamic moduli and gyration levels

The dynamic moduli obtained from Group B specimens at different gyration levels are shown in Table 5.7 and Figure 5.19. The response of the mix to the dynamic loads at varying frequencies is non-linear (Figure 5.19) because of the relatively large strain level (10^{-4}). The relationship between the number of gyrations and the dynamic moduli was examined by linear regression, as shown in Figure 5.20. The dynamic modulus at 25 Hz showed an excellent correlation (R^2 = 0.98) with the number of gyrations. Good correlations (R^2 > 0.87) exist when the dynamic modulus was measured under other cyclic loading frequencies (10 Hz, 5 Hz, 1Hz, 0.5Hz, and 0.1Hz).

Table 5.7: Dynamic moduli of HMA specimens at different gyrations

Description	Gyration number					
	40	**60**	**80**	**100**	**120**	**140**
***E* at 25Hz, MPa**	8110.1	9147.3	9878.6	10204.6	11027.3	11622.6
***E* at 10Hz, MPa**	6360.2	7349.6	8185.3	8258.7	9092.3	9689.8
***E* at 5Hz, MPa**	5151.4	6069.3	6898.2	6868.3	7658.1	8290.3
***E* at 1Hz, MPa**	2967.2	3677.8	4358.7	4162.2	4781.9	5391.7
***E* at 0.5Hz, MPa**	2274.8	2903.3	3496.7	3258.0	3797.3	4382.0
***E* at 0.1Hz, MPa**	1345.6	1680.6	2006.1	1805.0	2187.6	2611.7

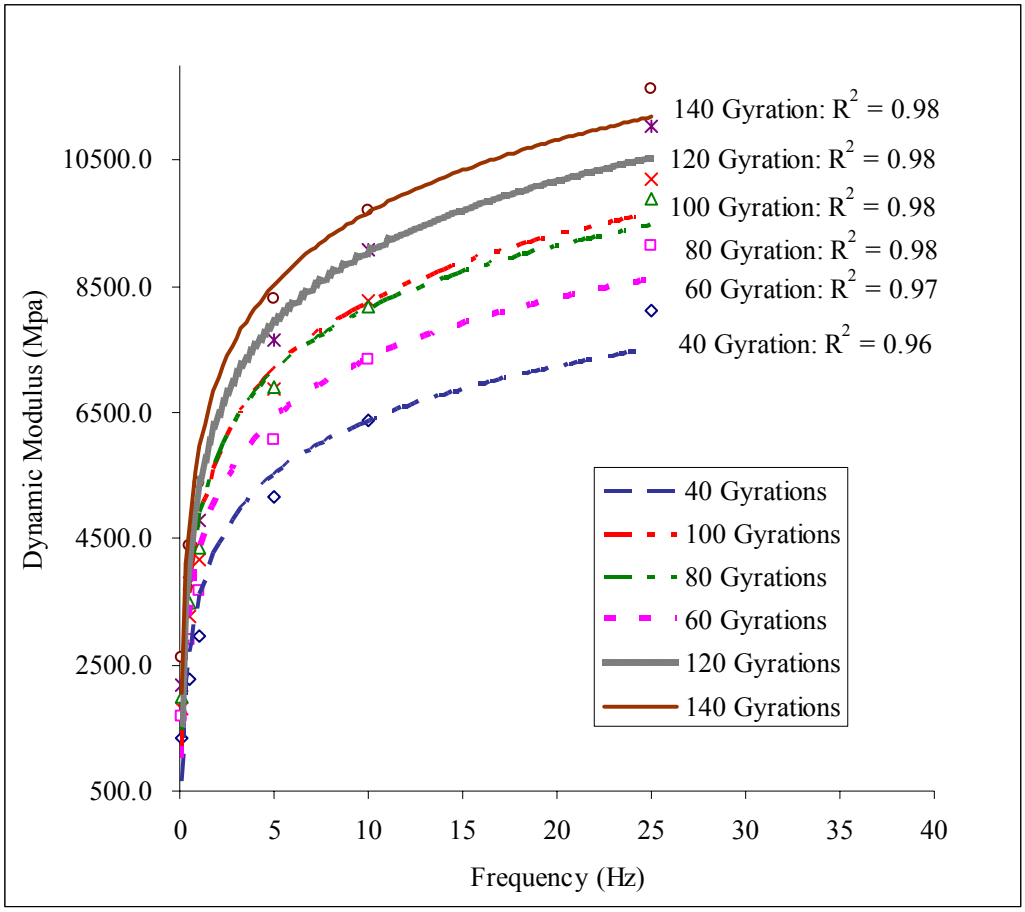

Figure 5.19: Dynamic moduli results (25 to 0.1Hz loading frequency)

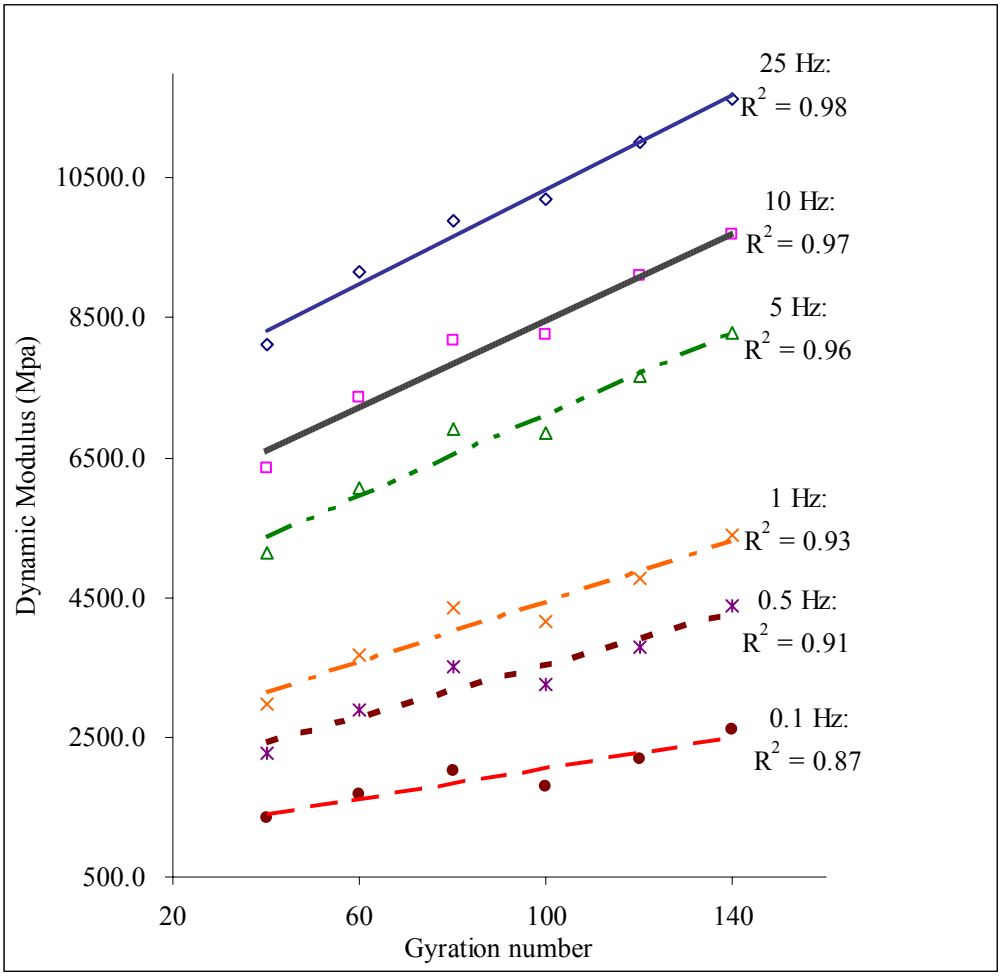

Figure 5.20: Dynamic moduli (25 to 0.1Hz loading frequency) vs. gyration number

Relationship between dynamic moduli and specimen densities

The correlations between dynamic moduli and specimen densities are illustrated in Figure 5.21. The moderate correlation support the previous observation that density measurements may not be sufficient to ensure good bonding between asphalt and aggregate to improve resistance to fatigue cracking.

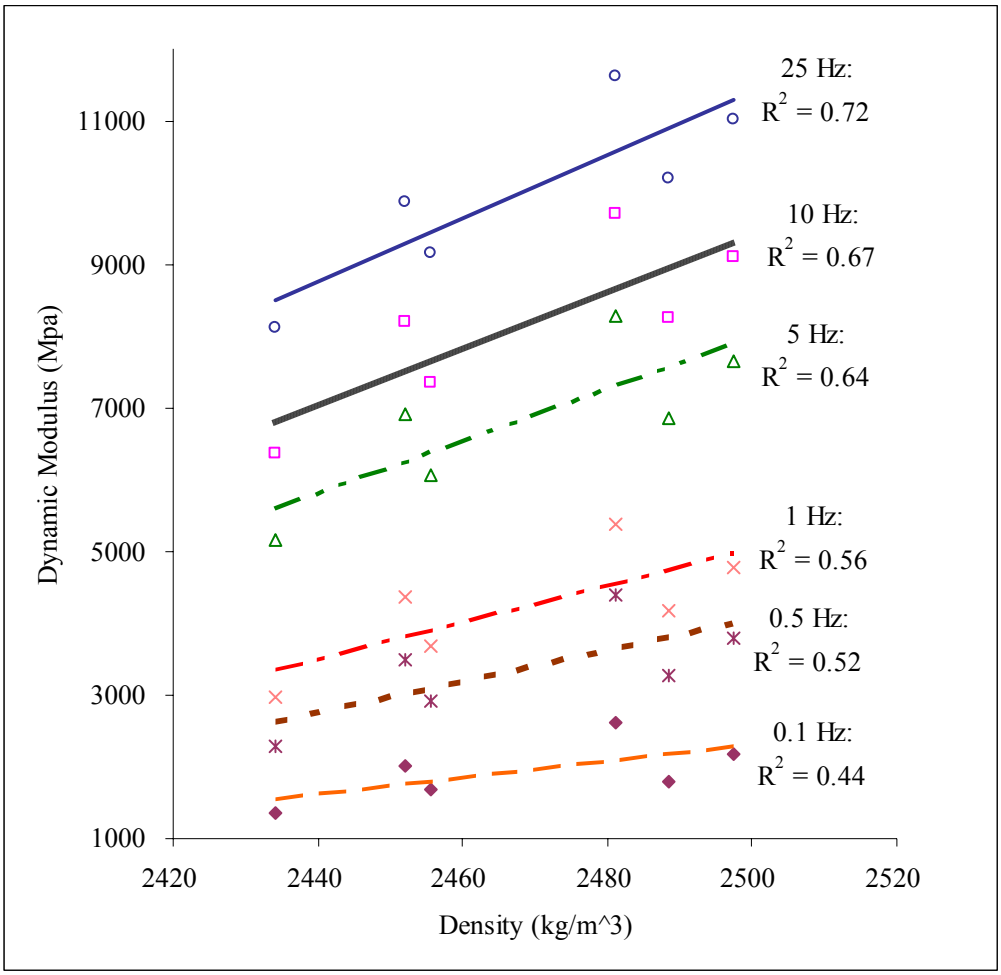

Figure 5.21: Dynamic moduli (25 to 0.1Hz loading frequency) vs. specimen densities

Relationship between wave characteristics and density

The correlations between the five wave characteristics and specimen densities are shown in Figure 5.22. The observed correlations with PTP, magnitude and area of spectrum are moderate, while the correlations with the velocity and frequency are less than moderate. This is expected because that density does not always reflect mix quality in terms of bonding between asphalt binder and the aggregates as aforementioned.

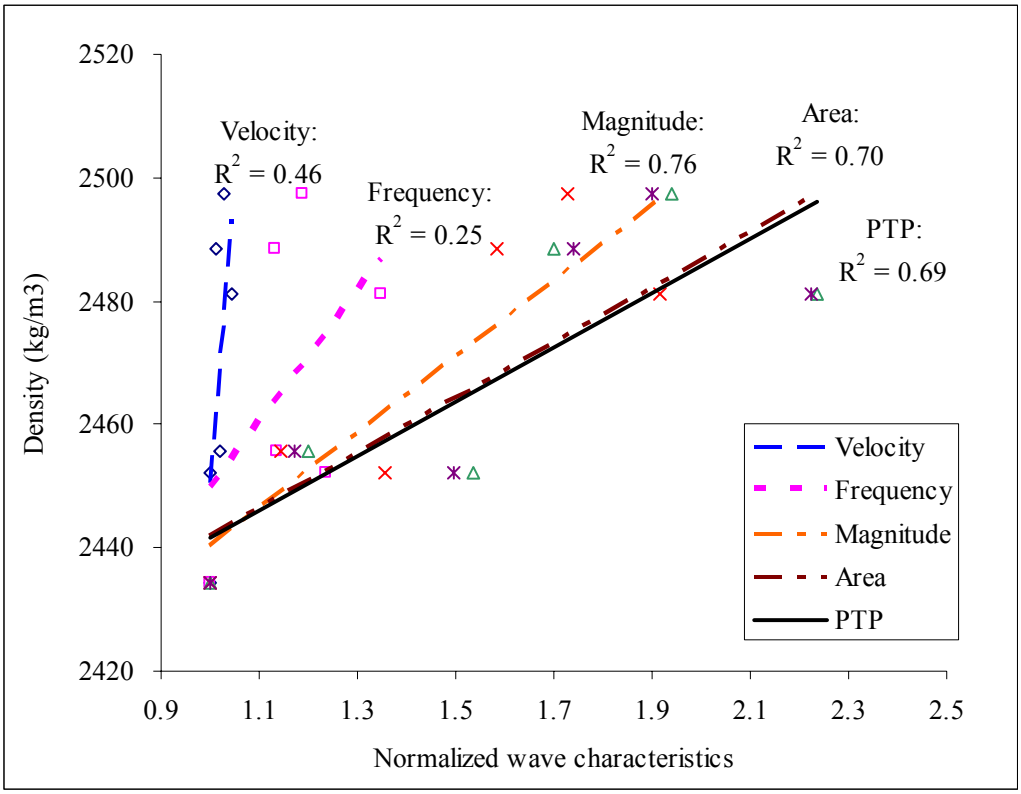

Figure 5.22: Wave characteristics vs. specimen densities (Note: velocity is normalized to 4318m/s, frequency to 93.75 kHz, magnitude to 0.096, spectral area to 1.435, and PTP to 1.2)

Relationship between wave characteristics and Dynamic modulus

The dynamic moduli were computed at different frequencies at room temperature. The selection of frequency depends on the type of truck loading of interest starting from fast moving traffic to slow moving traffic. The correlations between the dynamic moduli (at 25 Hz, 10 Hz, 5 Hz, 1Hz 0.5 Hz, and 0.1 Hz) and the PTP amplitude were examined, as shown in Figure 5.23. The PTP amplitude showed excellent correlations ($R^2 > 0.9$) with the dynamic moduli at the six loading frequencies. The correlation coefficients of the other wave characteristics with dynamic moduli at the six loading frequencies are summarized in Table 5.8. The corresponding figures showing the relationships of other wave characteristics with dynamic moduli at 0.1 to 25Hz loading frequencies are presented in Appendix B.

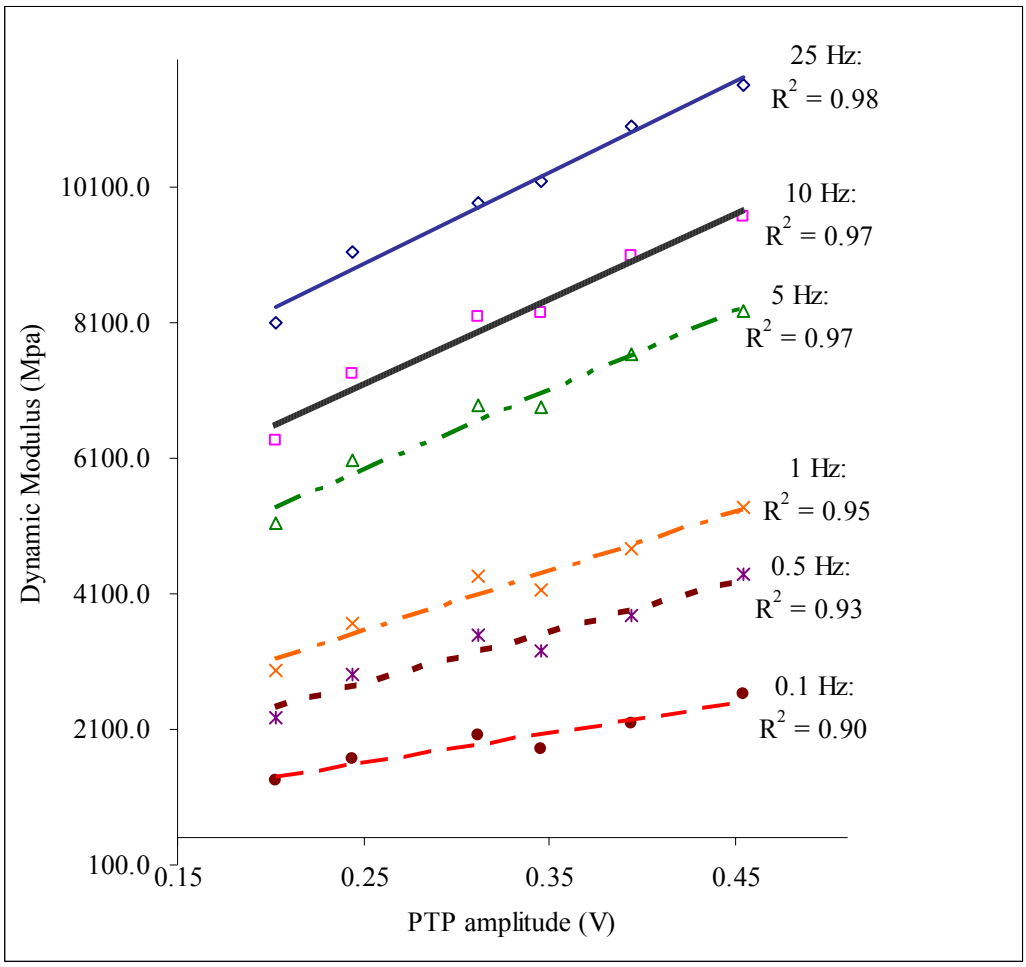

Figure 5.23: Dynamic moduli vs. PTP Amplitude

Table 5.8: Correlation coefficients for dynamic moduli vs. wave characteristics

Correlation coefficient	Wave characteristics				
	Velocity	**Frequency**	**PTP**	**Magnitude**	**Area**
at 25Hz loading	0.62	0.76	0.98	0.97	0.97
at 10Hz loading	0.59	0.80	0.97	0.95	0.95
at 5Hz loading	0.58	0.83	0.97	0.94	0.95
at 1Hz loading	0.57	0.88	0.95	0.90	0.92
at 0.5Hz loading	0.57	0.91	0.93	0.88	0.90
at 0.1Hz loading	0.61	0.92	0.90	0.84	0.87

Table 5.8 shows that the highest correlations ($R^2 > 0.9$) were between the dynamic modulus at 25 Hz and wave characteristics in terms of PTP, magnitude and spectrum area. This loading frequency corresponds to a pavement response under fast moving traffic that contributes to fatigue cracking under dynamic loading. The wave velocities showed moderate correlations with the dynamic moduli, which are similar to what was observed with gyrations as well. The possible reason is that the first arriving wave in UPV tests measures the dynamic stiffness at low strain levels ($< 10^{-6}$) and high frequencies (100 kHz); whereas, dynamic modulus test is performed at low frequencies (< 25 Hz) and larger strain levels (0.8 to 1.2 x 10^{-4}).

Slow moving traffic contributes to rutting at high temperature which corresponds to low loading frequency (e.g. 0.1 Hz). The dynamic moduli measured at 0.1 and 0.5 Hz showed excellent correlations with dominant frequencies of the first arriving P-waves (Table 5.8). This result implies that frequency contents of waves can be used to assess pavement failure caused by creep at slow moving traffic.

The correlations between the constraint moduli for the six specimens and the dynamic moduli at the six loading frequencies are illustrated in Figure 5.25. The constraint moduli are significantly larger because of the small strain level ($< 10^{-6}$) compared to that of dynamic moduli ($> 10^{-4}$). The moderate correlation was observed (Figure 5.25) also because of the difference in strain levels.

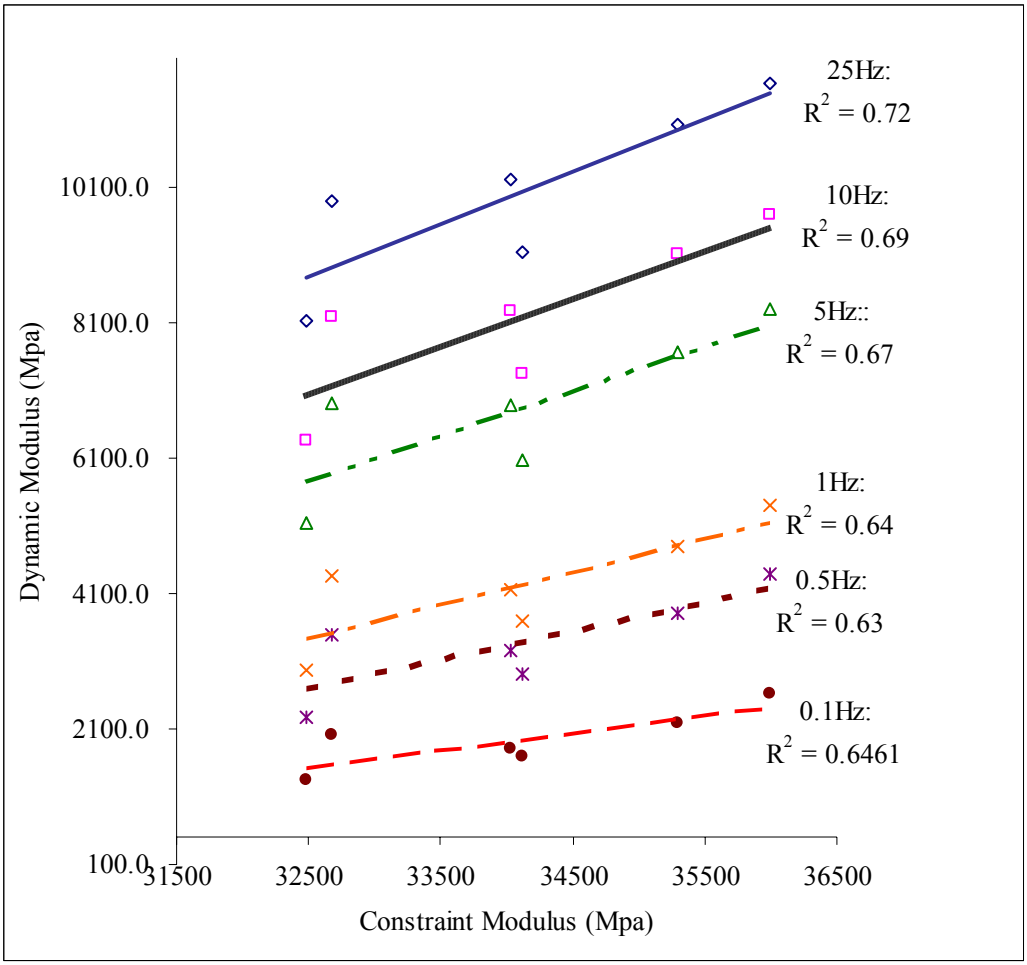

Figure 5.24: Dynamic moduli vs. constraint moduli

5.4 Summary

The main objective of the experimental program is described in this Chapter. The experiments of Phase I are the key topics covered by this chapter. The four major experiments involved in Phase I are calibration of UPV test system, UPV testing of the asphalt concrete mix, Bulk density measurements, and the dynamic modulus test. The detailed procedure of each test is described. Efficient signal processing techniques for obtaining wave characteristics from output signals are described. This chapter also provides experimental results from each test. The correlation among wave characteristics, density, dynamic modulus, and the number of gyrations were examined. The results showed strong relationship ($R^2 > 0.9$) between the wave characteristics (particularly the peak to peak amplitude) and the fundamental property of the mix. The strong correlation indicates the potential application of seismic wave techniques for pavement condition assessment. It is revealed that the wave attenuation is minimized if there is a good bonding at the aggregate-asphalt interface to ensure continuous medium of travel. This finding is very critical to moving forward the technology in the right direction. The observations provided in the chapter form an important basis for the experiments of Phase II.

CHAPTER 6
CONDITION ASSESSMENT OF LONGITUDINAL JOINTS IN ASPHALT PAVEMENTS SLAB TESTS: PHASE II

6.1 Introduction

The construction of asphalt pavements with good quality longitudinal joints between adjacent lanes enhances their long-term performance. Poor-quality longitudinal construction joints permit the seepage of water causing further deterioration by raveling of the hot mix asphalt (HMA). Previous research has shown that HMA is poorly compacted at the joints compared to the adjoining mat (Kilpatrick et al., 1967; Foster et al., 1969); thus, the longitudinal joint area is structurally inadequate to withstand repeated traffic load and traffic abrasion.

Traditionally, the quality of joints is evaluated in terms of achieving adequate density at the joints between adjacent and paving lanes. This evaluation is done by comparing the in-situ density obtained through pavement cores at five locations across the longitudinal joint of the pavement (typically at the centerline, 150 mm, and 450 mm on either side of the centerline). In general, good compaction at joints provides good bonding between the two adjacent pavement layers leading to good performance. The HMA density is currently used as a good indicator of the condition of the longitudinal joints. However, current density measurements are destructive and time consuming. Therefore, there is a need to develop a suitable nondestructive test (NDT) for evaluating the quality of longitudinal construction joints in asphalt pavements. Nondestructive testing techniques reduce the damage associated with coring and provide a more uniform condition assessment of the longitudinal joints.

Wave-based techniques were successfully used in testing asphalt specimens in Phase I experiments (Chapter 5, NDT testing of asphalt briquettes). The mix quality was

evaluated in terms of the PTP amplitude in time domain, maximum spectral magnitude, and spectrum area in the frequency domain. Experiments in Phase II are intended to examine the effectiveness of using the wave characteristics identified in the experiments of Phase I to assess the condition of longitudinal joints. The ultrasonic testing of three asphalt concrete slabs was performed in the laboratory. The purpose of these experiments is to develop a suitable field test procedure for the condition assessment of the longitudinal construction joints in asphalt pavements.

The first slab was fabricated in an effort to reproduce a good-quality joint. However, good bonding at the joint was not completely achieved because of the poor compaction technique used. Therefore, the second slab was fabricated using a different compaction procedure. The compaction procedure used in the fabrication of the third slab was modified to achieve a week-quality joint.

6.2 Instrumentation and Fabrication of Pavement Slab 1

The instrumentation used for the ultrasonic testing of the HMA slab 1 is schematically illustrated in Figure 6.1. Two identical transducers (Panametrics V102, 1 MHz, 2.5 cm diameter) were used as the pulse sources, whereas a miniature accelerometer (PCB 353B65, linear response up to 25 kHz, $\pm 3dB$ tolerance, resonant frequency > 40 kHz, sensitivity 100 mV/g) was used as the receiver. The transducers were driven by a pulser/receiver (Panametrics 5052PR), while the accelerometer was driven by a power supply (PCB 483A). The measured signals were amplified and filtered by a 200 kHz low-pass filter (Krohn-Hite 3384) before being displayed on the digital oscilloscope (HP 54610B). The signals were recorded in a desktop computer for further analysis.

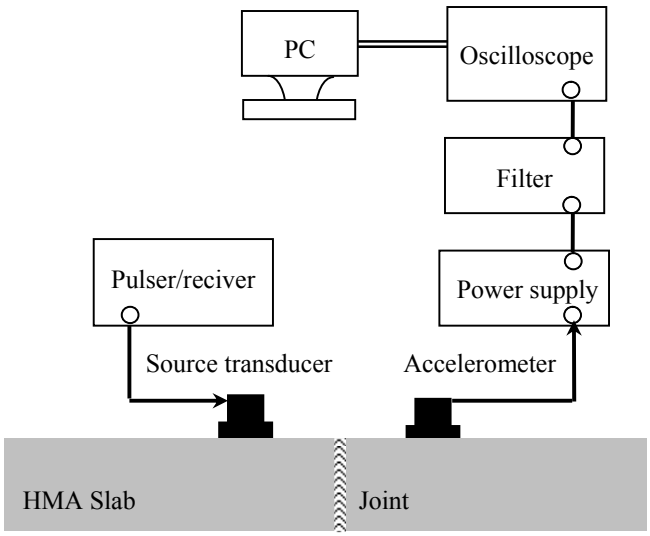

Figure 6.1: Ultrasonic experimental setup for HMA slab

A molding frame of $800 \times 600 \times 80$ mm internal dimensions was built to fabricate the test slabs in the laboratory. The frame was divided into two equal rectangles (sides A and B), by a piece of wood placed in the middle of the frame to create a joint as illustrated in Figure 6.2. The jointed slab was constructed in four stages using two lifts of 40 mm thick hot mix asphalt (HMA) as follows:

1. The necessary amount (approximately 23 kg) of loose HMA material required for fabrication of 40 mm thick HMA concrete was determined based on previous experiments (Chapter 5).
2. The material was heated in an oven up to 160^{o}C for 4 hours, in conjunction with a mixing bowl.
3. The material was thoroughly mixed in the bowl using the mechanical mixer (Figure 5.6a), then placed in the oven, and reheated to 160^{o}C.
4. Aluminium foil paper was placed covering the baseboard in order to facilitate the removal of the slab after fabrication.
5. About 23kg hot material was placed on side A and spread uniformly across the surface. Care was taken to ensure that there was no segregation during placement of HMA material.

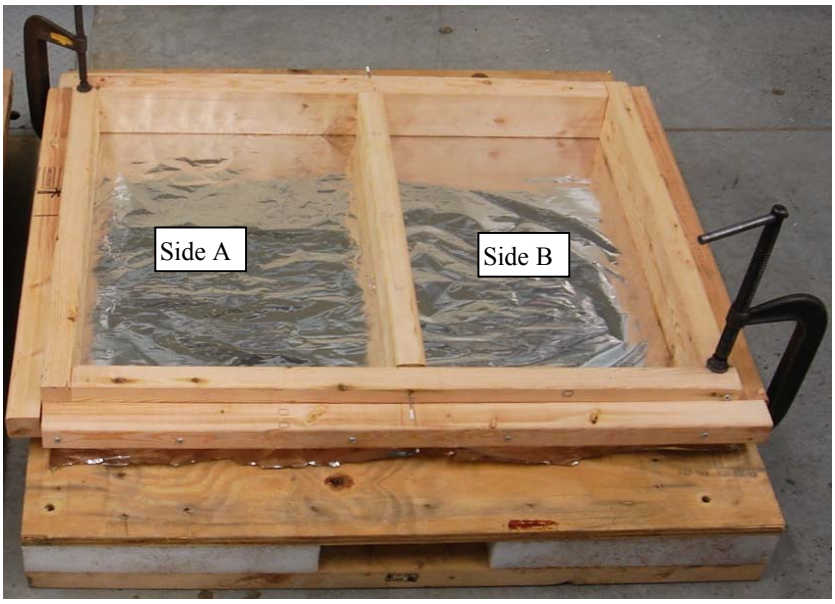

Figure 6.2: A molding frame for HMA slab preparation

6. The frame was removed and the mix was compacted with 300 lb steel roller until the mix was well compacted. The number of passes required for achieving the desire compaction was determined by trial and error (30 passes). The same number of passes was maintained while preparing the remaining of the slab.
7. The edges of the compacted mix were trimmed and the frame was fitted back to the finished portion of the HMA mix.
8. Steps 2 to 7 were repeated to fabricate the first lift on side B. The fabrication was done without the wooden divider such that the mix on side B could develop good bonding with the mix on side A during the roller compaction. The roller was allowed to roll over the joint to achieve a good joint strength.
9. Steps 2 to 8 were repeated to place HMA mixes on both sides and complete the fabrication of the slab. The slab was cooled down at room temperature to be ready for ultrasonic testing.

6.3 Ultrasonic Testing of Slab 1

Typical ultrasonic test results for slab 1 are presented in the following sections. The detailed results for slab 1 are given in Appendices C to G as described below.

- Signals in time and frequency domains in Appendix C
- Fourier transmission coefficient (FTC) vs. frequency in Appendix D
- Wavelet transform using Morlet wavelet in Appendix E
- Wavelet transform of signals using Mallat's algorithm in Appendix F available in the attached CD
- The signal processing MathCad files in Appendix G available in the attached CD

6.3.1 Wave velocities used for the condition assessment of the joint-free surface

Thin steel plates of 25mm diameter were epoxied to the slab 1 surface to achieve good coupling between the transducers and the mix surface (Figure 6.3). Sufficient pressure was applied on the plate such that the epoxy was uniformly distributed.

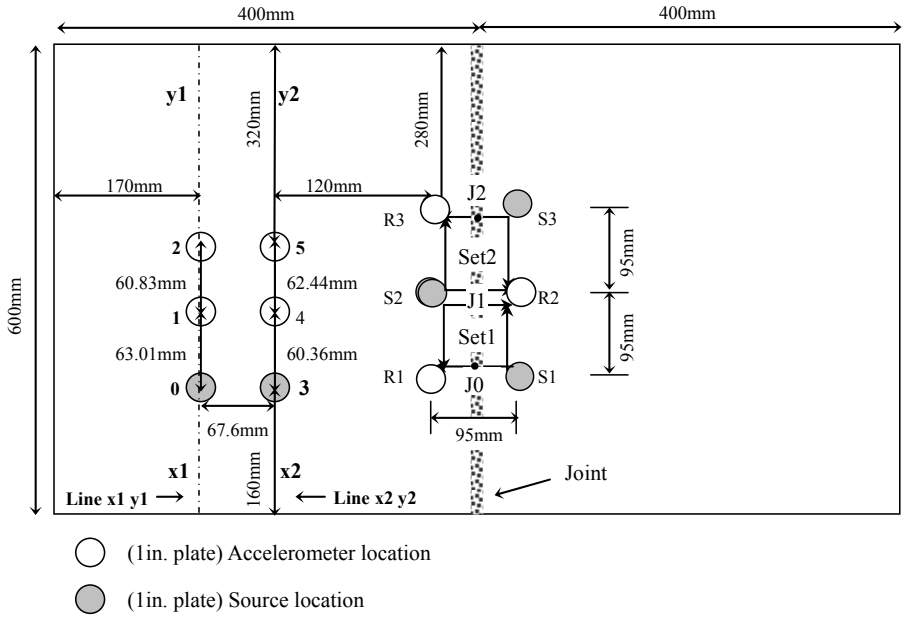

Figure 6.3: Ultrasonic testing geometry for HMA slab 1

Surface waves were generated on the joint-free surface of the slab along the lines x1-y1 and x2-y2 to measure P-wave and R-wave velocities; which are indicative of the strength of the material. The purpose of the wave velocity measurements taken along these two lines is to assess the uniformity of the mix placed. The locations for the source and the receivers in slab 1 are shown in Figure 6.3.

Typical time signals received at locations 1 and 2 of the line x1-y1 are shown in Figure 6.4. The first arriving wave is the fastest traveling P-wave. The P-wave velocity was determined from the distance and the travel time (Δt) between the two receiver locations (Figure 6.4). R-waves are slower than P-waves and thus appear after the P-wave arrival (Figure 6.4). However, the R-wave velocity was uncertain because its arrival at location 2 is not clear. The same uncertainty on the R-wave arrival at location 5 was also observed along the line x2-y2. An array with more data points (receiving locations) is required to improve the detection of R-wave arrivals.

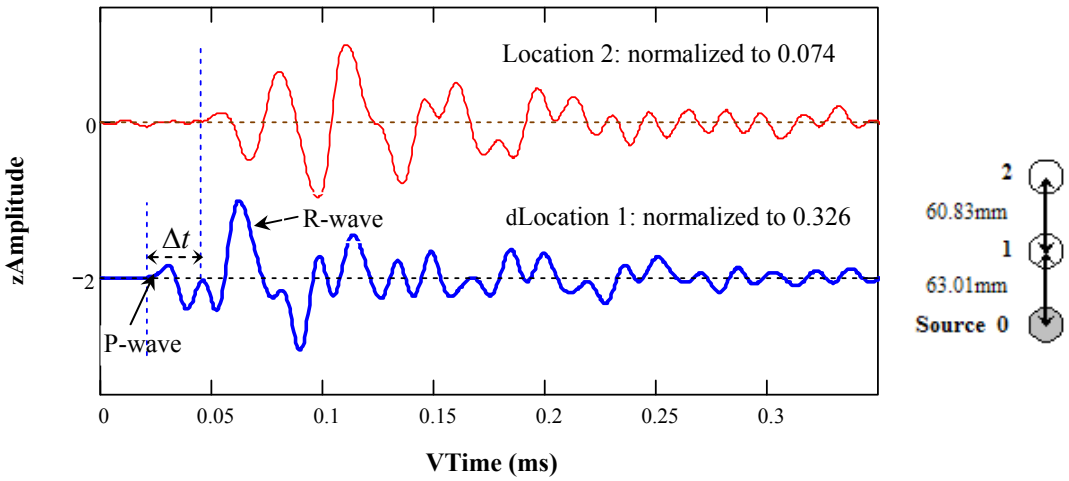

Figure 6.4: Time signals received along the Line x1-y1 in slab 1

6.3.2 Parameters used for the condition assessment of the joint

The source and receiver locations at both sides of the longitudinal joint were selected to assess the relative strength of the joint in terms of wave velocity and attenuation (Figure 6.3). The wave attenuation is measured in terms of six parameters:

1. PTP amplitude ratio in the time domain
2. Maximum magnitude ratio in the frequency domain
3. Spectrum area ratio in the frequency domain
4. Fourier transmission coefficient (FTC)
5. Wavelet transmission coefficients (WTC)
6. Equivalent damping ratio (D)

In addition to these six parameters, the frequency content of a signal was also analyzed using wavelet transform based on Mallat's algorithm (Mallat, 1998). This analysis provides a general picture of the frequency distribution of a signal over time that is not given by the Fourier transform (Chapter 3).

To assess the relative strength of the joint, wave attenuation was measured across the joint as well as along the joint-free area. Two sets of measurements were taken by placing the sources at locations S1, S2 and S3 and the receiver at locations R1, R2 and R3 (Figure 6.3). Each set includes two pairs of signals generated by two identical sources at different locations (e.g. S1 and S2) and received by a receiver placed at a selected location (e.g. R1). The locations were selected to capture the signal from locations S1 to R1 across the jointed surface and the signal from locations S2 to R1 along the joint-free surface. As a result, the ratio of the signal f_{S1_R1} to f_{S2_R1} reflects the relative strength of the joint across the wave path S1_R1 (Popovics et al., 2000). Table 6.1 summarizes the locations of the sources and receivers for the pairs of signals received for each set of measurements.

Table 6.1: Equal-spacing test arrangement in slab 1

Description	Locations	Measured Signals
Measurement Set 1	Pair 1 –sources at S1 and S2; receiver at R1	f_{S1_R1} and f_{S2_R1}
	Pair 2 –sources at S1 and S2; receiver at R2	f_{S1_R2} and f_{S2_R2}
Measurement Set 2	Pair 1 –sources at S2 and S3; receiver at R2	f_{S2_R2} and f_{S3_R2}
	Pair 2 –sources at S2 and S3; receiver at R3	f_{S2_R3} and f_{S3_R3}

More specifically, the condition of the joint was evaluated using the following procedure. First, the two identical transmitters of 1 MHz were placed at locations S1 and S2 as the sources. The surface waves generated at these locations were recorded by a 50 kHz accelerometer (receiver) placed at location R1 to measure the first signal f_{S1_R1} across the joint and the second signal f_{S2_R1} from the transmitter at S2 through the joint-free surface. The process was repeated by moving the receiver to location R2 to receive f_{S1_R2} and f_{S2_R2} from the sources at S1 and S2 (Figure 6.3). The signals f_{S1_R2} and f_{S2_R2} were analyzed using different methods to obtain wave characteristics (F_{S1_R1} and F_{S1_R2}) as discussed next.

Determination of the PTP ratio, spectral magnitude ratio, and spectrum area ratio

The relative strength of the joint at J0 across S1_R1 can be evaluated by transmission coefficient (TC) based on Equation 2.30 (Kramer, 1996):

$$TC(J0) = \frac{F_{S1\_R1}}{F_{S1\_R2}} \tag{6.1a}$$

where, F_{S1_R1} and F_{S1_R2} represent wave characteristics from signals f_{S1_R1} (across the joint) and f_{S1_R2} (through the joint-free surface on the right side of the joint) respectively; the first subscript refers to the source location and the second subscript refers to the receiver location.

For a perfect joint, the *TC* should be equal to 1, indicating no attenuation occurs across the joint. In theory, the *TC* is always between 0 (complete attenuation) and 1 (complete transmission). The underlying principle of the equal-spacing method (Yang et al., 2006) is that the signals (e.g. f_{S1_R1} and f_{S1_R2}) were sent by the same transmitter, traveled through the same geometry (distance), and were received by the same receiver. Thus, the wave amplitude reduction with distance (known as geometric attenuation) is cancelled out by the ratio of F_{S1_R1} to F_{S1_R2}. Therefore, any wave amplitude reduction across the joint is related only to the material properties of the medium. Alternatively, the relative strength of the joint at J0 across S1_R1 can also be evaluated by:

$$TC(J0) = \frac{F_{S1\_R1}}{F_{S2\_R1}} \tag{6.1b}$$

Similarly, the relative strength of the joint at J1 across S2_R2 is given by:

$$TC(J1) = \frac{F_{S2\_R2}}{F_{S2\_R1}} \tag{6.2}$$

where S2_R1 represents the joint-free wave path on the left side of the joint (Figure 6.3). In theory, the values given by equations 6.1a and 6.1b should be identical. Nevertheless, in reality, there are some differences because of the inherent variability associated with the joint-free surfaces (S1_R2 and S2_R1) on either side of the joint in the slab. This problem is addressed by the use of Fourier transmission coefficient (FTC) and Wavelet transmission coefficient (WTC) as discussed in the next section.

Determination of Fourier transmission coefficient (FTC) and Wavelet transmission coefficient (WTC)

The *FTC and WTC* can be considered an improvement to the *TC*. The *FTC* and *WTC* take into account the four signals in one set of measurements, giving an average condition index of the joint. Each of the four received time signals in one set of measurement can

be expressed as a product of transfer functions in the frequency domain (Chapter 4). Then, the FTC is given by (Popovics et al., 2000):

$$FTC = \sqrt{\frac{F_{S1\_R1} \cdot F_{S2\_R2}}{F_{S1\_R2} \cdot F_{S2\_R1}}} \tag{6.3}$$

where F_{S1_R1}, F_{S1_R2}, F_{S2_R2}, and F_{S2_R1} are the Fourier transforms of the time signals f_{S1_R1}, f_{S1_R2}, f_{S2_R2}, and f_{S2_R1}, respectively.

Hence, the calculation of *FTC* allows for elimination of the unknown characteristics of the transmitters, the receiver and the coupling, giving a more reliable index. The *FTC* and *WTC* are the key parameters considered in this study. The *FTC* implies that the presence of the joint can be considered the only factor causing reduction of the spectral amplitude. A typical variation of the *FTC* as a function of frequency is shown in Figure 6.5. The FTC decreases as the frequency increases because lower frequencies (lager wavelengths) are less sensitive to small changes in microstructure. Therefore, the wave attenuation measurements at low frequencies are generally small in comparison to the wave attenuation measured at high frequencies. The *FTC* also varies between 0 (complete attenuation) and 1 (complete transmission) similar to the TC. A comparison of the *FTC* vs. frequency for the two sets of measurements in slab 1 is given in Appendix D. The *FTC* is also computed as a global value using the maximum magnitudes in the frequency spectra of the four signals. For example, in Equation 6.3, instead of using the full frequency spectra (F_{S1_R1}, F_{S1_R2}, F_{S2_R1} and F_{S2_R2}) the corresponding maximum magnitudes in the frequency spectra of the time signals f_{S1_R1}, f_{S1_R2}, f_{S2_R1} and f_{S2_R2} are used to yield a global value.

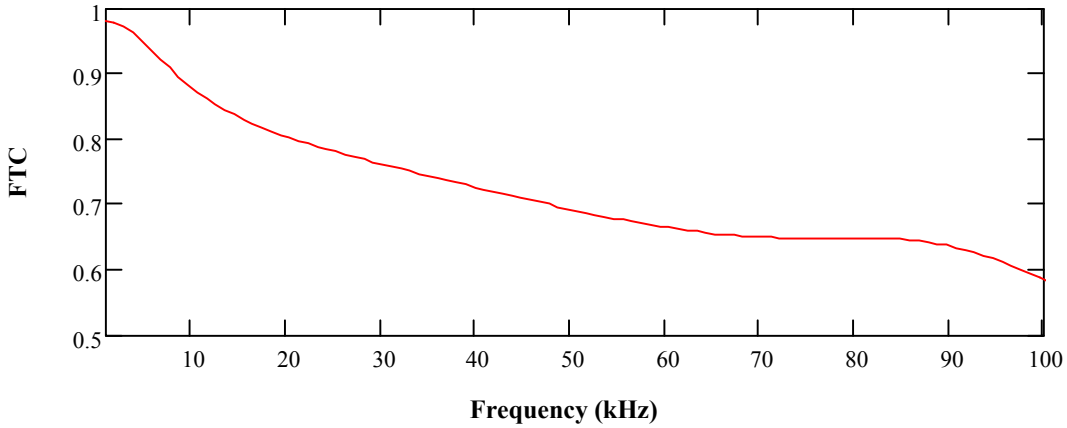

Figure 6.5: Typical example of FTC vs. frequency

The FTC has been found to be effective as a measure of energy transmission of each frequency component though a surface-breaking crack in concrete (Popovics et al., 2000; Song et al., 2003; Yang et al., 2006). Similarly, Wavelet transmission coefficient (WTC) based on wavelet transform was determined as a complementary parameter.

Wavelet transform measures the amount of overlap of a Morlet wavelet as it is shifted over the studied signal (Chapter 3). Four constants W_{S1_R1}, W_{S1_R2}, W_{S2_R1} and W_{S2_R2} were obtained as the peak amplitudes of the wavelet transforms of the four time signals f_{S1_R1}, f_{S1_R2}, f_{S2_R1} and f_{S2_R2} respectively. The wavelet transform of each signal was computed by using the dominant frequency of the signal as the center frequency for the Morlet wavelet. A typical wavelet transforms of signals f_{S2_R1} and f_{S2_R2} from measurements on slab 1 (Set 1) is shown in Figure 6.6. Using the same approach as for Equation 6.3, the WTC can be expressed as:

$$WTC = \sqrt{\frac{W_{S1\_R1} \cdot W_{S2\_R2}}{W_{S1\_R2} \cdot W_{S2\_R1}}} \tag{6.4}$$

The WTC is not a function of frequency. It indicates the transmission of a Morlet wavelet propagating though a joint. Analogous figures showing the wavelet transforms for slab 1 are available in Appendix E.

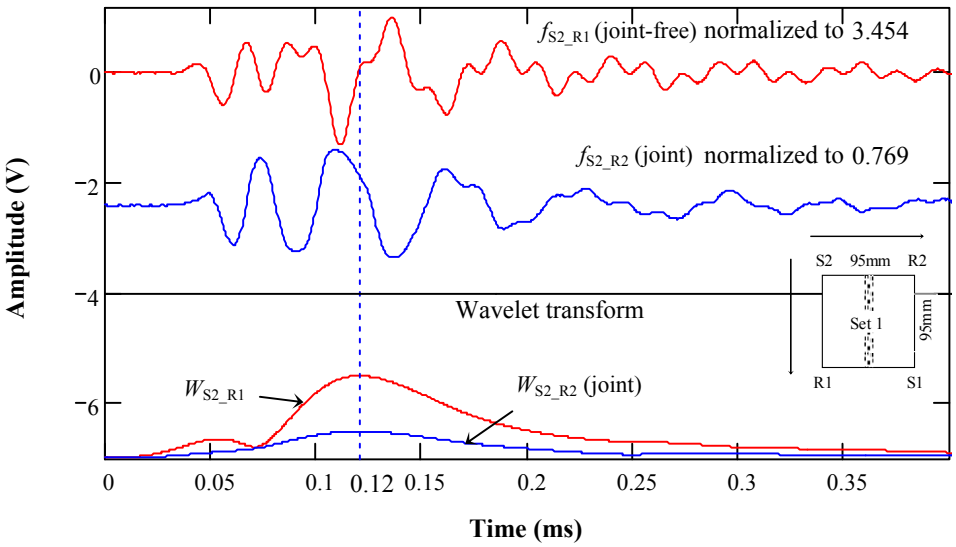

Figure 6.6: Typical Wavelet transform of the time signals f_{S2_R1} and f_{S2_R2} using Morlet wavelet (at center frequency of 21.484 kHz for f_{A_C} and 19.531 kHz for f_{A_B})

Determination of the equivalent damping ratio (D)

Equivalent damping ratio provides an alternative method to assess the condition of the joint. Damping ratio measures the wave energy dissipation during one cycle (Equation 2.32). In this study, the equivalent damping ratio coefficients for P- and R-waves across the joint were calculated using the FTC for P- and R-waves, instead of the Fourier spectral amplitudes. The condition of the joint was evaluated by comparing the damping ratios for the jointed surface with the damping ratios on the joint-free surfaces. The equivalent damping ratio in terms of the FTC can be expressed as:

$$\text{P-waves: } D = \frac{V_P}{2\pi f \Delta x} \ln\left(\frac{1}{FTC_P}\right) \tag{6.5a}$$

R-waves: $D = \frac{V_R}{2\pi f \Delta x} \ln\left(\frac{1}{FTC_R}\right)$ (6.5b)

where Δx is the average length of the four sides of the square pattern *S1_R1_S2_R2*; V_P and V_R are P-wave velocity and R-wave velocity respectively; FTC_P and FTC_R are Fourier transmission coefficients for P- waves and R-waves respectively. If FTC is a function of frequency, the resulting equivalent damping ratio is also a function of frequency. In this case, the *f* in Equations 6.5a and 6.5b is a range of frequency (e.g. 0 to 100 kHz) that is identical for all the signals analyzed. Selection of the frequency range is subjective depending on the frequency content of the analyzed signals. If FTC is a single value as aforementioned, the equivalent damping ratio is also a single value. In the last case, the *f* in Equations 6.5a and 6.5b represents a single frequency given by averaging the four dominant frequencies corresponding to the four signals concerned.

The required six parameters (Equations 6.1 to 6.5) were computed for the full time signals containing both P- and R-waves. Subsequently, the time signals were windowed to isolate the P-waves and the R-waves respectively. The same computation process was repeated for the P-wave portions and for the R-wave portions of the time signal to study the sensitivity of a specific type of wave to the presence of joints or flaws in an asphalt pavement. The differences between the analysis of whole-time signals and the analysis of windowed signals are summarized in Table 6.2a and 6.2b.

Table 6.2 (a): Differences between analysis of full signals and analysis of windowed signals for the PTP amplitude ratio, maximum magnitude ratio, and area ratio

Analyzed portion	PTP ratio	Magnitude ratio	Area ratio
Full signals	Use the PTP amplitudes of full signals in time domain	Use the maximum magnitudes of the frequency spectra of full signals	Use the areas of the frequency spectra of full signals
Windowed signals (P- or R-wave)	Use the PTP amplitudes of the windowed signals in time domain	Use the maximum magnitudes of the frequency spectra of the windowed signals	Use the areas of the frequency spectra of the windowed signals

Table 6.2 (b): Differences between analysis of full signals and analysis of windowed signals for FTC, WTC and equivalent damping ratio

Analyzed portion	FTC	WTC	Equivalent damping ratio
Full signals	1. For FTC vs. frequency, use the full frequency spectra of full signals. 2. For a single FTC value, use the maximum magnitudes of the frequency spectra of full signals.	Use the dominant frequency of the full $signal_i$ to compute the wavelet transform of the $signal_i$.	Same as in FTC
Windowed signals (P- or R-waves)	1. For FTC vs. frequency, use the full frequency spectra of the windowed potions. 2. For a single FTC value, use the maximum magnitudes of the frequency spectra of the windowed potions.	Use the dominant frequency of the windowed portion of the $signal_i$ to compute the wavelet transform of the $signal_i$.	Same as in FTC

Determination of frequency distribution over time

As the last step, wavelet transform based on Mallat's algorithm was performed to analyze the frequency distribution over time (Tallavo, 2007) (Chapter 3). An example of the Mallat's algorithm wavelet transform of the whole-time signal f_{S2_R1} is given in Figure 6.7a. The vertical axis in "scales" is indicative of frequency. The dominant frequency is 18.8 kHz (scale 76.5) arriving at around 0.00013 seconds (Figure 6.7b).

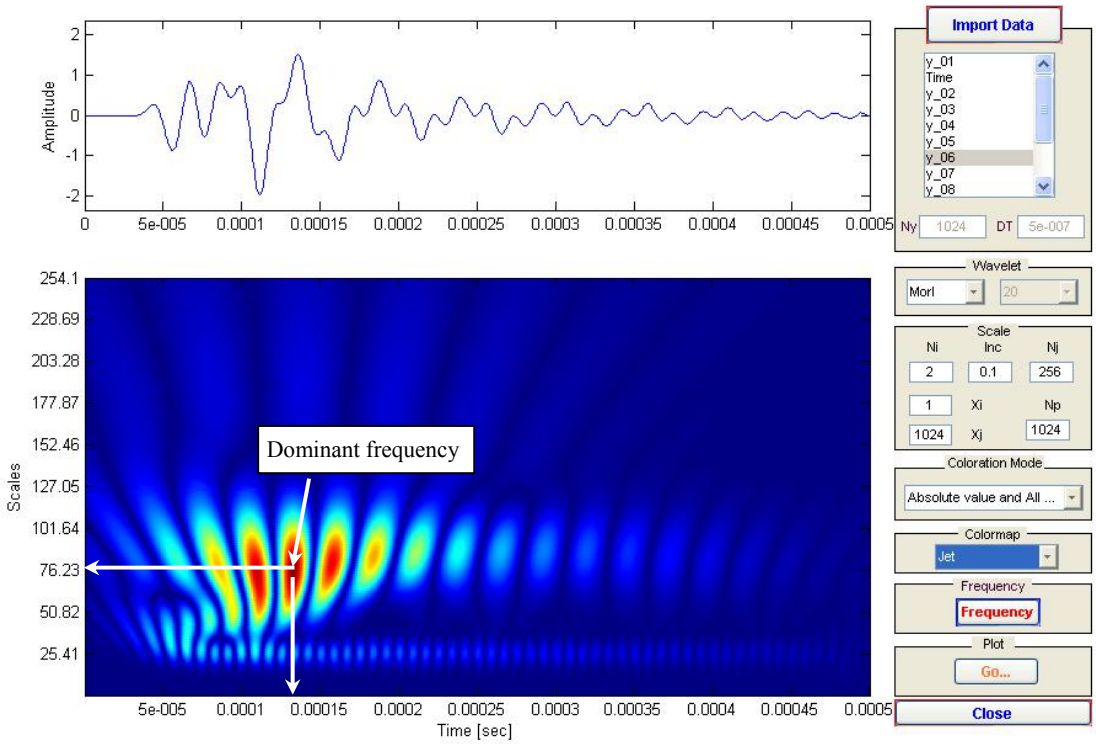

Figure 6.7 (a): Mallat's algorithm wavelet transform of f_{S2_R1} (Set 1, slab1) (Tallavo, 2007)

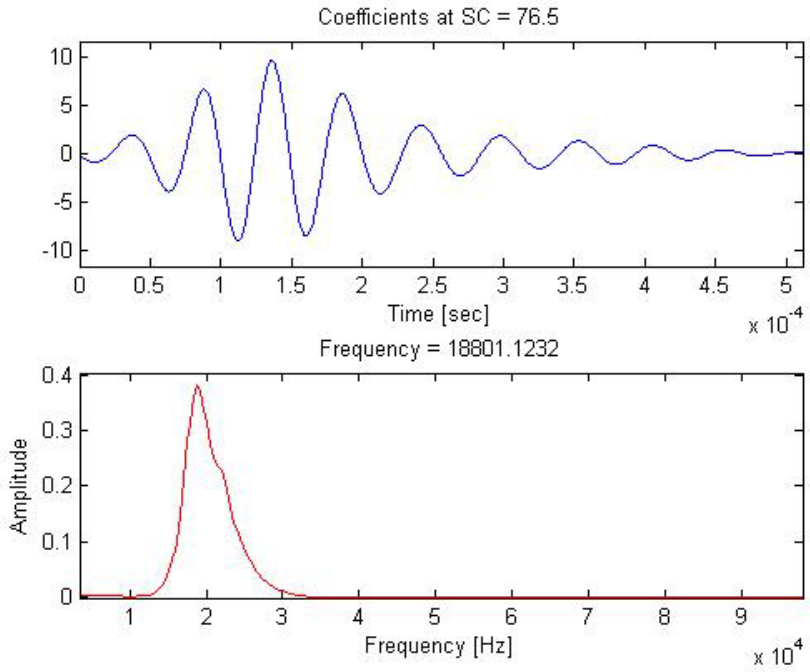

Figure 6.7 (b): Dominant frequency of the full time signal f_{S2_R1} (Set 1, slab1) (Tallavo, 2007)

6.4 Results and Discussions for Slab 1

Full signals and the windowed signals were analyzed for slab 1 using the techniques described in previous sections. The following sections provide the detailed results.

6.4.1 Analysis based on wave velocities

Typical time signals recorded at locations 1 and 2 of line x1-y1 are shown in Figure 6.4. The P-wave velocity was calculated from the distance (60.38mm) and the travel time ($\Delta t = 0.0239\ \mu s$) between locations 1 and 2. The resulting P-wave velocity (V_P) is 2524 m/s. Likewise, a V_P of 2800 m/s was obtained from Line x2-y2. Hence, an average V_P of 2662 m/s was obtained. The velocity variation also indicates the poor uniformity of the slab. Compared to the V_P = 4174m/s determined from UPV test on Group B cylindrical specimens in Phase I, the V_P of 2662 m/s indicates that the Group A specimens (at 100 gyrations) were compacted better than the slab 1. This result is expected because of the difficulty in compacting the large stone mix (SP19) using the roller. Thus, an alternative compaction method is required. An array with more receiving locations should be used to

detect the R-waves, as described previously. Wave velocities are necessary in the calculation of the dispersion curve of Lamb waves.

6.4.2 Analysis of full signals: PTP amplitude ratios

Figure 6.8 shows typical time-domain and frequency-domain representations of signals f_{S2_R1} and f_{S2_R2} from Set 1 measurements in slab 1. Each of these two signals was normalized to its PTP amplitude of the full signal for comparison purpose. The PTP amplitude of f_{S2_R2} across the joint at point J1 (Figure 6.3) was significantly lower than that of f_{S2_R1} through the joint-free surface. The PTP ratio for f_{S2_R2} / f_{S2_R1} equal to 0.22 was then used as a condition index for the joint at J1. Likewise, the PTP ratios for full signal analysis of Set 1 and Set 2 measurements were calculated and summarized in Table 6.3. The observed PTP ratios are less than 1, indicating that wave attenuation occurs across the joint. The PTP ratio (f_{S2_R2} / f_{S2_R1}) for the joint at J1 is less than the ratio (f_{S1_R1} / f_{S1_R2}) for the joint at J0, which implies that the strength of the joint at J1 is weaker than the joint at J0 (Figure 6.3). This comparison is based on the assumption that the material strength along the joint-free wave path S2_R1 is the same as or similar to that along the joint-free S1_R2. Yet in reality, there is a variation between the two joint-free surfaces that may contribute to the difference in PTP ratios for the joint at J0 and J1.

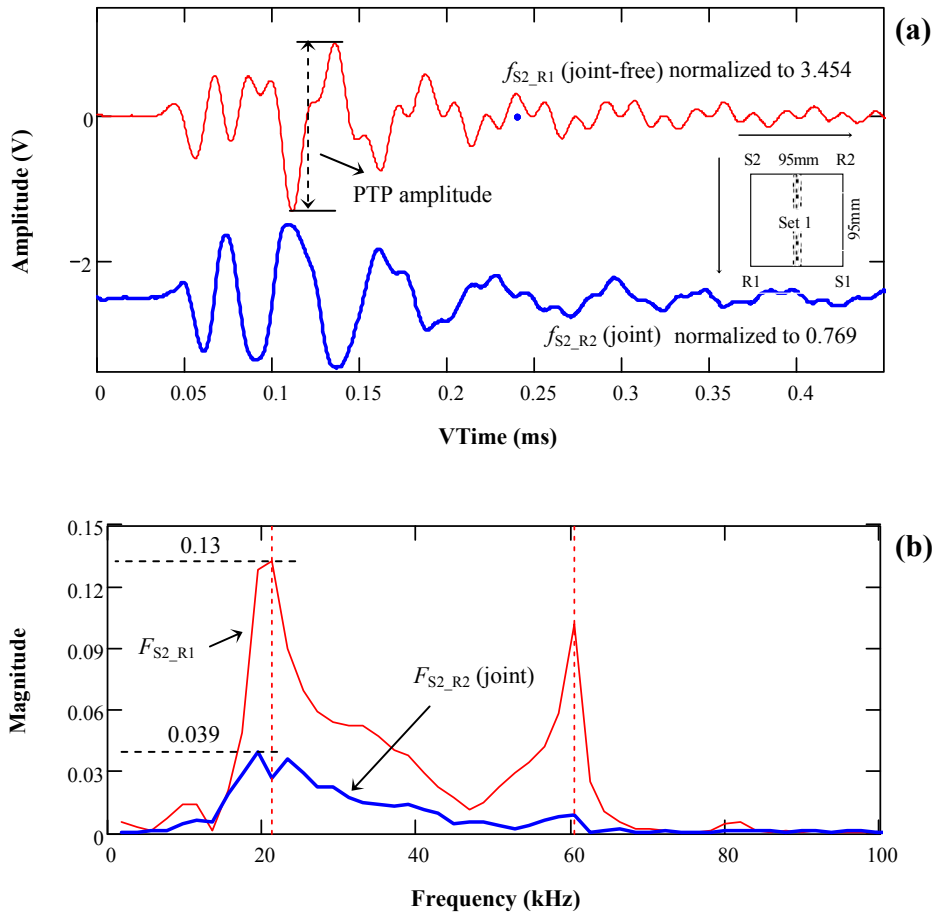

Figure 6.8: A pair of signals (Set 1, slab 1) across the joint and through the joint-free surface – (a) full signals in time and (b) full signals in frequency

6.4.3 Analysis of full signals: maximum magnitude ratios and spectrum area ratios

The maximum magnitudes of f_{S2_R1} and f_{S2_R2} were obtained in the frequency domain, as denoted by the horizontal dotted lines in Figure 6.8. The maximum magnitude ratio (f_{S2_R2} / f_{S2_R1}) is equal to 0.31 (Table 6.3). This value indicates the a frequency component of about 20 kHz traveling across the joint exhibits 69% reduction in wave amplitude. Likewise, the maximum magnitude ratios for full signal analysis of Set 1 and Set 2 measurements are summarized in Table 6.3. The spectrum areas of the signals in frequency domain were computed according to Equation 3.13. The spectrum area ratios for the two sets of measurements are also shown in Table 6.3. The results of the

magnitude ratios and the spectrum area ratios confirm that the relative strength of the joint at J1 is less than the strength of the joint at J0.

The frequency spectra for the full signals f_{S2_R2} and f_{S2_R1} showed larger magnitudes around 20 kHz and 60 kHz for both signals (Figure 6.8). Frequencies higher than 60 kHz are practically attenuated by the medium. Hence, two identical transmitters of 50 kHz should be used as the sources rather than the 1MHz transmitters.

Table 6.3: PTP ratio, magnitude ratio, and area ratio for slab 1

Location	Analyzed portion	Signal ratio (*SR*)	PTP ratio	Magnitude ratio	Area ratio
Jointed surface at locations S1, R1, S2 and R2 (Set 1)	Full signal	f_{S2_R2}/f_{S2_R1}	0.22	0.3	0.31
		f_{S1_R1}/f_{S1_R2}	0.83	0.82	0.84
	P-wave	f_{S2_R2}/f_{S2_R1}	0.30	0.31	0.30
		f_{S1_R1}/f_{S1_R2}	0.24	0.30	0.24
	R-wave	f_{S2_R2}/f_{S2_R1}	0.49	0.83	0.51
		f_{S1_R1}/f_{S1_R2}	0.77	0.61	0.81
Jointed surface at locations S2, R2, S3 and R3 (Set 2)	Full signal	f_{S2_R2}/f_{S2_R3}	0.35	0.57	0.45
		f_{S3_R3}/f_{S3_R2}	0.69	0.77	0.68
	P-wave	f_{S2_R2}/f_{S2_R3}	0.28	0.25	0.26
		f_{S3_R3}/f_{S3_R2}	0.26	0.27	0.29
	R-wave	f_{S2_R2}/f_{S2_R3}	0.30	0.3	0.31
		f_{S3_R3}/f_{S3_R2}	0.47	0.51	0.54
Jointed surface (Average for Set 1 and Set 2)	Full signal	$\frac{Set\ 1\ SR + Set\ 2\ SR}{2}$	0.52	0.62	0.57
	P-wave		0.27	0.28	0.27
	R-wave		0.51	0.56	0.54

6.4.4 Analysis of windowed signals: PTP, magnitude, and area ratios

A time window (Equation 3.12) was used to capture the P- and R-wave portions respectively for analysis in time and frequency domains, as shown in Figures 6.9 and 6.10. For consistency, the window was selected to cover an exact cycle of P-waves or R-waves for all the measurements. However, in some cases where the P- or R-wave cycle was distorted, the selection of the window width was subjective. In Figures 6.9 and 6.10, the PTP amplitudes in time domain are marked by the horizontal dotted lines, and the dominant frequencies of the windowed P- and R-waves in frequency domain are marked by the vertical dotted lines.

The PTP amplitudes of the four signals f_{S2_R2}, f_{S2_R1}, f_{S1_R1} and f_{S1_R2} were determined from their windowed signals in time domain (Figure 6.9). The PTP amplitude ratios for f_{S2_R2} / f_{S2_R1} and f_{S1_R1} / f_{S1_R2} are equal to 0.3 and 0.24 respectively (Table 6.3). Similarly, in frequency domain (Figure 6.9), the maximum magnitudes and spectrum areas of the four signals were determined. Then, the maximum magnitude ratios and the spectrum area ratios for f_{S2_R2} / f_{S2_R1} and f_{S1_R1} / f_{S1_R2} were calculated (Table 6.3). The analysis of the windowed P-waves showed that the three ratios (f_{S2_R2} / f_{S2_R1}) for the joint at J1 are close to the ratios (f_{S1_R1} / f_{S1_R2}) obtained for the joint at J0. In Set 2 measurements (Table 6.3), the analysis of windowed P-waves gave similar results.

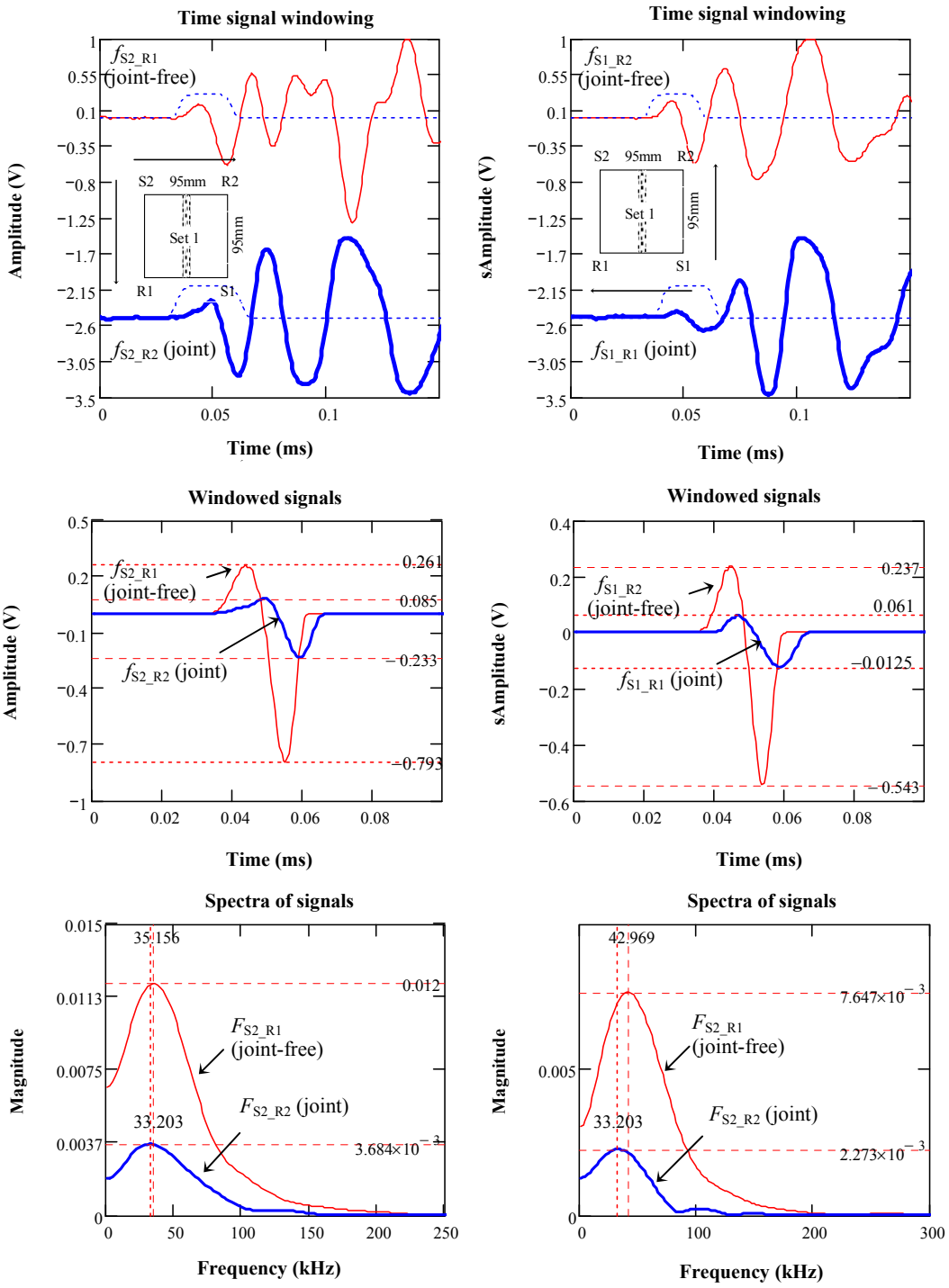

Figure 6.9: P-wave analysis in time and frequency domains (Set 1, slab 1) (Horizontal lines mark the peak amplitudes, and vertical lines dominant frequencies.)

R-waves were analyzed using the similar procedures used for P-waves (Figure 6.10). The resulting PTP amplitude ratios, the maximum magnitude ratios, and the spectrum area ratios for the two sets of measurements are summarized in Table 6.3. In Set 1, the PTP ratio and the area ratio for the joint at J1 are smaller than the ratio for the joint at J0. These results show the same trend as observed from the analysis of full signals of Set 1. This is expected because the full wave signal is generally dominated by R-waves. As described in Chapter 2, most of the energy from a surface impact propagates as R-waves, and thus R-waves virtually dominate the surface response. However, the magnitude ratio for the joint at J1 is larger than the magnitude ratio for the joint at J0. This discrepancy is caused by the interaction of R-waves with other waves mostly generated by reflections or scattering (Figure 6.10). Thus, the analysis of R-waves in the frequency domain for Set 1 measurements is considered not suitable. On the other hand, R-waves in Set 2 show that the three ratios obtained for the joint at J1 are smaller than the ratio for the joint at J2, which agree with the results of the analysis of full signals for Set 2.

Compared to the analysis of R-waves, the analysis of P-waves gave similar values with respect to the two signal pairs in a set of measurements (Table 6.3). A possible reason is that P-waves have larger wavelengths that provide the condition assessment of the full depth of the joint. R-waves are sensitive to the condition of the partial depth of the joint as the waves are concentrated on the top surface – 1/3 of the wavelength (< 20mm in depth).

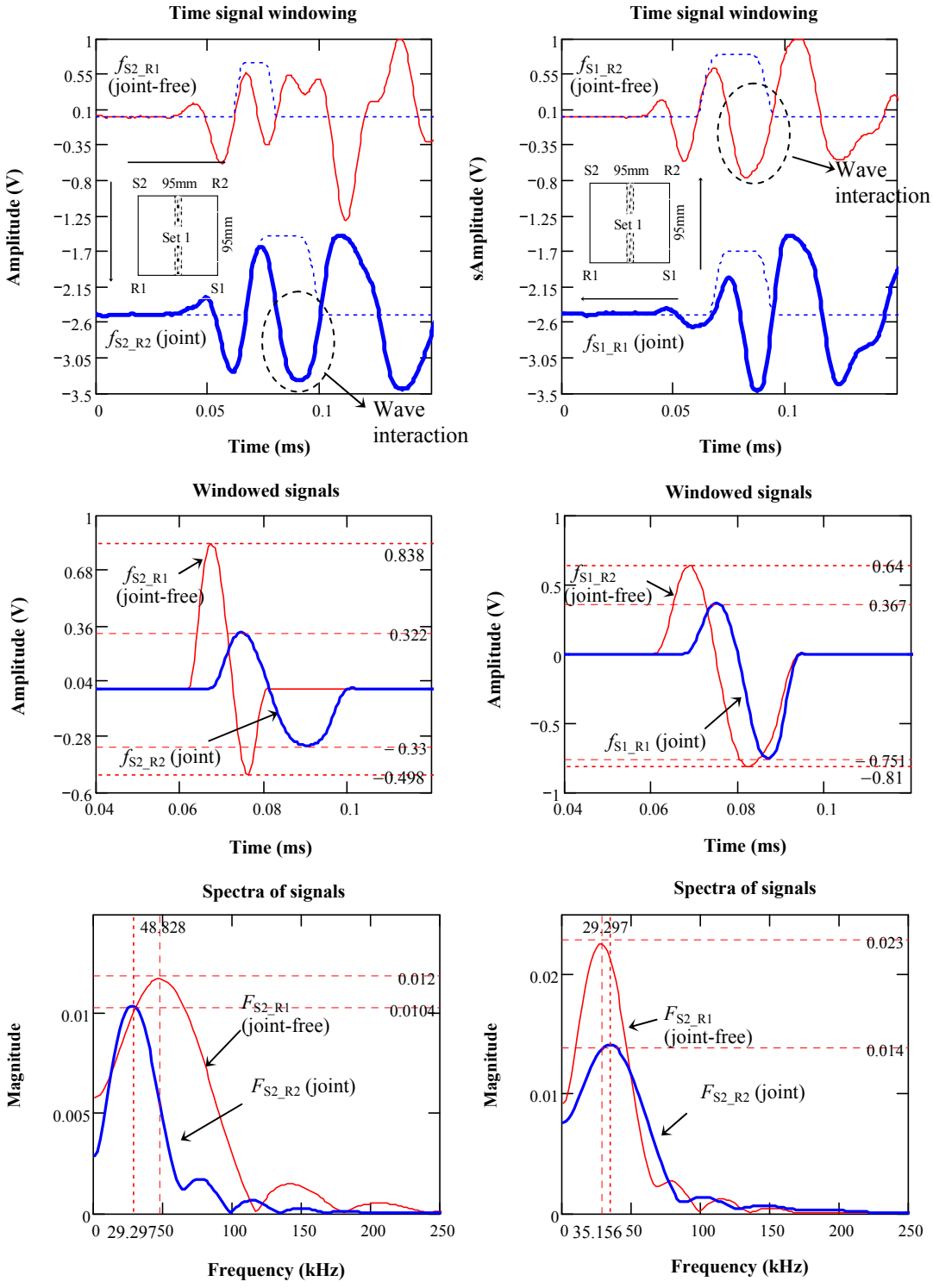

Figure 6.10: R-wave analysis in time and frequency domains (Set 1, slab 1) (Horizontal lines mark the peak amplitudes, and vertical lines dominant frequencies.)

6.4.5 Analysis of full signals: FTC, WTC and equivalent damping ratio

FTC and WTC give more reliable results with elimination of the coupling variability as described previously. The FTC and WTC provide the average condition of the joint between J0 and J1 for Set 1 measurements and between J1 and J2 for Set 2. The FTC and WTC results from the analysis of full signals for Set 1 and Set 2 measurements are summarized in Table 6.4. The analysis of full signals for Set 1 measurements across the joint between J0 and J1 show an FTC value of 0.49 and a WTC of 0.51 (Table 6.4). The results from Set 2 across the joint between J1 and J2 show a value of 0.58 for both FTC and WTC. Hence, it is implied that the joint between J1 and J2 is stronger than the joint between J0 and J1. The equivalent damping ratio is not available because no reliable R-wave velocity was obtained.

Table 6.4: FTC, WTC and equivalent damping ratio for slab 1

Location	Analyzed portion	Signal ratio (*SR*)	FTC	WTC	Damping ratio
Jointed surface at locations S1, R1, S2 and R2 (Set 1)	Full signal	$\sqrt{\frac{f_{S2\_R2} \cdot f_{S1\_R1}}{f_{S2\_R1} \cdot f_{S1\_R2}}}$	0.49 at 23kHz	0.51 at 23kHz	N/A
	P-wave		0.30 at 36kHz	0.59 at 36kHz	0.15 at 36kHz
	R-wave		0.71 at 35kHz	0.47 at 35kHz	N/A
Jointed surface at locations S2, R2, S3 and R3 (Set 2)	Full signal	$\sqrt{\frac{f_{S2\_R2} \cdot f_{S3\_R3}}{f_{S2\_R3} \cdot f_{S3\_R2}}}$	0.67 at 23kHz	0.64 at 23kHz	N/A
	P-wave		0.26 at 33kHz	0.53 at 33kHz	0.19 at 33kHz
	R-wave		0.39. at 34kHz	0.51 at 34kHz	N/A
Jointed surface (Average for Set 1 and Set 2)	Full signal	$\frac{Set\ 1\ SR + Set\ 2\ SR}{2}$	0.58 at 23kHz	0.58 at 23kHz	N/A
	P-wave		0.28 at 36kHz	0.56 at 36kHz	0.17
	R-wave		0.55 at 33kHz	0.49 at 33kHz	N/A

6.4.6 Analysis of windowed signals: FTC and WTC

The FTC as a global value obtained at dominant frequencies (e.g. 23 kHz) for each set of measurements is shown in Table 6.4 and Figure 6.11. In general, P- and R-wave analysis showed that Set 1 measurements (the joint between J0 and J1) have larger FTC than the values obtained for Set 2 (the joint between J1 and J2). This comparison implies that the joint between J0 and J1 is stronger. However, the results from the analysis of full signals showed the opposite trend. This discrepancy is because the frequency content of a full signal could be biased by the reflections or scattering following the first arriving P- and R waves. The average FTC value of the two set of measurements for full signals is 0.58, for the windowed P-waves is 0.28, and for the windowed R-waves 0.55. These values indicate wave attenuation has occurred across the joint. These values will be compared with the values obtained from slab 2 and slab 3 to examine the sensitivity of the FTC technique.

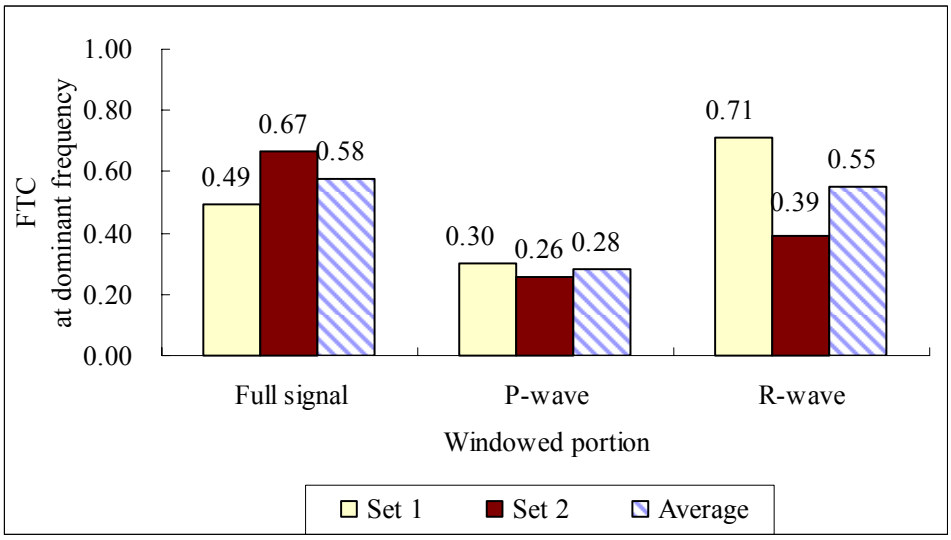

Figure 6.11: FTC at average dominant frequencies for the two sets of measurements (slab 1)

Similarly, WTC values for the windowed signals were obtained using the dominant frequencies of the windowed signals (Table 6.2b). The results for the two sets of measurements are shown in Table 6.4 and Figure 6.12. The WTC values remain nearly constant regardless of the selected frequencies (Figure 6.12). Thus, the WTC technique is

not sensitive to slight changes in frequency. In general, the frequency components of 23 kHz to 36 kHz across the joint in slab 1 had average WTC values between 0.58 and 0.49.

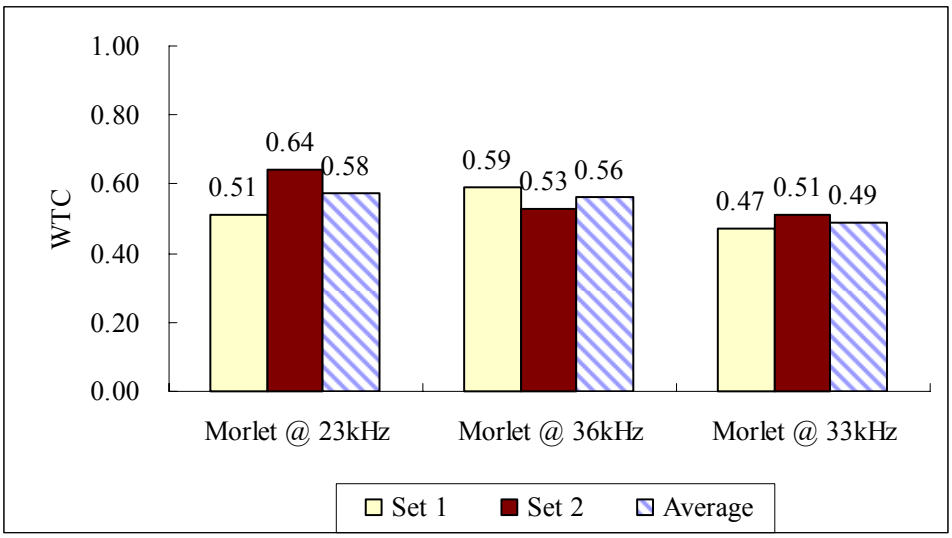

Figure 6.12: WTC using Morlet wavelet for the two sets of measurements (slab 1)

In addition, FTC values tend to decrease as frequency increases. Figure 6.13 shows typical results of FTC values against frequency obtained from windowed signals (f_{S2_R2}, f_{S2_R1}, f_{S1_R1} and f_{S1_R2} in Set 1). For Set 1 measurements, the dominant frequencies for the windowed P-waves are from 30 to 40 kHz (Figure 6.9) and for the windowed R-waves from 30 to 50 kHz (Figure 6.10). Thus, the analysis of FTC values should focus these frequency ranges. The corresponding FTC value for P-waves is 0.3 and for R-waves between 0.65 and 0.8. These FTC values are less than 1 showing that wave attenuation has occurred across the joint. Likewise, FTC values against frequency for Set 2 were obtained (Appendix D). The FTC values for both waves in Set 2 showed less variability compared to the FTC values observed in Set 1. This variation of FTC values between the two sets of measurements could be produced by the poor uniformity of the compaction with the roller.

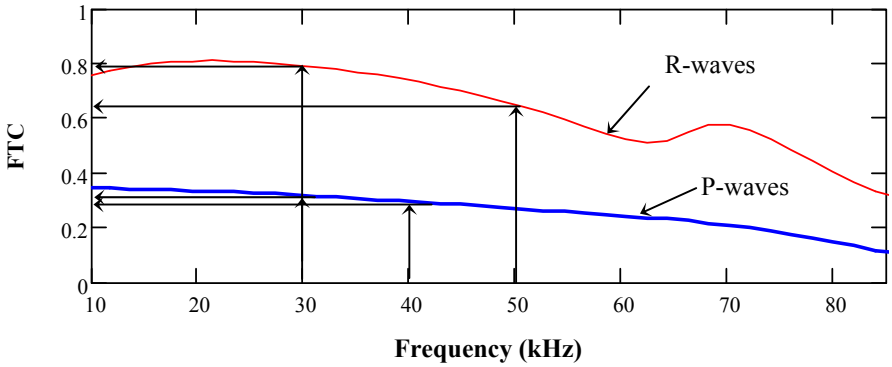

Figure 6.13: FTC values vs. frequency for the P-wave and R-wave portions (Set 1, slab 1)

6.4.7 Analysis of windowed signals: the equivalent damping ratio

The equivalent damping ratios for the two set of measurements were calculated using FTC (Equations 6.5a). An example of equivalent damping ratio against frequency for the windowed P-waves is illustrated in Figure 6.14. The P-wave equivalent damping ratio exhibits a pronounced decrease at low frequencies and approaches a constant value with increasing frequencies. The initial decrease is likely because the wavelengths of P-waves at low frequency range exceed the slab thickness. If the slab thickness is set as the maximum possible wavelength (about 85mm), the observed P-wave velocity (2650m/s) corresponds to the minimum frequency of 31 kHz. Therefore, P-waves propagating at lower frequencies than 30 kHz could be strongly affected by the slab boundaries, and hence, the resulting equivalent damping ratios at low frequencies are not indicative of material properties. The P-wave equivalent damping ratios from 30 kHz to 80 kHz varied from 0.181 to 0.106 (Figure 6.14). The equivalent damping ratios for R-waves are not available because no reliable R-wave velocity results were available.

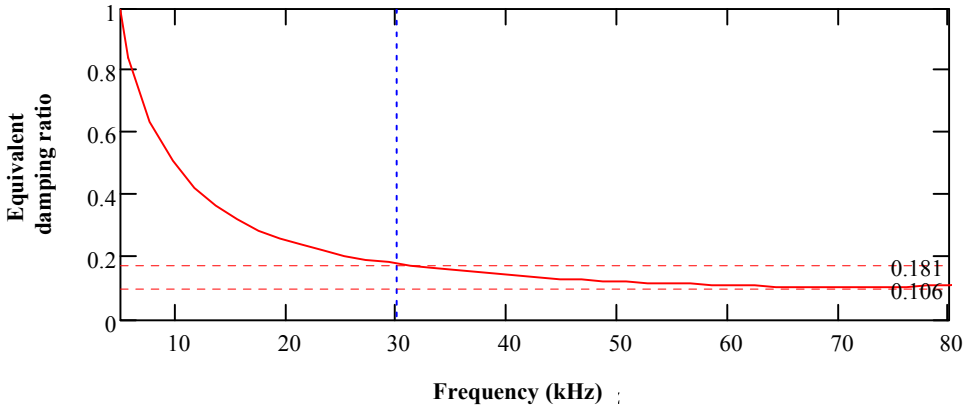

Figure 6.14: FTC-based damping ratios vs. frequency for P-waves (Set 1, slab 1)

6.4.8 Summary of test results for slab 1

1. The wave-based technique was suitable to assess the condition of the joint. The two sets of measurements across the joint gave average FTC values of 0.28 to 0.58 and average WTC values of 0.49 to 0.58. More specifically, the WTC may be more suitable because of the elimination of the errors associated with the subjective windowing of P- and R-waves.
2. P-waves propagating at lower frequencies than 30 kHz could be strongly affected by the slab boundaries.
3. The roller compaction technique was not suitable because of the difficulty in achieving a uniform compaction on the large stone mix (SP19).
4. Two identical transmitters of 50 kHz should be used as the sources because no dominant frequencies above 60 kHz were observed.
5. A new sensor array with more data points should be used to improve detection of R-waves and to select appropriate spacing between the source and the receiver to measure the wave attenuation because wave reflections have shown significant effects on the results.

6.5 Fabrication of Pavement Slab 2

The purpose of the second slab was to examine the sensitivity of the wave attenuation parameters for condition rating of a good joint. A procedure was developed to evaluate the suitability of the transducers for the ultrasonic testing of slab 2. This procedure involved the selection of a suitable spacing between the source and the receiver known as S-R spacing.

For the second slab, two identical transmitters of 50 kHz (narrow frequency band, center frequency: 50 kHz) were used as the sources. The transmitters were driven by a corresponding pulser (Pundit). In addition to the 50 kHz accelerometer used in the testing of slab 1, a 100 kHz accelerometer (PCB352A60, linear response up to 60 kHz at a tolerance of $\pm 3dB$, resonant frequency = 100 kHz, sensitivity 10mv/g) was used to verify results obtained using the 50 kHz accelerometer. The 50 kHz accelerometer is expected to receive non-amplified (real frequency response) signals up to 15kHz while amplifying the 50kHz component of the signals for analysis. The 100kHz accelerometer is expected to capture the real frequency response (up to 60kHz) of the slab. Another purpose of using the two accelerometers is to select one that is more suitable for testing of the slab. The equipment setup, such as the power supply (PCB483A) for the accelerometer, the low-pass filter (Krohn-Hite 3384), the digital oscilloscope (HP 54610B) and the desktop computer, was the same as used in slab 1.

As discussed previously, the roller compactor was not suitable to achieve the required compaction level (typically equivalent to 100 gyrations). An attempt to use a vibrating plate compactor also met with little success because the vibration resulted in the displacement of loose materials making it difficult to control the depth within the frame. Finally, the traditional method of compaction using a hand-held hammer (15 lbs) with a tamping foot of $20mm \times 20mm$ dimension was employed to prepare the second slab, as shown in Figure 6.15.

Figure 6.15: The hand-held hammer (15 lbs) used to compact slab 2

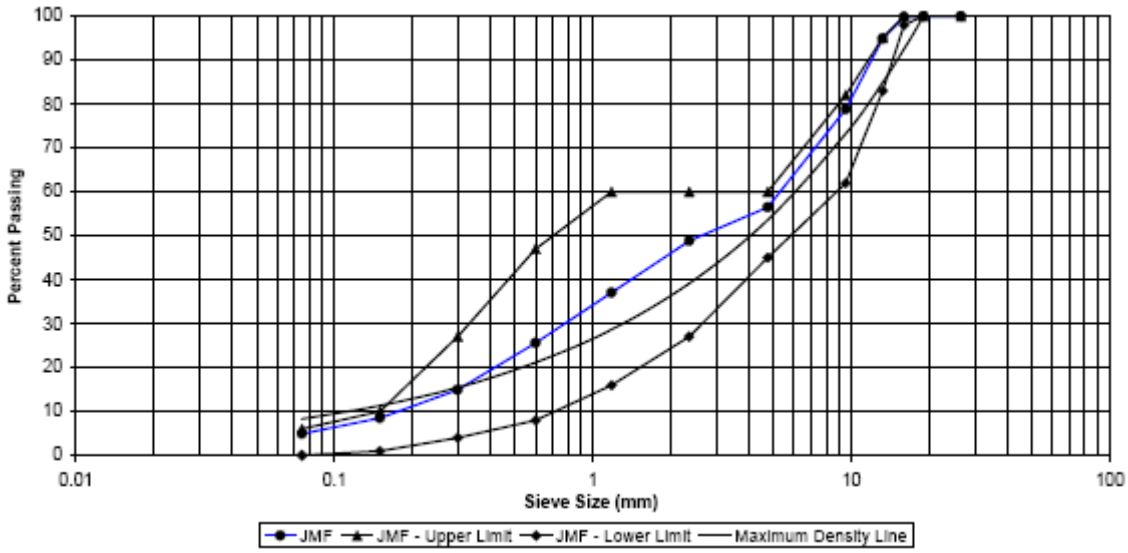

Figure 6.16: Aggregate gradation curve of HL4-20% recycle asphalt

In addition, a less stony material (HL4-20% recycle asphalt) was used in order to achieve a better compaction and to achieve a good joint adhesion. This mix is used in various highways in Canada. The gradation of batched aggregate was mixed according to Job Mix Formula using 5% asphalt cement, as indicated by the gradation curve in Figure 6.16. The procedure used in the fabrication of slab 2 is described as follows:

1. Followed the procedure outlined in the steps 1 to 5 for the fabrication of slab 1.
2. Started the compaction from one end of a corner of side A by tamping the mix with the hand-held hammer and moving the hammer along the side at 10 mm interval after each blow until it reached the other end, as shown in Figure 6.17. The process was repeated until the whole area was compacted. The same falling height (1m) was maintained while compacting the mix throughout.
3. Repeated steps 1 and 2 on side B without the wooden divider. An attempt was made to ensure the same compaction across the surface of the joint to achieve good adhesion at the joint
4. Repeated steps 1 to 2 with the divider in place to lay the second lift on the top of the mix laid on side A.
5. Repeated step 3 to place the second lift on the top of the mix on side B to complete the fabrication of the slab. The slab was allowed to cool down at room temperature making the slab ready for testing.

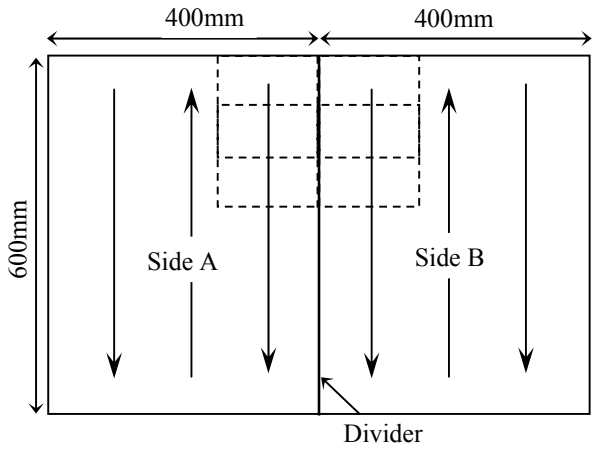

Figure 6.17: Compaction procedure of slab 2 with the 200mm square tamper

6.6 Ultrasonic Testing of Slab 2

Thin steel plates of 25mm and 15mm diameters were epoxied to the slab surface to improve the coupling between the slab and the transmitters/accelerometers, as illustrated in Figure 6.18.

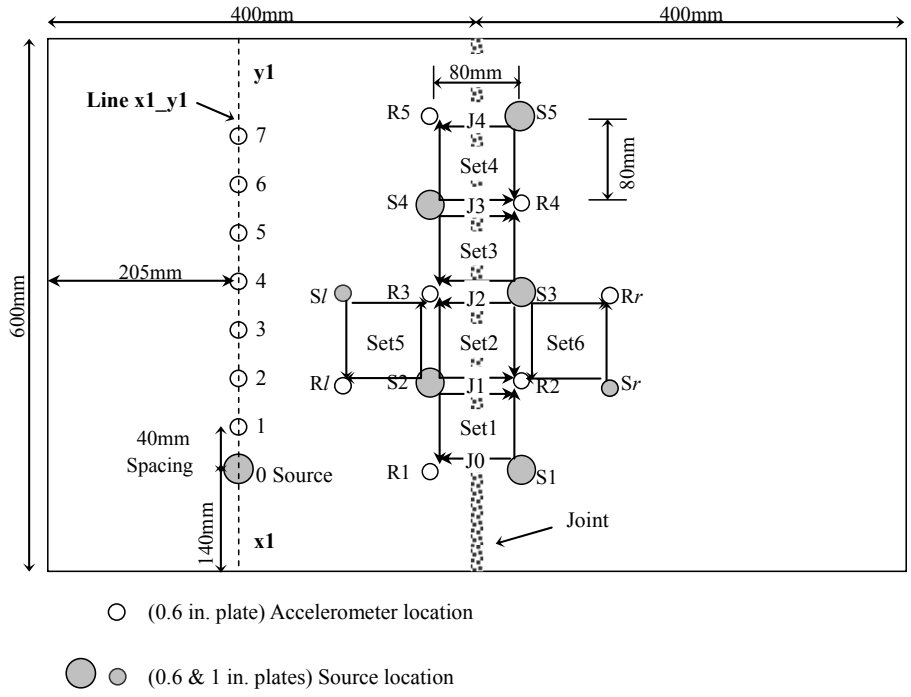

Figure 6.18: Ultrasonic testing geometry of HMA slab 2

As the first step, tests were carried out along the Line x1-y1 (Figure 6.18) to determine the wave velocities and geometric attenuation. The wave measurements taken at different intervals along the line x1-y1 were used to select a suitable S-R spacing required to receive a strong signal during testing of the joint. A spacing of 80mm was selected for the transmitter-receiver assembly in slab 2 because this spacing gives the signal with the least interference of arriving waves and best definition of R-wave arrival among the received signals (Figures 6.19a and 6.19b). For example, although location 1 shows a clear signal, the negative peak of the first arrival is disproportionately large, indicating interference with the following R-wave arrival (Figure 6.19a). The test results of slab 1 have shown

that the frequency contents of the windowed signals (Figure 6.10) are likely biased because of the wave interference, which affects the reliability of the results.

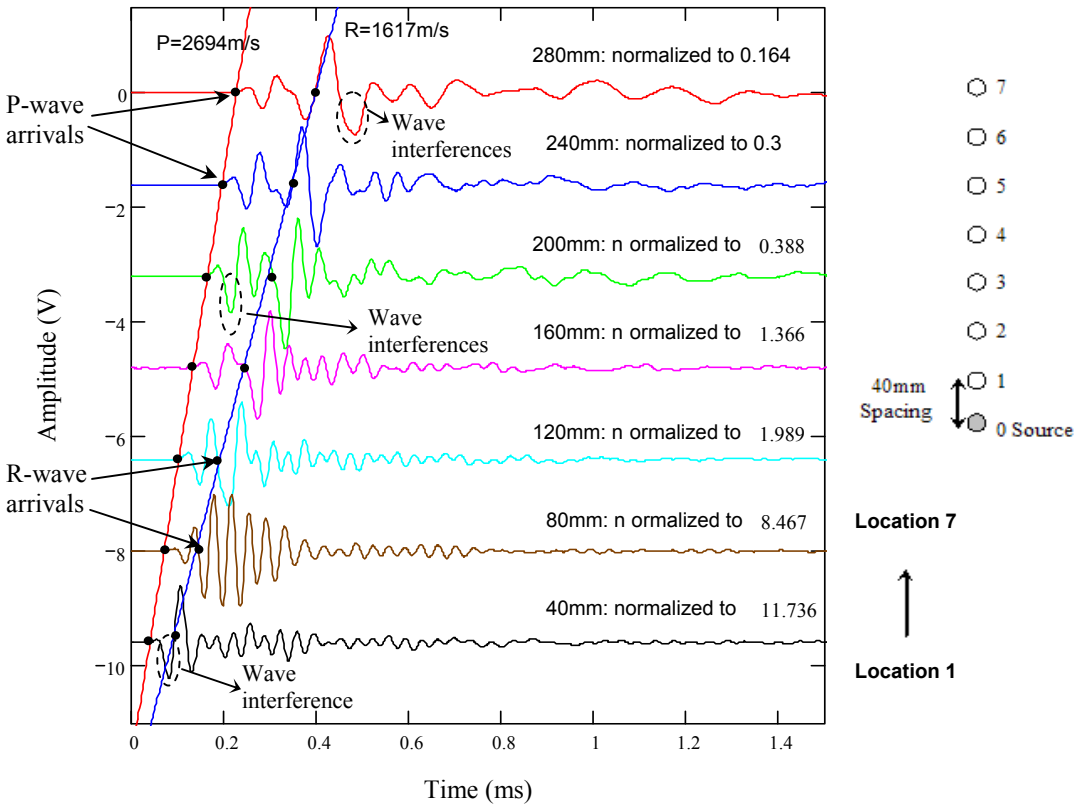

Figure 6.19 (a): Measurements using 50 kHz accelerometer along Line x1-y1 (slab 2)

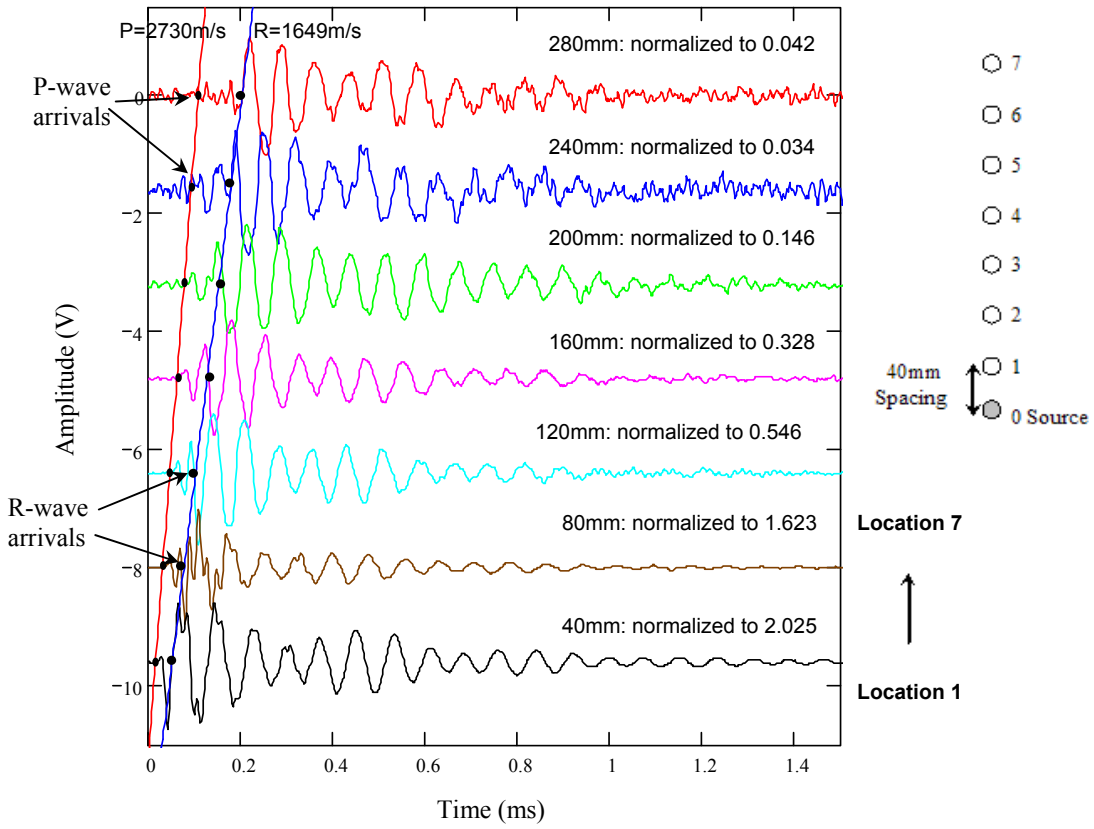

Figure 6.19 (b): Measurements using 100 kHz accelerometer along Line x1-y1 (slab 2)

In Figures 6.19a and 6.19 b, the P-wave and R-wave arrival points observed at different receiver locations are connected by two solid lines. The slopes of these lines will provide P- and R-wave velocities.

After the selection of the suitable S-R spacing, the source and receiver locations were selected following the equal-spacing configuration used in slab 1. The source and receiver locations for Set 1 to Set 4 measurements were developed to assess the wave attenuation across the joint in slab 2 (Figure 6.18). For ideal pavement sections where the material strength is uniform, the measured *FTC* should be constantly equal to 1. However, this condition is not always achieved even at the joint-free sections because the uniformity of compaction and material gradation cannot be achieved during the fabrication, as observed in slab 1. Wave measurements were taken at the joint-free

sections on either side of the joint in order to compare the compaction level achieved on both sides (Figure 6.18). The six sets of measurements are summarized in Table 6.5.

Table 6.5: Test arrangement in slab 2

Description	Locations	Measured signals
Jointed surface (Set 1)	Pair 1 –sources at S1 and S2; receiver at R1	f_{S1_R1} and f_{S2_R1}
	Pair 2 –sources at S1 and S2; receiver at R2	f_{S1_R2} and f_{S2_R2}
Jointed surface (Set 2)	Pair 1 –sources at S2 and S3; receiver at R2	f_{S2_R2} and f_{S3_R2}
	Pair 2 –sources at S2 and S3; receiver at R3	f_{S2_R3} and f_{S3_R3}
Jointed surface (Set 3)	Pair 1 –sources at S3 and S4; receiver at R3	f_{S3_R3} and f_{S4_R3}
	Pair 2 –sources at S3 and S4; receiver at R4	f_{S3_R4} and f_{S4_R4}
Jointed surface (Set 4)	Pair 1 –sources at S4 and S5; receiver at R4	f_{S4_R4} and f_{S5_R4}
	Pair 2 –sources at S4 and S5; receiver at R5	f_{S4_R5} and f_{S5_R5}
Joint-free surface (Set 5)	Pair 1 –sources at S2 and S*l*; receiver at R*l*	f_{S2_Rl} and f_{Sl_Rl}
	Pair 2 –sources at S2 and S*l*; receiver at R3	f_{S2_R3} and f_{Sl_R3}
Joint-free surface (Set 6)	Pair 1 –sources at S3 and S*r*; receiver at R2	f_{S3_R2} and f_{Sr_R2}
	Pair 2 –sources at S3 and S*r*; receiver at R*r*	f_{S3_Rr} and f_{Sr_Rr}

The received signals were analyzed in time and frequency domains using the same techniques used for slab 1. PTP amplitude ratio, maximum spectral amplitude ratio, maximum spectrum area ratio, FTC, WTC, and equivalent damping ratio were obtained to characterize the wave attenuation caused by the joint.

The joint-free wave path from set 1 to set 4 is close to the joint, and thus may have lower strength than does the joint-free sections away from the joint. Hence, the obtained FTC and WTC are probably not representative of true relative strength of the joint. Therefore, the FTC and WTC obtained from Set 5 and Set 6 (away from the joint) were used as the benchmark. The FTC and WTC obtained across the jointed sections were normalized to the benchmark FTC and WTC. The normalized FTC and WTC are expected to be representative of the relative strength of the joint.

6.7 Results and Discussions for Slab 2

The detailed results of the six sets of measurements in slab 2 are presented in Appendices H to O as described below.

- Signals in time and frequency domains in Appendix H
- The results of wave amplitude ratios in Appendix I
- The results of FTC vs. frequency and one-third wavelength in Appendix J
- The results of wavelet transform of full signals using Morlet wavelet in Appendix K
- Wavelet transform of signals using Mallat's algorithm in Appendix L available in the attached CD
- Equivalent damping ratio vs. frequency in Appendix M available in the attached CD
- The associated signal processing for Line x1-y1 and the six sets of measurements in slab in Appendices N and O available in the attached CD

6.7.1 Analysis based on wave velocities

Typical time signals at the seven locations measured using the 50 kHz and the 100 kHz accelerometers are shown in Figures 6.19a and 6.19b respectively. The P-wave and R-wave velocities were determined from the slope of the lines connecting the arrival points of P-waves and R-waves. The slopes of these lines were determined as the distance between two receiver locations divided by the travel time between the two corresponding locations. The P-wave velocity (V_P) of 2694 m/s and the R-wave velocity (V_R) of 1617 m/s were estimated from the wave measurements using the 50 kHz accelerometer (Figure 6.19a), For the measurements using the 100 kHz accelerometer (Figure 6.19b), V_P = 2730 m/s and V_R = 1649 m/s were obtained. The V_P was also estimated by measuring the time

taken by the wave traveling through the known depth of the slab (85mm). The measurement was conducted by placing one transducer (50 kHz, Pundit) on the slab surface and the other (50 kHz accelerometer) at the bottom. The velocity was then obtained by dividing the slab thickness by the wave travel time. An average V_P of 2765m/s and an average V_R of 1633m/s were obtained from these measurements. Based on the V_P and V_R, a Poisson's ratio of 0.12 was computed (Equation 4.2). The V_P and V_R were used to calculate to the Lamb wave dispersion curves.

Wave attenuation is attributed to two basic mechanisms: geometric attenuation and material attenuation/damping (Owino and Jacobs, 1999) (Chapter 2). The geometric attenuation in slab 1 was not evaluated because the data observed on the joint-free surface were limited. However, sufficient data were acquired to determine geometric attenuation in slab 2, as discussed in the following section.

6.7.2 Analysis based on geometric attenuation

Geometric attenuation is theoretically studied in a half space (Equation 2.33). However, in a slab, geometric attenuation could be affected by the presence of Lamb waves (caused by the P- and R-waves interacting with the boundaries) that do not exist in a half space (Chapter 2). The dispersive nature of Lamb waves may also affect the wave attenuation measured across the joint. The geometric attenuation study would contribute to understanding of the effect of Lamb waves.

The geometric attenuation in slab 2 was estimated by examining the relationship between the wave amplitude and the distance both in logarithmic scale as shown in Figures 6.20a and 6.20b. The wave attenuation is expressed in terms of signal PTP amplitude of the signal in time domain, maximum magnitude and spectrum area of the signal in frequency domain. The attenuation evaluation for P- and R-waves was achieved by analyzing the P-wave portions and the R-wave portions of the signals. The same techniques of windowing and Fourier transform used in slab 1 study were applied to slab 2 as well. In the analysis for P-waves, the signals received at locations 1 and 5 by the 50 kHz accelerometer and at locations 1, 6 and 7 using the 100 kHz accelerometer were excluded in the attenuation

evaluation. This was done because wave interference and noise lead to ambiguity and bias in windowing the P-wave portions of these signals. Noisy signals received (e.g. from locations 3 to 7) by the 100 kHz accelerometer is attributable to the low sensitivity (10mv/g) of the accelerometer. Also for the same reason, the 100 kHz accelerometer was then considered not suitable for the testing across the joint. For illustration of noise and wave interference, the front parts of the signals from Line x1-y1 measured with the 100 kHz accelerometer are enlarged in Figure 6.21. For the analysis of R-waves, only the signals measured with the 50 kHz accelerometer at locations 1 to 6 were studied. The signals measured with the 100 kHz accelerometer were not considered in the R-wave analysis because the R-wave portions are significantly affected by wave interference, as indicated by the dotted circles in Figure 6.21.

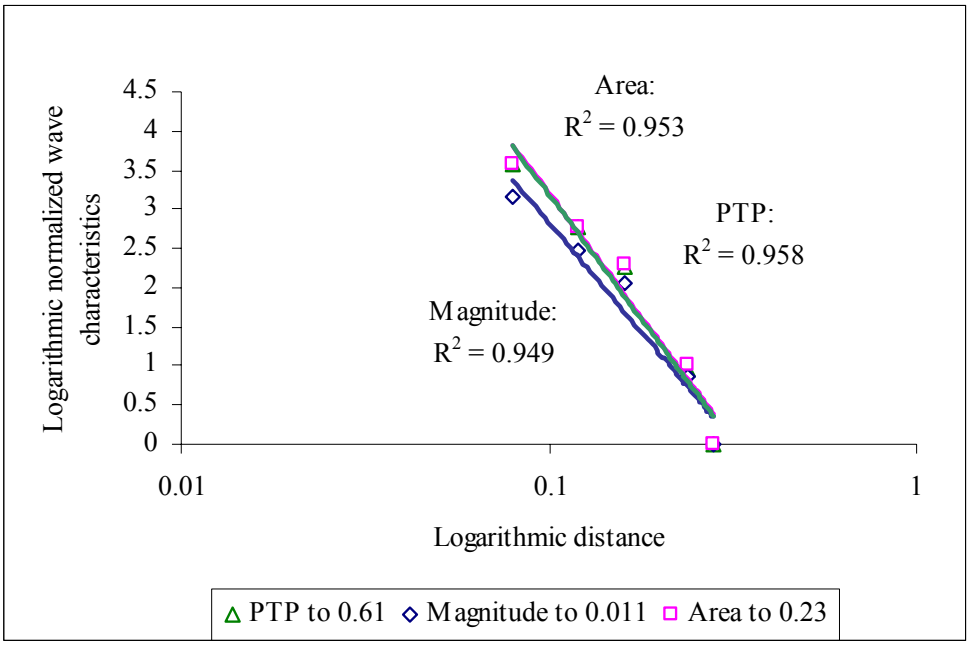

Figure 6.20 (a): P-wave attenuation measured using 50 kHz accelerometer (slab 2)

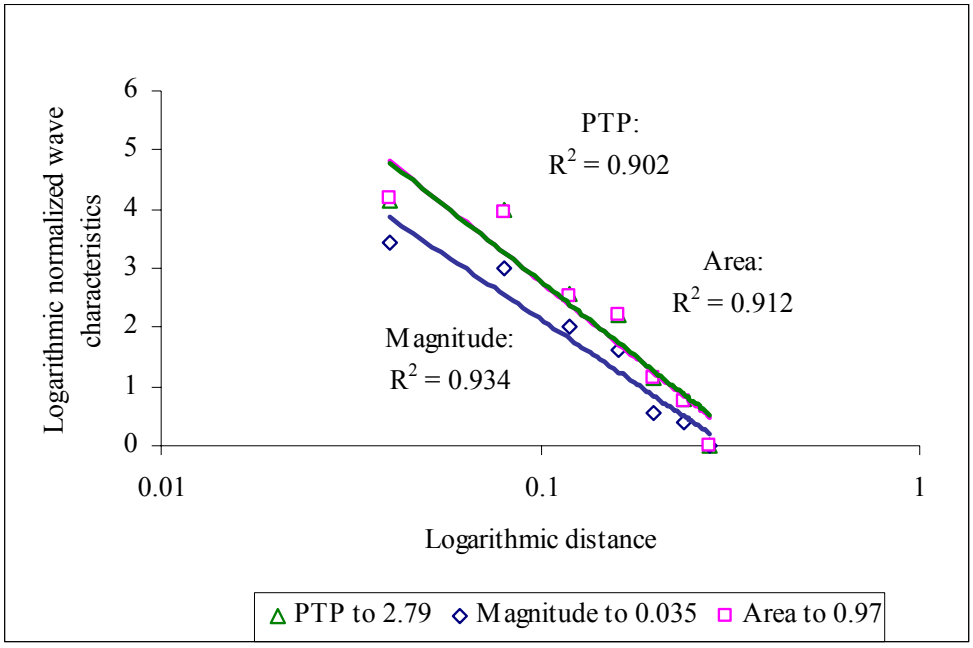

Figure 6.20 (b): R-wave attenuation measured using 50 kHz accelerometer (slab 2)

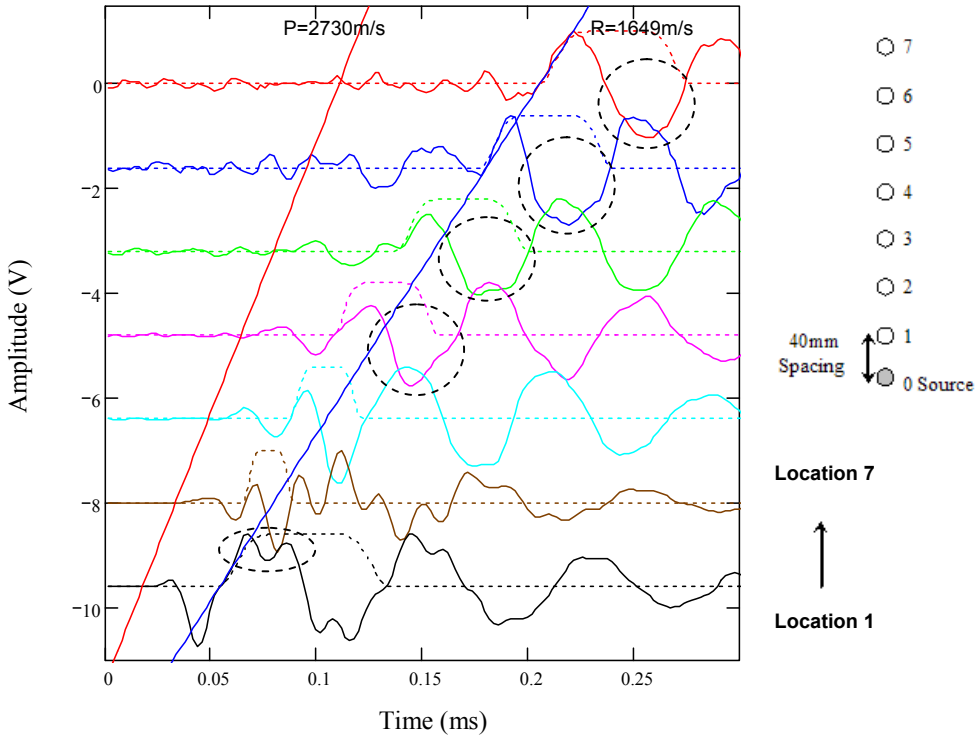

Figure 6.21: Enlarged view of signals measured with 100 kHz accelerometer (slab 2)

(Note: the dotted circles mark the wave interference.)

Figures 6.20a and 6.20b show the plots of normalized wave amplitudes vs. logarithmic distance between the source and receiver for the P- and R-wave signals measured by the 50 kHz accelerometer. The regression lines were fitted through the data. The average slope of the line for P-waves is -2.6 and for R-waves is -2.1 that are known as the geometric attenuation coefficients. The theoretical geometric attenuation coefficients for P- and R-waves (both waves at the surface) are -2 and -0.5 respectively (Chapter 2). The observed attenuation coefficients, especially for the R-waves, are significantly higher than the theoretical values. The possible reasons are as follows. The theoretical geometric attenuation is applicable to a homogeneous elastic half space where R-waves are non-dispersive. However, an asphalt concrete slab is an inhomogeneous viscoelastic confined space where dispersive Lamb waves instead of R-waves dominate low frequencies. The effect of Lamb waves will be minimized only after a certain *cut-off* frequency (f_{cut}) that depends on the slab thickness and the nature of the medium (Chapter 2). The dispersive nature of Lamb waves will affect the R-wave attenuation properties. In addition, while Equation 2.33 takes into account geometric attenuation only, material attenuation (damping) is also a source for reduction of signal amplitude. With both geometric and material attenuation effects, the waves lose their amplitude more rapidly. Besides, the interaction (i.e. superposition) between the first arriving P-waves and the following R-waves will also contaminate the attenuation results. On the other hand, the coupling variability at the seven receiving locations may also introduce inconsistency in the amplitude measurements. Thus, the effect of Lamb waves, material damping, mode superposition, and coupling variability are likely the explanations why the observed attenuation coefficients are higher than theoretical. Similar results of geometric attenuation observed using the 100 kHz accelerometer are shown in Table 6.6.

Table 6.6: Correlation between logarithmic wave amplitudes (y) vs. distance (x) for evaluation of geometric attenuation in slab 2

Accelerometer	Analyzed Portion	PTP	Magnitude	Area
50kHz (PCB353B65)	**P-wave (Figure 6.20a)**	y = -2.7429Ln(x) – 3.1255 (R^2 = 0.958)	y = -2.4183Ln(x) - 2.7335 (R^2 = 0.949)	y = -2.7354Ln(x) - 3.0878 (R^2 = 0.953)
	R-wave (Figure 6.20b)	y = -2.1923Ln(x) - 2.2672 (R^2 = 0.902)	y = -1.8773Ln(x) - 2.1836 (R^2 = 0.934)	y = -2.218Ln(x) - 2.3335 (R^2 = 0.912)
100kHz (PCB353A60)	**P-wave**	y = -2.3483Ln(x) - 3.5313 (R^2 = 0.977)	y = -1.8922Ln(x) - 2.8205 (R^2 = 0.964)	y = -2.3446Ln(x) - 3.5307 (R^2 = 0.975)
	R-wave	y = -2.2262Ln(x) - 2.4784 (R^2 = 0.875)	N/A	N/A

Note: N/A represents data not available because wave interference leads to biased windowing.

The specific effects of Lamb waves on measurements of wave attenuation (in terms of FTC, WTC, PTP amplitude ratio, maximum amplitude ratio, spectrum area ratio, and equivalent damping ratio) are yet to be fully understood. Thus, it is preferable to focus on analyzing the frequency components higher than the f_{cut} where the Lamb waves become non-dispersive and the effect is reduced. According to the Rayleigh-Lamb-frequency Equation 2.22, the Lamb wave dispersion curves in slab 2 were computed using MathCAD® as shown in Figure 6.22. The Lamb wave velocities approach V_R (see A0) or constant (see S0) at least beyond f_{cut} = 30 kHz (Figure 6.22). The f_{cut} was useful in understanding the variation of FTC values and equivalent damping ratio values with frequency in the subsequent study of the joint in slab 2.

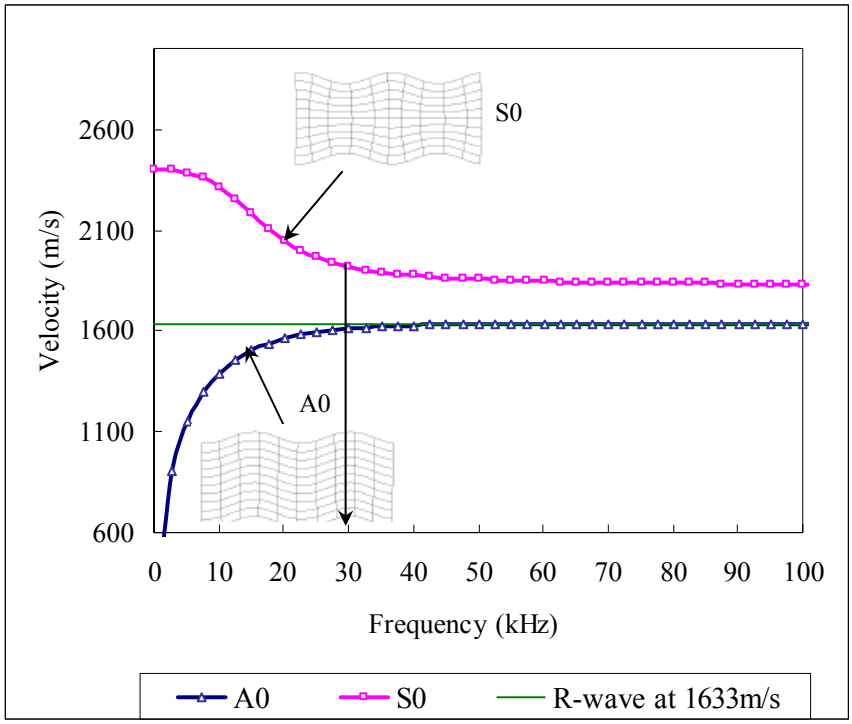

Figure 6.22: Dispersion curves of two Lamb wave modes in slab 2 (85mm thickness, V_P = 2765m/s, V_S = 1822m/s). (S0: Symmetric fundamental mode; A0: Anti-symmetric fundamental mode, (Kuttruff, 1991))

6.7.3 Analysis based on PTP ratio, maximum magnitude ratio, and spectrum area ratio

Figures 6.23 and 6.24 show the results of signal processing in both domains for a pair of signals (from Set 1) across the joint and through the joint-free surface respectively. In time domain, each of the two signals was normalized to its PTP amplitude for illustration purpose. In frequency domain, the real spectral amplitudes of the signals are given. The maximum spectral amplitudes of the two signals were indicated by the horizontal lines (Figures 6.23 and 6.24). A significant reduction (about 50% to 80%) in signal amplitudes across the joint was observed. In addition, the P-wave and R-wave portions are well defined with little interference between each other or noise (Figure 6.24). This result confirms that the selected source-receiver spacing (80 mm) is correct.

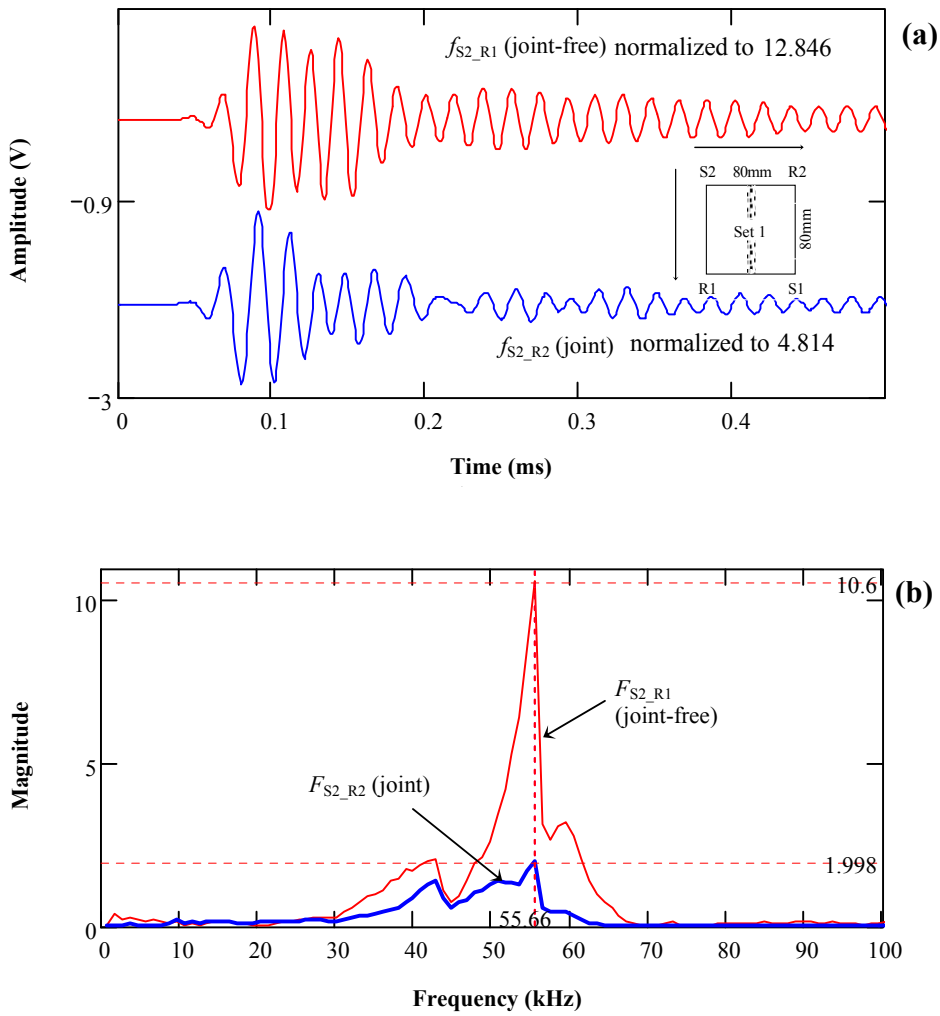

Figure 6.23: A pair of signals (Set 1, slab 2) across the joint and through the joint-free surface measured with 50kHz accelerometer - (a) full signals in time domain and (b) full signals in frequency domains

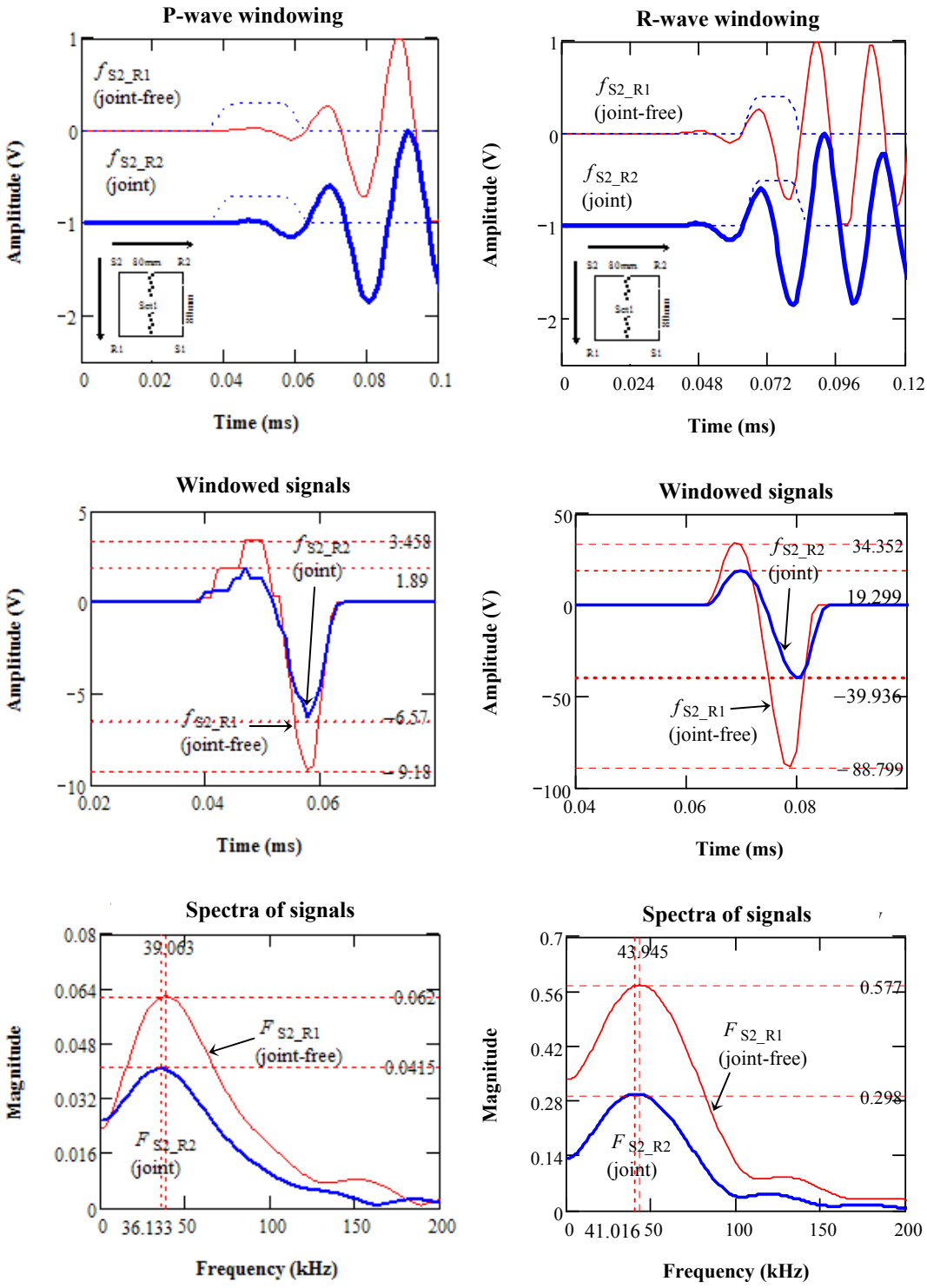

Figure 6.24: Windowing the P- and R-wave portions of the two signals (from Set 1) (Horizontal lines mark the peak amplitudes, and vertical lines the dominant frequencies)

The amplitude ratios (Appendix I) between the two pairs of signals in each set of measurements were compared in the same way it was done for slab 1. It was found that the strength of the joint decreases from J0 to J4 (Figure 6.18). This result could be to some degree attributed to the variability in compaction along the joint (Figure 6.17). The area compacted at higher mix temperatures achieved better compaction, and hence, higher strength. Thus, the joint-free surfaces near the joint at J4 would have received good compaction, resulting in lowest wave attenuation. Nevertheless, most of the amplitude ratios are less than 1, indicating occurrence of attenuation across the joint. In some cases (Appendix I), the maximum magnitude ratios or spectrum area ratios for the windowed signals are nearly 1 because the biased frequency contents of the windowed signals caused by wave interference. It is implied that caution must be exercised in the interpretation of the results from analysis of the windowed signals.

The average amplitude ratios for the six sets of measurements are summarized in Table 6.7. The amplitude ratios between the across-the-joint signals and the joint-free signals vary between 0.44 and 0.55. These values are slightly less then the values observed in slab 1 (0.51 to 0.72, *see* Table 6.3), indicating that the relative strength of the joint in slab 2 is slightly weaker than joint strength in slab 1. Although, an attempt was made to fabricate good joint in slab 2, the temperature drop caused by the delay in compacting the mix and insufficient weight of the hand-held hammer could have affected the mix compaction and hence the strength as indicated by the wave velocities (section 6.7.1).

The windowed P- waves and R-waves gave similar results (slightly larger than 1) associated with the Set 5 and Set 6 measurements for the joint-free surfaces. Yet, the results of the full wave signal are 20% to 46% larger than the values obtained from the P- and R-wave analyses. The possible reason is that a full signal contains scattering and wave reflections from boundaries in addition to the first arriving P- and R-waves. Amplitude ratios larger than 1 indicate that the farther the location from the joint, the better the mix quality.

Table 6.7: Average PTP ratio, magnitude ratio and area ratio for measurements on the jointed surface and the joint-free surfaces in slab 2

Locations	Analyzed Portion	PTP ratio	Magnitude ratio	Area ratio
Jointed surface (Set 1 to Set 4)	Full signal	0.44	0.47	0.45
	P-wave	0.51	0.55	0.53
	R-wave	0.49	0.53	0.49
Joint-free surface (Set 5 and Set 6)	Full signal	1.38	1.58	1.40
	P-wave	1.15	1.08	1.11
	R-wave	1.09	1.11	1.12

6.7.4 Analysis based on FTC and WTC

The FTC and WTC are better than the TC because they eliminate the coupling variability. Table 6.8 compares the average FTC and WTC of Set 1 to Set 4 measurements on the jointed surface. The FTC values between 0.48 and 0.57 were observed. The FTC values of 0.53 and 0.57 for P- and R-wave portions were observed. The average WTC values are between 0.41 and 0.44 as shown in Table 6.8 and Figure 6.26. The detailed FTC and WTC values for the six sets of measurements are given in Appendix I.

Figures 6.25 and 6.26 also display the average FTC and WTC values for Set 5 and Set 6 measurements on the joint-free surfaces in slab 2. The FTC and WTC values for Set 1 to Set 4 on the jointed surface in slab 2 are less than the values for Set 5 and Set 6 on the joint-free surfaces. As aforementioned, the FTC and WTC from Set 1 and Set 4 were normalized to the corresponding average FTC and WTC from Set 5 and Set 6 to obtain the FTC ratio and WTC ratio, as shown in Figure 6.27 and 6.28. For example, the average P-wave FTC from Set 5 and Set 6 was used as the divisor and to compute the P-wave FTC ratio. Likewise, for each selected frequency, the average WTC from Set 5 and Set 6 was used as the divisor.

The average FTC ratio for full signals and WTC ratios for different dominant frequencies give consistent ratios of around 0.35 (Figures 6.27 and 6.28). These parameters are suitable for condition assessment of the longitudinal joint in asphalt pavements. As aforementioned, caution must be exercised in the analysis of the windowed P- and R-waves.

Table 6.8: Average FTC, WTC and equivalent damping ratio for measurements on the jointed surface and the joint-free surfaces in slab 2

Locations	Analyzed Portion	FTC	WTC	Damping ratio
Jointed surface (Set 1 to Set 4)	Full signal	0.48 at 54kHz	0.41 at 54kHz	0.033 at 54kHz
	P-wave	0.53 at 36kHz	0.46 at 36kHz	0.09 at 36kHz
	R-wave	0.57 at 44kHz	0.44 at 44kHz	0.05 at 44kHz

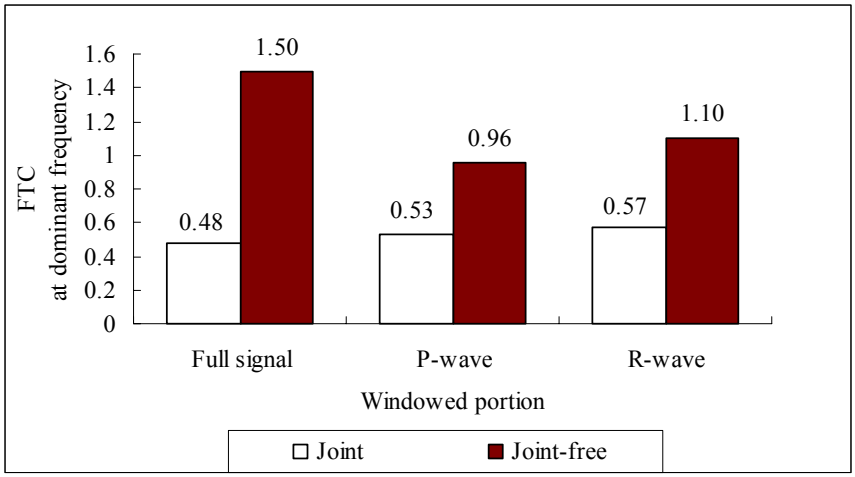

Figure 6.25: Comparison of average FTC between measurements on the jointed surface and the joint-free surfaces (slab 2)

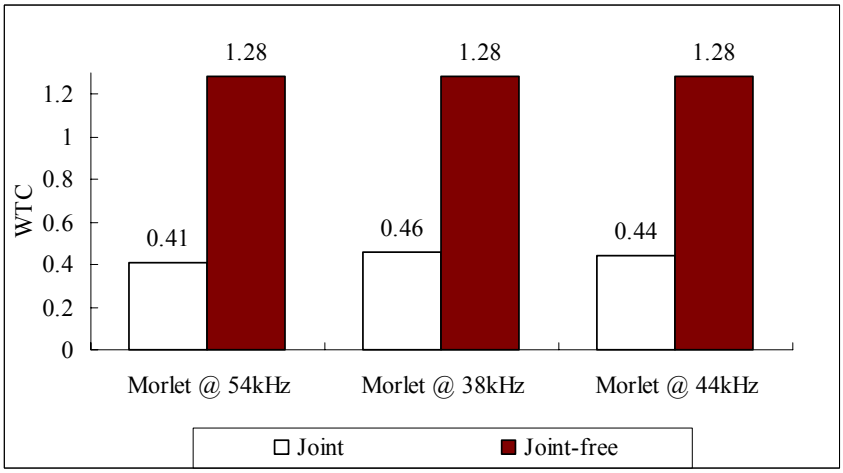

Figure 6.26: Comparison of average WTC between measurements on the jointed surface and the joint-free surface (Slab 2)

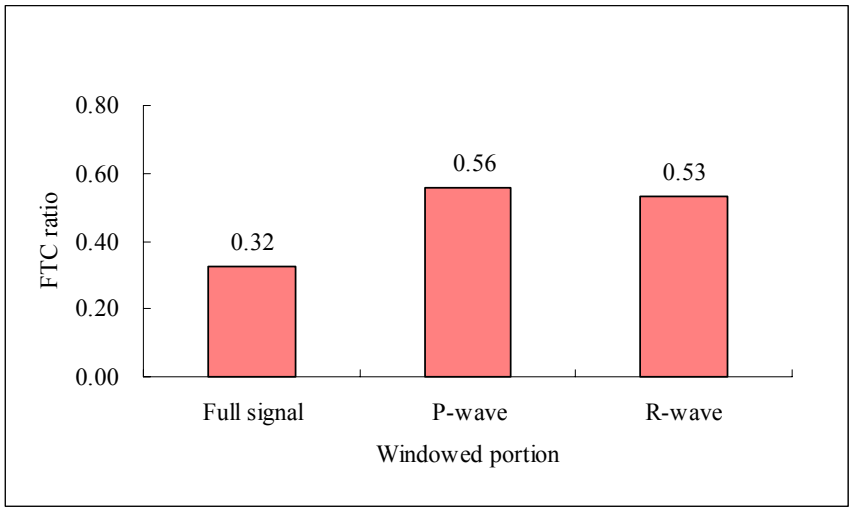

Figure 6.27: Average FTC ratio for Set 1 to Set 4 measurements on the jointed surface (slab 2)

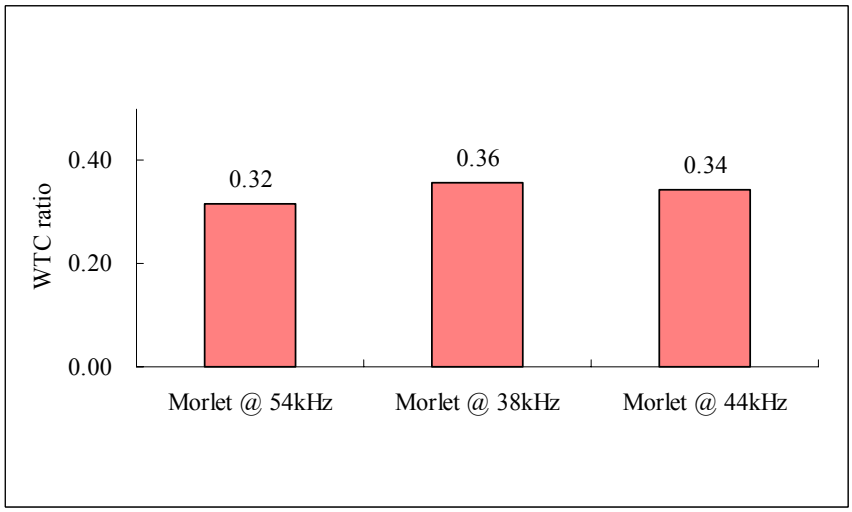

Figure 6.28: Average WTC ratio for Set 1 to Set 4 measurements on the jointed surface (slab 2)

For P-wave analysis, the FTC values for Set 5 and Set 6 in slab 2 are similar and are close to 1, as shown in Table 6.9. However, for R-waves, the FTC value for Set 5 is 1.31 and for Set 6 is 0.88. This could be because P-waves have larger wavelengths that are less sensitive to small changes in microstructures. In addition, P-waves enable sampling of the

full depth of the slab, giving an average condition. The FTC values obtained from the analysis of full signals for Set 5 and Set 6 are similar.

Table 6.9: Summary of FTC, WTC and equivalent damping ratio for Set 5 and Set 6 measurements on the joint-free surface in slab 2

Location	Analyzed Portion	Signal ratio (*SR*)	FTC	WTC	Damping ratio
Joint-free surface at left side of the joint (Set 5)	Full signal	$\sqrt{\frac{f_{S2\_Rl} \cdot f_{Sl\_R3}}{f_{S2\_R3} \cdot f_{Sl\_Rl}}}$	1.52 at 55kHz	1.36 at 55kHz	0.024 at 55kHz
	P-wave		0.95 at 41kHz	1.43 at 41kHz	-0.005 at 41kHz
	R-wave		1.31 at 45kHz	1.42 at 45kHz	0.02 at 45kHz
Joint-free surface at right side of the joint (Set 6)	Full signal	$\sqrt{\frac{f_{Sr\_R2} \cdot f_{S3\_Rr}}{f_{Sr\_Rr} \cdot f_{S3\_R2}}}$	1.47 at 48kHz	1.19 at 48kHz	0.025 at 48kHz
	P-wave		0.96 at 40kHz	1.13 at 40kHz	-0.01 at 40kHz
	R-wave		0.88 at 46kHz	1.13 at 46kHz	-0.01 at 46kHz
Joint-free surface (Average of the above 2 Sets)	Full signal	$\frac{Set\ 5\ SR + Set\ 6\ SR}{2}$	1.50 at 52kHz	1.28 at 52kHz	0.025 at 52kHz
	P-wave		0.96 at 40kHz	1.28 at 40kHz	-0.0075 at 40kHz
	R-wave		1.10 at 45kHz	1.28 at 45kHz	0.005 at 45kHz

FTC values were plotted against frequency and one-third the wavelength ($\lambda/3$) respectively (Appendix J), as shown in Figure 6.29. The one-third of the wavelength is typically the effective penetration depth for R-waves where the maximum displacements occur and most of the wave energy is concentrated (Stokoe and Nazarian 1983). As discussed previously, the 30 kHz is the *cut-off* frequency for R-waves, corresponding to $\lambda/3 =$ 18mm. After 30 kHz (or before 18mm), the FTC for R-waves shows a reasonable trend: the higher the frequencies (or the smaller the wavelengths), the smaller the FTC (Figure 6.23). It is indicated that the FTC for R-waves is suitable for condition assessment of the joint with a depth smaller than 18mm. The P-wave FTC values are slightly larger than the R-wave FTC values (Figure 6.23) because P-waves have larger wavelengths that enable more transmission.

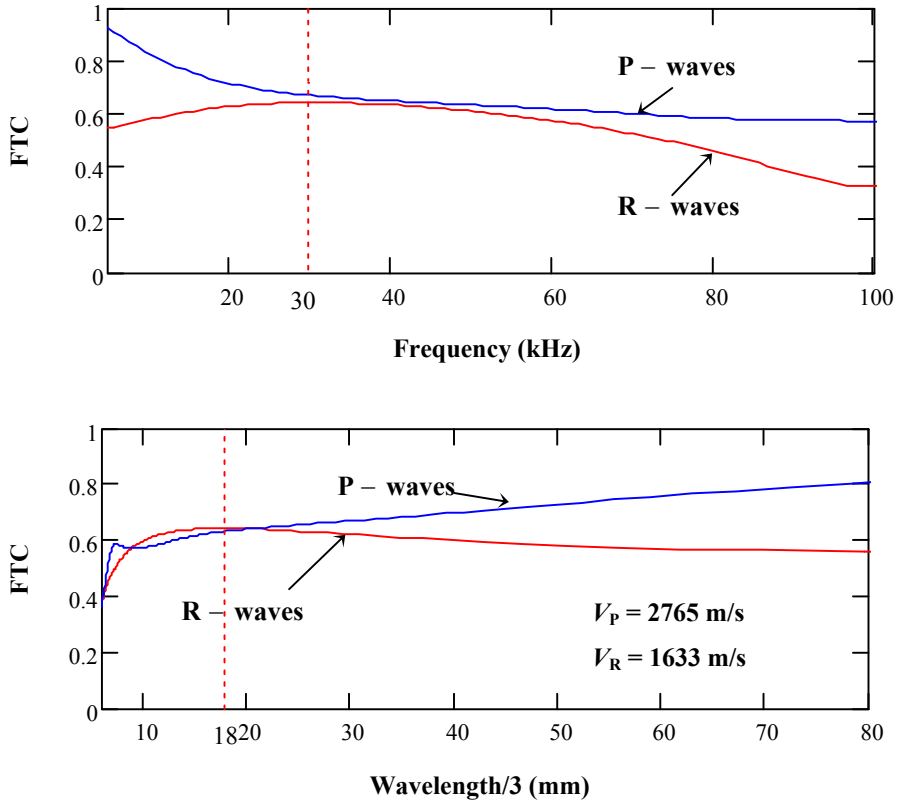

Figure 6.29: FTC from P- and R-wave portions for Set 1 (slab 2)

6.7.5 Analysis based on equivalent damping ratio for the joint

The equivalent damping ratios for the six sets of measurements (Appendix I) were computed according to Equations 6.5a and 6.5b. The equivalent damping ratios for the R-waves across the joint are in general smaller and more consistent than the equivalent damping ratios for the P-waves across the joint (Tables 6.8 and 6.9). The equivalent damping ratios for the R-waves are smaller because of the smaller velocity (Equation 6.5b).

Particular attention was given to comparing the equivalent damping ratios for the jointed surface with the equivalent damping ratios for the joint-free surfaces, as shown in Figure 6.30. The average equivalent damping ratios for Set 1 to Set 4 (on the jointed surface) were significant higher than the equivalent damping ratios for Set 5 and Set 6 (on the joint-free surfaces). This result indicates that the joint is strongly dissipative. The FTC-

based equivalent damping ratios are equal to zero only in the situation where the material strength is uniform (Equations 6.5a and 6.5b). Negative damping represents the situation where the material away from the joint is stronger than the material close to the joint. The equivalent damping ratio results in slab 2 will be compared with the equivalent damping ratios observed in slab 3, as will be discussed later.

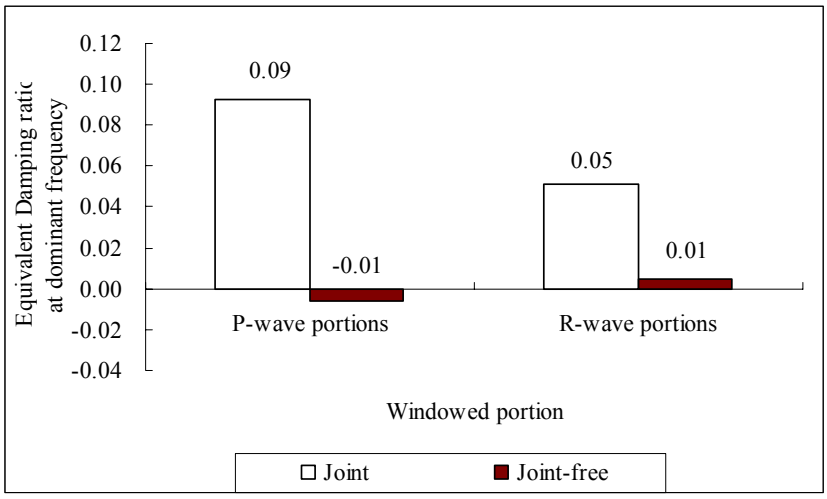

Figure 6.30: Average equivalent damping ratios for Set 1 to Set 4 and for Set 5 to Set 6

In addition, the equivalent damping ratio values as a function of frequency (Appendix M) were also studied to verify the effect of Lamb waves (caused by P-wave and S-waves interacting with two parallel boundary surfaces), as shown in Figure 6.31. The variation of the equivalent damping ratios for the P-waves at low frequencies is likely because the wavelengths of the P-waves at low frequency range exceed the slab thickness.

The initial decrease of the equivalent damping ratio values for R-waves (Figure 6.31) could be attributed to the presence of dispersive Lamb waves. The theoretical equivalent damping ratio calculation is applicable to R-waves in a half space where the R-wave velocity is constant as described by the V_R term in the Equation 2.32. Thus, the applicability of Equation 2.32 to a slab is limited at the high frequency range beyond the *cut-off* frequency (f_{cut}). The f_{cut} for the R-waves in slab 2 is 30 kHz, as determined previously. The equivalent damping ratios for the R-waves from 30 kHz to 100 kHz vary

from 0.046 to 0.031 (Figure 6.31). The equivalent damping ratios for the P-waves and the R-waves converge with increase of frequencies.

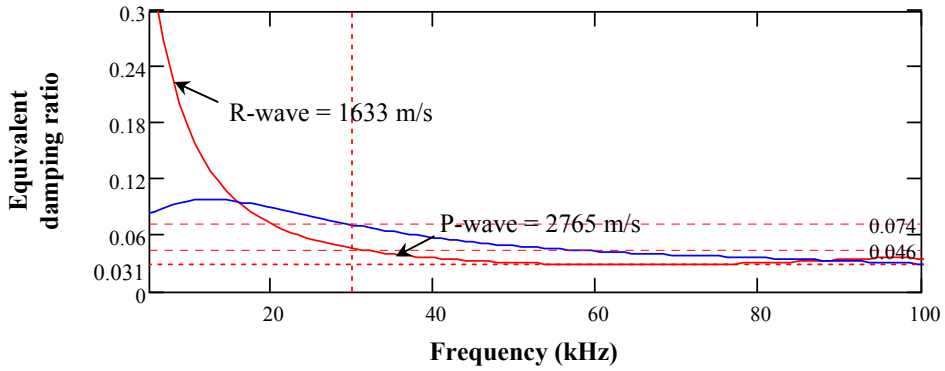

Figure 6.31: An example of equivalent damping ratios for P- and R-waves (Set 1, slab 2)

6.7.6 Summary of the results for slab 2

1. The wave attenuation parameters are suitable for condition assessment of longitudinal joints in asphalt pavements. More specifically, WTC and FTC for full signals and R-waves are quite promising. The FTC for R-waves is suitable for condition assessment of the longitudinal joint in slab 2 up to 18mm in depth.
2. The PTP ratio, maximum magnitude ratio and spectrum area ratio imply that the strength of the joint reduced from point J0 to J4.
3. The FTC and WTC show that the joint strength in slab 2 is weaker than the joint strength in slab 1.
4. The equivalent damping ratio results indicate that the joint is strongly dissipative.
5. The new sensor array on Line x1-y1 is applicable to evaluation of wave velocity and attenuation.
6. Appropriate spacing should be determined for condition assessment of the joint in terms of wave attenuation.
7. The observed relatively large geometric attenuation coefficients indicate the effects of Lamb waves and material damping.
8. The 100 kHz accelerometer is not suitable for testing of asphalt concrete slab because of its low sensitivity (10mv/g).

6.8 Fabrication of Pavement Slab 3

The purpose of the third slab was to assess the sensitivity of the wave attenuation parameters for condition rating of a week joint. Two identical transmitters of 50 kHz (narrow frequency band, center frequency: 50 kHz) were used as the sources, and the 50 kHz accelerometer as the receiver. The equipment setup used in the previous two tests, such as the power supply (PCB483(A) for the accelerometer, the low-pass filter (Krohn-hite 3384), the digital oscilloscope (HP 54610(B) and the desktop computer, was also used for testing of slab 3.

A modified hand-held hammer of a heavier weight (35 lbs) with a tamping foot of $20mm \times 20mm$ dimension was employed for the preparation of the third slab, as shown in Figure 6.32. The same mix (HL4-20% recycle asphalt) used in the preparation of slab 2 was used to fabricate the slab 3 with a weak joint. The procedure for fabrication of slab 3 is described as follows:

1. Followed the procedure used in steps 1 to 5 for the fabrication of slab 1.
2. Established a guideline parallel to the joint location and 20mm away from the divider, as shown in Figure 6.33.
3. Started the compaction from one end of a corner of side A near the guideline by tamping the mix with the hand-held hammer and moving the hammer along the guideline at 10 mm interval after every three blows until it reached the other end. The process was repeated until the whole area on side A up to the guideline was compacted to a desired level of compaction (60 blows). The same falling height (1m) was maintained when the compacting mix. The area between the guideline and the divider was compacted slightly using a piece of wood to create a weak joint.
4. Repeated steps 1 and 3 on side B without the divider. The whole area on side B up to the location of the joint (the divider) was fully compacted (60 blows).
5. Repeated steps 1 to 3 with the divider in place to lay the second lift on the top of the mix laid on side A.

Figure 6.32: The modified compactor (35 lbs) used in slab 3 fabrication

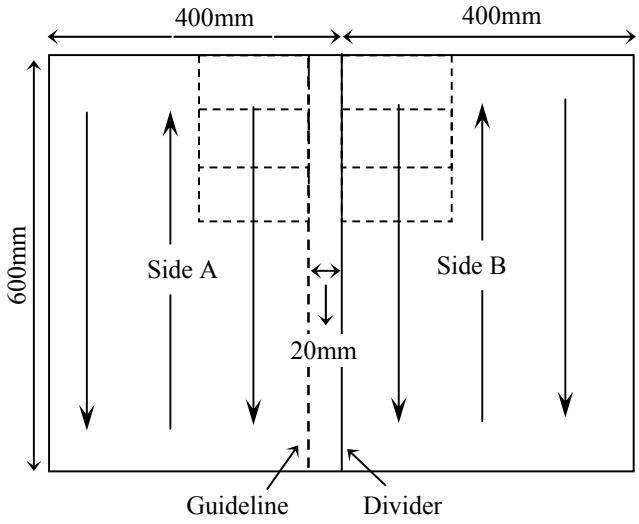

Figure 6.33: Compaction procedure of slab 3 with the 200mm square tamper

6. Repeated step 4 to place the second lift on the top of the mix on side B to complete the fabrication of the slab. The slab was allowed to cool down at room temperature making ready for testing.

6.9 Ultrasonic Testing of Slab 3

Thin steel plates of penny-size (15mm diameter) were epoxied to the slab surface, as illustrated in Figure 6.34a to 6.34c.

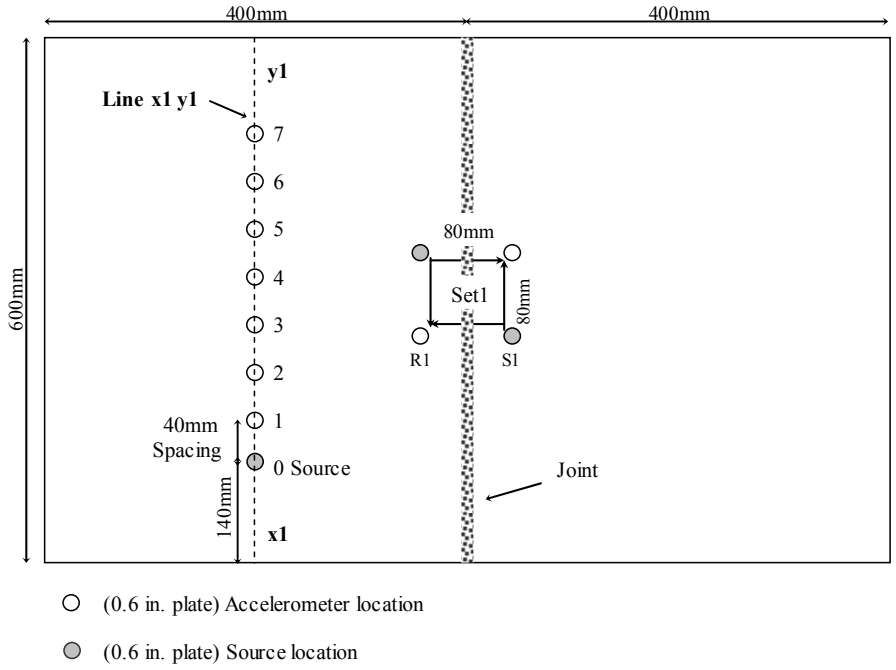

Figure 6.34 (a): Ultrasonic testing geometry for Set1 measurements (slab 3)

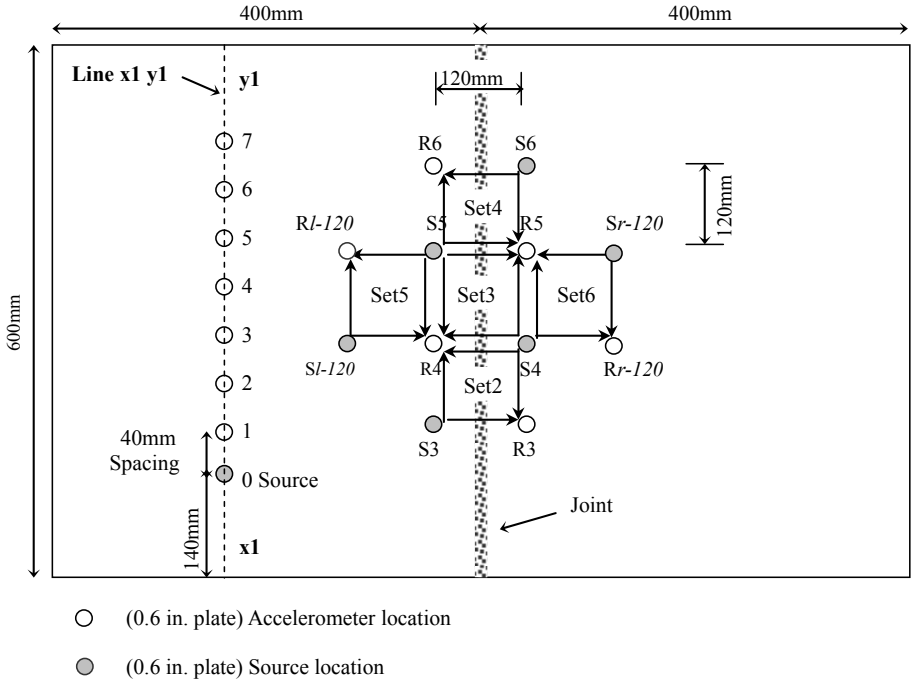

Figure 6.34 (b): Ultrasonic testing geometry for Set2 to Set 6 measurements (slab 3)

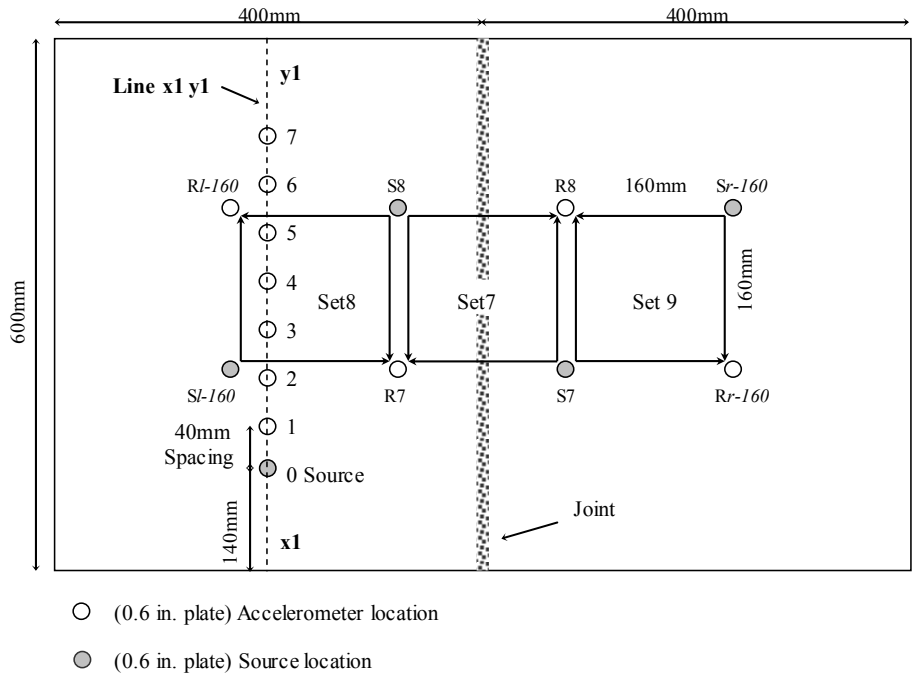

Figure 6.34 (c): Ultrasonic testing geometry for Set7 to Set 9 measurements (slab 3)

The same tests conducted along the Line x1-y1 in slab 2 were carried out in slab 3 to determine the wave velocities, attenuation, and suitable source-to-receiver (S-R) spacings (Figures 6.34a to 6.34c). The spacing requirement depends on the mix quality. Therefore, it is important to determine the appropriate S-R spacing before testing the slab. Each signal shown in the Figure 6.35 has been normalized to the maximum amplitude corresponding to the respective signal. Based on the testing, the spacings of 80mm, 120mm and 160mm were selected in slab 3 because of the clear detection of P- and R-waves with minimum wave interference (Figure 6.35). The spacings of 240mm and 280mm were not considered suitable because of the weak signals received far away from the source, as seen from the peak amplitudes of 0.19 and 0.122 respectively (Figure 6.35).

Based on the spacings determined, the source and receiver locations were selected to measure the signals across the jointed surface and the joint-free surface (Figures 6.34a to 6.34c). The effect of different spacings (80mm, 120mm and 160mm) on the output signals was studied from the measurements. The entire test and computation processes used in slab 2 were repeated here to measure the wave attenuation caused by the joint in slab 3. Typical results for slab 3 are given in the following sections. The detailed results of the nine sets of measurements for slab 3 are presented in Appendices P to W as described below.

- Signals in time and frequency domains in Appendix P
- Wave amplitude ratios in Appendix Q
- FTC vs. frequency and one-third the wavelength in Appendix R
- Wavelet transform of signals using Morlet wavelet in Appendix S
- Wavelet transform of signals using Mallat's algorithm in Appendix T available in the attached CD
- Equivalent damping ratio vs. frequency in Appendix U available in the attached CD
- The associated signal processing for Line x1-y1 and the nine sets of measurements in slab 3 in Appendices V and W available in the attached CD

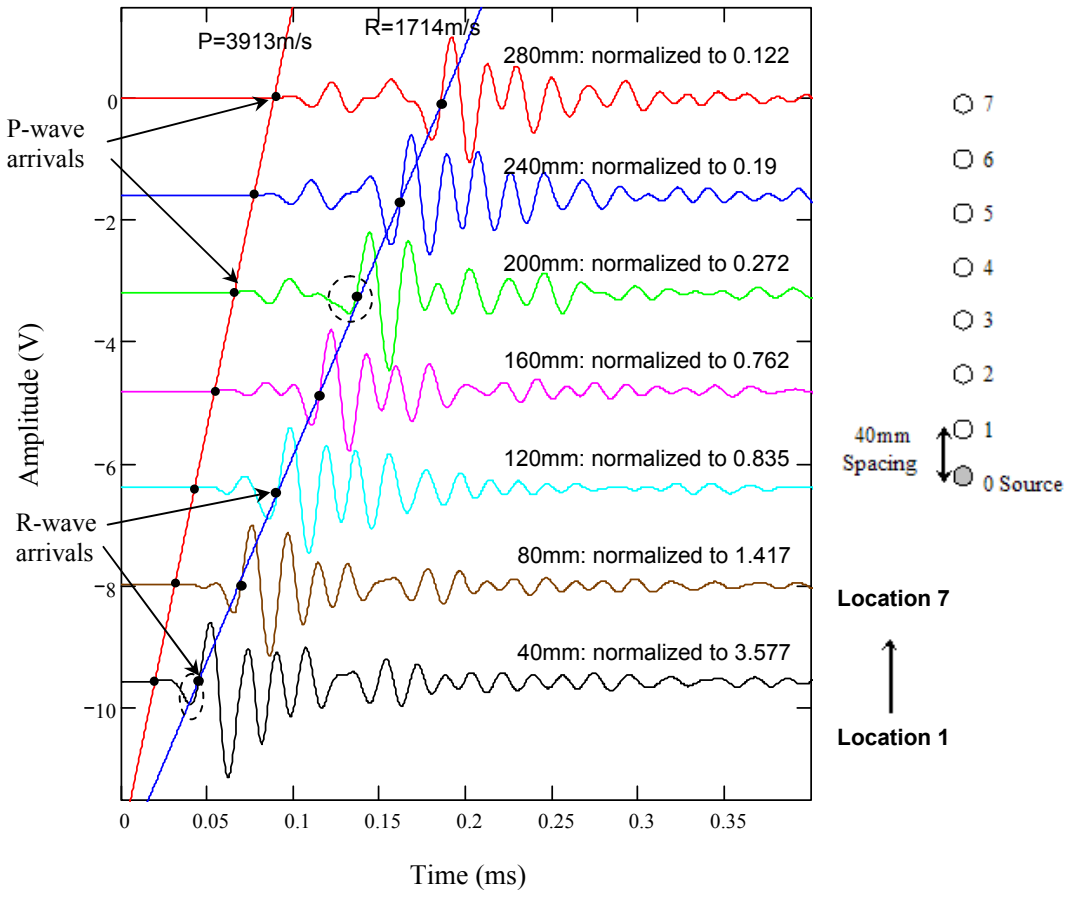

Figure 6.35: Measurements using 50 kHz accelerometer along Line x1-y1 (slab 3)

(Note: the dotted circles mark the wave interference.)

6.10 Results and Discussions for Slab 3

6.10.1 Analysis based on wave velocities

The purpose of the wave velocity measurements is to assess the level of compaction achieved during the fabrication of the slab. Typical time signals recorded at the seven locations are shown in Figure 6.35. The slopes of the lines connecting the P- and R-wave arrivals give the P-wave velocity (V_P = 3913 m/s) and the R-wave velocity (V_R = 1714 m/s). The V_P and V_R result in a Poisson's ratio of 0.36 (Equation 4.2). These values indicate that a better mix strength was achieved in slab 3 than in slab 2 that has a P-wave velocity of 2765 m/s, an R-wave velocity of 1633 m/s and a Poisson's ratio of 0.12. The

V_P and V_R were used to compute the Lamb wave dispersion curves and the equivalent damping ratios.

In order to reduce the effect of Lamb waves on the wave attenuation, the analysis of wave attenuation should focus the frequency components higher than the *cut-off* frequency (f_{cut}). This is because lamb waves become non-dispersive beyond the f_{cut}, and thus, the effect is minimized. The f_{cut} was useful in understanding the variation of FTC values and equivalent damping ratio values with frequency in the subsequent condition assessment of the joint. Based on the V_P and V_R determined, the Lamb wave dispersion curves in slab 3 were computed (Equation 2.22), as shown in Figure 6.36. The Lamb wave velocities approach V_R (see A0) or constant (see S0) at the f_{cut} of approximately 40 kHz (Figure 6.36).

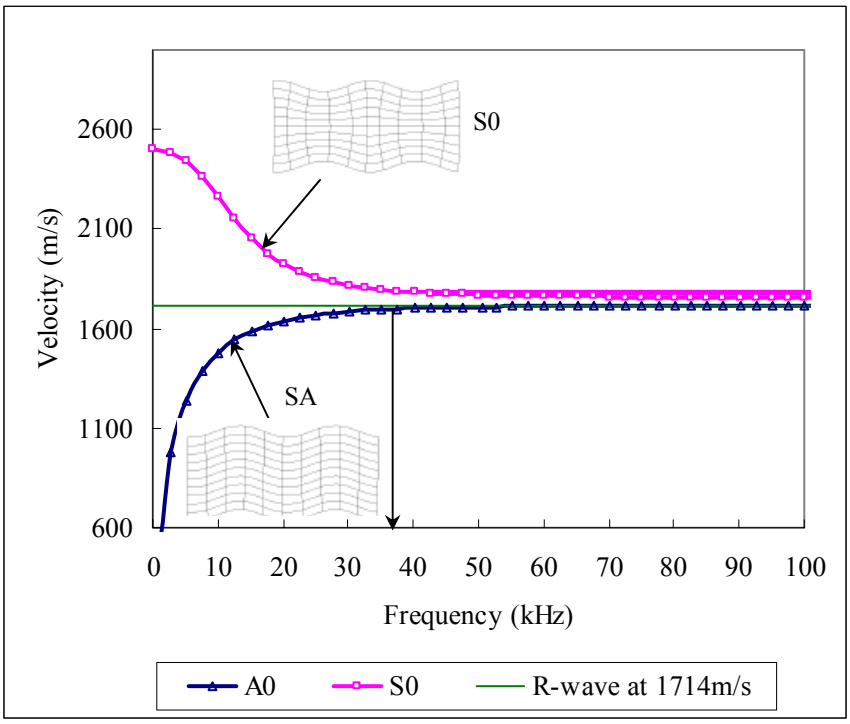

Figure 6.36: Dispersion curves of two Lamb wave modes in slab 3 (85mm thickness, V_P = 3913m/s, V_S = 1830m/s) (S0: Symmetric fundamental mode; A0: Anti-symmetric fundamental mode, (Kuttruff, 1991))

6.10.2 Analysis based on geometric attenuation

Wave attenuation is attributed to geometric attenuation and material attenuation/damping. Geometric attenuation (Equation 2.33) was estimated by examining the relationship between the wave amplitude and the distance both in logarithmic scale as shown in Figures 6.37a to 6.37c and Table 6.10. The signal received at location 1 was first excluded in the attenuation evaluation for P-waves because the interference of the arriving R-waves (Figure 6.35) impacted the windowing of P-waves. However, the observed correlations between the signal amplitudes and the distance are moderate (Figure 6.37a) because the amplitude at location 2 (80mm) is disproportionately smaller. The reason is not clear, which needs investigation. The attenuation for P-waves was then extrapolated based on the signal amplitudes from locations 3 to 7 (Figure 6.37b). For the R-wave geometric attenuation evaluation, all the signals were involved. The observed attenuation coefficient for P-wave is average -1.6, and for R-waves -1.8 (Table 6.10). These values are less than the values obtained in slab 2 probably because of less material attenuation (damping) in slab 3.

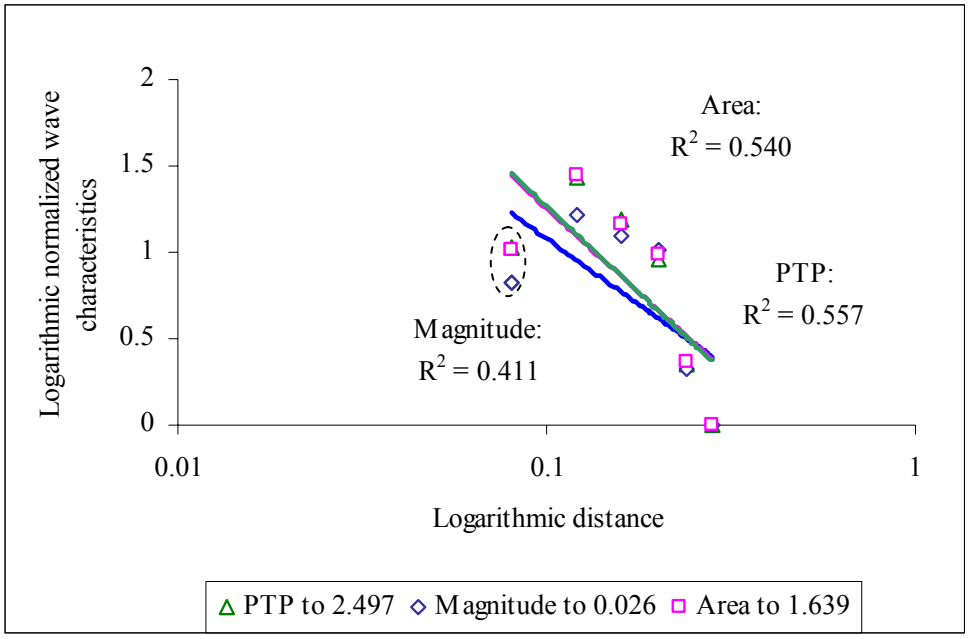

Figure 6.37 (a): P-wave attenuation based on locations from 2 to 7 (slab 3)

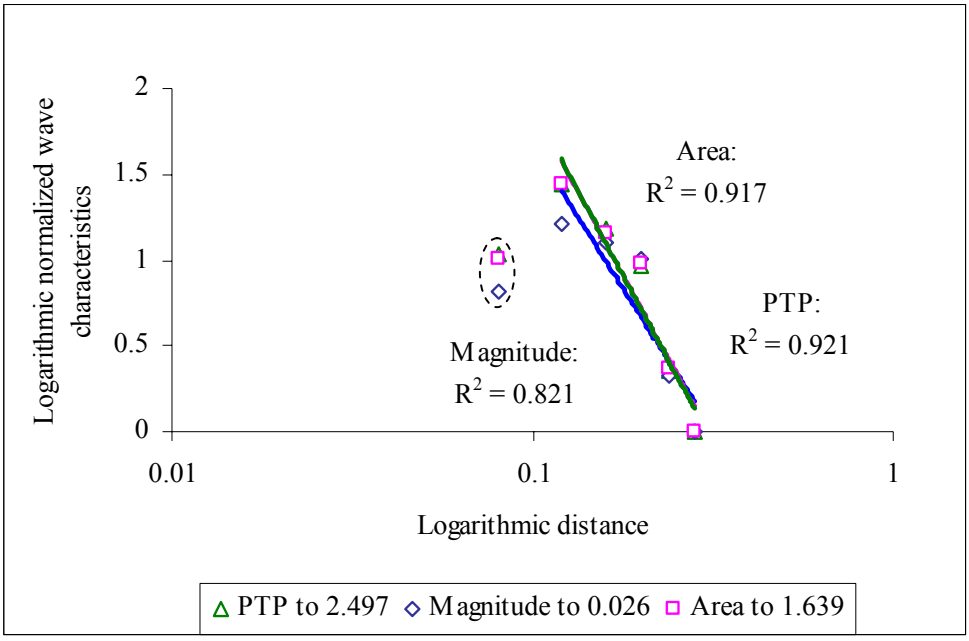

Figure 6.37 (b): P-wave attenuation based on locations from 3 to 7 (slab 3)

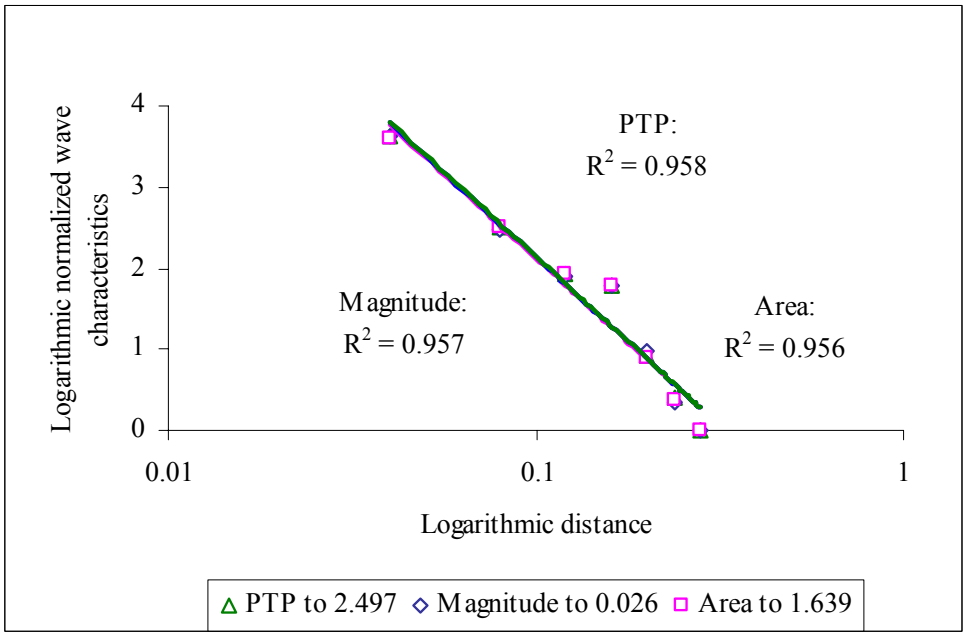

Figure 6.37 (c): R-wave attenuation based on locations from 1 to 7 (slab 3)

Table 6.10: Correlation between logarithmic wave amplitudes (y) vs. distance (x) for evaluation of geometric attenuation in slab 3

Accelerometer	Analyzed Portion	PTP	Magnitude	Area
50kHz (PCB353B65)	P-wave (Figure 6.37a)	y = -0.8676Ln(x) - 0.7325	y = -0.66Ln(x) - 0.4415	y = -0.8477Ln(x) - 0.6984
	P-wave (Figure 6.37b)	y = -1.7059Ln(x) - 2.0316	y = -1.4467Ln(x) - 1.6608	y = -1.6953Ln(x) - 2.012
	R-wave (Figure 6.37c)	y = -1.8095Ln(x) - 2.0246	y = -1.8037Ln(x) - 2.0178	y = -1.7897Ln(x) - 1.999

6.10.3 Analysis based on PTP ratio, maximum magnitude ratio, and spectrum area ratio

The joint in slab 3 was fabricated as a weak quality joint. Figures 6.38 and 6.39 compare the PTP amplitude and maximum spectral amplitude for a pair of signals (from Set 2) across the joint and through the joint-free surface respectively. A relatively large reduction (about 90%) in signal amplitude across the joint in slab 3 was observed in comparison to the observation from slab 2 (about 50%). There appears a delay in both P- and R-wave portions across the joint (Figure 6.39). In addition, the maximum spectral amplitude across the joint exhibits a shift towards lower frequencies (Figure 6.39). These observations indicate that the joint is analogous to a reflector, low pass filter and delay gate.

The average amplitude ratios for the nine sets of measurements are summarized in Table 6.11. In general, the signal amplitudes across the joint in slab 3 are more attenuated than in slab 2, as indicated by the smaller amplitude ratios in slab 3 (about 0.5 in slab 2, *see* Table 6.7). The results from the average amplitude ratios are analogous to the average FTC values. The following sections will present the FTC and WTC results.

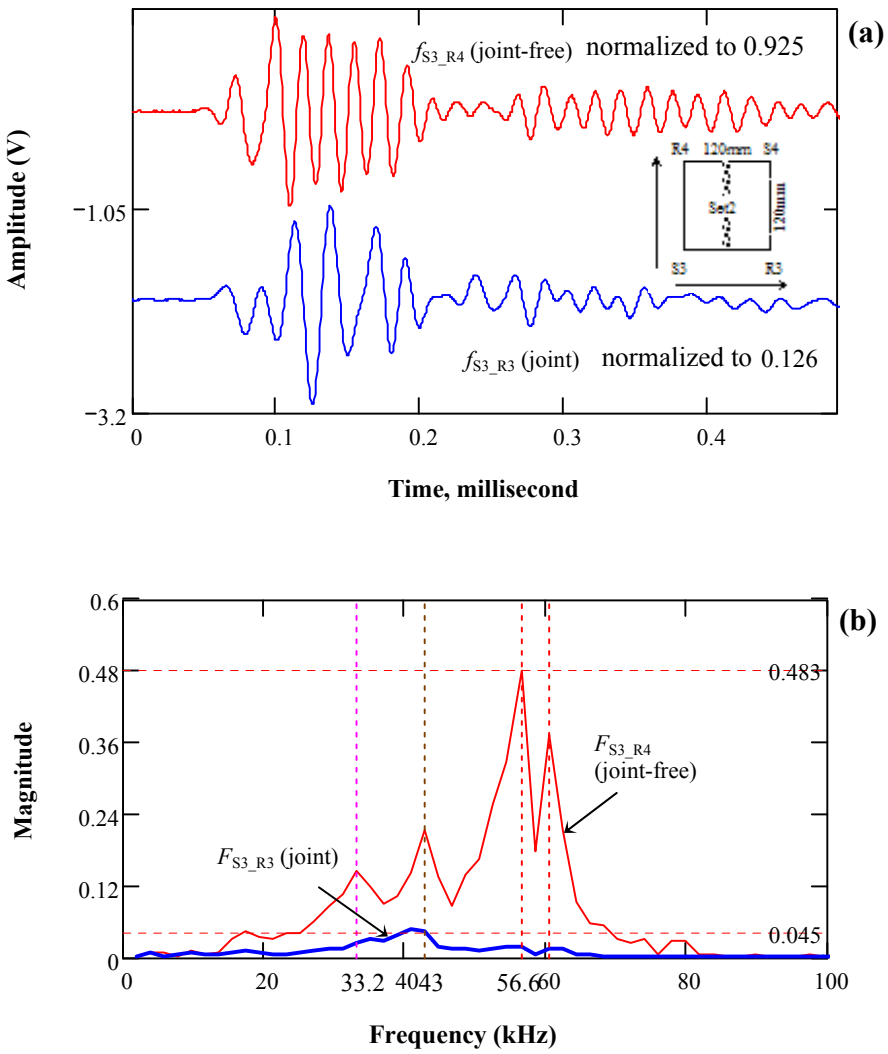

Figure 6.38: A pair of signals (Set 2, slab 3) across the joint and through the joint-free surface - (a) full signals in time domain and (b) full signals in frequency domain (Horizontal lines mark the maximum magnitude in frequency domain, and vertical lines mark the dominant frequencies)

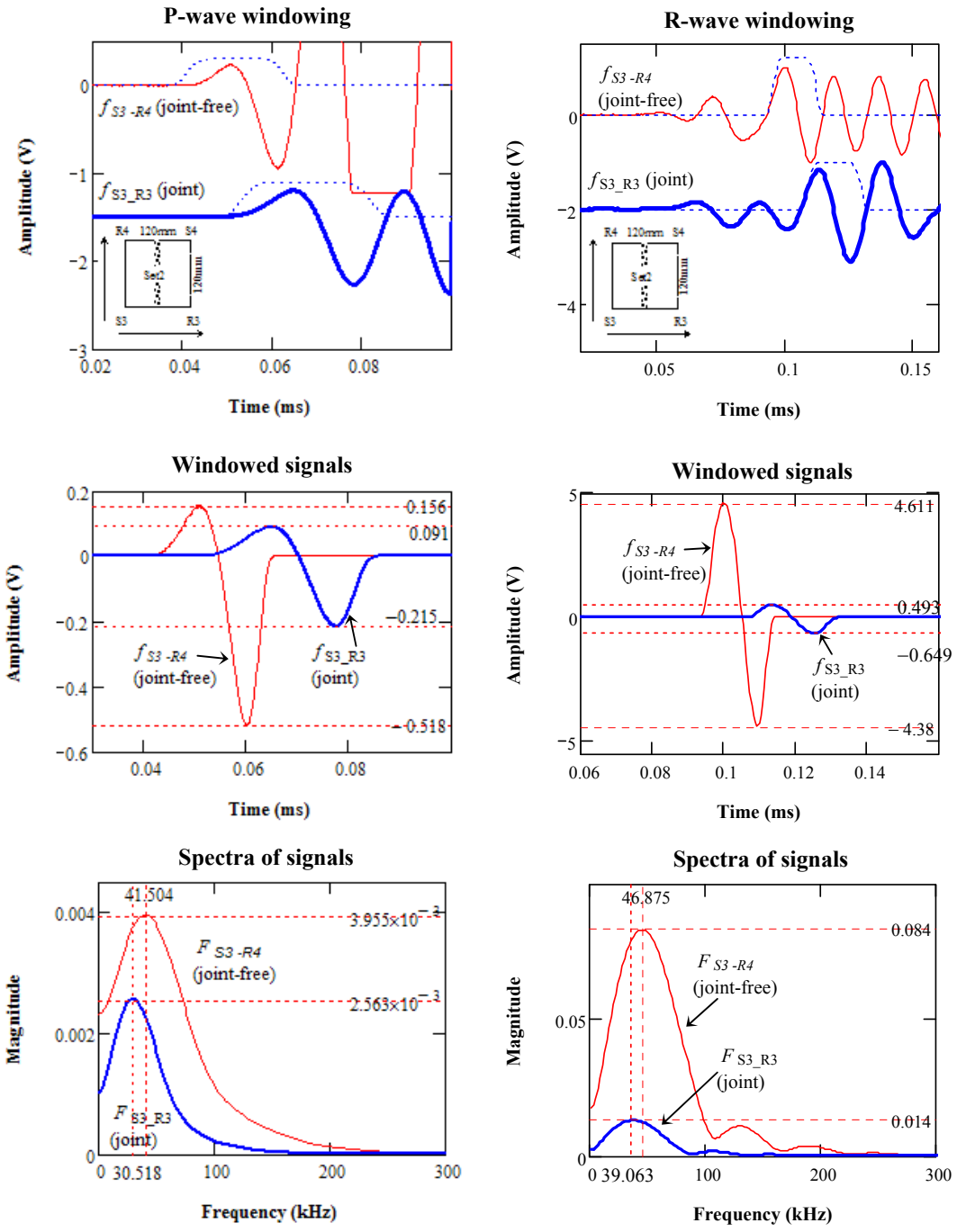

Figure 6.39: Windowing the P- and R-wave portions of the two signals (from Set 2) (Horizontal lines mark the PTP amplitudes in time and maximum magnitude in frequency, and vertical lines mark the dominant frequencies.)

Table 6.11: Average PTP ratio, maximum magnitude ratio, and spectrum area ratio for the measurements on the jointed and the joint-free surfaces

Location	Analyzed portion	PTP ratio	Magnitude ratio	Area ratio
Jointed surface (at 80mm S-R spacing)	Full signal	0.057	0.057	0.069
	P-wave	0.34	0.4	0.34
	R-wave	0.069	0.08	0.069
Jointed surface (at 120mm S-R spacing)	Full signal	0.10	0.09	0.11
	P-wave	0.29	0.43	0.27
	R-wave	0.10	0.11	0.10
Jointed surface (at 160mm S-R spacing)	Full signal	0.13	0.14	0.13
	P-wave	0.12	0.095	0.14
	R-wave	0.10	0.10	0.11
Joint-free surface (at 120mm S-R spacing)	Full signal	1.25	1.12	1.11
	P-wave	0.95	0.97	0.98
	R-wave	0.99	1.01	1.03
Joint-free surface (at 160mm S-R spacing)	Full signal	1.39	1.32	1.39
	P-wave	1.07	1.08	1.06
	R-wave	1.35	1.35	1.35

6.10.4 Analysis based on FTC and WTC for the joint

The FTC and WTC for the measurements on the jointed surface are shown in Figures 6.40 and 6.41. In general, the FTC values for P-waves are larger than the values for R-waves (Figures 6.40). The reason is that P-waves propagate with a larger wavelength because P-waves have a higher velocity. Thus, P-waves are less attenuated by the joint, giving higher FTC values (Figures 6.40). On the other hand, WTC was based on comparing the maximum amplitudes of the wavelet transform of the full signals, regardless of wave types. In addition, the WTC technique reduced the effect of different frequencies in the same way it reduced the coupling variation. Thus, the WTC values are more consistent (Figure 6.41). At 80mm and 120mm S-R spacing, the average FTC values for P-waves are between 0.4 and 0.42 and for R-waves between 0.08 and 0.10. At 160mm S-R spacing, the average FTC values for P- and R-waves are 0.13 and 0.11 respectively. WTC values varied from 0.06 to 0.13 when the S-R spacing increases from 80mm to 160mm. These values indicate a weak joint in slab 3 compared to slab 2 (*see*

Figures 6.25 and 6.26). On the other hand, the result of the repeated test for Set 3 (120mm S-R spacing) indicates high repeatability (Figures 6.40 and 6.41).

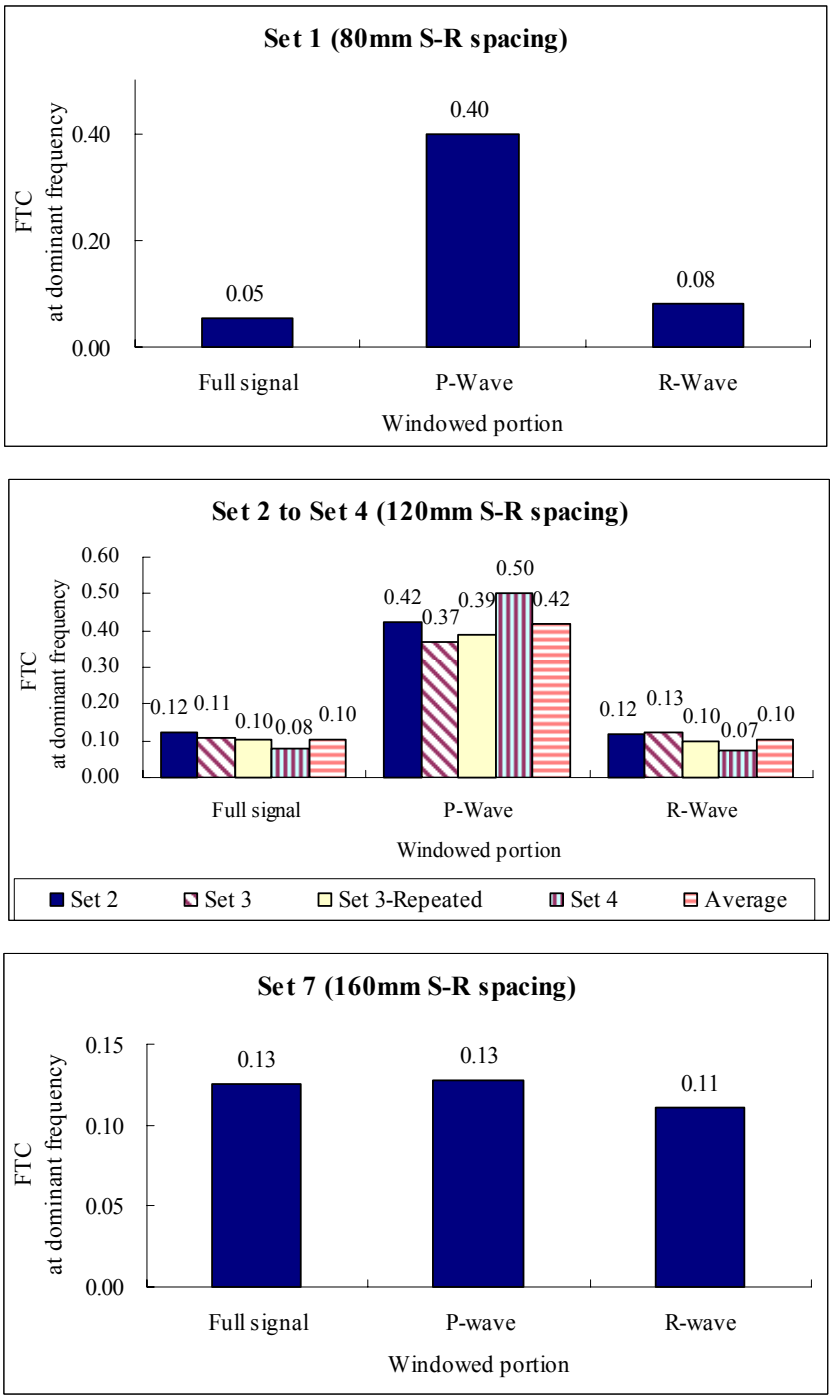

Figure 6.40: Comparison of FTC at dominant frequencies for measurements across the joint (slab 3) (Note: S-R spacing indicates source-to-receiver spacing)

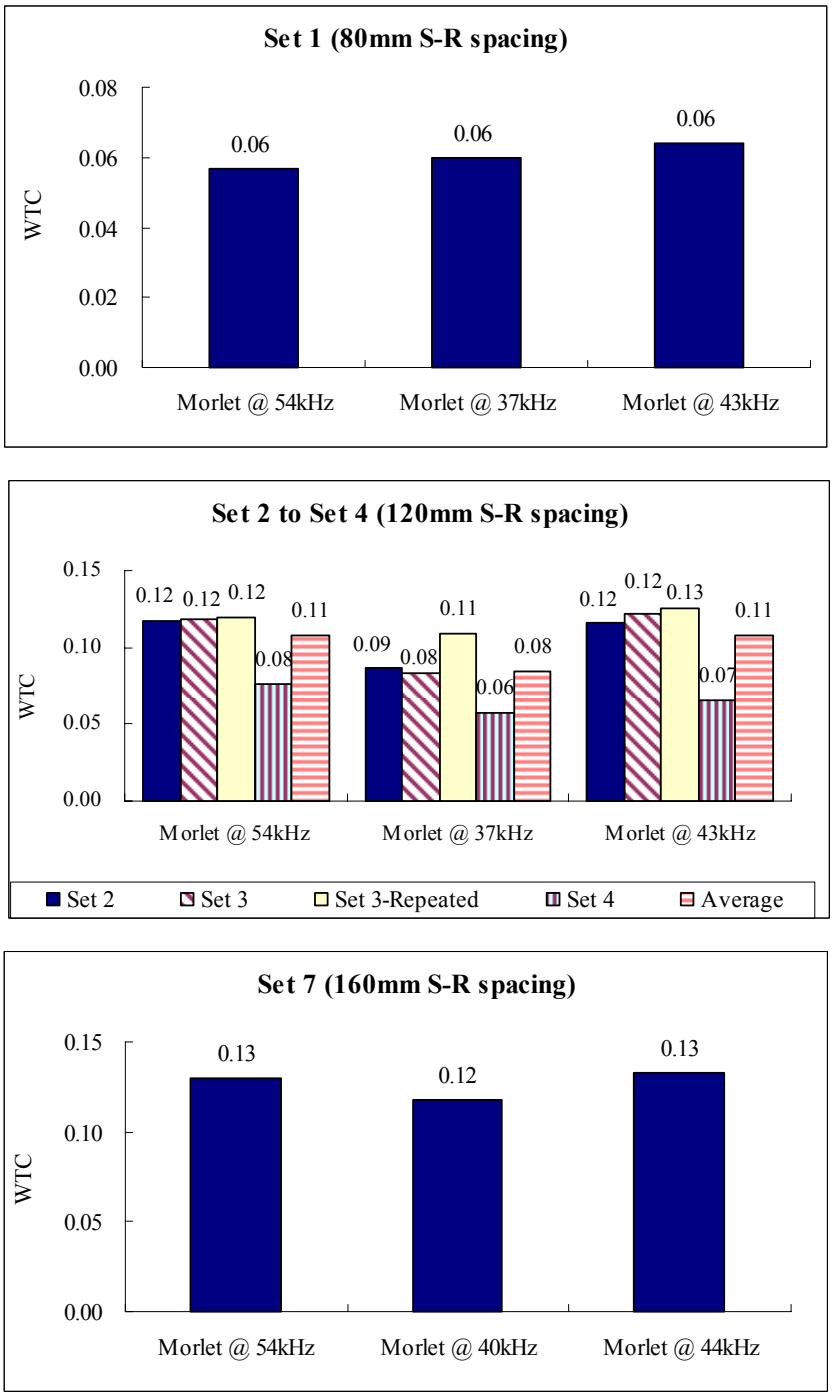

Figure 6.41: Comparison of WTC using Morlet wavelet for measurements across the joint (slab 3) (Note: S-R spacing indicates source-to-receiver spacing)

For the measurements on the jointed surface, 160mm S-R spacing gave significantly smaller FTC value for P-waves than did 80mm and 120mm S-R spacings (Figure 6.40). To understand this phenomenon, the following set of measurements were selected for comparison, Set 1 (80mm S-R spacing), Set 3 (120mm S-R spacing) and Set 7 (160mm S-R spacing), as shown in Figures 6.42a to 6.42c. Figure 6.42a shows that at 80mm S-R spacing, the negative peak of the first arriving P-wave of f_{S2_R2} is disproportionately amplified by the following R-wave arrival. In this case, windowing the P-wave portion is ambiguous. The inclusion of R-waves in the windowed P-waves results in higher amplitude because R-waves carry much larger energy than P-waves. The higher amplitude in the P-wave portion of the signal across the joint as a dividend results in a larger FTC. The interference between the first arriving P- and R-waves becomes less significant as the S-R spacing increases (Figures 6.42b and 6.42c). This observation indicates that the joint not only delays P- and R-wave arrivals, but also narrows the time interval between the two arrivals. The joint affects P-waves and R-waves differently. As shown in Figure 6.42a to 6.42c, the shorter the S-R spacing, the closer the two arrivals. When the S-R spacing increases to 160mm, the wave interference is practically insignificant. Hence, the 80mm S-R spacing is comparatively unsuitable for the measurements in slab 3.

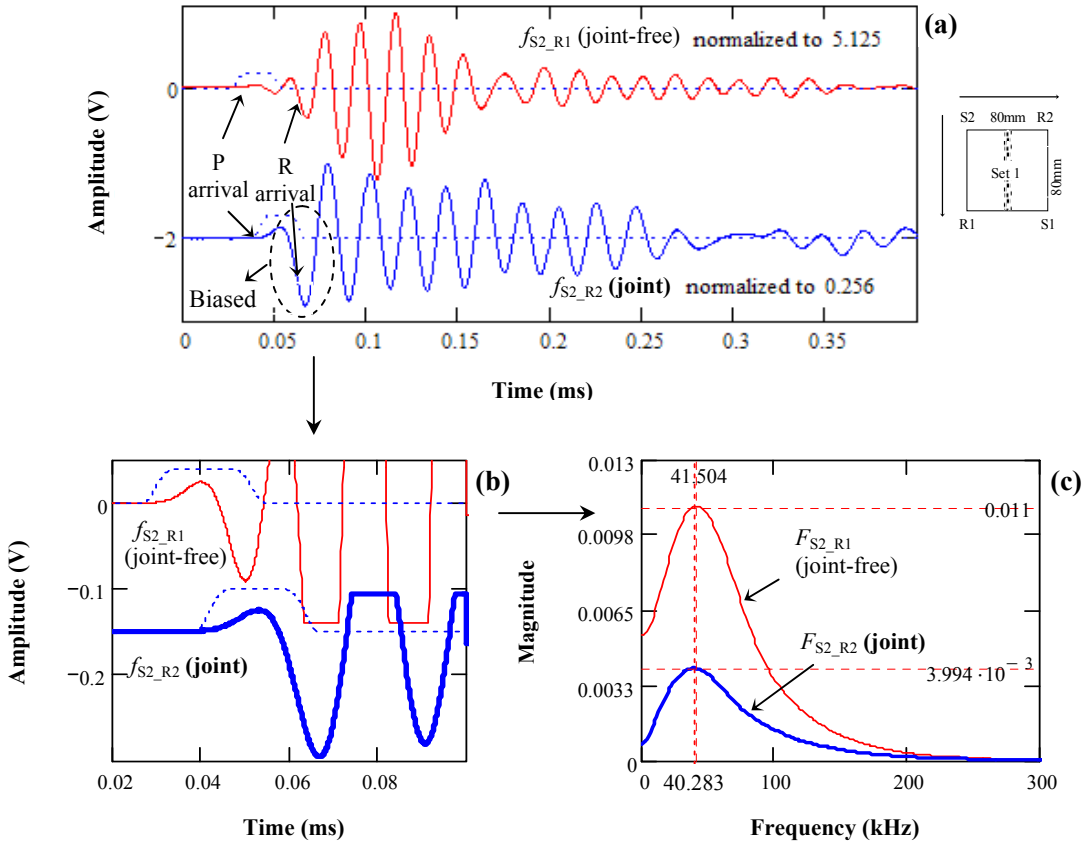

Figure 6.42 (a): A pair of signals from Set 1 (at 80mm S-R spacing) on the jointed surface in slab 3 - (a) full signals in time domain, (b) windowing P-wave portions and (c) windowed signals in frequency domain (Horizontal lines mark the maximum magnitudes in frequency domain, and vertical lines dominant frequencies.)

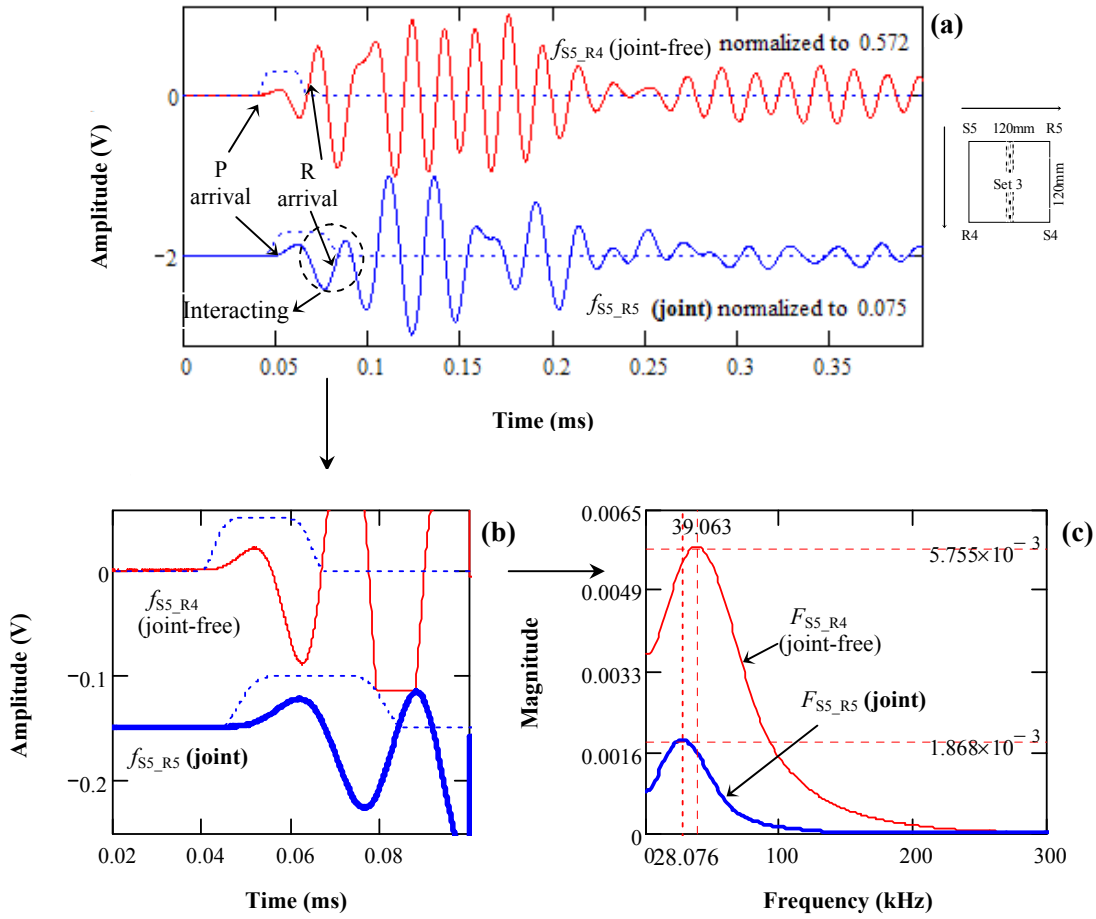

Figure 6.42 (b): A pair of signals from Set 3 (at 120mm S-R spacing) on the jointed surface in slab 3 - (a) full signals in time domain, (b) windowing P-wave portions and (c) windowed signals in frequency domain (Horizontal lines mark the maximum magnitudes in frequency domain, and vertical lines dominant frequencies.)

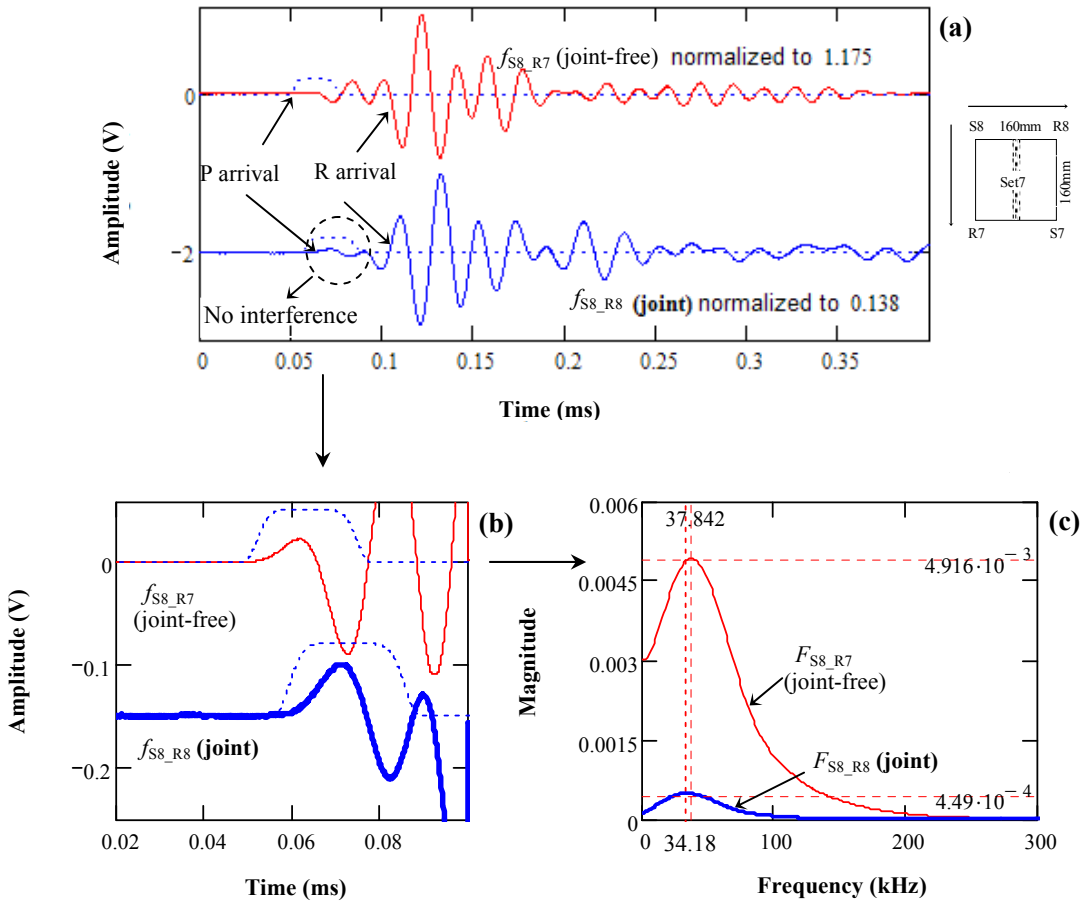

Figure 6.42 (c): A pair of signals from Set 7 (at 160mm S-R spacing) on the jointed surface in slab 3 - (a) full signals in time domain, (b) windowing P-wave portions and (c) windowed signals in frequency domain (Horizontal lines mark the maximum magnitudes in frequency domain, and vertical lines dominant frequencies.)

On the other hand, the observed average FTC and WTC values increase with the S-R spacing, as shown in Figure 6.43. To understand this phenomenon, the following set of measurements were considered for comparison, Set 1 (80mm S-R spacing) and Set 3 (120mm S-R spacing), as shown in Figures 6.44 and Table 6.12. The R-wave dominant frequency ($f_{dominant}$) of the signal f_{S2_R1} through the 80mm joint-free wave path is 48.828 kHz. However, the $f_{dominant}$ of f_{S5_R4} through the 120mm joint-free wave path is only 42.969 kHz because the longer distance leads to more attenuation. Thus, when there exists a joint, signal f_{S5_R5} through the 120mm distance exhibits a loss of $f_{dominant}$

components (from 42.969 kHz to 39.063 kHz) that is less than the loss for signal f_{S2_R2} through the 80mm distance (from 48.828 kHz to 41.016 kHz), as described in Table 6.8. The smaller difference between the $f_{dominant}$ component of signal f_{S5_R5} across the joint and the $f_{dominant}$ component of the joint-free signal f_{S5_R4} results in a higher amplitude ratio. WTC takes into account the full signals that are dominated by R-waves. Thus, the WTC for f_{S5_R5} / f_{S5_R4} at 120mm S-R spacing is expected to be higher as well. For the same reason, the FTC and WTC values at 160mm S-R spacing are the highest (Figure 6.43).

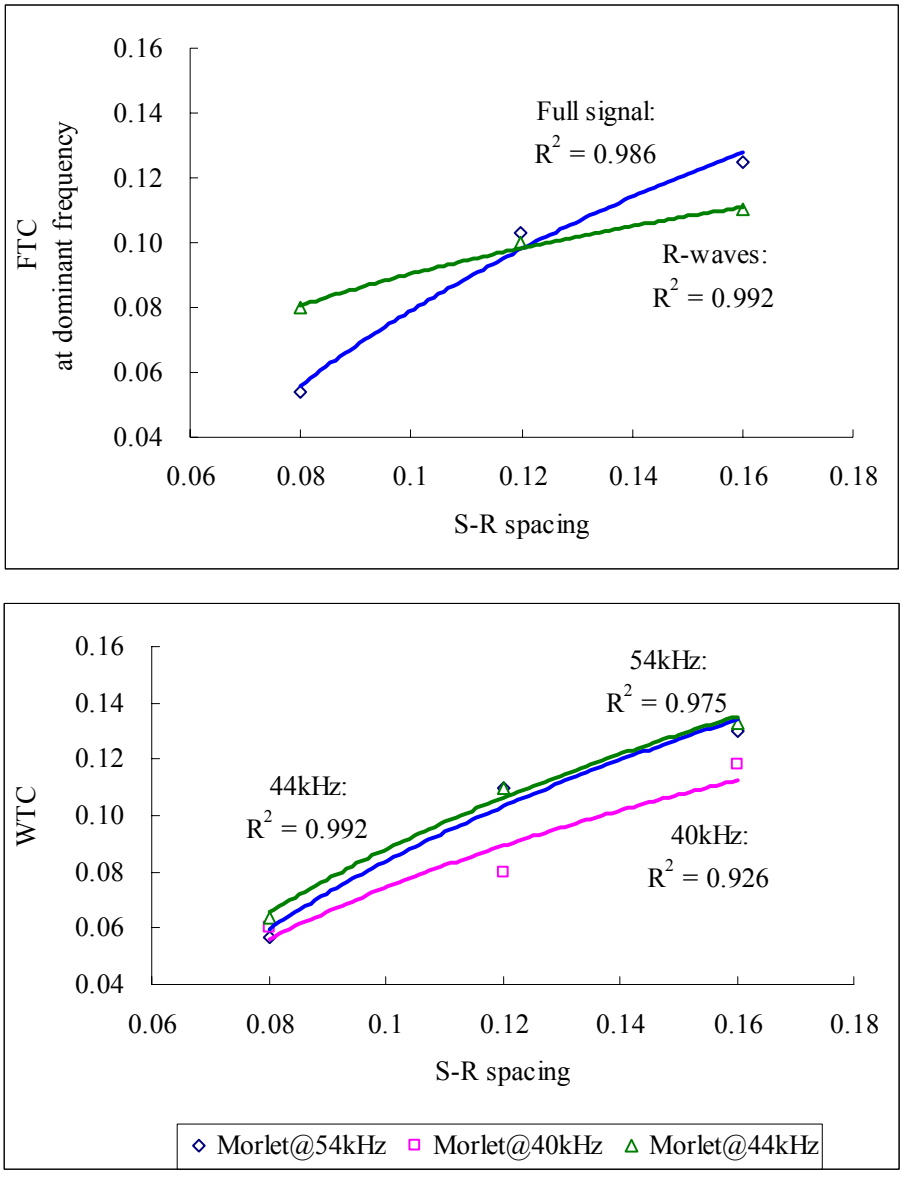

Figure 6.43: Average FTC and WTC values vs. source-to-receiver (S-R) spacing

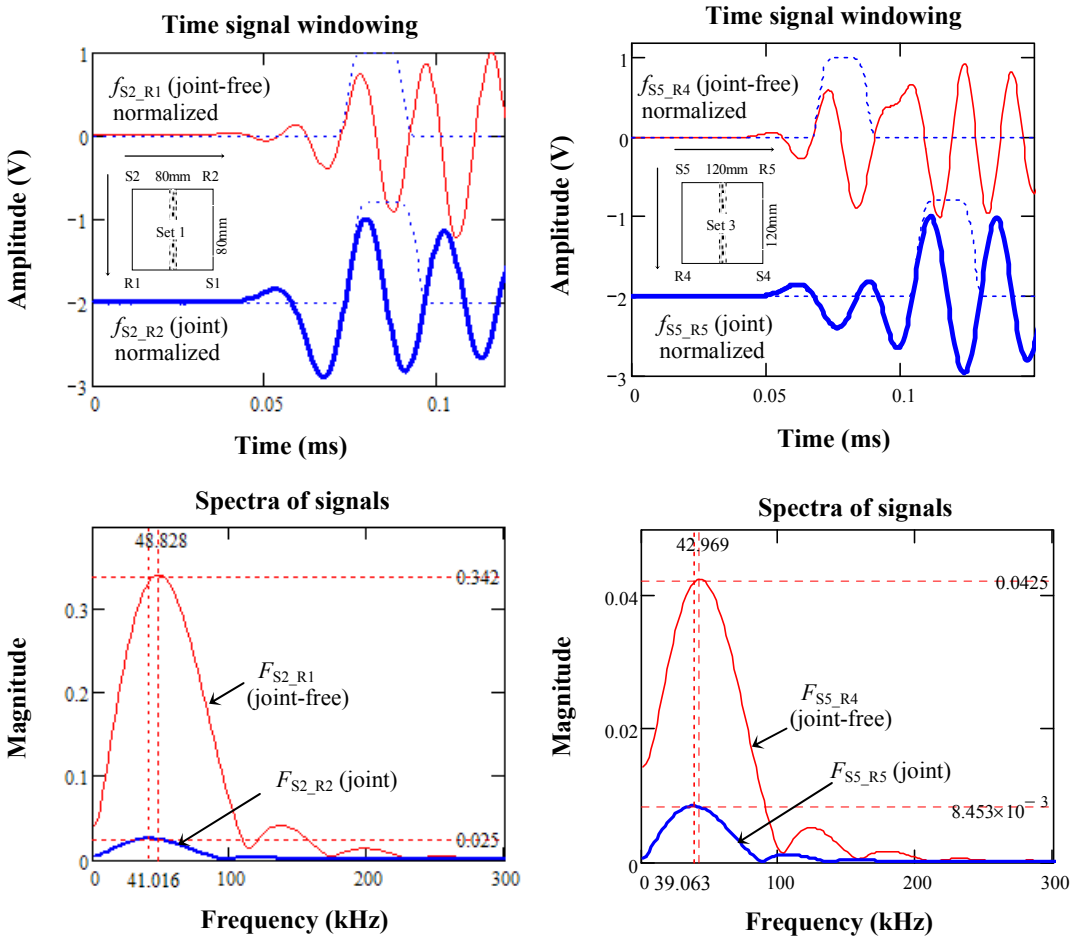

Figure 6.44: Comparison of the R-wave analysis between Set 1 (at 80mm S-R spacing) and Set 3 (at 120mm S-R spacing) on the jointed surface in slab 3 (Note: S-R is source-receiver; horizontal lines mark the maximum magnitude, and vertical lines dominant frequencies.)

Table 6.12: Comparison between Set 1 and Set 3 measurements

Description	**Set 1 (80mm S-R spacing)**	**Set 3 (120mm S-R spacing)**
$f_{dominant}$ for joint-free signals	48.828 kHz	42.969 kHz
$f_{dominant}$ for signals across the joint	41.016 kHz	39.063 kHz
Loss due to the joint	48.828 - 41.016 = 7.812 kHz	42.969 - 39.063 = 3.906 kHz
Conclusion	Loss across the joint at 80mm spacing is higher.	Loss across the joint at 120mm spacing is lower.

Note: $f_{dominant}$ represents dominant frequency of a windowed R-wave.

For the measurements (at 120mm S-R spacing) on the joint-free surfaces, the FTC and WTC for Set 6 (at the right side of the joint) are significantly smaller than those for Set 5 (at the left side of the joint) (Set6/Set5<50%), as shown in Figures 6.45 and 6.46. To explain this result, the signals from the two sets of measurements and their wavelet transforms (using Morlet at the dominant frequencies of their R-wave portions) were examined, as shown in Figures 6.47 and 6.48. Each time signal was normalized to its peak-to-peak amplitude in time domain. The amplitude of signal f_{S5_R4} is significantly smaller than the other signals likely because the wave path for f_{S5_R4} is parallel and close to the joint (Figure 6.47).

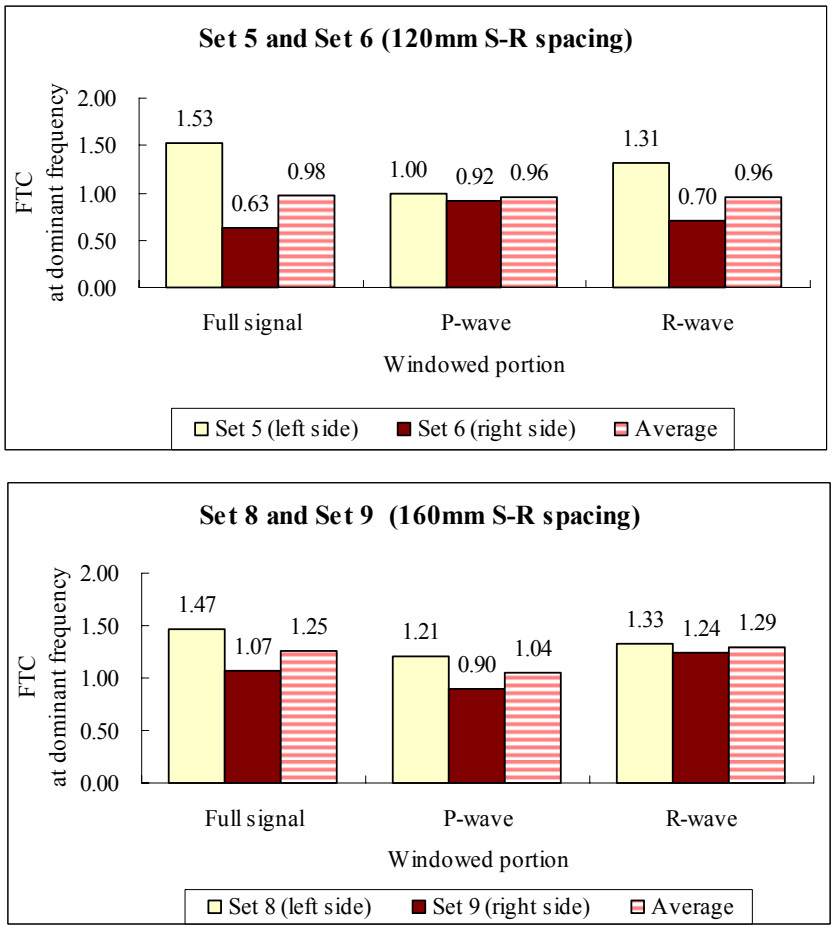

Figure 6.45: Comparison of FTC at dominant frequencies for the measurements on the joint-free surfaces (slab 3) (Note: S-R spacing indicates source-to-receiver spacing.)

FTC values were curved against frequency (f) and one-third the wavelength ($\lambda/3$) respectively (Appendix R), as shown in Figure 6.51. As discussed previously, the 40 kHz is the *cut-off* frequency for R-waves, corresponding to $\lambda/3 = 14$mm. It is implied that the FTC of R-waves is suitable for condition assessment of the joint with a depth smaller than 14mm. For P-waves, the FTC increases with frequencies at the low frequency range (< 40kHz) likely because the P-wave wavelengths at the low frequencies exceed the slab thickness. Based on the slab thickness (about 85mm) and the observed P-wave velocity ($V_P = 3913$m/s), a frequency of around 46 kHz ($f = V_P/\lambda$) was obtained. Thus, P-waves propagating at lower frequencies than 40 kHz could be strongly affected by the slab boundaries. After 40 kHz (or before $\lambda/3 =$ 33mm), the FTC for P-waves shows a reasonable trend: the higher the frequencies (or the smaller the wavelengths), the smaller the FTC (Figure 6.51). The P-wave FTC is much larger than the R-wave FTC because P-waves have larger wavelengths.

give similar FTC values for Set 5 (1.00) and Set 6 (0.92) likely because of the larger wavelength of P-waves. When considering the 160mm spacing (farther away from the joint), comparatively consistent values of the FTC and the WTC were observed (Figures 6.45 and 6.46). Values larger than 1 indicate that the farther the location from the joint, the better the mix quality. Nevertheless, all the FTC and WTC values across the joint are still significantly smaller than on the joint-free surface (Figures 6.40, 6.41, 6.45 and 6.46).

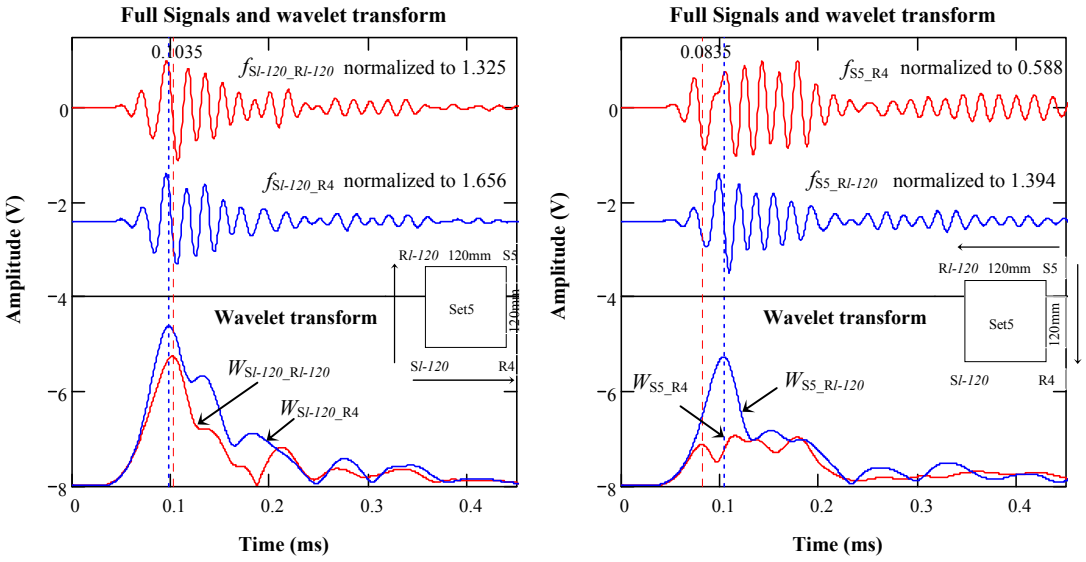

Figure 6.47: Signals from Set 5 (slab 3) and their wavelet transforms

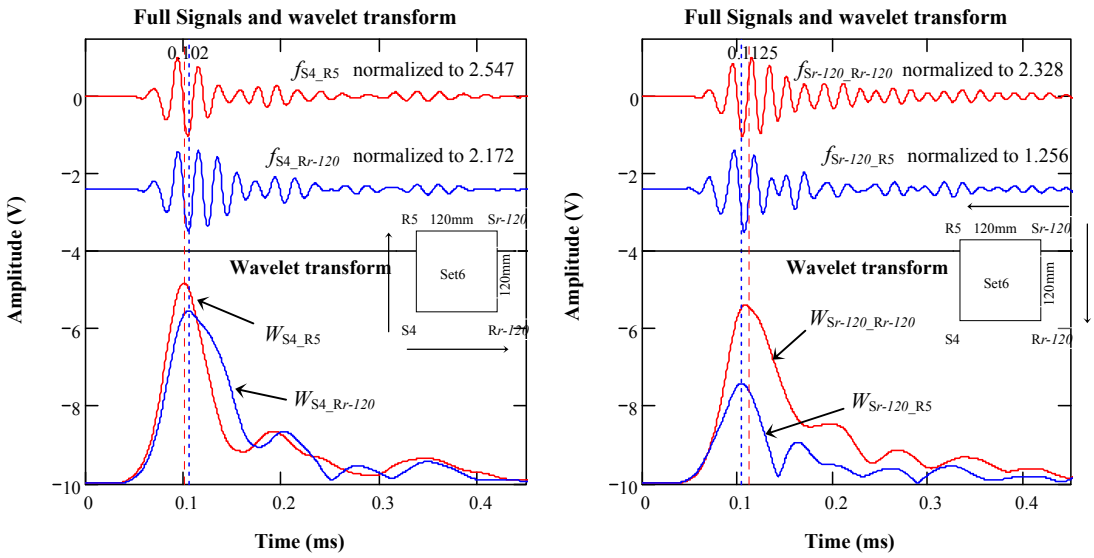

Figure 6.48: Signals from Set 6 (slab 3) and their wavelet transforms

The FTC and WTC for the jointed surfaces were correspondingly normalized to the average FTC and WTC for the joint-free squares to obtain the FTC ratios and WTC ratios. The average FTC ratio and average WTC ratio for slab 3 were compared with those for slab 1 and slab 2, as shown in Figures 6.49 and 6.50. Considering the suitability of the 80mm spacing in slab 3, no additional measurement on the joint-free surface was conducted, and hence the original measured FTC and WTC values were used in the comparison. Likewise, the average FTC and average WTC for slab 1 were used in the comparison.

In general, the average FTC ratios show that the relative strength of the joints in slab 1 and slab 2 are comparable. The relative strength of the joint in slab 3 is the weakest. However, the FTC for slab 1 may not be representative enough because wave interference biased the windowing, as explained previously. On the other hand, the WTC results show that the joint in slab 1 has the strongest relative strength and the joint in slab 3 the weakest. Hence, it is possible to conclude that slab 1 has a good-quality joint, slab 2 a medium-quality joint, slab 3 a weak-quality joint.

FTC values were curved against frequency (f) and one-third the wavelength ($\lambda/3$) respectively (Appendix R), as shown in Figure 6.51. As discussed previously, the 40 kHz is the *cut-off* frequency for R-waves, corresponding to $\lambda/3 = 14$mm. It is implied that the FTC of R-waves is suitable for condition assessment of the joint with a depth smaller than 14mm. For P-waves, the FTC increases with frequencies at low frequency range (< 40kHz) likely because the P-wave wavelengths at the low frequencies exceed the slab thickness. Based on the slab thickness (about 85mm) and the observed P-wave velocity ($V_P = 3913$m/s), a frequency of around 46 kHz ($f = V_P/\lambda$) was obtained. Thus, P-waves propagating at lower frequencies than 40 kHz could be strongly affected by the slab boundaries. After 40 kHz (or before $\lambda/3 =$ 33mm), the FTC for P-waves shows a reasonable trend: the higher the frequencies (or the smaller the wavelengths), the smaller the FTC (Figure 6.51). The P-wave FTC is much larger than the R-wave FTC because P-waves have larger wavelengths.

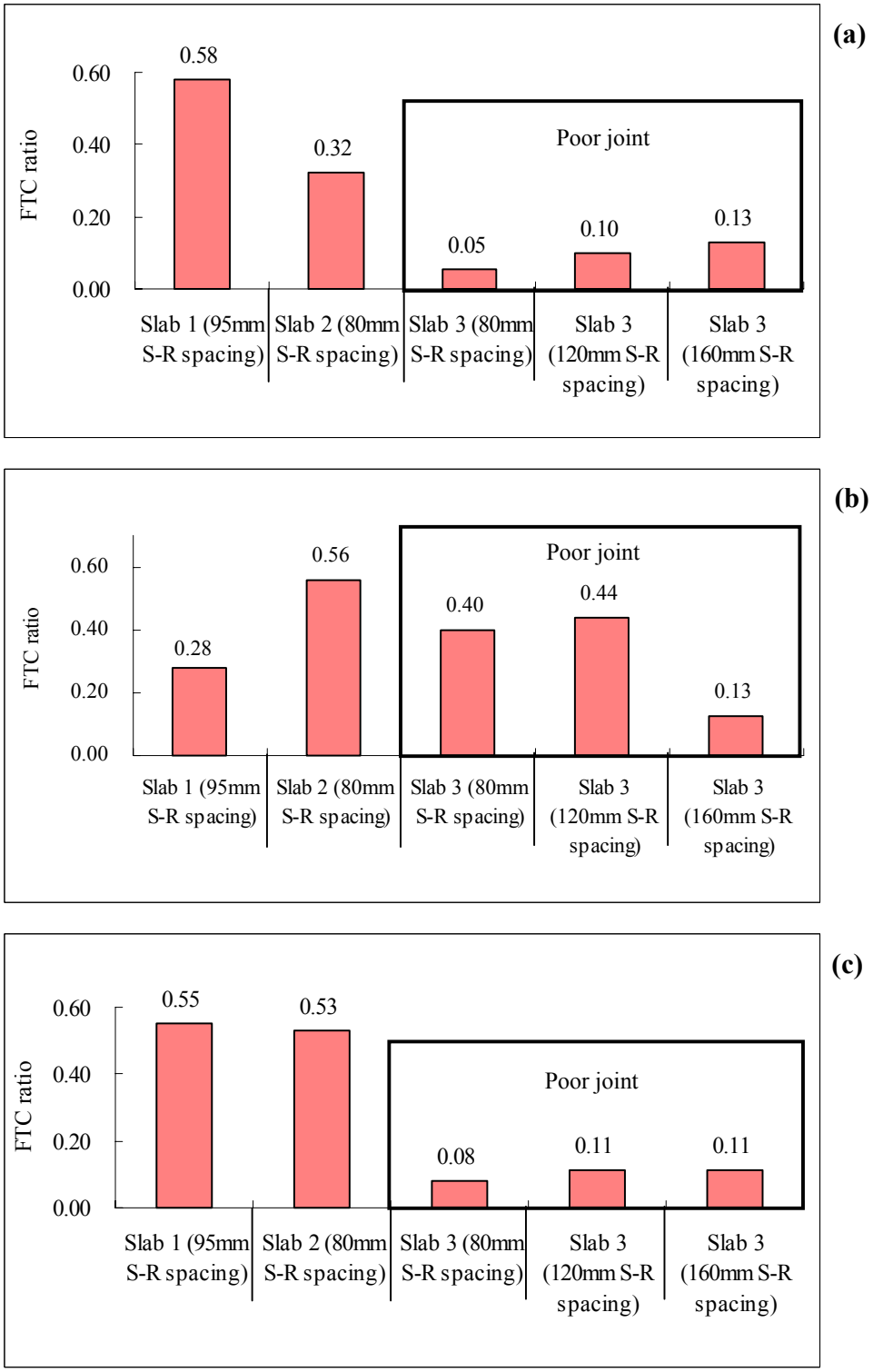

Figure 6.49: Comparison of average FTC ratios between slabs 2 and 3 – (a) full signals, (b) P-waves, and (c) R-waves (Note: S-R spacing indicates source-to-receiver (S-R) spacing)

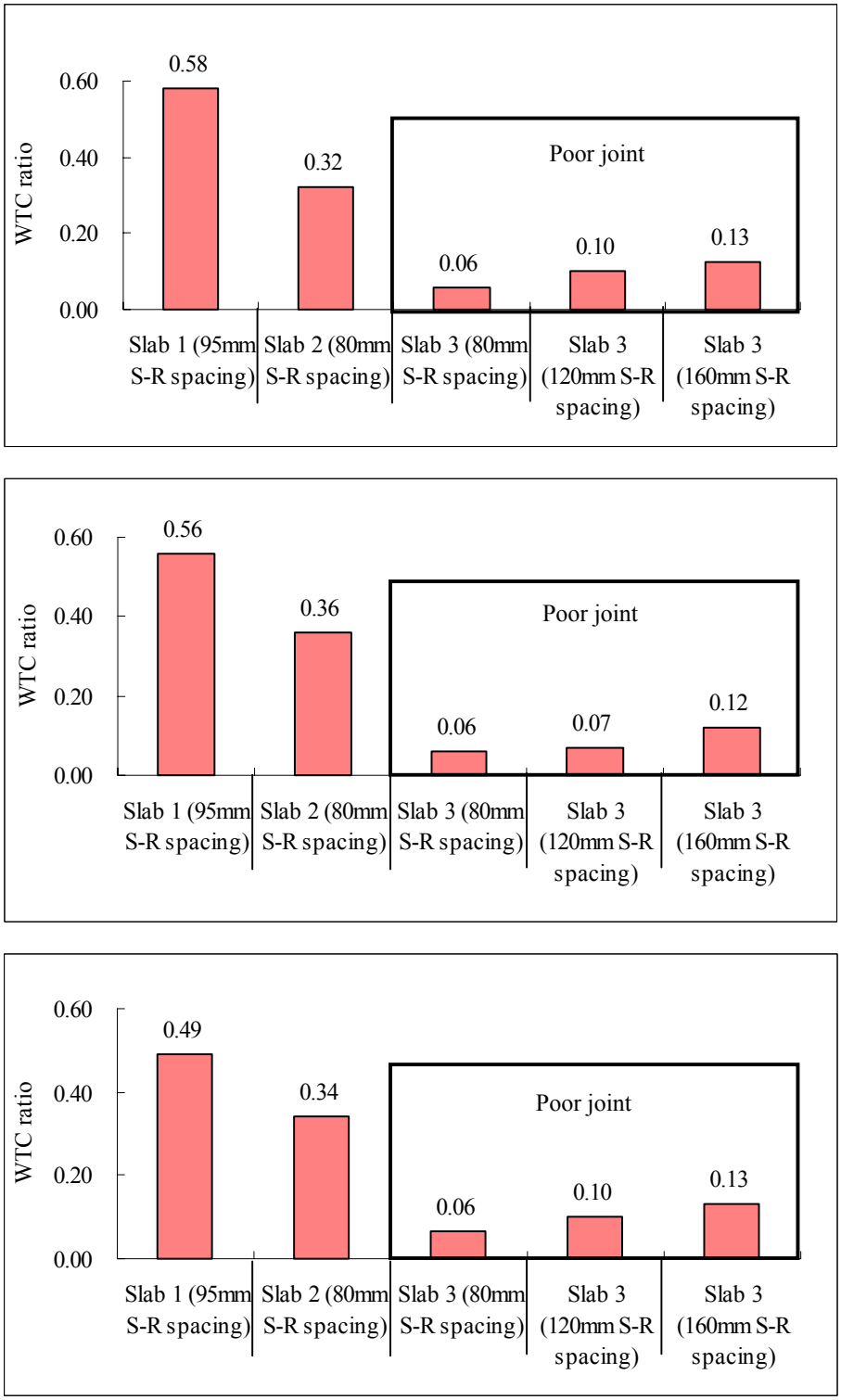

Figure 6.50: Comparison of average WTC ratios among the three slabs with average Morlet center frequency of (a) 54 kHz, (b) 37 kHz, and (c) 43kHz (Note: S-R spacing indicates source-to-receiver (S-R) spacing)

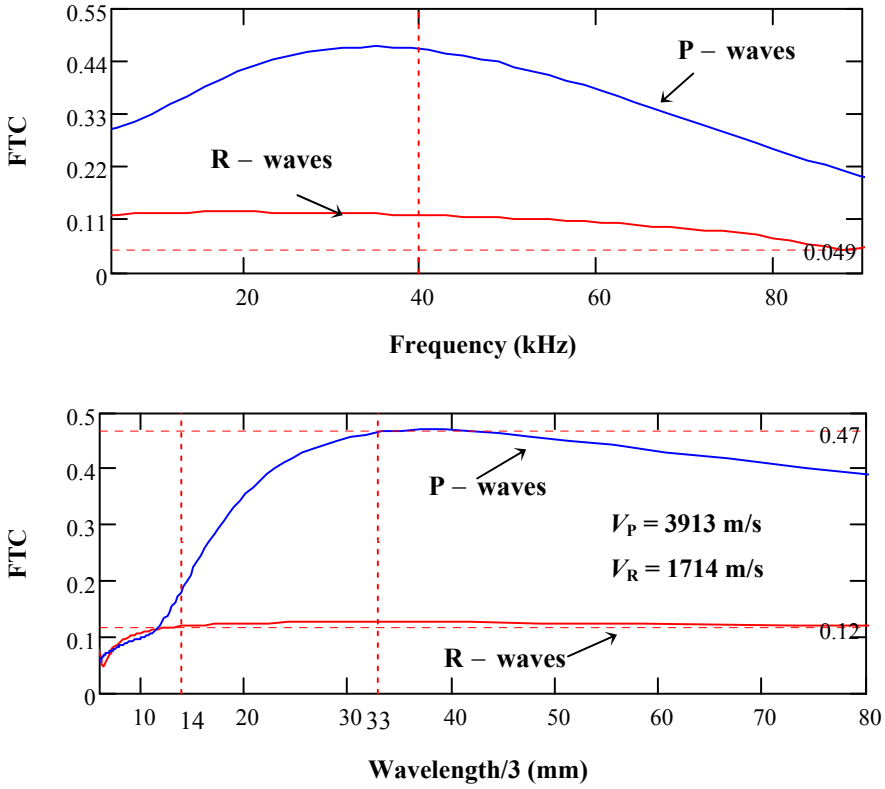

Figure 6.51: FTC of P- and R-waves for Set 2 at 120mm S-R spacing (slab 3)

6.10.5 Analysis based on equivalent damping ratio for the joint

The equivalent damping ratios for the jointed surface were compared with the equivalent damping ratios for the joint-free surfaces, as shown in Figures 6.52 and 6.53. The average equivalent damping ratios from the joint-free measurements in slab 2 and slab 3 were also given. The average equivalent damping ratio for R-waves for slab 1 was not available because no reliable R-wave velocity was obtained. The joint in slab 3 generally produced higher damping than did the joint in slab 2. This result confirms that the joint in slab 3 is more dissipative or has weaker bonding strength. The average equivalent damping ratio for R-waves decreases with the increasing S-R spacing in slab 3 because the FTC increases with the S-R spacing (Figure 6.43).

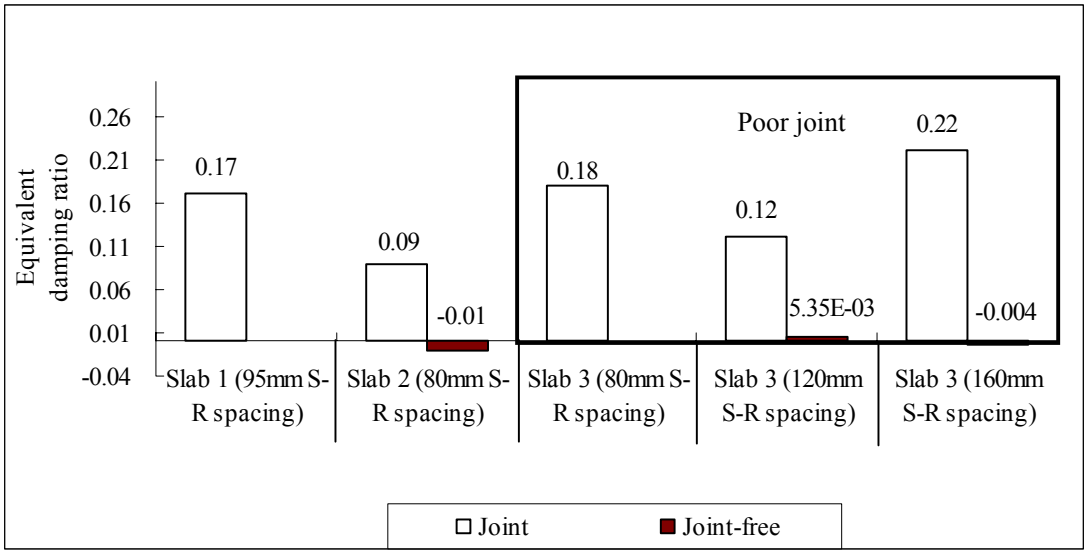

Figure 6.52: Comparison of P-wave equivalent damping ratios among the three slabs

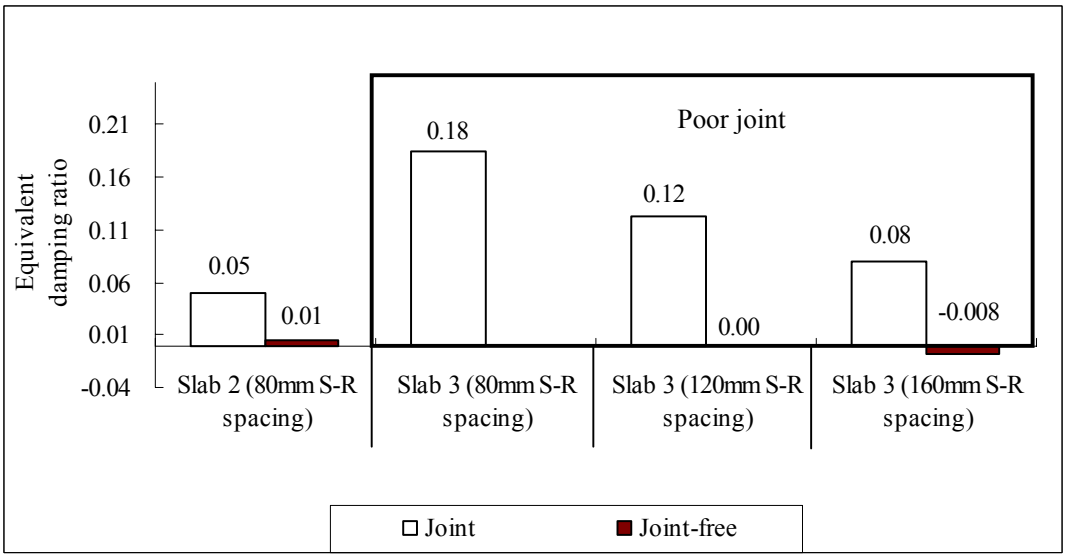

Figure 6.53: Comparison of R-wave equivalent damping ratios among the three slabs

6.10.6 Summary of the results

1. The wave attenuation measurements for the joint show that the joint in slab 3 is the weakest among the joints in the three slabs. The measured WTC values indicated that slab 1 has a good quality joint (WTC > 0.49), slab 2 a medium-quality joint (WTC between 0.32 and 0.34), slab 3 a weak-quality joint (WTC between 0.06 and 0.13).
2. The FTC of R-waves was suitable for condition assessment of the joint with a depth smaller than 14 mm.
3. The FTC and WTC values generally increase with the source-to-receiver (S-R) spacing.
4. The 80mm S-R spacing is not suitable for the observation of P-waves across the joint in slab 3 because of the wave interference.
5. The P- and R-wave velocities measured from the joint-free surface in slab 3 are higher than those measured in slab 2. This result indicates that the joint-free section in slab 3 is stronger than the joint-free section in slab 2.
6. The attenuation coefficients obtained from the geometric attenuation evaluation in slab 3 are smaller than the coefficients observed from slab 2. This result is probably because of the significant reduction in material attenuation (damping) in slab 3. This shows that a better mix strength was achieved in slab 3.

6.11 Summary

This chapter focused on examining the feasibility of using the wave characteristics identified in the experiments of Phase I to assess the condition of longitudinal joints in three laboratory-fabricated HMA slabs. The FTC and WTC techniques were used as improvements to the evaluation of wave characteristics using the PTP amplitude, maximum spectral amplitude, and spectrum area. The equivalent damping ratio based on the FTC provides an alternative method to assess the joint condition. This chapter described the experimental program for the experiments of Phase II. The detailed procedures of preparation of the three slabs and ultrasonic testing of the slabs were presented. The experimental results and analysis for the slabs are the key topic covered in this chapter. The data revealed that the seismic wave techniques indeed enable identification of good, fair, and poor construction joints. The methodology given in the chapter can potentially provide a tool for application of the wave-based techniques in the filed for in-situ condition assessment of asphalt pavements.

CHAPTER 7
SUMMARY AND CONCLUSIONS

7.1 Asphalt Concrete Specimen Tests - Phase I

The main objective of the experiments conducted in Phase I was to assess the suitability of using wave characteristics for the condition assessment of asphalt concrete specimens prepared in the laboratory. The asphalt concrete specimens were prepared using the identical aggregate types and asphalt binders. However, the specimens were compacted at different compaction levels to produce different volumetric properties. The quality of the specimens was evaluated in terms of bulk density and dynamic elastic modulus values. The main findings from these experiments are:

1. Wave attenuation parameters (PTP amplitude, maximum spectral magnitude, spectrum area) showed a strong correlation ($R^2 > 0.9$) with the gyration level. Thus, wave attenuation parameters are sensitive to the quality of the mix. These parameters can be used then to evaluate the performance of asphalt concrete pavements.
2. The strong correlation obtained between wave attenuation parameters and the dynamic modulus demonstrates that nondestructive tests are suitable for in situ condition assessment of asphalt concrete pavements. The use of NDT in the field will reduce the current dependence on time-consuming and large-strain tests.
3. Any of the three attenuation parameters (PTP amplitude, maximum spectral magnitude and spectrum area) can be used as a performance indicator. However, the PTP amplitude is more suitable for online monitoring because it can be determined readily from field measurements. The other parameters (maximum amplitude and spectral area) require the computation of frequency spectra.
4. The lack of correlation ($R^2 \sim 0.6$) between the wave velocity and the number of gyrations indicates that the use of wave velocity only is not sufficient for the condition assessment of HMA.
5. The moderate correlation ($R^2 \sim 0.8$) between the asphalt density and the level of compaction (number of gyrations) shows that the density of HMA is useful to assess

the quality of HMA in terms of densification of the material. However, the strong correlation observed between wave attenuation parameters and the dynamic modulus suggests that the material density only is not sufficient to assess the quality of the mix, which is associated with the durability and the long-term performance of the mix (good bonding between the aggregate and asphalt binder).

7.2 Asphalt Concrete Slab Tests - Phase II

The main objective of the experiments preformed in Phase II is two fold. The first objective was to determine the suitability of using wave characteristics (wave velocity and wave attenuation) for the condition assessment of longitudinal construction joints in asphalt pavements. The sensitivity of the wave characteristics to different types of joints was examined by testing three slabs with different joint conditions (good, fair, and poor). The second objective was to develop suitable test procedures for the condition assessment of the longitudinal construction joints in asphalt pavements. The main results from the experiment conducted in Phase II are summarized next.

1. Wave attenuation measurements using the wavelet transmission coefficient (WTC) can be used to identify good (WTC > 0.49), medium (0.32 < WTC < 0.34) and weak joints (WTC < 0.13). These findings provide the basis for future research on the use of wave-based techniques for the cost-effective condition assessment of longitudinal construction joints.
2. The PTP ratio, the maximum magnitude ratio and the spectrum area ratio can be used to assess the relative strength of longitudinal joints in asphalt pavements. However, care must be taken to ensure that good coupling exists between the transducers and the asphalt pavement.
3. The Fourier transmission coefficient (FTC) and the WTC provide an average condition index for a joint. However, The FTC can be affected by wave interference that leads to a biased time windowing. This limitation can be overcome by using an appropriate source-to-receiver spacing. The WTC is more suitable to be used as a condition index because it does not require time windowing.

4. The FTC of R-waves can be used for the condition assessment of a joint with a depth smaller than 20 mm, because of the stronger interaction of R-waves with the upper layer of the material (penetration depth = wavelength /3).
5. The damping ratio coefficient based on the FTC provides complementary information about the condition of the joint. However, the reliability of using the damping ratio coefficient depends on the accuracy of the wave velocity and the FTC measurements.
6. The source-to-receiver (S-R) spacing has an important effect on the measurements of the wave velocity and the FTC. An optimum S-R spacing must be selected to enhance signal- to-noise (S/N) ratio; which improves the detection of the first wave arrival.
7. Transducers with adequate sensitivity must be used. Low sensitivity reduces S/N ratio, and hence, the reliability of measurements.

7.3 Recommendations

The following steps are recommended for implementation of the wave-based technique for condition assessment of longitudinal joints in the field.

The first step is to select transducers that have high sensitivity and similar resonant frequencies. The sensitivity of the transducers is critical to obtain a strong and clear signal.

The second step is to select a suitable S-R spacing to avoid interference between P-waves and R-waves and to obtain a strong and clear signal (high S/N ratio).

The third step is to place the source and the receiver at the four corners of a square following the equal-spacing configuration suggested by Yang (2006). The spacing between the source and the receiver should meet the requirement given in step 2.

The final step is to select a reference location on a joint-free surface far away from the joint (e.g. the center of the lanes) to establish reference values of the FTC and WTC parameters. The FTC and WTC obtained from the jointed sections are normalized to the

reference values. The normalized FTC and WTC values are representative of the relative strength of the joint.

The following parameters are recommended for condition assessment of longitudinal joints in asphalt pavements: PTP ratio, FTC and WTC. Other parameters such as maximum magnitude ratio, spectrum area ratio, and damping ratio can be used as complementary observations.

7.4 Future Work

Further research will focus on assessing the quality of different types of mixtures prepared using different asphalt binders with identical volumetric design. The strength of the mix would be assessed in terms of wave attenuation parameters (PTP amplitude, maximum spectral amplitude and spectrum area). The small-strain wave-based measurements will be compared with large strain test results (e.g. dynamic modulus test).

REFERENCES

1) AASHTO TP 62-03, 2000, Standard method of test for: Determining dynamic modulus of hot-mix asphalt concrete mixtures, Washington DC
2) Achenbach, J. D., Komsky, I. N., Lee, Y. C. and Angel, Y. C., Jun. 1992, Self-calibrating ultrasonic technique for crack depth measurement, Journal of Nondestructive Evaluation, v11 n2, pp103-108
3) ACI Committee 228, June 1998, Nondestructive test methods for evaluation of concrete in structures, ACI 228.2R-98
4) Angel, Y.C. and Achenbach, J. D., 1984, Reflection and transmission of obliquely incident Rayleigh waves by a surface breaking crack, Journal of the Acoustical Society of America, v75, pp313-318
5) ASTM C597-02, Standard test method for pulse velocity through concrete, Book of Standards, Volume 04.02, ASTM International
6) ASTM D2726, Bulk Specific Gravity and Density of Compacted Bituminous Mixtures Using Saturated Surface Dry Specimens, Book of Standards, ASTM International
7) ASTM D2845-95, 1997a, Laboratory determination of pulse velocities and ultrasonic elastic constants of rock, Annual Book of ASTM Standards, Volume 04.08, ASTM, Philadelphia, Pa, pp. 254-259
8) ASTM, 1988, Concrete and aggregates, Annual Book of ASTM Standards, Volume 04.02, ASTM, Philadelphia, Pa
9) ASTM E494-95, 2001, Standard practice for measuring ultrasonic velocity in materials, Book of Standards, Volume 03.03, ASTM International
10) ASTM E494 – 95, Ultrasonic Velocity in Materials, Annual Book of ASTM Standards, Volume 03.03, ASTM International
11) Baker, M.R., Crain, K. and Nazarian S., August 1995, Determination of pavement thickness with a new ultrasonic device, Research report 1966-1F, Centre for Highway Material Research, University of Texas at EL Paso, Texas
12) Bedford, A. and Drumheller, D.S., 1994, Introduction to Elastic Wave Propagation, John Wiley and Sons

13) Blitz, J. and Simpson, G., 1996, Ultrasonic method of non-destructive testing, Chapman & Hall
14) Bonaquist, R.F., Christensen, D.W., and William Sump, III, 2003, Simple Performance Tester for Superpave Mix Design:First-Article Development and Evaluation, NCHRP Report 513, Transport Research Board, Washington D. C.
15) Brook, D. and R.J.Wynne, 1991, Introduction to signal processing, Wiley & Sons
16) Brown, L. F., Nov. 2000, Design considerations for piezoelectric polymer ultrasound transducers, IEEE Transactions on Ultrasonic, Ferroelectrics and Frequency Control, v47 n6, pp1377-1396
17) BSI 98/105795 DC, prEN 13296, Testing concrete determination of ultrasonic pulse velocity, British Standards
18) Carino, N.J., 1984, Laboratory Study of Flaw Detection in Concrete by the Pulse-echo Method, in In-Situ/Nondestructive Testing of Concrete, V.M. Malhotra, Editor, ACI SP-82, American Concrete Institute, pp 557-579
19) Carino, N. J., Sansalone, M. and Hsu, N. N., 1986, Flaw detection in concrete by frequency spectrum analysis of impact echo waveforms, International Advances in Nondestructive Testing, 12th Edition, New York, pp1-20
20) Carino, N. J. and Sansalone, M., 1990, Impact-echo: a new method for inspecting construction materials, Proceedings of Nondestructive Testing and Evaluation of Materials for Construction, University of Illinois, Aug., l988
21) Cartz, L., 1995, Non-destructive testing, Radiograph, Ultrasonic, Liquid penetrates, Magnetic particle, Eddy current, ASM International, USA
22) Chen, L., Zhu, J., Yan, X. and Song, C., July 2004, on arrangement of source and receivers in SASW testing, Soil Dynamics and Earthquake Engineering v24 n5, pp389-396
23) Cho, Y. S. and Lin, F. B., 2000, Integrity analysis of signal and multiplayer thin cement mortar slab structure using the spectral analysis of surface wave NDT method, Construction and Building Materials, v14, pp387-395
24) Cho, Y. S., June 2003, Non-destructive testing of high strength concrete using spectral analysis of surface waves, NDT & E International, v36 n4, pp229-235

25) Christensen, D.W., and Bonaquist, R.F., 2004, Evaluation of Indirect Tensile Test (IDT) Procedures for Low-Temperature Performance of Hot Mix Asphalt, NCHRP Report 530 Transport Research Board, Washington D. C.

26) Deng, C. J., Schmerr, L. W. and Sedov, A., Sep. 2002, Modeling and measuring all the elements of an ultrasonic nondestructive evaluation system 1: modeling foundation, Research in Nondestructive Evaluation, v14 n3, pp141-176

27) Deng, C. J., Schmerr, L. W. and Sedov, A., Dec. 2002, Modeling and measuring all the elements of an ultrasonic nondestructive evaluation system 2: model based measurements, Research in Nondestructive Evaluation, v14 n 4, pp177-201

28) EM350 lecture notes, 2005, Introduction to non-destructive evaluation engineering, Iowa State University, USA

29) Foti S., 2000, Multi-station methods for geotechnical characterisation using surface waves, PhD Diss., Politecnico di Torino, 229 pp

30) Gabor, D., 1946, Theory of communications. Journal of Institution of Electrical Engineers 93, pp 429-457

31) Galan A., 1990, Combined ultrasonic methods of concrete testing, Development in Civil Engineering 34, Elsevier

32) Geovision, www.geovision.com, Geovision Geophysical Services.

33) General Issues Asphalt Technology Committee (GIATC), September 2004, New Simple Performance Tests for Asphalt Mixes, Report, Number E-C068, ISSN 0097-8515, (AFK10), Transportation Research Board.

34) Graff, K.E. 1975, Wave motion in elastic solids, Oxford University Press, Lodon

35) Gucunski, N., 1991, Generation of low frequency Rayleigh waves for the Spectral-Analysis-of-Surface-Waves Method. Ph.D. dissertation, Department of Civil Engneering, the University of Michigan, Ann Arbor

36) Gucunski, N. and Woods, RD., 1992, "Numerical simulation of the SASW test" Soil Dynamics and Earthquake Engineering,vol.11, no.4, pp.213-227

37) Heisey, J. S., Stokoe, K. H., Hudson, W. R. and Meyer, A. H., 1982, Determination of in situ wave velocities from spectral analysis of surface waves, Research Report 256-2, Centre for Transportation Research, University of Texas at Austin, 277pp

38) Hellier, C.J., Drury, J., and Shakinovsky, M., 2001, Ultrasonic testing, Handbook of nondestructive evaluation, pp7.1-7.115

39) Herrmann R.B., Al-Eqabi G.I., 1991, Surface wave inversion for shear velocity, in: J.M.Hoven et al. (eds), Shear waves in marine sediments, Kluwer Academic Publisher, 545-556

40) Hevin, G., Abraham, O., Pedersen, H. A. and Campillo, M., Aug. 1998, Characterization of surface cracks with Rayleigh waves: a numerical model, NDT & E International, v31 n4, pp289-297

41) Horike M., 1985, Inversion of phase velocity of long-period microtremors to the s-wavevelocity structure down to the basement in urbanized areas, J.Phys.Earth, 33, 59-96

42) Hiltunen, D.R., 1988, Experimental evaluation of variables affecting the testing of pavements by the Spectral-analysis-of-surface-waves method, Ph.D. Dissertation, Civil Engineering Department, the University of Michigan, 303 pp.

43) Hiltunen, D. R. and Woods, R. D., 1988, SASW and cross hole test results compared, Geotechnical Special Publication, pp279-289

44) Hunter, S. C., 1957, Energy absorbed by elastic waves during impact, Journal of the Mechanics and Physics of Solids, v5, pp162-171

45) Huntingdon, H.B., 1940, J Acoustic Soc Am, 22, 362-4

46) Itasca, 2006, www.itascacg.com

47) Ingard, K.U., 1988, Fundamentals of waves and oscillations, Cambridge University Press, ISBN 0 521 33957

48) Jones, R., 1962, Surface wave technique for measuring the elastic properties and thickness of roads: theoretical development, Brit. J. Applied Phys., vol.13, pp 21-29

49) Krautkrämer, J. and Krautkrämer, H., 1990, Ultrasonic Testing of Materials, Springer-Verlag

50) Kuttruff, H., 1991, Ultrasonics fundamentals and applications, Elsevier Applied Science, New York.

51) Lamb, H., 1889, On waves in an elastic plate, Proceedings of the London Mathematical Society, v21, pp85-89

52) Lai C.G., 1998, Simultaneous inversion of Rayleigh phase velocity and attenuation for near-surface site characterization, PhD Diss., Georgia Inst. Of Techn., Atlanta (Georgia, USA) , 370 pp

53) Lai and Rix, 2002, BSSA

54) Leong, E., Yeo, S. and Rahardjo, H., 2004, Measurement of wave velocities and attenuation using an ultrasonic test system, Canadian Geotechnical Journal, 41(5): 844-860

55) Lin, Y. and Sansalone, M., Jul.-Aug. 1992, Detecting flaws in concrete beams and columns using the impact-echo method, ACI Materials Journal, v89 n4, pp396-405

56) Lin, Y. and Su, W. C., Sep.-Oct. 1996, Use of stress waves for determining the depth of surface-opening cracks in concrete structures, ACI Materials Journal, v93 n5, pp494-505

57) Liu, P. L., Tsai, C. D. and Wu, T. T., Oct. 1996, Imagine of surface-breaking concrete cracks using transient elastic waves, NDT & E International v29 n5, pp323-331

58) Love, A.E.H., 1911, Some Problems of Geodynamics, Cambridge, U.K.: Cambridge University Press, pp. 160-165.

59) Lysmer, J., 1965, Vertical motion of rigid footings, Contract Report No. 3-115, conducted for WES, Vicksburg, Mississippi, 137 pp

60) Malhotra, V.M. and Carette, 1980, In-situ testing – A Review, Progress in Concrete Technology, V.M. Malhotra, Ed., Energy, Mines, and Resources Canada, Ottawa, Canada, pp750-796

61) Mallat S., 1998, A wavelet tour of signal processing, Academic Press, USA

62) Martincek, G., 1994, Dynamics of pavement structures, E&FN Spon and Ister Science Press, Bratislava, Slovak Republic

63) McMaster, Robert C., 1963, Nondestructive Testing Handbook, Volume II, The Ronald Press Company, New York

64) Miller, G. G. and Pursey, H., 1955, on the partition of energy between elastic waves in a semi-infinite solid, Proceeding of the Royal Society of London, Series A, v233, pp251-541

65) Morrison, N., 1994, Introduction to Fourier analysis, John Wiley & Sons Inc., pp563

66) Moore, W., Hanson, D., and Hall, J., 1978, An introduction to nondestructive structural evaluation of pavements, Transportation Research Circular 189, Washington, D.C.

67) Murigendrappa, S. M., Maiti, S. K. and Srirangarajan, H. R., Sep. 2004, Frequency-based experimental and theoretical identification of multiple cracks in straight pipes filled with fluid, NDT & E International 37, v37 n6, pp431-438

68) Murigendrappa, S. M., Maiti, S. K. and Srirangarajan, H. R., Mar. 2004, Experimental and theoretical study on cracks detection in pipes filled with fluid, Journal of Sound and Vibration, v270 n4-5, pp1013-1032

69) Naik, T. and Malhotra, M., 1991, Handbook on nondestructive testing of concrete, CRC Press

70) Witczak, M.W., Kaloush, K., Pellinen, T., El-Basyouny, M., and Von Quintus, H., 2002, Simple Performance Test for Superpave Mix Design, NCHRP Report 465, Transport Research Board, Washington D. C.

71) National Institute of Quality Supervision for Civil Structures (China), 1997, Nondestructive testing techniques for concrete structures (in Chinese)

72) Nazarian S, Stokoe K.H. II, and Hudson WR, 1983, Use of spectral analysis of surface waves method for determination of moduli and thicknesses of pavement systems. Transportation research record, 921, TRB. Washington, DC: National Research Council, pp. 38-45

73) Nazarian, S., 1984, "In situ determination of soil deposits and pavement systems by spectral analysis of surface waves method." PhD thesis, Univ. of Texas at Austin

74) Nazarian, S., and Stokoe, K.H. II, 1986, Use of surface waves in pavement evaluation, Transportation Research Record, No. 1070, pp. 132-144

75) Ovanesova, A. V. and Suarez, L. E., 2004, Application of wavelet transforms to damage detection in frame structures, Engineering Structures 26(2004), pp39-49

76) Panametraics INC., August 22, 1984, Instruction manual: Ultrasonic pulser/receiver model 5052PR, Panametraics INC., Waltham, Massachusetts

77) Popovics, S., June, 1969, "Effect of Porosity on the Strength of Concrete," Journal of Materials, JMLSA, , v4, n2, pp356-371

78) Popovics, S., Rose, J. L., and Popovics, J. S., 1990, The behavior of ultrasonic pulse in concrete, Cement and Concrete Research, v20, n2, pp183-191

79) Popovics, S. and Popovics, J.S. 1992, A critique of the ultrasonic pulse velocity method for testing concrete, in: NDT of Concrete Elem. And Struct., / ed. F. Ansari and S. Strue/, Proc. ASCE: San Antonio, 94 – 103

80) Popovics JS and Rose JL, November, 1994, A survey of developments in ultrasonic NDE of concrete, IEEE Transactions on Ultrasonics, Ferroelectrics, and Frequency Control, v41, n1, pp140-143

81) Popovics, J. S., Rose, J. L., etc., Mar. 1995, Approaches for the generation of stress waves in concrete, Experimental Mechanics, v35 n1, pp36-41

82) Popovics, J. S., Song, W. J. and Achenbach, J. D., 1998, One-sided stress wave velocity measurement in concrete, ASCE Journal of Engineering mechanics, v124, pp1346-1353

83) Popovics, J. S., Song, W. J. and Achenbach, J. D., 1998, A study of surface wave attenuation measurement for application to pavement characterization, Proceedings of SPIE, pp300-308

84) Popovics, J. S., Song, W. J., Ghandehari, M., etc., 2000, Application of surface transmission measurements for crack depth determination in concrete, ACI Materials Journal, v97 n2, pp127-135

85) Porat, B., 1997, A course in digital signal processing, John Wiley & Sons Inc.

86) Proctor, T. M. and Breckenridge, F. R., 1992, Source force waveforms: the use of a calibrated transducer in obtaining an accurate waveform of a source, Journal of Acoustic Emission, v10:3, pp43-48

87) Pratt, D. and Sansalone, M., Mar.-Apr., 1992, Impact-echo signal interpretation using artificial intelligence, ACI Materials Journal, v 89 n 2, pp178-187

88) Qian, Shie, 2002, Time-frequency and wavelet transforms, Prentice-Hall Inc.

89) Rayleigh, L., 1885, On waves propagated along the plane surface of an elastic solid, Proceedings of the London Mathematical Society, v17, pp4-11

90) Richart, F. E., Hall, J. R. and Woods, R. D., 1970, Vibrations of soils and foundations, Prentice-Hall Inc, 414pp

91) Roesset, JM, Chang, D.-W., Stokoe, KH, II and Aouad, M., 1989, "Modulus and Thickness of the Pavement Surface Layer from SASW Tests," Transportation Research Record, No. 1260, pp. 52-63

92) Rose, J.L., April, 1985, Ultrasonic wave propagation principles in composite material inspection, Materials Evaluation, Vol. 43, No. 5, pp. 481-483

93) Rose, J.L., Pilarski, A., Balasubramaniam, K., Dale, J., and Diprimeo, D., June 21-26, 1987, Wave scattering and guided wave considerations. in anisotropic media, Proceedings of the 14th Annual Review of Progress in Quantitative NDE, Williamsburg, Va.

94) Rose, J.L., and Pilarski, A., Apr. 1988, Surface and plate waves in layered structures, Materials Evaluation, v46

95) Sanchez-Salinero, I., Roesset, J.M., Shao, K-Y., Stokoe, K.H., Ii, Rix, G.J., 1987, Analytical Evaluation Of Variables Affecting Surface Wave Testing Of Pavements, Transportation Research Record, No.1136, pp.86-95

96) Sachse, W. and Pao, Y., 1978, On the determination of phase and group velocities of dispersive waves in solids, Journal of applied Physics, v49(8), pp4320-4327

97) Santamarina, J. Carlos, 1998, Introduction to discrete signals and inverse problems in civil engineering, ASCE Press, USA, 327 pp

98) Sansalone, M., Lin, J. M. and Streett, W. B., Mar.-Apr. 1998, Determining the depth of surface-opening cracks using impact-generated stress waves and time-of-flight techniques, ACI Materials Journal, v 95 n 2, pp168-177

99) Sansalone, M., Nov.–Dec. 1997, Impact-Echo: the complete story, ACI Structural Journal, v 94 n 6, pp777-786

100) Sansalone, M., Lin, J. M. and Streett, W. B., Nov.-Dec. 1997, A procedure for determining P-wave speed in concrete for use in impact-echo testing using a direct P-wave speed measurement technique, ACI Materials Journal, v94 n6, pp531-539

101) Sansalone, M., and Carino, N.J., Sept., 1986, Impact-Echo: A Method for Flaw Detection in Concrete Using Transient Stress Waves, NBSIR 86-3452, National

Bureau of Standards, Gaithersburg, Maryland, 222 pp. order from NTIS, PB#87-104444/AS

102) Sansalone, M., Carino, N. J. and Hsu, N. J., Jul.-Aug. 1987, Finite element study of transient wave propagation in plates, Journal of Research of the National Bureau of Standards, v92 n4, pp267-278

103) Sansalone, M., and Carino, N.J., 1988, "Laboratory and Field Study of the Impact-Echo Method for Flaw Detection in Concrete," in Nondestructive Testing of Concrete, ACI SP-112 of the American Concrete Institute, pp 1-20

104) Sansalone, M. and Carino, N.J., Mar.-Apr. 1989, "Detecting Delaminations in Concrete Slabs with and without Overlays Using the Impact-Echo Method," ACI Materials Journal, V. 85, No. 2, pp 175-184

105) Sansalone, M., and Streett, W. B., 1997, Impact-Echo: Nondestructive Evaluation of Concrete and Masonry, Bullbrier Press, 339 pp.

106) Schickert, G., 1984, Critical reflections on nondestructive testing of concrete, Materials and Structures, 5/6 (1984) 99, pp. 217-220

107) Sheu, J. C., 1987, Applications and limitations of the spectral-analysis-of-surface-waves method, Ph.D. Thesis, Department of Civil Engineering, University of Texas at Austin

108) Sheu JC, Stokoe KH, Roesset JM., 1988, Effects of reflected waves on SASW testing of pavements. Transportation research record, No. 1196, pp51-61

109) Sheu, JC, Rix, GJ, and Stokoe, KH, II., 1988, Rapid Determination of Modulus and Thickness of Pavement Surface. Layer", presented at the Transportation Research Board annual meeting

110) Silk, M. G., 1976, The determination of crack penetration using ultrasonic surface waves, Ultrasonics, v38, pp290-297

111) Smith R. and Lytton, R., 1985, Operating characteristics and user satisfaction of commercially available ND equipment, Transportation Research Record 1007

112) Song, W. J., Popovics, J. S. and Achenbach, J. D., Apr. 1999, Crack depth determination in concrete slabs using wave propagation measurements, Proceedings of the Federal Aviation Administration Technology Transfer Conference, Atlantic City, NJ, USA

113) Song, W. J., Popovics, J. S., Aldrin, J. C. and Shah, S. P., Feb. 2003, Measurement of surface wave transmission coefficient across surface-breaking cracks and notches in concrete, Journal of Acoustical Society of America 113(2), pp717-725

114) Staszewski, WJ, 1998, Structural and mechanical damage detection using wavelets, The Shock and Vibration Digest, v30(6), pp457-472

115) Stokoe, K. H. and Nazarian S., 1983, Effectiveness of ground improvement from spectral analysis of surface waves, Proceedings of the European Conference on Soil Mechanics and Foundation Engineering, v1, pp91-94

116) Strobbia, C., 2003, Surface wave methods, Ph.D. Thesis, http://www2.polito.it/ricerca/engel/downloads/ClaudioStrobbia.pdf

117) Sturrup, V.R., Vecchio, F.J., and Caratin H., 1984, Pulse velocity as a measure of concrete compressive strengths, Nondestructive testing of concrete ACI SP 82-11, V.M. Malhotra, ed., American Concrete Institute, Detroit, U.S.A., 201-227.

118) Tallavo, F.J., 2007, PhD thesis.

119) Toutanji, H. A., Apr. 2003, Development of a new experimental approval for bridge deck evaluation, UTCA Report (01327), University of Alabama, USA

120) Olson Engineering, Inc., January 23, 2004, Ultrasonic Pulse Velocity (UPV), available at http://www.olsonengineering.com/testmethods.html

121) Olson Engineering, Inc., January 23, 2004, Spectral Analysis Of Spectral Waves (SASW), available at http://www.olsonengineering.com/testmethods.html

122) Ullidtz, P., 1987, Pavement Analysis, Development in Civil Engineering, Vol.19, Elsevier, ISBN 0-444-42817-8

123) Vary A., 1991, Material property characterization, Non-destructive testing handbook – ultrasonic testing, Vol. 7, American Society for Non-destructive Testing, Columbus, Ohio, pp. 383-431

124) Vidale, RF, 1964, The dispersion of stress waves in layered media overlaying a half space of lesser acoustic rigidity. PhD thesis, Univ. of Wisconsin

125) Viktorov, I. A., 1967, Rayleigh and Lamb waves, Plenum Press, New York

126) Wikipedia, 2007, Seismic wave, available at http://en.wikipedia.org/wiki/Seismic_wave

127) Witczak, M.W., Kaloush, K., Pellinen, T., El-Basyouny, M., and Von Quintus, H., 2002, Simple Performance Test for Superpave Mix Design, NCHRP Report 465, Transport Research Board, Washington D. C.

128) Wolf, J. P. and Obernhulber, P., 1981, Free-field response from surface and inclined body waves, Transactions of the International Conference on Structural Mechanics in Reactor Technology, 14pp

129) Yang, Y., Cascante, G., and Polak, A., 2007, Numerical and experimental evaluation of depth of surface-breaking cracks in concrete plates, University of Waterloo, ON, Canada.

130) Zerwer, A., 1999, Near surface fracture detection in structural elements: investigation using Rayleigh waves, Ph. D. Thesis, University of Waterloo, ON, Canada

131) Zerwer, A., Cascante, G., and Hutchinson, J., 2002, Parameter estimation in finite element simulations of Rayleigh waves, Journal of Geotechnical and Geoenvironmental Engineering, v128 n3, pp250-261

132) Zerwer, A., Polak, M. A. and Santamarina, J. C., June 2003, Rayleigh wave propagation for the detection of near surface discontinuities: finite element study, Journal of Nondestructive Evaluation, v22 n2, pp39-52

133) Zerwer, A., Polak, M. A., Santamarina, J. C., 2000, Wave Propagation in thin Plexiglas plates: Implications for Rayleigh waves, NDT & E International, v33, pp33-41

134) Zukas, J. A., Nicholas, T., Swift, H. F., etc., 1982, Impact dynamics, John Wiley & Sons

Appendix A

Signal Processing for Gyratory Samples

This appendix is a PDF file available in the Appendix CD.

The file name of this PDF file is “Appendix A - Signal processing for gyratory samples.pdf”.

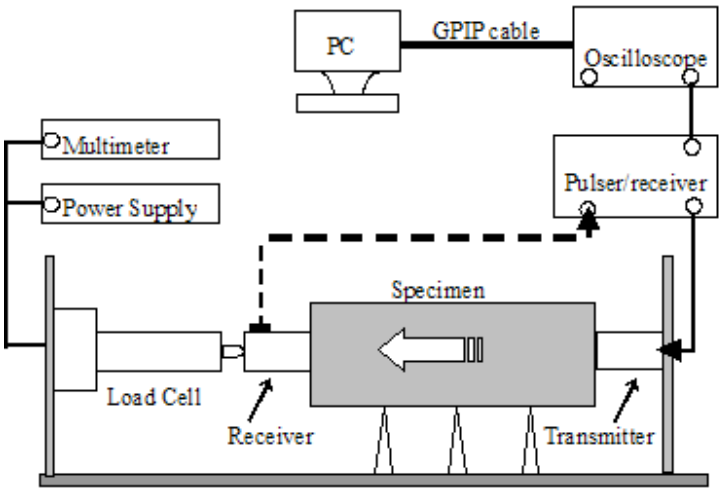

Figure A - 1: UPV testing of a gyratory specimen

Measure Gyratory samples using 1MHz P-Wave Transducers:

Pulse receiver parameter setting for 1MHz P-Wave transducers				
Rep. Rate: 2		Pressure: 14 mv (about 45lb)		
Energy: 4				
Atten. (dB): 0				
GAIN (dB): 40				
Damping: 4.0				
Mode: 2				

Oscilloscope setting: **Sampling Rate Δt:** $\frac{50\mu s}{100}$ **1000 Points in Total**

Index $N := 2^{10}$ $i := 1 .. N$ $u := 1 .. \frac{N}{2}$ $ORIGIN \equiv 1$

all := Reading data $f_u := \frac{u}{N \cdot 5 \cdot 10^{-4}}$

Definition of signals: AC indicates Asphalt Concrete, while the following number indicates the number of gyrations.

$AC40_i := all_{i,1}$ $AC60_i := all_{i,2}$ $AC80_i := all_{i,3}$

$AC100_i := all_{i,4}$ $AC120_i := all_{i,5}$ $AC140_i := all_{i,6}$

$signal40_i := AC40_i - mean(AC40)$ $signal140_i := AC140_i - mean(AC140)$

$signal60_i := AC60_i - mean(AC60)$ $signal80_i := AC80_i - mean(AC80)$

$signal100_i := AC100_i - mean(AC100)$ $signal120_i := AC120_i - mean(AC120)$

$signal := (signal40 \ signal60 \ signal80 \ signal100 \ signal120 \ signal140)^T$

Analysis of the full time signals:

Parameter $p := 1 .. 6$ $\omega o_p := 2\pi \cdot 1.2$

Arrival Time (AT) of the signal: $AT := (0.0485 \;\; 0.0475 \;\; 0.0535 \;\; 0.0485 \;\; 0.0445 \;\; 0.0465 \;\; 0 \;\; 0)^T$

$$tp_p := ceil\left(\left(\frac{AT_p}{0.0005}\right)\right) \cdot 0.000$$

$$wp(t, \omega o) := \begin{cases} 10\left|\cos(\omega o \cdot t)^{5000} - 1\right| & \text{if } 0 \le t \le \frac{\pi}{\omega o} \\ 0 & \text{otherwise} \end{cases}$$

Define **Time Window** (Twind) to amplify the arrival of the signals:

$$Twind := \left| \begin{array}{l} \text{for } p \in 1 .. 6 \\ \quad \text{for } i \in 1 .. N \\ \quad\quad ampl_{i,p} \leftarrow wp(i \cdot 0.0005 - tp_p, \omega o_p) \\ ampl \end{array} \right.$$

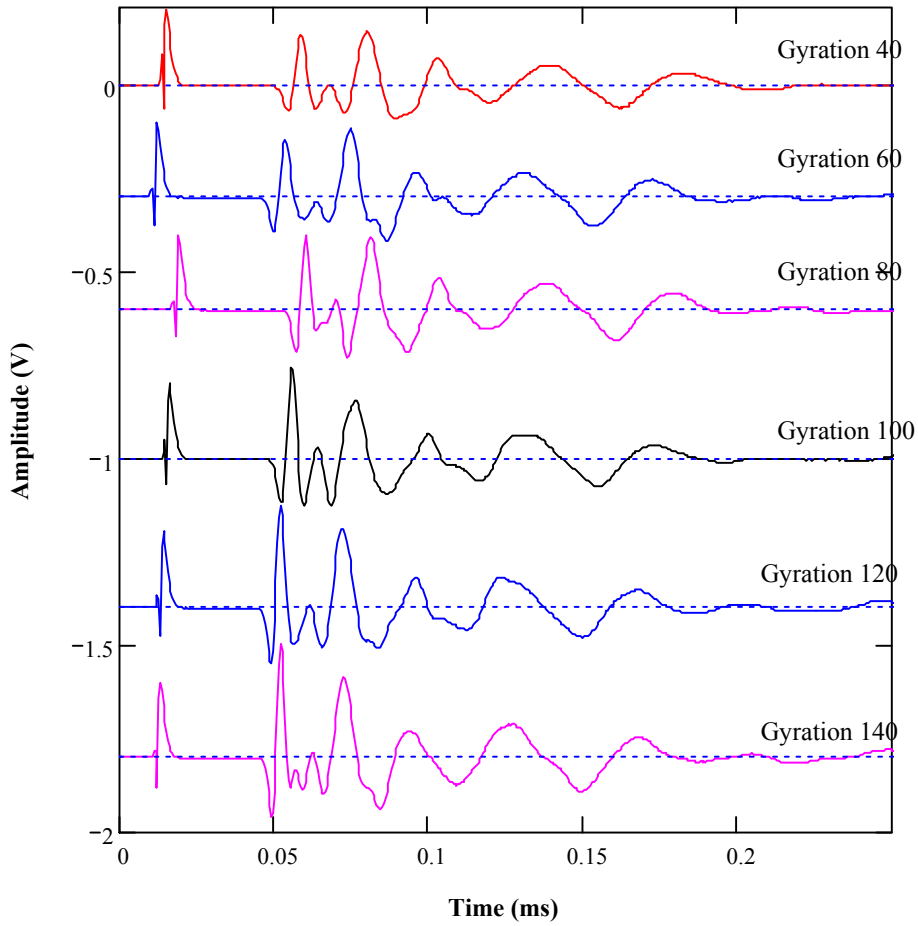

Fourier Transform of the Windowed Signals: $FTW^{\langle p \rangle} := CFFT\left(\overrightarrow{\left(Twind^{\langle p \rangle} \cdot signal_p\right)}\right)$

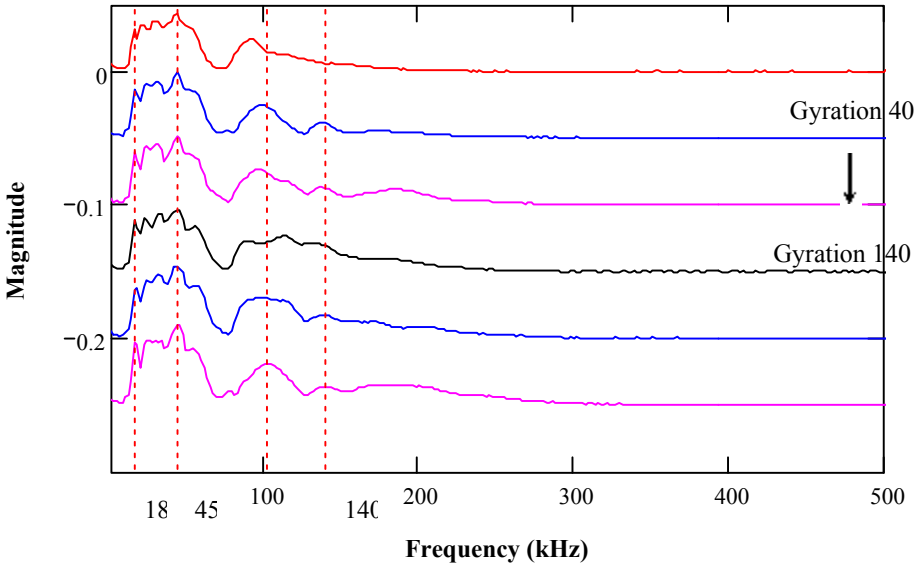

Window the 1st peak of the time signals:

Parameter $\omega o_1 := 2\pi \cdot 42$ $\omega o_2 := 2\pi \cdot 53$ $\omega o_3 := 2\pi \cdot 51$ $\omega o_4 := 2\pi \cdot 51$

$\omega o_5 := 2\pi \cdot 55$ $\omega o_6 := 2\pi \cdot 58$

Arrival Time (AT):

$AT := (\ 0.0505 \quad 0.0475 \quad 0.0535 \quad 0.049 \quad 0.046 \quad 0.0465 \quad 0 \quad 0\ )^T$

$p := 1 .. 6$

$tp_p := ceil\left(\left(\frac{AT_p}{0.0005}\right)\right) \cdot 0.000$

$wp(t, \omega o) := \begin{cases} 10\left|\cos(\omega o \cdot t)^{10} - 1\right| & \text{if } 0 \le t \le \frac{\pi}{\omega o} \\ 0 & \text{otherwise} \end{cases}$

Define **Time Window** (Twind) to amplify the arrival of the signals:

$$Twind := \left| \begin{array}{l} \text{for } p \in 1 .. 6 \\ \quad \text{for } i \in 1 .. N \\ \quad\quad ampl_{i,p} \leftarrow wp\left(i \cdot 0.0005 - tp_p, \omega o_p\right) \\ ampl \end{array} \right.$$

Fourier Transform of the Windowed Signals: $FTW^{\langle p \rangle} := CFFT\left(\overrightarrow{\left(Twind^{\langle p \rangle} \cdot signal_p\right)}\right)$

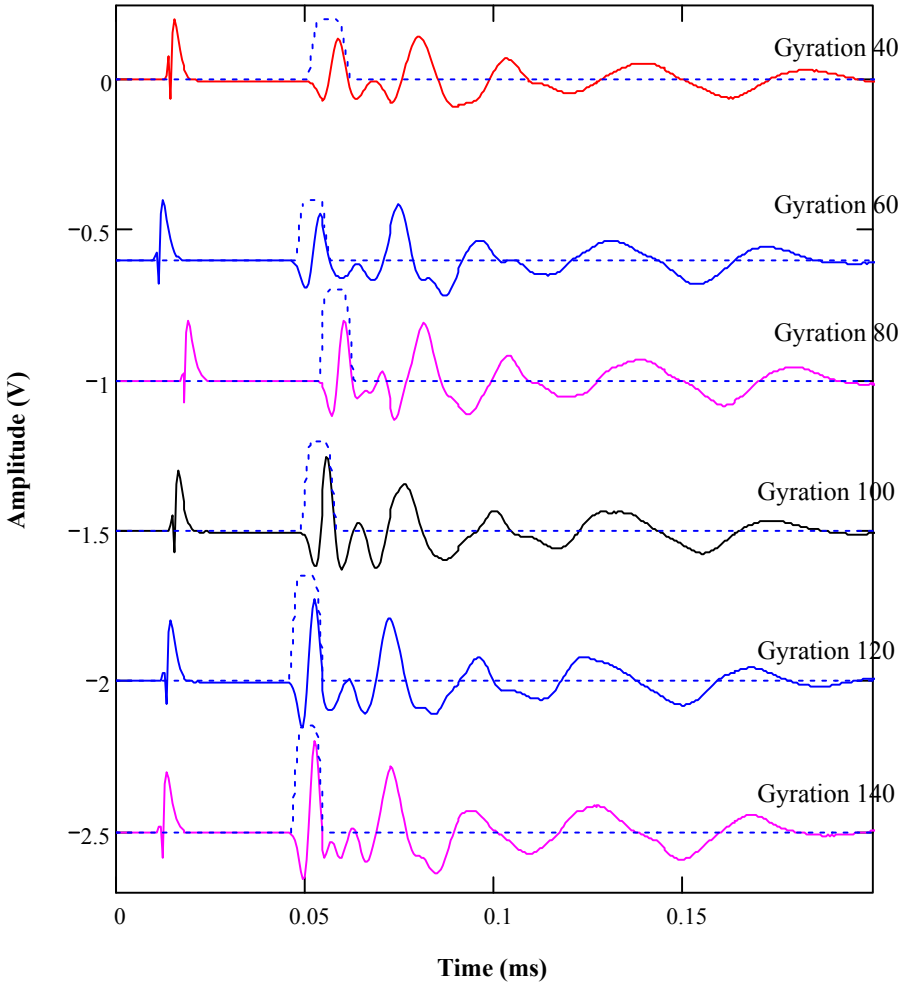
Gyration 40
Gyration 60
Gyration 80
Gyration 100
Gyration 120
Gyration 140
0
−0.5
−1
−1.5
−2
−2.5
0
0.05
0.1
0.15
Amplitude (V)
Time (ms)

The First Arrivals in time domain after windowing are as follows:

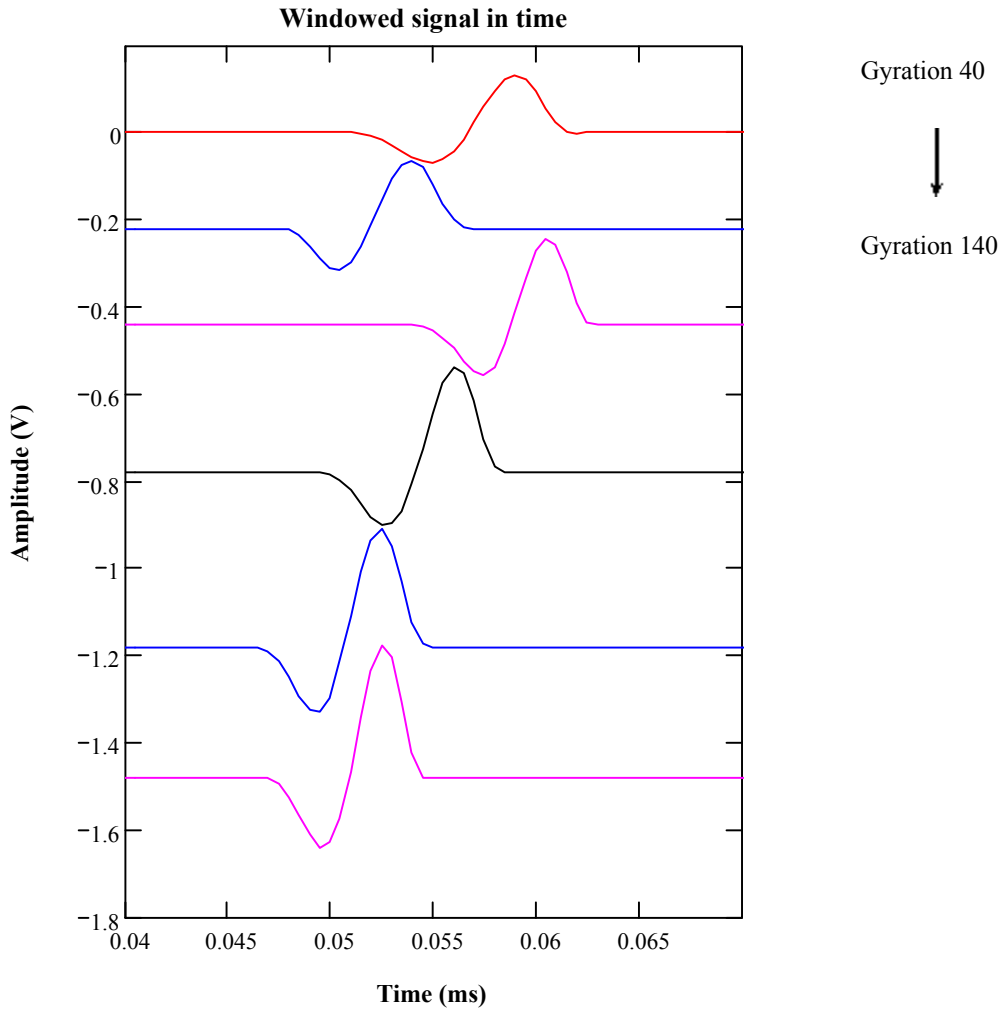

The frequency spectra for the above first arrivals are as follows:

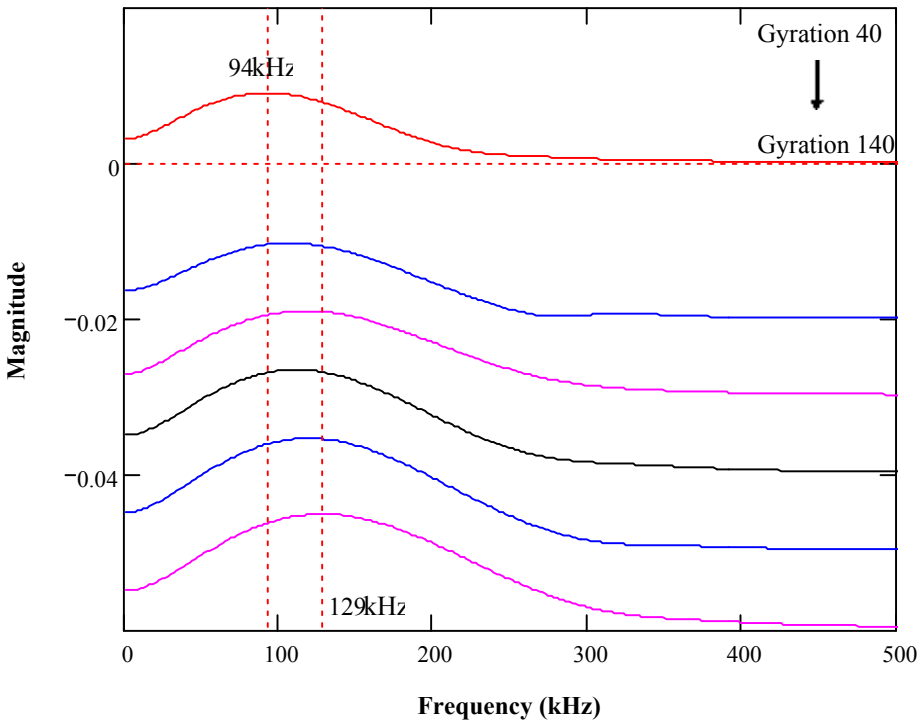

Calibration of the small difference in length:

Peak-to-Peak (PTP) values of the windowed signals (ws) :

$j := 80..125$ $k := 80..113$ $m := 80..127$ $n := 80..117$ $o := 80..111$

$ws40_j := signal40_j$ $ws140_o := signal140_o$ $ws100_n := signal100_n$

$ws60_k := signal60_k$ $ws80_m := signal80_m$ $ws120_o := signal120_o$

$PTP40 := \max(ws40) - \min(ws40)$ $PTP60 := \max(ws60) - \min(ws60)$

$PTP80 := \max(ws80) - \min(ws80)$ $PTP100 := \max(ws100) - \min(ws100)$

$PTP120 := \max(ws120) - \min(ws120)$ $PTP140 := \max(ws140) - \min(ws140)$

Calibration of the small difference in length:

$gyration := (40 \quad 60 \quad 80 \quad 100 \quad 120 \quad 140)^T$

PTP vs. Gyration

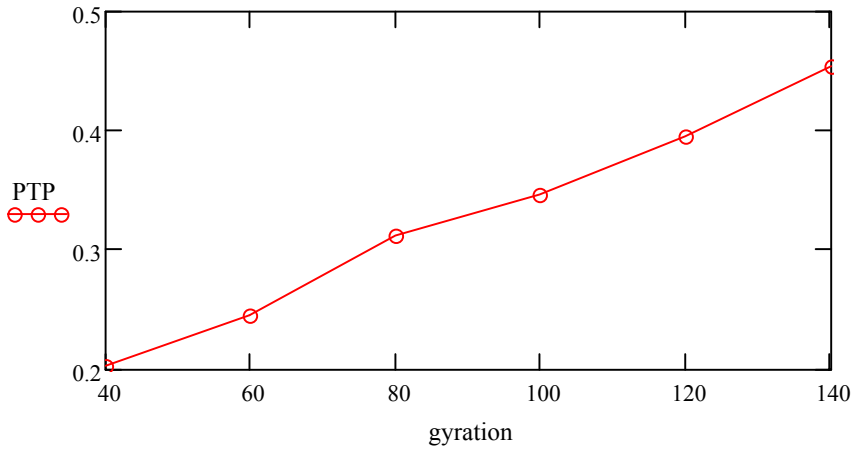

Maximum Area in Frequency Domain for the Windowed Signal (MA):

$$p := 1 .. 6 \qquad MA_p := \sum_{u=1}^{300} \frac{|FTW_{u,p}|}{N \cdot 0.0005}$$

Calibration of the small difference in length:

$$MA1 := \left(MA_1 \cdot \frac{160.6575}{160.6575} \quad MA_2 \cdot \frac{159.065}{160.6575} \quad MA_3 \cdot \frac{158.825}{160.6575} \quad MA_4 \cdot \frac{153}{160.6575} \quad MA_5 \cdot \frac{150.22}{160.6575} \quad MA_6 \cdot \frac{157.595}{160.6575} \right)^T$$

MA vs. Gyration

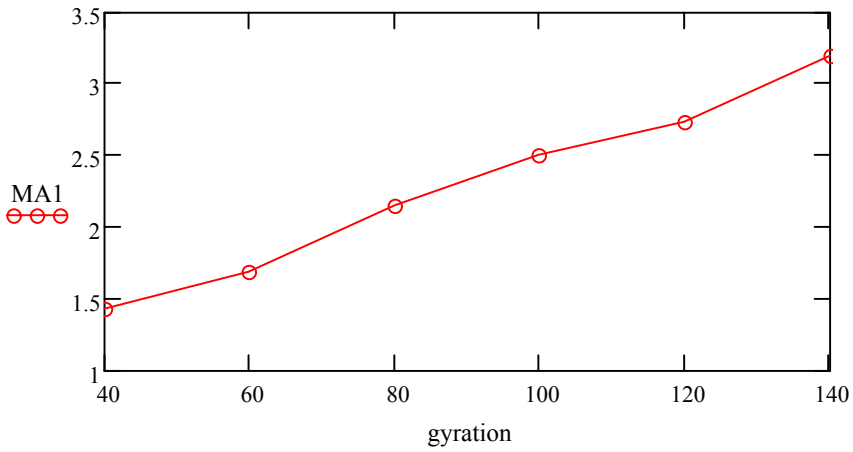

$$MA1 = \begin{pmatrix} 1.435 \\ 1.681 \\ 2.146 \\ 2.496 \\ 2.729 \\ 3.19 \end{pmatrix}$$

Maximum Magnitude in Frequency Domain (MM):

$p := 1 .. 6$ $\quad MM_p := \max\left(\left|FTW^{\langle p \rangle}\right|\right)$

Calibration of the small difference in length:

MM vs. Gyration

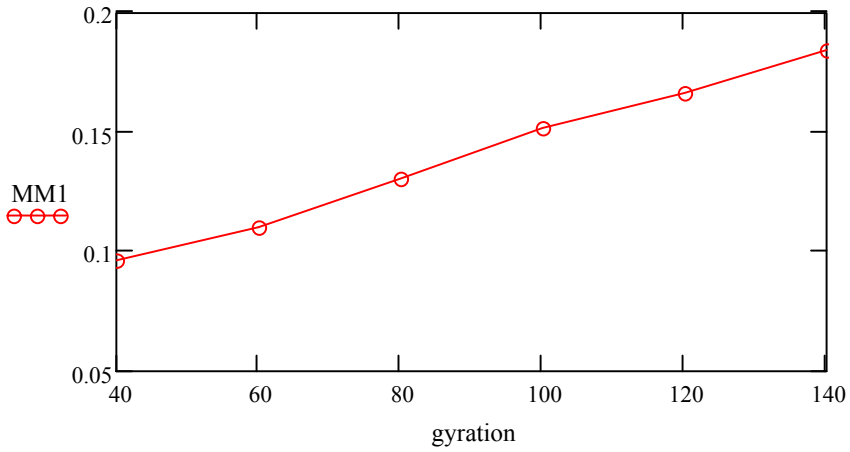

$$MM1 = \begin{pmatrix} 0.096 \\ 0.11 \\ 0.13 \\ 0.152 \\ 0.166 \\ 0.184 \end{pmatrix}$$

Summary

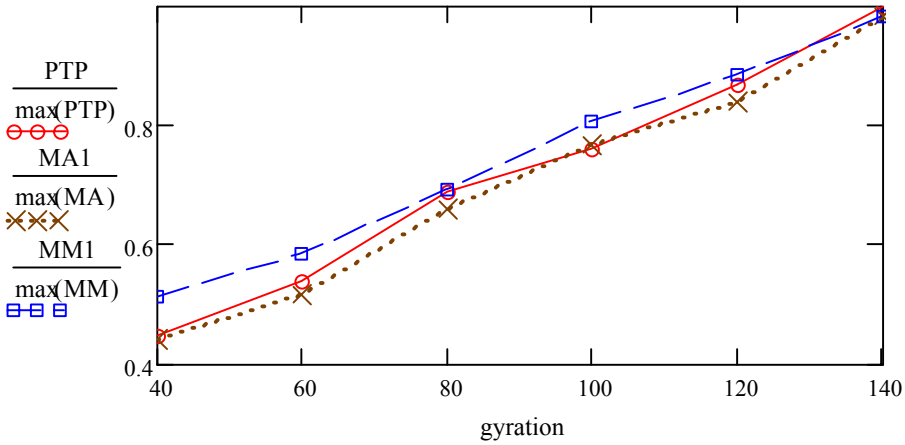

Window one and a half cycle of the time signals:

Parameter $\omega o_1 := 2\pi \cdot 28$ $\omega o_2 := 2\pi \cdot 30$ $\omega o_3 := 2\pi \cdot 31$ $\omega o_4 := 2\pi \cdot 33$

$\omega o_6 := 2\pi \cdot 45$ $\omega o_5 := 2\pi \cdot 30$

Arrival Time (AT):

$AT := (\ 0.0505 \quad 0.0475 \quad 0.0535 \quad 0.049 \quad 0.046 \quad 0.0465 \quad 0 \quad 0\ )^T$

$p := 1 .. 6$

$tp_p := ceil\left(\left(\frac{AT_p}{0.0005}\right)\right) \cdot 0.000$

$wp(t, \omega o) := \begin{cases} 10\left|\cos(\omega o \cdot t)^{10} - 1\right| & \text{if } 0 \le t \le \frac{\pi}{\omega o} \\ 0 & \text{otherwise} \end{cases}$

Define **Time Window** (Twind) to amplify the arrival of the signals:

$Twind := \left| \begin{array}{l} \text{for } p \in 1 .. 6 \\ \quad \text{for } i \in 1 .. N \\ \quad\quad ampl_{i,p} \leftarrow wp\left(i \cdot 0.0005 - tp_p, \omega o_p\right) \\ ampl \end{array} \right.$

Fourier Transform of the Windowed Signals: $FTW^{\langle p \rangle} := CFFT\left(\overrightarrow{\left(Twind^{\langle p \rangle} \cdot signal_p\right)}\right)$

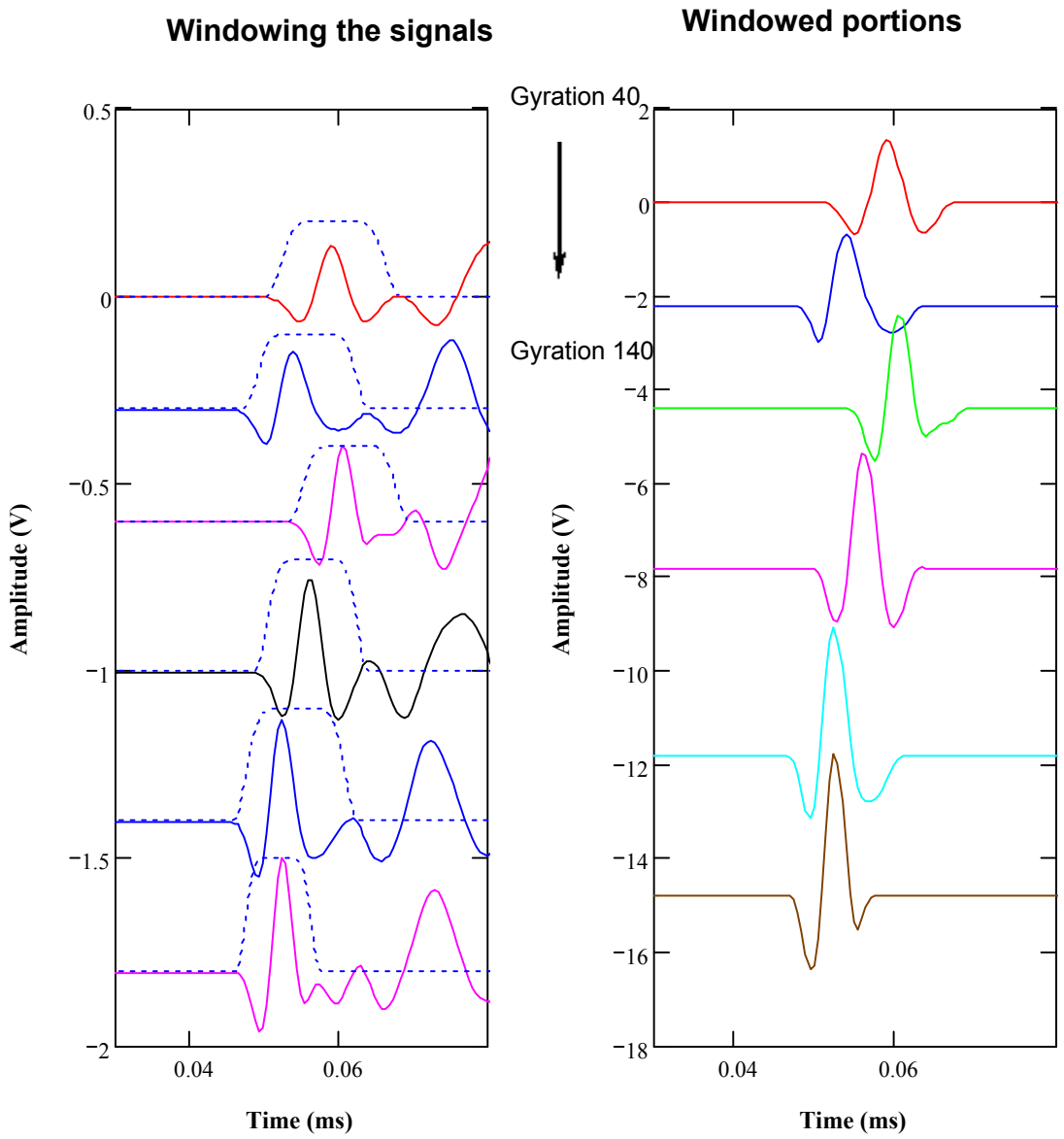
Windowing the signals
Windowed portions
Gyration 40
Gyration 140
Amplitude (V)
Time (ms)
0.5
0
−0.5
−1
−1.5
−2
0.04
0.06
2
0
−2
−4
−6
−8
−10
−12
−14
−16
−18

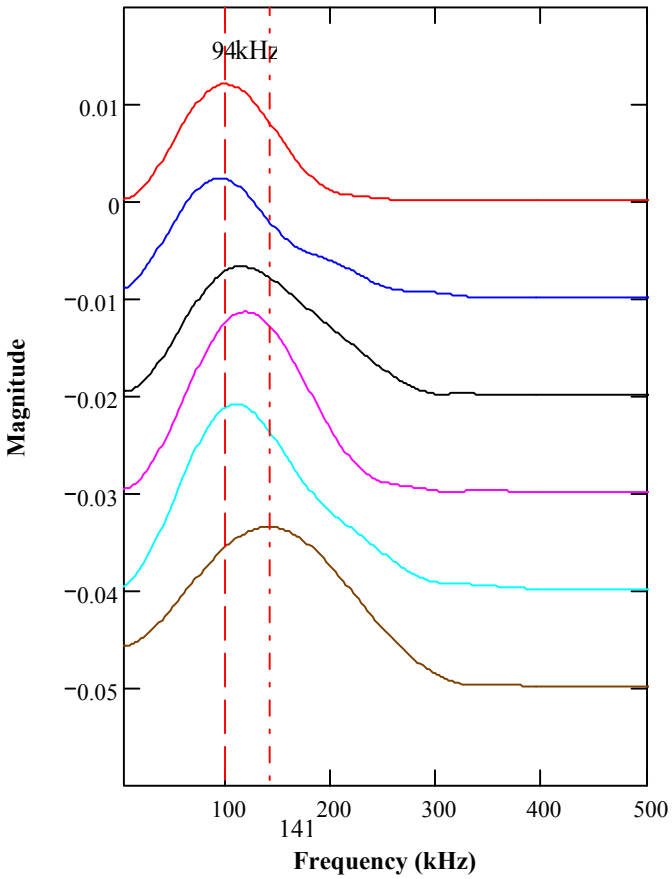

Gyraton 40

Gyraton 140

Calibration of the small difference in length:

Peak-to-Peak (PTP) value of the windowed signals (ws) :

$j := 80..125 \qquad k := 80..113 \qquad m := 80..127 \qquad n := 80..117 \qquad o := 80..111$

$ws40_j := signal40_j \qquad ws140_o := signal140_o \qquad ws100_n := signal100_n$

$ws60_k := signal60_k \qquad ws80_m := signal80_m \qquad ws120_o := signal120_o$

$PTP40 := \max(ws40) - \min(ws40) \qquad PTP60 := \max(ws60) - \min(ws60)$

$PTP80 := \max(ws80) - \min(ws80) \qquad PTP100 := \max(ws100) - \min(ws100)$

$PTP120 := \max(ws120) - \min(ws120) \qquad PTP140 := \max(ws140) - \min(ws140)$

Calibration of the small difference in length:

$gyration := (40 \quad 60 \quad 80 \quad 100 \quad 120 \quad 140)^T$

PTP vs. Gyration

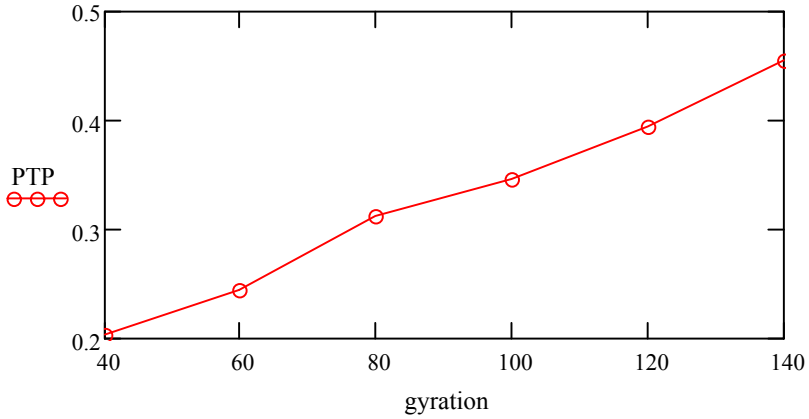

$$PTP = \begin{pmatrix} 0.203 \\ 0.244 \\ 0.312 \\ 0.345 \\ 0.394 \\ 0.454 \end{pmatrix}$$

Maximum Area in Frequency Domain for the Windowed Signal (MA):

$p := 1 .. 6$

$$MA1_p := \sum_{u=1}^{300} \frac{|FTW_{u,p}|}{N \cdot 0.0005}$$

Calibration of the small difference in length:

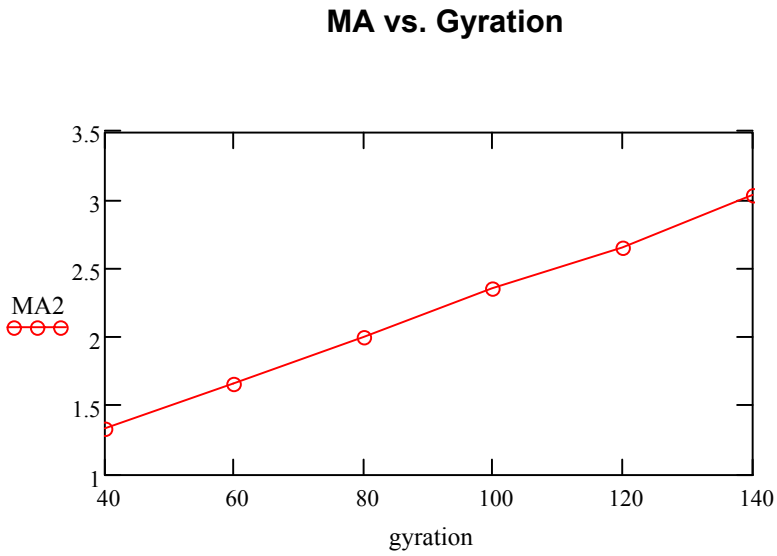

$$MA2 = \begin{pmatrix} 1.335 \\ 1.66 \\ 2.005 \\ 2.355 \\ 2.656 \\ 3.033 \end{pmatrix}$$

Maximum Magnitude in Frequency Domain (MM):

$p := 1 .. 6$ $\qquad MM_p := \max\left(\left|FTW^{\langle p \rangle}\right|\right)$

Calibration of the small difference in length:

MM vs. Gyration

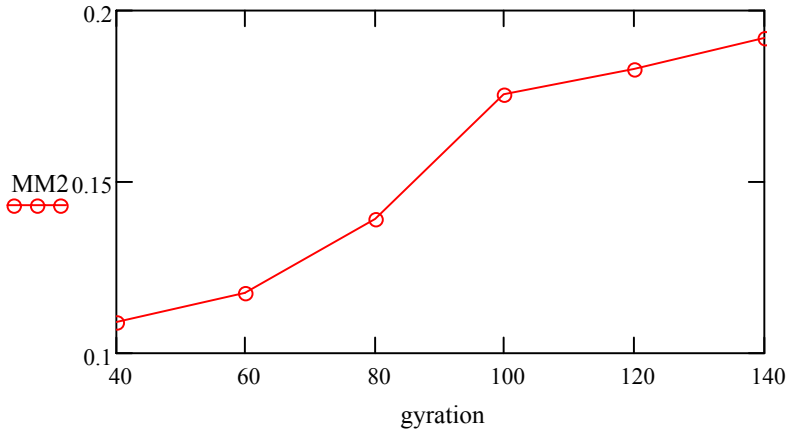

$$MM2 = \begin{pmatrix} 0.109 \\ 0.117 \\ 0.139 \\ 0.175 \\ 0.182 \\ 0.192 \end{pmatrix}$$

Summary

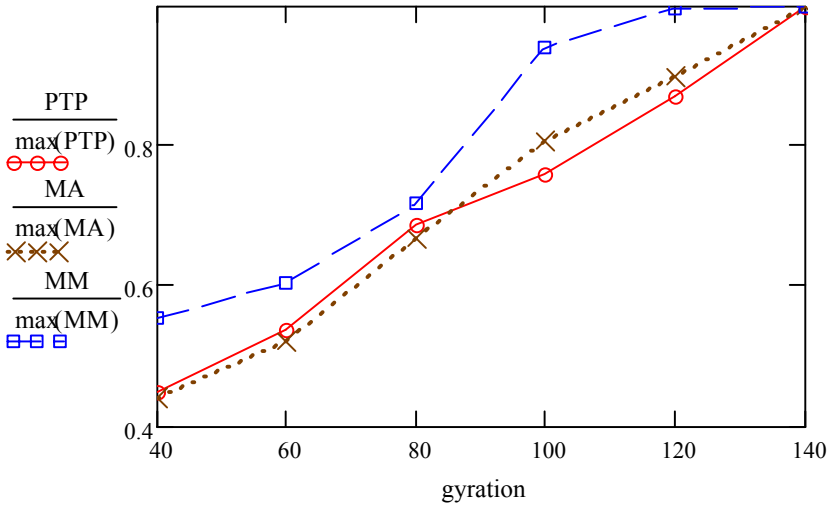

Appendix B

Relationships between Wave Characteristics and Dynamic Moduli at 0.1 to 25Hz Loading Frequencies

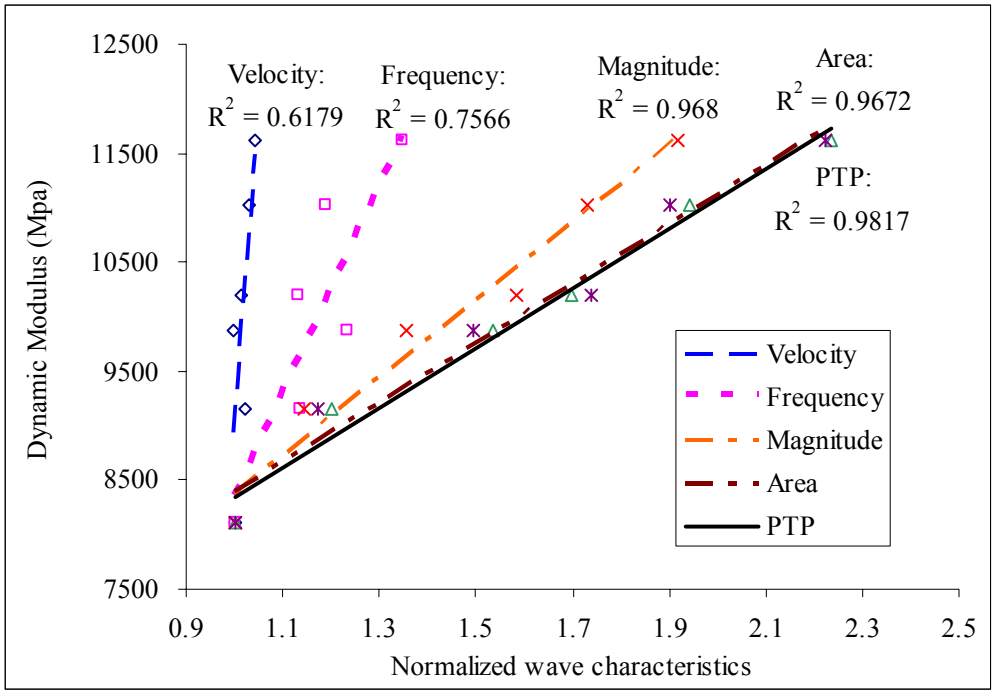

Figure B-1: Wave characteristics vs. dynamic moduli at 25 Hz loading frequency

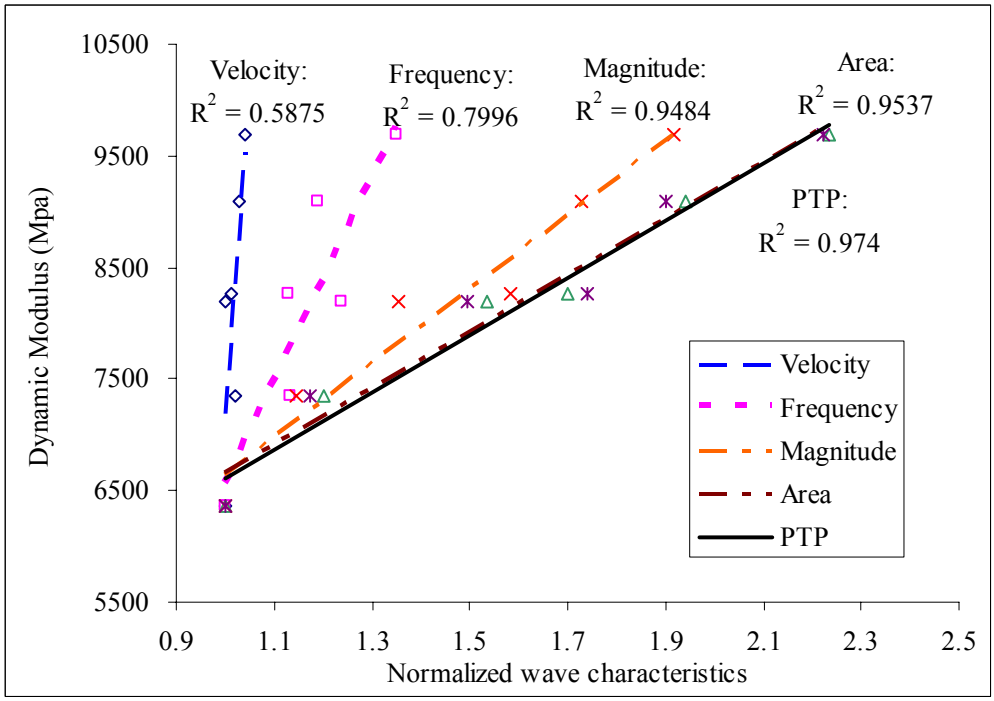

Figure B-2: Wave characteristics vs. dynamic moduli at 10 Hz loading frequency

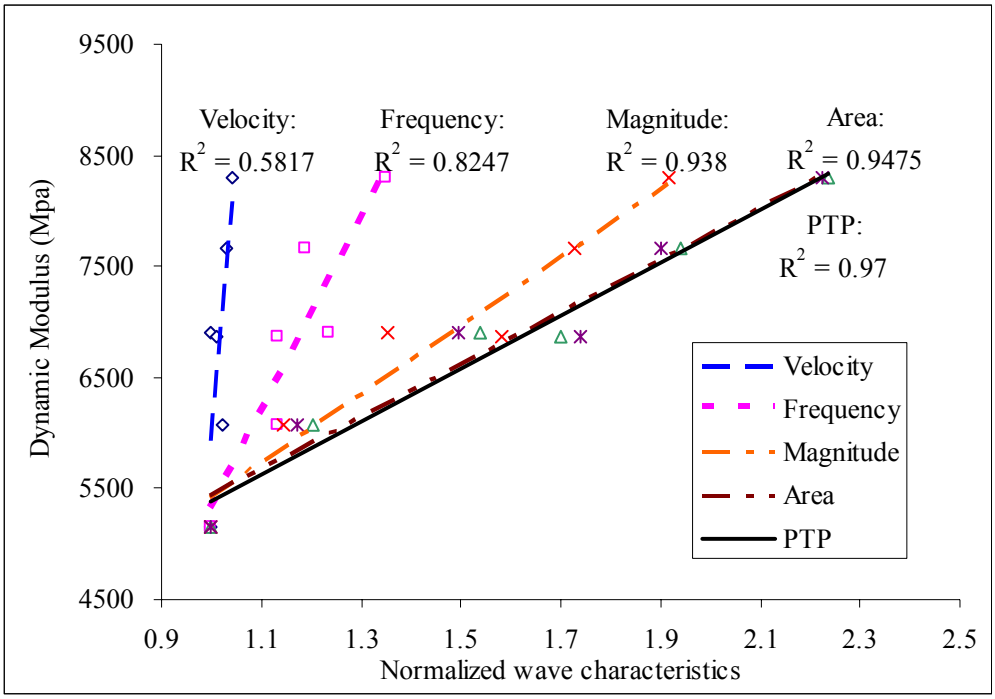

Figure B-3: Wave characteristics vs. dynamic moduli at 5 Hz loading frequency

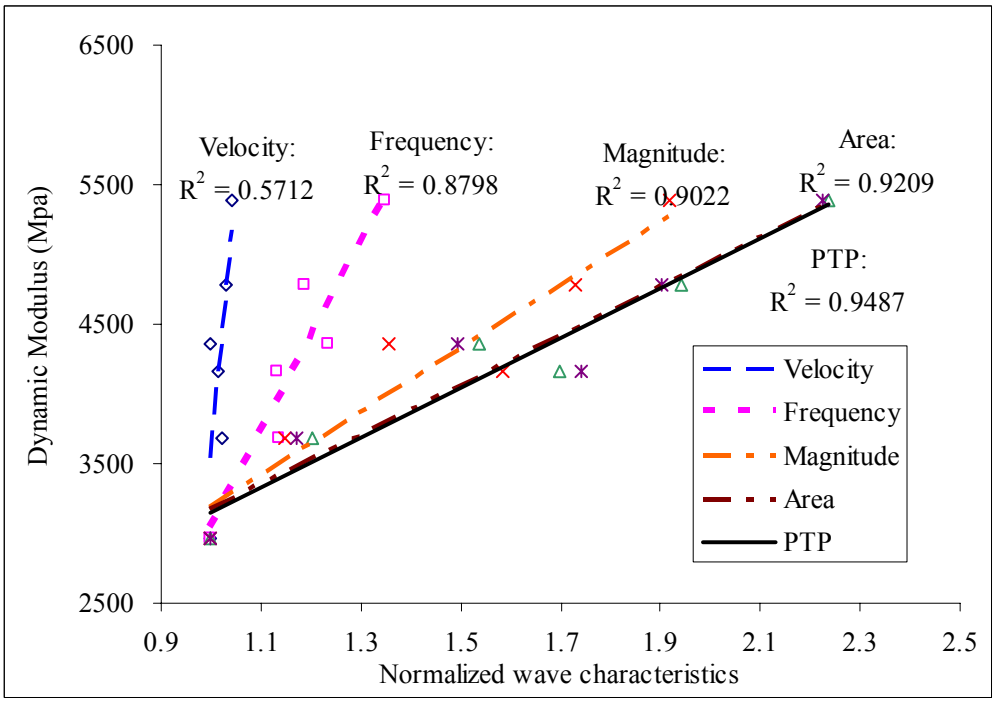

Figure B-4: Wave characteristics vs. dynamic moduli at 1 Hz loading frequency

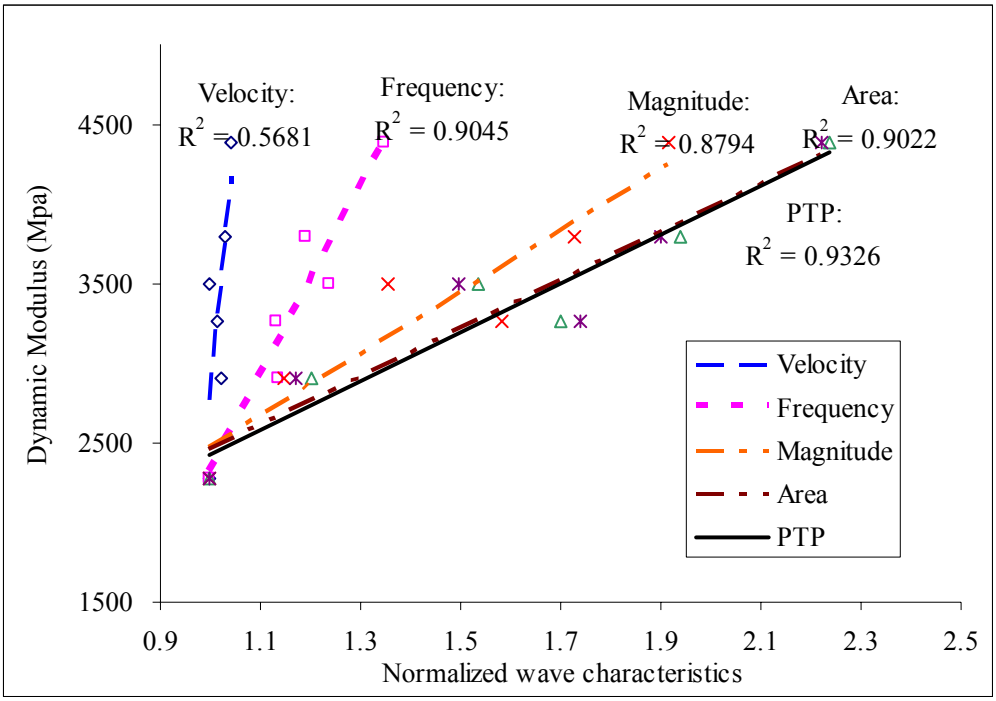

Figure B-5: Wave characteristics vs. dynamic moduli at 0.5 Hz loading frequency

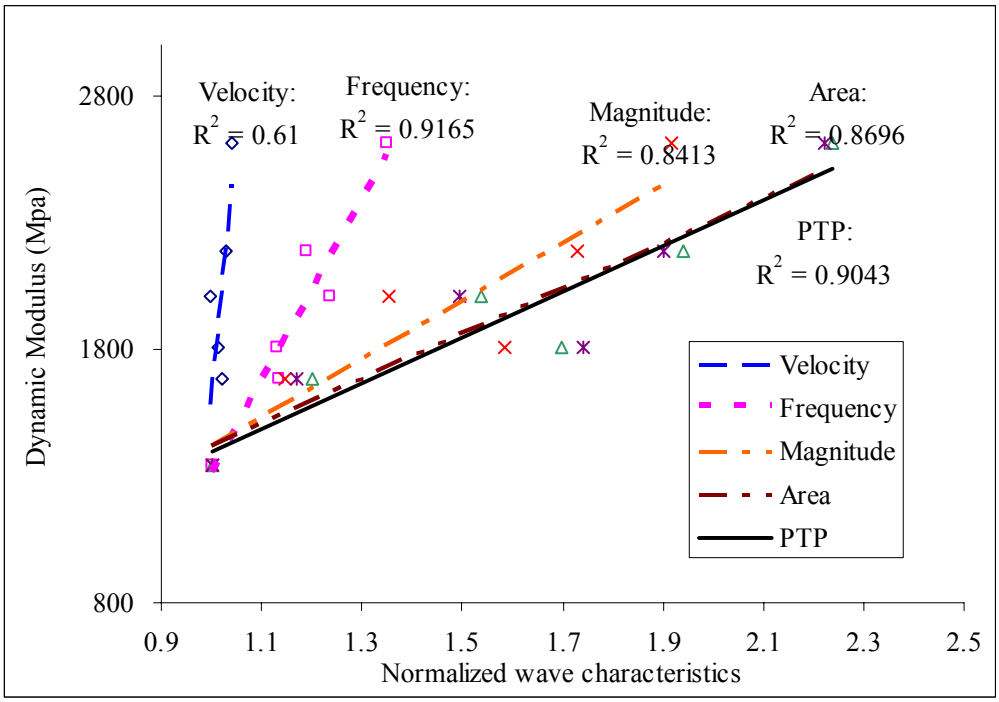

Figure B-6: Wave characteristics vs. dynamic moduli at 0.1 Hz loading frequency

Appendix C

Signals in Time and Frequency Domains for Slab 1

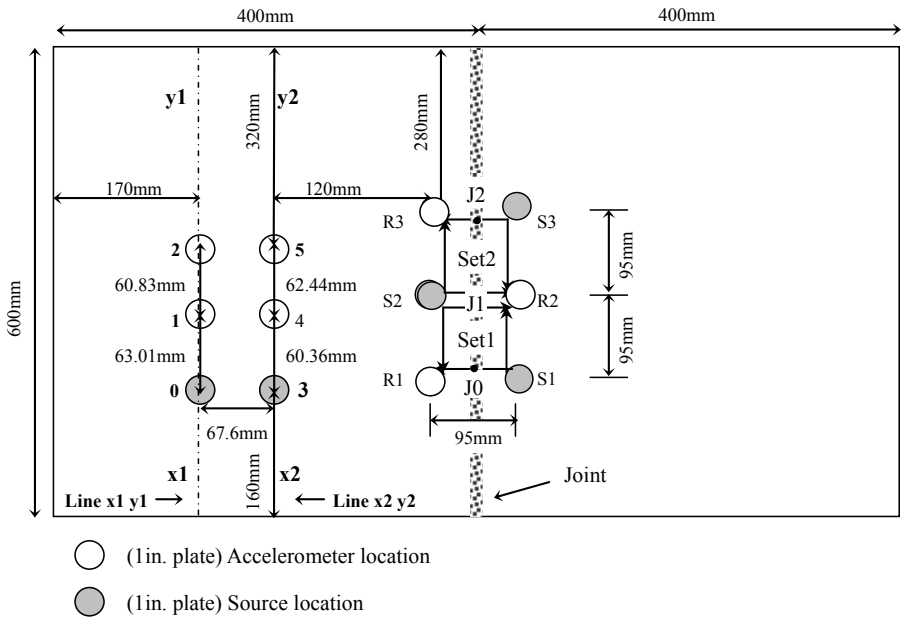

Figure C-1: Ultrasonic testing configuration of HMA slab 1

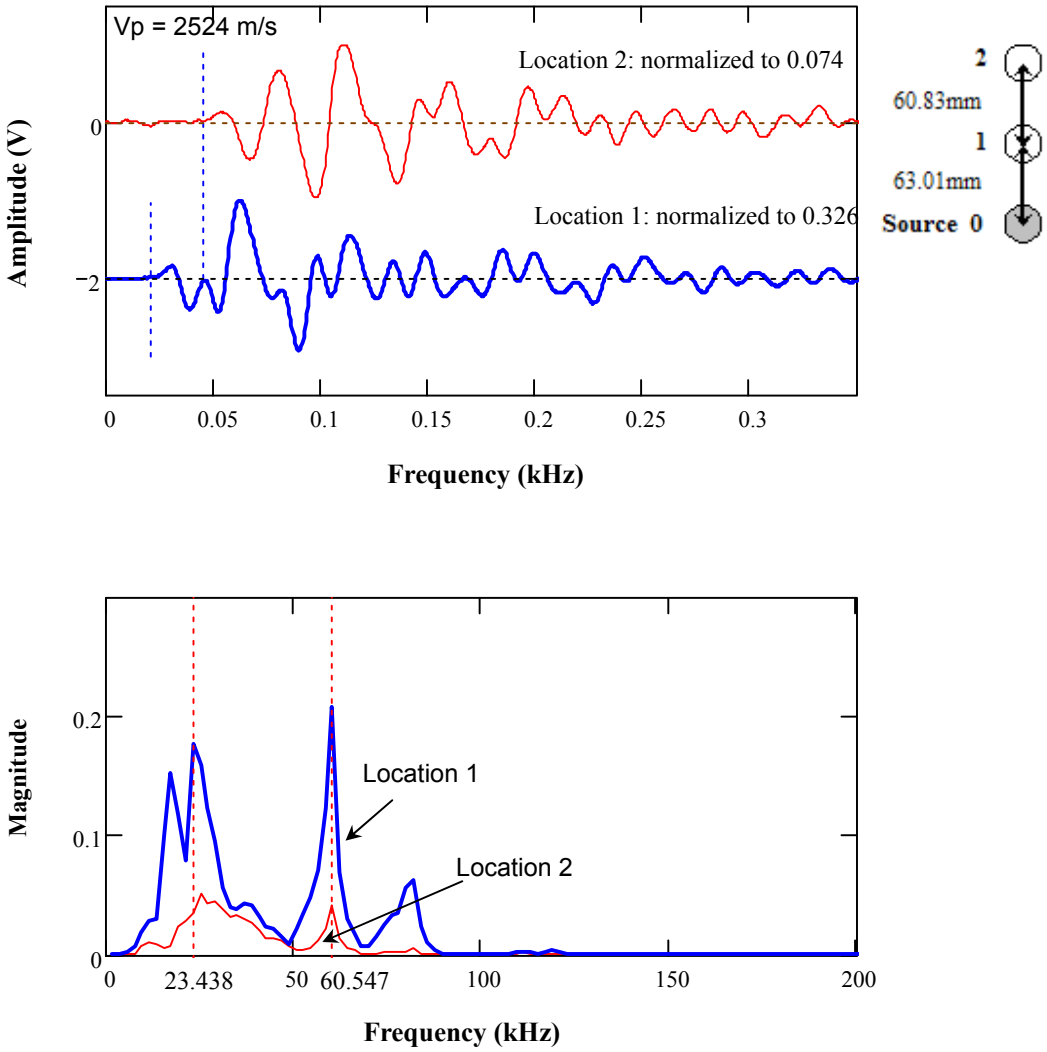

Figure C-2: Full signals in time and frequency domains received along the Line x1 y1

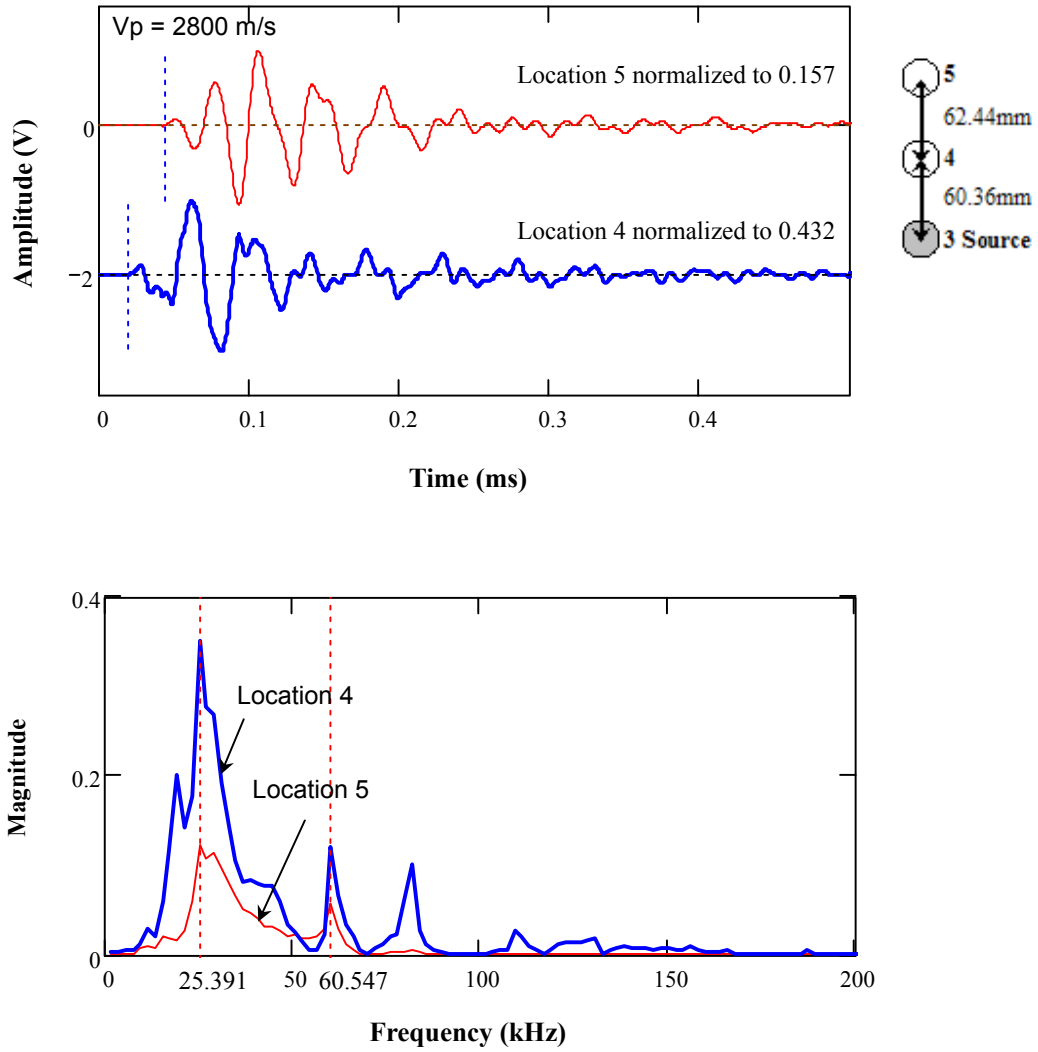

Figure C-3: Full signals in time and frequency domains received along the Line x2 y2

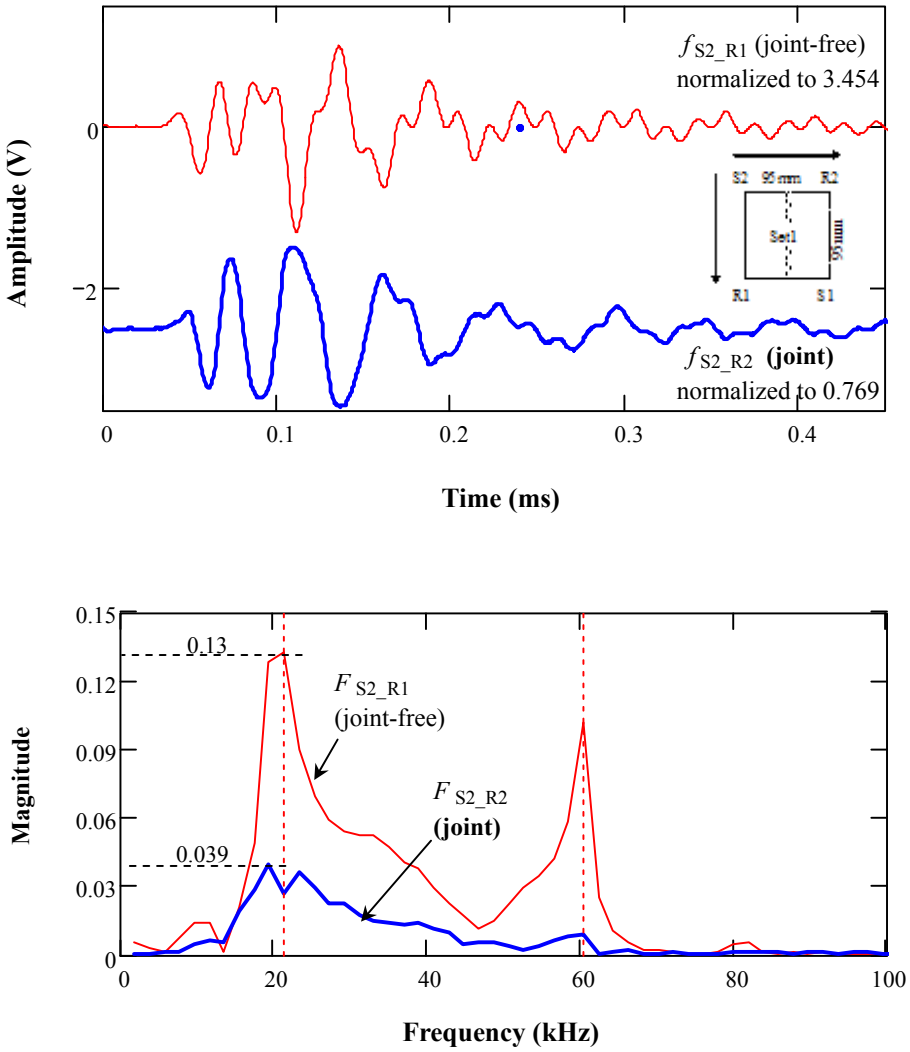

Figure C-3: A pair of signals in time and frequency domains for Set 1

(Horizontal lines mark the peak amplitudes and vertical lines dominant frequencies.)

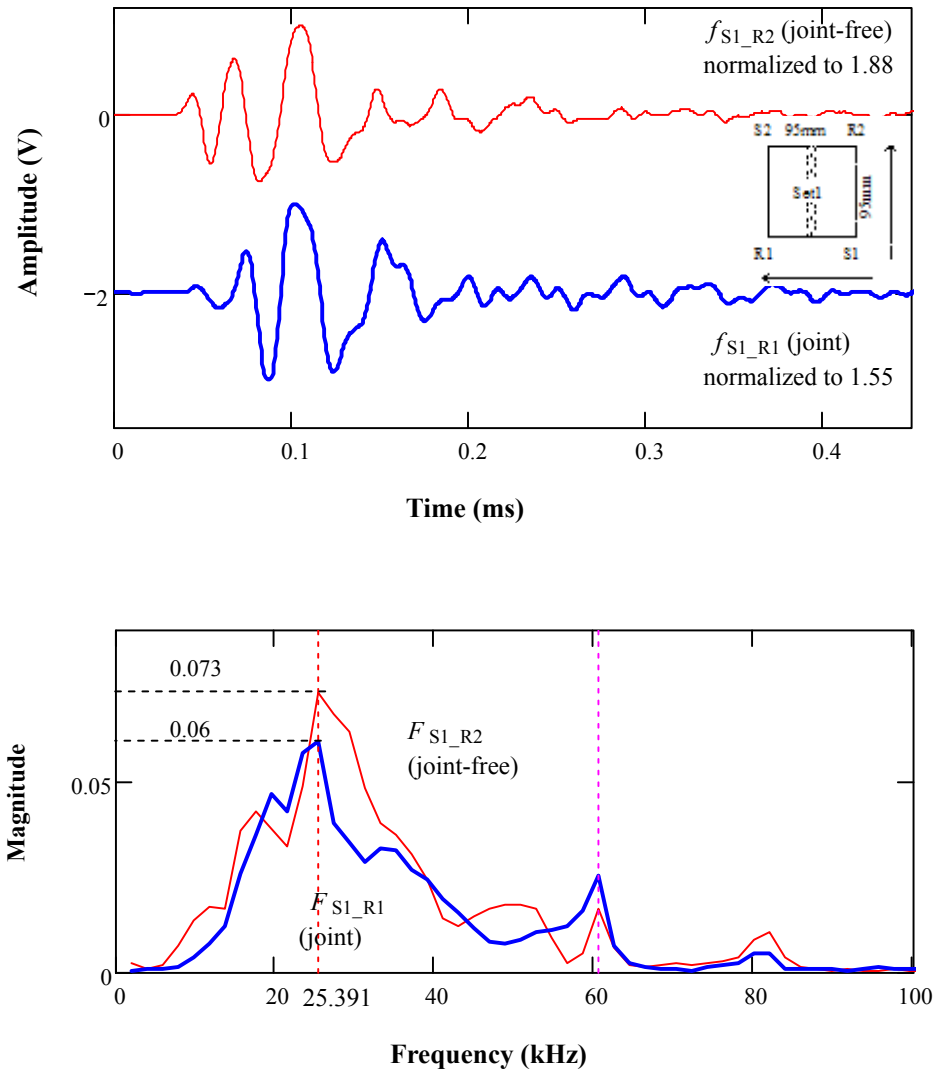

Figure C-4: A pair of signals in time and frequency domains for Set 1

(Horizontal lines mark the peak amplitudes and vertical lines dominant frequencies.)

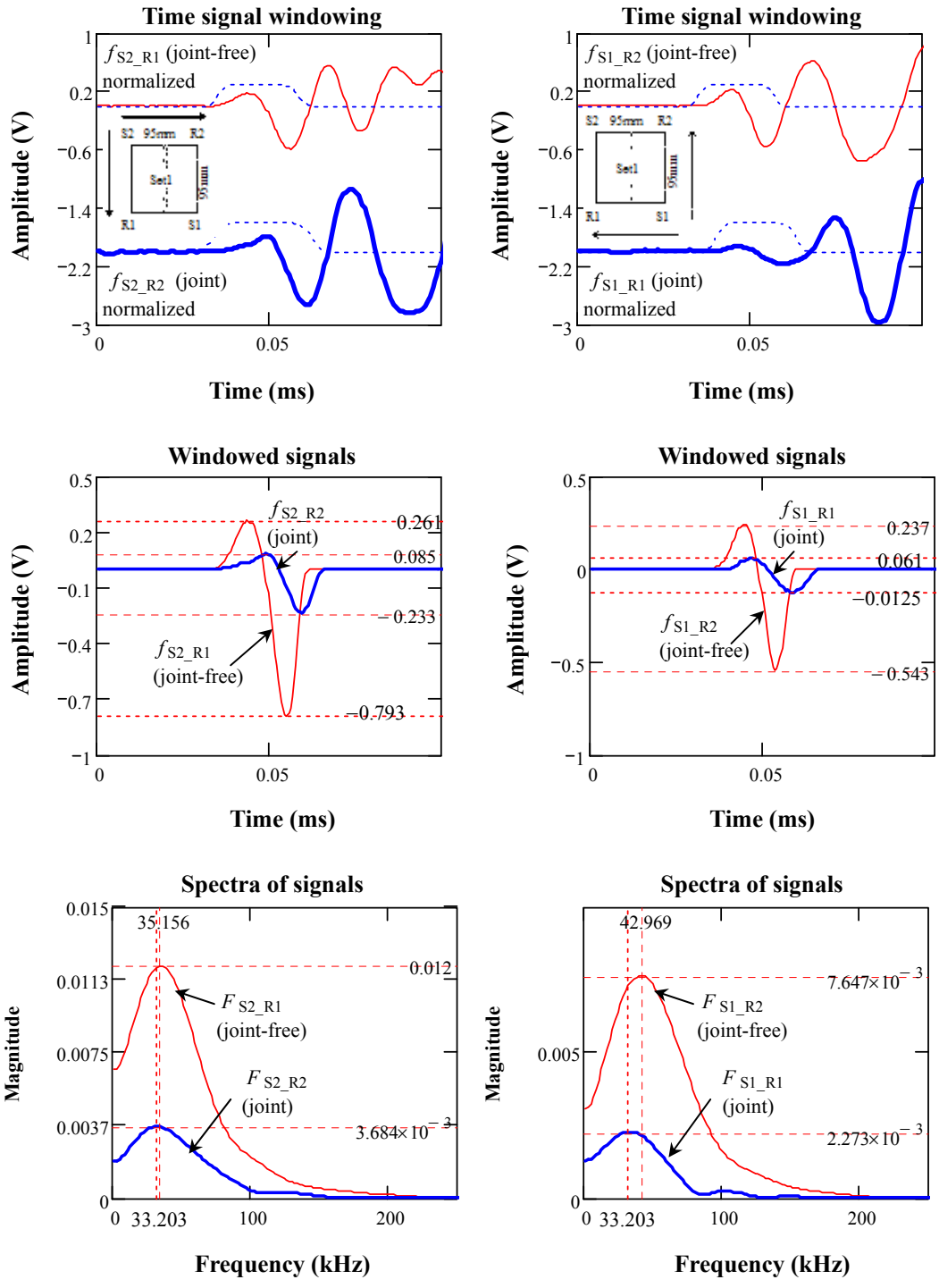

Figure C-5: P-wave analyses in time and frequency domains for Set 1

(Horizontal lines mark the peak amplitudes and vertical lines dominant frequencies.)

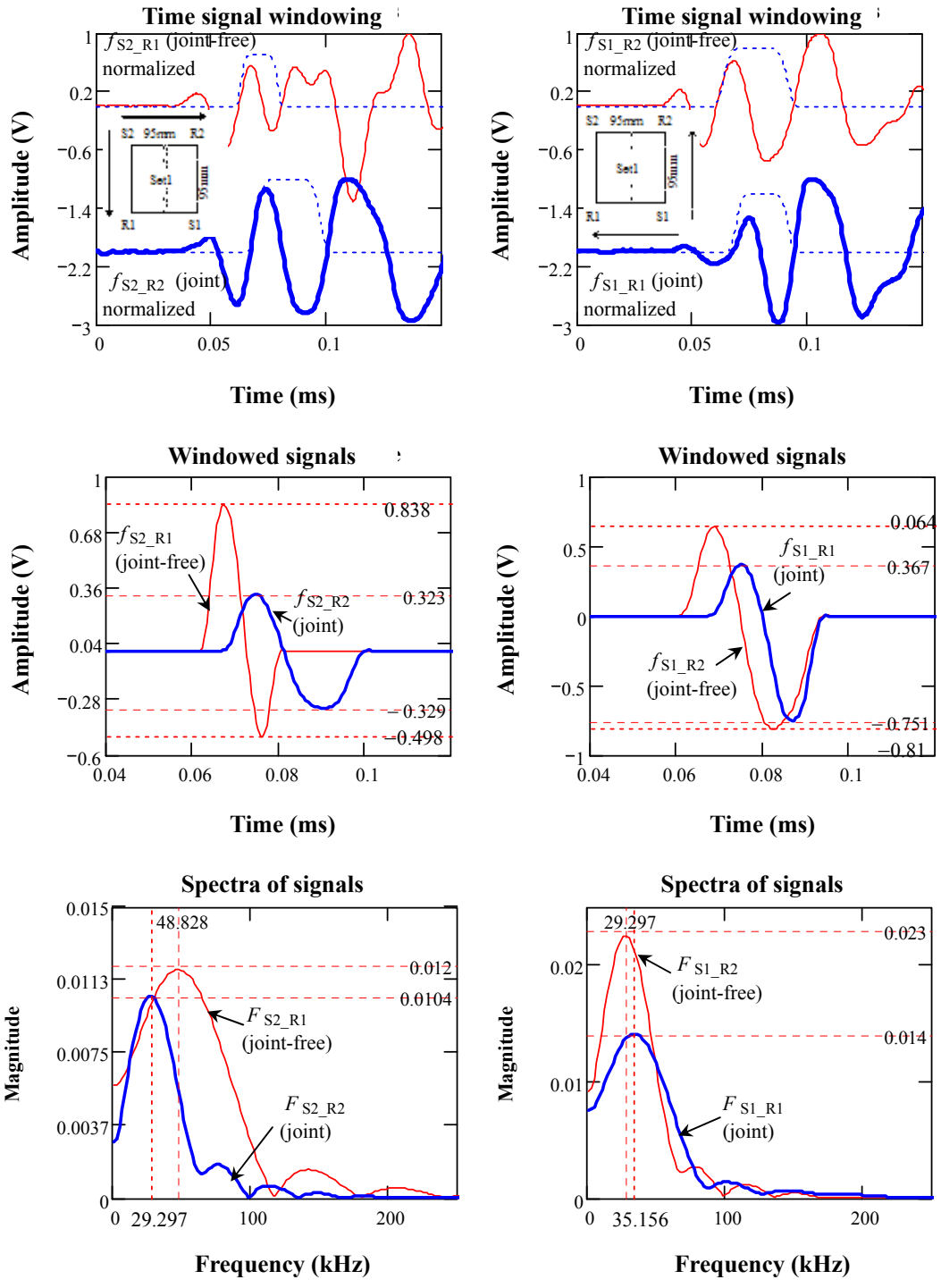

Figure C-6: R-wave analyses in time and frequency domains for Set 1

(Horizontal lines mark the peak amplitudes and vertical lines dominant frequencies.)

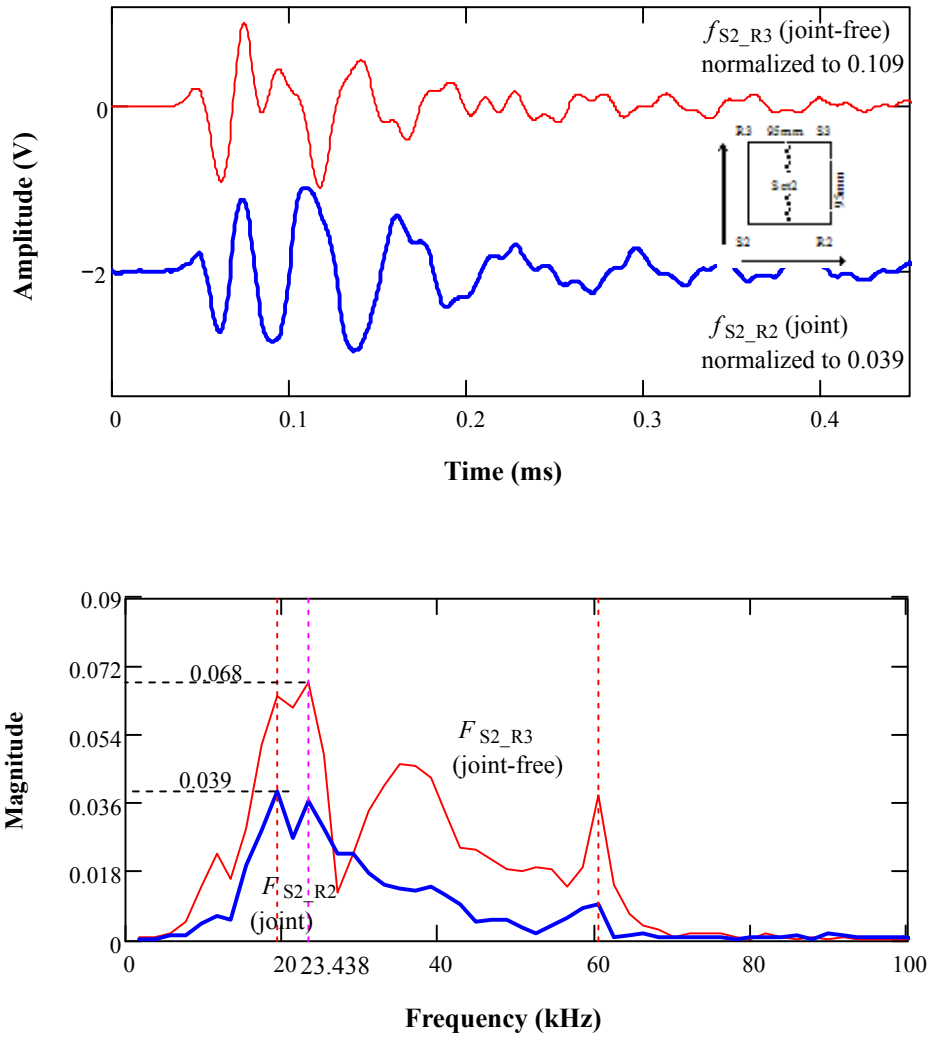

Figure C-7: A pair of signals in time and frequency domains for Set 2

(Horizontal lines mark the peak amplitudes and vertical lines dominant frequencies.)

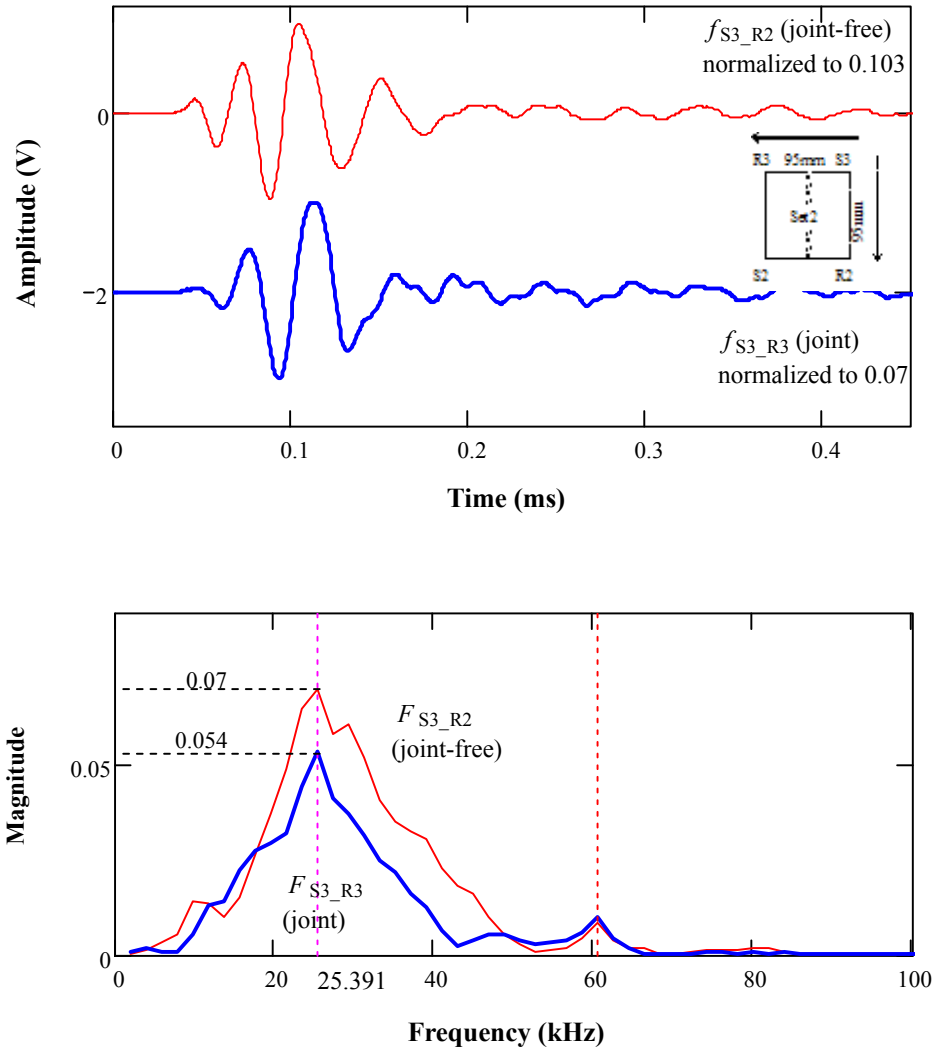

Figure C-8: A pair of signals in time and frequency domains for Set 2

(Horizontal lines mark the peak amplitudes and vertical lines dominant frequencies.)

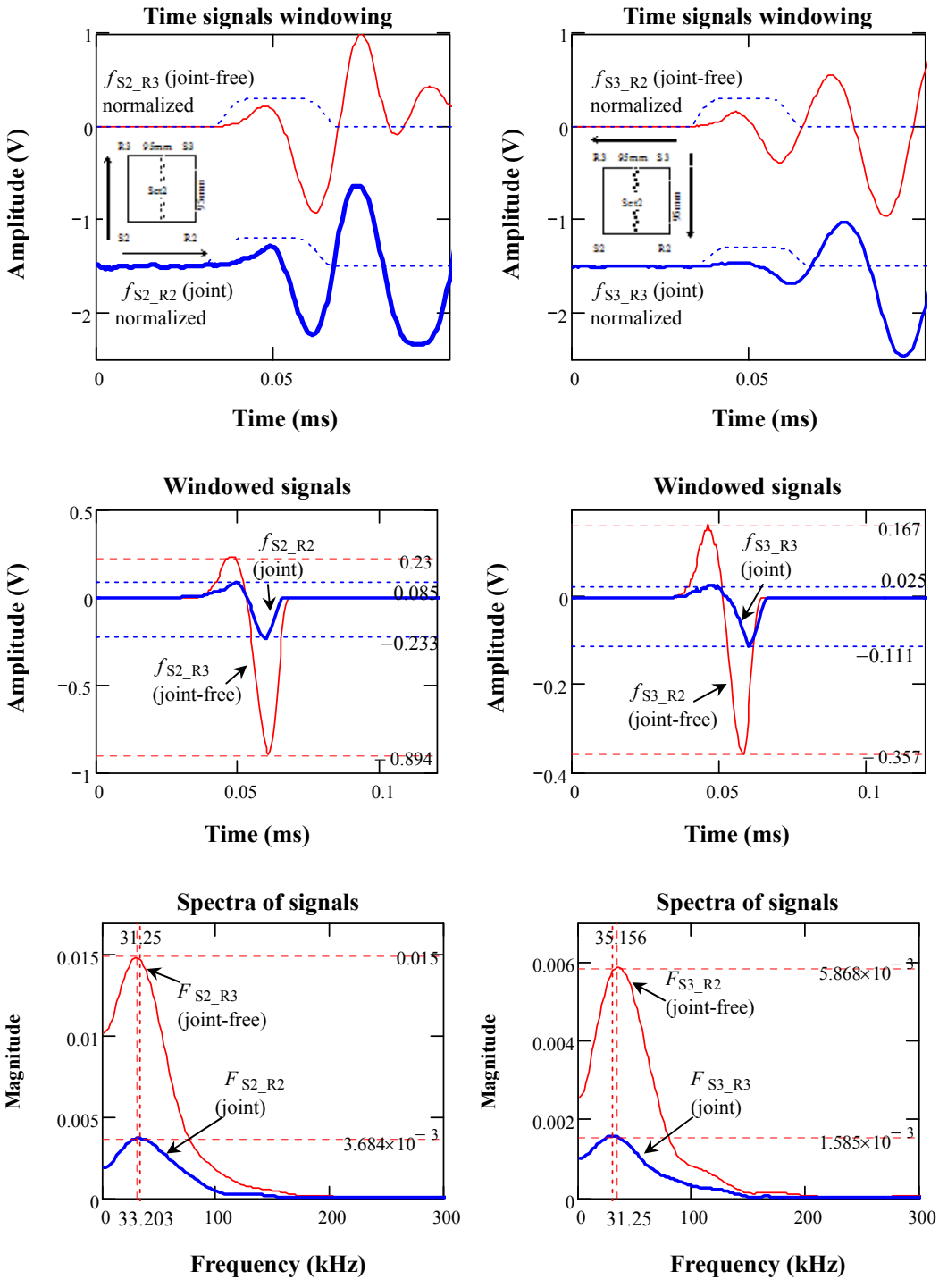

Figure C-9: P-wave analyses in time and frequency domains for Set 2

(Horizontal lines mark the peak amplitudes and vertical lines dominant frequencies.)

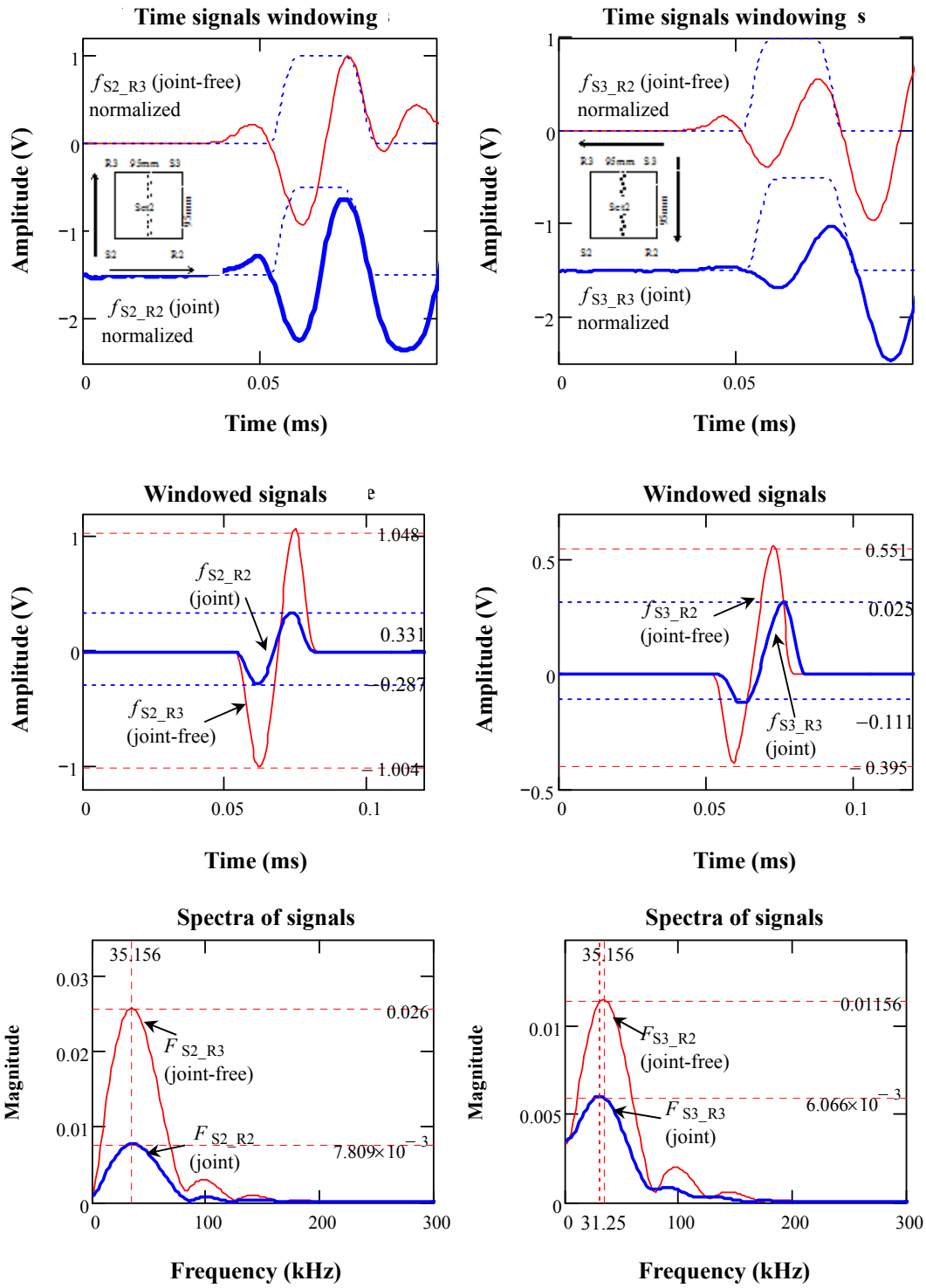

Figure C-10: R-wave analyses in time and frequency domains for Set 2

(Horizontal lines mark the peak amplitudes and vertical lines dominant frequencies.)

Appendix D

Fourier Transmission Coefficient (FTC) vs. Frequency for Slab 1

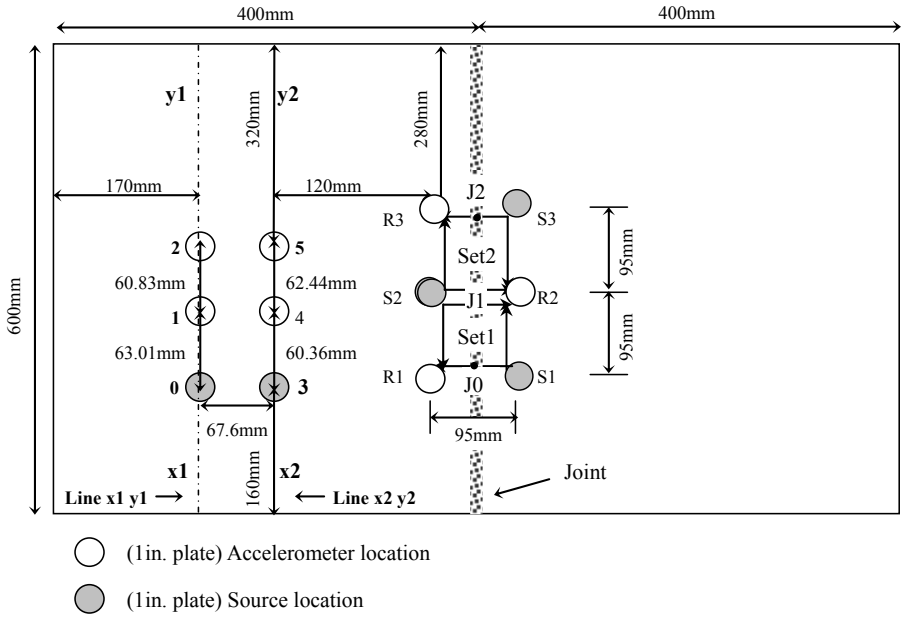

Figure D-1: Ultrasonic testing configuration of HMA slab 1

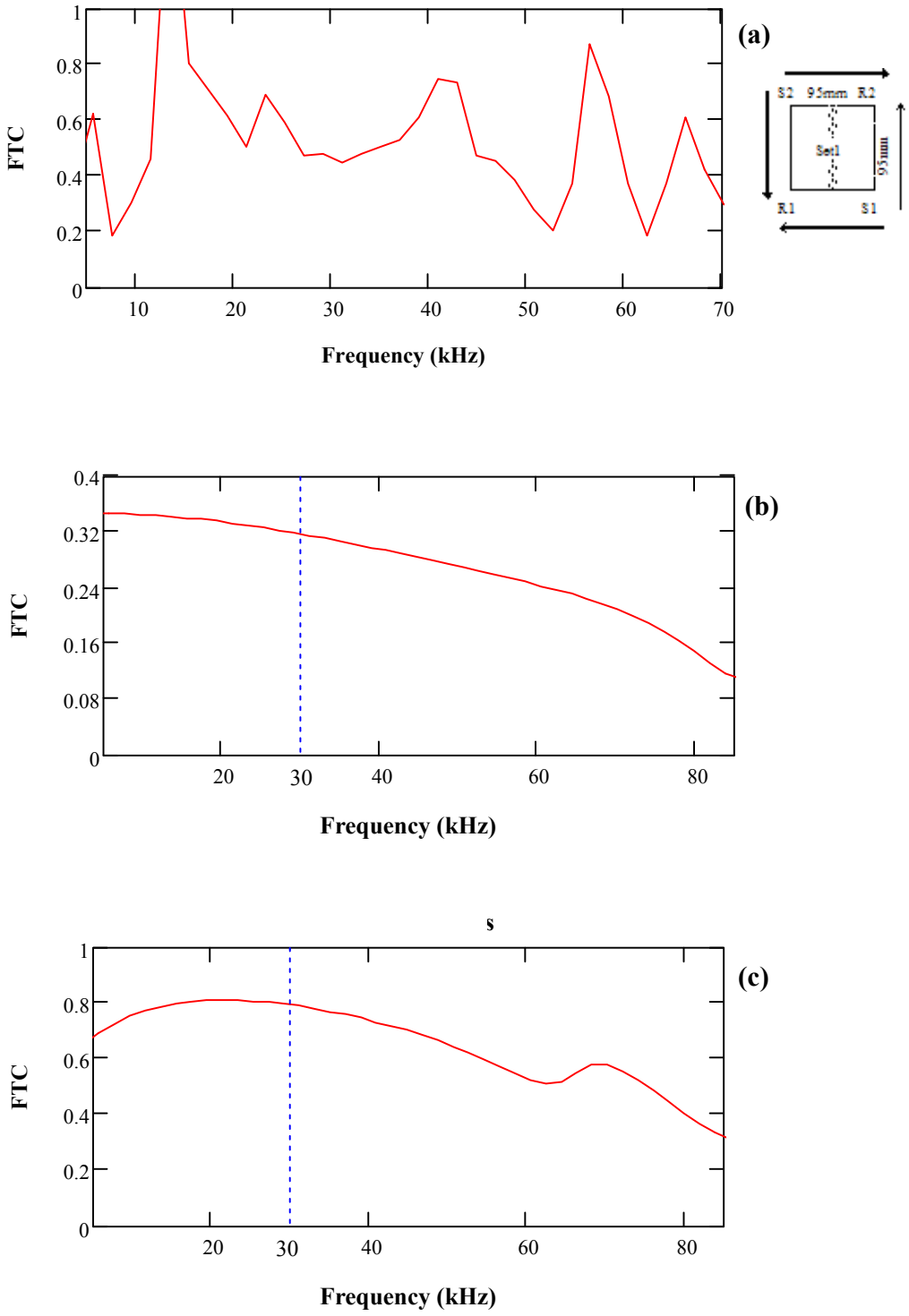

Figure D-2: FTC vs. frequency for (a) full signals, (b) P-waves and (c) R-waves for set 1

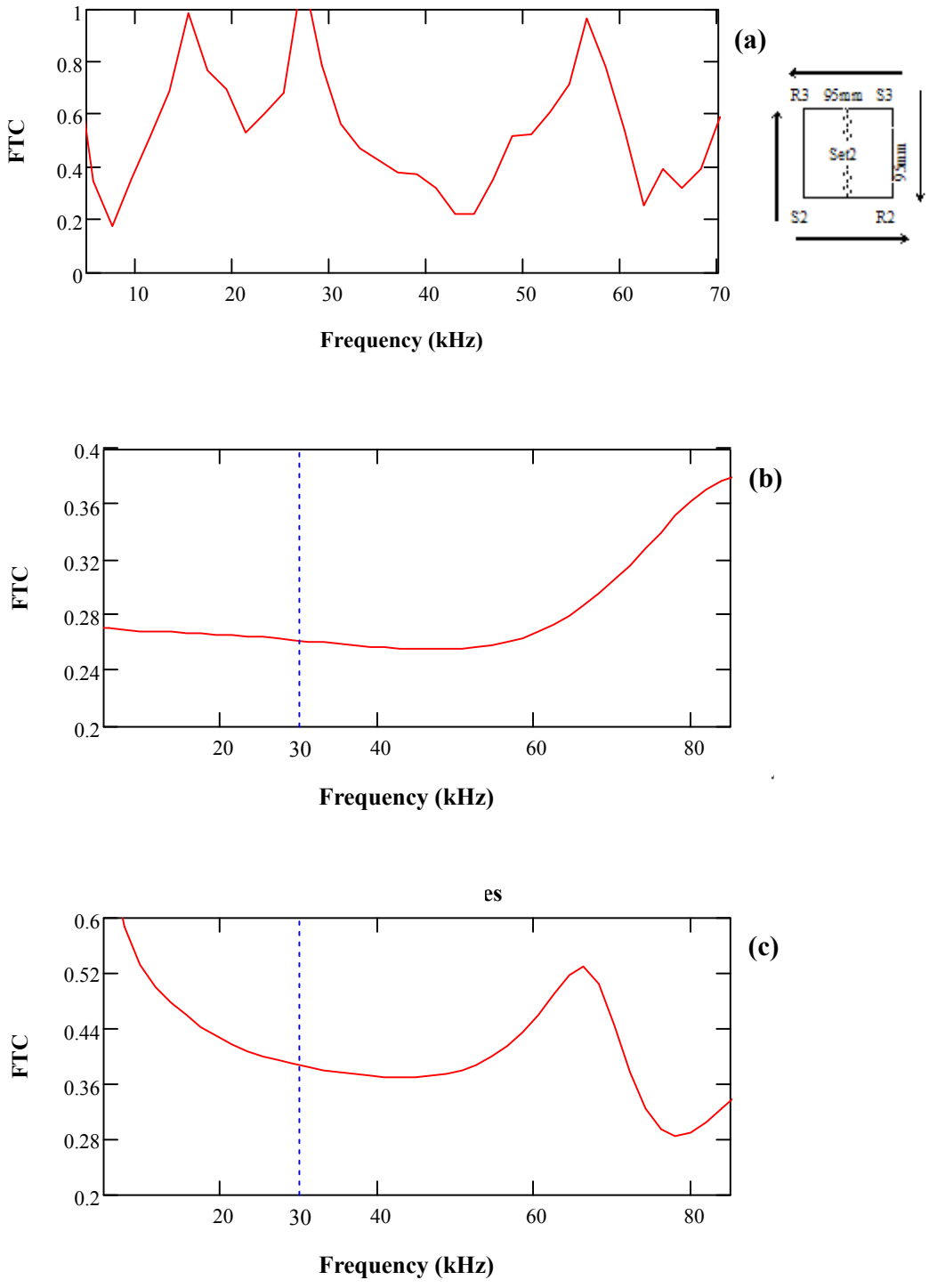

Figure D-3: FTC vs. frequency for (a) full signals, (b) P-waves and (c) R-waves for set 2

Appendix E

Wavelet Transform Using Morlet Wavelet for Slab 1 - Measurements on the Jointed Surface

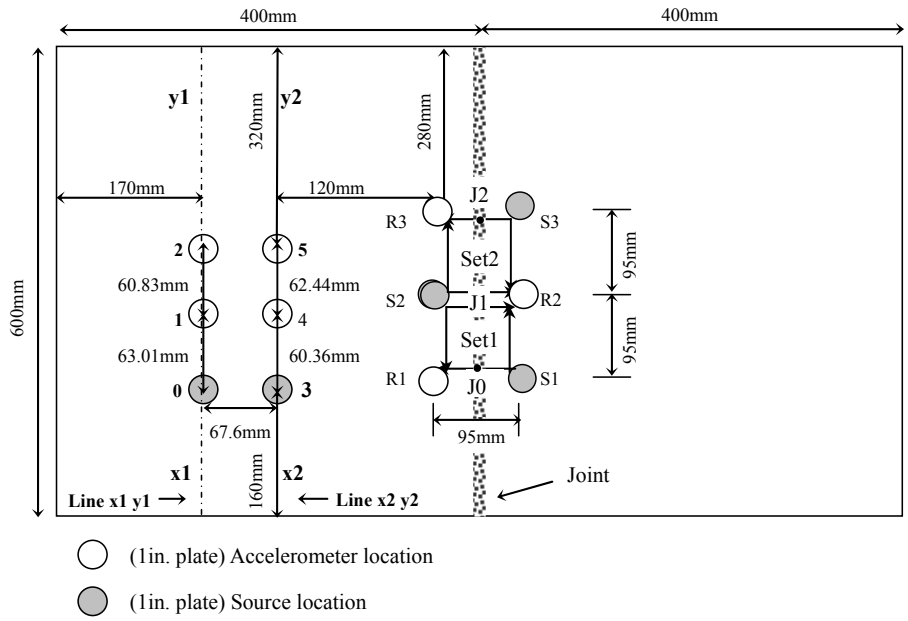

Figure E-1: Ultrasonic testing configuration of HMA slab 1

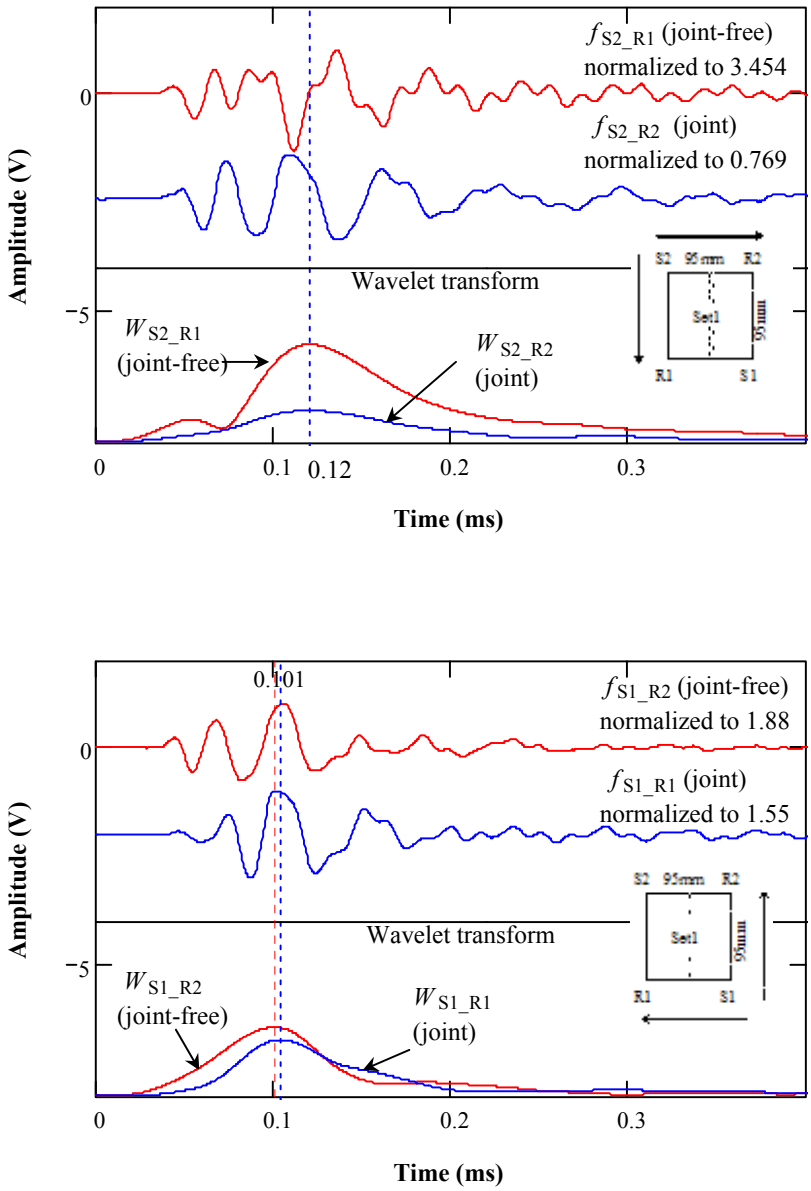

Figure E-2: Wavelet transform of set 1 measurements using Morlet wavelet at the dominant frequencies of full signals (Morlet center frequency of 21.484 kHz for f_{S2_R1}; 19.531 kHz for f_{S2_R2}; and 25.445 kHz for both f_{S1_R2} and f_{S1_R1})

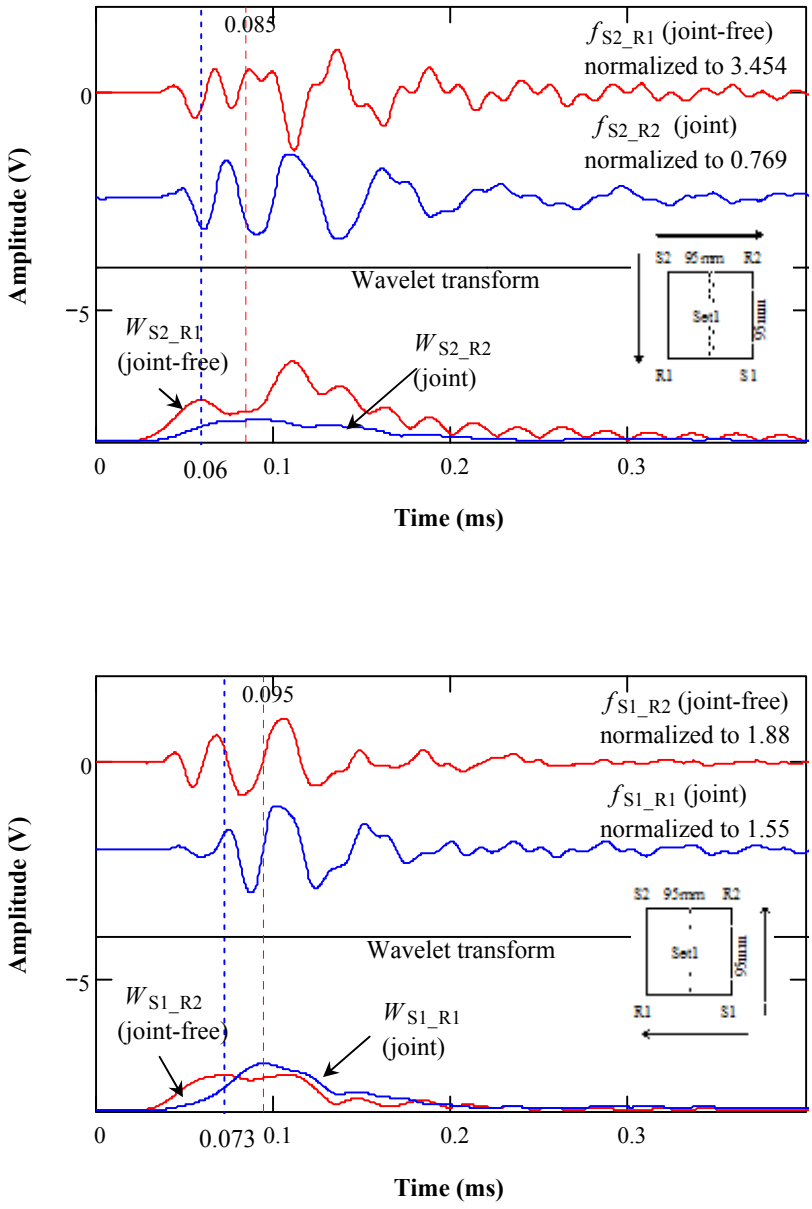

Figure E-3: Wavelet transform of set 1 measurements using Morlet wavelet at dominant frequencies of P-waves (Morlet center frequency of 35.156 kHz for f_{S2_R1}; 33.203 kHz for f_{S2_R2}; 42.969 kHz for f_{S1_R2}; and 22.203 kHz for f_{S1_R1})

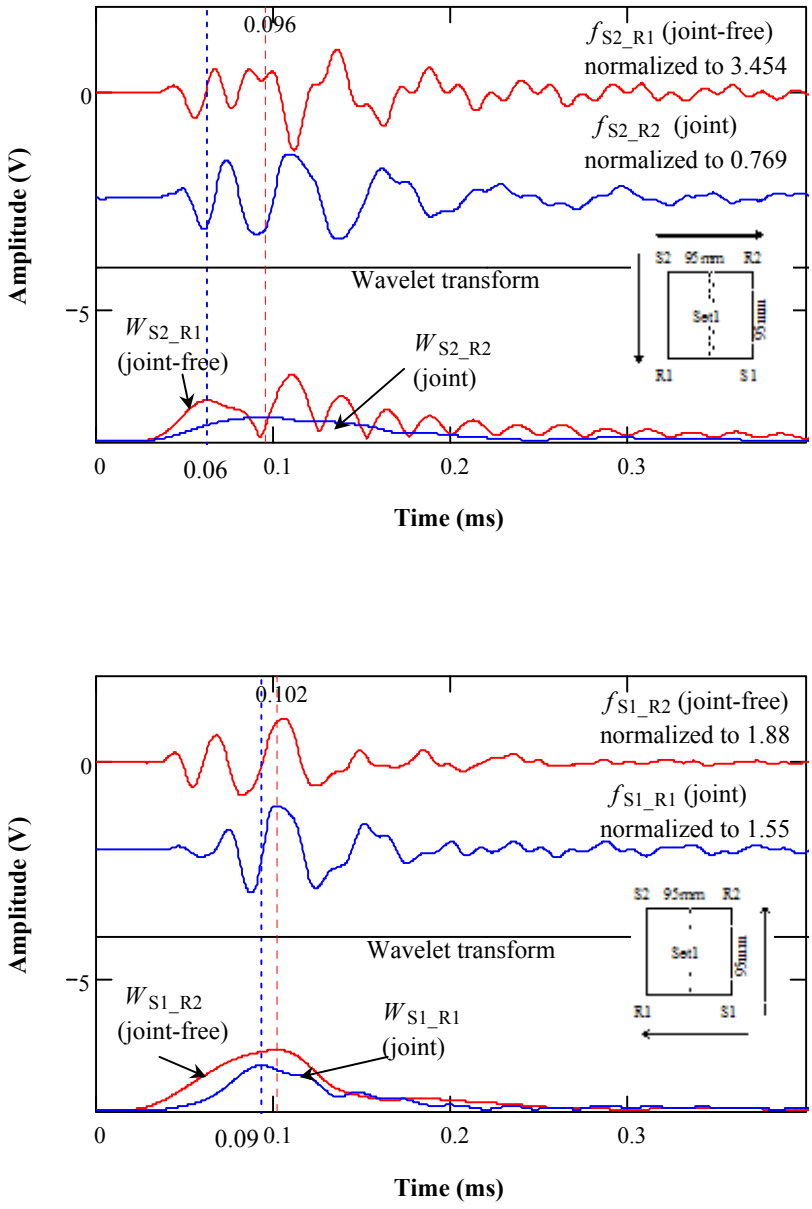

Figure E-4: Wavelet transform of set 1 measurements using Morlet wavelet at the dominant frequencies of R-waves (Morlet center frequency of 48.828 kHz for f_{S2_R1}; 29.297 kHz for f_{S2_R2}; 29.297 kHz for f_{S1_R2}; and 35.156 kHz for f_{S1_R1}).

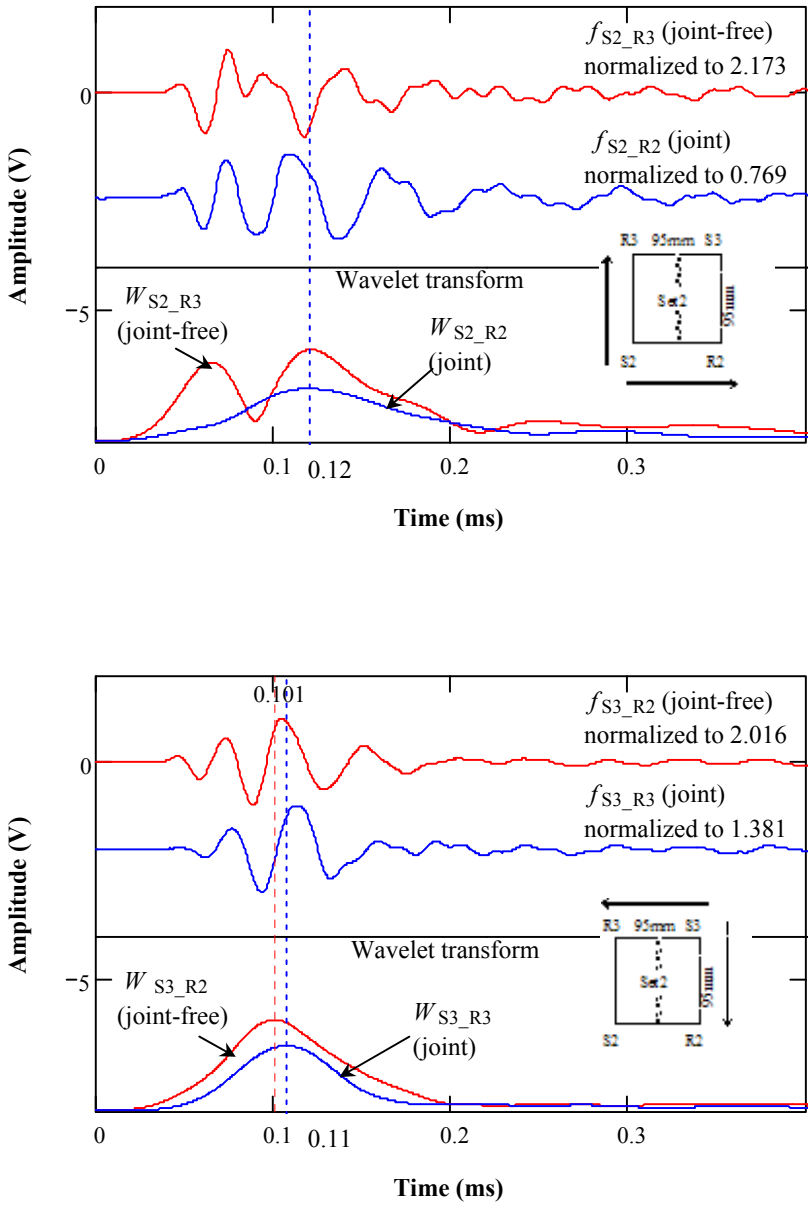

Figure E-5: Wavelet transform of set 2 measurements using Morlet wavelet at dominant frequencies of full signals (Morlet center frequency of 23.438 kHz for f_{S2_R3}; 19.531 kHz for f_{S2_R2}; and 25.391 kHz for both f_{S3_R2} and f_{S3_R3})

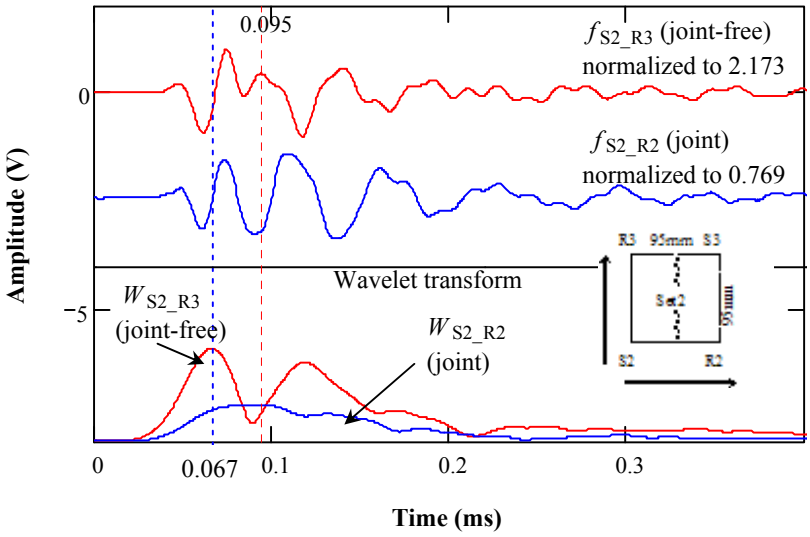

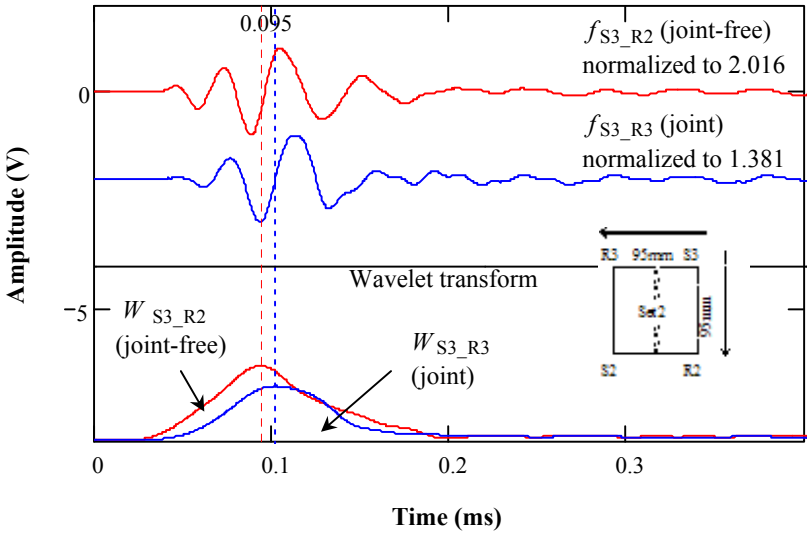

Figure E-6: Wavelet transform of pair 2 of signals from set 1 using Morlet wavelet (Morlet center frequency of 31.25 kHz for f_{S2_R3}; and 33.203 kHz for f_{S2_R2}; 35.156 kHz for f_{S3_R2}; and 31.25 kHz for f_{S3_R3})

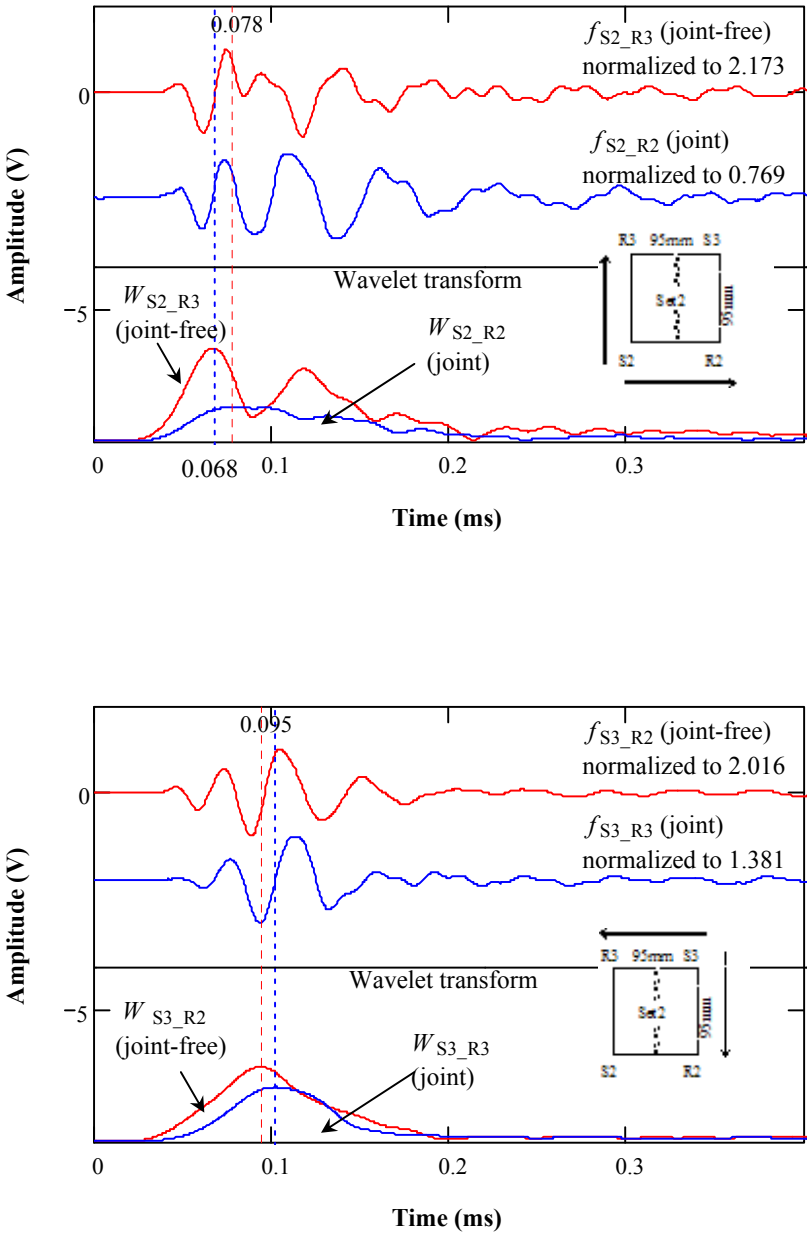

Figure E-7: Wavelet transform of set 2 measurements using Morlet wavelet at the dominant frequencies of R-waves (Morlet center frequency of 35.156 kHz for both f_{S2_R3} and f_{S2_R2}; 35.156 kHz for f_{S3_R2}; and 31.25 kHz for f_{S3_R3})

Appendix F
Wavelet Transform of Signals
Using Mallat's Algorithm for Slab 1

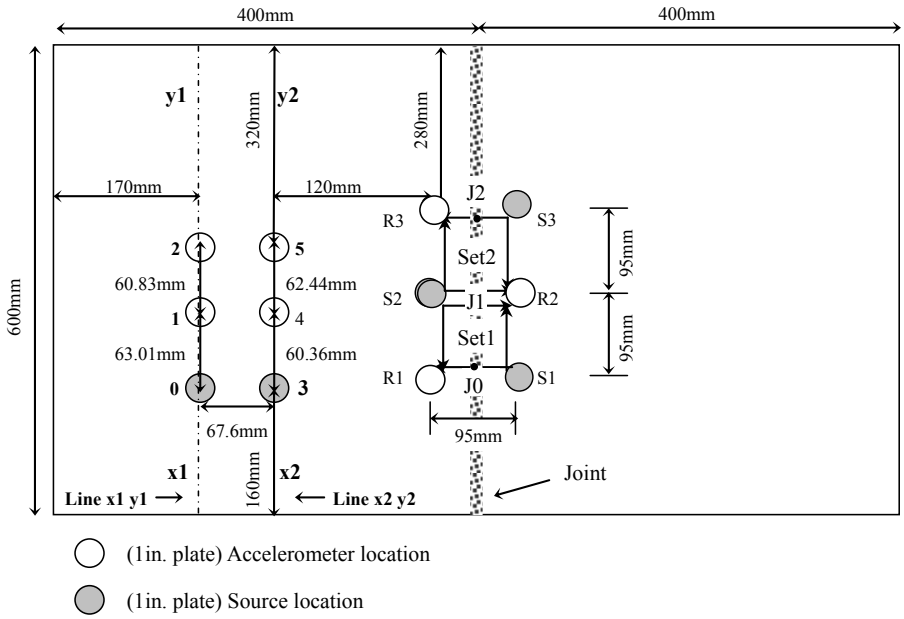

Figure F-1: Ultrasonic testing configuration of HMA slab 1

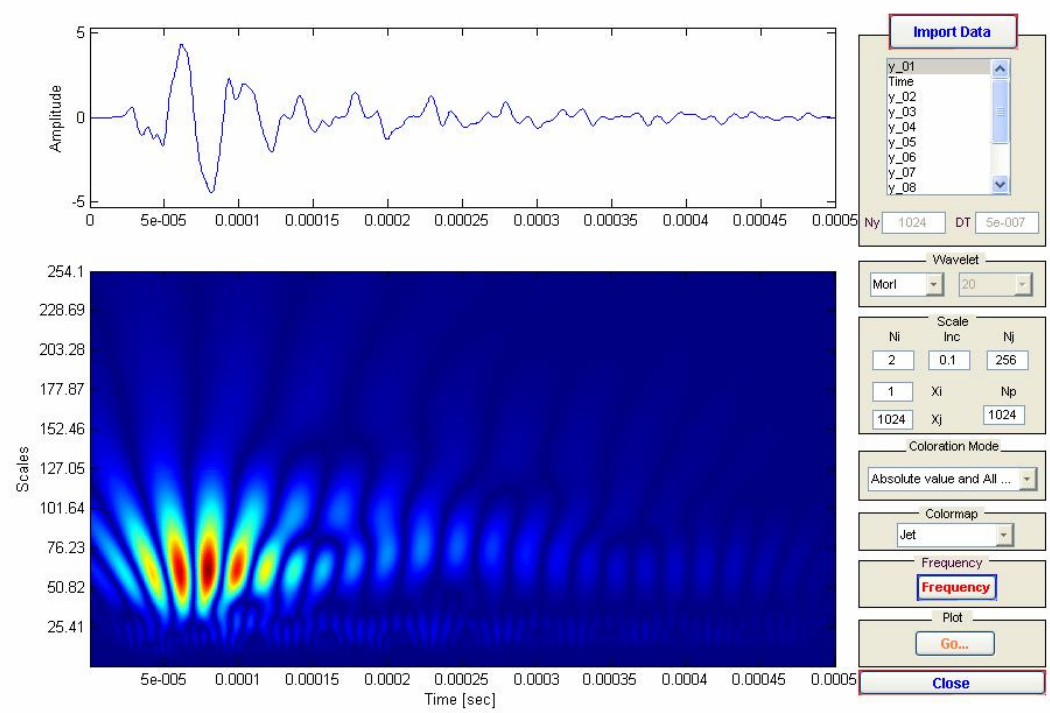

Figure F-2: Wavelet transform of signal at location 1 in Line x1 y using Mallat's algorithm

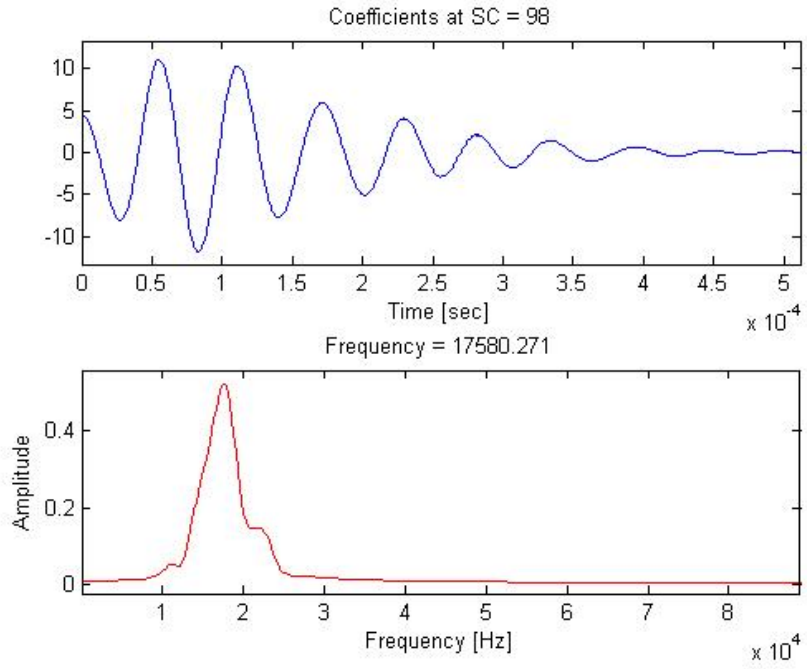

Figure F-3: Frequency content at a given scale from Figure F-2

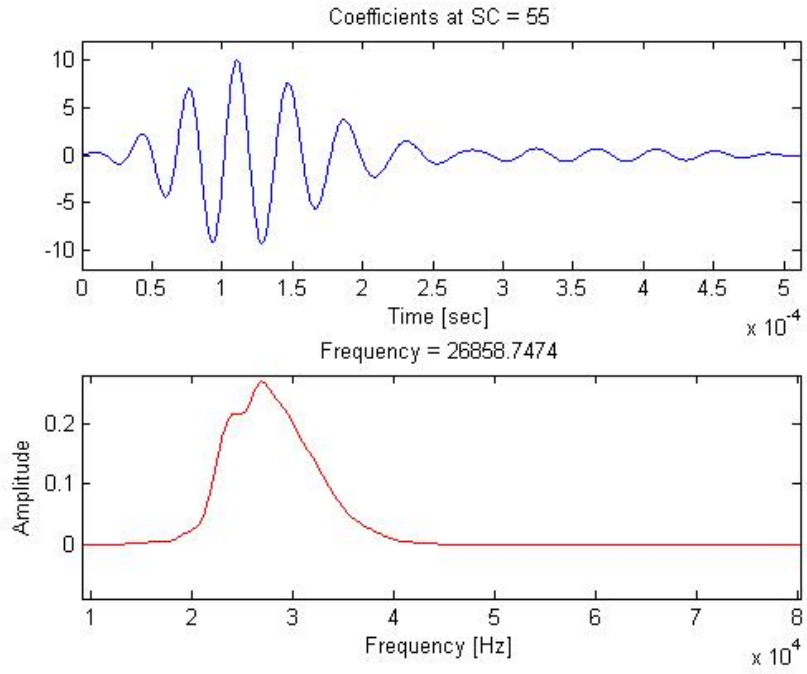

Figure F-4: Frequency content at a given scale from Figure F-2

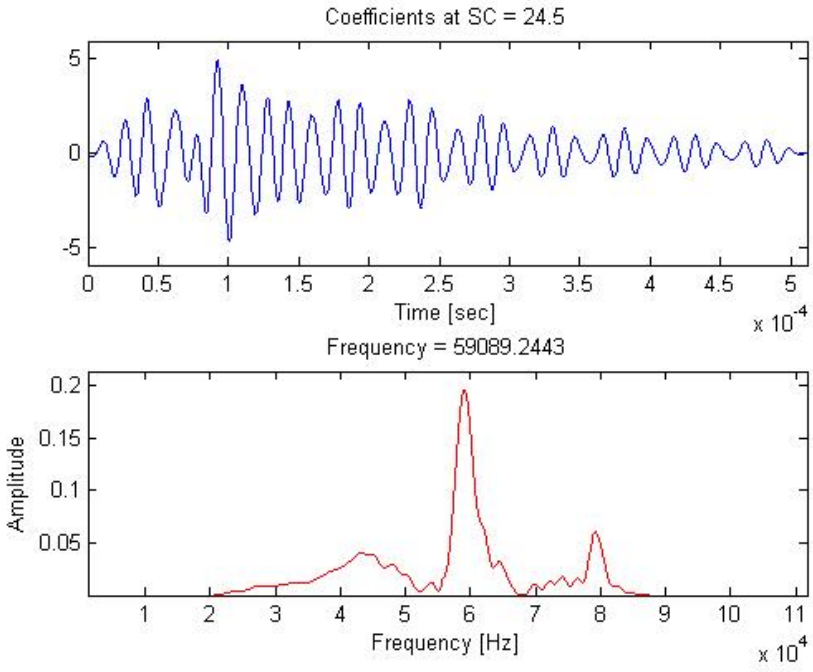

Figure F-5: Frequency content at a given scale from Figure F-2

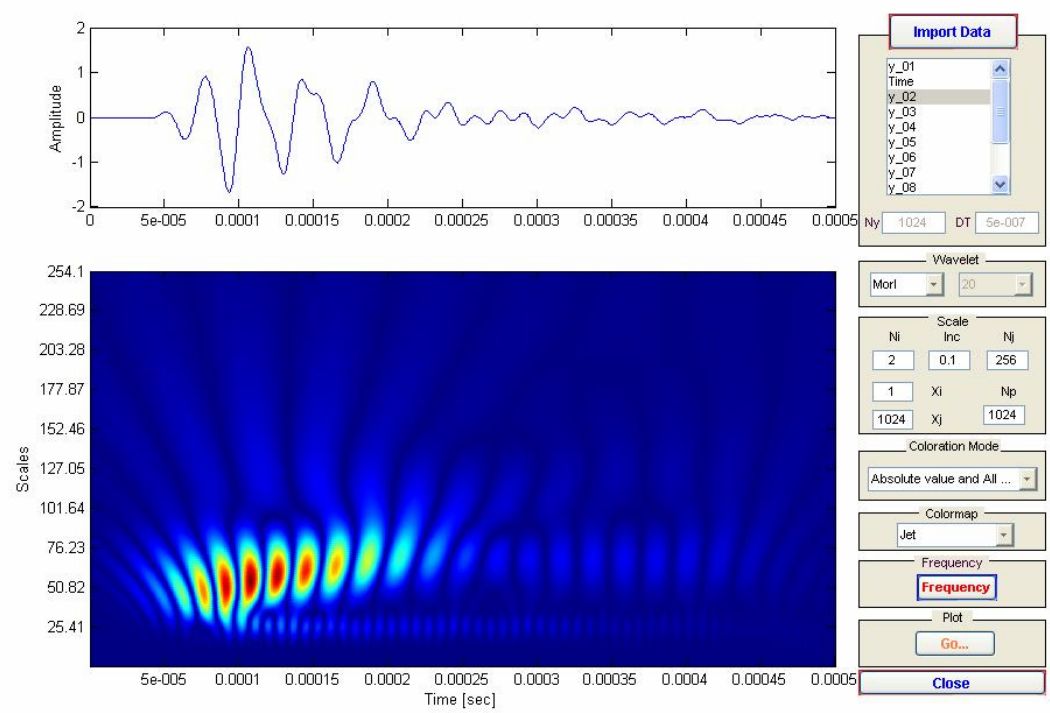

Figure F-6: Wavelet transform of signal at location 2 in Line x1 y using Mallat's algorithm

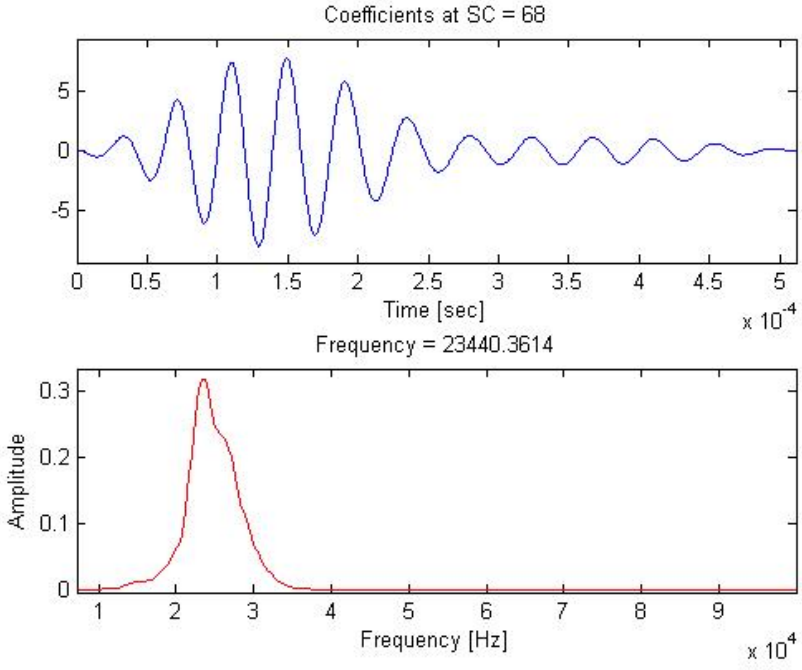

Figure F-7: Frequency content at a given scale from Figure F-6

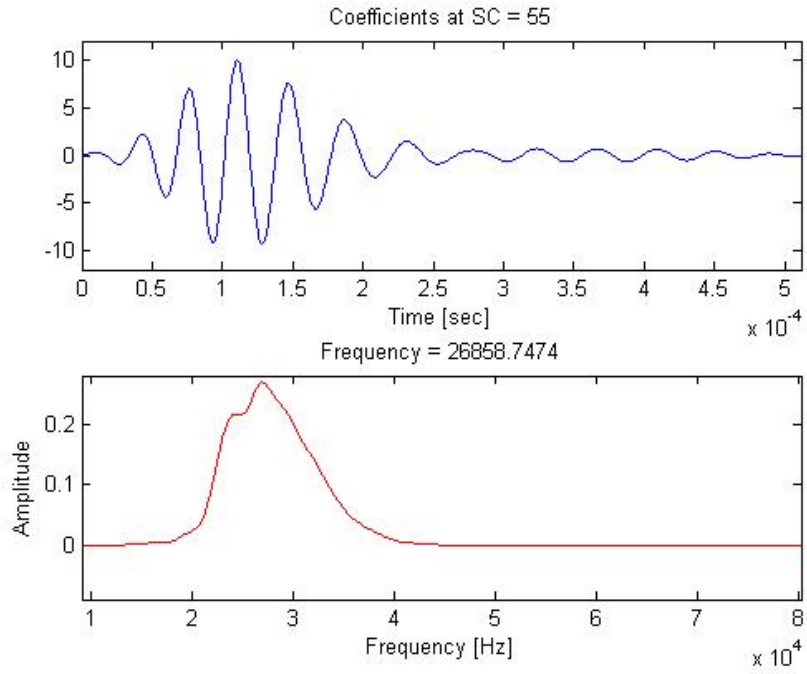

Figure F-8: Frequency content at a given scale from Figure F-6

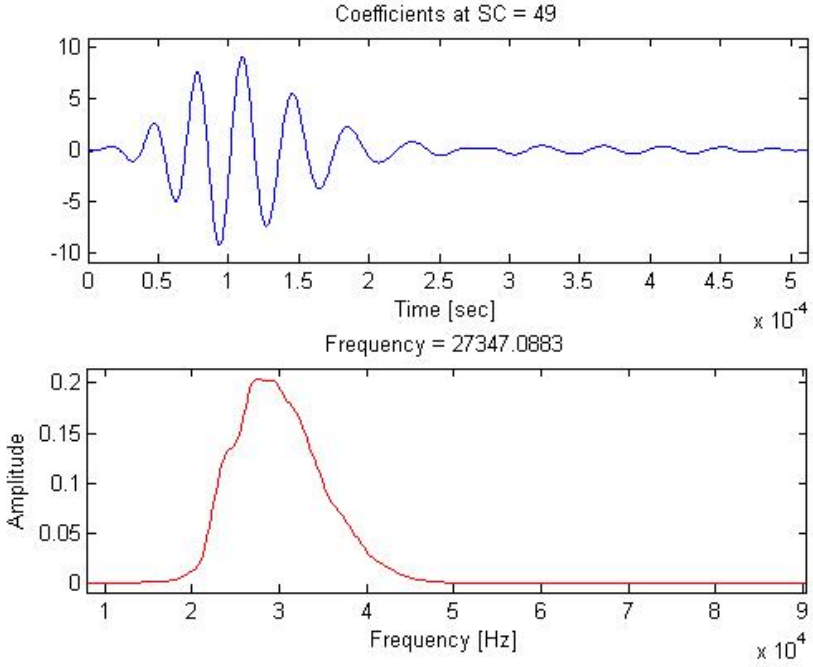

Figure F-9: Frequency content at a given scale from Figure F-6

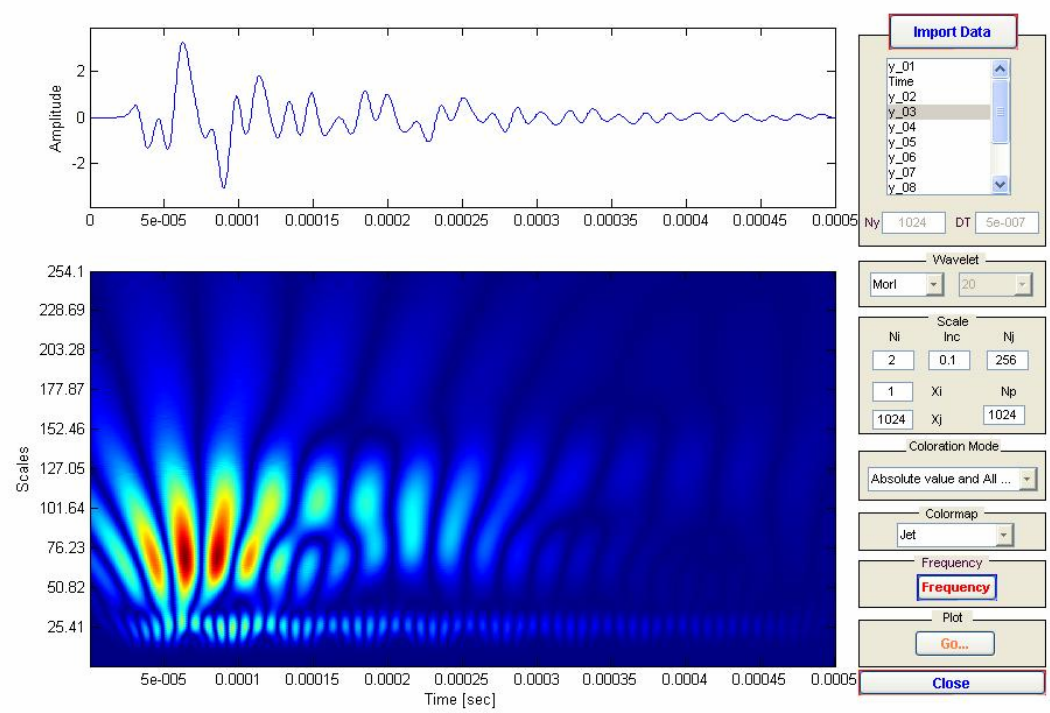

Figure F-10: Wavelet transform of signal at location 3 in Line x1 y using Mallat's algorithm

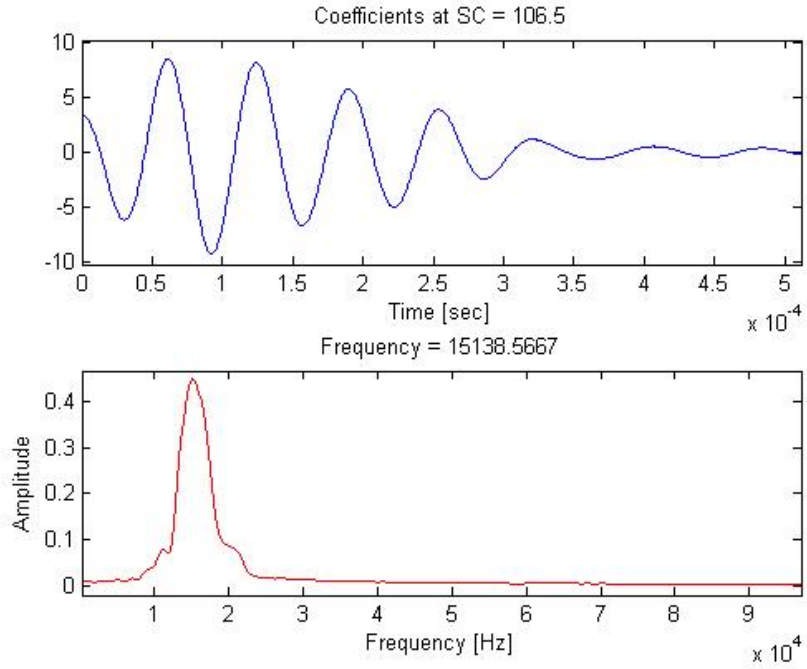

Figure F-11: Frequency content at a given scale from Figure F-10

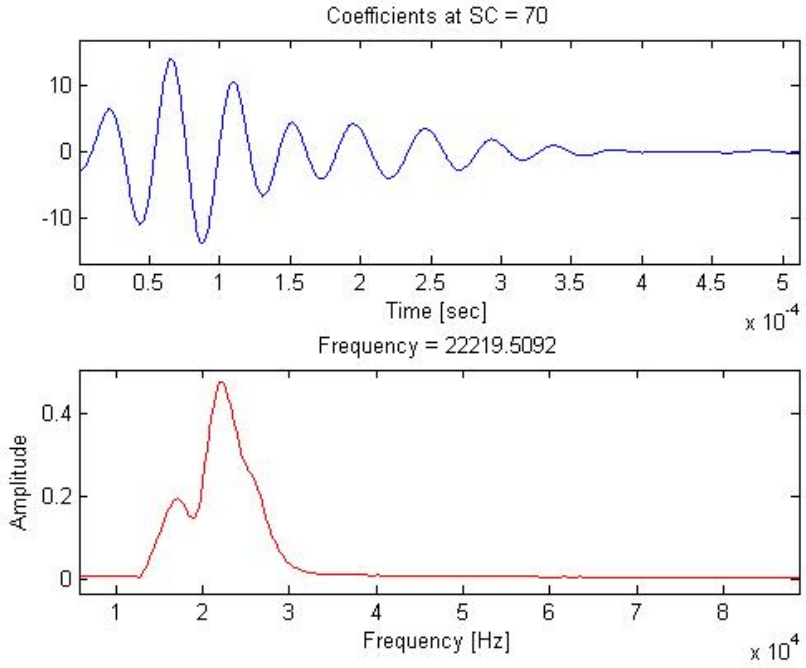

Figure F-12: Frequency content at a given scale from Figure F-10

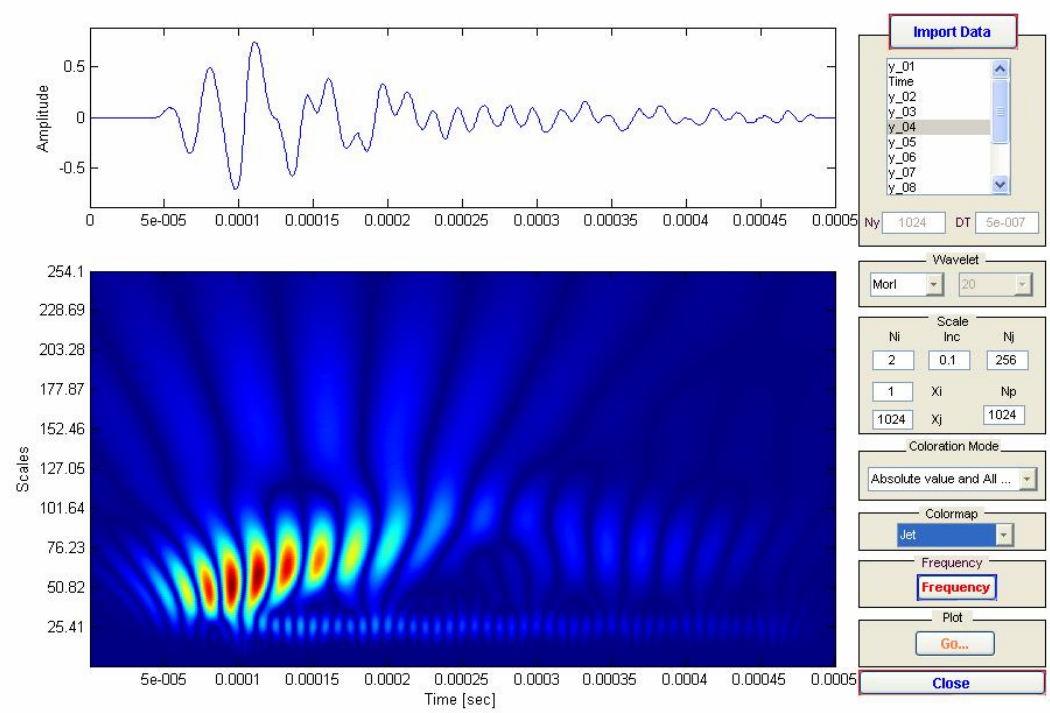

Figure F-13: Wavelet transform of signal at location 4 in Line x1 y using Mallat's algorithm

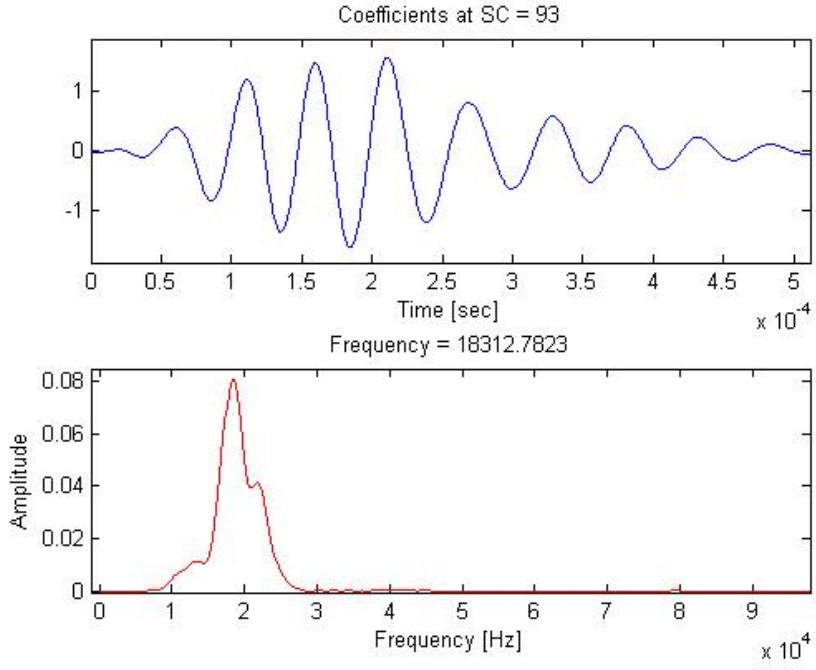

Figure F-14: Frequency content at a given scale from Figure F-13

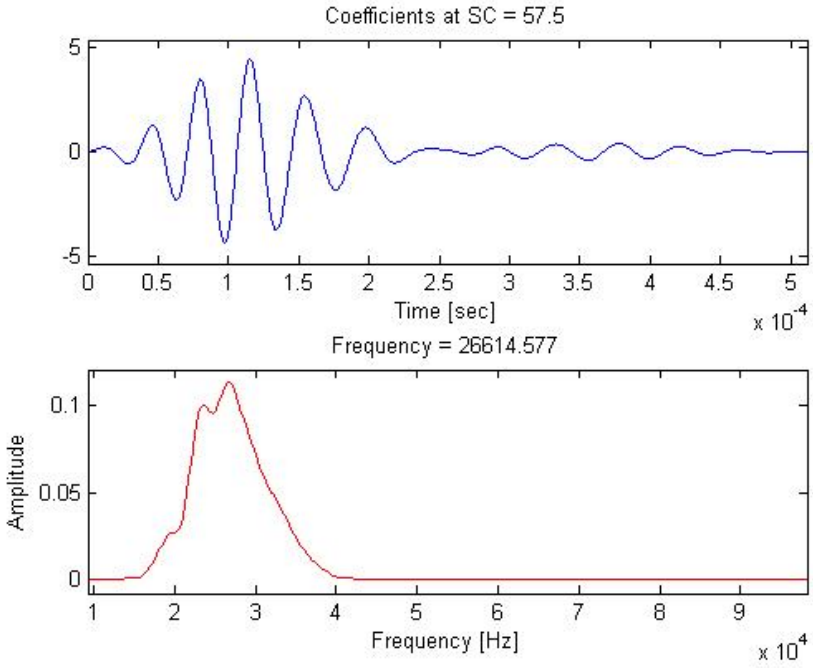

Figure F-15: Frequency content at a given scale from Figure F-10

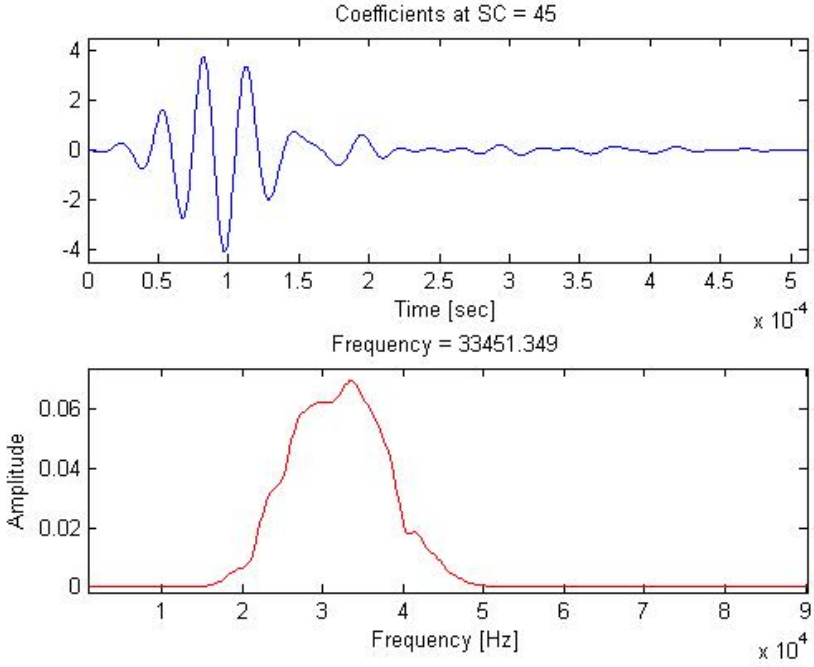

Figure F-16: Frequency content at a given scale from Figure F-10

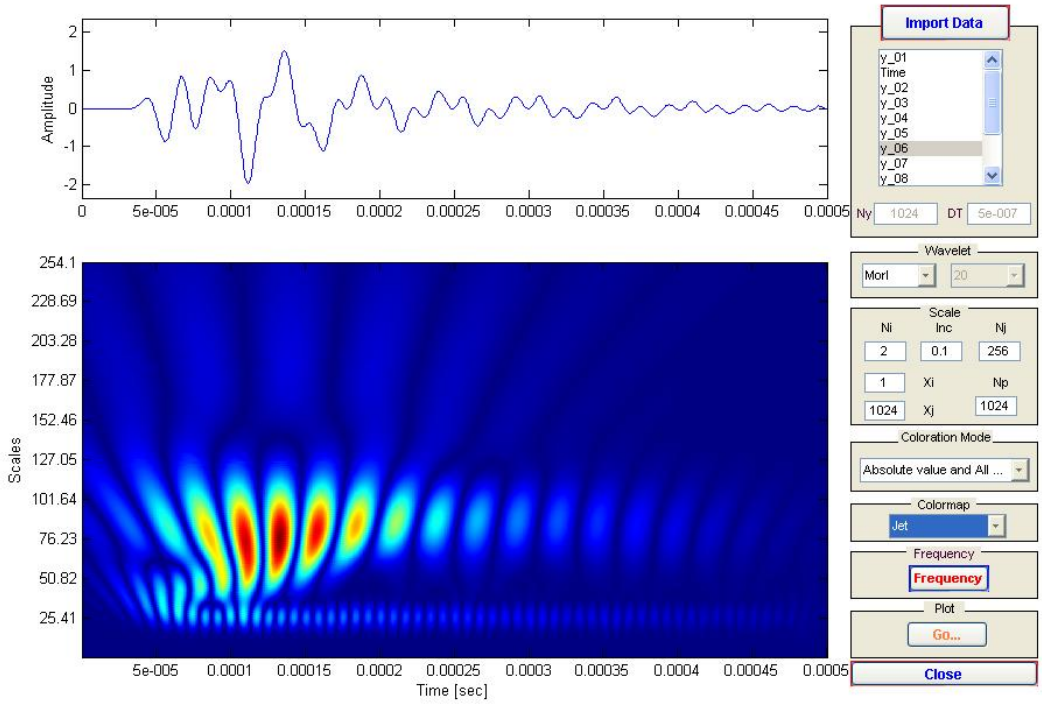

Figure F-17: Wavelet transform of signal f_{S2_R1} through the joint-free surface using Mallat's algorithm

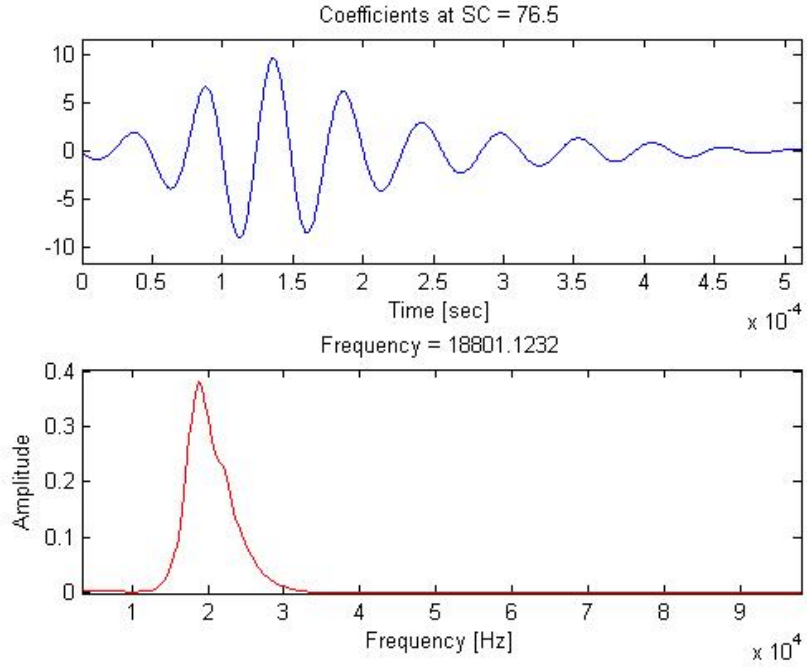

Figure F-18: Frequency content at a given scale from Figure F-16

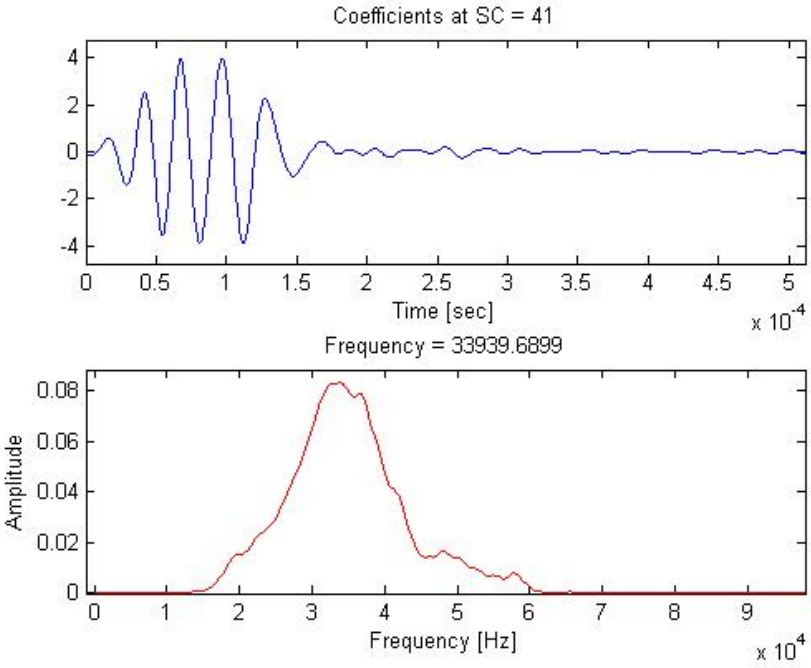

Figure F-19: Frequency content at a given scale from Figure F-16

Acceleration signal of AB

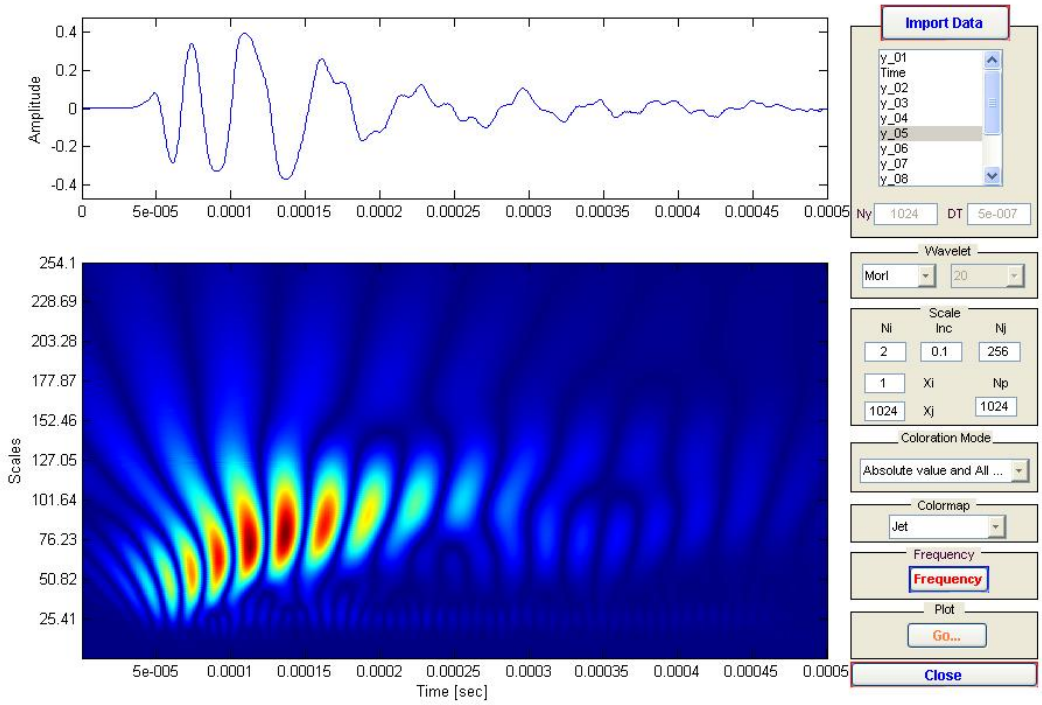

Figure F-20: Wavelet transform of signal f_{S2_R2} across the joint using Mallat's algorithm

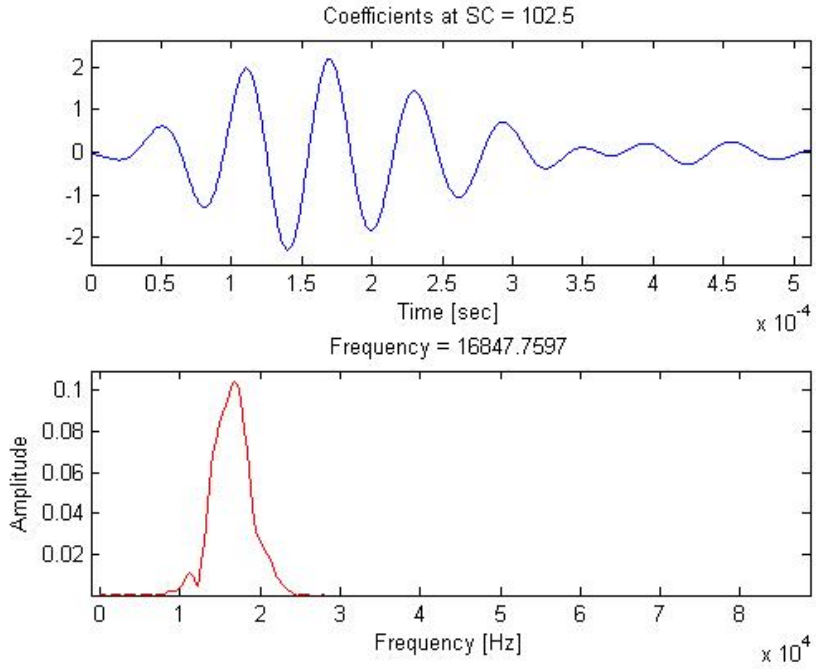

Figure F-21: Frequency content at a given scale from Figure F-20

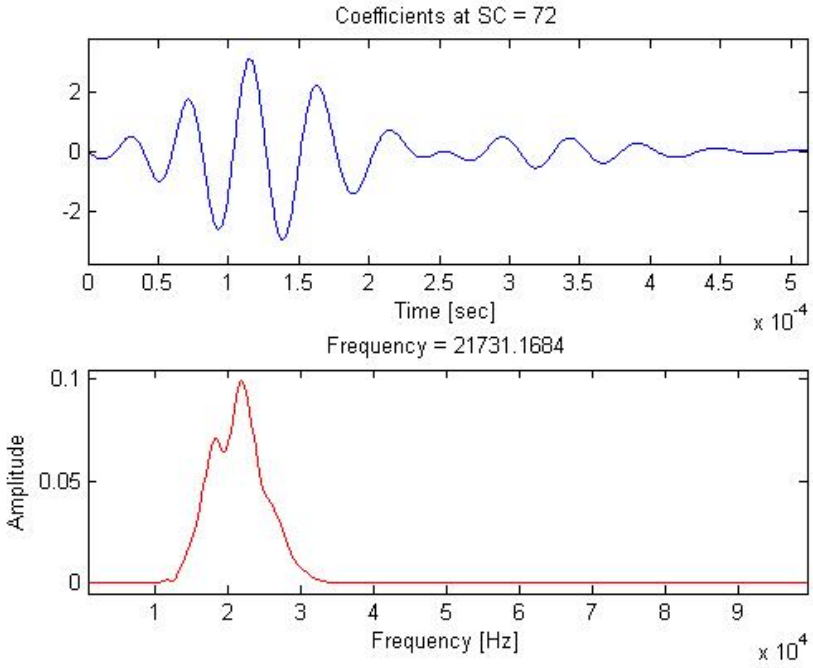

Figure F-22: Frequency content at a given scale from Figure F-20

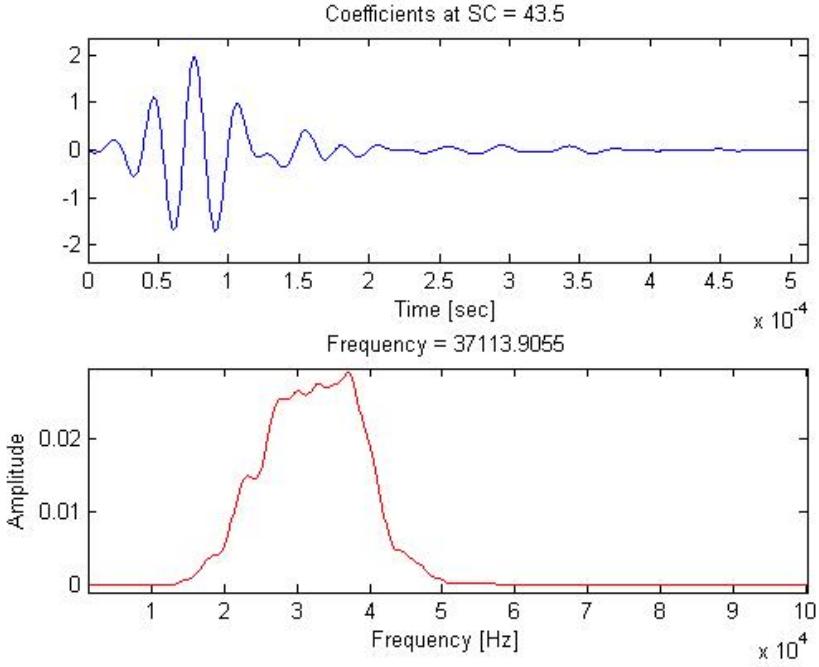

Figure F-23: Frequency content at a given scale from Figure F-20

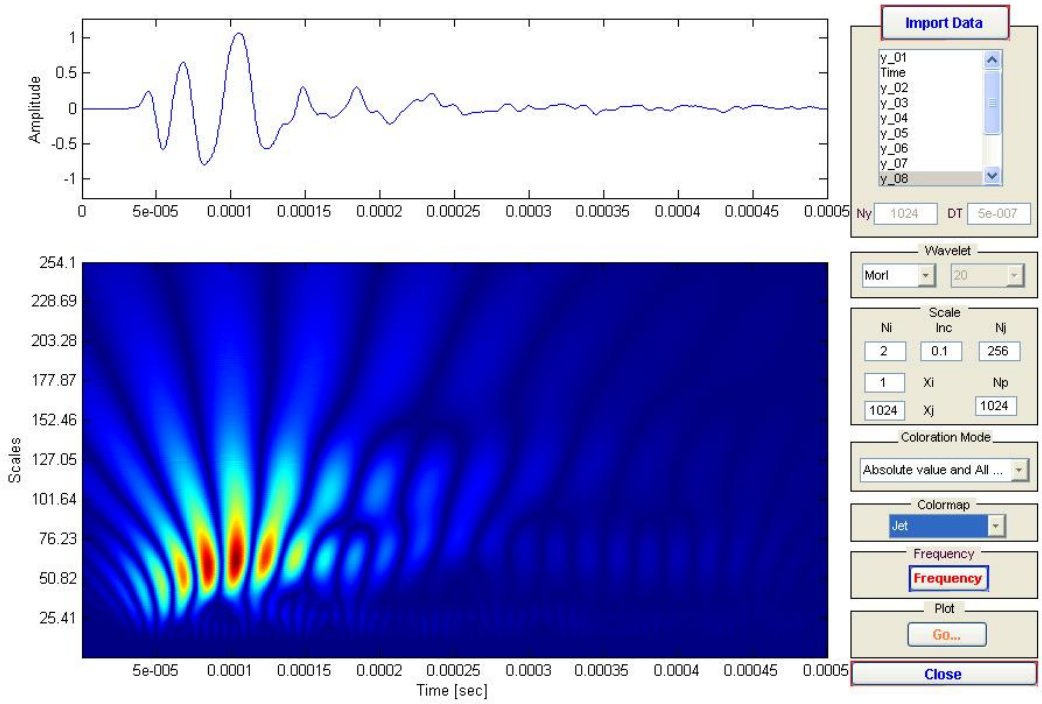

Figure F-24: Wavelet transform of signal f_{S1_R2} through the joint-free surface using Mallat's algorithm

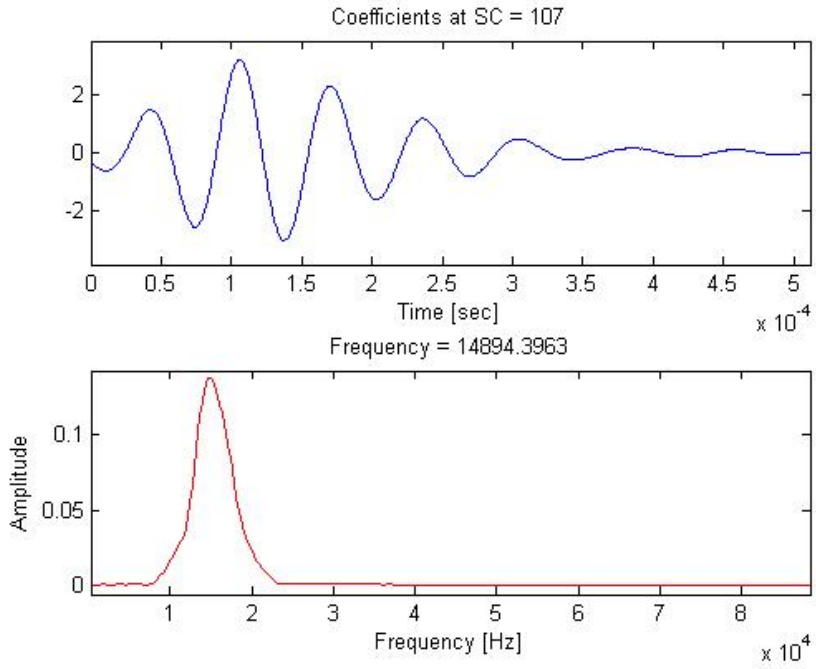

Figure F-25: Frequency content at a given scale from Figure F-24

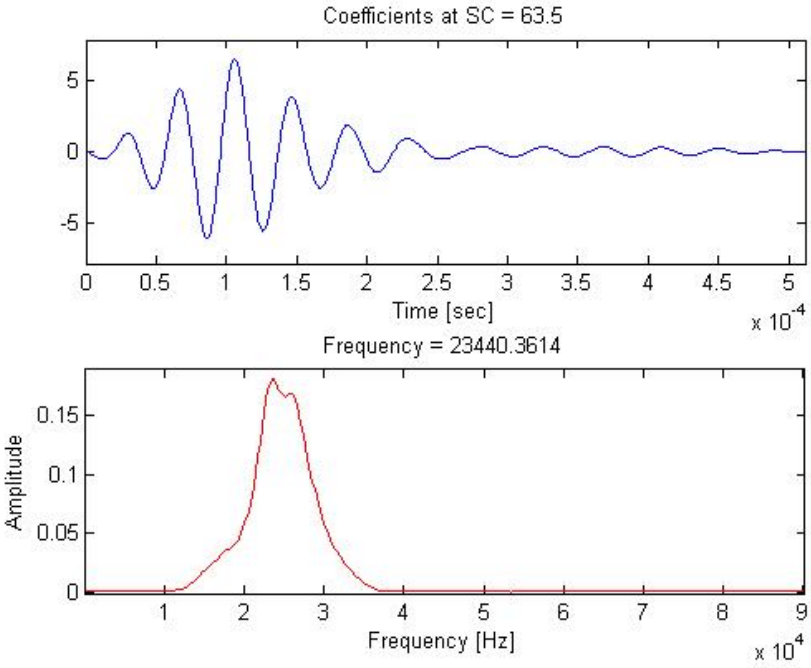

Figure F-26: Frequency content at a given scale from Figure F-24

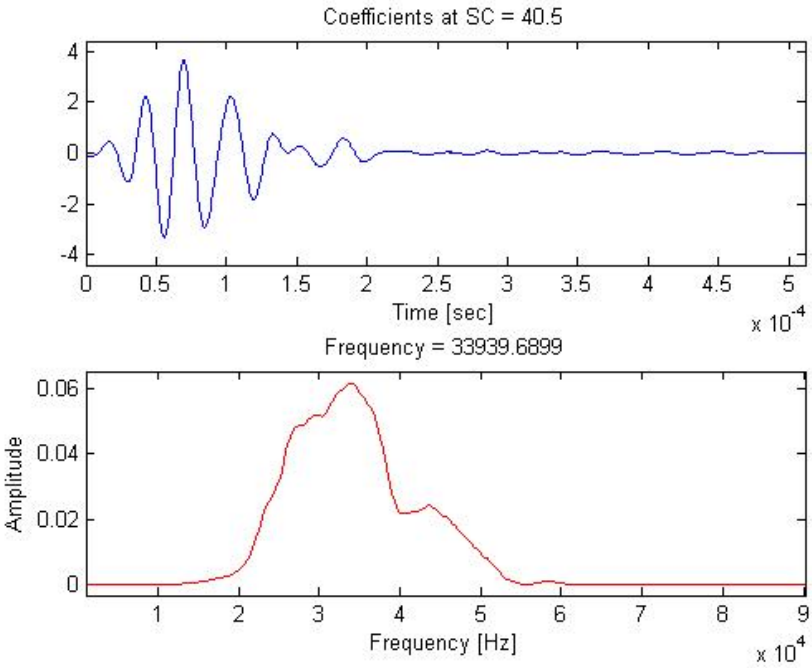

Figure F-27: Frequency content at a given scale from Figure F-24

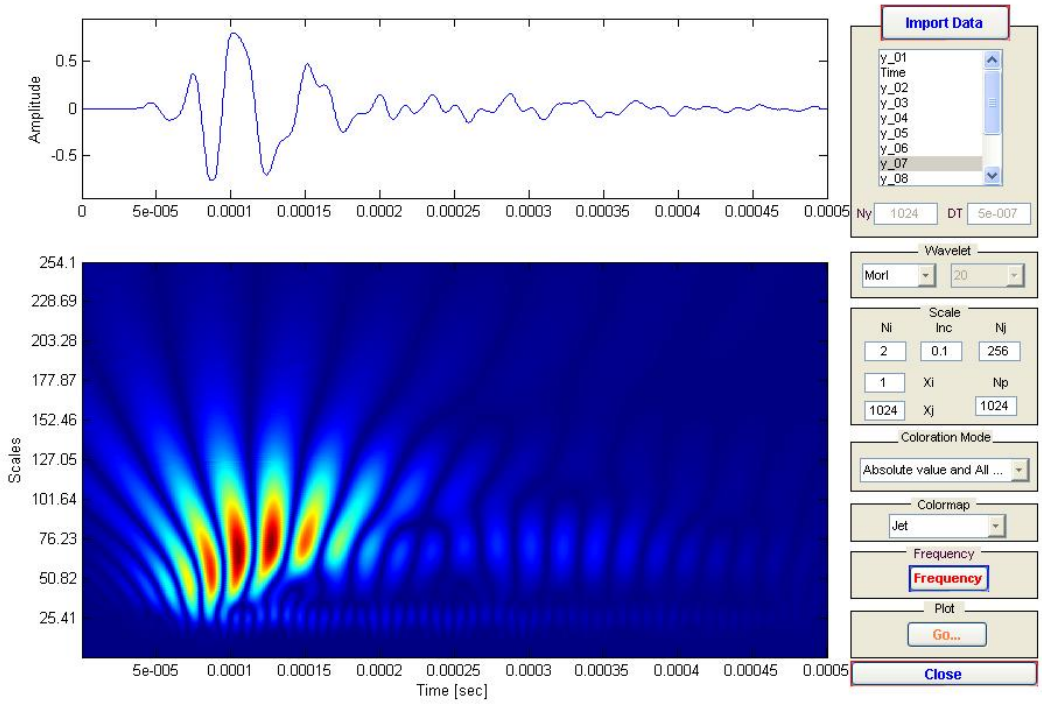

Figure F-28: Wavelet transform of signal f_{S1_R1} across the joint using Mallat's algorithm

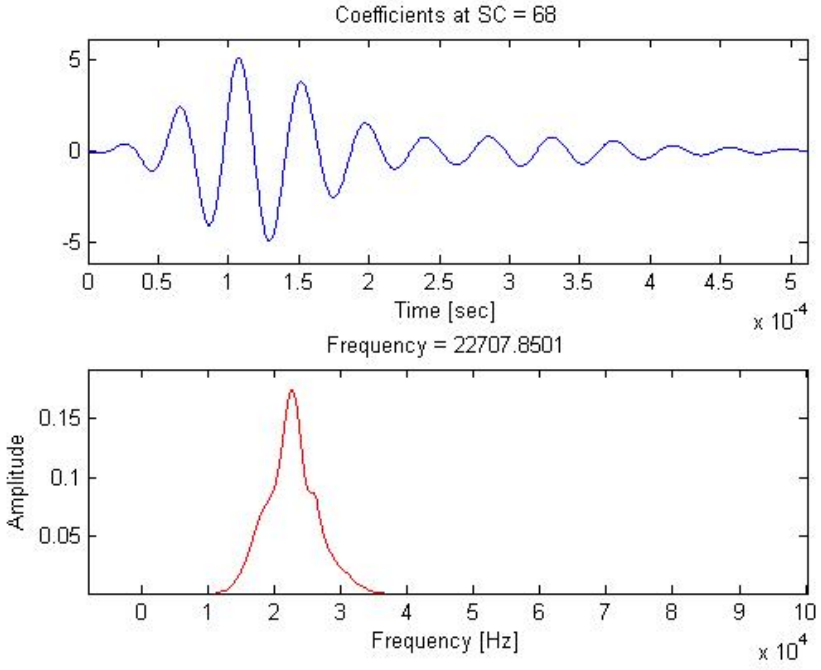

Figure F-29: Frequency content at a given scale from Figure F-28

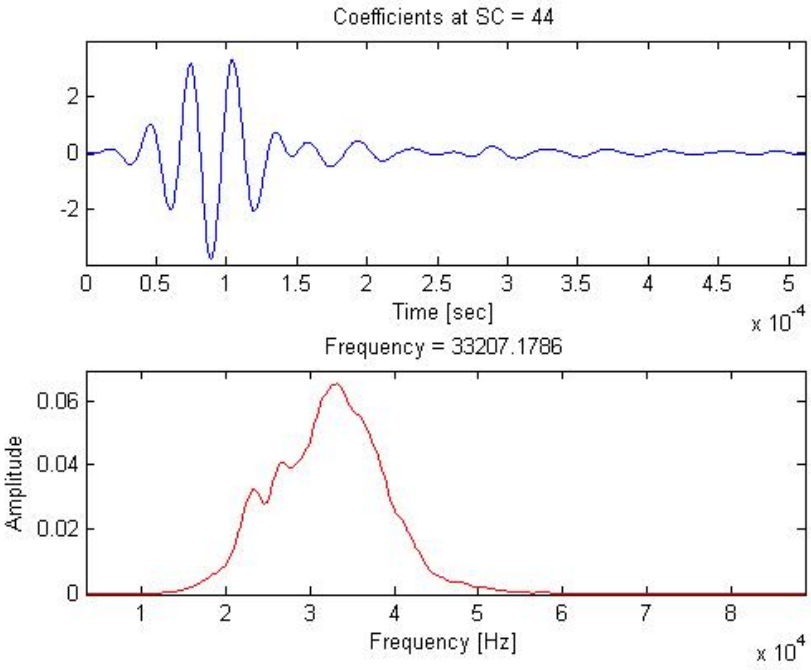

Figure F-30: Frequency content at a given scale from Figure F-28

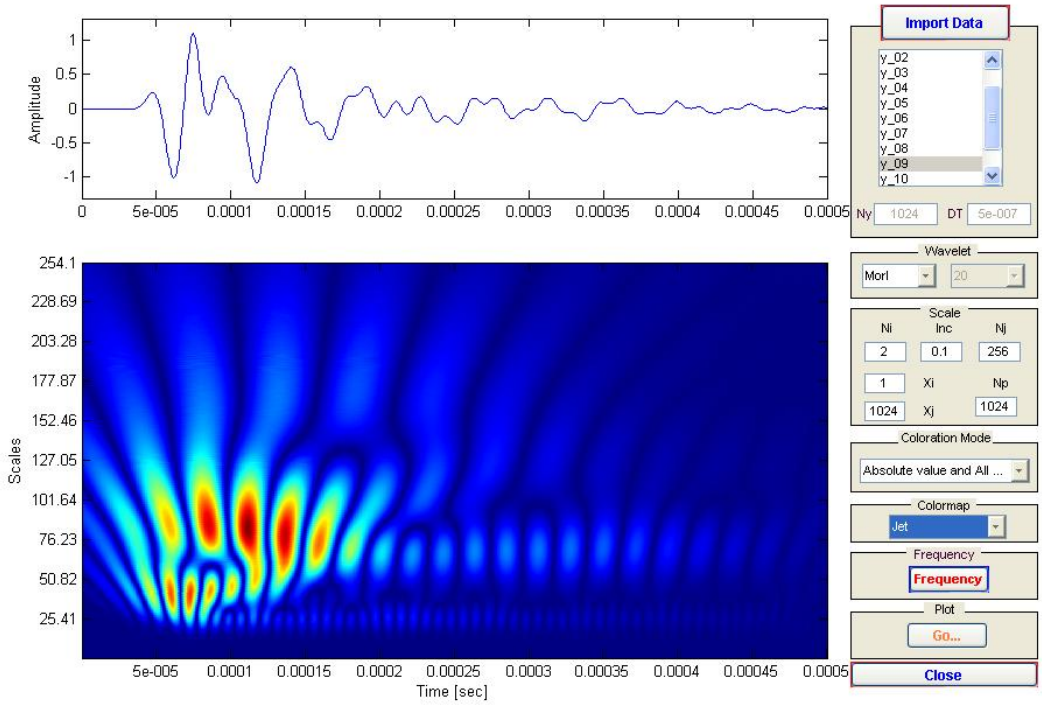

Figure F-31: Wavelet transform of signal f_{S2_R3} through the joint-free surface using Mallat's algorithm

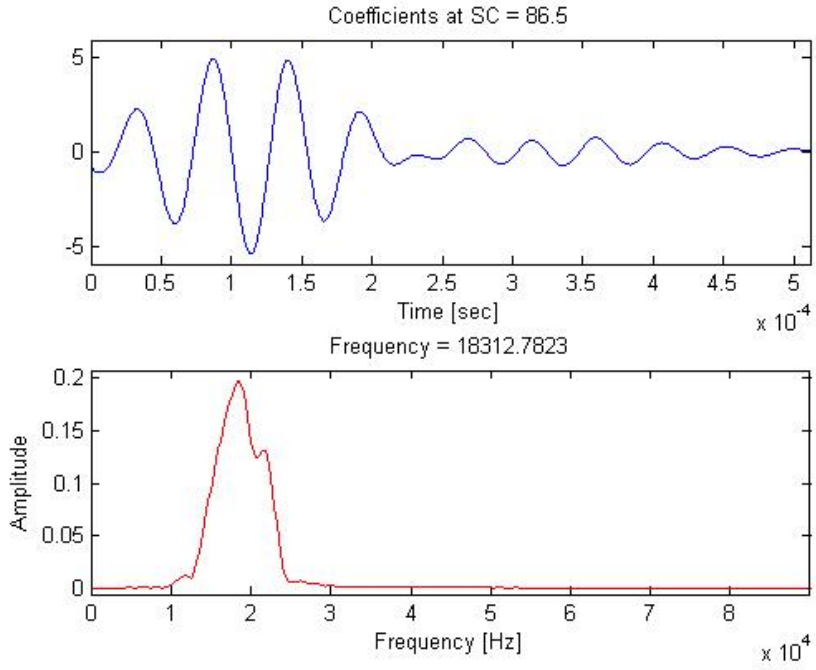

Figure F-32: Frequency content at a given scale from Figure F-31

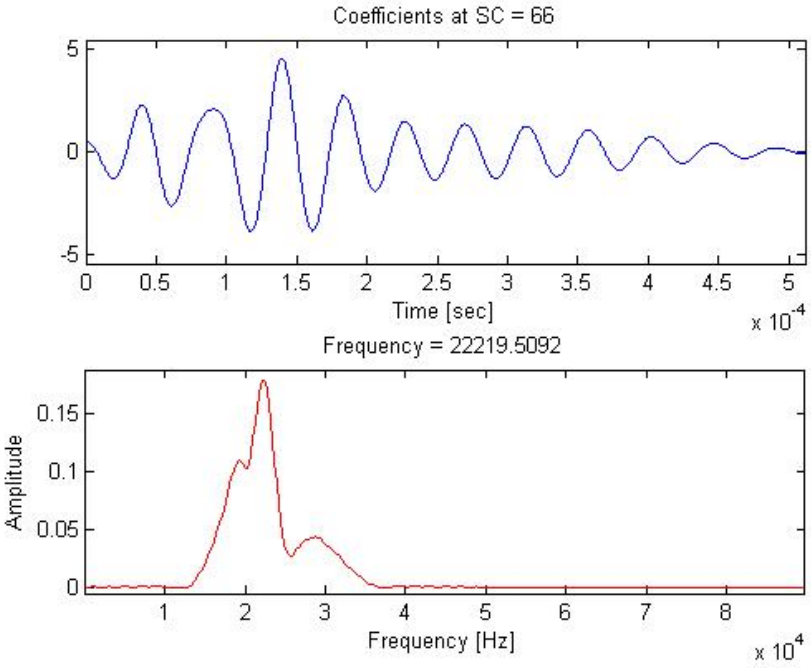

Figure F-33: Frequency content at a given scale from Figure F-31

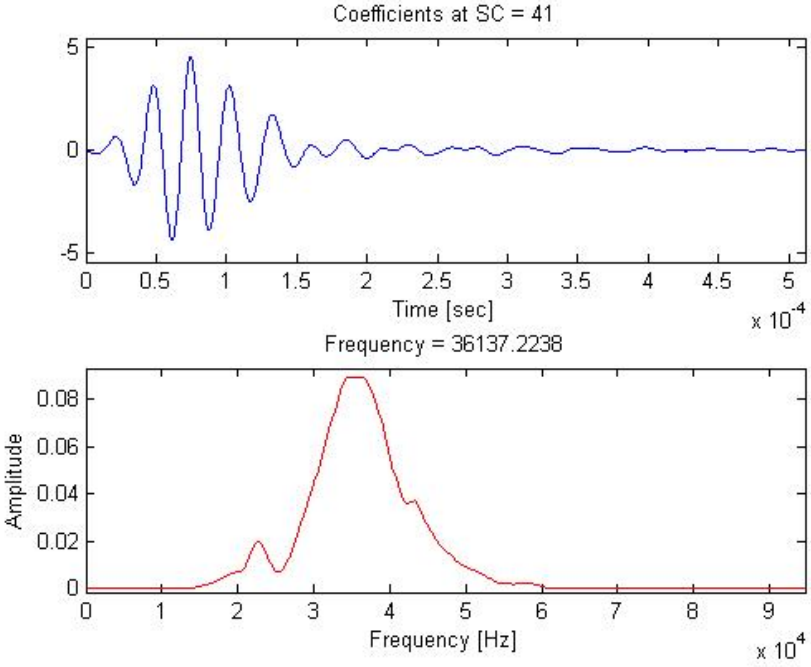

Figure F-34: Frequency content at a given scale from Figure F-31

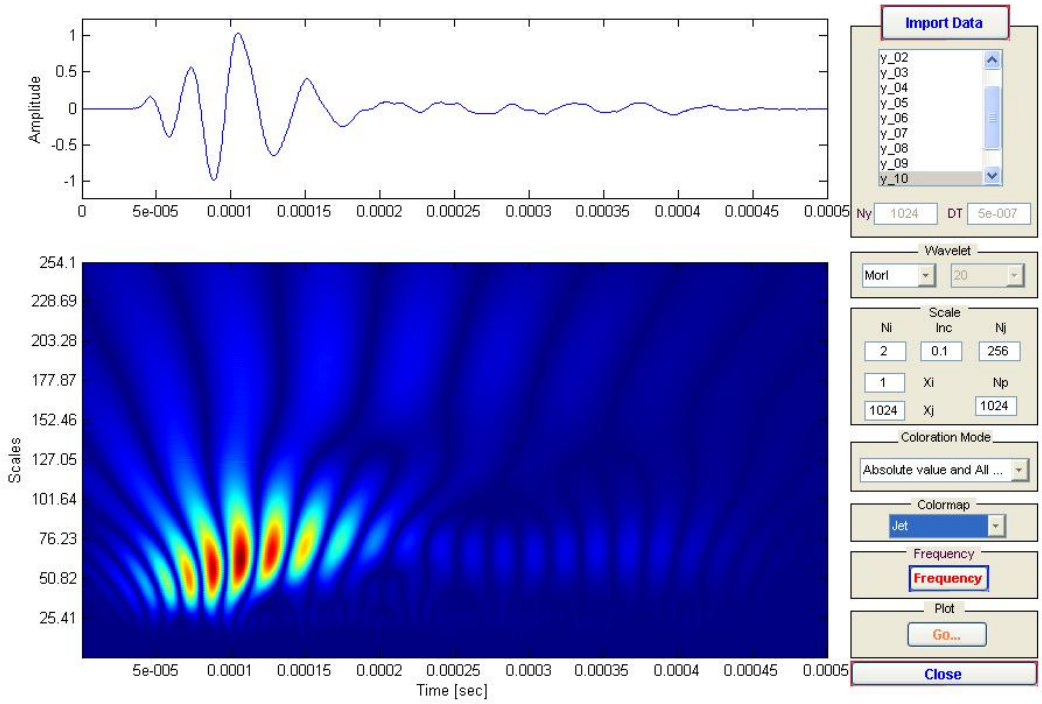

Figure F-35: Wavelet transform of signal f_{S3_R2} through the joint-free surface using Mallat's algorithm

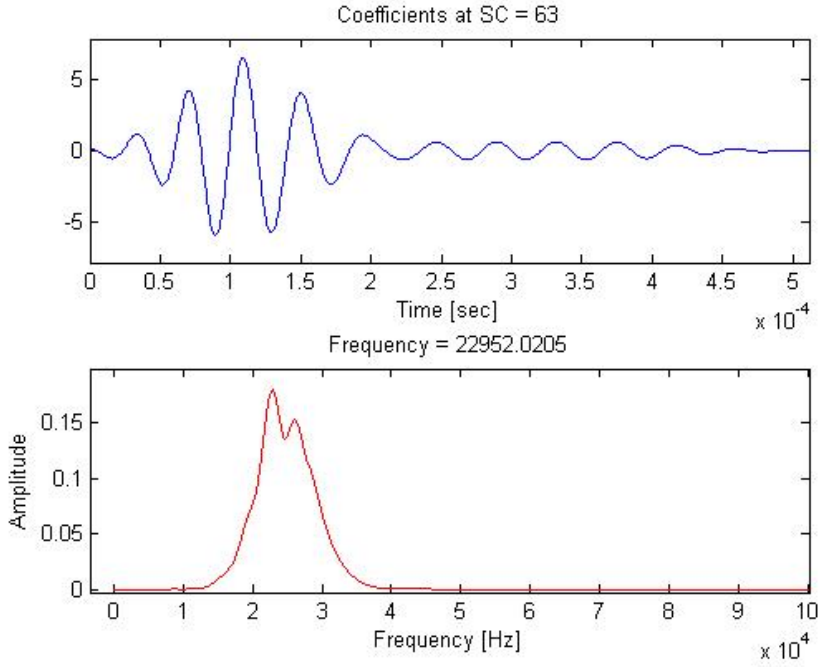

Figure F-36: Frequency content at a given scale from Figure F-35

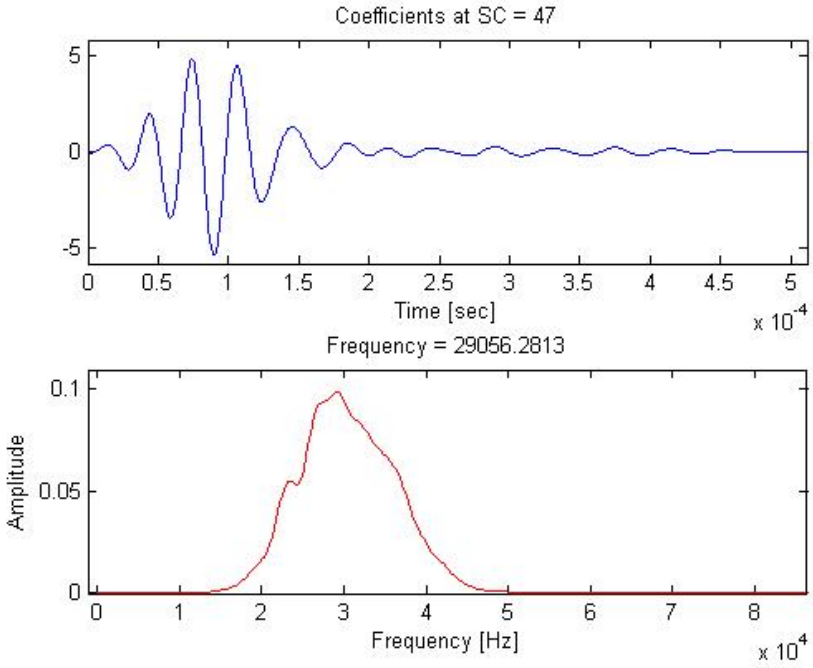

Figure F-37: Frequency content at a given scale from Figure F-35

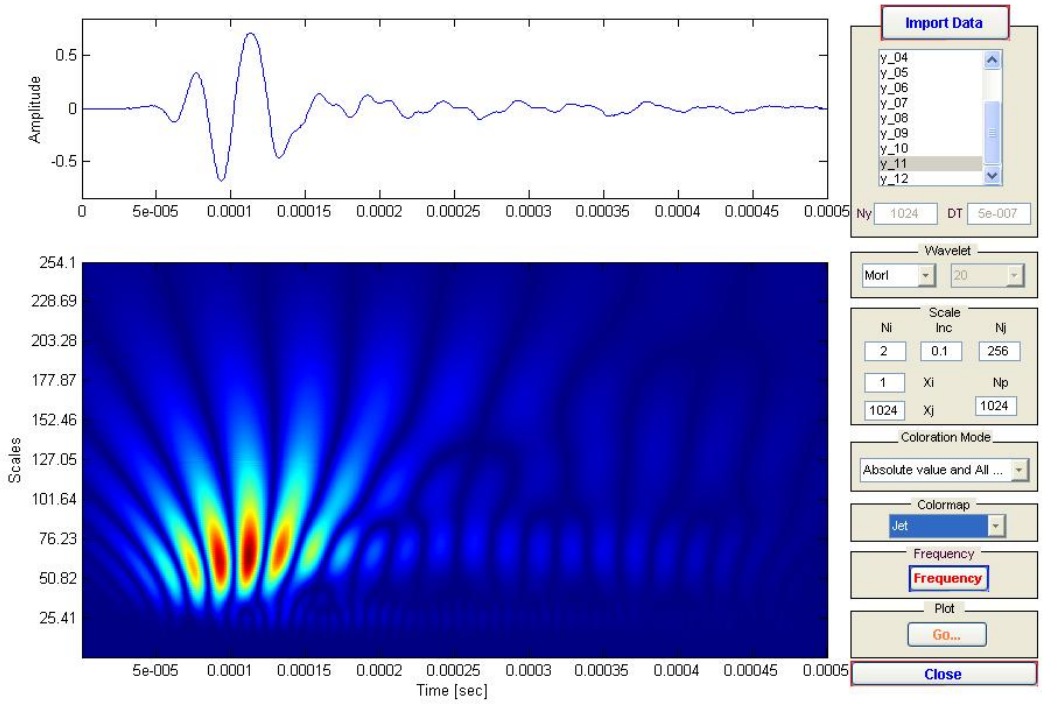

Figure F-38: Wavelet transform of signal f_{S3_R3} across the joint using Mallat's algorithm

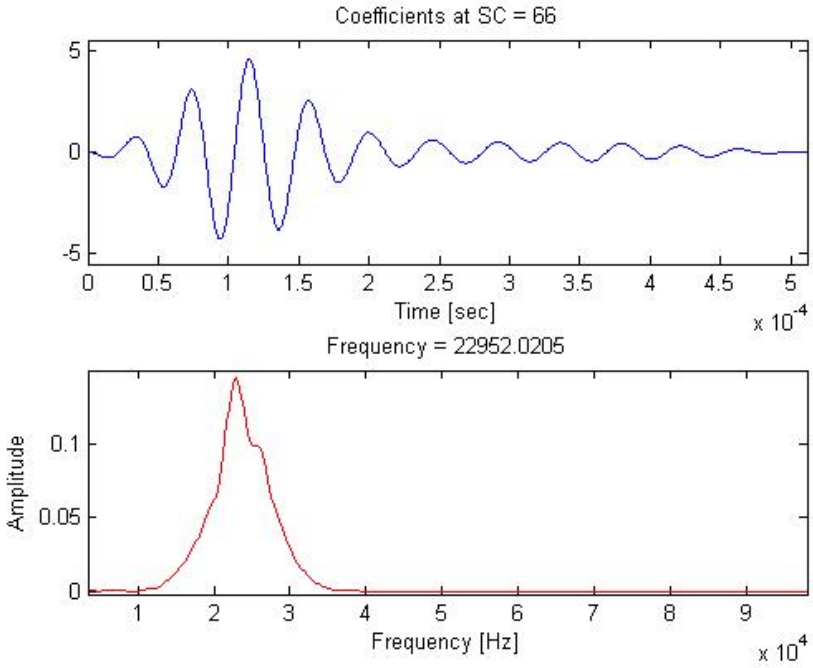

Figure F-39: Frequency content at a given scale from Figure F-38

Appendix G
Signal Processing for Slab 1
- Lines X1-Y1 and X2-Y2, Set 1 and Set 2

This appendix is a PDF file available in the Appendix CD.

The file name of this PDF file is “Appendix G - Signal processing for Slab 1.pdf”.

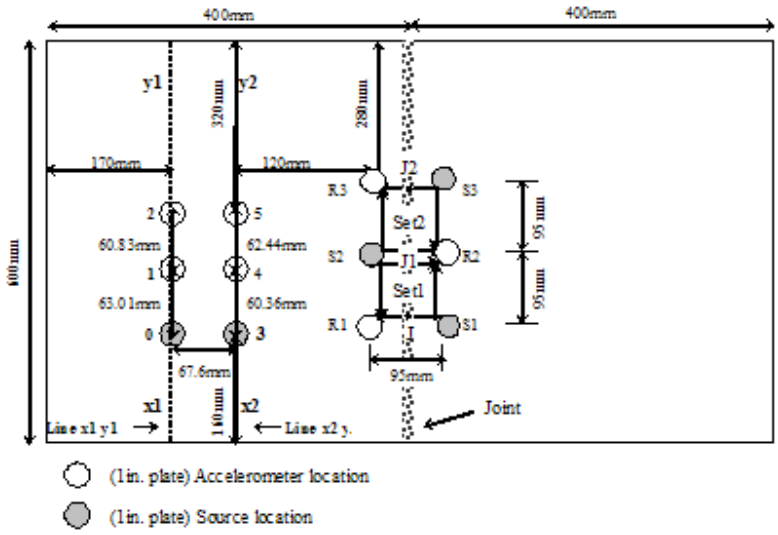

Figure G-1: Schematic illustration of ultrasonic testing configuration of HMA slab 1.

Measure Slab 1 using 1MHz P-wave Transducer as the transmitter and 50kHz accelerometer as the reveiver:

Pulse receiver and filter parameter setting			
Pulse receiver setting:	Rep. Rate: 2	**Filter setting:**	20db input
	Energy: 4		10db output
	Atten. (dB): 0		180 cutoff frequency
	GAIN (dB): 40	**Accelerometer (PCB353B65) setting:**	Resonant frequency > 40 kHz
	Damping: 4.0		sensitivity 100mV/g
	Mode: 2		

Oscilloscope setting: **Sampling Rate Δt:** $\frac{50\mu s}{100}$ **1000 Points in Total**

Index $N := 2^{10}$ $i := 1 .. N$ $u := 1 .. \frac{N}{2}$ $ORIGIN \equiv 1$ $fl_u := \frac{u}{N \cdot 5 \cdot 10^{-4}}$

all :=

$J := 1 .. 24$

$avg_J := mean(all^{\langle J \rangle})$ $signal^{\langle J \rangle} := all^{\langle J \rangle} - avg_J$

Definition of full signal:

Line x1 y1: $position1 := signal^{\langle 3 \rangle}$ $position2 := signal^{\langle 4 \rangle}$

Line x2 y2: $position3 := signal^{\langle 1 \rangle}$ $position4 := signal^{\langle 2 \rangle}$

Set1 $S2\_R2 := signal^{\langle 5 \rangle}$ $S2\_R1 := signal^{\langle 6 \rangle}$

$S1\_R1 := signal^{\langle 7 \rangle}$ $S1\_R2 := signal^{\langle 8 \rangle}$

Set2 $S2\_R3 := signal^{\langle 9 \rangle}$ $S3\_R2 := signal^{\langle 10 \rangle}$

$S3\_R3 := signal^{\langle 11 \rangle}$

Definition of front part signal:

Line x1 y1: $position1\_front := signal^{\langle 13 \rangle}$ $position2\_front := signal^{\langle 14 \rangle}$

Analyses of the full time signals:

Parameter $p := 1 .. 12$ $\omega o_p := 2\pi \cdot 1.03$ $\omega o_{12} := 2\pi \cdot 1.04$ $\omega o_2 := 2\pi \cdot 1.1$

$\omega o_4 := 2\pi \cdot 1.13$ $\omega o_6 := 2\pi \cdot 1.07$ $\omega o_5 := 2\pi \cdot 1.06$ $\omega o_7 := 2\pi \cdot 1.08$

$\omega o_9 := 2\pi \cdot 1.06$ $\omega o_{10} := 2\pi \cdot 1.07$ $\omega o_{11} := 2\pi \cdot 1.07$

Arrival Time (AT) of the signal: $\omega o_8 := 2\pi \cdot 1.07$

$AT := (\ 0.015 \quad 0.041 \quad 0.015 \quad 0.044 \quad 0.03 \quad 0.032 \quad 0.037 \quad 0.032 \quad 0.03 \quad 0.03 \quad 0.03 \quad 0.02 \quad 0\ )^T$

$tp_p := \text{ceil}\left(\left(\frac{AT_p}{0.0005}\right)\right) \cdot 0.0005$

$$wp(t, \omega o) := \begin{cases} 10\left|\cos(\omega o \cdot t)^{5000} - 1\right| & \text{if } 0 \le t \le \frac{\pi}{\omega o} \\ 0 & \text{otherwise} \end{cases}$$

Define **Time Window** (Twind) to amplify the arrival of the signals:

$$Twind := \left| \begin{array}{l} \text{for } p \in 1 .. 12 \\ \quad \text{for } i \in 1 .. N \\ \quad\quad ampl_{i,p} \leftarrow wp\left(i \cdot 0.0005 - tp_p, \omega o_p\right) \\ ampl \end{array} \right.$$

Fourier Transform of the Windowed Signals: $FTW^{\langle p \rangle} := CFFT\left(\overrightarrow{\left(Twind^{\langle p \rangle} \cdot signal^{\langle p \rangle}\right)}\right)$

Windowed Signals: $P_{i,p} := Twind_{i,p} \cdot signal_{i,p}$

Spectrum Area $MA_{u,p} := \sum_{u=1}^{u} \frac{\left|FTW_{u,p}\right|}{N \cdot 0.0005}$

Normalize each signal: $maxSiganl_J := \max\left(\overrightarrow{\left|signal^{\langle J \rangle}\right|}\right)$ $SINGAL^{\langle J \rangle} := \frac{signal^{\langle J \rangle}}{maxSiganl_J}$

Line x1 y1- Locations 1 and 2

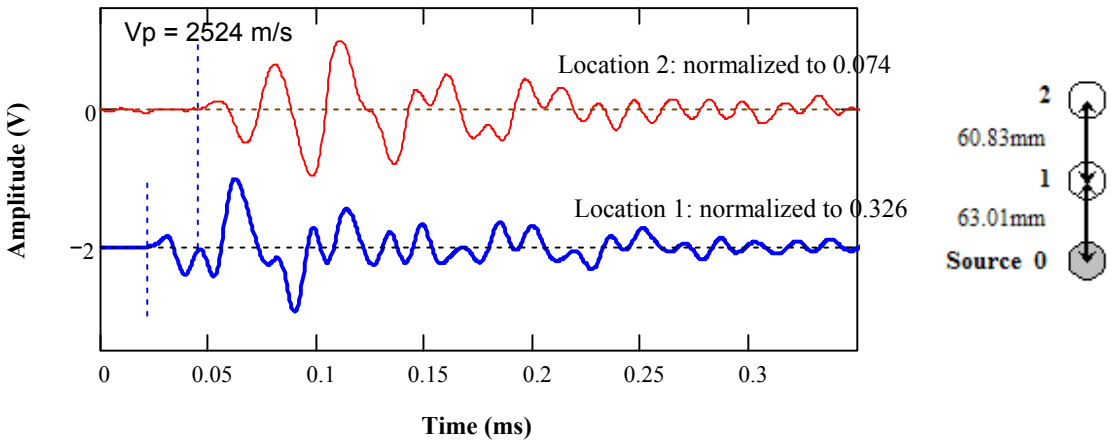

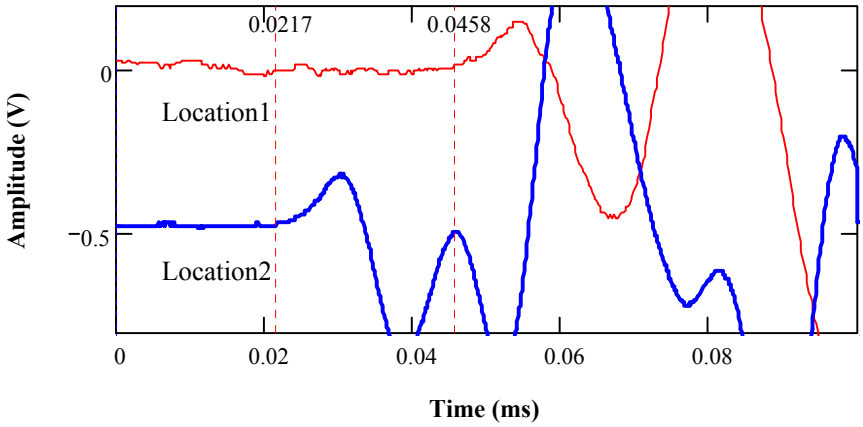

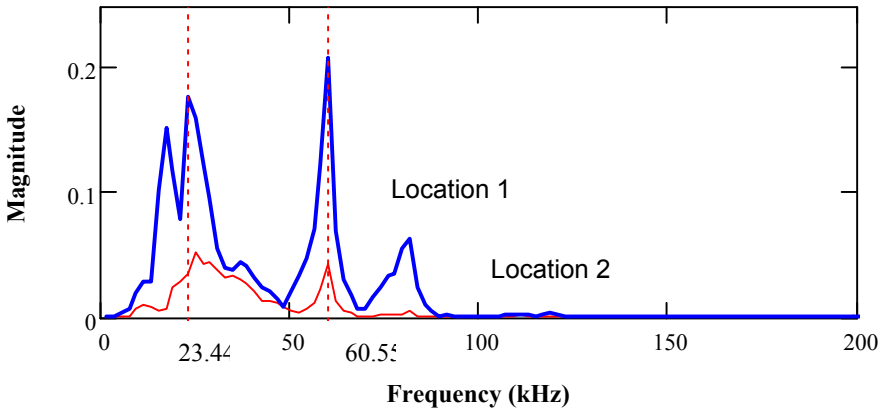

Line x2 y2 - Locations 4 and 5

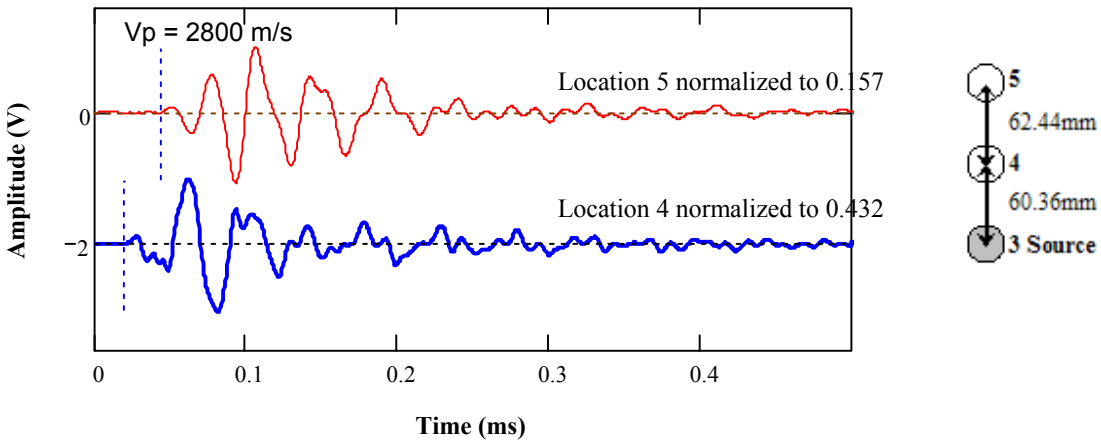

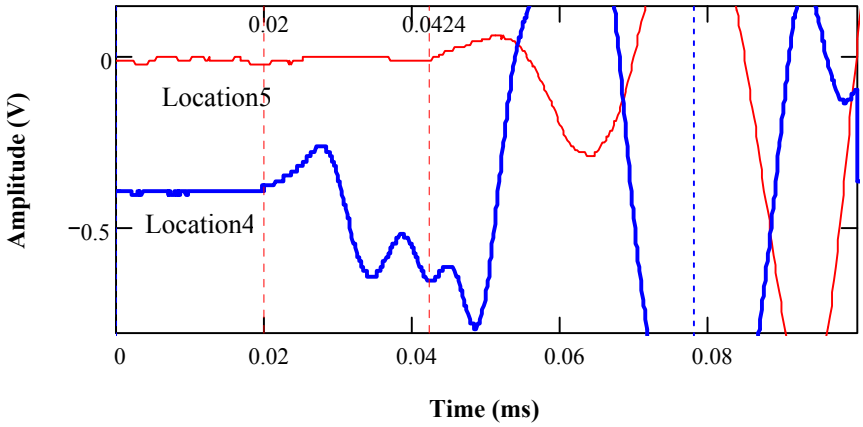

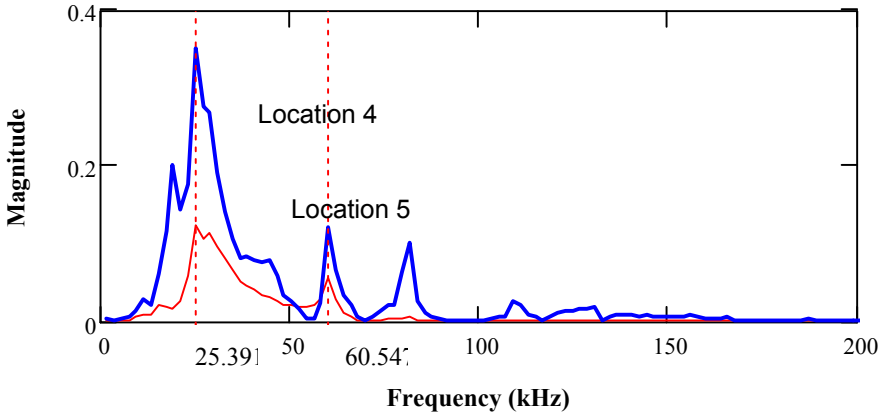

Damping ratio @ 24kHz

$fre := 24$

For location 1 & 2

$$\left(\frac{2\pi fre \cdot 61}{2.775\times 10^{3}}\right)^{-1} \cdot \ln\left(\frac{0.177}{0.052}\right) = 0.37$$

For location 3 & 4

$$\left(\frac{2\pi fre \cdot 61}{2.775\times 10^{3}}\right)^{-1} \cdot \ln\left(\frac{0.351}{0.123}\right) = 0.316$$

Damping analysis for full signals:

$$\Delta\Phi 1_{u} := \left(\frac{2\pi\, f1_{u} \cdot 61}{2.775\times 10^{3}}\right)^{-1}$$

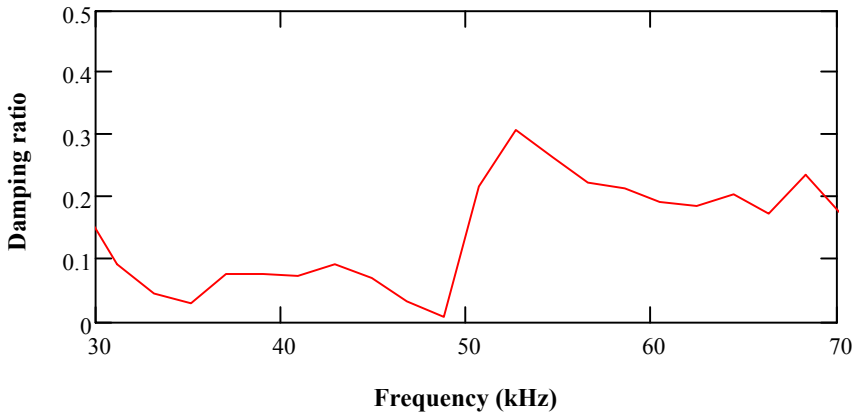

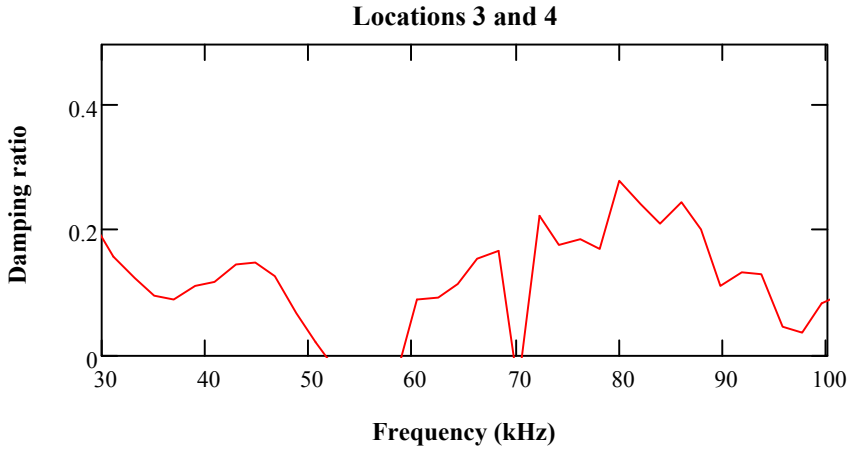

Analysis of joint - Set 1 $f_{S2\text{-}R1}$ (joint-free) & $f_{S2\text{-}R2}$ (joint)

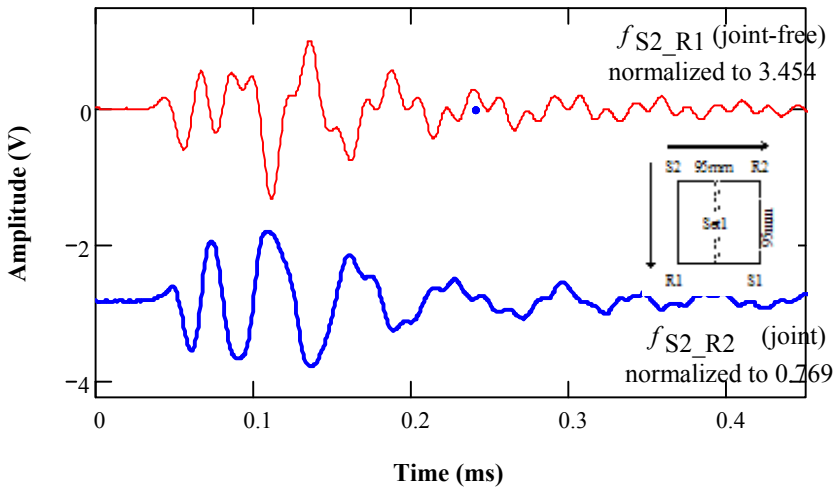

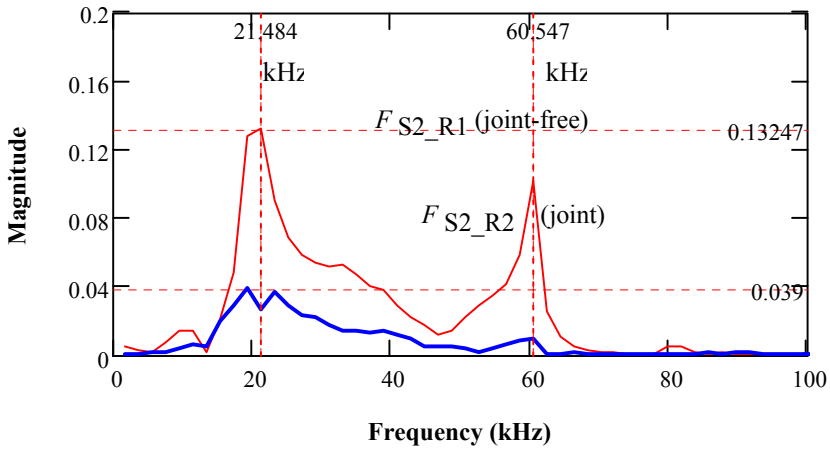

PTP ratio: $\frac{\text{Joint}}{\text{No} - \text{Joint}}$ $\frac{\max\left(P^{\langle 5\rangle}\right) - \min\left(P^{\langle 5\rangle}\right)}{\max\left(P^{\langle 6\rangle}\right) - \min\left(P^{\langle 6\rangle}\right)} = 0.223$

Maximum Area for the Windowed Signal (MA):

$\frac{\text{Joint}}{\text{No} - \text{Joint}}$ $\frac{MA_{100,5}}{MA_{100,6}} = 0.308$

Maximum Magnitude in Frequency Domain (MM):

$\frac{\text{Joint}}{\text{No} - \text{Joint}}$ $MM1 := \frac{0.039}{0.132}$ $MM1 = 0.295$

$f_{S1\text{-}R2}$ (joint-free) & $f_{S1\text{-}R1}$ (joint)

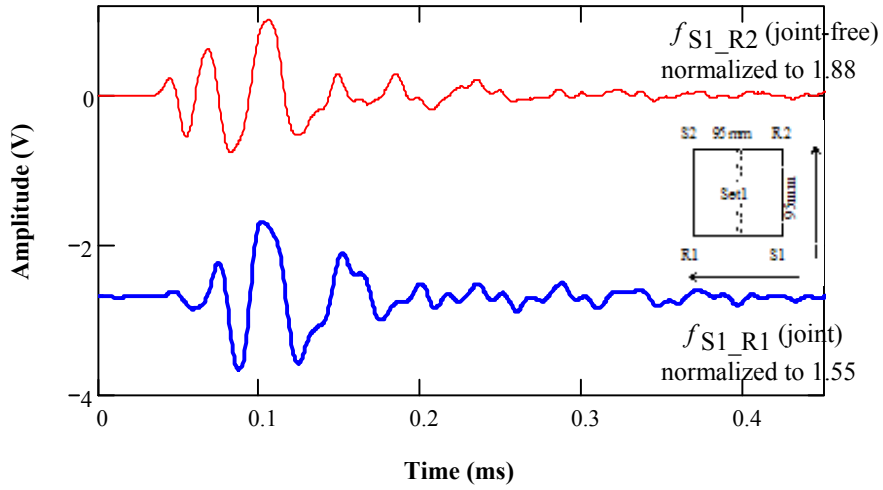

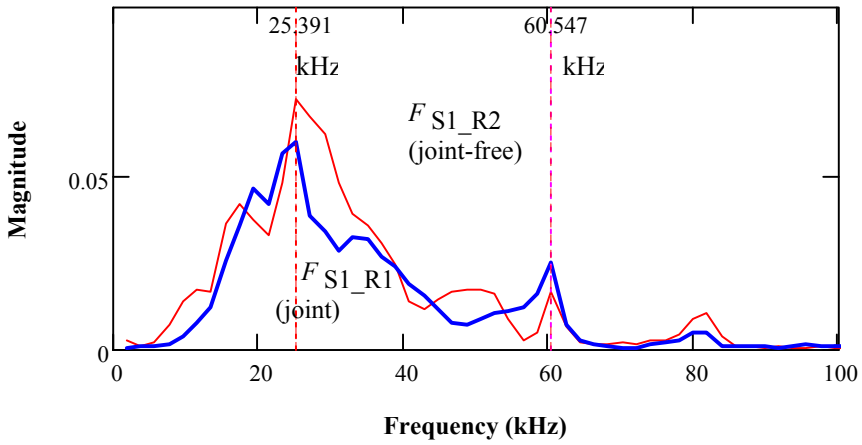

PTP ratio: $\frac{\text{Joint}}{\text{No} - \text{Joint}}$ $\frac{\max\left(P^{\langle 7\rangle}\right) - \min\left(P^{\langle 7\rangle}\right)}{\max\left(P^{\langle 8\rangle}\right) - \min\left(P^{\langle 8\rangle}\right)} = 0.826$

Maximum Area for the Windowed Signal (MA)

$\frac{\text{Joint}}{\text{No} - \text{Joint}}$ $\frac{MA_{100,7}}{MA_{100,8}} = 0.842$

Transmission Coefficient (TC)

$$TC_u := \sqrt{\frac{|FTW_{u,5}| \cdot |FTW_{u,7}|}{|FTW_{u,6}| \cdot |FTW_{u,8}|}}$$

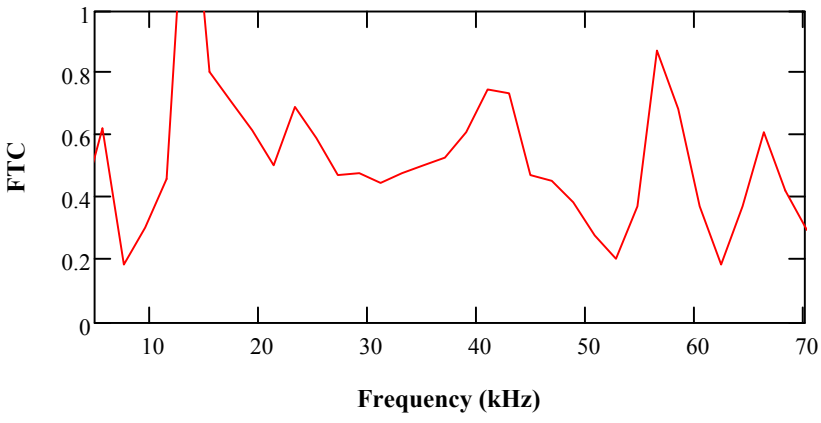

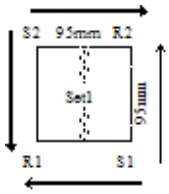

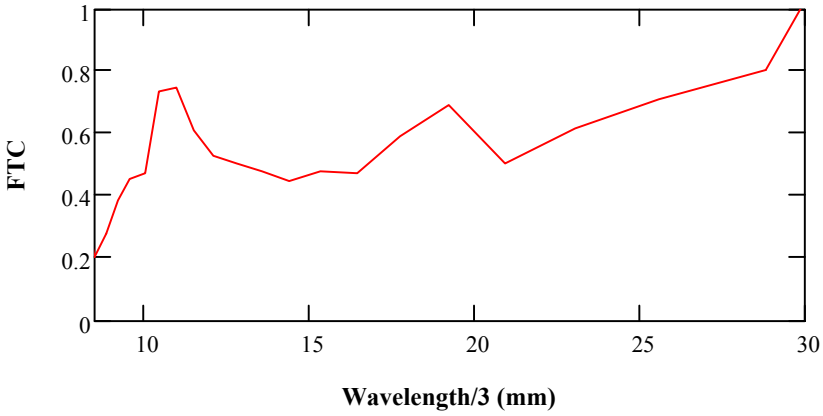

Damping ratio @ 23kHz

fre := 22.9

$f_{S2\text{-}R1}$ (joint-free) & $f_{S2\text{-}R2}$ (joint)

$$\left(\frac{2\pi fre \cdot 95}{1352}\right)^{-1} \cdot \ln\left(\frac{1}{MM1}\right) = 0.12$$

$f_{S1\text{-}R2}$ (joint-free) & $f_{S1\text{-}R1}$ (joint)

$$\left(\frac{2\pi fre \cdot 95}{1352}\right)^{-1} \cdot \ln\left(\frac{1}{MM2}\right) = 0.019$$

Damping analysis for full signals:

$$\Delta\Phi 1_u := \left(\frac{2\pi f 1_u \cdot 95}{1352}\right)^{-1}$$

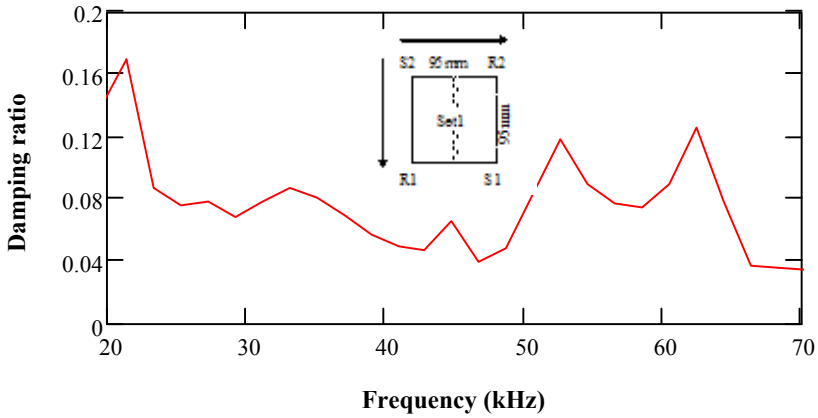

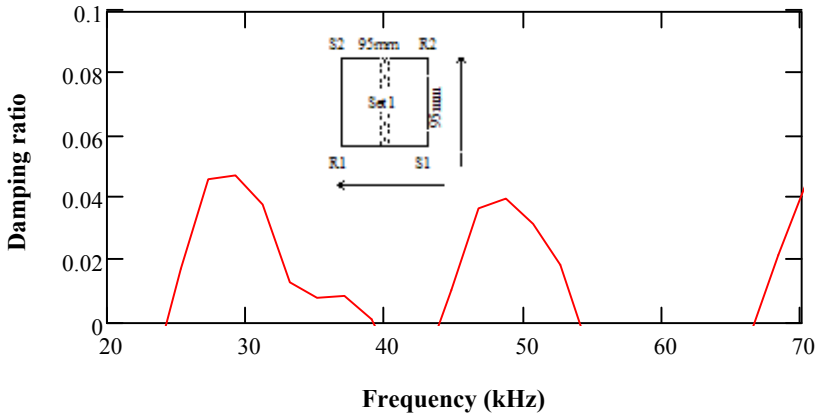

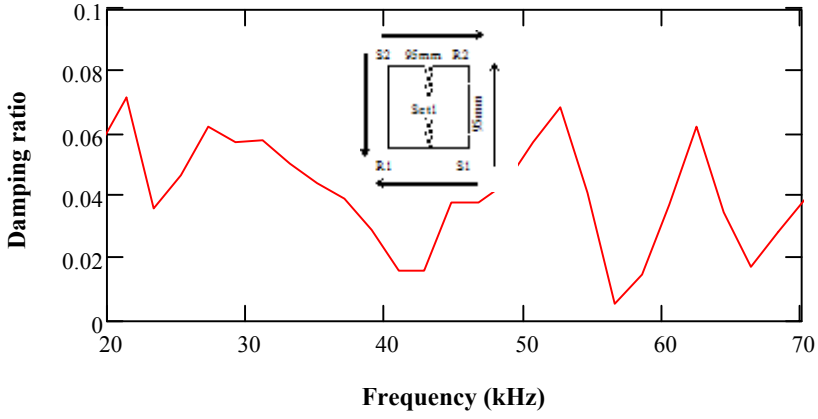

Damping analysis for full signals - using spectrum area:

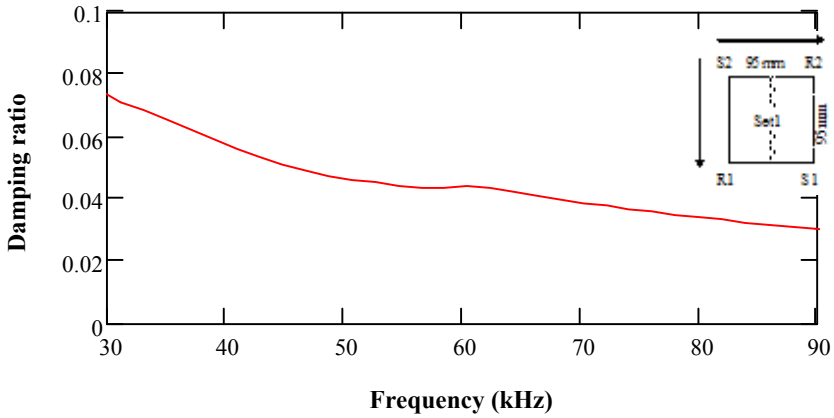

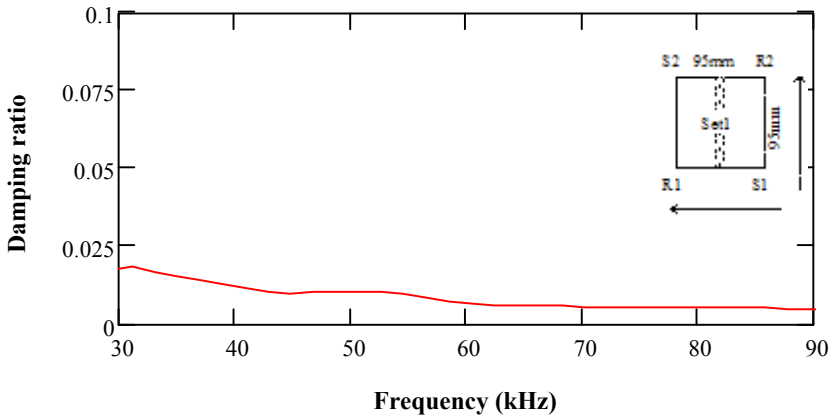

Analysis of joint -SET 2 $f_{S2\text{-}R3}$ (joint-free) & $f_{S2\text{-}R2}$ (joint)

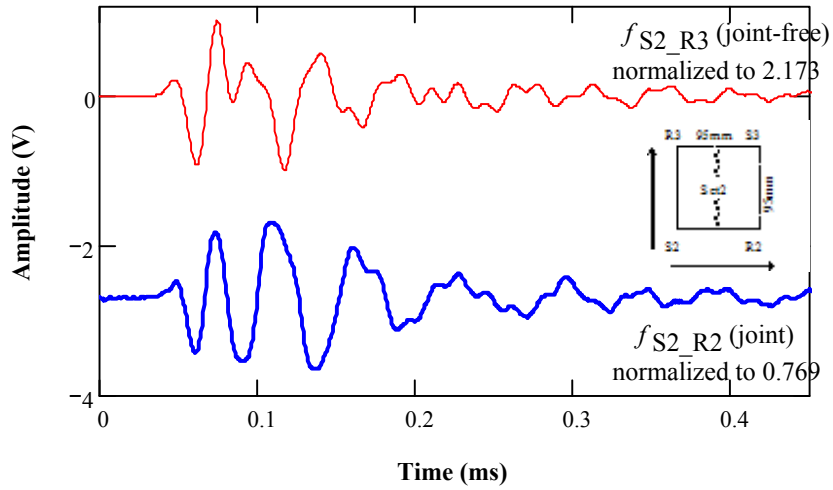

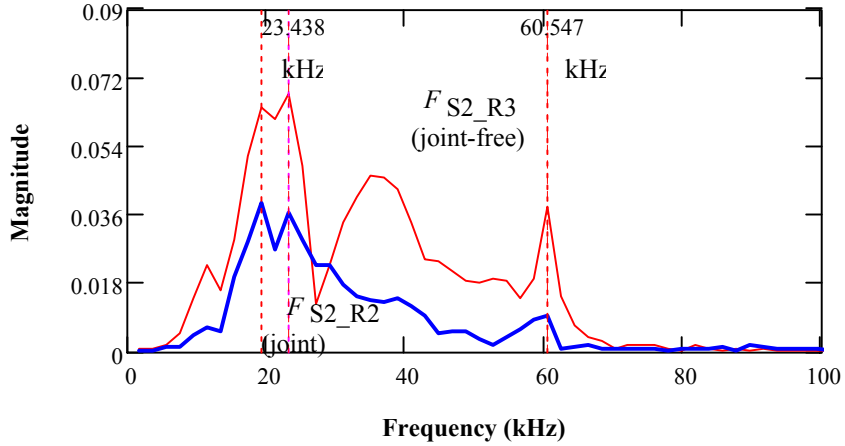

PTP ratio: $\frac{\text{Joint}}{\text{No} - \text{Joint}}$ $\frac{\max\left(P^{\langle 5\rangle}\right) - \min\left(P^{\langle 5\rangle}\right)}{\max\left(P^{\langle 9\rangle}\right) - \min\left(P^{\langle 9\rangle}\right)} = 0.354$

Maximum Area in Frequency Domain for the Windowed Signal (MA):

$\frac{\text{Joint}}{\text{No} - \text{Joint}}$ $\frac{MA_{100,5}}{MA_{100,9}} = 0.448$

$f_{S3\text{-}R2}$ (joint-free) & $f_{S3\text{-}R3}$ (joint)

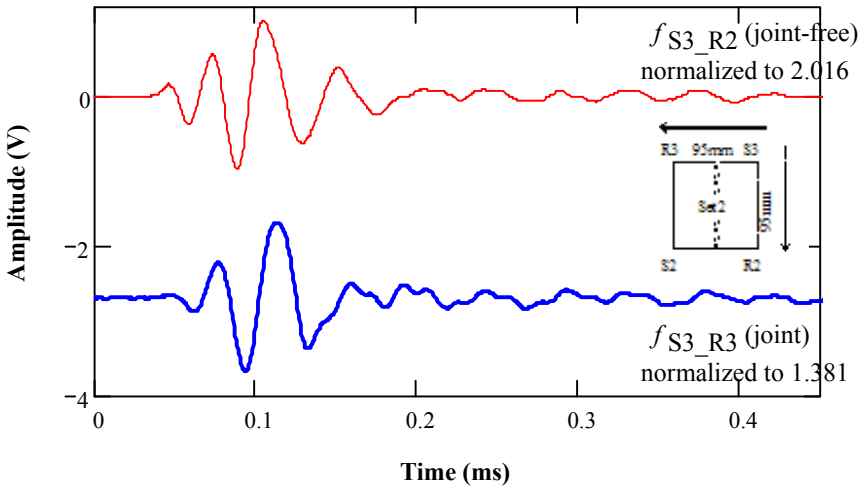

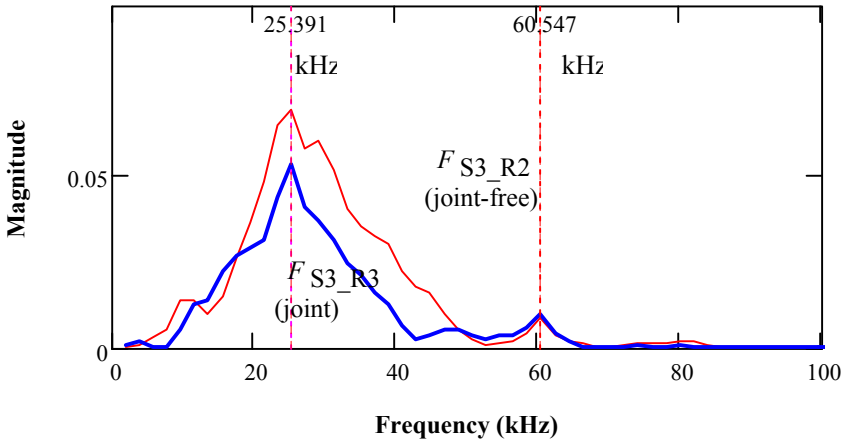

PTP ratio: $\frac{\text{Joint}}{\text{No} - \text{Joint}}$ $\frac{\max\left(P^{\langle 11\rangle}\right) - \min\left(P^{\langle 11\rangle}\right)}{\max\left(P^{\langle 10\rangle}\right) - \min\left(P^{\langle 10\rangle}\right)} = 0.685$

Maximum Area in Frequency Domain for the Windowed Signal (MA):

$\frac{\text{Joint}}{\text{No} - \text{Joint}}$ $\frac{MA_{100,11}}{MA_{100,10}} = 0.682$

Transmission Coefficient (TC)

$$TC_u := \sqrt{\frac{|FTW_{u,5}| \cdot |FTW_{u,11}|}{|FTW_{u,9}| \cdot |FTW_{u,10}|}}$$

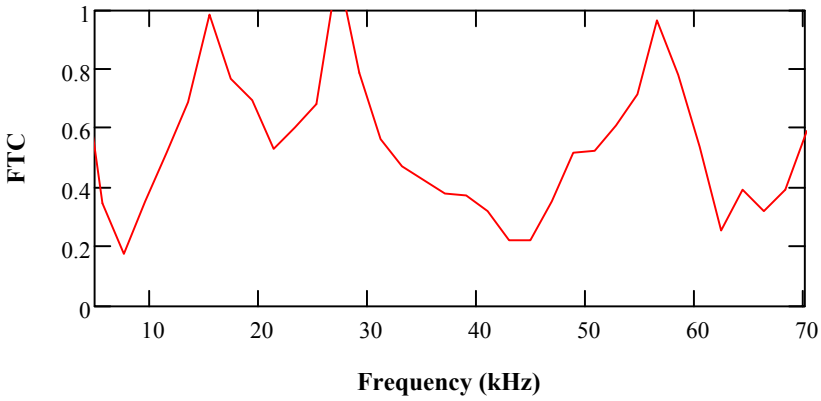

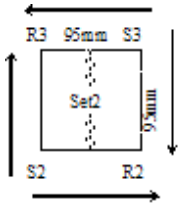

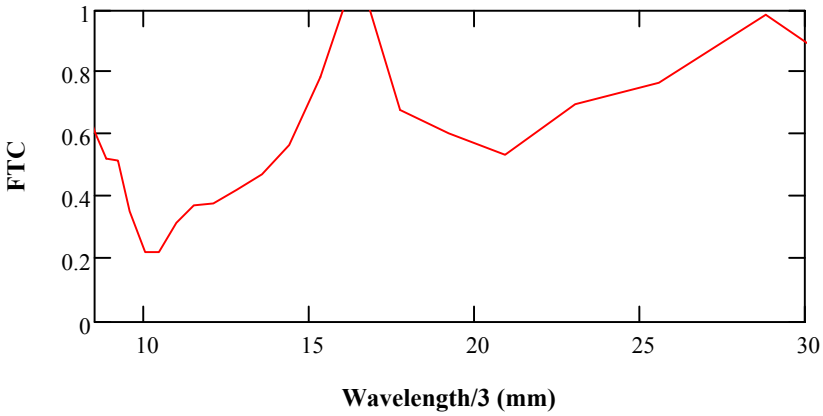

Damping ratio @ 23kHz

fre := 23.4

$f_{S2\text{-}R3}$ (joint-free) & $f_{S2\text{-}R2}$ (joint) $\left(\frac{2\pi fre \cdot 95}{1352}\right)^{-1} \cdot \ln\left(\frac{1}{MM1}\right) = 0.054$

$f_{S3\text{-}R2}$ (joint-free) & $f_{S3\text{-}R3}$ (joint) $\left(\frac{2\pi fre \cdot 95}{1352}\right)^{-1} \cdot \ln\left(\frac{1}{MM2}\right) = 0.025$

For the set $\left(\frac{2\pi fre \cdot 95}{1352}\right)^{-1} \cdot \ln\left(\sqrt{\frac{1}{MM2 \cdot MM1}}\right) = 0.039$

Damping analysis for full signals:

$$\Delta\Phi 1_u := \left(\frac{2\pi f 1_u \cdot 95}{1352}\right)^{-1}$$

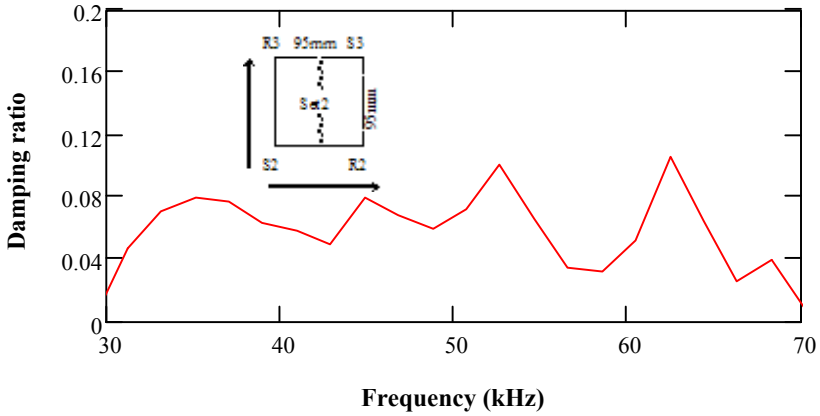

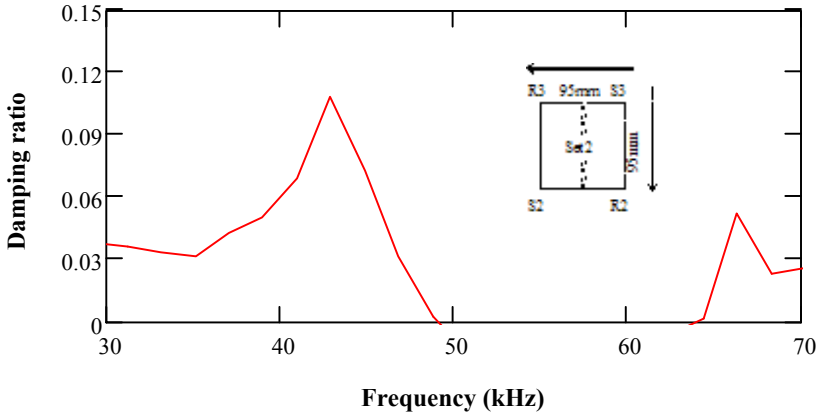

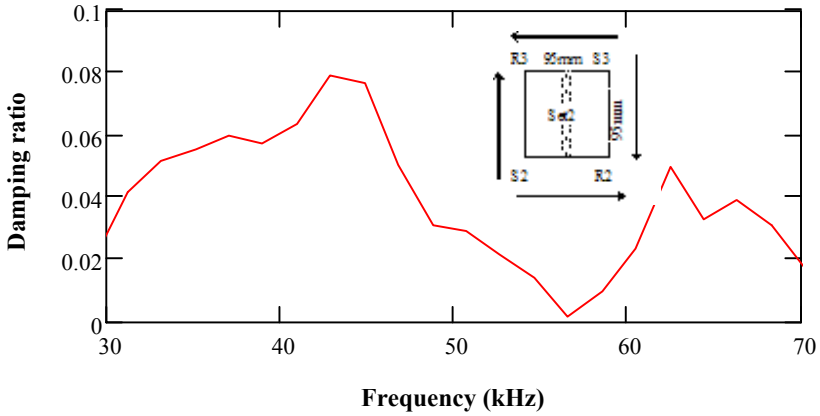

Damping analysis for full signals - using spectrum area:

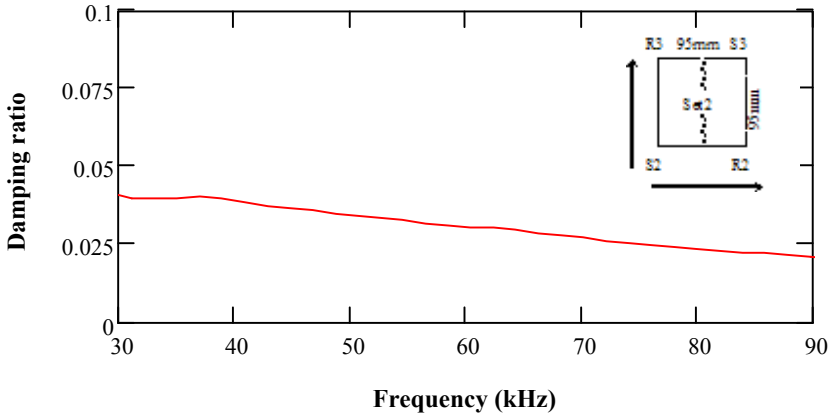

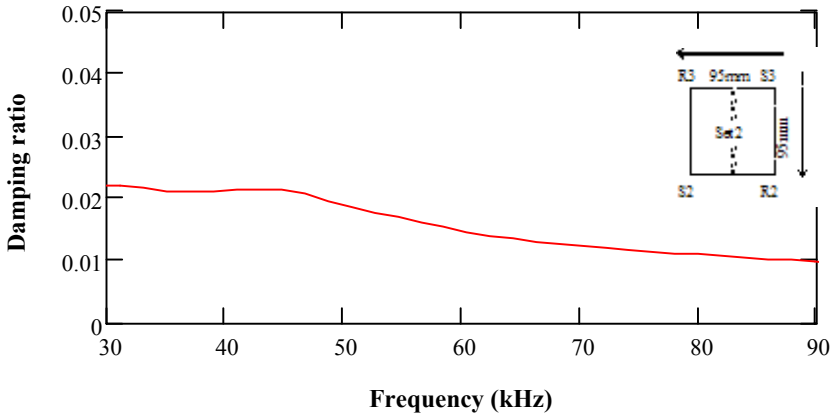

Wavelet transform - for dominat frequency in full signals of set 1, deifferent center frequency for 4 signals defined by "aX"; Time shift by "τ".

$aAC := 46.5$ $\frac{1}{2 \cdot aAC \cdot 5 \cdot 10^{-4}} = 21.482$ kHz $aDB := 39.3$ $\frac{1}{2 \cdot aDB \cdot 5 \cdot 10^{-4}} = 25.445$ kHz

$aAB := 51.2$ $\frac{1}{2 \cdot aAB \cdot 5 \cdot 10^{-4}} = 19.531$ kHz $aDC := 39.3$ $\frac{1}{2 \cdot aDC \cdot 5 \cdot 10^{-4}} = 25.445$ kHz

Definition of Morlet wavelet $\tau := 1 .. N$

f_{S2_R1} (joint-free) $w\_AC_{i,\tau} := aAC^{-\frac{1}{2}} \cdot \left[e^{j \cdot \frac{-\pi}{aAC} \cdot (\tau - i)} \cdot e^{-1 \cdot \left(\frac{\tau - i}{aAC} \right)^2} \right]$

f_{S2_R2} **(joint)** $w\_AB_{i,\tau} := aAB^{-\frac{1}{2}} \cdot \left[e^{j \cdot \frac{-\pi}{aAB} \cdot (\tau - i)} \cdot e^{-1 \cdot \left(\frac{\tau - i}{aAB} \right)^2} \right]$

f_{S1_R2} (joint-free) $w\_DB_{i,\tau} := aDB^{-\frac{1}{2}} \cdot \left[e^{j \cdot \frac{-\pi}{aDB} \cdot (\tau - i)} \cdot e^{-1 \cdot \left(\frac{\tau - i}{aDB} \right)^2} \right]$

f_{S1_R1} (joint) $w\_DC_{i,\tau} := aDC^{-\frac{1}{2}} \cdot \left[e^{j \cdot \frac{-\pi}{aDC} \cdot (\tau - i)} \cdot e^{-1 \cdot \left(\frac{\tau - i}{aDC} \right)^2} \right]$

Wavelet transform

f_{S2_R1} (joint-free) $WAC_\tau := \sum_i \left(w\_AC_{i,\tau} \cdot AC_i \right)$

$WAC_\tau := \left| WAC_\tau \right|$

f_{S2_R2} **(joint)** $WAB_\tau := \sum_i \left(w\_AB_{i,\tau} \cdot AB_i \right)$

$WAB_\tau := \left| WAB_\tau \right|$

f_{S1_R2} (joint-free) $WDB_\tau := \sum_i \left(w\_DB_{i,\tau} \cdot DB_i \right)$

$WDB_\tau := \left| WDB_\tau \right|$

f_{S1_R1} (joint) $WDC_\tau := \sum_i \left(w\_DC_{i,\tau} \cdot DC_i \right)$

$WDC_\tau := \left| WDC_\tau \right|$

$f_{S2\text{-}R1}$ (joint-free) & $f_{S2\text{-}R2}$ (joint)

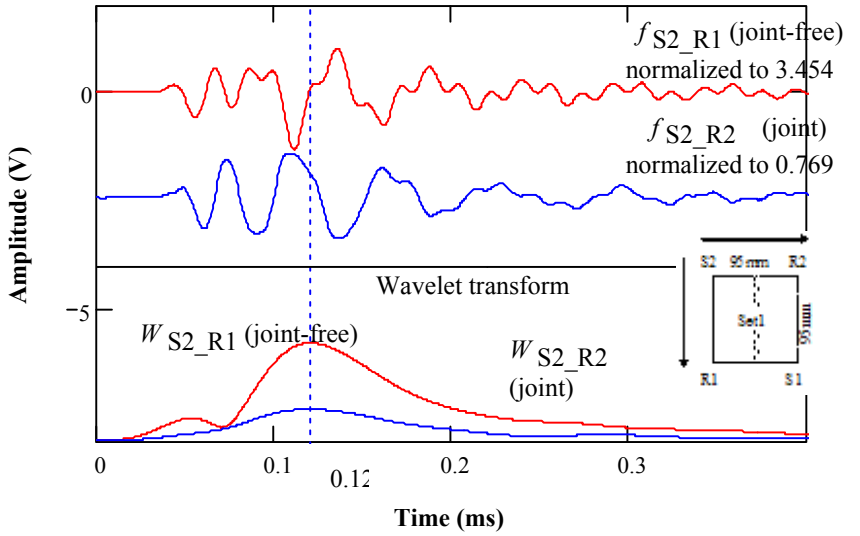

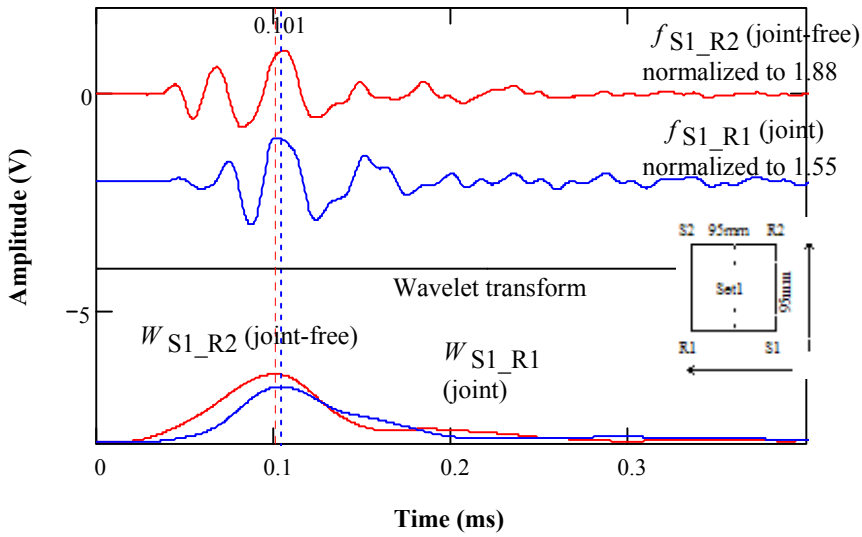

Amplitude ratio

$$\frac{\max(WAB)}{\max(WAC)} = 0.324 \qquad \frac{\max(WDC)}{\max(WDB)} = 0.816 \qquad \sqrt{\frac{\max(WAB)}{\max(WAC)}\frac{\max(WDC)}{\max(WDB)}} = 0.514$$

Wavelet transform - for dominat frequency in full signals of set 2, deifferent center frequencies for 4 signals defined by "aX"; Time shift by "τ".

$aAC2 := 42.67$ $\dfrac{1}{2 \cdot aAC2 \cdot 5 \cdot 10^{-4}} = 23.436$ kHz $aD2B := 39.3$ $\dfrac{1}{2 \cdot aD2B \cdot 5 \cdot 10^{-4}} = 25.445$ kHz

$aAB := 51.2$ $\dfrac{1}{2 \cdot aAB \cdot 5 \cdot 10^{-4}} = 19.531$ kHz $aD2C2 := 39.3$ $\dfrac{1}{2 \cdot aD2C2 \cdot 5 \cdot 10^{-4}} = 25.445$

Definition of Morlet wavelet $\tau := 1 .. N$

f_{S2_R3} (joint-free) $w\_AC2_{i,\tau} := aAC2 \cdot \left[e^{j \cdot \frac{-\pi}{aAC2} \cdot (\tau - i)} \cdot e^{-1 \cdot \left(\frac{\tau - i}{aAC2} \right)^2} \right]^{-\frac{1}{2}}$

f_{S2_R2} (joint) $w\_AB_{i,\tau} := aAB \cdot \left[e^{j \cdot \frac{-\pi}{aAB} \cdot (\tau - i)} \cdot e^{-1 \cdot \left(\frac{\tau - i}{aAB} \right)^2} \right]^{-\frac{1}{2}}$

f_{S3_R2} (joint-free) $w\_D2B_{i,\tau} := aD2B \cdot \left[e^{j \cdot \frac{-\pi}{aD2B} \cdot (\tau - i)} \cdot e^{-1 \cdot \left(\frac{\tau - i}{aD2B} \right)^2} \right]^{-\frac{1}{2}}$

f_{S3_R3} (joint) $w\_D2C2_{i,\tau} := aD2C2 \cdot \left[e^{j \cdot \frac{-\pi}{aD2C2} \cdot (\tau - i)} \cdot e^{-1 \cdot \left(\frac{\tau - i}{aD2C2} \right)^2} \right]^{-\frac{1}{2}}$

Wavelet transform

f_{S2_R3} (joint-free) $WAC2_\tau := \sum_i \left(w\_AC2_{i,\tau} \cdot AC2_i \right)$ f_{S2_R2} (joint) $WAB_\tau := \sum_i \left(w\_AB_{i,\tau} \cdot AB_i \right)$

$WAC2_\tau := \left| WAC2_\tau \right|$ $WAB_\tau := \left| WAB_\tau \right|$

f_{S3_R2} (joint-free) $WD2B_\tau := \sum_i \left(w\_D2B_{i,\tau} \cdot D2B_i \right)$ f_{S3_R3} (joint) $WD2C2_\tau := \sum_i \left(w\_D2C2_{i,\tau} \cdot D2C2_i \right)$

$WD2B_\tau := \left| WD2B_\tau \right|$ $WD2C2_\tau := \left| WD2C2_\tau \right|$

$f_{S2\text{-}R3}$ (joint-free) & $f_{S2\text{-}R2}$ (joint)

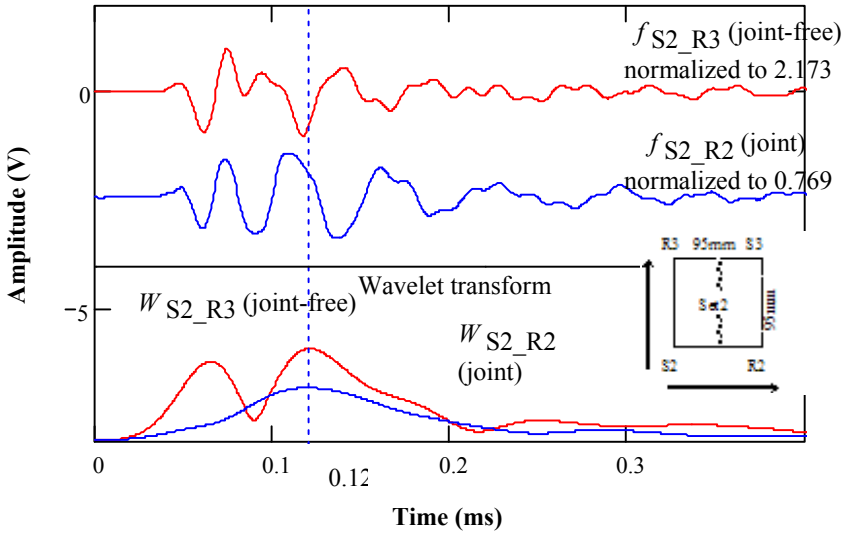

$f_{S3\text{-}R2}$ (joint-free) & $f_{S3\text{-}R3}$ (joint)

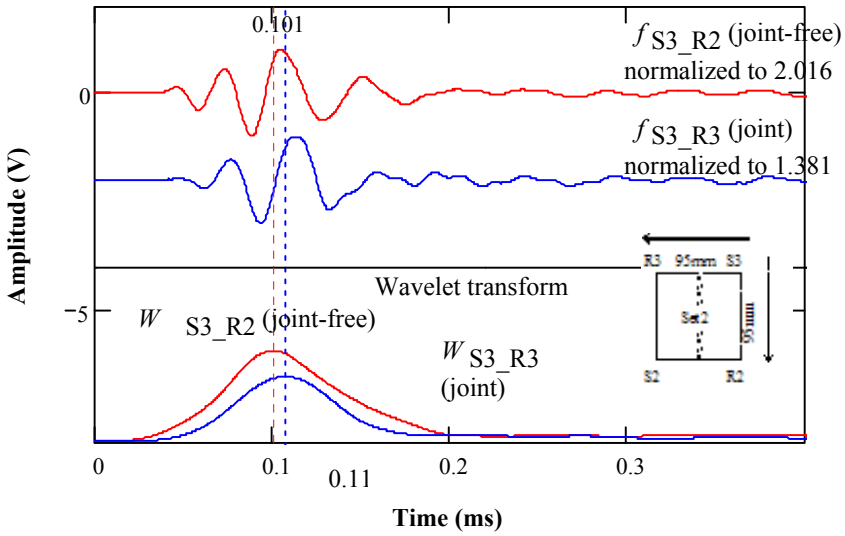

Amplitude ratio

$$\frac{\max(WAB)}{\max(WAC2)} = 0.575 \qquad \frac{\max(WD2C2)}{\max(WD2B)} = 0.714 \qquad \sqrt{\frac{\max(WAB)}{\max(WAC2)}\frac{\max(WD2C2)}{\max(WD2B)}} = 0.641$$

Window the P-wave portion of the time signals - set 1:

Parameter $p := 1 .. 12$ $\omega o_p := 2\pi \cdot 16.5$ $\omega o_5 := 2\pi \cdot 13.5$ $\omega o_7 := 2\pi \cdot 16.5$

$\omega o_{11} := 2\pi \cdot 15.5$ $\omega o_8 := 2\pi \cdot 17.5$ $\omega o_9 := 2\pi \cdot 14$ $\omega o_{10} := 2\pi \cdot 15.5$

Arrival Time (AT) of the signal:

$AT := (\ 0.02 \quad 0.042 \quad 0.015 \quad 0.045 \quad 0.03 \quad 0.032 \quad 0.037 \quad 0.032 \quad 0.033 \quad 0.033 \quad 0.035 \quad 0.02 \quad 0\ )^T$

$tp_p := ceil\left(\left(\frac{AT_p}{0.0005}\right)\right) \cdot 0.000$

$wp(t, \omega o) := \begin{cases} 10\left|\cos(\omega o \cdot t)^{10} - 1\right| & \text{if } 0 \le t \le \frac{\pi}{\omega o} \\ 0 & \text{otherwise} \end{cases}$

Define **Time Window** (Twind) to amplify the arrival of the signals:

$$Twind := \left| \begin{array}{l} \text{for } p \in 1 .. 12 \\ \quad \text{for } i \in 1 .. N \\ \quad\quad ampl_{i,p} \leftarrow wp\left(i \cdot 0.0005 - tp_p, \omega o_p\right) \\ ampl \end{array} \right.$$

Fourier Transform of the Windowed Signals: $FTW^{\langle p \rangle} := CFFT\left(\overrightarrow{\left(Twind^{\langle p \rangle} \cdot signal^{\langle p \rangle}\right)}\right)$

Windowed Signals: $P_{i,p} := Twind_{i,p} \cdot signal_{i,p}$

Spectrum Area: $MA_{u,p} := \sum_{u=1}^{u} \frac{\left|FTW_{u,p}\right|}{N \cdot 0.001}$

$f_{S2\text{-}R1}$ (joint-free) & $f_{S2\text{-}R2}$ (joint)

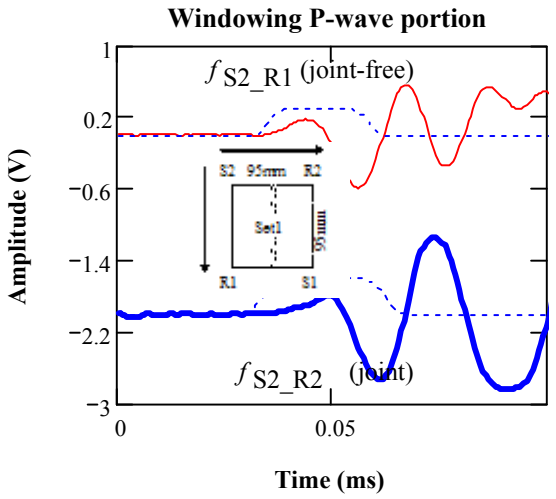

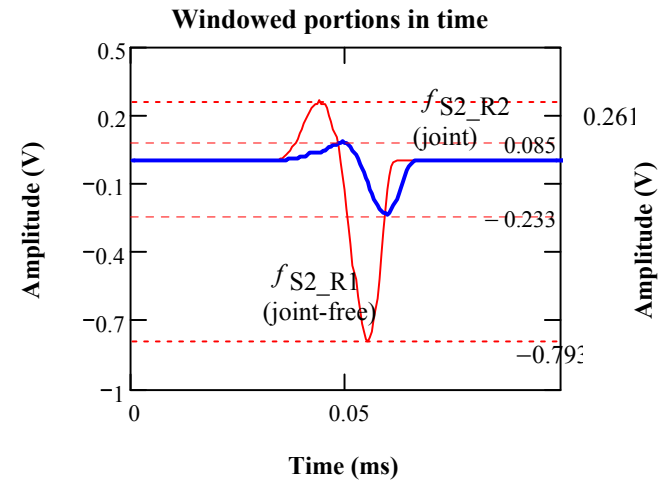

$f_{S1\text{-}R2}$ (joint-free) & $f_{S1\text{-}R1}$ (joint)

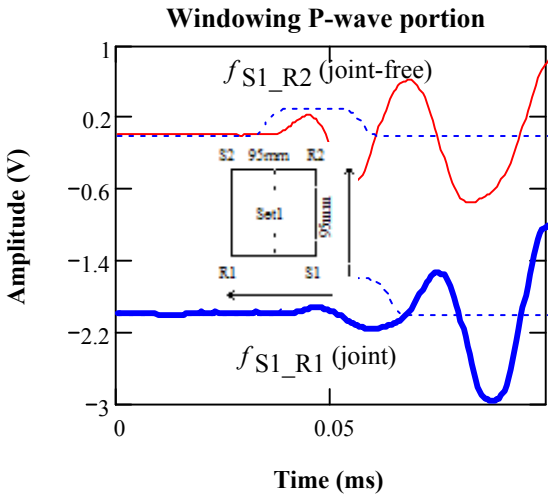

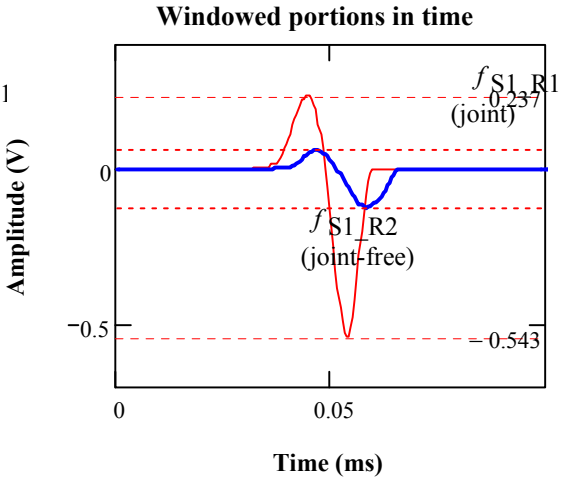

Transmission Coefficient (TC)

$$TC_u := \sqrt{\frac{|FTW_{u,5}| \cdot |FTW_{u,7}|}{|FTW_{u,6}| \cdot |FTW_{u,8}|}}$$

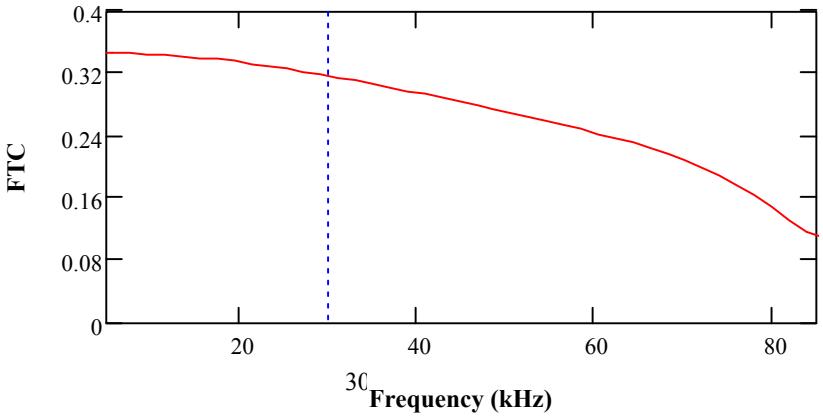

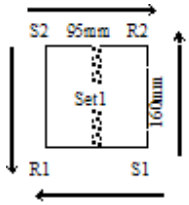

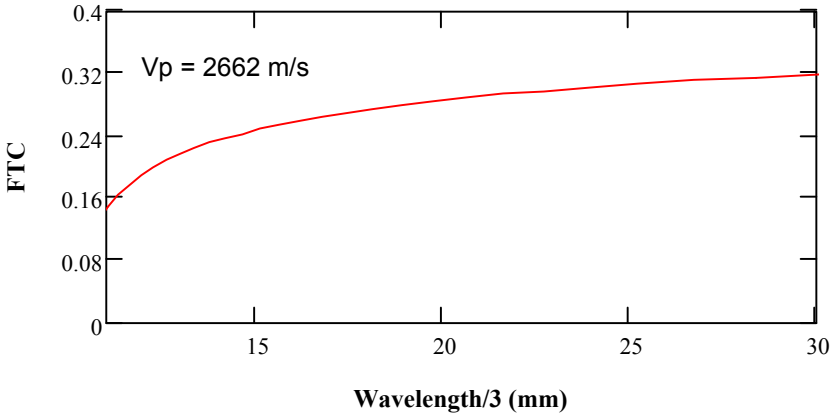

Damping ratio @ 36kHz

$fre := 36.13$

Damping ratio Based on Spetrum Area

$f_{S2\text{-}R1}$ (joint-free) & $f_{S2\text{-}R2}$ (joint)	$\left(\frac{2\pi fre \cdot 95}{2775}\right)^{-1} \cdot \ln\left(\frac{1}{MM1}\right) = 0.152$	$\left(\frac{2\pi fre \cdot 95}{2775}\right)^{-1} \cdot \ln\left(\frac{MA_{300,6}}{MA_{300,5}}\right) = 0.157$
$f_{S1\text{-}R2}$ (joint-free) & $f_{S1\text{-}R1}$ (joint)	$\left(\frac{2\pi fre \cdot 95}{2775}\right)^{-1} \cdot \ln\left(\frac{1}{MM2}\right) = 0.156$	$\left(\frac{2\pi fre \cdot 95}{2775}\right)^{-1} \cdot \ln\left(\frac{MA_{300,8}}{MA_{300,7}}\right) = 0.182$
For the set	$\left(\frac{2\pi fre \cdot 95}{2775}\right)^{-1} \cdot \ln\left(\sqrt{\frac{1}{MM2 \cdot MM1}}\right) = 0.154$	$\sqrt{MM2 \cdot MM1} = 0.302$

Damping analysis for full signals:

$$\Delta\Phi 1_u := \left(\frac{2\pi \, f1_u \cdot 95}{2.775 \times 10^3} \right)^{-1}$$

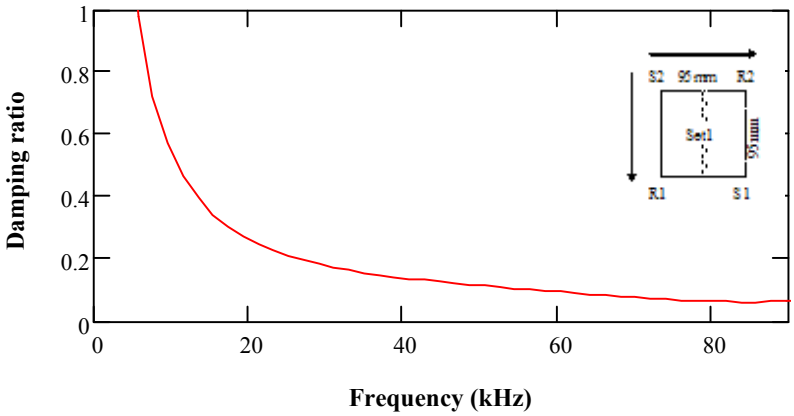

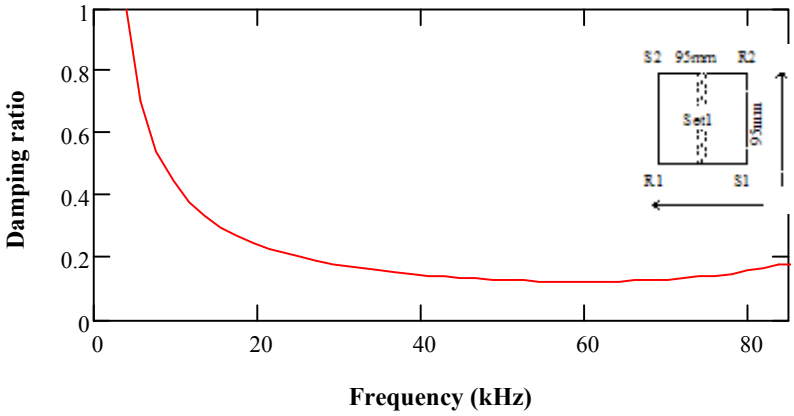

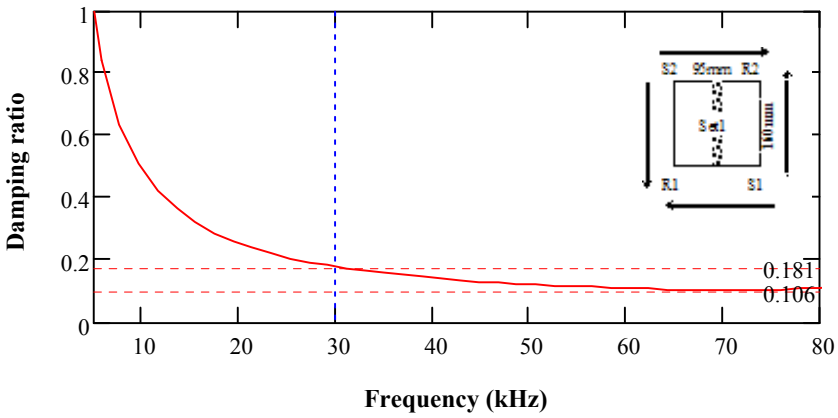

Damping analysis for full signals - using spectrum area:

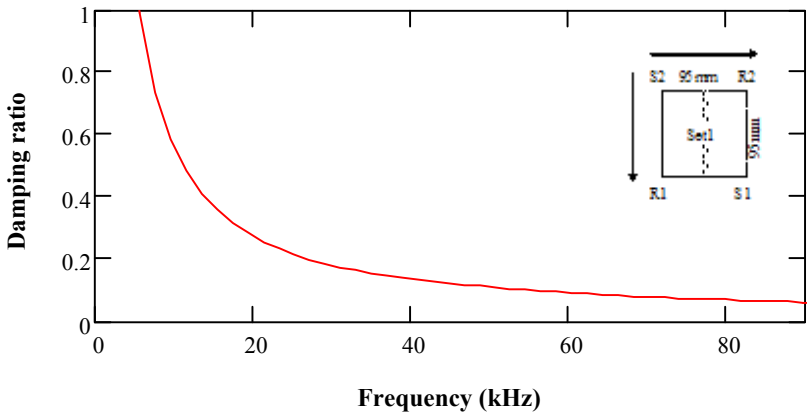

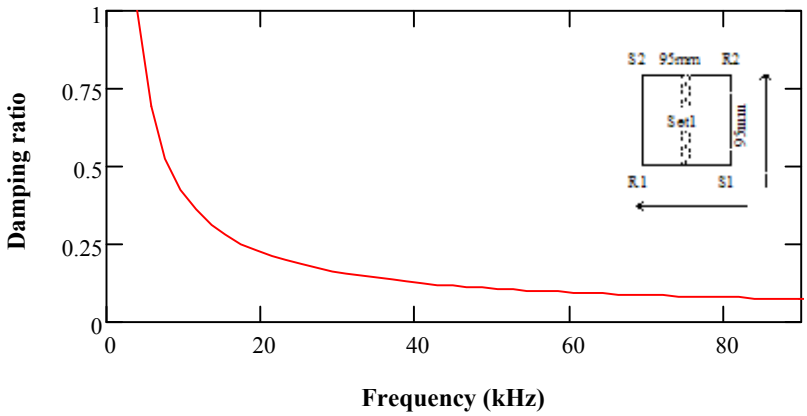

Window the R-wave of the time signals:

Parameter $p := 1 .. 12$ $\omega o_p := 2\pi \cdot 24.5$ $\omega o_5 := 2\pi \cdot 14$ $\omega o_7 := 2\pi \cdot 17$

$\omega o_{11} := 2\pi \cdot 15.5$ $\omega o_8 := 2\pi \cdot 14$ $\omega o_9 := 2\pi \cdot 14$ $\omega o_{10} := 2\pi \cdot 15.5$

Arrival Time (AT) of the signal:

$AT := (\ 0.02 \quad 0.042 \quad 0.015 \quad 0.045 \quad 0.066 \quad 0.061 \quad 0.066 \quad 0.06 \quad 0.033 \quad 0.033 \quad 0.035 \quad 0.02 \quad 0\ )^T$

$tp_p := ceil\left(\left(\frac{AT_p}{0.0005}\right)\right) \cdot 0.000$

$$wp(t, \omega o) := \begin{cases} 10\left|\cos(\omega o \cdot t)^{10} - 1\right| & \text{if } 0 \le t \le \frac{\pi}{\omega o} \\ 0 & \text{otherwise} \end{cases}$$

Define **Time Window** (Twind) to amplify the arrival of the signals:

$$Twind := \left| \begin{array}{l} \text{for } p \in 1 .. 12 \\ \quad \text{for } i \in 1 .. N \\ \quad\quad ampl_{i,p} \leftarrow wp\left(i \cdot 0.0005 - tp_p, \omega o_p\right) \\ ampl \end{array} \right.$$

Fourier Transform of the Windowed Signals: $FTW^{\langle p \rangle} := CFFT\left(\overrightarrow{\left(Twind^{\langle p \rangle} \cdot signal^{\langle p \rangle}\right)}\right)$

Windowed Signals: $P_{i,p} := Twind_{i,p} \cdot signal_{i,p}$

Spectrum Area: $MA_{u,p} := \sum_{u=1}^{u} \frac{\left|FTW_{u,p}\right|}{N \cdot 0.001}$

$f_{S2\text{-}R1}$ (joint-free) & $f_{S2\text{-}R2}$ (joint)

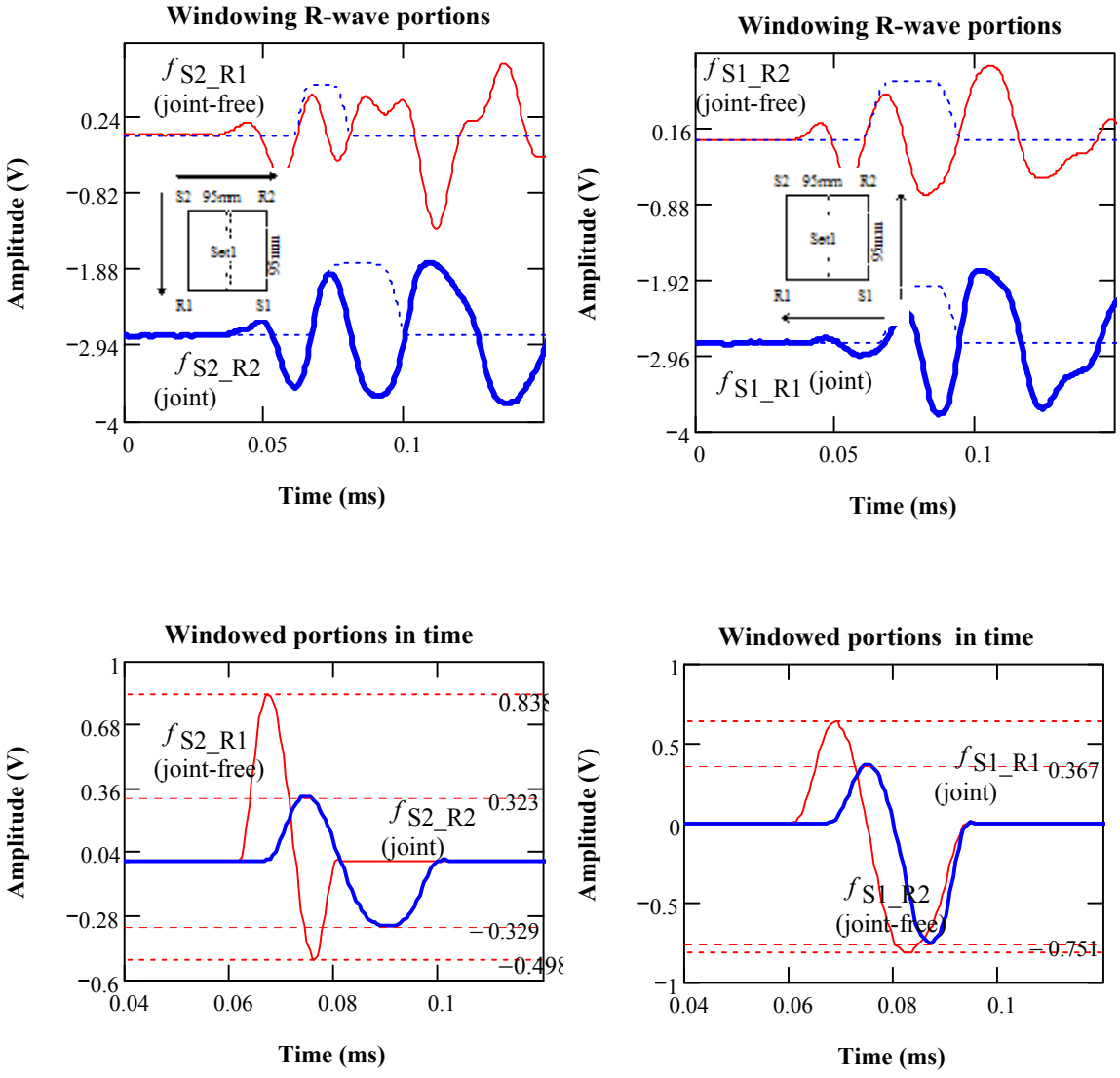

Transmission Coefficient (TC)

$$TC_u := \sqrt{\frac{|FTW_{u,5}| \cdot |FTW_{u,7}|}{|FTW_{u,6}| \cdot |FTW_{u,8}|}}$$

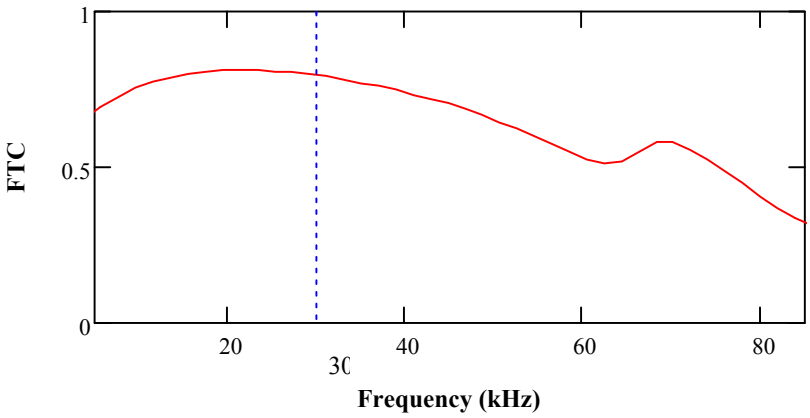

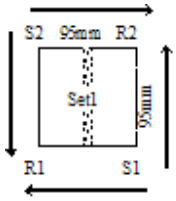

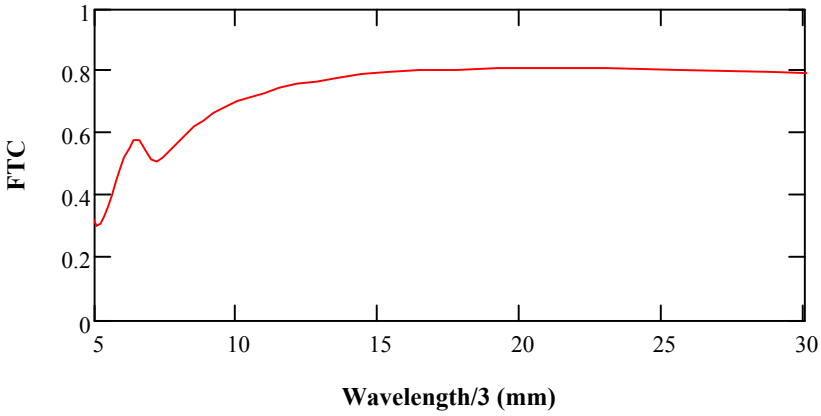

Damping ratio @ 36kHz

$fre := 35.64$

$f_{S2\text{-}R1}$ (joint-free) & $f_{S2\text{-}R2}$ (joint)

$$\left(\frac{2\pi fre \cdot 95}{1352}\right)^{-1} \cdot \ln\left(\frac{1}{MM1}\right) = 0.012$$

$f_{S1\text{-}R2}$ (joint-free) & $f_{S1\text{-}R1}$ (joint)

$$\left(\frac{2\pi fre \cdot 95}{1352}\right)^{-1} \cdot \ln\left(\frac{1}{MM2}\right) = 0.032$$

For the set

$$\left(\frac{2\pi fre \cdot 95}{1352}\right)^{-1} \cdot \ln\left(\sqrt{\frac{1}{MM2 \cdot MM1}}\right) = 0.022$$

Damping analysis for R-wave signals:

$$\Delta\Phi 1_u := \left(\frac{2\pi f1_u \cdot 95}{2.775 \times 10^3} \right)^{-1}$$

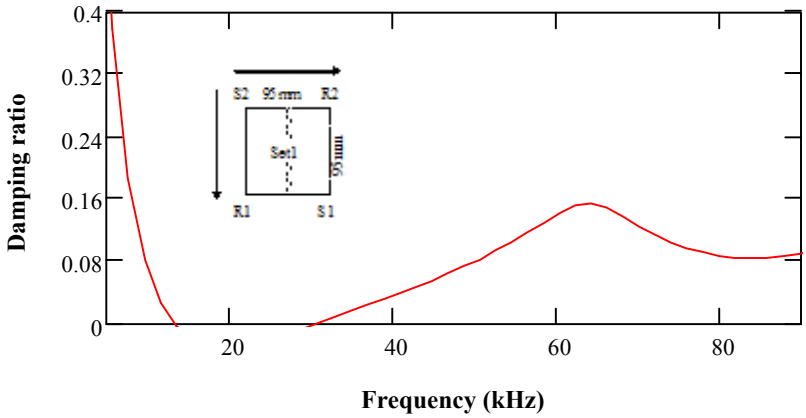

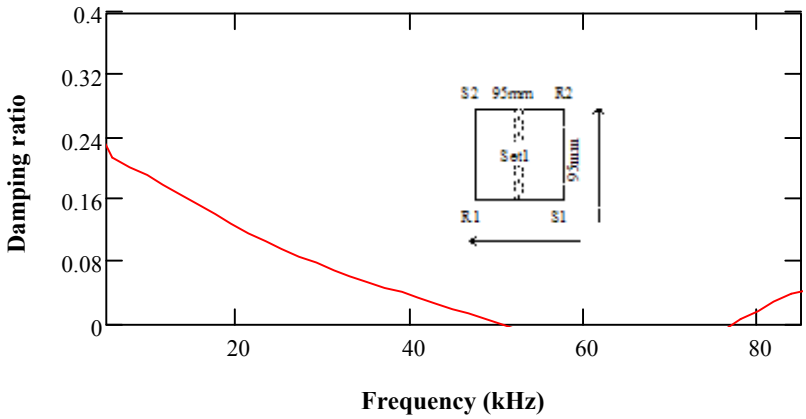

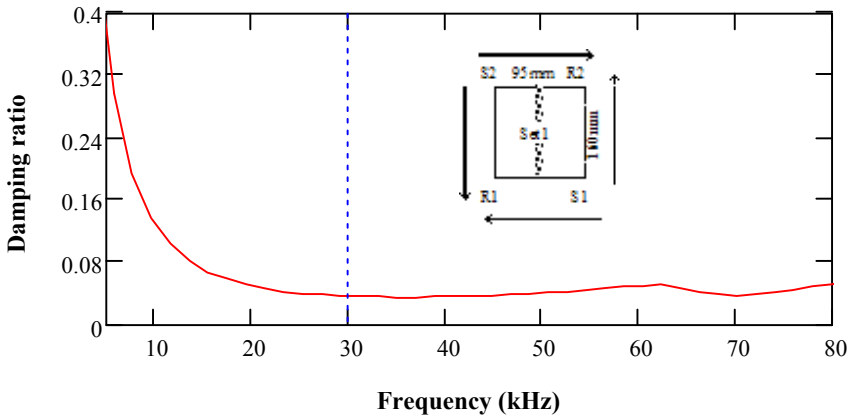

Damping analysis for R-waves - using spectrum area:

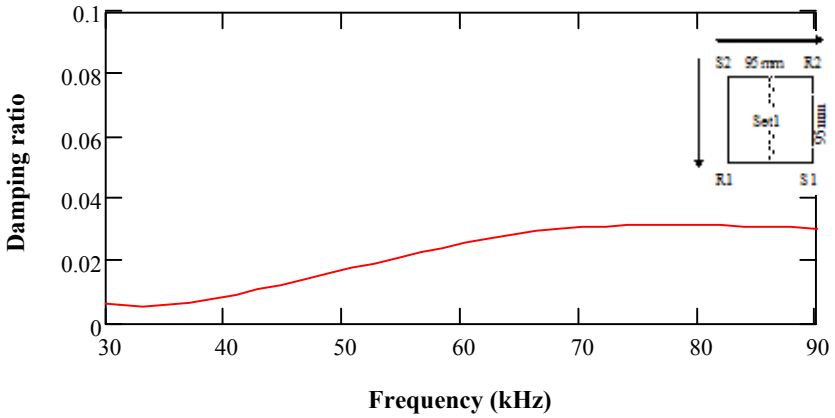

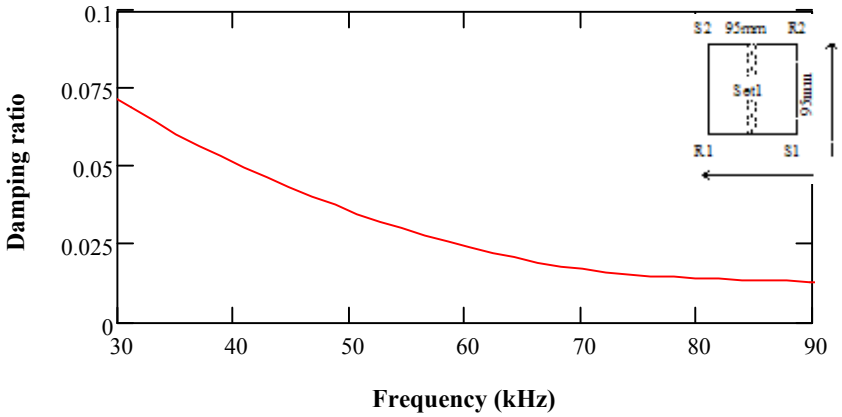

Wavelet transform - for dominat frequency in P-wave portion of set 1, frequency for 4 signals defined by "aX"; Time shift by "τ".

$aAC := 28.4$ $\frac{1}{2 \cdot aAC \cdot 5 \cdot 10^{-4}} = 35.162$ kHz $aDB := 23.27$ $\frac{1}{2 \cdot aDB \cdot 5 \cdot 10^{-4}} = 42.9$

$aAB := 30.12$ $\frac{1}{2 \cdot aAB \cdot 5 \cdot 10^{-4}} = 33.201$ kHz $aDC := 30.12$ $\frac{1}{2 \cdot aDC \cdot 5 \cdot 10^{-4}} = 33.2$

Definition of Morlet wavelet $\tau := 1 .. N$

f_{S2_R1} (joint-free) $w\_AC_{i,\tau} := aAC \cdot e^{-\frac{1}{2} \cdot \left[j \cdot \frac{-\pi}{aAC} \cdot (\tau - i) - 1 \cdot \left(\frac{\tau - i}{aAC} \right)^2 \right]}$

f_{S2_R2} **(joint)** $w\_AB_{i,\tau} := aAB \cdot e^{-\frac{1}{2} \cdot \left[j \cdot \frac{-\pi}{aAB} \cdot (\tau - i) - 1 \cdot \left(\frac{\tau - i}{aAB} \right)^2 \right]}$

f_{S1_R2} (joint-free) $w\_DB_{i,\tau} := aDB \cdot e^{-\frac{1}{2} \cdot \left[j \cdot \frac{-\pi}{aDB} \cdot (\tau - i) - 1 \cdot \left(\frac{\tau - i}{aDB} \right)^2 \right]}$

f_{S1_R1} (joint) $w\_DC_{i,\tau} := aDC \cdot e^{-\frac{1}{2} \cdot \left[j \cdot \frac{-\pi}{aDC} \cdot (\tau - i) - 1 \cdot \left(\frac{\tau - i}{aDC} \right)^2 \right]}$

Wavelet transform

f_{S2_R1} (joint-free) $WAC_\tau := \sum_i \left(w\_AC_{i,\tau} \cdot AC_i \right)$

$WAC_\tau := \left| WAC_\tau \right|$

f_{S2_R2} **(joint)** $WAB_\tau := \sum_i w\_AB_{i,\tau} \cdot$

$WAB_\tau := \left| WAB_\tau \right|$

f_{S1_R2} (joint-free) $WDB_\tau := \sum_i \left(w\_DB_{i,\tau} \cdot DB_i \right)$

$WDB_\tau := \left| WDB_\tau \right|$

f_{S1_R1} (joint) $WDC_\tau := \sum_i w\_DC_{i,\tau} \cdot$

$WDC_\tau := \left| WDC_\tau \right|$

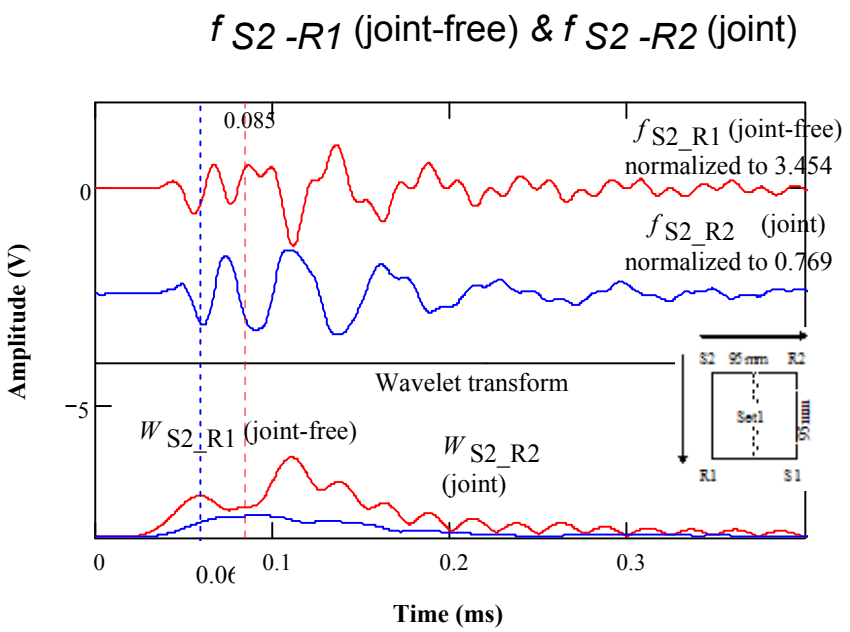

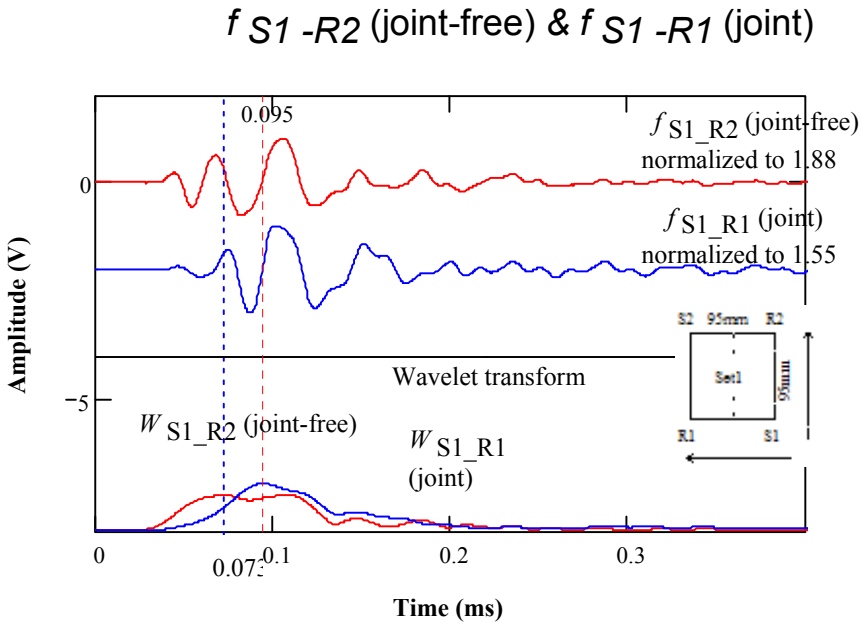

Amplitude ratio

$$\frac{\max(WAB)}{5-4.363} = 0.258 \qquad \frac{\max(WDC)}{\max(WDB)} = 1.314 \qquad \sqrt{\frac{\max(WAB)}{5-4.363}\,\frac{\max(WDC)}{\max(WDB)}} = 0.583$$

Wavelet transform - for dominat frequency in R-wave portion of set 1, center frequencyfor 4 signals defined by "aX"; Time shift by "τ".

aAC := 20.48 $\frac{1}{2 \cdot aAC \cdot 5 \cdot 10^{-4}} = 48.828$ kHz aDB := 34.13 $\frac{1}{2 \cdot aDB \cdot 5 \cdot 10^{-4}} = 29.3$

aAB := 34.13 $\frac{1}{2 \cdot aAB \cdot 5 \cdot 10^{-4}} = 29.3$ kHz aDC := 28.44 $\frac{1}{2 \cdot aDC \cdot 5 \cdot 10^{-4}} = 35.1$

Definition of Morlet wavelet

$\tau := 1 .. N$

f_{S2_R1} (joint-free) $w\_AC_{i,\tau} := aAC^{-\frac{1}{2}} \cdot \left[e^{j \cdot \frac{-\pi}{aAC} \cdot (\tau - i)} \cdot e^{-1 \cdot \left(\frac{\tau - i}{aAC} \right)^2} \right]$

f_{S2_R2} **(joint)** $w\_AB_{i,\tau} := aAB^{-\frac{1}{2}} \cdot \left[e^{j \cdot \frac{-\pi}{aAB} \cdot (\tau - i)} \cdot e^{-1 \cdot \left(\frac{\tau - i}{aAB} \right)^2} \right]$

f_{S1_R2} (joint-free) $w\_DB_{i,\tau} := aDB^{-\frac{1}{2}} \cdot \left[e^{j \cdot \frac{-\pi}{aDB} \cdot (\tau - i)} \cdot e^{-1 \cdot \left(\frac{\tau - i}{aDB} \right)^2} \right]$

f_{S1_R1} (joint) $w\_DC_{i,\tau} := aDC^{-\frac{1}{2}} \cdot \left[e^{j \cdot \frac{-\pi}{aDC} \cdot (\tau - i)} \cdot e^{-1 \cdot \left(\frac{\tau - i}{aDC} \right)^2} \right]$

Wavelet transform

f_{S2_R1} (joint-free) $WAC_\tau := \sum_i \left(w\_AC_{i,\tau} \cdot AC_i \right)$

$WAC_\tau := \left| WAC_\tau \right|$

f_{S2_R2} **(joint)** $WAB_\tau := \sum_i \left(w\_AB_{i,\tau} \cdot \right.$

$WAB_\tau := \left| WAB_\tau \right|$

f_{S1_R2} (joint-free) $WDB_\tau := \sum_i \left(w\_DB_{i,\tau} \cdot DB_i \right)$

$WDB_\tau := \left| WDB_\tau \right|$

f_{S1_R1} (joint) $WDC_\tau := \sum_i \left. \right) w\_DC_{i,\tau} \cdot D$

$WDC_\tau := \left| WDC_\tau \right|$

$f_{S2\text{-}R1}$ (joint-free) & $f_{S2\text{-}R2}$ (joint)

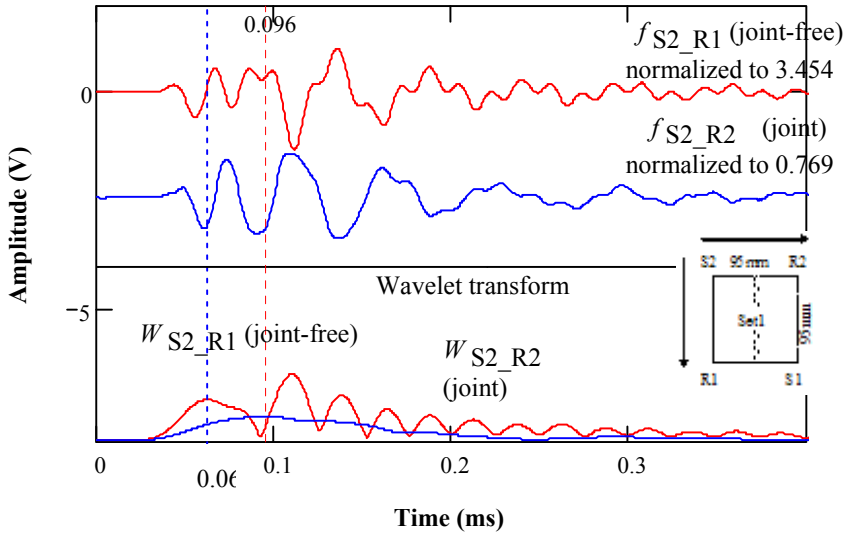

$f_{S1\text{-}R2}$ (joint-free) & $f_{S1\text{-}R1}$ (joint)

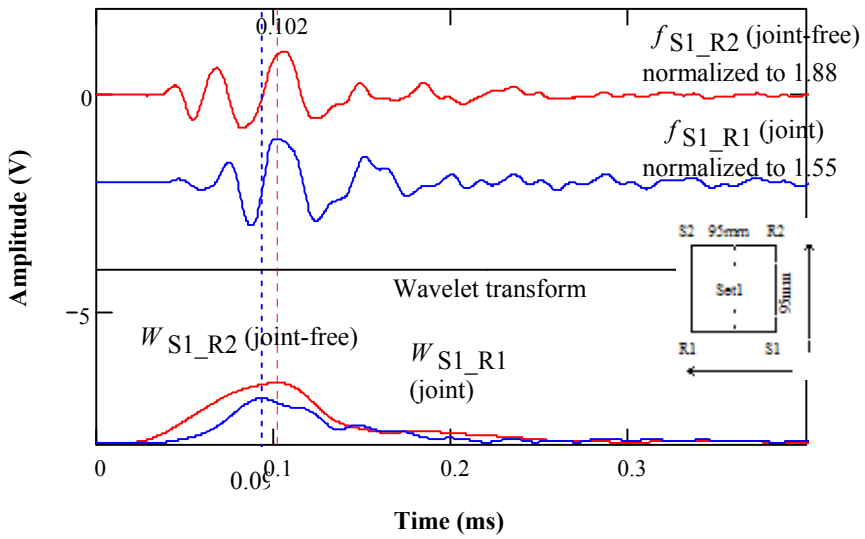

Amplitude ratio

$$\frac{\max(WAB)}{5-4.366} = 0.297 \qquad \frac{\max(WDC)}{\max(WDB)} = 0.745 \qquad \sqrt{\frac{\max(WAB)}{5-4.366}\,\frac{\max(WDC)}{\max(WDB)}} = 0.47$$

Window the P-wave portion of the time signals-set 2:

Parameter $p := 1 .. 12$ $\omega o_p := 2\pi \cdot 16.5$ $\omega o_5 := 2\pi \cdot 13.5$ $\omega o_7 := 2\pi \cdot 16.5$

$\omega o_{11} := 2\pi \cdot 15.5$ $\omega o_8 := 2\pi \cdot 17.5$ $\omega o_9 := 2\pi \cdot 14$ $\omega o_{10} := 2\pi \cdot 15.5$

Arrival Time (AT) of the signal:

$AT := (\ 0.02 \quad 0.042 \quad 0.015 \quad 0.045 \quad 0.03 \quad 0.032 \quad 0.037 \quad 0.032 \quad 0.033 \quad 0.033 \quad 0.035 \quad 0.02 \quad 0\ )^T$

$tp_p := ceil\left(\left(\frac{AT_p}{0.0005}\right)\right) \cdot 0.000$

$$wp(t, \omega o) := \begin{cases} 10\left|\cos(\omega o \cdot t)^{10} - 1\right| & \text{if } 0 \le t \le \frac{\pi}{\omega o} \\ 0 & \text{otherwise} \end{cases}$$

Define **Time Window** (Twind) to amplify the arrival of the signals:

$$Twind := \left| \begin{array}{l} \text{for } p \in 1 .. 12 \\ \quad \text{for } i \in 1 .. N \\ \quad\quad ampl_{i,p} \leftarrow wp\left(i \cdot 0.0005 - tp_p, \omega o_p\right) \\ ampl \end{array} \right.$$

Fourier Transform of the Windowed Signals: $FTW^{\langle p \rangle} := CFFT\left(\overrightarrow{\left(Twind^{\langle p \rangle} \cdot signal^{\langle p \rangle}\right)}\right)$

Windowed Signals: $P_{i,p} := Twind_{i,p} \cdot signal_{i,p}$

Spectrum Area $MA_{u,p} := \sum_{u=1}^{u} \frac{\left|FTW_{u,p}\right|}{N \cdot 0.001}$

f S2 -R3 (joint-free) & *f S2 -R2* (joint)

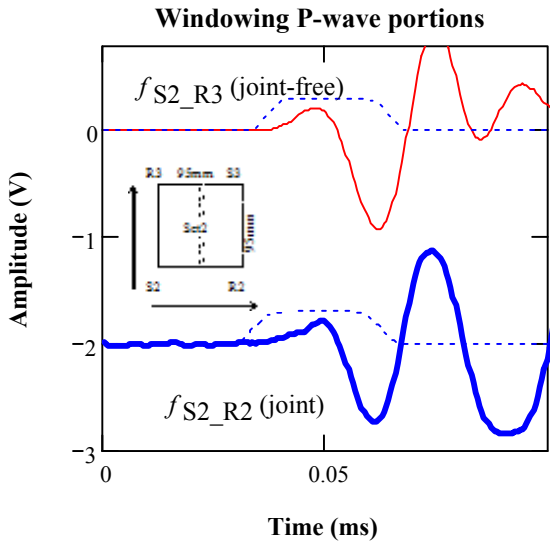

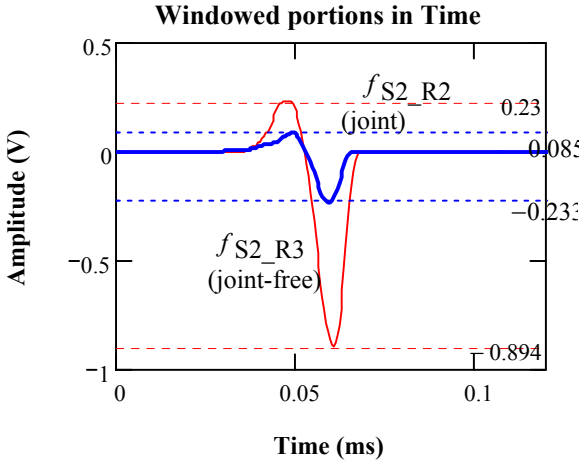

f S3 -R2 (joint-free) & *f S3 -R3* (joint)

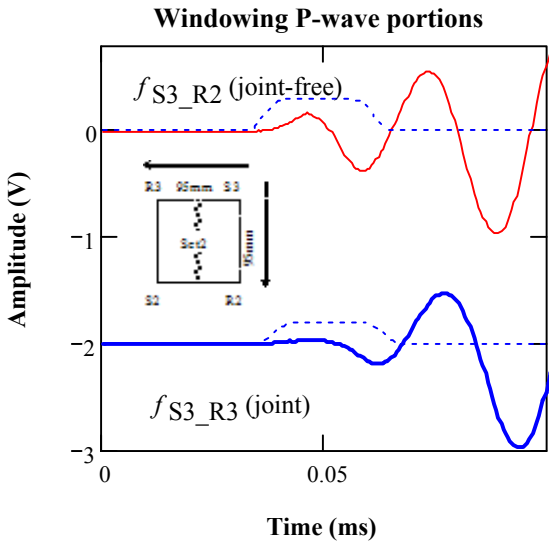

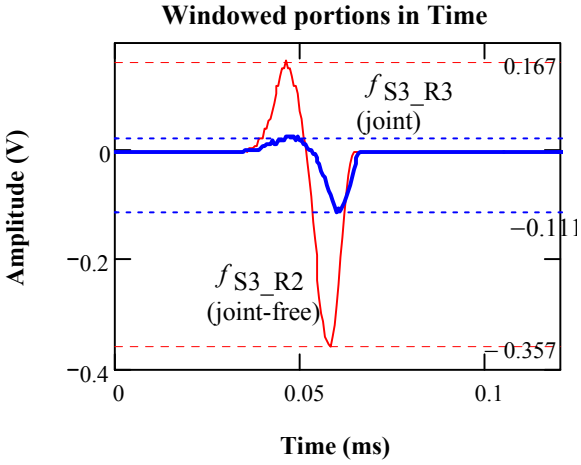

Transmission Coefficient (TC)

$$TC_u := \sqrt{\frac{|FTW_{u,5}| \cdot |FTW_{u,11}|}{|FTW_{u,9}| \cdot |FTW_{u,10}|}}$$

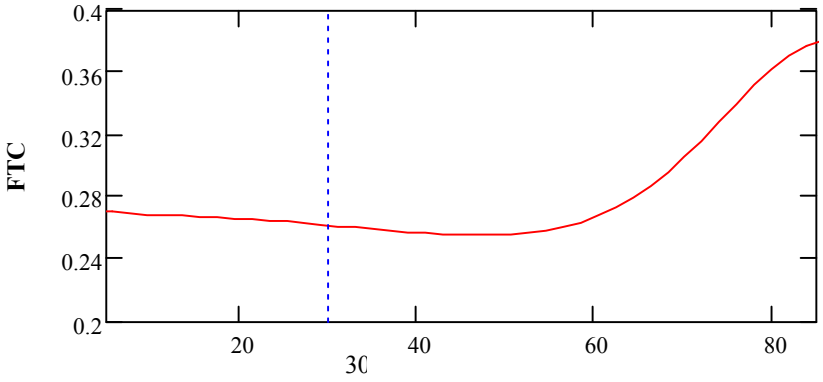

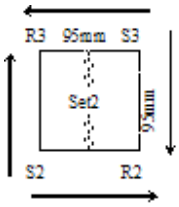

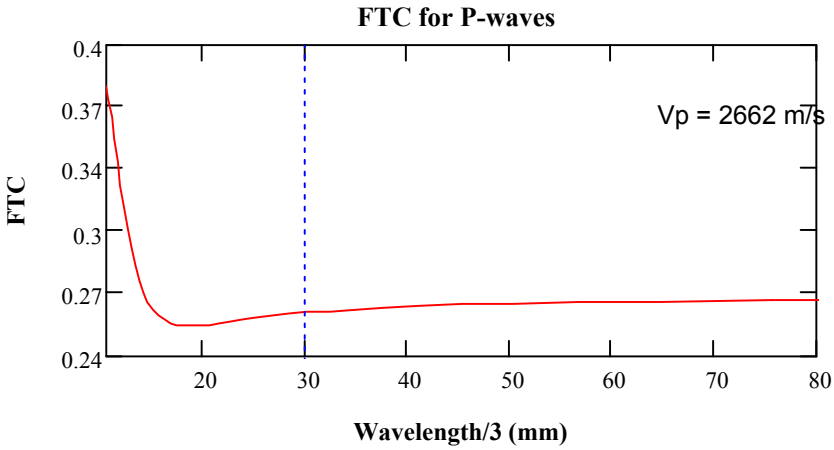

Damping ratio @ 33kHz

$fre := 32.71$

$f_{S2\text{-}R3}$ (joint-free) & $f_{S2\text{-}R2}$ (joint)

$$\left(\frac{2\pi fre \cdot 95}{2775}\right)^{-1} \cdot \ln\left(\frac{1}{MM1}\right) = 0.2$$

$f_{S3\text{-}R2}$ (joint-free) & $f_{S3\text{-}R3}$ (joint)

$$\left(\frac{2\pi fre \cdot 95}{2775}\right)^{-1} \cdot \ln\left(\frac{1}{MM2}\right) = 0.186$$

For the set

$$\left(\frac{2\pi fre \cdot 95}{2775}\right)^{-1} \cdot \ln\left(\sqrt{\frac{1}{MM2 \cdot MM1}}\right) = 0.193$$

Damping analysis for P-waves:

$$\Delta\Phi 1_u := \left(\frac{2\pi f1_u \cdot 95}{2.775 \times 10^3} \right)^{-1}$$

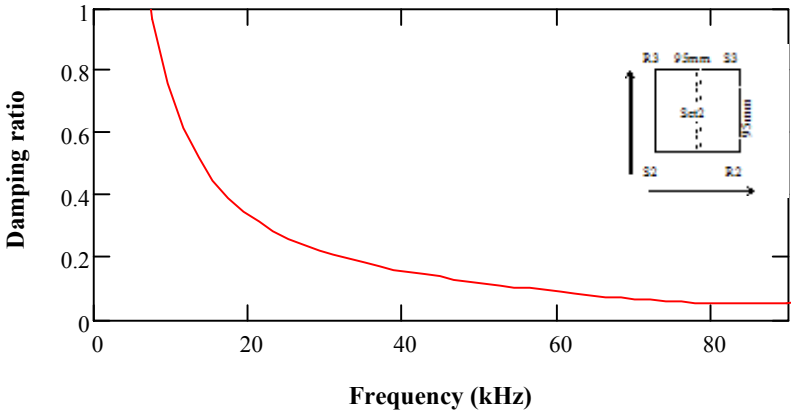

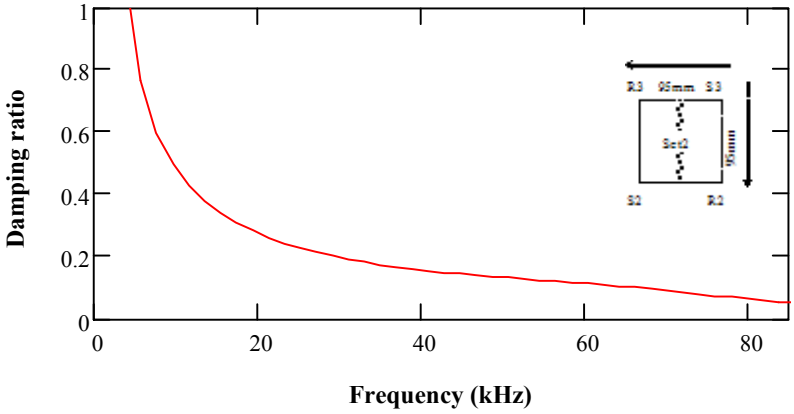

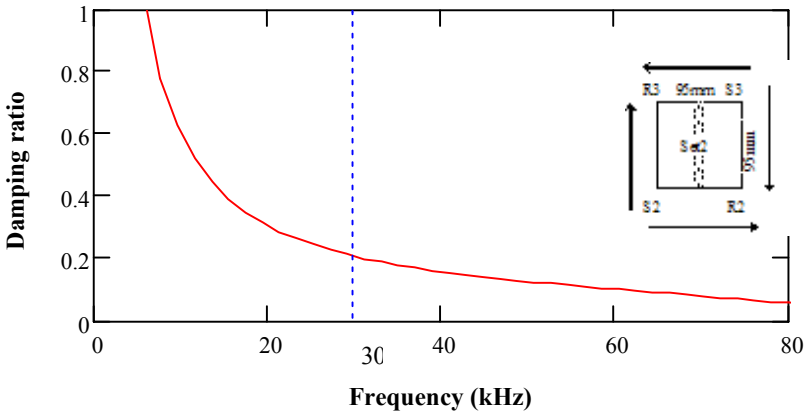

Damping analysis for P-waves - using spectrum area:

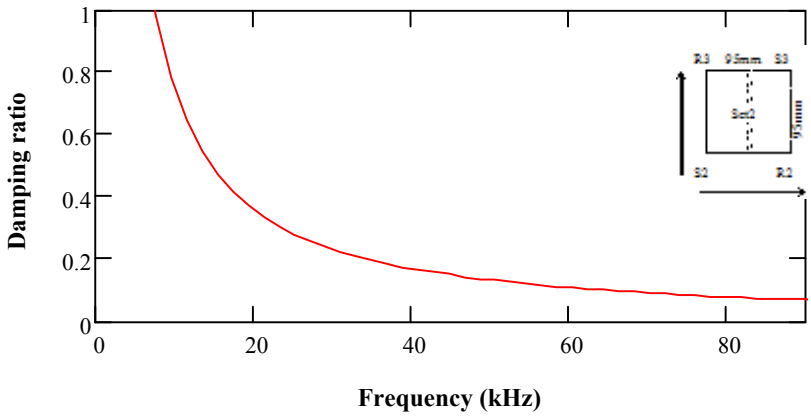

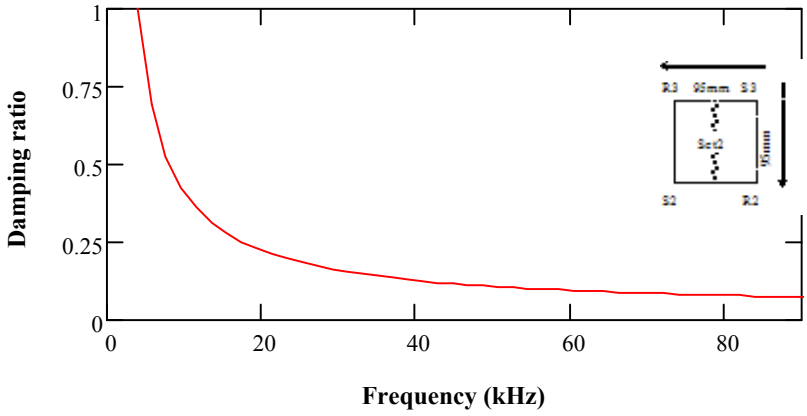

Original time signals analysis --
Window the 2 peaks of the original time signals of the set 2:

Parameter $p := 1 .. 12$ $\omega o_9 := 2\pi \cdot 9.8$ $\omega o_{10} := 2\pi \cdot 10.3$ $\omega o_5 := 2\pi \cdot 9.2$ $\omega o_{11} := 2\pi \cdot 9.9$

Arrival Time (AT) of the signal:

$AT := (\ 0.02 \quad 0.042 \quad 0.015 \quad 0.045 \quad 0.03 \quad 0.032 \quad 0.037 \quad 0.032 \quad 0.033 \quad 0.033 \quad 0.035 \quad 0.02 \quad 0\ )^T$

$tp_p := ceil\left(\left(\frac{AT_p}{0.0005}\right)\right) \cdot 0.000$

$$wp(t, \omega o) := \begin{cases} 10\left|\cos(\omega o \cdot t)^{20} - 1\right| & \text{if } 0 \le t \le \frac{\pi}{\omega o} \\ 0 & \text{otherwise} \end{cases}$$

Define **Time Window** (Twind) to amplify the arrival of the signals:

$$Twind := \left| \begin{array}{l} \text{for } p \in 1 .. 12 \\ \quad \text{for } i \in 1 .. N \\ \quad\quad ampl_{i,p} \leftarrow wp\left(i \cdot 0.0005 - tp_p, \omega o_p\right) \\ ampl \end{array} \right.$$

Fourier Transform of the Windowed Signals: $FTW^{\langle p \rangle} := CFFT\left(\overrightarrow{\left(Twind^{\langle p \rangle} \cdot signal^{\langle p \rangle}\right)}\right)$

Windowed Signals: $P_{i,p} := Twind_{i,p} \cdot signal_{i,p}$

Spectrum Area $MA_{u,p} := \sum_{u=1}^{u} \frac{\left|FTW_{u,p}\right|}{N \cdot 0.001}$

Damping analysis for full signals:

$$\Delta\Phi 1_u := \left(\frac{2\pi f1_u \cdot 95}{1.352 \times 10^3} \right)^{-1}$$

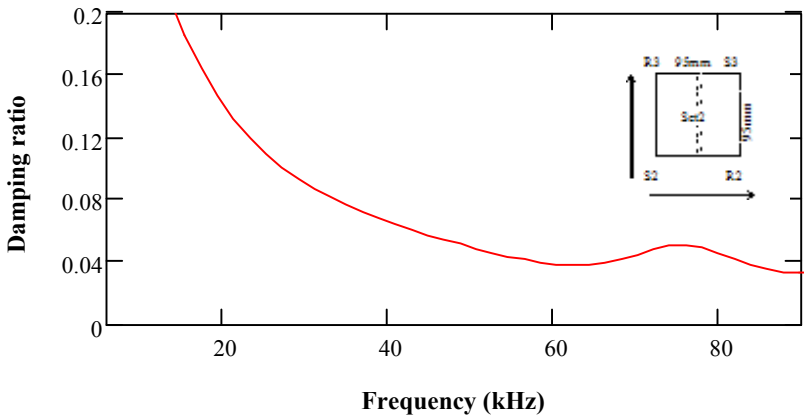

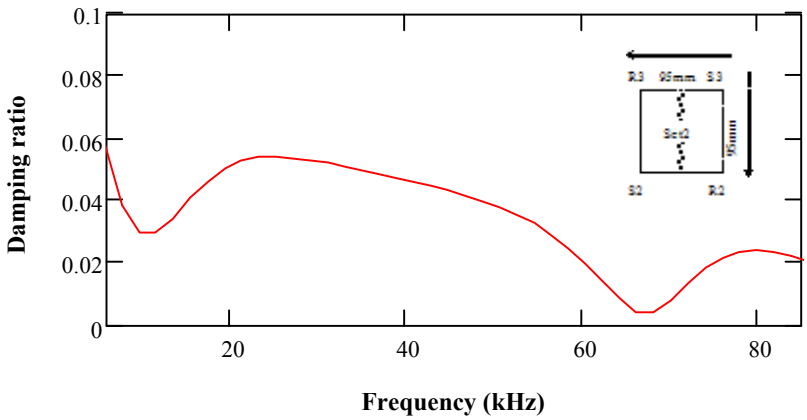

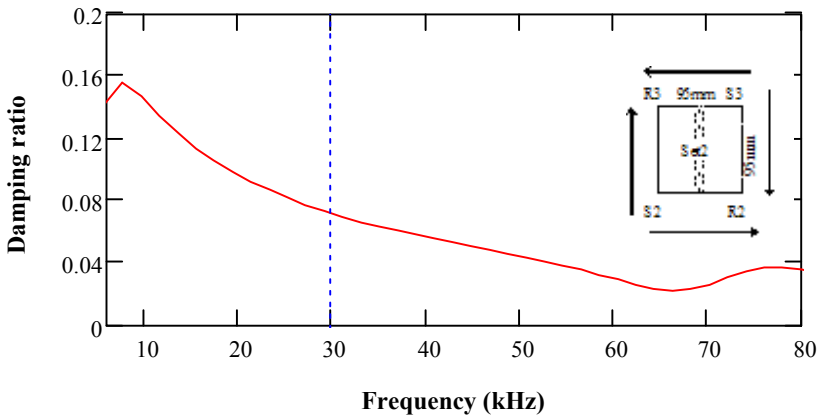

Damping analysis for R-waves - using spectrum area:

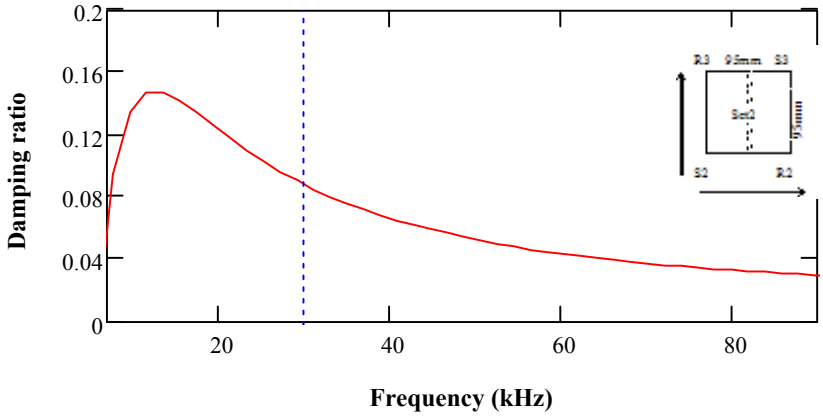

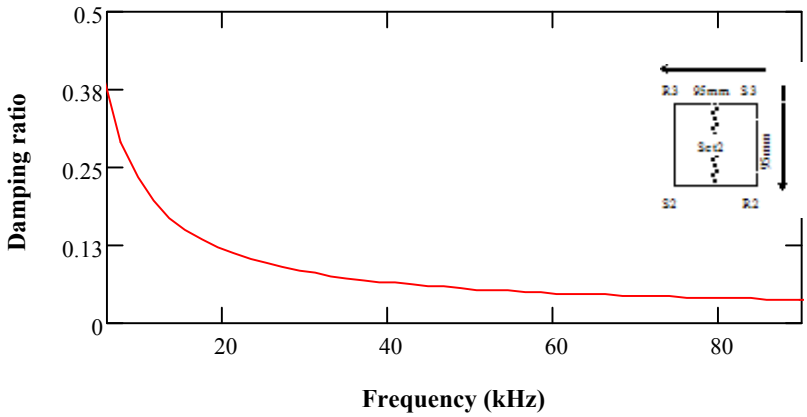

Original signal analysis --
Window the front part of the original time signals of the set 2:

Parameter $p := 1 .. 11$

$AT := (\ 0.02 \quad 0.042 \quad 0.015 \quad 0.045 \quad 0.053 \quad 0.032 \quad 0.037 \quad 0.032 \quad 0.053 \quad 0.052 \quad 0.053 \quad 0.02 \quad 0\ )^T$

$\omega o_9 := 2\pi \cdot 16.8$ $\omega o_{10} := 2\pi \cdot 17.6$ $\omega o_5 := 2\pi \cdot 17.2$ $\omega o_{11} := 2\pi \cdot 15.9$

Arrival Time (AT) of the signal:

$$tp_p := ceil\left(\left(\frac{AT_p}{0.0005}\right)\right) \cdot 0.000$$

$$wp(t, \omega o) := \begin{cases} 10\left|\cos(\omega o \cdot t)^{10} - 1\right| & \text{if } 0 \le t \le \frac{\pi}{\omega o} \\ 0 & \text{otherwise} \end{cases}$$

Define **Time Window** (Twind) to amplify the arrival of the signals:

$$Twind := \left| \begin{array}{l} \text{for } p \in 1 .. 11 \\ \quad \text{for } i \in 1 .. N \\ \quad\quad ampl_{i,p} \leftarrow wp\left(i \cdot 0.0005 - tp_p, \omega o_p\right) \\ ampl \end{array} \right.$$

Fourier Transform of the Windowed Signals: $FTW^{\langle p \rangle} := CFFT\left(\overrightarrow{\left(Twind^{\langle p \rangle} \cdot signal^{\langle p \rangle}\right)}\right)$

Windowed Signals: $P_{i,p} := Twind_{i,p} \cdot signal_{i,p}$

Spectrum Area $MA_{u,p} := \sum_{u=1}^{u} \frac{\left|FTW_{u,p}\right|}{N \cdot 0.001}$

Transmission Coefficient (TC) =

$$TC_u := \sqrt{\frac{|FTW_{u,5}| \cdot |FTW_{u,11}|}{|FTW_{u,9}| \cdot |FTW_{u,10}|}}$$

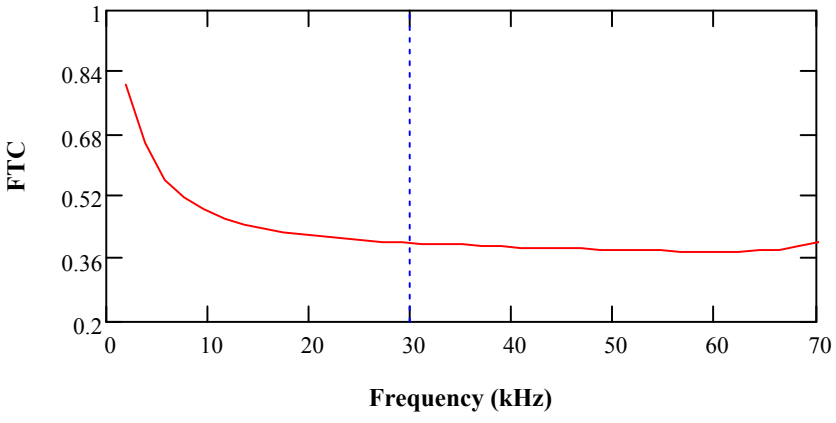

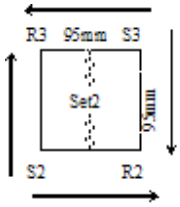

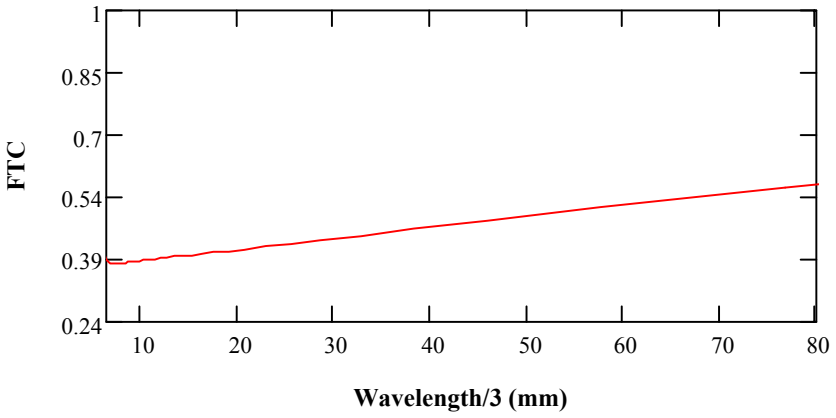

Damping ratio @ 34kHz

fre := 34.18

$f_{S2\text{-}R3}$ (joint-free) & $f_{S2\text{-}R2}$ (joint)

$$\left(\frac{2\pi fre \cdot 95}{2775}\right)^{-1} \cdot \ln\left(\frac{1}{MM1}\right) = 0.164$$

$f_{S3\text{-}R2}$ (joint-free) & $f_{S3\text{-}R3}$ (joint)

$$\left(\frac{2\pi fre \cdot 95}{2775}\right)^{-1} \cdot \ln\left(\frac{1}{MM2}\right) = 0.093$$

Damping analysis for full signals:

$$\Delta\Phi 1_u := \left(\frac{2\pi f1_u \cdot 95}{1.352 \times 10^3} \right)^{-1}$$

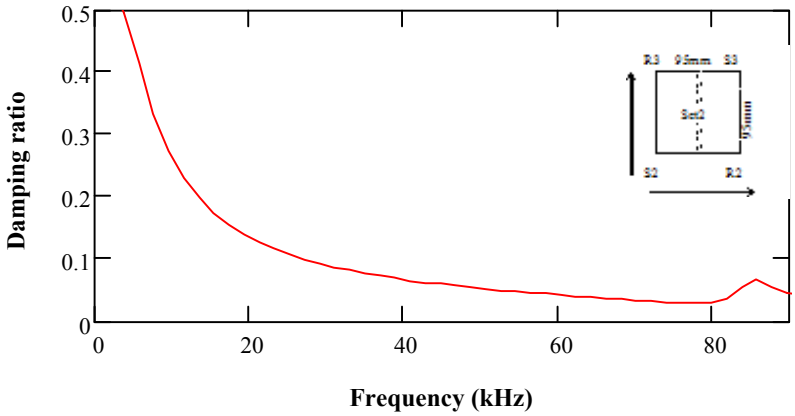

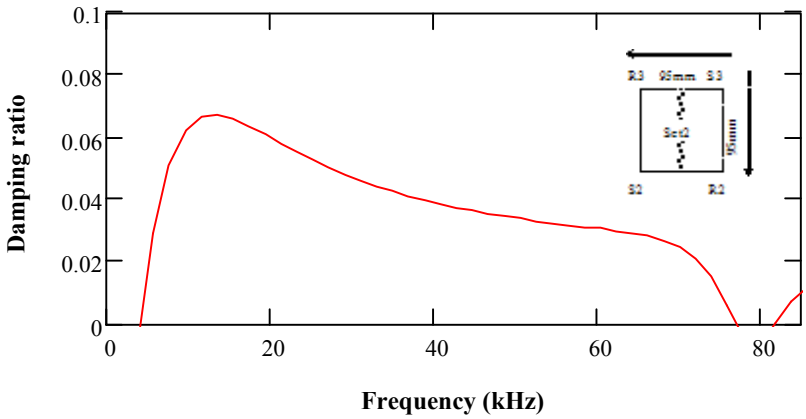

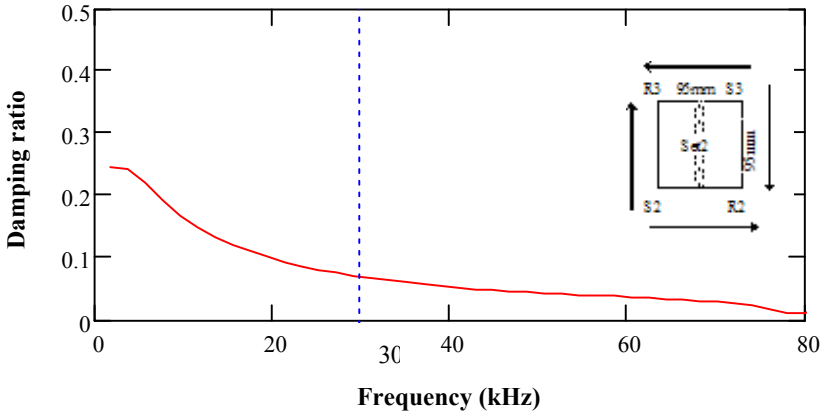

Damping analysis for full signals - using spectrum area:

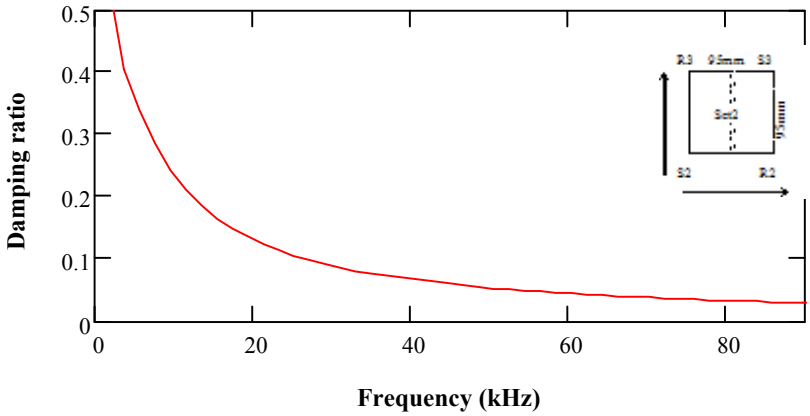

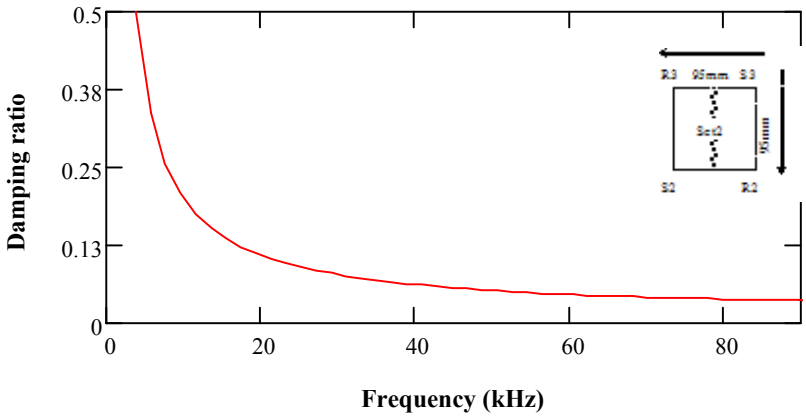

Wavelet transform - for dominat frequency in P-wave portions of set 2, center frequency for 4 signals defined by "aX"; Time shift by "τ".

$aAC2 := 32 \quad \frac{1}{2 \cdot aAC2 \cdot 5 \cdot 10^{-4}} = 31.25$ kHz $\quad aD2B := 28.44 \quad \frac{1}{2 \cdot aD2B \cdot 5 \cdot 10^{-4}} = 35.162$

$aAB := 30.12 \quad \frac{1}{2 \cdot aAB \cdot 5 \cdot 10^{-4}} = 33.201$ kHz $\quad aD2C2 := 32 \quad \frac{1}{2 \cdot aD2C2 \cdot 5 \cdot 10^{-4}} = 31.25$

Definition of Morlet wavelet $\tau := 1 .. N$

f_{S2_R3} (joint-free) $\quad w\_AC2_{i,\tau} := aAC2 \cdot \left[e^{j \cdot \frac{-\pi}{aAC2} \cdot (\tau - i)} \cdot e^{-1 \cdot \left(\frac{\tau - i}{aAC2} \right)^2} \right]^{-\frac{1}{2}}$

f_{S2_R2} (joint) $\quad w\_AB_{i,\tau} := aAB \cdot \left[e^{j \cdot \frac{-\pi}{aAB} \cdot (\tau - i)} \cdot e^{-1 \cdot \left(\frac{\tau - i}{aAB} \right)^2} \right]^{-\frac{1}{2}}$

f_{S3_R2} (joint-free) $\quad w\_D2B_{i,\tau} := aD2B \cdot \left[e^{j \cdot \frac{-\pi}{aD2B} \cdot (\tau - i)} \cdot e^{-1 \cdot \left(\frac{\tau - i}{aD2B} \right)^2} \right]^{-\frac{1}{2}}$

f_{S3_R3} (joint) $\quad w\_D2C2_{i,\tau} := aD2C2 \cdot \left[e^{j \cdot \frac{-\pi}{aD2C2} \cdot (\tau - i)} \cdot e^{-1 \cdot \left(\frac{\tau - i}{aD2C2} \right)^2} \right]^{-\frac{1}{2}}$

Wavelet transform

f_{S2_R3} (joint-free) $\quad WAC2_\tau := \sum_i \left(w\_AC2_{i,\tau} \cdot AC2_i \right)$

$WAC2_\tau := \left| WAC2_\tau \right|$

f_{S2_R2} (joint) $\quad WAB_\tau := \sum_i \left(w\_AB_{i,\tau} \cdot AB_i \right)$

$WAB_\tau := \left| WAB_\tau \right|$

f_{S3_R2} (joint-free) $\quad WD2B_\tau := \sum_i \left(w\_D2B_{i,\tau} \cdot D2B_i \right)$

f_{S3_R3} (joint) $\quad WD2C2_\tau := \sum_i \left) w\_D2C2_{i,\tau} \cdot D2$

$f_{S2\text{-}R3}$ (joint-free) & $f_{S2\text{-}R2}$ (joint)

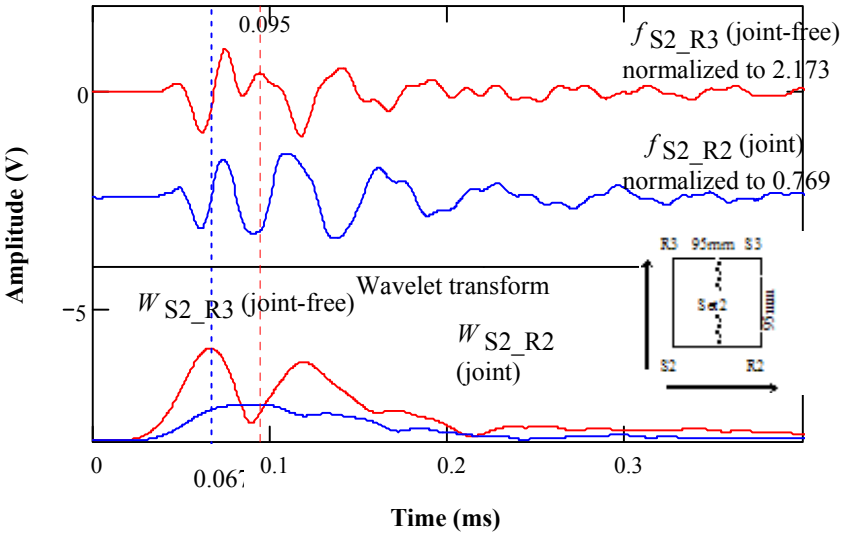

$f_{S3\text{-}R2}$ (joint-free) & $f_{S3\text{-}R3}$ (joint)

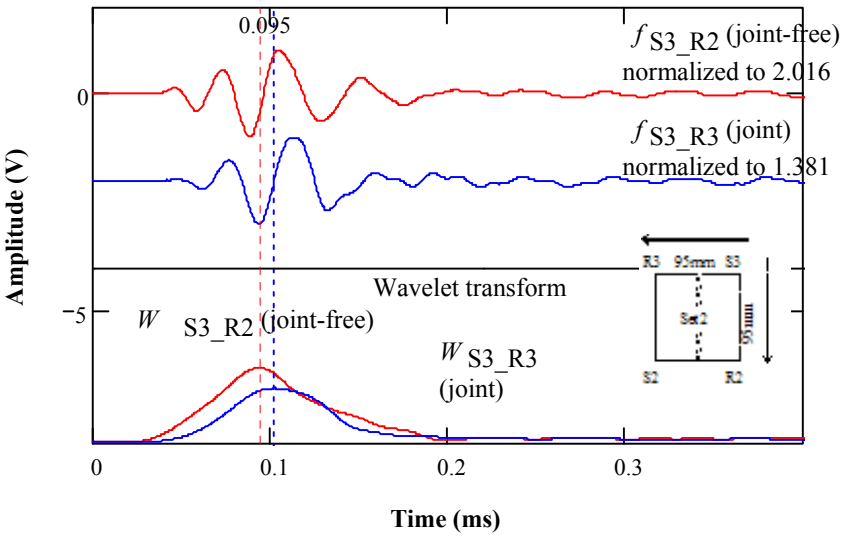

Amplitude ratio

$$\frac{\max(WAB)}{\max(WAC2)} = 0.386 \qquad \frac{\max(WD2C2)}{\max(WD2B)} = 0.727 \qquad \sqrt{\frac{\max(WAB)}{\max(WAC2)}\frac{\max(WD2C2)}{\max(WD2B)}} = 0.53$$

Wavelet transform - for dominat frequency in R-wave portions of set 2, center frequency for 4 signals defined by "aX"; Time shift by "τ".

$aAC2 := 28.4 \quad \frac{1}{2 \cdot aAC2 \cdot 5 \cdot 10^{-4}} = 35.162 \quad kHz$

$aD2B := 28.4 \quad \frac{1}{2 \cdot aD2B \cdot 5 \cdot 10^{-4}} = 35.162$

$aAB := 28.4 \quad \frac{1}{2 \cdot aAB \cdot 5 \cdot 10^{-4}} = 35.162 \quad kHz$

$aD2C2 := 32 \quad \frac{1}{2 \cdot aD2C2 \cdot 5 \cdot 10^{-4}} = 31.25$

Definition of Morlet wavelet $\tau := 1 .. N$

f_{S2_R3} (joint-free) $w\_AC2_{i,\tau} := aAC2^{-\frac{1}{2}\cdot\left[e^{j\cdot\frac{-\pi}{aAC2}\cdot(\tau-i)} \cdot e^{-1\cdot\left(\frac{\tau-i}{aAC2}\right)^2}\right]}$

f_{S2_R2} (joint) $w\_AB_{i,\tau} := aAB^{-\frac{1}{2}\cdot\left[e^{j\cdot\frac{-\pi}{aAB}\cdot(\tau-i)} \cdot e^{-1\cdot\left(\frac{\tau-i}{aAB}\right)^2}\right]}$

f_{S3_R2} (joint-free) $w\_D2B_{i,\tau} := aD2B^{-\frac{1}{2}\cdot\left[e^{j\cdot\frac{-\pi}{aD2B}\cdot(\tau-i)} \cdot e^{-1\cdot\left(\frac{\tau-i}{aD2B}\right)^2}\right]}$

f_{S3_R3} (joint) $w\_D2C2_{i,\tau} := aD2C2^{-\frac{1}{2}\cdot\left[e^{j\cdot\frac{-\pi}{aD2C2}\cdot(\tau-i)} \cdot e^{-1\cdot\left(\frac{\tau-i}{aD2C2}\right)^2}\right]}$

Wavelet transform

f_{S2_R3} (joint-free) $WAC2_\tau := \sum_i \left(w\_AC2_{i,\tau} \cdot AC2_i\right)$

f_{S2_R2} (joint) $WAB_\tau := \sum_i \left(w\_AB_{i,\tau} \cdot A$

$WAC2_\tau := \left|WAC2_\tau\right|$

$WAB_\tau := \left|WAB_\tau\right|$

f_{S3_R2} (joint-free) $WD2B_\tau := \sum_i \left(w\_D2B_{i,\tau} \cdot D2B_i\right)$

f_{S3_R3} (joint) $WD2C2_\tau := \sum_i w\_D2C2_{i,\tau} \cdot$

$f_{S2\text{-}R3}$ (joint-free) & $f_{S2\text{-}R2}$ (joint)

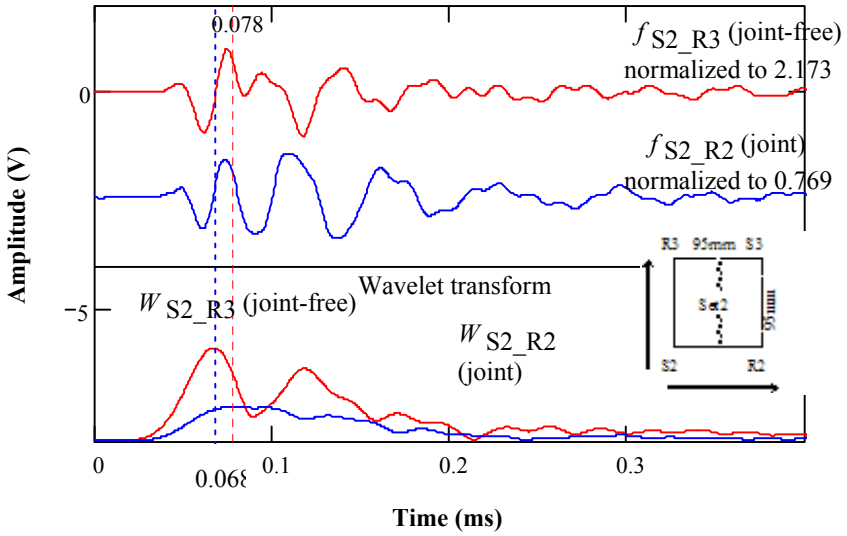

$f_{S3\text{-}R2}$ (joint-free) & $f_{S3\text{-}R3}$ (joint)

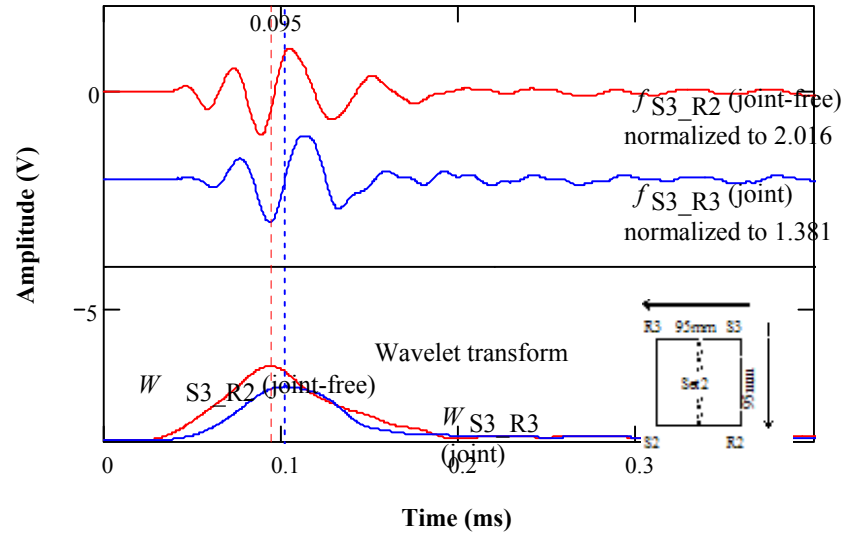

Amplitude ratio

$$\frac{\max(WAB)}{\max(WAC2)} = 0.364 \qquad \frac{\max(WD2C2)}{\max(WD2B)} = 0.727 \qquad \sqrt{\frac{\max(WAB)}{\max(WAC2)}\frac{\max(WD2C2)}{\max(WD2B)}} = 0.514$$

Appendix H

Signals in Time and Frequency Domains for Slab 2

- Measurements on the Jointed and the Joint-free Surfaces

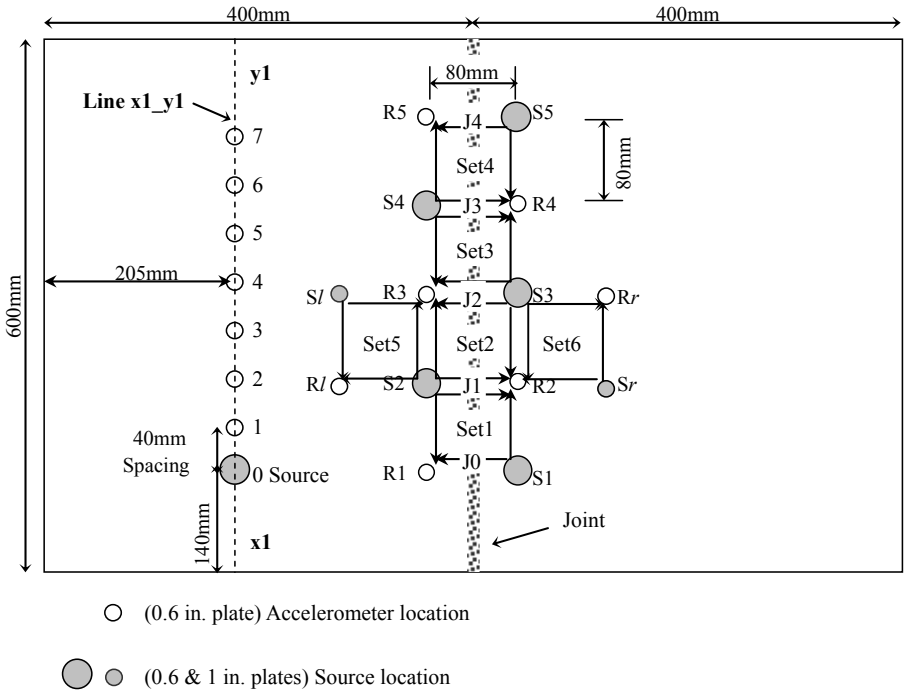

Figure H-1: Ultrasonic testing configuration of HMA slab 2

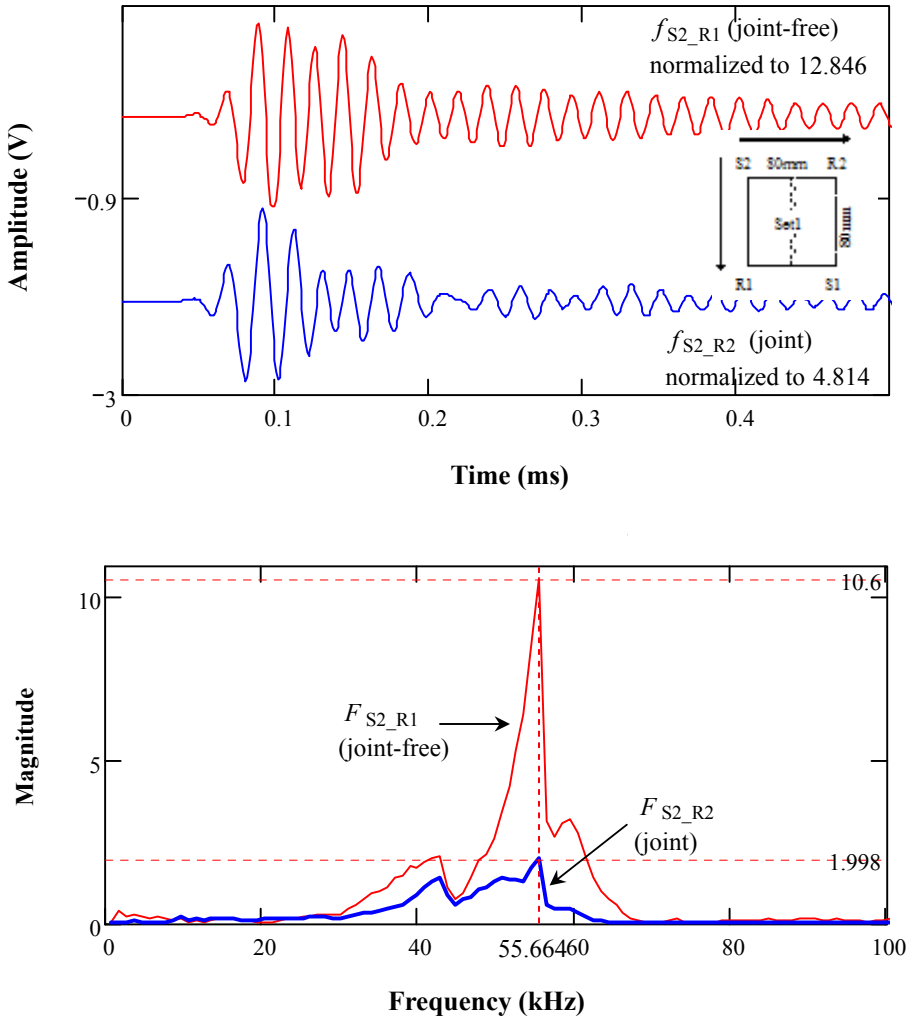

Figure H-2: Signal Pair 1 in time and frequency domains for Set 1

(Horizontal lines mark the peak amplitudes and vertical lines dominant frequencies.)

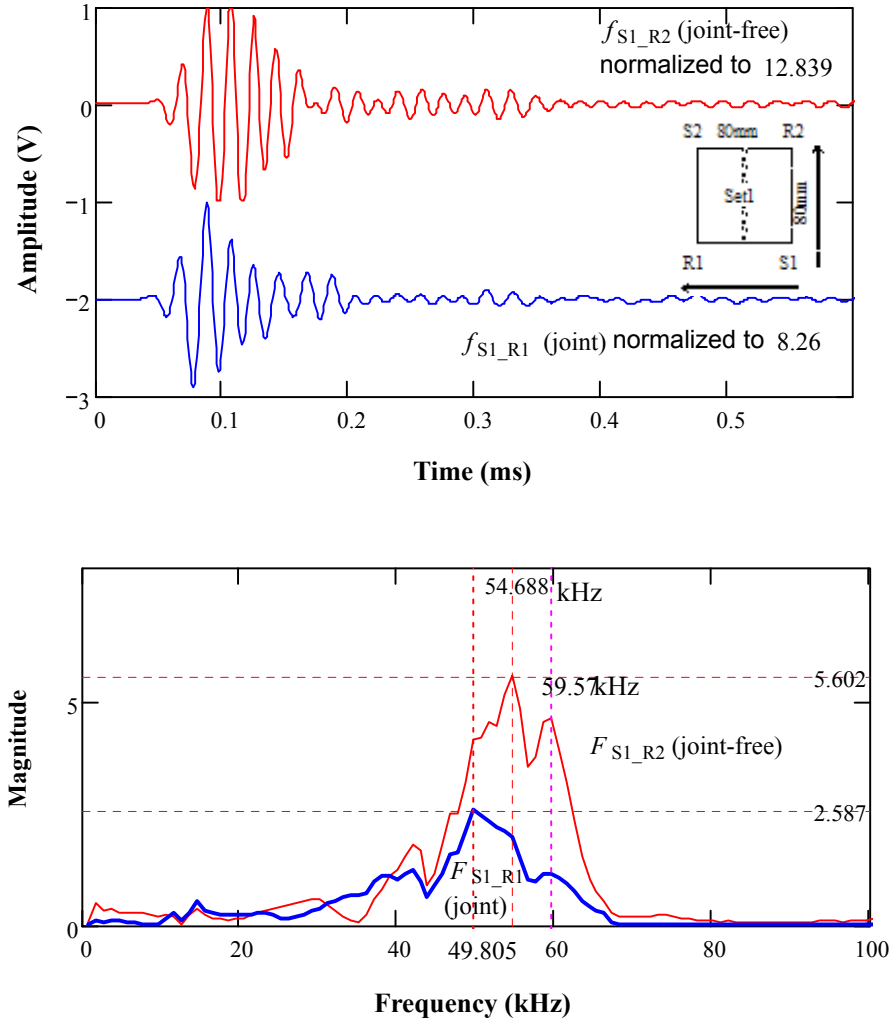

Figure H-3: Signal Pair 2 in time and frequency domains for Set 1

(Horizontal lines mark the peak amplitudes and vertical lines dominant frequencies.)

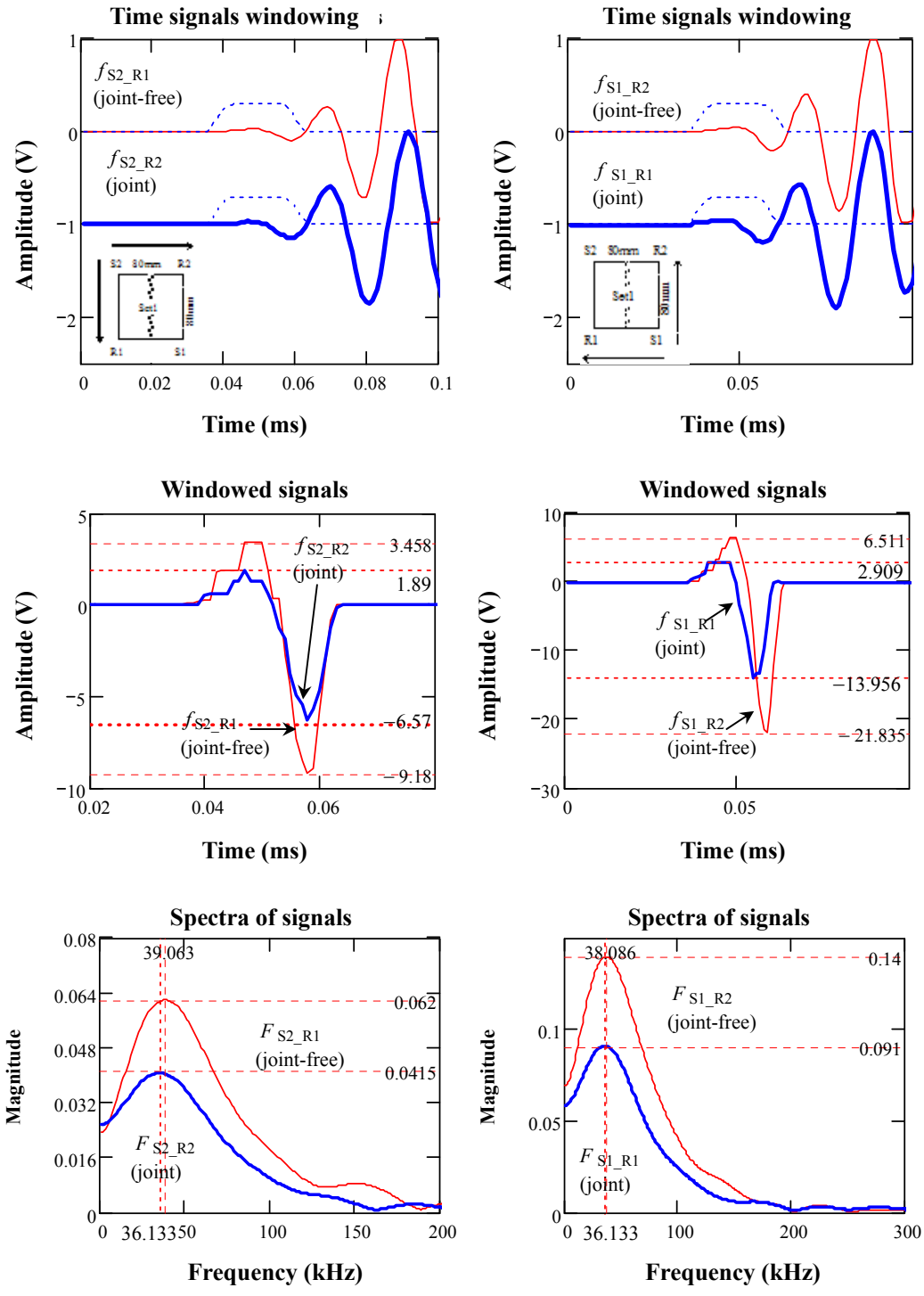

Figure H-4: P-wave analyses in time and frequency domains for Set 1

(Horizontal lines mark the peak amplitudes and vertical lines dominant frequencies.)

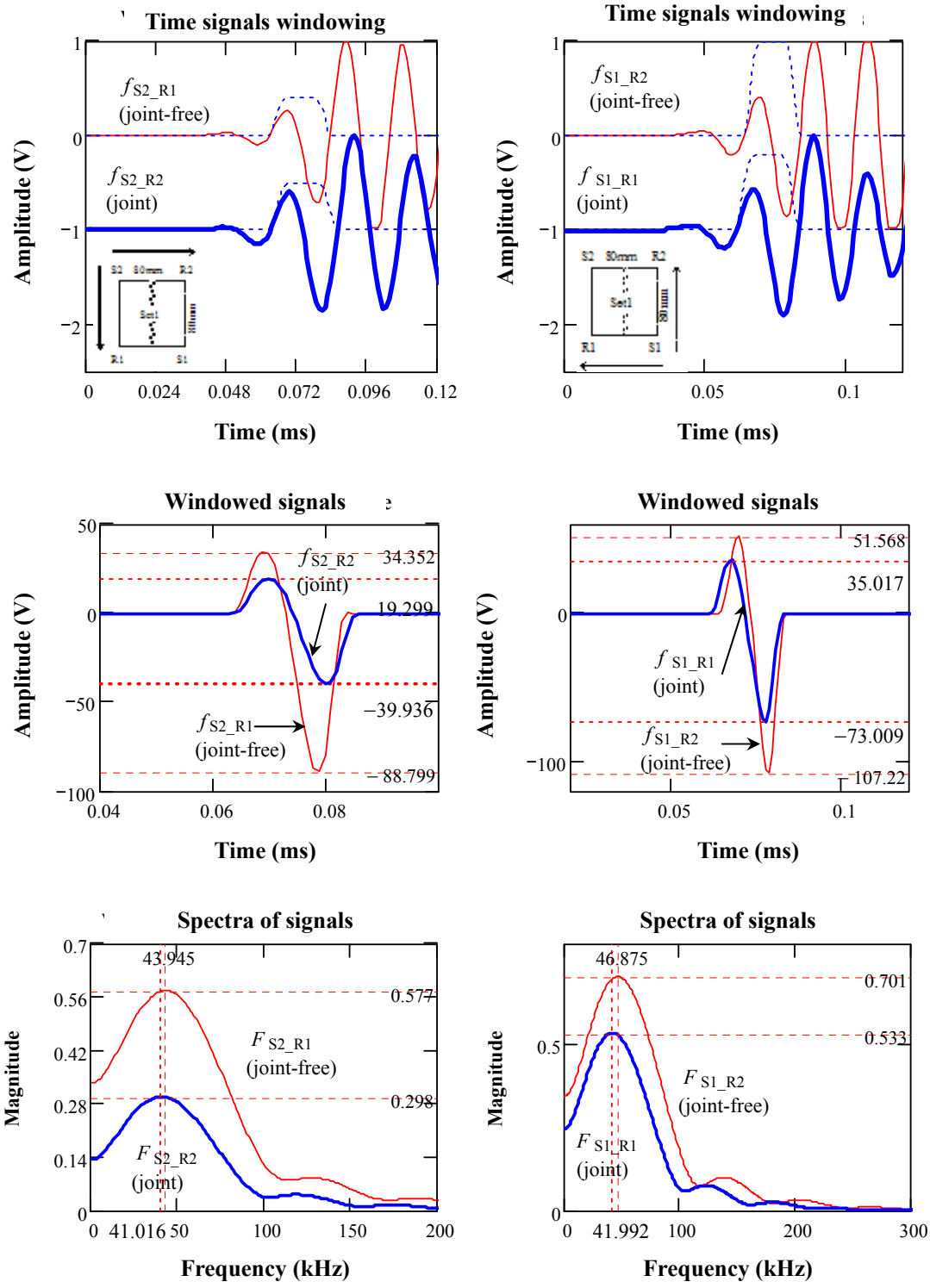

Figure H-5: R-wave analyses in time and frequency domains for Set 1

(Horizontal lines mark the peak amplitudes and vertical lines dominant frequencies.)

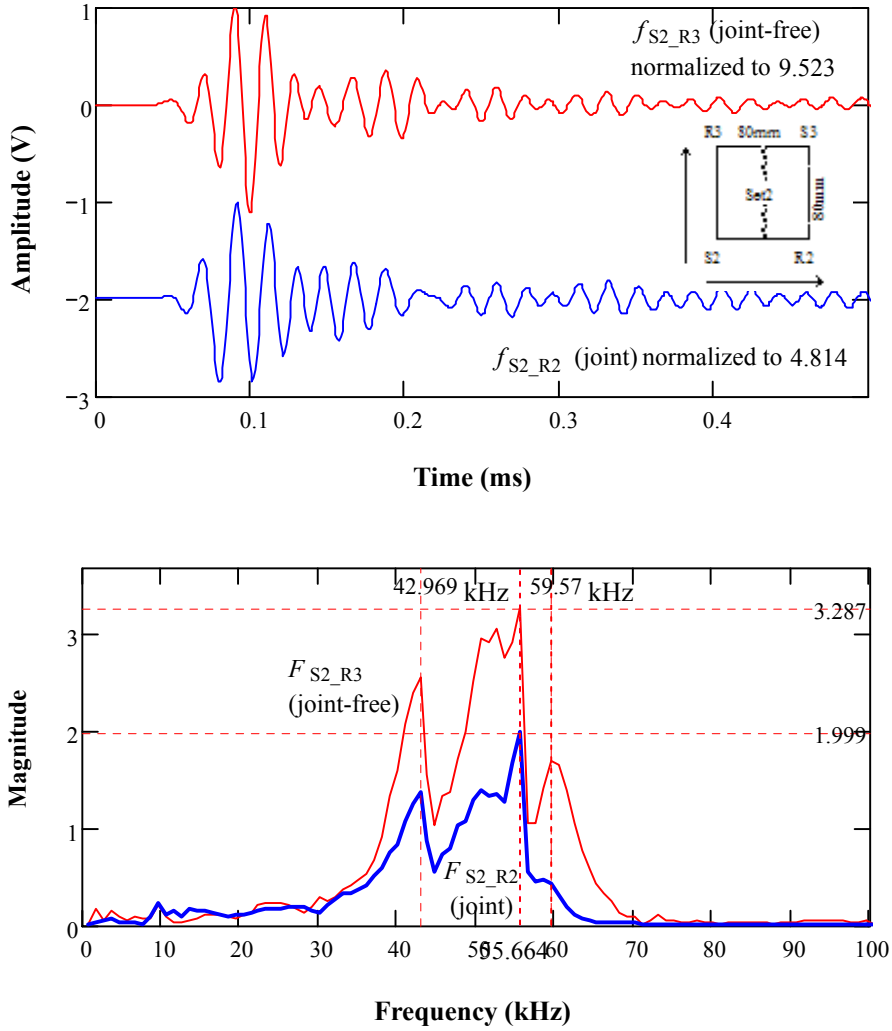

Figure H-6: Signal Pair 1 in time and frequency domains for Set 2

(Horizontal lines mark the peak amplitudes and vertical lines dominant frequencies.)

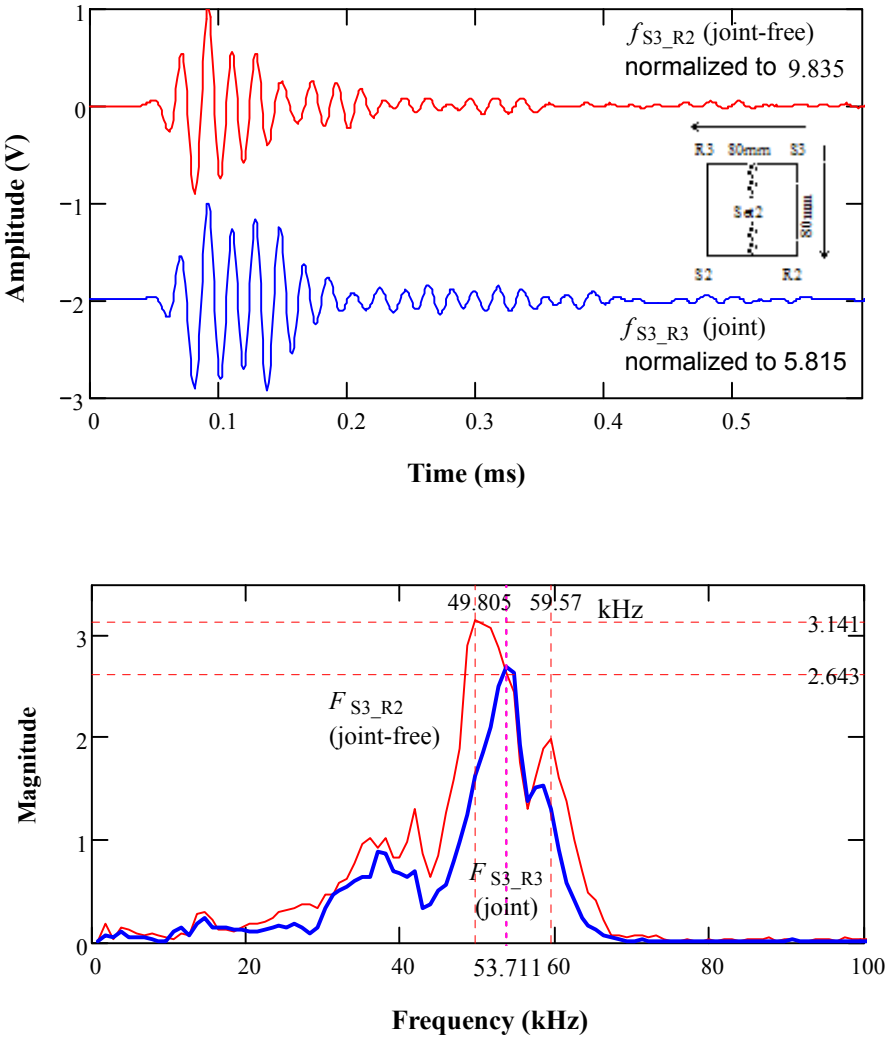

Figure H-7: Signal Pair 2 in time and frequency domains for Set 2

(Horizontal lines mark the peak amplitudes and vertical lines dominant frequencies.)

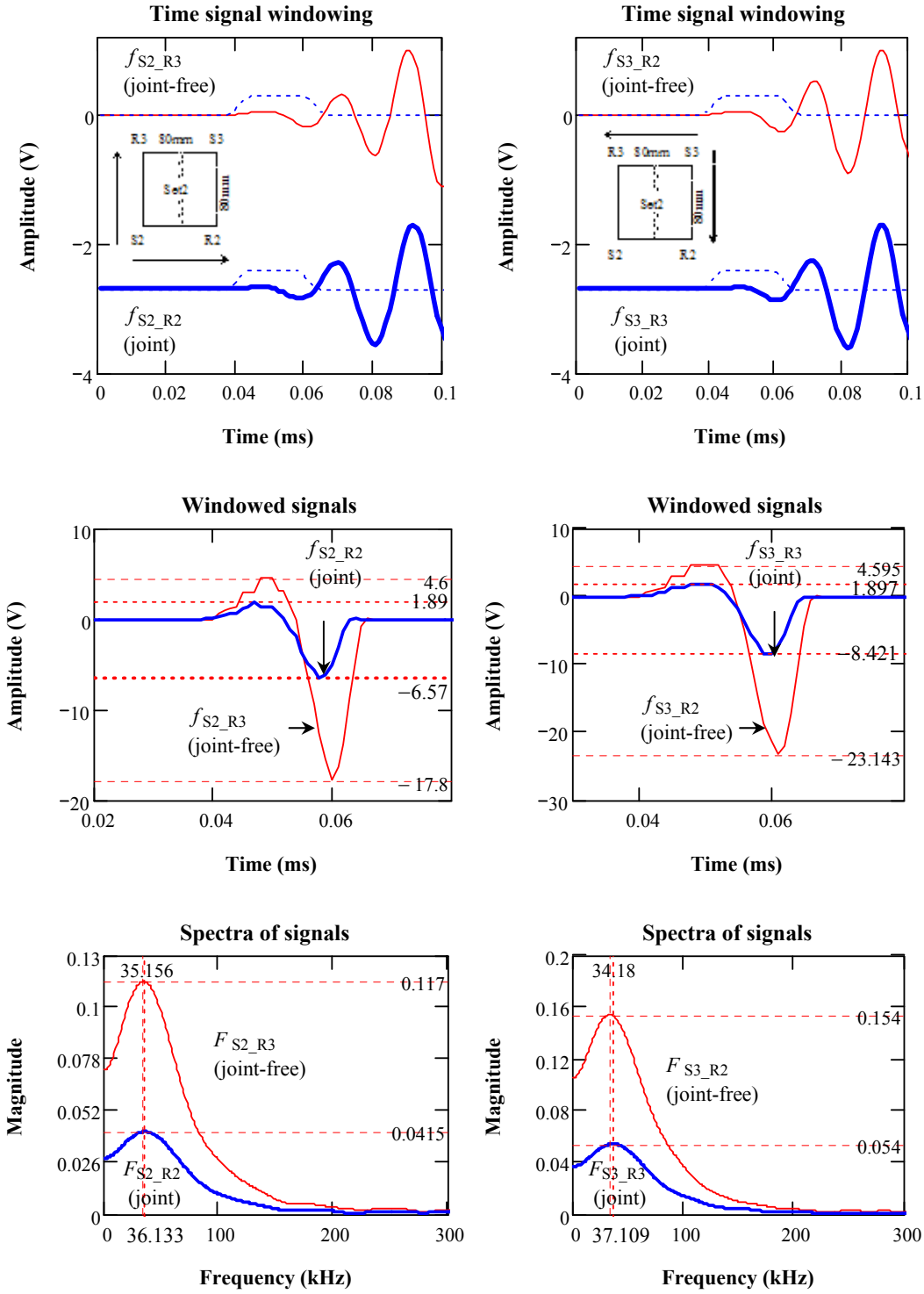

Figure H-8: P-wave analyses in time and frequency domains for Set 2

(Horizontal lines mark the peak amplitudes and vertical lines dominant frequencies.)

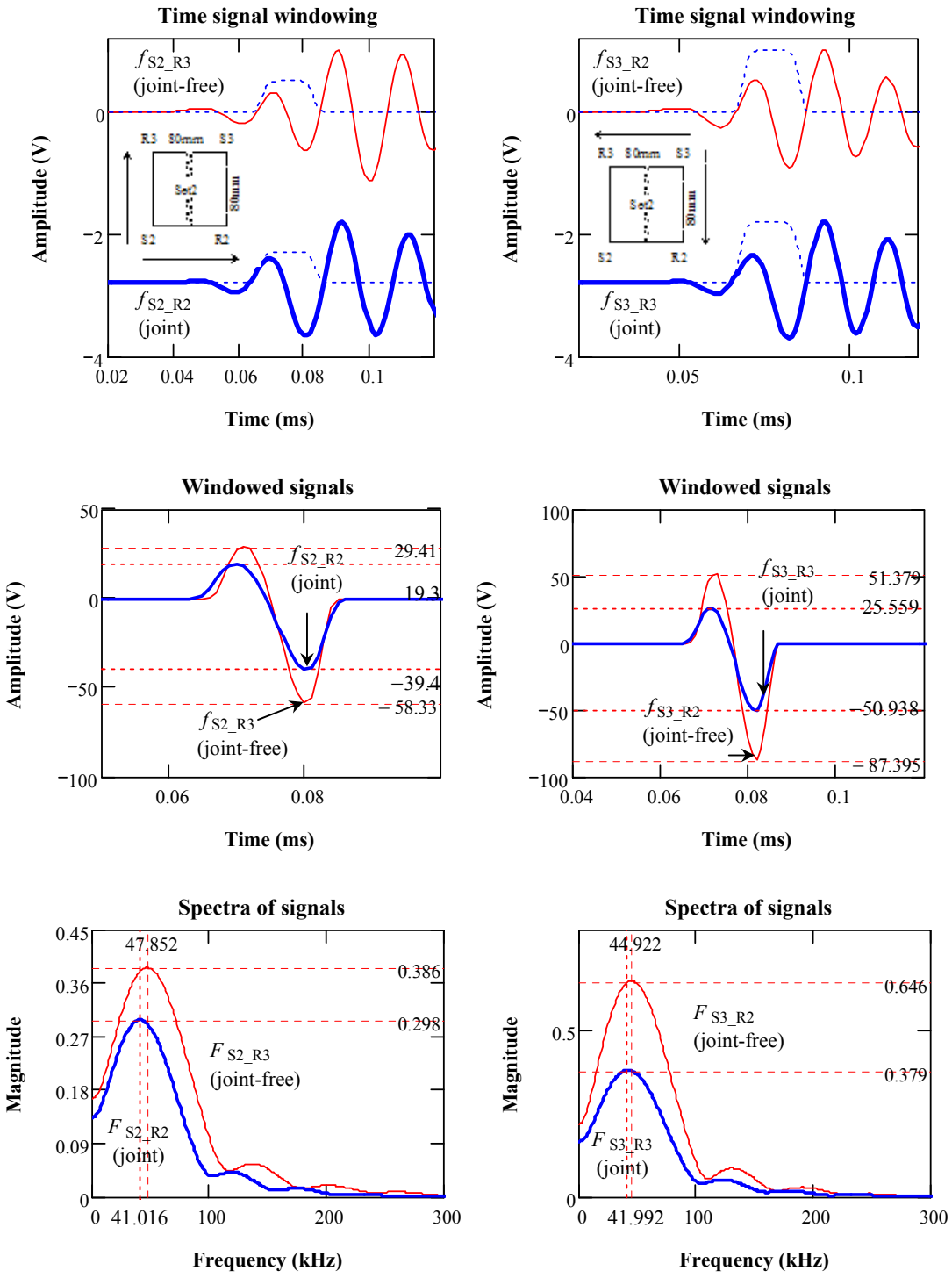

Figure H-9: R-wave analyses in time and frequency domains for Set 2

(Horizontal lines mark the peak amplitudes and vertical lines dominant frequencies.)

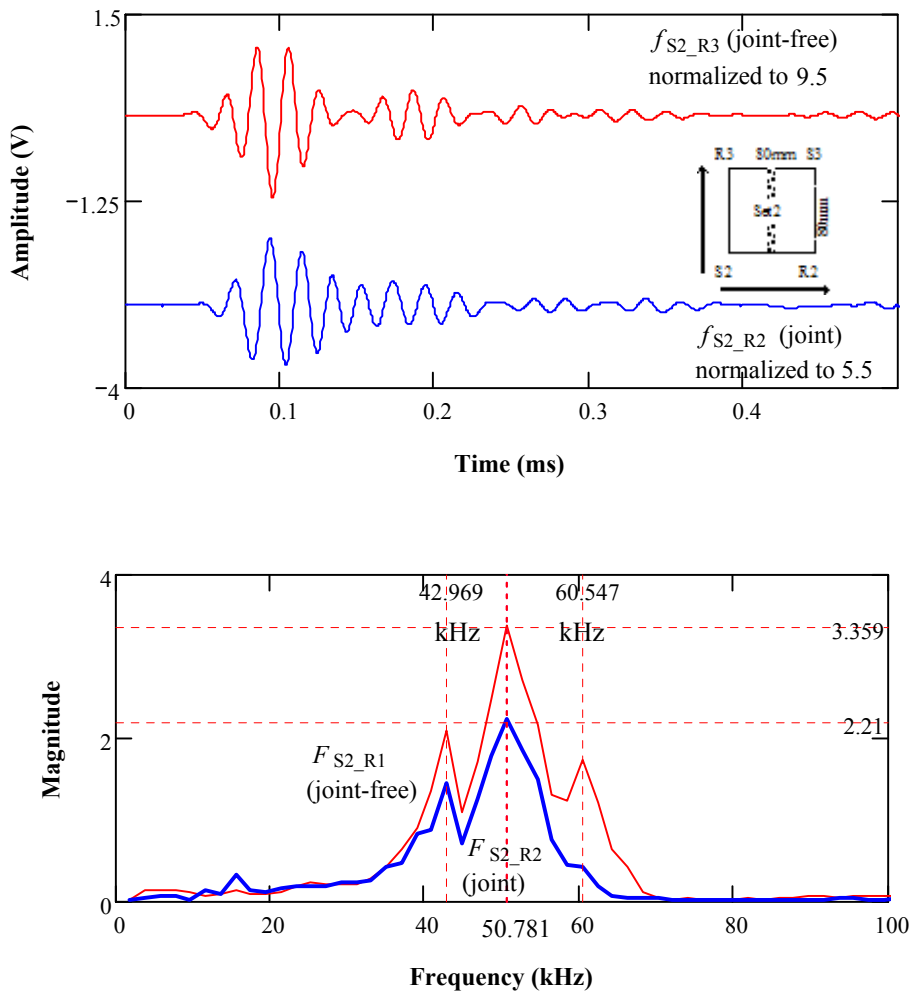

Figure H-10: Signal Pair 1 in time and frequency domains for repeated Set 2 measurements (Horizontal lines mark the peak amplitudes and vertical lines dominant frequencies)

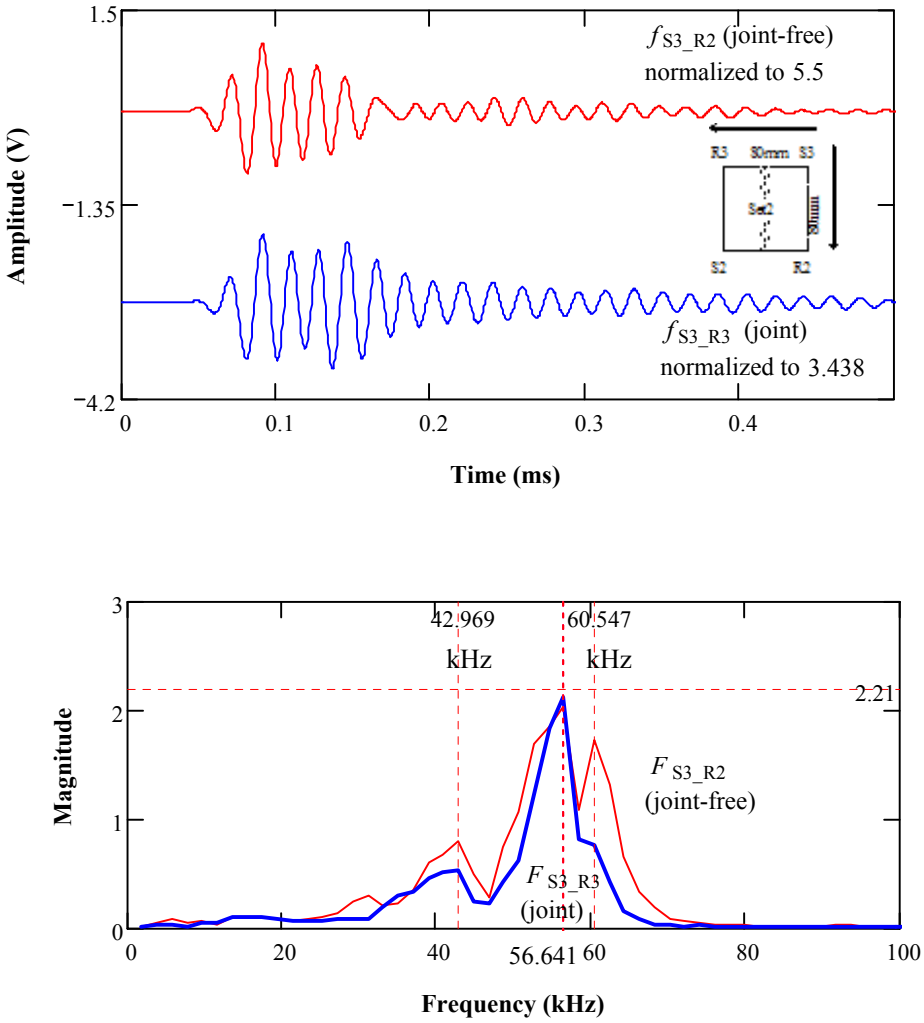

Figure H-11: Signal Pair signals in time and frequency domains for repeated Set 2 measurements (Horizontal lines mark the peak amplitudes and vertical lines dominant frequencies)

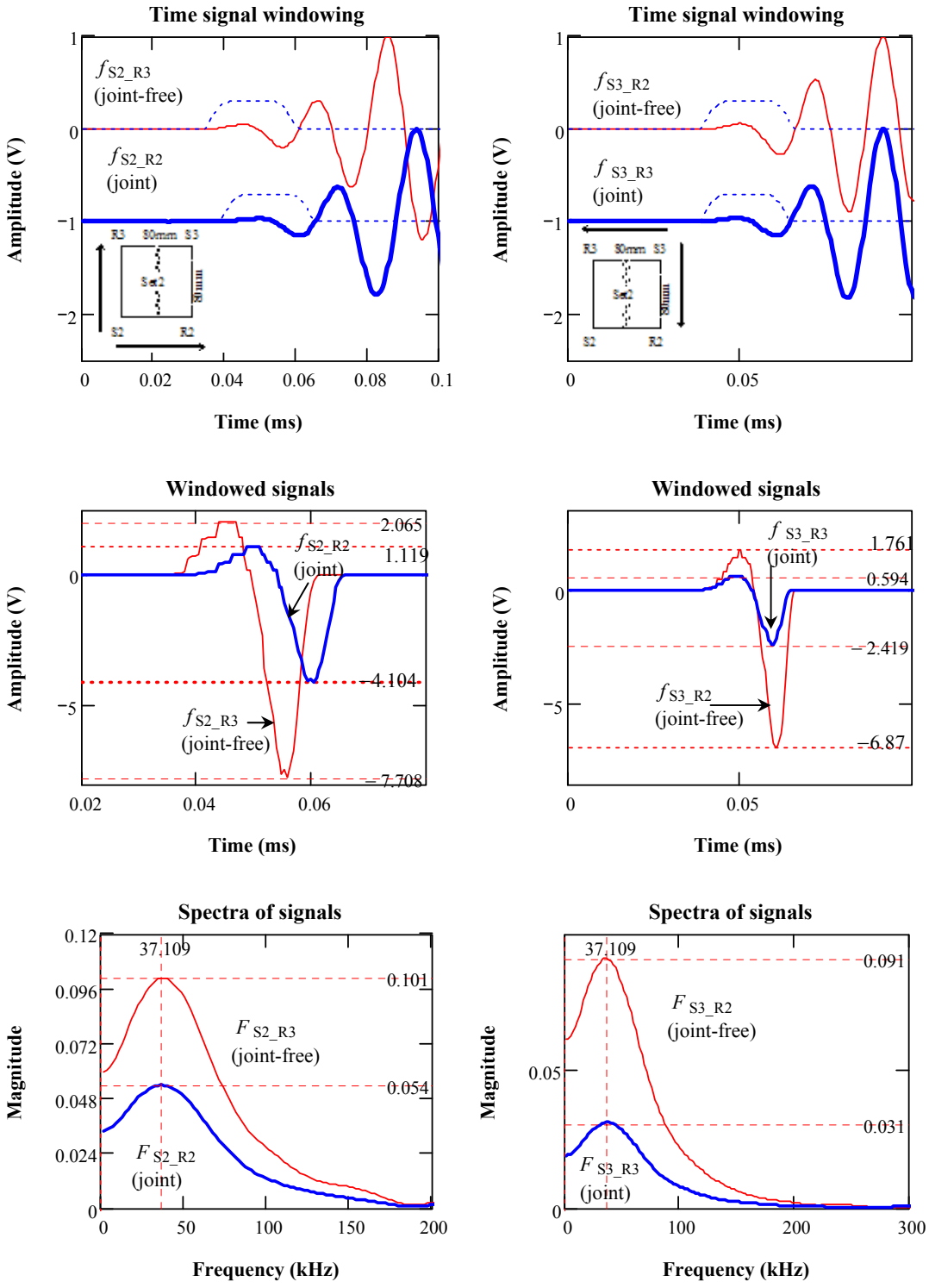

Figure H-12: P-wave analyses in time and frequency domains for repeated Set 2 (Horizontal lines mark the peak amplitudes and vertical lines dominant frequencies.)

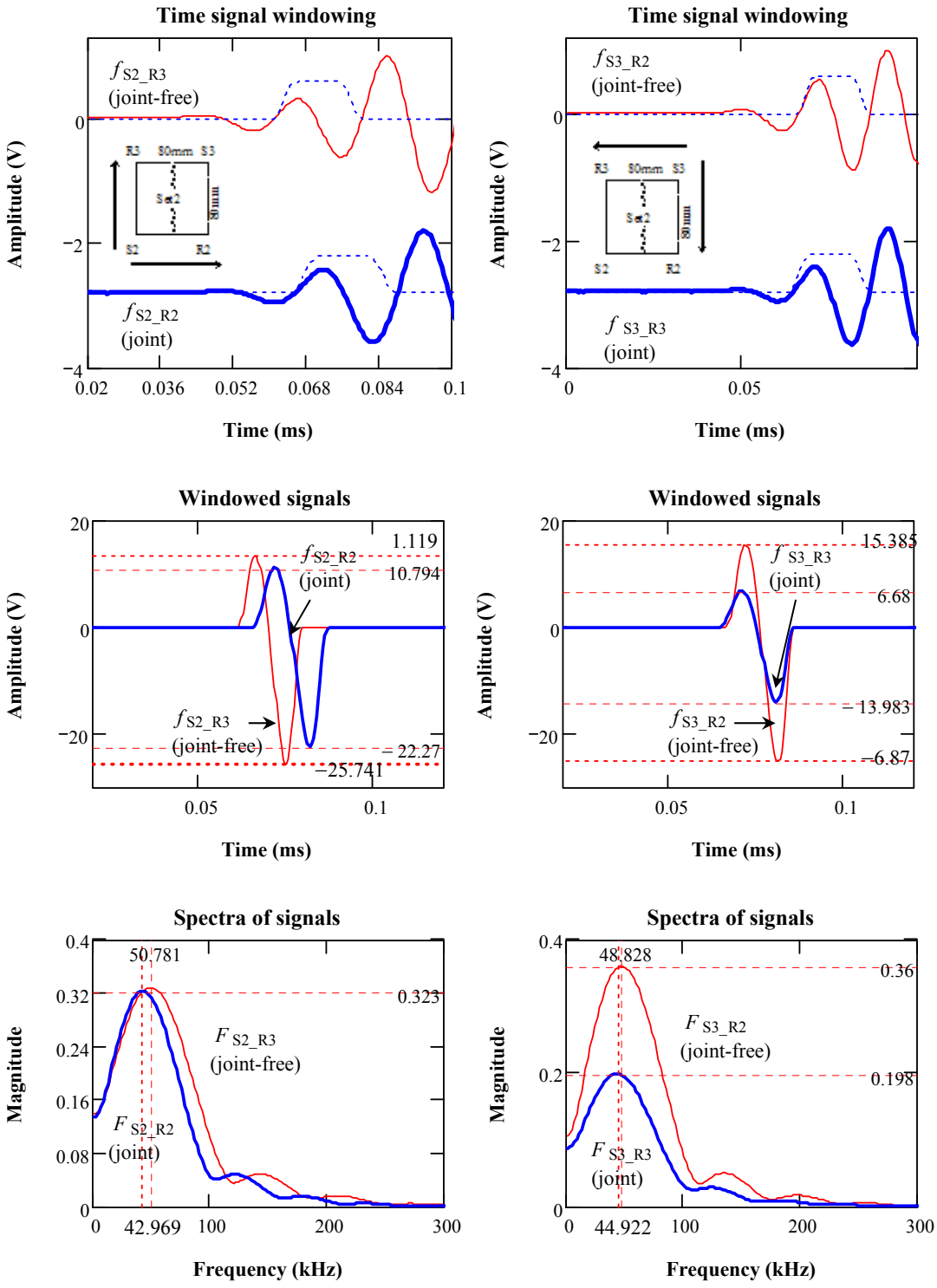

Figure H-13: R-wave analyses in time and frequency domains for repeated Set 2 (Horizontal lines mark the peak amplitudes and vertical lines dominant frequencies.)

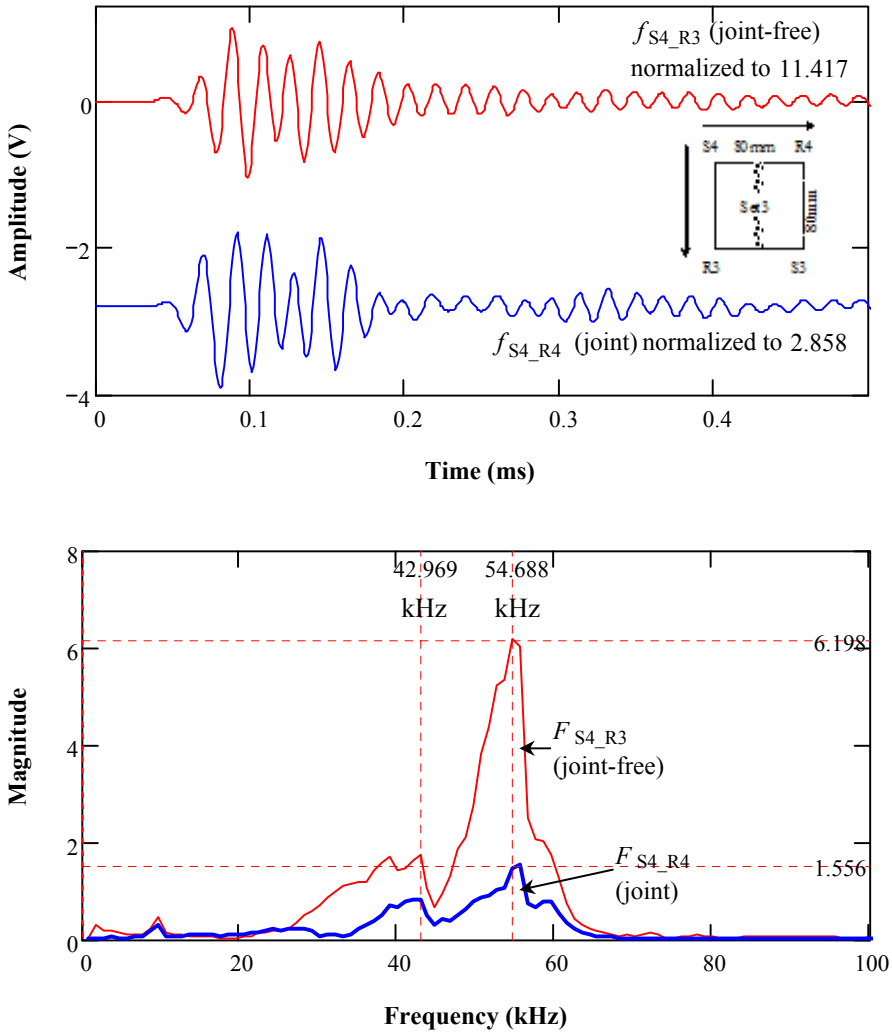

Figure H-14: Signal Pair 1 in time and frequency domains for Set 3

(Horizontal lines mark the peak amplitudes and vertical lines dominant frequencies.)

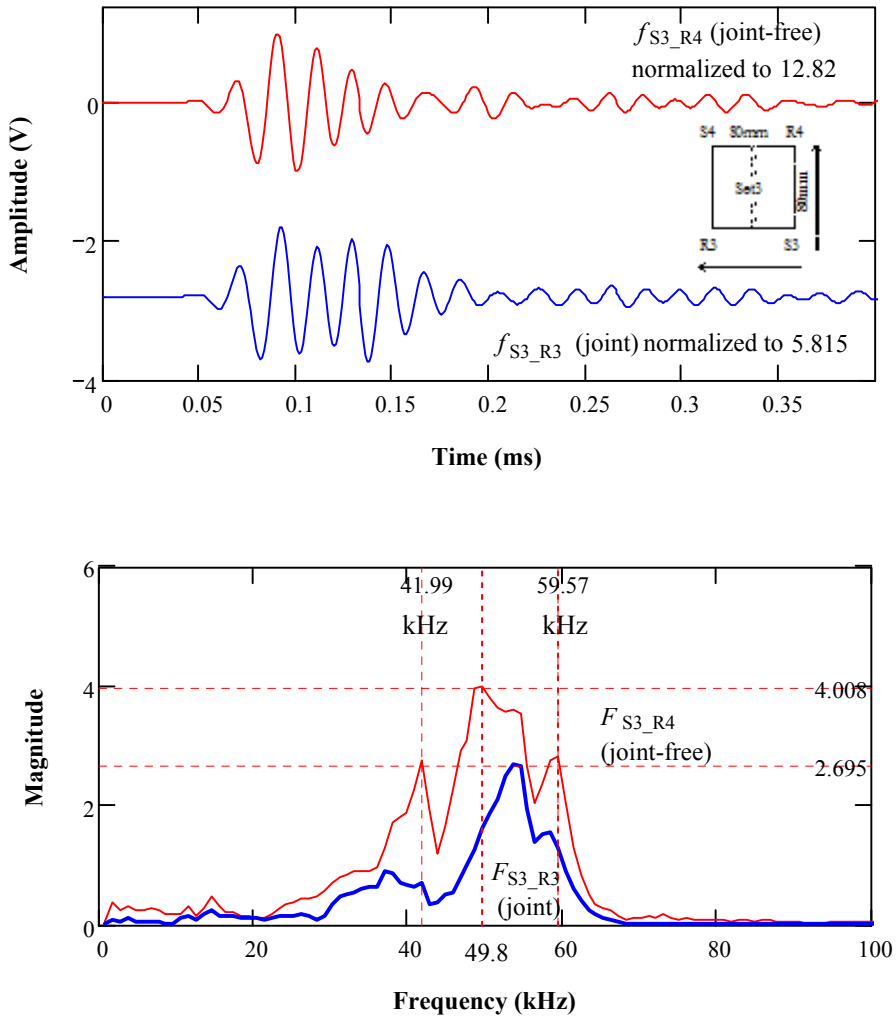

Figure H-15: Signal Pair 2 in time and frequency domains for Set 3

(Horizontal lines mark the peak amplitudes and vertical lines dominant frequencies.)

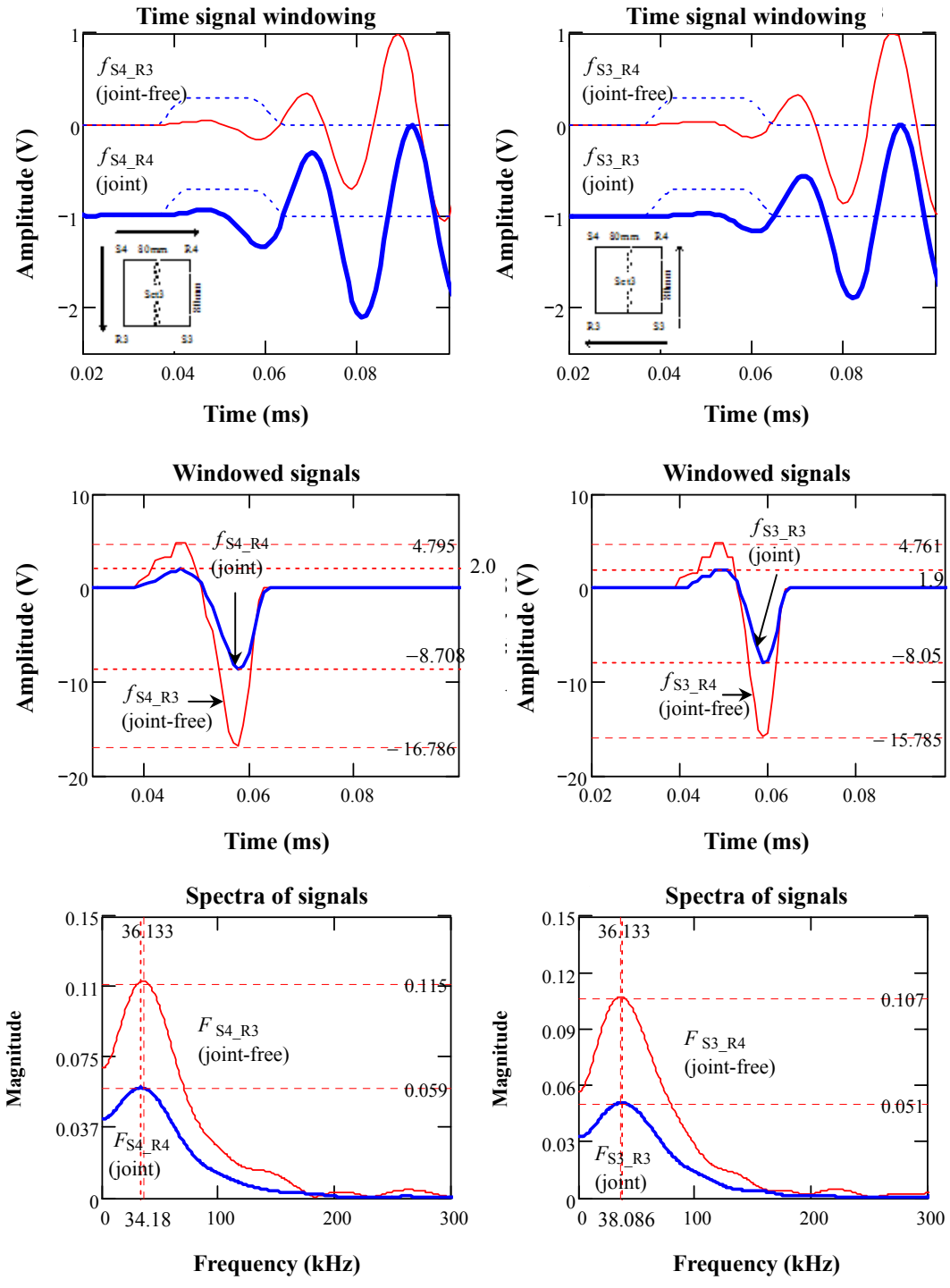

Figure H-16: P-wave analyses in time and frequency domains for Set 3

(Horizontal lines mark the peak amplitudes and vertical lines dominant frequencies.)

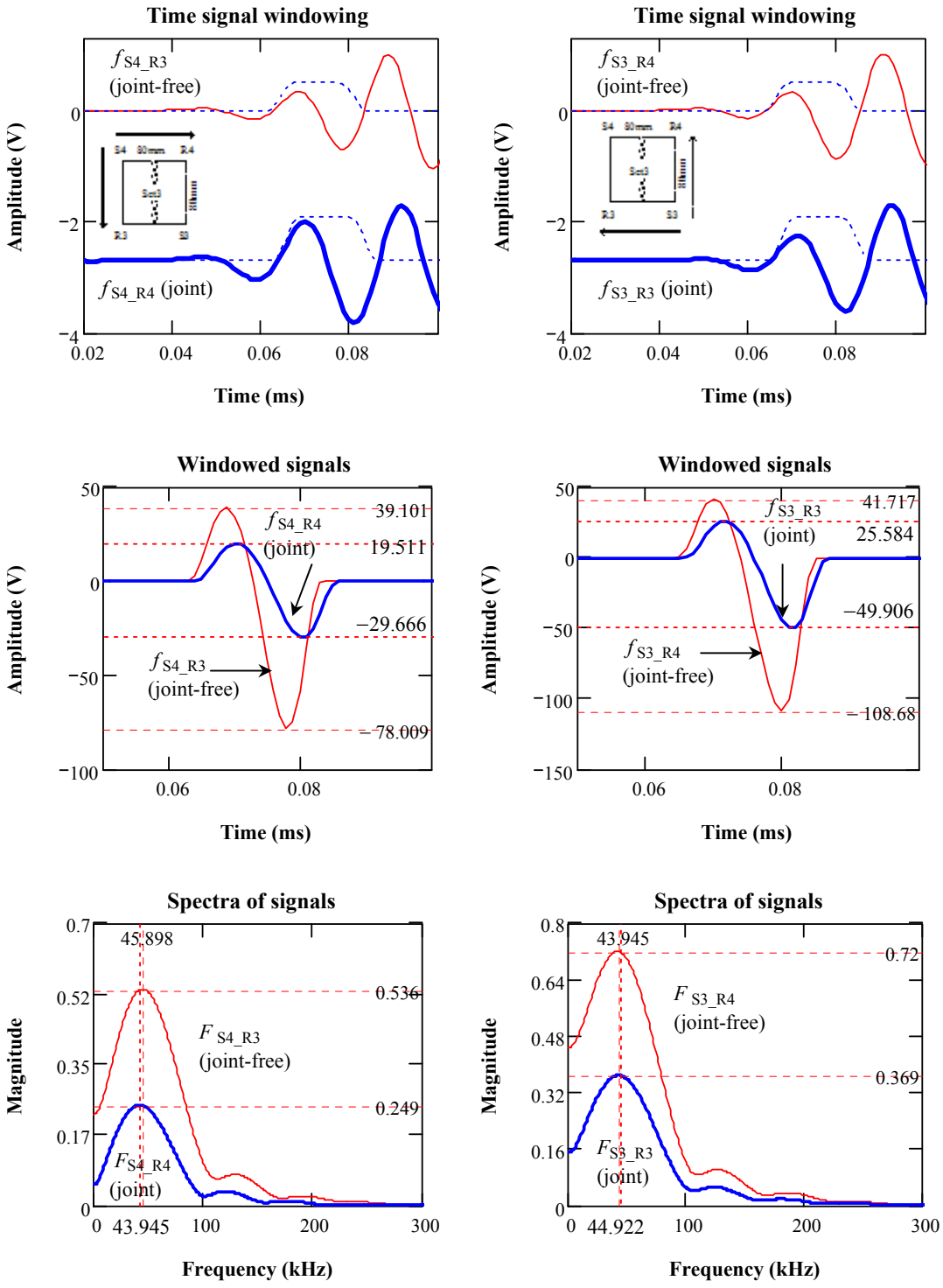

Figure H-17: R-wave analyses in time and frequency domains for Set 3

(Horizontal lines mark the peak amplitudes and vertical lines dominant frequencies.)

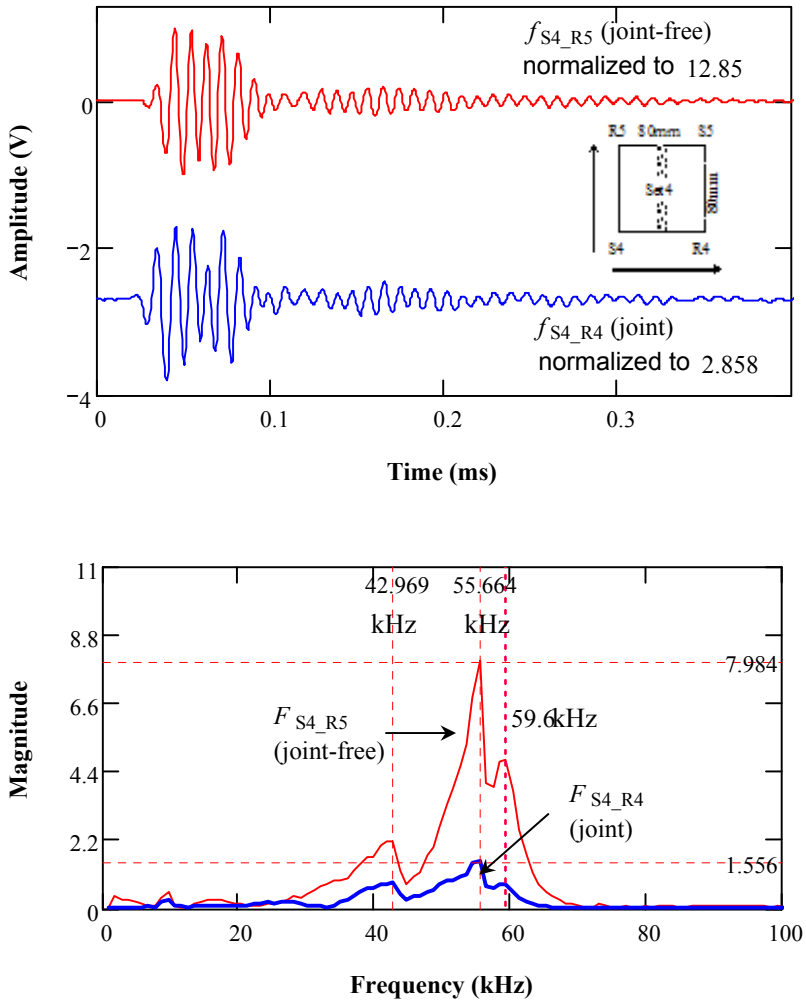

Figure H-18: Signal Pair 1 in time and frequency domains for Set 4

(Horizontal lines mark the peak amplitudes and vertical lines dominant frequencies.)

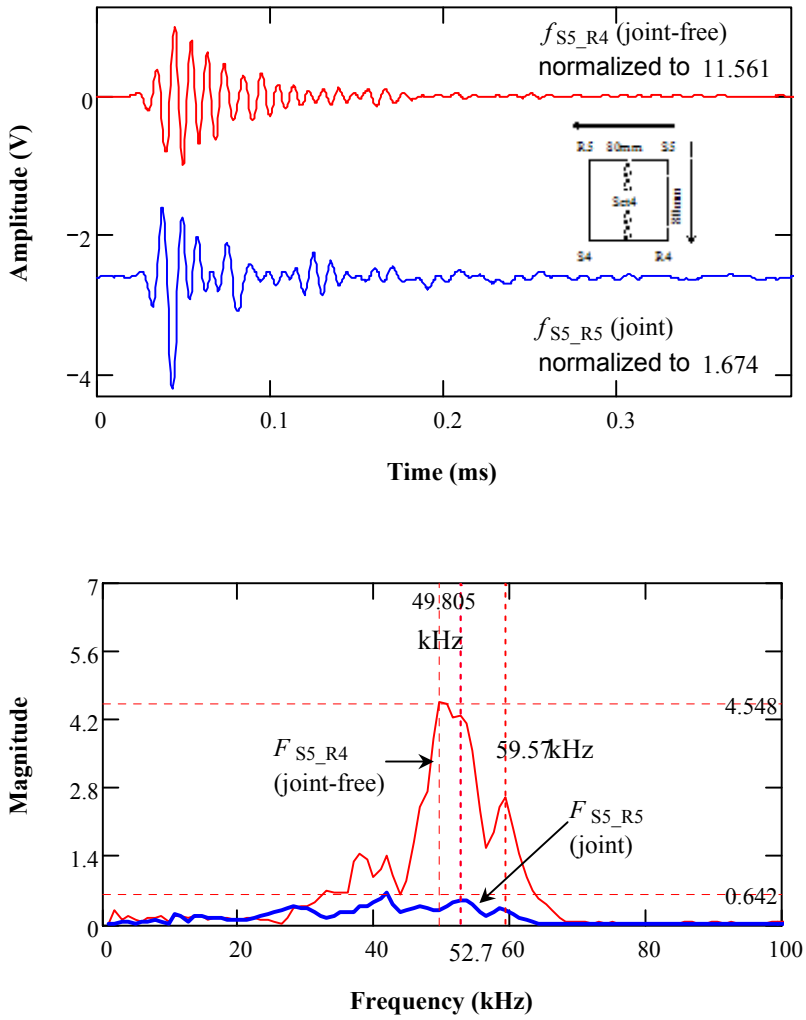

Figure H-19: Signal Pair 2 in time and frequency domains for Set 3

(Horizontal lines mark the peak amplitudes and vertical lines dominant frequencies.)

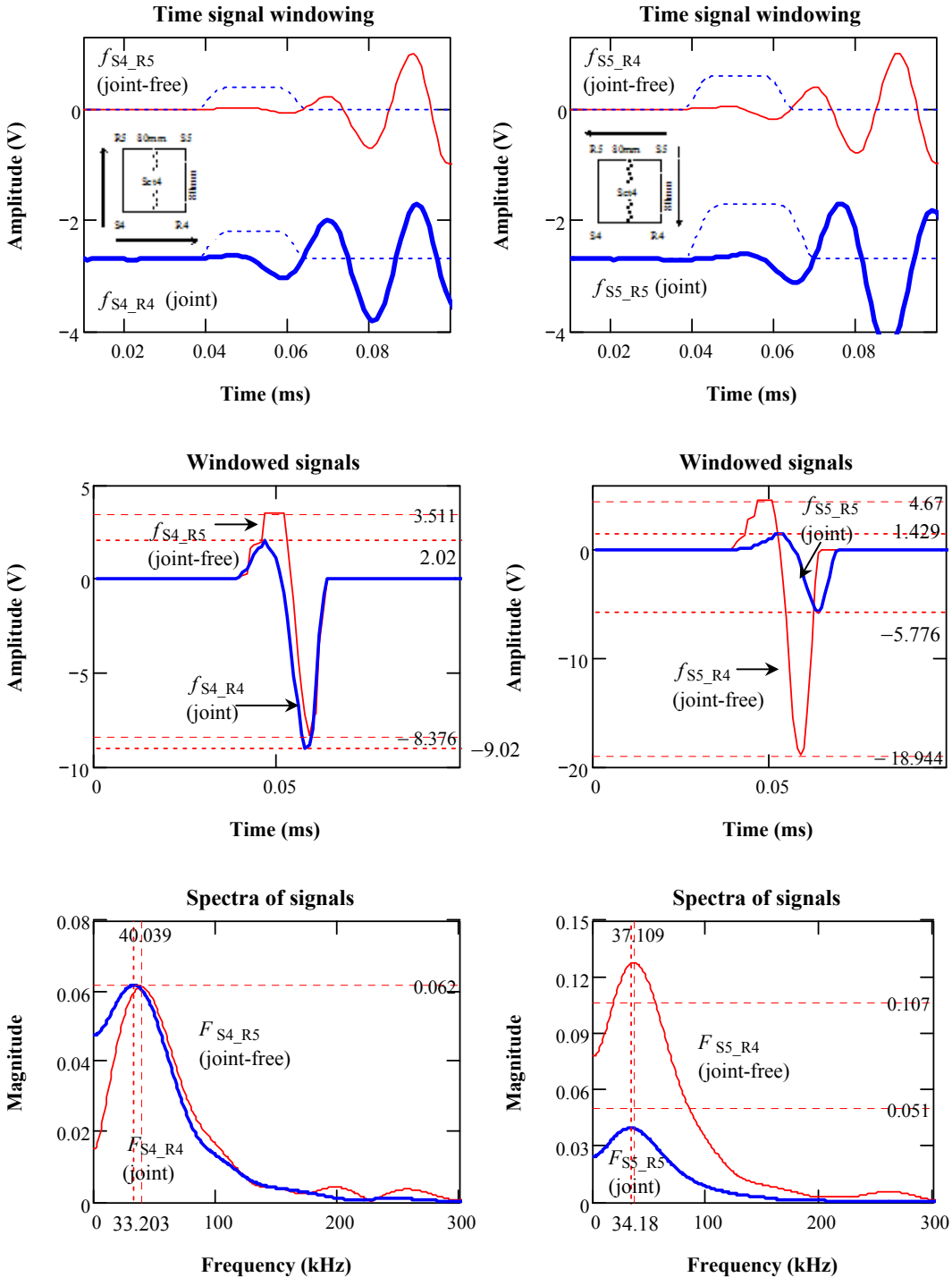

Figure H-20: P-wave analyses in time and frequency domains for Set 4

(Horizontal lines mark the peak amplitudes and vertical lines dominant frequencies.)

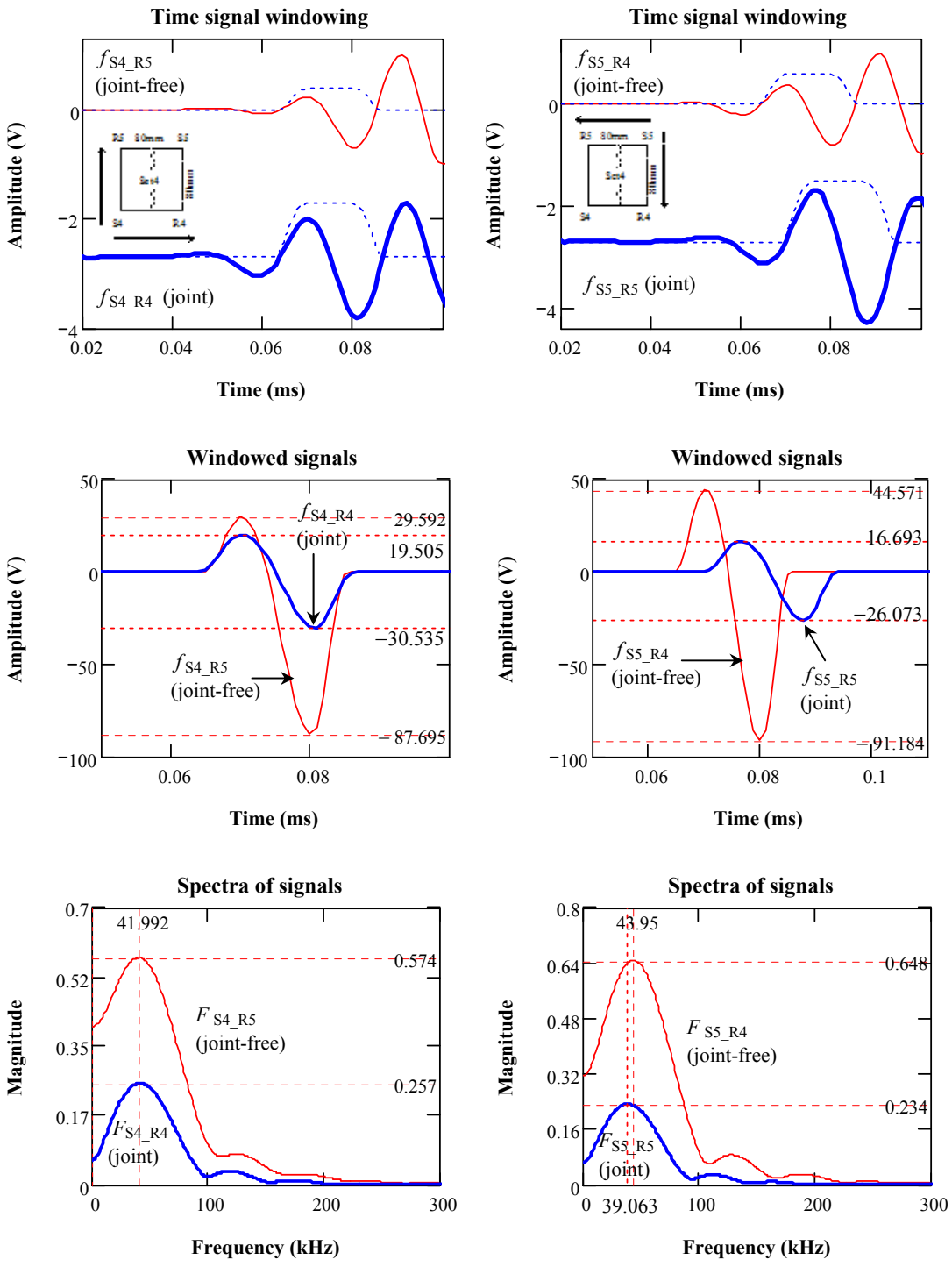

Figure H-21: R-wave analyses in time and frequency domains for Set 4

(Horizontal lines mark the peak amplitudes and vertical lines dominant frequencies.)

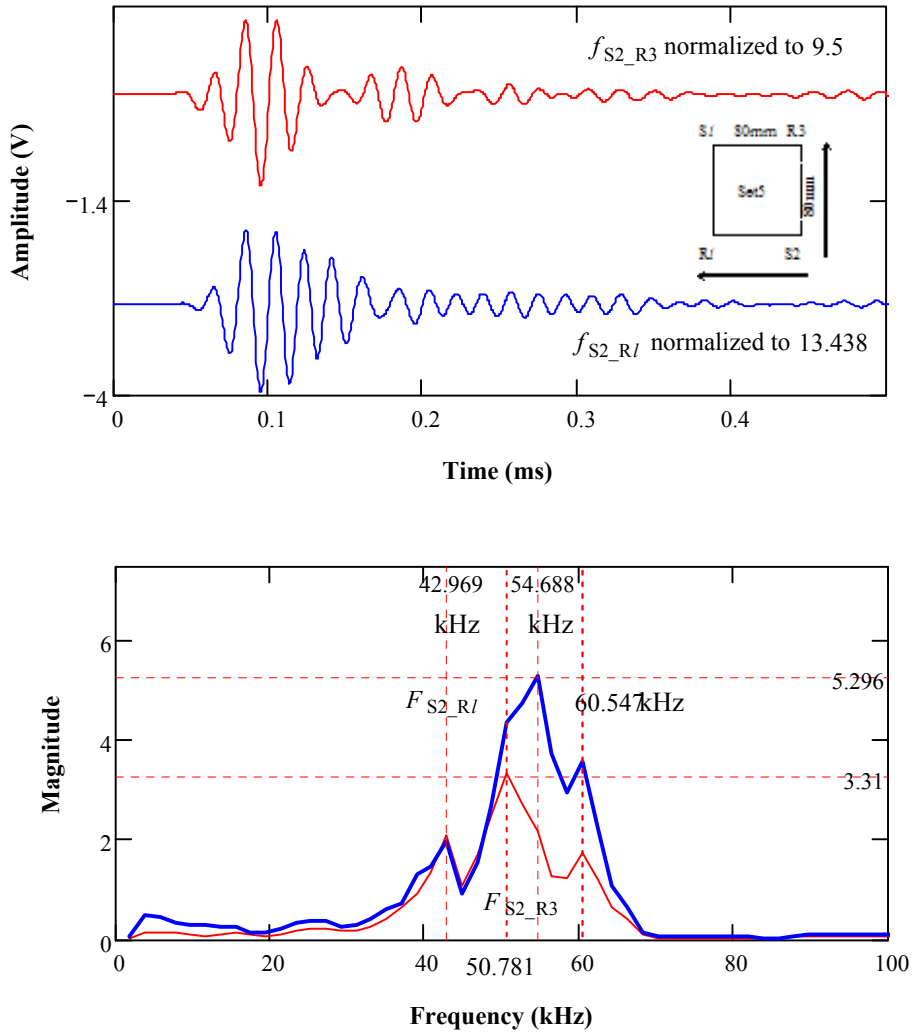

Figure H-22: Signal Pair 1 in time and frequency domains for Set 5 at the left side of the joint (Horizontal lines mark the peak amplitudes and vertical lines dominant frequencies.)

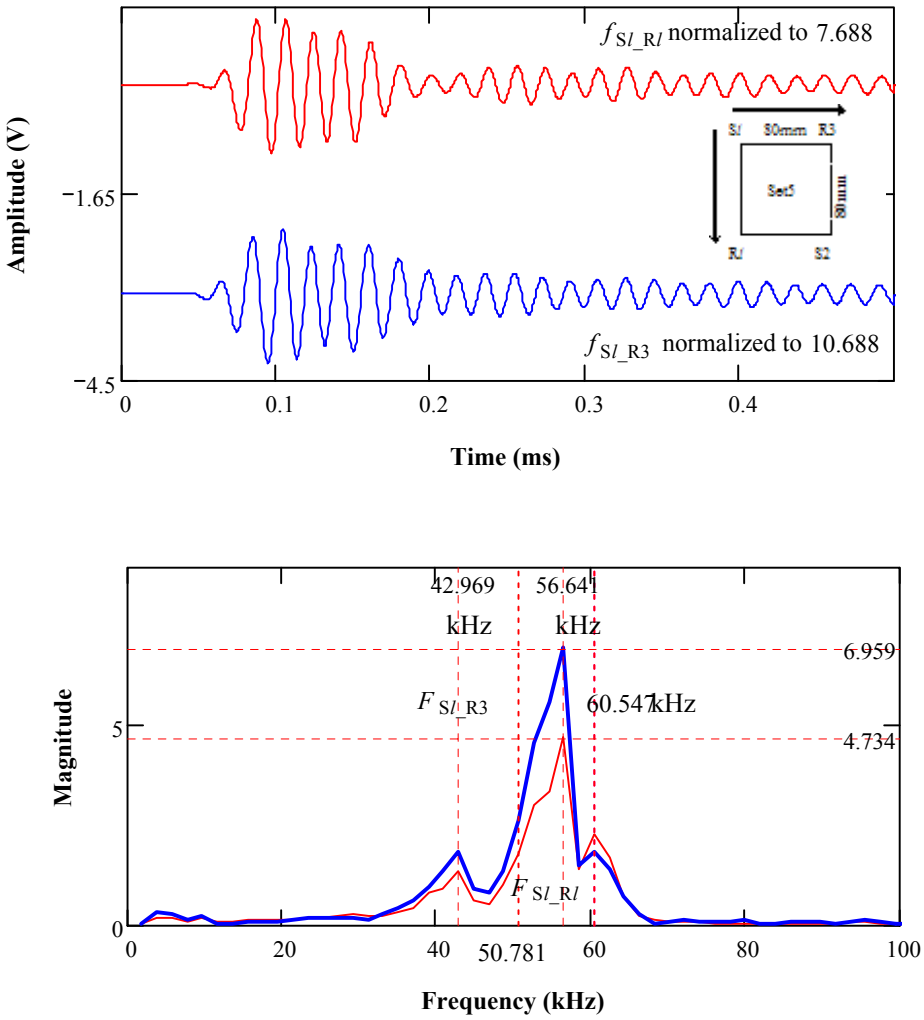

Figure H-23: Signal Pair 2 in time and frequency domains for Set 5 at the left side of the joint (Horizontal lines mark the peak amplitudes and vertical lines dominant frequencies.)

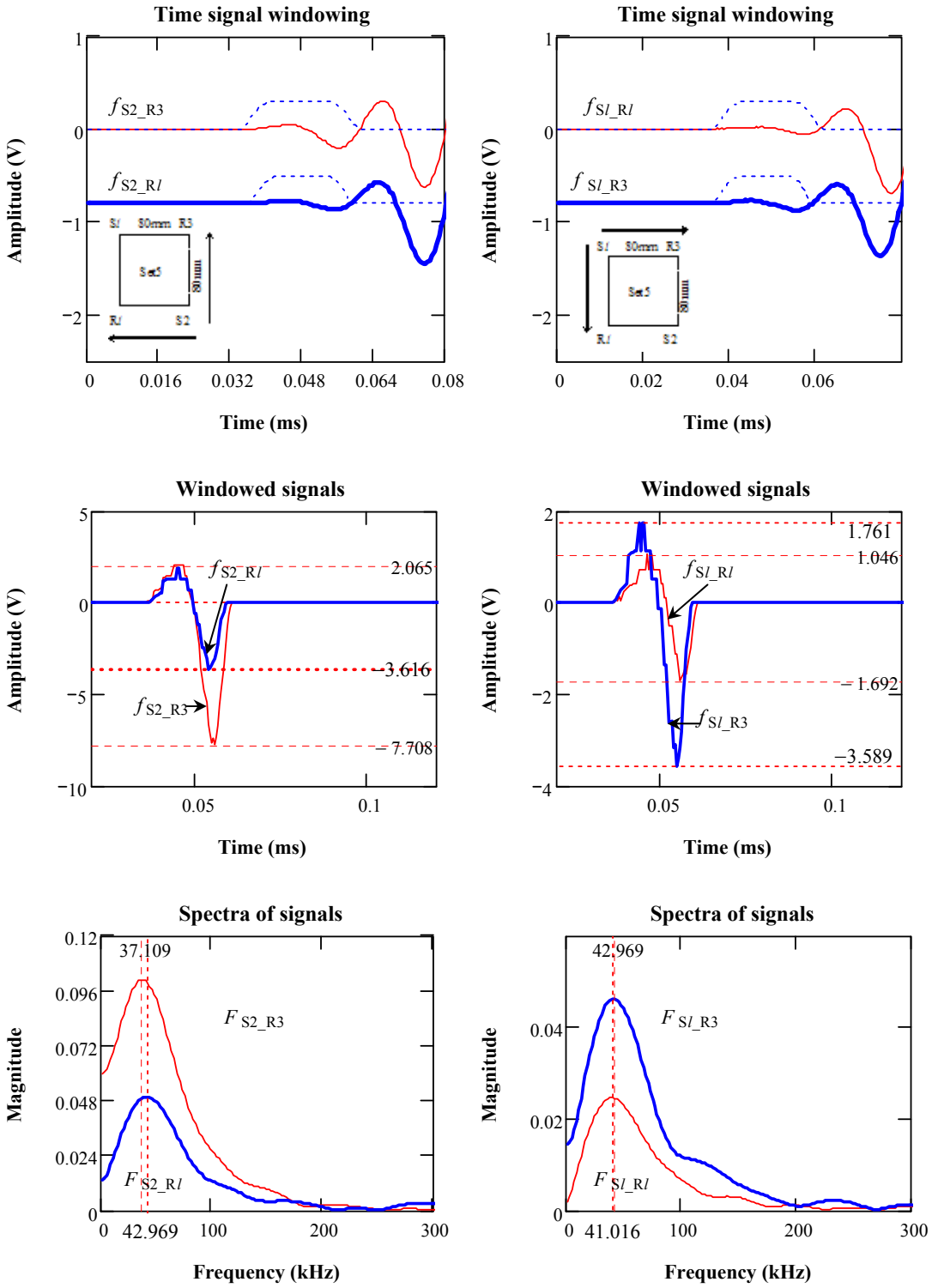

Figure H-24: P-wave analyses in time and frequency domains for Set 5

(Horizontal lines mark the peak amplitudes and vertical lines dominant frequencies.)

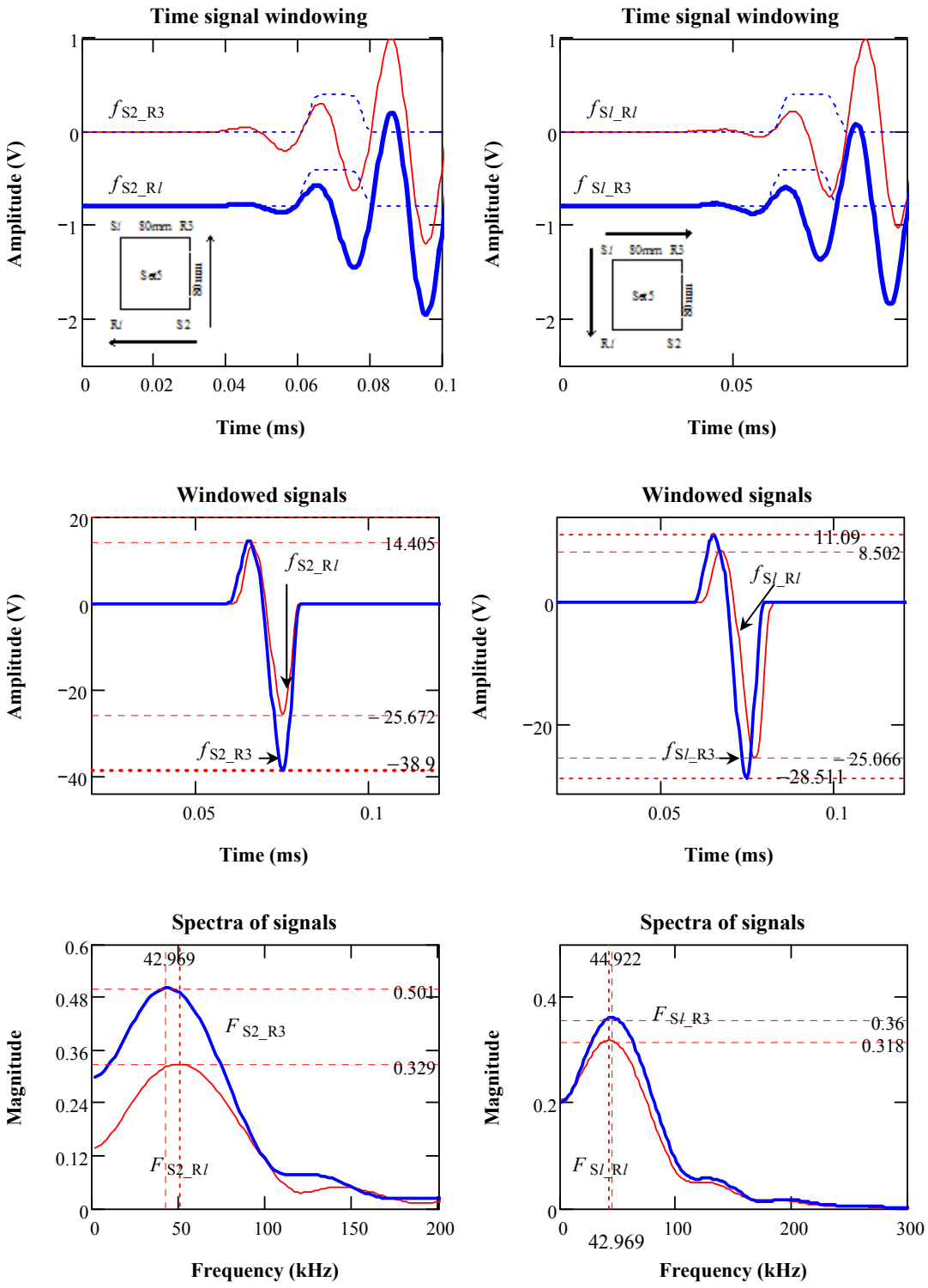

Figure H-25: R-wave analyses in time and frequency domains for Set 5

(Horizontal lines mark the peak amplitudes and vertical lines dominant frequencies.)

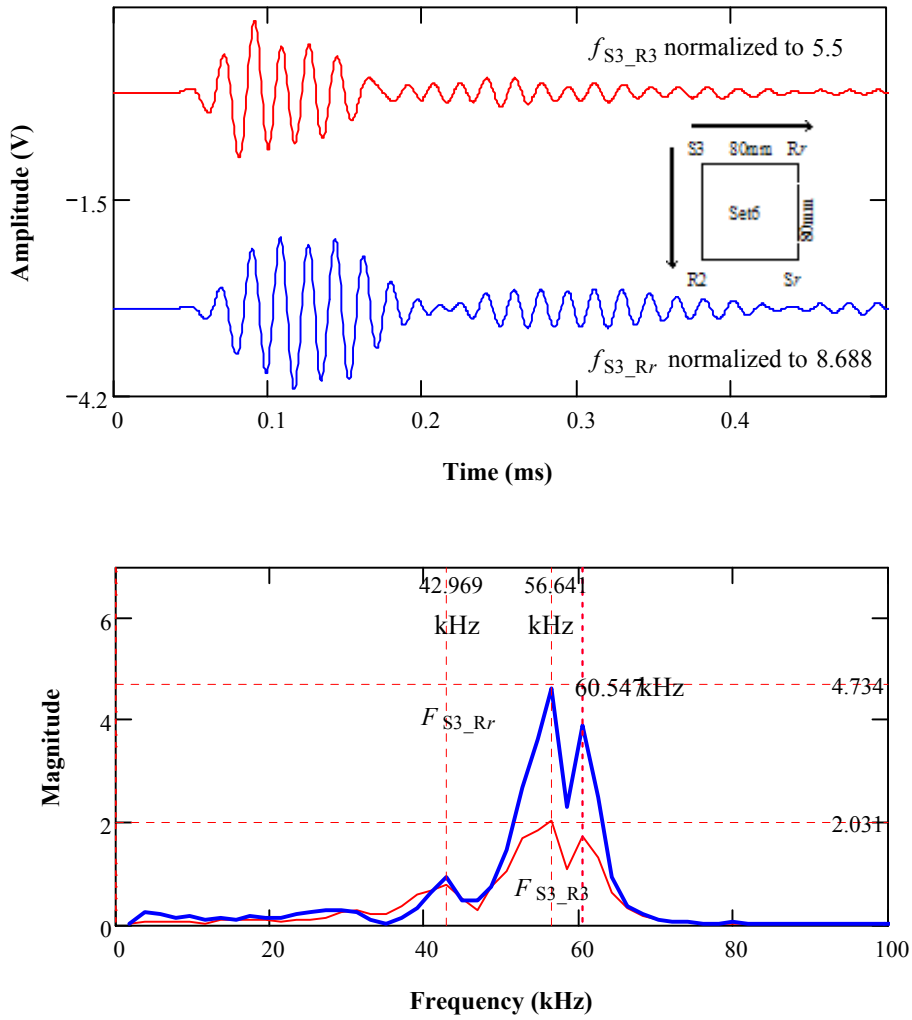

Figure H-26: Signal Pair 1 in time and frequency domains for Set 6 at the right side of the joint (Horizontal lines mark the peak amplitudes and vertical lines dominant frequencies.)

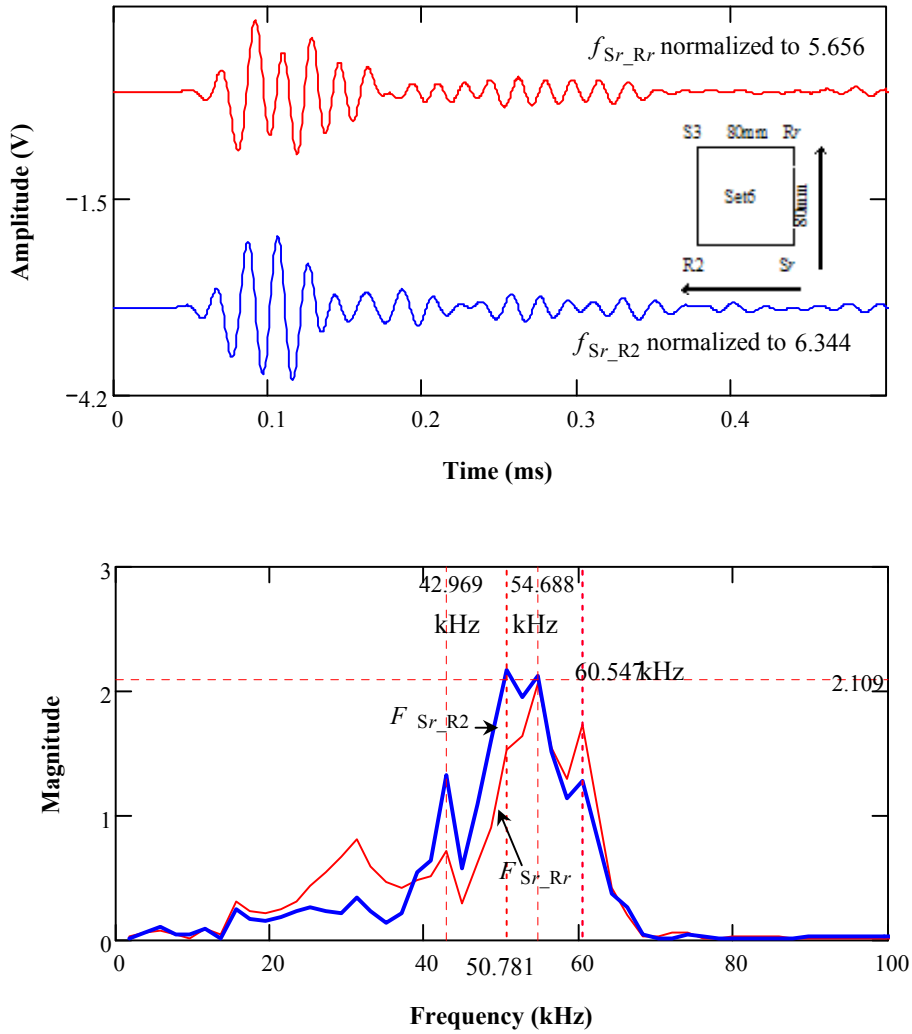

Figure H-27: Signal Pair 2 in time and frequency domains for Set 6 at the right side of the joint (Horizontal lines mark the peak amplitudes and vertical lines dominant frequencies.)

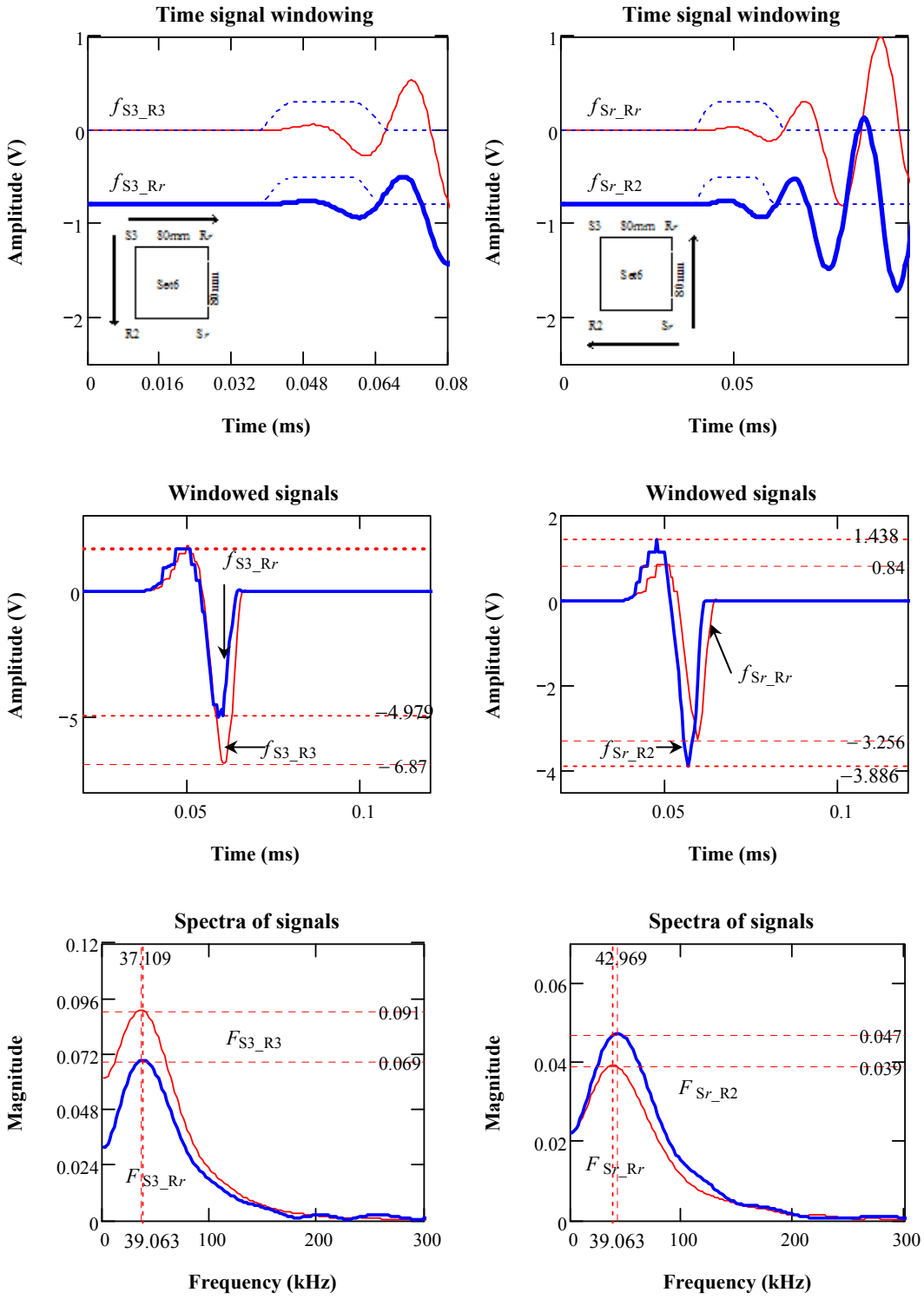

Figure H-28: P-wave analyses in time and frequency domains for Set 6

(Horizontal lines mark the peak amplitudes and vertical lines dominant frequencies.)

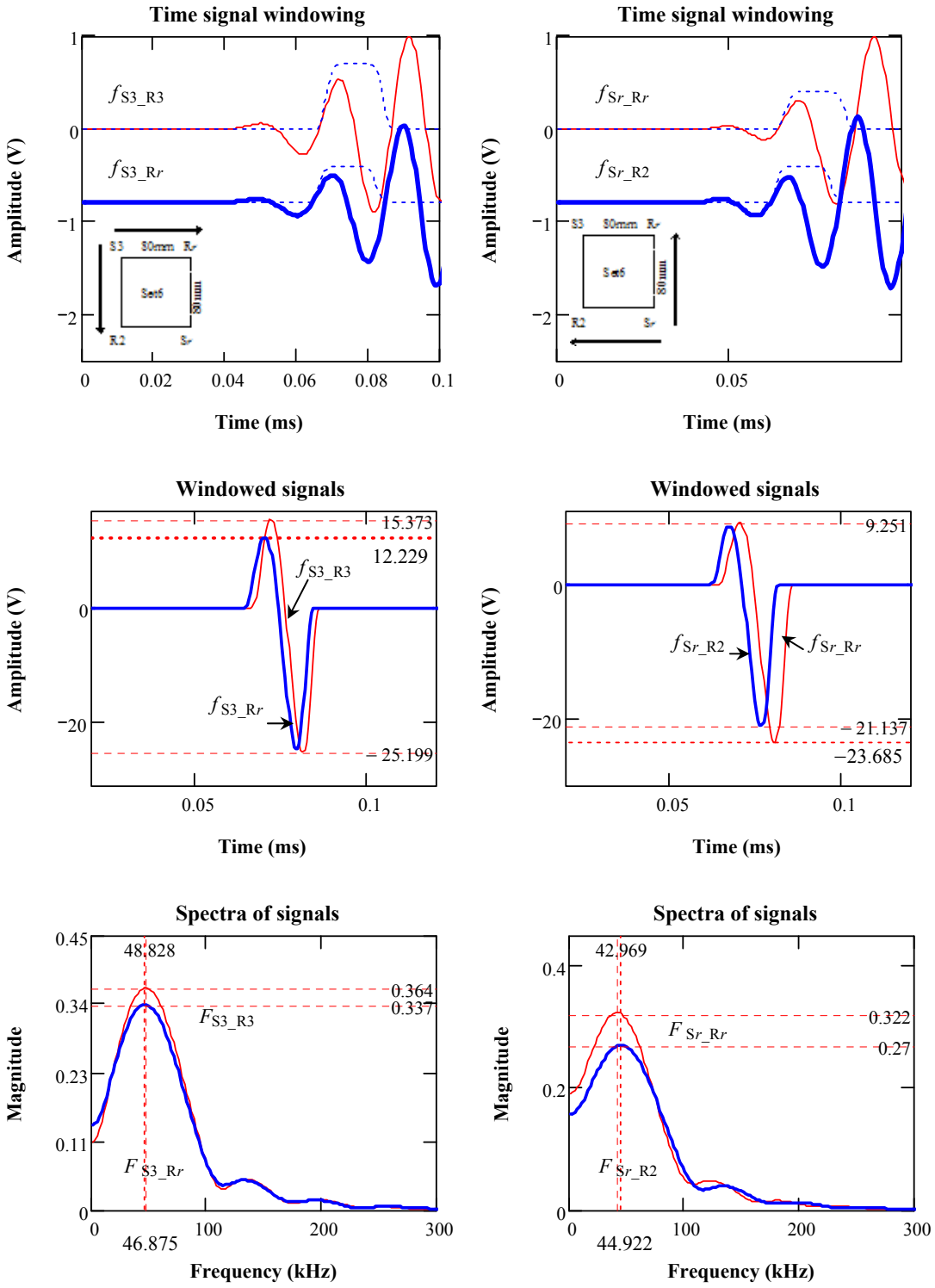

Figure H-29: R-wave analyses in time and frequency domains for Set 6

(Horizontal lines mark the peak amplitudes and vertical lines dominant frequencies.)

Appendix I

Detailed Results of Wave Amplitude Ratios for Slab 2

- Measurements on the Jointed and the Joint-free Surfaces

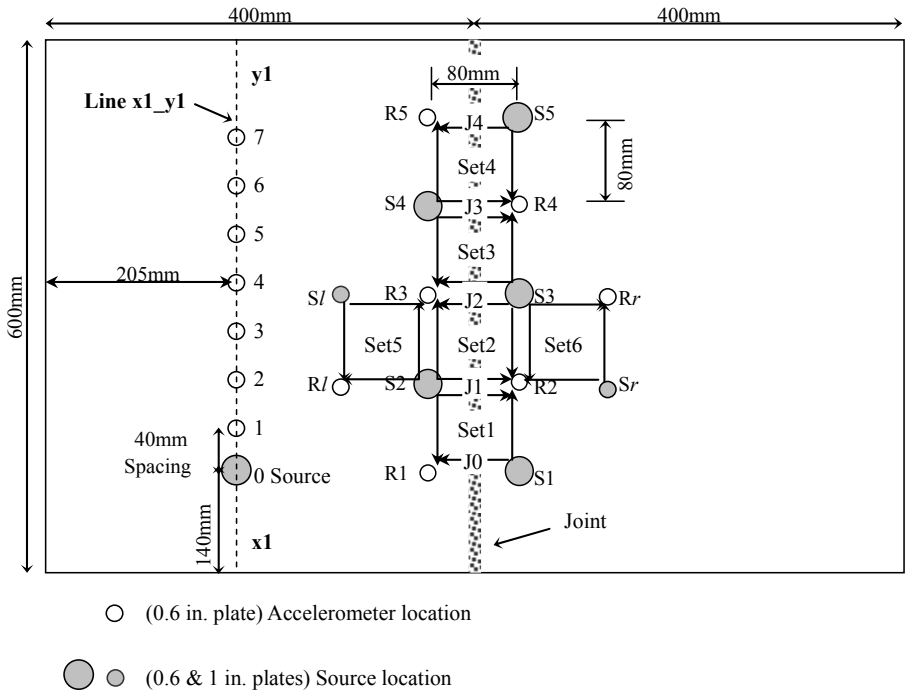

Figure I-1: Ultrasonic test configuration of HMA slab 2

Table I-1: PTP ratio, maximum spectral magnitude ratio, and spectrum area ratio for the jointed surface in slab 2

Locations	Analyzed Portion	Signal ratio (*SR*)	PTP ratio	Magnitude ratio	Area ratio
Jointed surface (Set 1)	Full signal	f_{S2_R2}/f_{S2_R1}	0.35	0.19	0.31
		f_{S1_R1}/f_{S1_R2}	0.62	0.45	0.47
	P-wave	f_{S2_R2}/f_{S2_R1}	0.65	0.66	0.64
		f_{S1_R1}/f_{S1_R2}	0.6	0.65	0.66
	R-wave	f_{S2_R2}/f_{S2_R1}	0.48	0.52	0.45
		f_{S1_R1}/f_{S1_R2}	0.68	0.76	0.68
Jointed surface (Set 2)	Full signal	f_{S2_R2}/f_{S2_R3}	0.44	0.61	0.50
		f_{S3_R3}/f_{S3_R2}	0.6	0.52	0.68
	P-wave	f_{S2_R2}/f_{S2_R3}	0.38	0.35	0.37
		f_{S3_R3}/f_{S3_R2}	0.37	0.35	0.37
	R-wave	f_{S2_R2}/f_{S2_R3}	0.68	0.77	0.69
		f_{S3_R3}/f_{S3_R2}	0.55	0.59	0.58
Jointed surface (Repeated Set 2)	Full signal	f_{S2_R2}/f_{S2_R3}	0.58	0.66	0.62
		f_{S3_R3}/f_{S3_R2}	0.63	1.04	0.68
	P-wave	f_{S2_R2}/f_{S2_R3}	0.53	0.54	0.53
		f_{S3_R3}/f_{S3_R2}	0.35	0.34	0.35
	R-wave	f_{S2_R2}/f_{S2_R3}	0.86	1	0.85
		f_{S3_R3}/f_{S3_R2}	0.51	0.55	0.54
Jointed surface (Set 3)	Full signal	f_{S4_R4}/f_{S4_R3}	0.26	0.25	0.31
		f_{S3_R3}/f_{S3_R4}	0.44	0.67	0.46
	P-wave	f_{S4_R4}/f_{S4_R3}	0.49	0.51	0.51
		f_{S3_R3}/f_{S3_R4}	0.48	0.48	0.49
	R-wave	f_{S4_R4}/f_{S4_R3}	0.43	0.47	0.41
		f_{S3_R3}/f_{S3_R4}	0.50	0.51	0.48
Jointed surface (Set 4)	Full signal	f_{S4_R4}/f_{S4_R5}	0.24	0.2	0.24
		f_{S5_R5}/f_{S5_R4}	0.19	0.067	0.21
	P-wave	f_{S4_R4}/f_{S4_R5}	0.93	1.1	1.1
		f_{S5_R5}/f_{S5_R4}	0.31	0.5	0.3
	R-wave	f_{S4_R4}/f_{S4_R5}	0.43	0.45	0.37
		f_{S5_R5}/f_{S5_R4}	0.32	0.24	0.30
Jointed Surface (Average)	Full signal	$\frac{Set\ 1\ SR + \cdots + Set\ 4\ SR}{5}$	0.44	0.47	0.45
	P-wave		0.51	0.55	0.53
	R-wave		0.49	0.53	0.49

Table I-2: PTP ratio, magnitude ratio and area ratio for the joint-free surfaces in slab 2

Location	Analyzed Portion	Signal ratio (*SR*)	PTP ratio	Magnitude ratio	Area ratio
Joint-free surface (Set 5)	Full signal	f_{S2_Rl}/f_{S2_R3}	1.41	1.58	1.61
		f_{Sl_R3}/f_{Sl_Rl}	1.39	1.47	1.33
	P-wave	f_{S2_Rl}/f_{S2_R3}	0.57	0.5	0.5
		f_{Sl_R3}/f_{Sl_Rl}	1.95	1.84	2
	R-wave	f_{S2_Rl}/f_{S2_R3}	1.37	1.53	1.47
		f_{Sl_R3}/f_{Sl_Rl}	1.17	1.13	1.14
Joint-free surface (Set 6)	Full signal	f_{Sr_R2}/f_{Sr_Rr}	1.58	2.28	1.65
		f_{S3_Rr}/f_{S3_R2}	1.12	1	0.99
	P-wave	f_{Sr_R2}/f_{Sr_Rr}	0.77	0.76	0.75
		f_{S3_Rr}/f_{S3_R2}	1.3	1.21	1.2
	R-wave	f_{Sr_R2}/f_{Sr_Rr}	0.91	0.93	0.96
		f_{S3_Rr}/f_{S3_R2}	0.90	0.84	0.9
Joint-free surface (Average)	Full signal	$\frac{Set\ 5\ SR + Set\ 6\ SR}{2}$	1.38	1.58	1.40
	P-wave		1.15	1.08	1.11
	R-wave		1.09	1.11	1.12

Table I-3: FTC, WTC and damping ratio for the jointed surface in slab 2

Location	Analyzed Portion	Signal ratio (*SR*)	FTC	WTC	Damping ratio
Jointed surface (Set 1)	Full signal	$\sqrt{\frac{f_{S2\_R2}\cdot f_{S1\_R1}}{f_{S2\_R1}\cdot f_{S1\_R2}}}$	0.29 at 55kHz	0.41 at 55kHz	0.07 at 55kHz
	P-wave		0.65 at 37kHz	0.48 at 37kHz	0.06 at 37kHz
	R-wave		0.63 at 44kHz	0.49 at 44kHz	0.03 at 44kHz
Jointed surface (Set 2)	Full signal	$\sqrt{\frac{f_{S2\_R2}\cdot f_{S3\_R3}}{f_{S2\_R3}\cdot f_{S3\_R2}}}$	0.72 at 54kHz	0.51 at 54kHz	0.019 at 54kHz
	P-wave		0.35 at 36kHz	0.6 at 36kHz	0.16 at 36kHz
	R-wave		0.67 at 47kHz	0.53 at 47kHz	0.03 at 47kHz

Table I-3: FTC, WTC and damping ratio for the jointed surface in slab 2 (continuous)

Location	Analyzed Portion	Signal ratio (*SR*)	FTC	WTC	Damping ratio
Jointed surface (Repeated Set 2)	Full signal	$\sqrt{\frac{f_{S2\_R2} \cdot f_{S3\_R3}}{f_{S2\_R3} \cdot f_{S3\_R2}}}$	0.83 at 54kHz	0.58 at 54kHz	0.011 at 54kHz
	P-wave		0.43 at 37kHz	0.64 at 37kHz	0.1 at 37kHz
	R-wave		0.74 at 47kHz	0.61 at 47kHz	0.05 at 47kHz
Jointed surface (Set 3)	Full signal	$\sqrt{\frac{f_{S4\_R4} \cdot f_{S3\_R3}}{f_{S4\_R3} \cdot f_{S3\_R4}}}$	0.41 at 52kHz	0.33 at 52kHz	0.054 at 52kHz
	P-wave		0.49 at 36kHz	0.34 at 36kHz	0.1 at 36kHz
	R-wave		0.49 at 42kHz	0.33 at 42kHz	0.05 at 42kHz
Jointed surface (Set 4)	Full signal	$\sqrt{\frac{f_{S4\_R4} \cdot f_{S5\_R5}}{f_{S4\_R5} \cdot f_{S5\_R4}}}$	0.17 at 51kHz	0.2 at 51kHz	0.11 at 51kHz
	P-wave		0.74 at 36kHz	0.22 at 36kHz	0.04 at 36kHz
	R-wave		0.33 at 41kHz	0.23 at 41kHz	0.09 at 41kHz
Jointed surface (Average)	Full signal	$\frac{Set\ 1\ SR + \cdots + Set\ 4\ SR}{5}$	0.48 at 54kHz	0.41 at 54kHz	0.033 at 54kHz
	P-wave		0.53 at 36kHz	0.46 at 36kHz	0.09 at 36kHz
	R-wave		0.57 at 44kHz	0.44 at 44kHz	0.05 at 44kHz

Table I-4: FTC, WTC and damping ratio for the joint-free surfaces in slab 2

Location	Analyzed Portion	Signal ratio (*SR*)	FTC	WTC	Damping ratio
Joint-free surface (Set 5)	Full signal	$\sqrt{\frac{f_{S2\_Rl} \cdot f_{Sl\_R3}}{f_{S2\_R3} \cdot f_{Sl\_Rl}}}$	1.52 at 55kHz	1.36 at 55kHz	0.024 at 55kHz
	P-wave		0.95 at 41kHz	1.43 at 41kHz	-0.005 at 41kHz
	R-wave		1.31 at 45kHz	1.42 at 45kHz	0.02 at 45kHz
Joint-free surface (Set 6)	Full signal	$\sqrt{\frac{f_{Sr\_R2} \cdot f_{S3\_Rr}}{f_{Sr\_Rr} \cdot f_{S3\_R2}}}$	1.47 at 48kHz	1.19 at 48kHz	0.025 at 48kHz
	P-wave		0.96 at 40kHz	1.13 at 40kHz	-0.01 at 40kHz
	R-wave		0.88 at 46kHz	1.13 at 46kHz	-0.01 at 46kHz
Joint-free surface (Average)	Full signal	$\frac{Set\ 5\ SR + Set\ 6\ SR}{2}$	1.50 at 52kHz	1.28 at 52kHz	0.025 at 52kHz
	P-wave		0.96 at 40kHz	1.28 at 40kHz	-0.0075 at 40kHz
	R-wave		1.10 at 45kHz	1.28 at 45kHz	0.005 at 45kHz

Appendix J

FTC vs. Frequency and Wavelength/3 for Slab 2

- Measurements on the Jointed and the Joint-free Surfaces

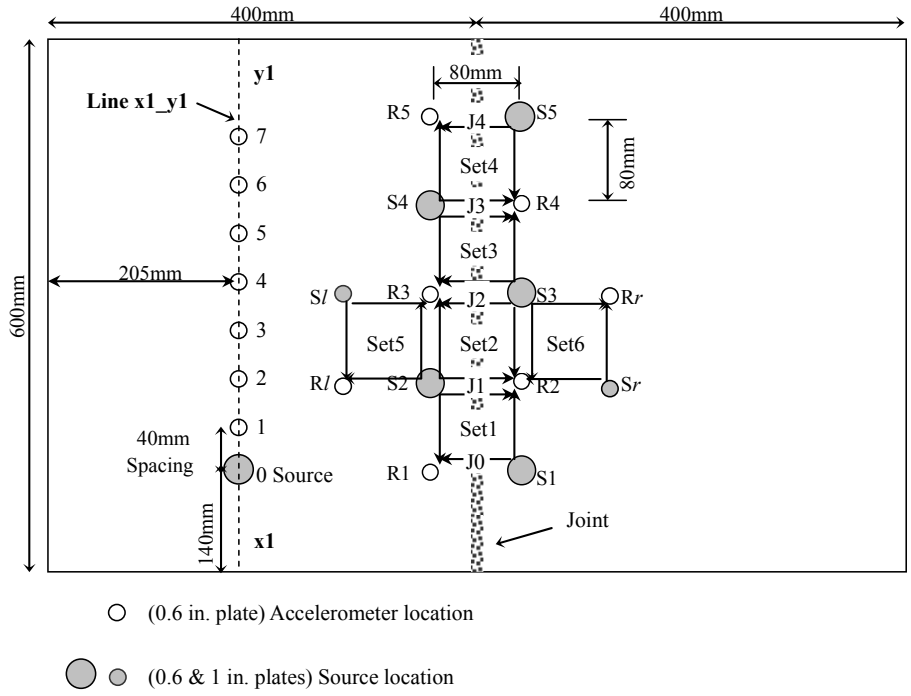

Figure J-1: Ultrasonic test configuration of HMA slab 2

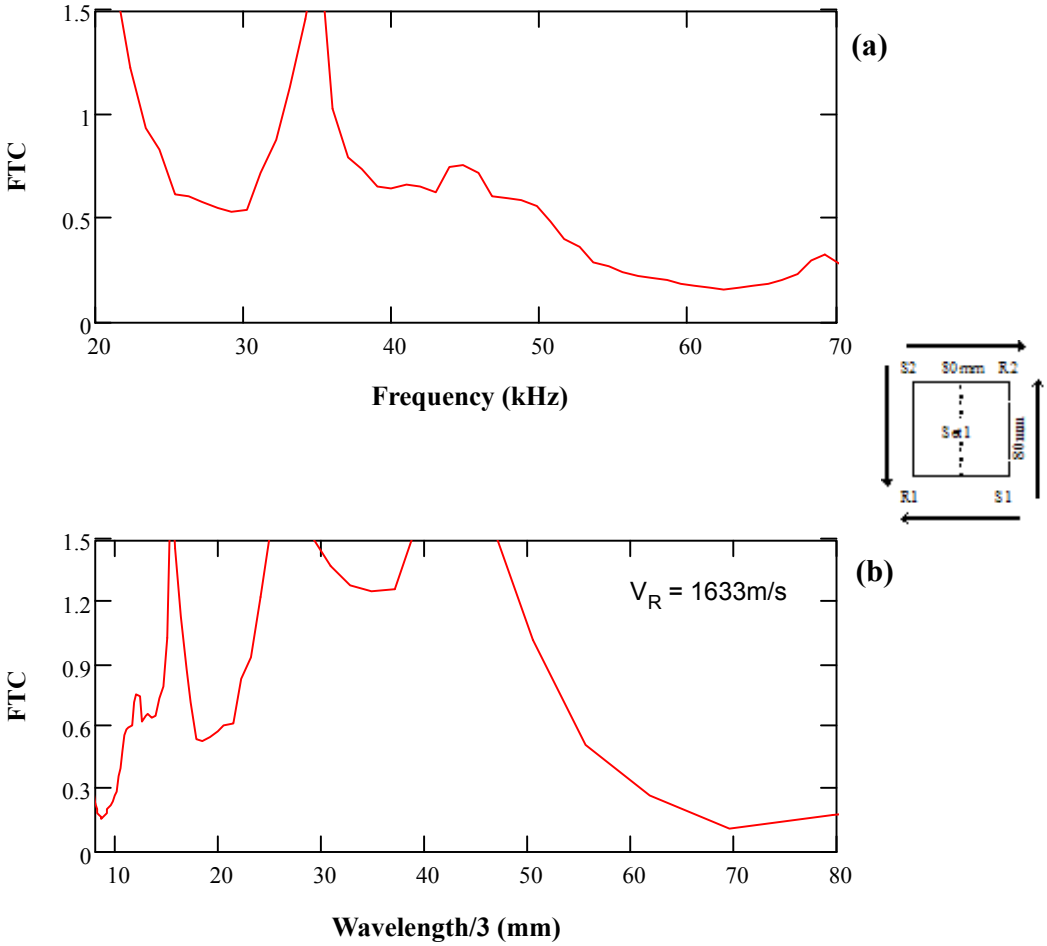

Figure J-2: (a) FTC vs. frequency and (b) FTC vs. wavelength/3 for full signals of set 1 measurements

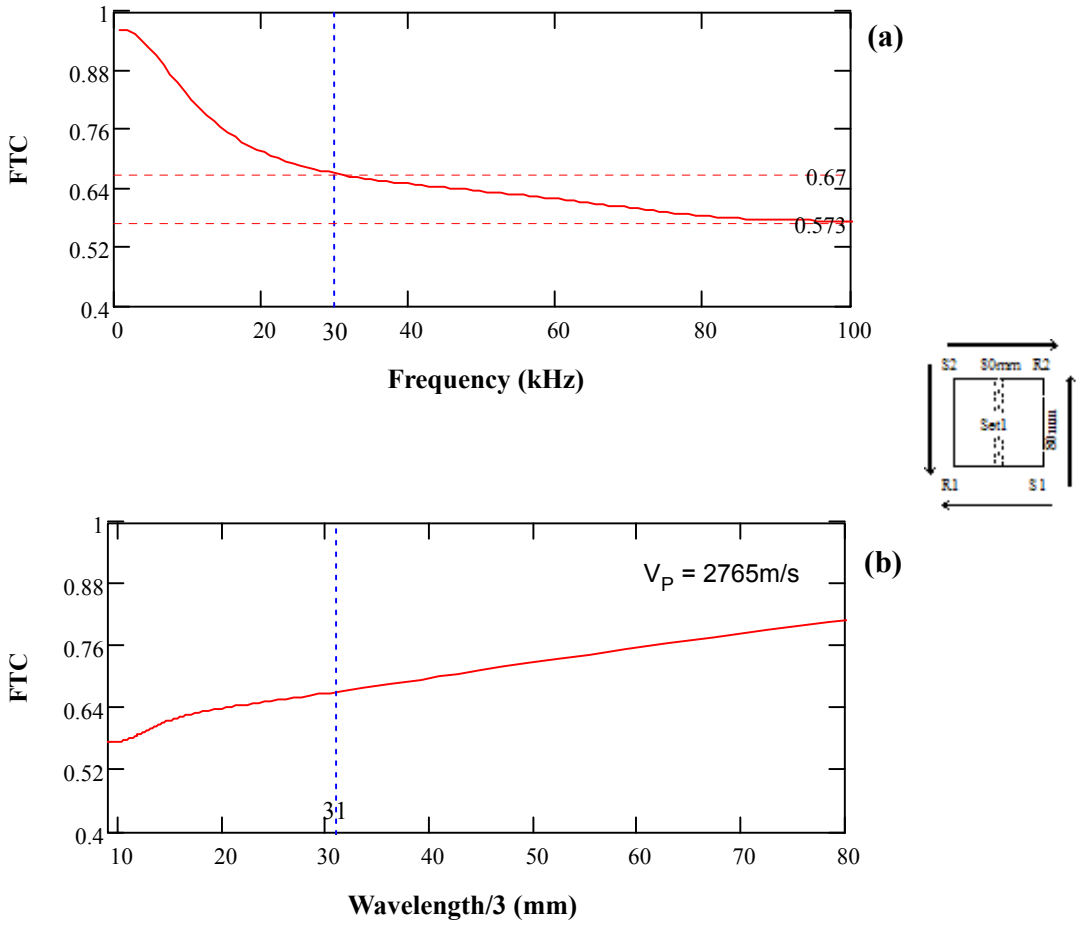

Figure J-3: (a) FTC vs. frequency and (b) FTC vs. wavelength/3 for P-waves for set 1 measurements

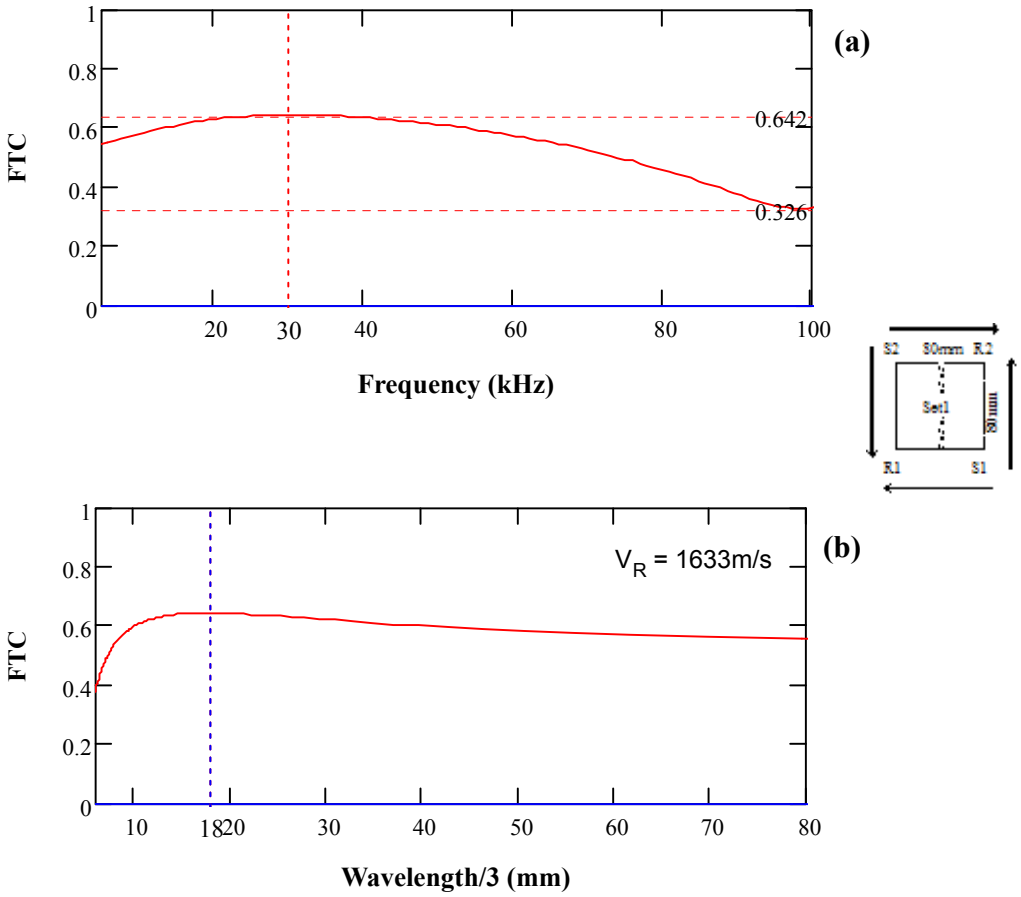

Figure J-4: (a) FTC vs. frequency and (b) FTC vs. wavelength/3 for P-waves for set 1 measurements

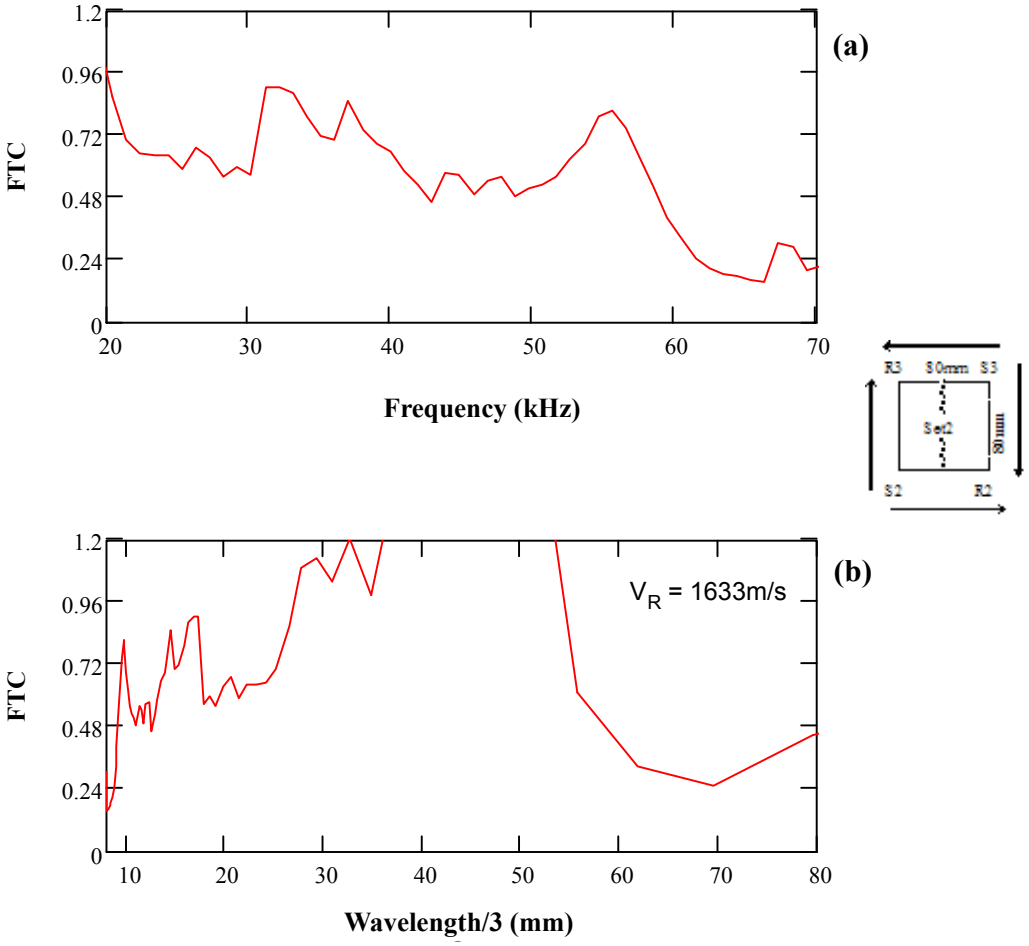

Figure J-5: (a) FTC vs. frequency and (b) FTC vs. wavelength/3 for full signals of set 2 measurements

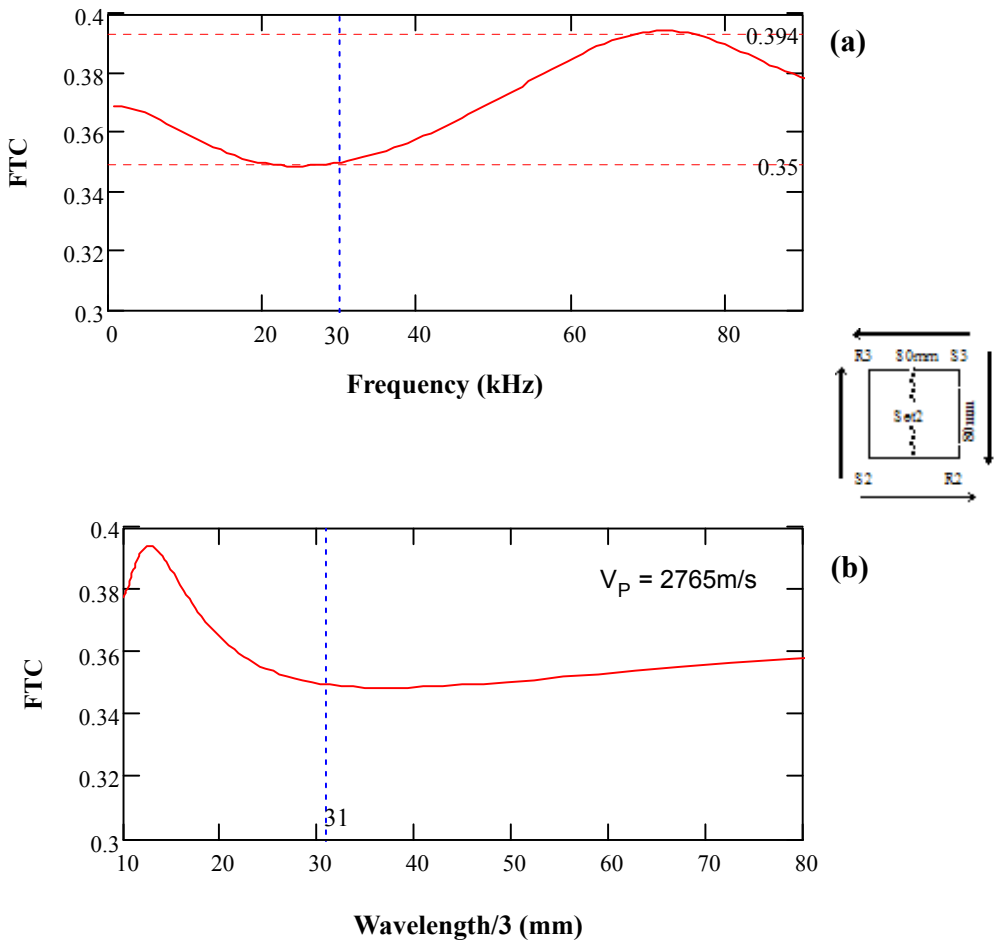

Figure J-6: (a) FTC vs. frequency and (b) FTC vs. wavelength/3 for P-waves for set 2 measurements

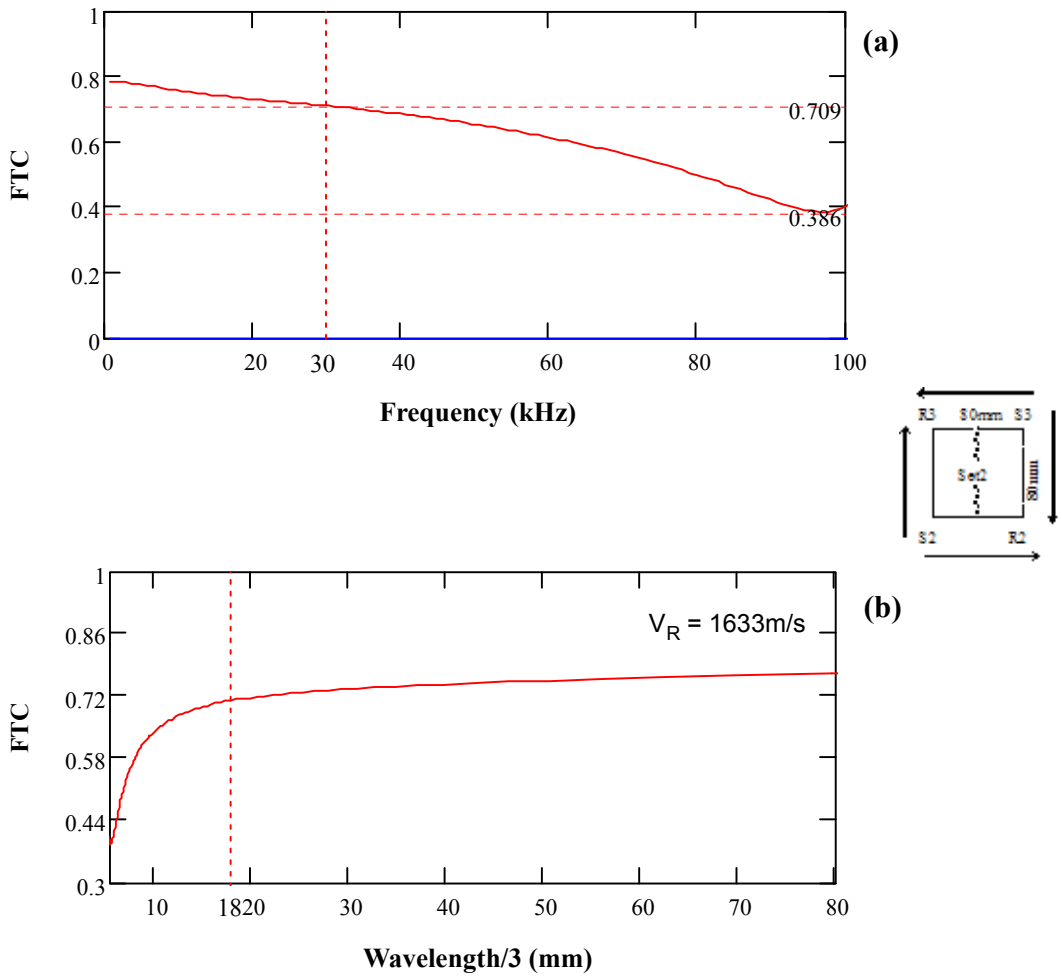

Figure J-7: (a) FTC vs. frequency and (b) FTC vs. wavelength/3 for R-waves for set 2 measurements

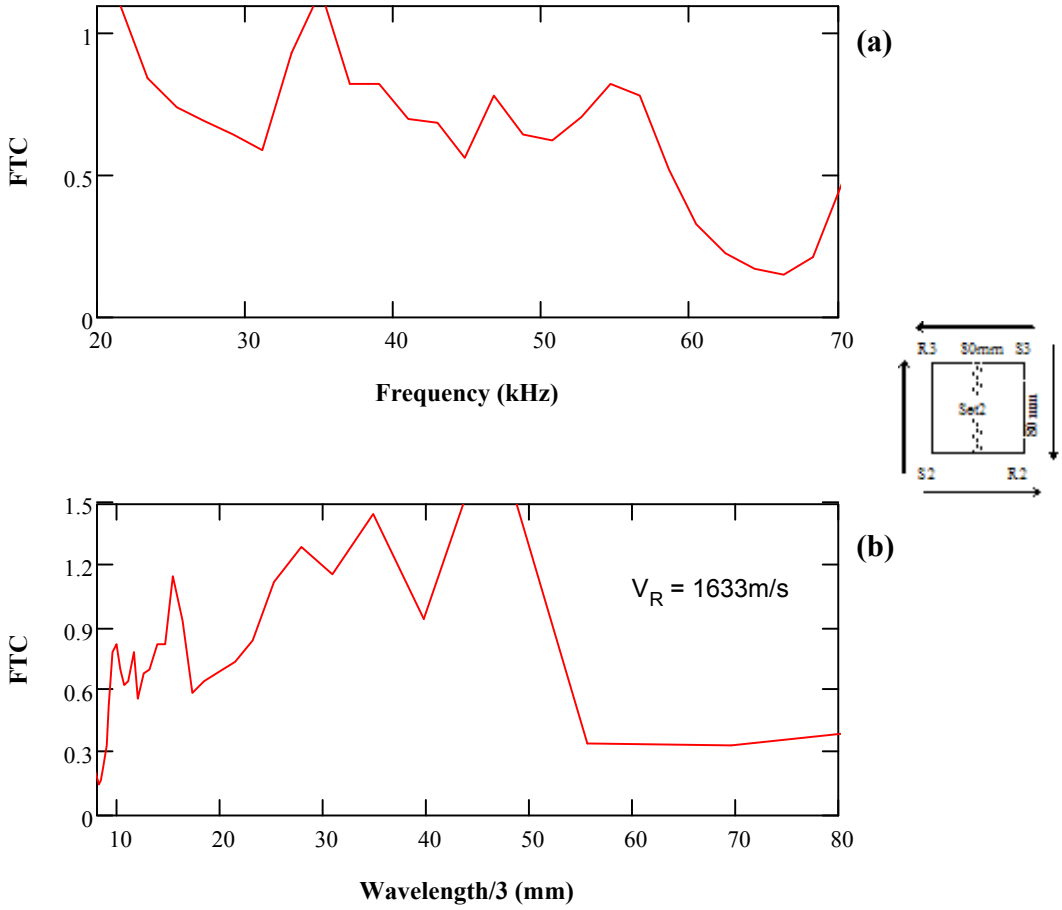

Figure J-8: (a) FTC vs. frequency and (b) FTC vs. wavelength/3 for full signals for repeated set 2 measurements

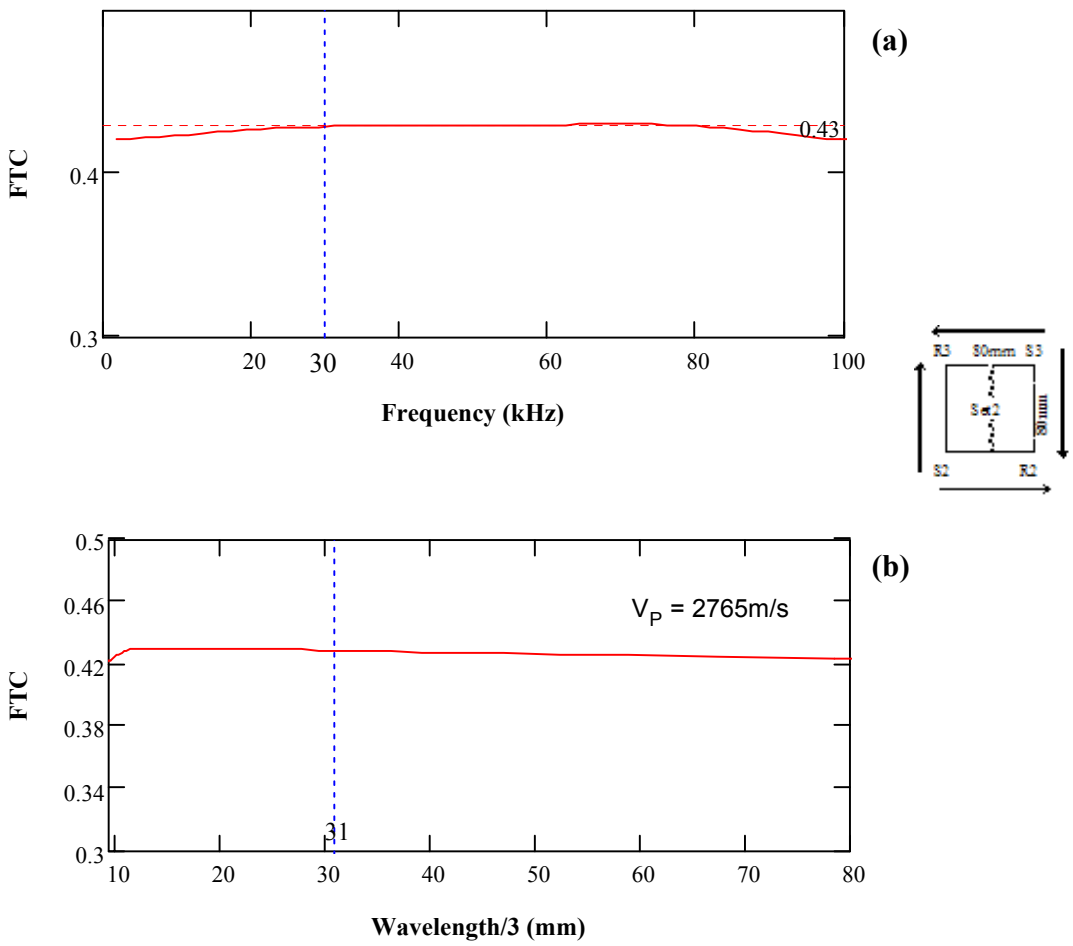

Figure J-9: (a) FTC vs. frequency and (b) FTC vs. wavelength/3 for P-waves for repeated set 2 measurements

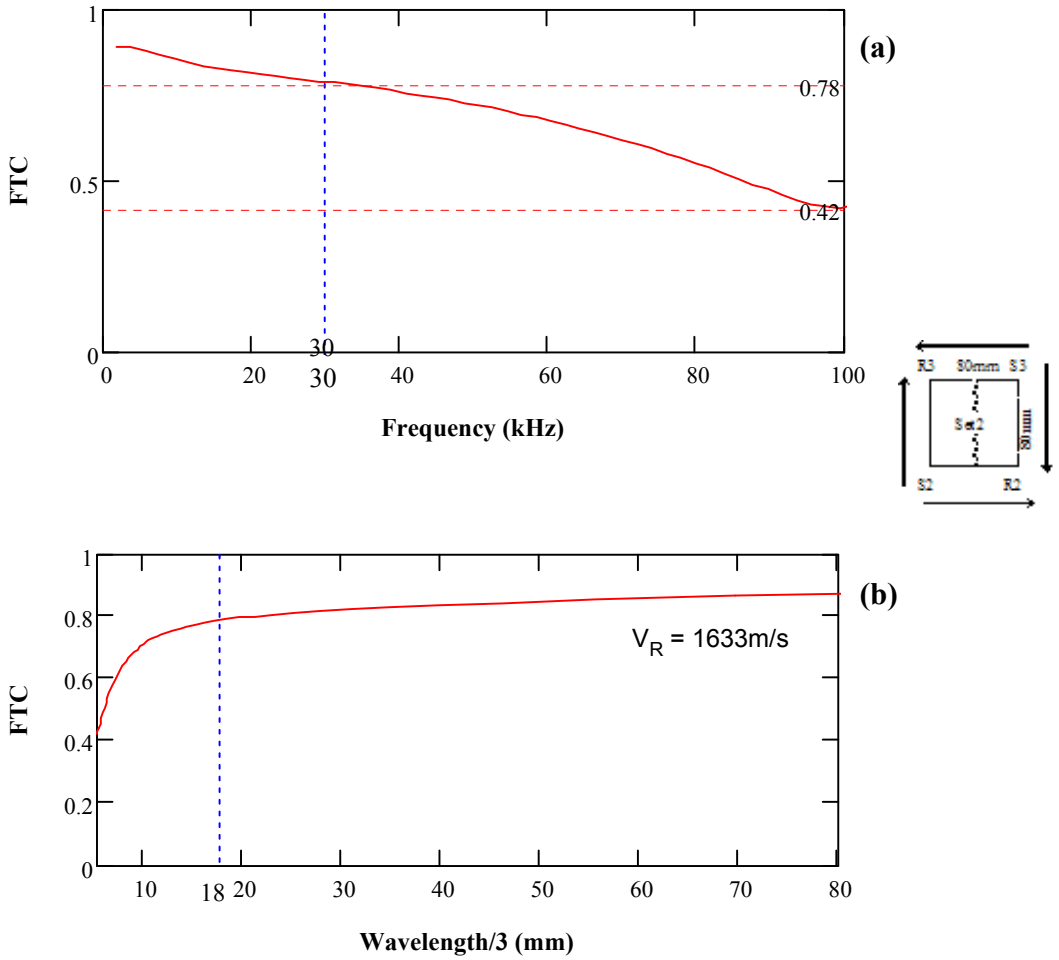

Figure J-10: (a) FTC vs. frequency and (b) FTC vs. wavelength/3 for R-waves for repeated set 2 measurements

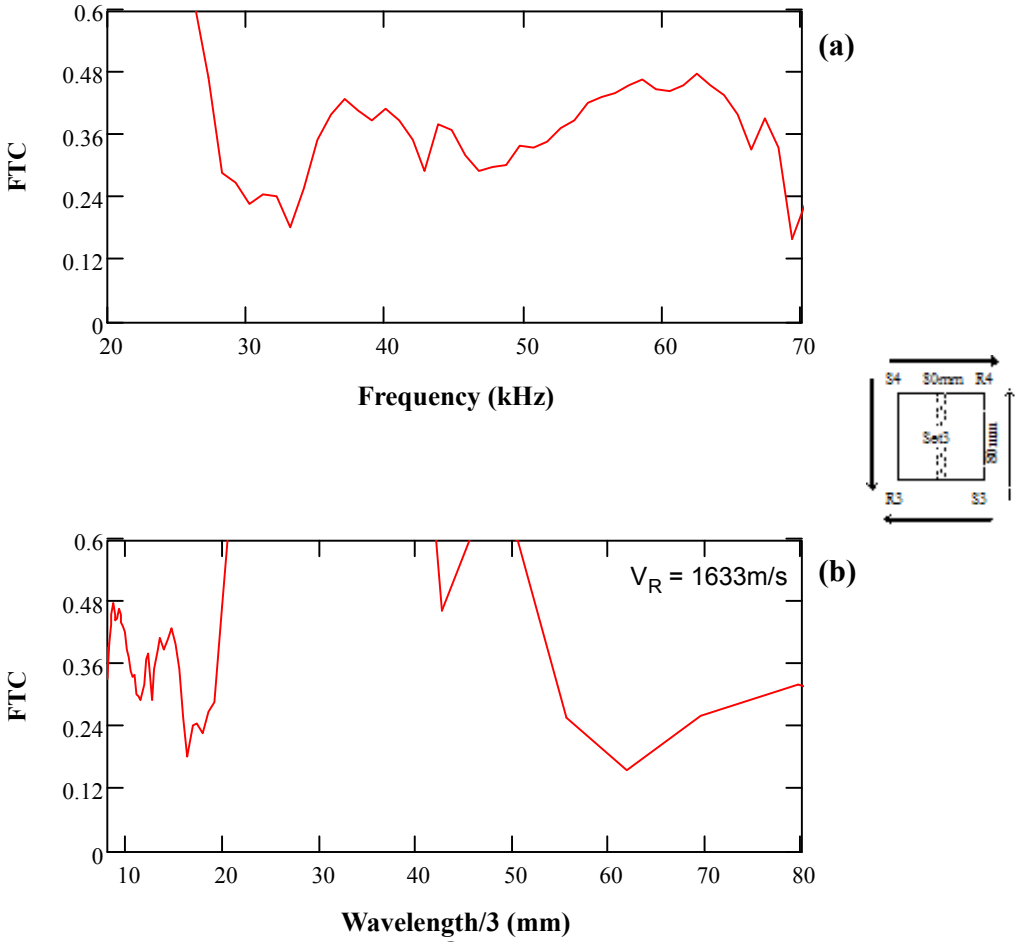

Figure J-11: (a) FTC vs. frequency and (b) FTC vs. wavelength/3 for full signals of set 3 measurements

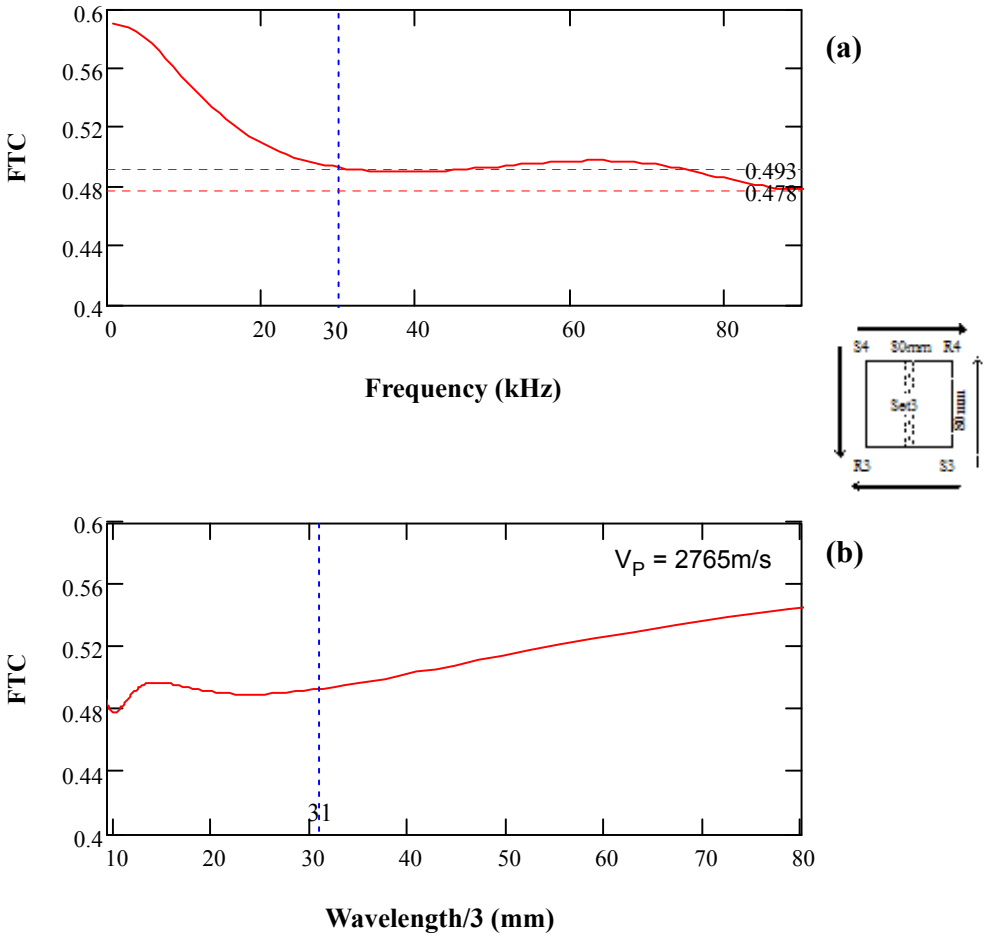

Figure J-12: (a) FTC vs. frequency and (b) FTC vs. wavelength/3 for P-waves for set 3 measurements

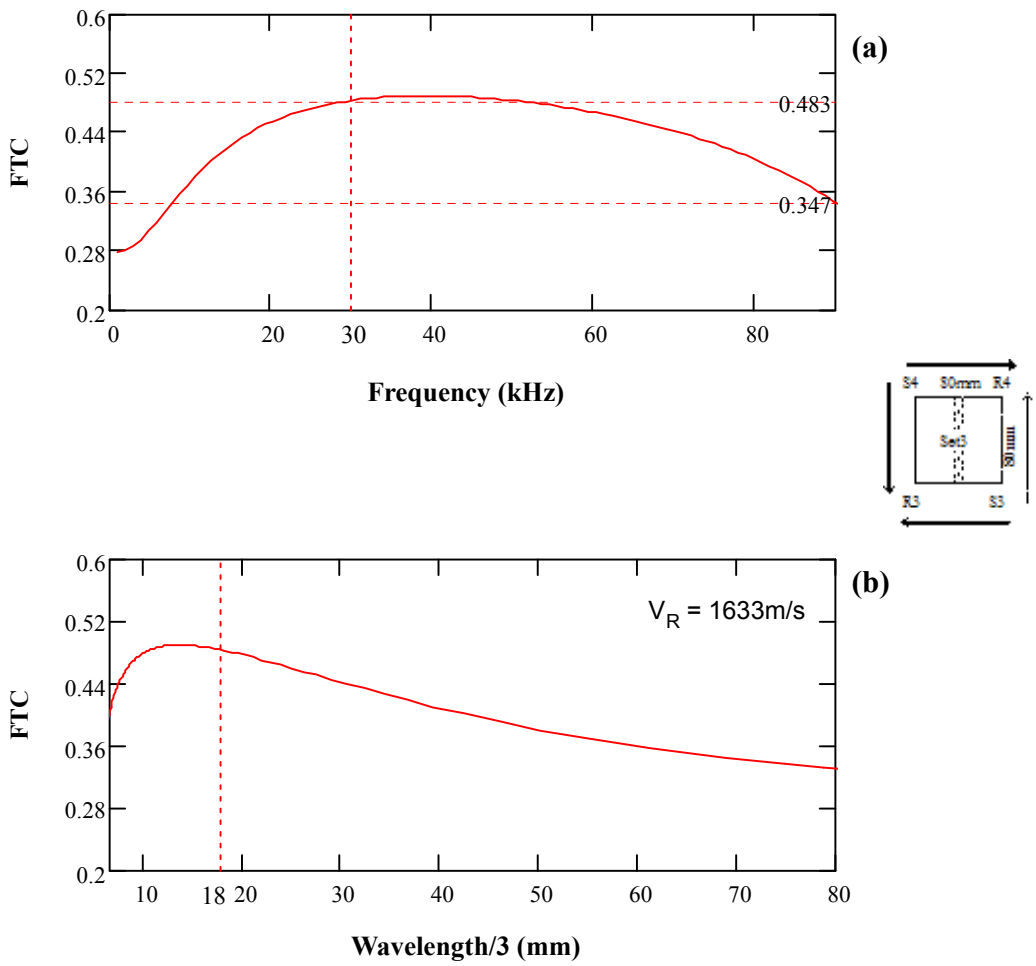

Figure J-13: (a) FTC vs. frequency and (b) FTC vs. wavelength/3 for R-waves for set 3 measurements

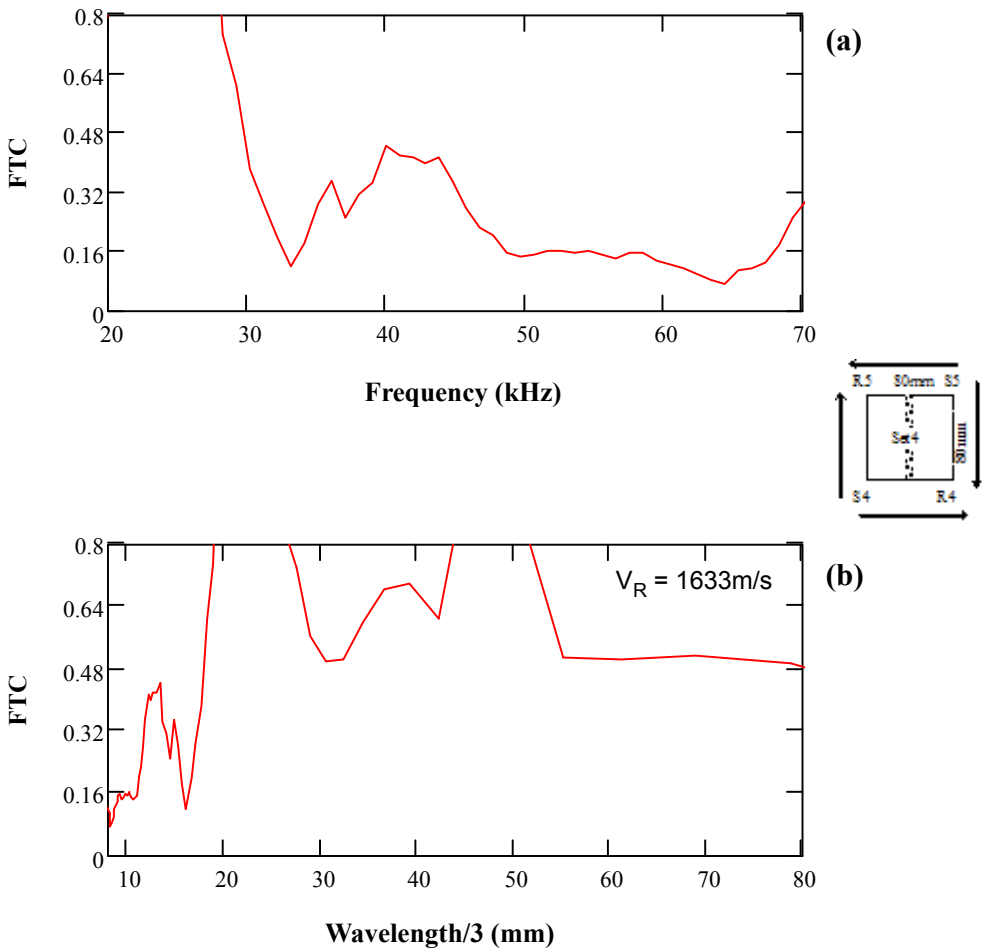

Figure J-14: (a) FTC vs. frequency and (b) FTC vs. wavelength/3 for full signals of set 4 measurements

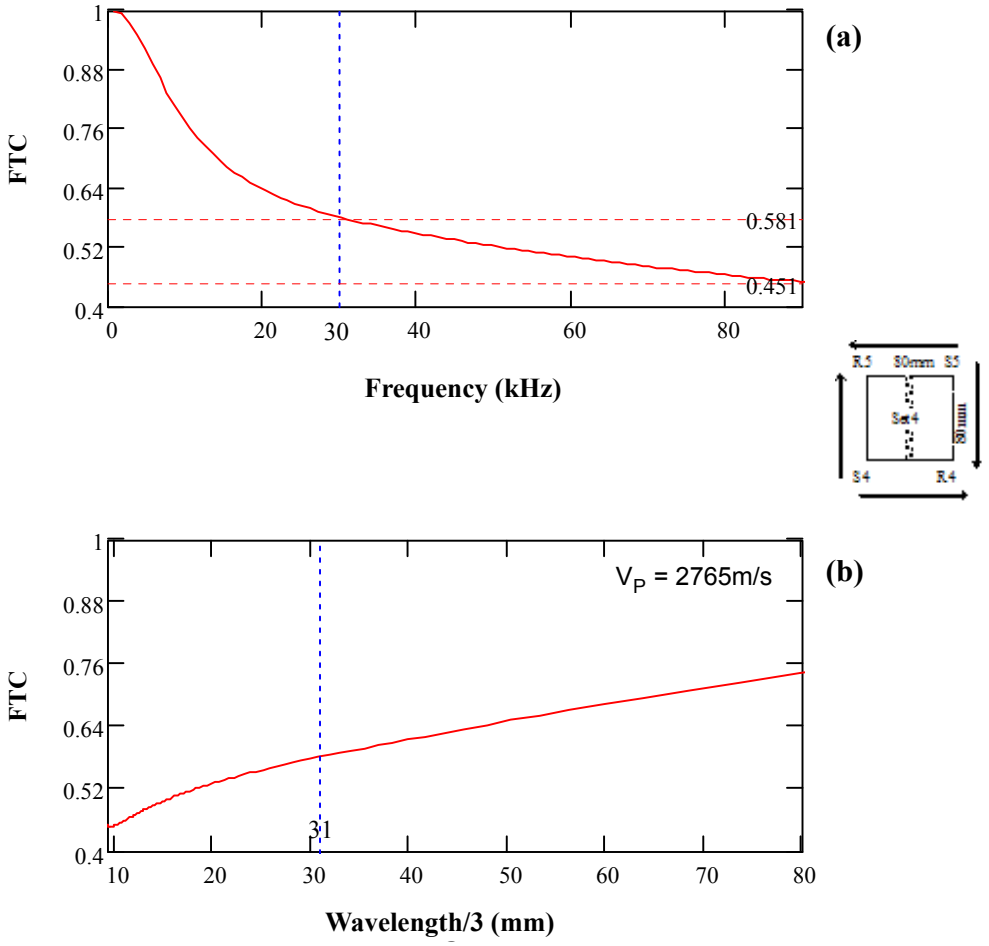

Figure J-15: (a) FTC vs. frequency and (b) FTC vs. wavelength/3 for P-waves for set 4 measurements

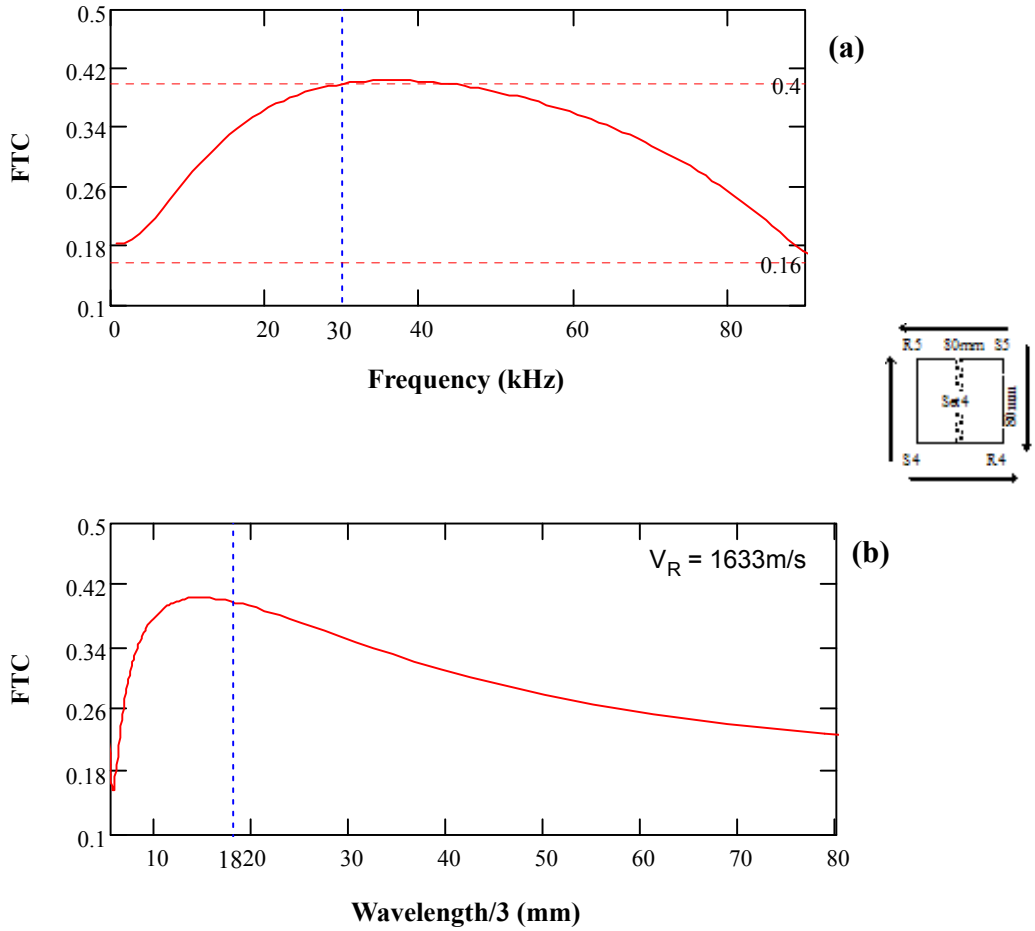

Figure J-16: (a) FTC vs. frequency and (b) FTC vs. wavelength/3 for R-waves for set 4 measurements

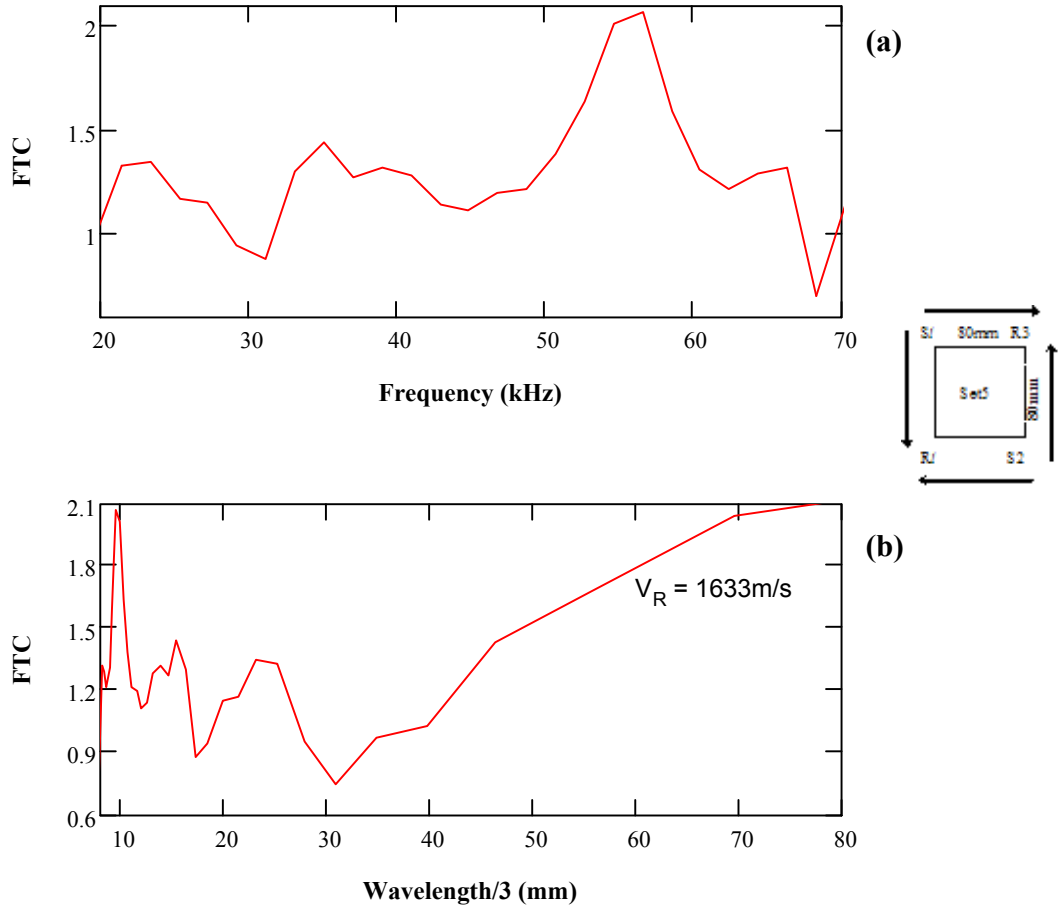

Figure J-17: (a) FTC vs. frequency and (b) FTC vs. wavelength/3 for full signals for set 5 measurements at the left side of the joint

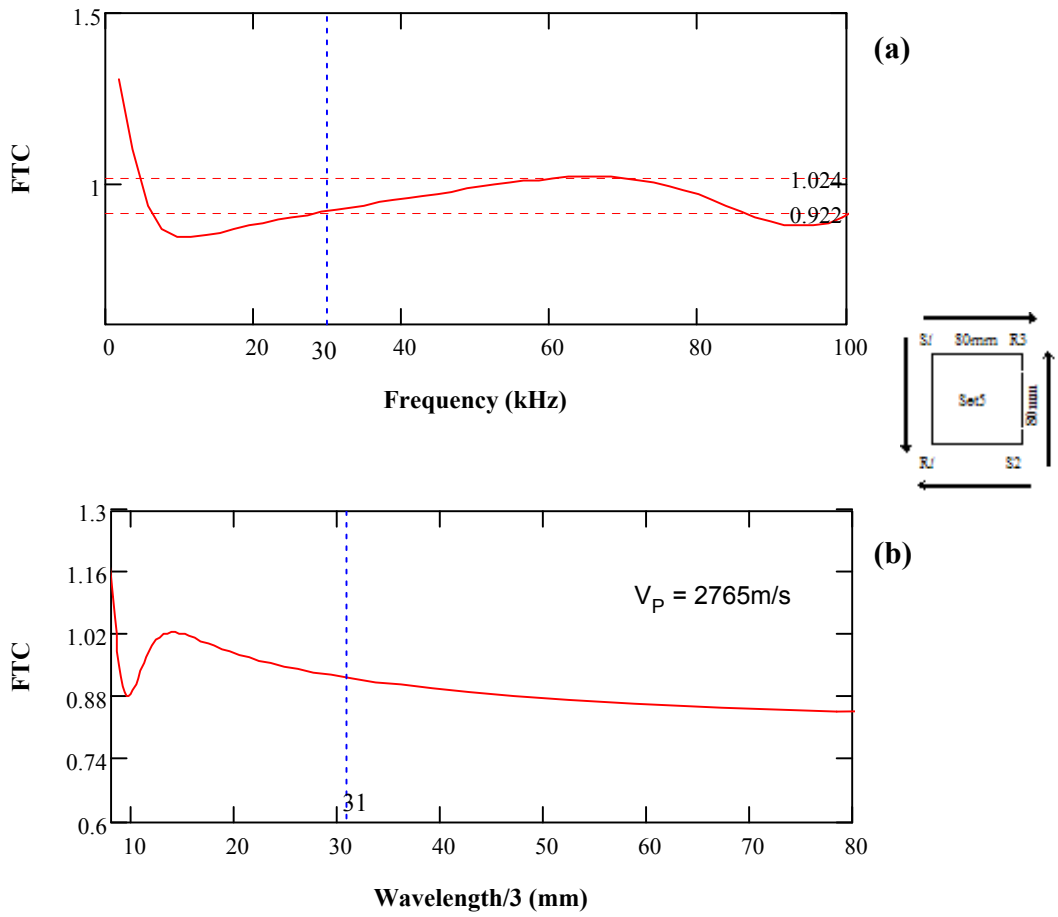

Figure J-18: (a) FTC vs. frequency and (b) FTC vs. wavelength/3 for P-waves for set 5 measurements at the left side of the joint

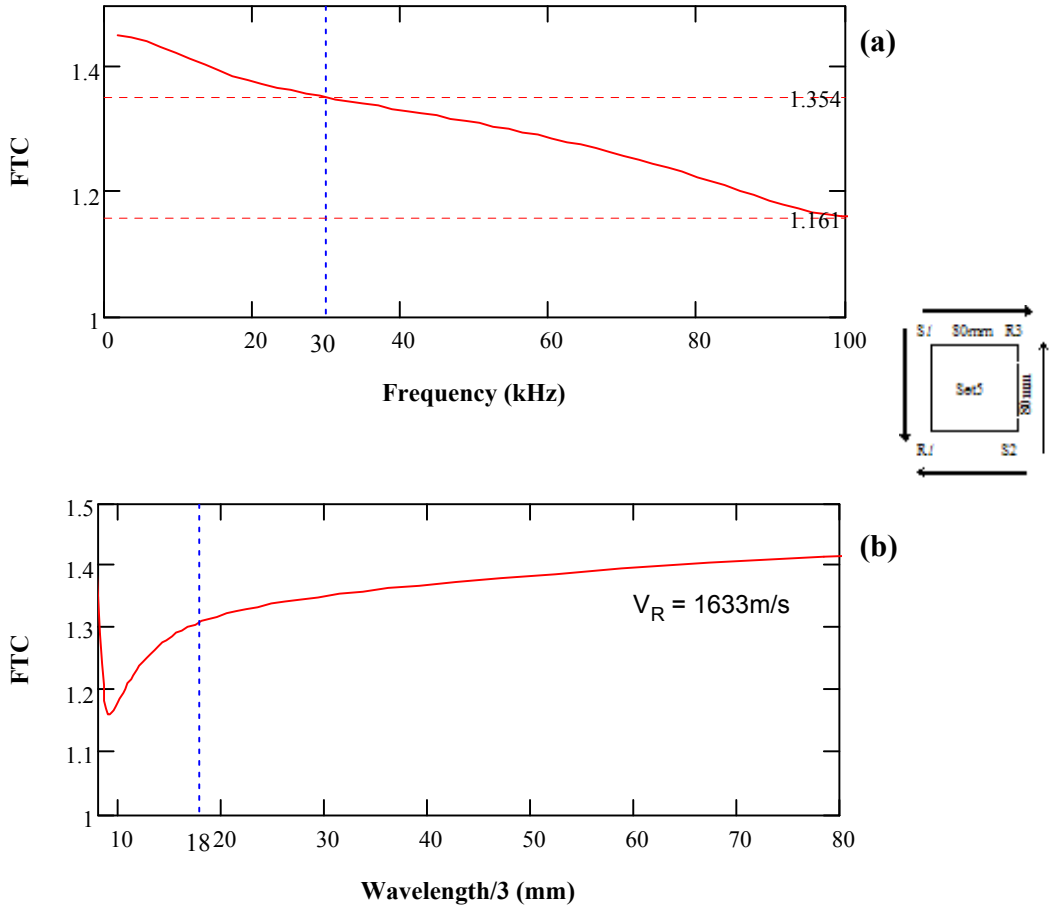

Figure J-19: (a) FTC vs. frequency and (b) FTC vs. wavelength/3 for R-waves for set 5 measurements at the left side of the joint

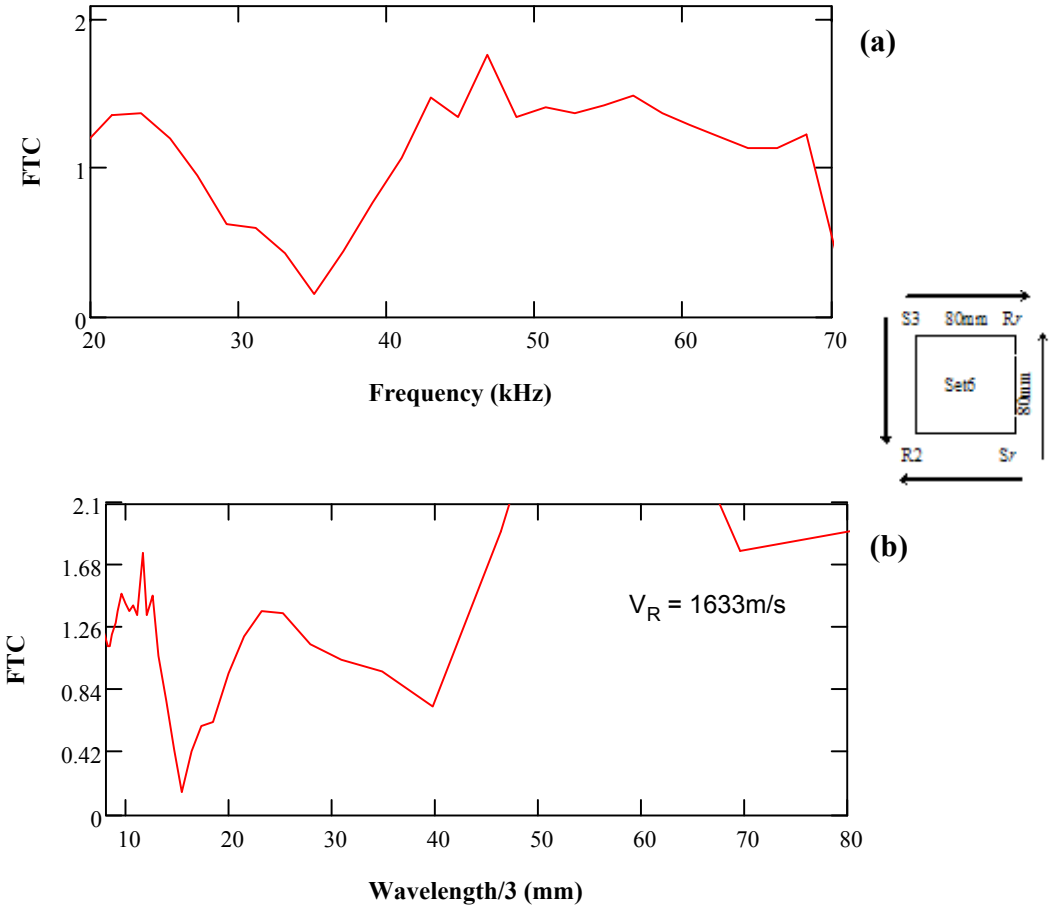

Figure J-20: (a) FTC vs. frequency and (b) FTC vs. wavelength/3 for full signals of set 6 measurements at the right side of the joint

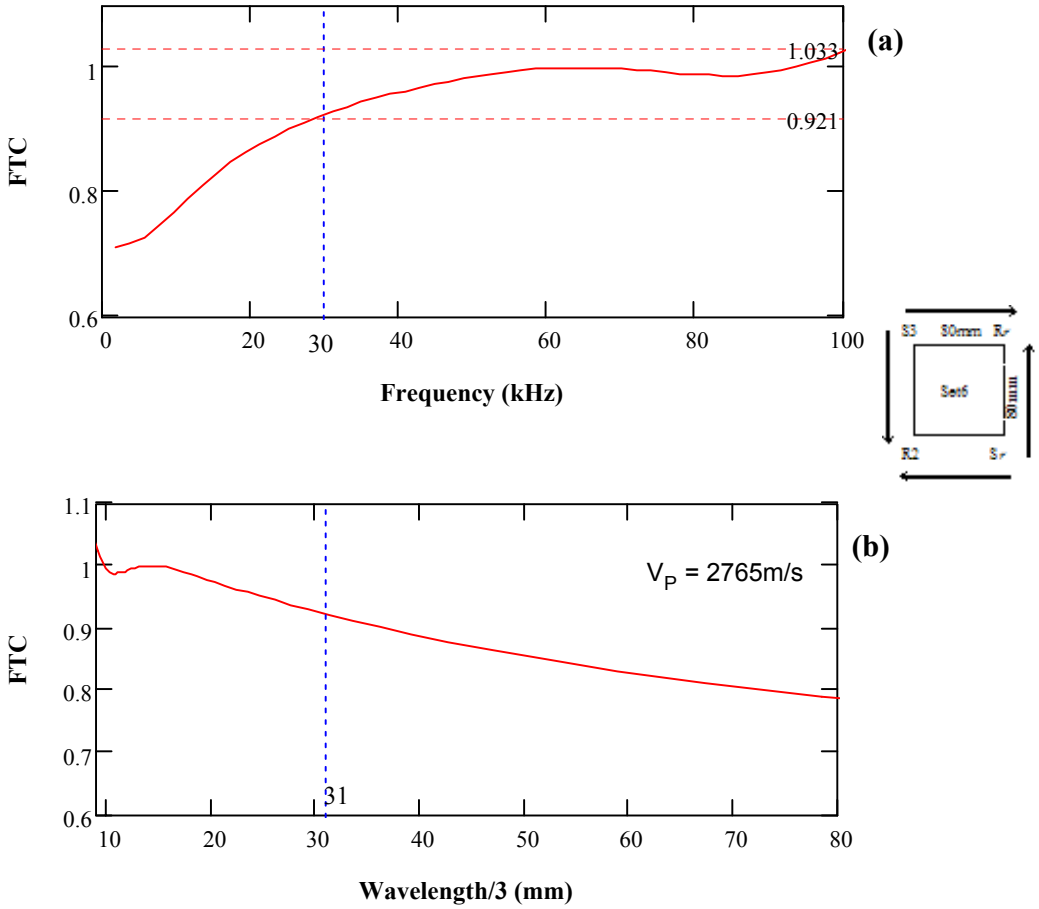

Figure J-21: (a) FTC vs. frequency and (b) FTC vs. wavelength/3 for full signals of set 6 measurements at the left side of the joint

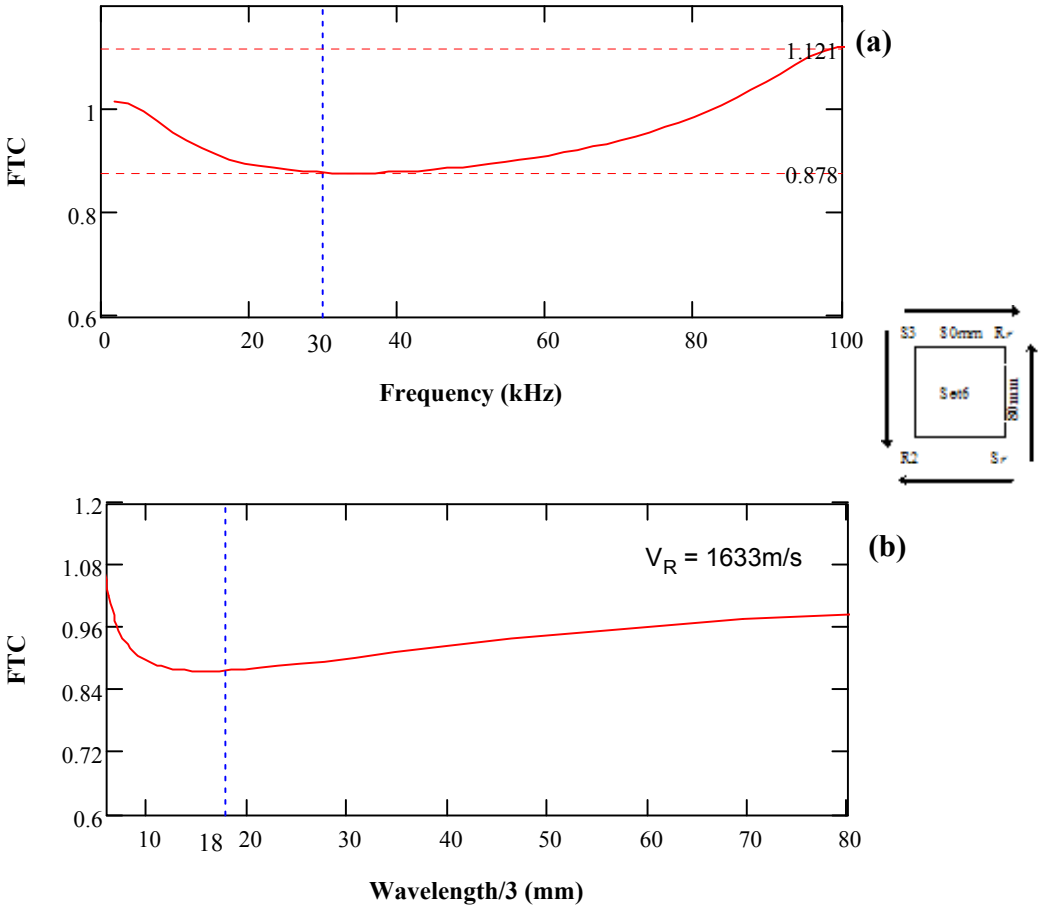

Figure J-22: (a) FTC vs. frequency and (b) FTC vs. wavelength/3 for full signals of set 6 measurements at the left side of the joint

Appendix K

Wavelet Transform Using Morlet Wavelet for Slab 2

- Measurements on the Jointed and the Joint-free Surfaces

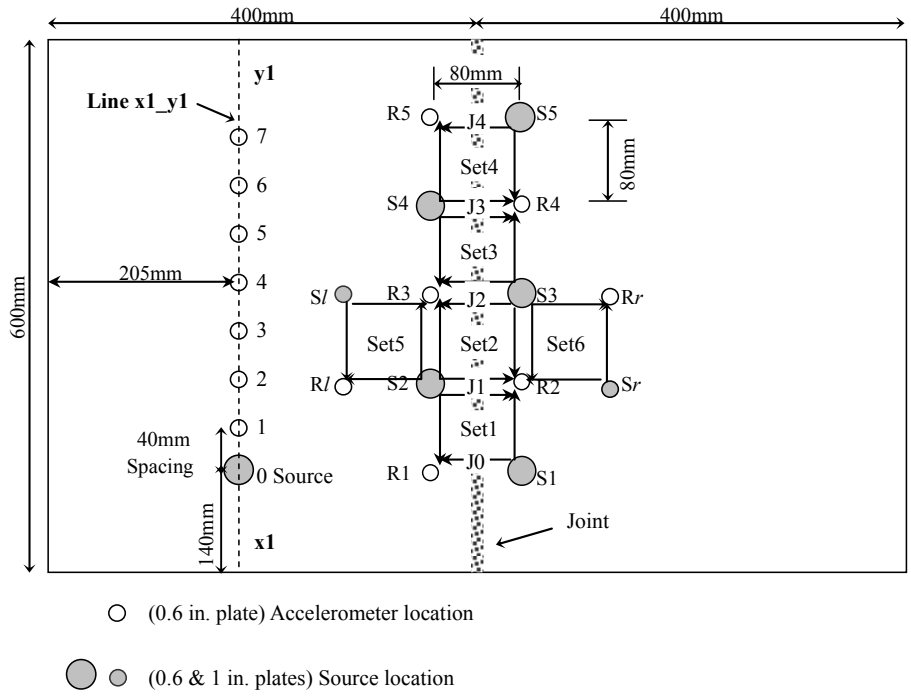

Figure K-1: Ultrasonic test configuration of HMA slab 2

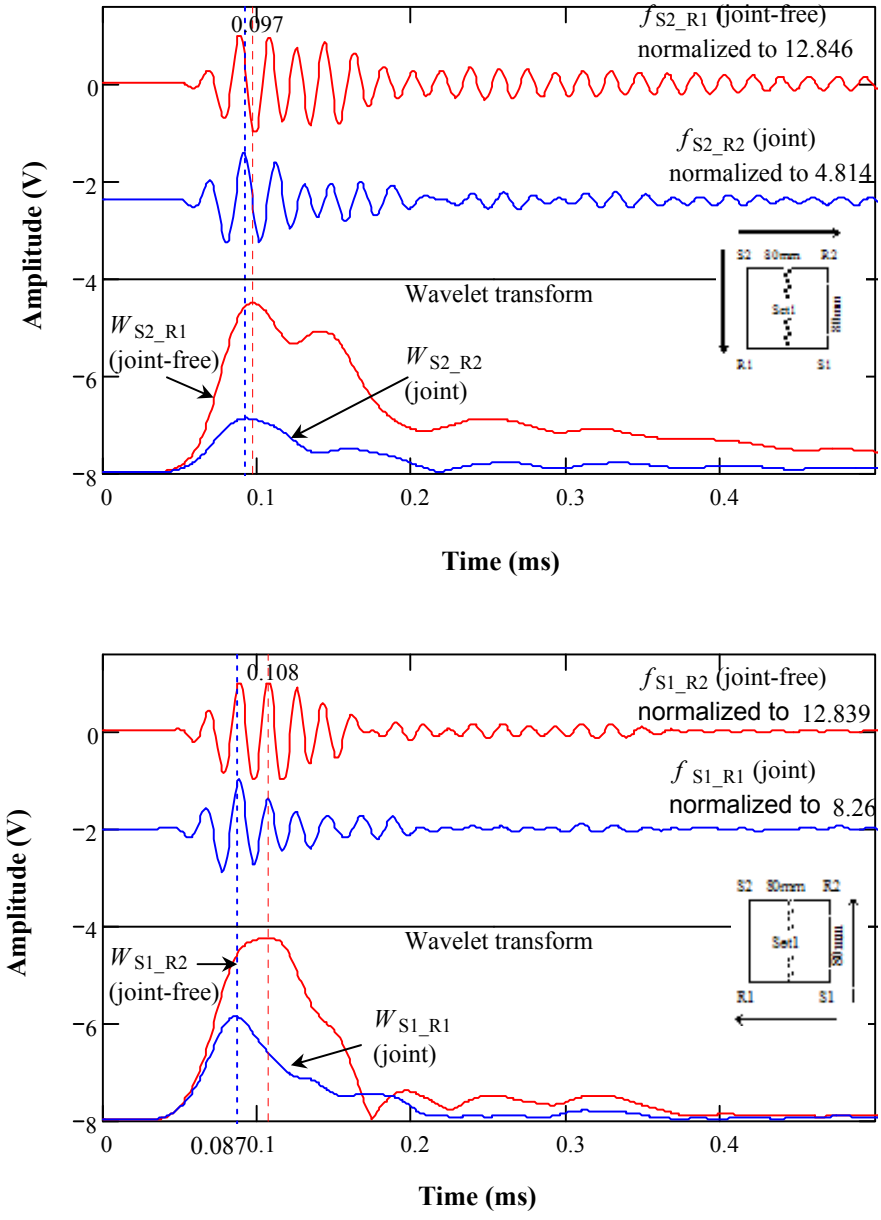

Figure K-2: Wavelet transform of set 1 measurements using Morlet wavelet at dominant frequencies of full signals (Morlet center frequency of 55.664 kHz for both f_{S2_R1} and f_{S2_R2}; 54.688 kHz for f_{S1_R2}; and 49.805 kHz for f_{S1_R1})

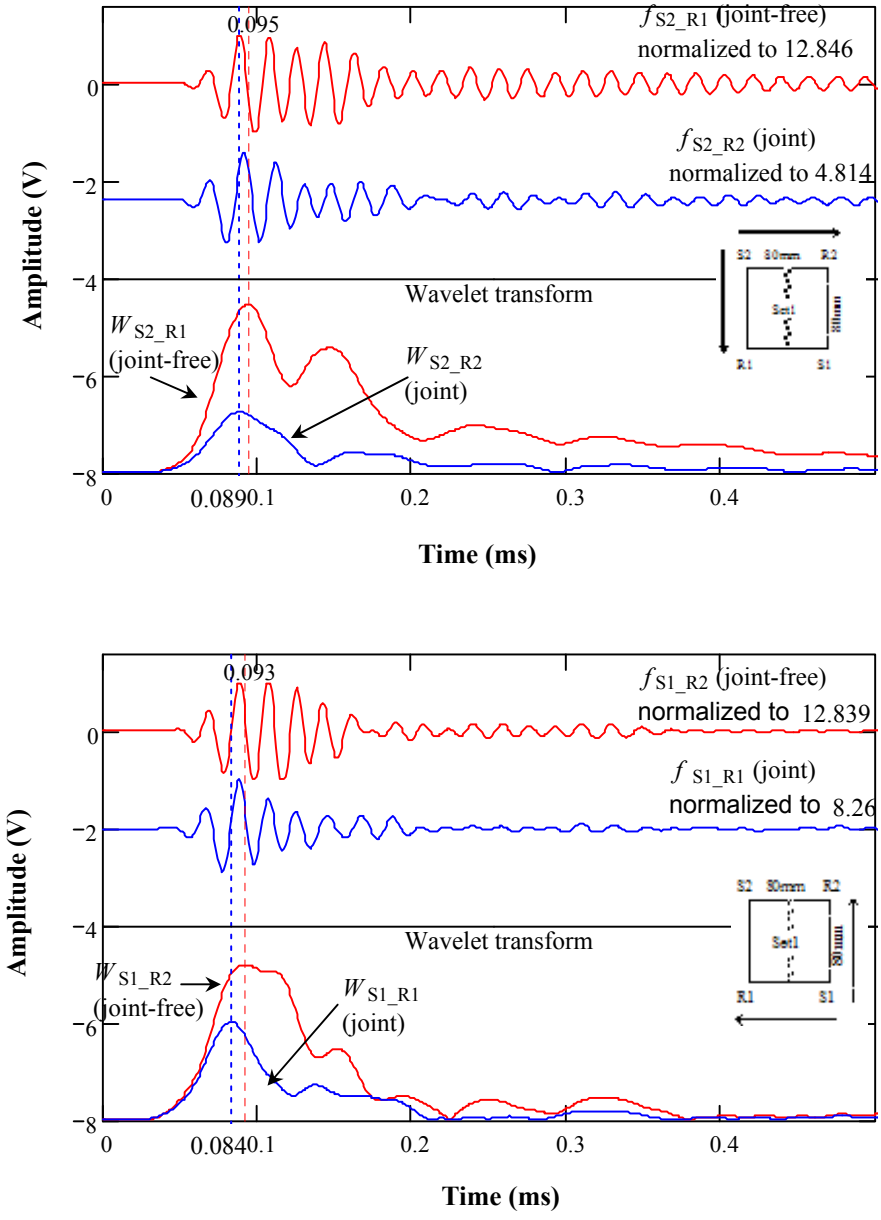

Figure K-3: Wavelet transform of set 1 measurements using Morlet wavelet at dominant frequencies of P-waves (Morlet center frequency of 39.063 kHz for f_{S2_R1}; 36.133 kHz for f_{S2_R2}; 38.086 kHz for f_{S1_R2}; and 36.133 kHz for f_{S1_R1}).

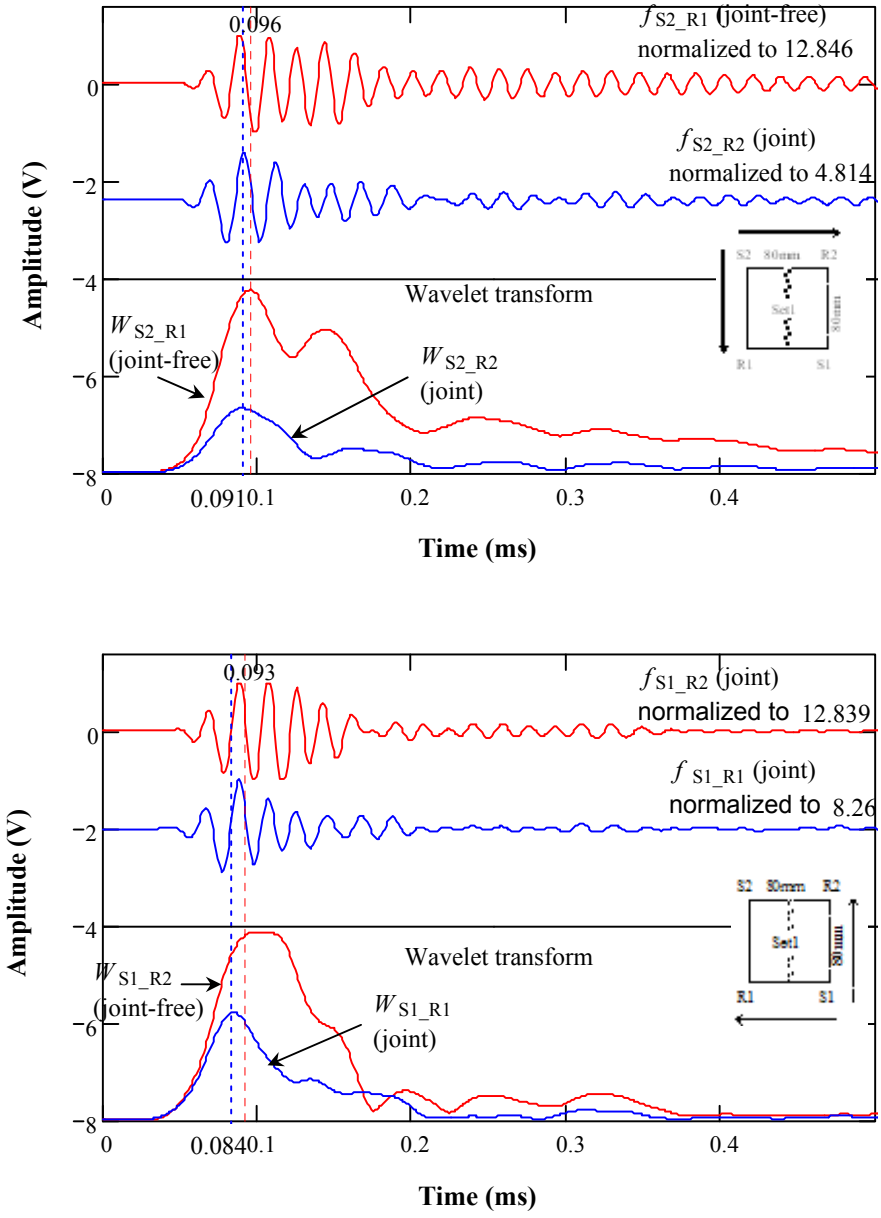

Figure K-4: Wavelet transform of set 1 measurements using Morlet wavelet at dominant frequencies of R-waves (Morlet center frequency of 43.945 kHz for f_{S2_R1}; 41.016 kHz for f_{S2_R2}; 46.875 kHz for f_{S1_R2}; and 41.992 kHz for f_{S1_R1})

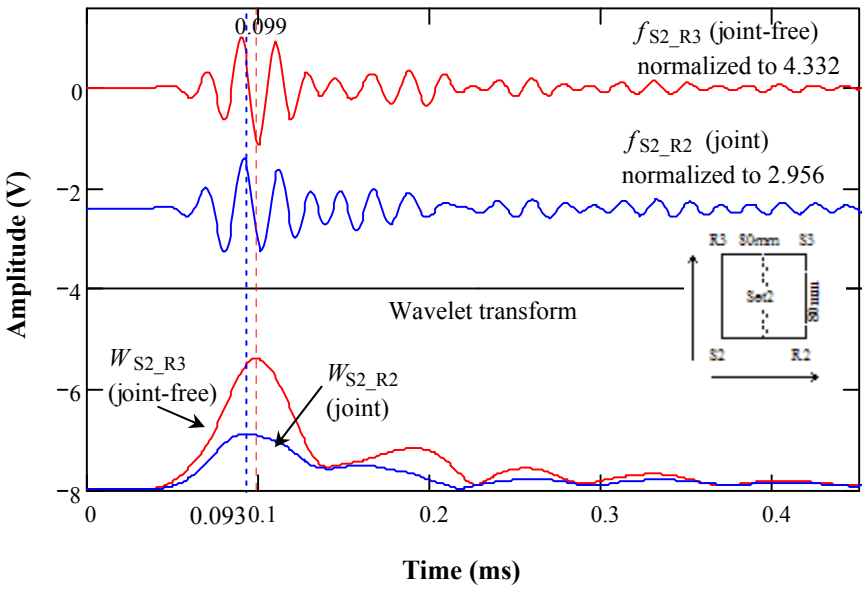

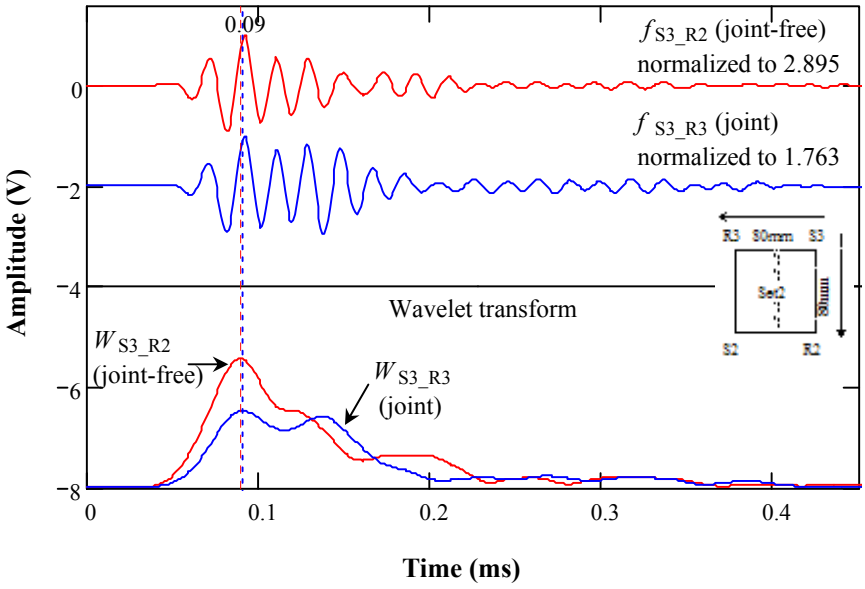

Figure K-5: Wavelet transform of set 2 measurements using Morlet wavelet at dominant frequencies of full signals (Morlet center frequency of 55.664 kHz for both f_{S2_R3} and f_{S2_R2}; 49.805 kHz for f_{S3_R2}; and 53.711 kHz for f_{S3_R3})

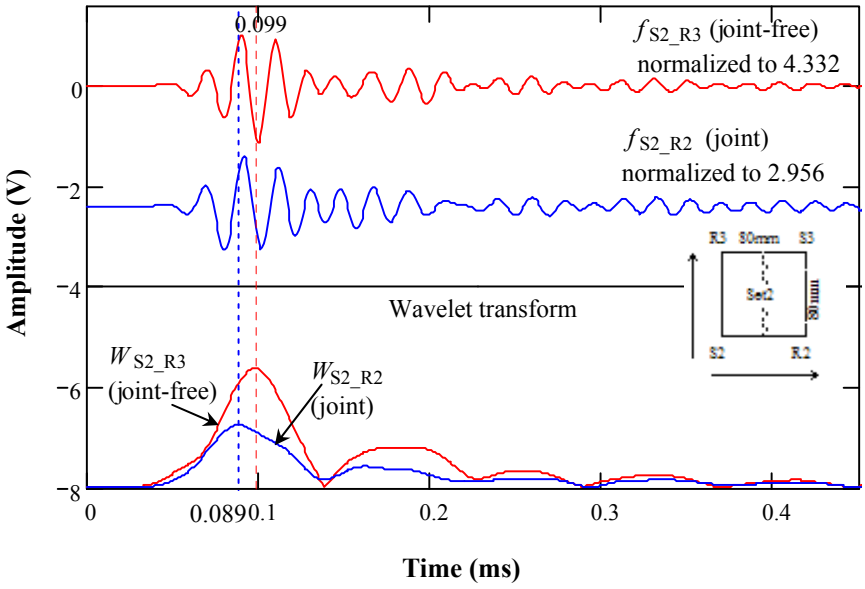

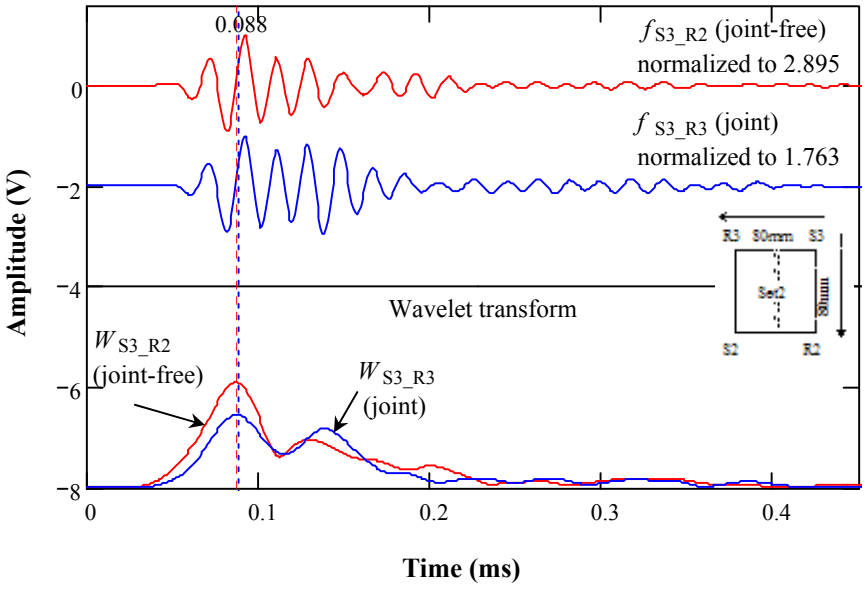

Figure K-6: Wavelet transform of set 2 measurements using Morlet wavelet at dominant frequencies of P-waves (Morlet center frequency of 35.156 kHz for f_{S2_R3}; 36.133 kHz for f_{S2_R2}; 34.18 kHz for f_{S3_R2}; and 37.108 kHz for f_{S3_R3}).

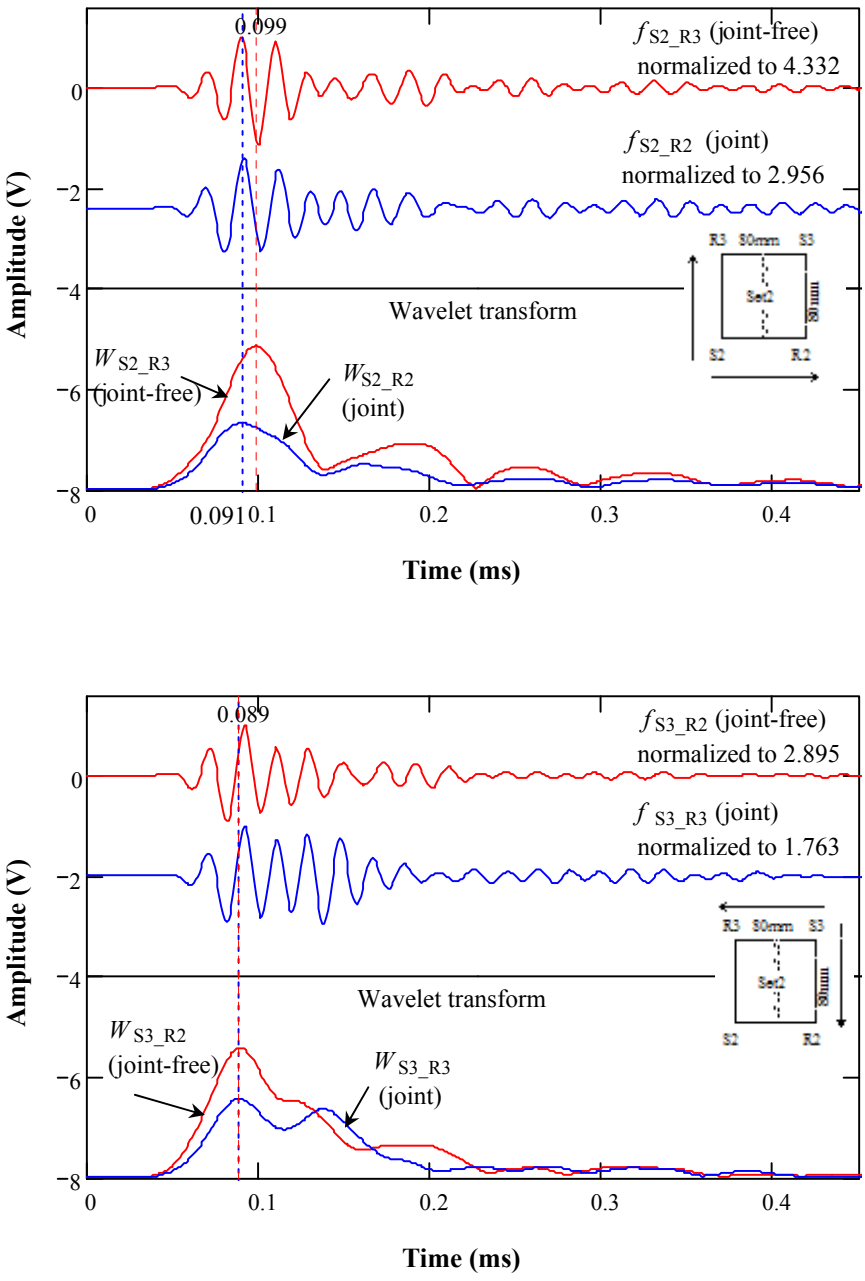

Figure K-7: Wavelet transform of set 2 measurements using Morlet wavelet at dominant frequencies of R-waves (Morlet center frequency of 47.852 kHz for f_{S2_R3}; 41.016 kHz for f_{S2_R2}; 44.922 kHz for f_{S3_R2}; and 41.992 kHz for f_{S3_R3})

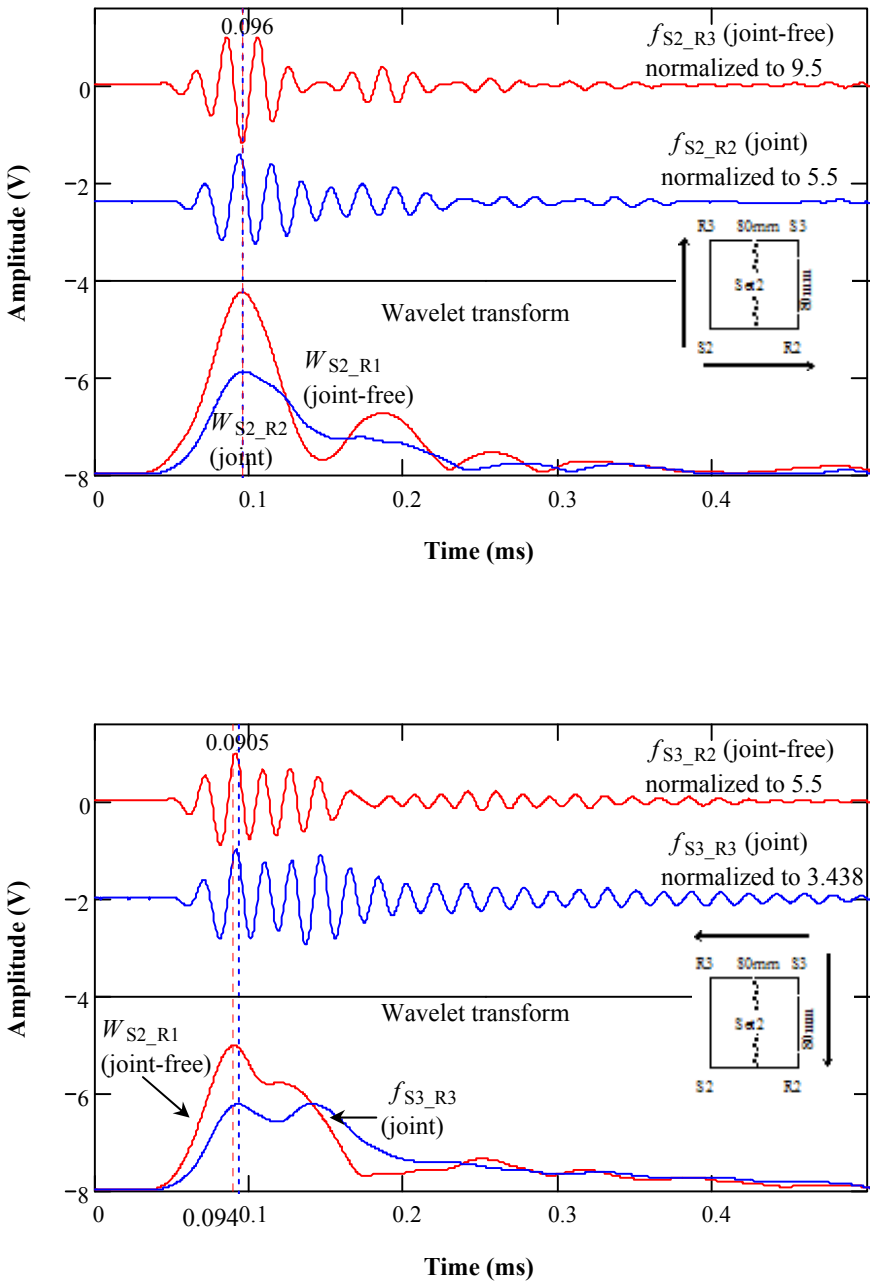

Figure K-8: Wavelet transform of repeated set 2 measurements using Morlet wavelet at dominant frequencies of full signals (Morlet center frequency of 50.781 kHz for both f_{S2_R3} and f_{S2_R2}; 56.641 kHz for both f_{S3_R2} and f_{S3_R3})

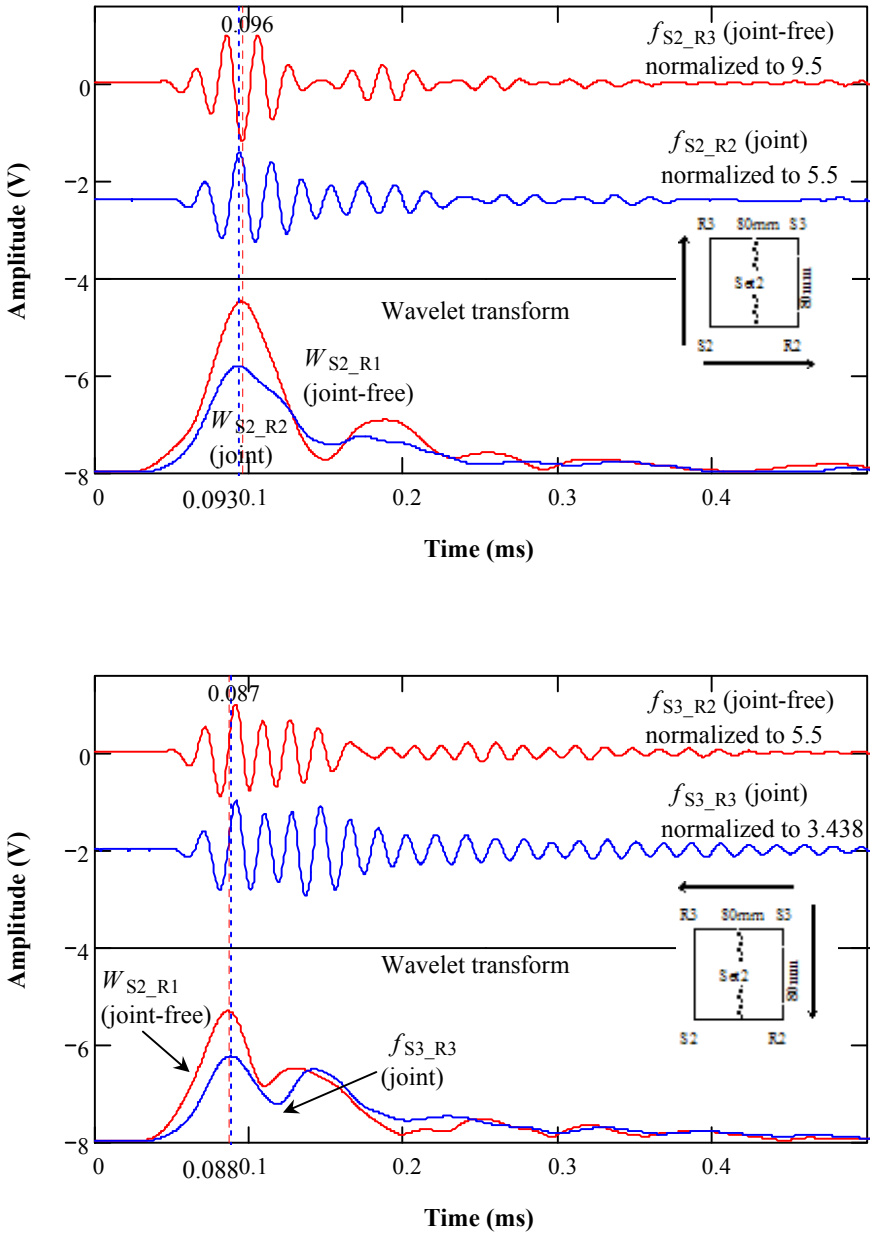

Figure K-9: Wavelet transform of repeated set 2 measurements using Morlet wavelet at dominant frequencies of P-waves (Morlet center frequency of 37.109 kHz for all the signals in repeated set 2 measurements)

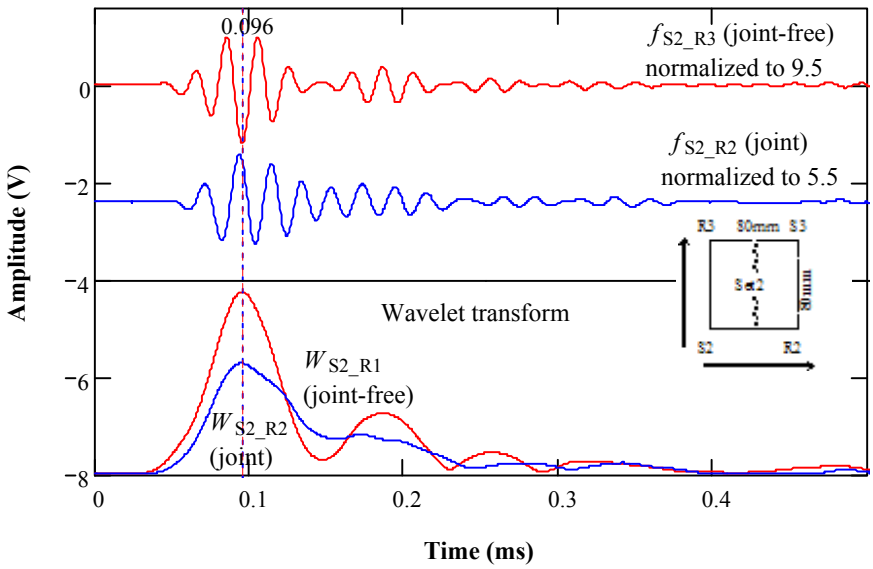

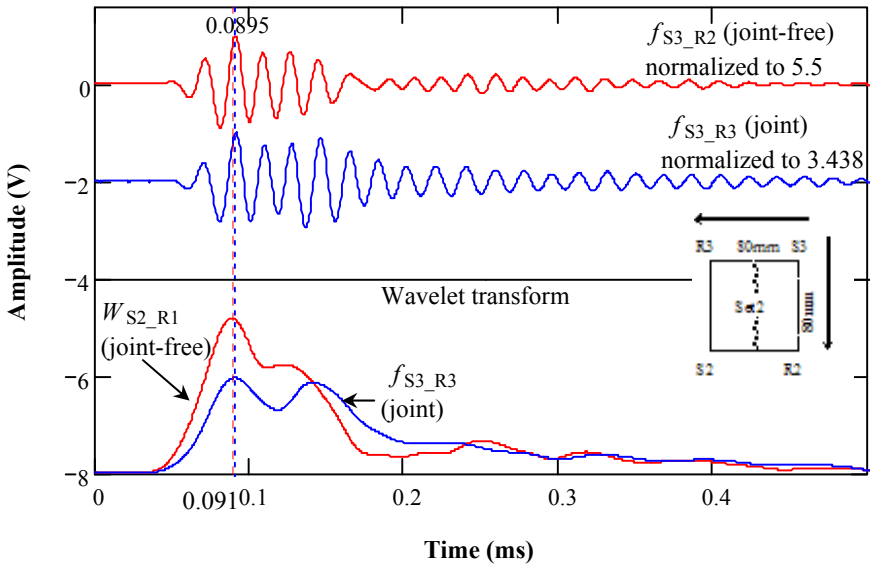

Figure K-10: Wavelet transform of repeated set 2 measurements using Morlet wavelet at dominant frequencies of R-waves (Morlet center frequency of 50.781 kHz for f_{S2_R3}; 42.969 kHz for f_{S2_R2}; 48.828 kHz for f_{S3_R2}; and 44.929 kHz for f_{S3_R3})

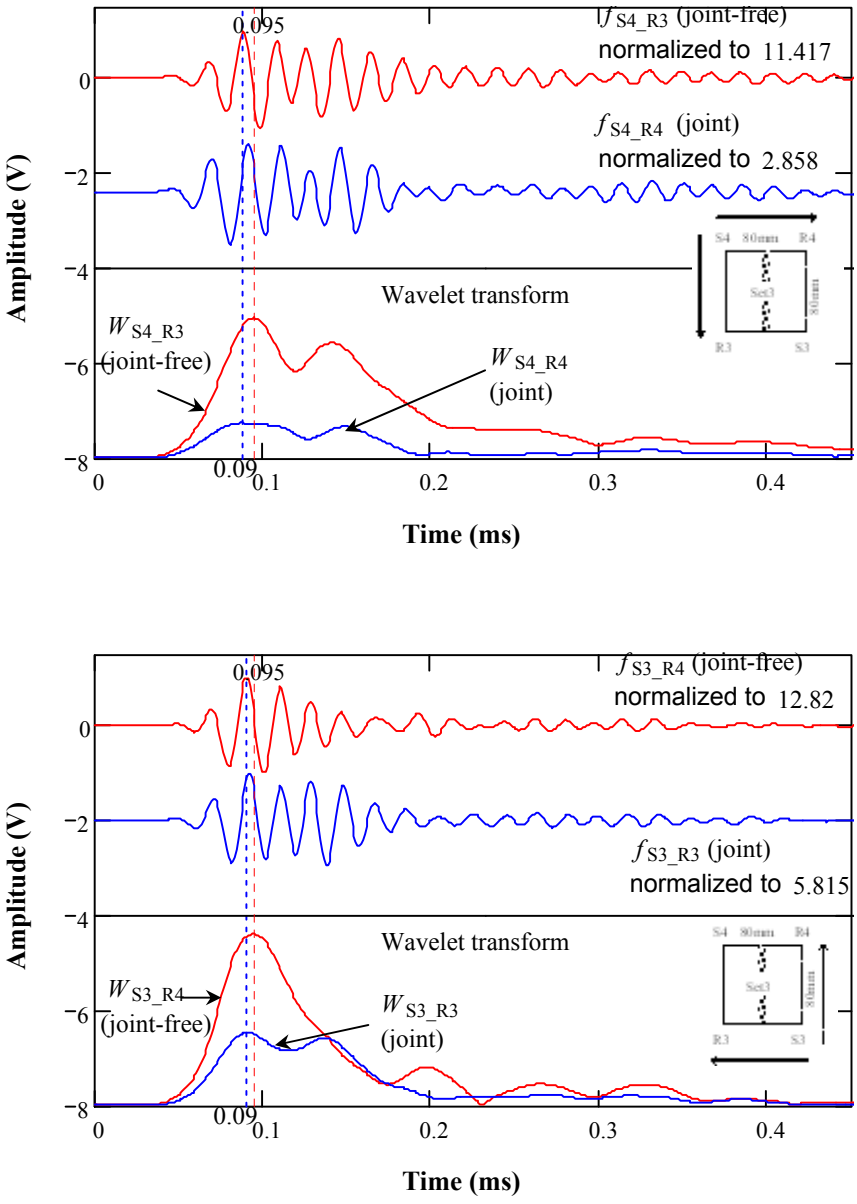

Figure K-11: Wavelet transform of set 3 measurements using Morlet wavelet at dominant frequencies of full signals (Morlet center frequency of 54.688 kHz for both f_{S4_R3} and f_{S4_R4}; 49.81 kHz for f_{S3_R4}; and 53.711 kHz for f_{S3_R3})

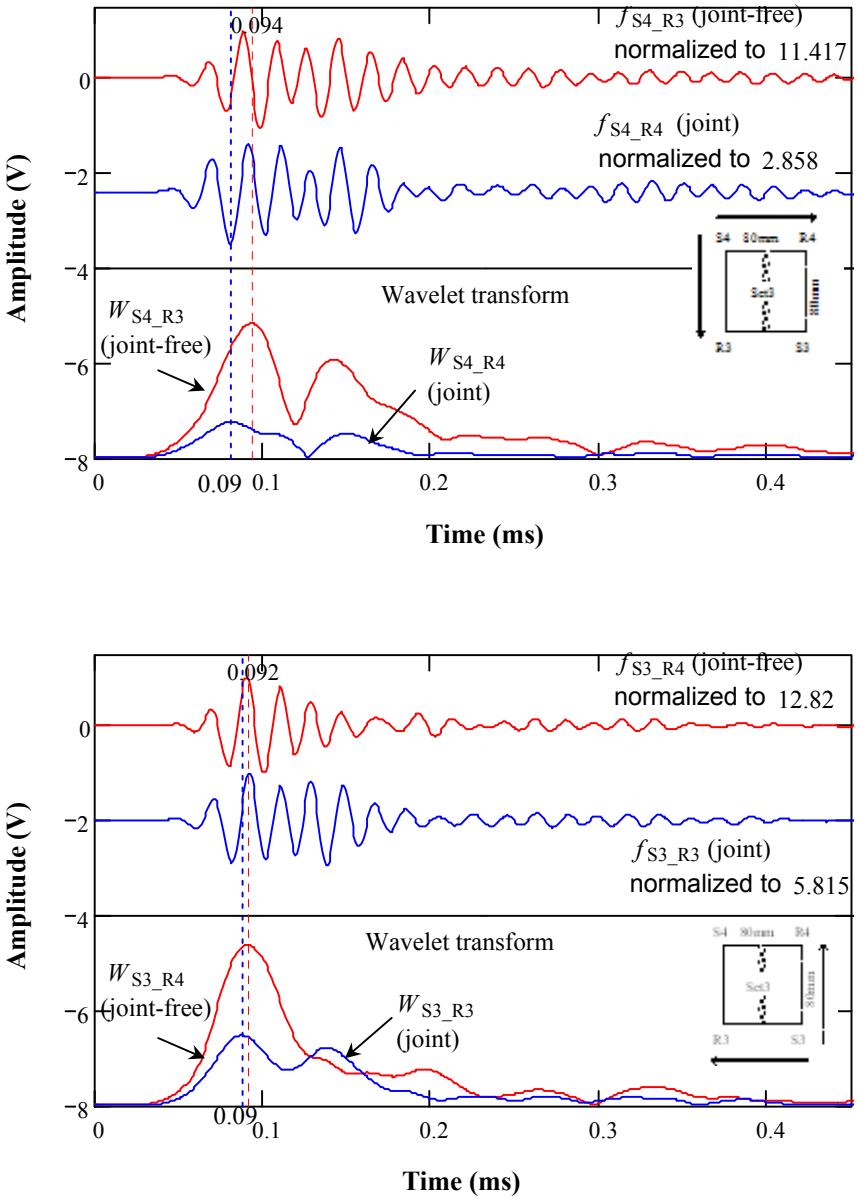

Figure K-12: Wavelet transform of set 3 measurements using Morlet wavelet at dominant frequencies of P-waves (Morlet center frequency of 36.133 kHz for f_{S4_R3}; and 34.18 kHz for f_{S4_R4}; 36.133 kHz for f_{S3_R4}; and 38.086 kHz for f_{S3_R3})

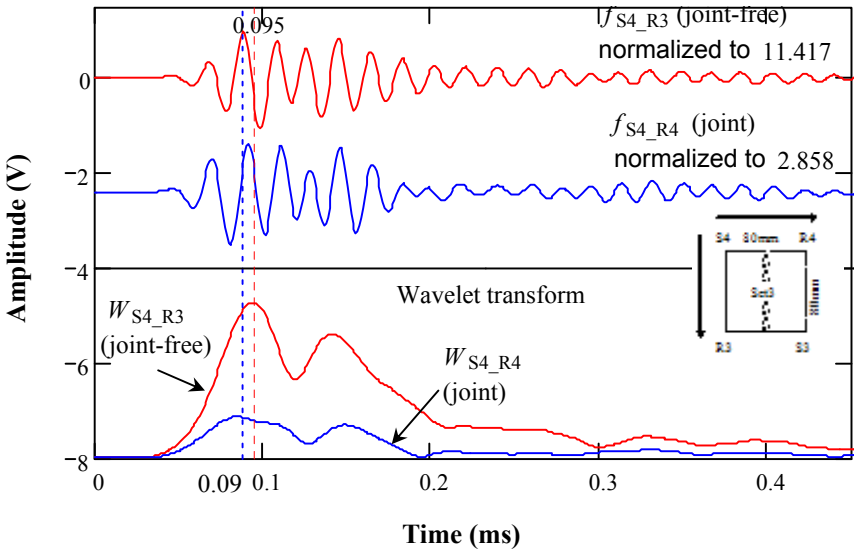

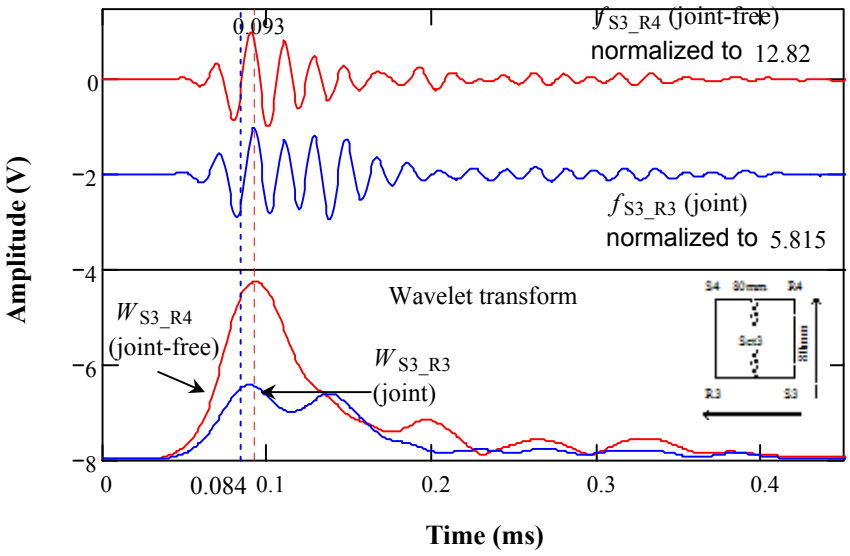

Figure K-13: Wavelet transform of set 3 measurements using Morlet wavelet at dominant frequencies of R-waves (Morlet center frequency of 45.898 kHz for f_{S4_R3}; 43.945 kHz for f_{S4_R4}; 43.945 kHz for f_{S3_R4}; and 44.922 kHz for f_{S3_R3})

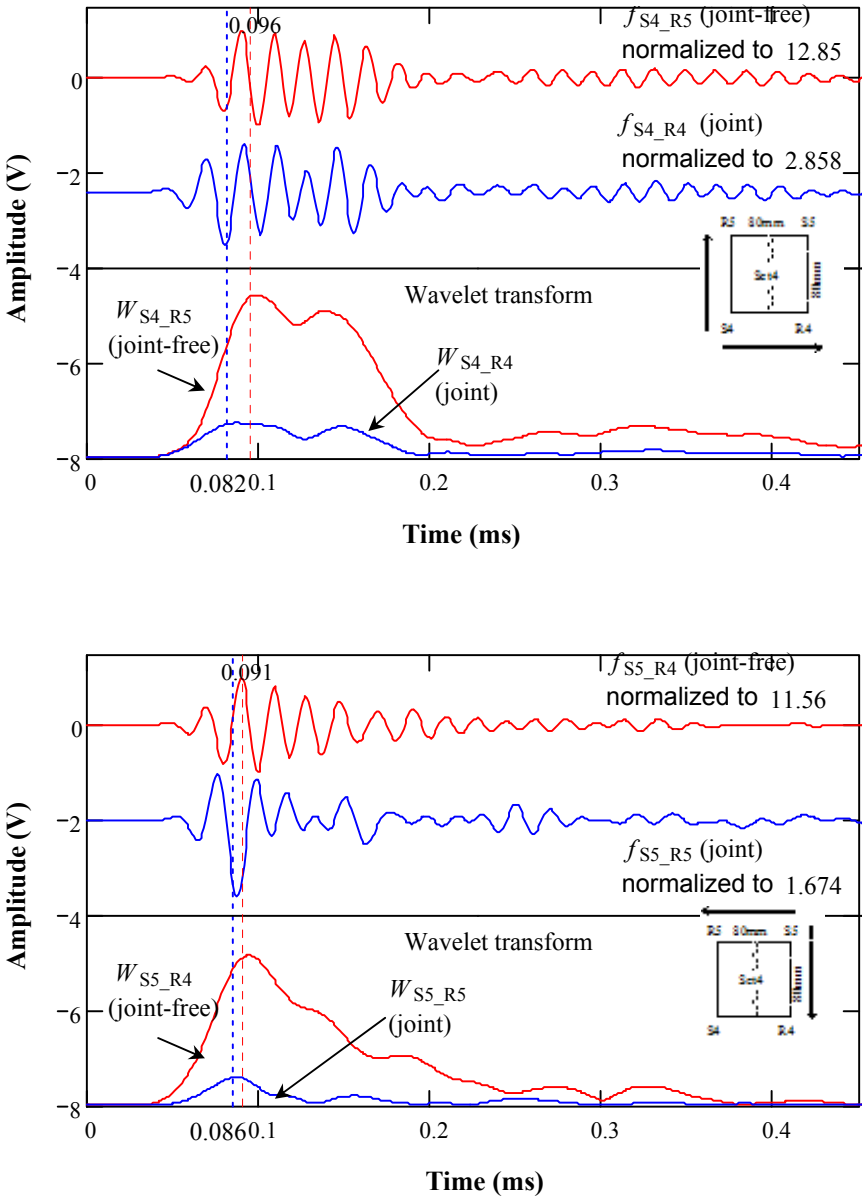

Figure K-14: Wavelet transform of set 4 measurements using Morlet wavelet at dominant frequencies of full signals (Morlet center frequency of 55.664 kHz for both f_{S4_R5} and f_{S4_R4}; 49.805 kHz for f_{S5_R4}; and 41.922 kHz for f_{S5_R5})

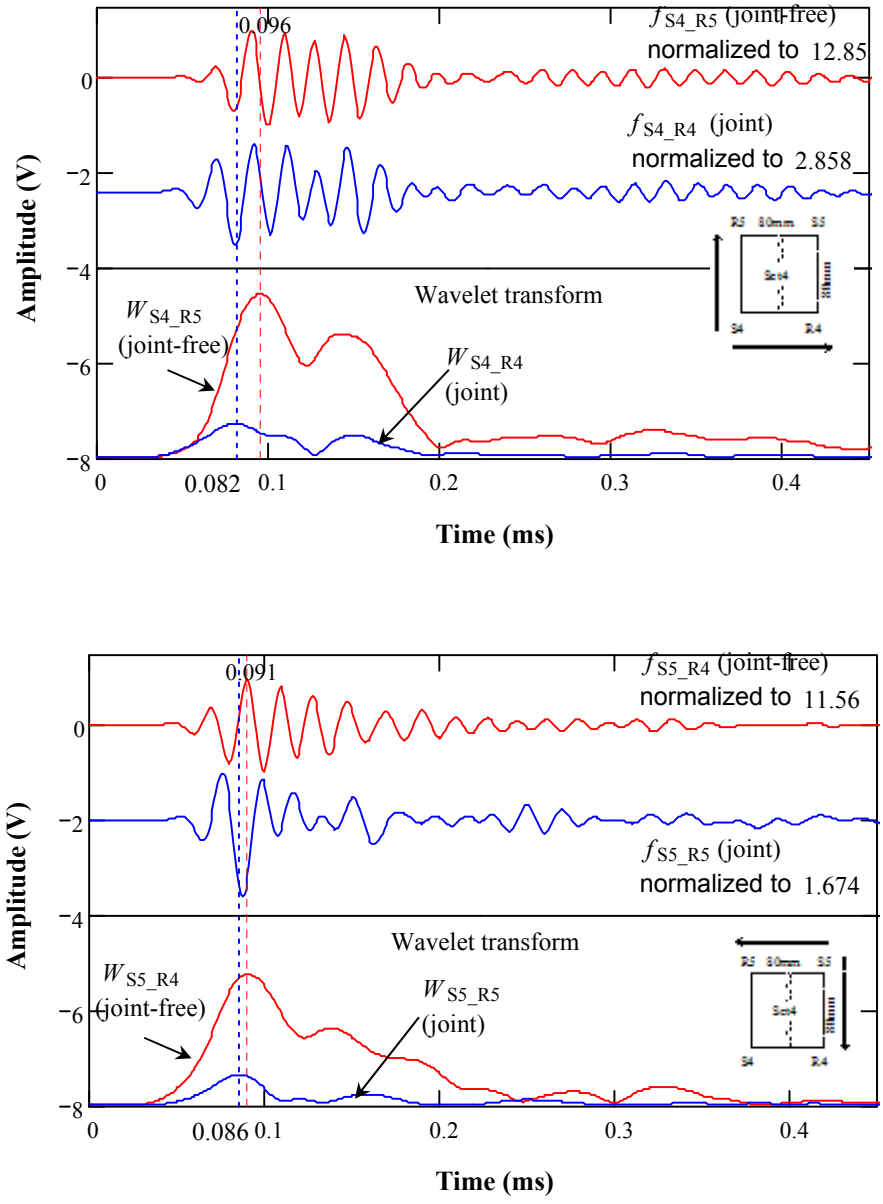

Figure K-15: Wavelet transform of set 4 measurements using Morlet wavelet at dominant frequencies of P-waves (Morlet center frequency of 40.039 kHz for f_{S4_R5}; and 33.203 kHz for f_{S4_R4}; 37.109 kHz for f_{S5_R4}; and 34.18 kHz for f_{S5_R5})

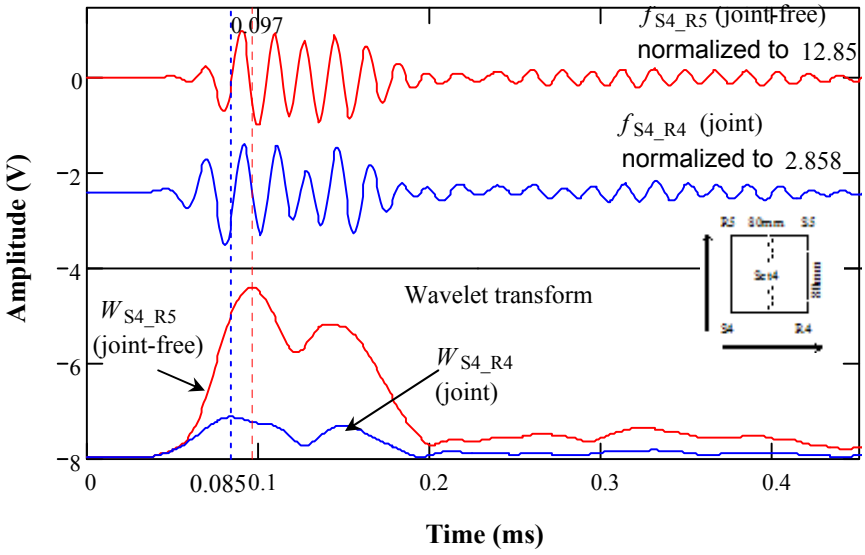

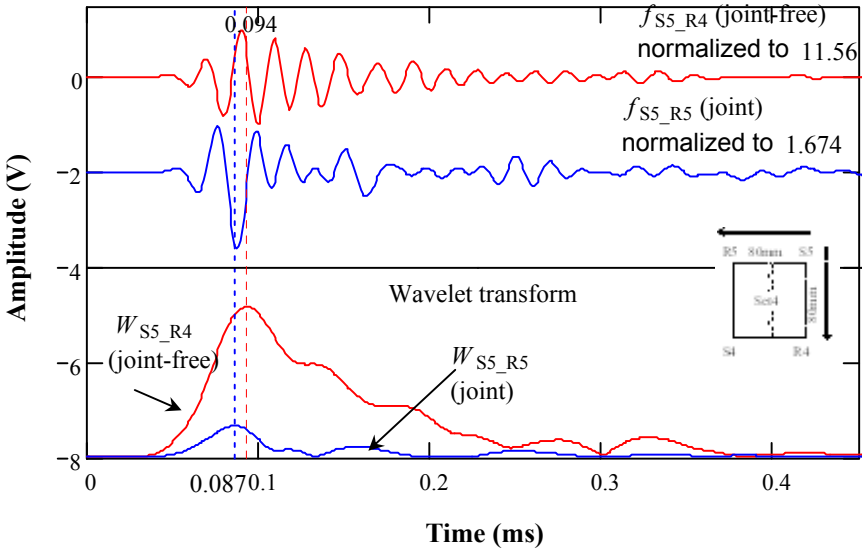

Figure K-16: Wavelet transform of set 4 measurements using Morlet wavelet at dominant frequencies of R-waves (Morlet center frequency of 41.992 kHz for both f_{S4_R5} and f_{S4_R4}; 43.95 kHz for f_{S5_R4}; and 39.063 kHz for f_{S5_R5})

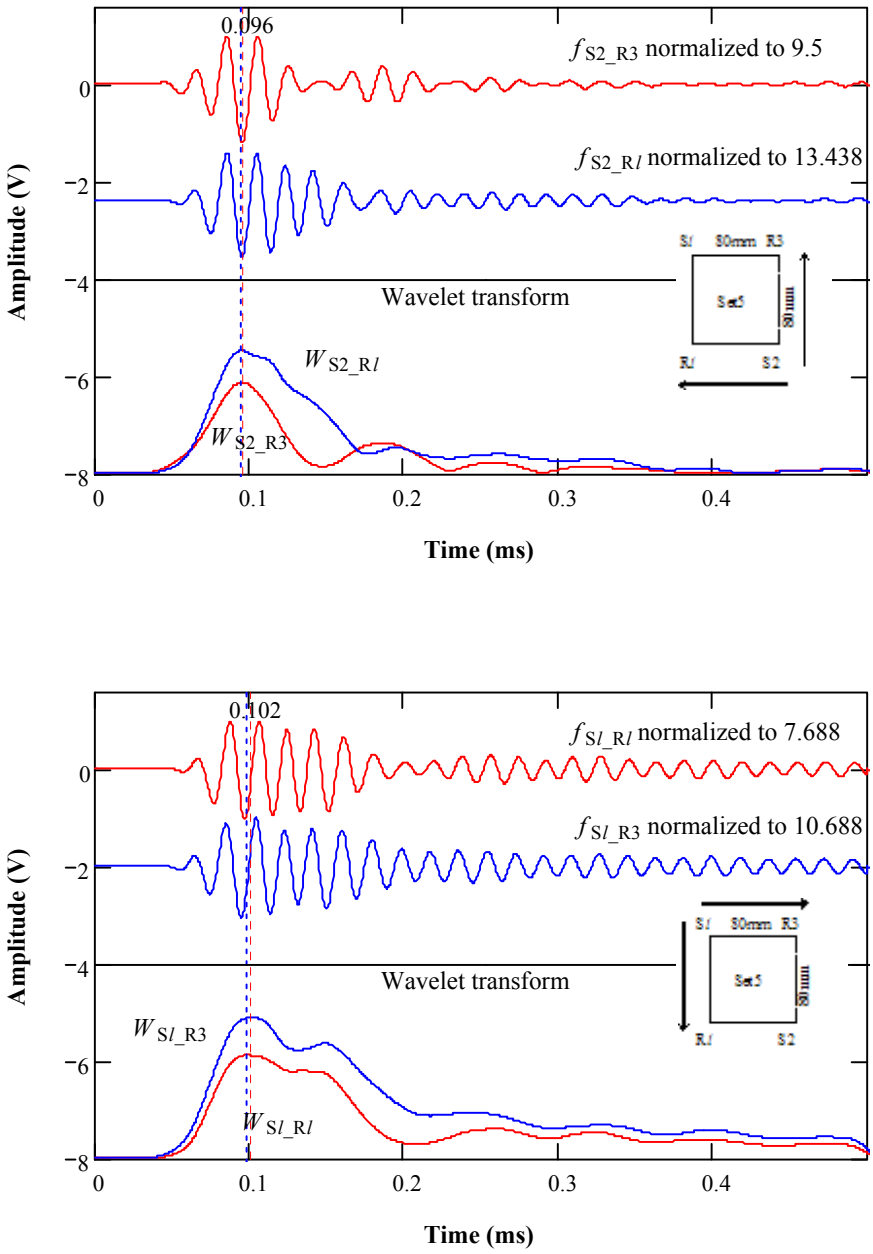

Figure K-17: Wavelet transform of set 5 measurements at the left side of the joint using Morlet wavelet at dominant frequencies of full signals (Morlet center frequency of 54.688 kHz for both f_{S2_R3} and f_{S2_Rl}; 56.641 kHz for both f_{Sl_Rl} and f_{Sl_R3})

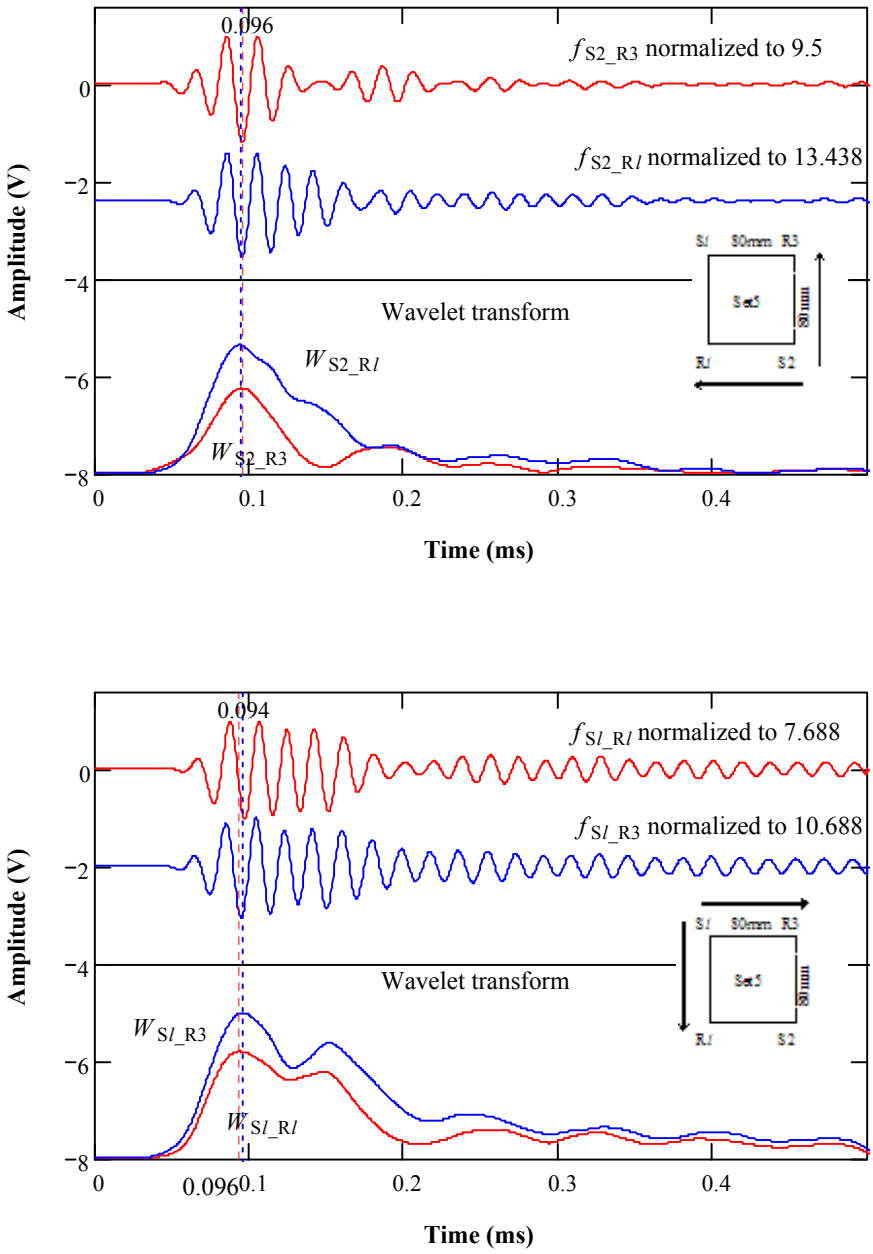

Figure K-18: Wavelet transform of set 5 measurements at the left side of the joint using Morlet wavelet at dominant frequencies of P-waves (Morlet center frequency of 37.109 kHz for f_{S2_R3}; 42.969 for f_{S2_Rl}; 41.016 kHz for f_{Sl_Rl}; and 42.969 kHz for f_{Sl_R3})

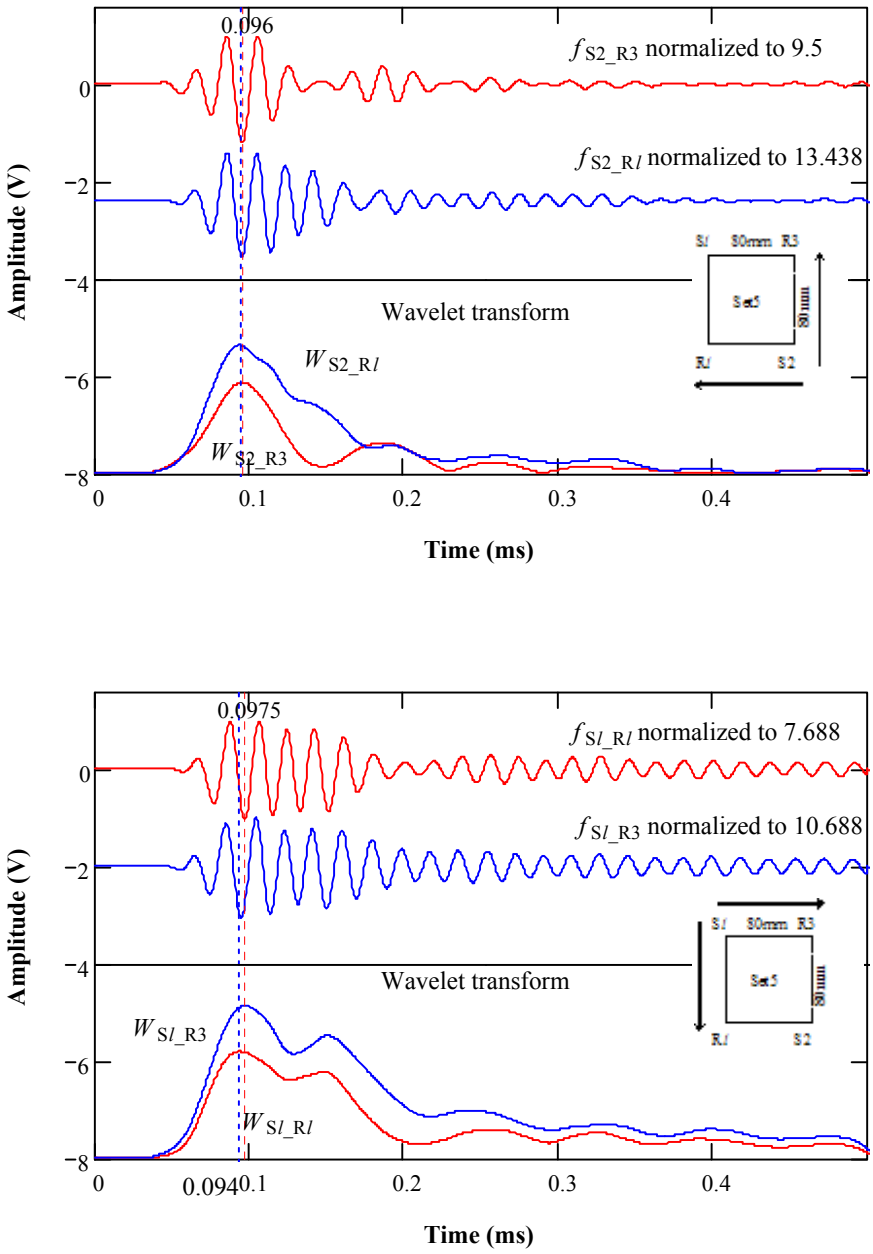

Figure K-19: Wavelet transform of set 5 measurements at the left side of the joint using Morlet wavelet at dominant frequencies of R-waves (Morlet center frequency of 50.781 kHz for f_{S2_R3}; 42.969 for f_{S2_Rl}; 42.969 kHz for f_{Sl_Rl}; and 44.922 kHz for f_{Sl_R3})

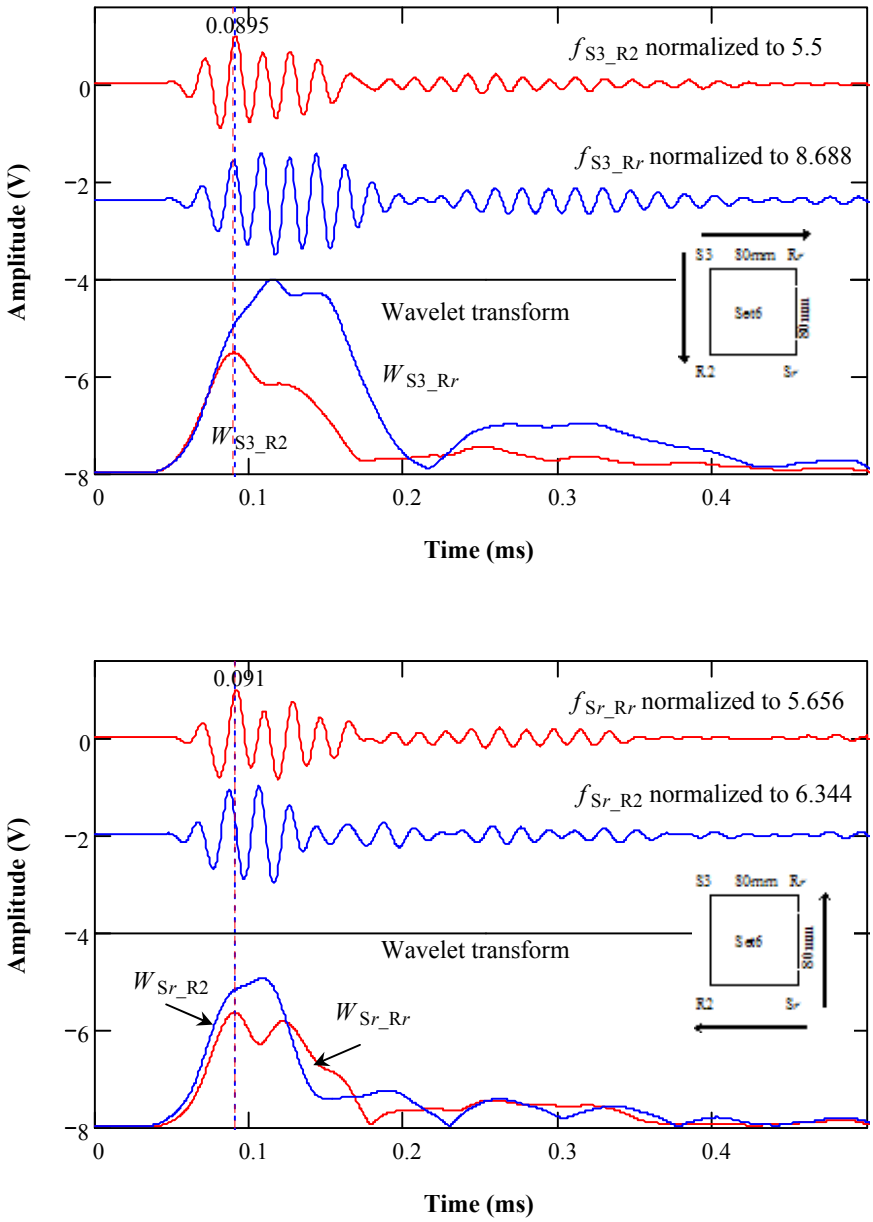

Figure K-20: Wavelet transform of set 6 measurements at the right side of the joint using Morlet wavelet at dominant frequencies of full signals (Morlet center frequency of 56.641 kHz for both f_{S3_R2} and f_{S3_Rr}; 54.688 kHz for both f_{Sr_Rr} and f_{Sr_R2})

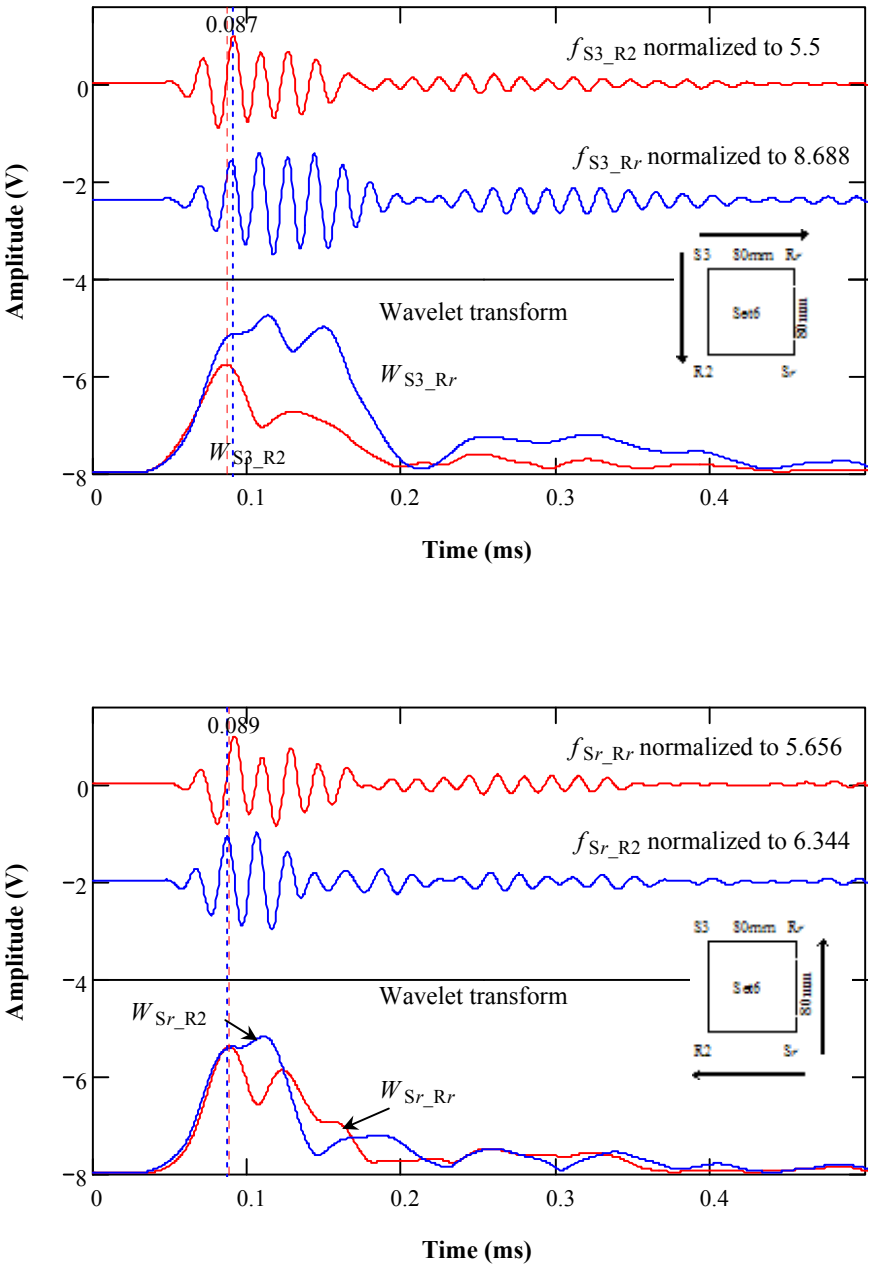

Figure K-21: Wavelet transform of set 6 measurements at the right side of the joint using Morlet wavelet at dominant frequencies of P-waves (Morlet center frequency of 37.109 kHz for f_{S3_R2}; 39.036 kHz for f_{S3_Rr}; 39.063 kHz for f_{Sr_Rr}; and 42.969 kHz for f_{Sr_R2})

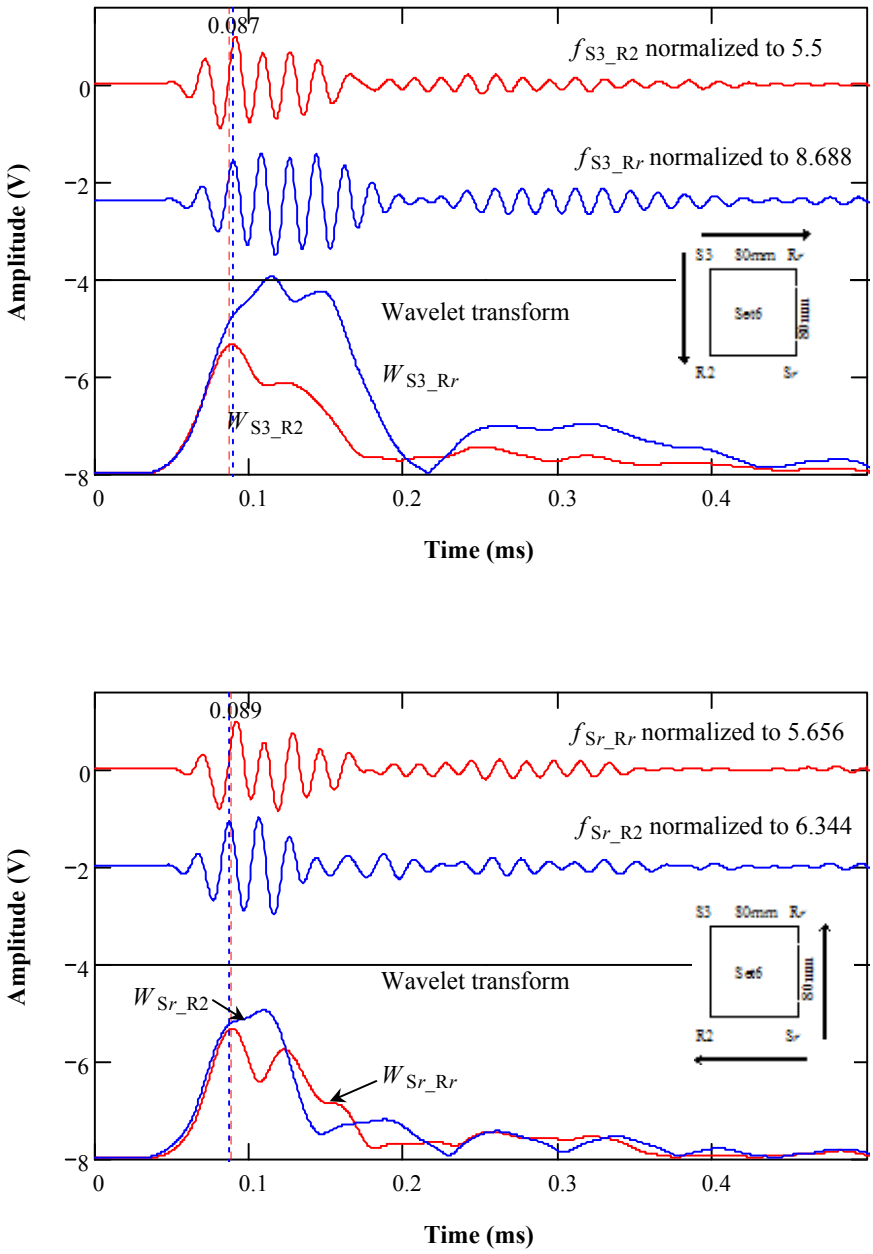

Figure K-22: Wavelet transform of set 6 measurements at the right side of the joint using Morlet wavelet at dominant frequencies of R-waves (Morlet center frequency of 48.828 kHz for f_{S3_R2}; 46.875 kHz for f_{S3_Rr}; 42.969 kHz for f_{Sr_Rr}; and 44.922 kHz for f_{Sr_R2})

Appendix L
Wavelet Transform of Signals
Using Mallat's Algorithm for Slab 2

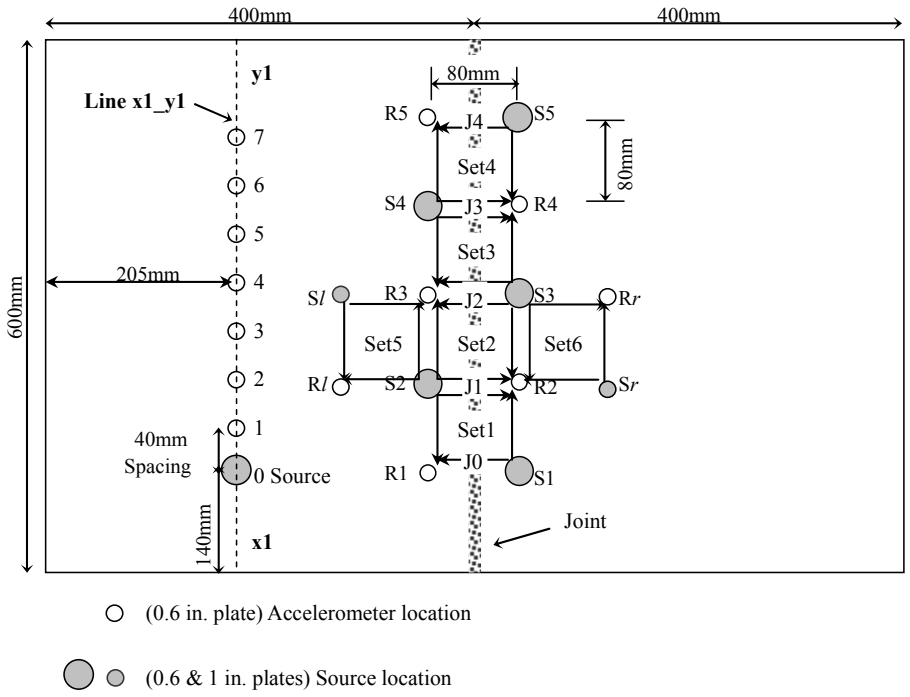

Figure L-1: Ultrasonic test configuration of HMA slab 2

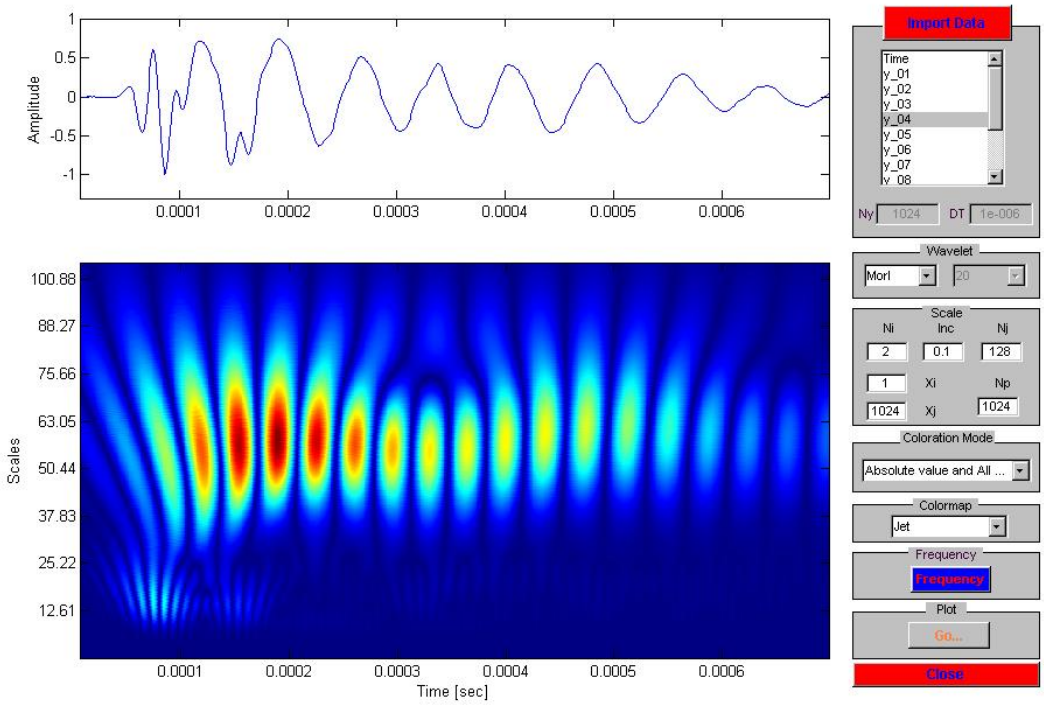

Figure F-2: Wavelet transform of signal f_{S1_R1} across the joint using Mallat's algorithm

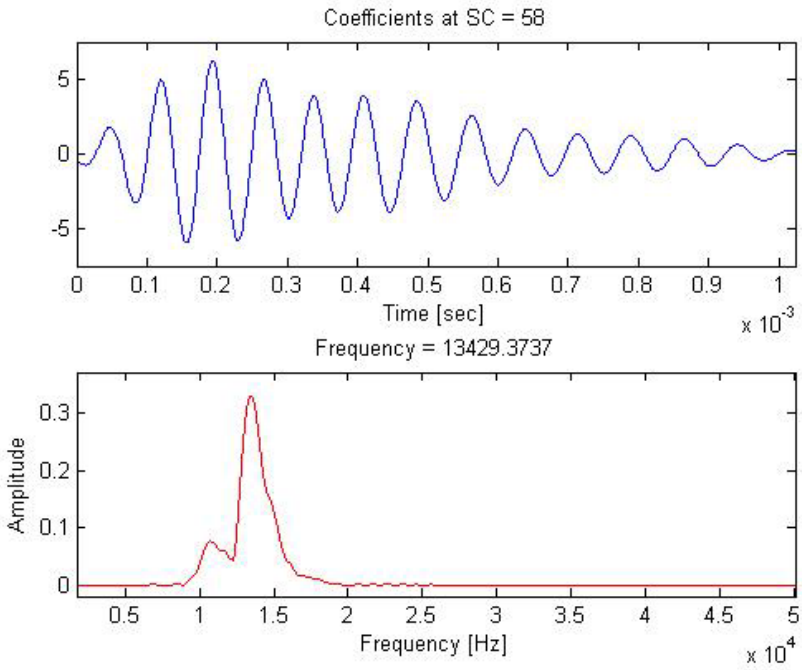

Figure F-3: Frequency content at a given scale from Figure F-2

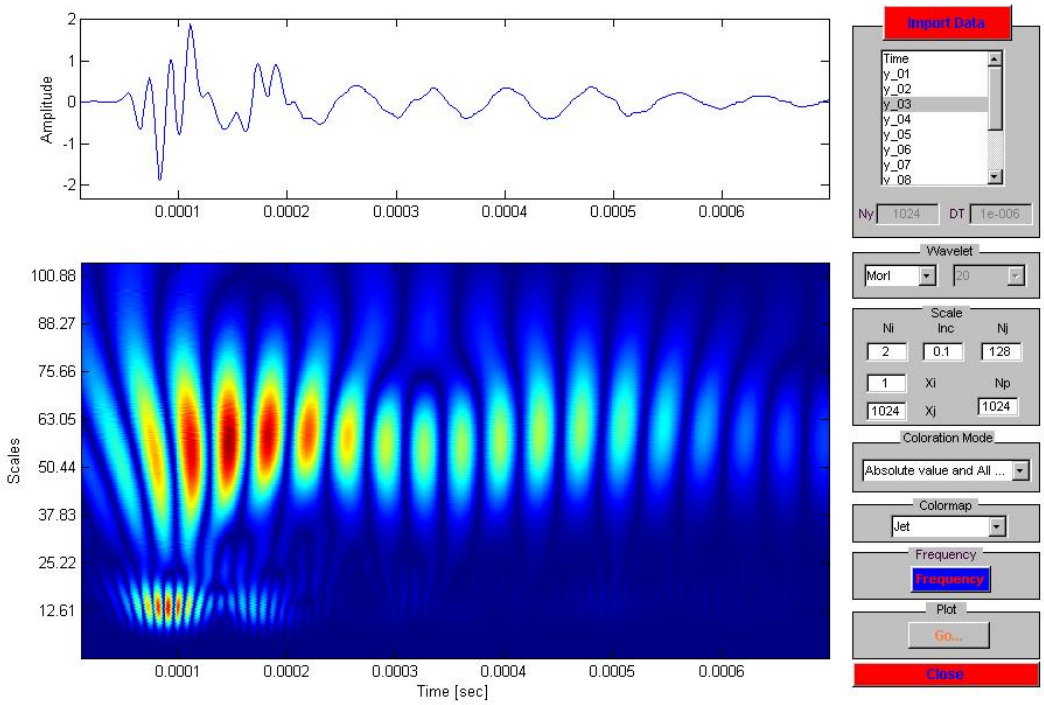

Figure F-4: Wavelet transform of signal f_{S1_R2} through the joint-free surface using Mallat's algorithm

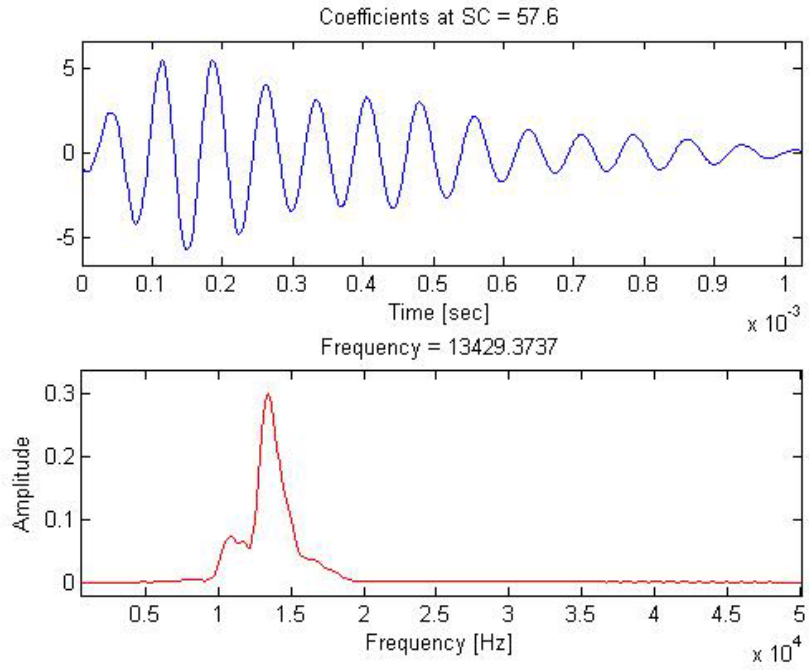

Figure F-5: Frequency content at a given scale from Figure F-4

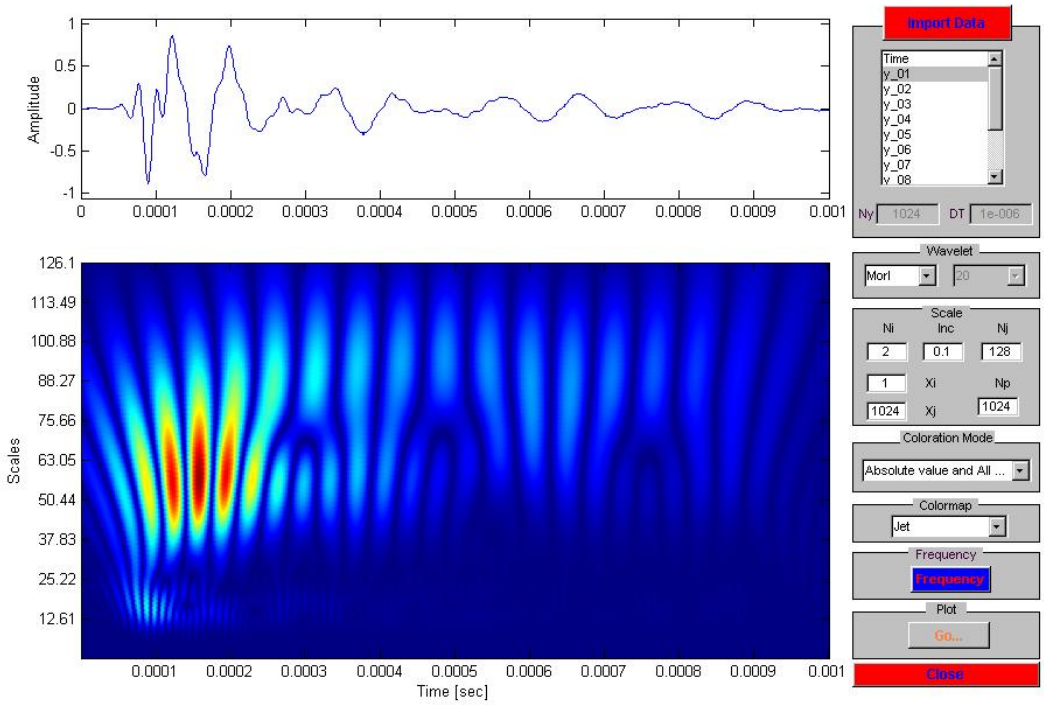

Figure F-6: Wavelet transform of signal f_{S2_R2} across the joint using Mallat's algorithm

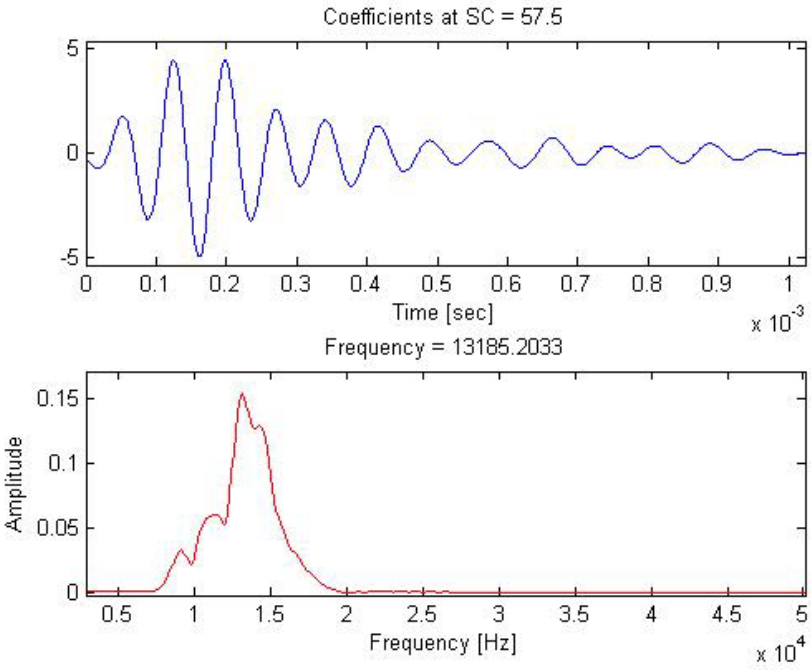

Figure F-7: Frequency content at a given scale from Figure F-6

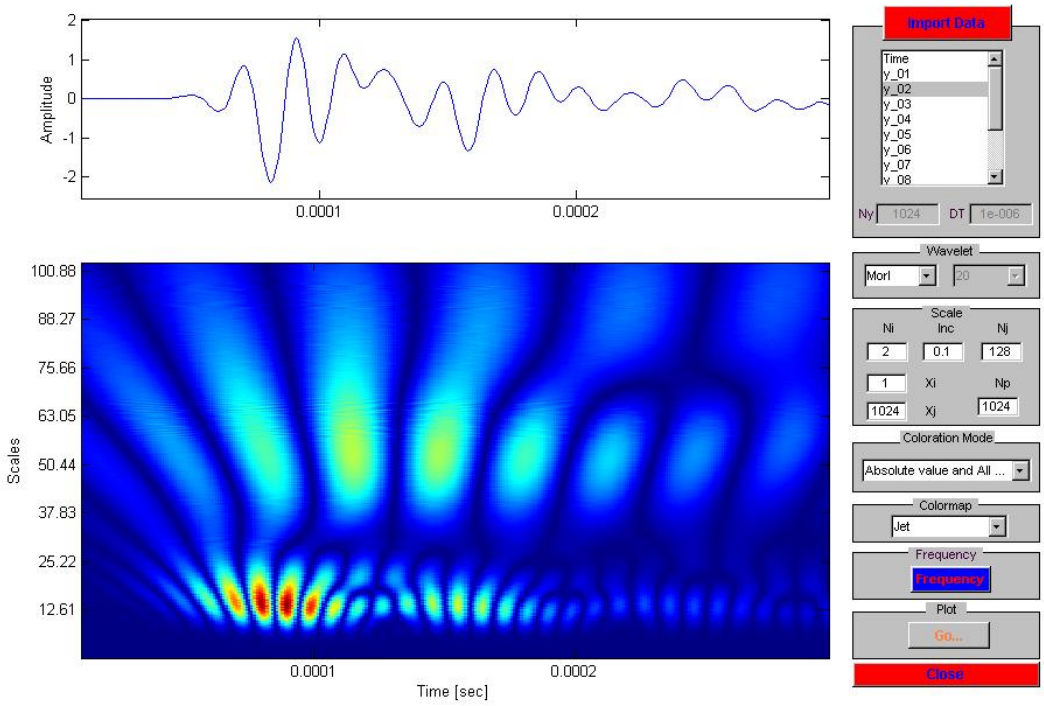

Figure F-8: Wavelet transform of signal f_{S2_R1} through the joint-free surface using Mallat's algorithm

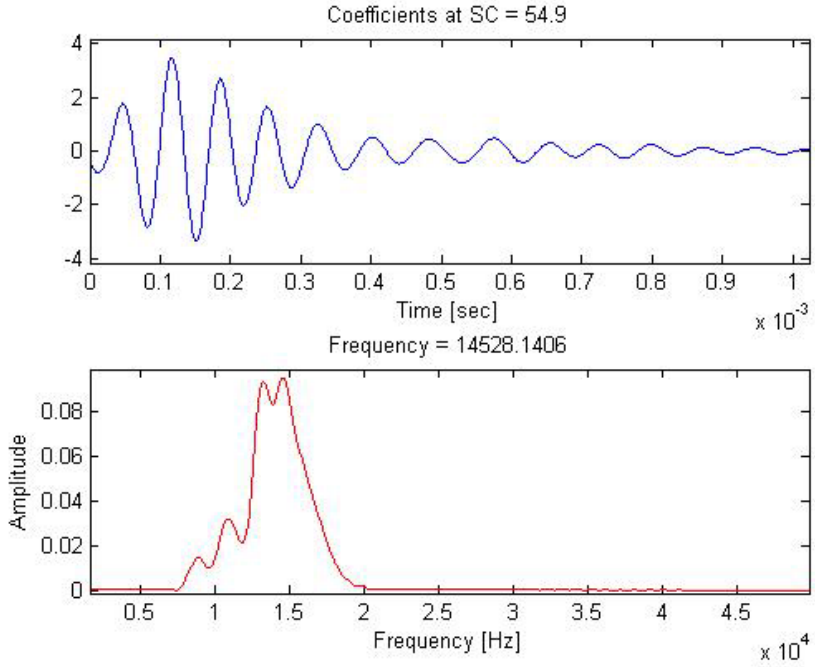

Figure F-9: Frequency content at a given scale from Figure F-8

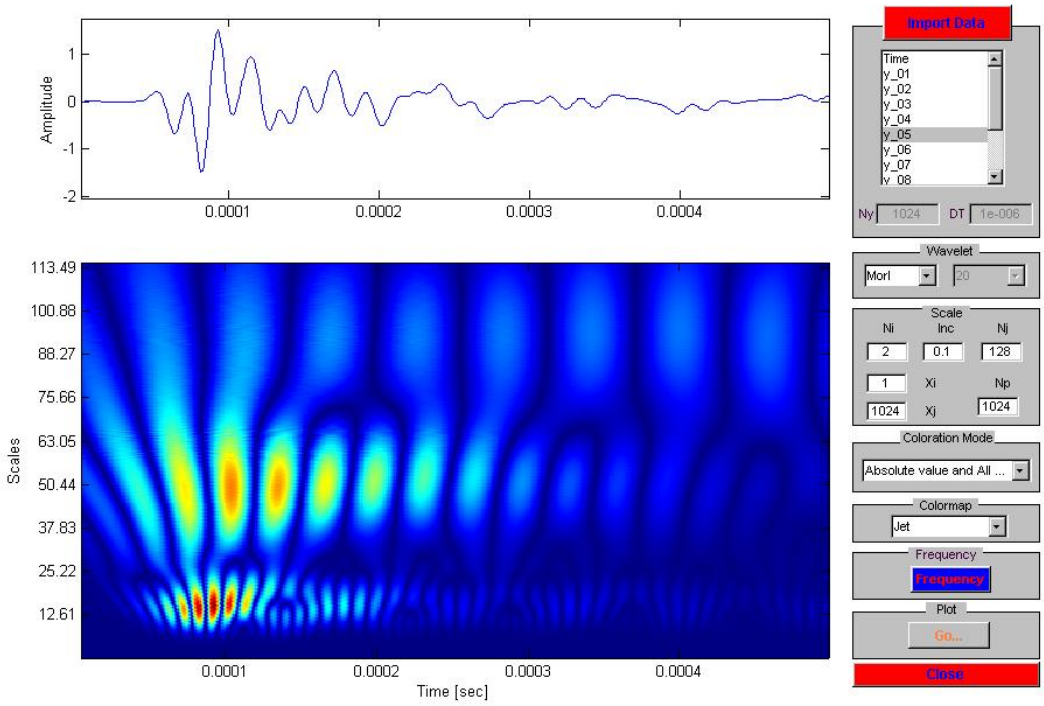

Figure F-10: Wavelet transform of signal f_{S2_R3} through the joint-free surface using Mallat's algorithm

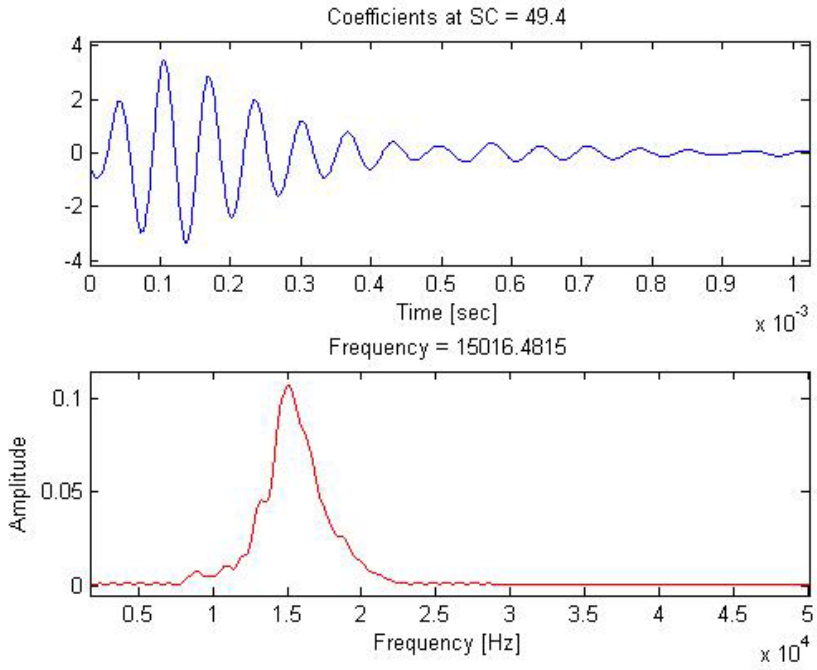

Figure F-11: Frequency content at a given scale from Figure F-10

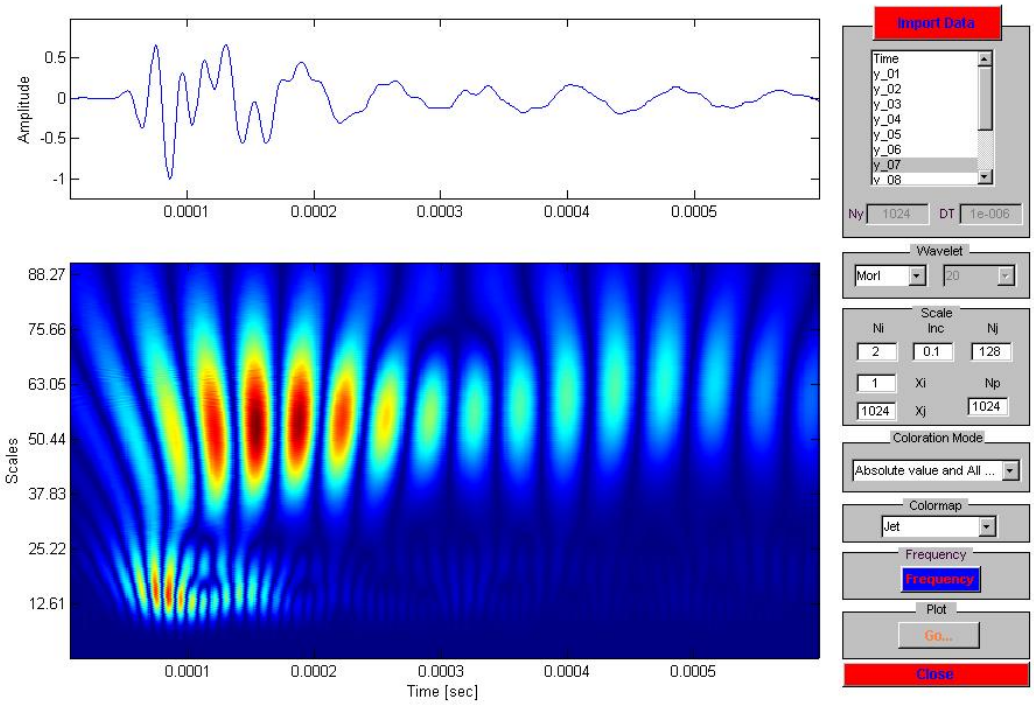

Figure F-12: Wavelet transform of signal f_{S3_R3} across the joint using Mallat's algorithm

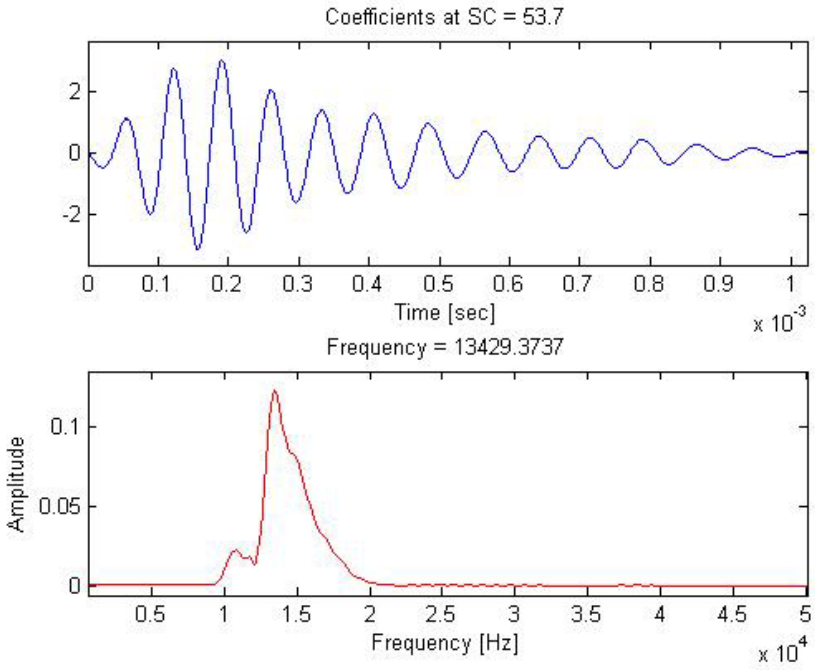

Figure F-13: Frequency content at a given scale from Figure F-12

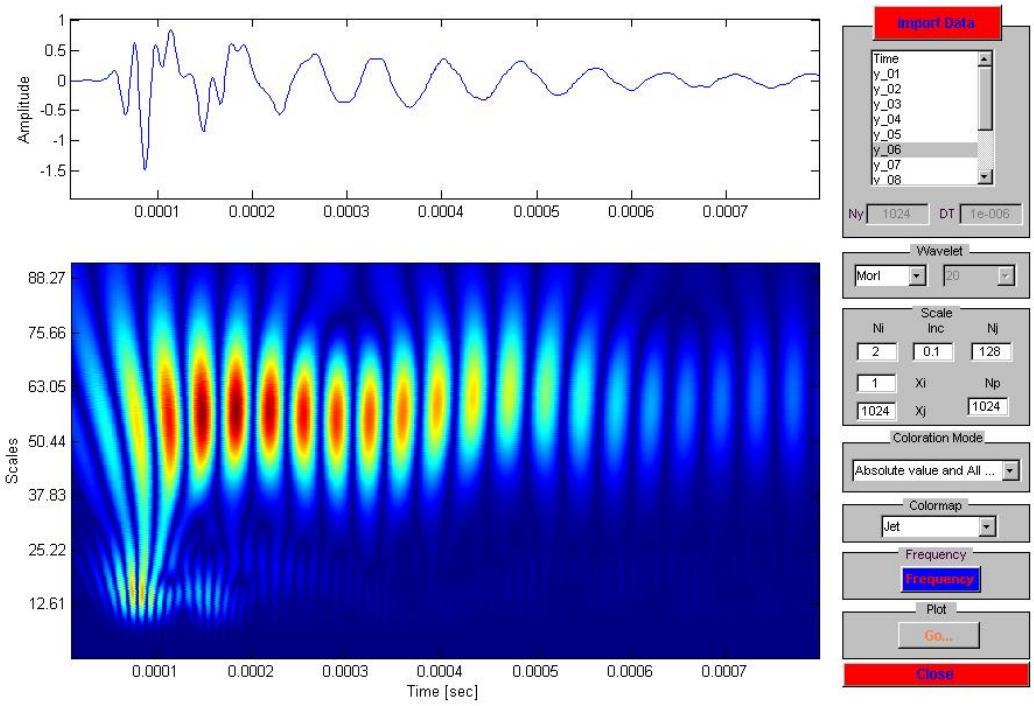

Figure F-14: Wavelet transform of signal f_{S3_R2} through the joint-free surface using Mallat's algorithm

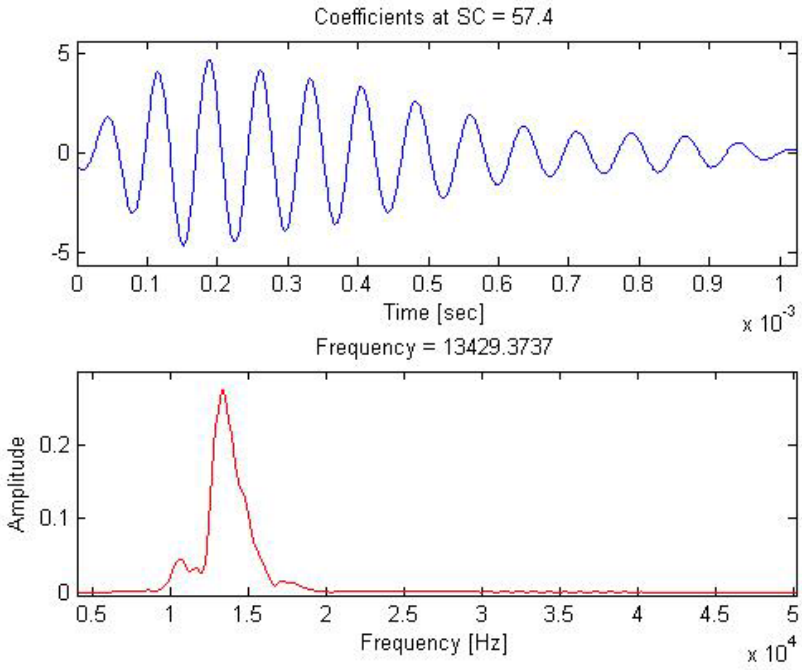

Figure F-15: Frequency content at a given scale from Figure F-14

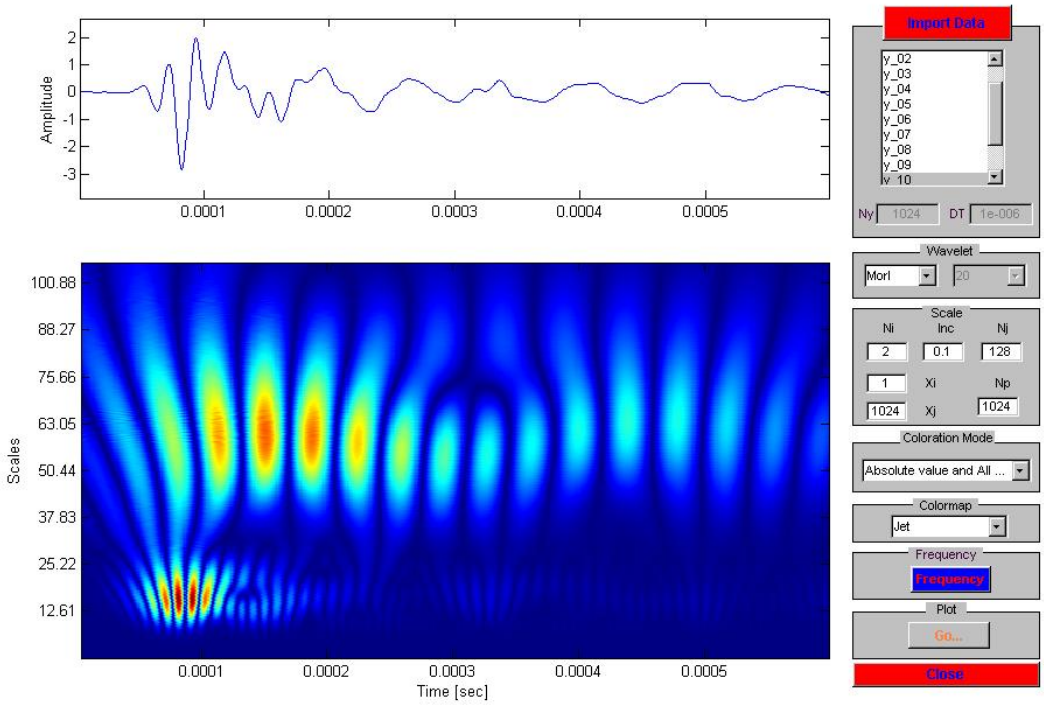

Figure F-16: Wavelet transform of signal f_{S3_R4} through the joint-free surface using Mallat's algorithm

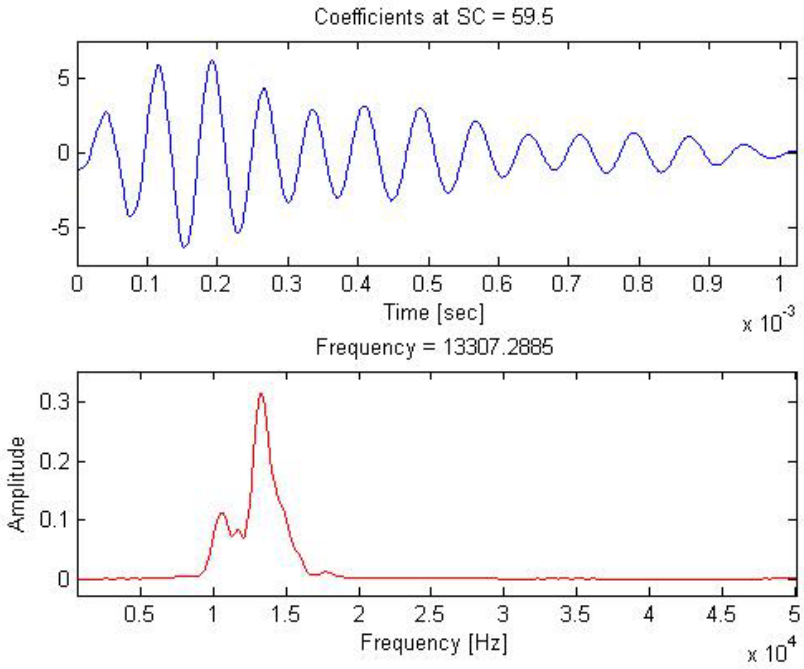

Figure F-17: Frequency content at a given scale from Figure F-16

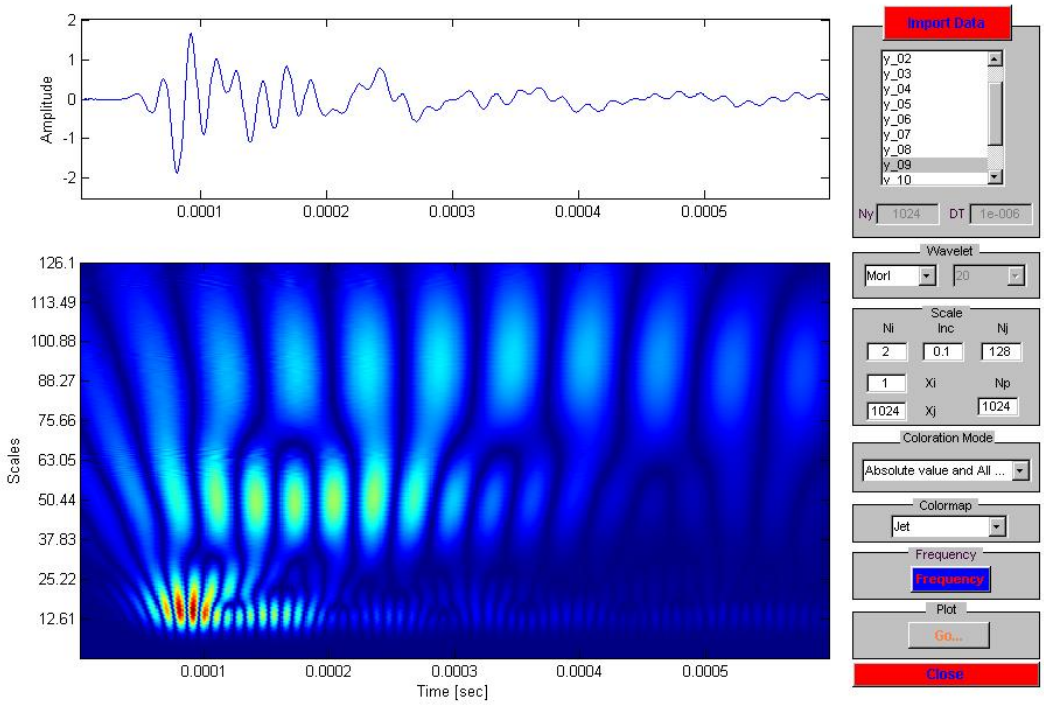

Figure F-18: Wavelet transform of signal f_{S4_R3} through the joint-free surface using Mallat's algorithm

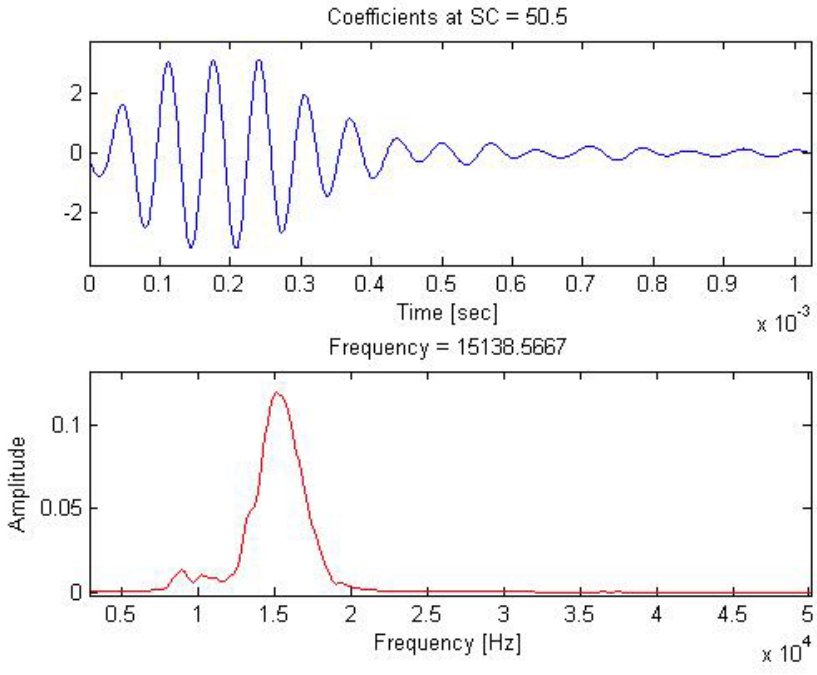

Figure F-19: Frequency content at a given scale from Figure F-18

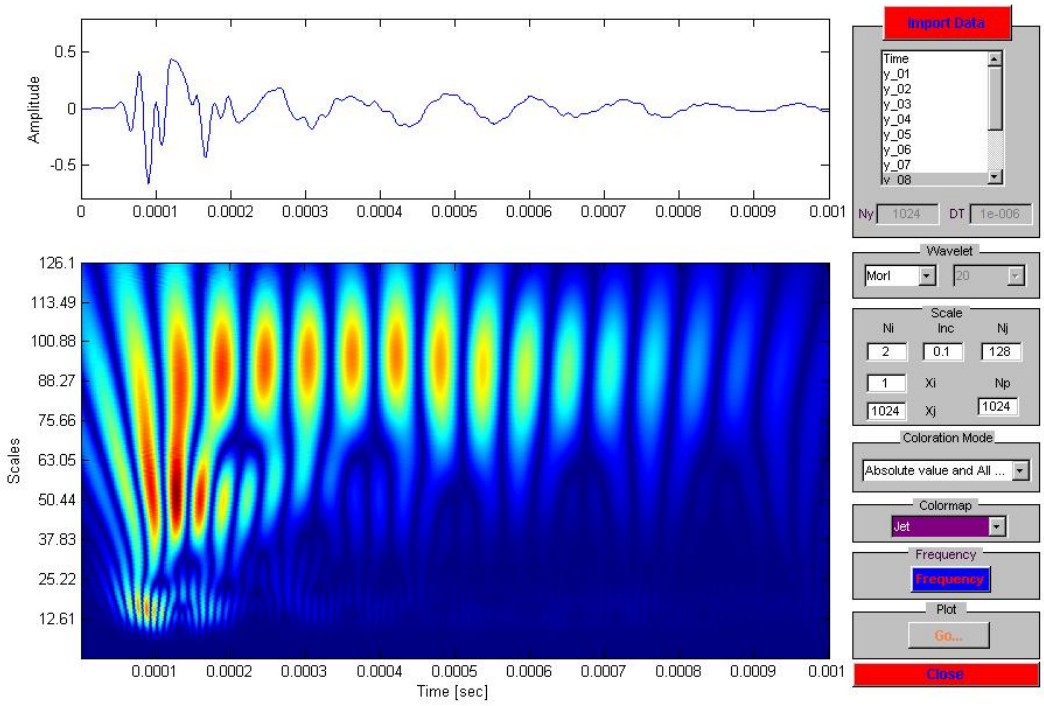

Figure F-20: Wavelet transform of signal f_{S4_R4} across the joint using Mallat's algorithm

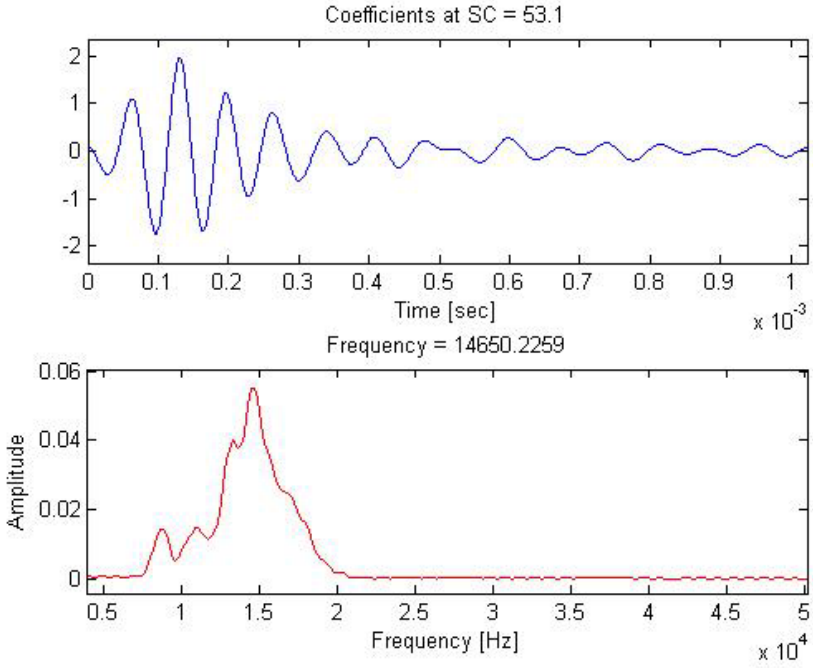

Figure F-21: Frequency content at a given scale from Figure F-20

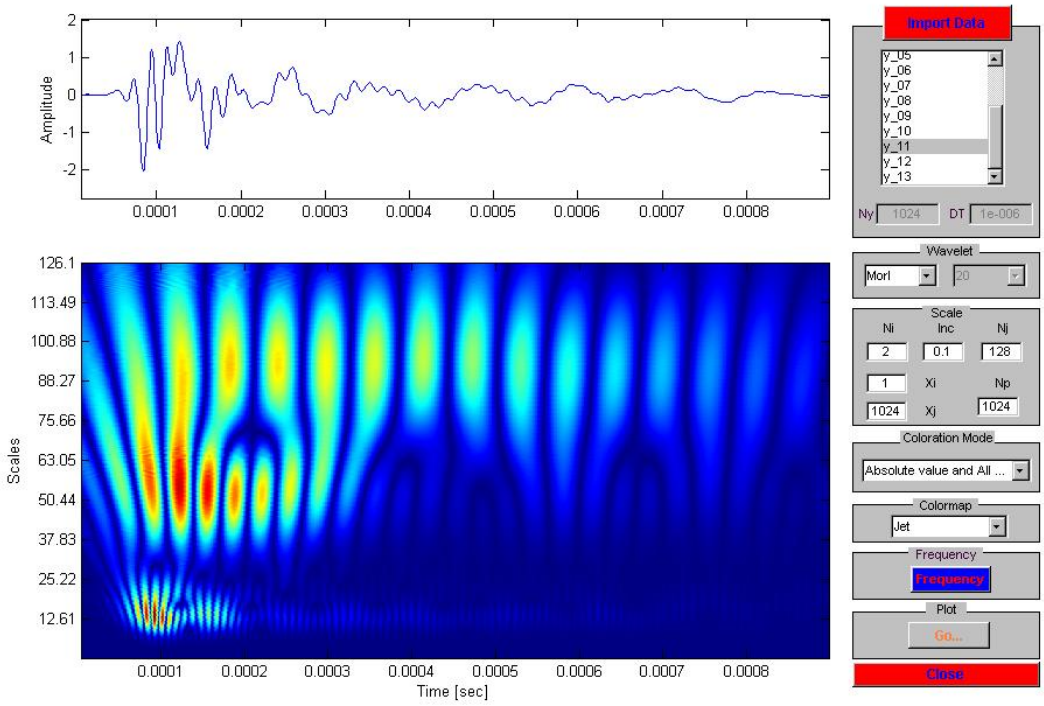

Figure F-22: Wavelet transform of signal f_{S4_R5} through the joint-free surface using Mallat's algorithm

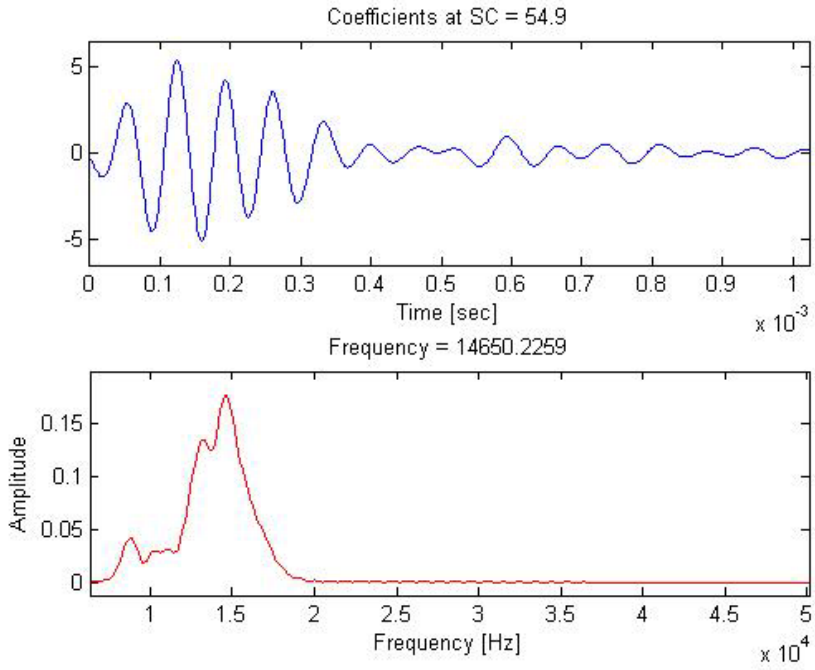

Figure F-23: Frequency content at a given scale from Figure F-22

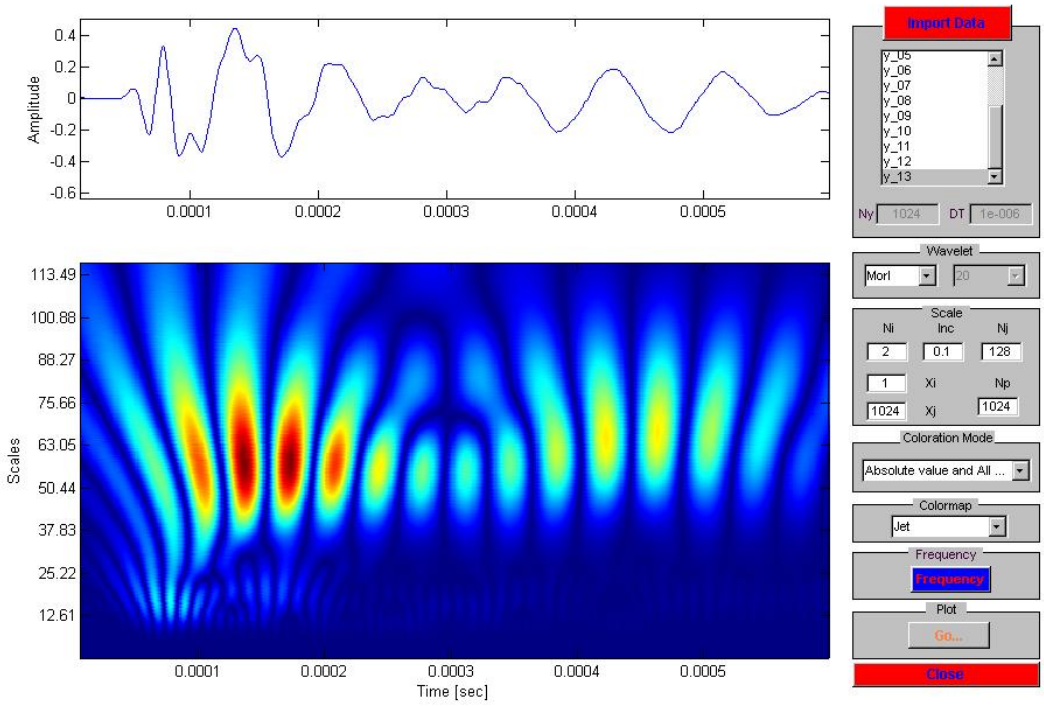

Figure F-24: Wavelet transform of signal f_{S5_R5} across the joint using Mallat's algorithm

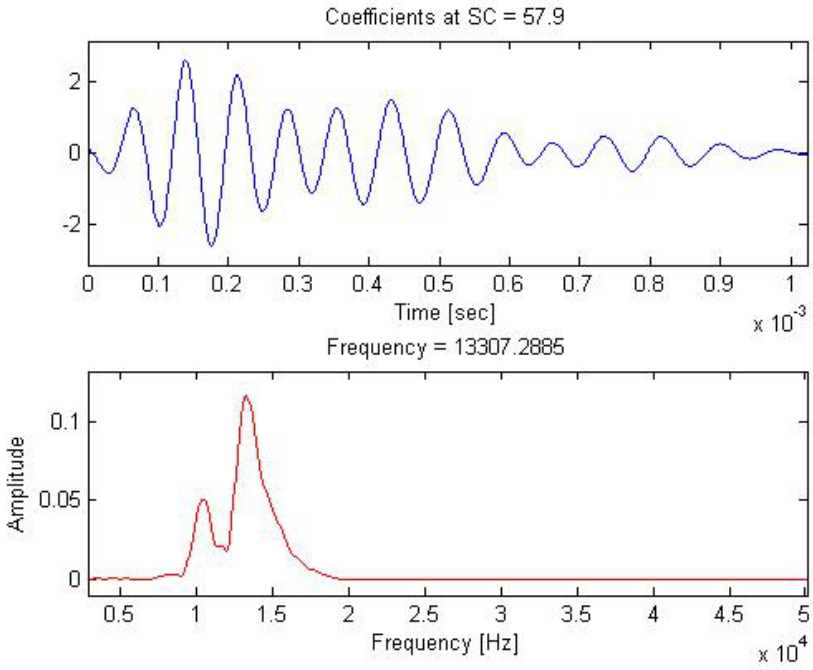

Figure F-25: Frequency content at a given scale from Figure F-24

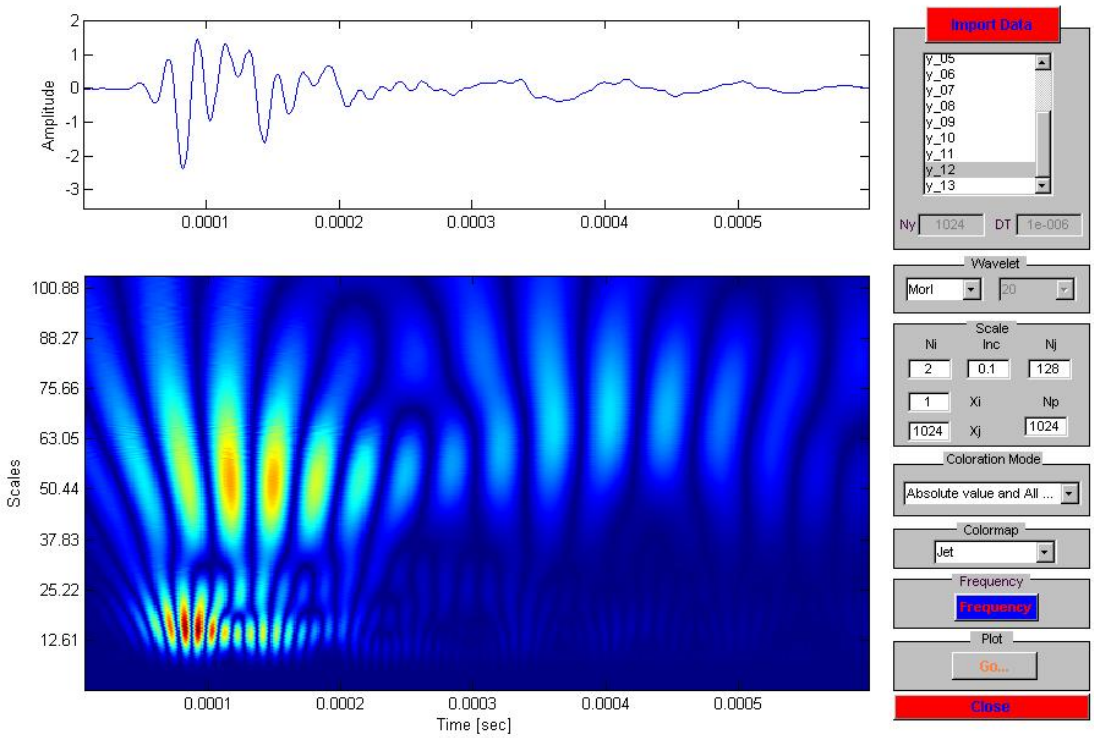

Figure F-26: Wavelet transform of signal f_{S5_R4} through the joint-free surface using Mallat's algorithm

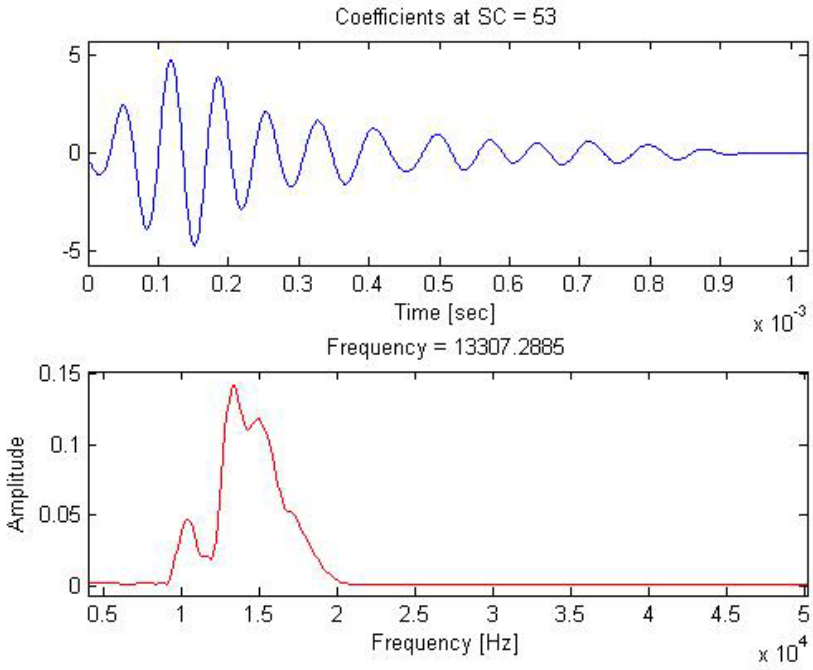

Figure F-27: Frequency content at a given scale from Figure F-26

Appendix M

Equivalent Damping ratio vs. Frequency for slab 2

- Measurements on the Jointed and the Joint-free Surfaces

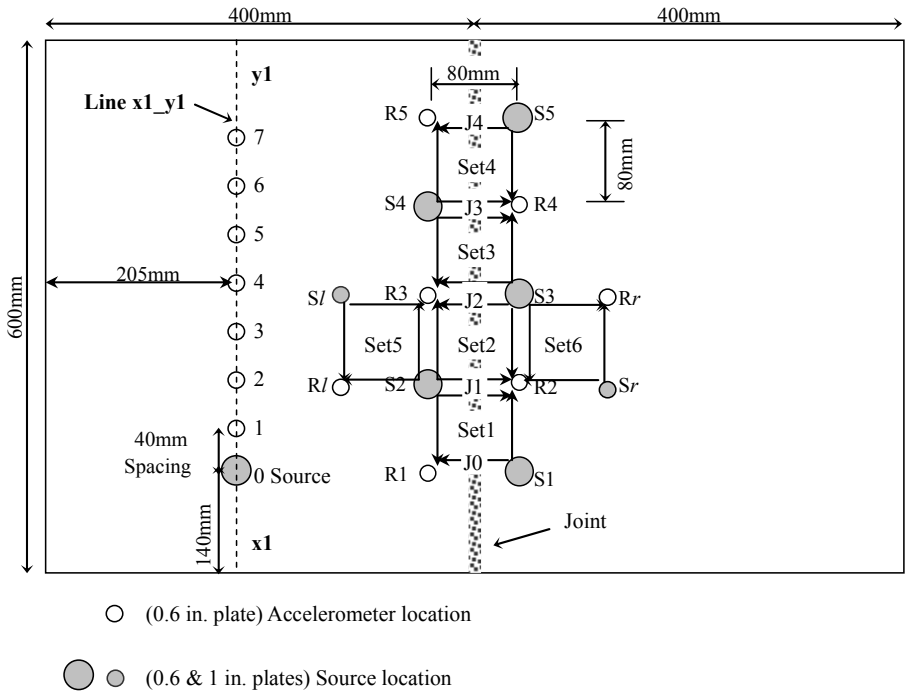

Figure M-1: Ultrasonic test configuration of HMA slab 2

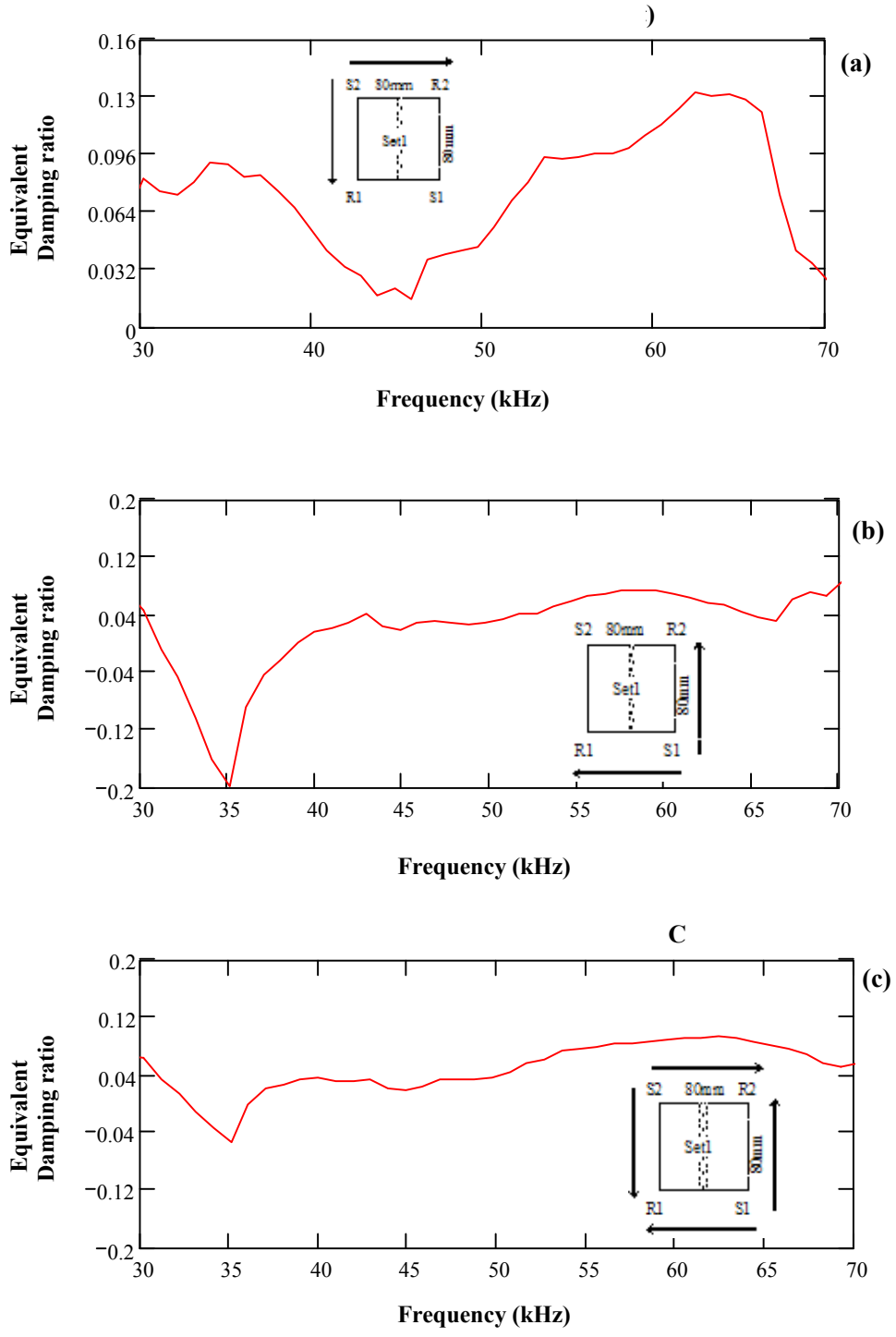

Figure M-2: Equivalent damping ratio (D) vs. frequency for full signals of set 1 measurements on the jointed surface – (a) D for Signal Pair 1 of set 1 (b) D for Signal Pair 2 of set 1 (c) D for entire set 1 measurements

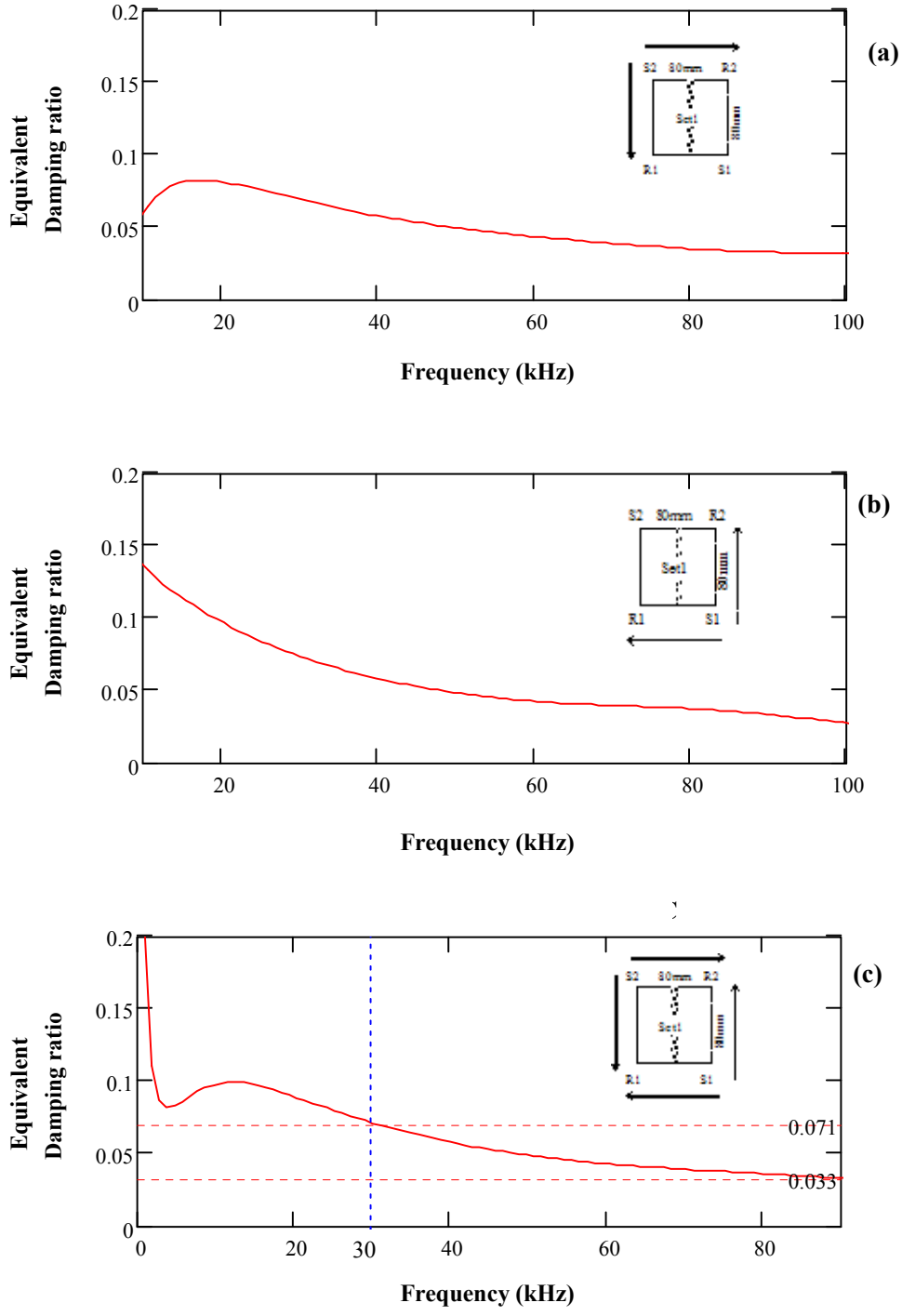

Figure M-3: Equivalent damping ratio (D) vs. frequency for P-waves for set 1 measurements on the jointed surface – (a) D for Signal Pair 1 of set 1 (b) D for Signal Pair 2 of set 1 (c) D for entire set 1 measurements

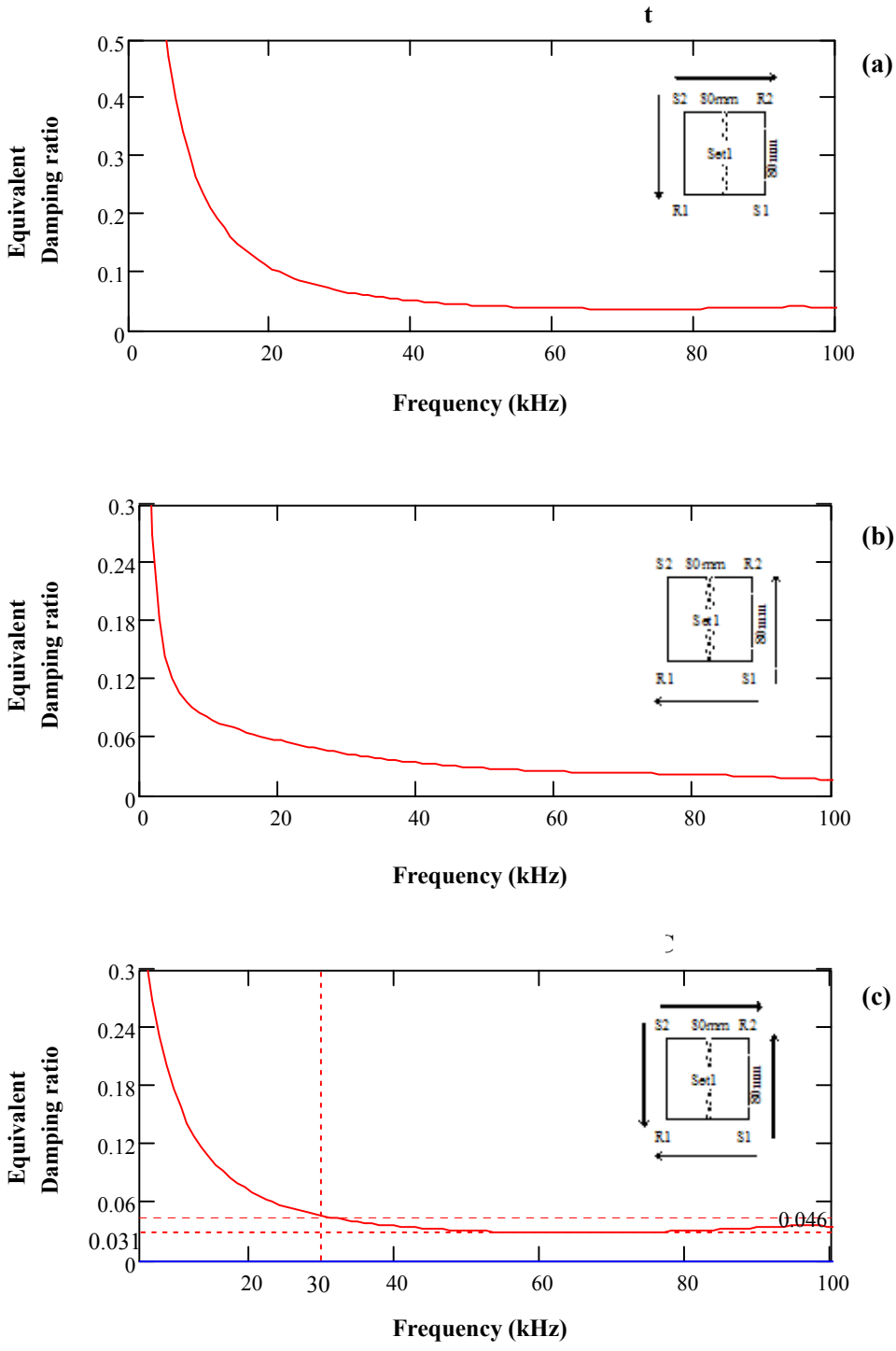

Figure M-4: Equivalent damping ratio (D) vs. frequency for R-waves for set 1 measurements on the jointed surface – (a) D for Signal Pair 1 of set 1 (b) D for Signal Pair 2 of set 1 (c) D for entire set 1 measurements

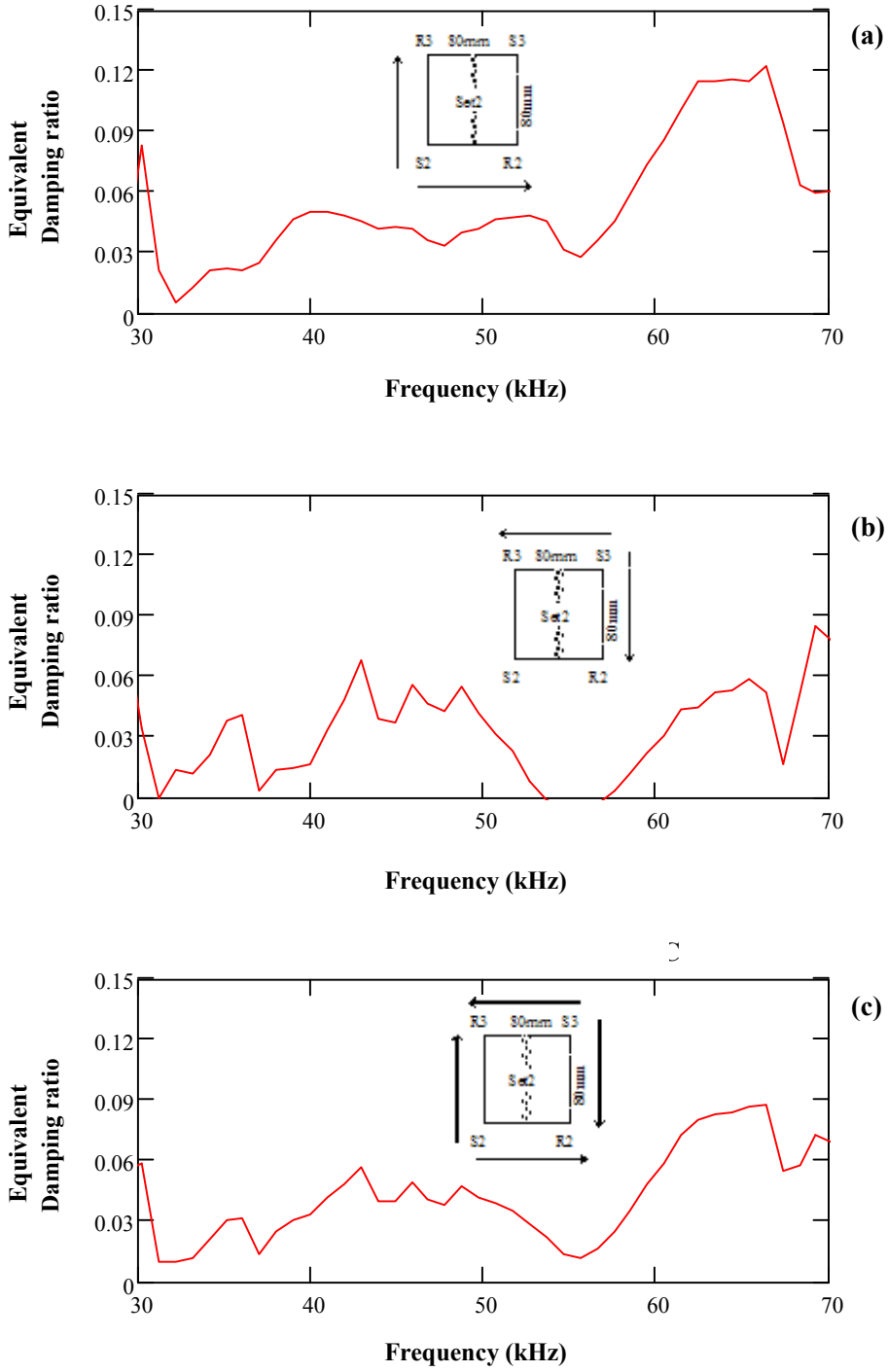

Figure M-5: Equivalent damping ratio (D) vs. frequency for full signals for set 2 measurements on the jointed surface – (a) D for Signal Pair 1 of set 2 (b) D for Signal Pair 2 of set 2 (c) D for entire set 2 measurements

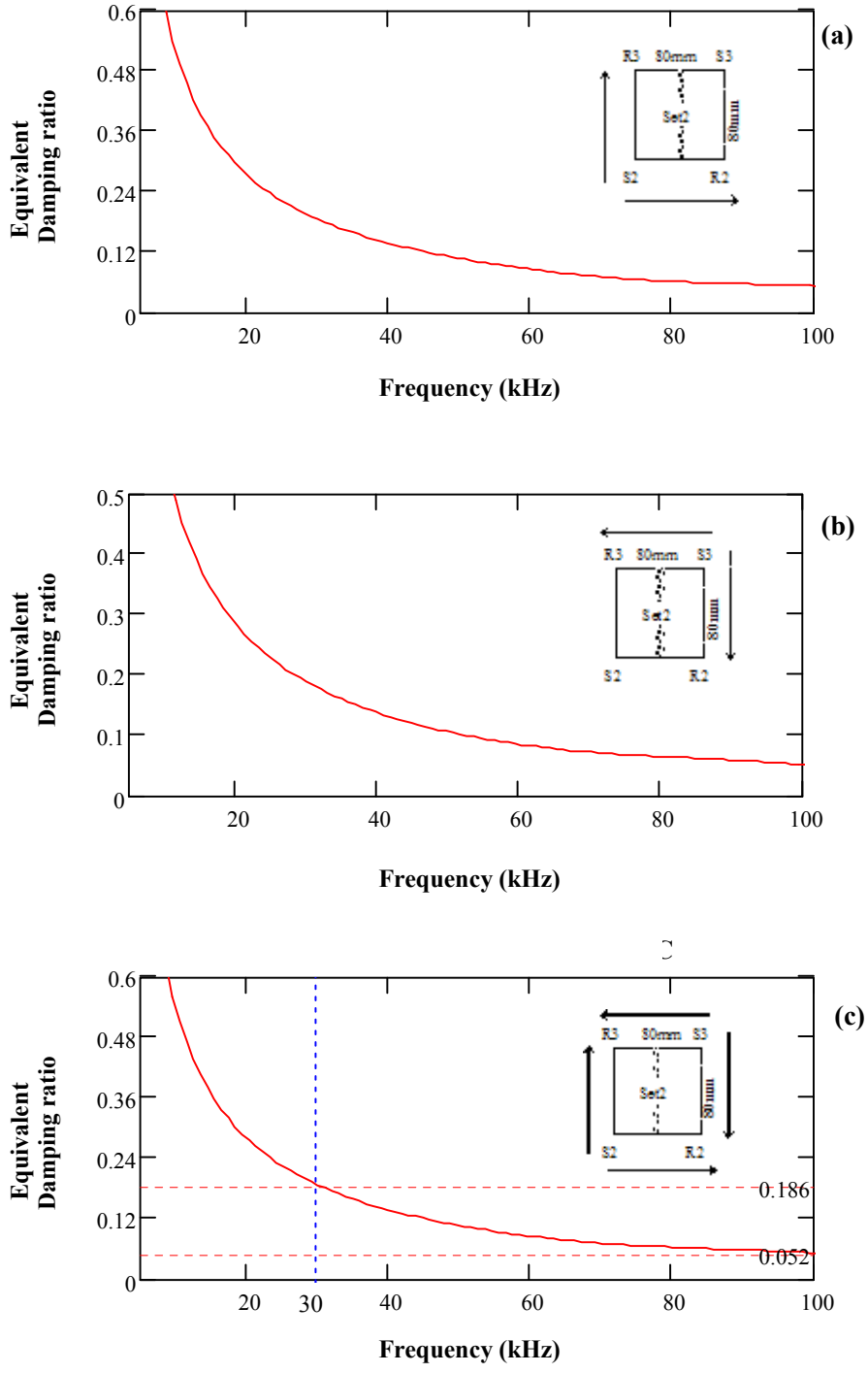

Figure M-6: Equivalent damping ratio (D) vs. frequency for P-waves for set 2 measurements on the jointed surface – (a) D for Signal Pair 1 of set 2 (b) D for Signal Pair 2 of set 2 (c) D for entire set 2 measurements

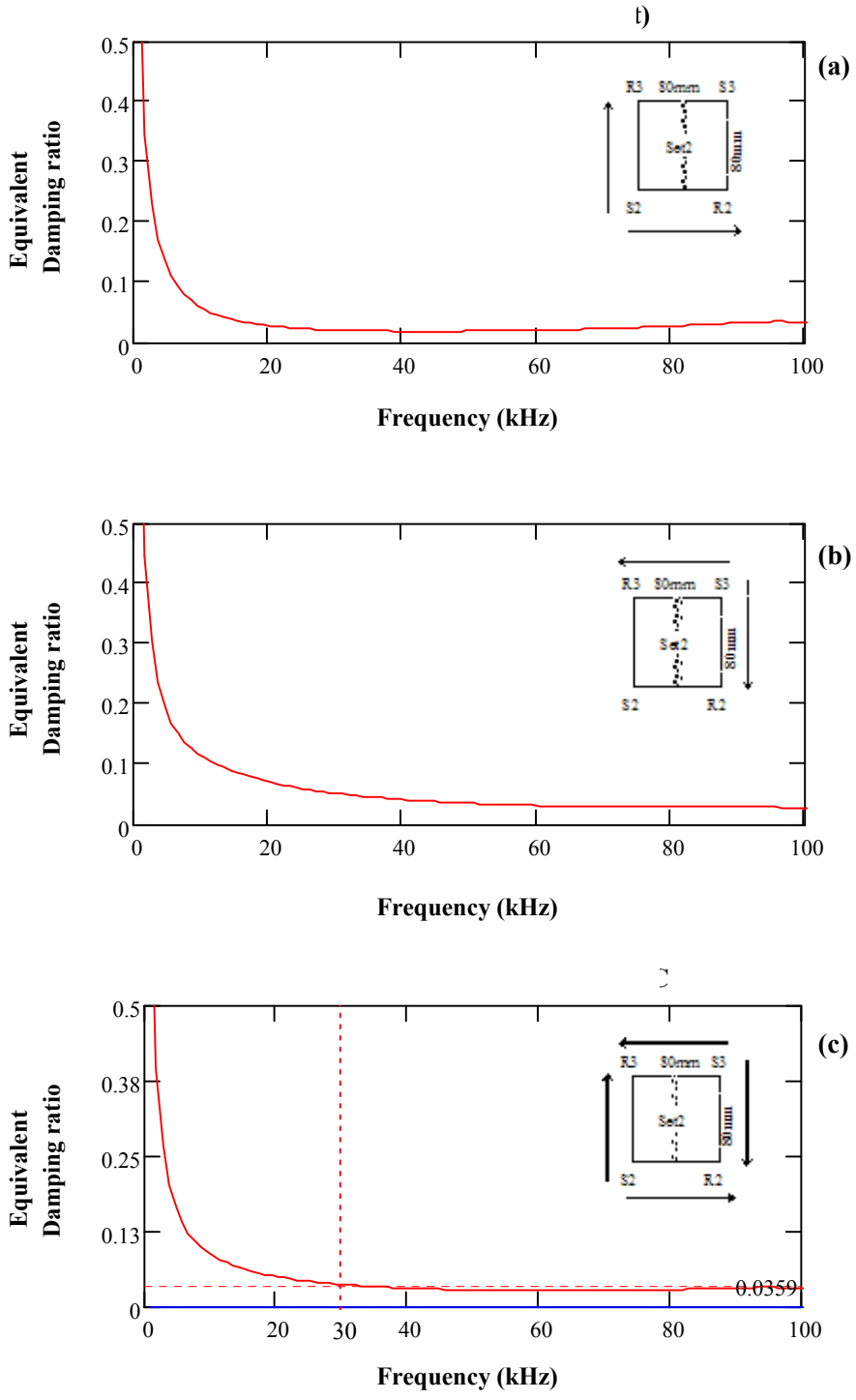

Figure M-7: Equivalent damping ratio (D) vs. frequency for R-waves for set 2 measurements on the jointed surface – (a) D for Signal Pair 1 of set 2 (b) D for Signal Pair 2 of set 2 (c) D for entire set 2 measurements

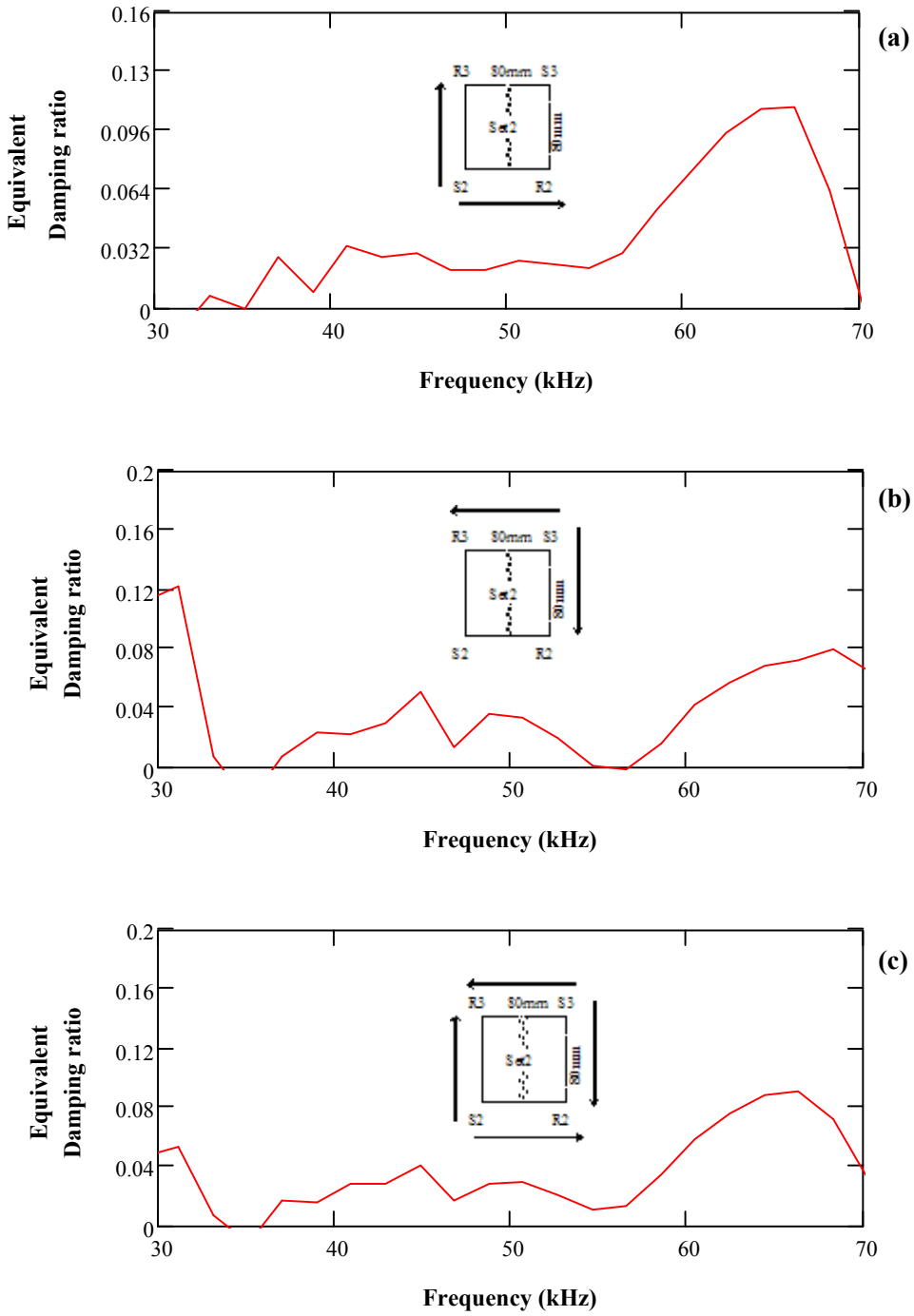

Figure M-8: Equivalent damping ratio (D) vs. frequency for full signals for repeated set 2 measurements on the jointed surface – (a) D for Signal Pair 1 of repeated set 2 (b) D for Signal Pair 2 of repeated set 2 (c) D for entire repeated set 2 measurements

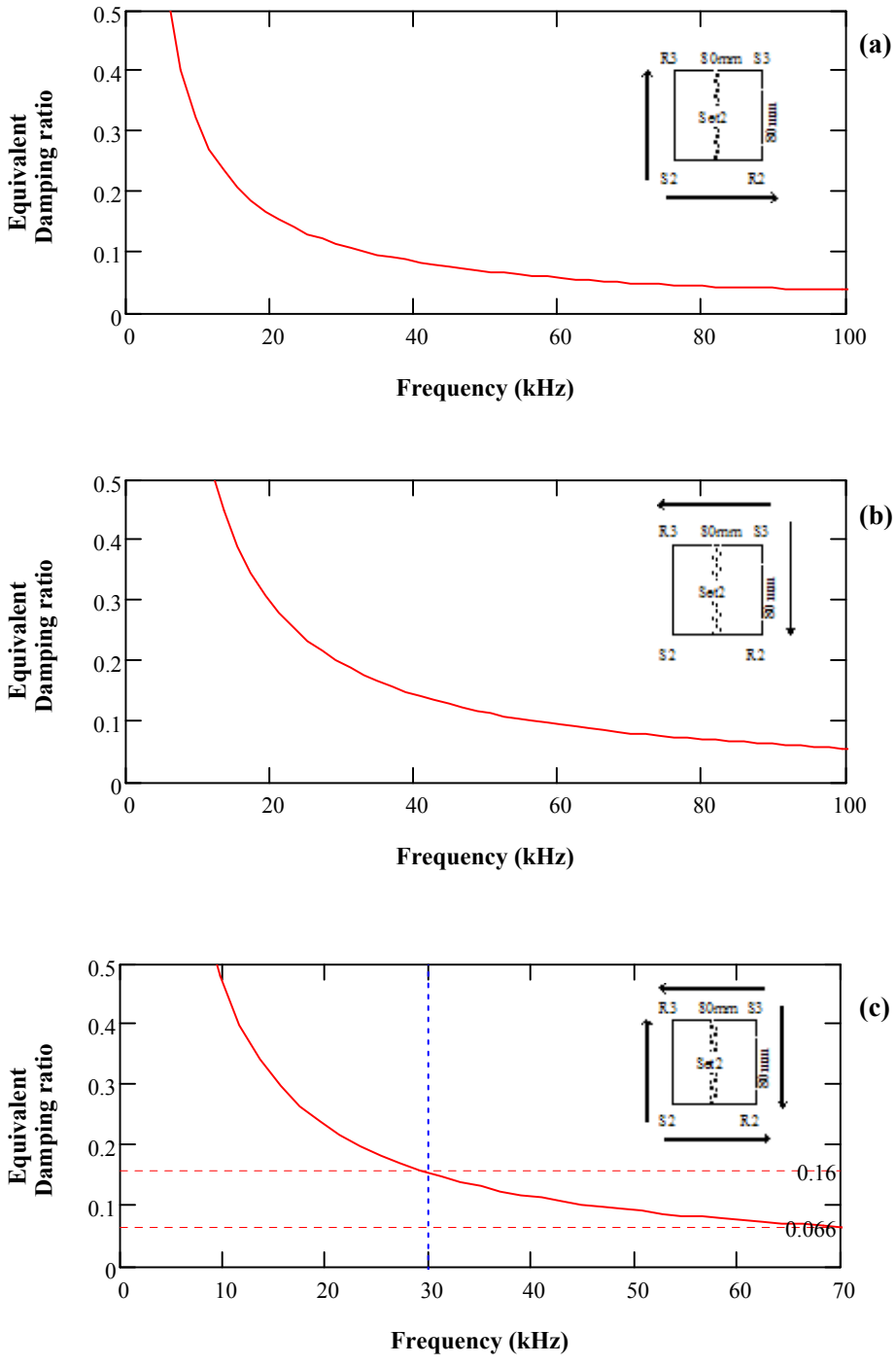

Figure M-9: Equivalent damping ratio (D) vs. frequency for P-waves for repeated set 2 measurements on the jointed surface – (a) D for Signal Pair 1 of repeated set 2 (b) D for Signal Pair 2 of repeated set 2 (c) D for entire repeated set 2 measurements

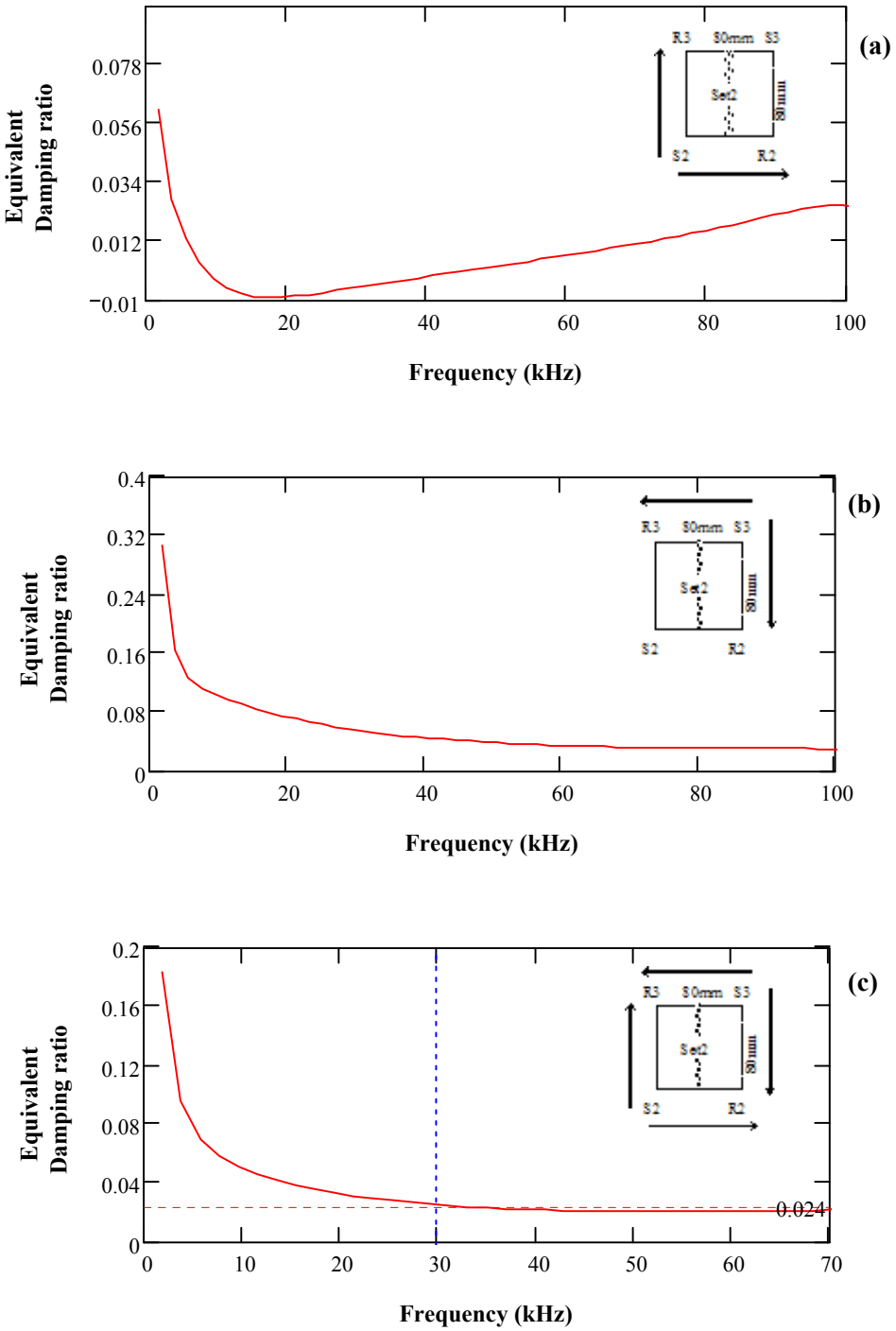

Figure M-10: Equivalent damping ratio (D) vs. frequency for R-waves for repeated set 2 measurements on the jointed surface – (a) D for Signal Pair 1 of repeated set 2 (b) D for Signal Pair 2 of repeated set 2 (c) D for entire repeated set 2 measurements

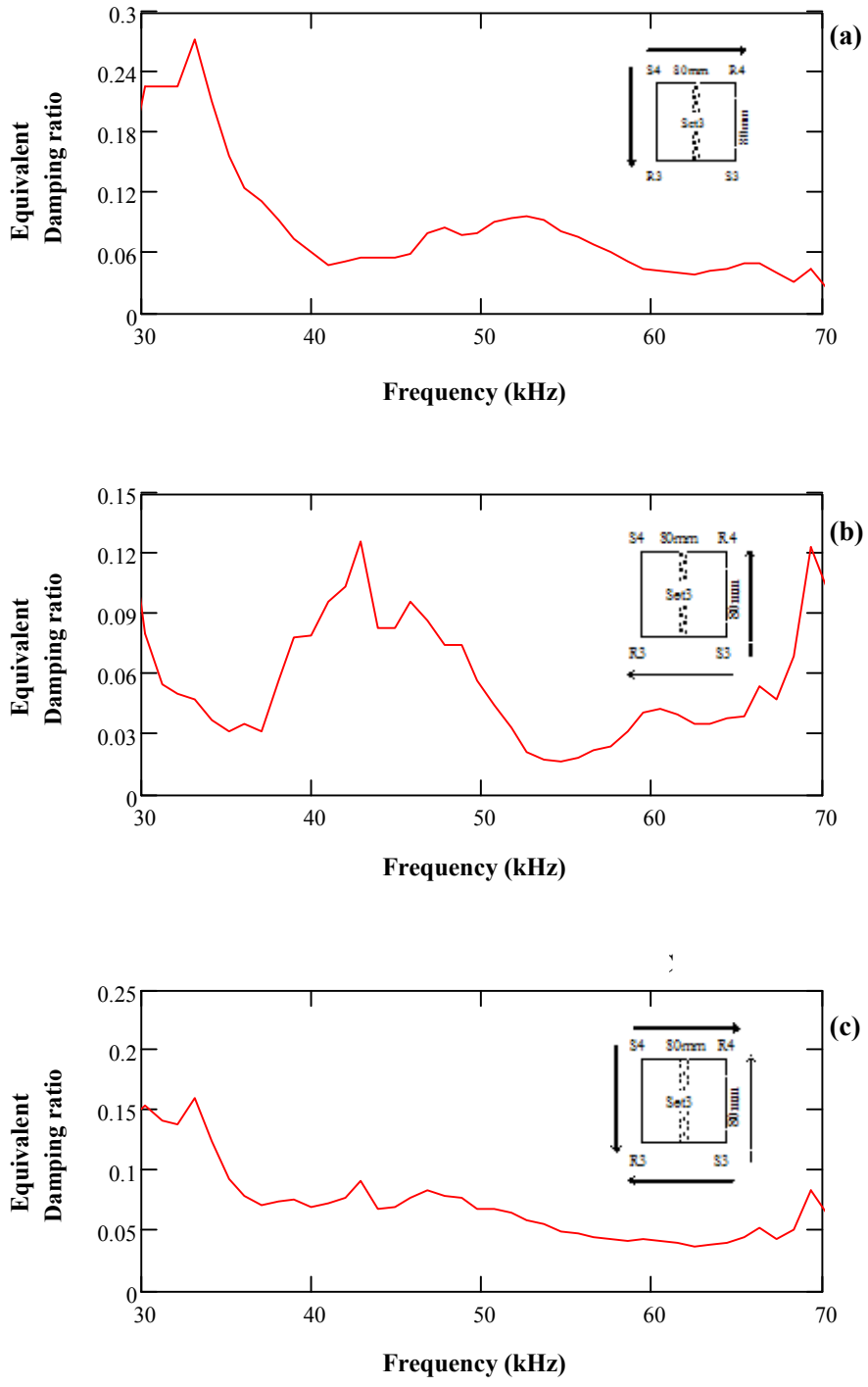

Figure M-11: Equivalent damping ratio (D) vs. frequency for full signals for set 3 measurements on the jointed surface – (a) D for Signal Pair 1 of set 3 (b) D for Signal Pair 2 of set 3 (c) D for entire set 3 measurements

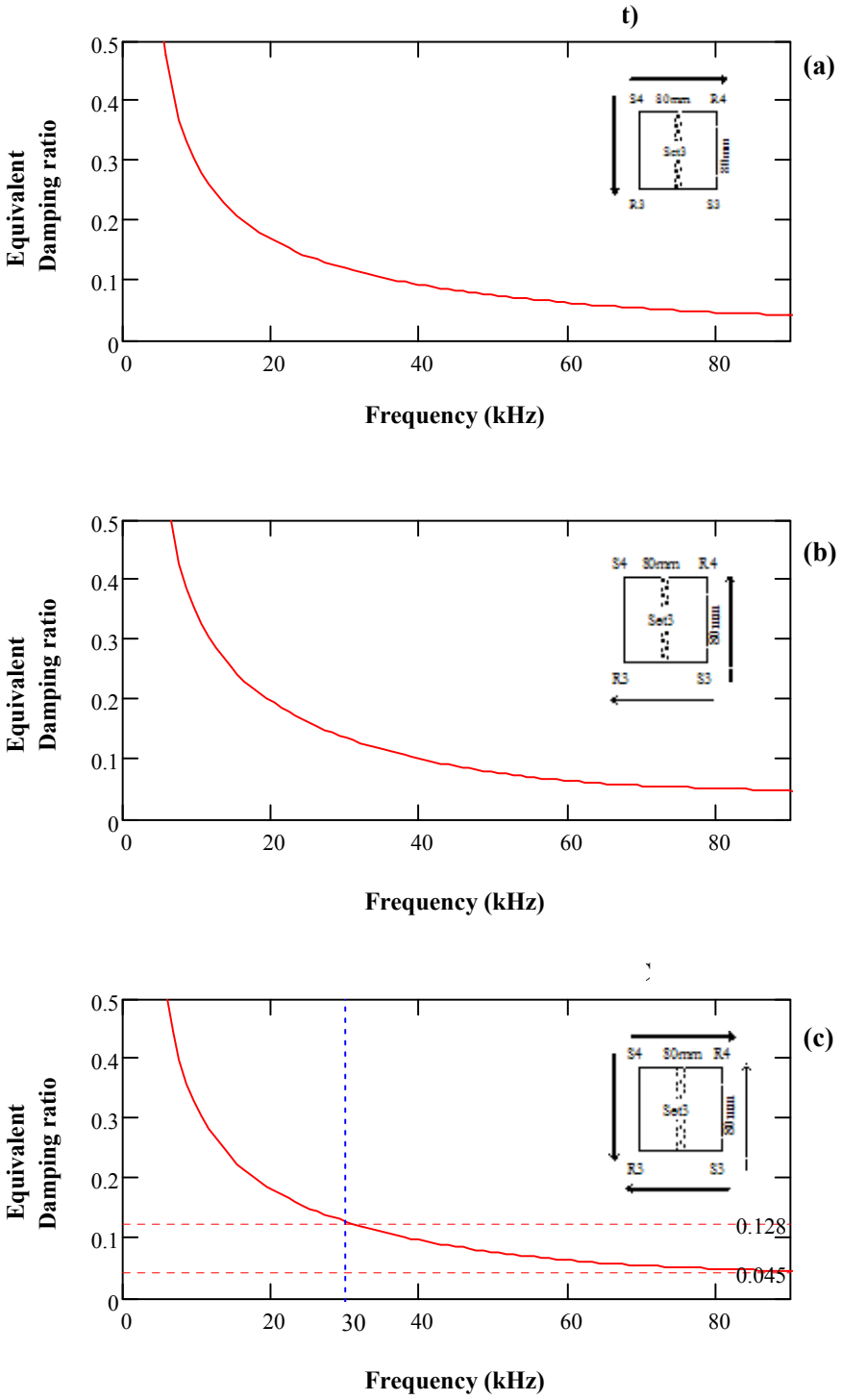

Figure M-12: Equivalent damping ratio (D) vs. frequency for P-waves for set 3 measurements on the jointed surface – (a) D for Signal Pair 1 of set 3 (b) D for Signal Pair 2 of set 3 (c) D for entire set 3 measurements

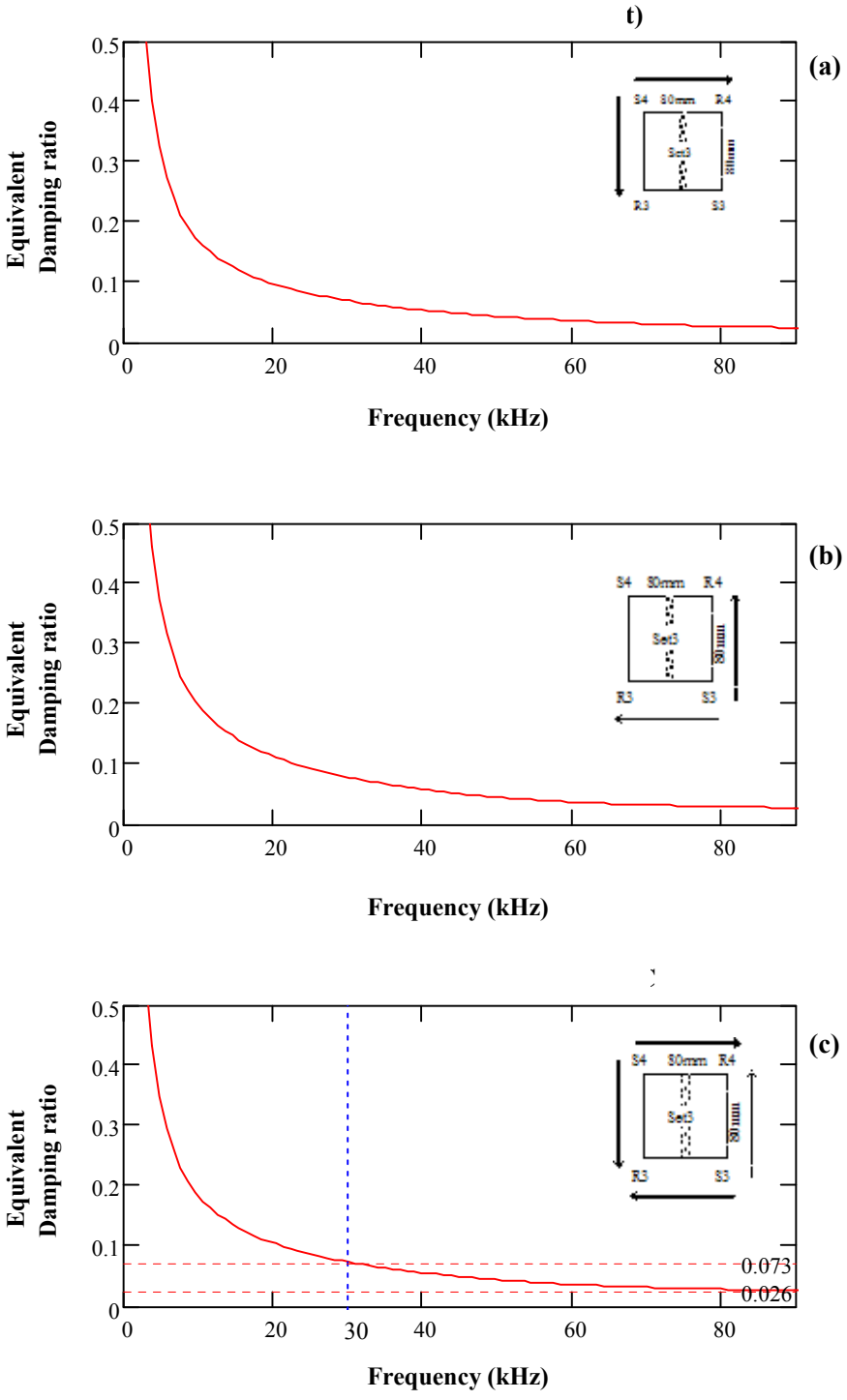

Figure M-13: Equivalent damping ratio (D) vs. frequency for R-waves for set 3 measurements on the jointed surface – (a) D for Signal Pair 1 of set 3 (b) D for Signal Pair 2 of set 3 (c) D for entire set 3 measurements

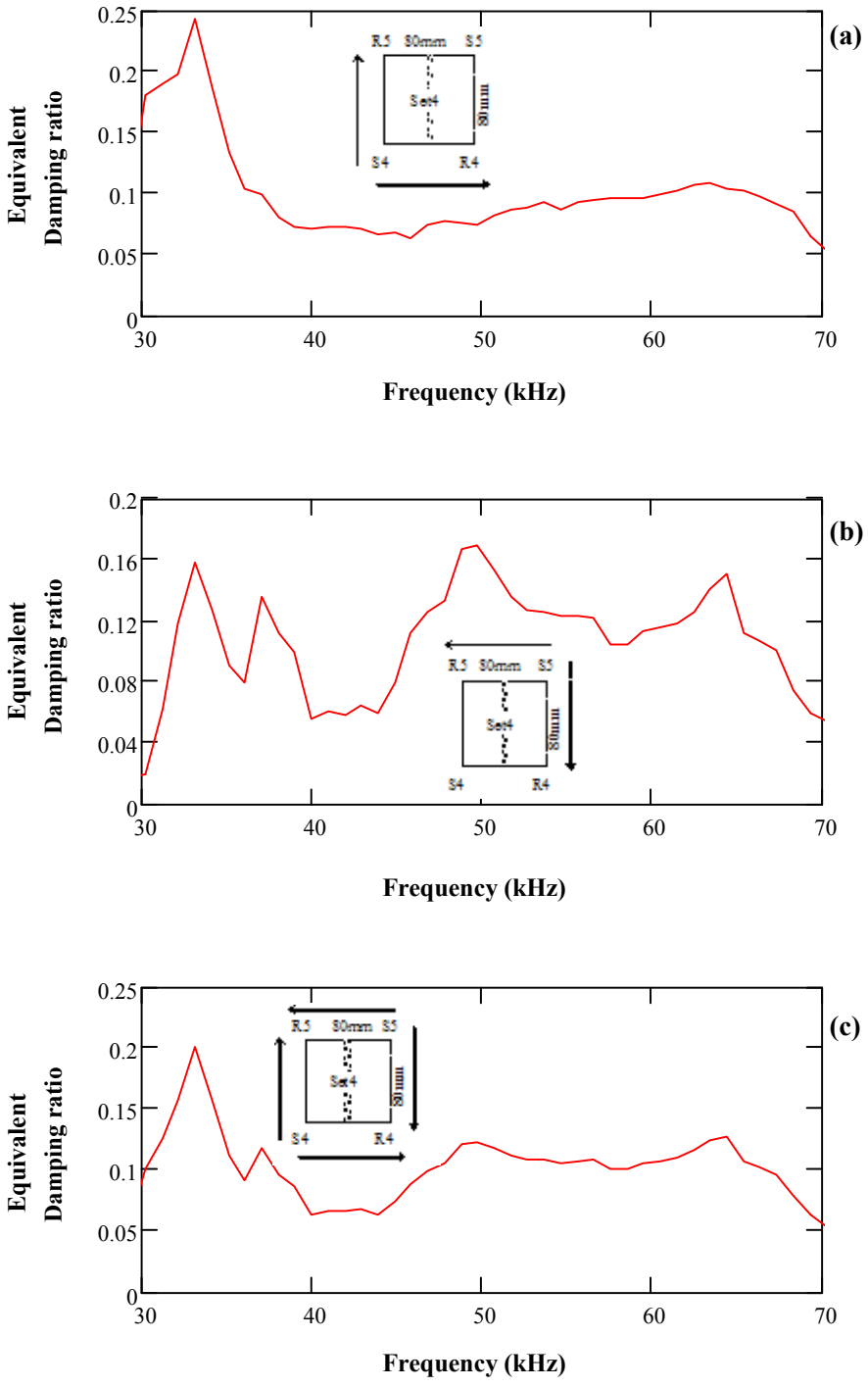

Figure M-14: Equivalent damping ratio (D) vs. frequency for full signals for set 4 measurements on the jointed surface – (a) D for Signal Pair 1 of set 4 (b) D for Signal Pair 2 of set 4 (c) D for entire set 4 measurements

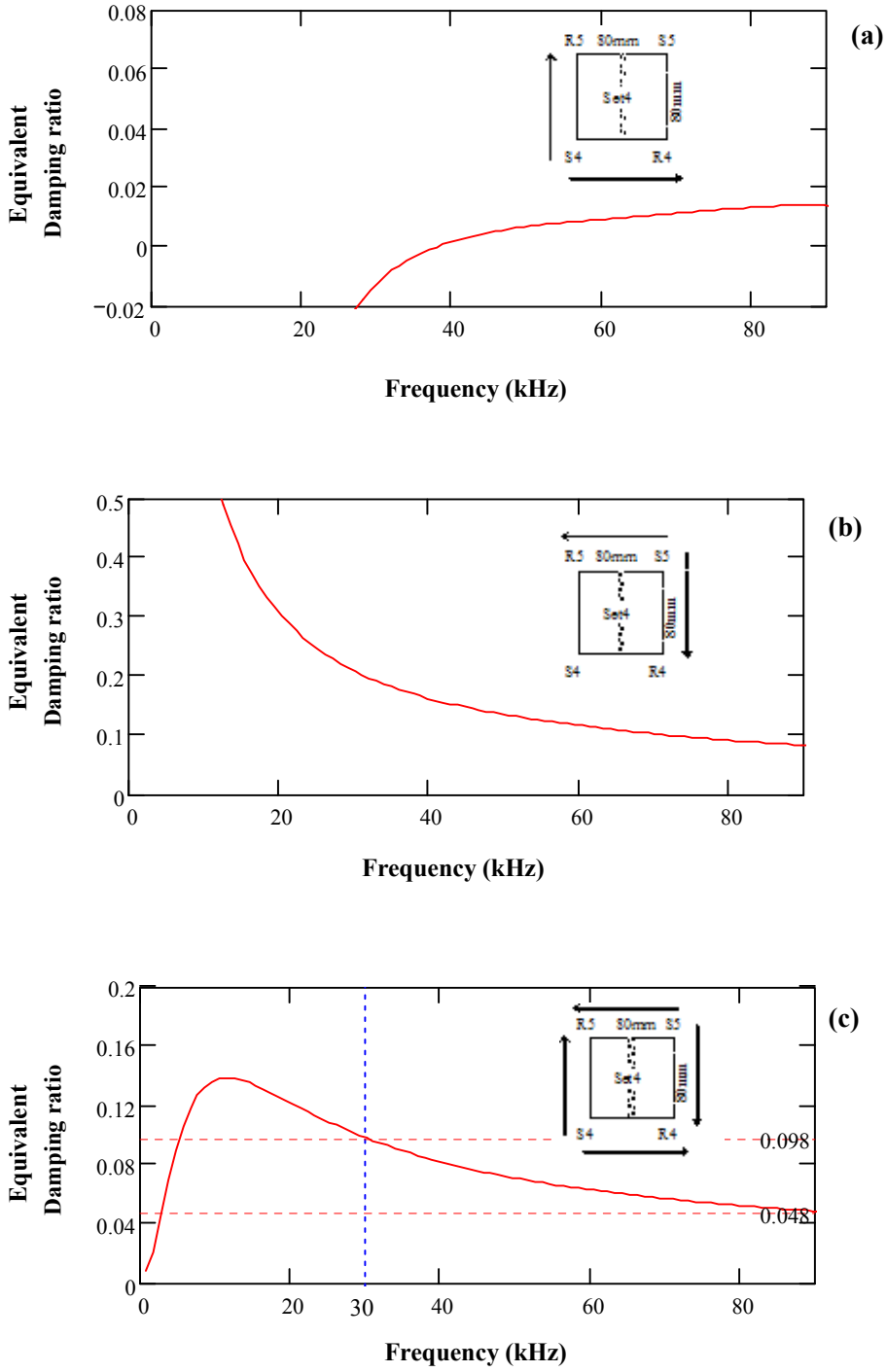

Figure M-15: Equivalent damping ratio (D) vs. frequency for P-waves for set 4 measurements on the jointed surface – (a) D for Signal Pair 1 of set 4 (b) D for Signal Pair 2 of set 4 (c) D for entire set 4 measurements

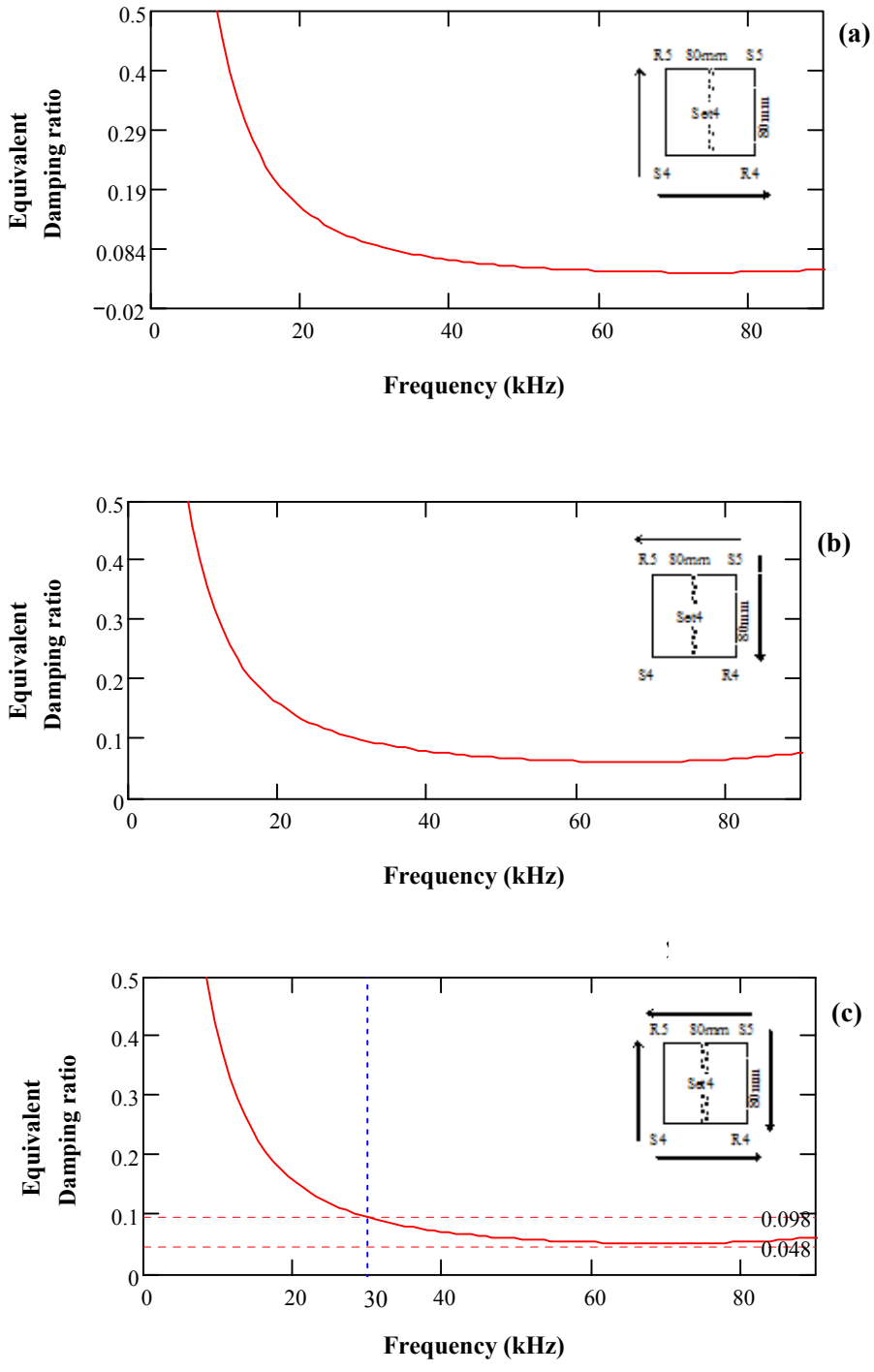

Figure M-16: Equivalent damping ratio (D) vs. frequency for R-waves for set 4 measurements on the jointed surface – (a) D for Signal Pair 1 of set 4 (b) D for Signal Pair 2 of set 4 (c) D for entire set 4 measurements

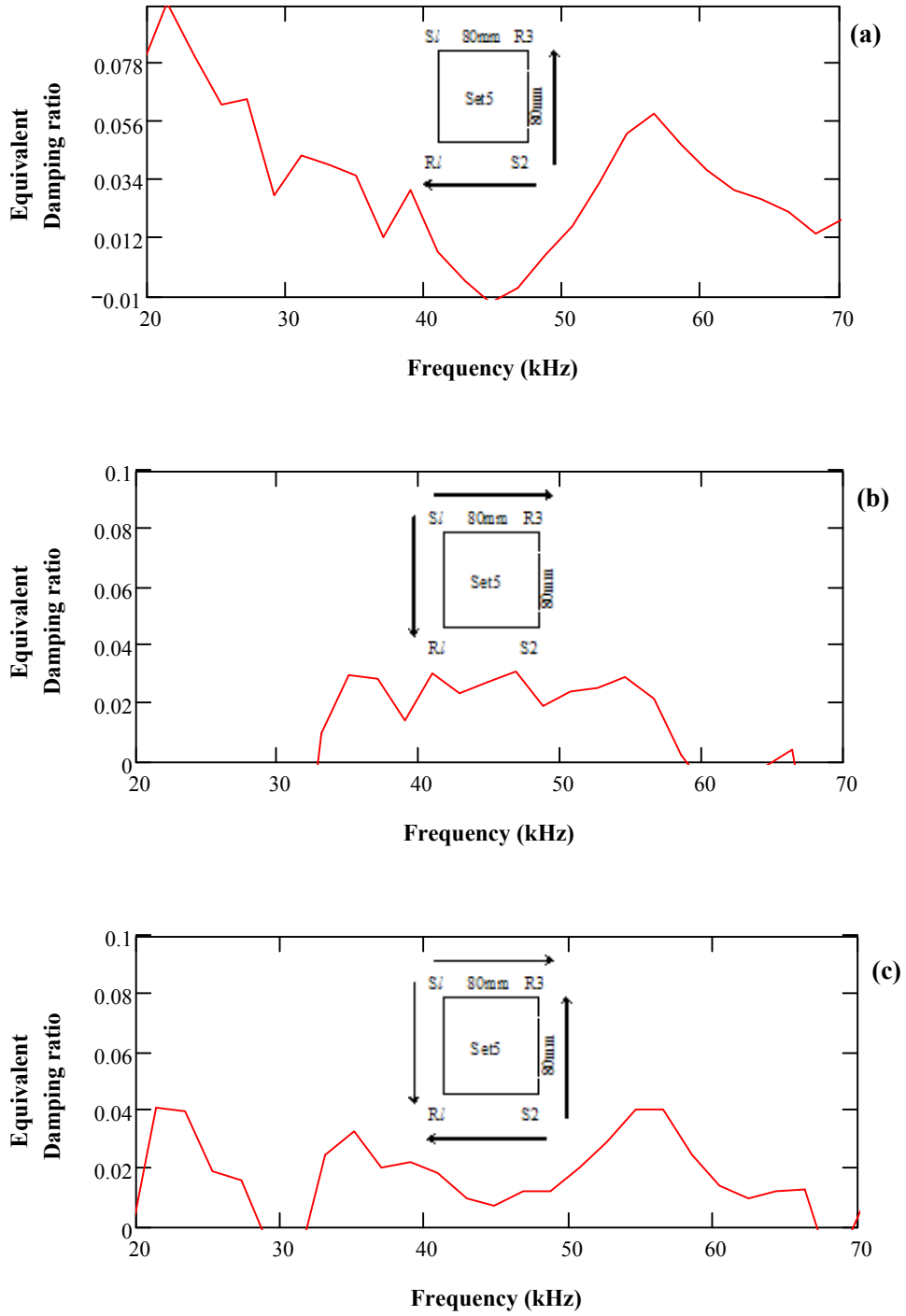

Figure M-17: Equivalent damping ratio (D) vs. frequency for full signals for set 5 measurements on the joint-free surface – (a) D for Signal Pair 1 of set 5 (b) D for Signal Pair 2 of set 5 (c) D for entire set 5 measurements

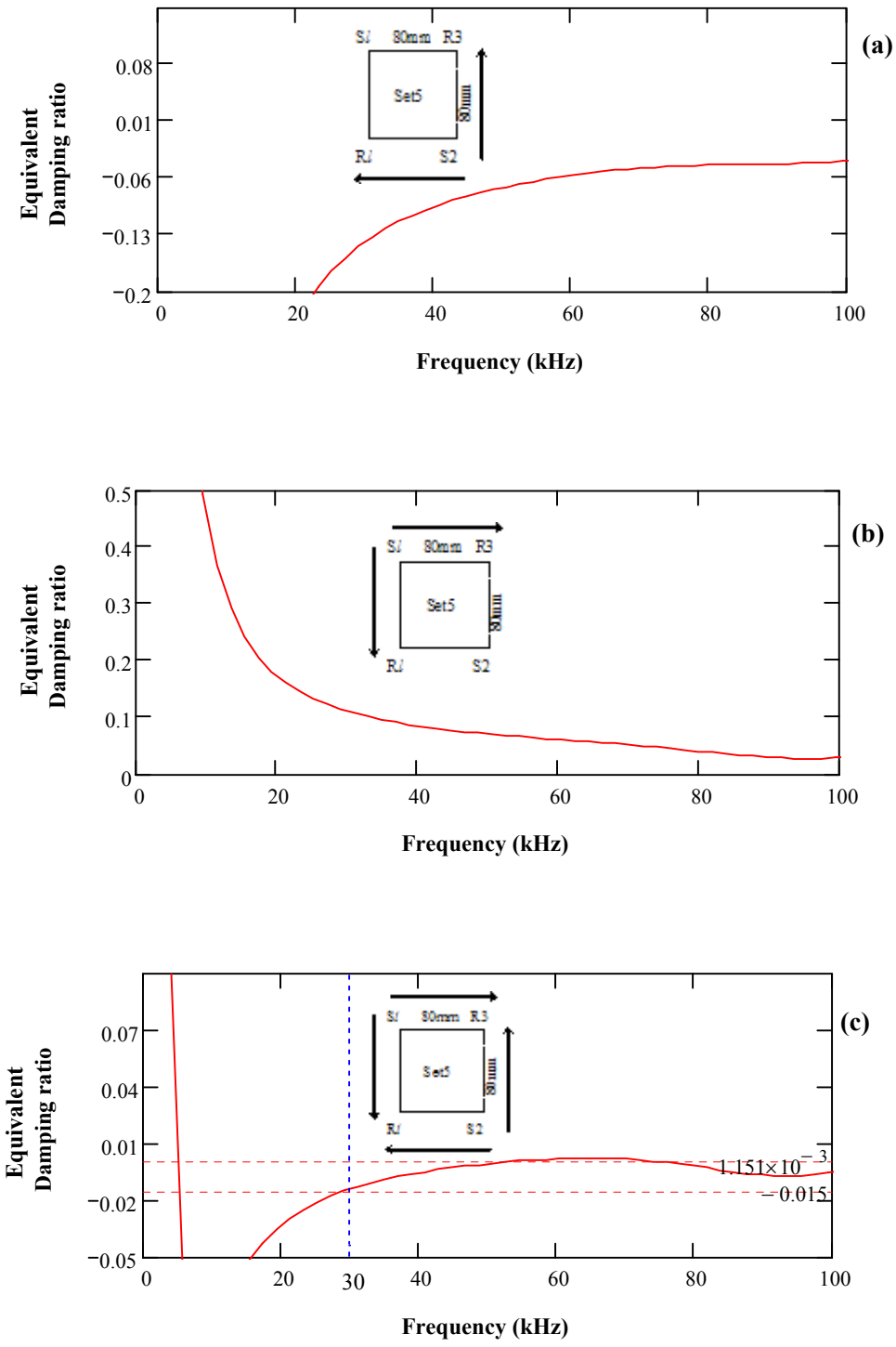

Figure M-18: Equivalent damping ratio (D) vs. frequency for P-waves for set 5 measurements on the joint-free surface – (a) D for Signal Pair 1 of set 5 (b) D for Signal Pair 2 of set 5 (c) D for entire set 5 measurements

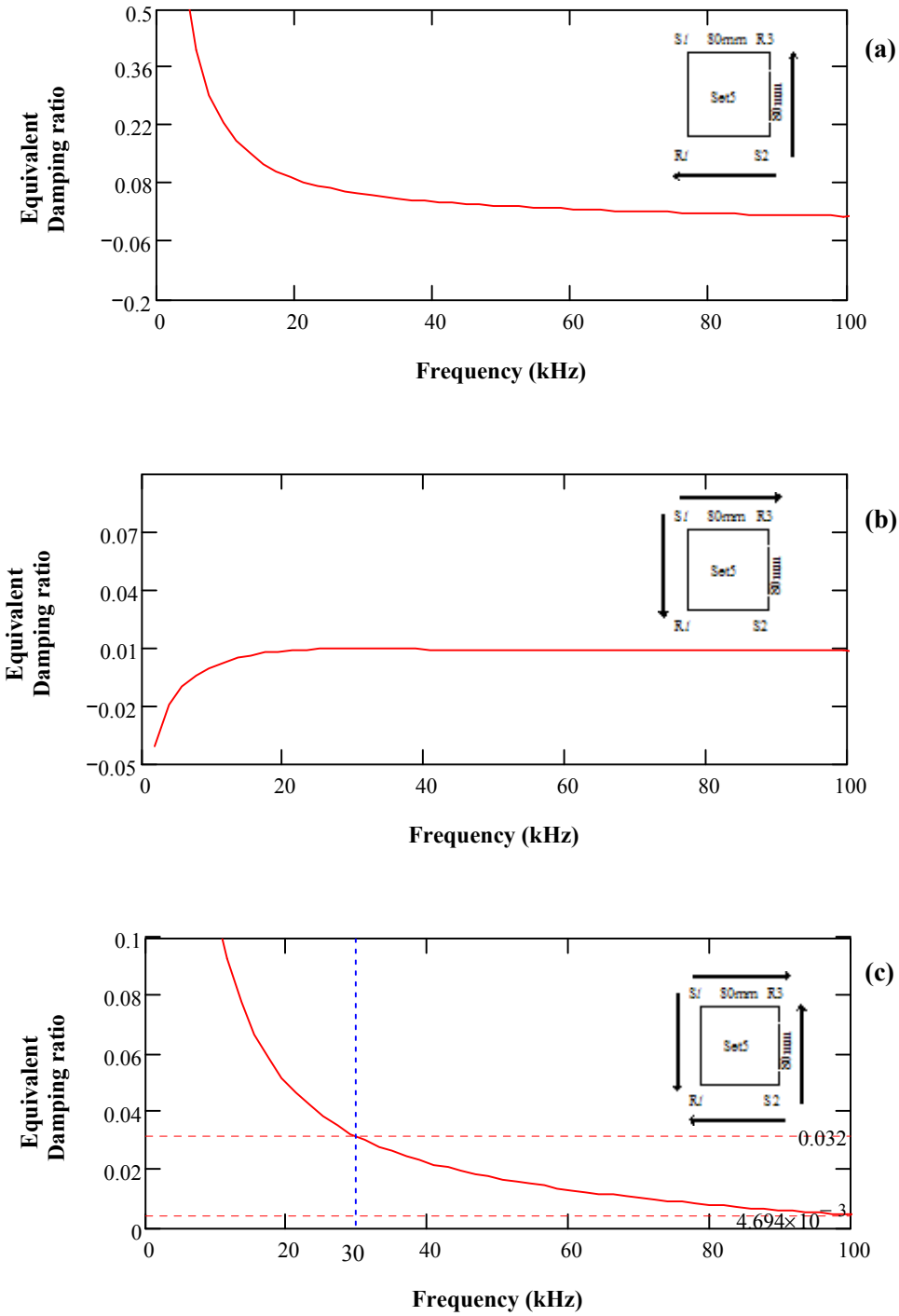

Figure M-19: Equivalent damping ratio (D) vs. frequency for R-waves for set 5 measurements on the joint-free surface – (a) D for Signal Pair 1 of set 5 (b) D for Signal Pair 2 of set 5 (c) D for entire set 5 measurements

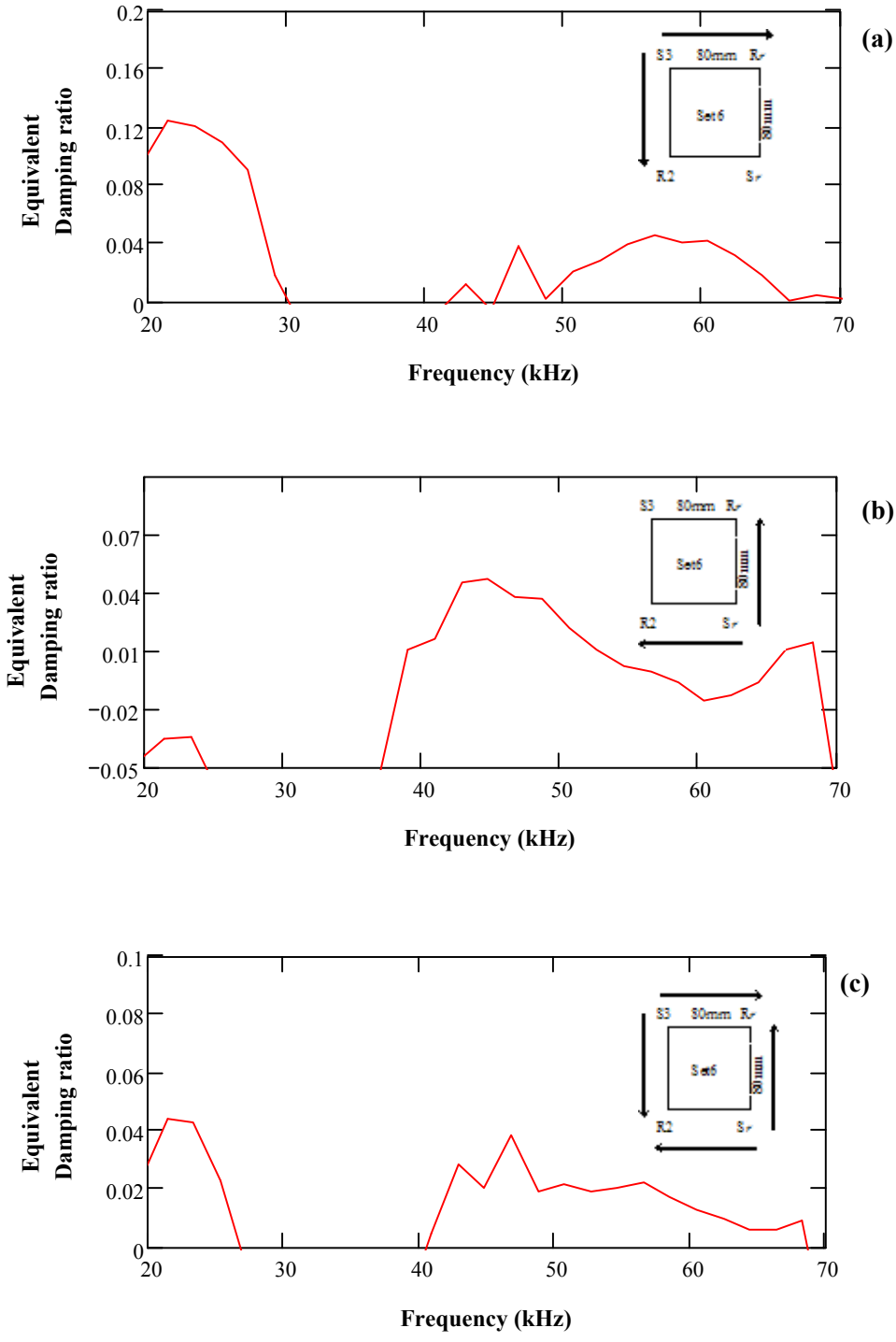

Figure M-20: Equivalent damping ratio (D) vs. frequency for full signals for set 6 measurements on the joint-free surface – (a) D for Signal Pair 1 of set 6 (b) D for Signal Pair 2 of set 6 (c) D for entire set 6 measurements

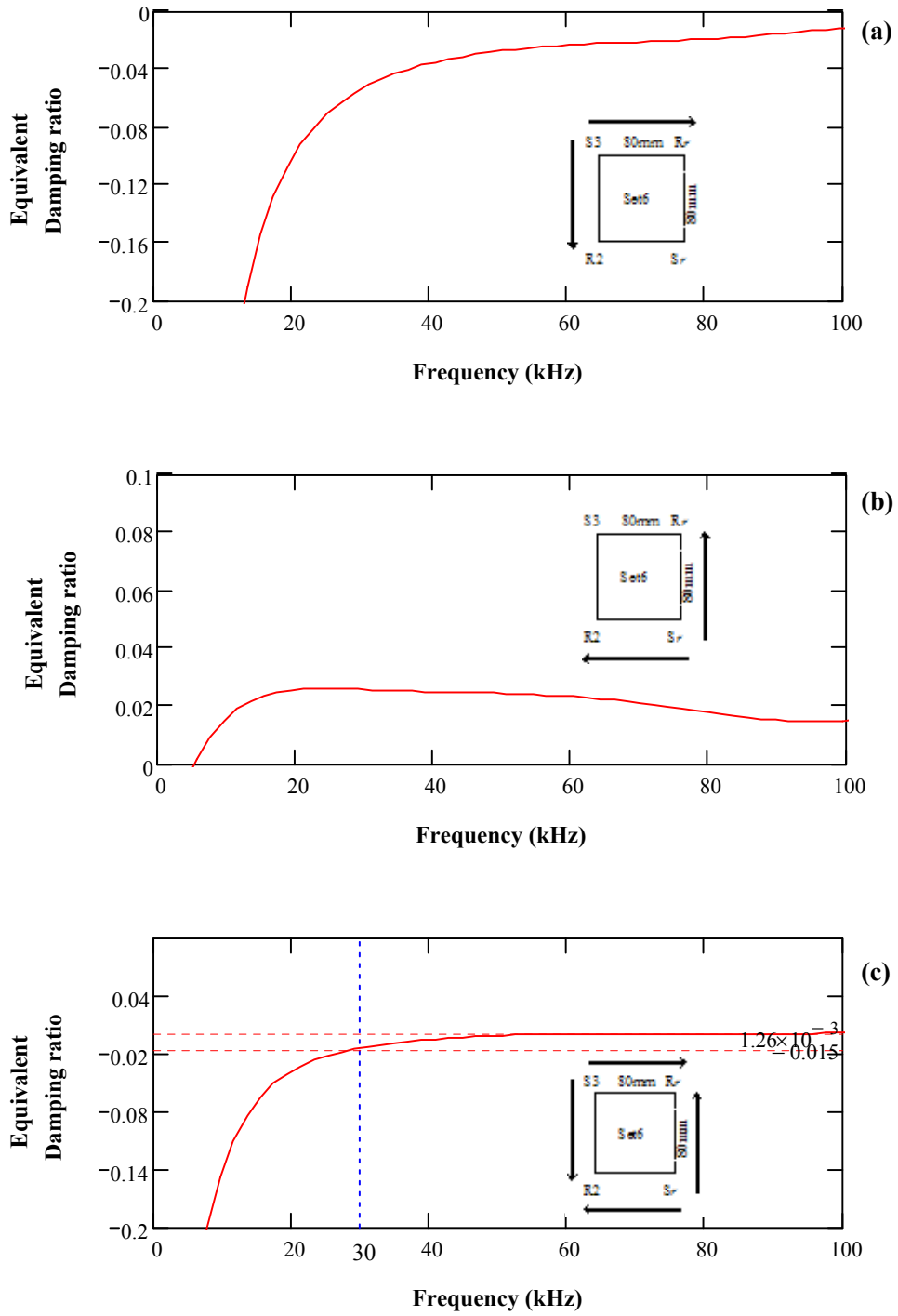

Figure M-21: Equivalent damping ratio (D) vs. frequency for P-waves for set 6 measurements on the joint-free surface – (a) D for Signal Pair 1 of set 6 (b) D for Signal Pair 2 of set 6 (c) D for entire set 6 measurements

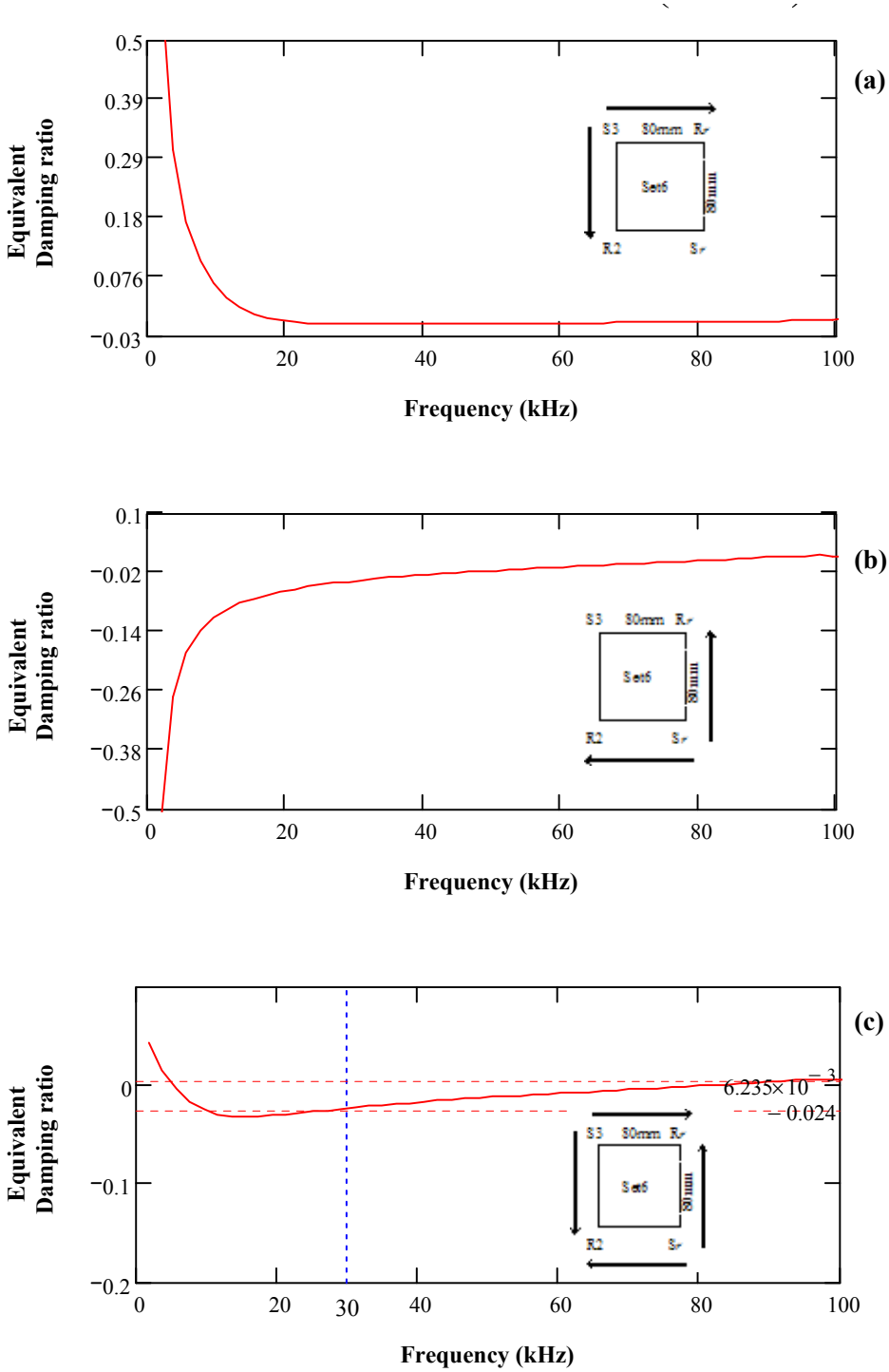

Figure M-22: Equivalent damping ratio (D) vs. frequency for R-waves for set 6 measurements on the joint-free surface – (a) D for Signal Pair 1 of set 6 (b) D for Signal Pair 2 of set 6 (c) D for entire set 6 measurements

Appendix N

Signal Processing for Slab 2 – Line X1 Y1

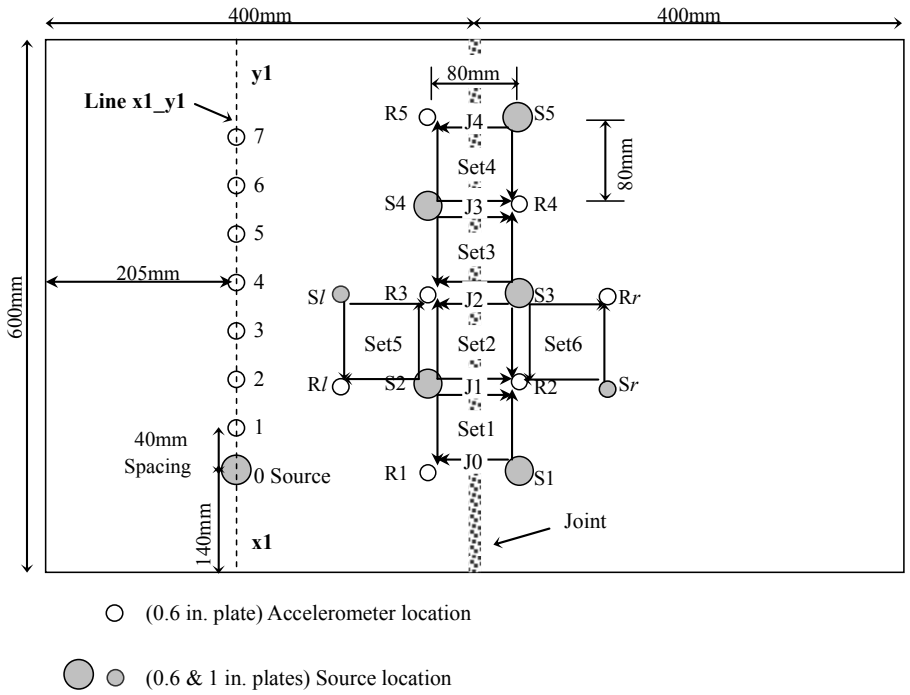

Figure N-1: Ultrasonic testing configuration of HMA slab 2

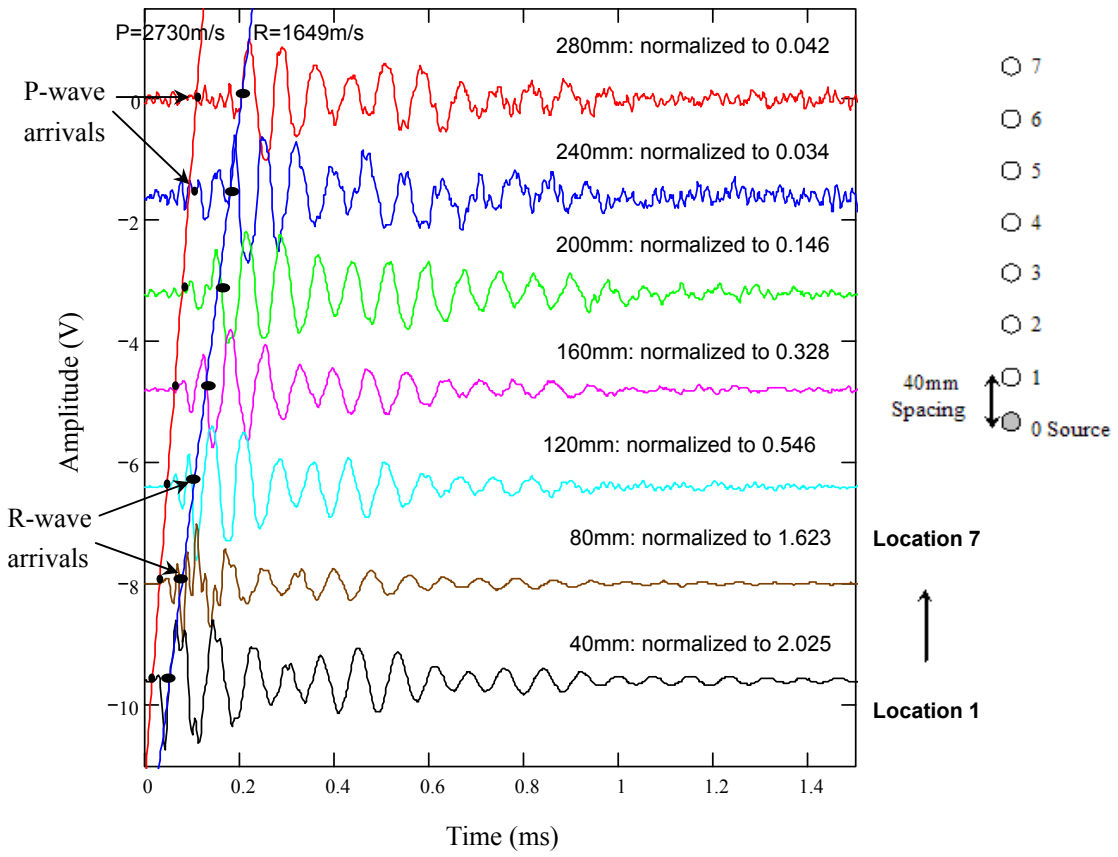

Figure N-2: Signals received using 100 kHz accelerometer along Line x1 y1

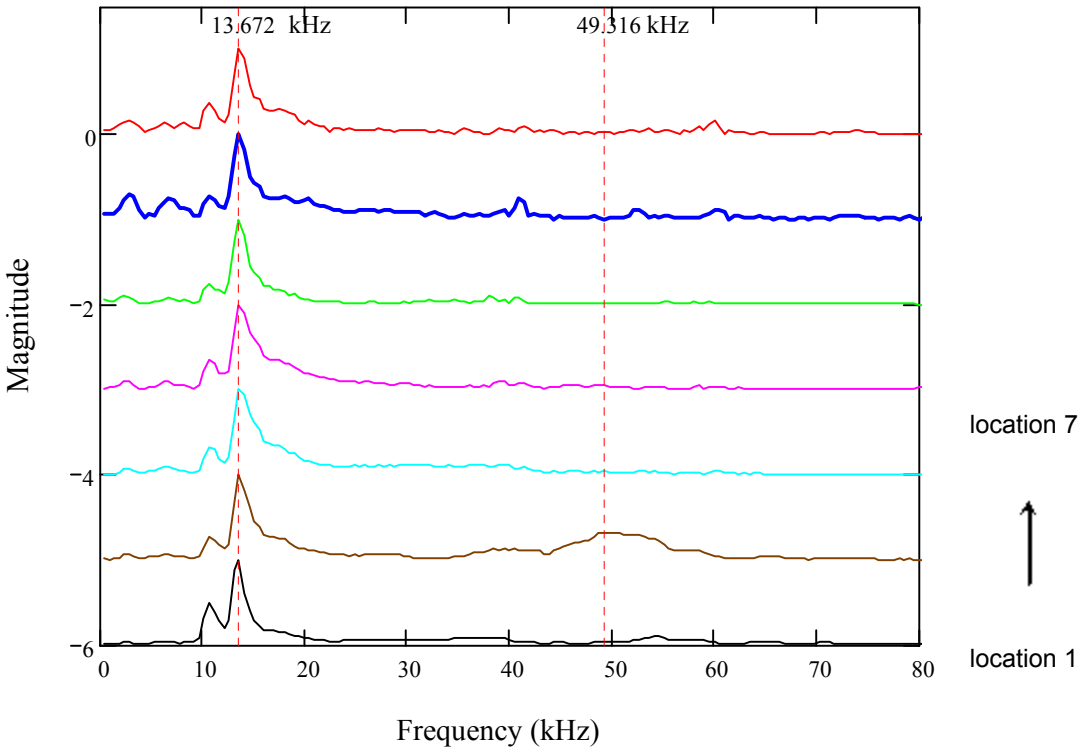

Figure N-3: Normalized **f**requency spectra of the signals received using 100 kHz accelerometer along Line x1 y1

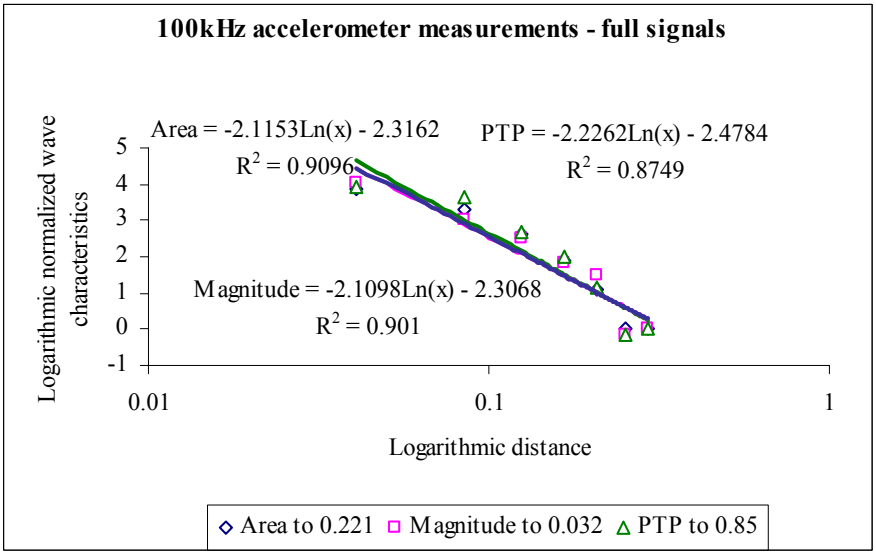

Figure N-4: Geometric attenuation evaluation based on full signals

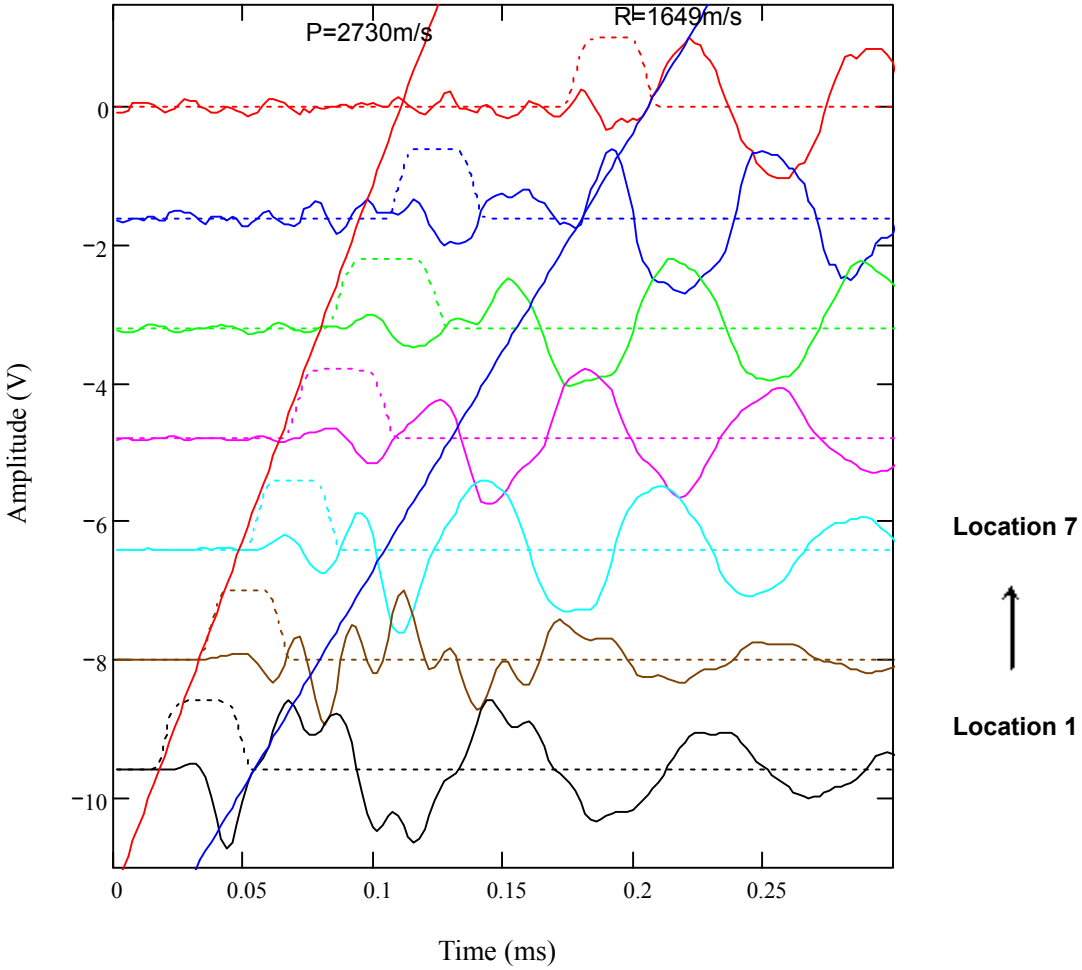

Figure N-5: Windowing P-waves of the signals received using 100 kHz accelerometer along Line x1 y1

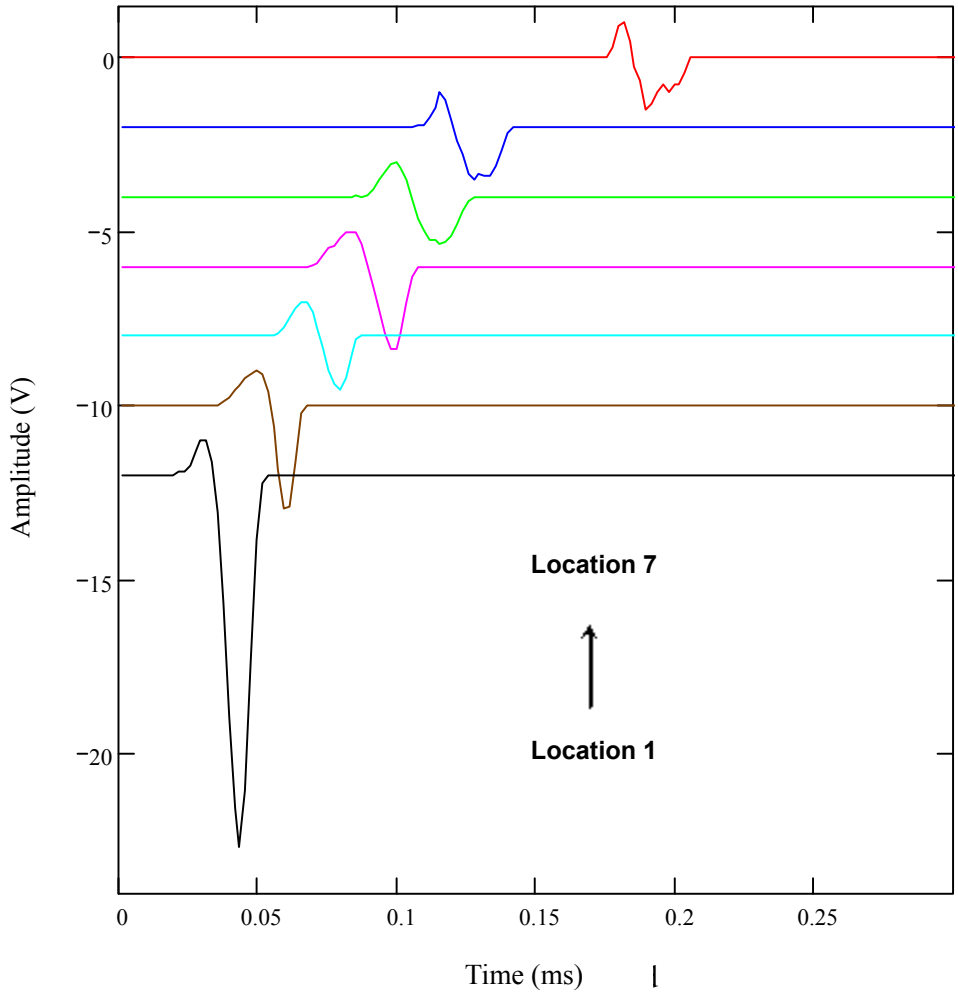

Figure N-6: Windowed P-wave portions of the signals received using 100 kHz accelerometer along Line x1 y1

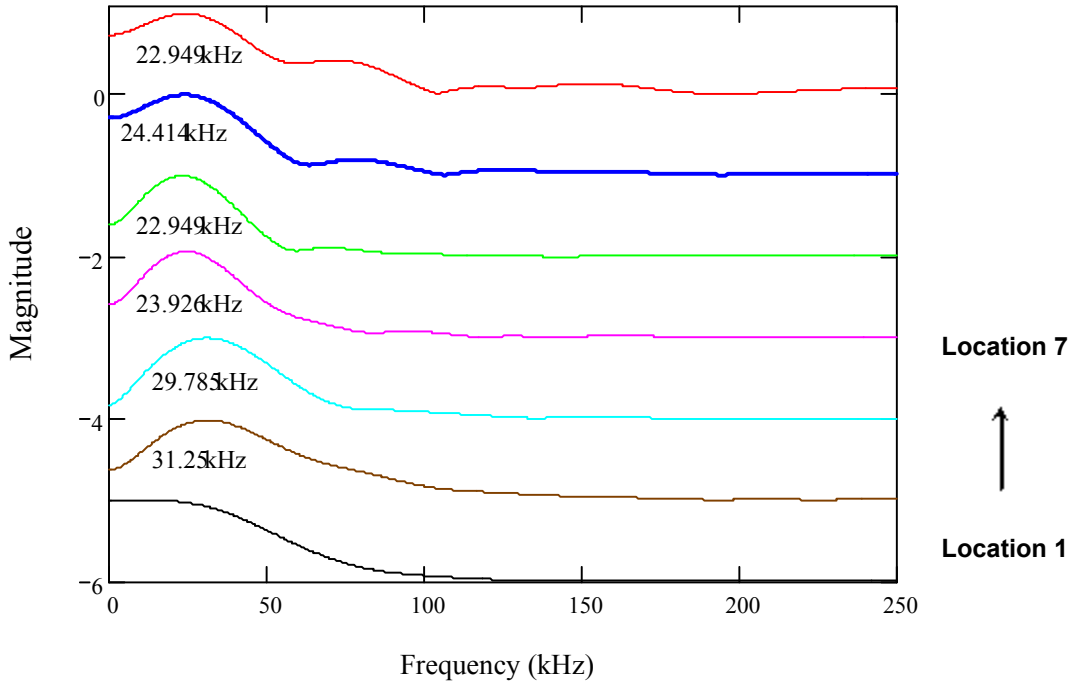

Figure N-7: Normalized frequency spectra of the windowed P-wave portions of the signals received using 100 kHz accelerometer along Line x1 y1

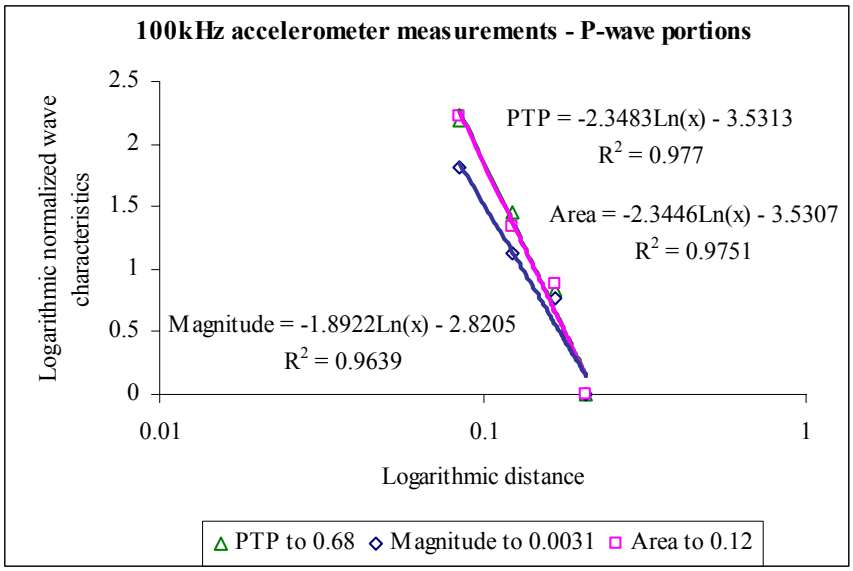

Figure N-8: Geometric attenuation evaluation based on P-waves.

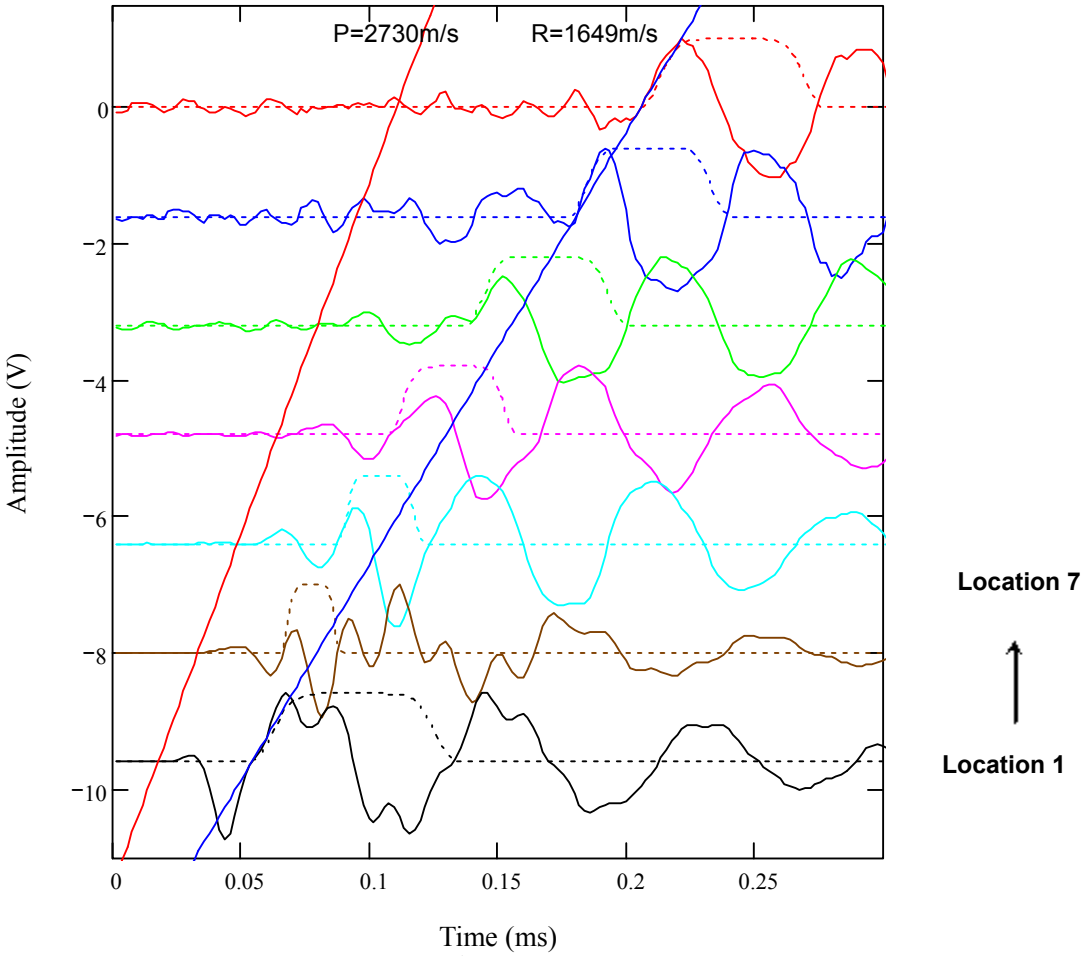

Figure N-9: Windowing R-waves of the signals received using 100 kHz accelerometer along Line x1 y1

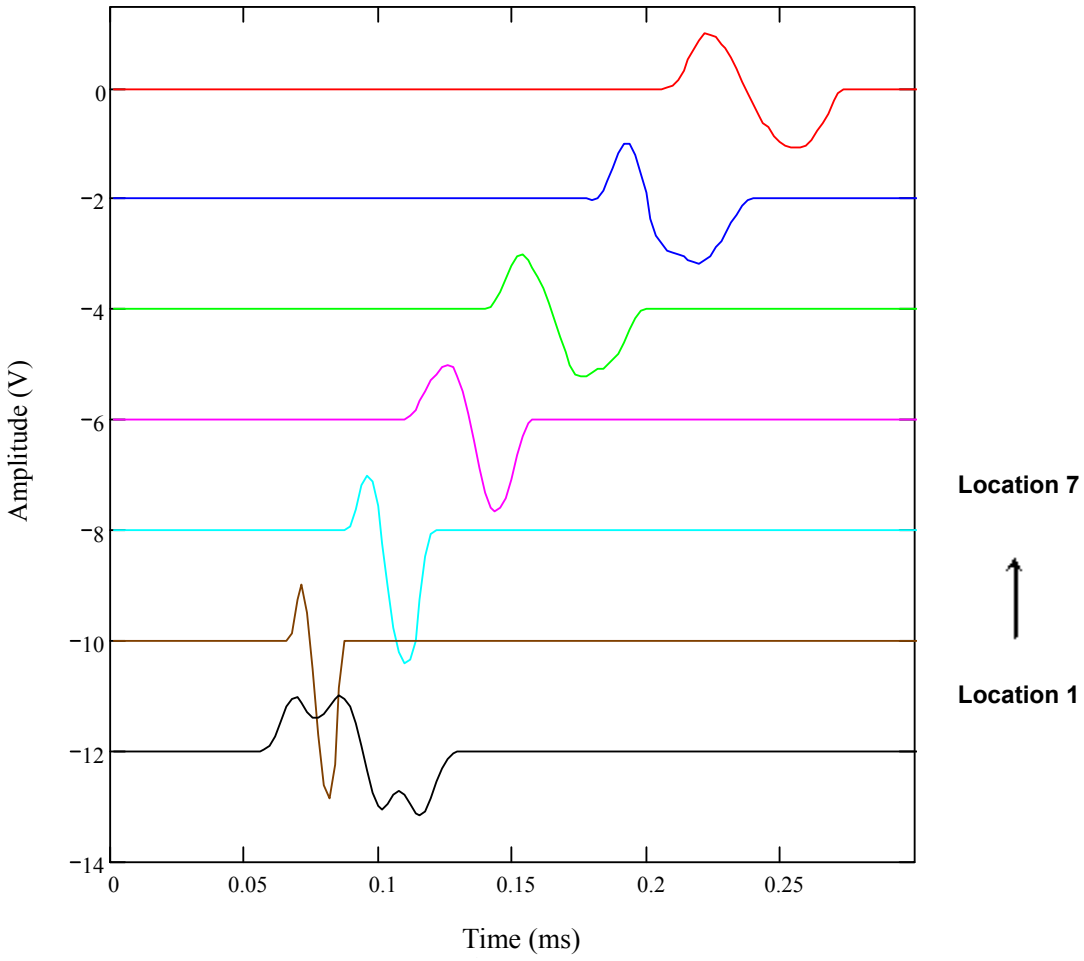

Figure N-10: Windowed R-waves of the signals received using 100 kHz accelerometer along Line x1 y1

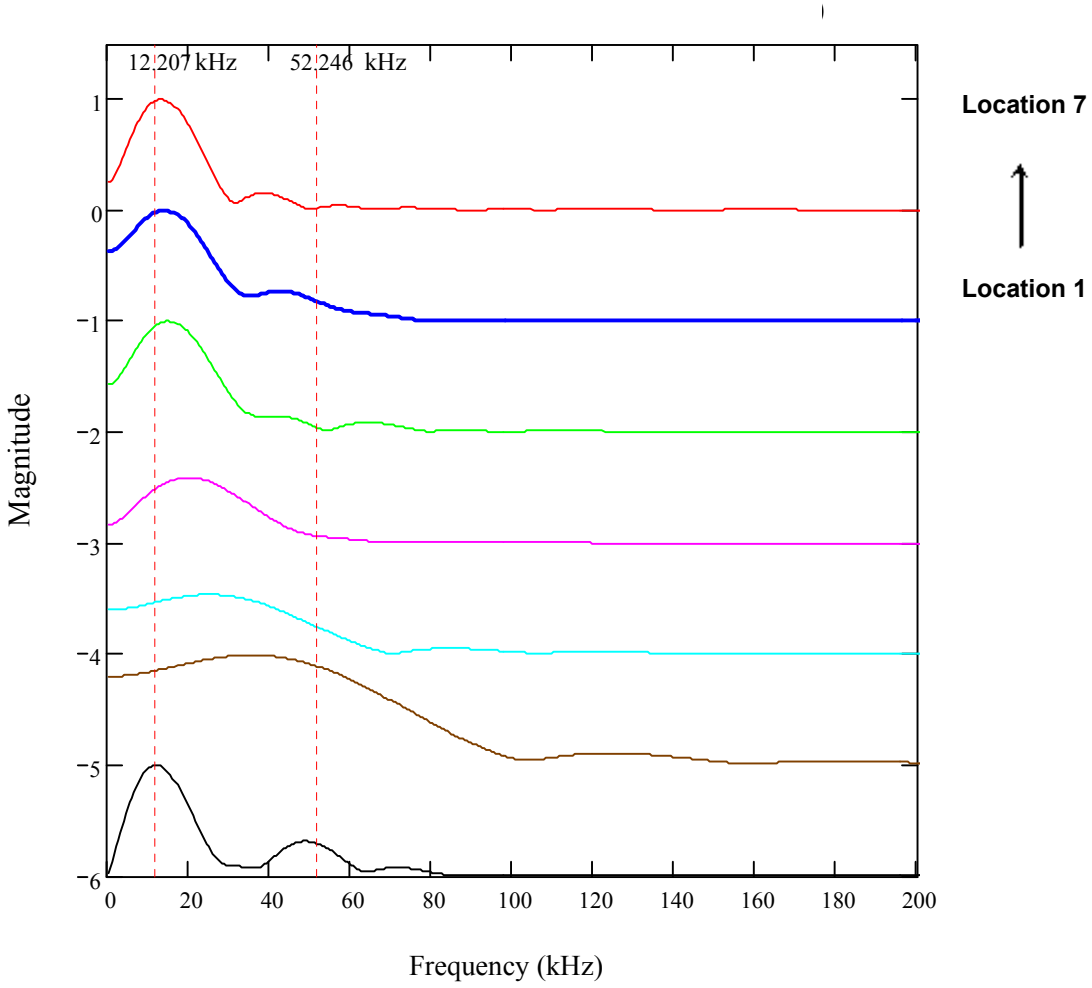

Figure N-11: Normalized **f**requency spectra of the windowed R-wave portions of the signals received using 100 kHz accelerometer along Line x1 y1

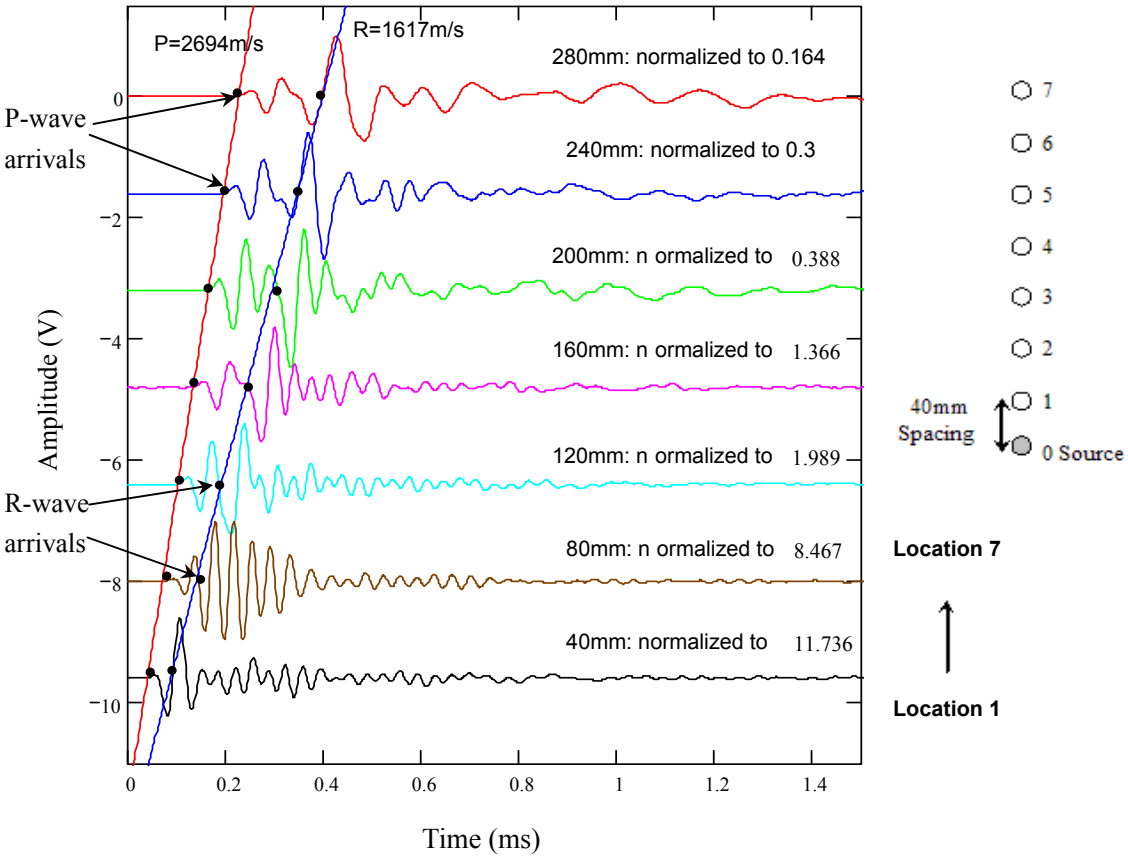

Figure N-12: Signals received using 50 kHz accelerometer along Line x1 y1

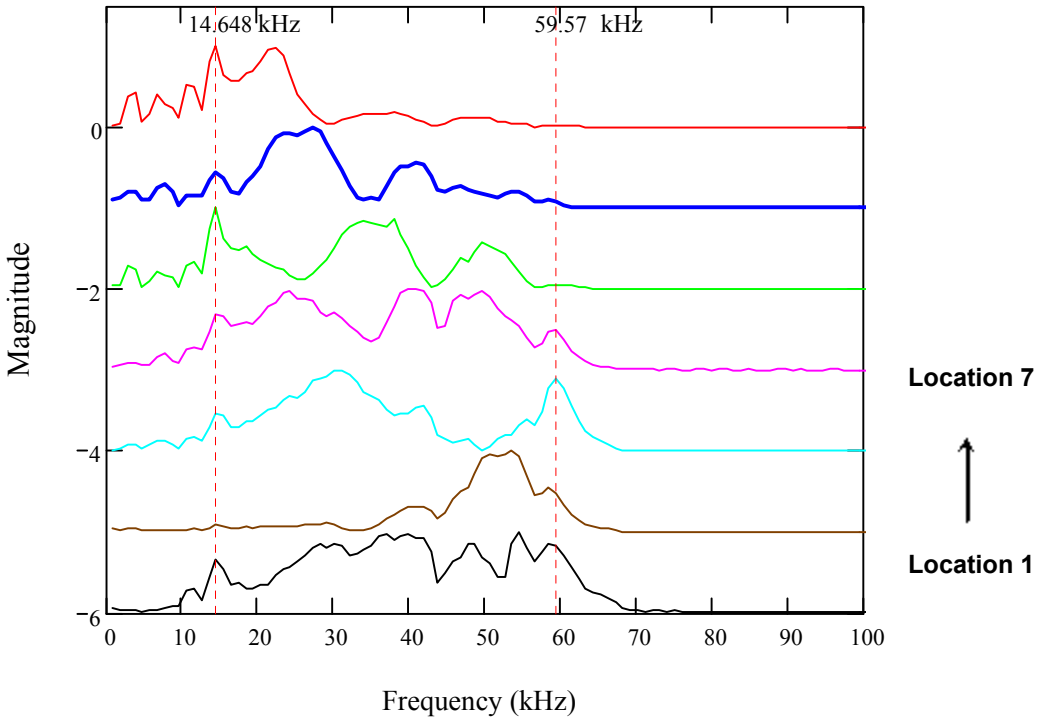

Figure N-13: Normalized frequency spectra of the signals received using 50 kHz accelerometer along Line x1 y1

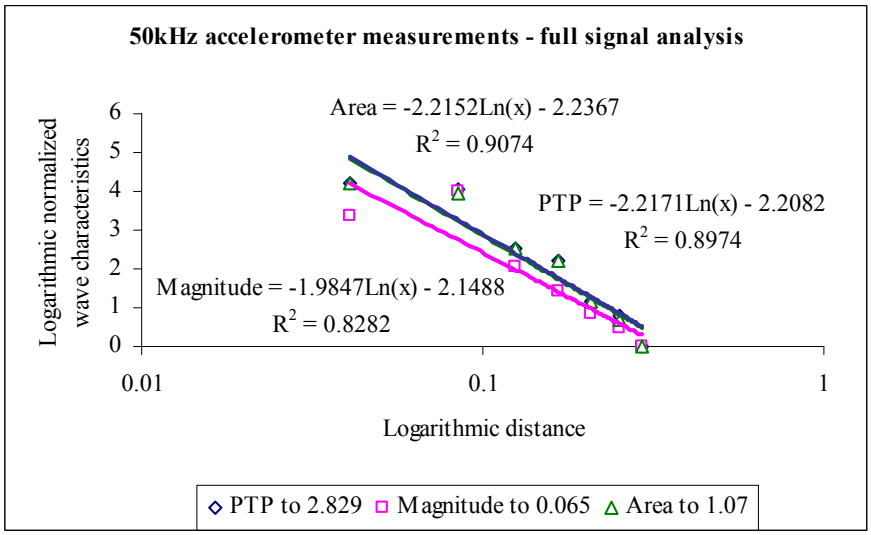

Figure N-14: Geometric attenuation evaluation based on full signals

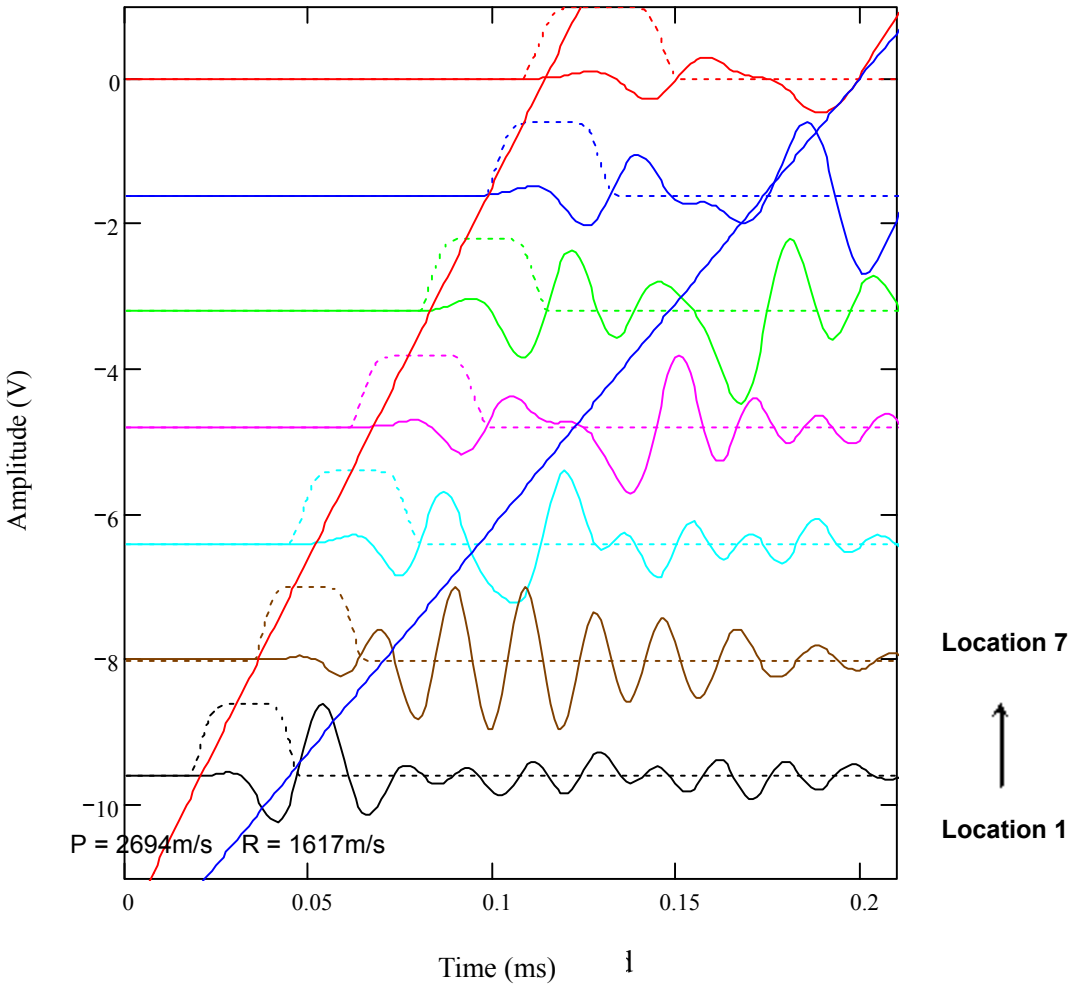

Figure N-15: Windowing P-waves of the signals received using 50 kHz accelerometer along Line x1 y1

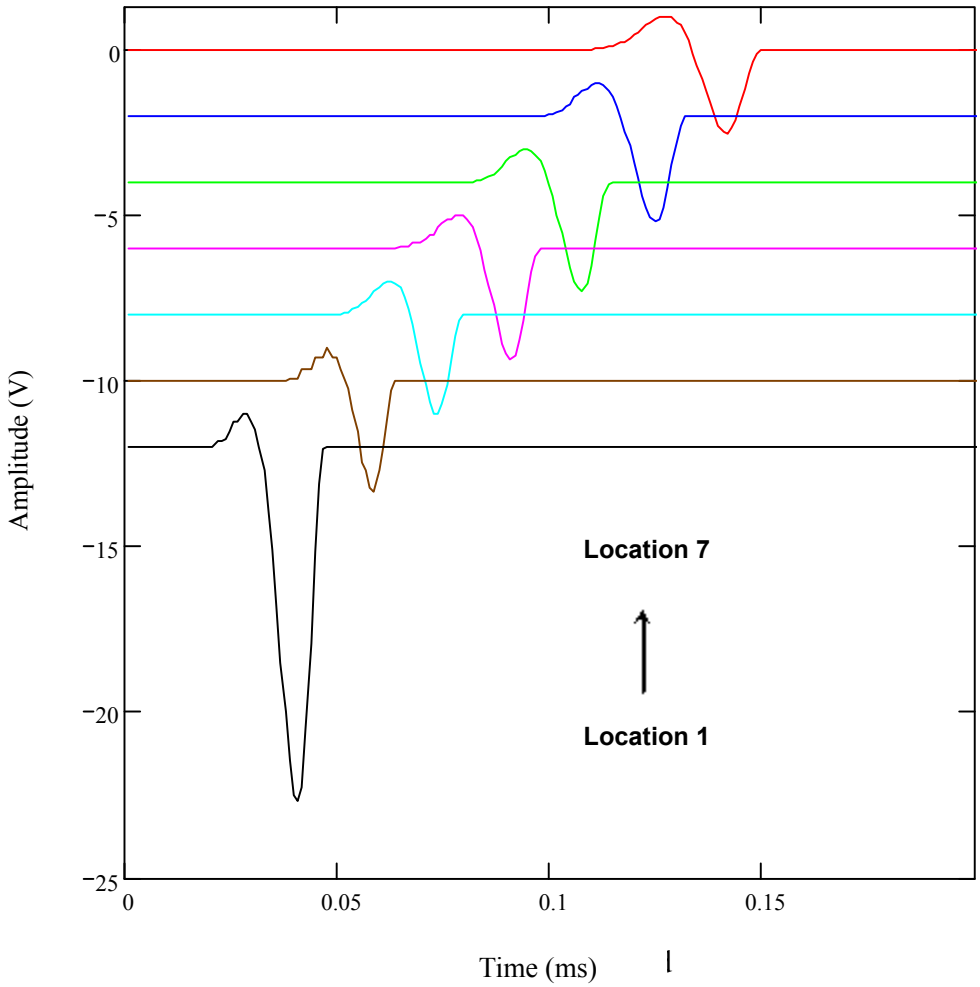

Figure N-16: Windowed P-waves of the signals received using 50 kHz accelerometer along Line x1 y1

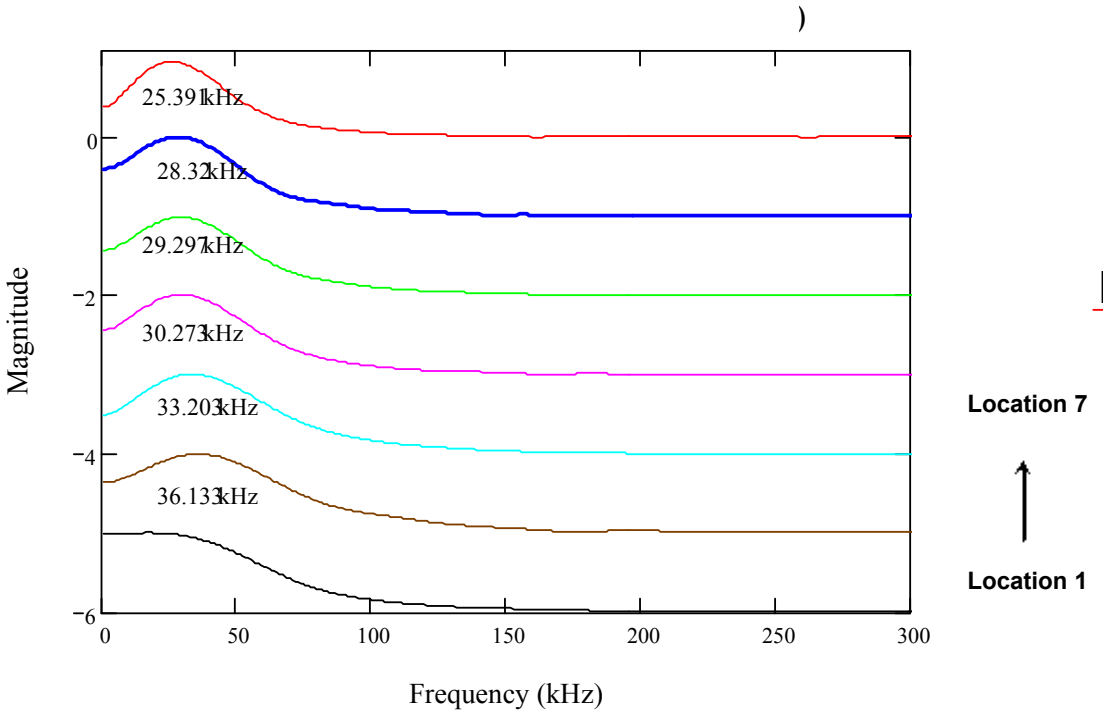

Figure N-17: Normalized frequency spectra of windowed P-waves of the signals received using 50 kHz accelerometer along Line x1 y1

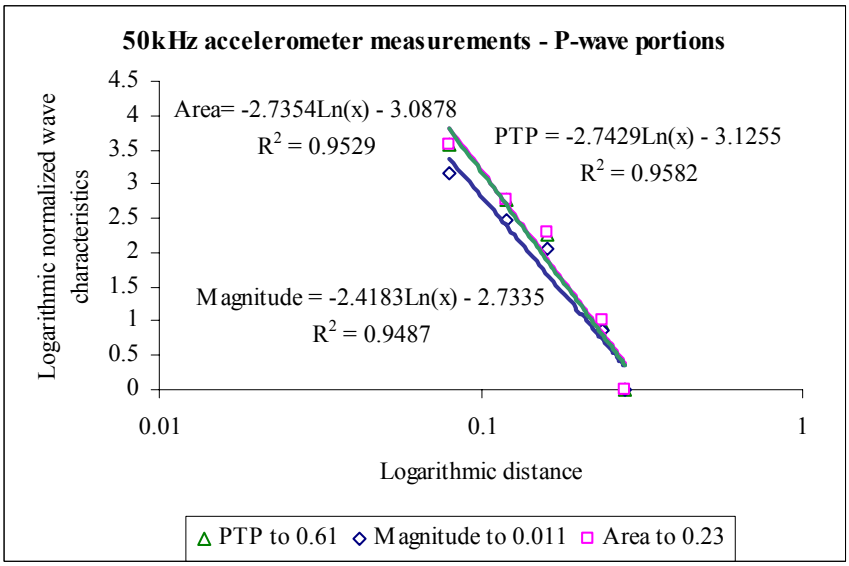

Figure N-18: Geometric attenuation evaluation based on P-waves

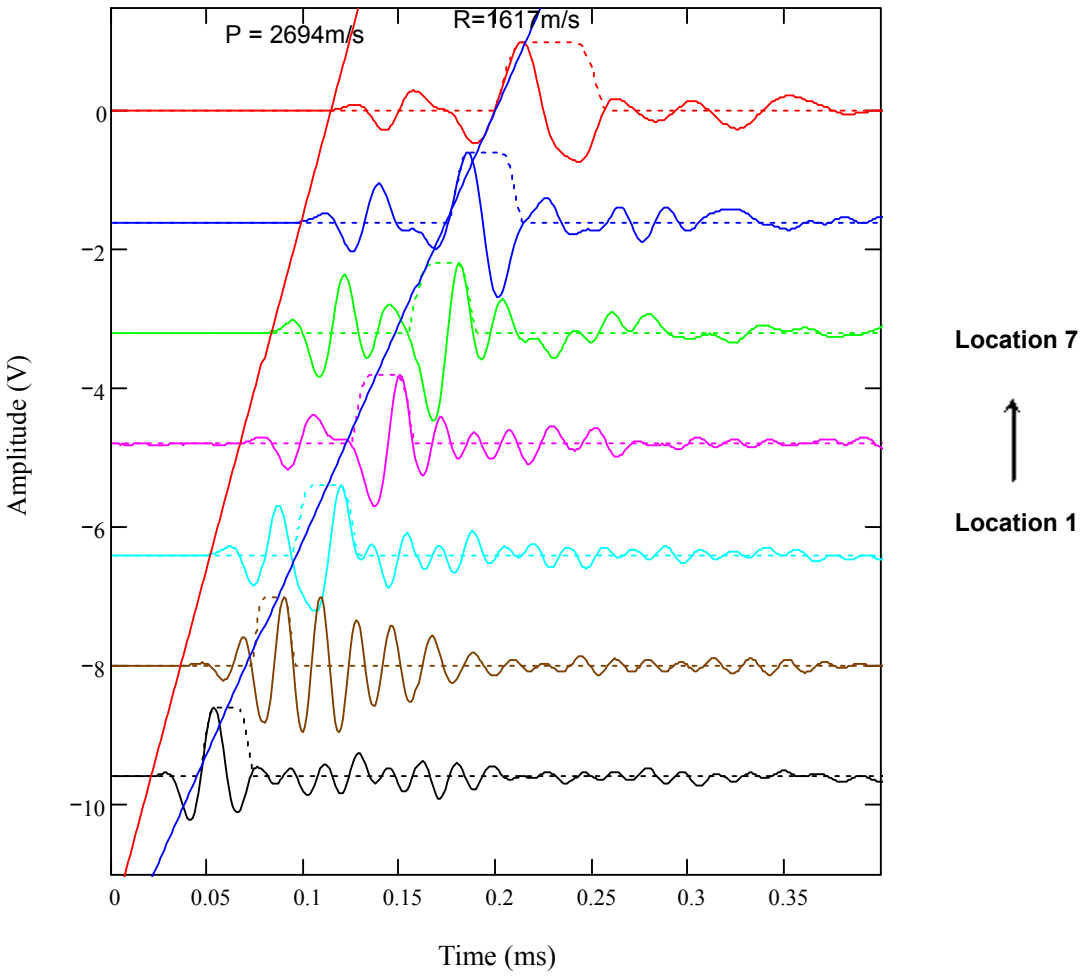

Figure N-19: Windowing R-waves of the signals received using 50 kHz accelerometer along Line x1 y1

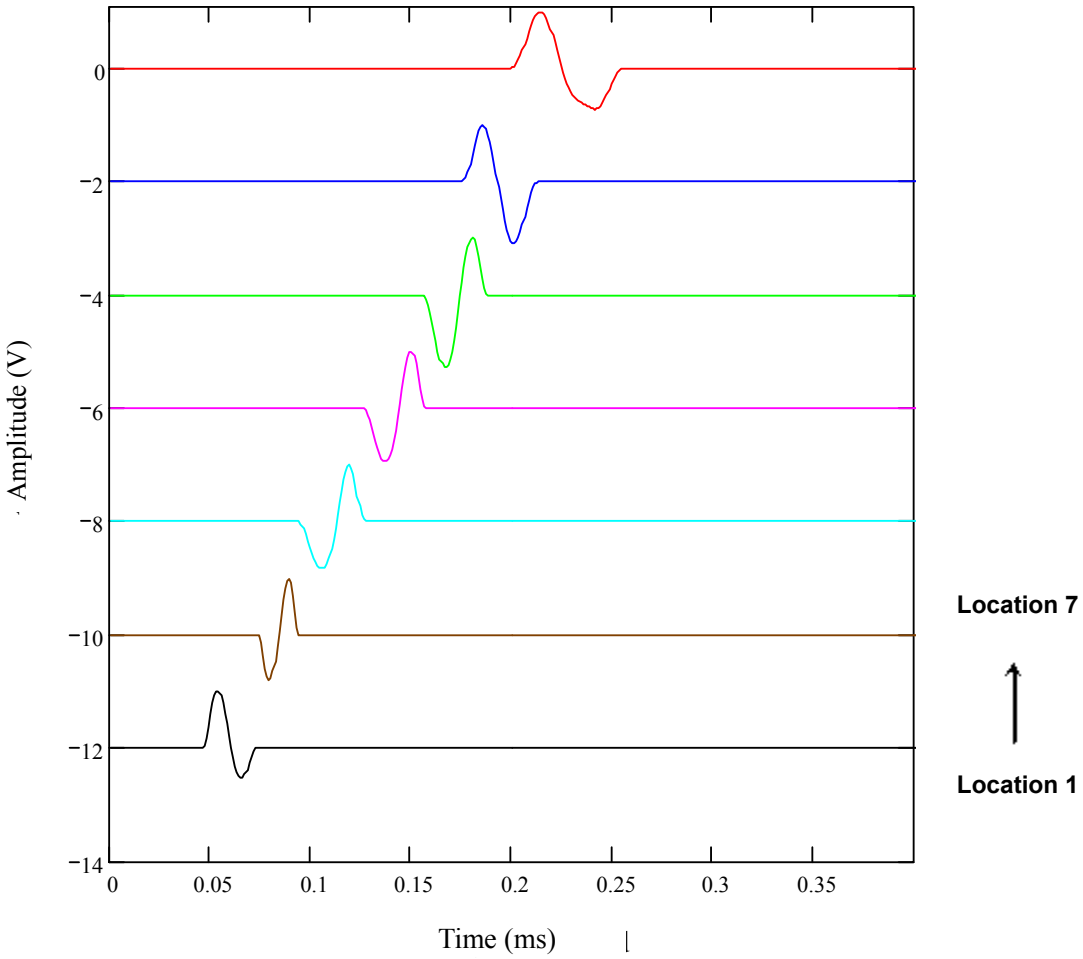

Figure N-20: Windowed R-waves of the signals received using 50 kHz accelerometer along Line x1 y1

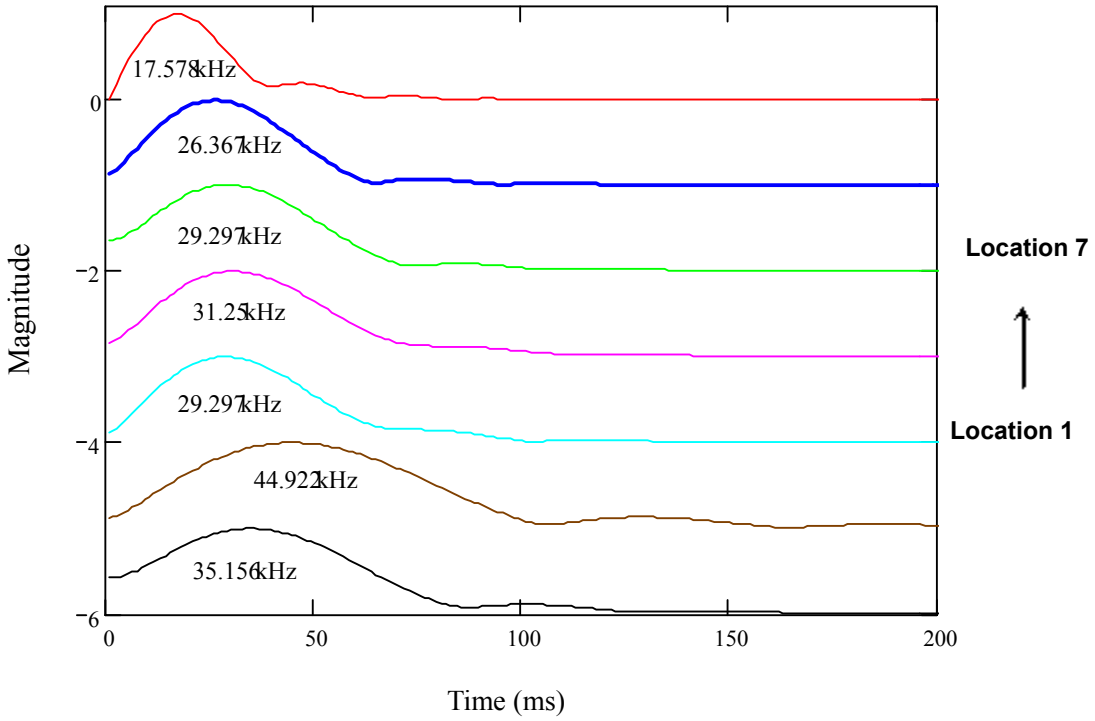

Figure N-21: Normalized frequency spectra of windowed R-waves of the signals received using 50 kHz accelerometer along Line x1 y1

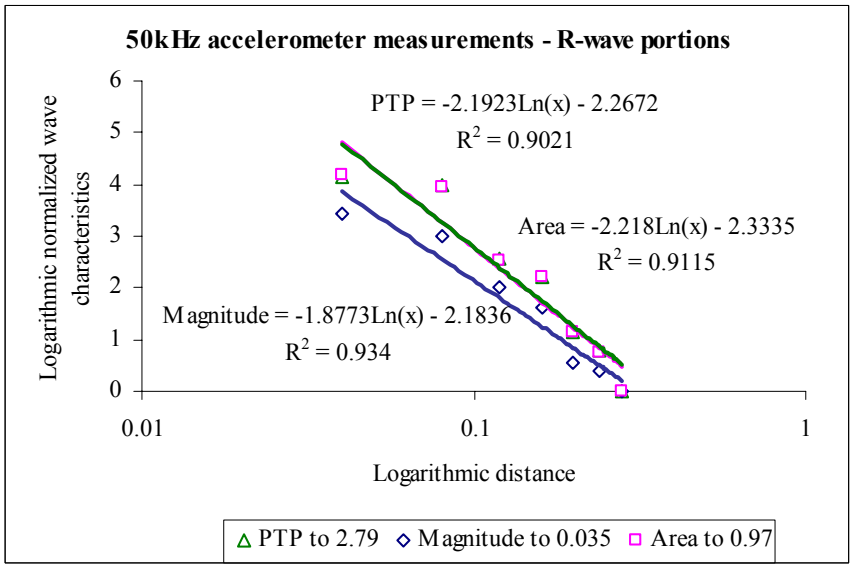

Figure N-22: Geometric attenuation evaluation based on R-waves

Appendix O

Signal Processing for Slab 2

- Measurements on the Jointed and the Joint-free Surfaces

This appendix is a PDF file available in the Appendix CD.

The file name of this PDF file is “Appendix O - Signal processing for jointed and joint-free surfaces.pdf”.

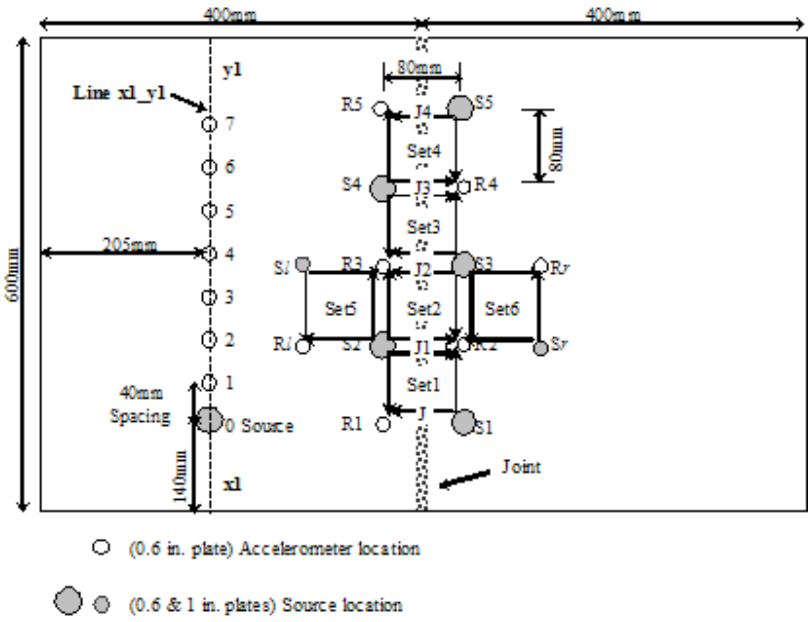

Figure O-1: Ultrasonic testing configuration of HMA slab 2

Measure Slab 2- using 50kHz P-Wave Transducer as the and 50kHz accelerometer as the reveiver:

Pulse receiver and filter parameter setting					
Pulse receiver setting:	Pundit	**Filter setting:**	20db input		
			0db output		
			100kHz cutoff frequency		
		Transducers setting:	Transmitter: Resonant frequency = 50kHz		
			Accelerometer (PCB353B65): Resonant frequency = 50kHz		

Oscilloscope setting: **Sampling Rate Δt:** $\frac{100\mu s}{100}$ **1000 Points in Total**

Index $N := 2^{10}$ $i := 1 .. N$ $u := 1 .. \frac{N}{2}$ $ORIGIN \equiv 1$ $f_u := \frac{u}{N \cdot 1 \cdot 10^{-3}}$

all :=

Reading data $J := 1 .. 13$ $avg_J := mean\left(all^{\langle J \rangle}\right)$ $signal^{\langle J \rangle} := all^{\langle J \rangle} - avg_J$

Definition of full signals for the measurements on jointed

Set 1 $S2\_R2 := signal^{\langle 1 \rangle}$ $S2\_R1 := signal^{\langle 2 \rangle}$ Set 2 $S2\_R3 := signal^{\langle 5 \rangle}$

$S1\_R2 := signal^{\langle 3 \rangle}$ $S1\_R1 := signal^{\langle 4 \rangle}$ $S3\_R3 := signal^{\langle 7 \rangle}$

Set 3 $S4\_R4 := signal^{\langle 8 \rangle}$ $S4\_R3 := signal^{\langle 9 \rangle}$ Set 4 $S4\_R5 := signal^{\langle 11 \rangle}$

$S3\_R4 := signal^{\langle 10 \rangle}$ $S5\_R5 := signal^{\langle 13 \rangle}$

Analysis of set 1 - the full time signals:

Parameter $p := 1 .. 4$ $\omega o_p := 2\pi \cdot 0.55$ **Arrival Time (AT) of the signal:**

$tp := ceil\left(\left(\frac{AT}{0.001}\right)\right) \cdot 0.001$

$$wp(t, \omega o) := \begin{cases} 10\left|\cos(\omega o \cdot t)^{5000} - 1\right| & \text{if } 0 \le t \le \frac{\pi}{\omega o} \\ 0 & \text{otherwise} \end{cases}$$

Define **Time Window** (Twind) to amplify the arrival of the signals:

$$\text{Twind} := \left| \begin{array}{l} \text{for } p \in 1..4 \\ \quad \text{for } i \in 1..N \\ \quad\quad \text{ampl}_{i,p} \leftarrow \text{wp}\left(i \cdot 0.001 - \text{tp}, \omega o_p\right) \\ \text{ampl} \end{array} \right.$$

Fourier Transform of the Windowed Signals: $\text{FTW}^{\langle p \rangle} := \text{CFFT}\left(\overrightarrow{\left(\text{Twind}^{\langle p \rangle} \cdot \text{signal}^{\langle p \rangle}\right)}\right)$

Windowed Signals: $P_{i,p} := \text{Twind}_{i,p} \cdot \text{signal}_{i,p}$

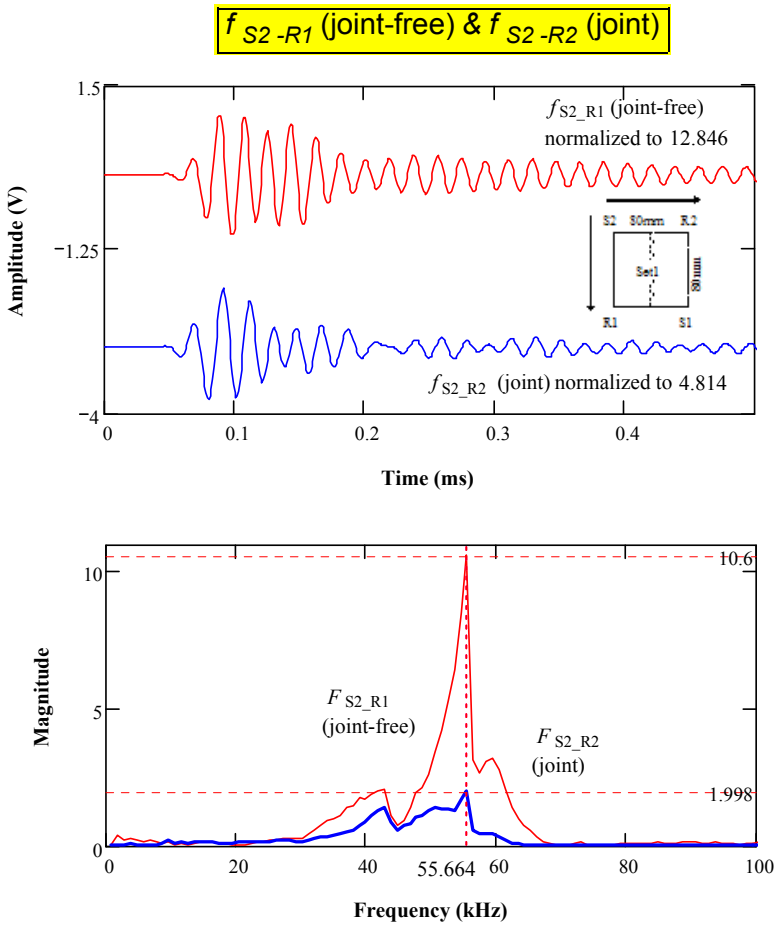

PTP ratio: $\dfrac{\text{Joint}}{\text{No} - \text{Joint}} \qquad \dfrac{\max\left(P^{\langle 1 \rangle}\right) - \min\left(P^{\langle 1 \rangle}\right)}{\max\left(P^{\langle 2 \rangle}\right) - \min\left(P^{\langle 2 \rangle}\right)} = 0.351$

$f_{S1\text{-}R2}$ (joint-free) & $f_{S1\text{-}R1}$ (joint)

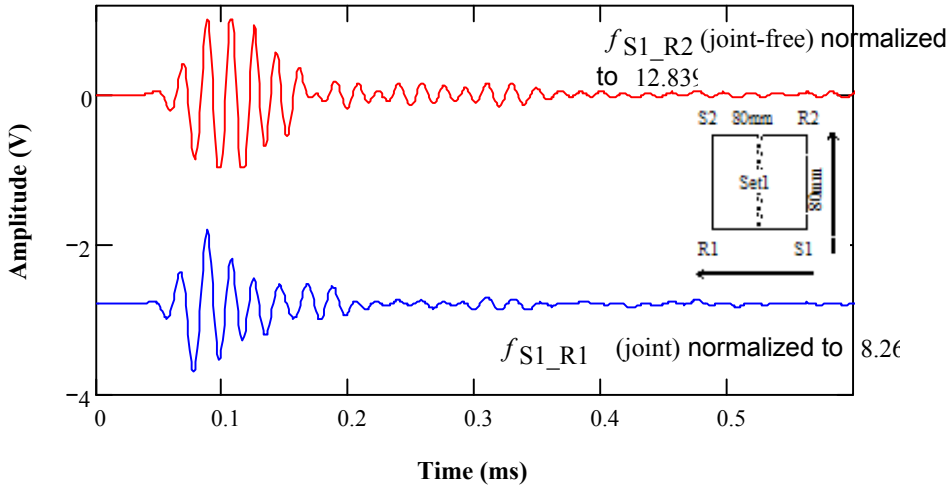

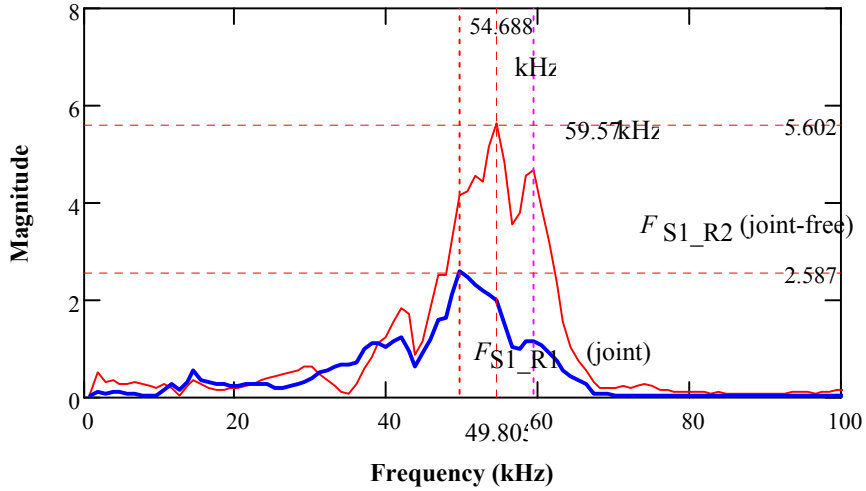

PTP ratio: $\frac{\text{Joint}}{\text{No} - \text{Joint}}$ $\frac{\max\left(P^{\langle 4\rangle}\right) - \min\left(P^{\langle 4\rangle}\right)}{\max\left(P^{\langle 3\rangle}\right) - \min\left(P^{\langle 3\rangle}\right)} = 0.62$

Transmission Coefficient (TC) =

$$TC_u := \sqrt{\frac{|FTW_{u,1}| \cdot |FTW_{u,4}|}{|FTW_{u,2}| \cdot |FTW_{u,3}|}}$$

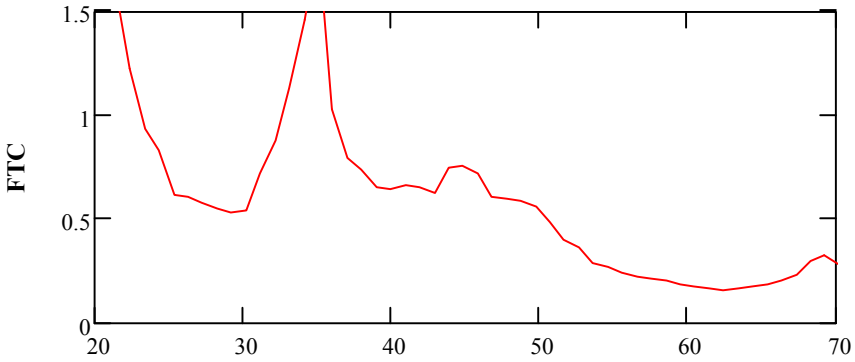

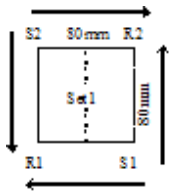

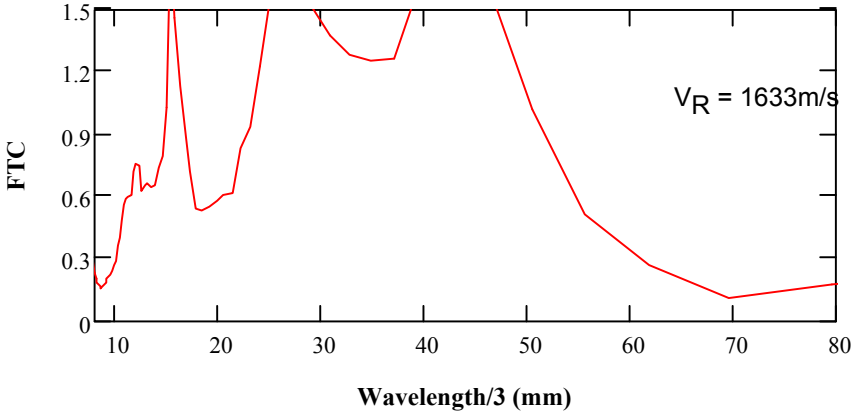

Damping ratio @ 55kHz

fre := 55

$f_{S2\text{-}R1}$ (joint-free) & $f_{S2\text{-}R2}$ (joint)

$$\left(\frac{2\pi fre \cdot 82}{1.617\times 10^3}\right)^{-1} \cdot \ln(MM1) = 0.095$$

$f_{S1\text{-}R2}$ (joint-free) & $f_{S1\text{-}R1}$ (joint)

$$\left(\frac{2\pi fre \cdot 82}{1.617\times 10^3}\right)^{-1} \cdot \ln(MM2) = 0.045$$

For the Set 1

$$\left(\frac{2\pi fre \cdot 82}{1.617\times 10^3}\right)^{-1} \cdot \ln\left(\sqrt{MM2 \cdot MM1}\right) = 0.07$$

Damping analysis for full signals:

$$\Delta\Phi 1_u := \left(\frac{2\pi f_u \cdot 82}{1.617 \times 10^3} \right)^{-1}$$

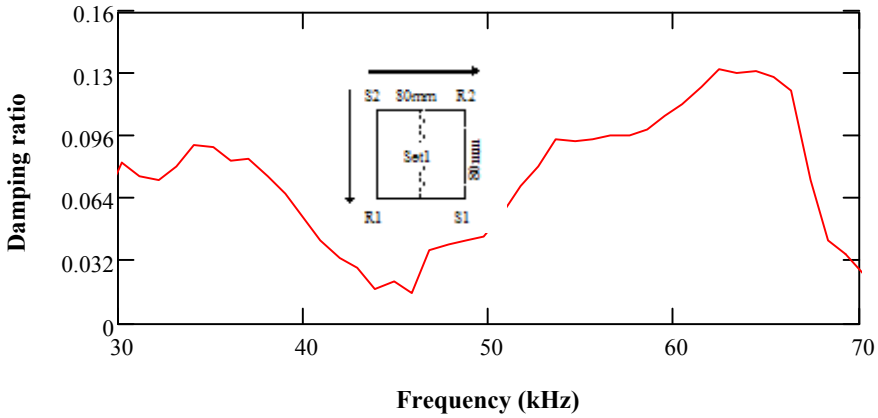

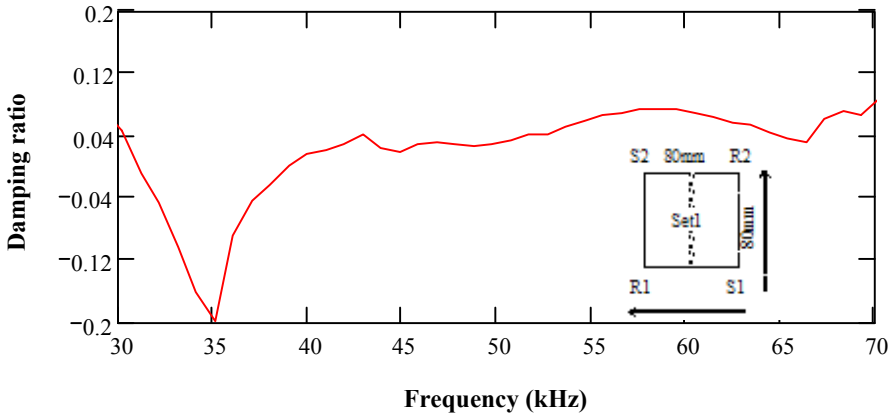

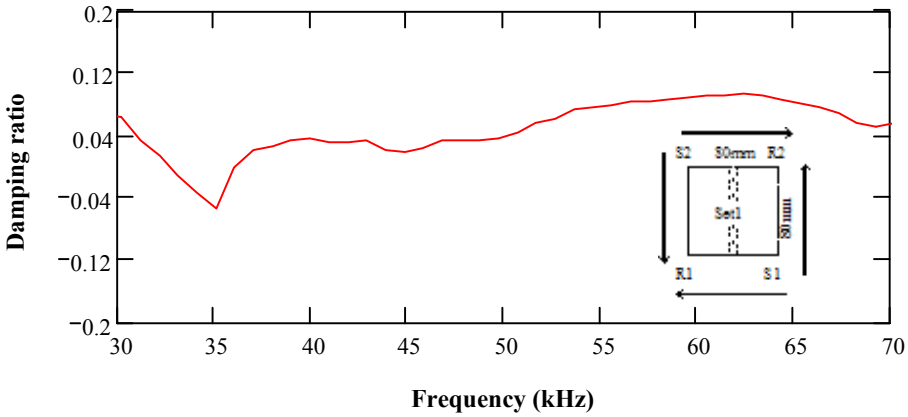

Damping analysis for full signals - using spectrum area:

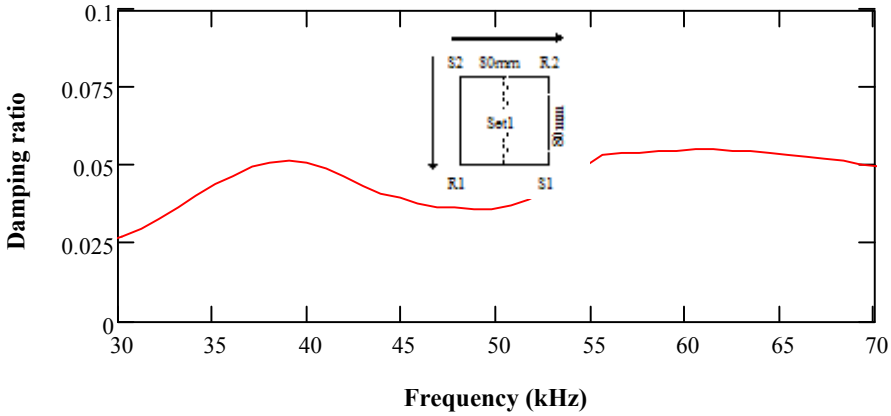

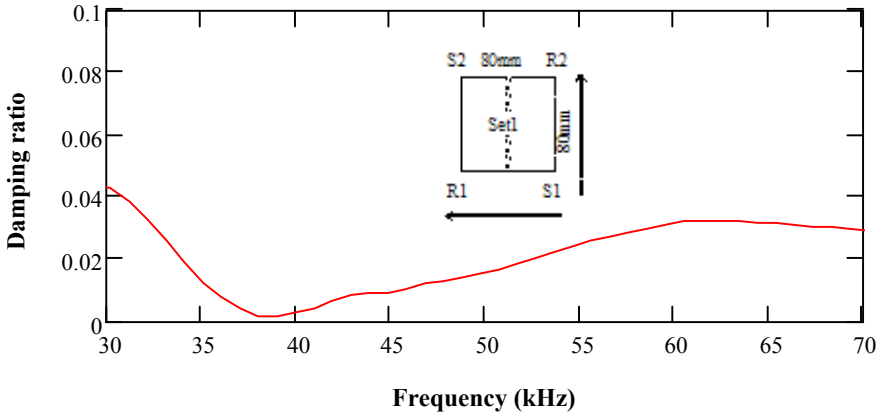

Window the P-wave of the time signals - window 1:

Parameter $p := 1 .. 4$ $\omega o_p := 2\pi \cdot 17$

$\omega o_2 := 2\pi \cdot 17.5$ $\omega o_3 := 2\pi \cdot 17$ $\omega o_4 := 2\pi \cdot 18.5$

Arrival Time (AT) of the signal: $AT := 0.035$

$$tp_p := ceil\left(\left(\frac{AT}{0.001}\right)\right) \cdot 0.001$$

$$wp(t, \omega o) := \begin{cases} 10\left|\cos(\omega o \cdot t)^{10} - 1\right| & \text{if } 0 \le t \le \frac{\pi}{\omega o} \\ 0 & \text{otherwise} \end{cases}$$

Define **Time Window** (Twind) to amplify the arrival of the signals:

$$Twind := \left| \begin{array}{l} \text{for } p \in 1 .. 4 \\ \quad \text{for } i \in 1 .. N \\ \quad\quad ampl_{i,p} \leftarrow wp\left(i \cdot 0.001 - tp_p, \omega o_p\right) \\ ampl \end{array} \right.$$

Fourier Transform of the Windowed Signals: $FTW^{\langle p \rangle} := CFFT\left(\overrightarrow{\left(Twind^{\langle p \rangle} \cdot signal^{\langle p \rangle}\right)}\right)$

Windowed Signals: $P_{i,p} := Twind_{i,p} \cdot signal_{i,p}$

Spectrum area: $$MA_{u,p} := \sum_{u=1}^{u} \frac{\left|FTW_{u,p}\right|}{N \cdot 0.001}$$

$f_{S2\text{-}R1}$ (joint-free) & $f_{S2\text{-}R2}$ (joint)

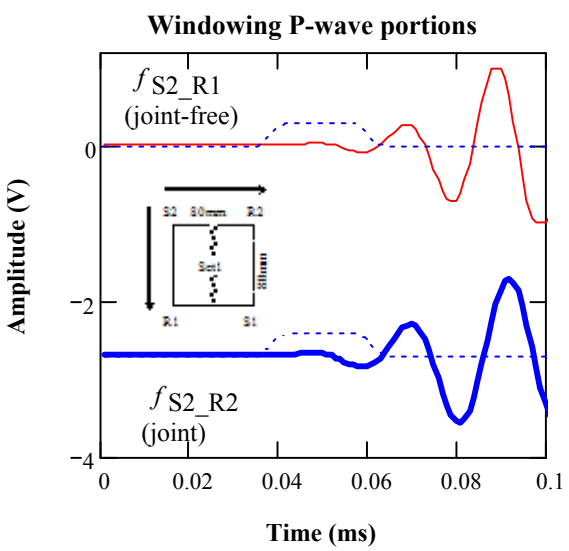

$f_{S1\text{-}R2}$ (joint-free) & f_{S1}

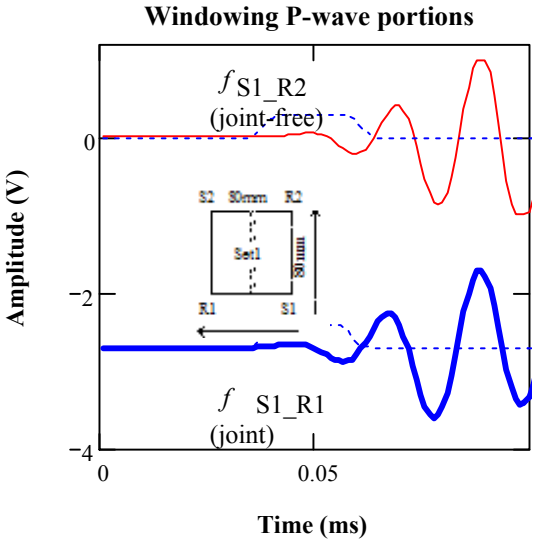

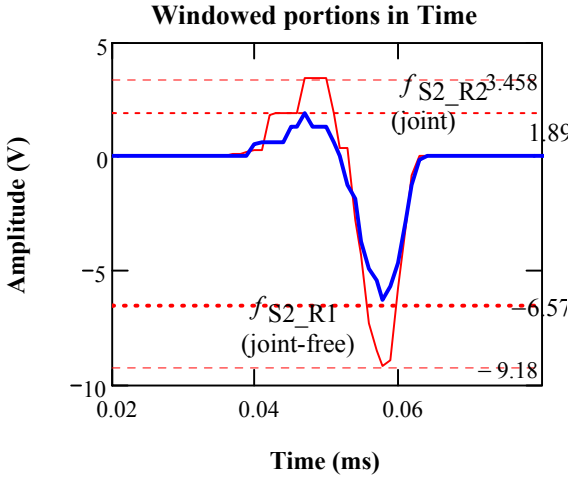

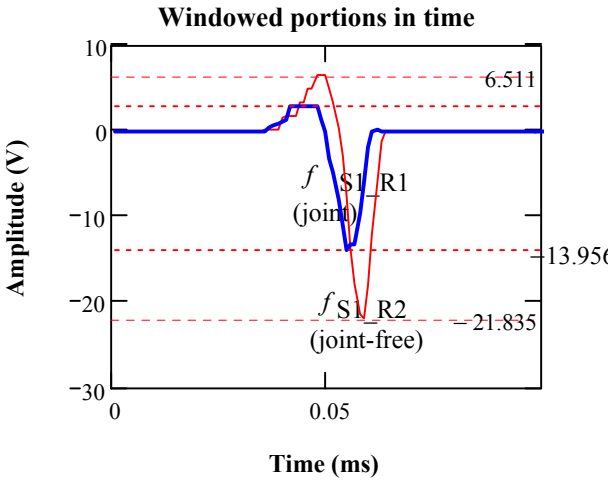

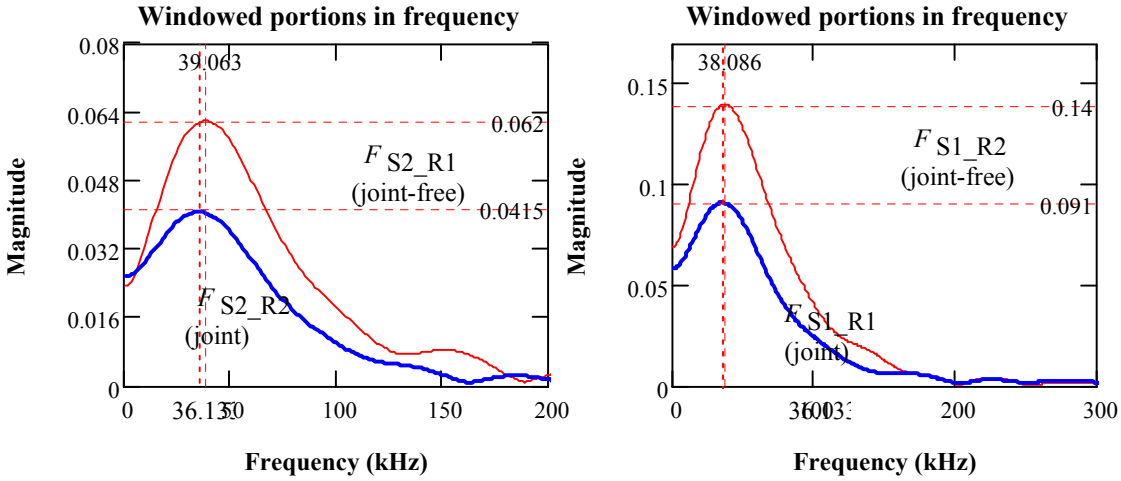

PTP ratio: $\frac{\text{Joint}}{\text{No}-\text{Joint}}$ $\frac{\max\left(P^{\langle 1\rangle}\right)-\min\left(P^{\langle 1\rangle}\right)}{\max\left(P^{\langle 2\rangle}\right)-\min\left(P^{\langle 2\rangle}\right)}=0.65$ $\frac{\max\left(P^{\langle 4\rangle}\right)-\min\left(P^{\langle 4\rangle}\right)}{\max\left(P^{\langle 3\rangle}\right)-\min\left(P^{\langle 3\rangle}\right)}=0.595$

Maximum Area in Frequency Domain for the Windowed Signal

$\frac{\text{Joint}}{\text{No}-\text{Joint}}$ $\frac{MA_{300,1}}{MA_{300,2}}=0.637$ $\frac{MA_{300,4}}{MA_{300,3}}=0.655$

Maximum Magnitude in Frequency Domain (MM):

$\frac{\text{Joint}}{\text{No}-\text{Joint}}$ $MM1:=\frac{0.062}{0.041}$ $\frac{1}{MM1}=0.661$ $MM2:=\frac{0.14}{0.091}$ $\frac{1}{MM2}=0.65$

Window the P-wave portion of the time signals-set 2:

Parameter $p := 1 .. 12$ $\omega o_p := 2\pi \cdot 16.5$ $\omega o_5 := 2\pi \cdot 13.5$ $\omega o_7 := 2\pi \cdot 16.5$

$\omega o_{11} := 2\pi \cdot 15.5$ $\omega o_8 := 2\pi \cdot 17.5$ $\omega o_9 := 2\pi \cdot 14$ $\omega o_{10} := 2\pi \cdot 15.5$

Arrival Time (AT) of the signal:

$AT := (\ 0.02 \quad 0.042 \quad 0.015 \quad 0.045 \quad 0.03 \quad 0.032 \quad 0.037 \quad 0.032 \quad 0.033 \quad 0.033 \quad 0.035 \quad 0.02 \quad 0\ )^T$

$tp_p := ceil\left(\left(\frac{AT_p}{0.0005}\right)\right) \cdot 0.000$ $wp(t, \omega o) := \begin{cases} 10\left|\cos(\omega o \cdot t)^{10} - 1\right| & \text{if } 0 \le t \le \frac{\pi}{\omega o} \\ 0 & \text{otherwise} \end{cases}$

Define **Time Window** (Twind) to amplify the arrival of the signals:

$$Twind := \left| \begin{array}{l} \text{for } p \in 1 .. 12 \\ \quad \text{for } i \in 1 .. N \\ \quad\quad ampl_{i,p} \leftarrow wp\left(i \cdot 0.0005 - tp_p, \omega o_p\right) \\ ampl \end{array} \right.$$

Fourier Transform of the Windowed Signals: $FTW^{\langle p \rangle} := CFFT\left(\overrightarrow{\left(Twind^{\langle p \rangle} \cdot signal^{\langle p \rangle}\right)}\right)$

Windowed Signals: $P_{i,p} := Twind_{i,p} \cdot signal_{i,p}$

Spectrum Area $MA_{u,p} := \sum_{u=1}^{u} \frac{\left|FTW_{u,p}\right|}{N \cdot 0.001}$

Transmission Coefficient (TC) =

$$TC_u := \sqrt{\frac{|FTW_{u,1}| \cdot |FTW_{u,4}|}{|FTW_{u,2}| \cdot |FTW_{u,3}|}}$$

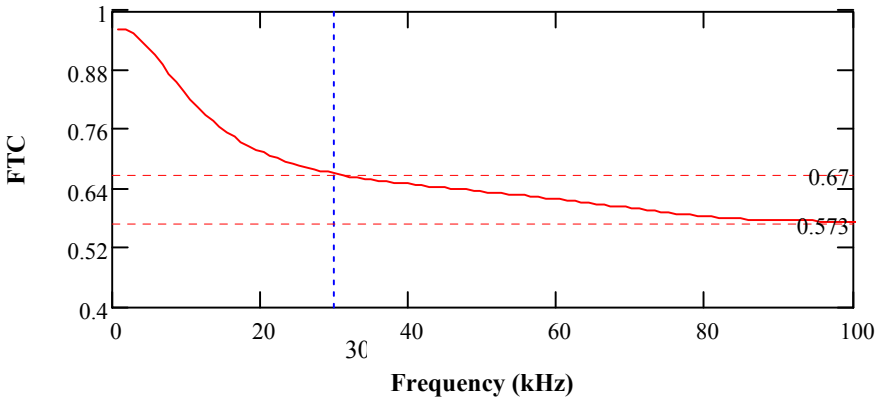

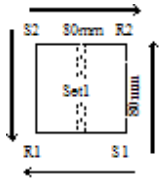

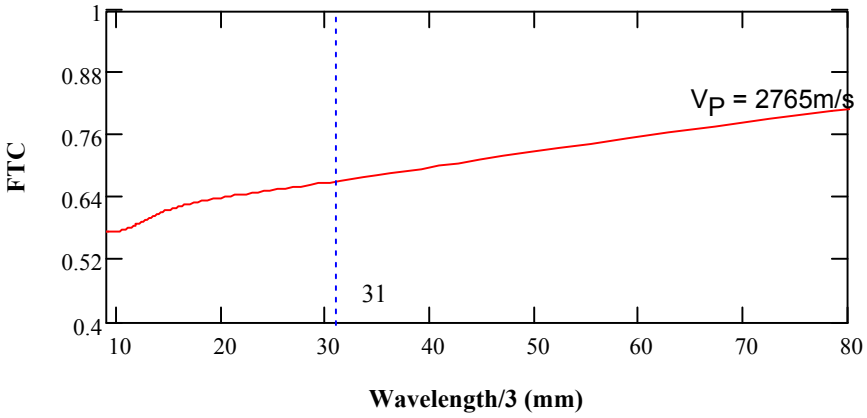

Damping ratio @ 37kHz

fre := 37.35

$f_{S2\text{-}R1}$ (joint-free) & $f_{S2\text{-}R2}$ (joint)

$$\left(\frac{2\pi fre \cdot 82}{2.811 \times 10^3}\right)^{-1} \cdot \ln(MM1) = 0.06$$

$f_{S1\text{-}R2}$ (joint-free) & $f_{S1\text{-}R1}$ (joint)

$$\left(\frac{2\pi fre \cdot 82}{2.811 \times 10^3}\right)^{-1} \cdot \ln(MM2) = 0.063$$

Damping analysis for P-wave signals:

$$\Delta\Phi 1_u := \left(\frac{2\pi f_u \cdot 82}{2.765 \times 10^3} \right)^{-1}$$

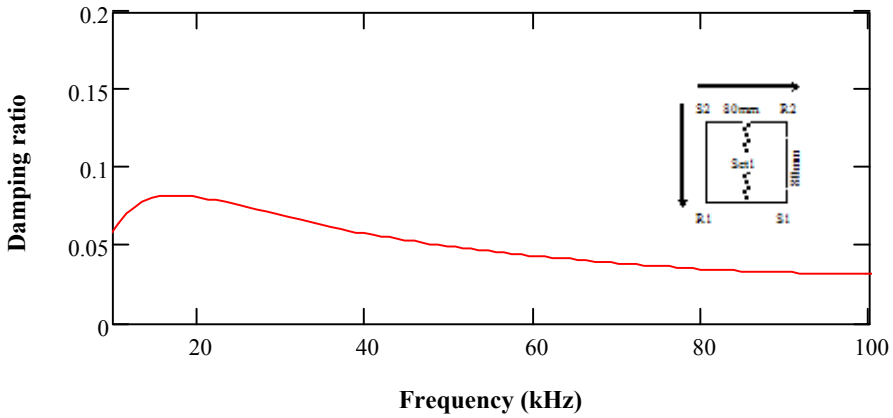

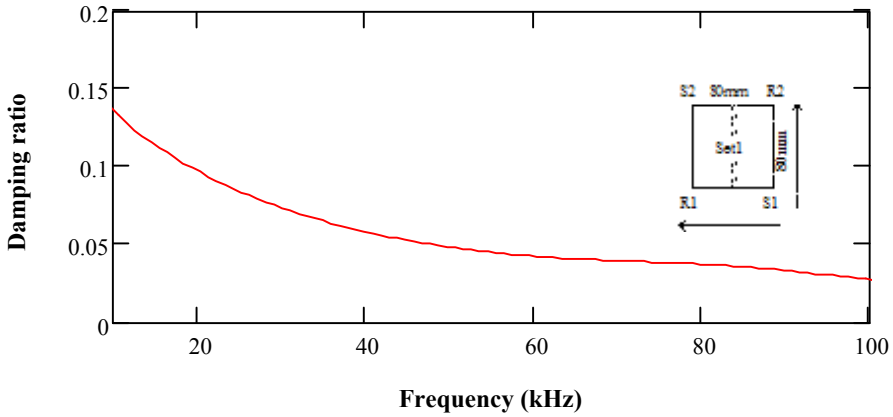

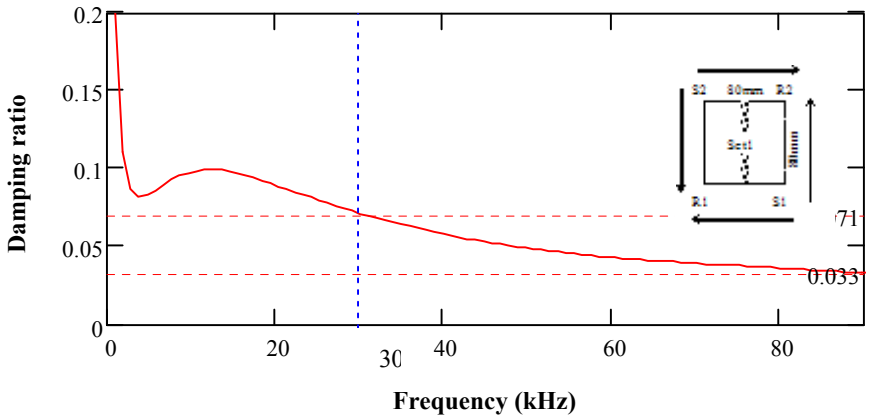

Damping analysis for P-wave signals -- using spectrum area

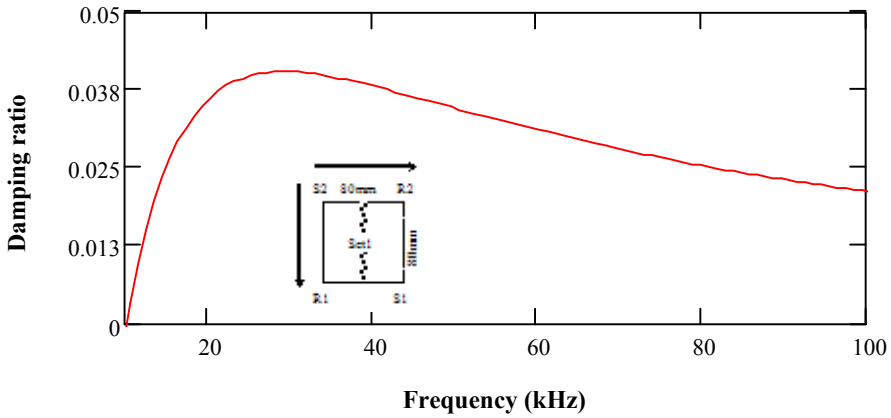

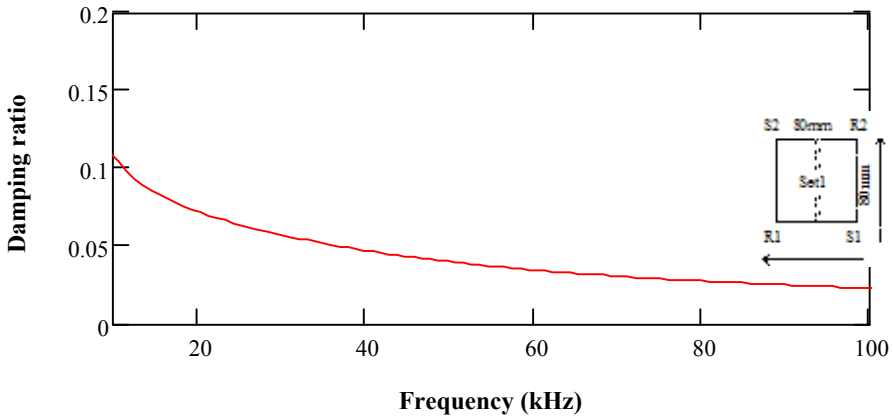

Window the R-wave arrival of time signals - window 2:

Parameter $p := 1 .. 4$ $\omega o_p := 2\pi \cdot 21.5$

$\omega o_2 := 2\pi \cdot 23.5$ $\omega o_3 := 2\pi \cdot 25$ $\omega o_4 := 2\pi \cdot 22$

Arrival Time (AT) of the signal: $AT := (0.063 \quad 0.063 \quad 0.064 \quad 0.061)^T$

$$tp_p := ceil\left(\left(\frac{AT_p}{0.001}\right)\right) \cdot 0.001$$

$$wp(t, \omega o) := \begin{cases} 10\left|\cos(\omega o \cdot t)^{10} - 1\right| & \text{if } 0 \le t \le \frac{\pi}{\omega o} \\ 0 & \text{otherwise} \end{cases}$$

Define **Time Window** (Twind) to amplify the arrival of the signals:

$$Twind := \left| \begin{array}{l} \text{for } p \in 1 .. 4 \\ \quad \text{for } i \in 1 .. N \\ \quad\quad ampl_{i,p} \leftarrow wp\left(i \cdot 0.001 - tp_p, \omega o_p\right) \\ ampl \end{array} \right.$$

Fourier Transform of the Windowed Signals: $FTTW^{\langle p \rangle} := CFFT\left(\overrightarrow{\left(Twind^{\langle p \rangle} \cdot signal^{\langle p \rangle}\right)}\right)$

Windowed Signals: $P_{i,p} := Twind_{i,p} \cdot signal_{i,p}$

Spectrum area: $$MA_{u,p} := \sum_{u=1}^{u} \frac{\left|FTTW_{u,p}\right|}{N \cdot 0.001}$$

$f_{S2\text{-}R1}$ (joint-free) & $f_{S2\text{-}R2}$ (joint)

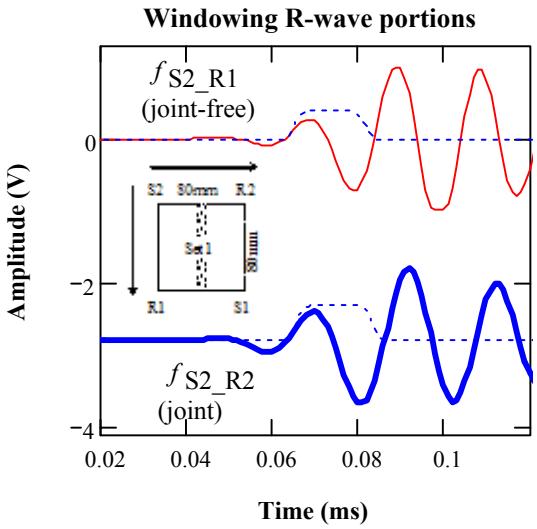

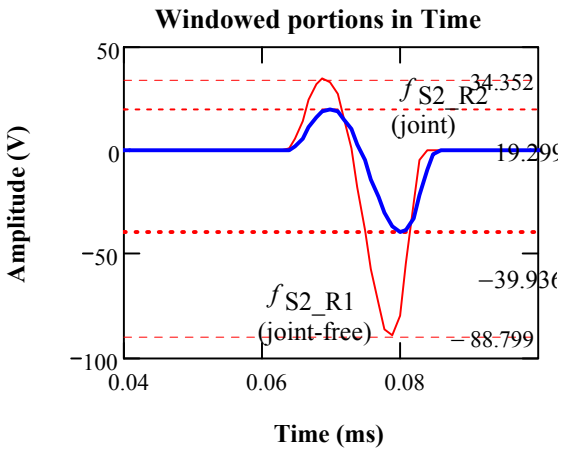

$f_{S1\text{-}R2}$ (joint-free) & $f_{S1\text{-}R1}$ (joint)

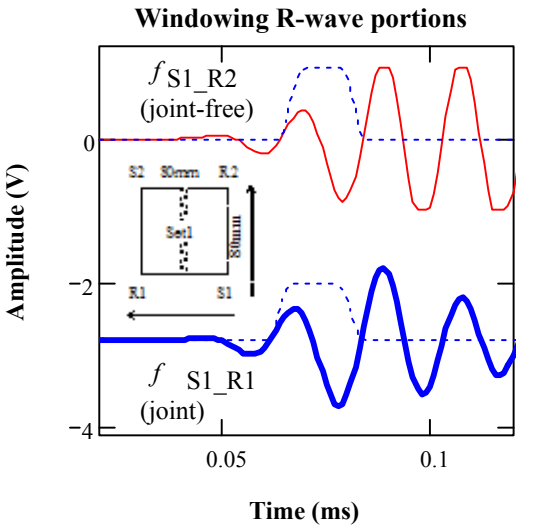

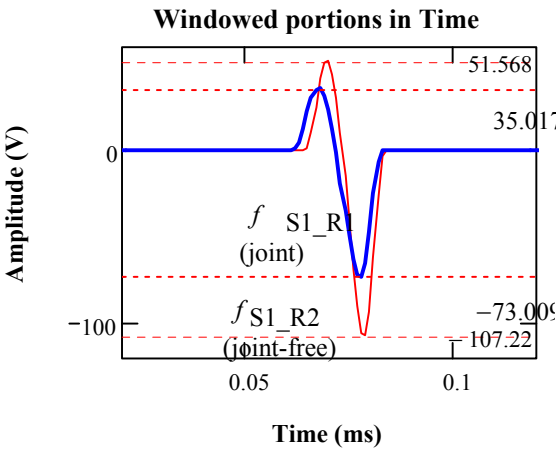

Transmission Coefficient (TC) =

$$TTC_u := \sqrt{\frac{|FTTW_{u,1}| \cdot |FTTW_{u,4}|}{|FTTW_{u,2}| \cdot |FTTW_{u,3}|}}$$

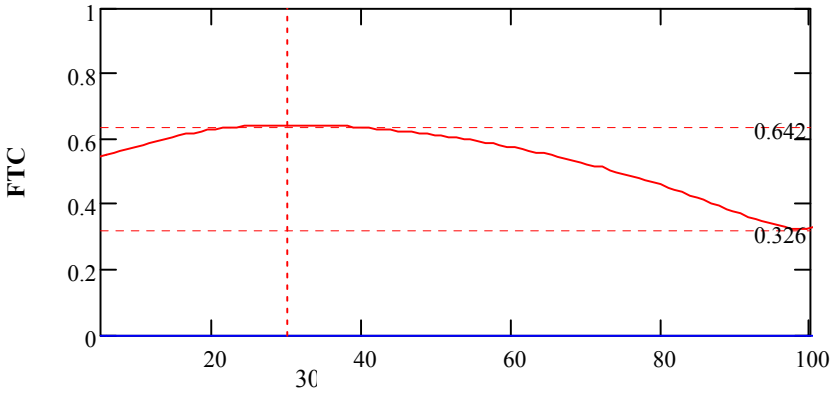

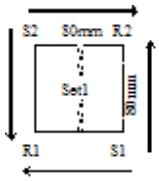

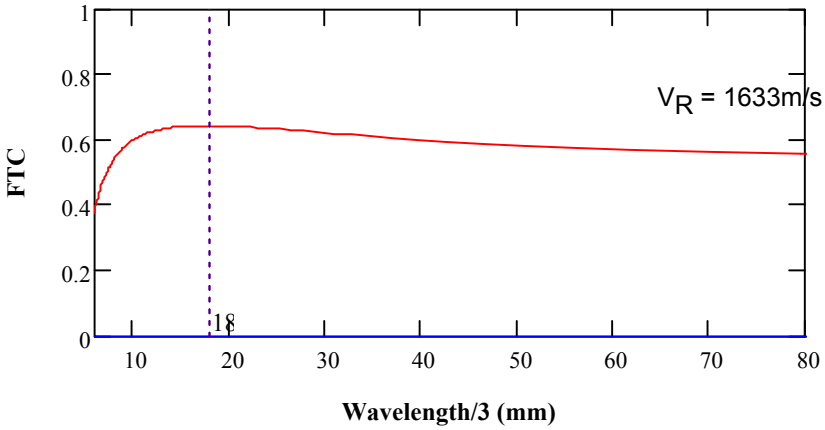

Damping ratio @ 43kHz

fre := 43.21

$f_{S2\text{-}R1}$ (joint-free) & $f_{S2\text{-}R2}$ (joint)

$$\left(\frac{2\pi fre \cdot 82}{1.617\times 10^3}\right)^{-1} \cdot \ln(MM1) = 0.048$$

$f_{S1\text{-}R2}$ (joint-free) & $f_{S1\text{-}R1}$ (joint)

$$\left(\frac{2\pi fre \cdot 82}{1.617\times 10^3}\right)^{-1} \cdot \ln(MM2) = 0.02$$

For the set

$$\left(\frac{2\pi fre \cdot 82}{1.633\times 10^3}\right)^{-1} \cdot \ln\left(\sqrt{MM2 \cdot MM1}\right) = 0.034$$

Damping analysis for R-wave signals:

$$\Delta\Phi 2_u := \left(\frac{2\pi f_u \cdot 82}{1.617 \times 10^3} \right)^{-1}$$

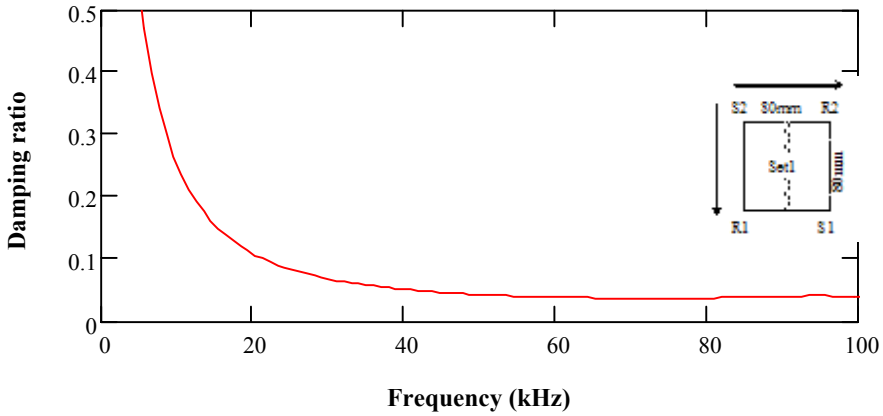

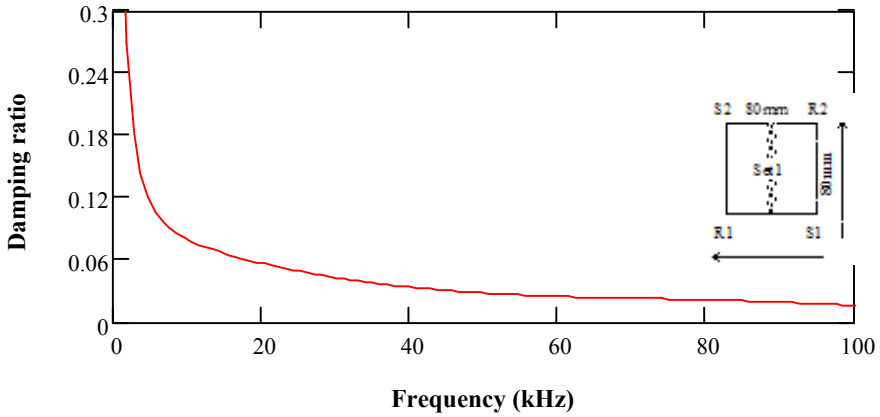

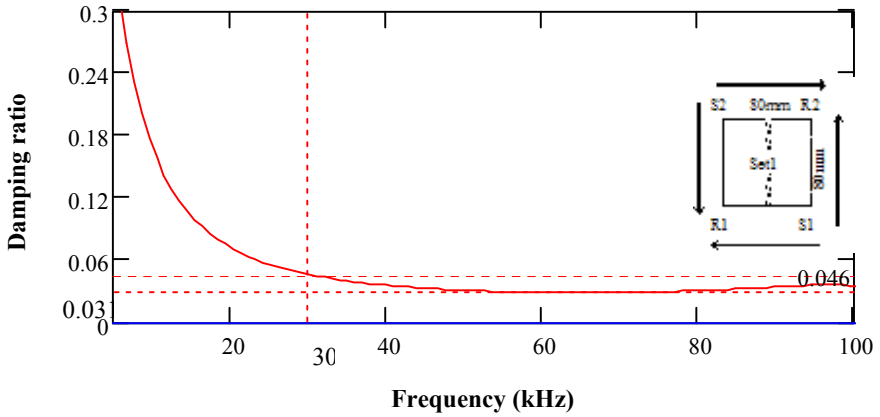

Damping analysis for R-wave signals:

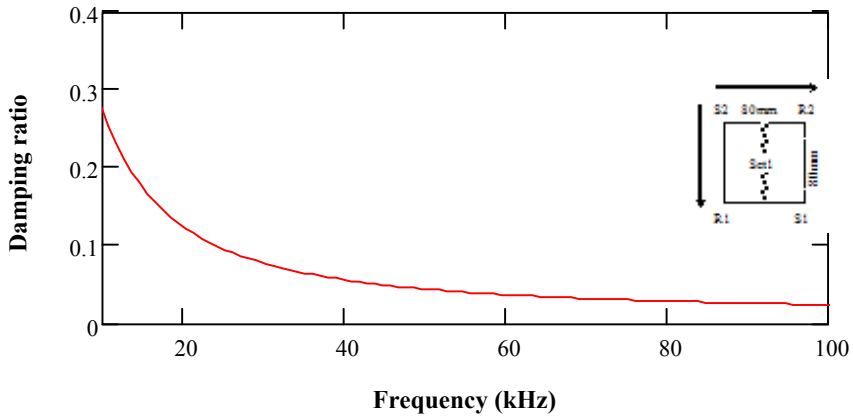

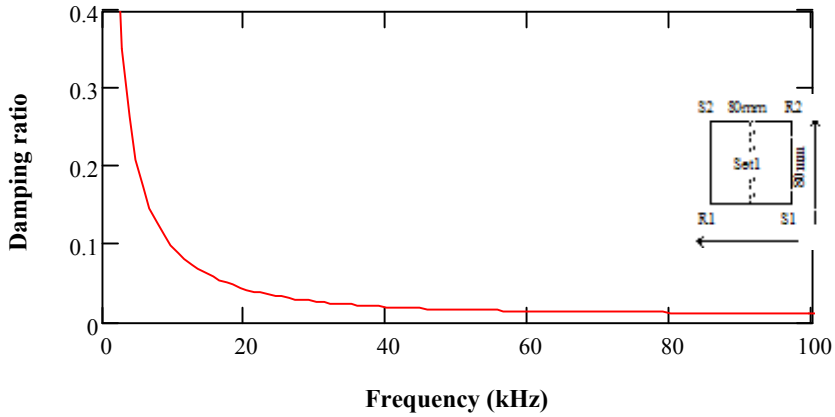

Wavelet transform - for dominant freuency in full signals, deifferent center frequencies for 4 signals defined by "aX"; Time shift by "τ".

$aAC := 8.9$ $\frac{1}{2 \cdot aAC \cdot 1 \cdot 10^{-3}} = 55.679$ kHz $aDB := 9.14$ $\frac{1}{2 \cdot aDB \cdot 1 \cdot 10^{-3}} = 54.70$

$aAB := 8.9$ $\frac{1}{2 \cdot aAB \cdot 1 \cdot 10^{-3}} = 55.679$ kHz $aDC := 10$ $\frac{1}{2 \cdot aDC \cdot 1 \cdot 10^{-3}} = 50$

Definition of Morlet wavelet

$\tau := 1 .. N$

f_{S2_R1} (joint-free) $w\_AC_{i,\tau} := aAC^{-\frac{1}{2}} \cdot \left[e^{j \cdot \frac{-\pi}{aAC} \cdot (\tau - i)} \cdot e^{-1 \cdot \left(\frac{\tau - i}{aAC} \right)^2} \right]$

f_{S2_R2} **(joint)** $w\_AB_{i,\tau} := aAB^{-\frac{1}{2}} \cdot \left[e^{j \cdot \frac{-\pi}{aAB} \cdot (\tau - i)} \cdot e^{-1 \cdot \left(\frac{\tau - i}{aAB} \right)^2} \right]$

f_{S1_R2} (joint-free) $w\_DB_{i,\tau} := aDB^{-\frac{1}{2}} \cdot \left[e^{j \cdot \frac{-\pi}{aDB} \cdot (\tau - i)} \cdot e^{-1 \cdot \left(\frac{\tau - i}{aDB} \right)^2} \right]$

f_{S1_R1} **(joint)** $w\_DC_{i,\tau} := aDC^{-\frac{1}{2}} \cdot \left[e^{j \cdot \frac{-\pi}{aDC} \cdot (\tau - i)} \cdot e^{-1 \cdot \left(\frac{\tau - i}{aDC} \right)^2} \right]$

Wavelet transform

f_{S2_R1} (joint-free) $WAC_\tau := \sum_i \left(w\_AC_{i,\tau} \cdot AC_i \right)$

$WAC_\tau := \left| WAC_\tau \right|$

f_{S2_R2} **(joint)** $WAB_\tau := \sum_i w\_AB_{i,\tau} \cdot$

$WAB_\tau := \left| WAB_\tau \right|$

f_{S1_R2} (joint-free) $WDB_\tau := \sum_i \left(w\_DB_{i,\tau} \cdot DB_i \right)$

f_{S1_R1} **(joint)** $WDC_\tau := \sum_i w\_DC_{i,\tau} \cdot$

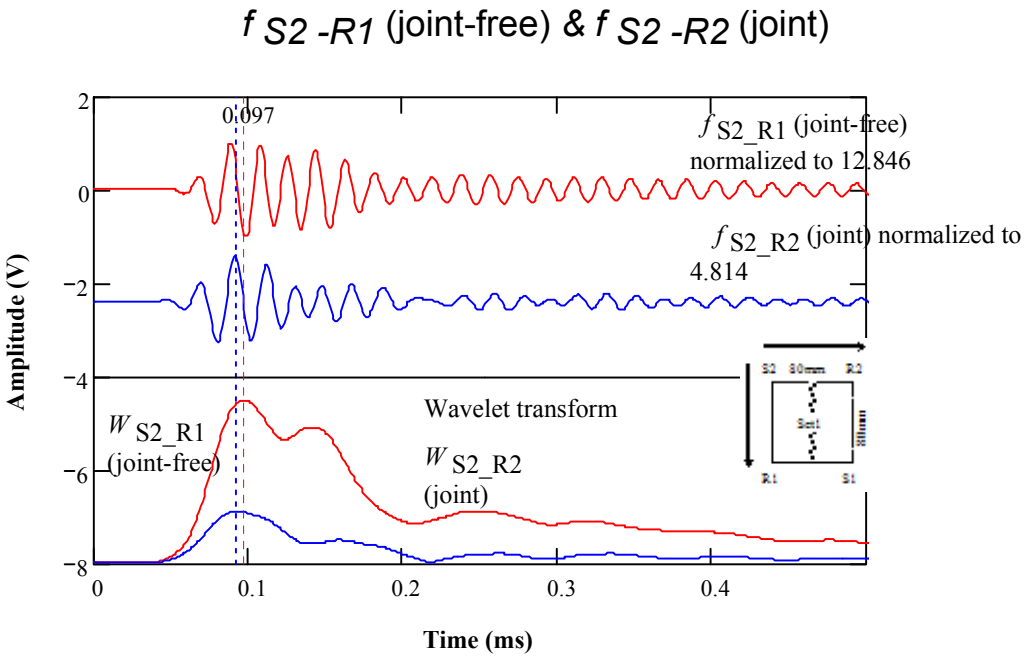

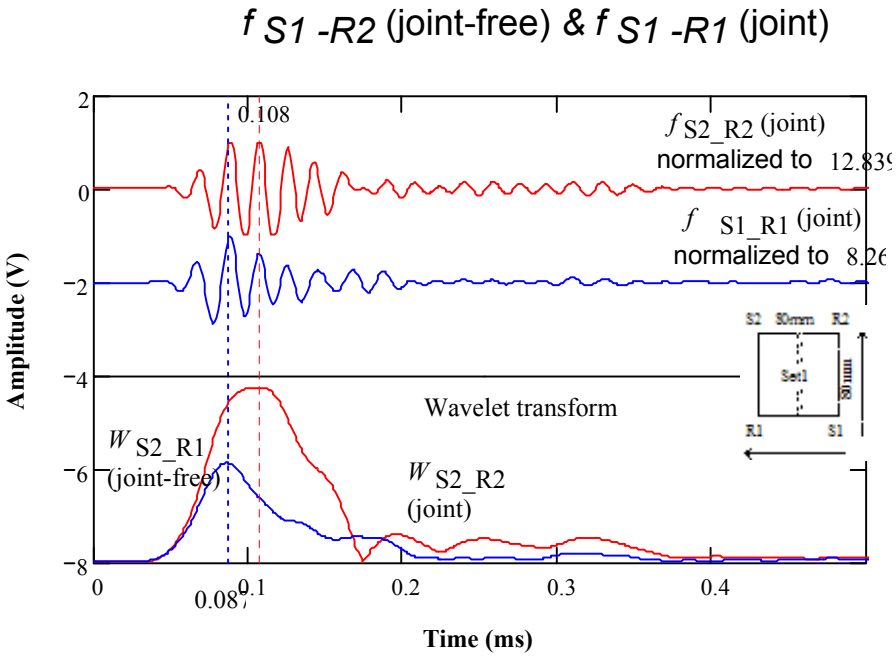

Amplitude ratio

$$\frac{\max(WAB)}{\max(WAC)} = 0.321 \qquad \frac{\max(WDC)}{\max(WDB)} = 0.569 \qquad \sqrt{\frac{\max(WAB)}{\max(WAC)}\frac{\max(WDC)}{\max(WDB)}} = 0.427$$

Wavelet transform - for P-wave, deifferent center frequency for 4 signals defined by "aX"; Time shift by "τ".

$aAC := 12.8$ $\frac{1}{2 \cdot aAC \cdot 1 \cdot 10^{-3}} = 39.063$ kHz $aDB := 13.13$ $\frac{1}{2 \cdot aDB \cdot 1 \cdot 10^{-3}} = 38.0$

$aAB := 13.84$ $\frac{1}{2 \cdot aAB \cdot 1 \cdot 10^{-3}} = 36.127$ kHz $aDC := 13.84$ $\frac{1}{2 \cdot aDC \cdot 1 \cdot 10^{-3}} = 36.1$

Definition of Morlet wavelet $\tau := 1 .. N$

f_{S2_R1} (joint-free) $w\_AC_{i,\tau} := aAC^{-\frac{1}{2}} \cdot \left[e^{j \cdot \frac{-\pi}{aAC} \cdot (\tau - i)} \cdot e^{-1 \cdot \left(\frac{\tau - i}{aAC} \right)^2} \right]$

f_{S2_R2} **(joint)** $w\_AB_{i,\tau} := aAB^{-\frac{1}{2}} \cdot \left[e^{j \cdot \frac{-\pi}{aAB} \cdot (\tau - i)} \cdot e^{-1 \cdot \left(\frac{\tau - i}{aAB} \right)^2} \right]$

f_{S1_R2} (joint-free) $w\_DB_{i,\tau} := aDB^{-\frac{1}{2}} \cdot \left[e^{j \cdot \frac{-\pi}{aDB} \cdot (\tau - i)} \cdot e^{-1 \cdot \left(\frac{\tau - i}{aDB} \right)^2} \right]$

f_{S1_R1} (joint) $w\_DC_{i,\tau} := aDC^{-\frac{1}{2}} \cdot \left[e^{j \cdot \frac{-\pi}{aDC} \cdot (\tau - i)} \cdot e^{-1 \cdot \left(\frac{\tau - i}{aDC} \right)^2} \right]$

Wavelet transform

f_{S2_R1} (joint-free) $WAC_\tau := \sum_i \left(w\_AC_{i,\tau} \cdot AC_i \right)$

$WAC_\tau := \left| WAC_\tau \right|$

f_{S2_R2} (joint) $WAB_\tau := \sum_i w\_AB_{i,\tau} \cdot$

$WAB_\tau := \left| WAB_\tau \right|$

f_{S1_R2} (joint-free) $WDB_\tau := \sum_i \left(w\_DB_{i,\tau} \cdot DB_i \right)$

f_{S1_R1} (joint) $WDC_\tau : \sum_i w\_DC_{i,\tau} \cdot$

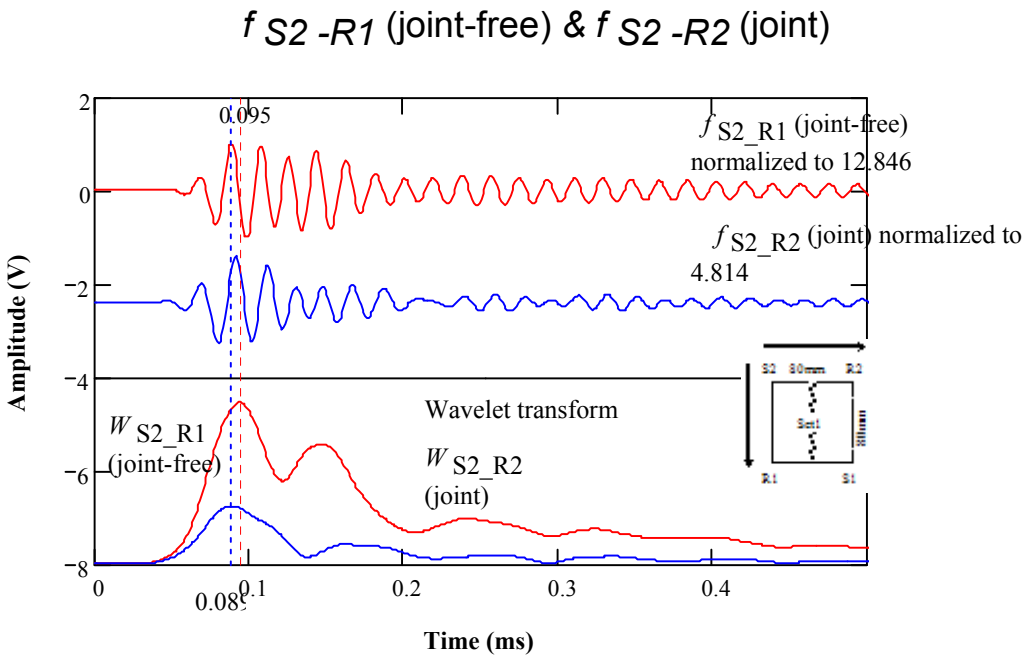

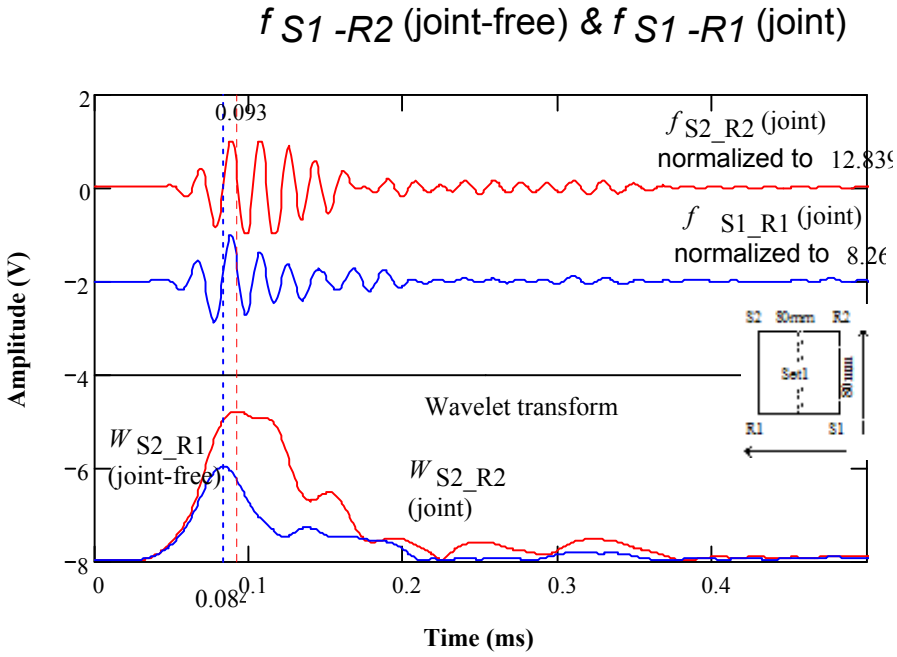

Amplitude ratio

$$\frac{\max(WAB)}{\max(WAC)} = 0.36 \qquad \frac{\max(WDC)}{\max(WDB)} = 0.633 \qquad \sqrt{\frac{\max(WAB)}{\max(WAC)}\frac{\max(WDC)}{\max(WDB)}} = 0.478$$

Wavelet transform - for R-wave, different center frequency for 4 signals defined by "aX"; Time shift by "τ".

$aAC := 11.38$ $\frac{1}{2 \cdot aAC \cdot 1 \cdot 10^{-3}} = 43.937$ kHz $aDB := 10.67$ $\frac{1}{2 \cdot aDB \cdot 1 \cdot 10^{-3}} = 46.86$

$aAB := 12.18$ $\frac{1}{2 \cdot aAB \cdot 1 \cdot 10^{-3}} = 41.051$ kHz $aDC := 11.91$ $\frac{1}{2 \cdot aDC \cdot 1 \cdot 10^{-3}} = 41.982$

Definition of Morlet wavelet $\tau := 1 .. N$

f_{S2_R1} (joint-free) $w\_AC_{i,\tau} := aAC^{-\frac{1}{2}} \cdot \left[e^{j \cdot \frac{-\pi}{aAC} \cdot (\tau - i)} \cdot e^{-1 \cdot \left(\frac{\tau - i}{aAC} \right)^2} \right]$

f_{S2_R2} **(joint)** $w\_AB_{i,\tau} := aAB^{-\frac{1}{2}} \cdot \left[e^{j \cdot \frac{-\pi}{aAB} \cdot (\tau - i)} \cdot e^{-1 \cdot \left(\frac{\tau - i}{aAB} \right)^2} \right]$

f_{S1_R2} (joint-free) $w\_DB_{i,\tau} := aDB^{-\frac{1}{2}} \cdot \left[e^{j \cdot \frac{-\pi}{aDB} \cdot (\tau - i)} \cdot e^{-1 \cdot \left(\frac{\tau - i}{aDB} \right)^2} \right]$

f_{S1_R1} **(joint)** $w\_DC_{i,\tau} := aDC^{-\frac{1}{2}} \cdot \left[e^{j \cdot \frac{-\pi}{aDC} \cdot (\tau - i)} \cdot e^{-1 \cdot \left(\frac{\tau - i}{aDC} \right)^2} \right]$

Wavelet transform

f_{S2_R1} (joint-free) $WAC_\tau := \sum_i \left(w\_AC_{i,\tau} \cdot AC_i \right)$

$WAC_\tau := \left| WAC_\tau \right|$

f_{S2_R2} (joint) $WAB_\tau := \sum_i w\_AB_{i,\tau} \cdot$

$WAB_\tau := \left| WAB_\tau \right|$

f_{S1_R2} (joint-free) $WDB_\tau := \sum_i \left(w\_DB_{i,\tau} \cdot DB_i \right)$

f_{S1_R1} (joint) $WDC_\tau := \sum_i \left(w\_DC_{i,\tau} \cdot \right.$

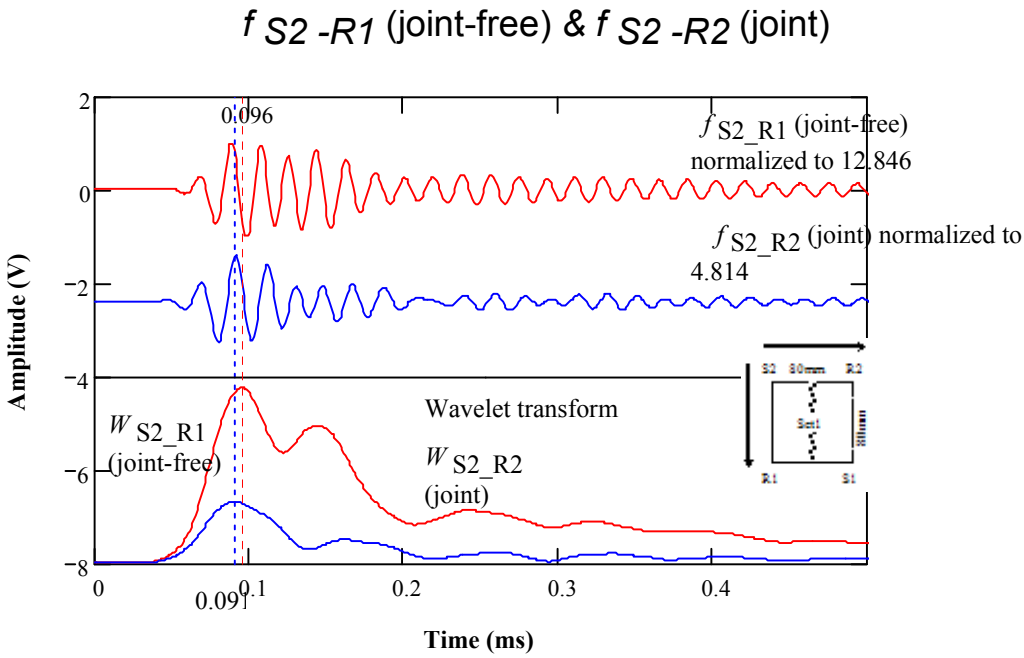

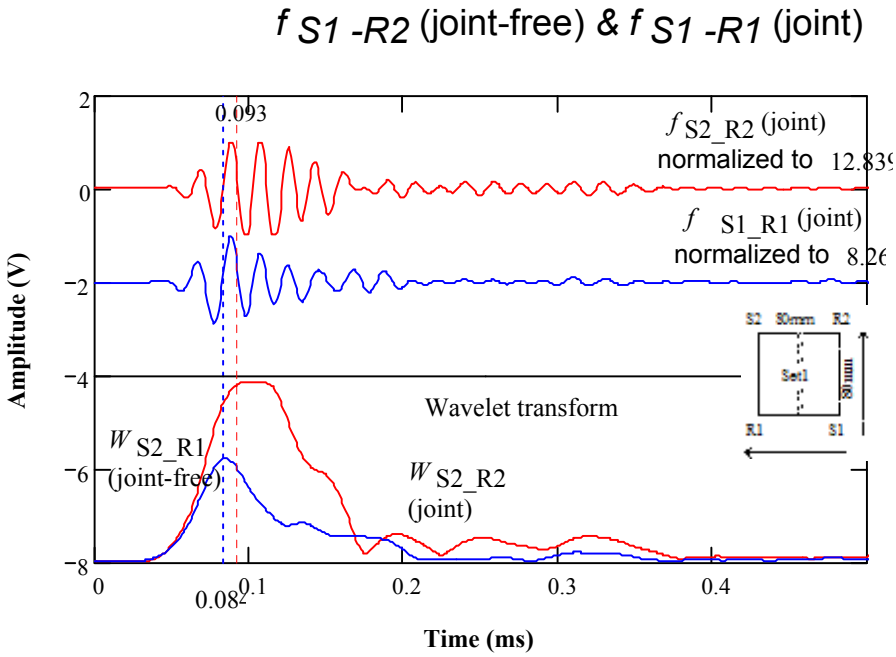

Amplitude ratio

$$\frac{\max(WAB)}{\max(WAC)} = 0.353 \qquad \frac{\max(WDC)}{\max(WDB)} = 0.572 \qquad \sqrt{\frac{\max(WAB)}{\max(WAC)}\frac{\max(WDC)}{\max(WDB)}} = 0.449$$

Appendix P

Signals in Time and Frequency Domains for Slab 3

- Measurements on the Jointed and the Joint-free Surfaces

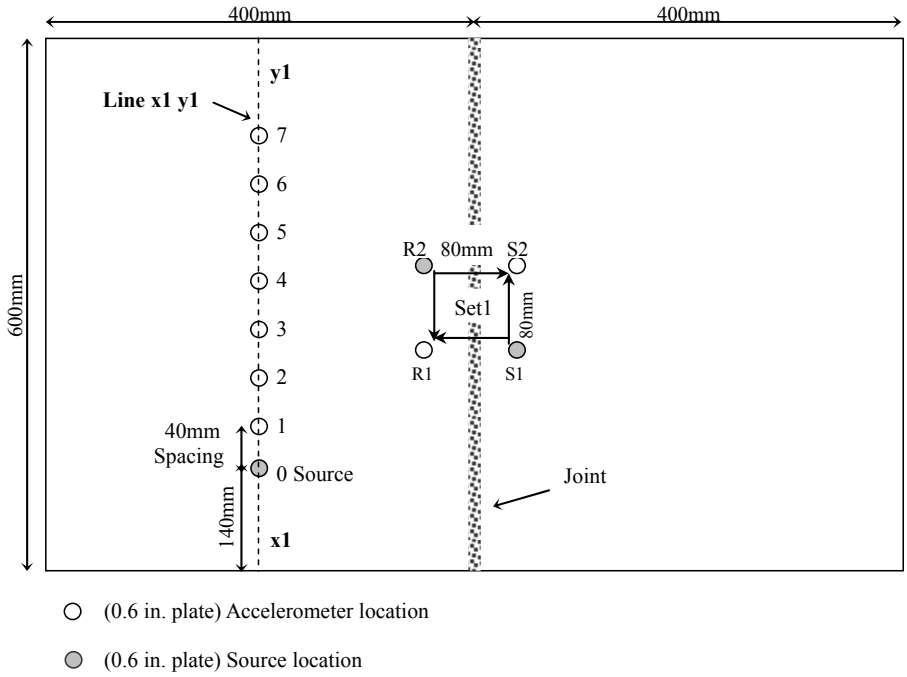

Figure P-1: 80mm S-R spacing configuration of HMA slab 3

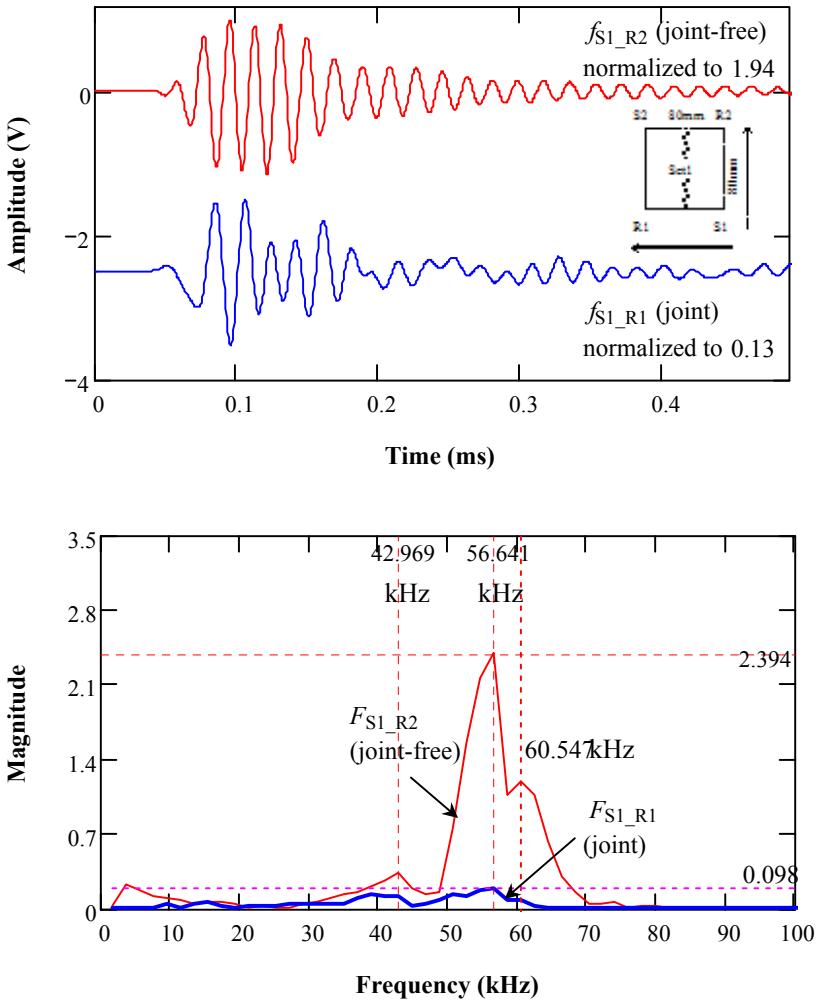

Figure P-2: Signal Pair 1 of Set 1 measurements in time and frequency domains (80mm S-R spacing) on jointed surface (Horizontal lines mark the peak amplitudes and vertical lines dominant frequencies.)

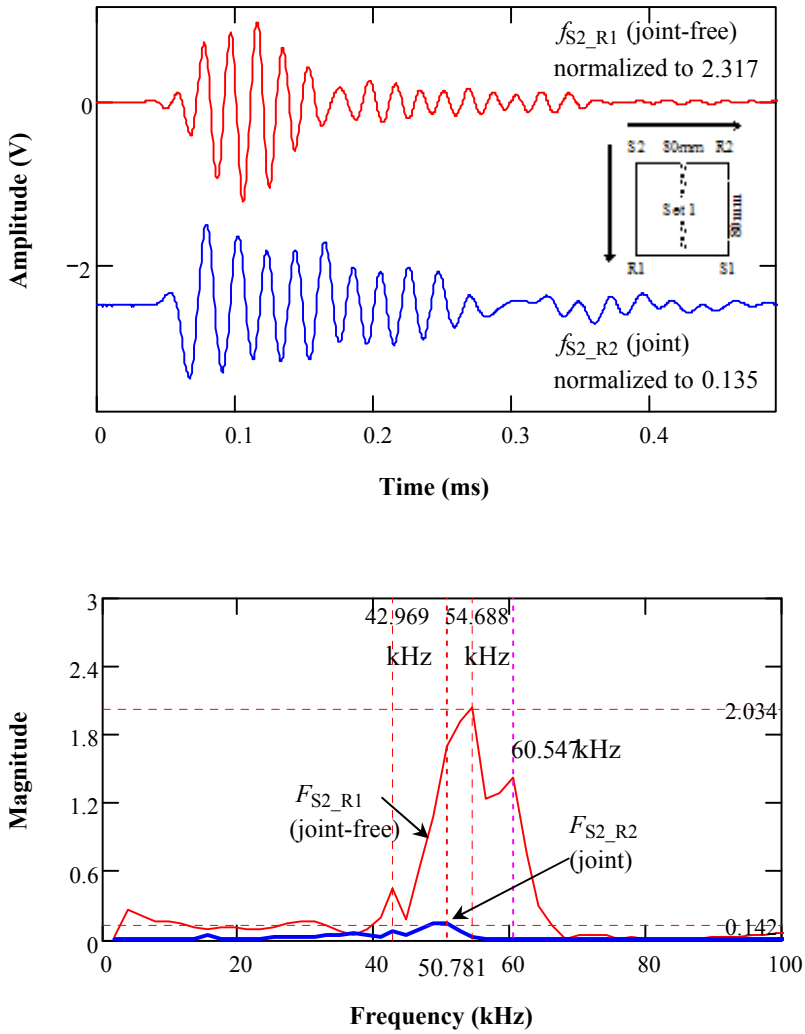

Figure P-3: Signal Pair 2 of Set 1 measurements in time and frequency domains (80mm S-R spacing) on jointed surface (Horizontal lines mark the peak amplitudes and vertical lines dominant frequencies.)

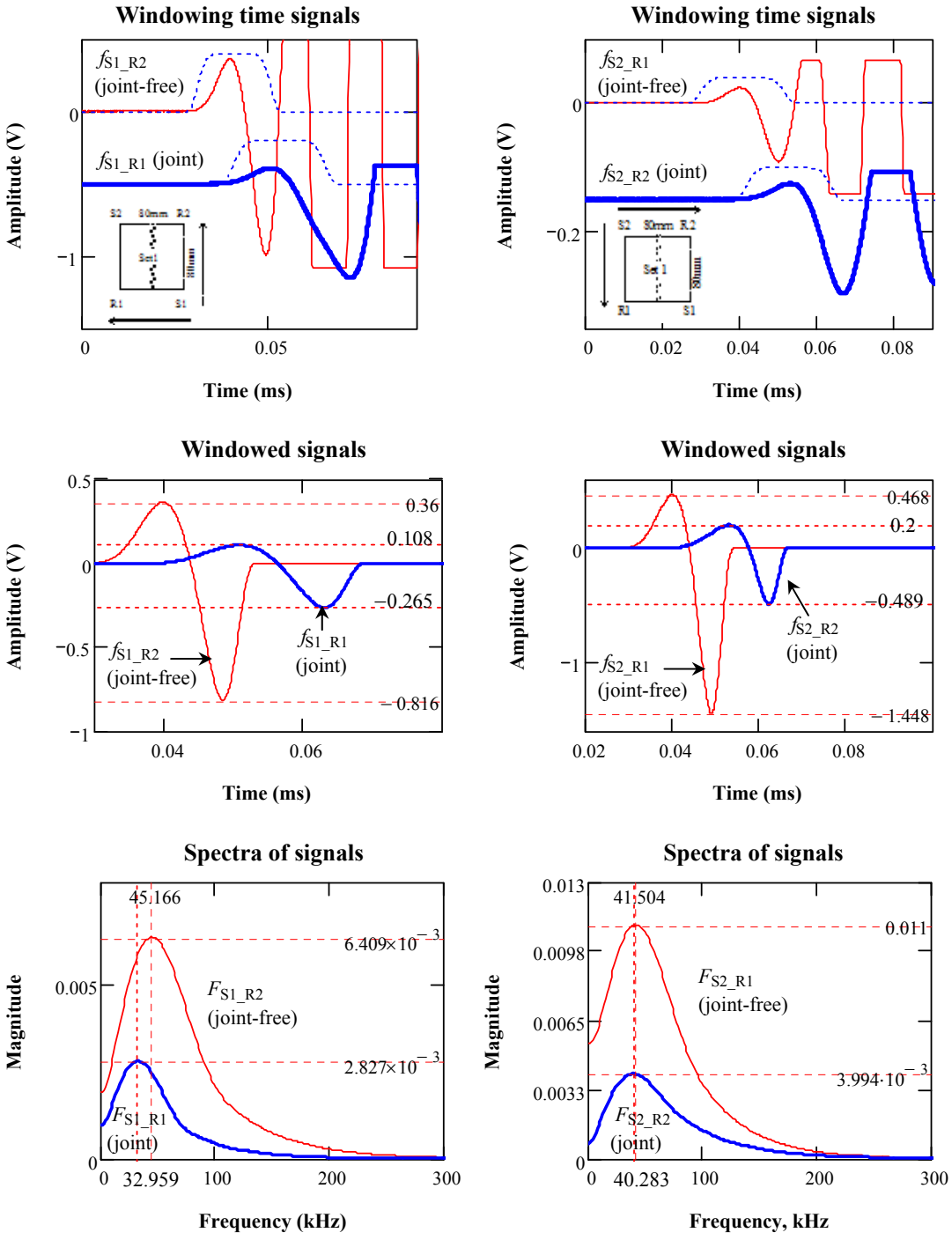

Figure P-4: P-wave analyses in time and frequency domains for Set 1 (80mm S-R spacing) on jointed surface (Horizontal lines mark the peak amplitudes and vertical lines dominant frequencies.)

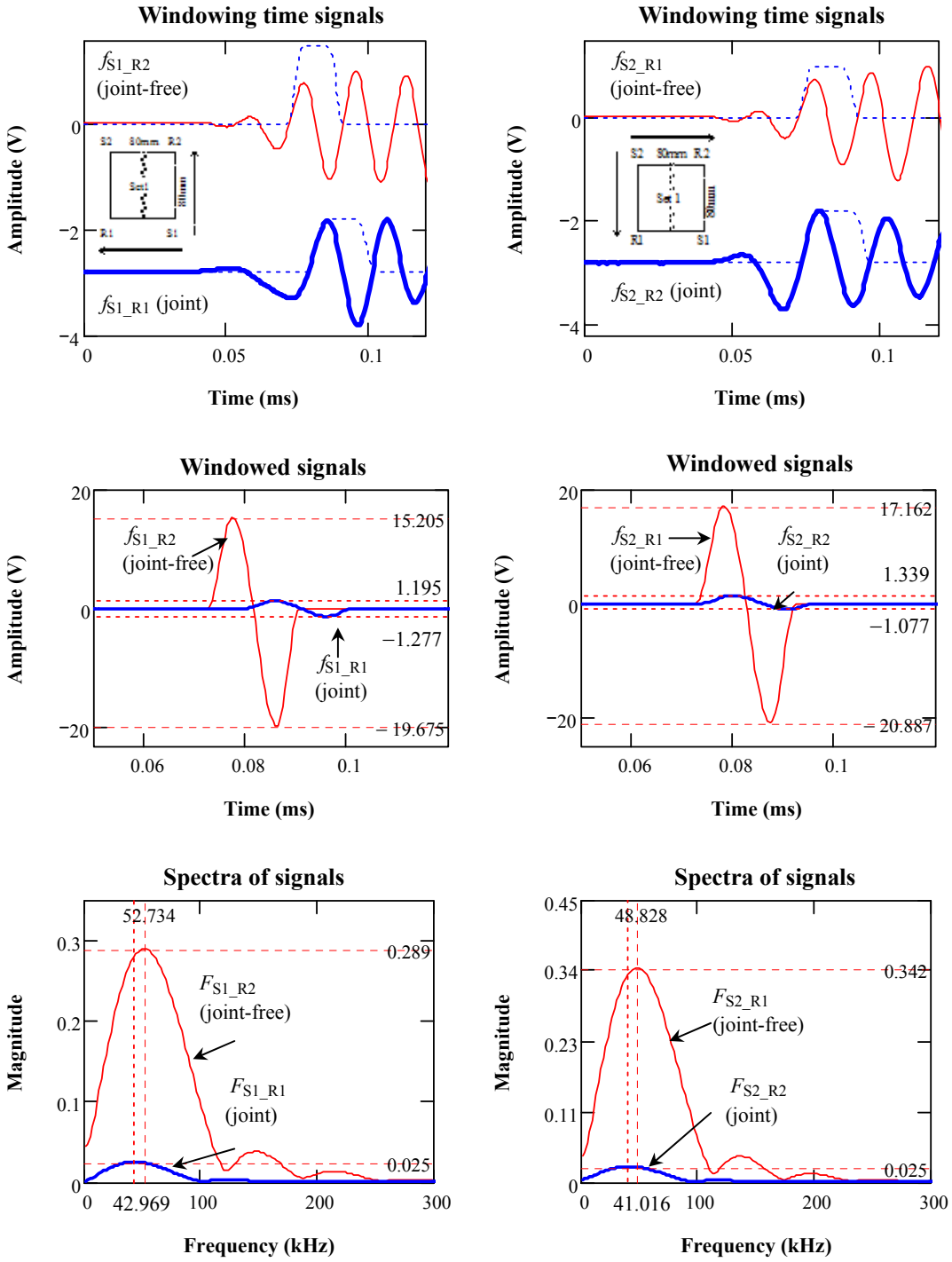

Figure P-5: R-wave analyses in time and frequency domains for Set 1 (80mm S-R spacing) on jointed surface (Horizontal lines mark the peak amplitudes and vertical lines dominant frequencies.)

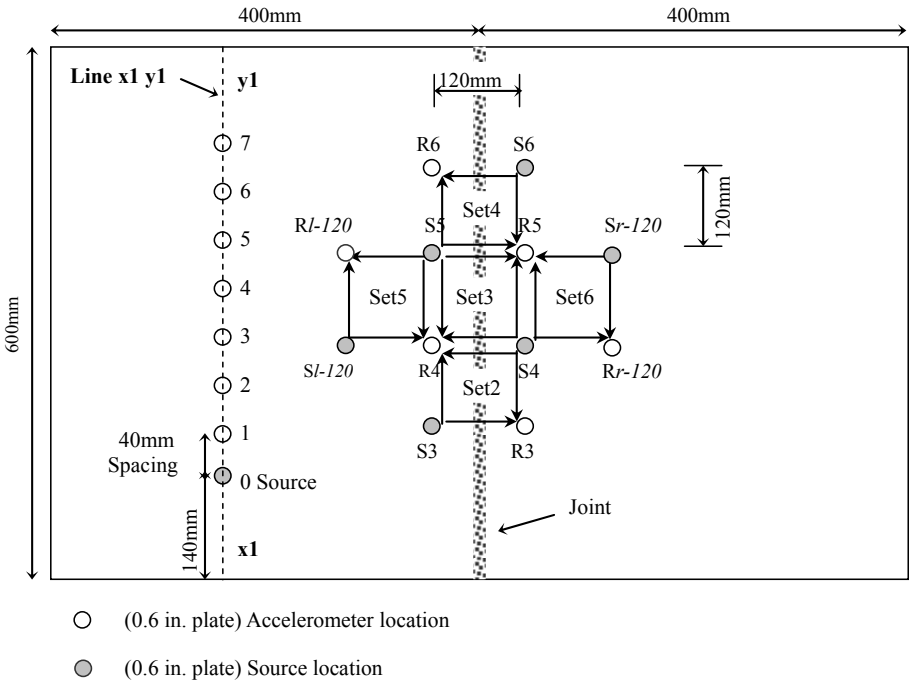

Figure P-6: 120mm S-R spacing configuration of HMA slab 3

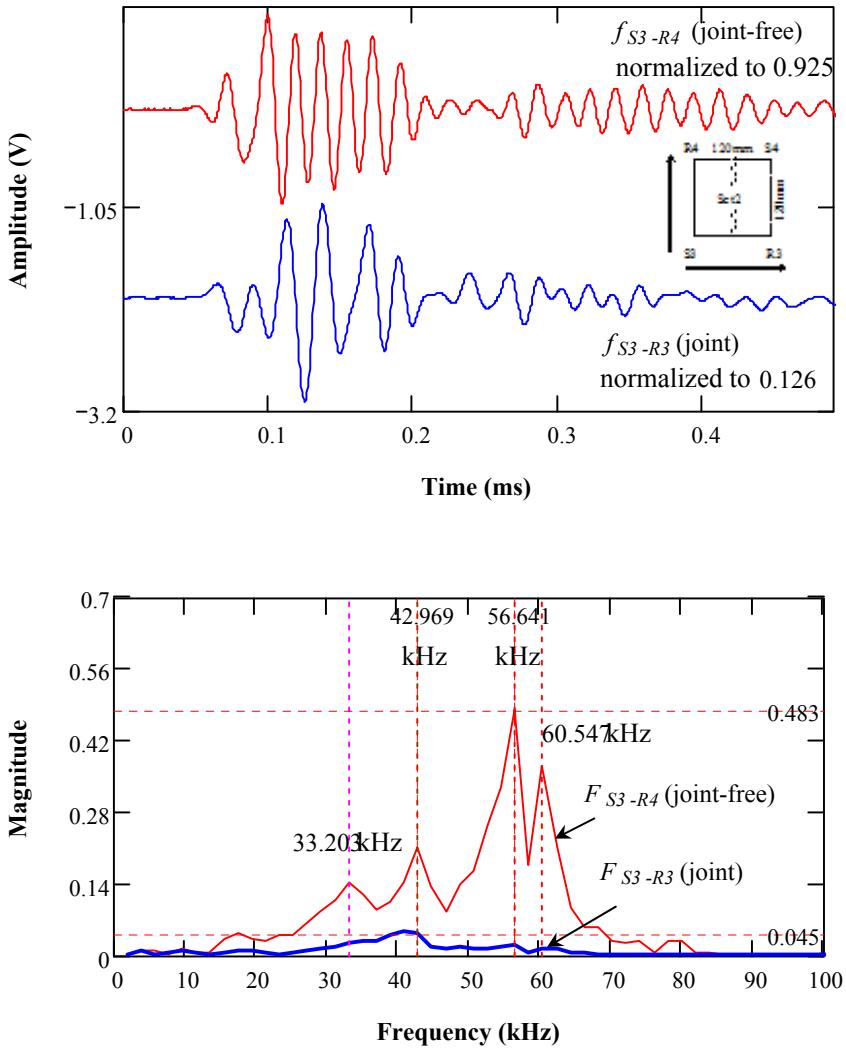

Figure P-7: Signal Pair 1 of Set 2 measurements in time and frequency domains (120mm S-R spacing) on jointed surface (Horizontal lines mark the peak amplitudes and vertical lines dominant frequencies.)

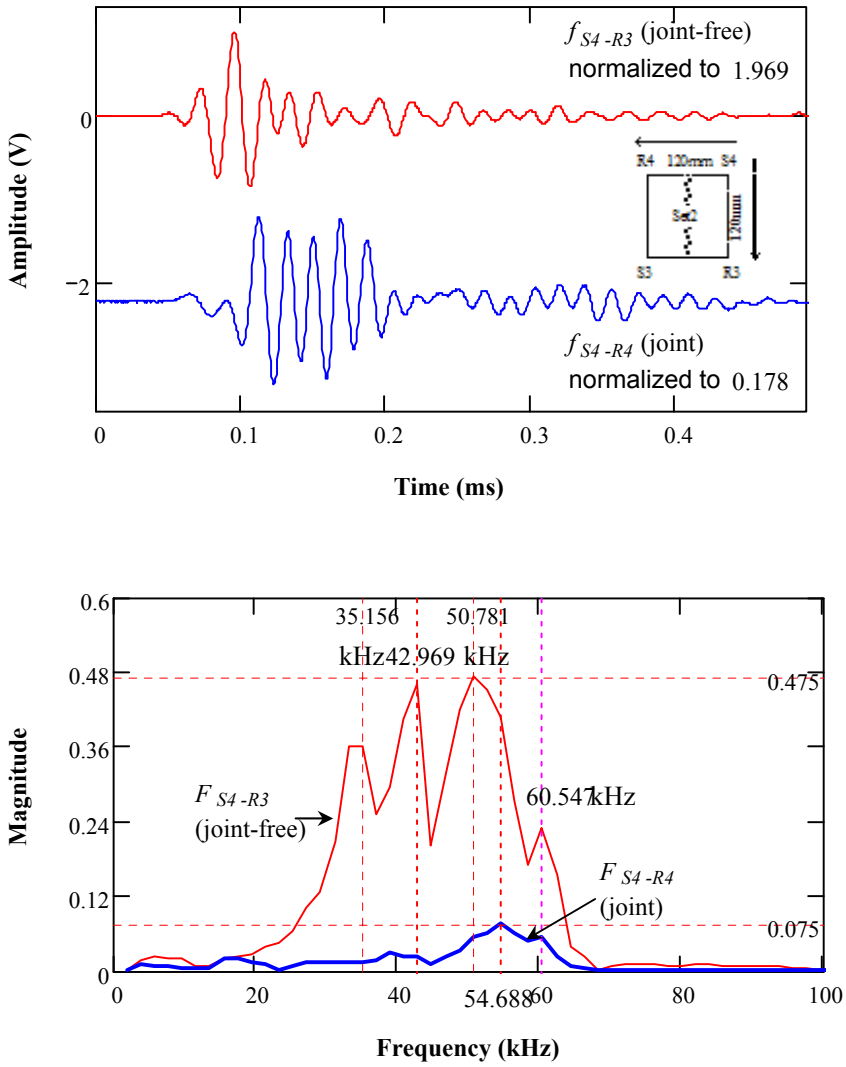

Figure P-8: Signal Pair 2 of Set 2 measurements in time and frequency domains (120mm S-R spacing) on jointed surface (Horizontal lines mark the peak amplitudes and vertical lines dominant frequencies.)

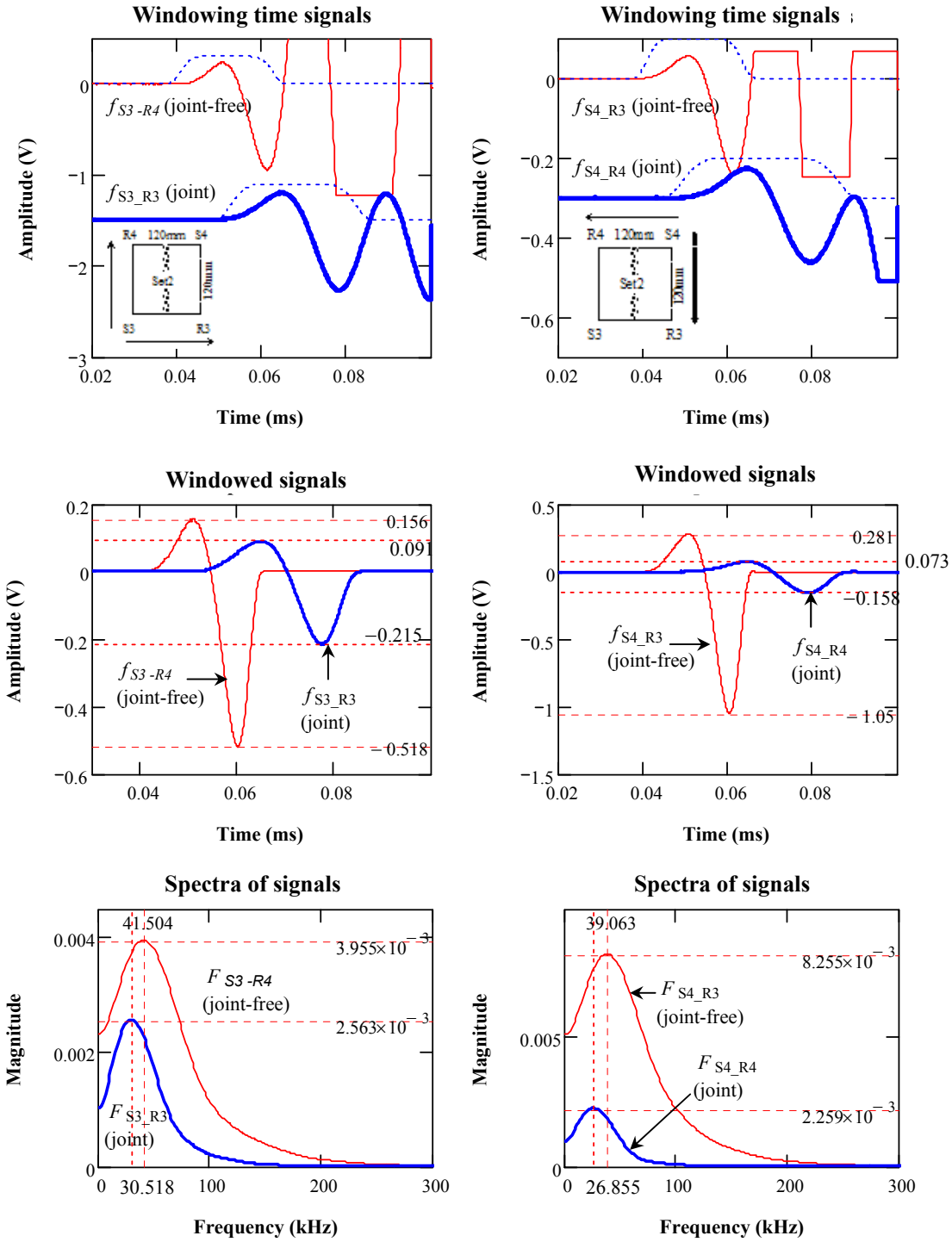

Figure P-9: P-wave analyses in time and frequency domains for Set 2 (120mm S-R spacing) on jointed surface (Horizontal lines mark the peak amplitudes and vertical lines dominant frequencies.)

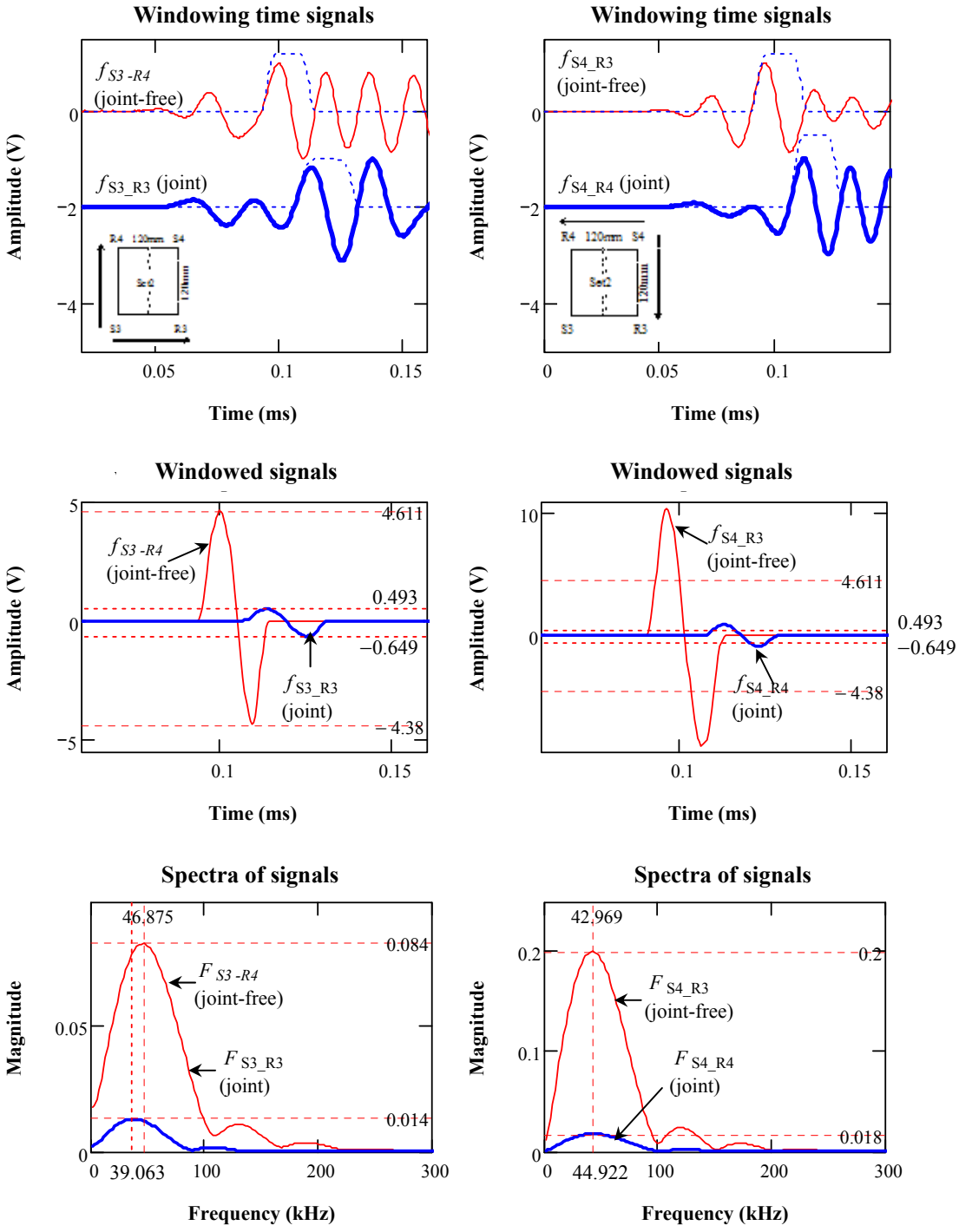

Figure P-10: R-wave analyses in time and frequency domains for Set 2 (120mm S-R spacing) on jointed surface (Horizontal lines mark the peak amplitudes and vertical lines dominant frequencies.)

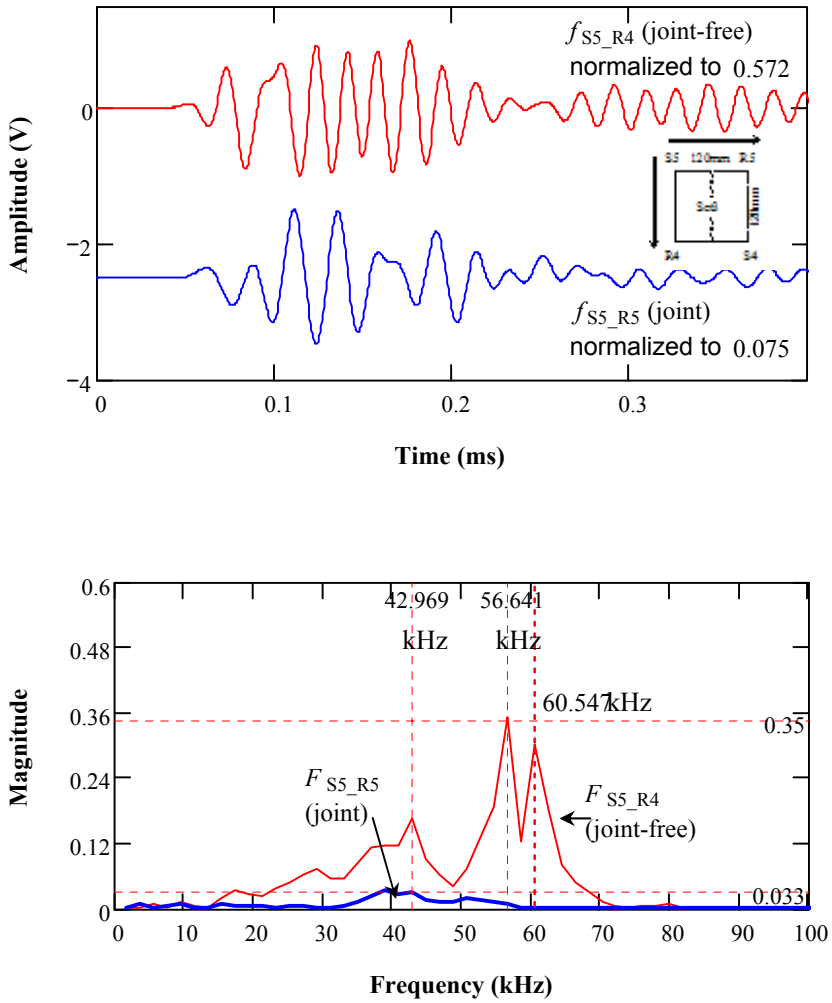

Figure P-11: Signal Pair 1 of Set 3 measurements in time and frequency domains (120mm S-R spacing) on jointed surface (Horizontal lines mark the peak amplitudes and vertical lines dominant frequencies.)

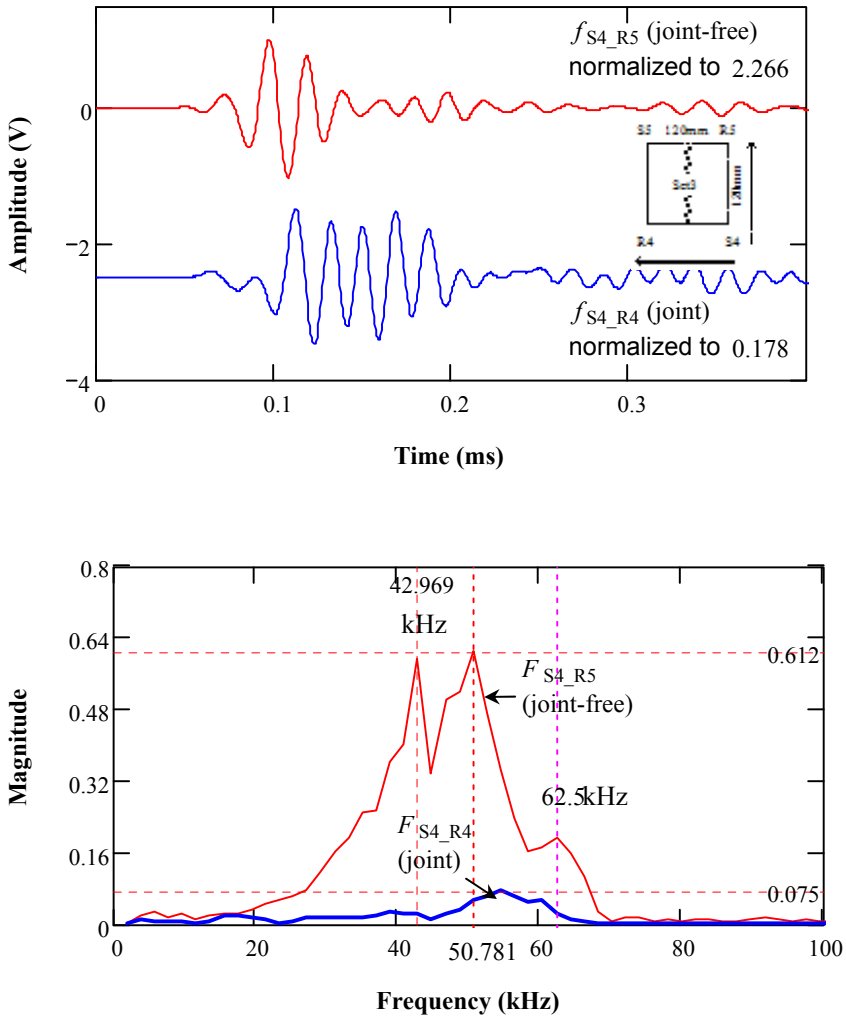

Figure P-12: Signal Pair 2 of Set 3 measurements in time and frequency domains (120mm S-R spacing) on jointed surface (Horizontal lines mark the peak amplitudes and vertical lines dominant frequencies.)

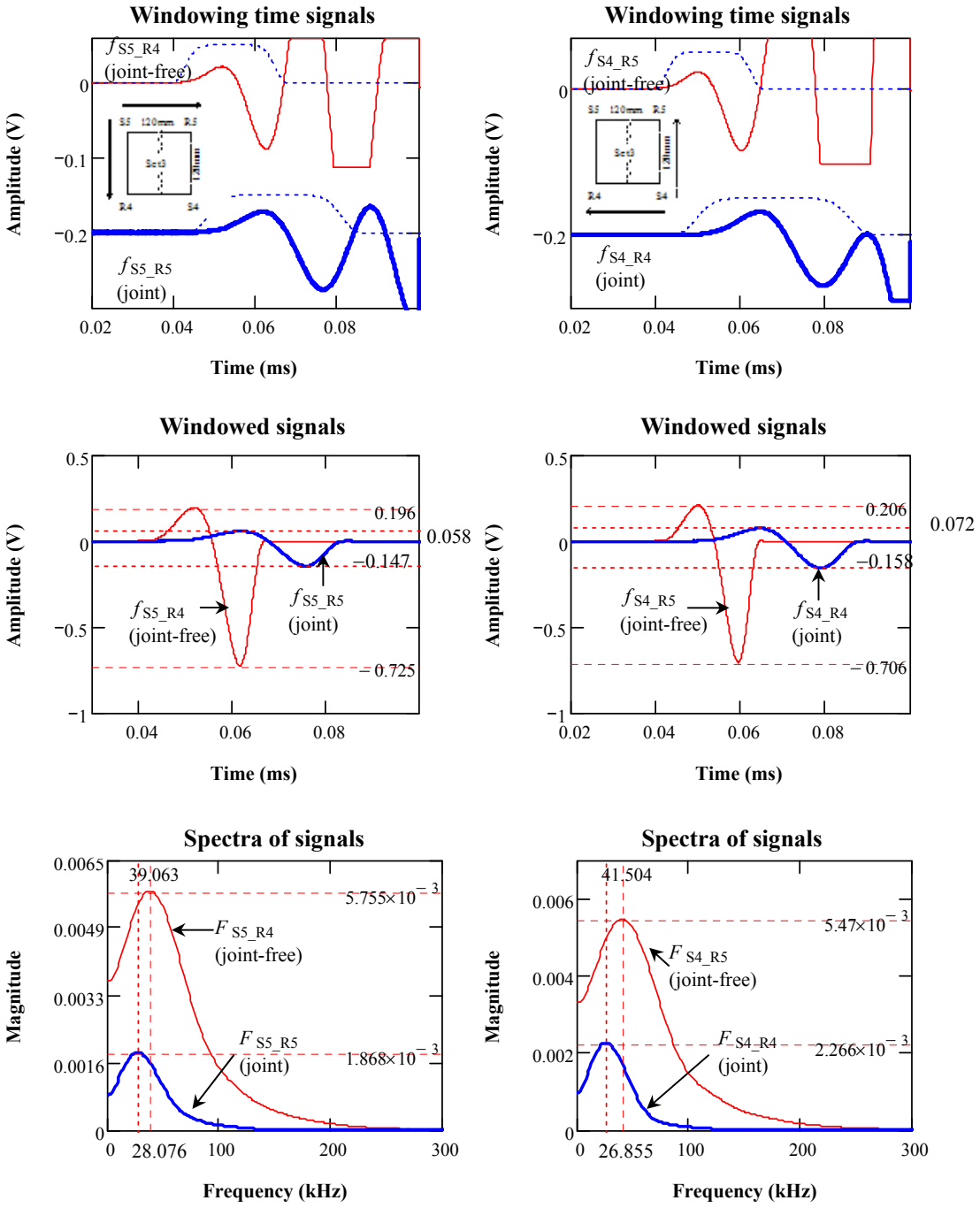

Figure P-13: P-wave analyses in time and frequency domains for Set 3 (120mm S-R spacing) on jointed surface (Horizontal lines mark the peak amplitudes and vertical lines dominant frequencies.)

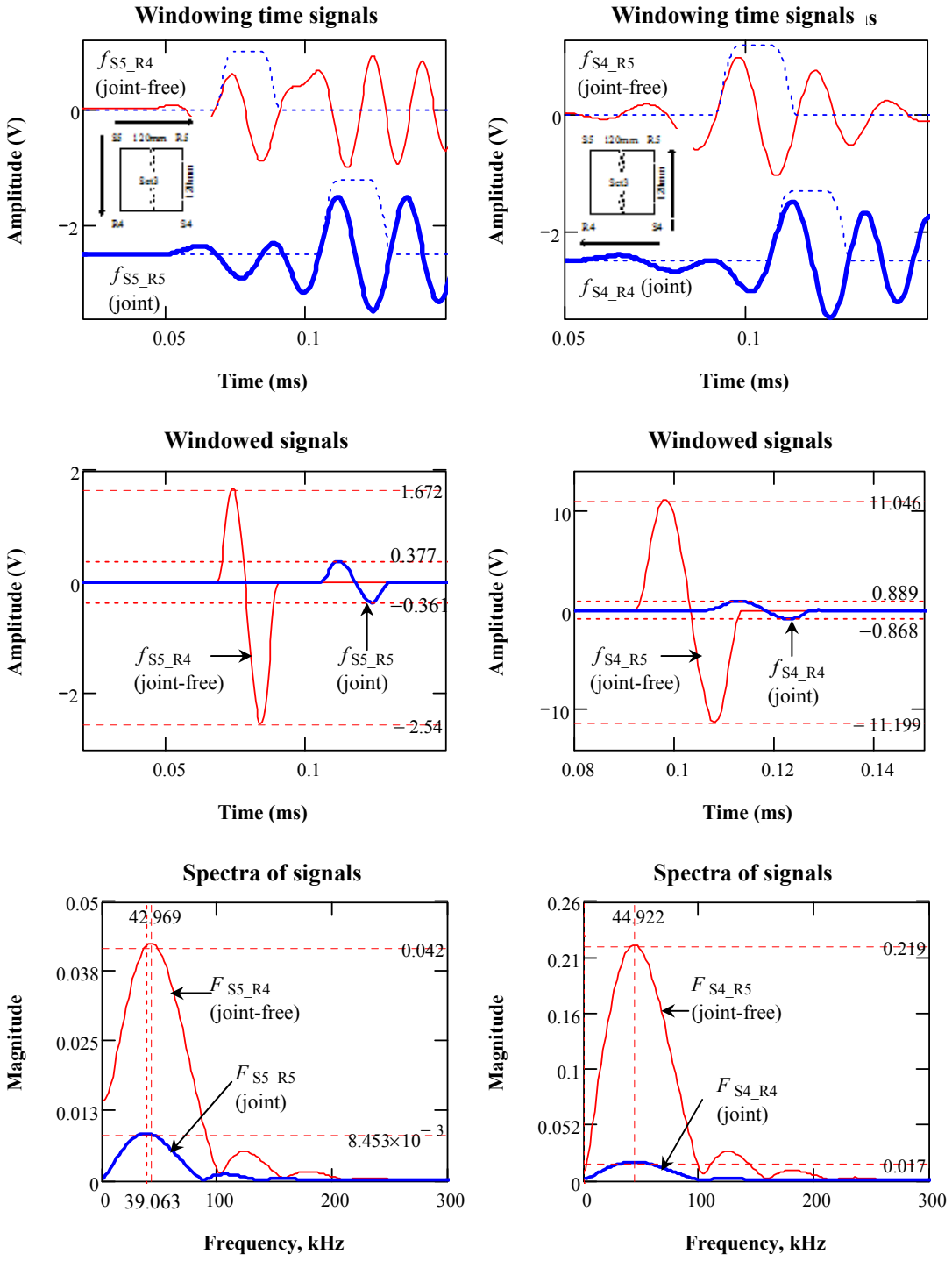

Figure P-14: R-wave analyses in time and frequency domains for Set 3 (120mm S-R spacing) on jointed surface (Horizontal lines mark the peak amplitudes and vertical lines dominant frequencies.)

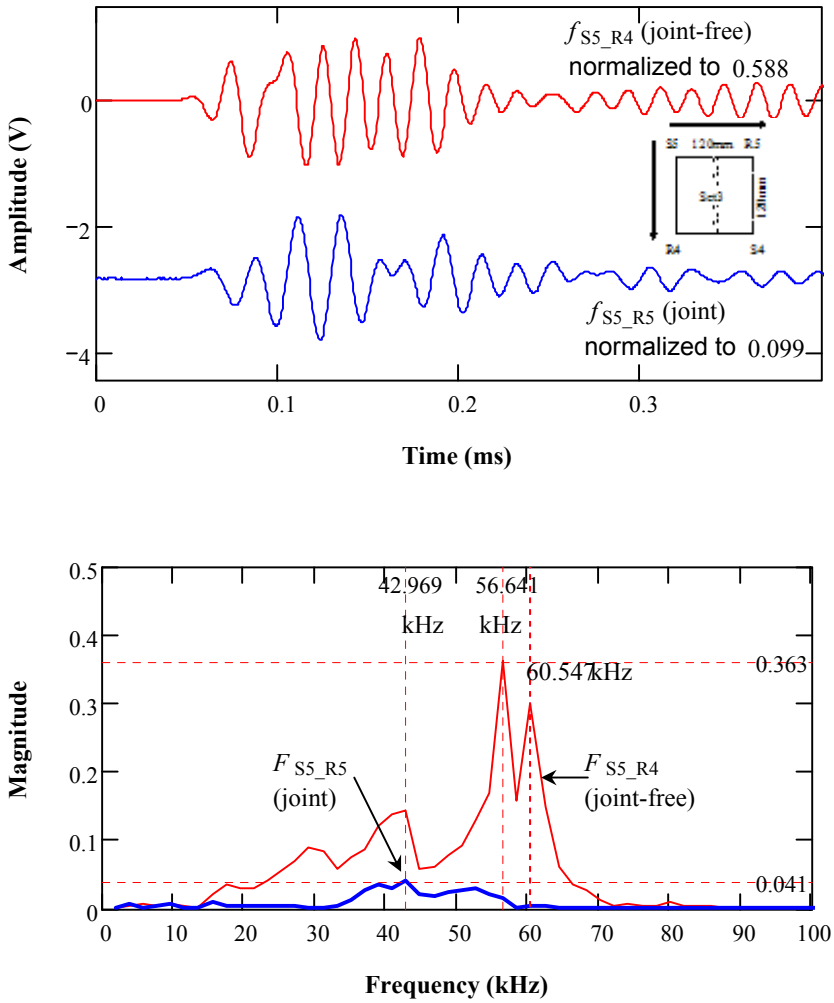

Figure P-15: Signal Pair 1 of repeated Set 3 measurements in time and frequency domains (120mm S-R spacing) on jointed surface (Horizontal lines mark the peak amplitudes and vertical lines dominant frequencies.)

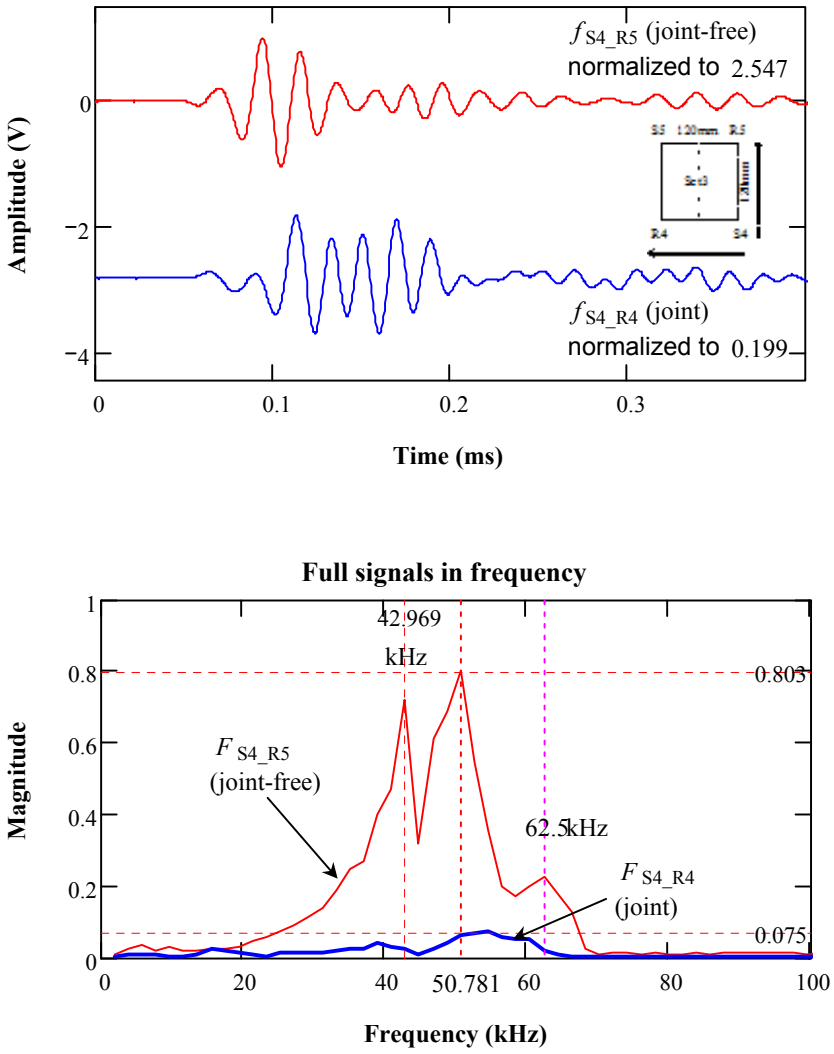

Figure P-16: Signal Pair 2 of repeated Set 3 measurements in time and frequency domains (120mm S-R spacing) on jointed surface (Horizontal lines mark the peak amplitudes and vertical lines dominant frequencies.)

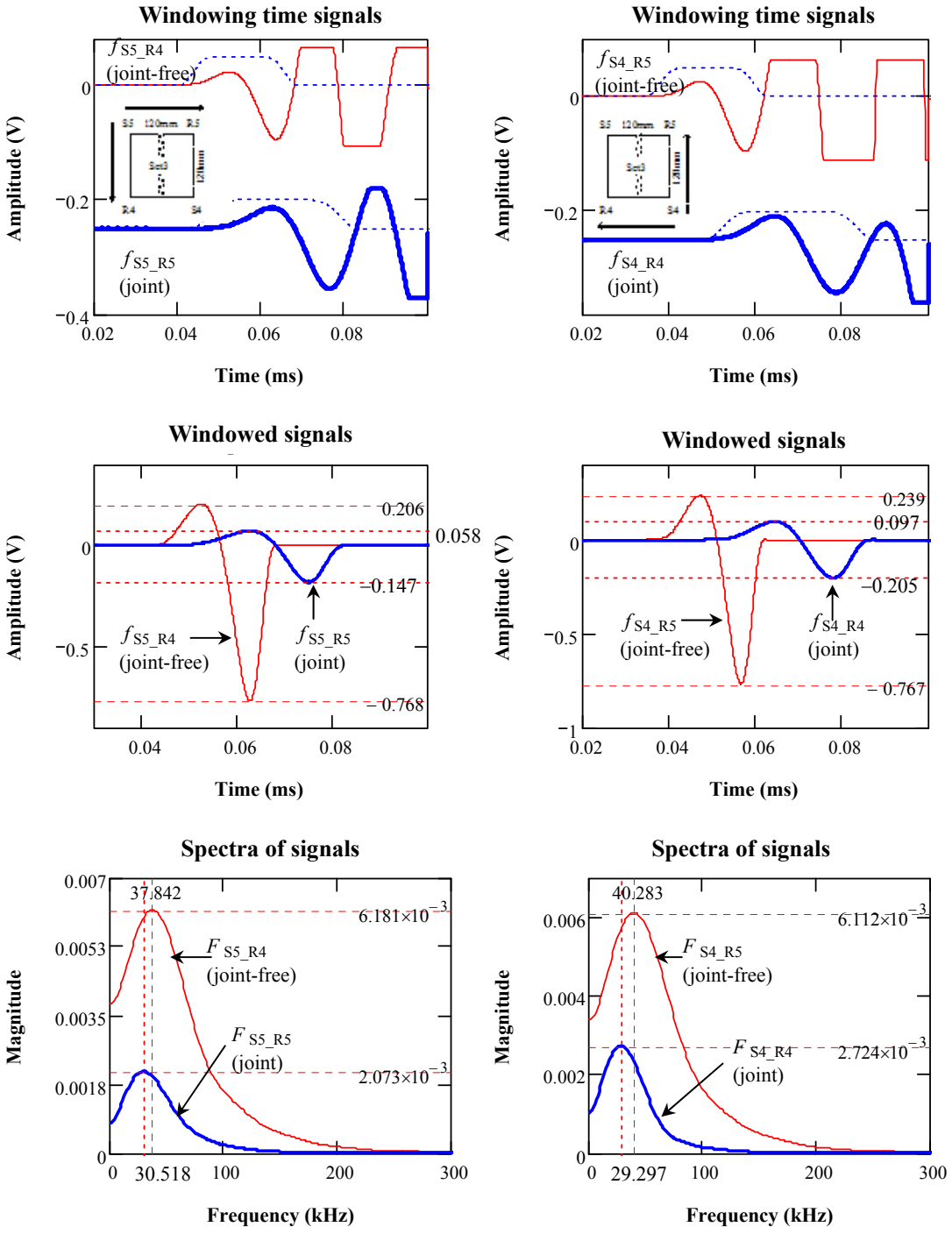

Figure P-17: P-wave analyses in time and frequency domains for repeated Set 3 measurements (120mm S-R spacing) on jointed surface (Horizontal lines mark the peak amplitudes and vertical lines dominant frequencies.)

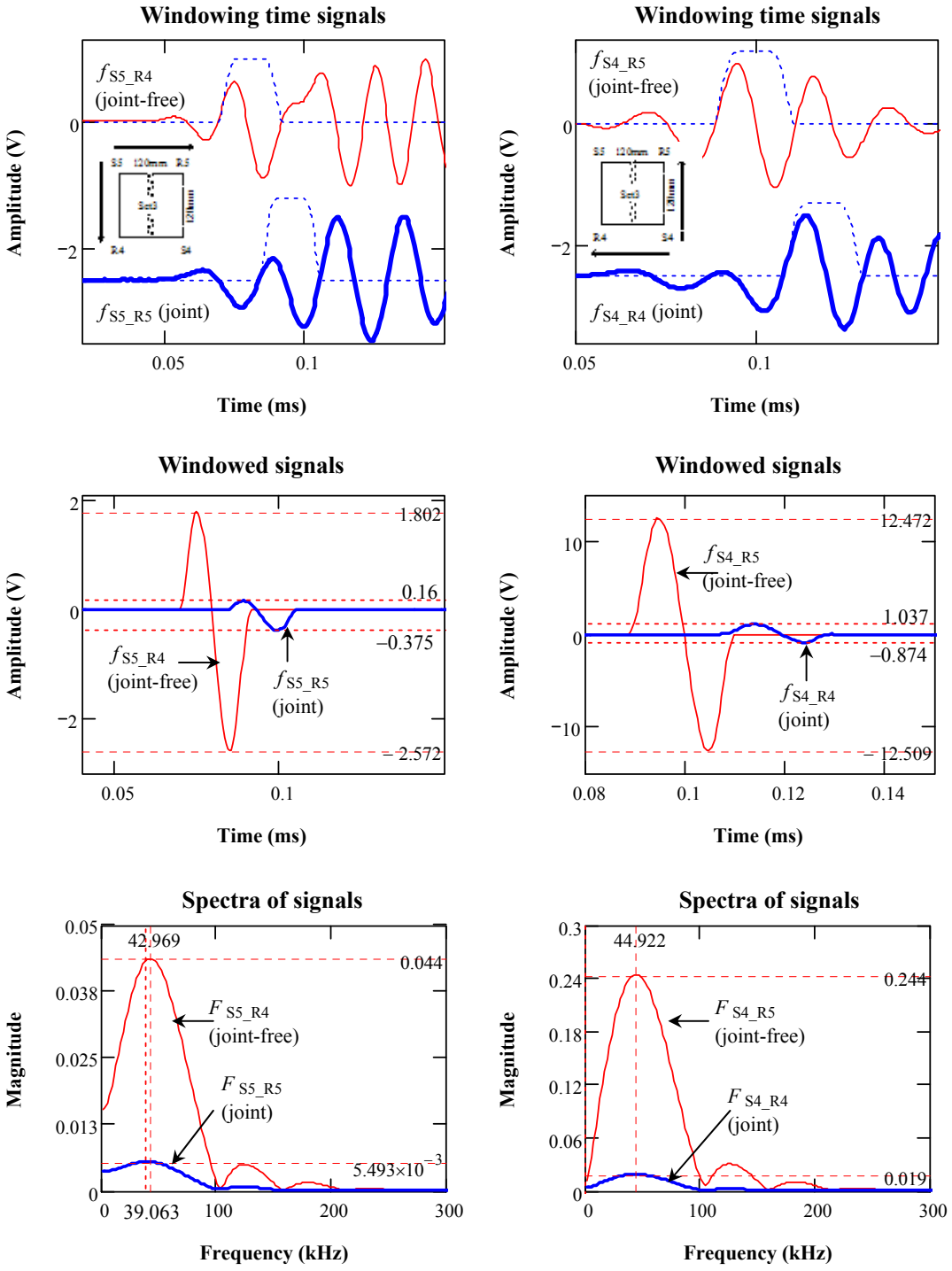

Figure P-18: R-wave analyses in time and frequency domains for repeated Set 3 measurements (120mm S-R spacing) on jointed surface (Horizontal lines mark the peak amplitudes and vertical lines dominant frequencies.)

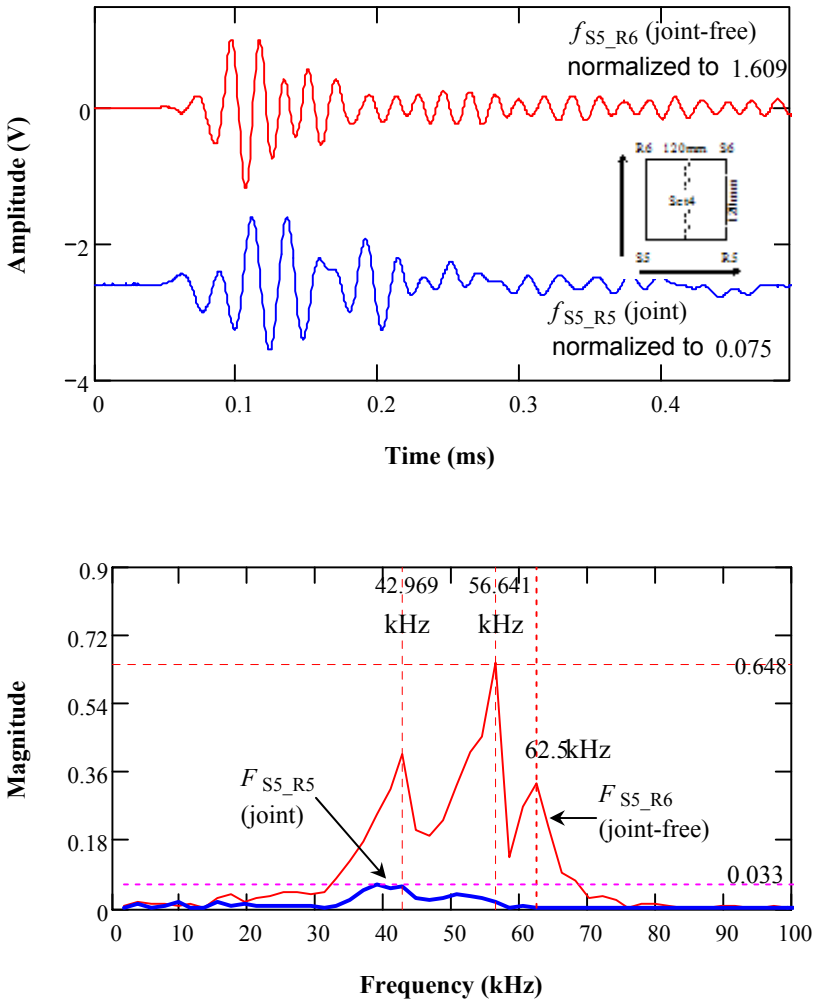

Figure P-19: Signal Pair 1 of Set 4 measurements in time and frequency domains (120mm S-R spacing) on jointed surface (Horizontal lines mark the peak amplitudes and vertical lines dominant frequencies.)

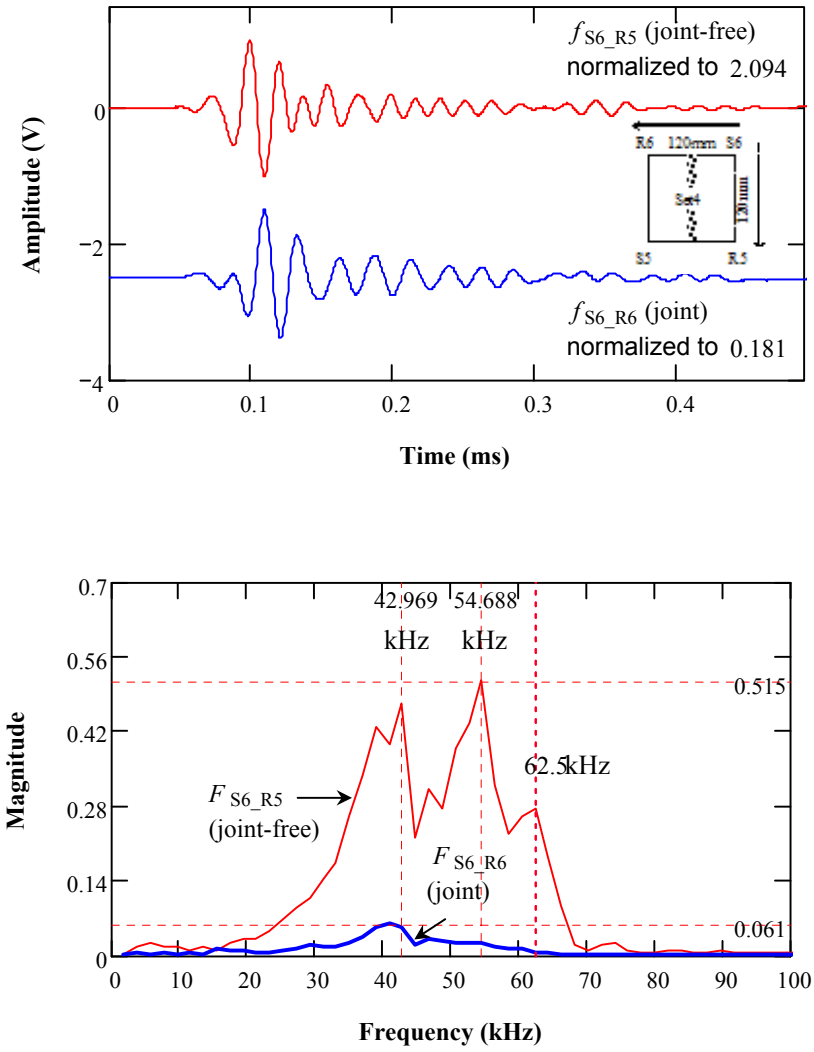

Figure P-20: Signal Pair 2 of Set 4 measurements in time and frequency domains (120mm S-R spacing) on jointed surface (Horizontal lines mark the peak amplitudes and vertical lines dominant frequencies.)

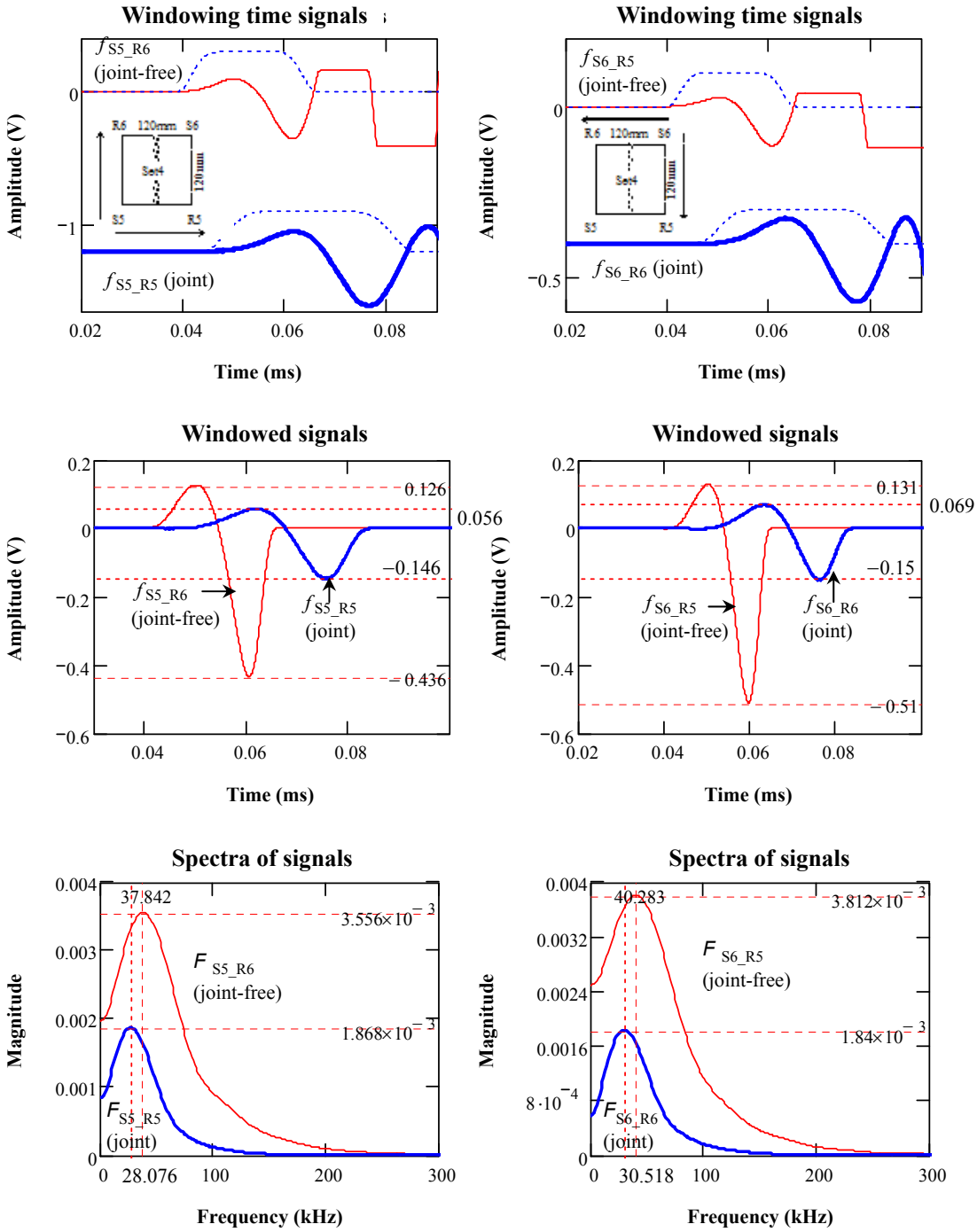

Figure P-21: P-wave analyses in time and frequency domains for Set 4 (120mm S-R spacing) on jointed surface (Horizontal lines mark the peak amplitudes and vertical lines dominant frequencies.)

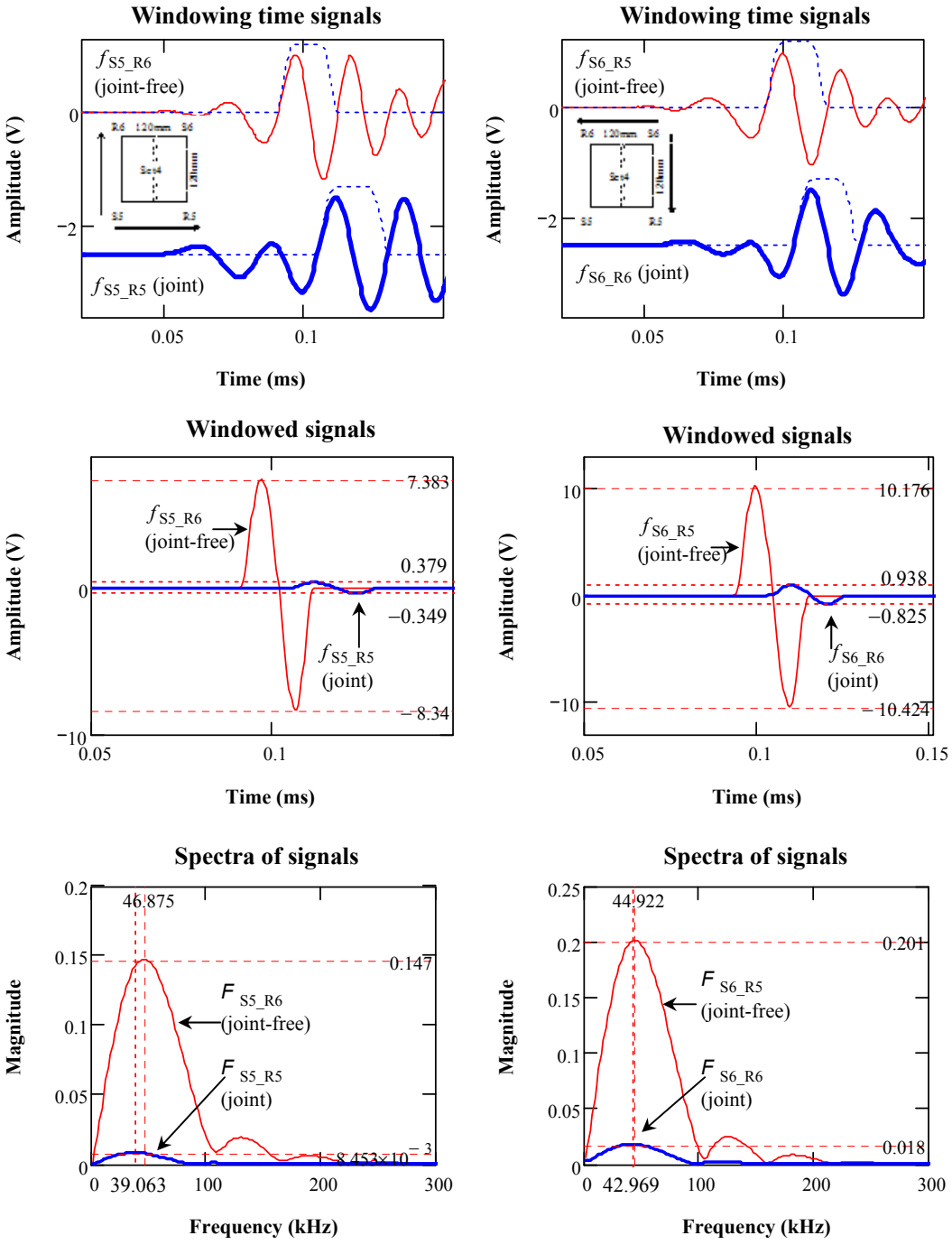

Figure P-22: R-wave analyses in time and frequency domains for Set 4 (120mm S-R spacing) on jointed surface (Horizontal lines mark the peak amplitudes and vertical lines dominant frequencies.)

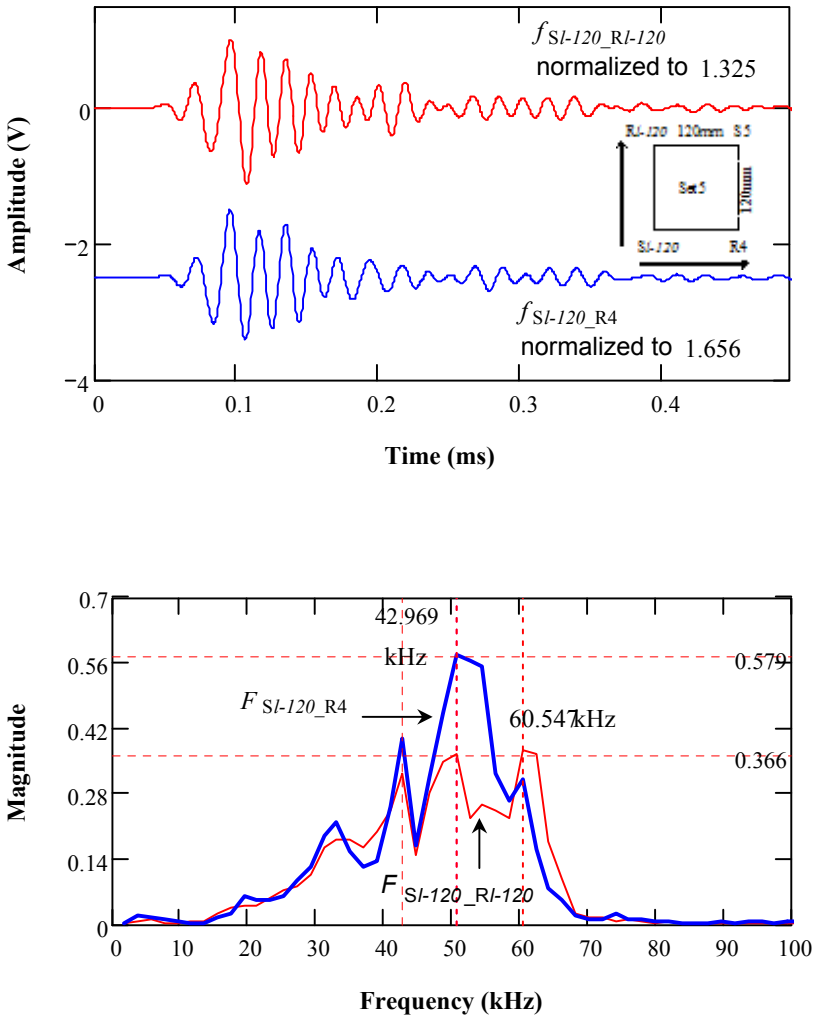

Figure P-23: Signal Pair 1 of Set 5 measurements in time and frequency domains (120mm S-R spacing) on the joint-free surface (Horizontal lines mark the peak amplitudes and vertical lines dominant frequencies.)

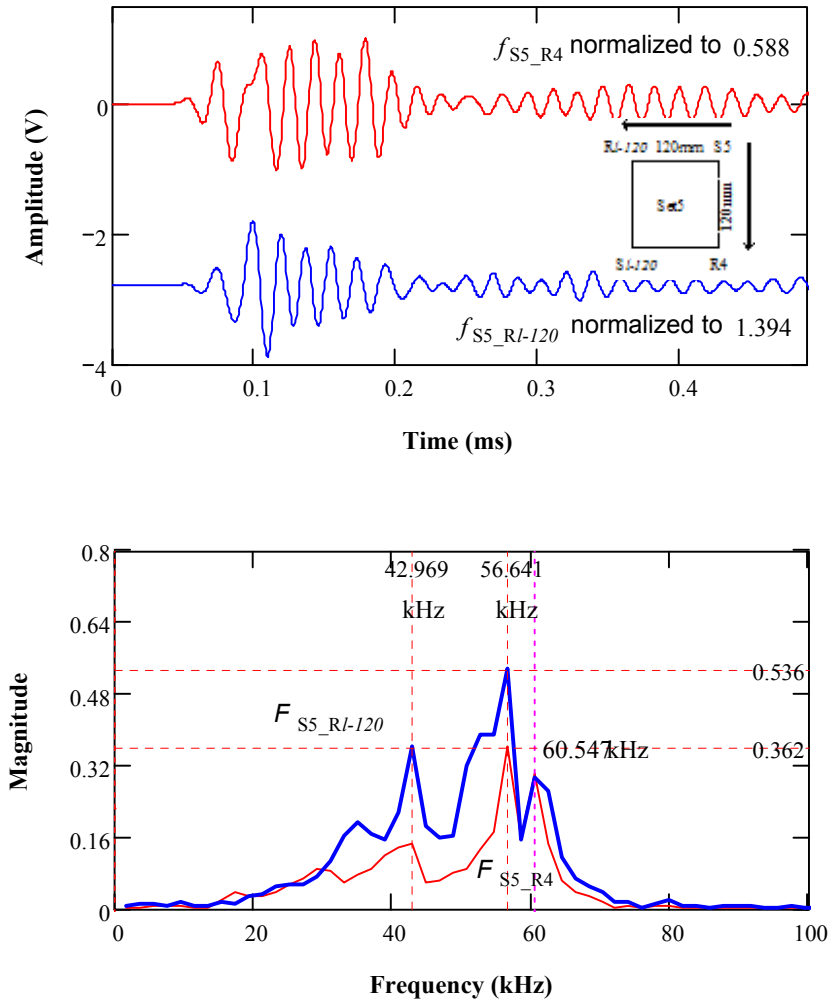

Figure P-24: Signal Pair 2 of Set 5 measurements in time and frequency domains (120mm S-R spacing) on the joint-free surface (Horizontal lines mark the peak amplitudes and vertical lines dominant frequencies.)

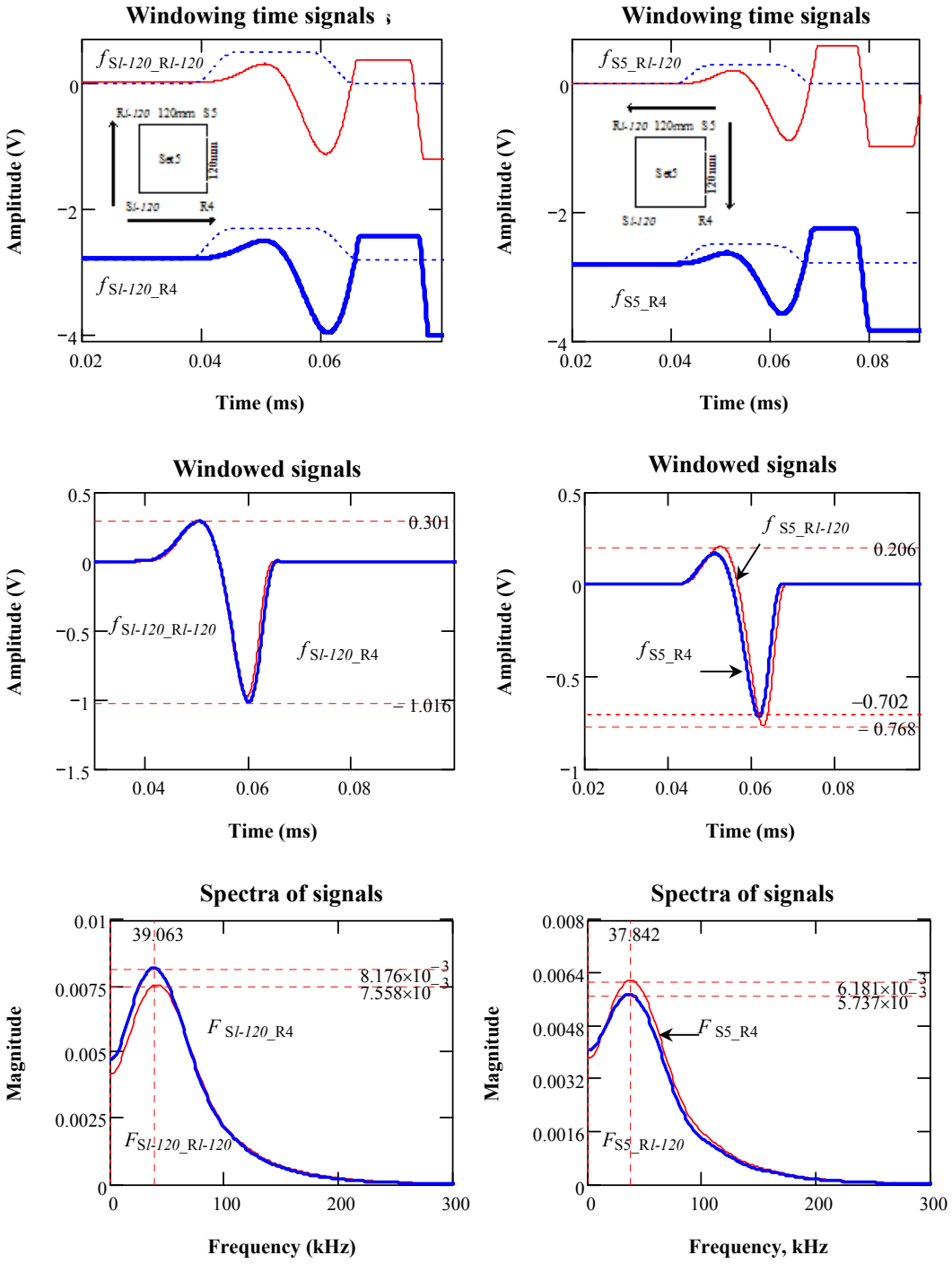

Figure P-25: P-wave analyses in time and frequency domains for Set 5 (120mm S-R spacing) on the joint-free surface (Horizontal lines mark the peak amplitudes and vertical lines dominant frequencies.)

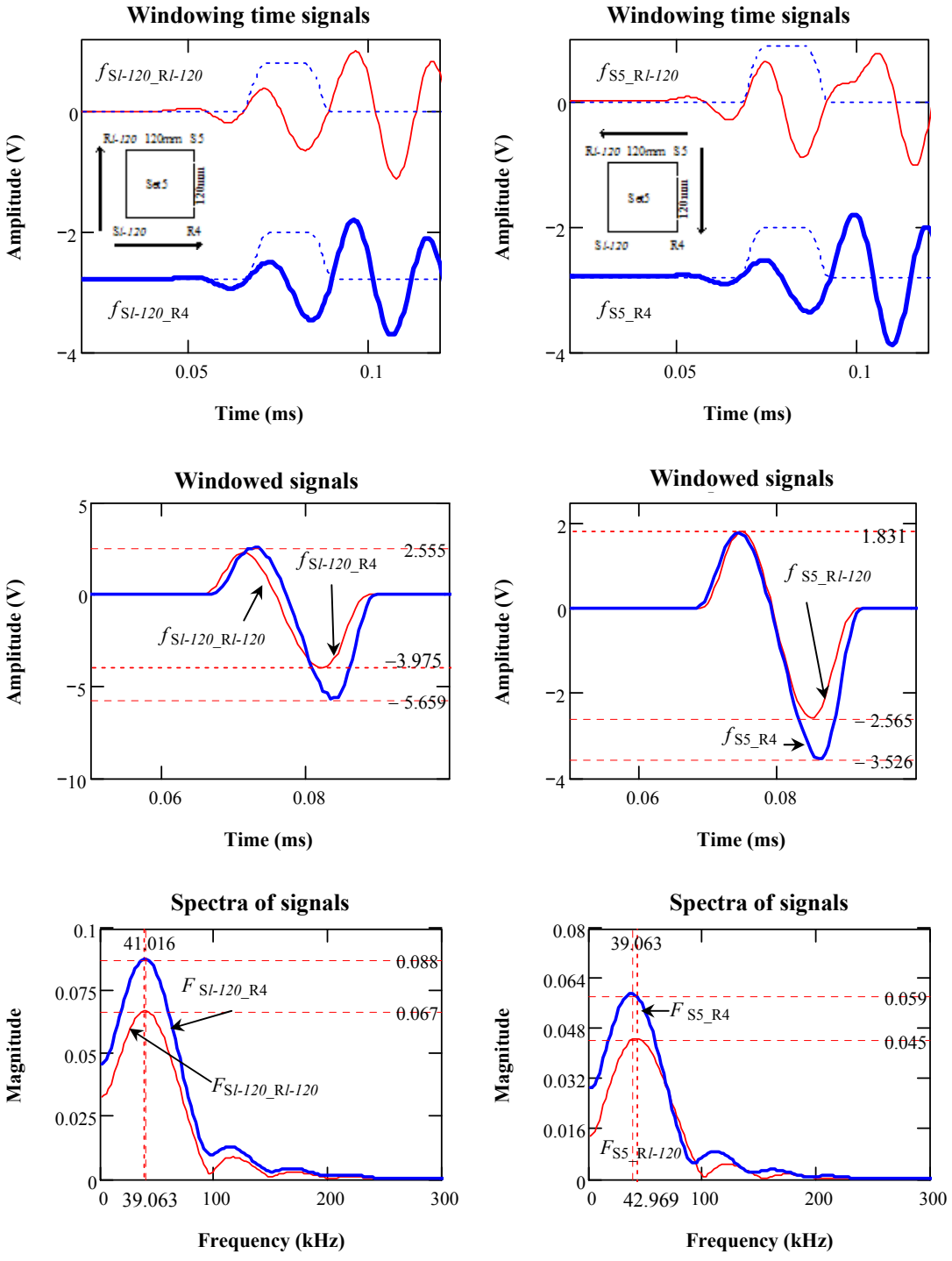

Figure P-26: R-wave analyses in time and frequency domains for Set 5 (120mm S-R spacing) on the joint-free surface (Horizontal lines mark the peak amplitudes and vertical lines dominant frequencies.)

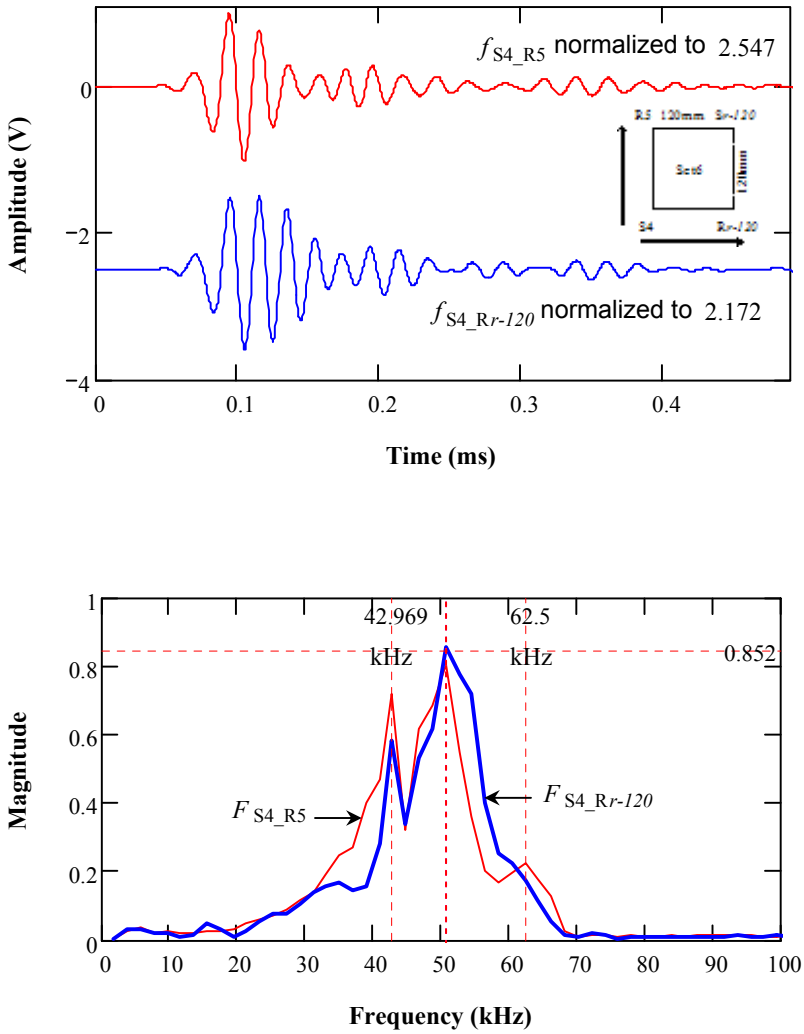

Figure P-27: Signal Pair 1 of Set 6 measurements in time and frequency domains (120mm S-R spacing) on the joint-free surface (Horizontal lines mark the peak amplitudes and vertical lines dominant frequencies.)

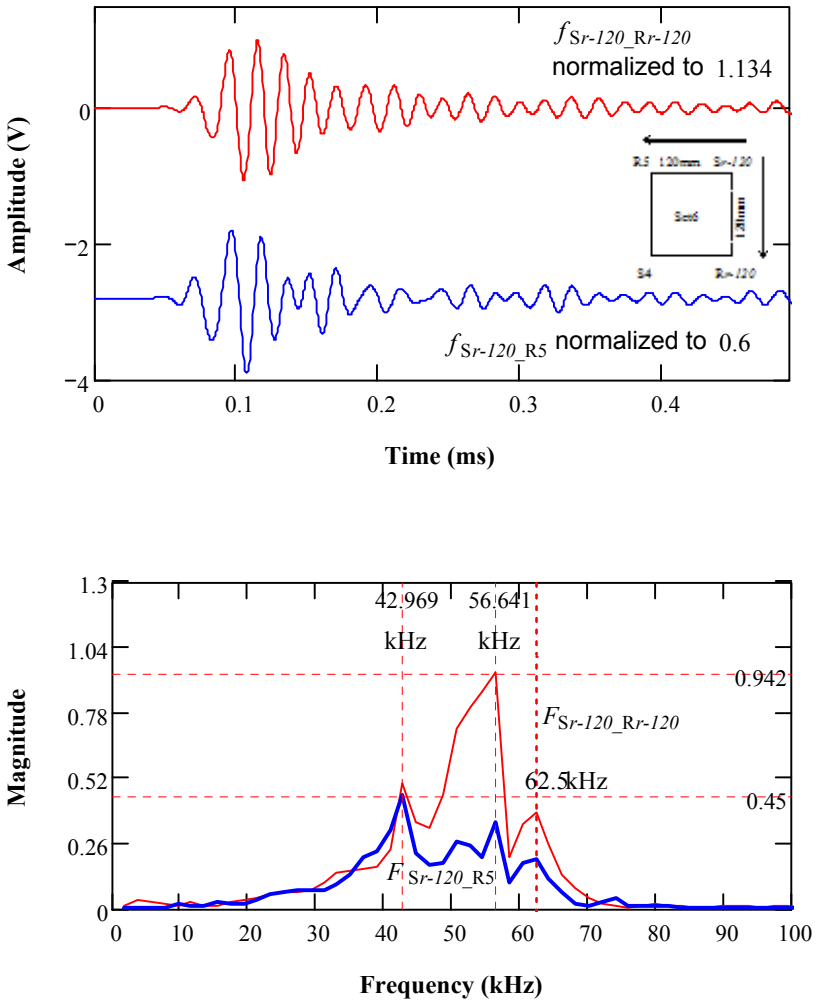

Figure P-28: Signal Pair 2 of Set 6 measurements in time and frequency domains (120mm S-R spacing) on the joint-free surface (Horizontal lines mark the peak amplitudes and vertical lines dominant frequencies.)

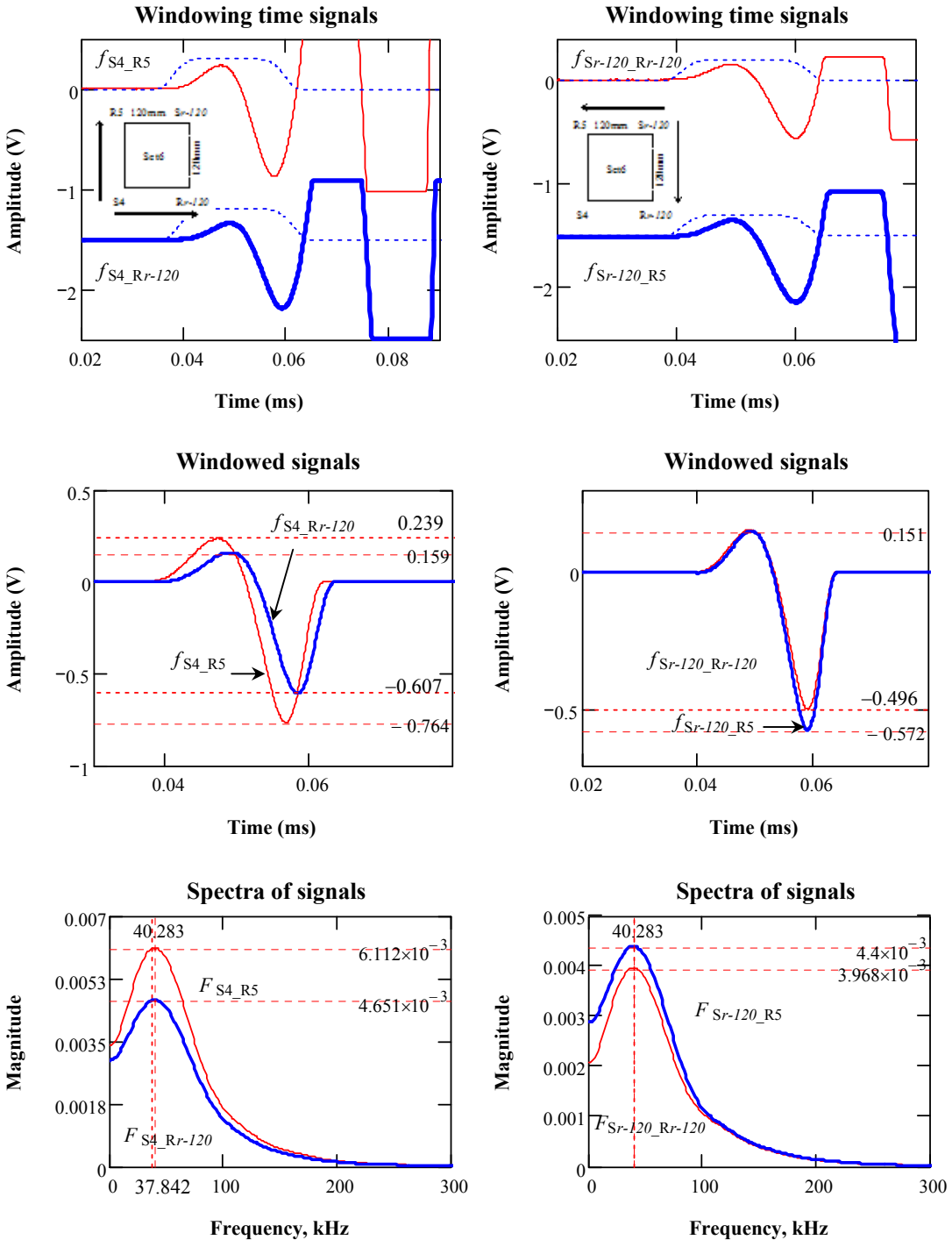

Figure P-29: P-wave analyses in time and frequency domains for Set 6 (120mm S-R spacing) on the joint-free surface (Horizontal lines mark the peak amplitudes and vertical lines dominant frequencies.)

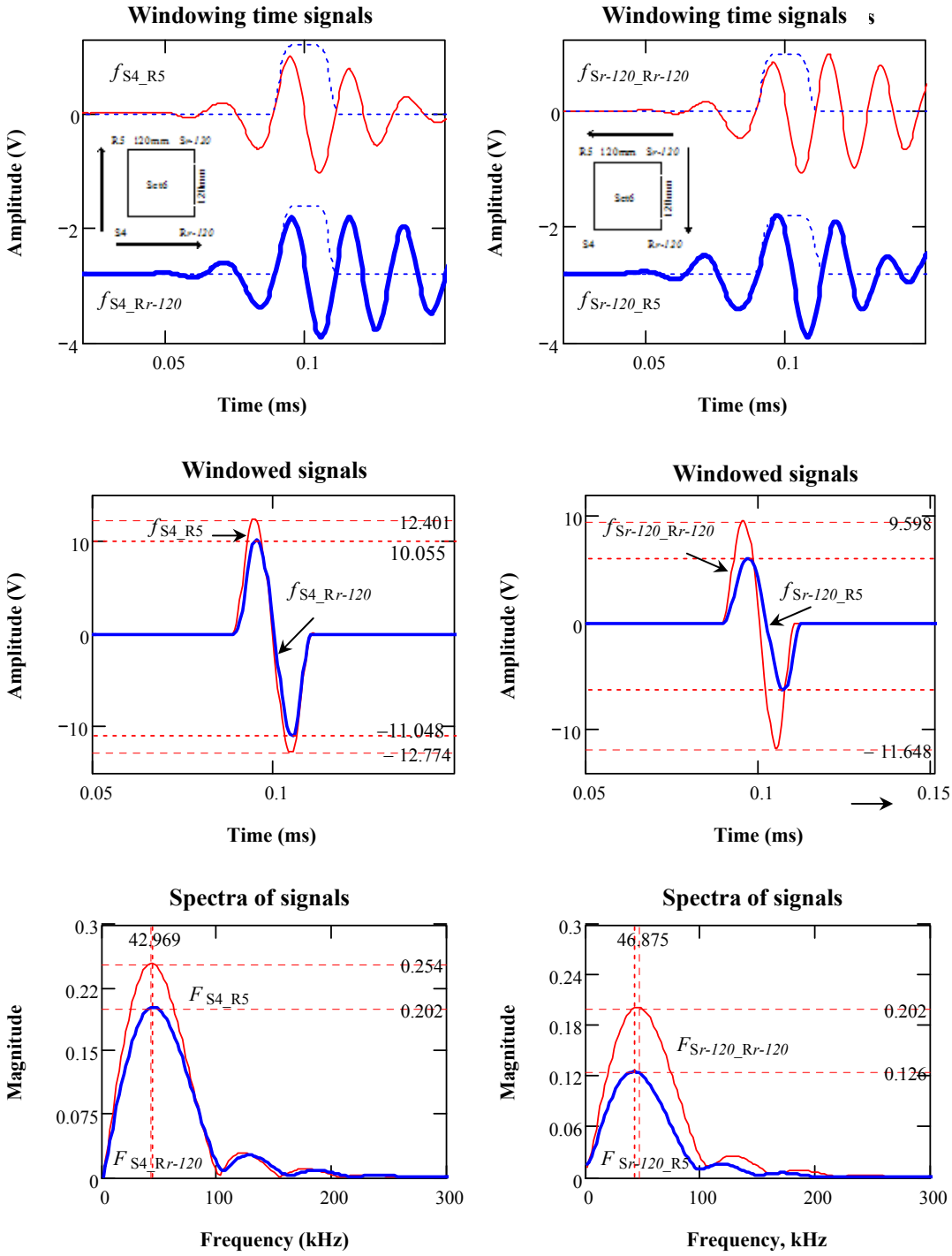

Figure P-30: R-wave analyses in time and frequency domains for Set 6 (120mm S-R spacing) on the joint-free surface (Horizontal lines mark the peak amplitudes and vertical lines dominant frequencies.)

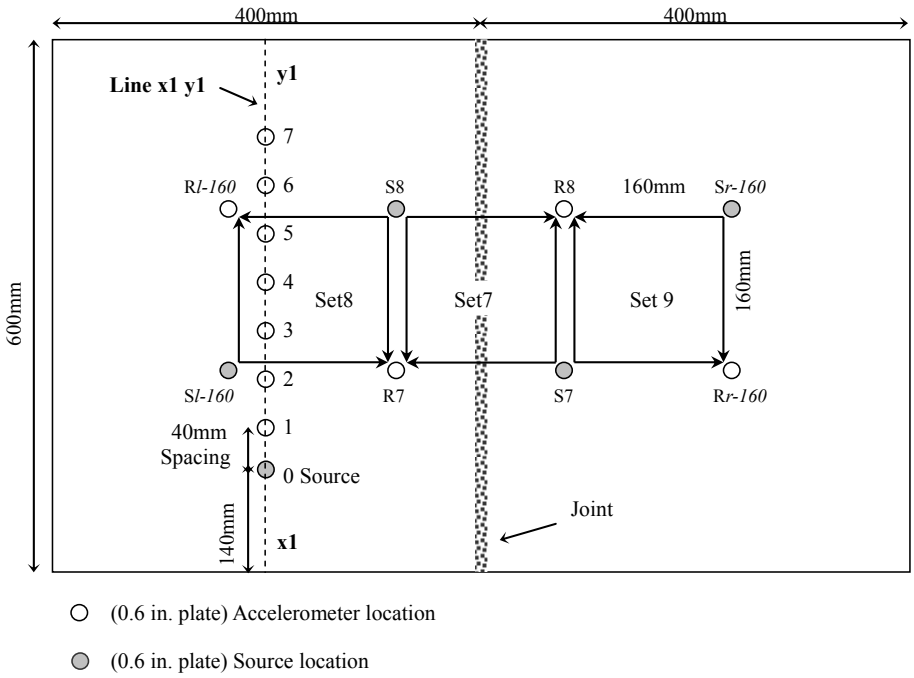

Figure P-31: 160mm S-R spacing configuration of HMA slab 3

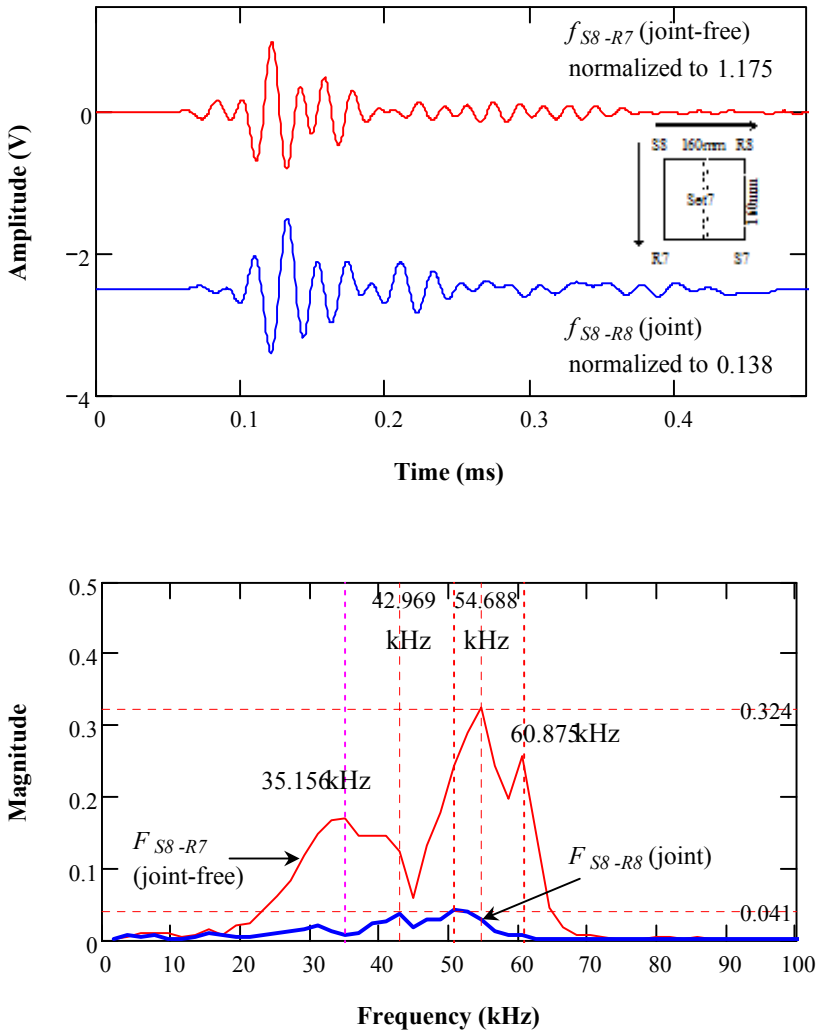

Figure P-32: Signal Pair 1 of Set 7 measurements in time and frequency domains (160mm S-R spacing) on the jointed surface (Horizontal lines mark the peak amplitudes and vertical lines dominant frequencies.)

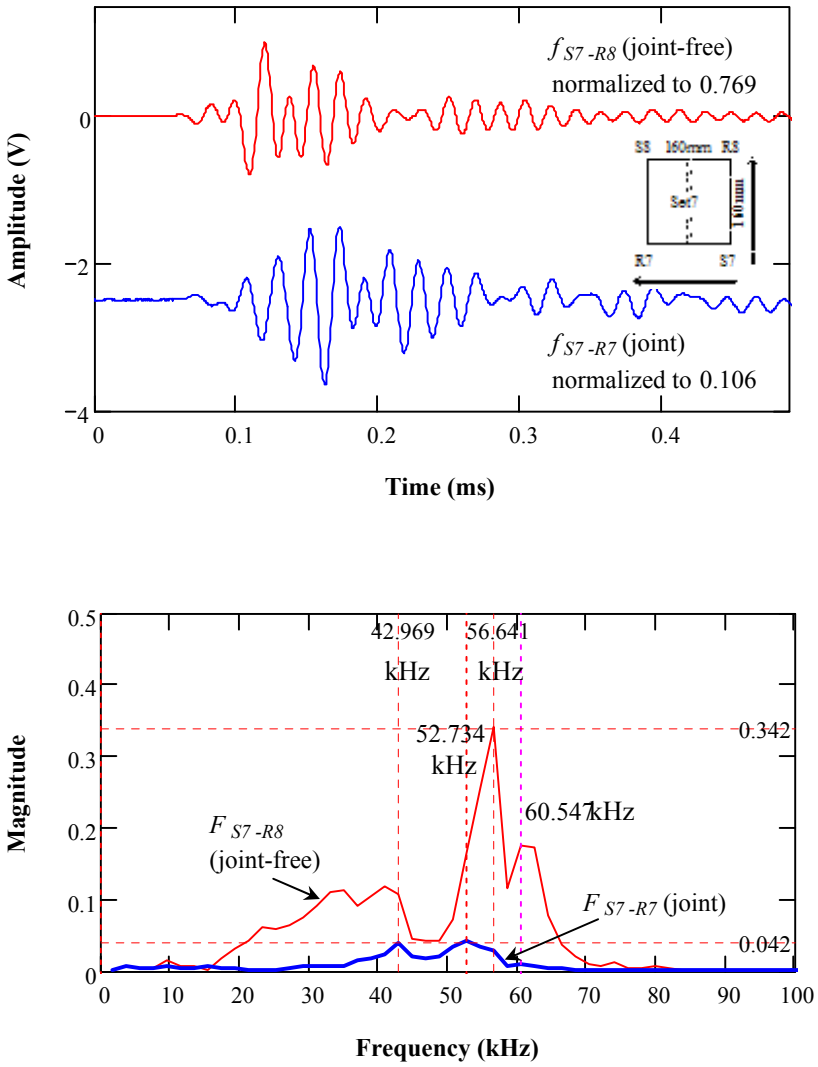

Figure P-33: Signal Pair 2 of Set 7 measurements in time and frequency domains (160mm S-R spacing) on the jointed surface (Horizontal lines mark the peak amplitudes and vertical lines dominant frequencies.)

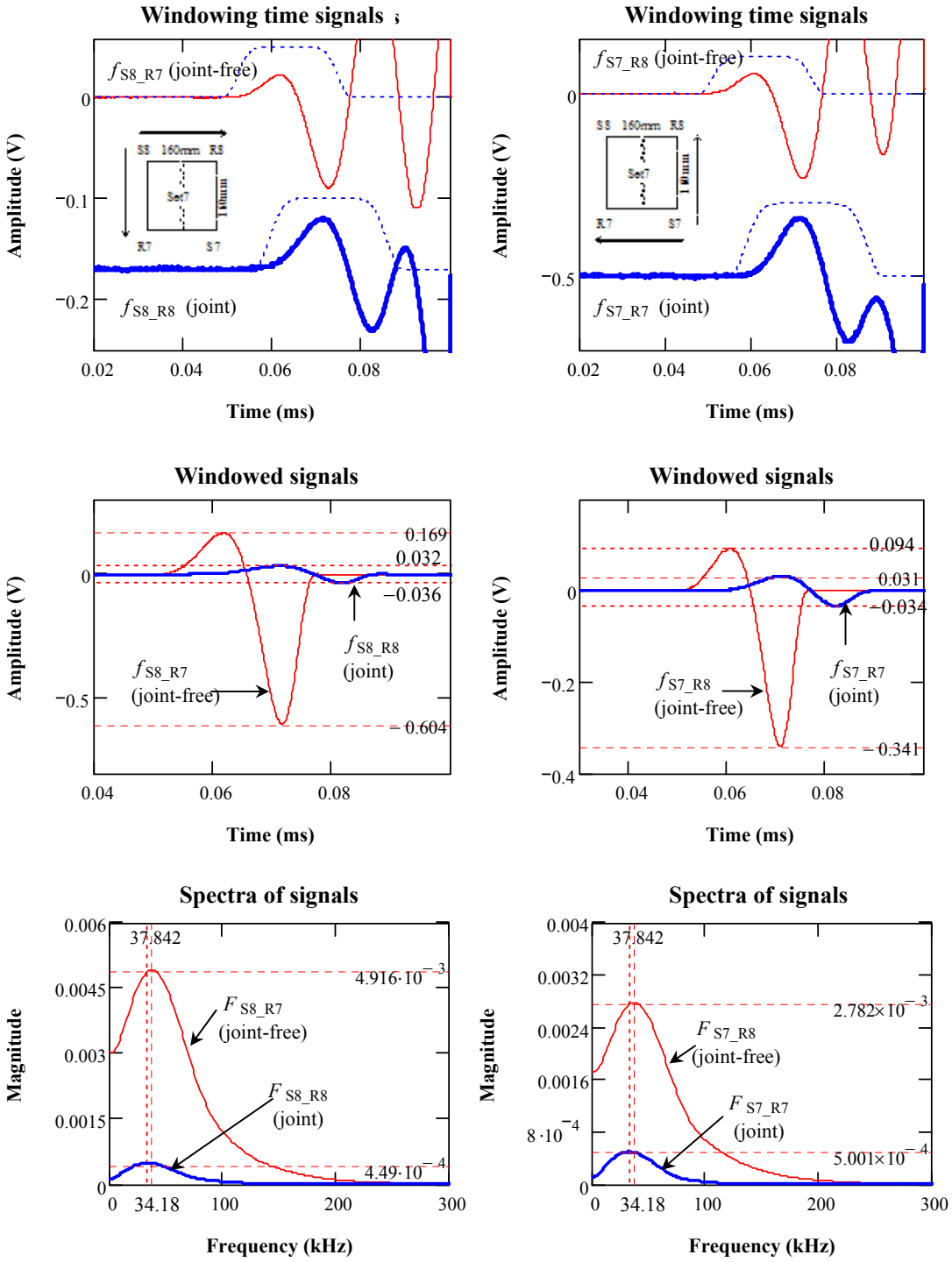

Figure P-34: P-wave analyses in time and frequency domains for Set 7 (160mm S-R spacing) on the jointed surface (Horizontal lines mark the peak amplitudes and vertical lines dominant frequencies.)

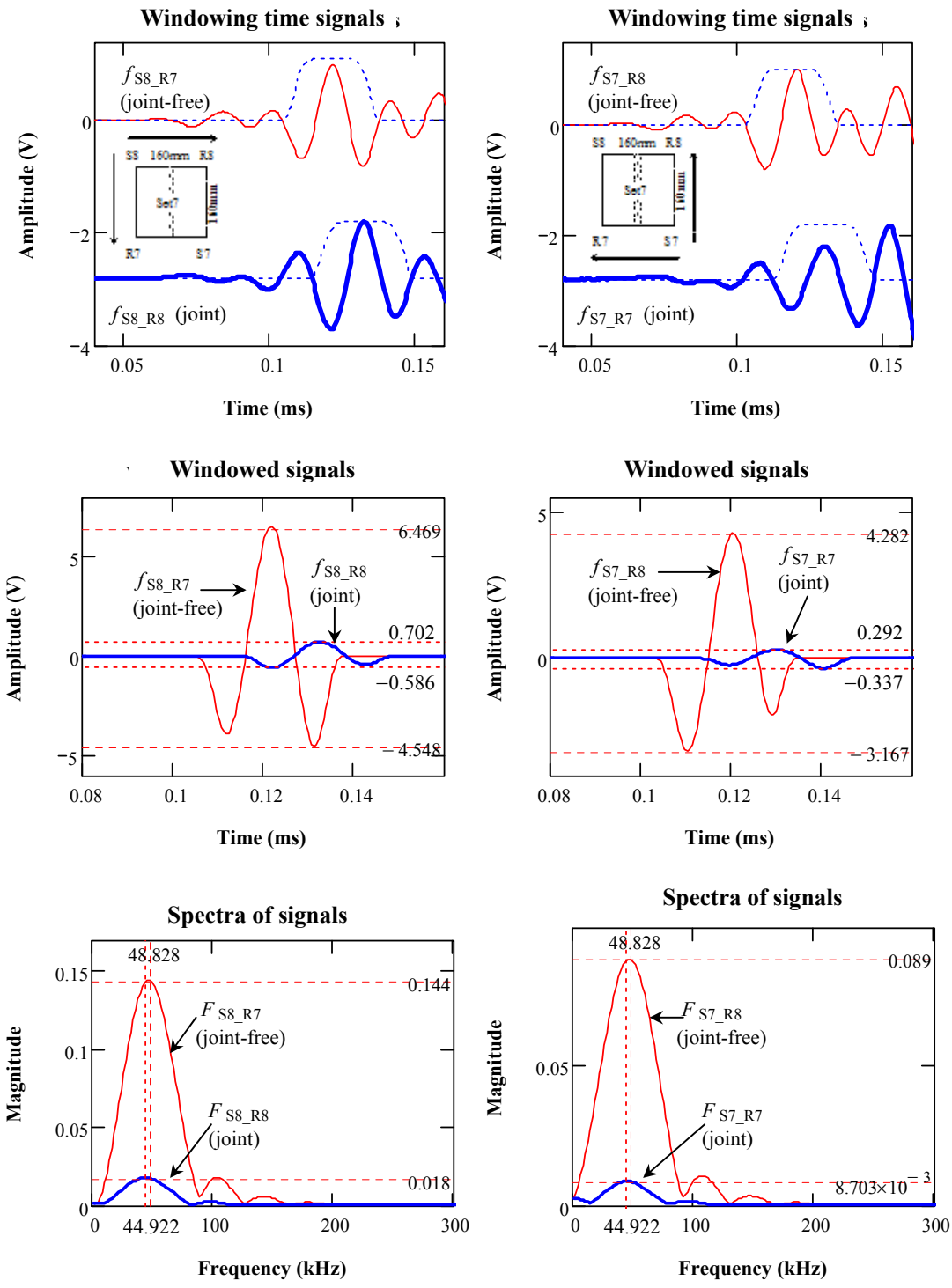

Figure P-35: R-wave analyses in time and frequency domains for Set 7 (160mm S-R spacing) on the jointed surface (Horizontal lines mark the peak amplitudes and vertical lines dominant frequencies.)

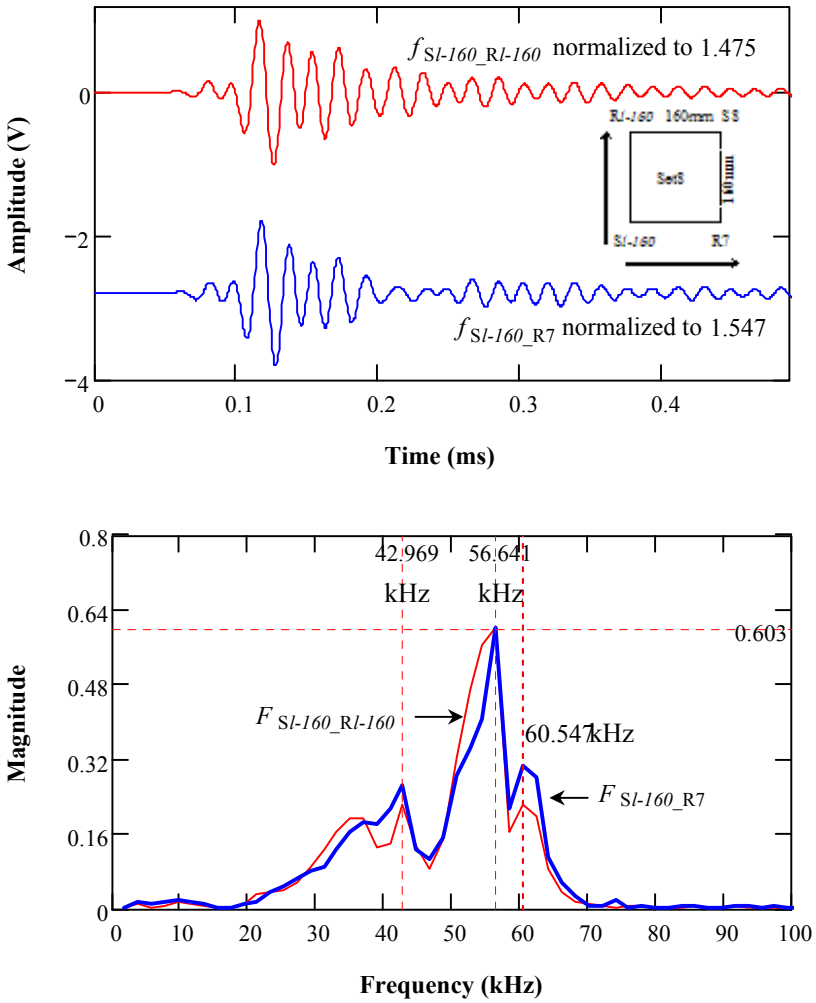

Figure P-36: Signal Pair 1 of Set 8 measurements in time and frequency domains (160mm S-R spacing) on the joint-free surface (Horizontal lines mark the peak amplitudes and vertical lines dominant frequencies.)

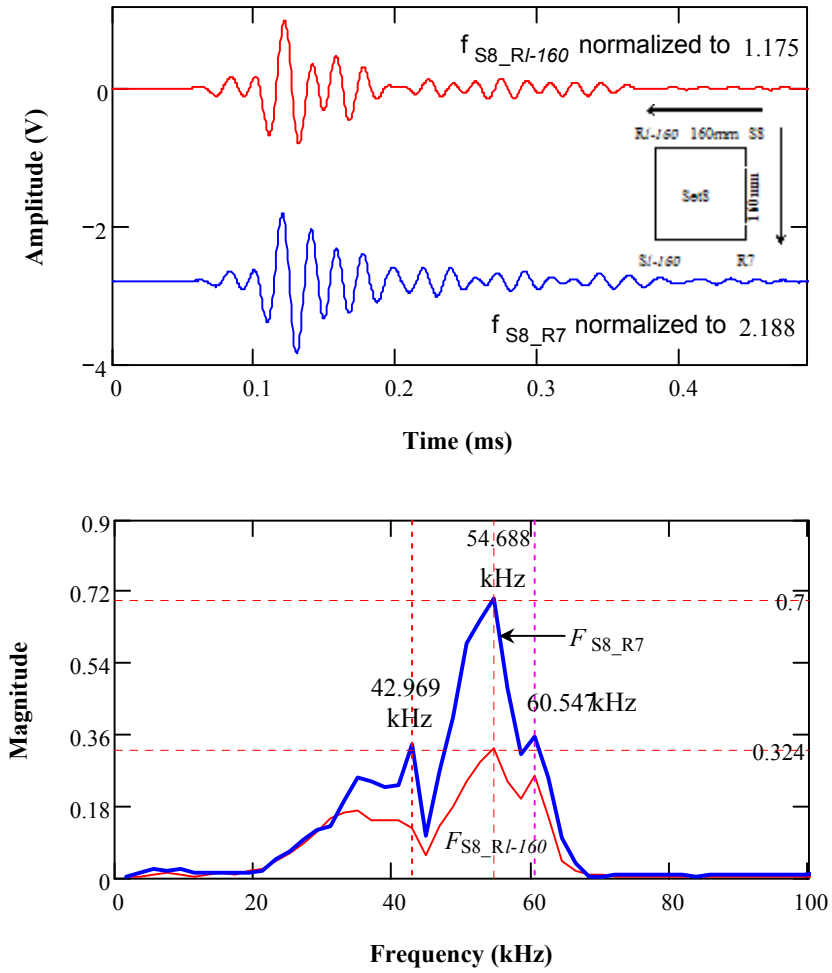

Figure P-37: Signal Pair 2 of Set 8 measurements in time and frequency domains (160mm S-R spacing) on the joint-free surface (Horizontal lines mark the peak amplitudes and vertical lines dominant frequencies.)

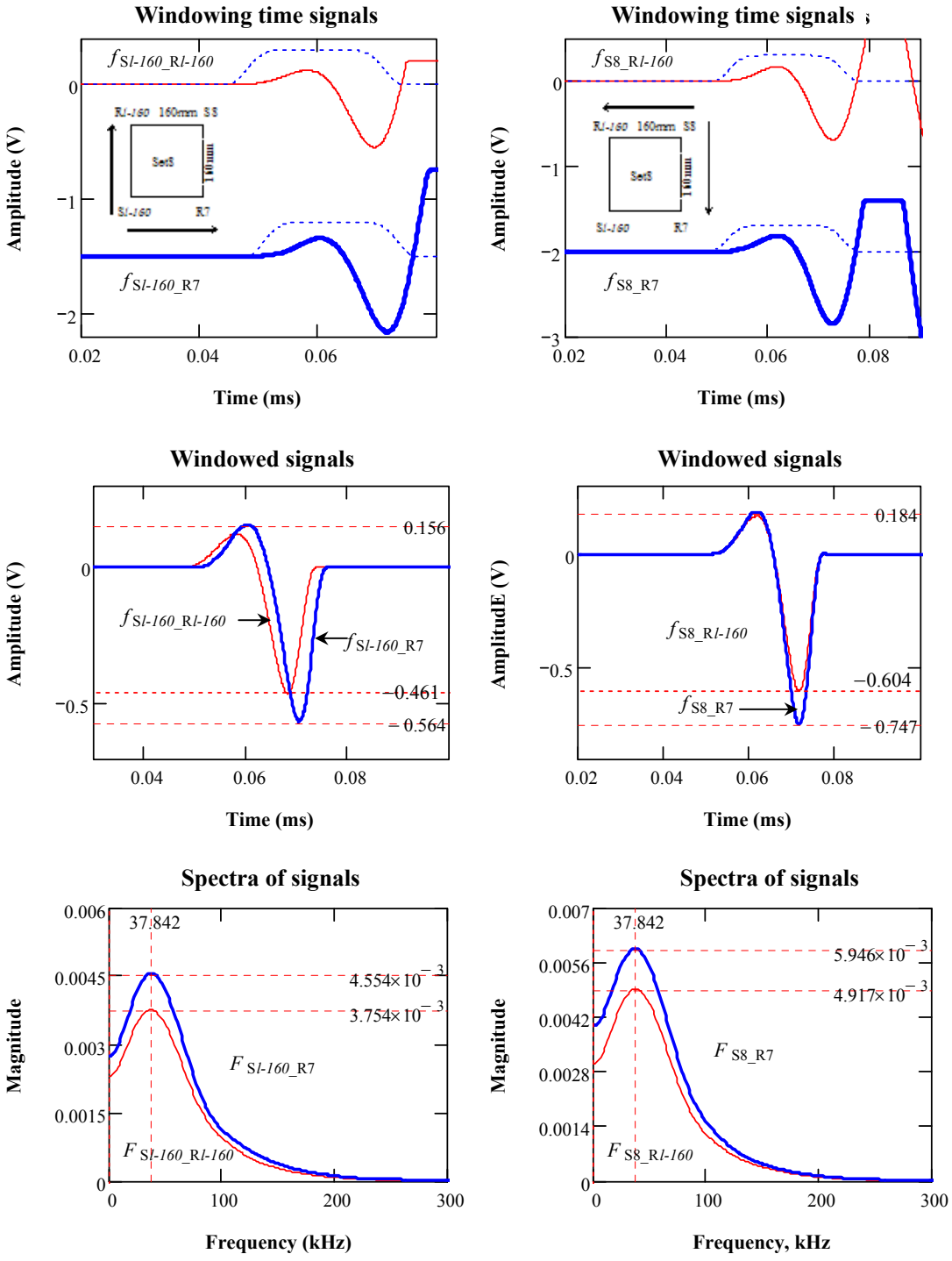

Figure P-38: P-wave analyses in time and frequency domains for Set 8 (160mm S-R spacing) on the joint-free surface (Horizontal lines mark the peak amplitudes and vertical lines dominant frequencies.)

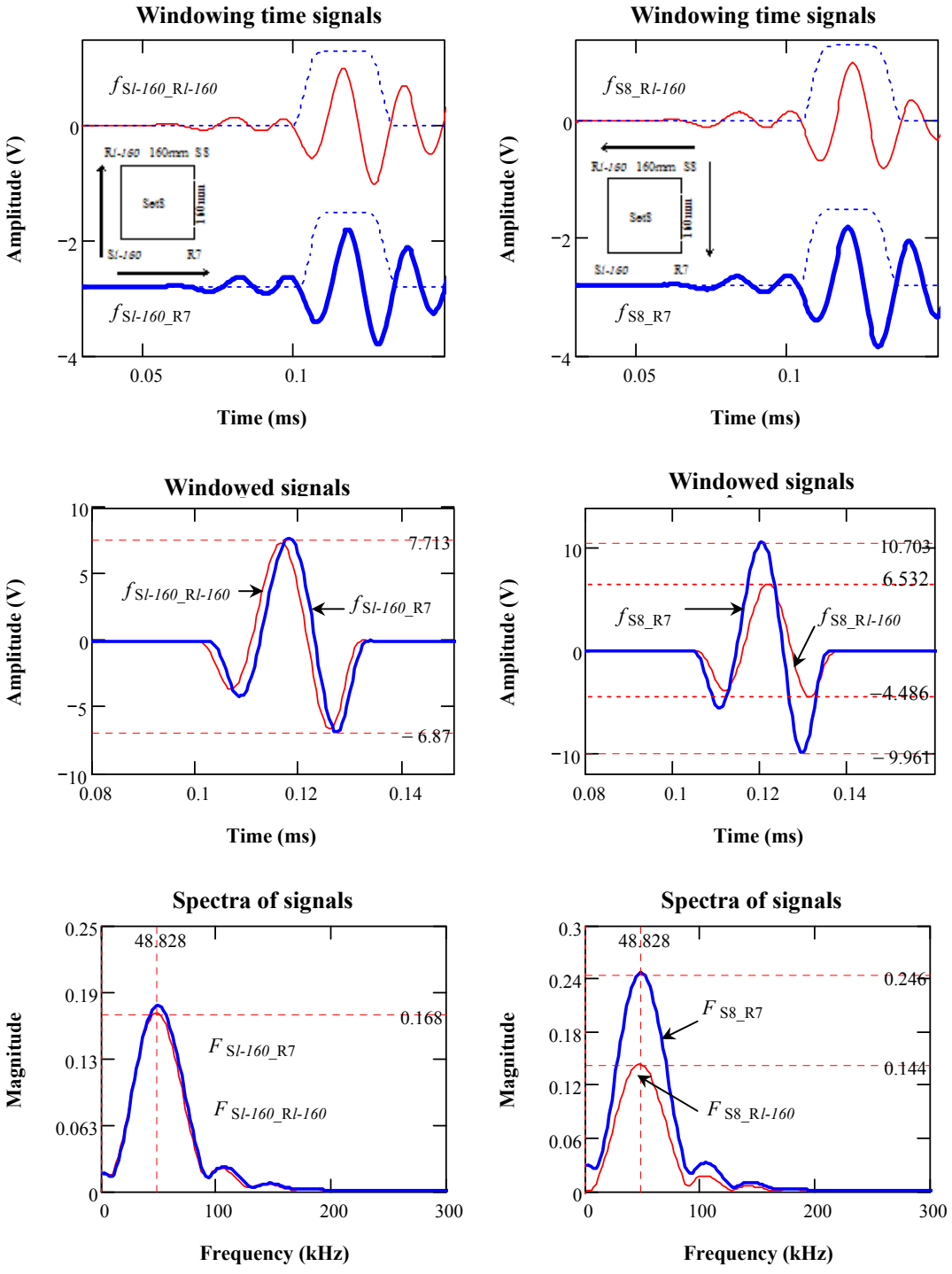

Figure P-39: R-wave analyses in time and frequency domains for Set 8 (160mm S-R spacing) on the joint-free surface (Horizontal lines mark the peak amplitudes and vertical lines dominant frequencies.)

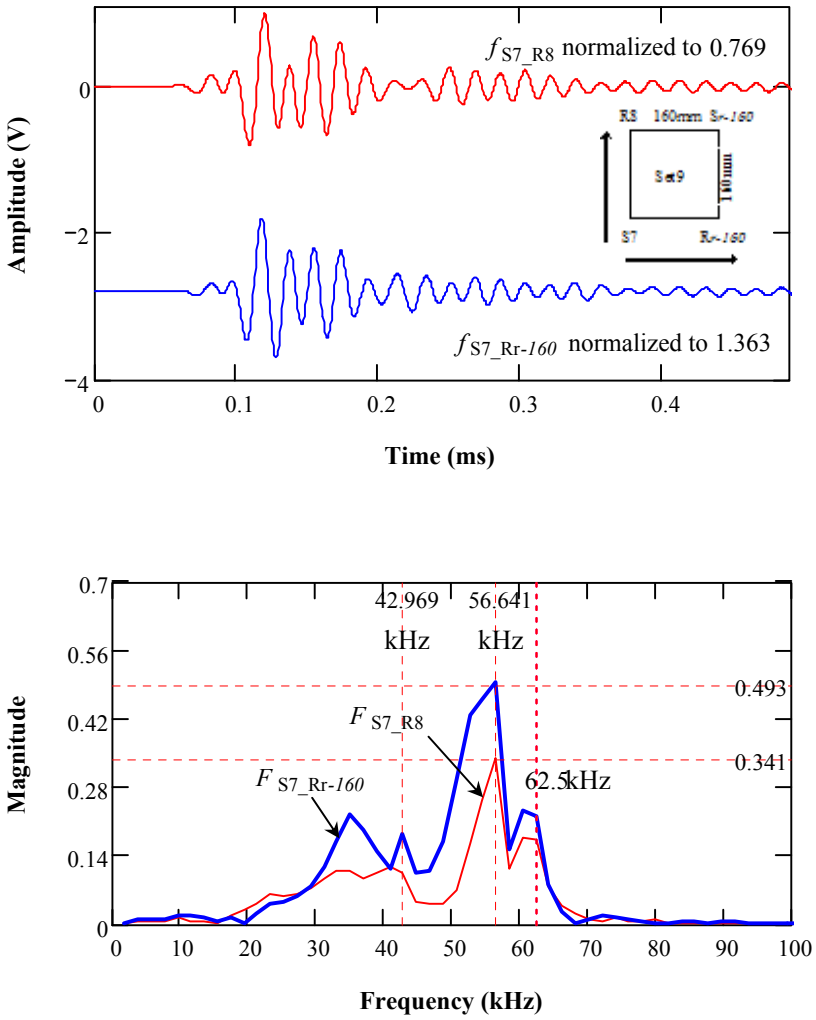

Figure P-40: Signal Pair 1 of Set 9 measurements in time and frequency domains (160mm S-R spacing) on the joint-free surface (Horizontal lines mark the peak amplitudes and vertical lines dominant frequencies.)

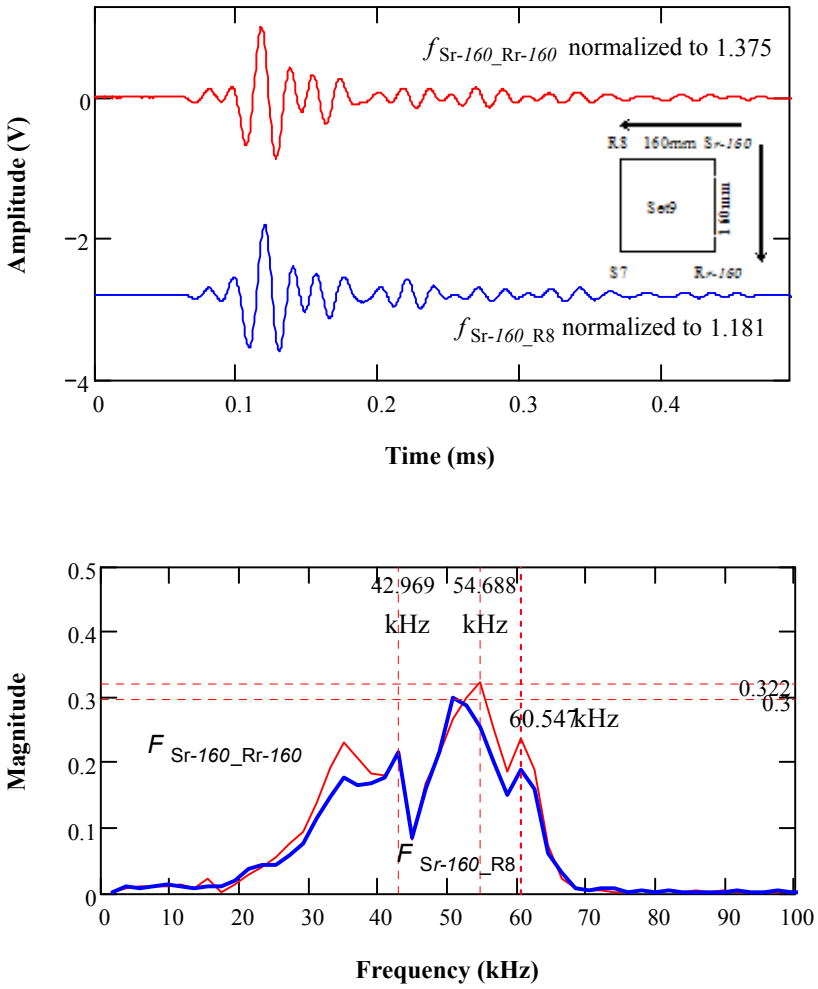

Figure P-41: Signal Pair 2 of Set 9 measurements in time and frequency domains (160mm S-R spacing) on the joint-free surface (Horizontal lines mark the peak amplitudes and vertical lines dominant frequencies.)

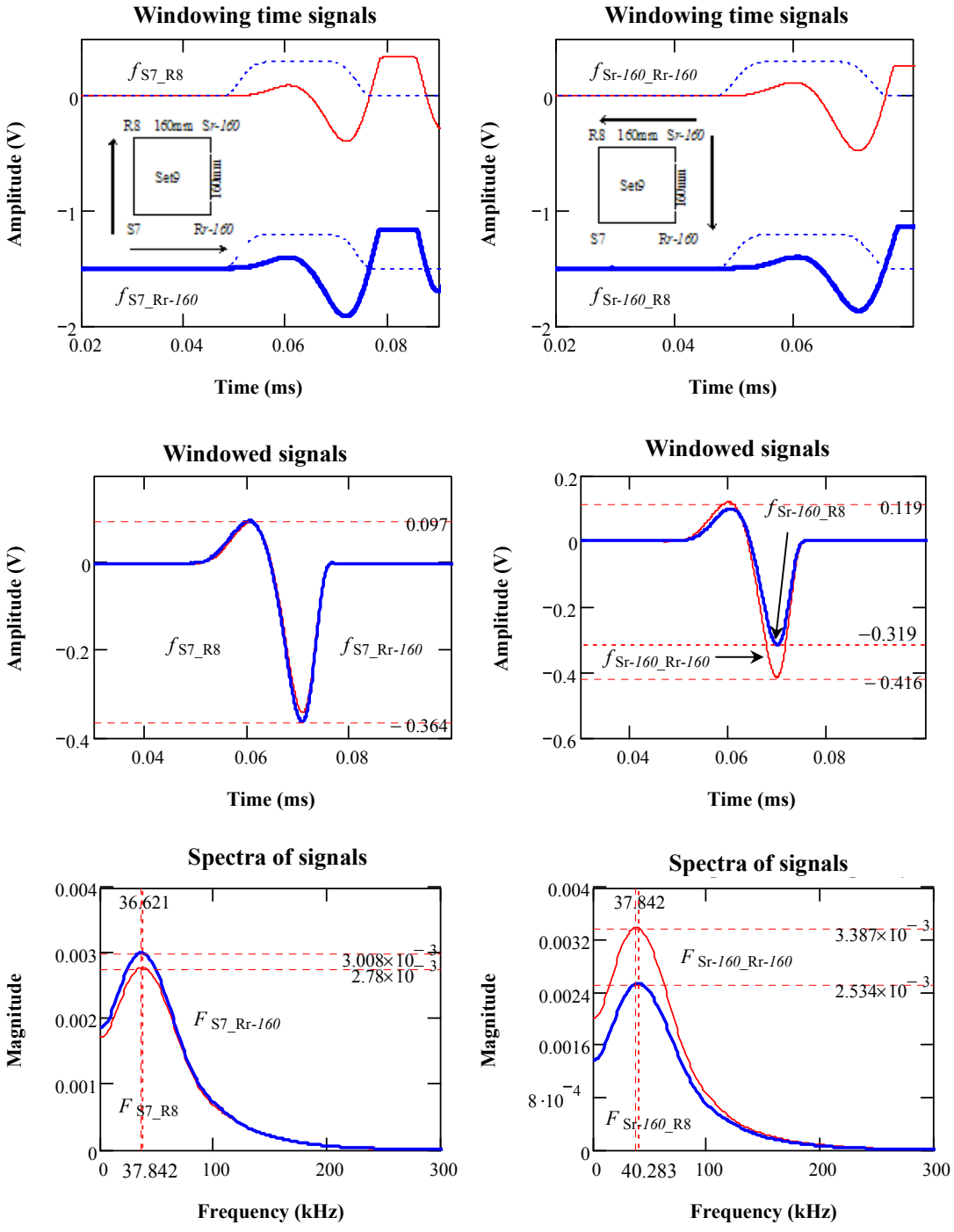

Figure P-42: P-wave analyses in time and frequency domains for Set 9 (160mm S-R spacing) on the joint-free surface (Horizontal lines mark the peak amplitudes and vertical lines dominant frequencies.)

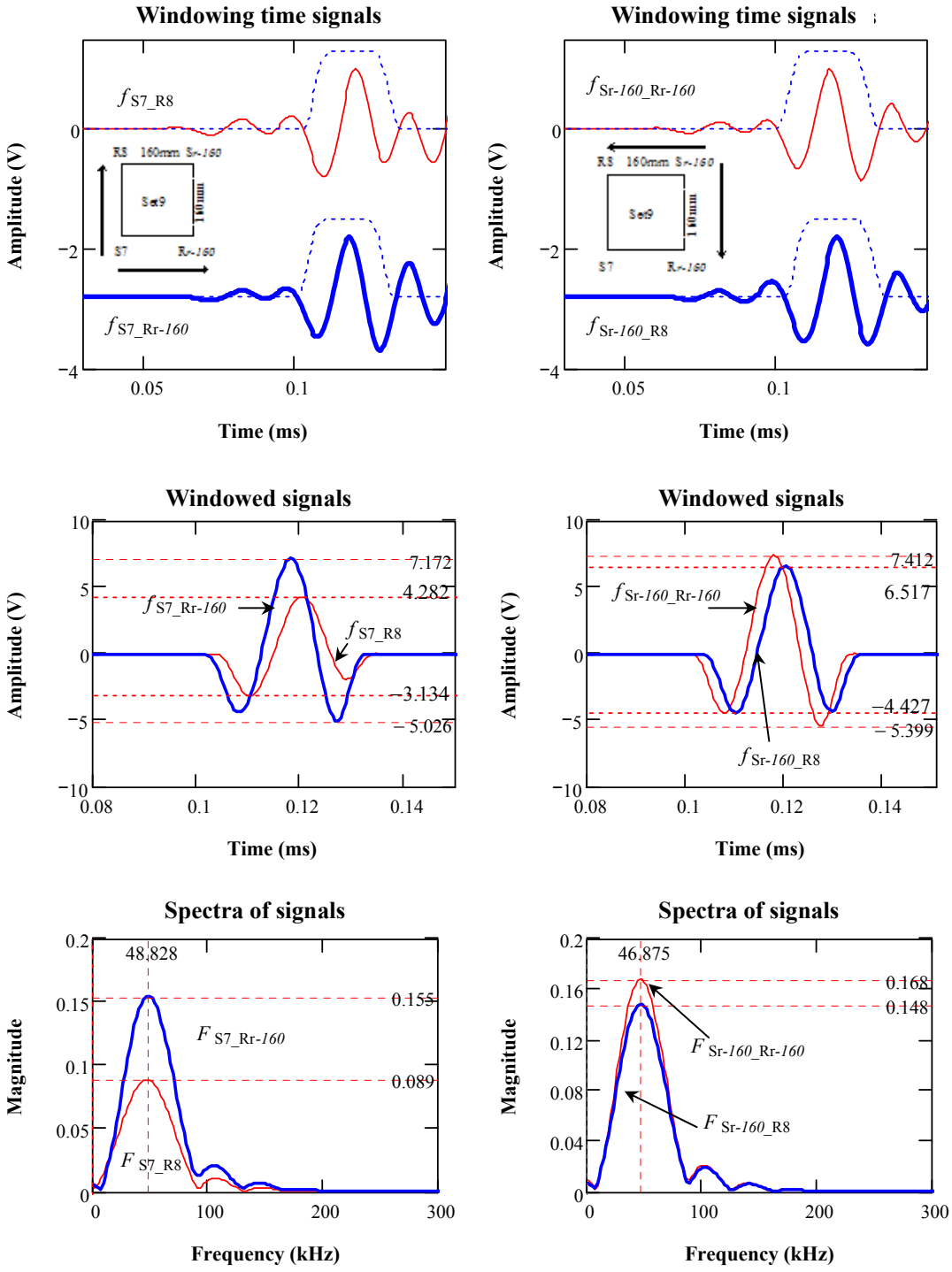

Figure P-43: R-wave analyses in time and frequency domains for Set 9 (160mm S-R spacing) on the joint-free surface (Horizontal lines mark the peak amplitudes and vertical lines dominant frequencies.)

Appendix Q
Source-to-Receiver (S-R) Arrangement and Detailed Results of Wave Amplitude Ratios for Slab 3 - Measurements on the Jointed and the Joint-free Surfaces

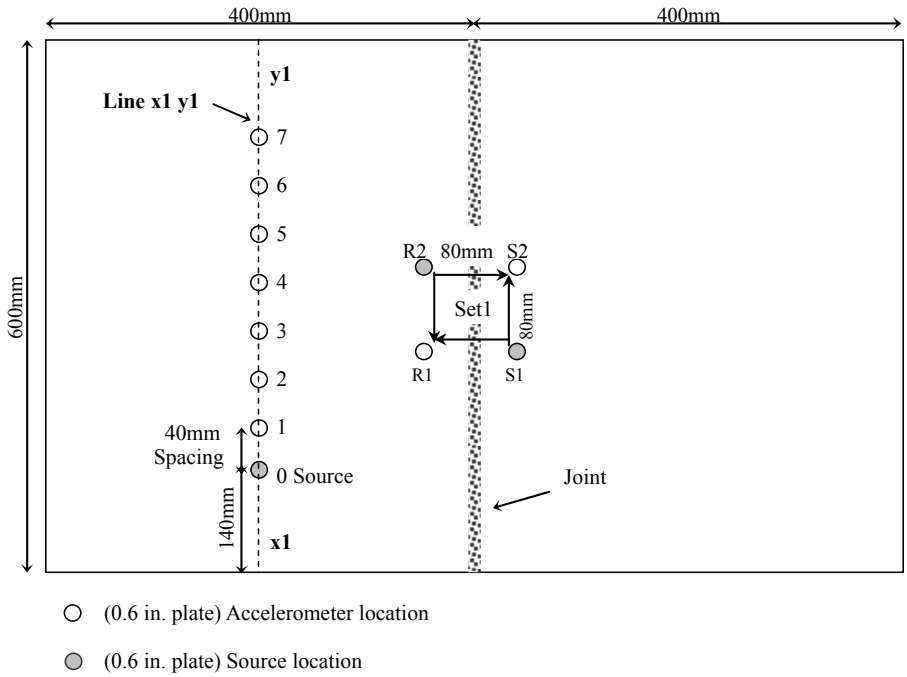

Figure Q-1: 80mm S-R spacing configuration of HMA slab 3

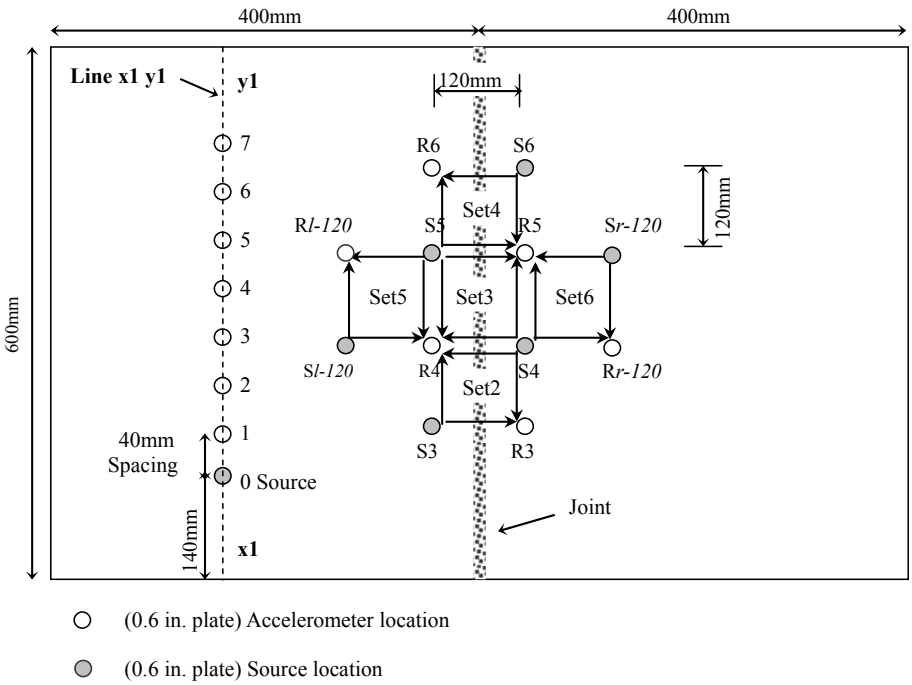

Figure Q-2: 120mm S-R spacing configuration of HMA slab 3

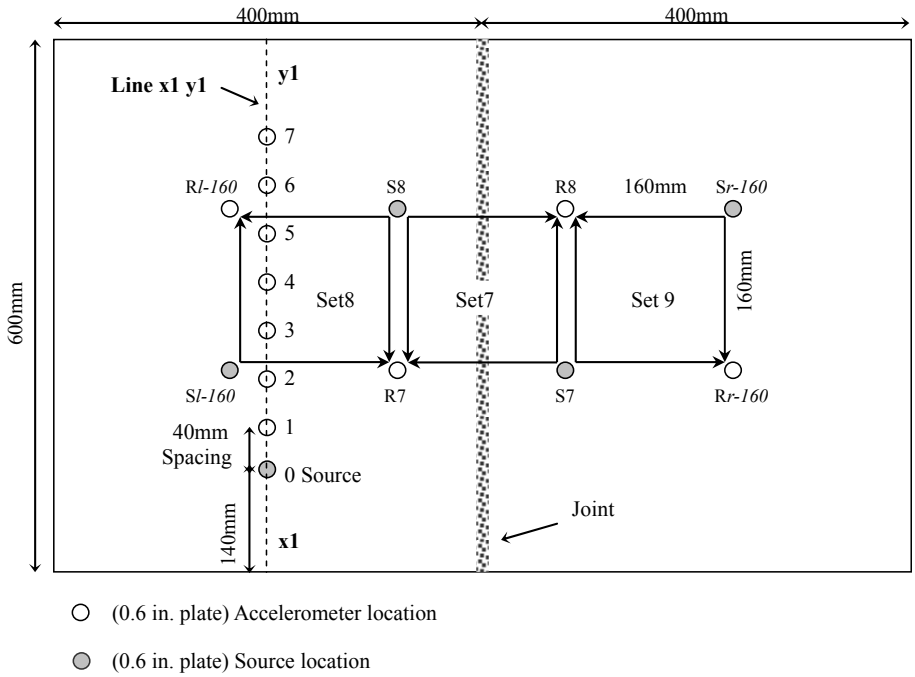

Figure Q-3: 160mm S-R spacing configuration of HMA slab 3

Table Q-1: Source and receiver arranged at 80mm spacing in slab 3

Locations	Description	Signals received
Jointed surface at locations S1, R1, S2 and R2 (Set 1)	Pair 1 –sources at S1 and S2; receiver at R1	f_{S1_R1} and f_{S2_R1}
	Pair 2 –sources at S1 and S2; receiver at R2	f_{S2_R2} and f_{S1_R2}

Table Q-2: Source and receiver arranged at 120mm spacing in slab 3

Locations	Description	Signals received
Jointed surface at locations S3, R3, S4 and R4 (Set 2)	Pair 1 –sources at S3 and S4; receiver at R3	f_{S3_R3} and f_{S4_R3}
	Pair 2 –sources at S3 and S4; receiver at R4	f_{S4_R4} and f_{S3_R4}
Jointed surface at locations S4, R4, S5 and R5 (Set 3)	Pair 1 –sources at S4 and S5; receiver at R4	f_{S4_R4} and f_{S5_R4}
	Pair 2 –sources at S4 and S5; receiver at R5	f_{S5_R5} and f_{S4_R5}
Jointed surface at locations S5, R5, S6 and R6 (Set 4)	Pair 1 –sources at S5 and S6; receiver at R5	f_{S5_R5} and f_{S6_R5}
	Pair 2 –sources at S5 and S6; receiver at R6	f_{S6_R6} and f_{S5_R6}
Joint-free surface at locations S*l-120*, R*l-120*, S5 and R4 (Set 5)	Pair 1 –sources at S*l-120* and S5; receiver at R4	$f_{Sl\text{-}120\_R4}$ and f_{S5_R4}
	Pair 2 –sources at S*l-120* and S5; receiver at R*l-120*	$f_{S5\_Rl\text{-}120}$ and $f_{Sl\text{-}120\_Rl\text{-}120}$
Joint-free surface at locations S*r-120*, R*r-120*, S4 and R5 (Set 1)	Pair 1 –sources at S4 and S*r-120*; receiver at R*r-120*	$f_{S4\_Rr\text{-}120}$ and $f_{Sr\text{-}120\_Rr\text{-}120}$
	Pair 2 –sources at S4 and S*r-120*; receiver at R5	$f_{Sr\text{-}120\_R5}$ and f_{S4_R5}

Table Q-3: Source and receiver arranged at 160mm spacing in slab 3

Locations	Description	Signals received
Jointed surface at locations S7, R7, S8 and R8 (Set 7)	Pair 1 –sources at S7 and S8; receiver at R7	f_{S7_R7} and f_{S8_R7}
	Pair 2 –sources at S7 and S8; receiver at R8	f_{S8_R8} and f_{S7_R8}
Joint-free surface at locations S*l-160*, R*l-160*, S8 and R7 (Set 8)	Pair 1 –sources at S*l-160* and S8; receiver at R7	$f_{Sl\text{-}160\_R7}$ and f_{S8_R7}
	Pair 2 –sources at S*l-160* and S8; receiver at R*l-160*	$f_{S8\_Rl\text{-}160}$ and $f_{Sl\text{-}160\_Rl\text{-}160}$
Joint-free surface at locations S*r-160*, R*r-160*, S7 and R8 (Set 9)	Pair 1 –sources at S*r-160* and S7; receiver at R*r-160*	$f_{S7\_Rr\text{-}160}$ and $f_{Sr\text{-}160\_Rr\text{-}160}$
	Pair 2 –sources at S*r-160* and S7; receiver at R8	$f_{Sr\text{-}160\_R8}$ and f_{S7_R8}

Table Q-4: PTP ratio, magnitude ratio and area ratio for Set 1 measurements (80mm source-to-receiver spacing) on the jointed surface in slab 3

Location	Analyzed portion	Signal ratio (*SR*)	PTP ratio	Magnitude ratio	Area ratio
Jointed surface (Set 1)	Full signal	f_{S1_R1}/f_{S1_R2}	0.063	0.041	0.071
		f_{S2_R2}/f_{S2_R1}	0.05	0.072	0.066
	P-wave	f_{S1_R1}/f_{S1_R2}	0.32	0.44	0.33
		f_{S2_R2}/f_{S2_R1}	0.36	0.36	0.35
	R-wave	f_{S1_R1}/f_{S1_R2}	0.073	0.087	0.073
		f_{S2_R2}/f_{S2_R1}	0.064	0.073	0.065
Jointed surface (Set 1 average)	Full signal	$\frac{1}{2}\cdot\left(\frac{f_{S1\_R1}}{f_{S1\_R2}}+\frac{f_{S2\_R2}}{f_{S2\_R1}}\right)$	0.057	0.057	0.069
	P-wave		0.34	0.4	0.34
	R-wave		0.069	0.08	0.069

Table Q-5: PTP ratio, magnitude ratio and area ratio for Set 2 to Set 4 measurements (120mm source-to-receiver spacing) on the jointed surface in slab 3

Locations	Analyzed portion	Signal ratio (*SR*)	PTP ratio	Magnitude ratio	Area ratio
Jointed surface (Set 2)	Full signal	f_{S3_R3}/f_{S3_R4}	0.14	0.09	0.12
		f_{S4_R4}/f_{S4_R3}	0.09	0.16	0.12
	P-wave	f_{S3_R3}/f_{S3_R4}	0.45	0.65	0.42
		f_{S4_R4}/f_{S4_R3}	0.17	0.28	0.15
	R-wave	f_{S3_R3}/f_{S3_R4}	0.13	0.16	0.13
		f_{S4_R4}/f_{S4_R3}	0.09	0.09	0.09
Jointed surface (Set 3)	Full signal	f_{S5_R5}/f_{S5_R4}	0.13	0.09	0.11
		f_{S4_R4}/f_{S4_R5}	0.08	0.12	0.11
	P-wave	f_{S5_R5}/f_{S5_R4}	0.22	0.33	0.21
		f_{S4_R4}/f_{S4_R5}	0.25	0.41	0.23
	R-wave	f_{S5_R5}/f_{S5_R4}	0.18	0.20	0.17
		f_{S4_R4}/f_{S4_R5}	0.08	0.08	0.08
Jointed surface (Set 3 repeated)	Full signal	f_{S5_R5}/f_{S5_R4}	0.17	0.11	0.13
		f_{S4_R4}/f_{S4_R5}	0.08	0.09	0.10
	P-wave	f_{S5_R5}/f_{S5_R4}	0.26	0.34	0.24
		f_{S4_R4}/f_{S4_R5}	0.3	0.45	0.27
	R-wave	f_{S5_R5}/f_{S5_R4}	0.12	0.13	0.14
		f_{S4_R4}/f_{S4_R5}	0.077	0.078	0.079
Jointed surface (Set 4)	Full signal	f_{S5_R5}/f_{S5_R6}	0.05	0.01	0.06
		f_{S6_R6}/f_{S6_R5}	0.09	0.05	0.09
	P-wave	f_{S5_R5}/f_{S5_R6}	0.36	0.53	0.34
		f_{S6_R6}/f_{S6_R5}	0.34	0.48	0.30
	R-wave	f_{S5_R5}/f_{S5_R6}	0.05	0.06	0.05
		f_{S6_R6}/f_{S6_R5}	0.09	0.09	0.09
Jointed surface (average)	Full signal	$\frac{Set\ 2\ SR + \cdots + Set\ 4\ SR}{4}$	0.10	0.09	0.11
	P-wave		0.29	0.43	0.27
	R-wave		0.10	0.11	0.10

Table Q-6: PTP ratio, magnitude ratio and area ratio for Set 5 to Set 6 measurements (120mm source-to-receiver spacing) on the joint-free surfaces in slab 3

Location	Analyzed portion	Signal ratio (*SR*)	PTP ratio	Magnitude ratio	Area ratio
Joint-free surface at the left side of the joint (Set 5)	Full signal	$f_{Sl\text{-}120\_R4}/f_{Sl\text{-}120\_Rl\text{-}120}$	1.25	1.58	1.17
		$f_{S5\_Rl\text{-}120}/f_{S5\_R4}$	2.37	1.48	1.75
	P-wave	$f_{Sl\text{-}120\_R4}/f_{Sl\text{-}120\_Rl\text{-}120}$	1.02	1.08	1.04
		$f_{S5\_Rl\text{-}120}/f_{S5\_R4}$	0.91	0.93	0.94
	R-wave	$f_{Sl\text{-}120\_R4}/f_{Sl\text{-}120\_Rl\text{-}120}$	1.31	1.31	1.37
		$f_{S5\_Rl\text{-}120}/f_{S5\_R4}$	1.21	1.31	1.33
Joint-free surface at the right side of the joint (Set 6)	Full signal	$f_{S4\_Rr\text{-}120}/f_{S4\_R5}$	0.85	1.06	0.96
		$f_{Sr\text{-}120\_R4}/f_{Sr\text{-}120\_Rr\text{-}120}$	0.54	0.37	0.55
	P-wave	$f_{S4\_Rr\text{-}120}/f_{S4\_R5}$	0.76	0.76	0.79
		$f_{Sr\text{-}120\_R4}/f_{Sr\text{-}120\_Rr\text{-}120}$	1.11	1.11	1.14
	R-wave	$f_{S4\_Rr\text{-}120}/f_{S4\_R5}$	0.84	0.80	0.84
		$f_{Sr\text{-}120\_R4}/f_{Sr\text{-}120\_Rr\text{-}120}$	0.58	0.62	0.59
Joint-free surface (average)	Full signal	$\frac{Set\ 5\ SR + Set\ 6\ SR}{2}$	1.25	1.12	1.11
	P-wave		0.95	0.97	0.98
	R-wave		0.99	1.01	1.03

Table Q-7: PTP ratio, magnitude ratio and area ratio for Set 7 measurements (160mm source-to-receiver spacing) on the jointed surface in slab 3

Location	Analyzed portion	Signal ratio (*SR*)	PTP ratio	Magnitude ratio	Area ratio
Jointed surface (Set 7)	Full signal	f_{S8_R8}/f_{S8_R7}	0.12	0.12	0.13
		f_{S7_R7}/f_{S7_R8}	0.14	0.15	0.12
	P-wave	f_{S8_R8}/f_{S8_R7}	0.08	0.07	0.091
		f_{S7_R7}/f_{S7_R8}	0.15	0.12	0.18
	R-wave	f_{S8_R8}/f_{S8_R7}	0.12	0.12	0.13
		f_{S7_R7}/f_{S7_R8}	0.085	0.088	0.098
Jointed surface (average)	Full signal	$\frac{1}{2}\cdot\left(\frac{f_{S8\_R8}}{f_{S8\_R7}}+\frac{f_{S7\_R7}}{f_{S7\_R8}}\right)$	0.13	0.14	0.13
	P-wave		0.12	0.095	0.14
	R-wave		0.10	0.10	0.11

Table Q-8: PTP ratio, magnitude ratio and area ratio for Set 7 measurements (160mm source-to-receiver spacing) on the joint-free surfaces in slab 3

Location	Analyzed portion	Signal ratio (*SR*)	PTP ratio	Magnitude ratio	Area ratio
Joint-free surface at the left side of the joint (Set 8)	Full signal	$f_{Sl\text{-}160\_R7} / f_{Sl\text{-}160\_Rl\text{-}160}$	1.05	1.02	1.00
		$f_{S8\_Rl\text{-}160} / f_{S8\_R7}$	1.86	1.78	2.16
	P-wave	$f_{Sl\text{-}160\_R7} / f_{Sl\text{-}160\_Rl\text{-}160}$	1.23	1.22	1.21
		$f_{S8\_Rl\text{-}160} / f_{S8\_R7}$	1.21	1.24	1.21
	R-wave	$f_{Sl\text{-}160\_R7} / f_{Sl\text{-}160\_Rl\text{-}160}$	1.04	1.05	1.04
		$f_{S8\_Rl\text{-}160} / f_{S8\_R7}$	1.87	1.79	1.72
Joint-free surface at the right side of the joint (Set 9)	Full signal	$f_{S7\_Rr\text{-}160} / f_{S7\_R8}$	1.77	1.59	1.45
		$f_{Sr\text{-}160\_R8} / f_{Sr\text{-}160\_Rr\text{-}160}$	0.86	0.9	0.93
	P-wave	$f_{S7\_Rr\text{-}160} / f_{S7\_R8}$	1.06	1.07	1.08
		$f_{Sr\text{-}160\_R8} / f_{Sr\text{-}160\_Rr\text{-}160}$	0.78	0.77	0.75
	R-wave	$f_{S7\_Rr\text{-}160} / f_{S7\_R8}$	1.64	1.68	1.74
		$f_{Sr\text{-}160\_R8} / f_{Sr\text{-}160\_Rr\text{-}160}$	0.86	0.89	0.88
Joint-free surface (average)	Full signal	$\frac{Set\ 8\ SR + Set\ 9\ SR}{2}$	1.39	1.32	1.39
	P-wave		1.07	1.08	1.06
	R-wave		1.35	1.35	1.35

Table Q-9: FTC, WTC, and damping ratio for Set 1 measurements (80mm source-to-receiver spacing) on the jointed surface in slab 3

Location	Analyzed portion	Signal ratio (*SR*)	FTC	WTC	Damping ratio
Jointed surface (Set 1)	Full signal	$\sqrt{\frac{f_{S1\_R1} \cdot f_{S2\_R2}}{f_{S1\_R2} \cdot f_{S2\_R1}}}$	0.054 at 54kHz	0.057 at 54kHz	0.18 at 54kHz
	P-wave		0.4 at 39kHz	0.06 at 39kHz	0.18 at 39kHz
	R-wave		0.08 at 47kHz	0.064 at 47kHz	0.18 at 47kHz

.

Table Q-10: FTC, WTC, and damping ratio for Set 2 to Set 4 measurements (120mm source-to-reciver spacing) on the jointed surface in slab 3

Location	Analyzed portion	Signal ratio (*SR*)	FTC	WTC	Damping ratio
Jointed surface (Set 2)	Full signal	$\sqrt{\frac{f_{S2\_R2}\cdot f_{S3\_R3}}{f_{S2\_R3}\cdot f_{S3\_R2}}}$	0.12 at 51kHz	0.12 at 51kHz	0.09 at 51kHz
	P-wave		0.42 at 37kHz	0.087 at 37kHz	0.12 at 37kHz
	R-wave		0.12 at 43kHz	0.12 at 43kHz	0.11 at 43kHz
Jointed surface (Set 3)	Full signal	$\sqrt{\frac{f_{S4\_R4}\cdot f_{S3\_R3}}{f_{S4\_R3}\cdot f_{S3\_R4}}}$	0.11 at 50kHz	0.12 at 50kHz	0.10 at 50kHz
	P-wave		0.37 at 38kHz	0.083 at 38kHz	0.14 at 38kHz
	R-wave		0.13 at 43kHz	0.12 at 43kHz	0.11 at 43kHz
Jointed surface (Set 3 repeated)	Full signal	$\sqrt{\frac{f_{S4\_R4}\cdot f_{S5\_R5}}{f_{S4\_R5}\cdot f_{S5\_R4}}}$	0.10 at 51kHz	0.12 at 51kHz	0.10 at 51kHz
	P-wave		0.39 at 34kHz	0.1 at 34kHz	0.13 at 34kHz
	R-wave		0.10 at 43kHz	0.13 at 43kHZ	0.12 at 43kHz
Jointed surface (Set 4)	Full signal	$\sqrt{\frac{f_{S4\_R4}\cdot f_{S5\_R5}}{f_{S4\_R5}\cdot f_{S5\_R4}}}$	0.078 at 50kHz	0.076 at 50kHz	0.11 at 50kHz
	P-wave		0.50 at 34kHz	0.058 at 34kHz	0.10 at 34kHz
	R-wave		0.072 at 43kHz	0.066 at 43kHz	0.14 at 43kHz
Jointed surface (average)	Full signal	$\frac{Set\ 2\ SR+\cdots+Set\ 4\ SR}{4}$	0.10 at 51kHz	0.11 at 51kHz	0.10 at 51kHz
	P-wave		0.42 at 36kHz	0.08 at 36kHz	0.12 at 36kHz
	R-wave		0.10 at 43kHz	0.11 at 43kHz	0.12 at 43kHz

Table Q-11: FTC, WTC, and damping ratio for Set 5 to Set 6 measurements (120mm source-to-reciver spacing) on the joint-free surface in slab 3

Location	Analyzed portion	Signal ratio (*SR*)	FTC	WTC	Damping ratio
Joint-free surface at the left side of the joint (Set 5)	Full signal	$\sqrt{\frac{f_{Sl-120\_R4} \cdot f_{S5\_Rl-120}}{f_{Sl-120\_Rl-120} \cdot f_{S5\_R4}}}$	1.53 at 54kHz	1.69 at 54kHz	-0.018 at 54kHz
	P-wave		1.00 at 39kHz	1.8 at 39kHz	$-2.95*10^{-4}$ at 39kHz
	R-wave		1.31 at 47kHz	1.78 at 47kHz	-0.02 at 47kHz
Joint-free surface at the right side of the joint (Set 6)	Full signal	$\sqrt{\frac{f_{S4\_Rr-120} \cdot f_{Sr-120\_R5}}{f_{S4\_R5} \cdot f_{Sr-120\_Rr-120}}}$	0.63 at 54kHz	0.68 at 54kHz	0.02 at 54kHz
	P-wave		0.92 at 39kHz	0.71 at 39kHz	0.01 at 39kHz
	R-wave		0.70 at 47kHz	0.7 at 47kHz	0.01 at 47kHz
Joint-free surface (average)	Full signal	$\frac{Set\ 5\ SR + Set\ 6\ SR}{2}$	1.08 at 54kHz	1.19 at 54kHz	0.02 at 54kHz
	P-wave		0.92 at 39kHz	0.71 at 39kHz	$4.9*10^{-3}$ at 39kHz
	R-wave		1.01 at 47kHz	1.24 at 47kHz	$-5*10^{-3}$ at 47kHz

Table Q-12: FTC, WTC, and damping ratio for Set 7 measurements (160mm source-to-reciver spacing) on the jointed surface in slab 3

Location	Analyzed portion	Signal ratio (*SR*)	FTC	WTC	Damping ratio
Jointed surface (Set 7)	Full signal	$\sqrt{\frac{f_{S8\_R8} \cdot f_{S7\_R7}}{f_{S8\_R7} \cdot f_{S7\_R8}}}$	0.13 at 54kHz	0.13 at 54kHz	0.066 at 54kHz
	P-wave		0.13 at 36kHz	0.12 at 36kHz	0.22 at 36kHz
	R-wave		0.11 at 47kHz	0.13 at 47kHz	0.08 at 47kHz

Table Q-13: FTC, WTC, and damping ratio for Set 8 and Set 9 measurements (160mm source-to-reciver spacing) on the joint-free surfaces in slab 3

Location	Analyzed portion	Signal ratio (*SR*)	FTC	WTC	Damping ratio
Joint-free surface at the left side of the joint (Set 8)	Full signal	$\sqrt{\frac{f_{Sl-160\_R7} \cdot f_{S8\_Rl-160}}{f_{Sl-160\_Rl-160} \cdot f_{S8\_R7}}}$	1.47 at 56kHz	1.39 at 56kHz	-0.012 at 56kHz
	P-wave		1.21 at 36kHz	1.34 at 36kHz	-0.02 at 36kHz
	R-wave		1.33 at 49kHz	1.39 at 49kHz	-0.01 at 49kHz
Joint-free surface at the right side of the joint (Set 9)	Full signal	$\sqrt{\frac{f_{S7\_Rr-160} \cdot f_{Sr-160\_R8}}{f_{S7\_R8} \cdot f_{Sr-160\_Rr-160}}}$	1.07 at 56kHz	1.3 at 56kHz	$-4.6*10^{-3}$ at 56kHz
	P-wave		0.90 at 34kHz	1.27 at 34kHz	0.012 at 34kHz
	R-wave		1.24 at 48kHz	1.26 at 48kHz	-0.008 at 48kHz
Joint-free surface (average)	Full signal	$\frac{Set\ 8\ SR + Set\ 9\ SR}{2}$	1.47 at 56kHz	1.39 at 56kHz	-0.0083 at 56kHz
	P-wave		0.9 at 35kHz	1.27 at 35kHz	0.012 at 35kHz
	R-wave		1.24 at 49kHz	1.26 at 49kHz	-0.008 at 49kHz

Appendix R

FTC vs. Frequency and Wavelength/3 for Slab 3

- Measurements on the Jointed and the Joint-free Surfaces

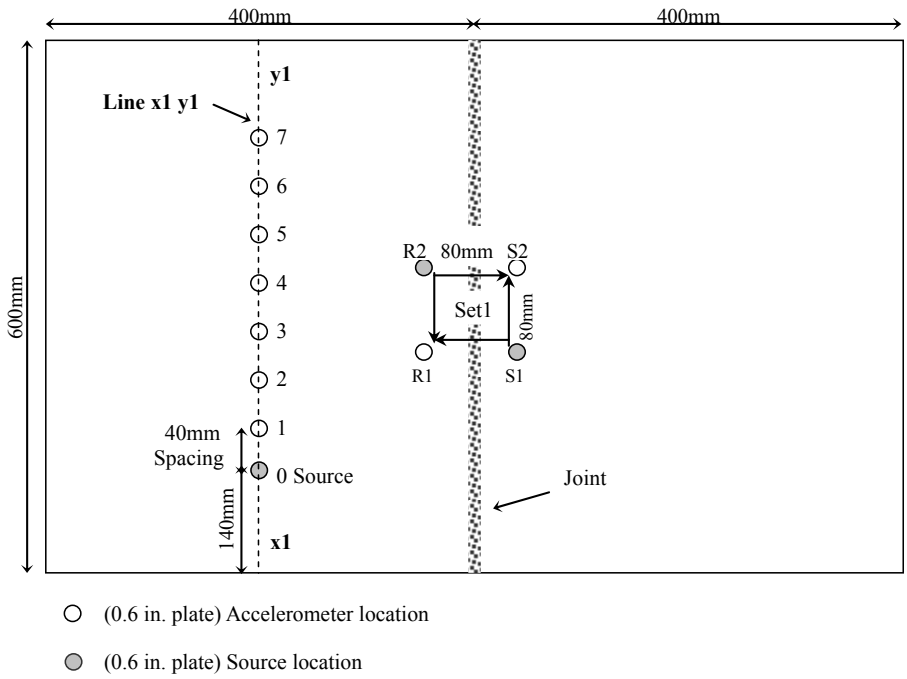

Figure R-1: 80mm S-R spacing configuration of HMA slab 3

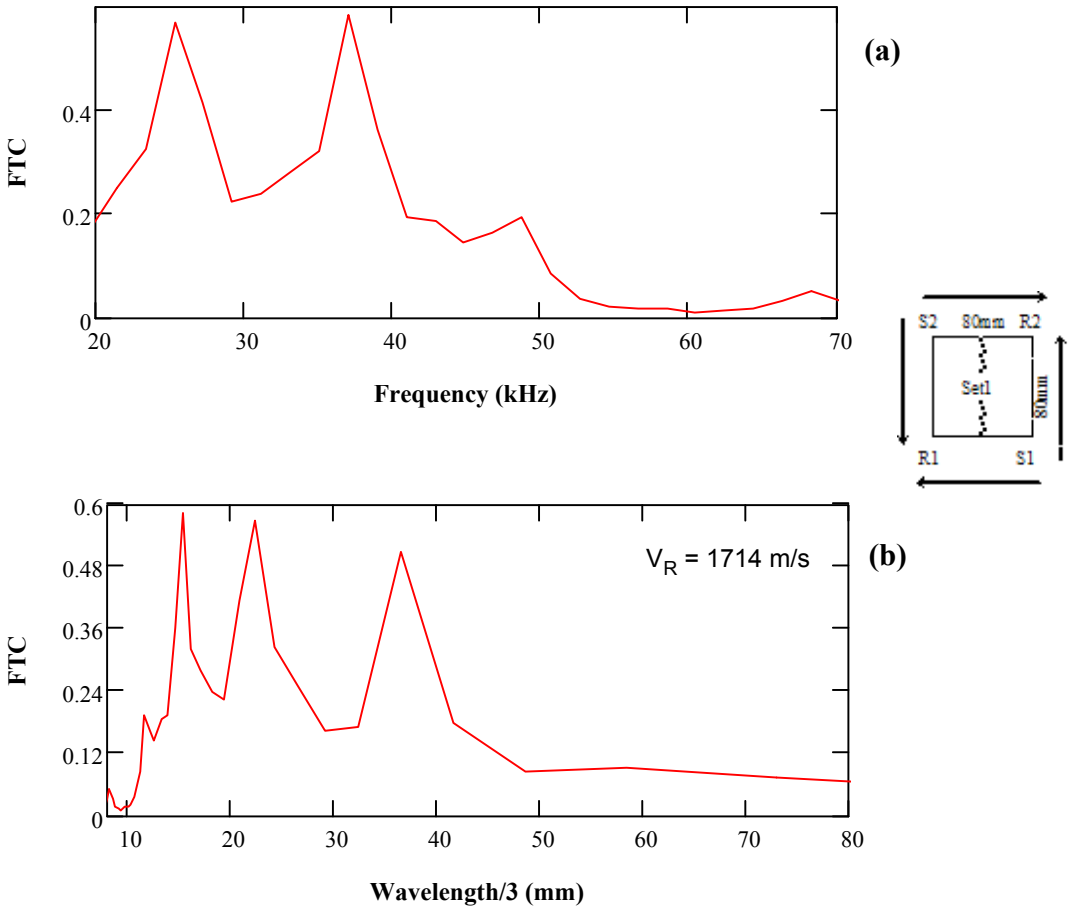

Figure R-2: (a) FTC vs. frequency and (b) FTC vs. wavelength/3 for full signals of set 1 measurements (80mm S-R spacing) on jointed surface

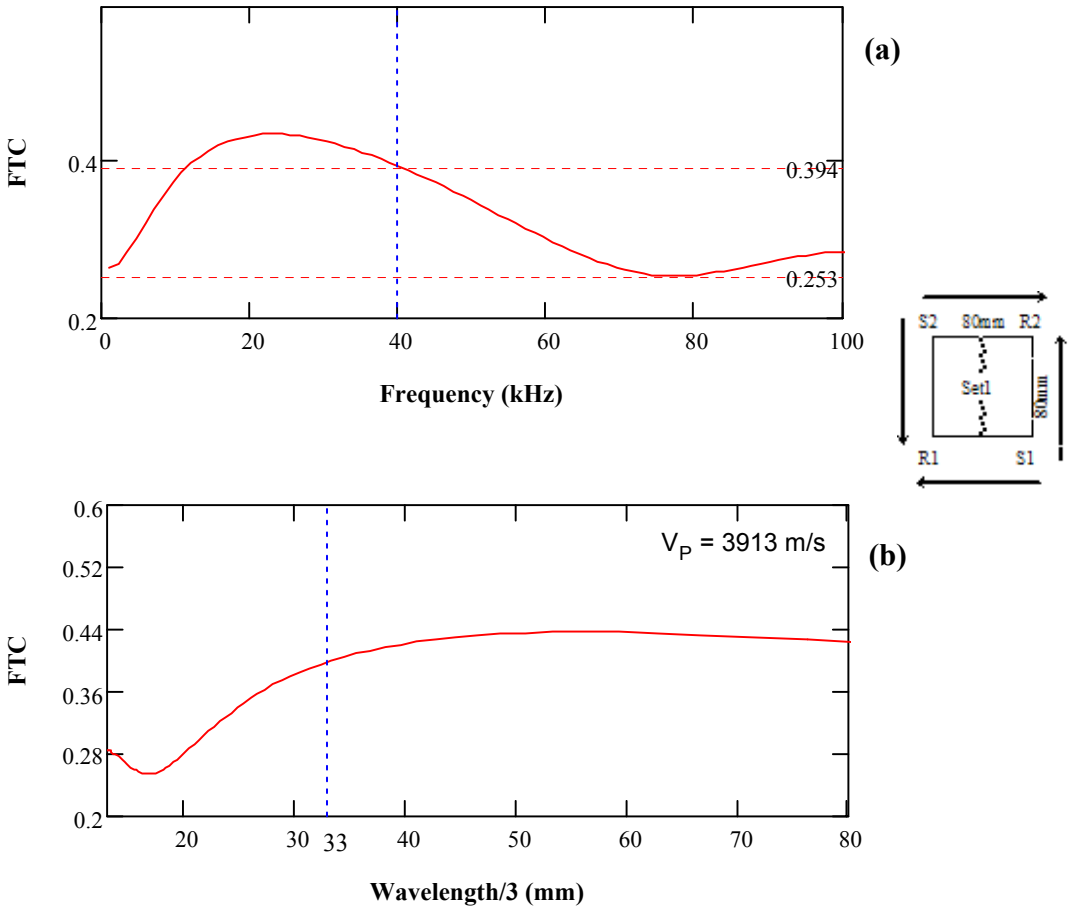

Figure R-3: (a) FTC vs. frequency and (b) FTC vs. wavelength/3 for P-waves for set 1 measurements (80mm S-R spacing) on jointed surface

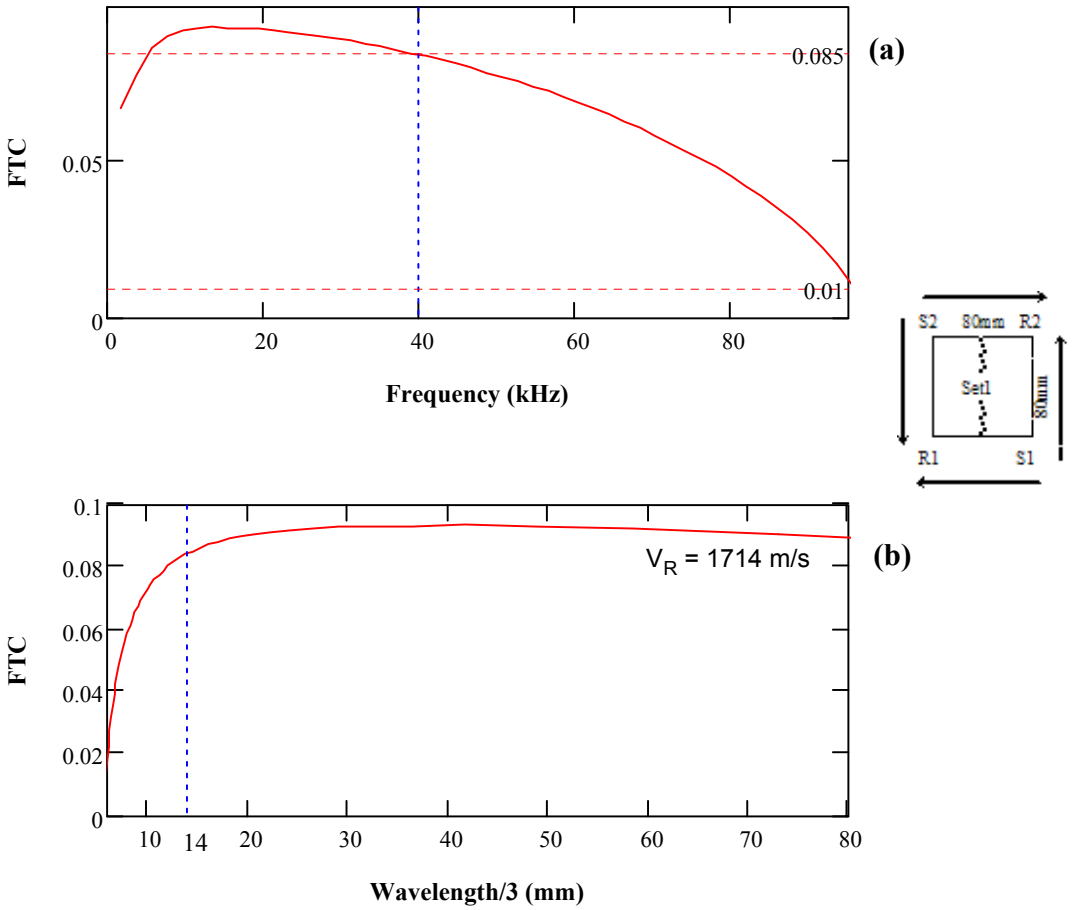

Figure R-4: (a) FTC vs. frequency and (b) FTC vs. wavelength/3 for R-waves for set 1 measurements (80mm S-R spacing) on jointed surface

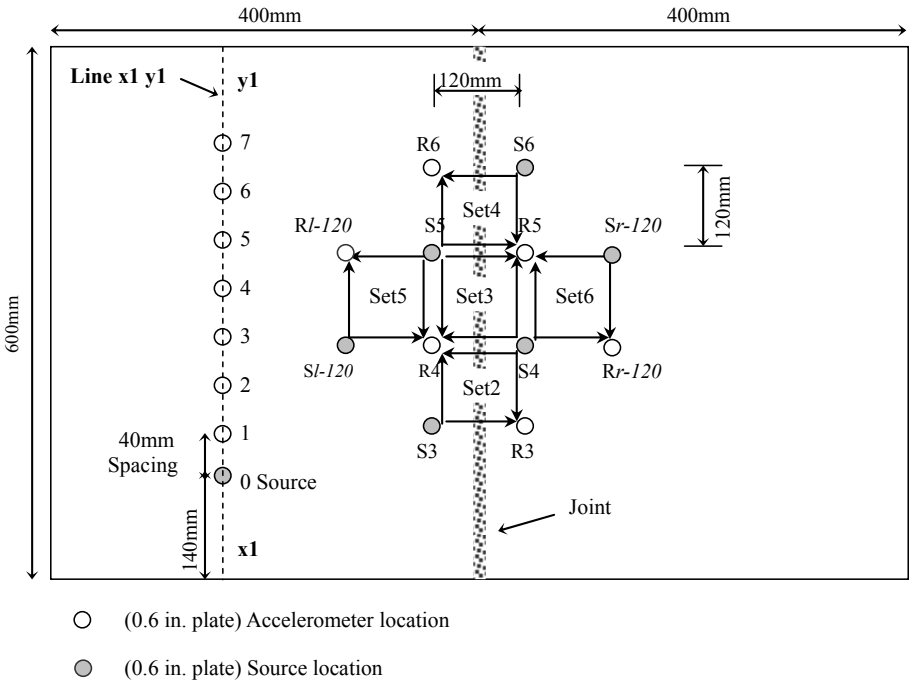

Figure R-5: 120mm S-R spacing configuration of HMA slab 3

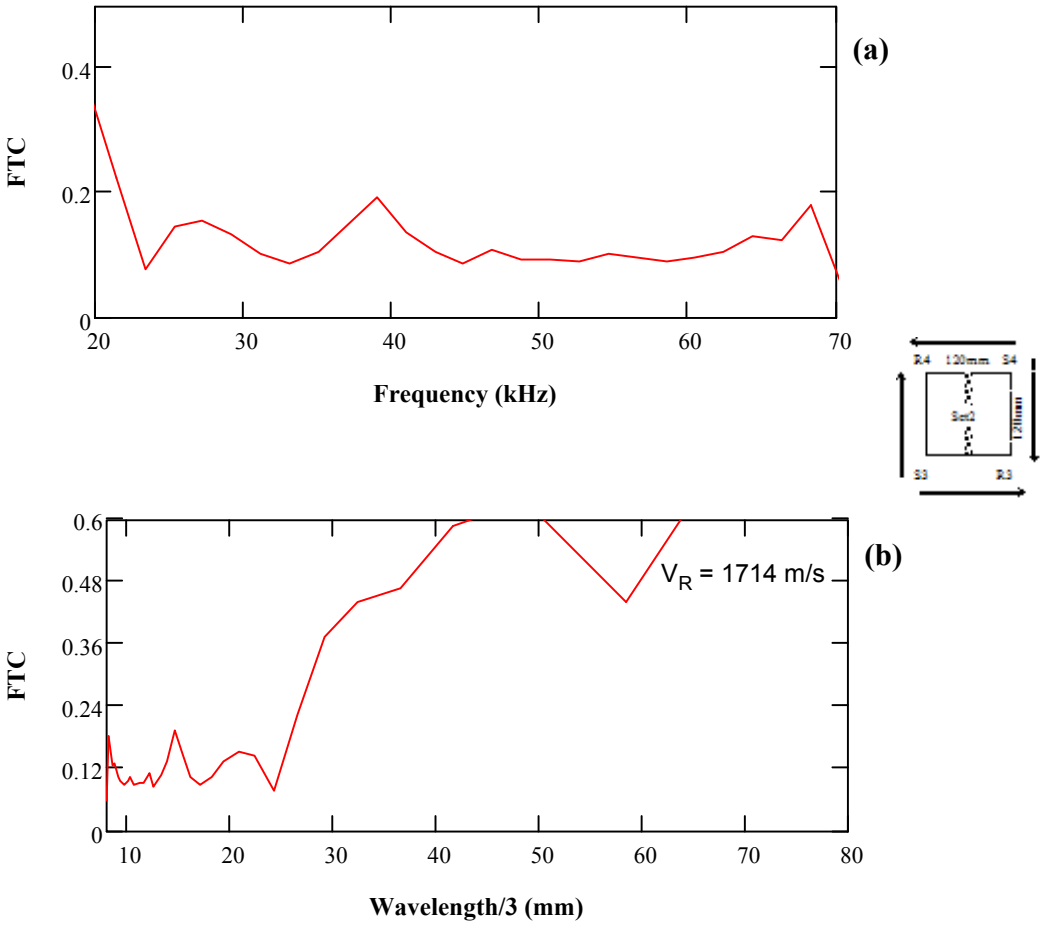

Figure R-6: (a) FTC vs. frequency and (b) FTC vs. wavelength/3 for full signals of set 2 measurements (120mm S-R spacing) on jointed surface

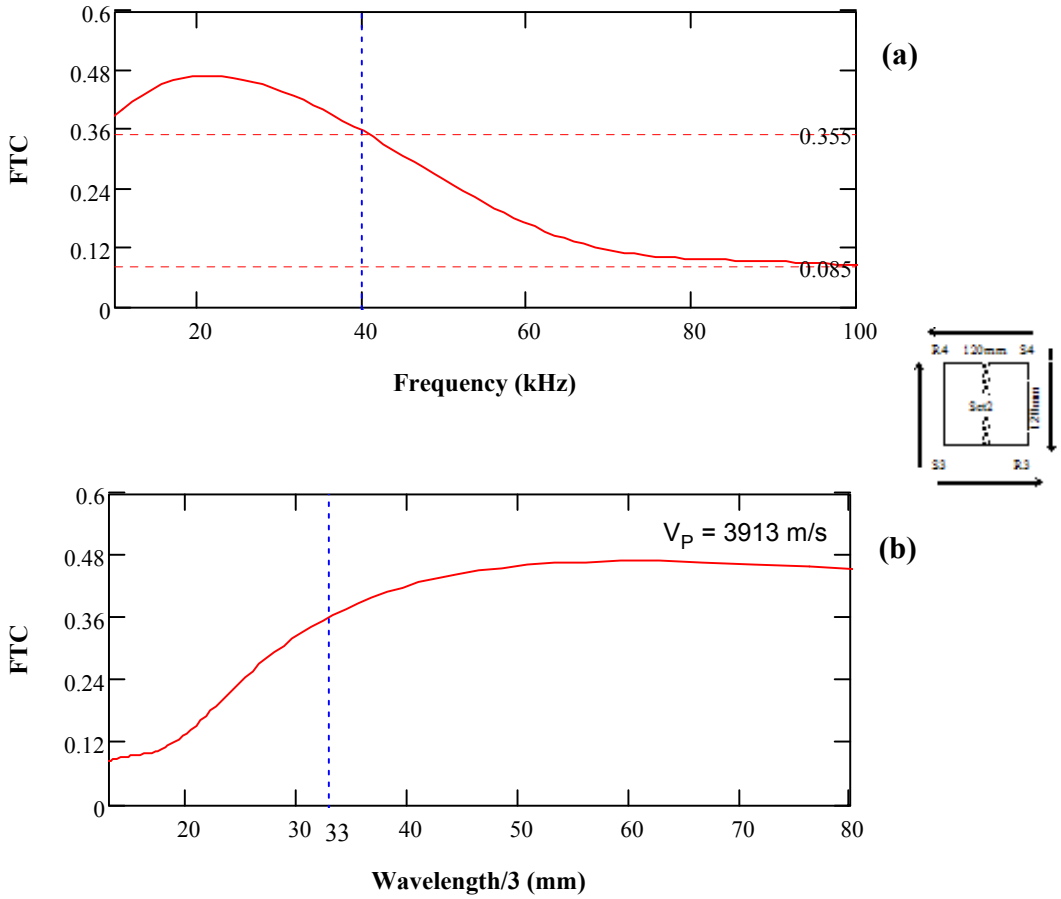

Figure R-7: (a) FTC vs. frequency and (b) FTC vs. wavelength/3 for P-waves for set 2 measurements (120mm S-R spacing) on jointed surface

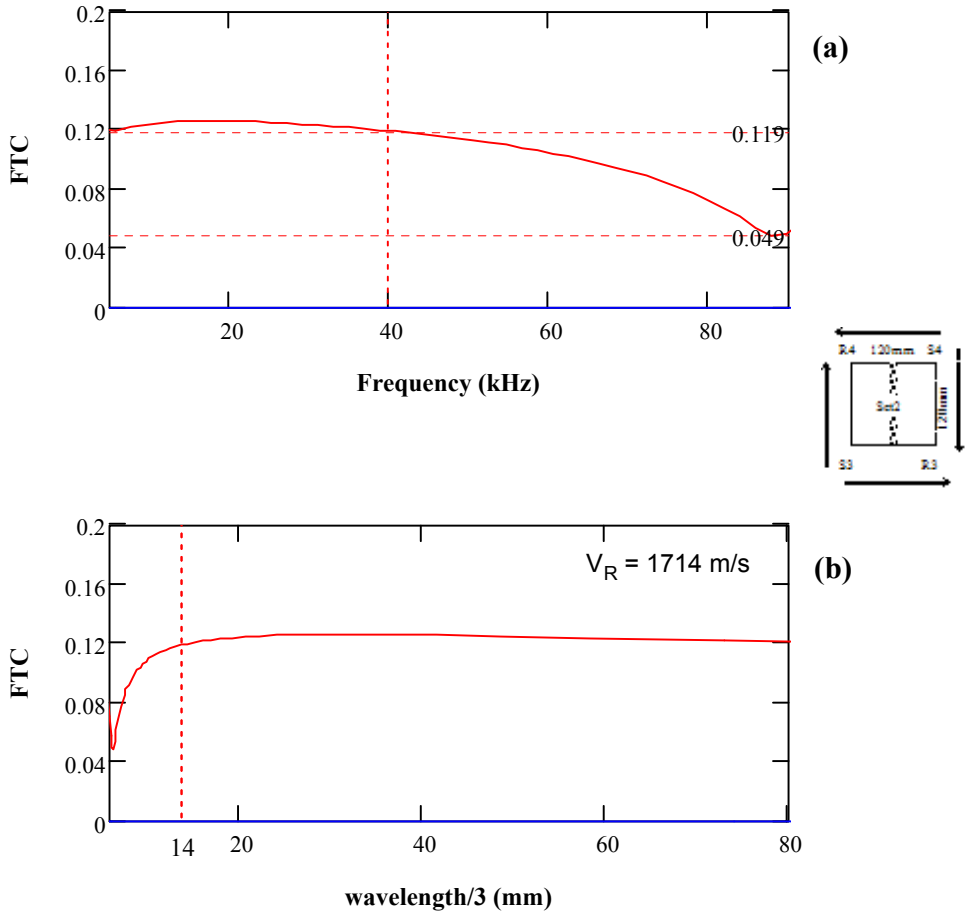

Figure R-8: (a) FTC vs. frequency and (b) FTC vs. wavelength/3 for R-waves for set 2 measurements (120mm S-R spacing) on jointed surface

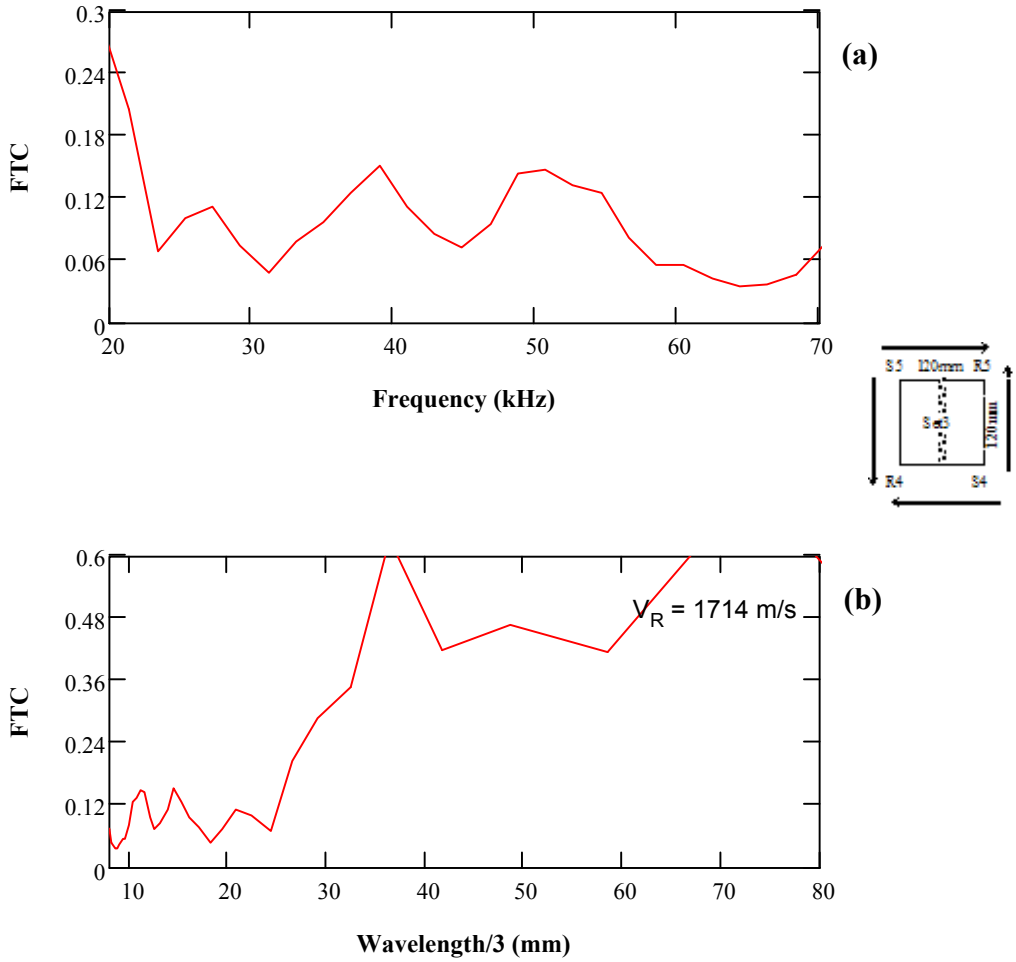

Figure R-9: (a) FTC vs. frequency and (b) FTC vs. wavelength/3 for full signals of set 3 measurements (120mm S-R spacing) on jointed surface

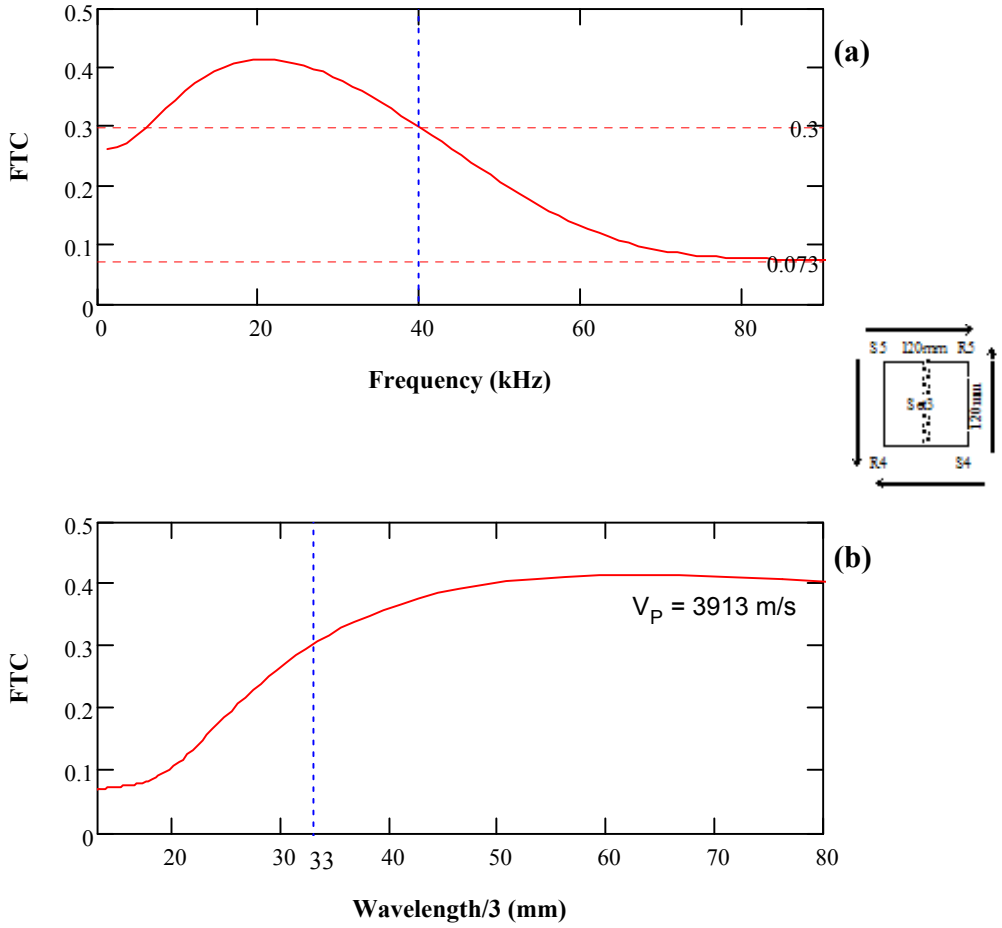

Figure R-10: (a) FTC vs. frequency and (b) FTC vs. wavelength/3 for P-waves for set 3 measurements (120mm S-R spacing) on jointed surface

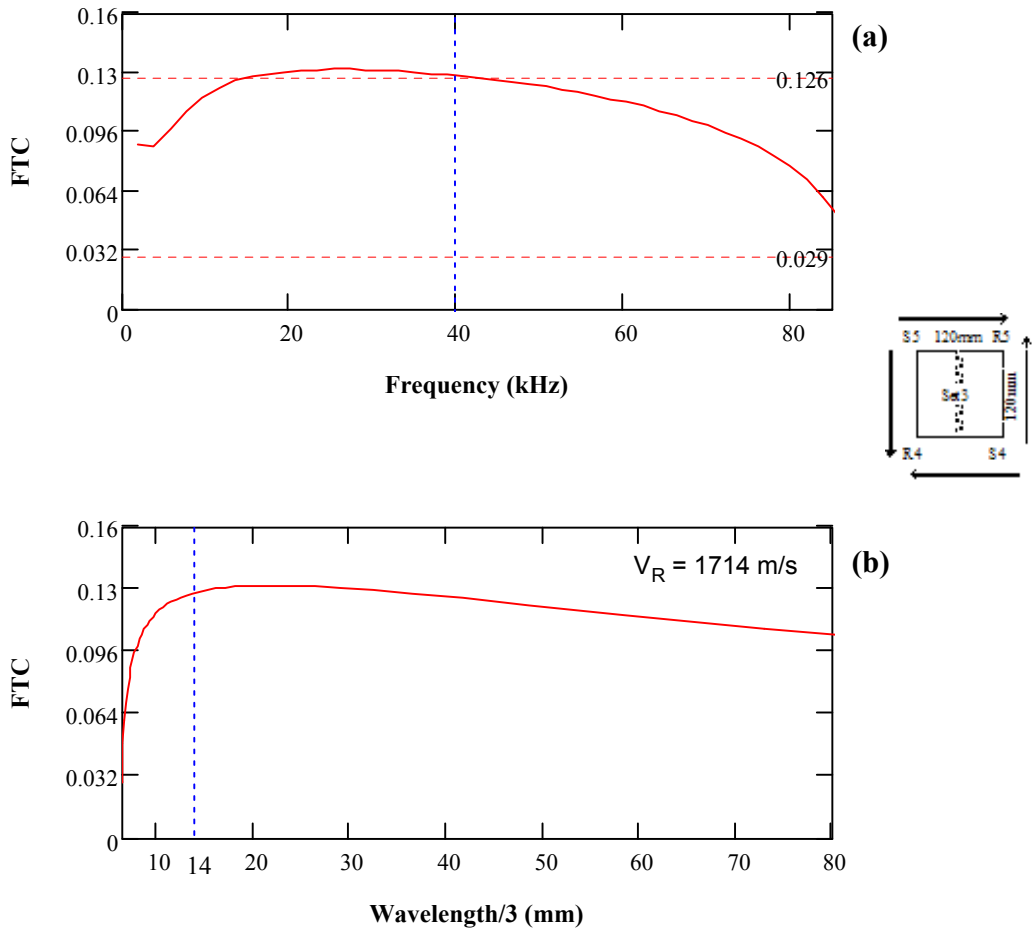

Figure R-11: (a) FTC vs. frequency and (b) FTC vs. wavelength/3 for R-waves for set 3 measurements (120mm S-R spacing) on jointed surface

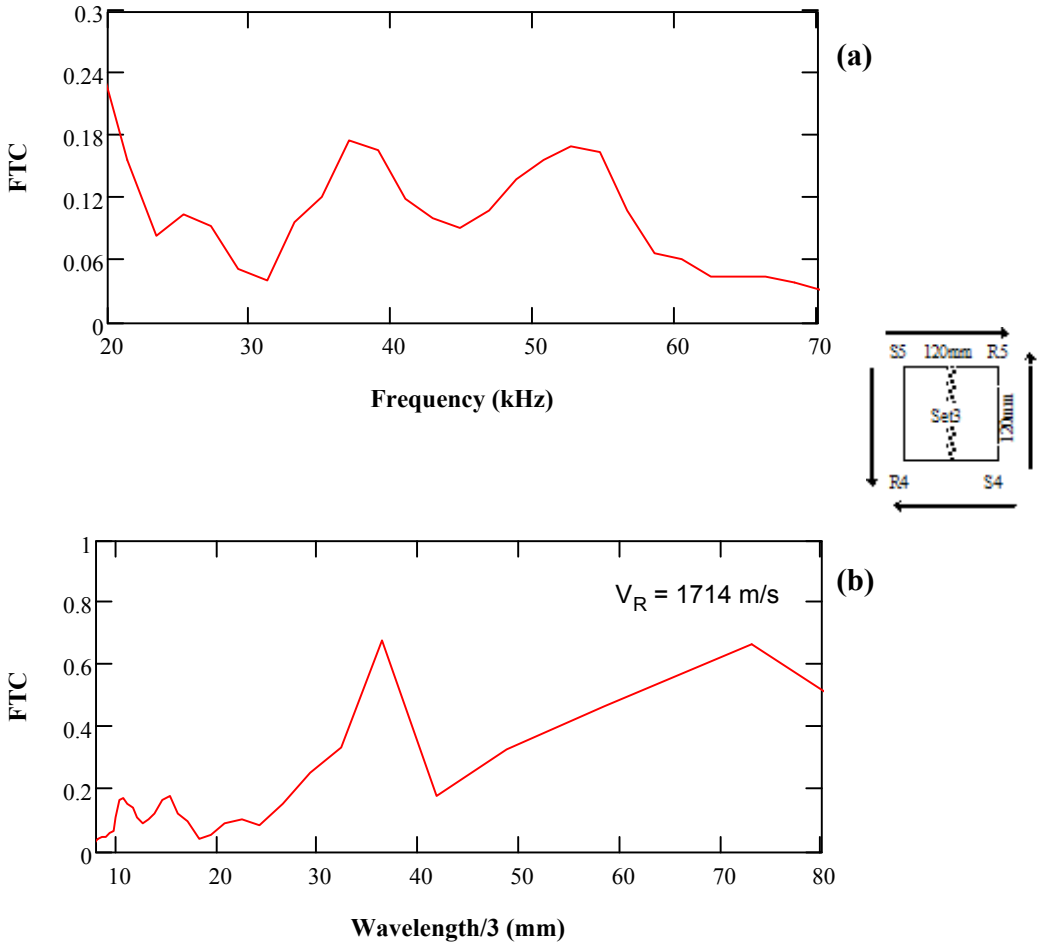

Figure R-12: (a) FTC vs. frequency and (b) FTC vs. wavelength/3 for full signals of repeated set 3 measurements (120mm S-R spacing) on jointed surface

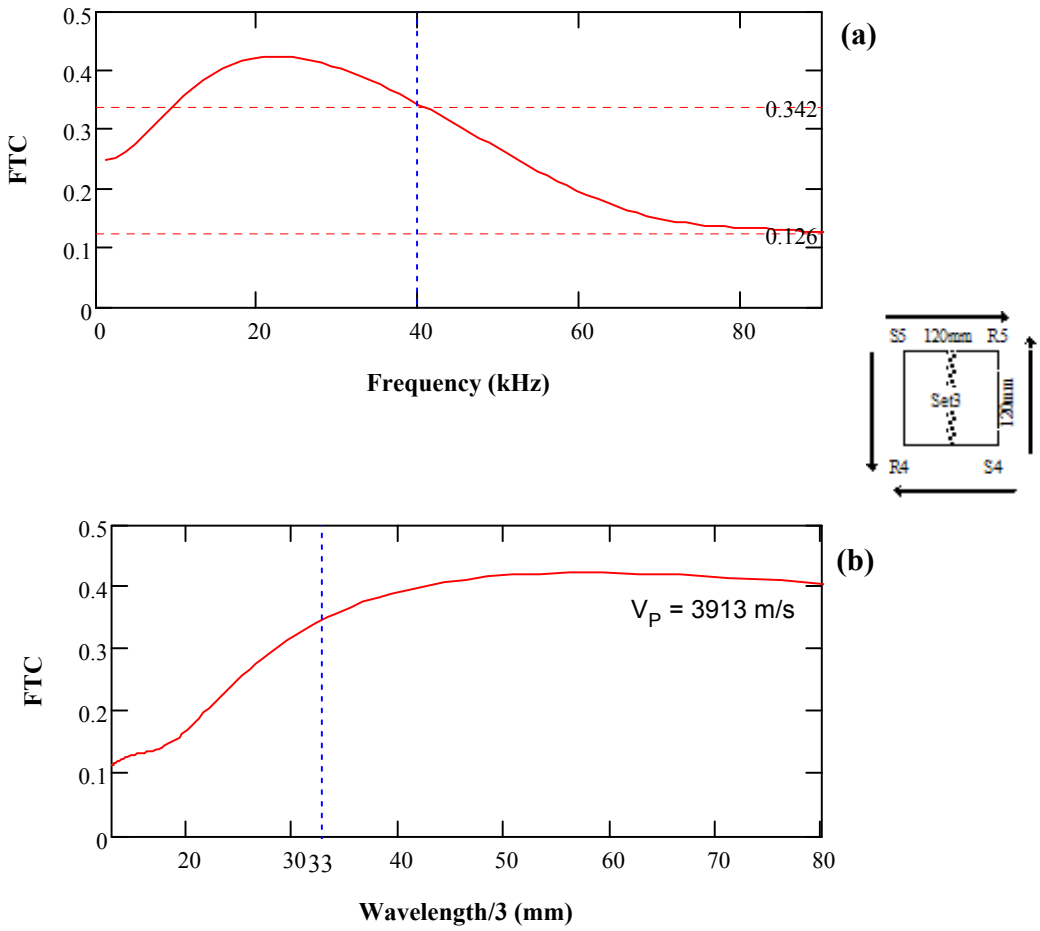

Figure R-13: (a) FTC vs. frequency and (b) FTC vs. wavelength/3 for P-waves for repeated set 3 measurements (120mm S-R spacing) on jointed surface

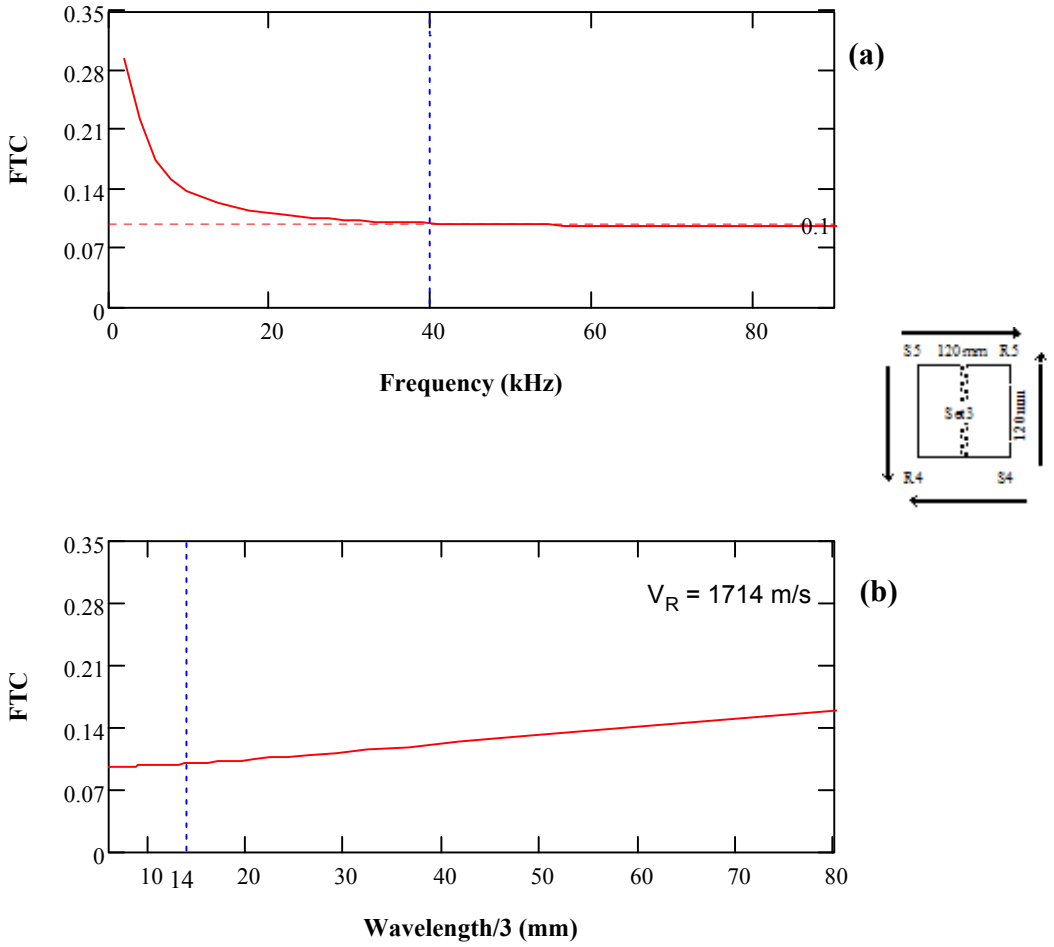

Figure R-14: (a) FTC vs. frequency and (b) FTC vs. wavelength/3 for R-waves for repeated set 3 measurements (120mm S-R spacing) on jointed surface

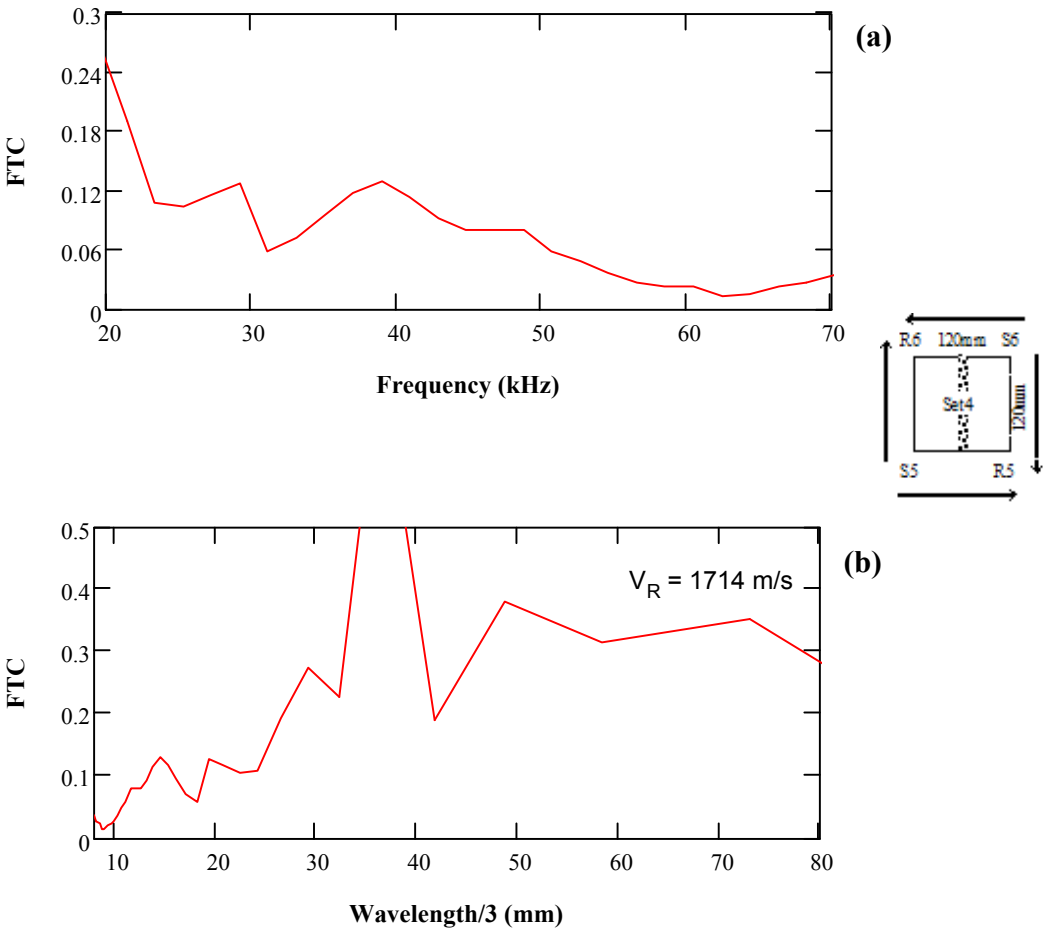

Figure R-15: (a) FTC vs. frequency and (b) FTC vs. wavelength/3 for full signals of set 4 measurements (120mm S-R spacing) on jointed surface

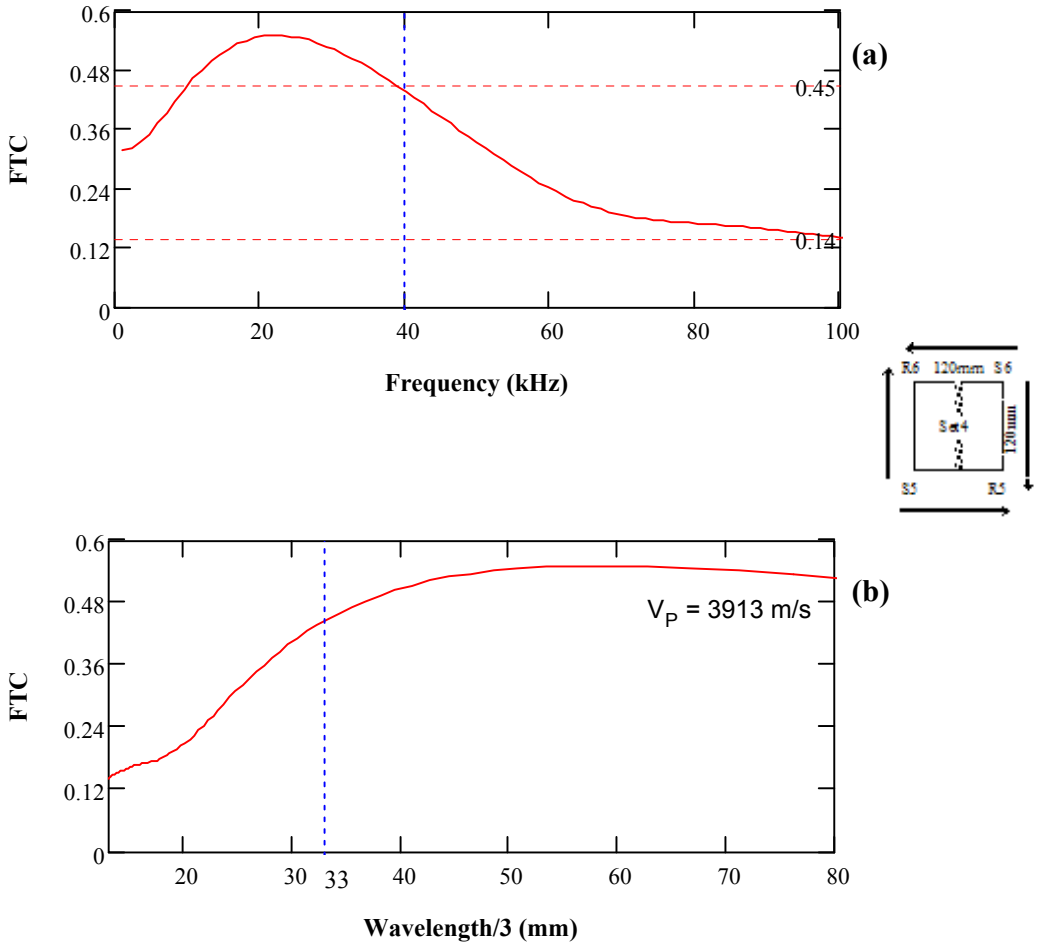

Figure R-16: (a) FTC vs. frequency and (b) FTC vs. wavelength/3 for P-waves for set 4 measurements (120mm S-R spacing) on jointed surface

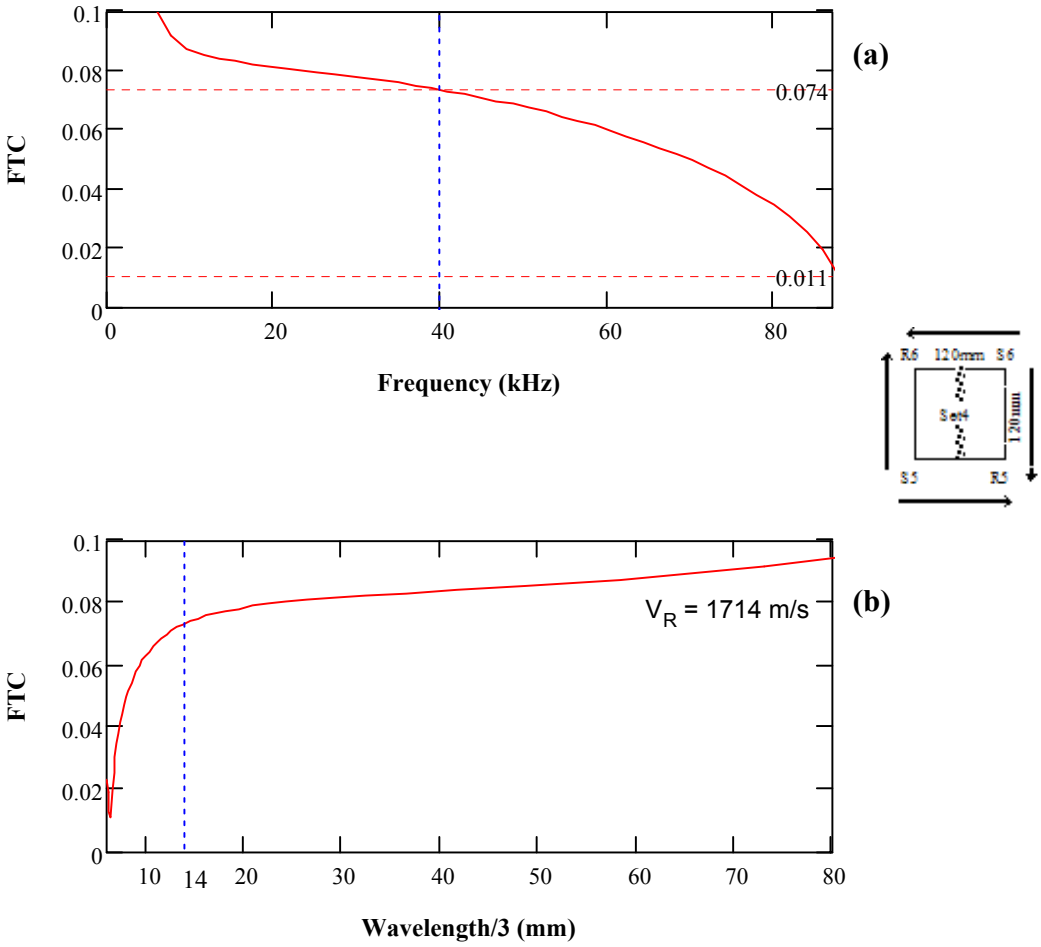

Figure R-17: (a) FTC vs. frequency and (b) FTC vs. wavelength/3 for R-waves for set 4 measurements (120mm S-R spacing) on jointed surface

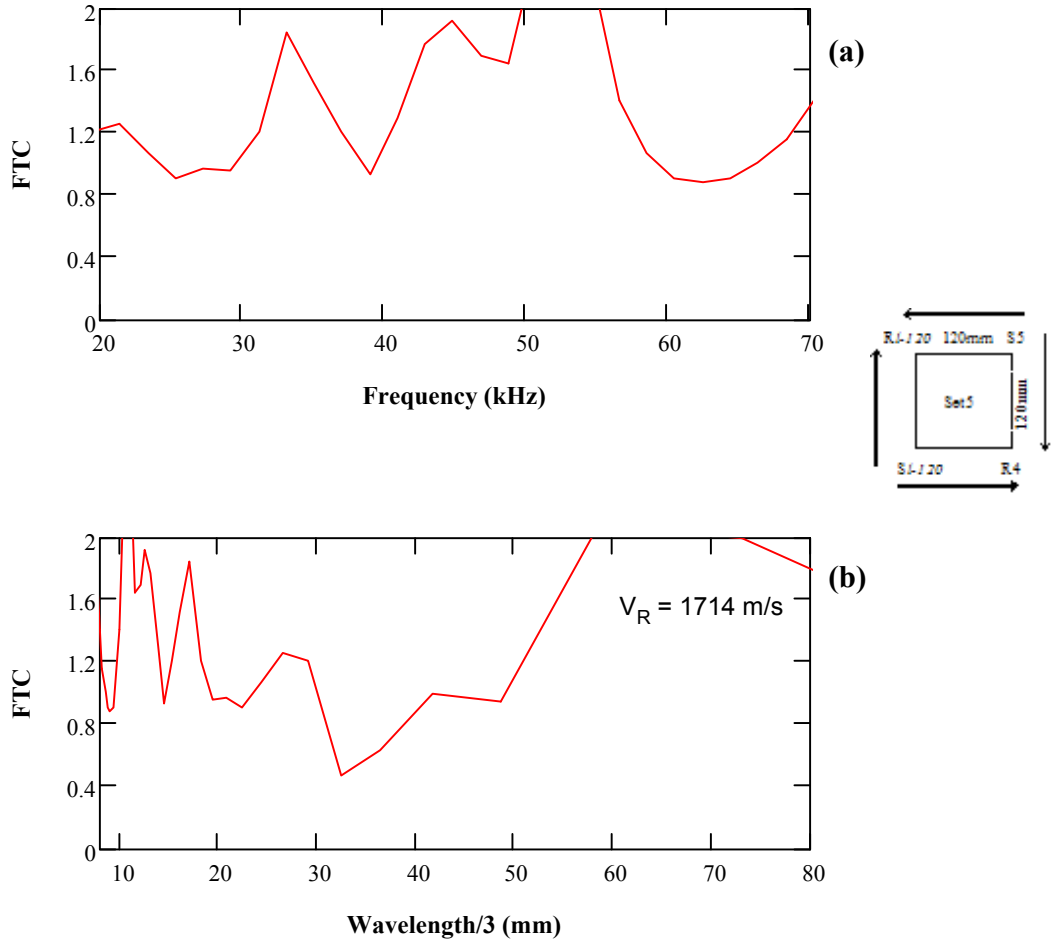

Figure R-18: (a) FTC vs. frequency and (b) FTC vs. wavelength/3 for full signals of set 5 measurements (120mm S-R spacing) on joint-free surface

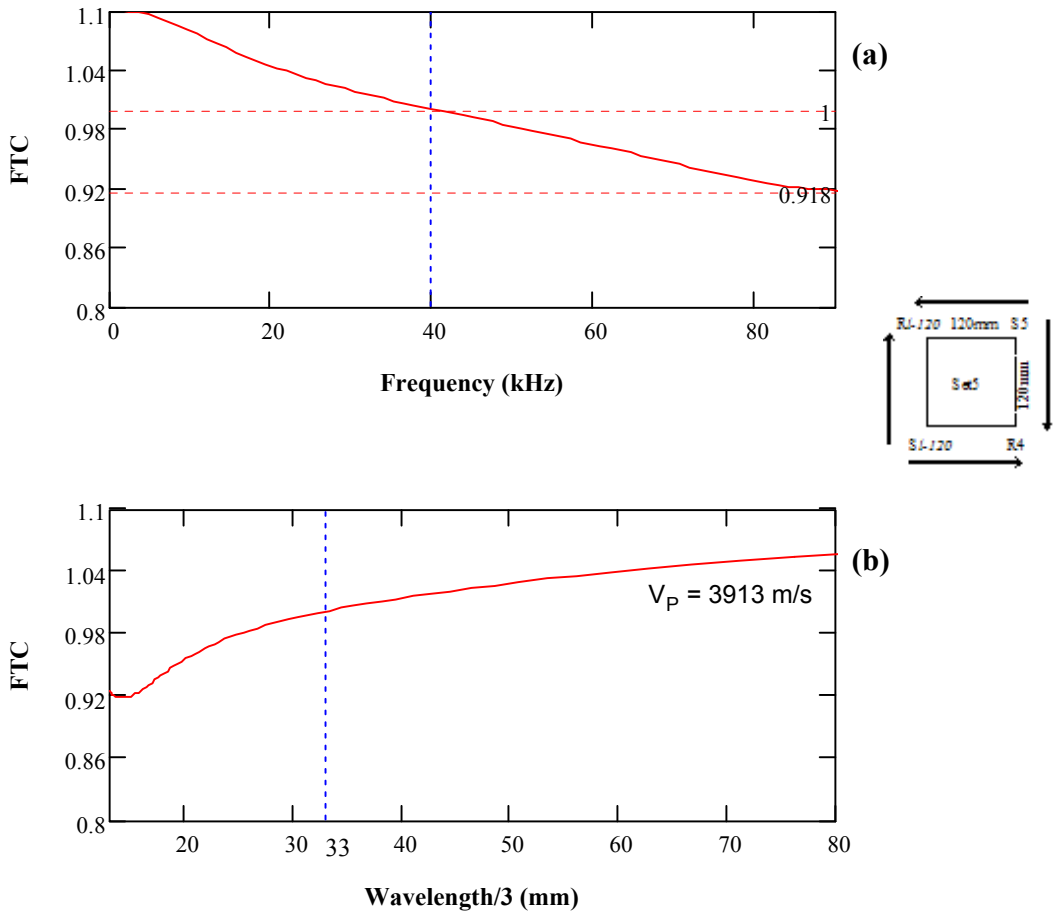

Figure R-19: (a) FTC vs. frequency and (b) FTC vs. wavelength/3 for P-waves for set 5 measurements (120mm S-R spacing) on joint-free surface

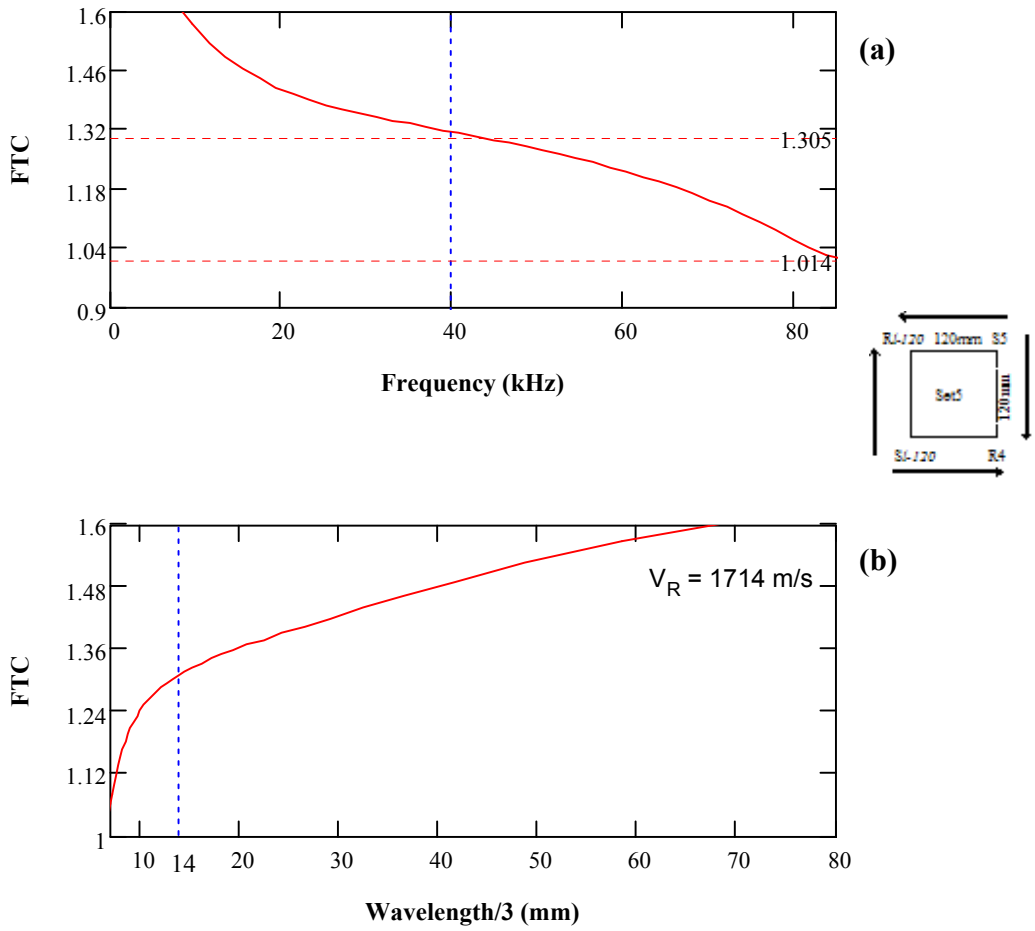

Figure R-20: (a) FTC vs. frequency and (b) FTC vs. wavelength/3 for R-waves for set 5 measurements (120mm S-R spacing) on joint-free surface

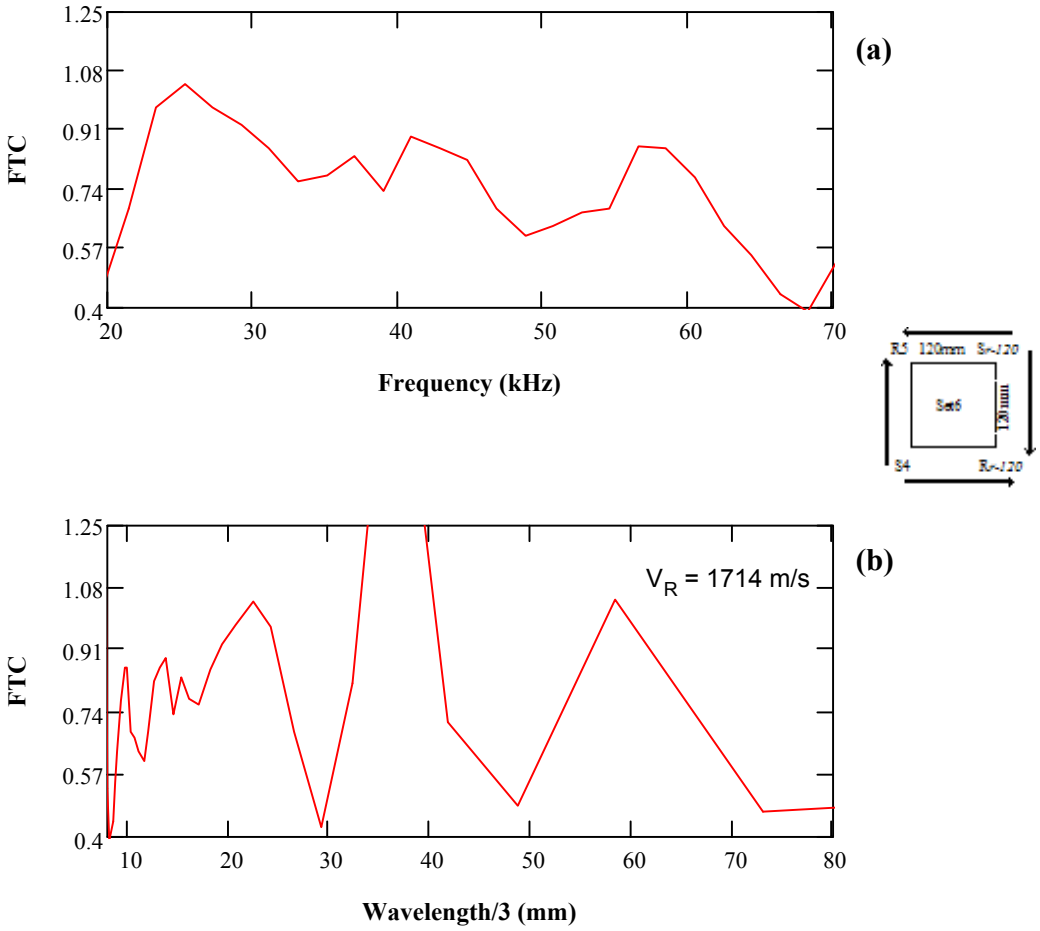

Figure R-21: (a) FTC vs. frequency and (b) FTC vs. wavelength/3 for full signals of set 6 measurements (120mm S-R spacing) on joint-free surface

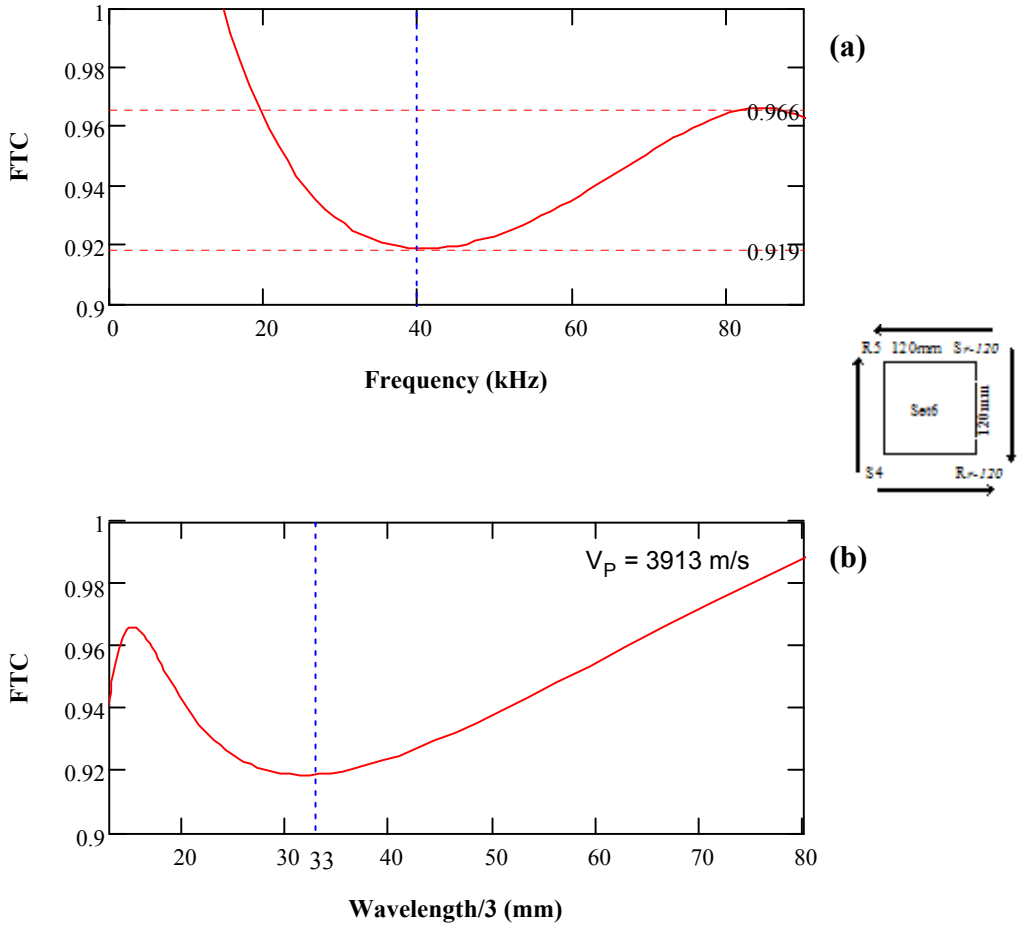

Figure R-22: (a) FTC vs. frequency and (b) FTC vs. wavelength/3 for P-waves for set 6 measurements (120mm S-R spacing) on joint-free surface

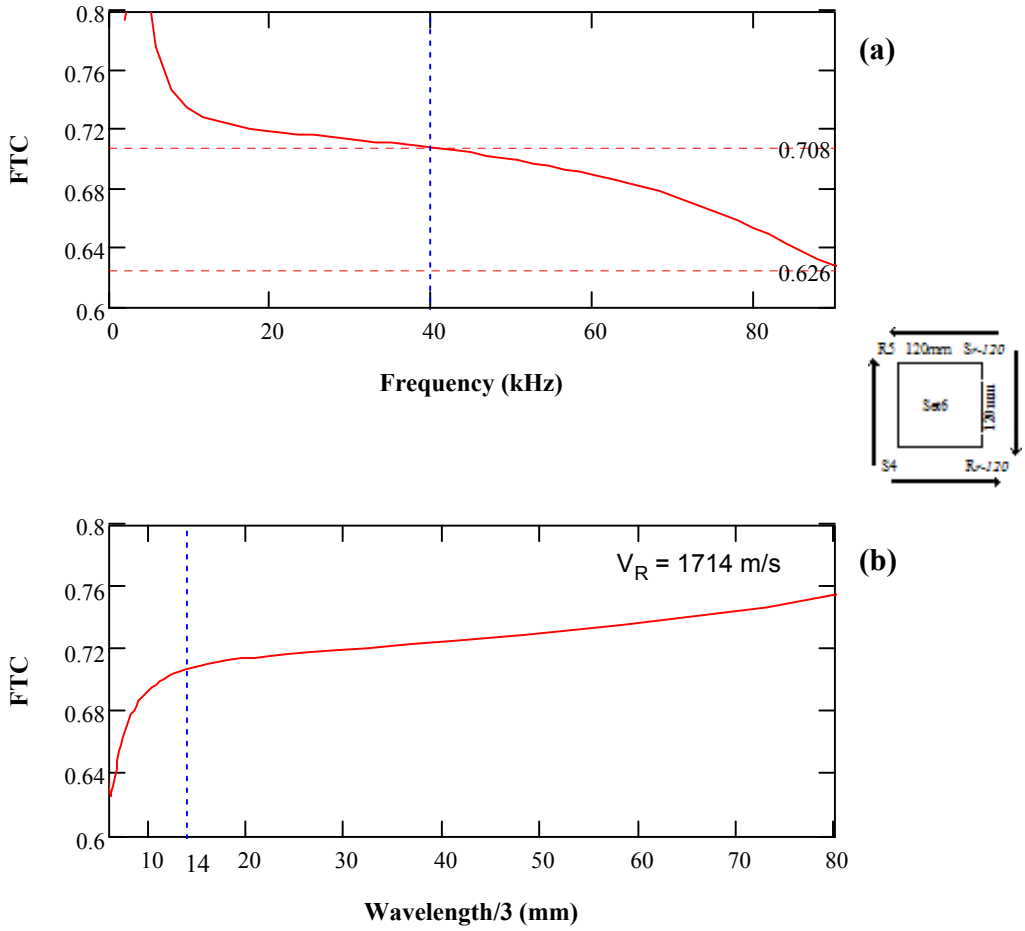

Figure R-23: (a) FTC vs. frequency and (b) FTC vs. wavelength/3 for R-waves for set 6 measurements (120mm S-R spacing) on joint-free surface

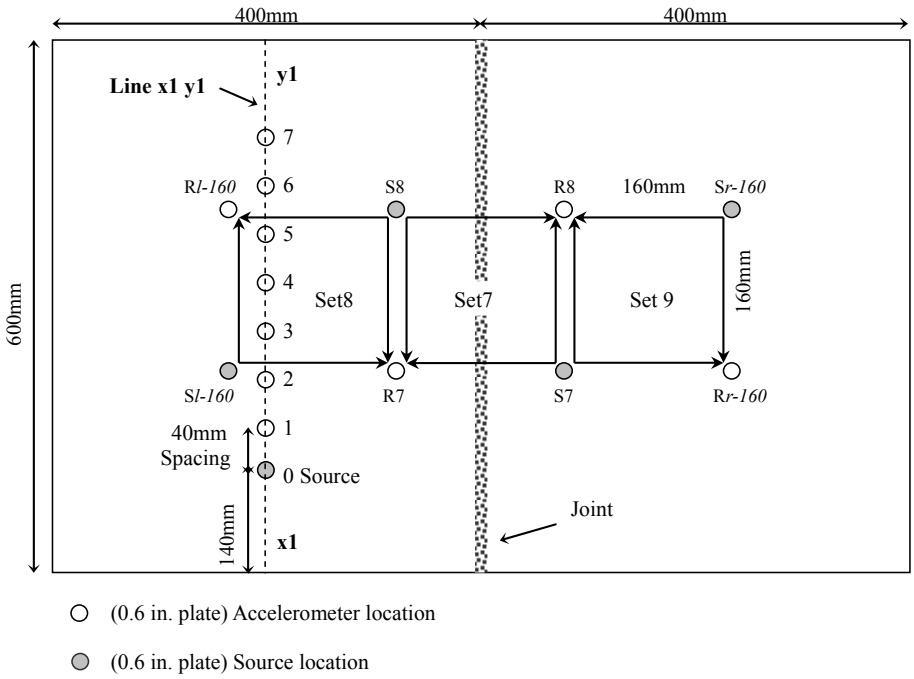

Figure R-24: 160mm S-R spacing configuration of HMA slab 3

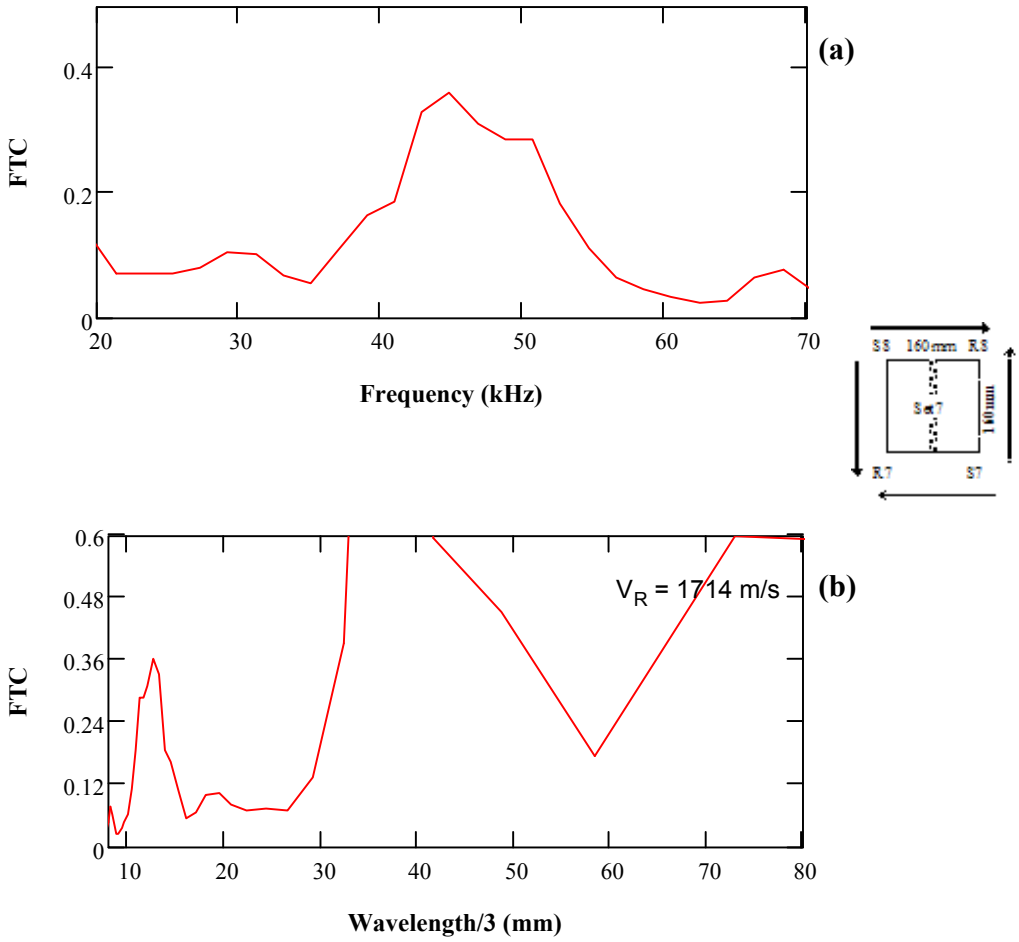

Figure R-25: (a) FTC vs. frequency and (b) FTC vs. wavelength/3 for full signals of set 7 measurements (160mm S-R spacing) on jointed surface

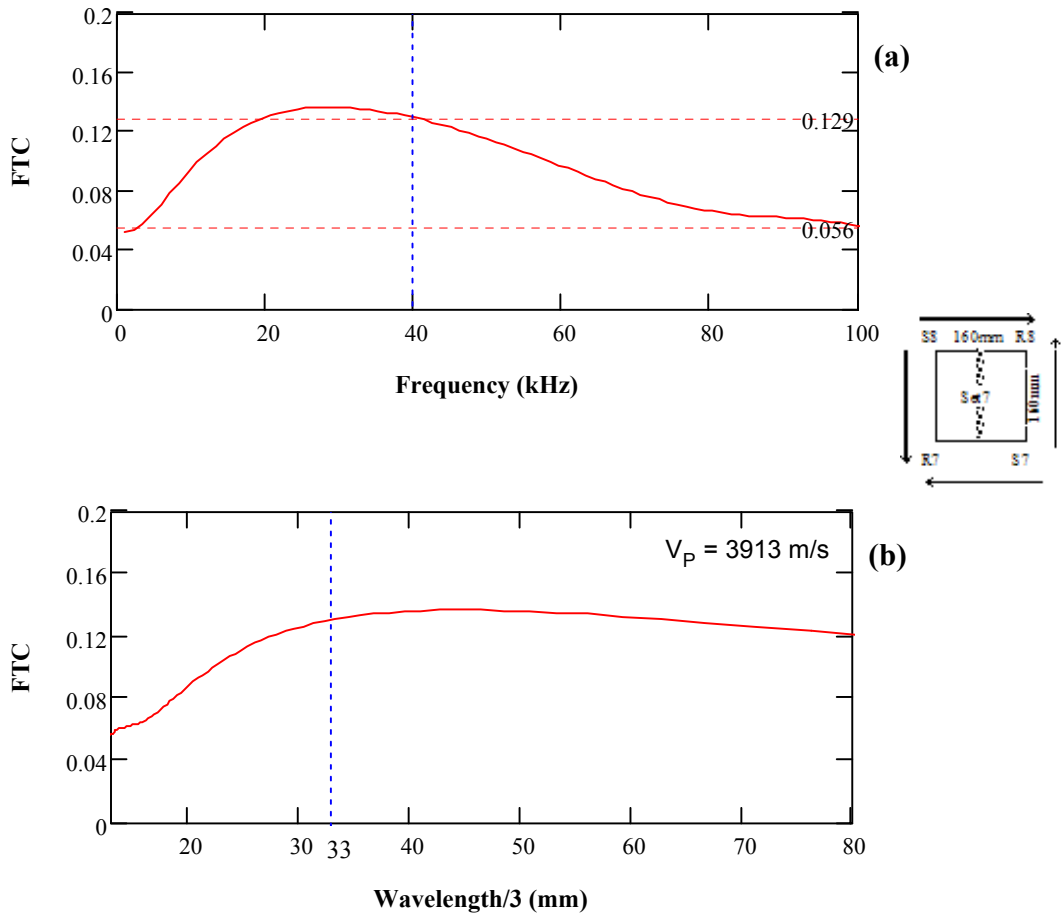

Figure R-26: (a) FTC vs. frequency and (b) FTC vs. wavelength/3 for P-waves for set 7 measurements (160mm S-R spacing) on jointed surface

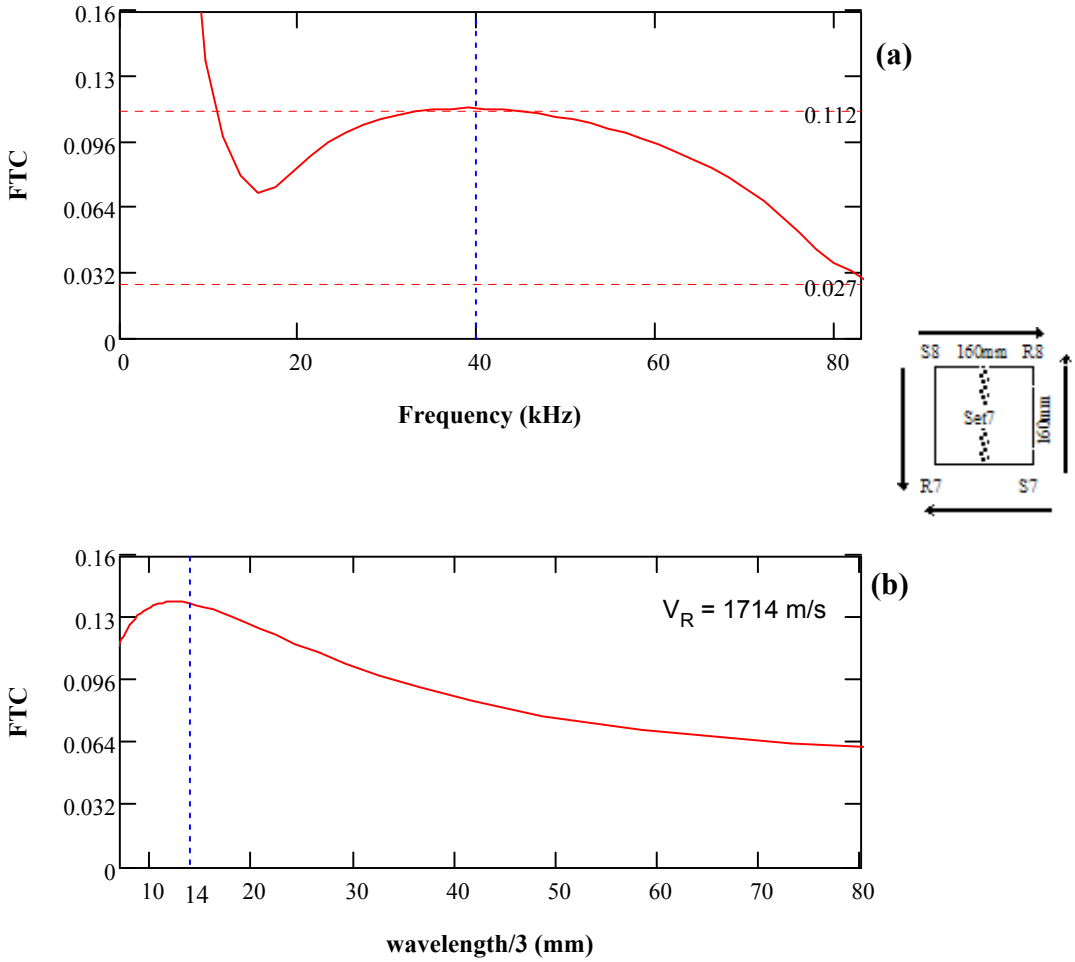

Figure R-27: (a) FTC vs. frequency and (b) FTC vs. wavelength/3 for R-waves for set 7 measurements (160mm S-R spacing) on jointed surface

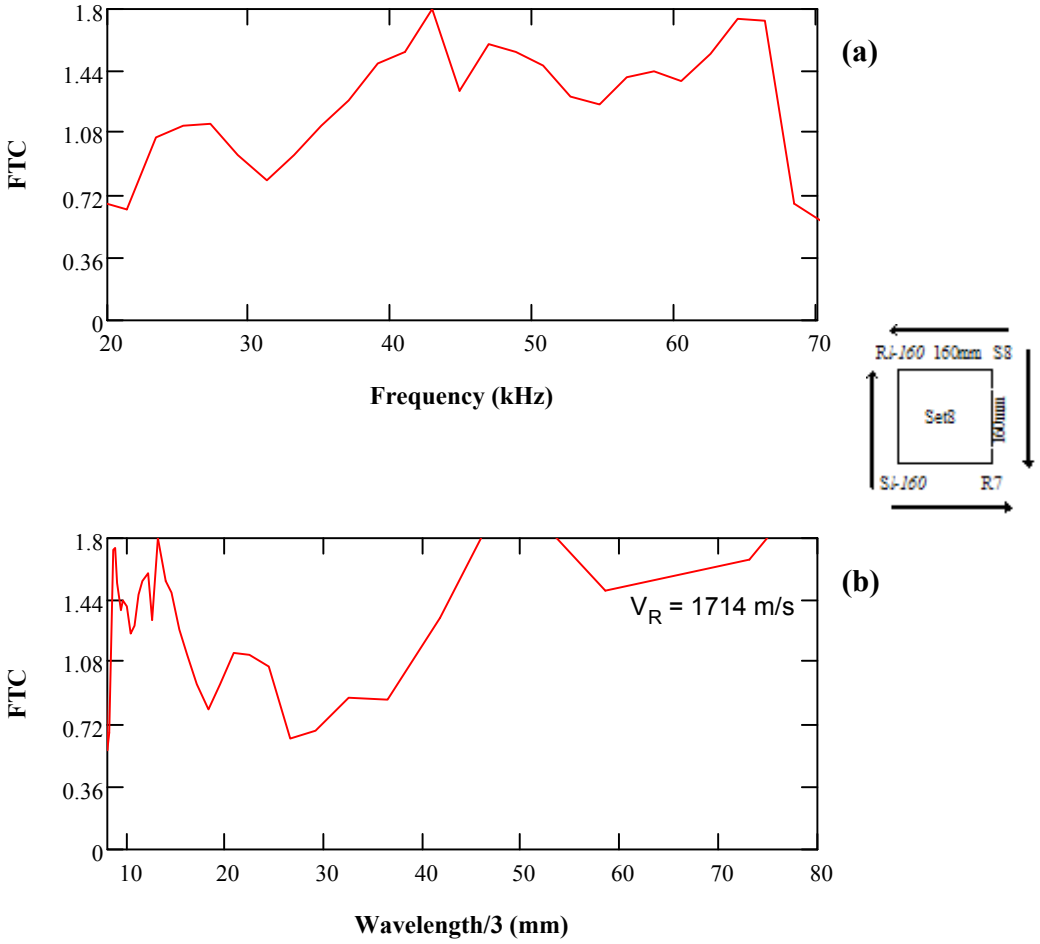

Figure R-28: (a) FTC vs. frequency and (b) FTC vs. wavelength/3 for full signals of set 8 measurements (160mm S-R spacing) on joint-free surface

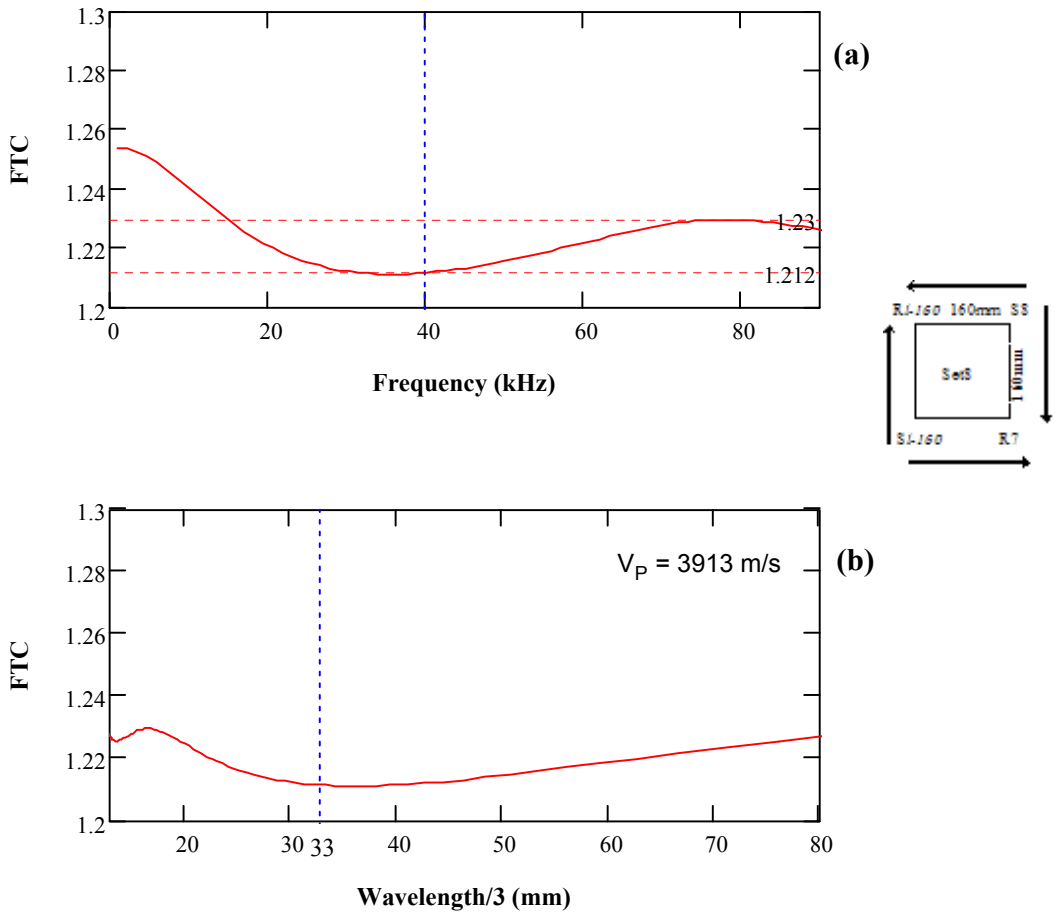

Figure R-29: (a) FTC vs. frequency and (b) FTC vs. wavelength/3 for P-waves for set 8 measurements (160mm S-R spacing) on joint-free surface

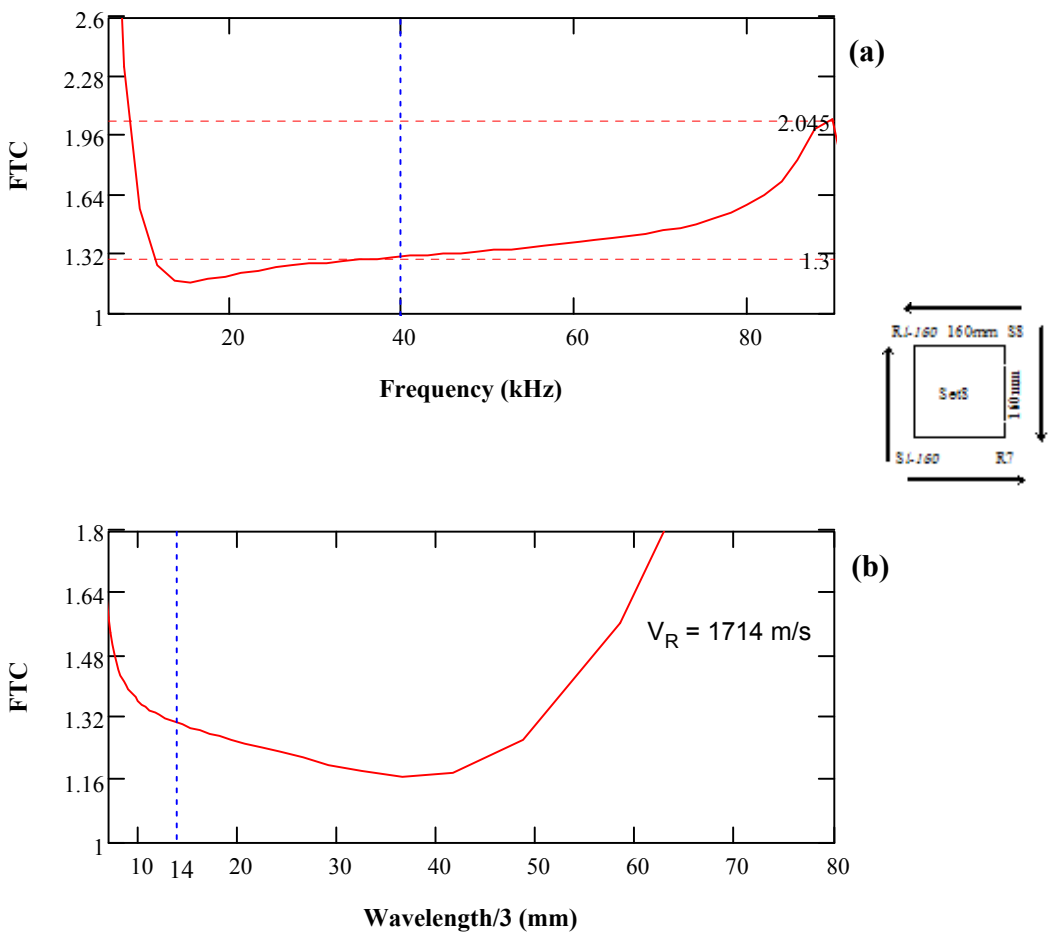

Figure R-30: (a) FTC vs. frequency and (b) FTC vs. wavelength/3 for R-waves for set 8 measurements (160mm S-R spacing) on joint-free surface

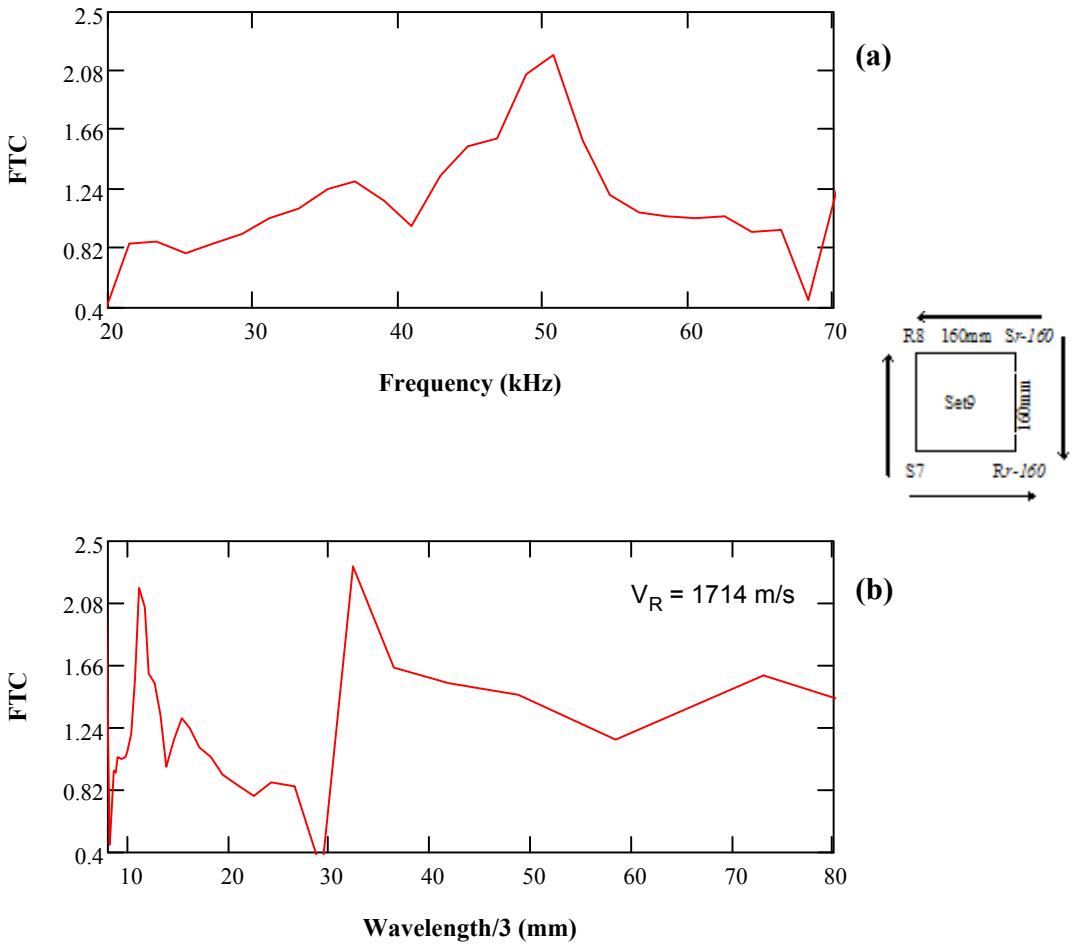

Figure R-31: (a) FTC vs. frequency and (b) FTC vs. wavelength/3 for full signals of set 9 measurements (160mm S-R spacing) on joint-free surface

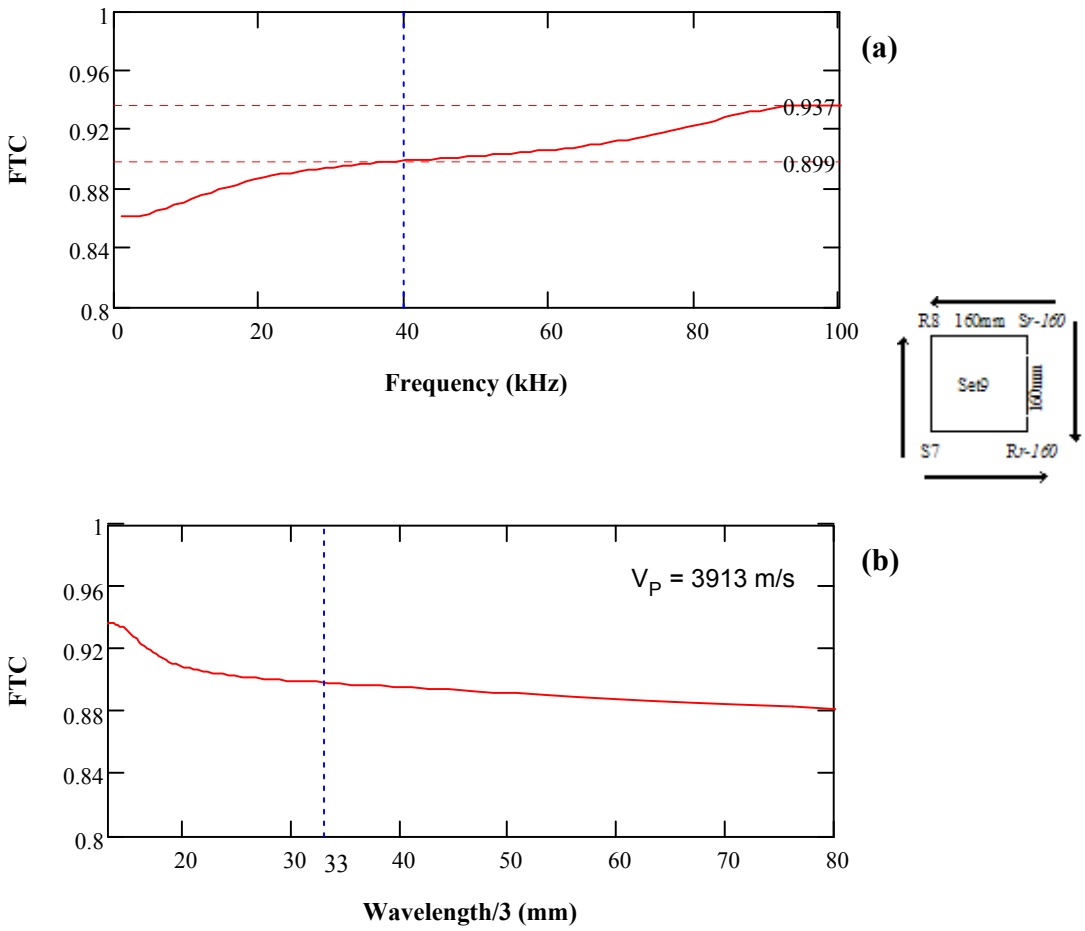

Figure R-32: (a) FTC vs. frequency and (b) FTC vs. wavelength/3 for P-waves for set 9 measurements (160mm S-R spacing) on joint-free surface

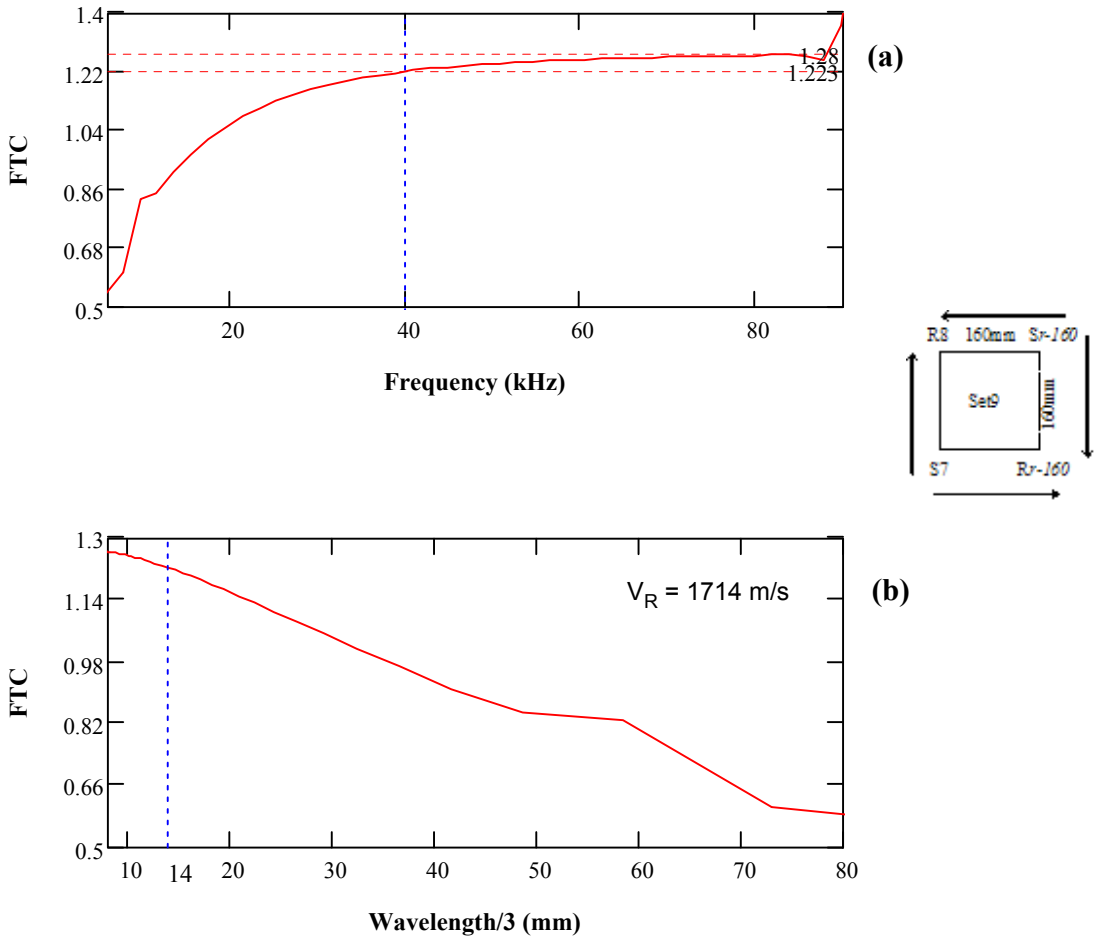

Figure R-33: (a) FTC vs. frequency and (b) FTC vs. wavelength/3 for P-waves for set 9 measurements (160mm S-R spacing) on joint-free surface

Appendix S

Wavelet Transform Using Morlet Wavelet for Slab 3 - Measurements on the Jointed and the Joint-free Surfaces

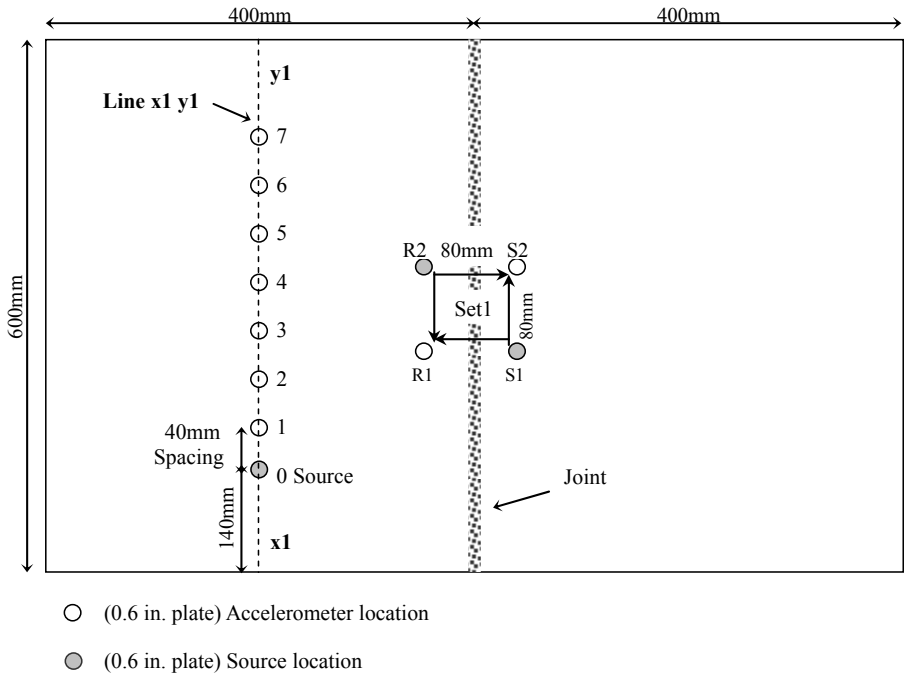

Figure S-1: 80mm S-R spacing configuration of HMA slab 3

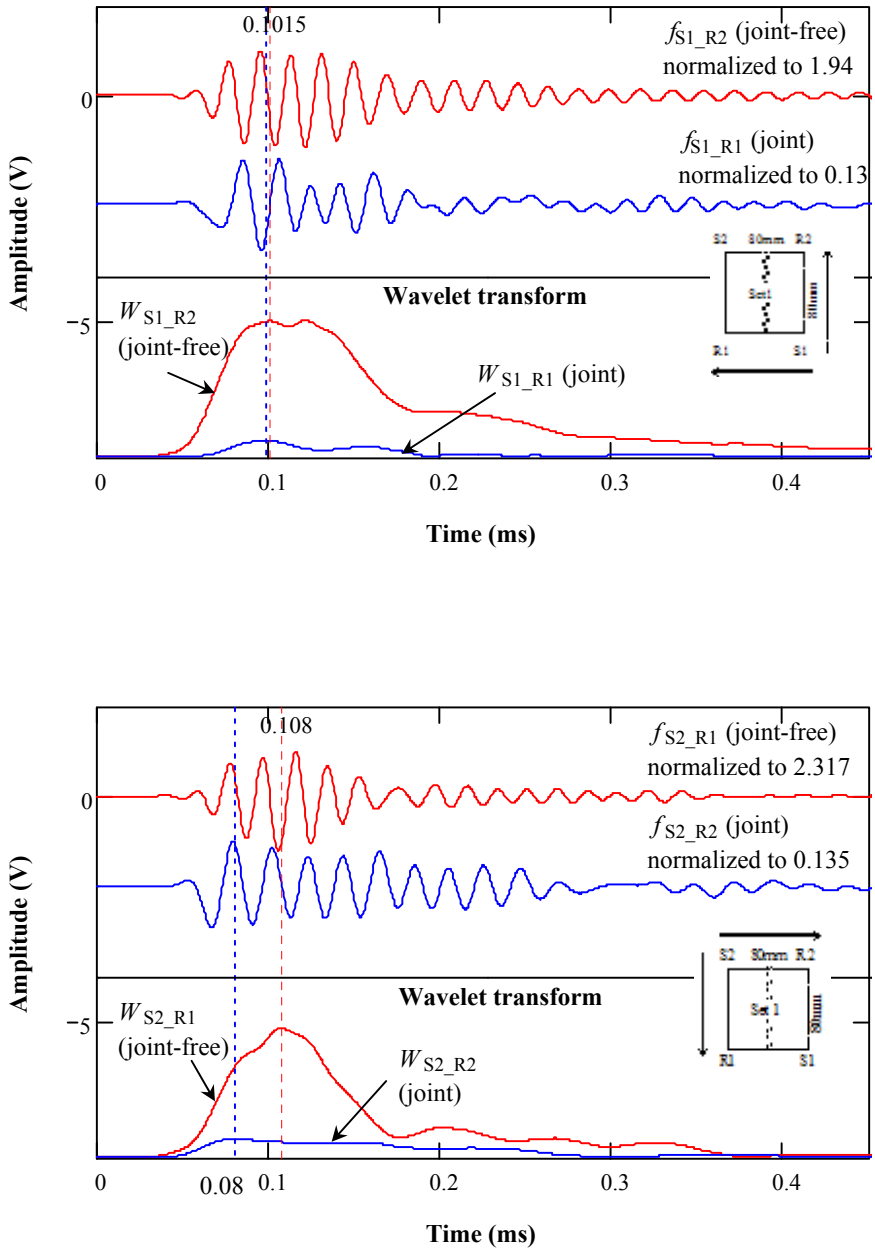

Figure S-2: Wavelet transform of set 1 measurements (80mm S-R spacing) using Morlet wavelet at the dominant frequencies of full signals (Morlet center frequency of 56.641 kHz for both f_{S1_R2} and f_{S1_R1}; 54.688 kHz for f_{S2_R1}; and 50.781 kHz for f_{S2_R2})

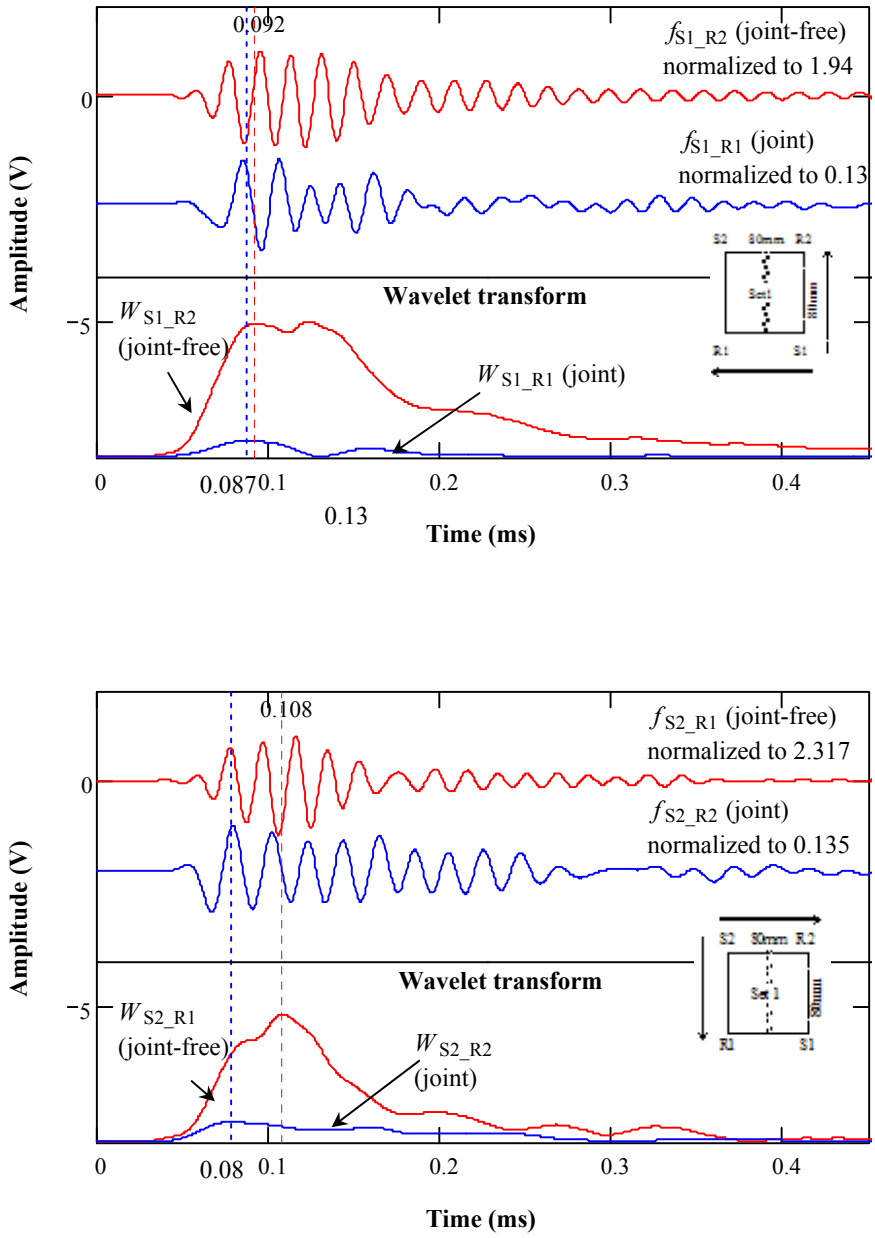

Figure S-3: Wavelet transform of set 1 measurements (80mm S-R spacing) using Morlet wavelet at the dominant frequencies of P-waves (Morlet center frequency of 45.166 kHz for f_{S1_R2}; 32.959 kHz for f_{S1_R1}; 41.504 kHz for f_{S2_R1}; and 40.283 kHz for f_{S2_R2})

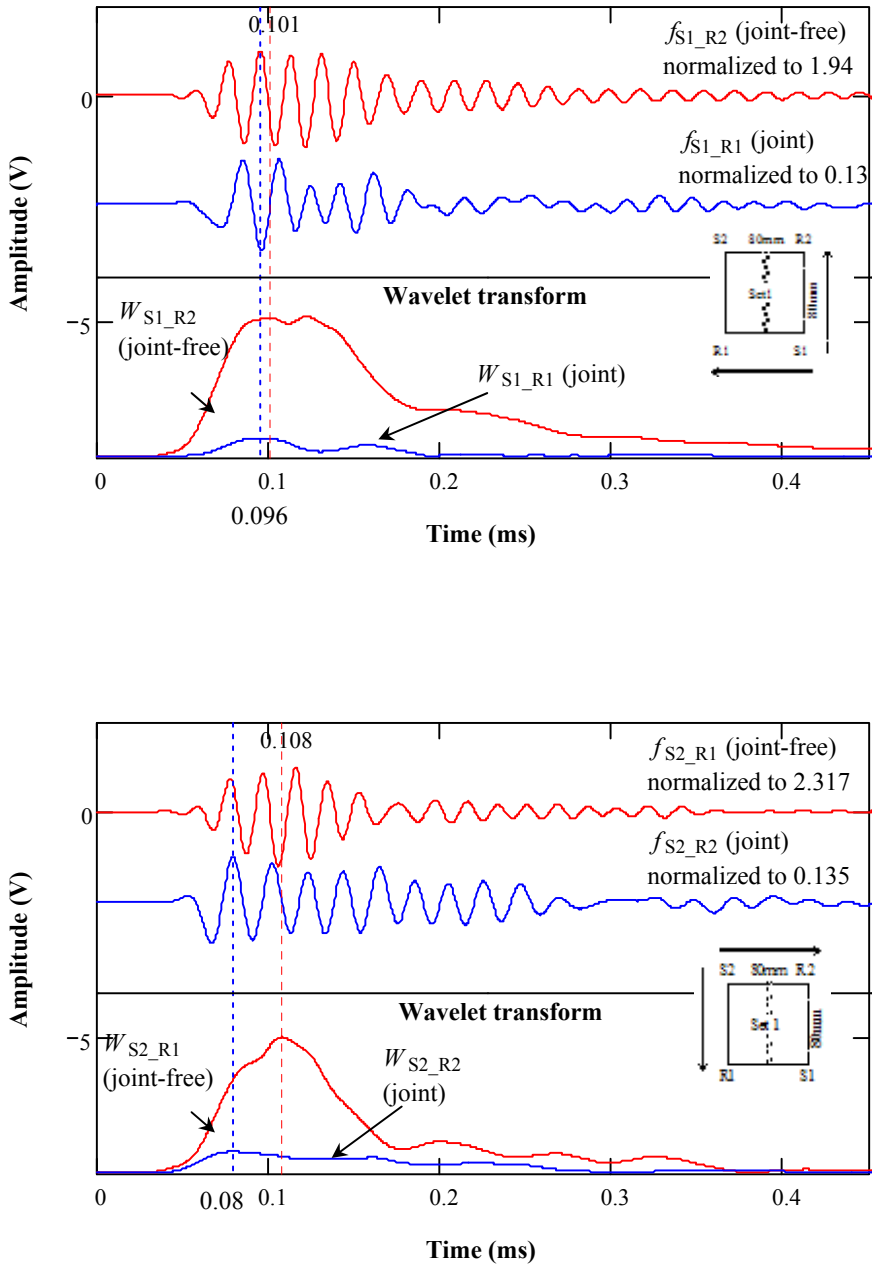

Figure S-4: Wavelet transform of set 1 measurements (80mm S-R spacing) using Morlet wavelet at the dominant frequencies of R-waves (Morlet center frequency of 52.734 kHz for f_{S1_R2}; 42.969 kHz for f_{S1_R1}; 48.828 kHz for f_{S2_R1}; and 41.016 kHz for f_{S2_R2})

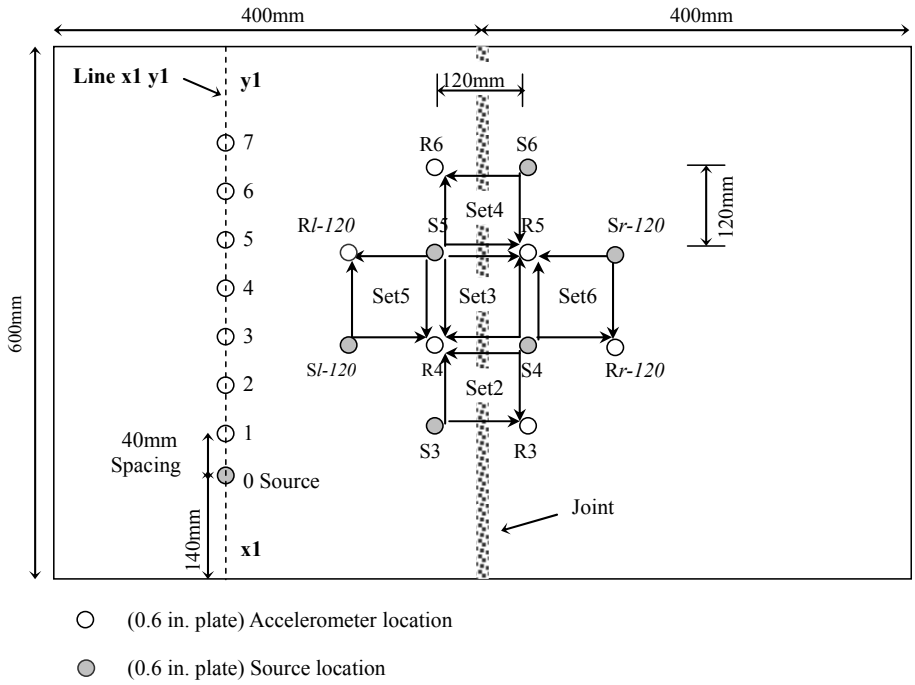

Figure S-5: 120mm S-R spacing configuration of HMA slab 3

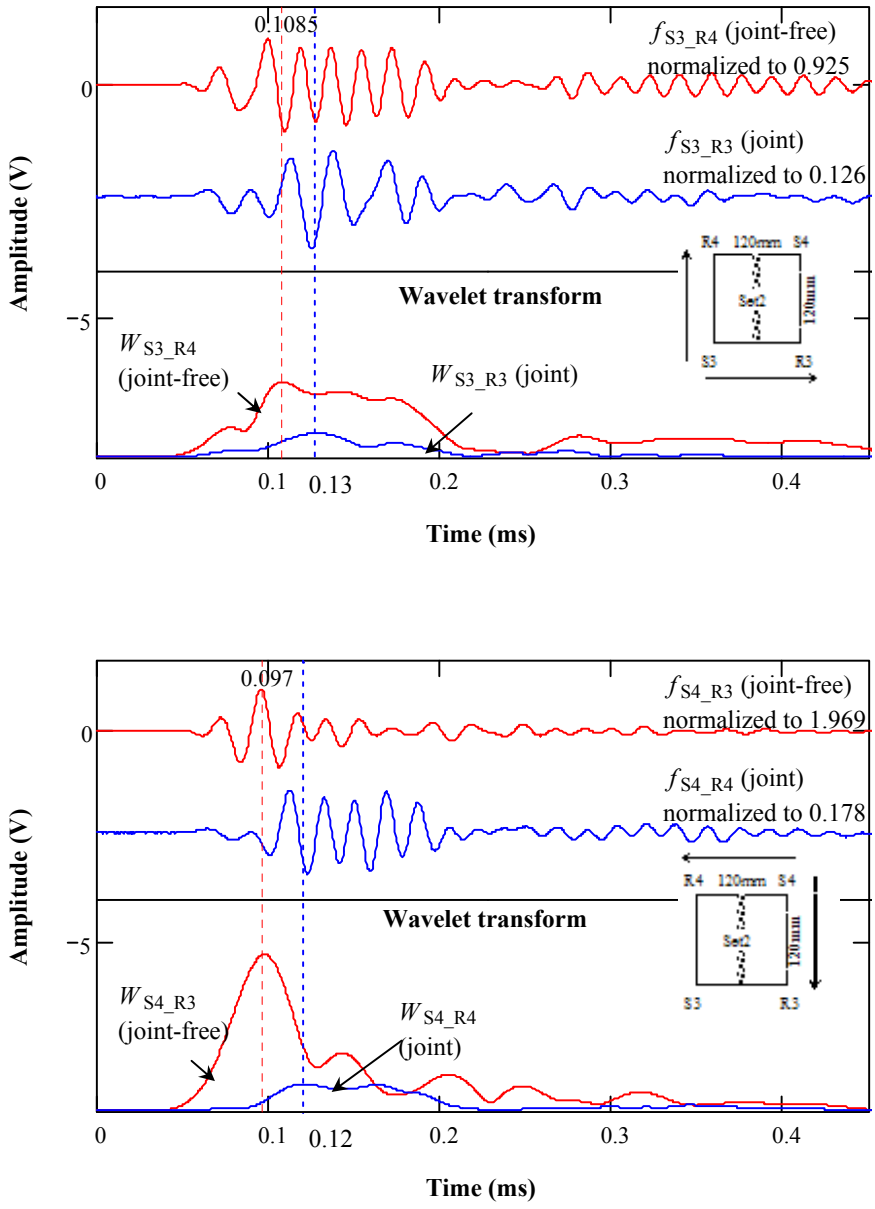

Figure S-6: Wavelet transform of set 2 measurements (120mm S-R spacing) using Morlet wavelet at the dominant frequencies of full signals (Morlet center frequency of 56.641 kHz for f_{S3_R3}; 42.969 kHz for f_{S3_R3}; 50.781 kHz for f_{S4_R3}; and 54.688 kHz for f_{S4_R4})

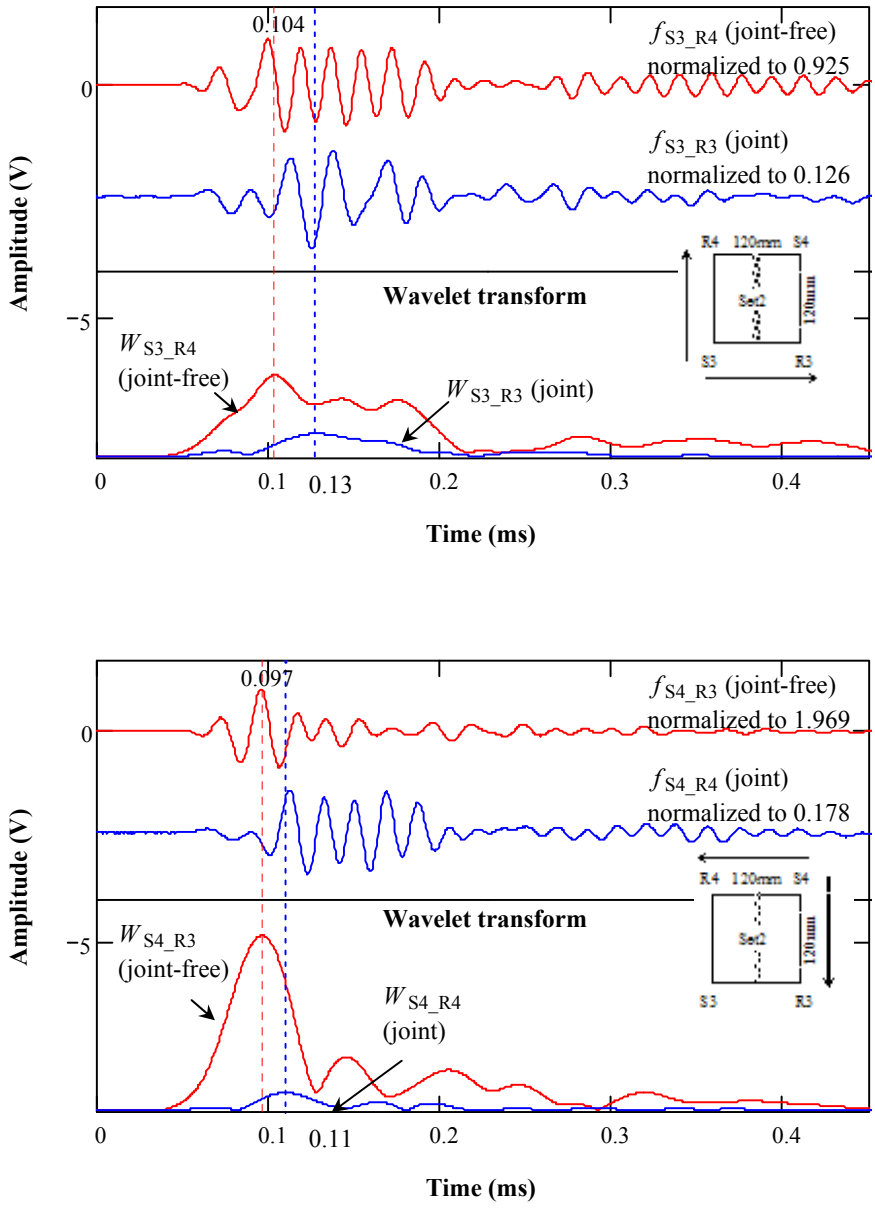

Figure S-7: Wavelet transform of set 2 measurements (120mm S-R spacing) using Morlet wavelet at the dominant frequencies of P-waves (Morlet center frequency of 41.504 kHz for f_{S3_R3}; 30.518 kHz for f_{S3_R3}; 39.063 kHz for f_{S4_R3}; and 26.855 kHz for f_{S4_R4})

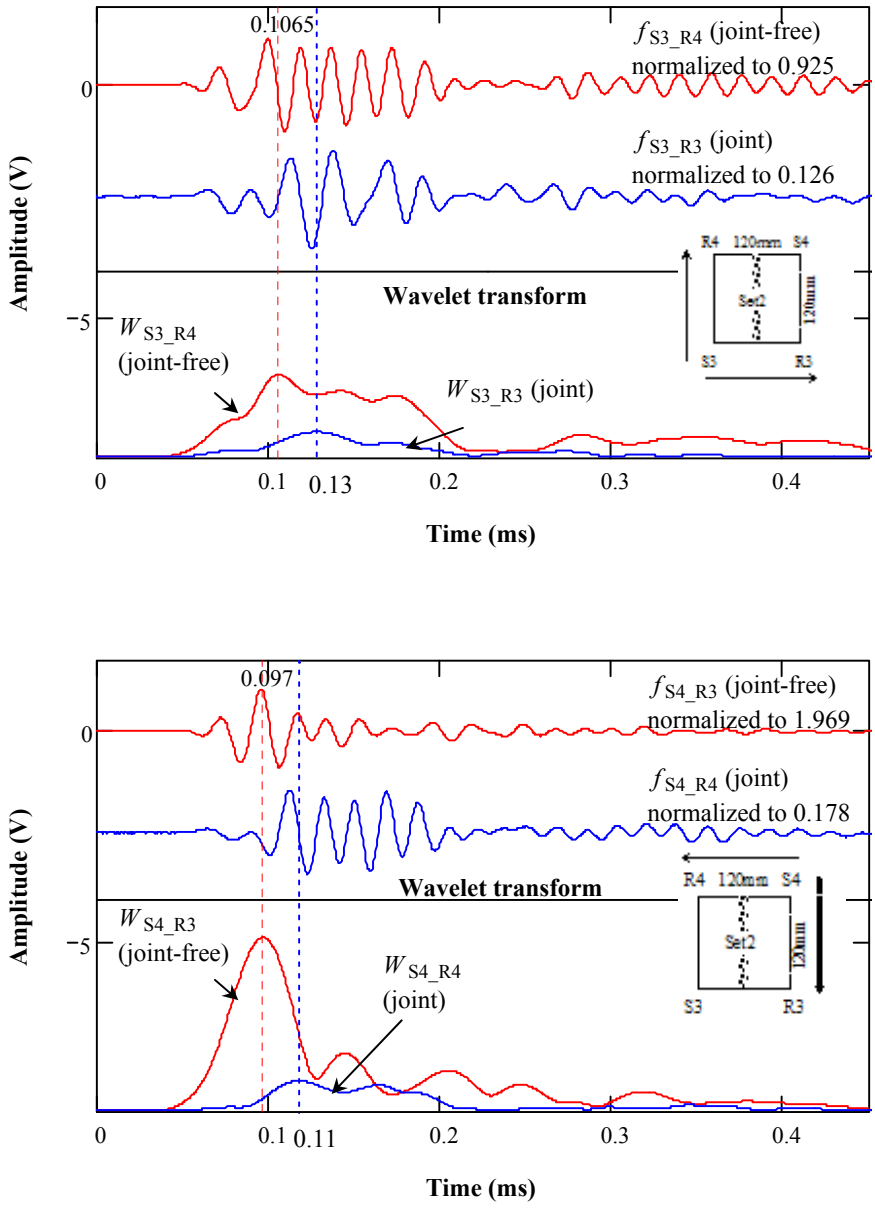

Figure S-8: Wavelet transform of set 2 measurements (120mm S-R spacing) using Morlet wavelet at the dominant frequencies of R-waves (Morlet center frequency of 46.875 kHz for f_{S3_R3}; 39.063 kHz for f_{S3_R3}; 42.969 kHz for f_{S4_R3}; and 44.922 kHz for f_{S4_R4})

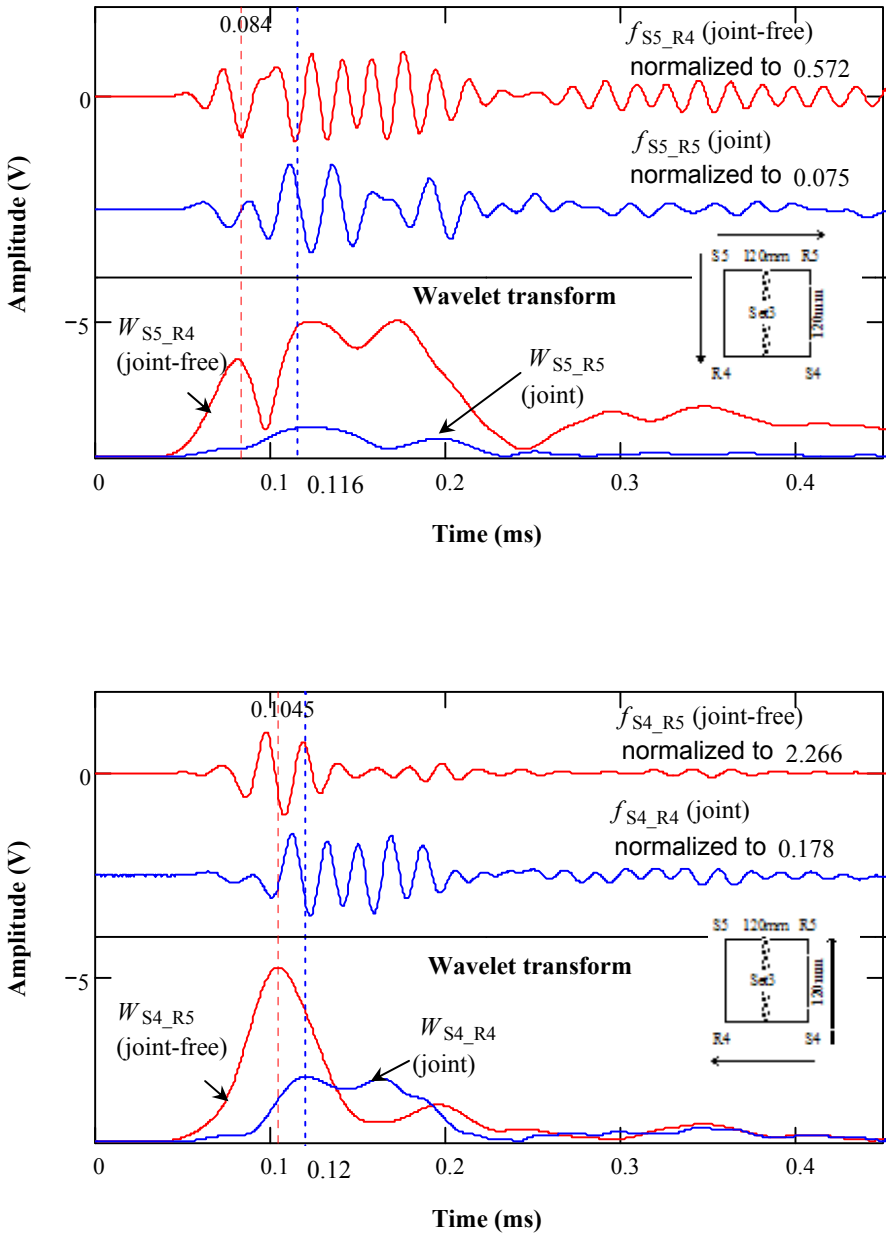

Figure S-9: Wavelet transform of set 3 measurements (120mm S-R spacing) using Morlet wavelet at the dominant frequencies of full signals (Morlet center frequency of 56.641 kHz for f_{S5_R4}; 42.969 kHz for f_{S5_R5}; 50.781 kHz for f_{S4_R5}; and 54.688 kHz for f_{S4_R4})

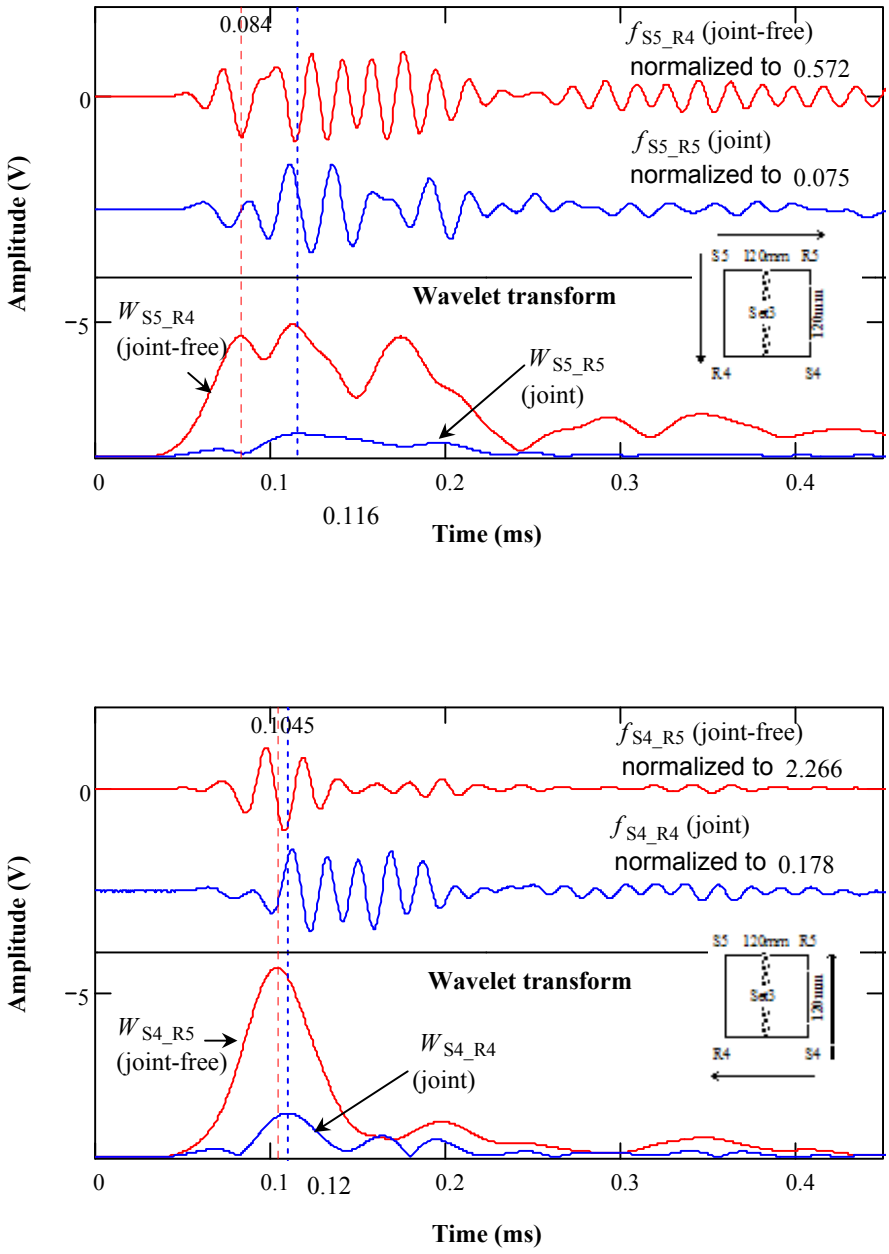

Figure S-10: Wavelet transform of set 3 measurements (120mm S-R spacing) using Morlet wavelet at the dominant frequencies of P-waves (Morlet center frequency of 39.063 kHz for f_{S5_R4}; 28.075 kHz for f_{S5_R5}; 40.504 kHz for f_{S4_R5}; and 26.855 kHz for f_{S4_R4})

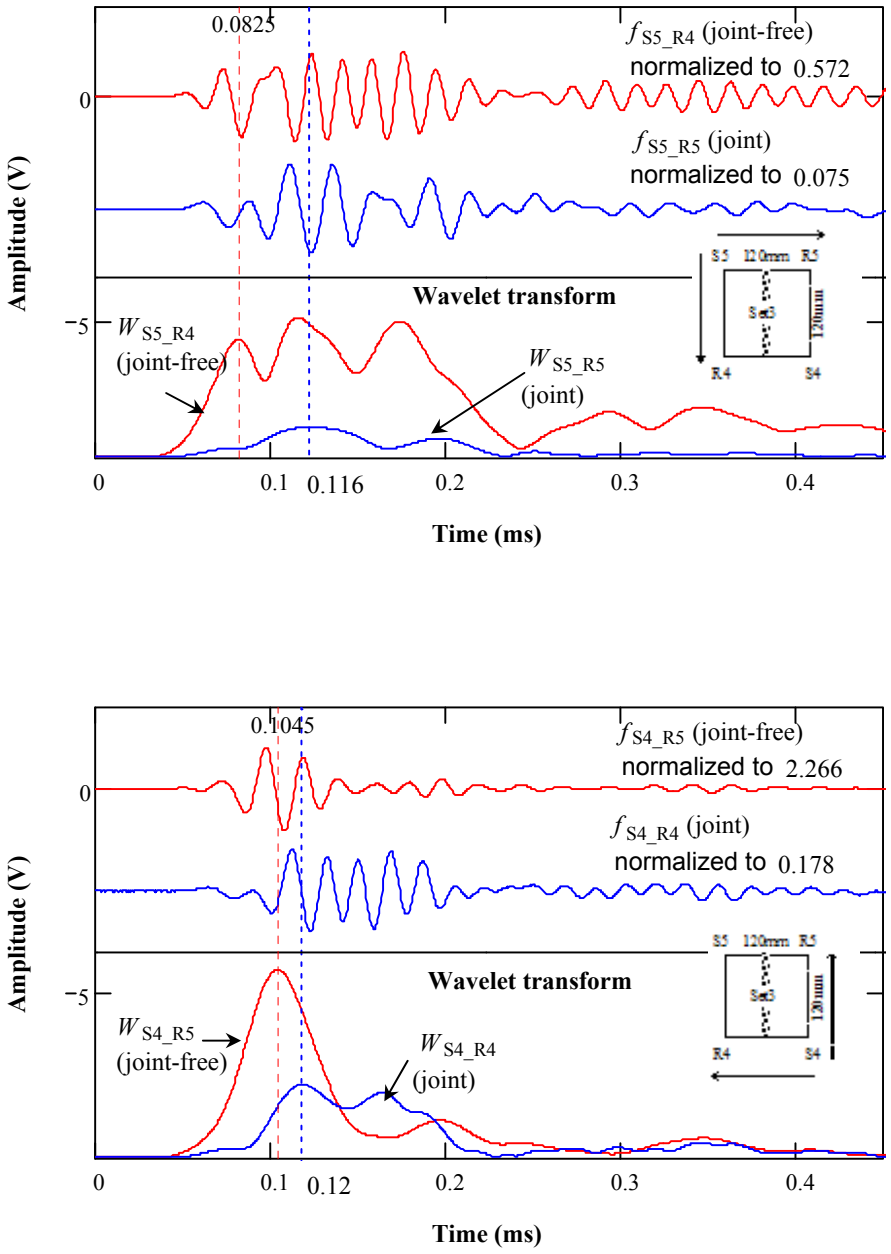

Figure S-11: Wavelet transform of set 3 measurements (120mm S-R spacing) using Morlet wavelet at the dominant frequencies of R-waves (Morlet center frequency of 42.969 kHz for f_{S5_R4}; 39.063 kHz for f_{S5_R5}; 44.922 kHz for f_{S4_R5}; and 44.922 kHz for f_{S4_R4})

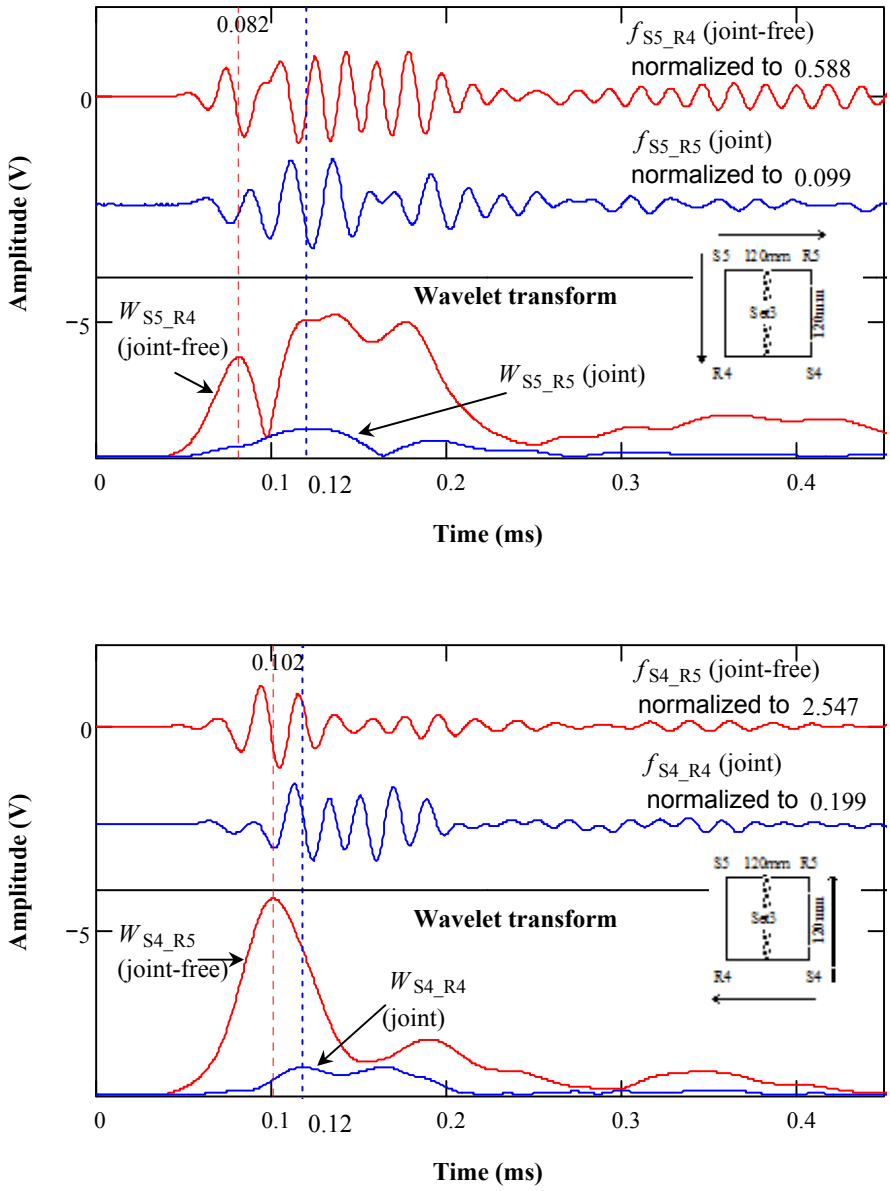

Figure S-12: Wavelet transform of repeated set 3 measurements (120mm S-R spacing) using Morlet wavelet at the dominant frequencies of full signals (Morlet center frequency of 56.641 kHz for f_{S5_R4}; 42.969 kHz for f_{S5_R5}; 50.781 kHz for f_{S4_R5}; and 50.781 kHz for f_{S4_R4})

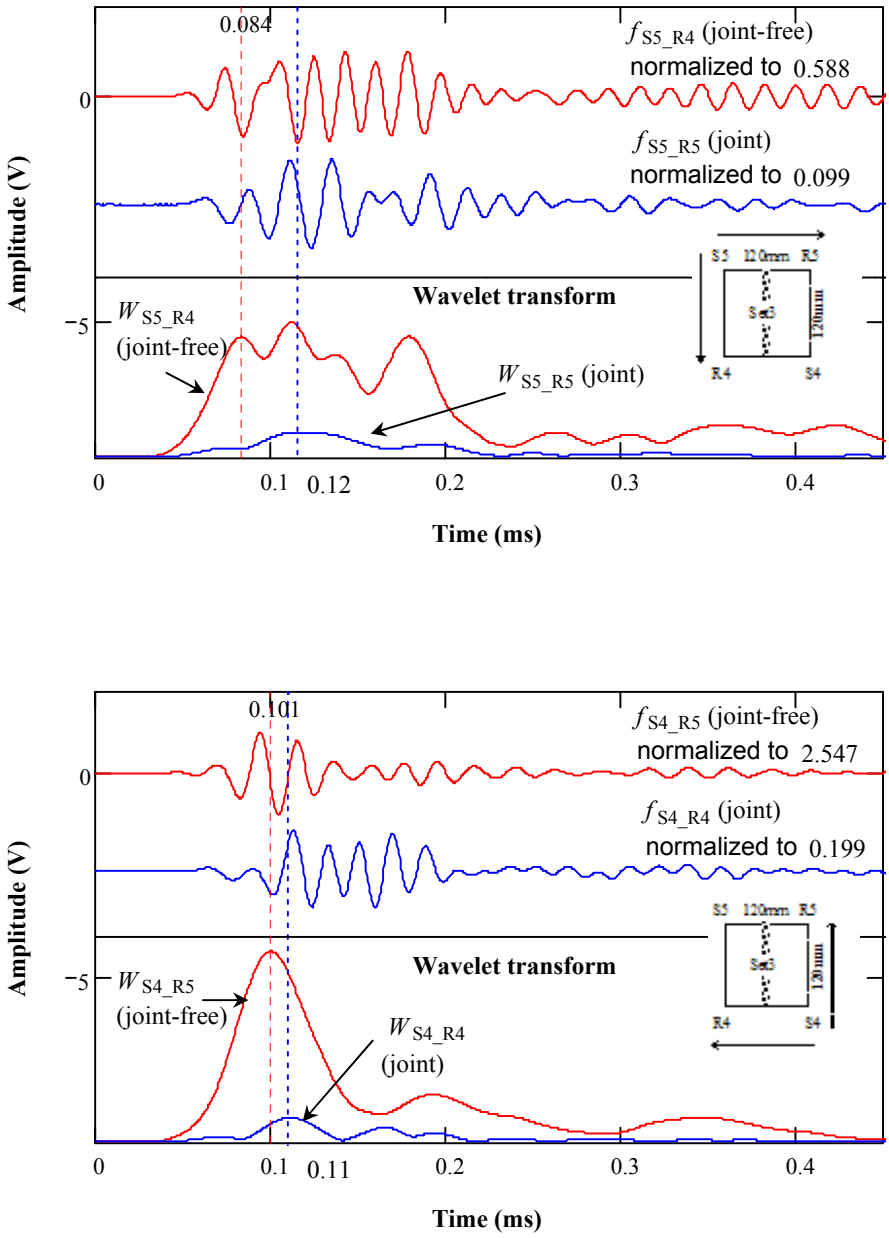

Figure S-13: Wavelet transform of repeated set 3 measurements (120mm S-R spacing) using Morlet wavelet at the dominant frequencies of P-waves (Morlet center frequency of 37.842 kHz for f_{S5_R4}; 30.578 kHz for f_{S5_R5}; 42.283 kHz for f_{S4_R5}; and 29.297 kHz for f_{S4_R4})

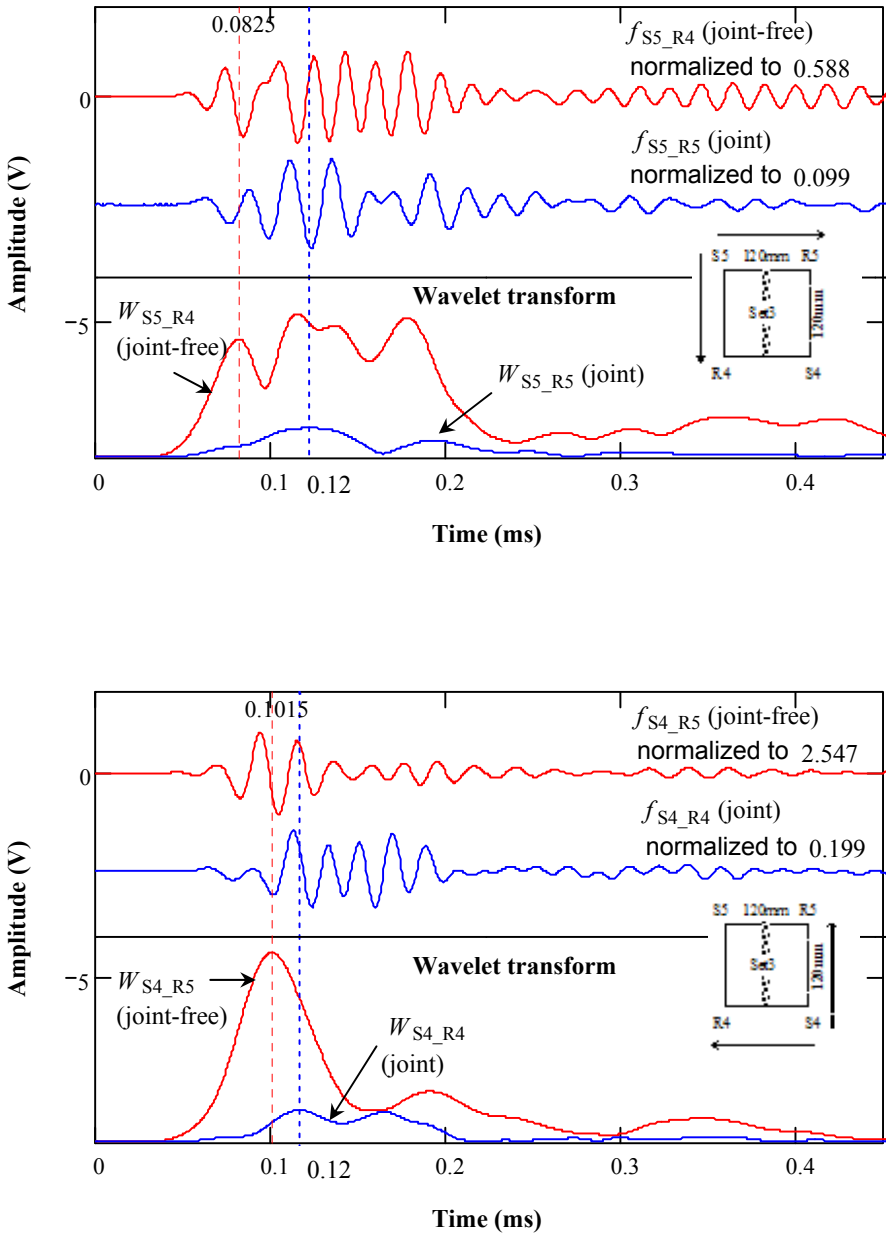

Figure S-14: Wavelet transform of repeated set 3 measurements (120mm S-R spacing) using Morlet wavelet at the dominant frequencies of P-waves (Morlet center frequency of 42.969 kHz for f_{S5_R4}; 39.063 kHz for f_{S5_R5}; 44.922 kHz for f_{S4_R5}; and 44.922 kHz for f_{S4_R4})

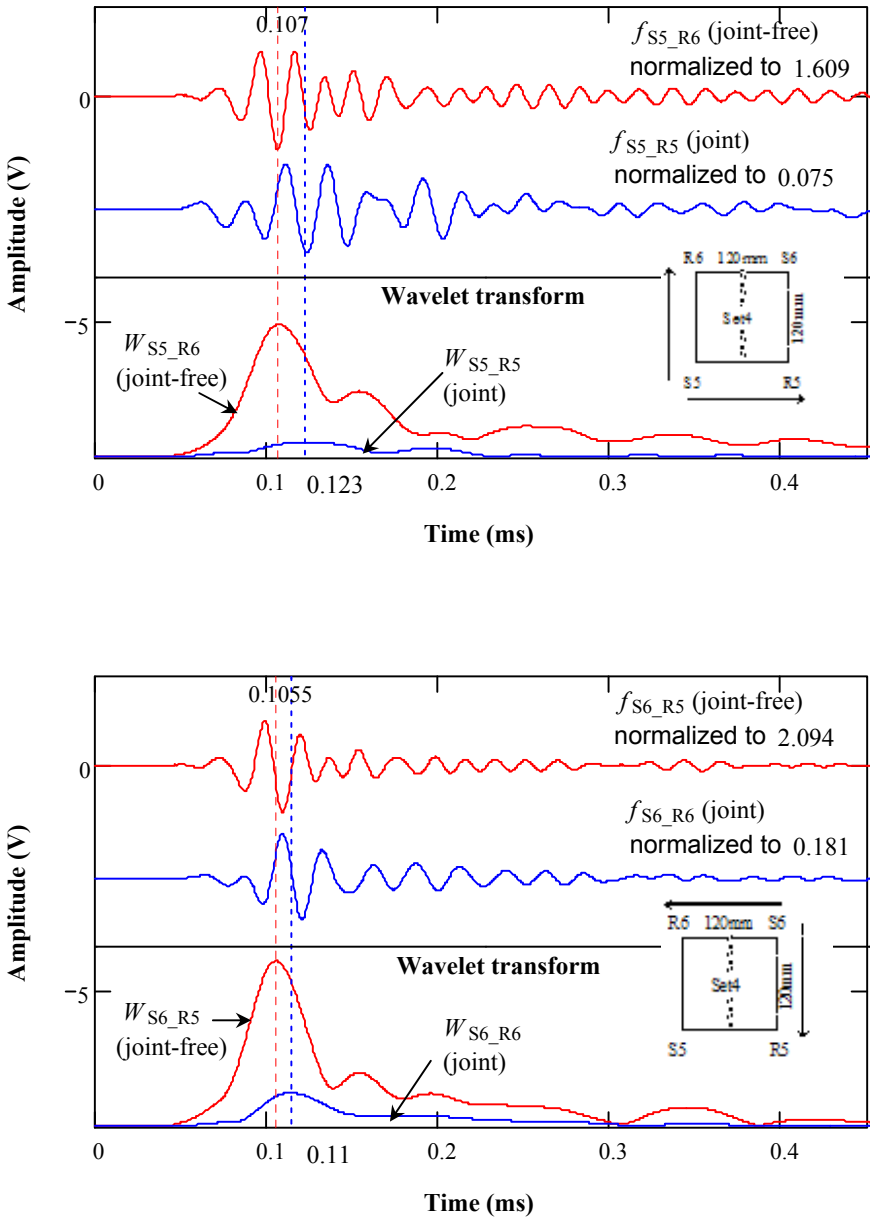

Figure S-15: Wavelet transform of set 4 measurements (120mm S-R spacing) using Morlet wavelet at the dominant frequencies of full signals (Morlet center frequency of 56.641 kHz for f_{S5_R6}; 42.969 kHz for f_{S5_R5}; 54.688 kHz for f_{S6_R5}; and 42.969 kHz for f_{S6_R6})

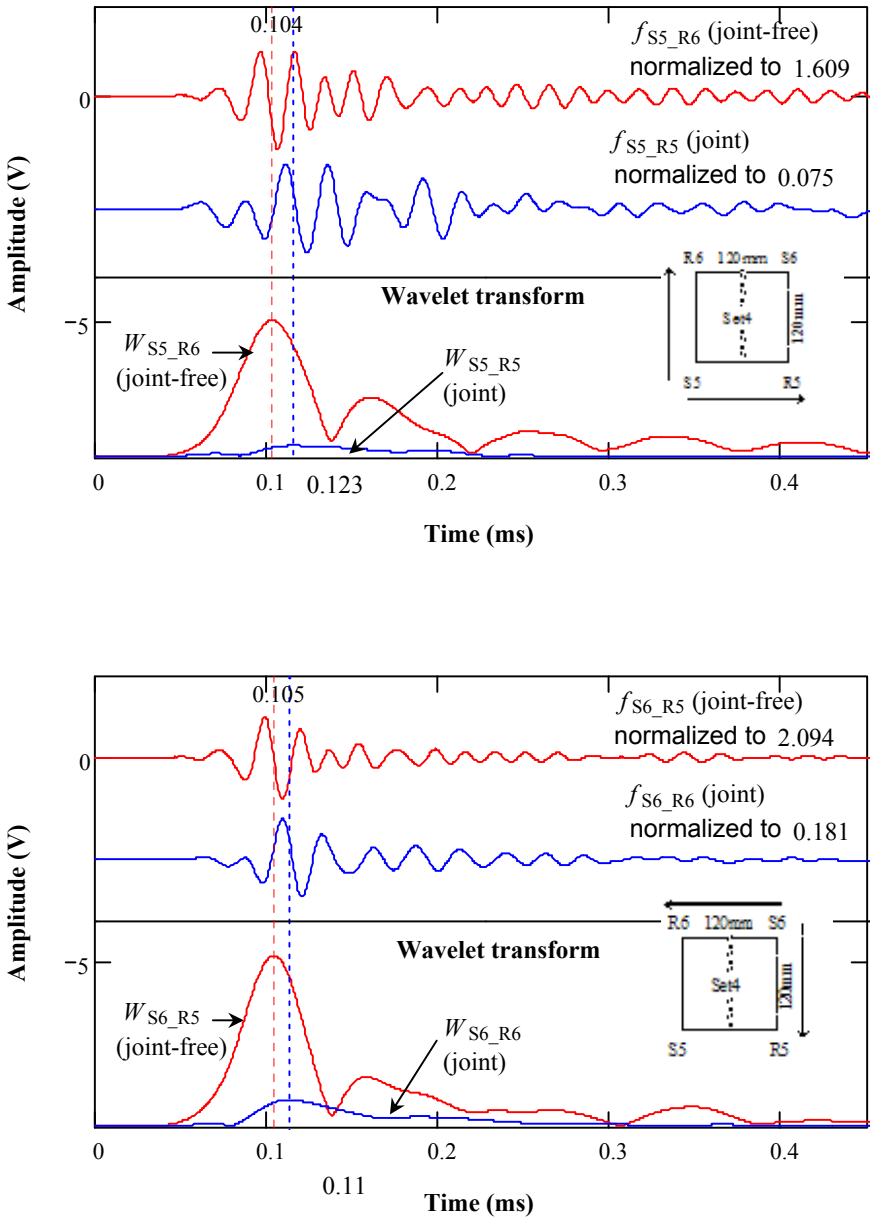

Figure S-16: Wavelet transform of set 4 measurements (120mm S-R spacing) using Morlet wavelet at the dominant frequencies of P-waves (Morlet center frequency of 37.842 kHz for f_{S5_R6}; 28.076 kHz for f_{S5_R5}; 40.283 kHz for f_{S6_R5}; and 30.518 kHz for f_{S6_R6})

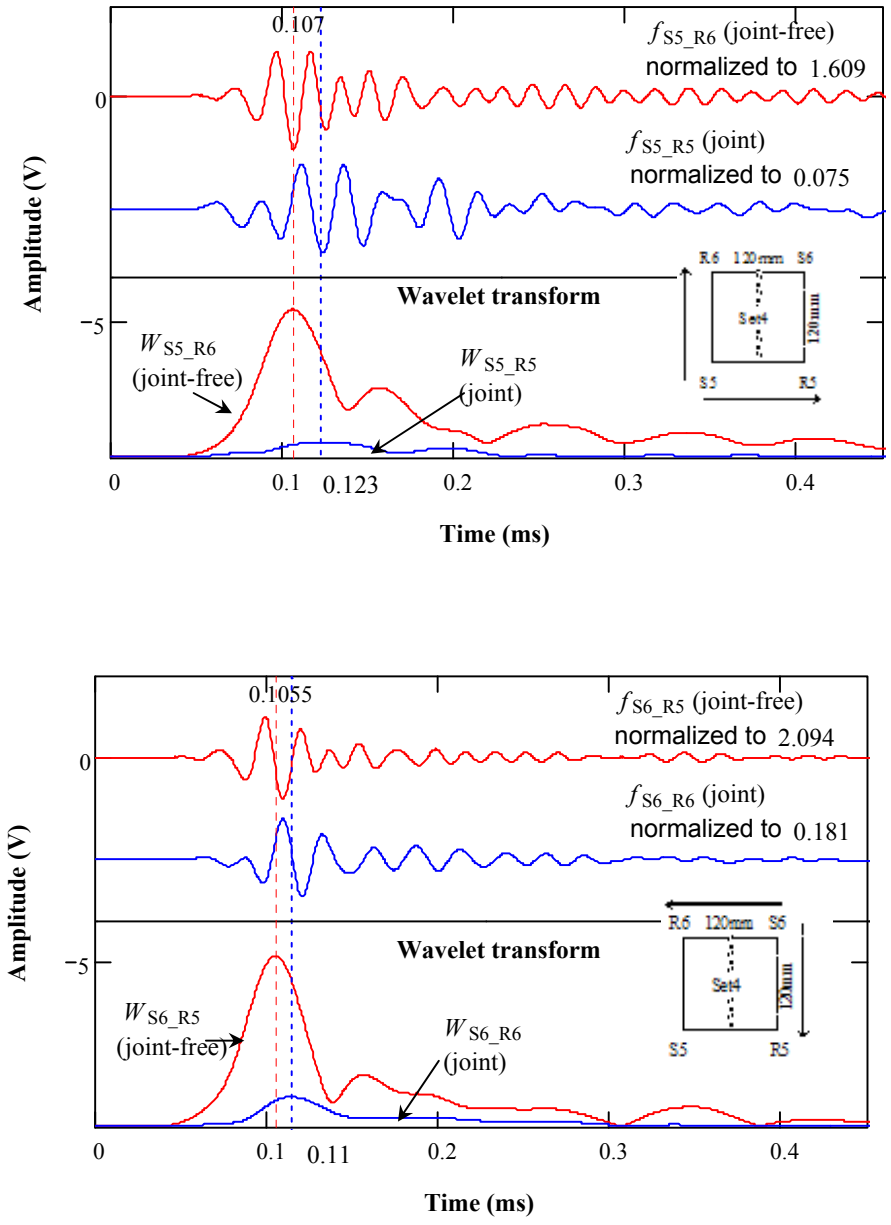

Figure S-17: Wavelet transform of set 4 measurements (120mm S-R spacing) using Morlet wavelet at the dominant frequencies of R-waves (Morlet center frequency of 46.787 kHz for f_{S5_R6}; 39.063 kHz for f_{S5_R5}; 44.922 kHz for f_{S6_R5}; and 42.969 kHz for f_{S6_R6})

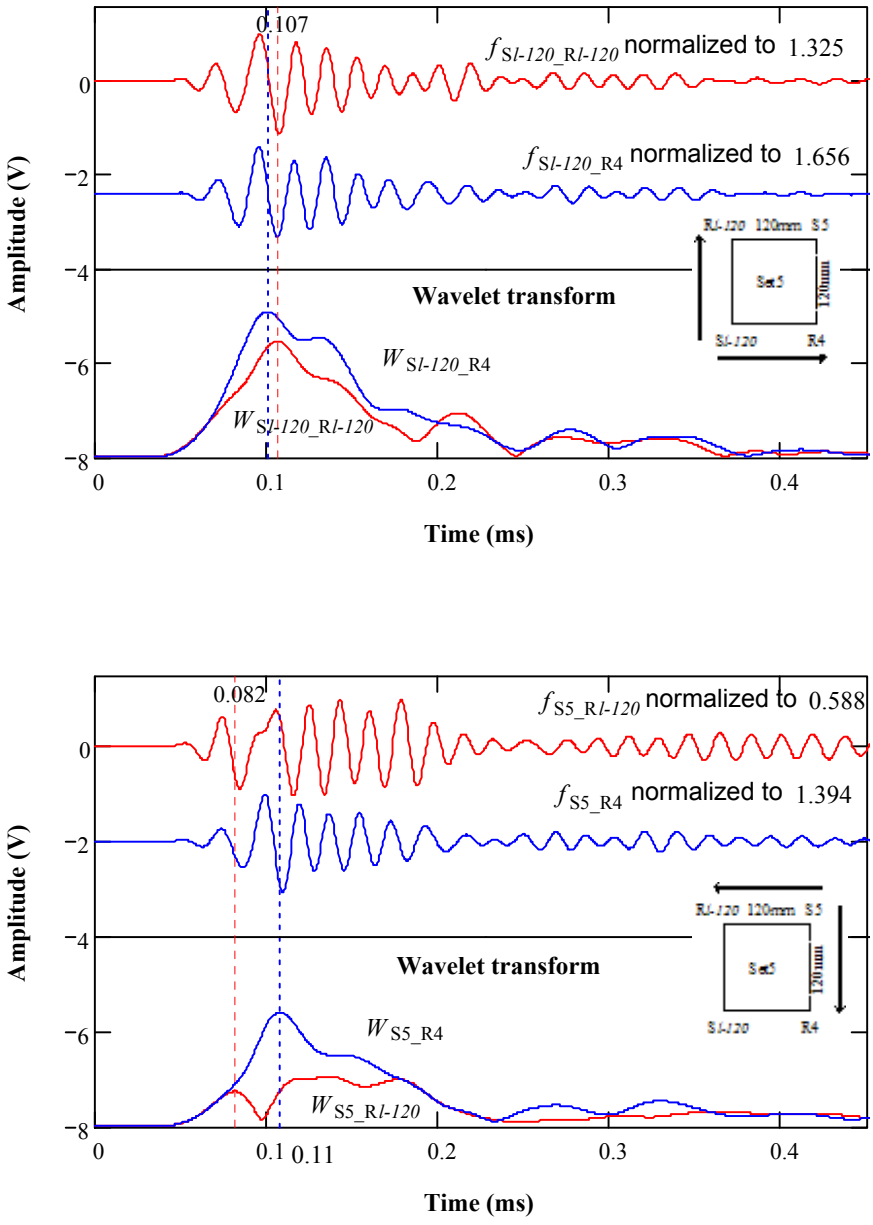

Figure S-18: Wavelet transform of set 5 measurements (120mm S-R spacing) using Morlet wavelet at the dominant frequencies of full signals (Morlet center frequency of 50.781 kHz for both $f_{Sl\text{-}120\_Rl\text{-}120}$ and $f_{Sl\text{-}120\_R4}$; 56.641 kHz for both $f_{S5\_Rl\text{-}120}$ and f_{S5_R4})

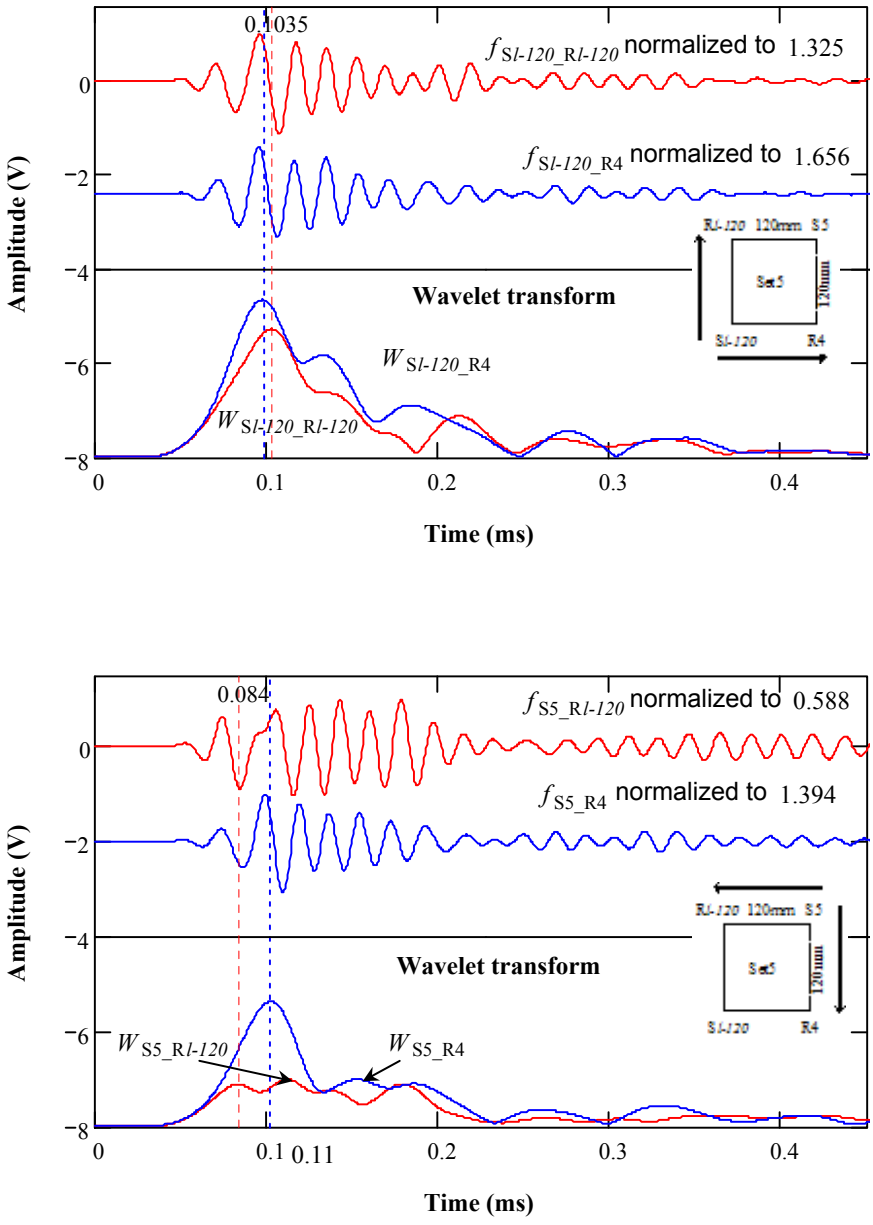

Figure S-19: Wavelet transform of set 5 measurements (120mm S-R spacing) using Morlet wavelet at the dominant frequencies of P-waves (Morlet center frequency of 39.063 kHz for both $f_{Sl\text{-}120\_Rl\text{-}120}$ and $f_{Sl\text{-}120\_R4}$; 37.842 kHz for both $f_{S5\_Rl\text{-}120}$ and f_{S5_R4})

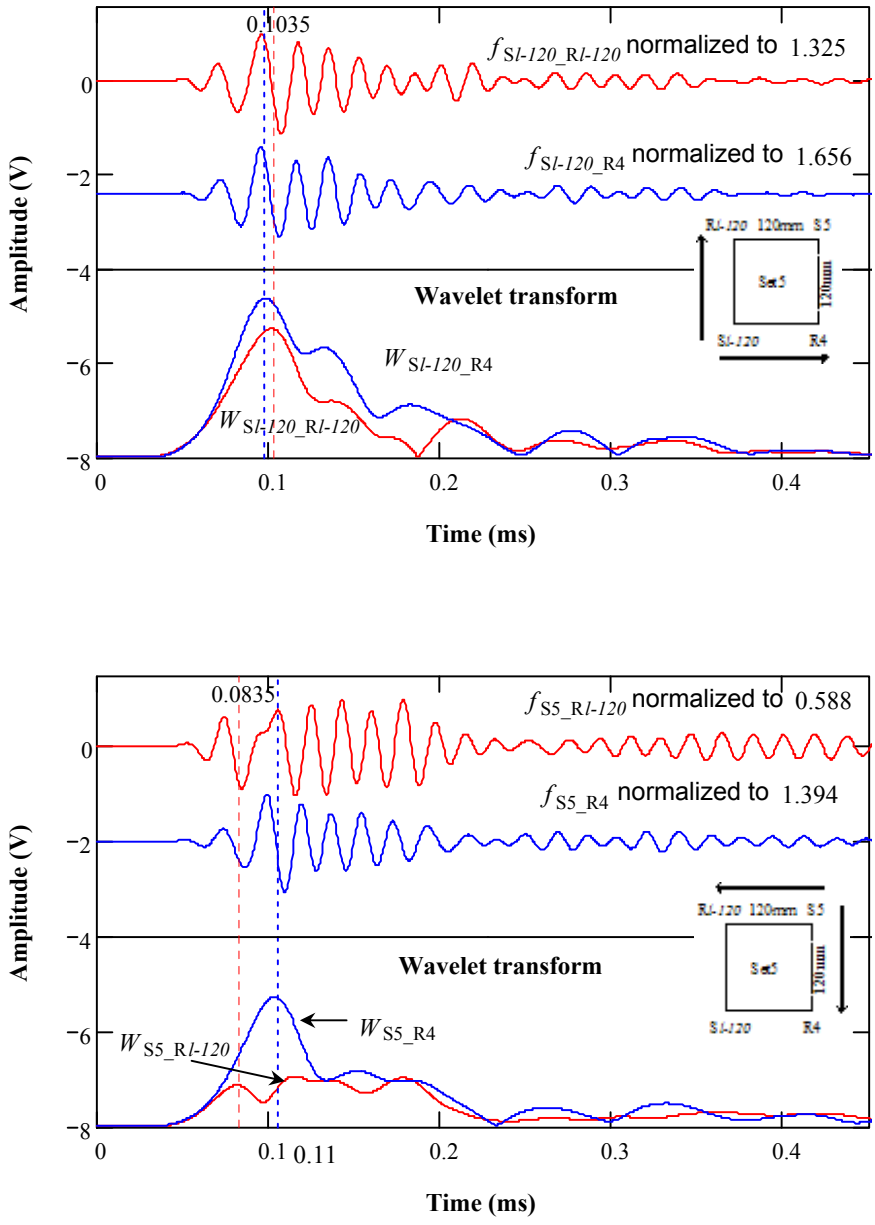

Figure S-20: Wavelet transform of set 5 measurements (120mm S-R spacing) using Morlet wavelet at the dominant frequencies of R-waves (Morlet center frequency of 41.016 kHz for $f_{Sl\text{-}120\_Rl\text{-}120}$; 39.063 kHz for $f_{Sl\text{-}120\_R4}$; 39.063 kHz for $f_{S5\_Rl\text{-}120}$; and 42.969 for f_{S5_R4})

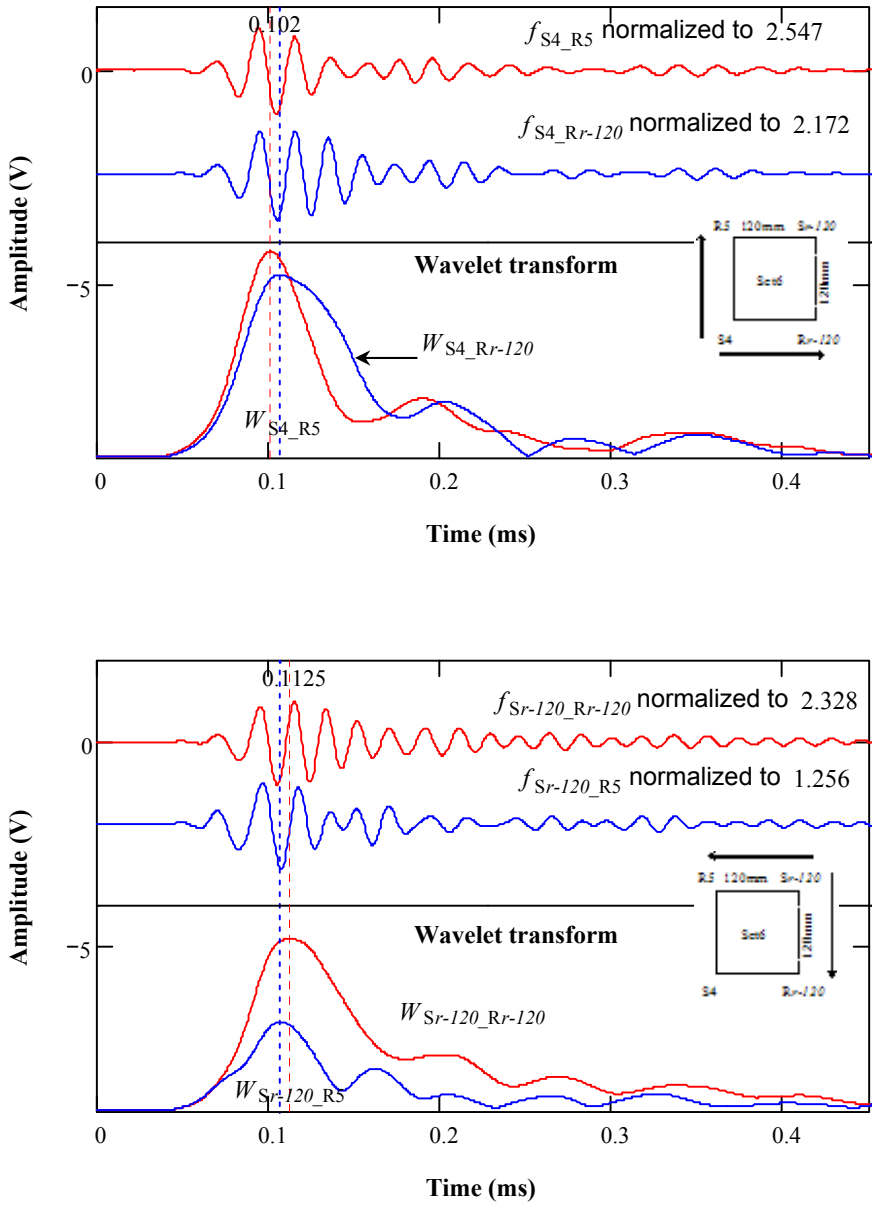

Figure S-21: Wavelet transform of set 6 measurements (120mm S-R spacing) using Morlet wavelet at the dominant frequencies of full signals (Morlet center frequency of 50.781 kHz for both f_{S4_R5} and $f_{S4\_Rr\text{-}120}$; and 56.641 kHz for both $f_{Sr\text{-}120\_Rr\text{-}120}$ and $f_{Sr\text{-}120\_R5}$)

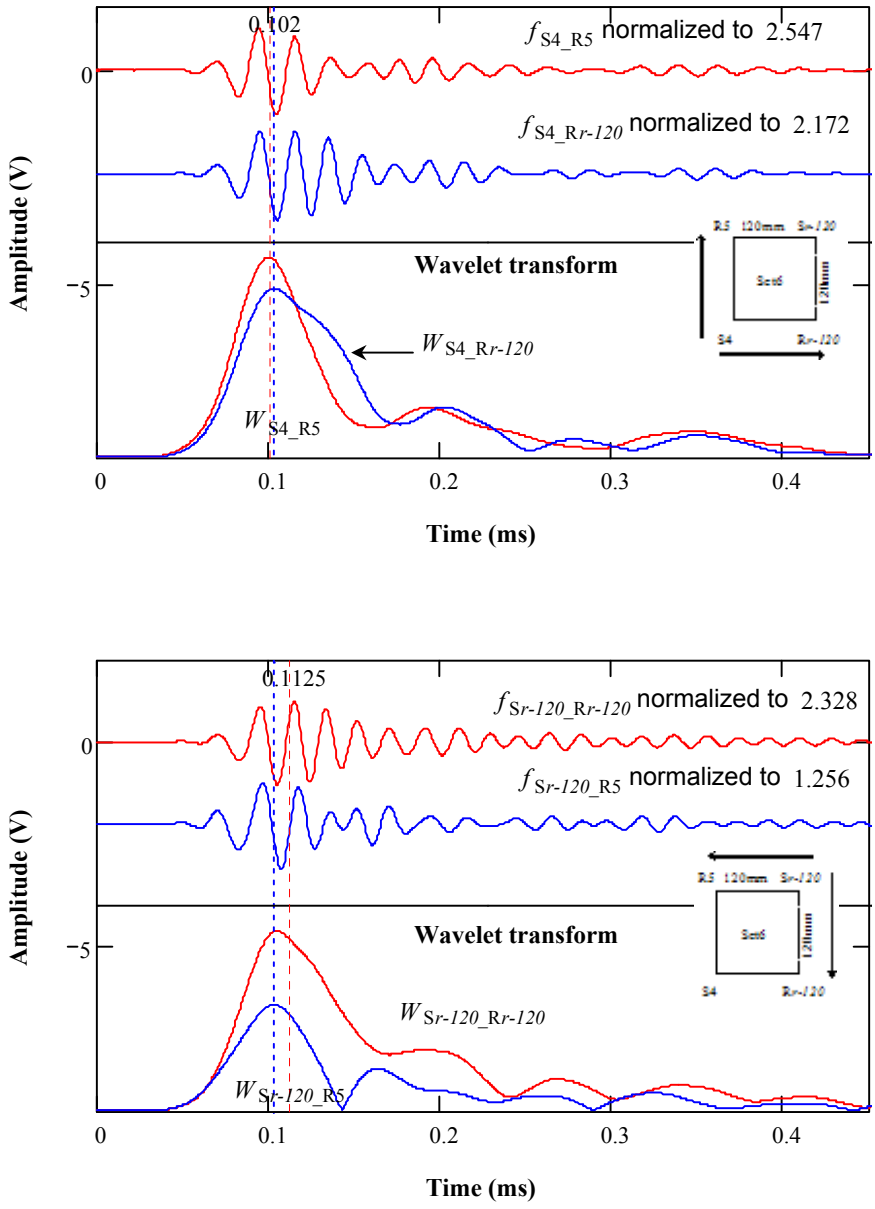

Figure S-22: Wavelet transform of set 6 measurements (120mm S-R spacing) using Morlet wavelet at the dominant frequencies of P-waves (Morlet center frequency of 40.283 kHz for f_{S4_R5}; 37.842 kHz for $f_{S4\_Rr\text{-}120}$; and 40.283 kHz for both $f_{Sr\text{-}120\_Rr\text{-}120}$ and $f_{Sr\text{-}120\_R5}$)

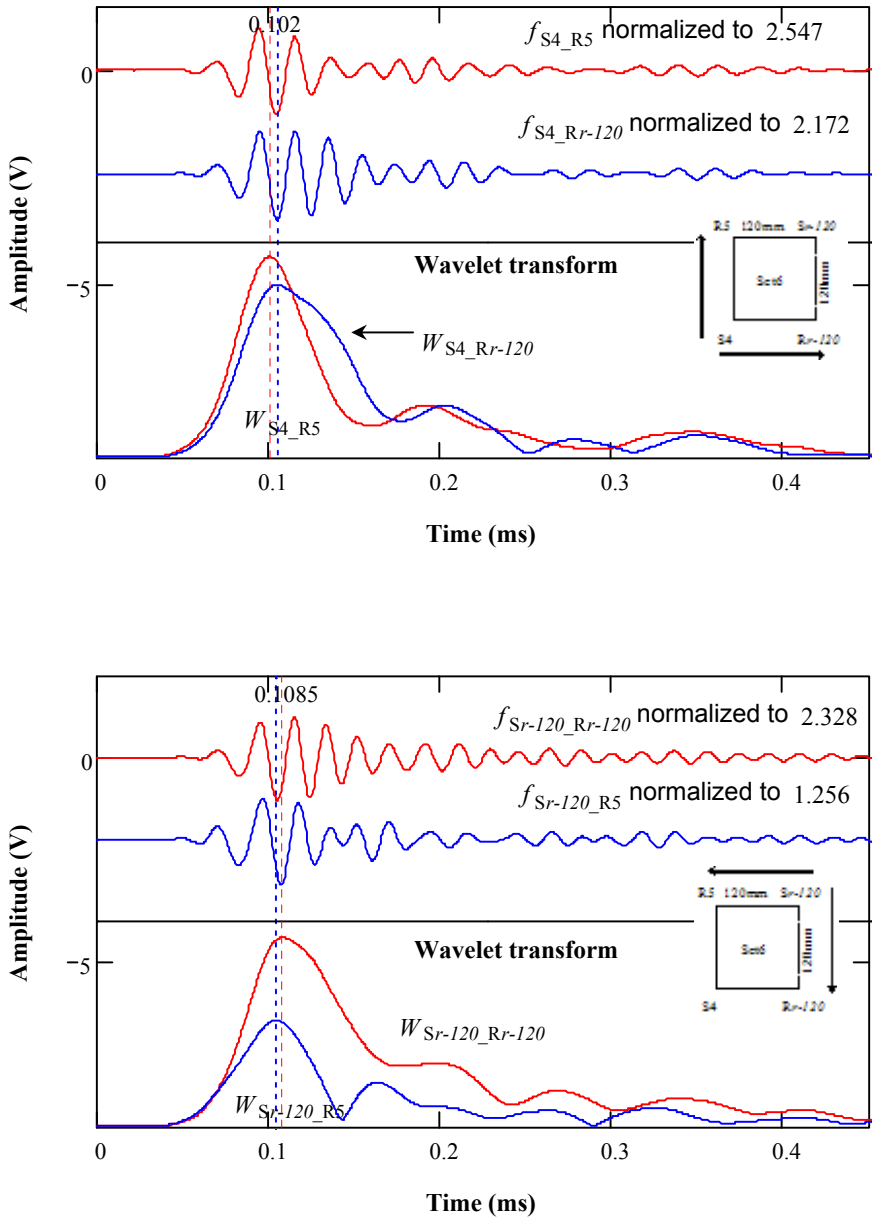

Figure S-23: Wavelet transform of set 6 measurements (120mm S-R spacing) using Morlet wavelet at the dominant frequencies of R-waves (Morlet center frequency of 42.969 kHz for both f_{S4_R5} and $f_{S4\_Rr\text{-}120}$; and 46.875 kHz for both $f_{Sr\text{-}120\_Rr\text{-}120}$ and $f_{Sr\text{-}120\_R5}$)

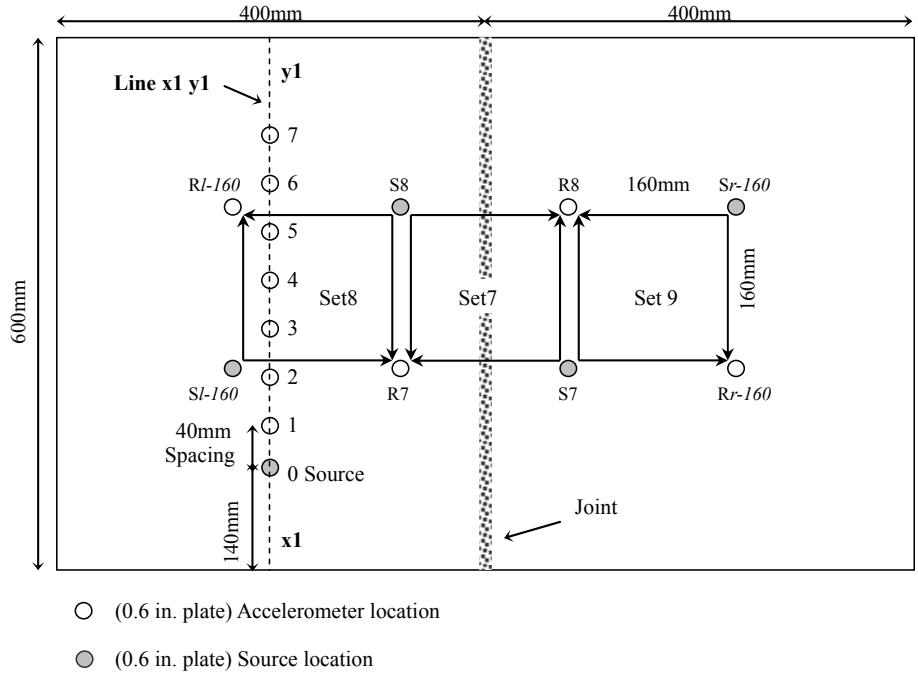

Figure S-24: 160mm S-R spacing configuration of HMA slab 3

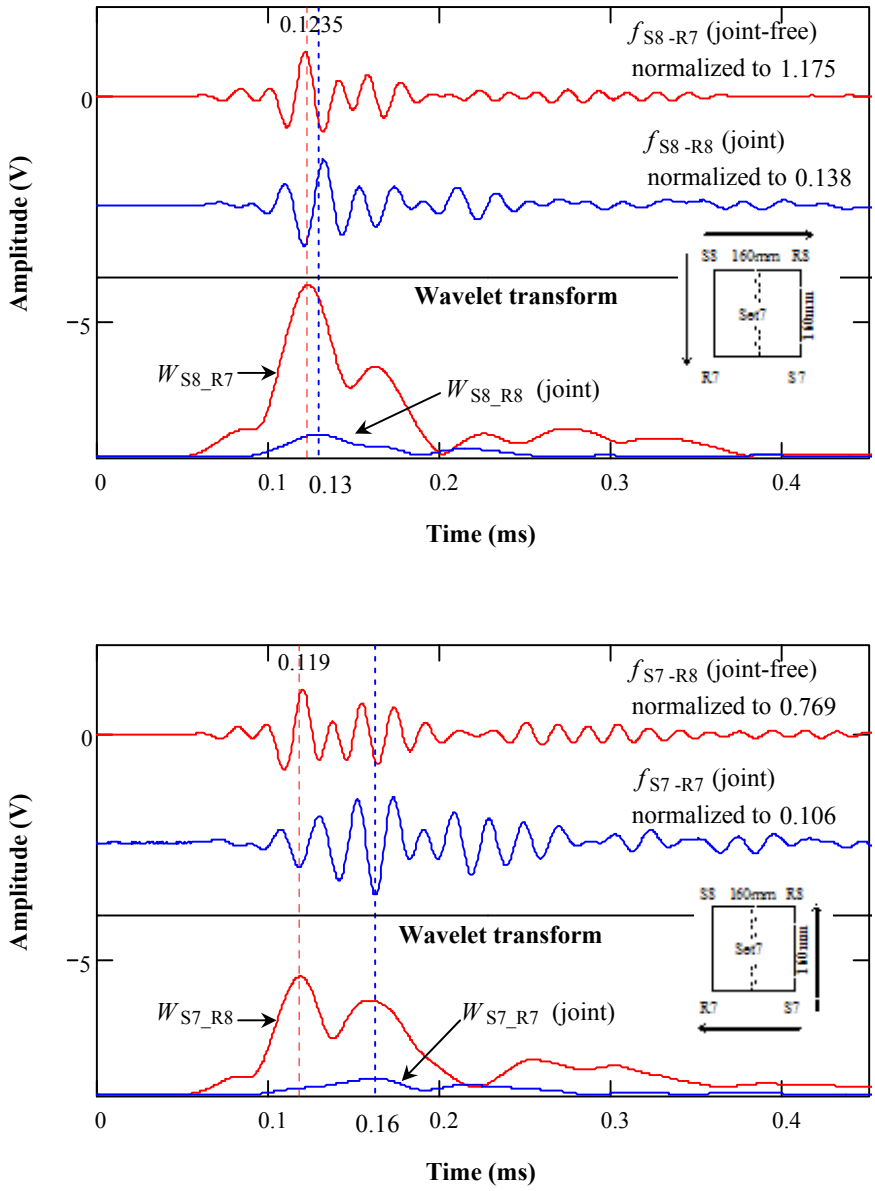

Figure S-25: Wavelet transform of set 7 measurements (160mm S-R spacing) using Morlet wavelet at the dominant frequencies of full signals (Morlet center frequency of 54.688 kHz for f_{S8_R7}; 50.781 kHz for f_{S8_R8}; 56.641 kHz for f_{S7_R8}; and 52.734 kHz for f_{S7_R7})

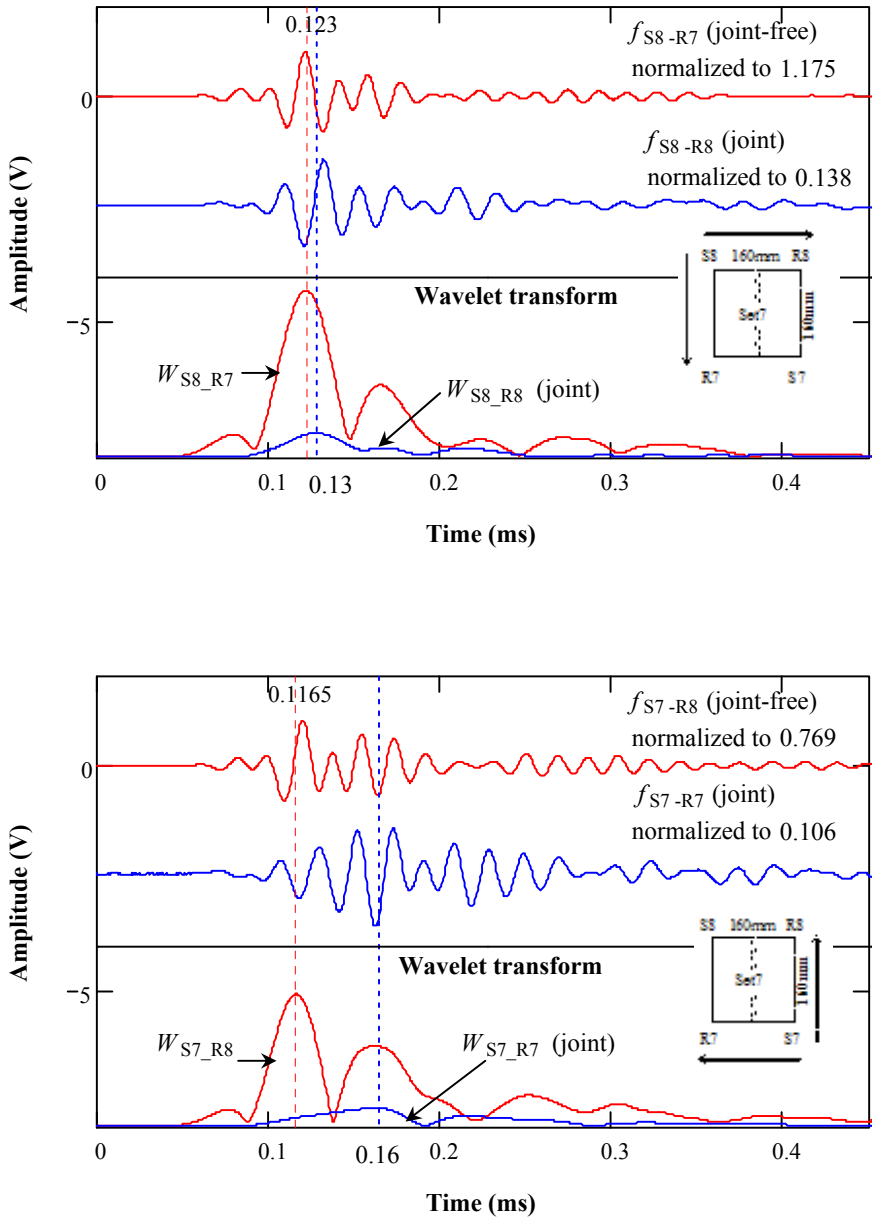

Figure S-26: Wavelet transform of set 7 measurements (160mm S-R spacing) using Morlet wavelet at the dominant frequencies of P-waves (Morlet center frequency of 37.842 kHz for f_{S8_R7}; 34.18 kHz for f_{S8_R8}; 37.842 kHz for f_{S7_R8}; and 34.18 kHz for f_{S7_R7})

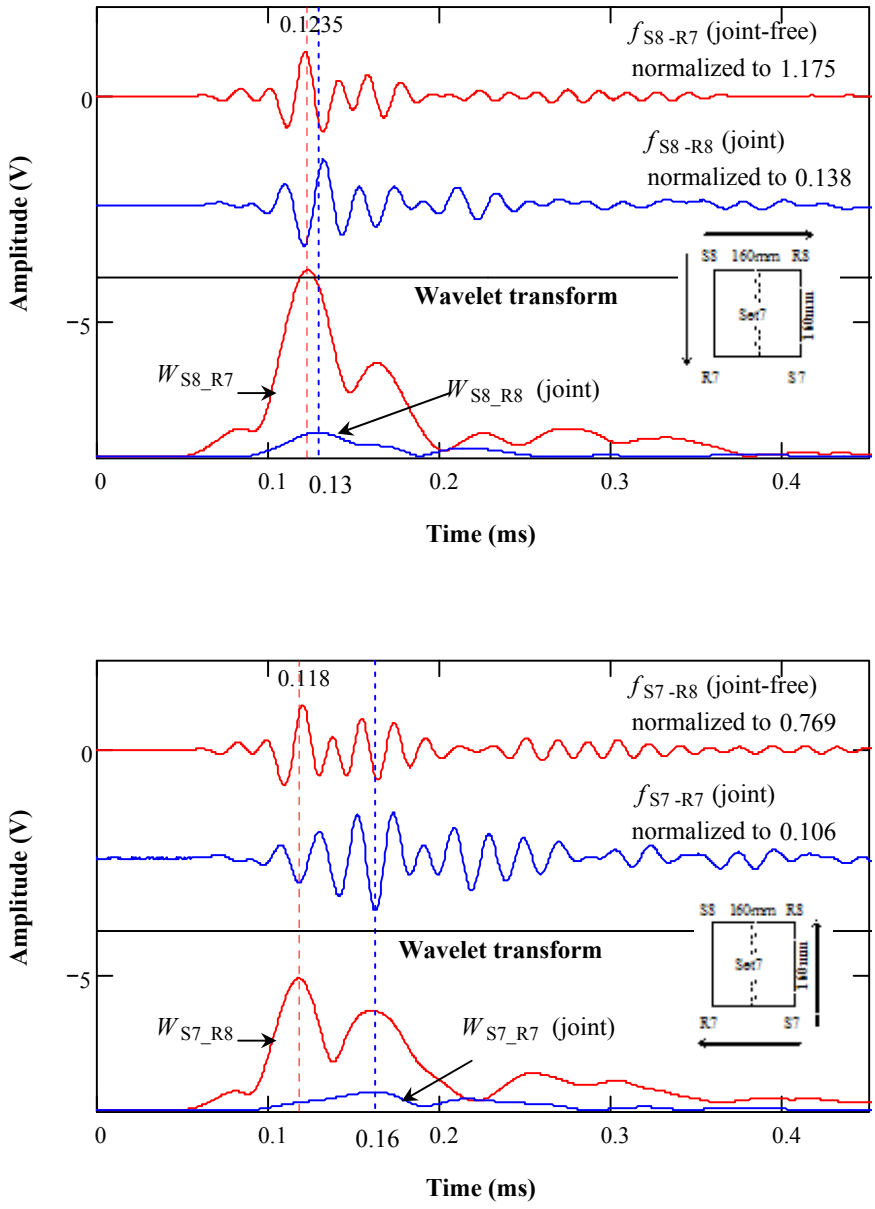

Figure S-27: Wavelet transform of set 7 measurements (160mm S-R spacing) using Morlet wavelet at the dominant frequencies of R-waves (Morlet center frequency of 48.828 kHz for f_{S8_R7}; 44.922 kHz for f_{S8_R8}; 48.828 kHz for f_{S7_R8}; and 44.922 kHz for f_{S7_R7})

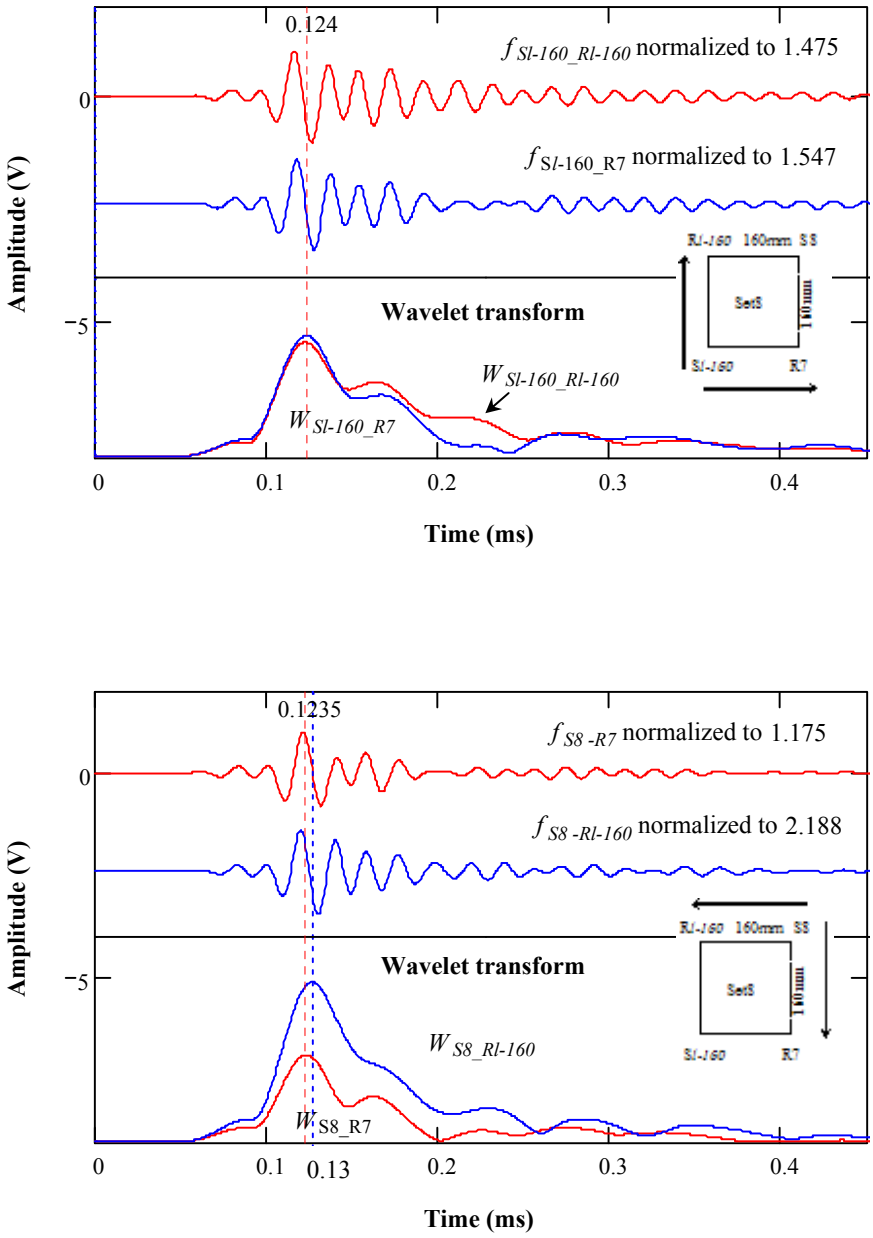

Figure S-28: Wavelet transform of set 8 measurements (160mm S-R spacing) using Morlet wavelet at the dominant frequencies of full signals (Morlet center frequency of 56.641 kHz for both $f_{Sl\text{-}160\_Rl\text{-}160}$ and $f_{Sl\text{-}160\_R7}$; 54.688 kHz for both f_{S8_R7} and $f_{S8\_Rl\text{-}160}$)

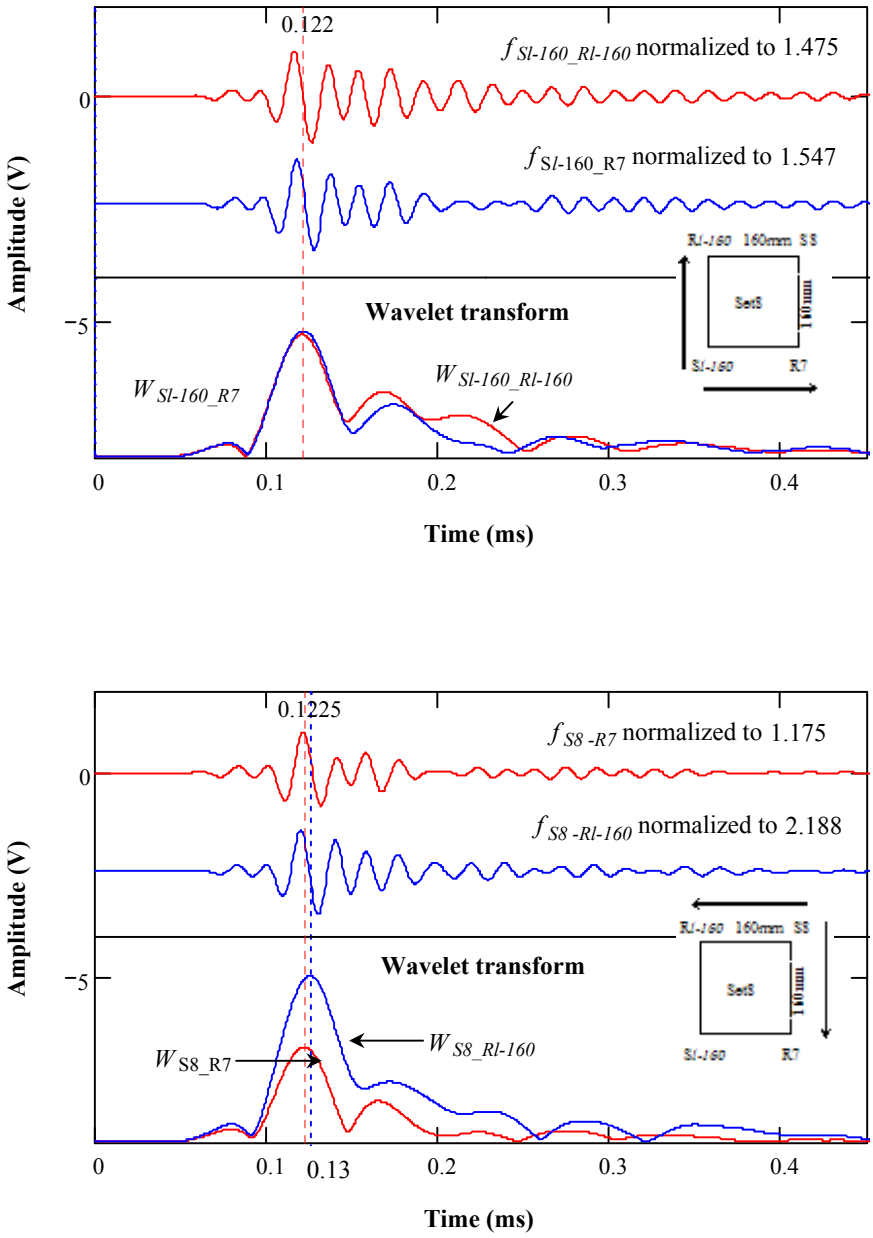

Figure S-29: Wavelet transform of set 8 measurements (160mm S-R spacing) using Morlet wavelet at the dominant frequencies of P-waves (Morlet center frequency of 37.842 kHz for all the signals of Set 8)

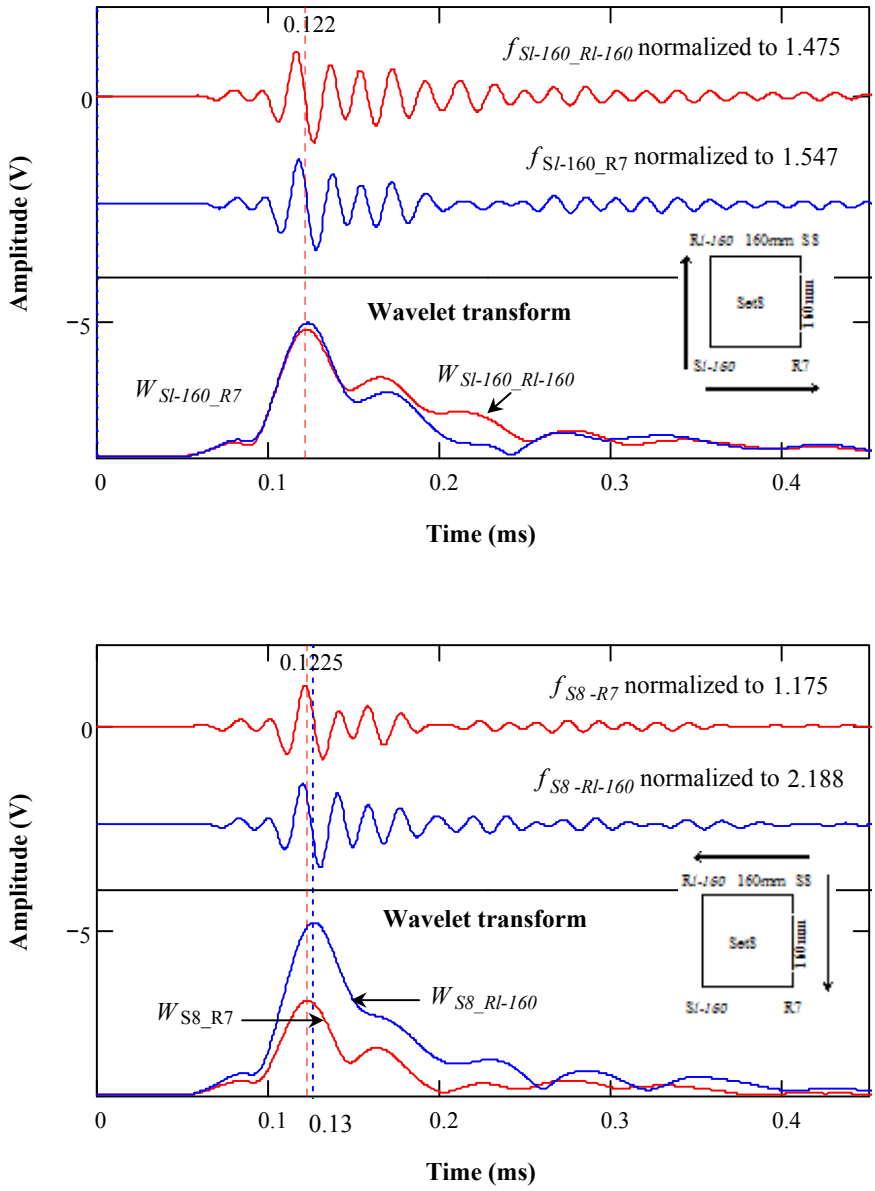

Figure S-30: Wavelet transform of set 8 measurements (160mm S-R spacing) using Morlet wavelet at the dominant frequencies of R-waves (Morlet center frequency of 48.828 kHz for all the signals of Set 8)

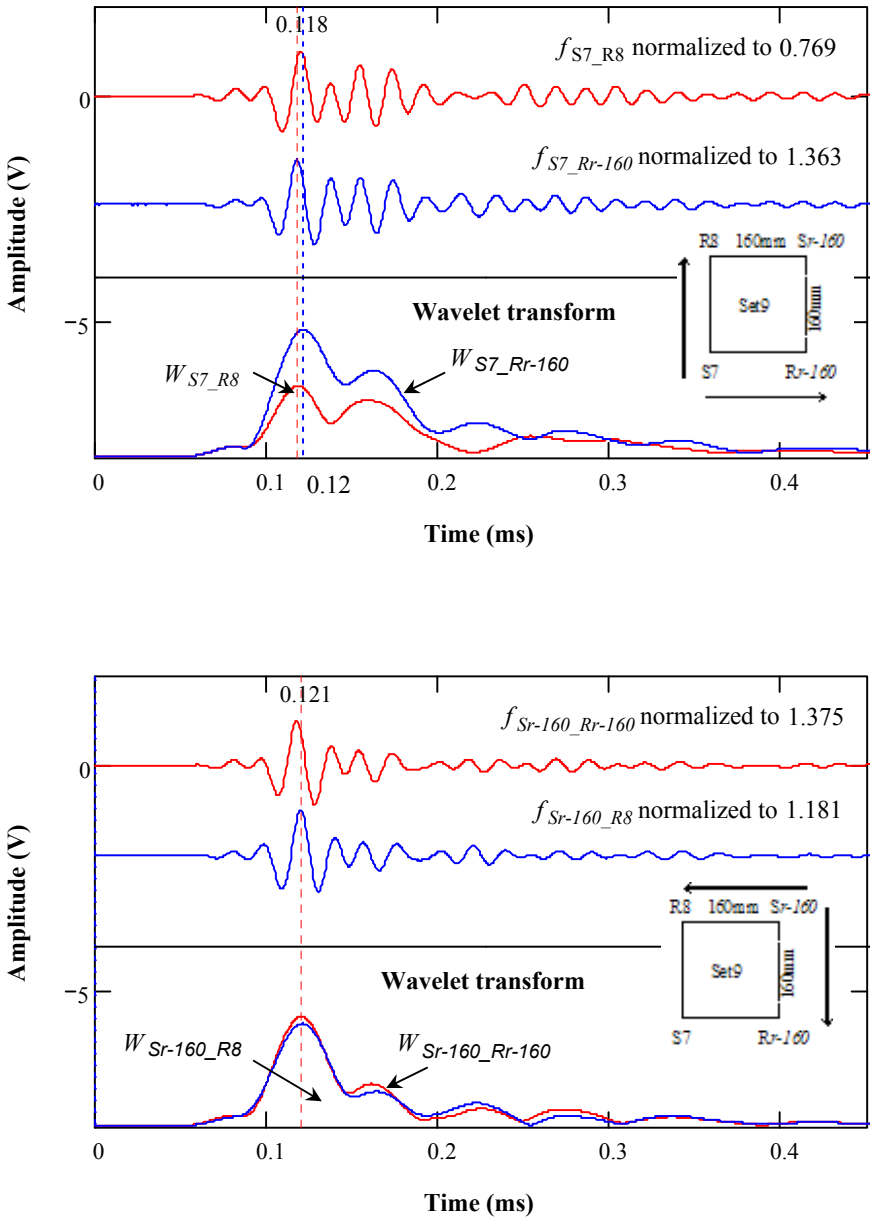

Figure S-31: Wavelet transform of set 9 measurements (160mm S-R spacing) using Morlet wavelet at the dominant frequencies of full signals (Morlet center frequency of 56.641 kHz for both f_{S7_R8} and $f_{S7\_Rr\text{-}160}$; 54.688 kHz for $f_{Sr\text{-}160\_Rr\text{-}160}$; and 50.781 kHz for $f_{Sr\text{-}160\_R8}$)

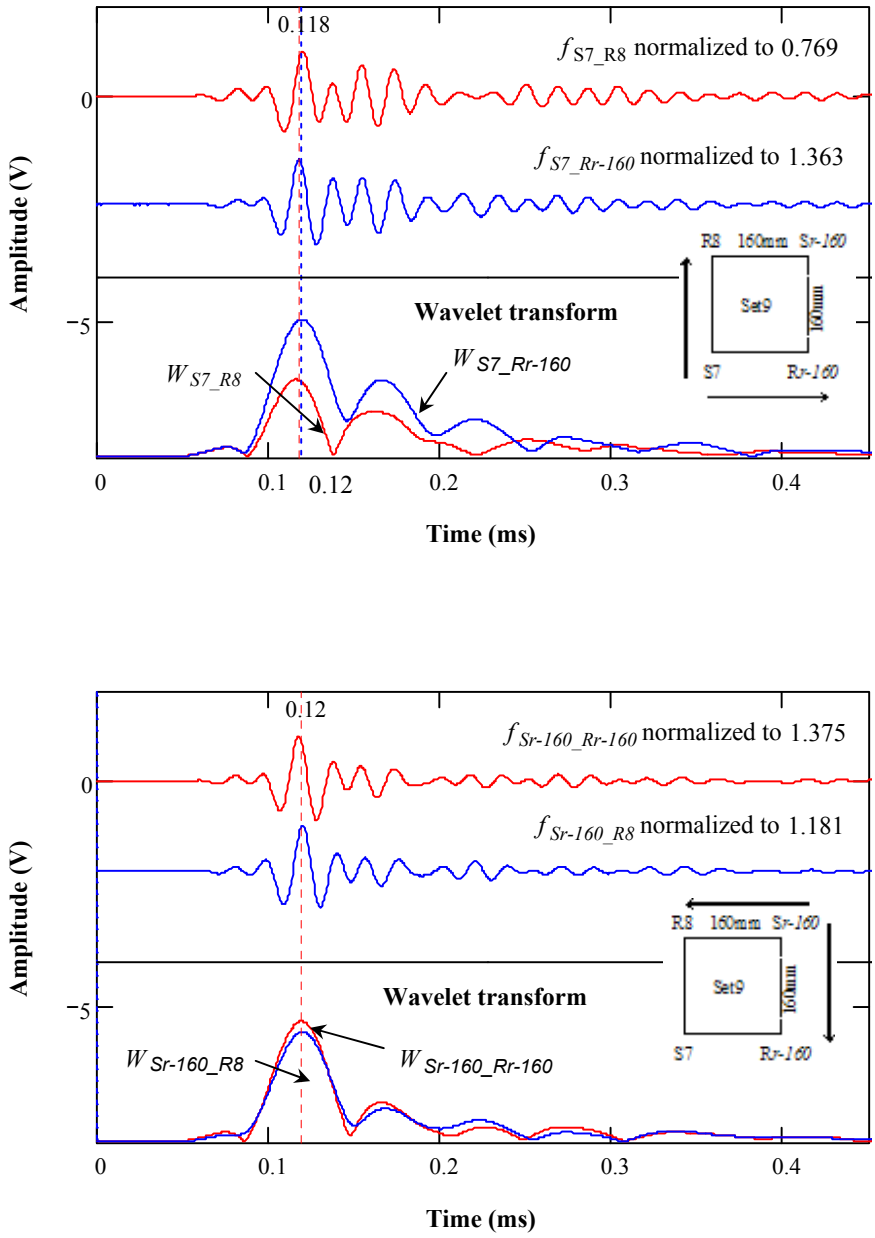

Figure S-32: Wavelet transform of set 9 measurements (160mm S-R spacing) using Morlet wavelet at the dominant frequencies of P-waves (Morlet center frequency of 36.621 kHz for f_{S7_R8}; 37.842 kHz for $f_{S7\_Rr\text{-}160}$; 37.842 kHz for $f_{Sr\text{-}160\_Rr\text{-}160}$; and 40.283 kHz for $f_{Sr\text{-}160\_R8}$)

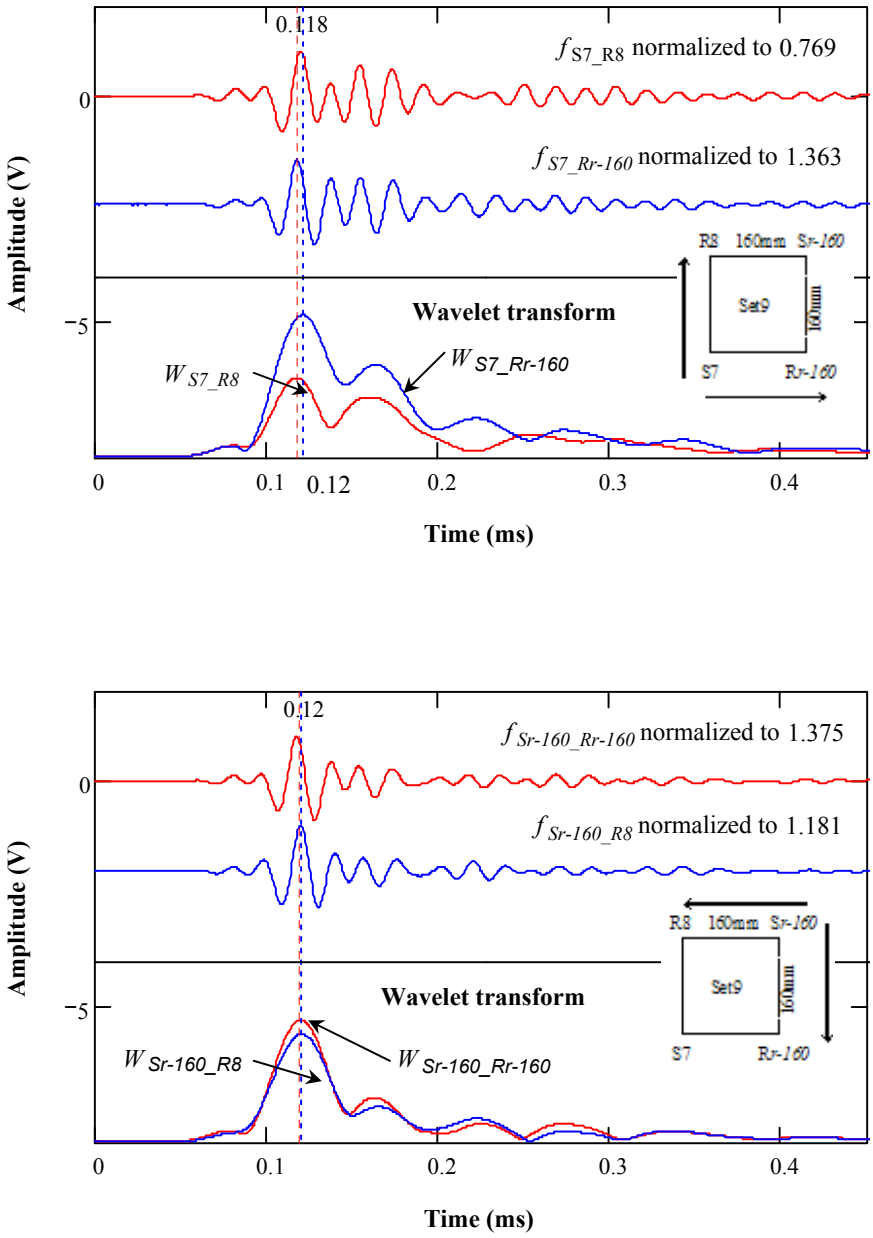

Figure S-33: Wavelet transform of set 9 measurements (160mm S-R spacing) using Morlet wavelet at the dominant frequencies of R-waves (Morlet center frequency of 48.828 kHz for both f_{S7_R8} and $f_{S7\_Rr\text{-}160}$; 46.875 kHz for both $f_{Sr\text{-}160\_Rr\text{-}160}$ and $f_{Sr\text{-}160\_R8}$)

Appendix T

Wavelet Transform of Signals

Using Mallat's Algorithm for Slab 3

This appendix is a PDF file available in the Appendix CD.

The file name of this PDF file is "Appendix T - Wavelet transform using Mallat's.pdf".

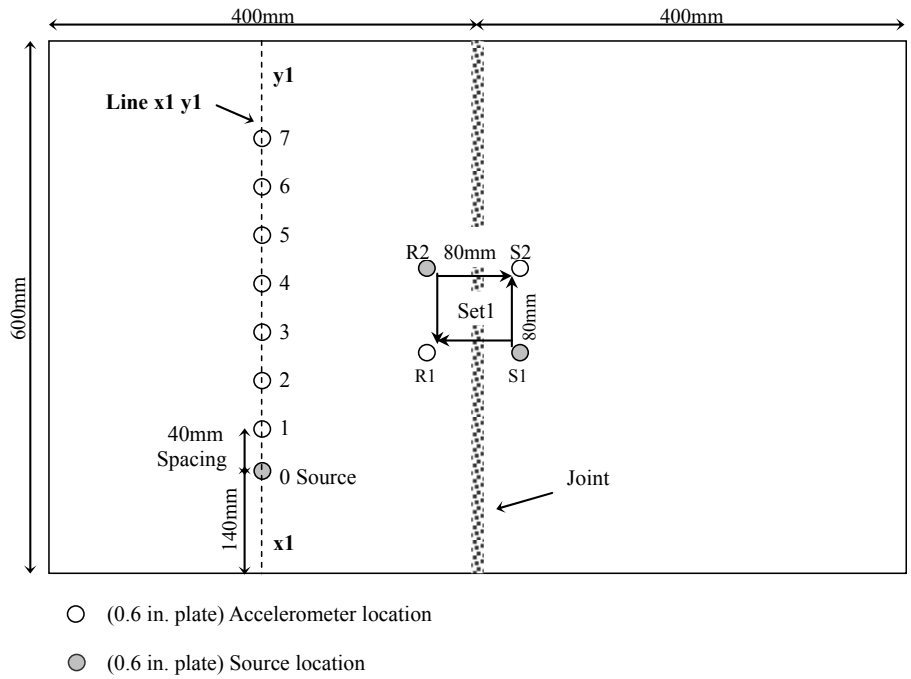

Figure T-1: 80mm S-R spacing configuration of HMA slab 3

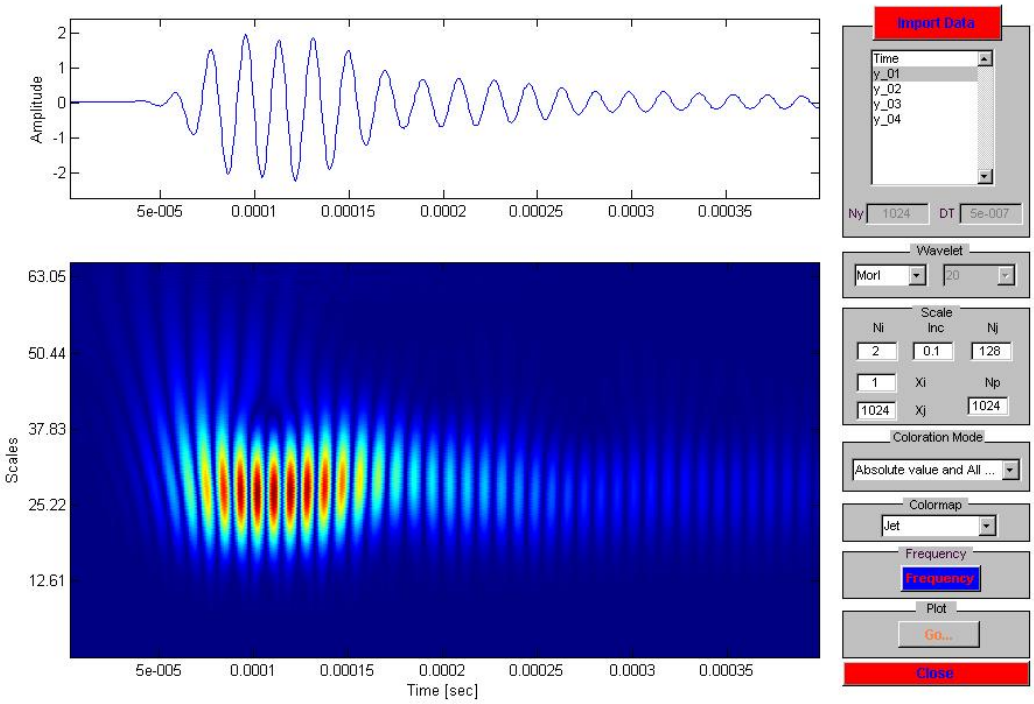

Figure T-2: Wavelet transform using Mallat's algorithm for signal f_{S1_R2} through the joint-free surface at 80mm S-R spacing

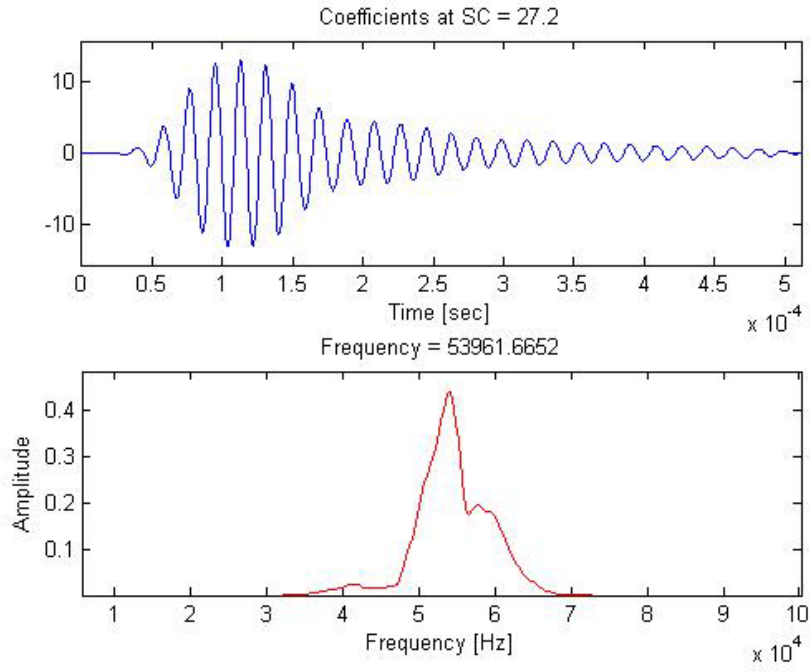

Figure T-3: Frequency content at a given scale from Figure T-2

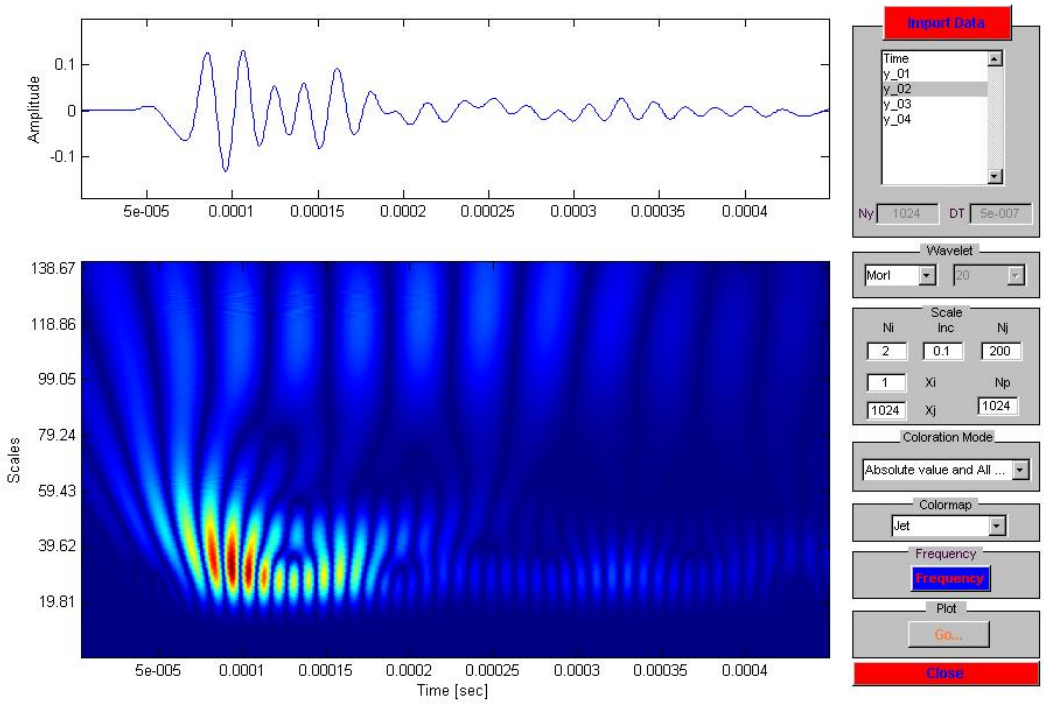

Figure T-4: Wavelet transform using Mallat's algorithm for signal f_{S1_R1} across the joint (at 80mm S-R spacing)

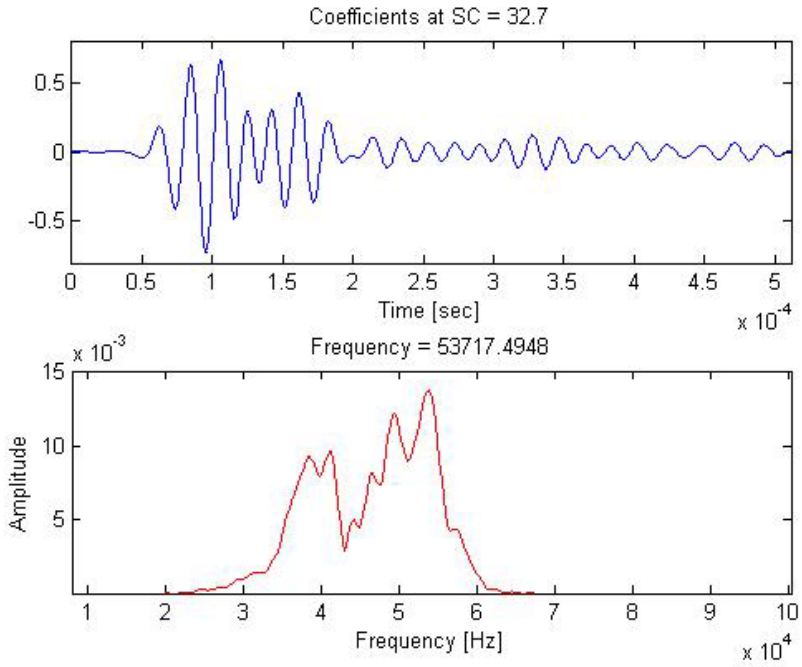

Figure T-5: Frequency content at a given scale from Figure T-4

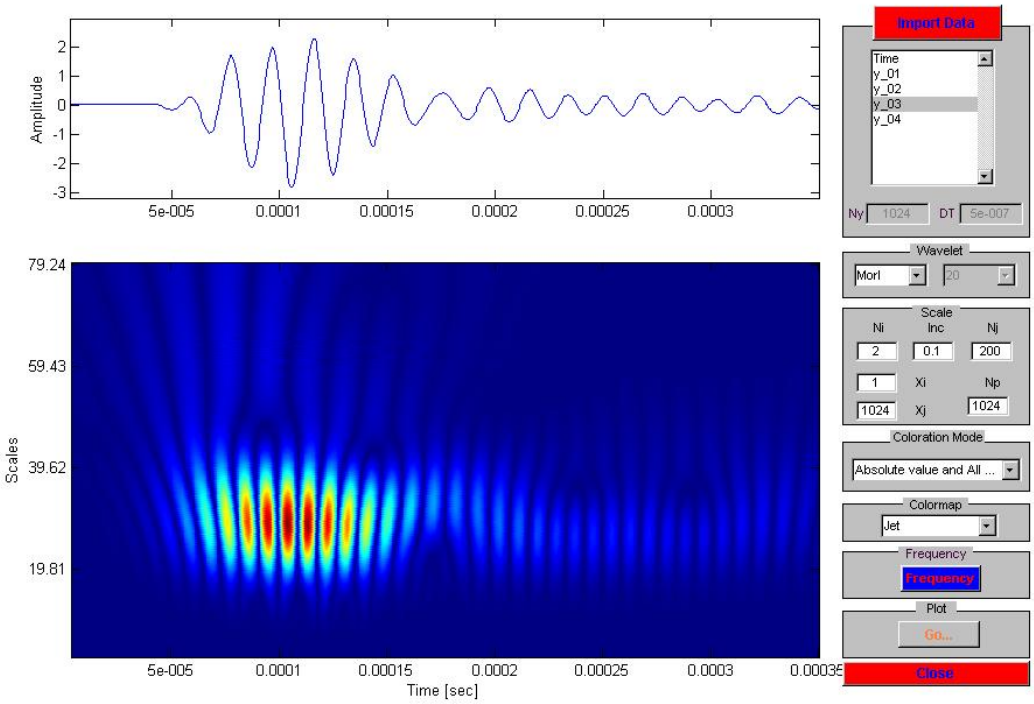

Figure T-6: Wavelet transform using Mallat's algorithm for signal f_{S2_R1} hrough the joint-free surface (at 80mm S-R spacing)

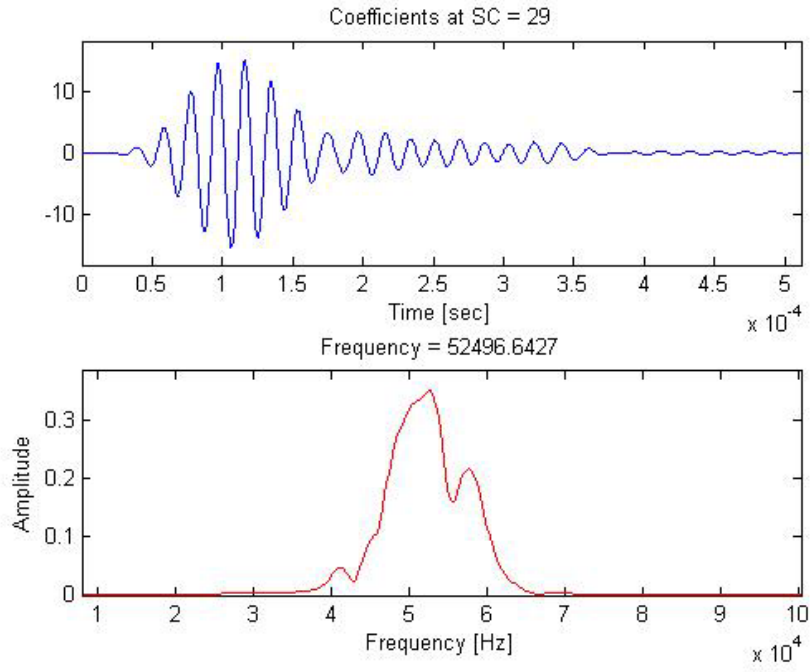

Figure T-7: Frequency content at a given scale from Figure T-6

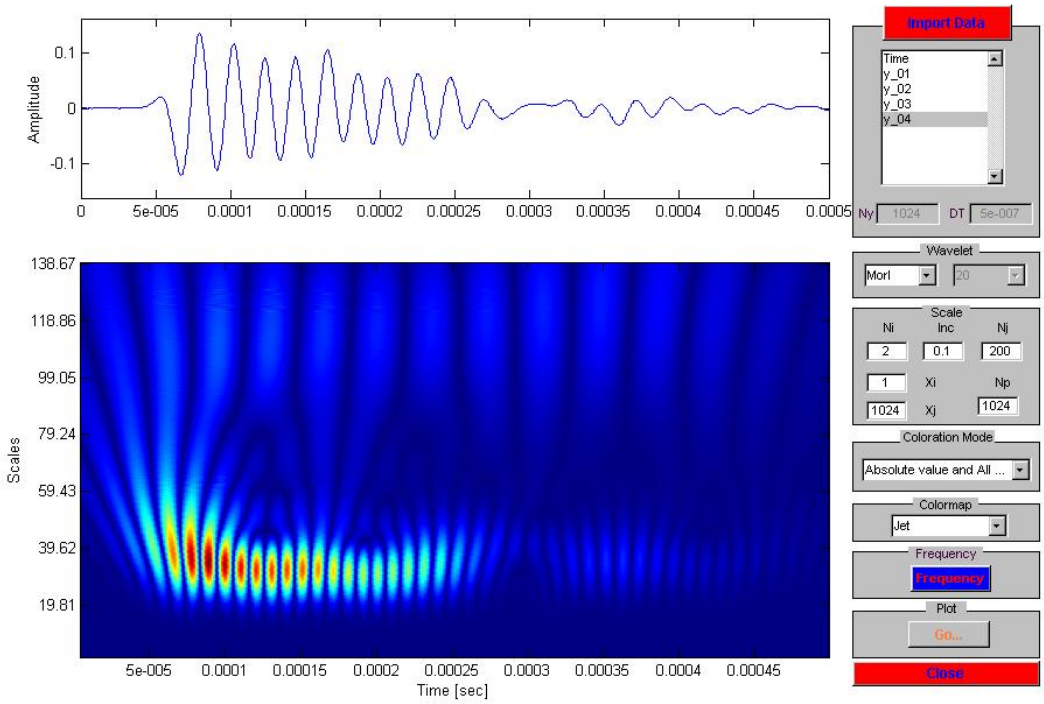

Figure T-8: Wavelet transform using Mallat's algorithm for signal f_{S2_R2} across the joint (at 80mm S-R spacing)

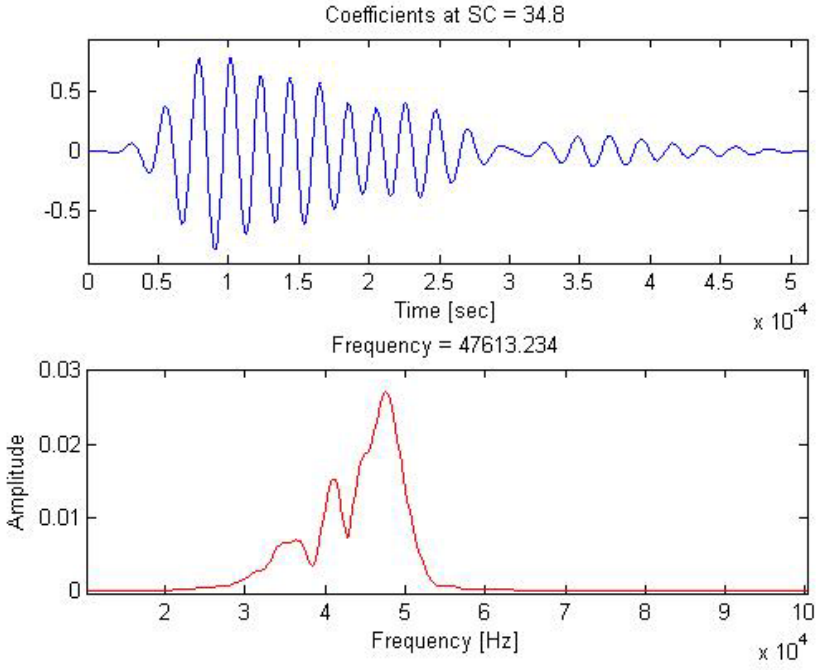

Figure T-9: Frequency content at a given scale from Figure T-8

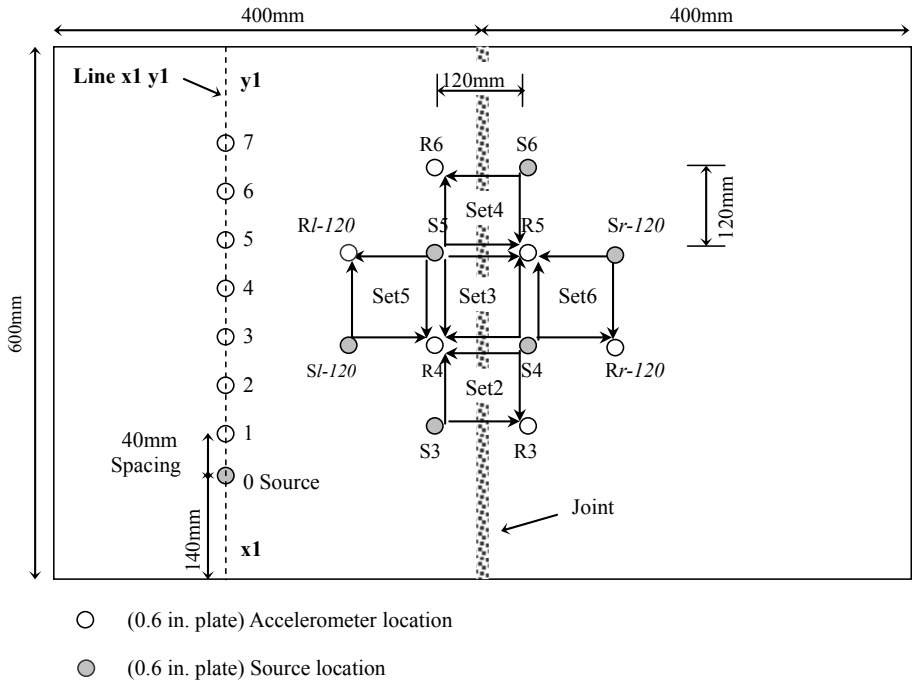

Figure T-10: 120mm S-R spacing configuration of HMA slab 3

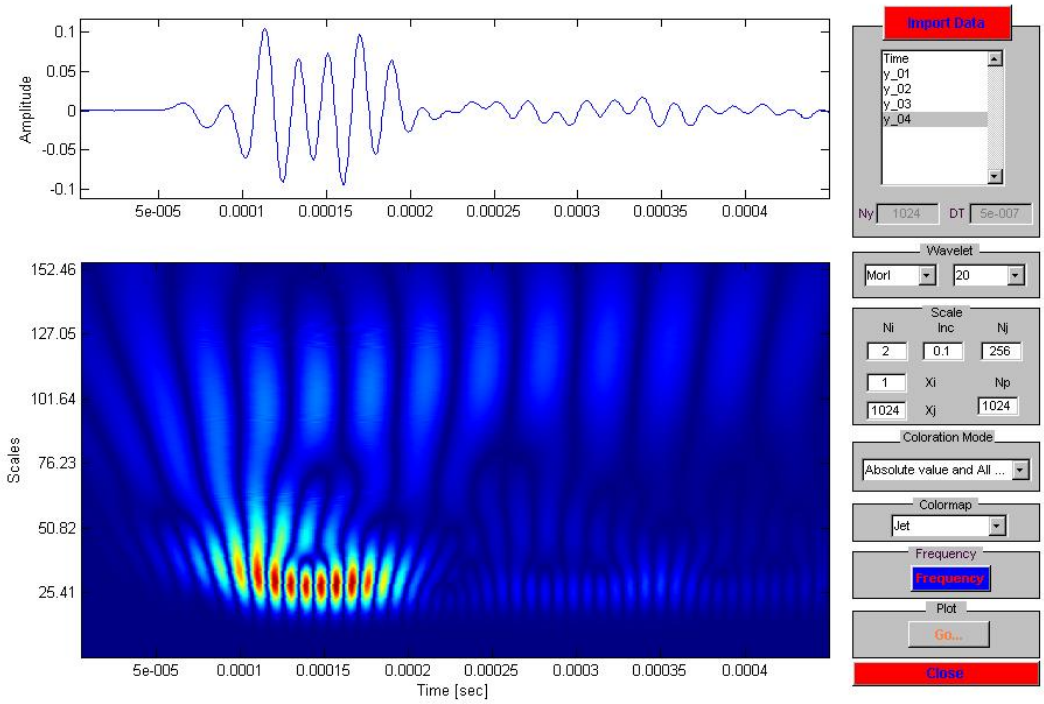

Figure T-11: Wavelet transform using Mallat's algorithm for signal f_{S4_R4} across the joint (at 120mm S-R spacing)

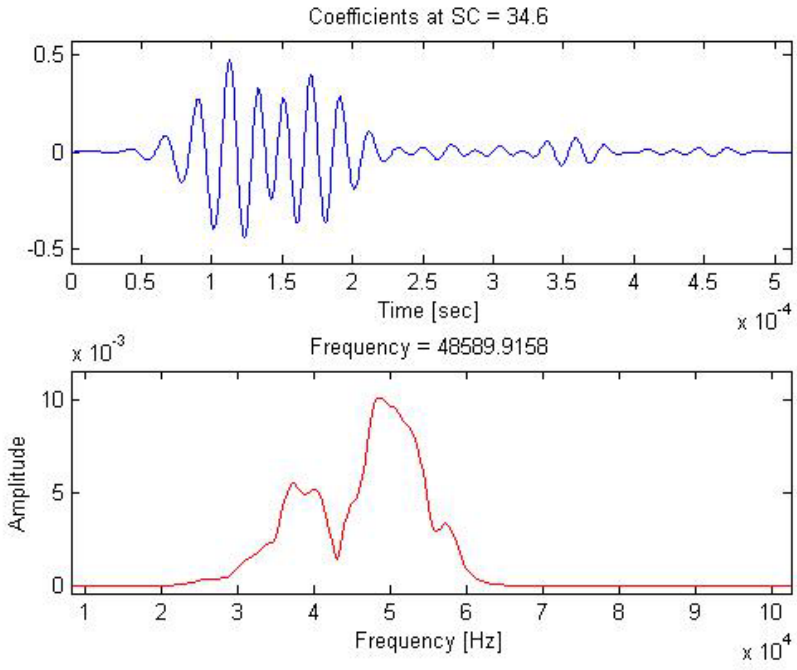

Figure T-12: Frequency content at a given scale from Figure T-11

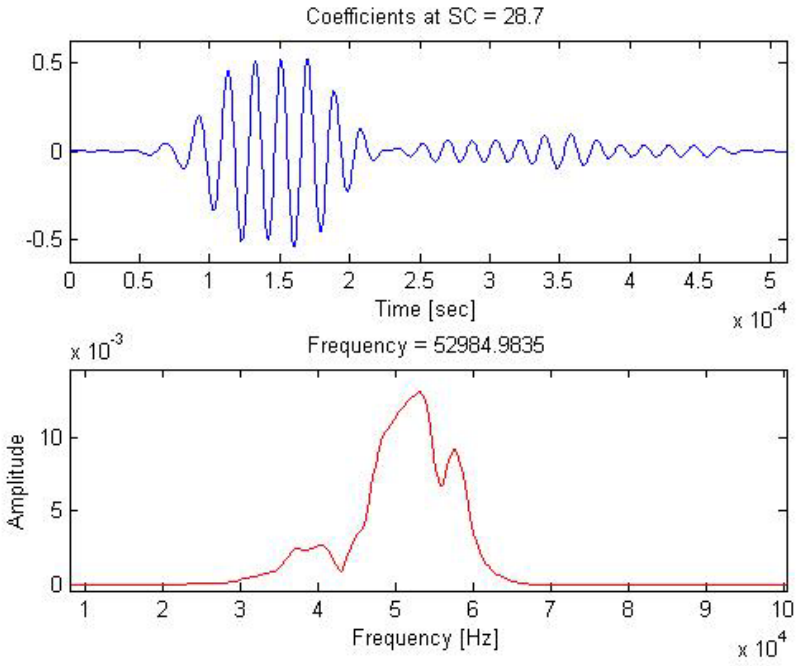

Figure T-13: Frequency content at a given scale from Figure T-11

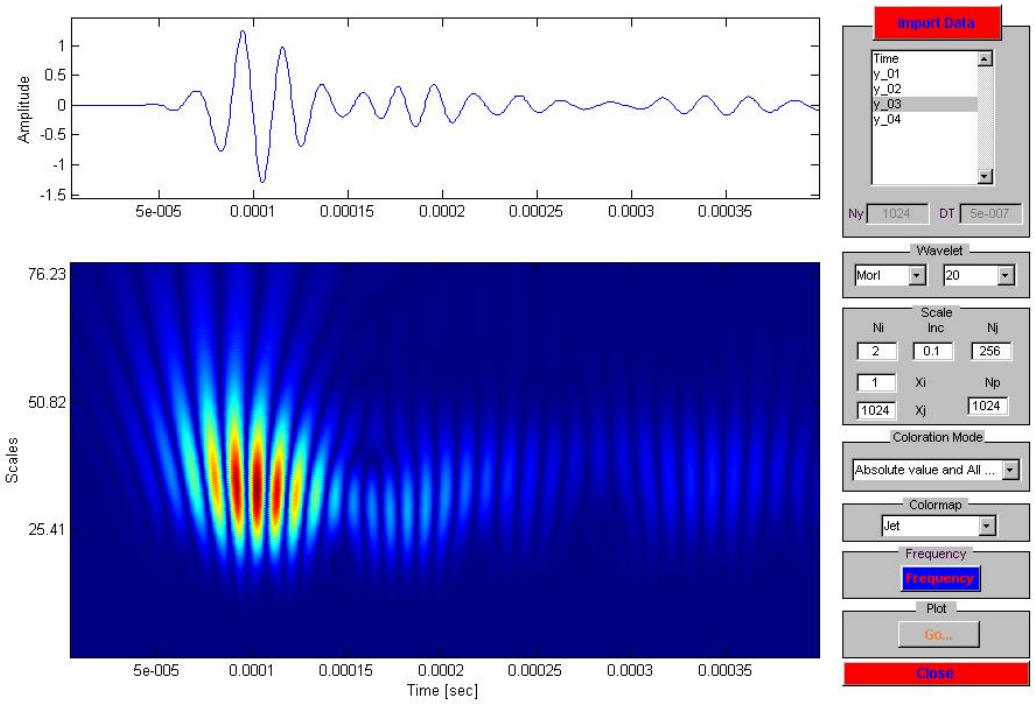

Figure T-14: Wavelet transform using Mallat's algorithm for signal f_{S4_R5} through the joint-free surface (at 120mm S-R spacing)

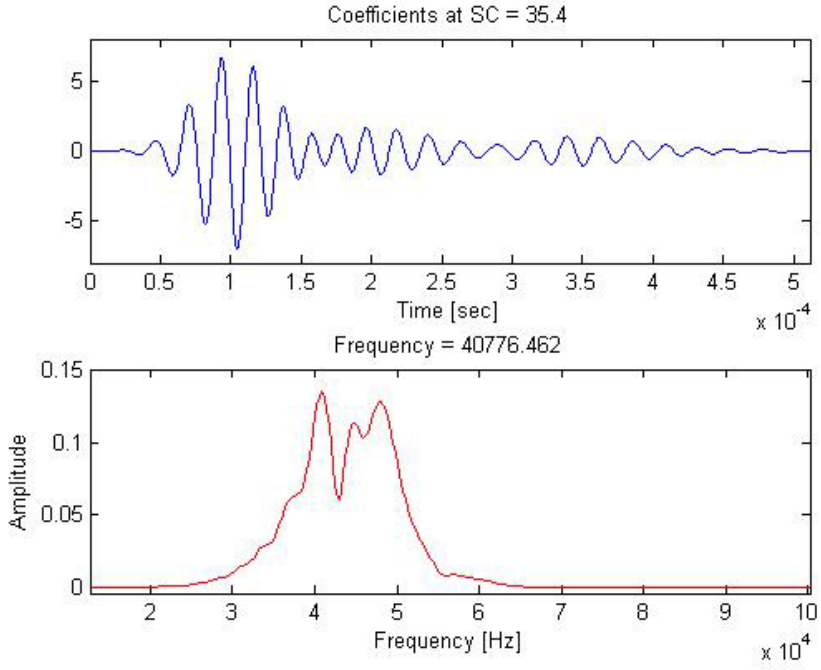

Figure T-15: Frequency content at a given scale from Figure T-14

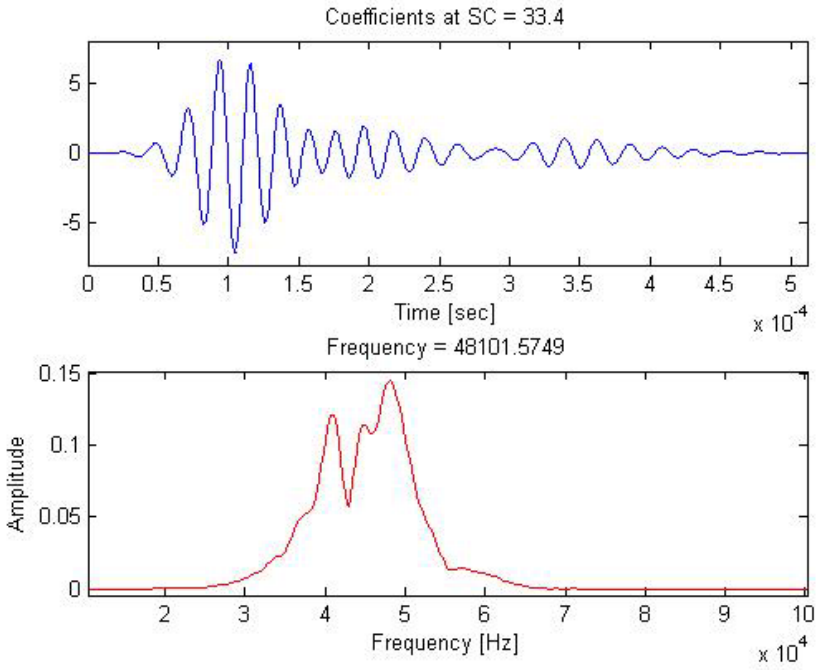

Figure T-16: Frequency content at a given scale from Figure T-14

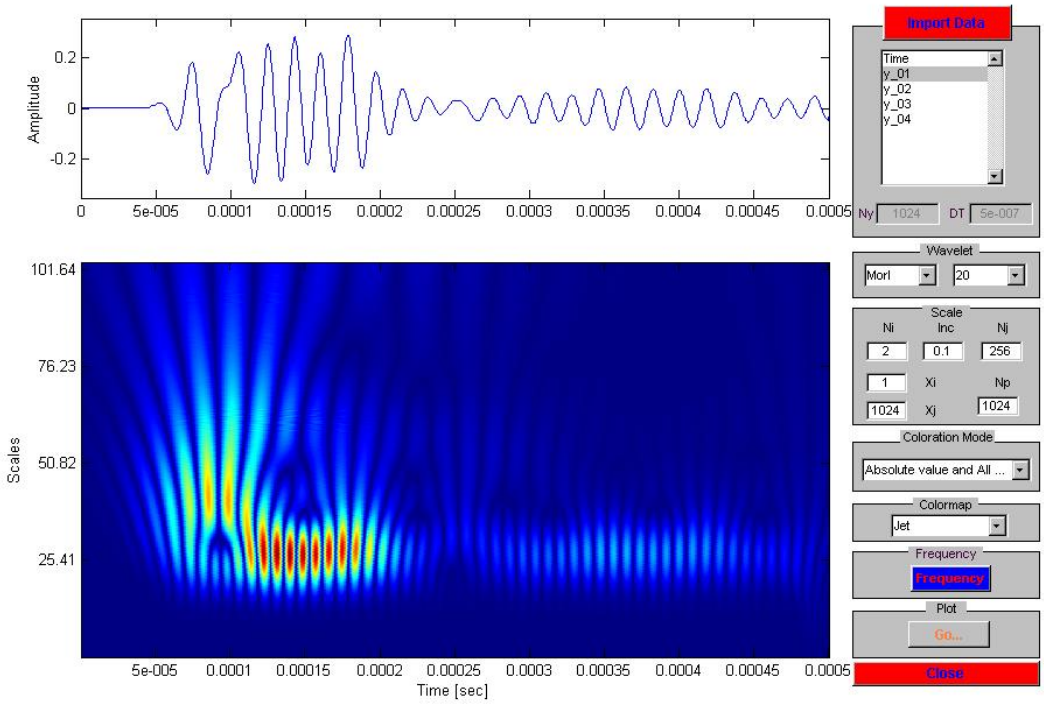

Figure T-17: Wavelet transform using Mallat's algorithm for signal f_{S5_R4} through the joint-free surface (at 120mm S-R spacing)

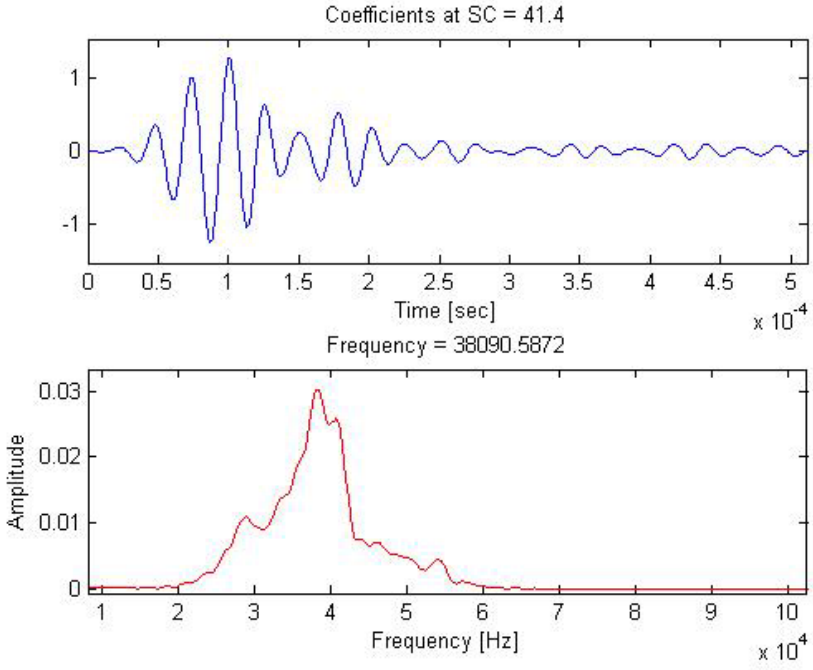

Figure T-18: Frequency content at a given scale from Figure T-17

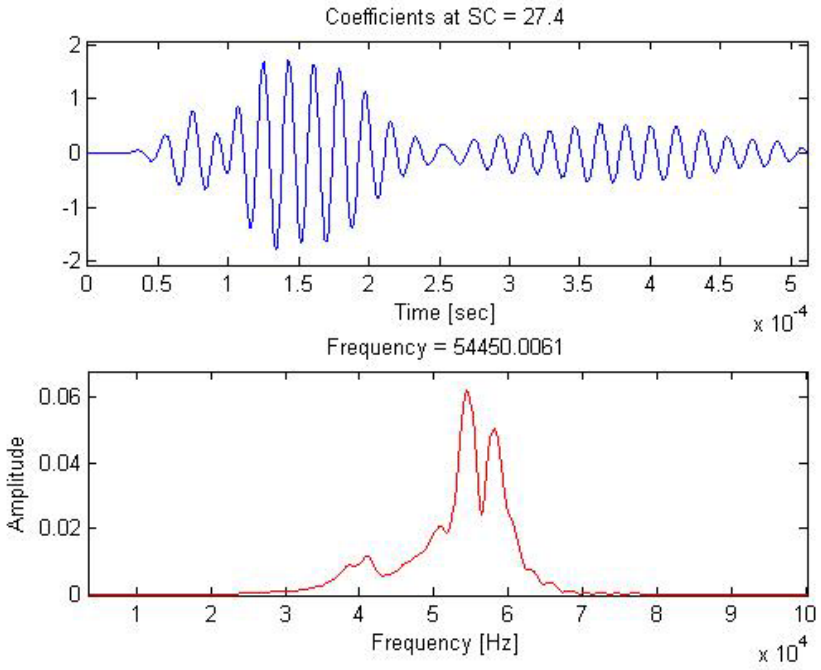

Figure T-19: Frequency content at a given scale from Figure T-17

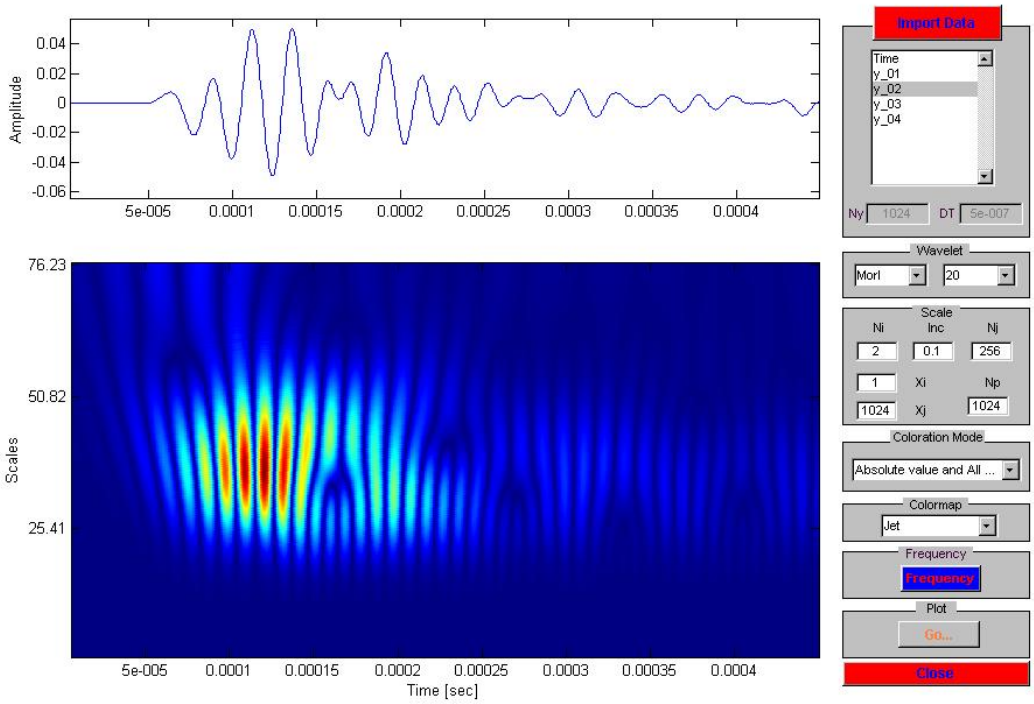

Figure T-20: Wavelet transform using Mallat's algorithm for signal f_{S5_R5} across the joint (at 120mm S-R spacing)

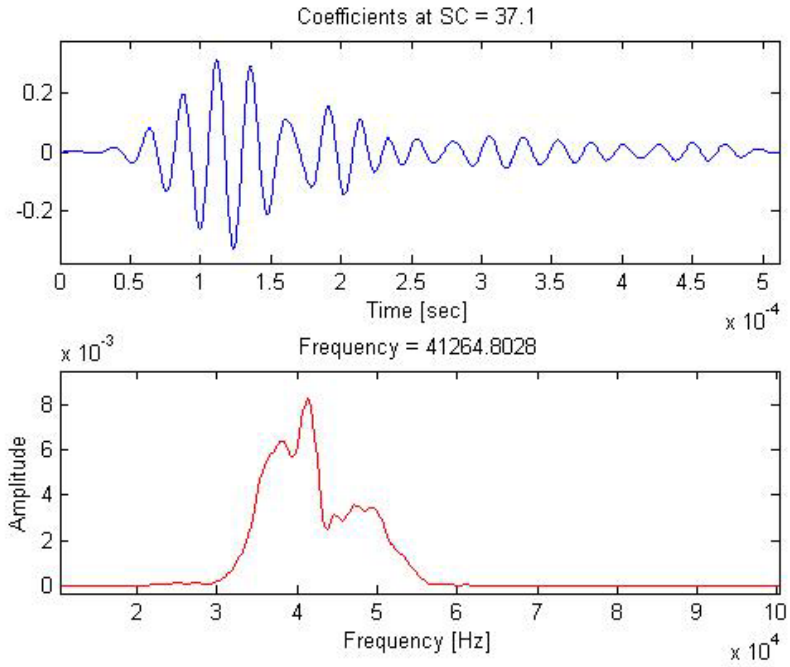

Figure T-21: Frequency content at a given scale from Figure T-20

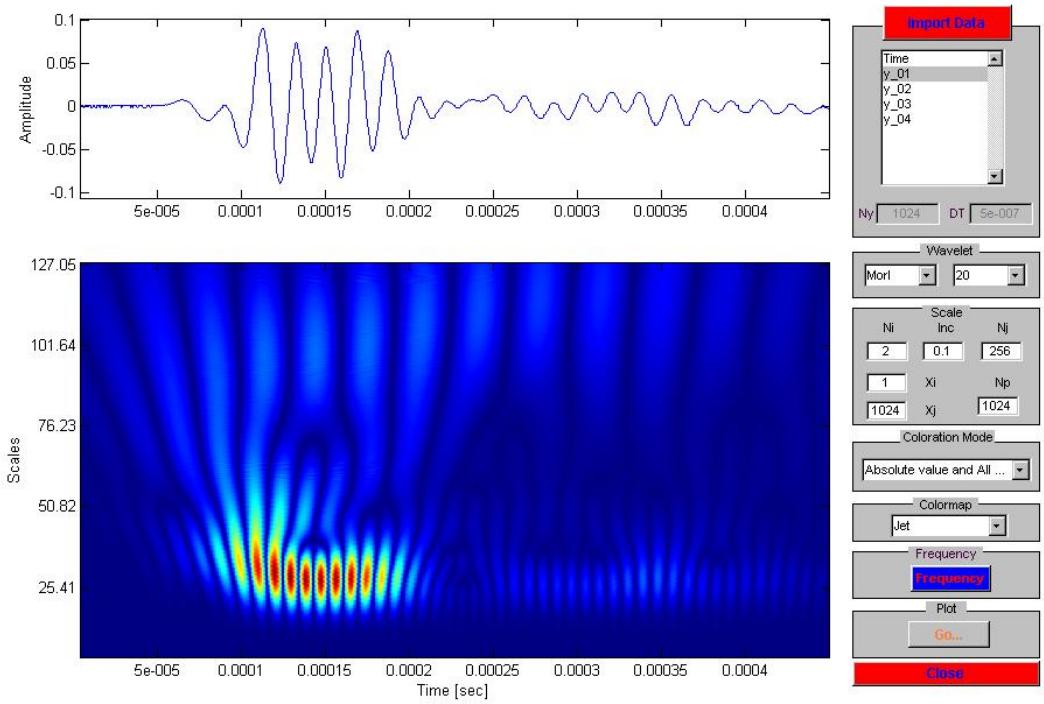

Figure T-22: Wavelet transform using Mallat's algorithm for signal f_{S5_R4} (repeated test) through the joint-free surface (at 120mm S-R spacing)

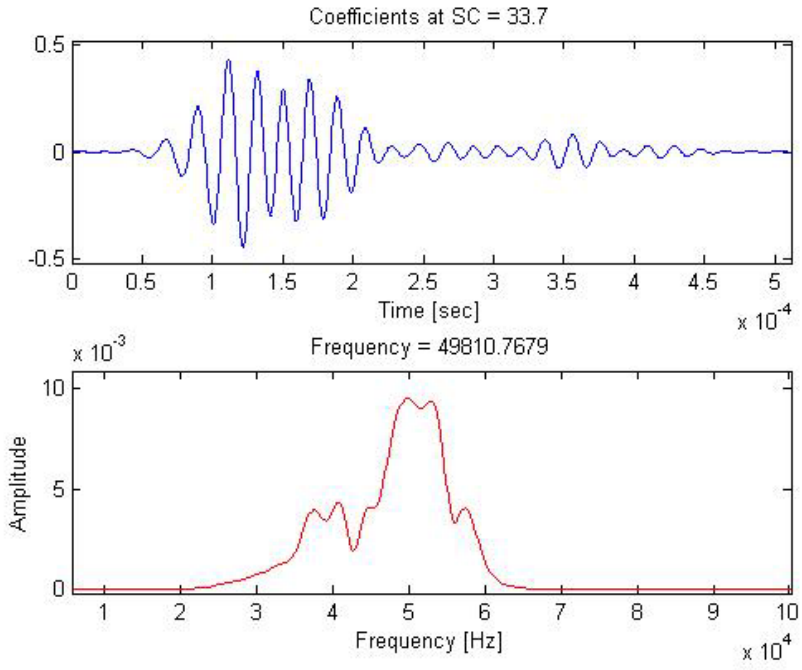

Figure T-23: Frequency content at a given scale from Figure T-22

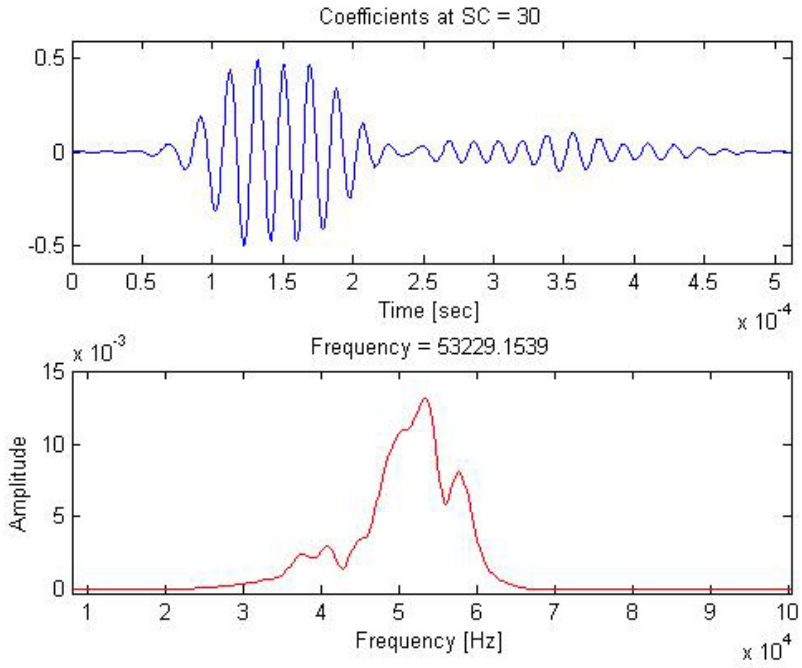

Figure T-24: Frequency content at a given scale from Figure T-22

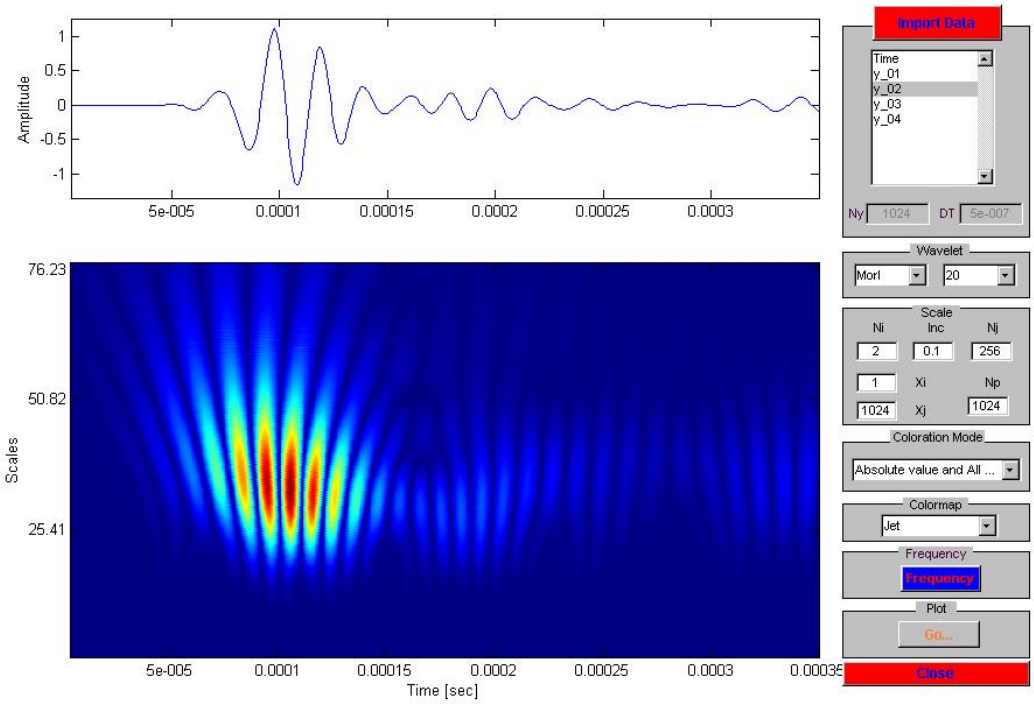

Figure T-25: Wavelet transform using Mallat's algorithm for signal f_{S5_R5} (repeated test) across the joint (at 120mm S-R spacing)

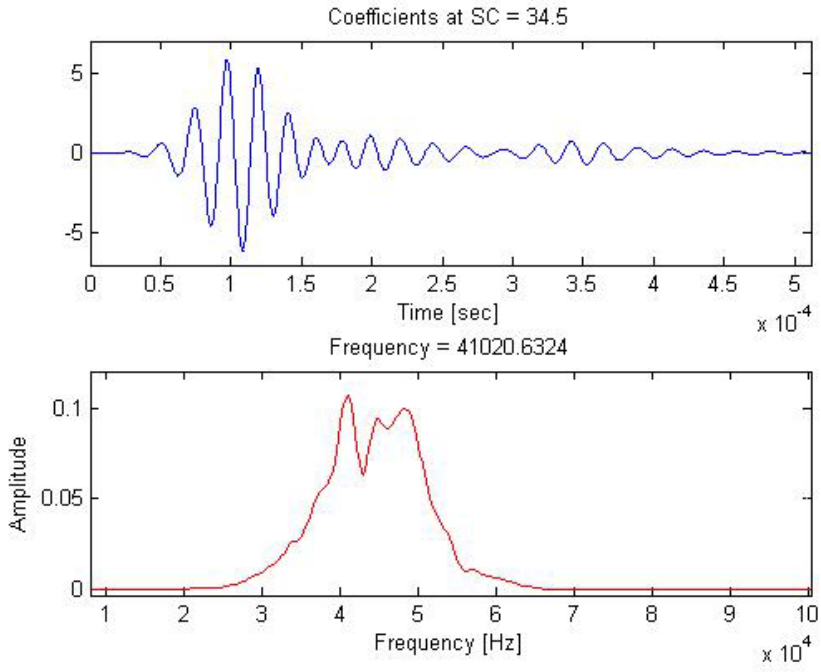

Figure T-26: Frequency content at a given scale from Figure T-25

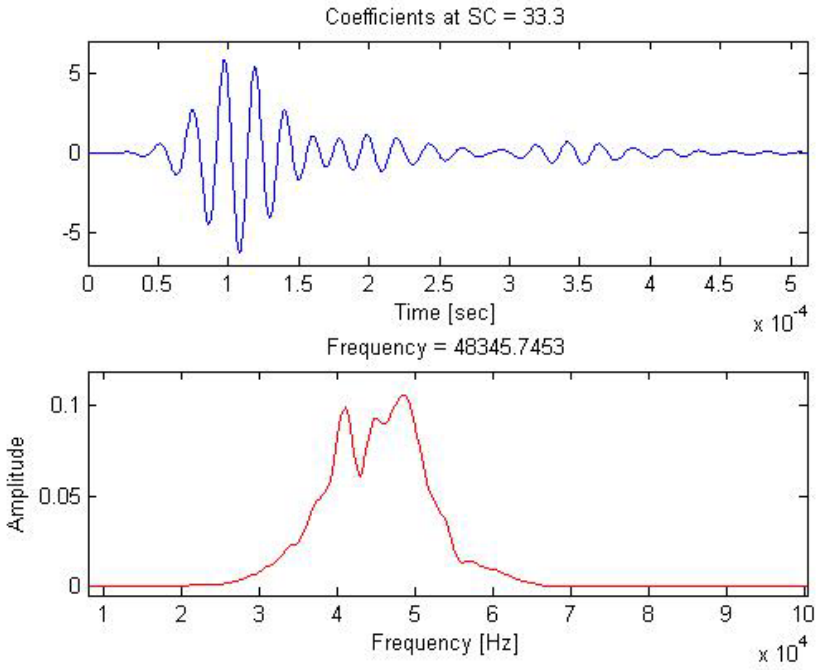

Figure T-27: Frequency content at a given scale from Figure T-25

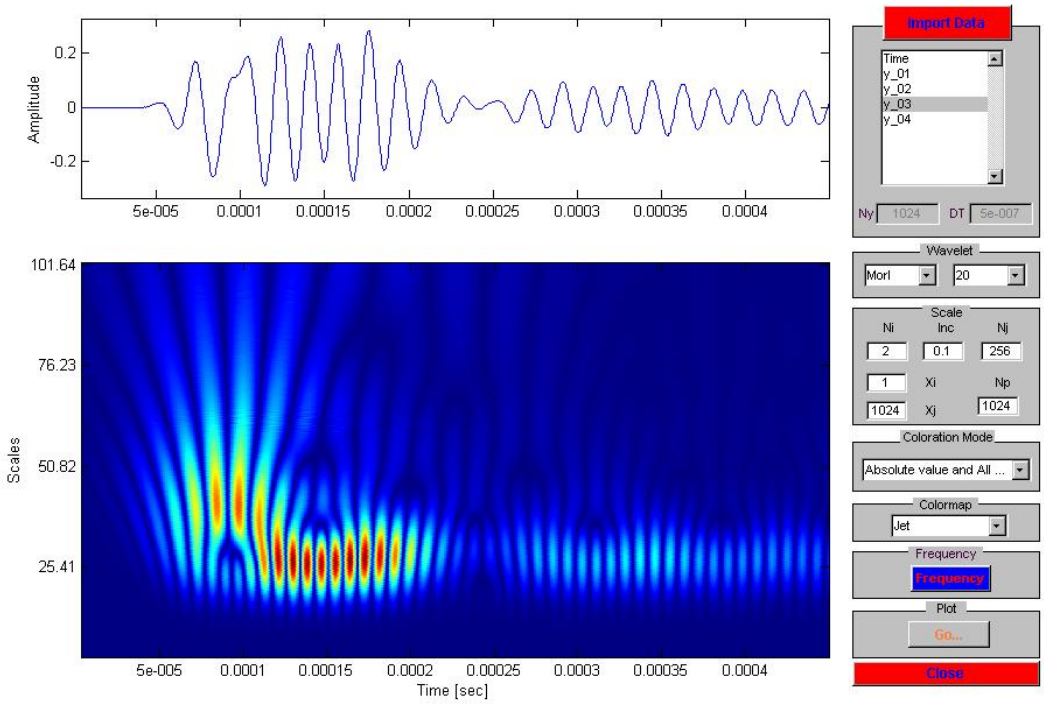

Figure T-28: Wavelet transform using Mallat's algorithm for signal f_{S4_R5} (repeated test) through the joint-free surface (at 120mm S-R spacing)

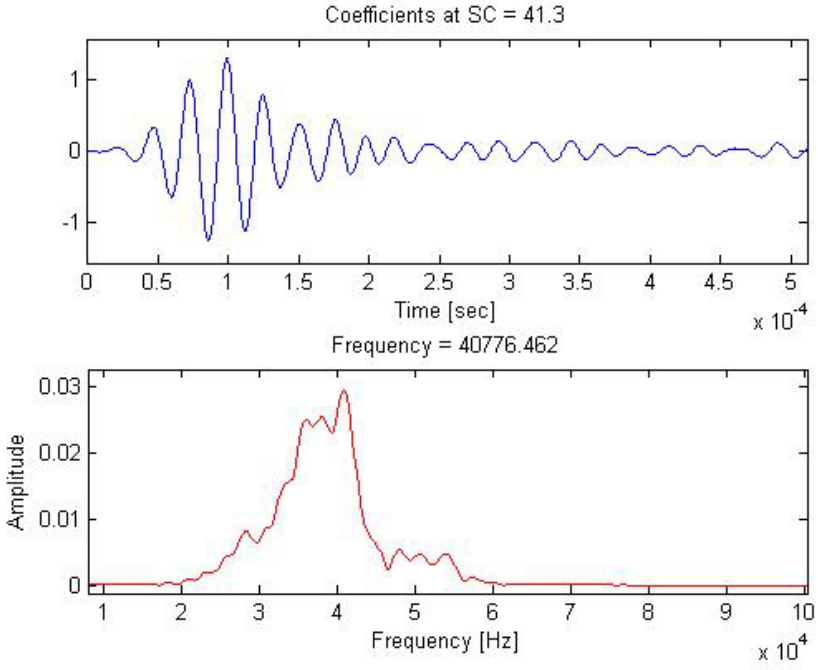

Figure T-29: Frequency content at a given scale from Figure T-28

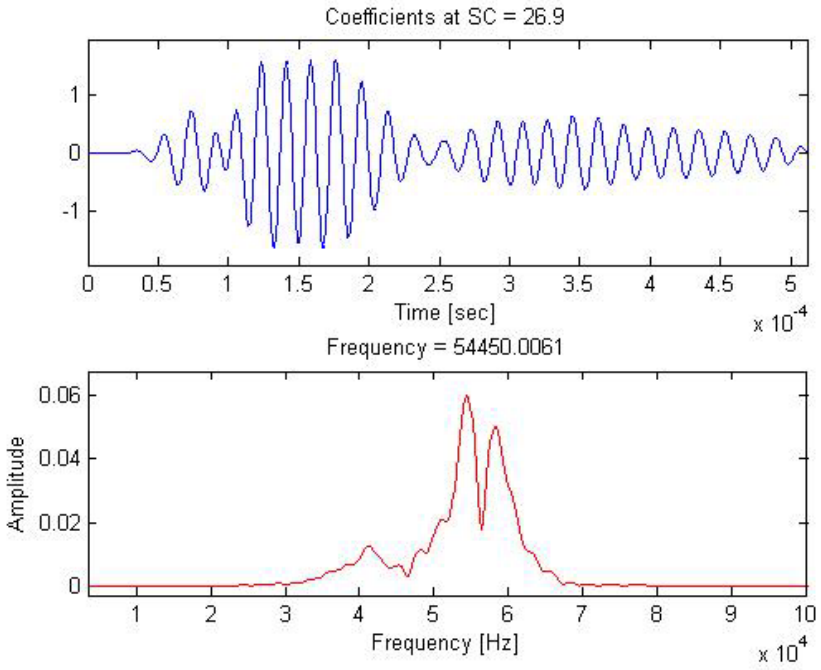

Figure T-30: Frequency content at a given scale from Figure T-28

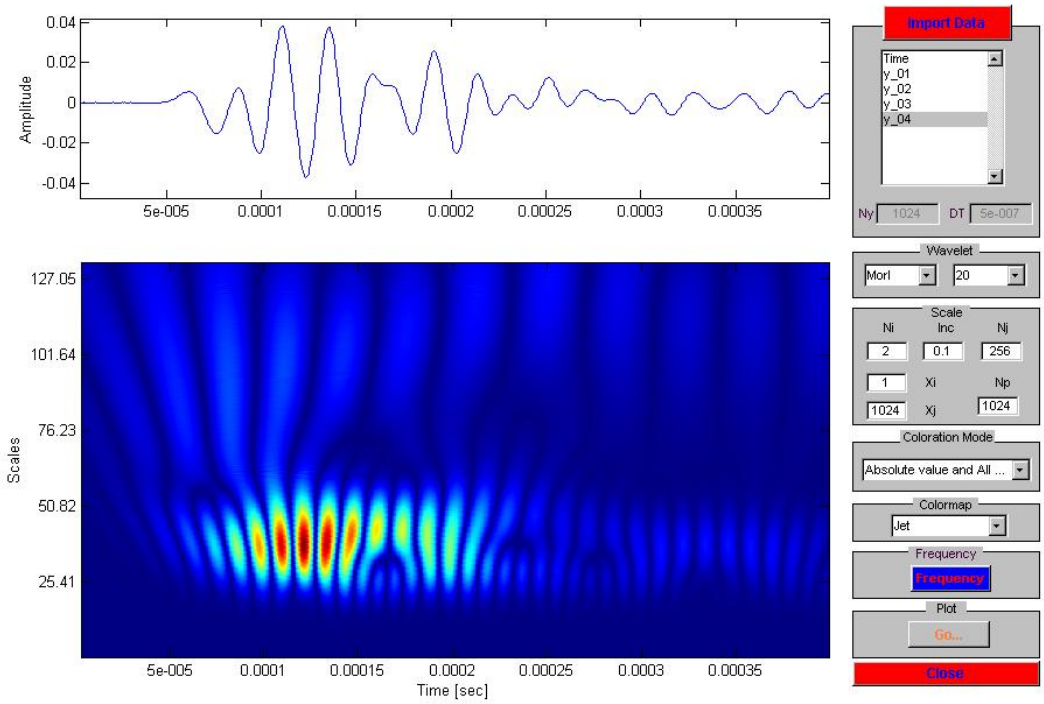

Figure T-31: Wavelet transform using Mallat's algorithm for signal f_{S4_R4} (repeated test) across the joint (at 120mm S-R spacing)

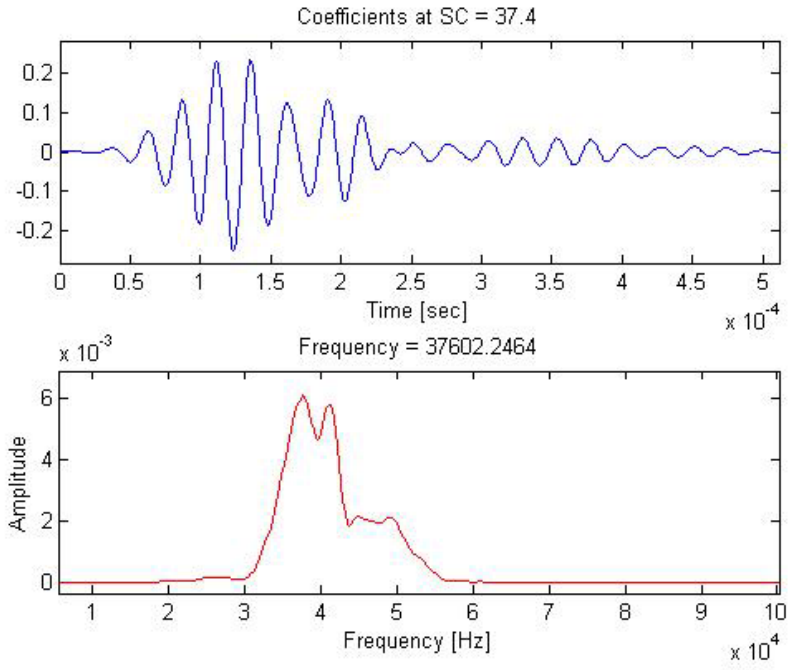

Figure T-32: Frequency content at a given scale from Figure T-31

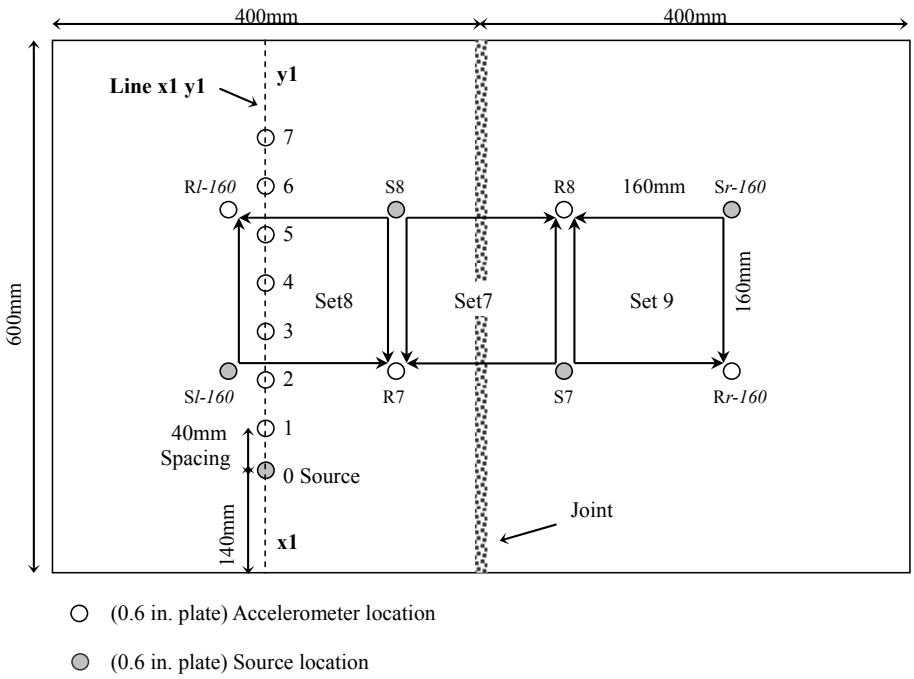

Figure T-33: 160mm S-R spacing configuration of HMA slab 3

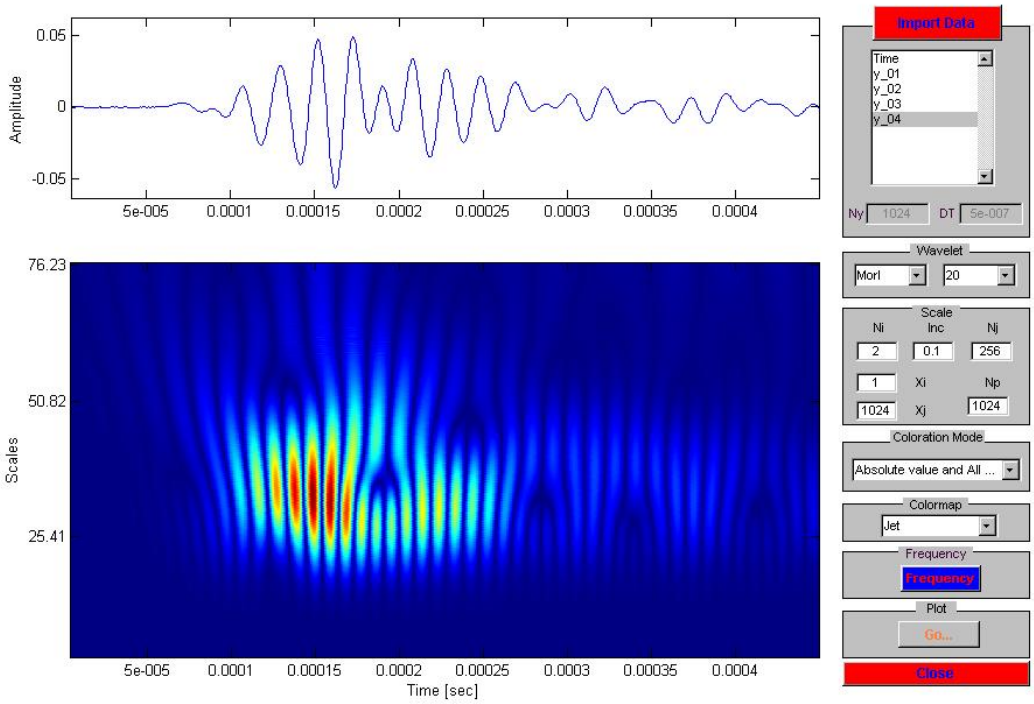

Figure T-34: Wavelet transform using Mallat's algorithm for signal f_{S7_R7} across the joint (at 160mm S-R spacing)

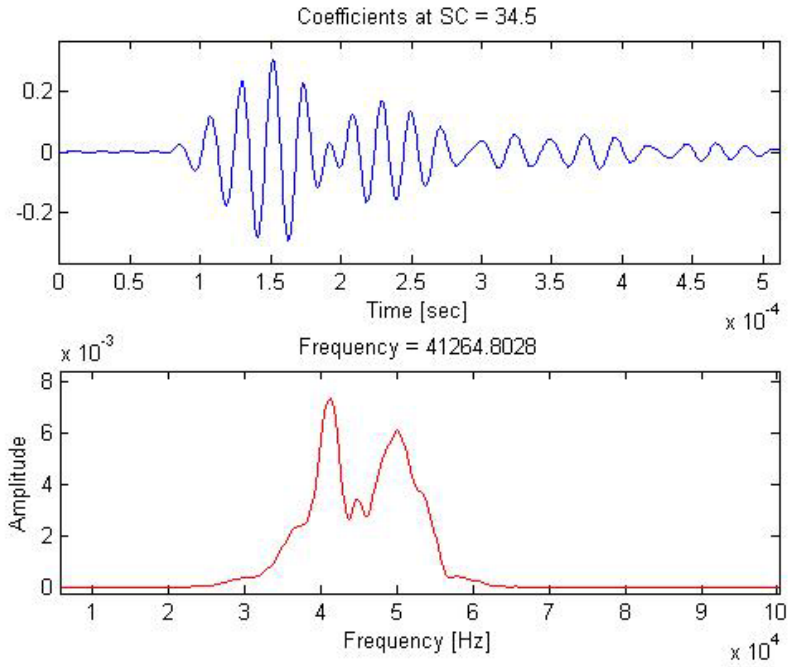

Figure T-35: Frequency content at a given scale from Figure T-34

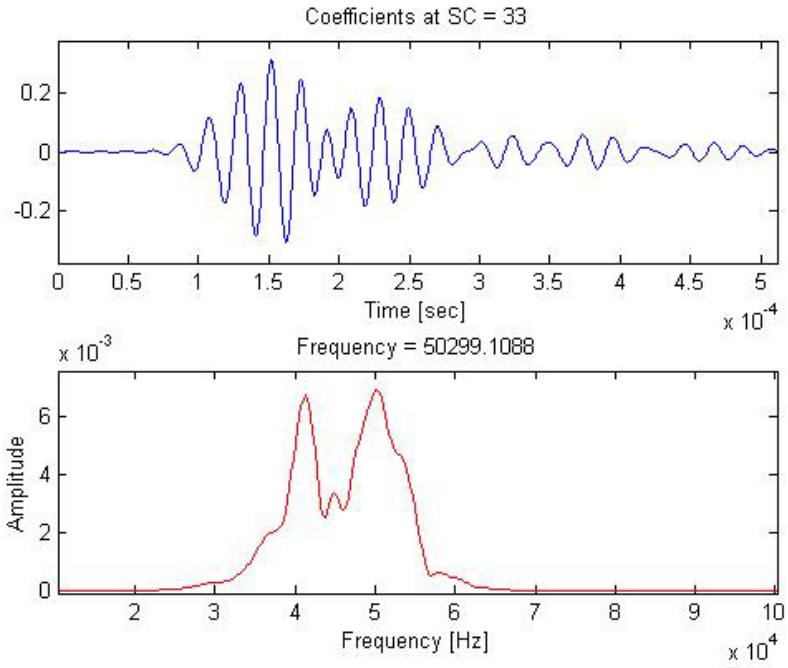

Figure T-36: Frequency content at a given scale from Figure T-34

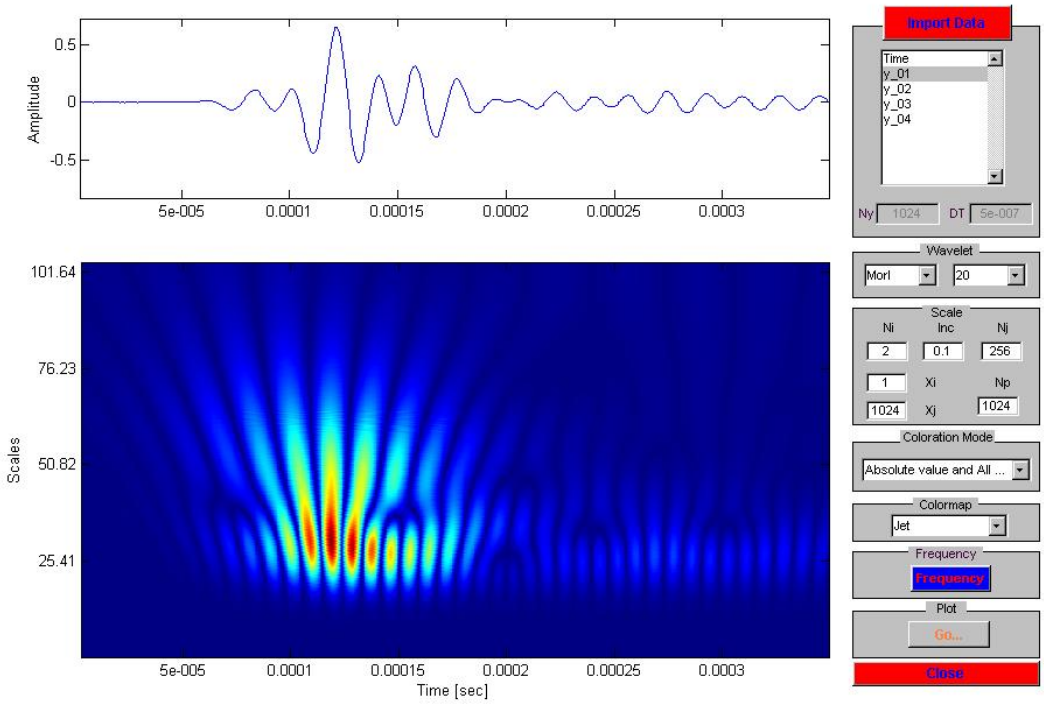

Figure T-37: Wavelet transform using Mallat's algorithm for signal f_{S8_R7} through the joint-free surface (at 160mm S-R spacing)

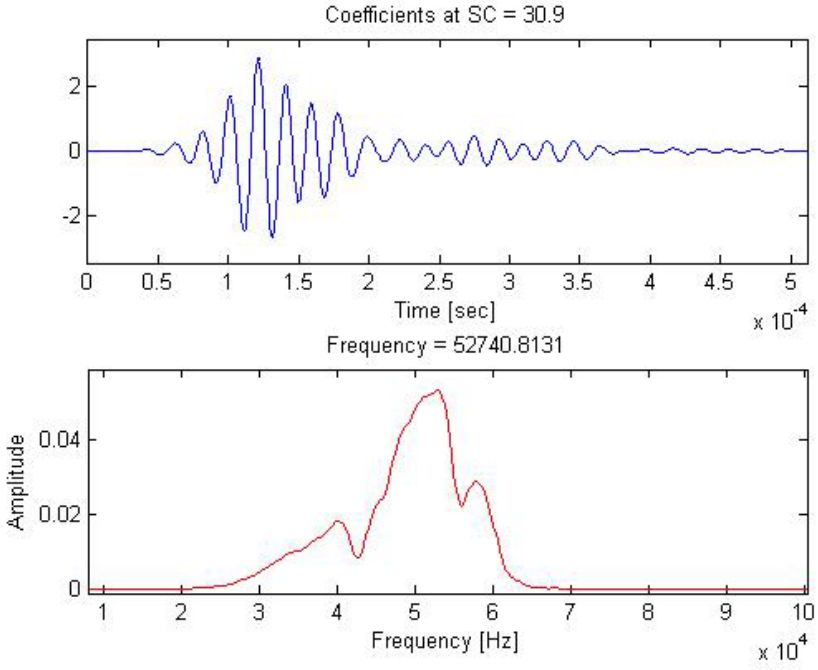

Figure T-38: Frequency content at a given scale from Figure T-37

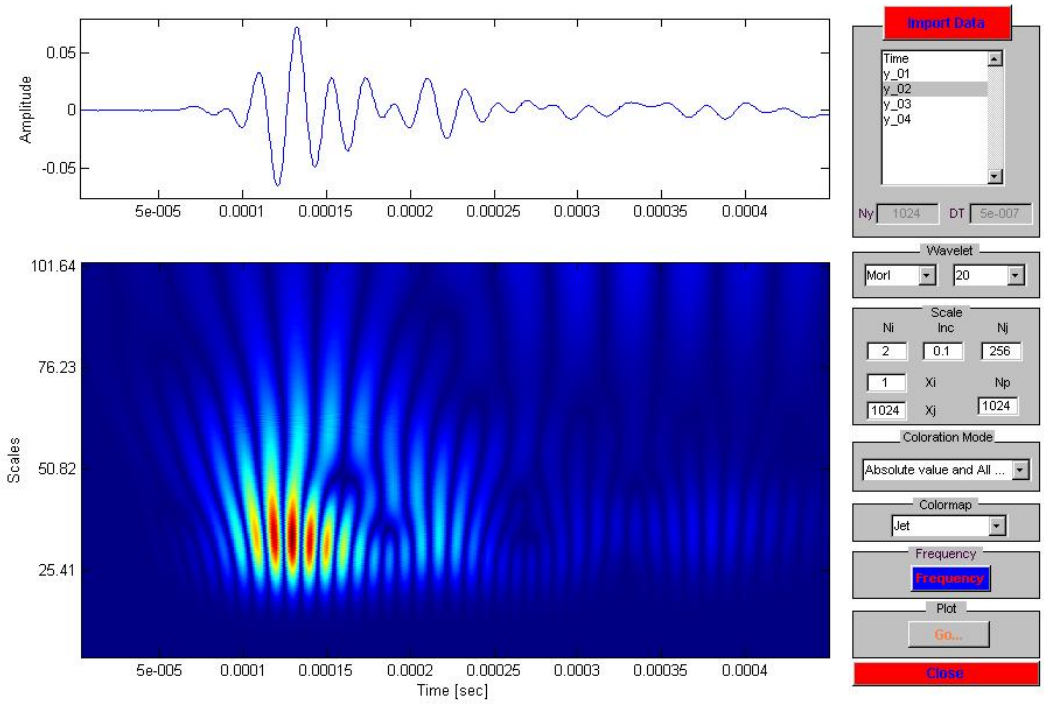

Figure T-39: Wavelet transform using Mallat's algorithm for signal f_{S8_R8} across the joint (at 160mm S-R spacing)

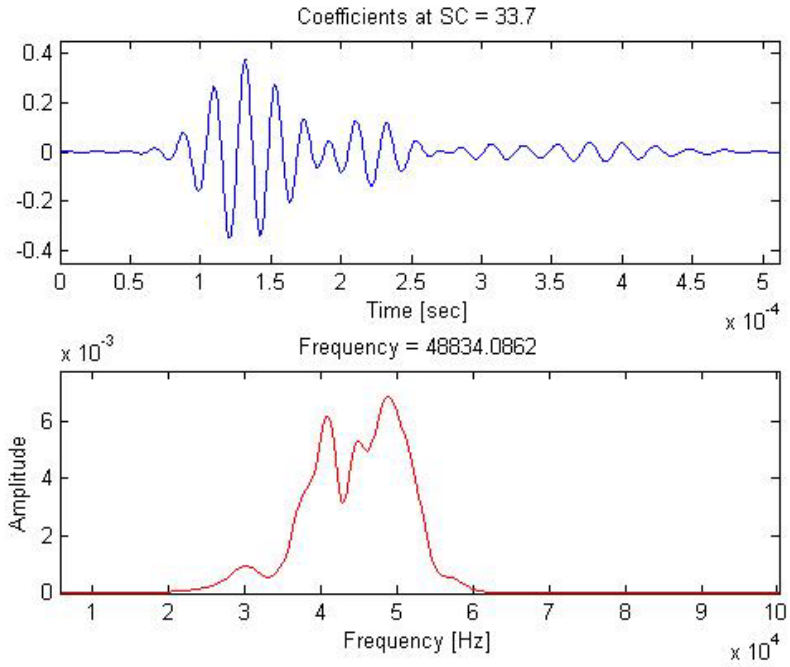

Figure T-40: Frequency content at a given scale from Figure T-39

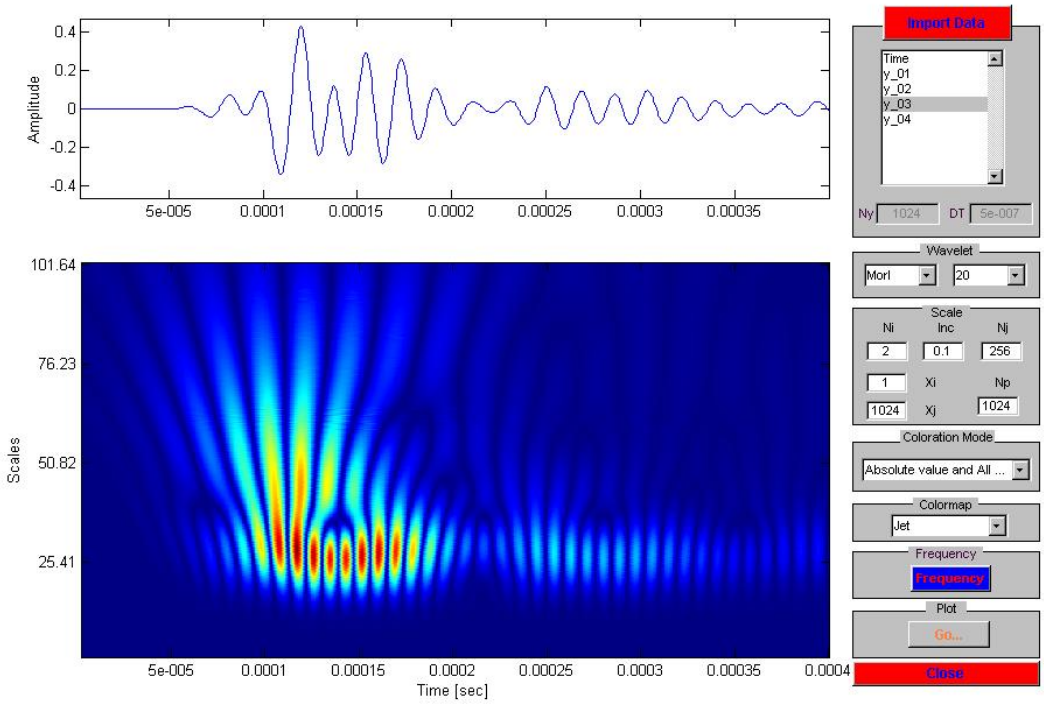

Figure T-41: Wavelet transform using Mallat's algorithm for signal f_{S7_R8} through the joint-free surface (at 160mm S-R spacing)

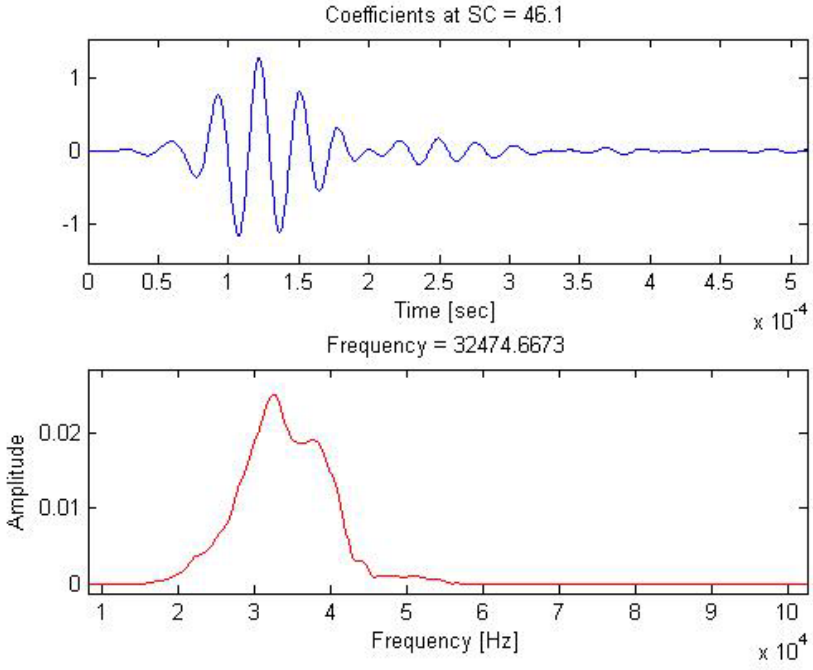

Figure T-42: Frequency content at a given scale from Figure T-41

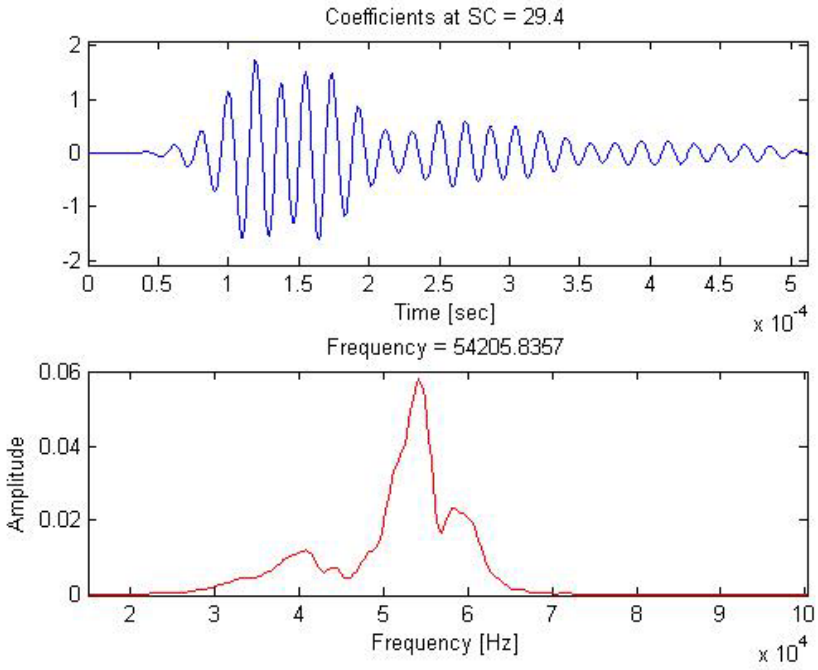

Figure T-43: Frequency content at a given scale from Figure T-41

Appendix U

Equivalent Damping Ratio vs. Frequency for Slab 3

- Measurements on the Jointed and the Joint-free Surfaces

This appendix is a PDF file available in the Appendix CD.

The file name of this PDF file is “Appendix U－Equivalent damping ratio vs. frequency.pdf”.

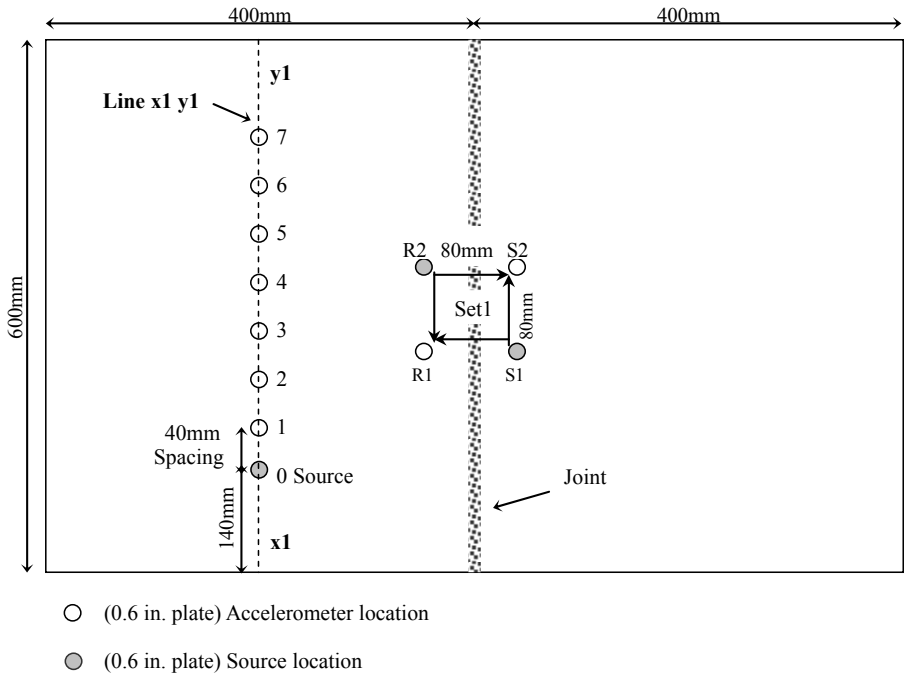

Figure U-1: 80mm S-R spacing configuration of HMA slab 3

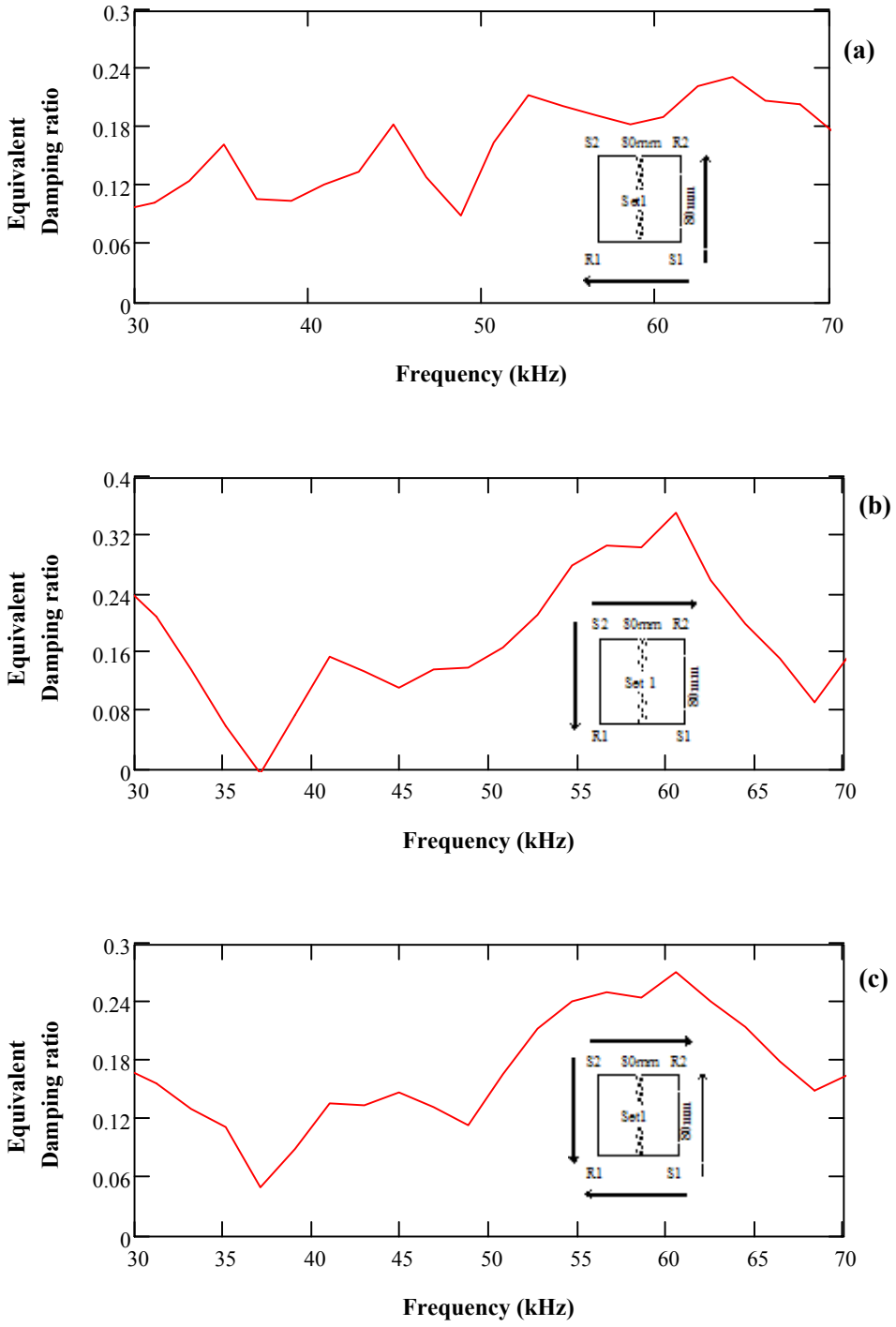

Figure U-2: Equivalent damping ratio (D) vs. frequency for full signals of set 1 measurements (80mm S-R spacing) on the jointed surface – (a) D for Signal Pair 1 of set 1 (b) D for Signal Pair 2 of set 1 (c) D for entire set 1 measurements

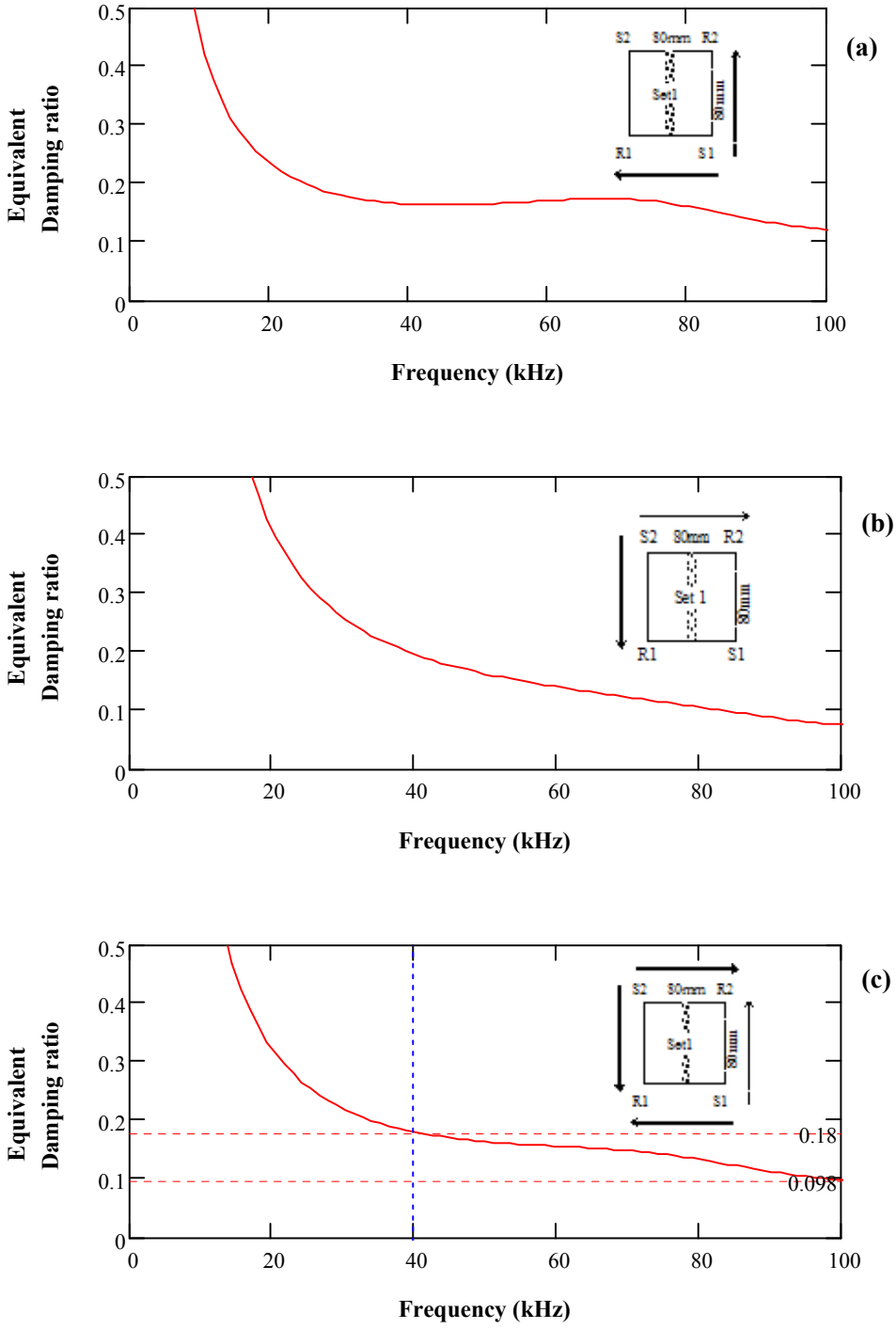

Figure U-3: Equivalent damping ratio (D) vs. frequency for P-waves for set 1 measurements (80mm S-R spacing) on the jointed surface - (a) D for Signal Pair 1 of set 1 (b) D for Signal Pair 2 of set 1 (c) D for entire set 1 measurements

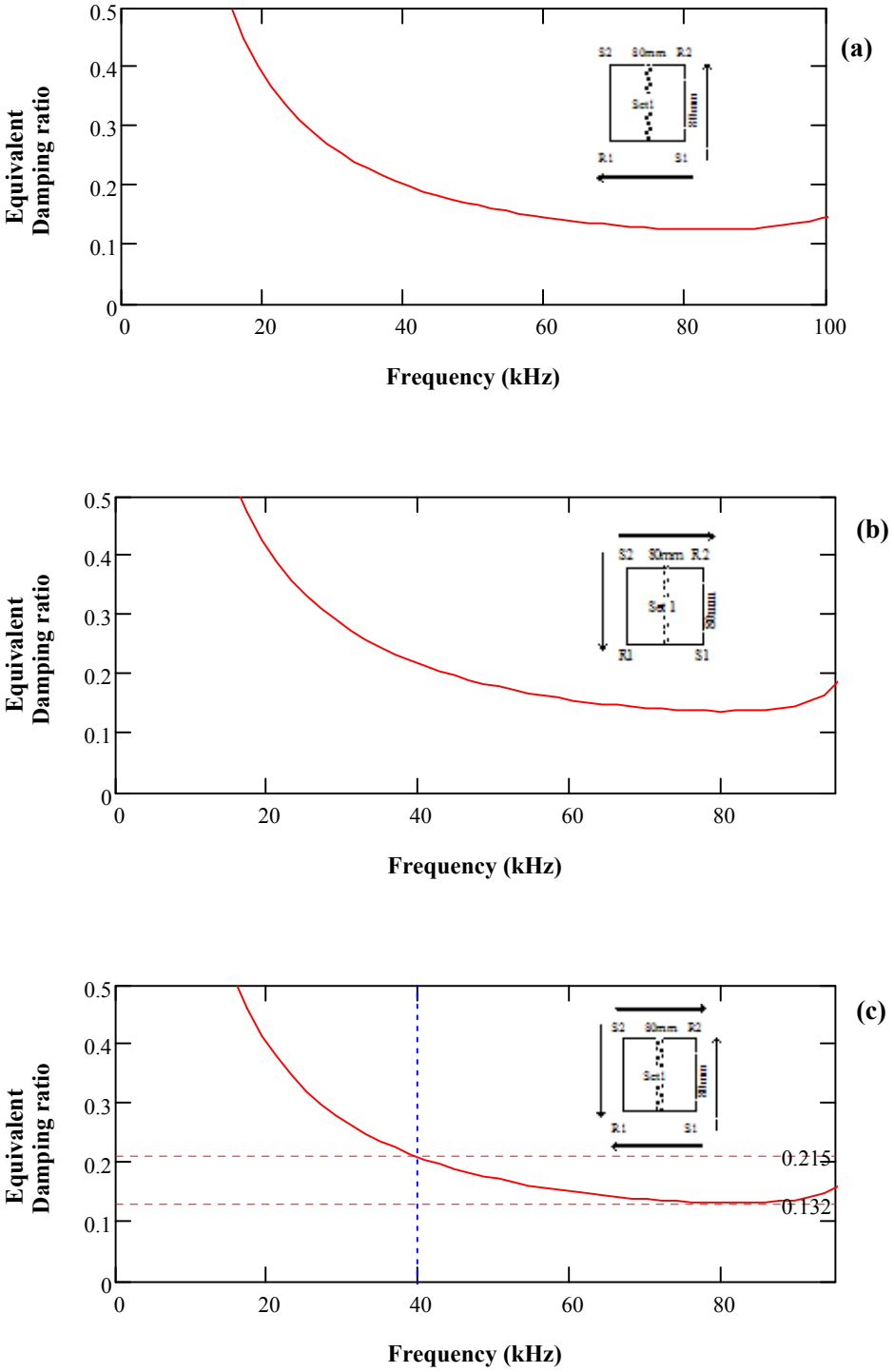

Figure U-4: Equivalent damping ratio (D) vs. frequency for R-waves for set 1 measurements (80mm S-R spacing) on the jointed surface - (a) D for Signal Pair 1 of set 1 (b) D for Signal Pair 2 of set 1 (c) D for entire set 1 measurements

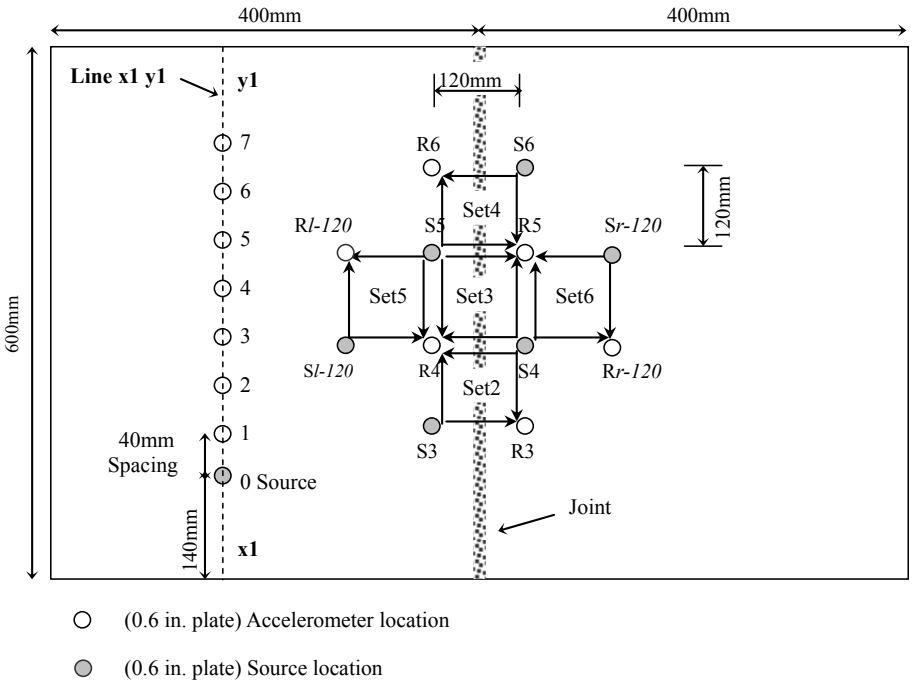

Figure U-5: 120mm S-R spacing configuration of HMA slab 3

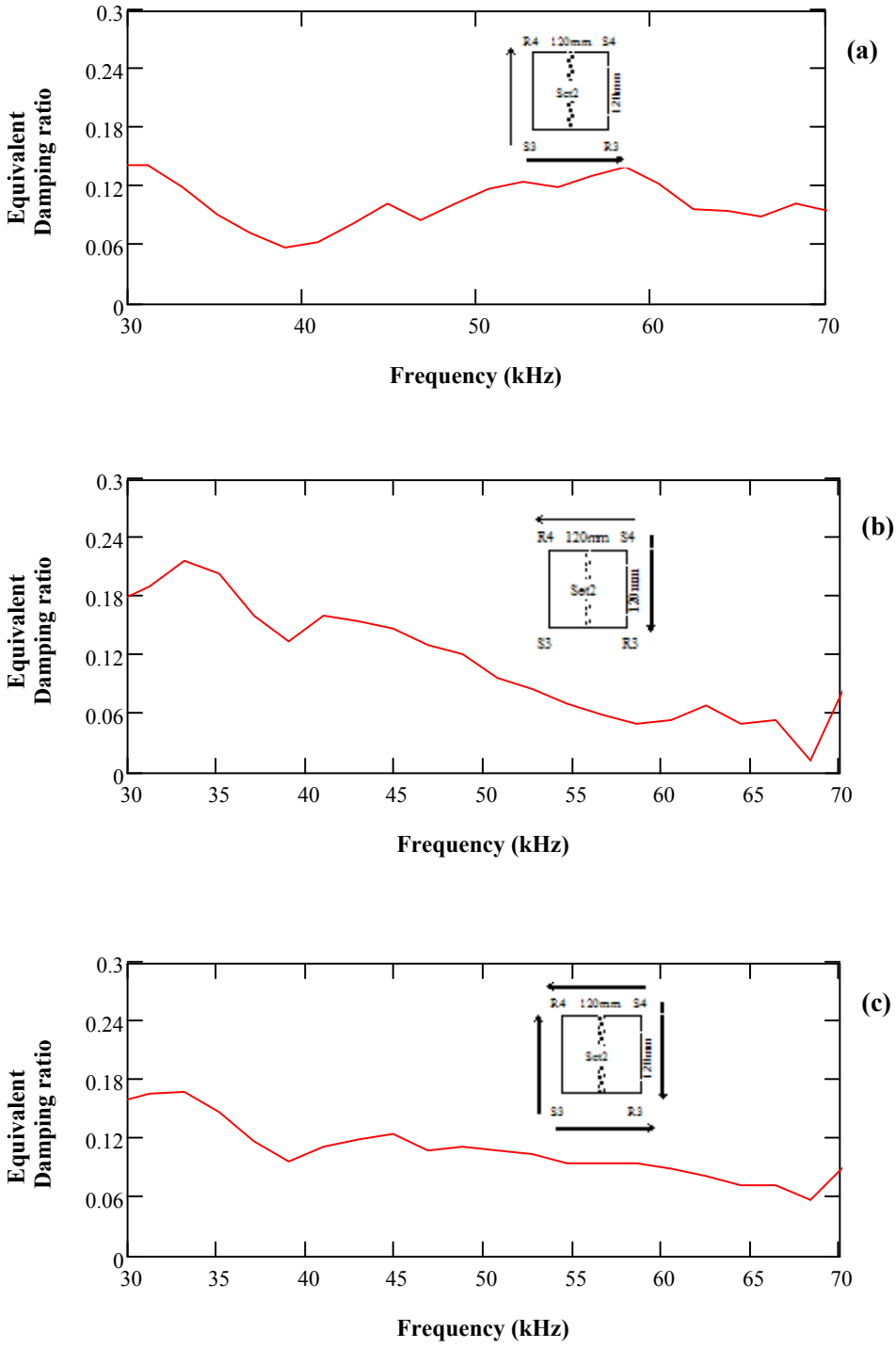

Figure U-6: Equivalent damping ratio (D) vs. frequency for full signals of set 2 measurements (120mm S-R spacing) on the jointed surface - (a) D for Signal Pair 1 of set 2 (b) D for Signal Pair 2 of set 2 (c) D for entire set 2 measurements

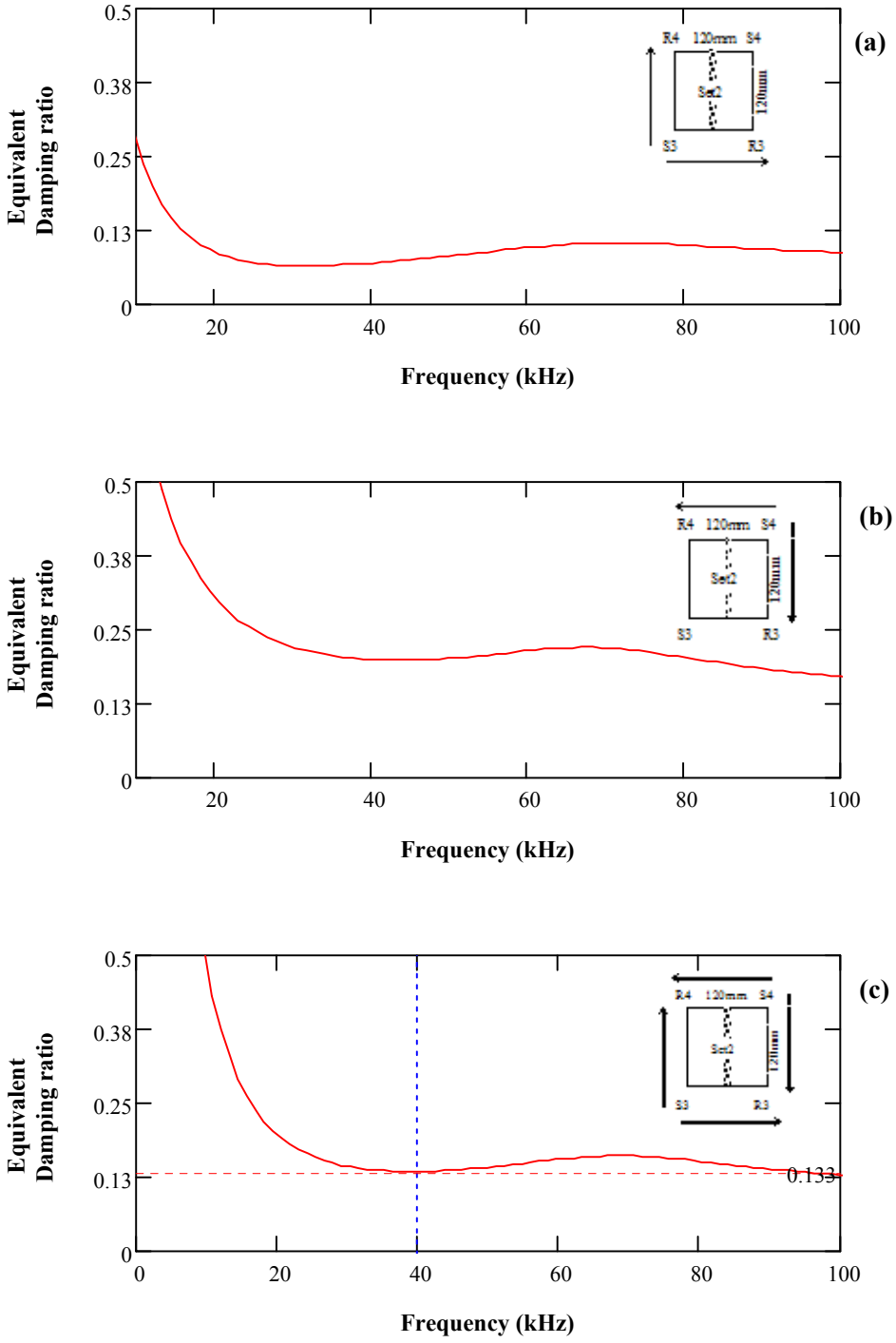

Figure U-7: Equivalent damping ratio (D) vs. frequency for P-waves for set 2 measurements (120mm S-R spacing) on the jointed surface - (a) D for Signal Pair 1 of set 2 (b) D for Signal Pair 2 of set 2 (c) D for entire set 2 measurements

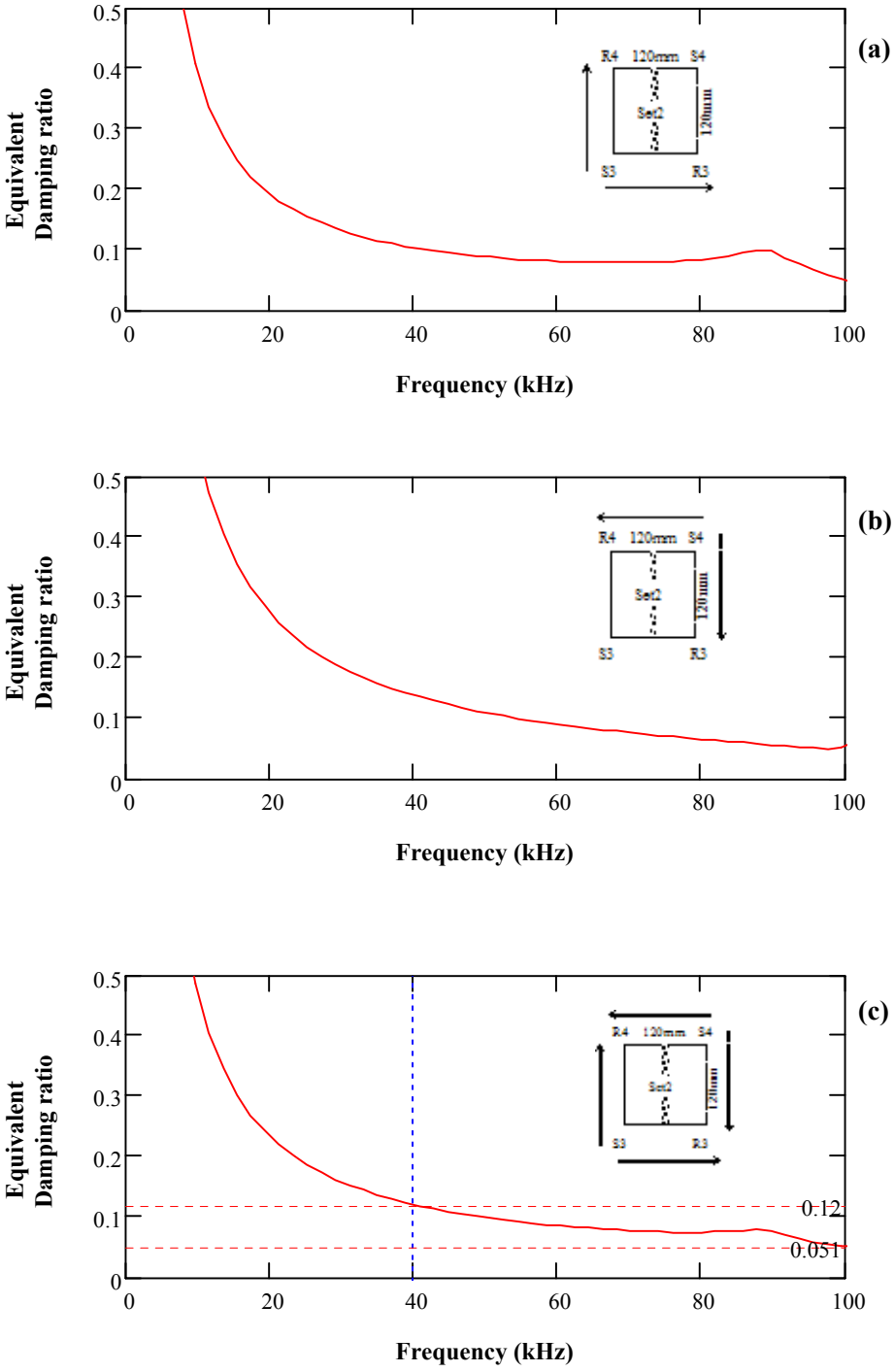

Figure U-8: Equivalent damping ratio (D) vs. frequency for R-waves for set 2 measurements (120mm S-R spacing) on the jointed surface - (a) D for Signal Pair 1 of set 2 (b) D for Signal Pair 2 of set 2 (c) D for entire set 2 measurements

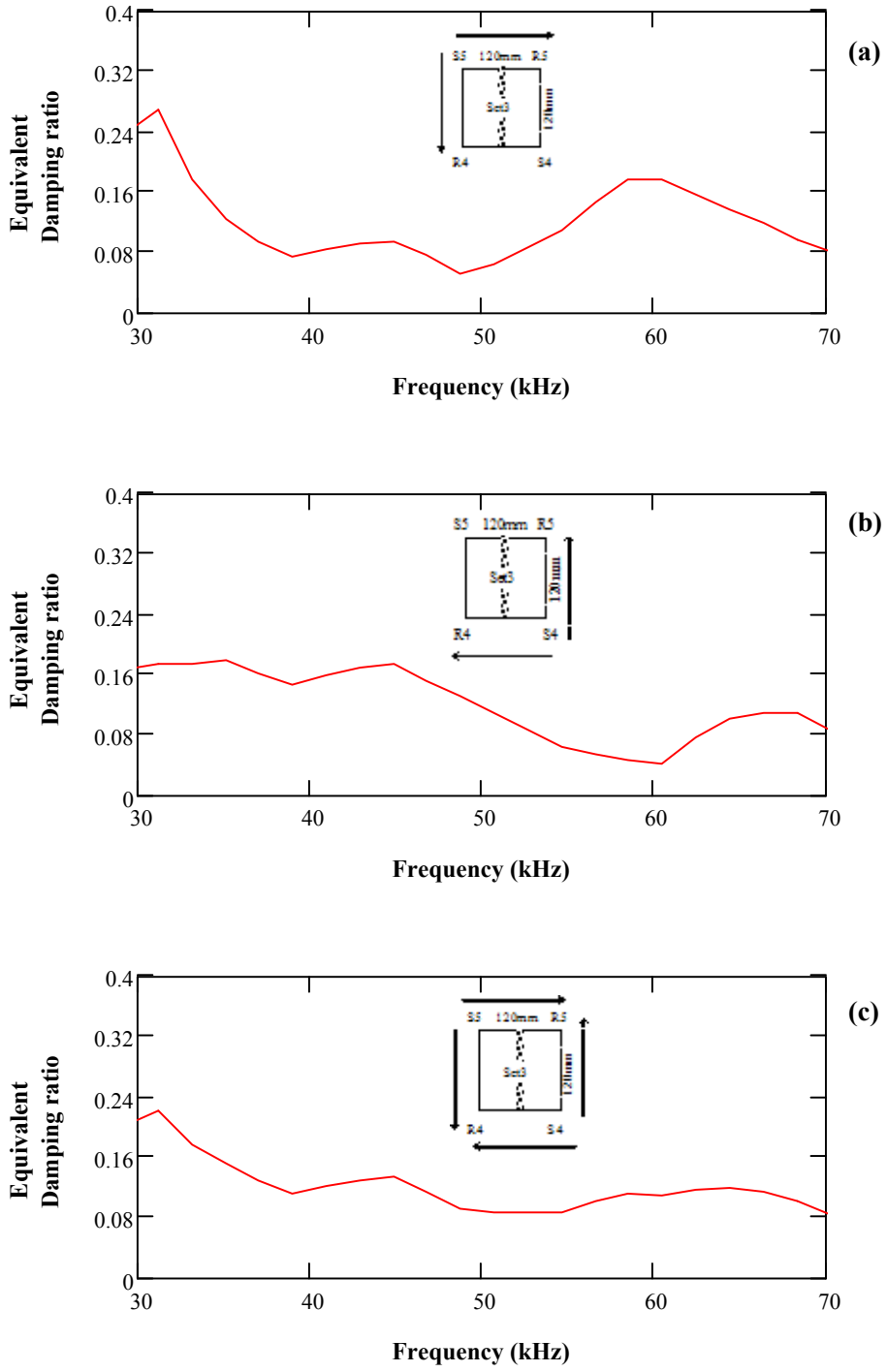

Figure U-9: Equivalent damping ratio (D) vs. frequency for full signals of set 3 measurements (120mm S-R spacing) on the jointed surface - (a) D for Signal Pair 1 of set 3 (b) D for Signal Pair 2 of set 3 (c) D for entire set 3 measurements

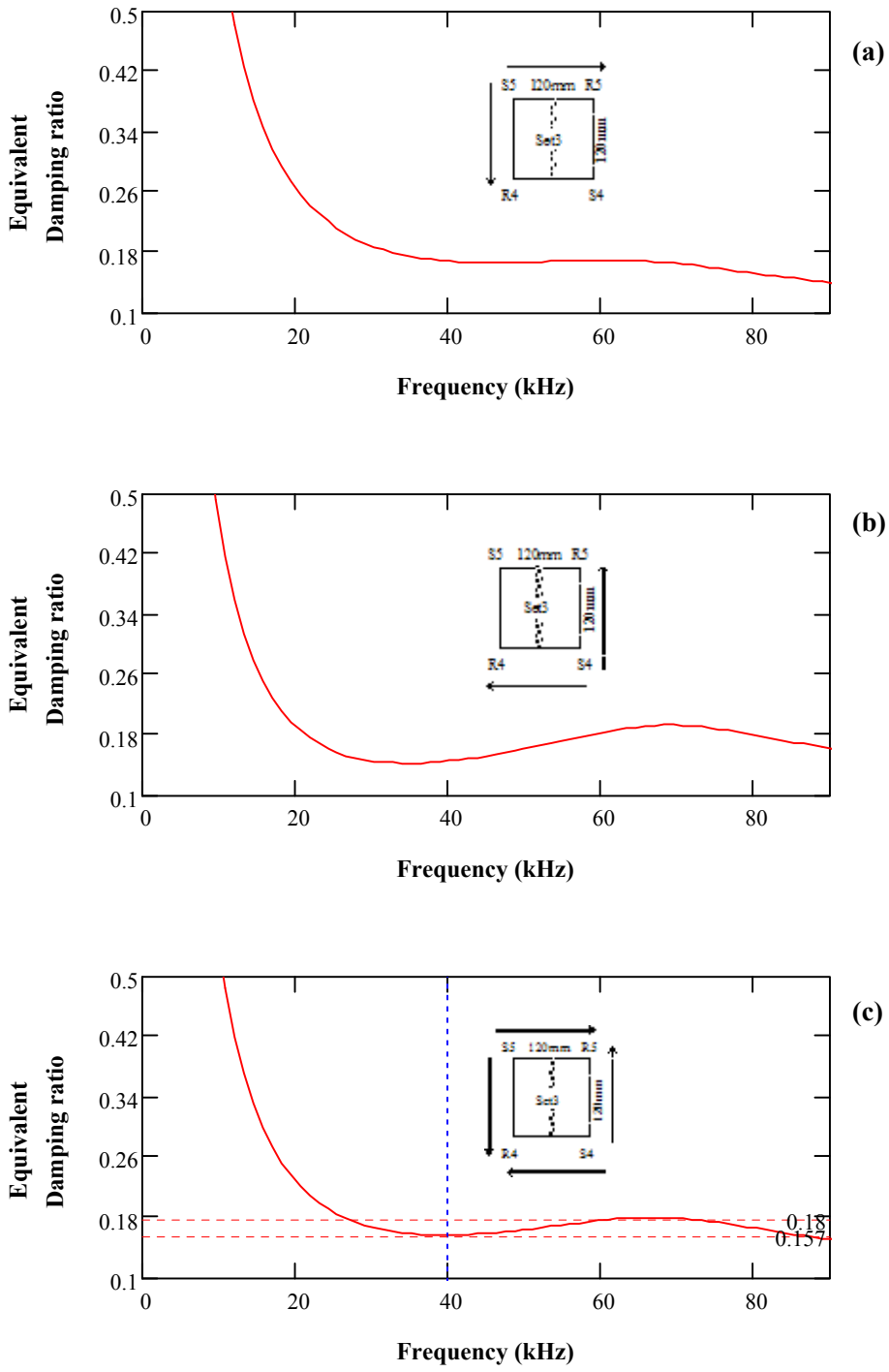

Figure U-10: Equivalent damping ratio (D) vs. frequency for P-waves for set 3 measurements (120mm S-R spacing) on the jointed surface - (a) D for Signal Pair 1 of set 3 (b) D for Signal Pair 2 of set 3 (c) D for entire set 3 measurements

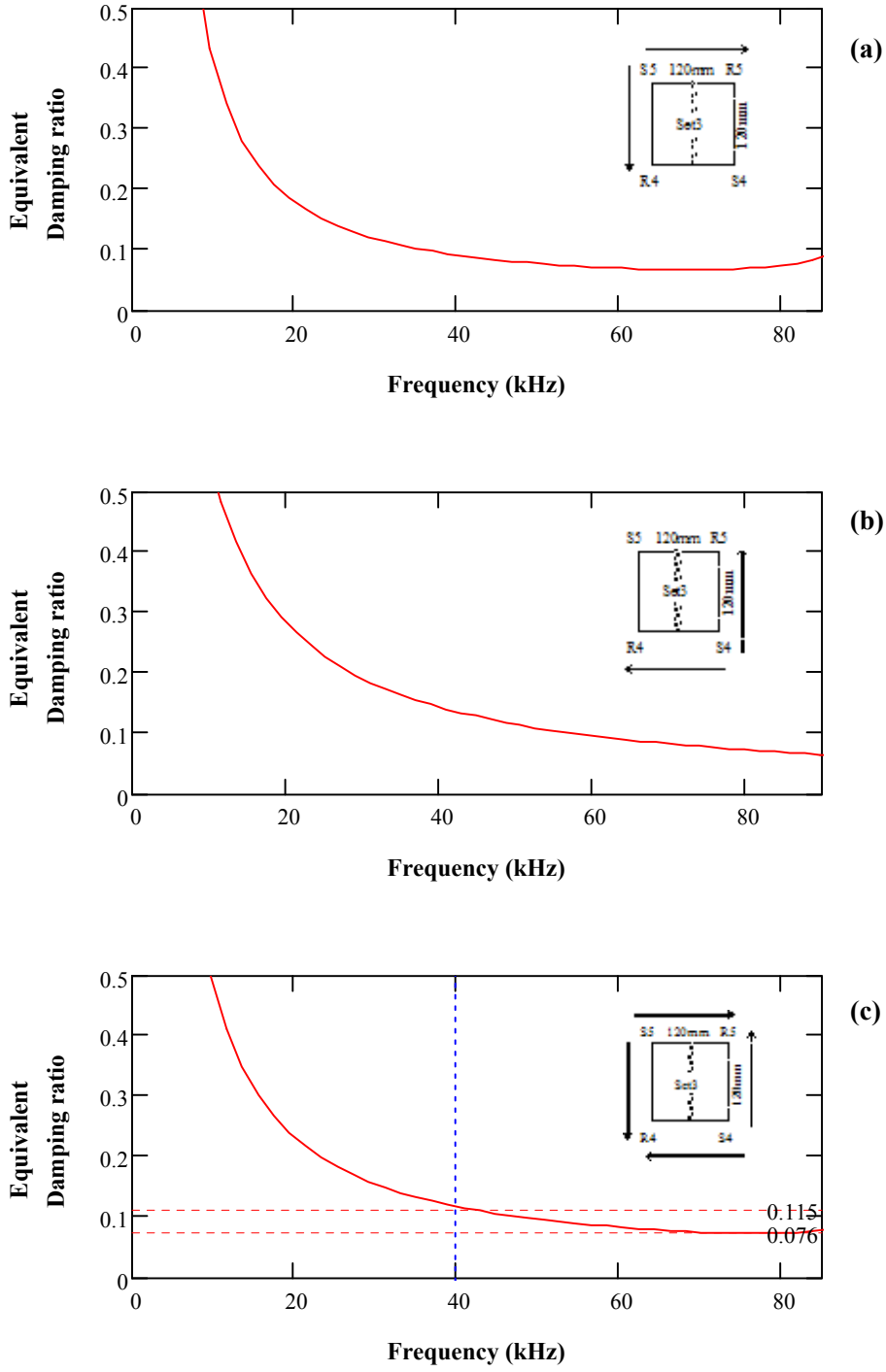

Figure U-11: Equivalent damping ratio (D) vs. frequency for R-waves for set 3 measurements (120mm S-R spacing) on the jointed surface - (a) D for Signal Pair 1 of set 3 (b) D for Signal Pair 2 of set 3 (c) D for entire set 3 measurements

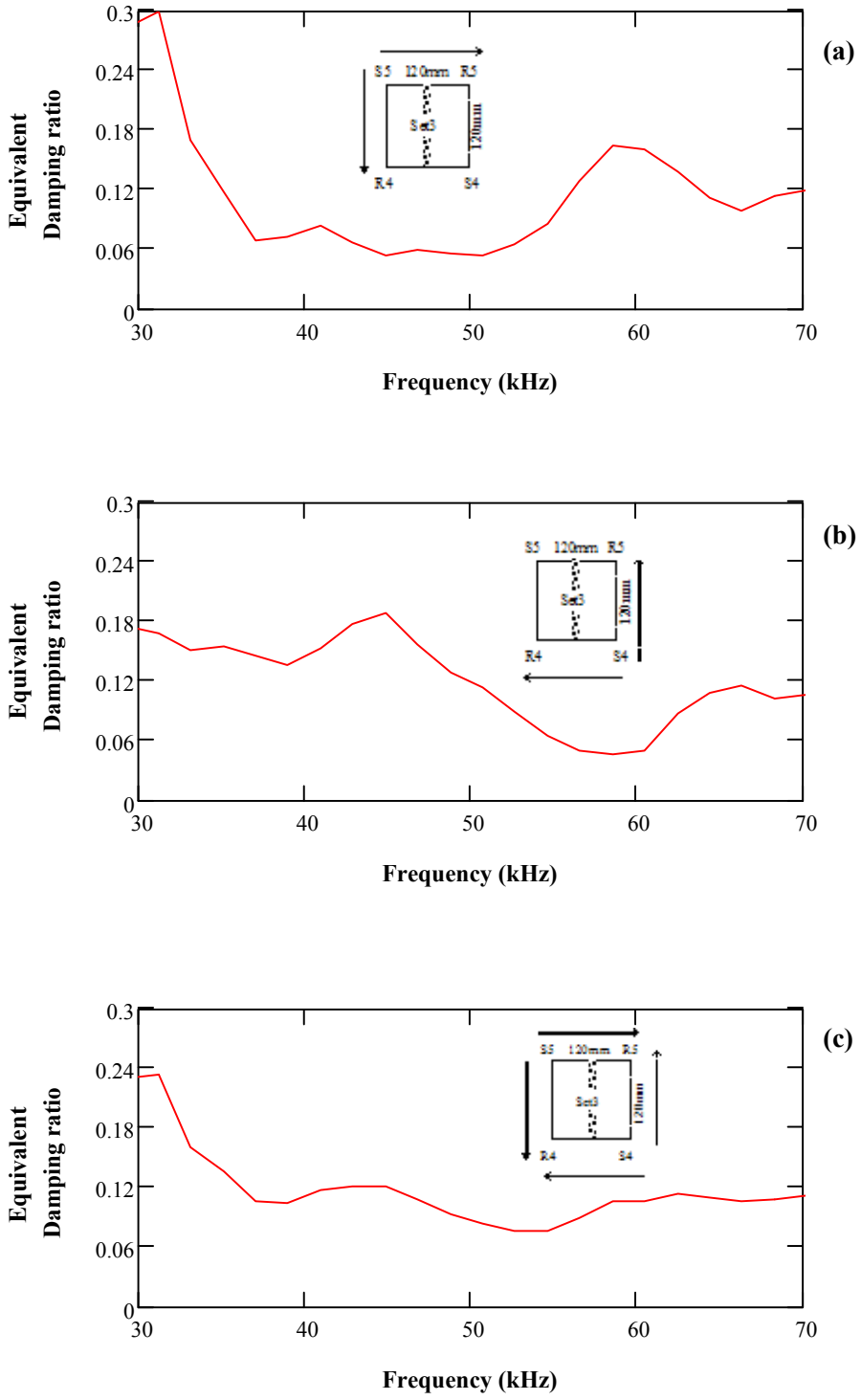

Figure U-12: Equivalent damping ratio (D) vs. frequency for full signals of repeated set 3 measurements (120mm S-R spacing) on the jointed surface - (a) D for Signal Pair 1 of set 3 (b) D for Signal Pair 2 of set 3 (c) D for entire set 3 measurements

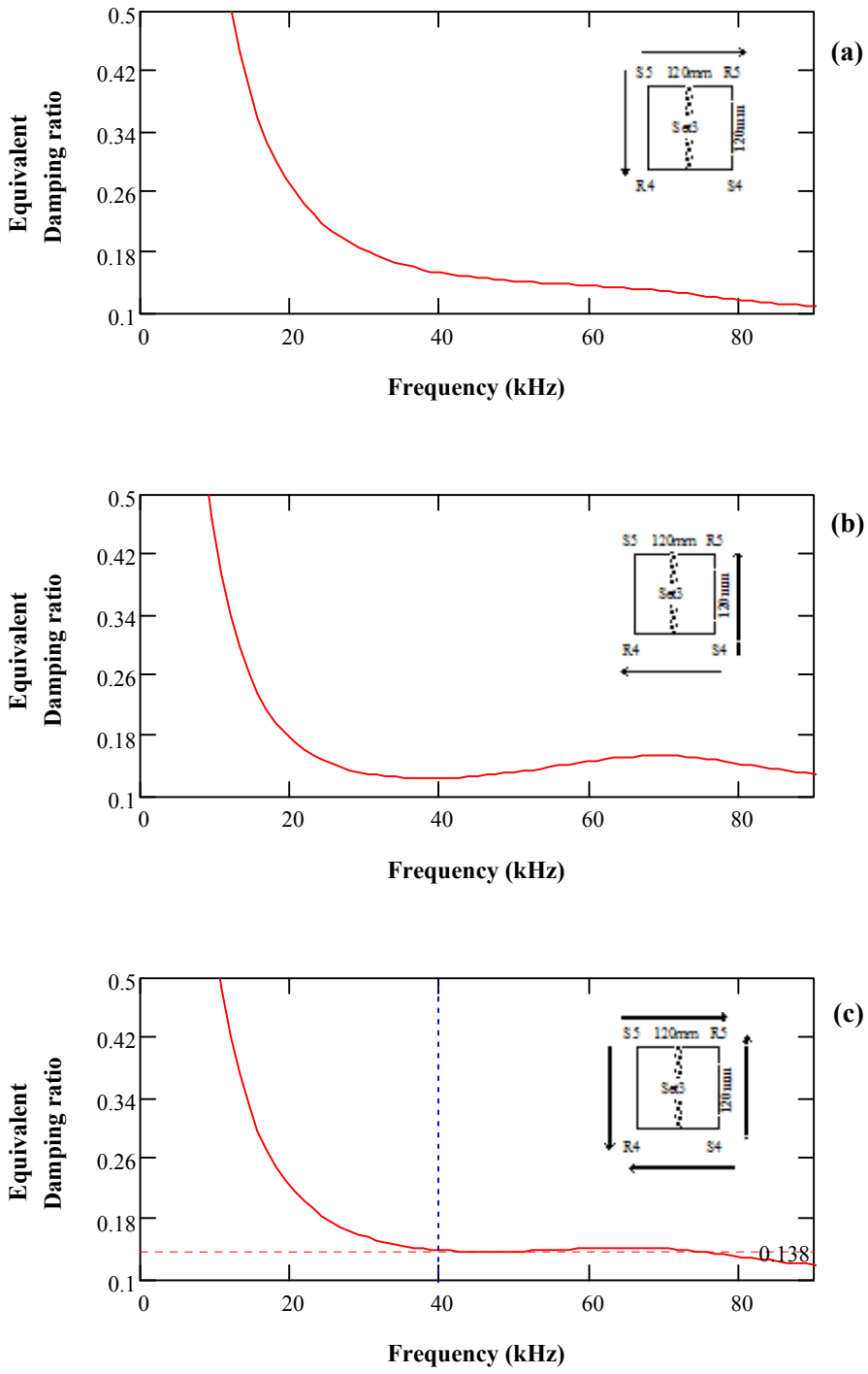

Figure U-13: Equivalent damping ratio (D) vs. frequency for P-wave for repeated set 3 measurements (120mm S-R spacing) on the jointed surface - (a) D for Signal Pair 1 of set 3 (b) D for Signal Pair 2 of set 3 (c) D for entire set 3 measurements

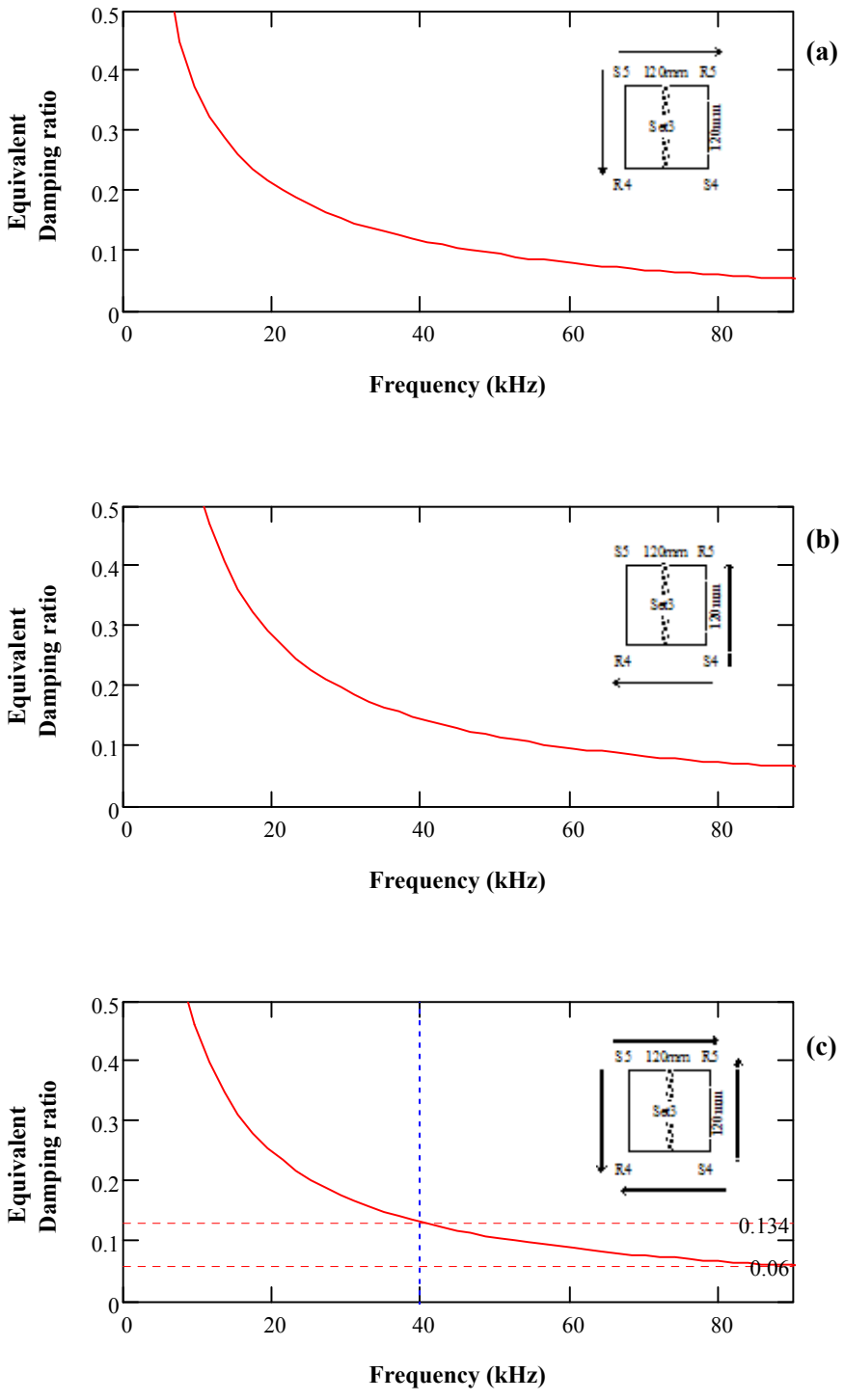

Figure U-14: Equivalent damping ratio (D) vs. frequency for R-wave for repeated set 3 measurements (120mm S-R spacing) on the jointed surface - (a) D for Signal Pair 1 of set 3 (b) D for Signal Pair 2 of set 3 (c) D for entire set 3 measurements

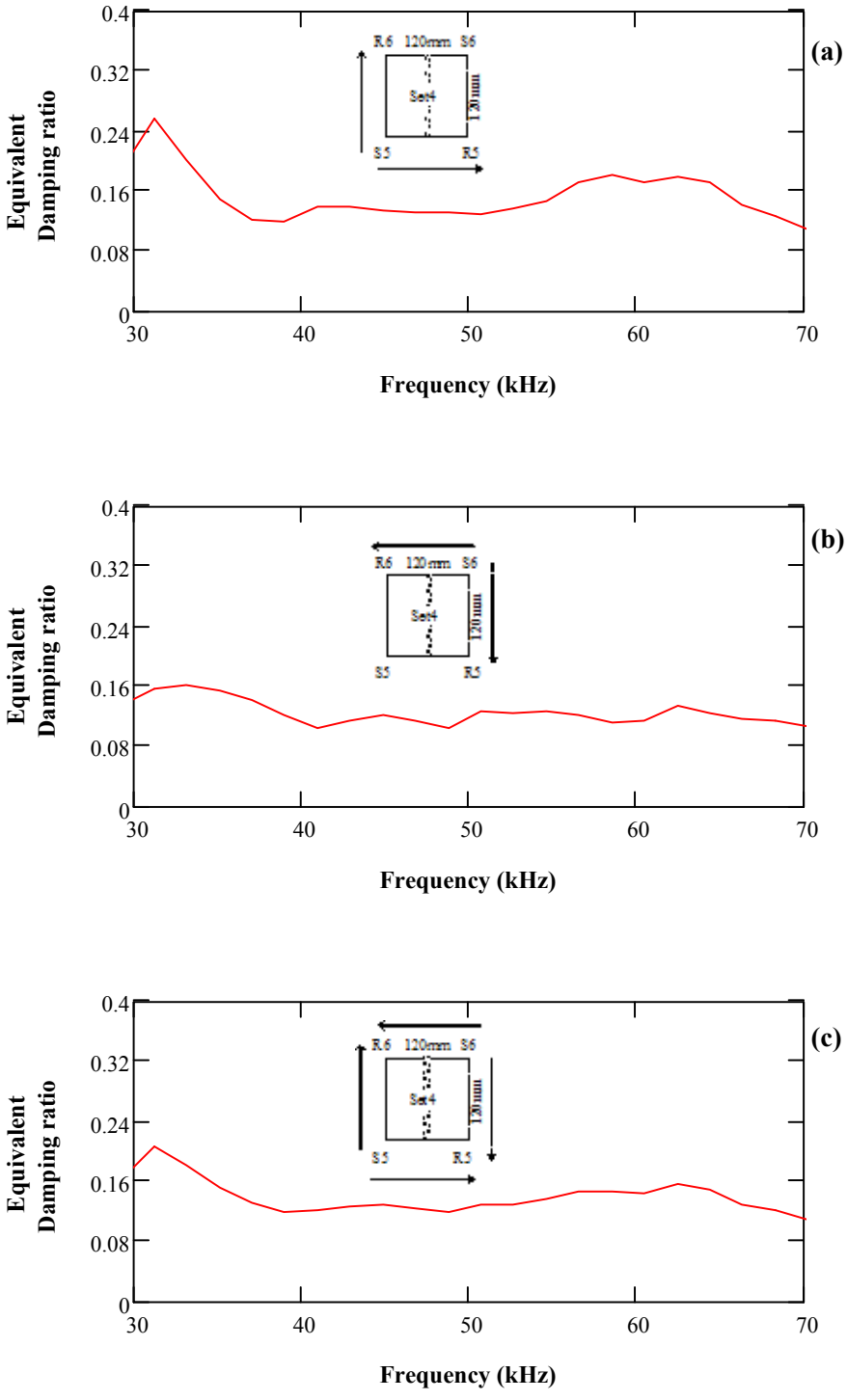

Figure U-15: Equivalent damping ratio (D) vs. frequency for full signals of set 4 measurements (120mm S-R spacing) on the jointed surface - (a) D for Signal Pair 1 of set 4 (b) D for Signal Pair 2 of set 4 (c) D for entire set 4 measurements

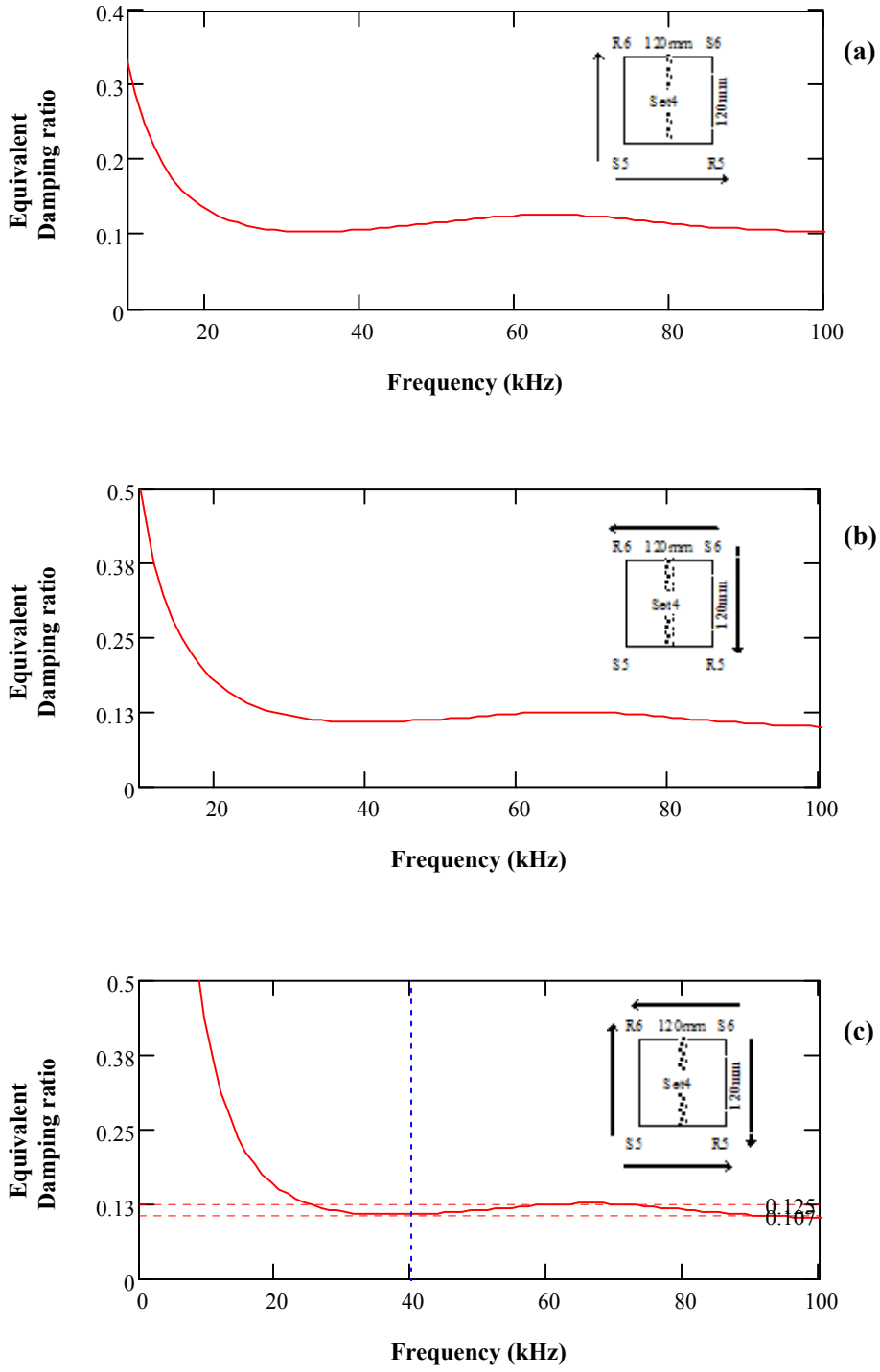

Figure U-16: Equivalent damping ratio (D) vs. frequency for P-waves for set 4 measurements (120mm S-R spacing) on the jointed surface - (a) D for Signal Pair 1 of set 4 (b) D for Signal Pair 2 of set 4 (c) D for entire set 4 measurements

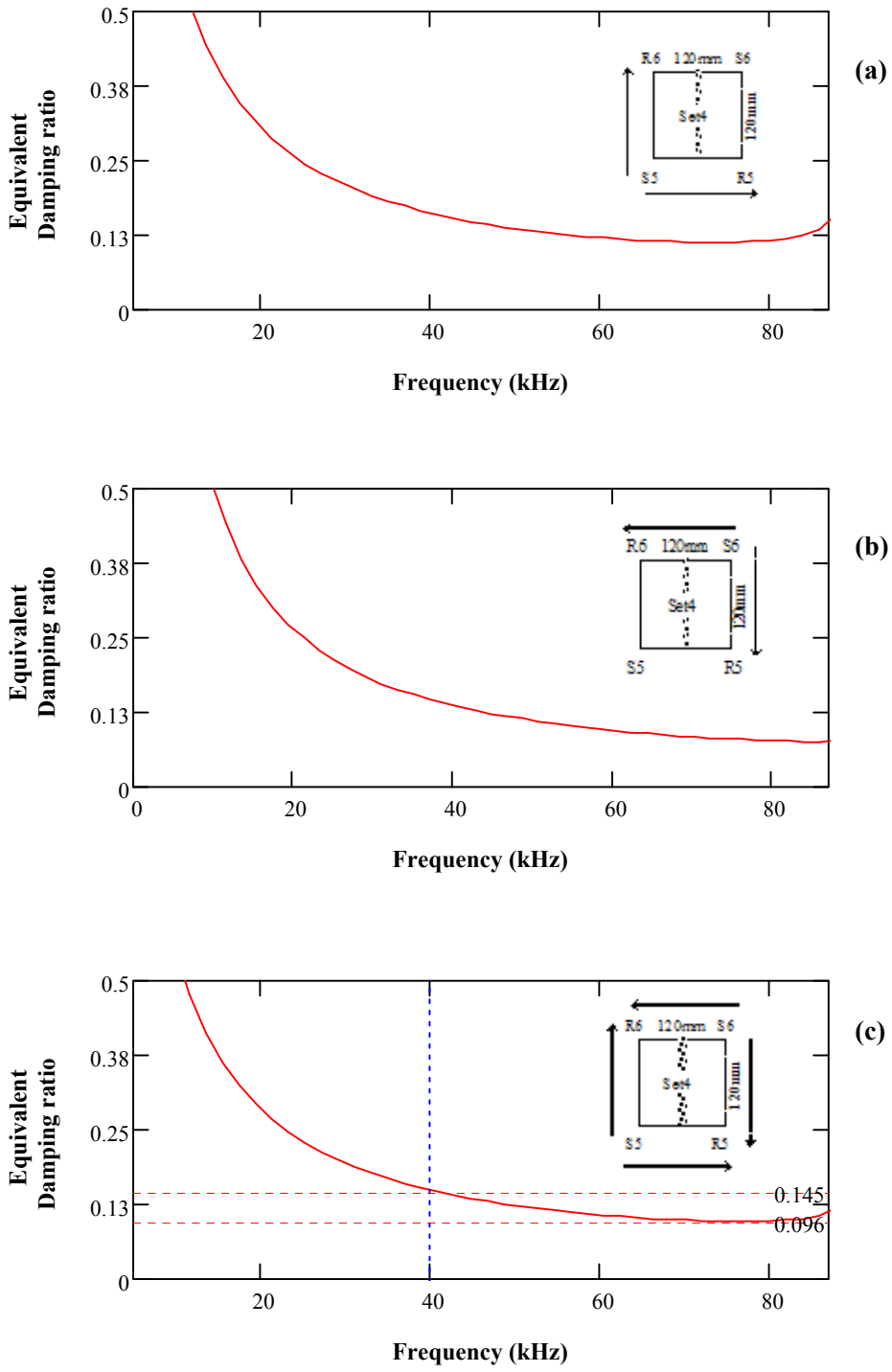

Figure U-17: Equivalent damping ratio (D) vs. frequency for R-waves for set 4 measurements (120mm S-R spacing) on the jointed surface - (a) D for Signal Pair 1 of set 4 (b) D for Signal Pair 2 of set 4 (c) D for entire set 4 measurements

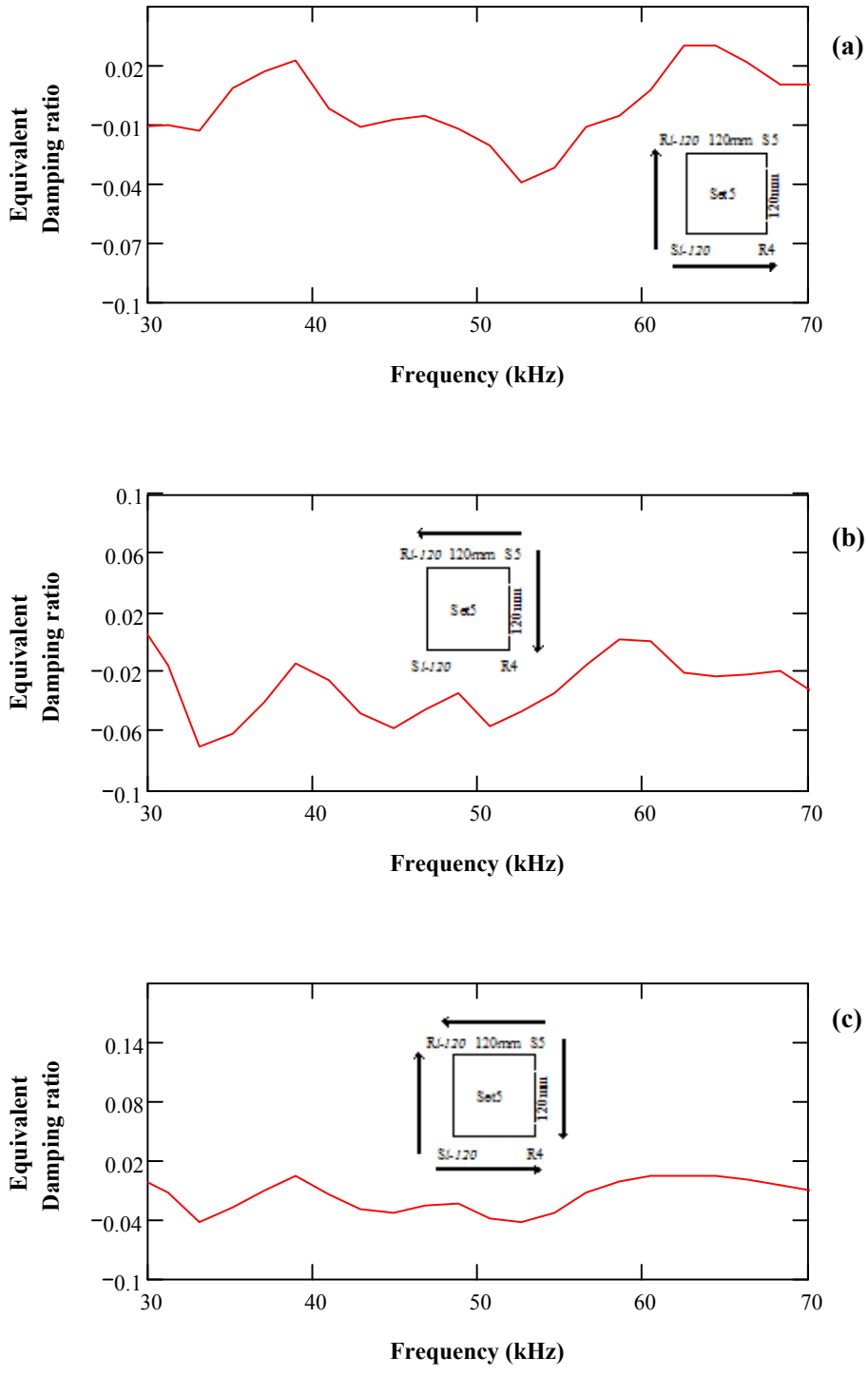

Figure U-18: Equivalent damping ratio (D) vs. frequency for full signals of set 5 measurements (120mm S-R spacing) on the joint-free surface - (a) D for Signal Pair 1 of set 5 (b) D for Signal Pair 2 of set 5 (c) D for entire set 5 measurements

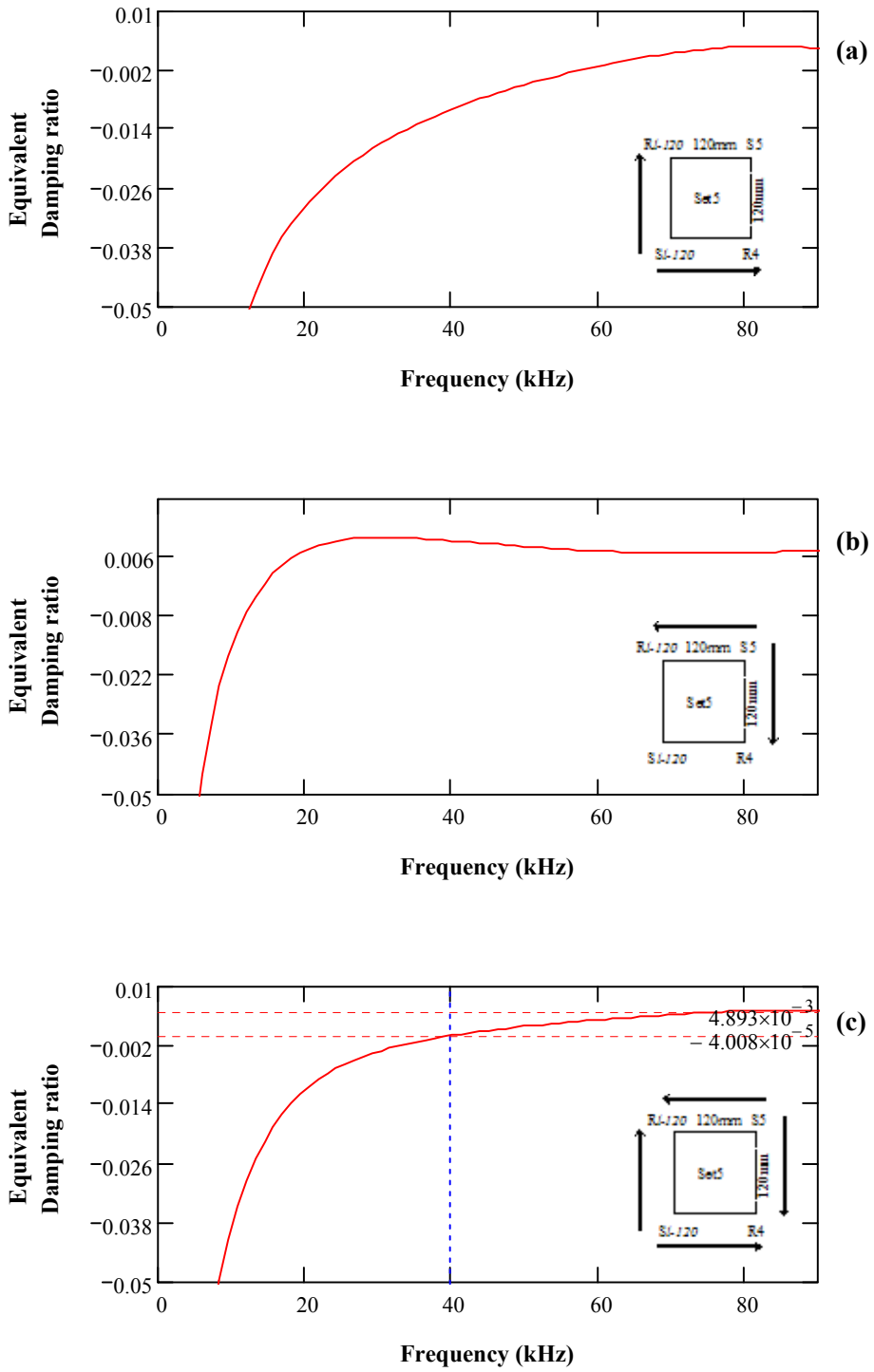

Figure U-19: Equivalent damping ratio (D) vs. frequency for P-waves for set 5 measurements (120mm S-R spacing) on the joint-free surface - (a) D for Signal Pair 1 of set 5 (b) D for Signal Pair 2 of set 5 (c) D for entire set 5 measurements

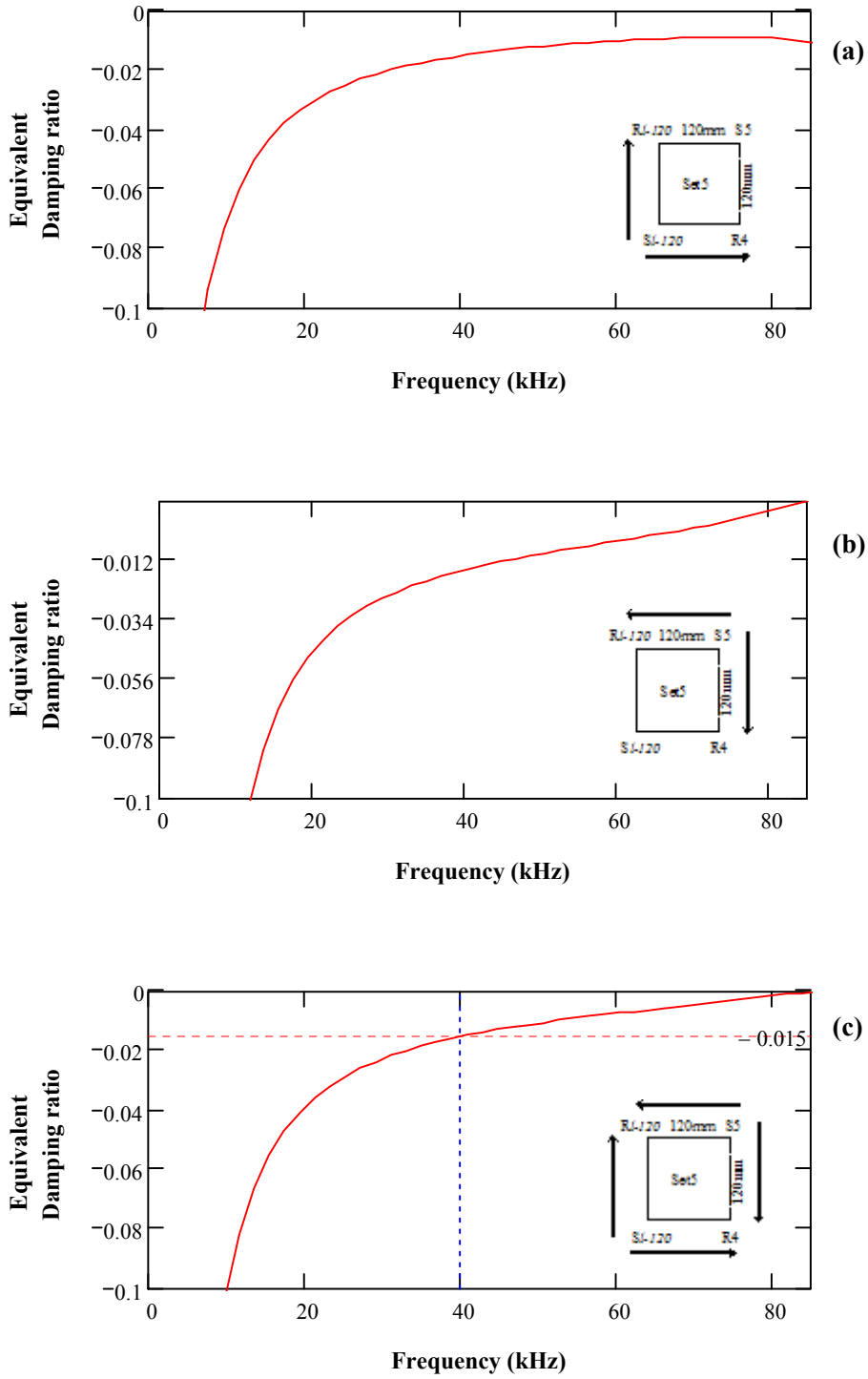

Figure U-20: Equivalent damping ratio (D) vs. frequency for R-waves for set 5 measurements (120mm S-R spacing) on the joint-free surface - (a) D for Signal Pair 1 of set 5 (b) D for Signal Pair 2 of set 5 (c) D for entire set 5 measurements

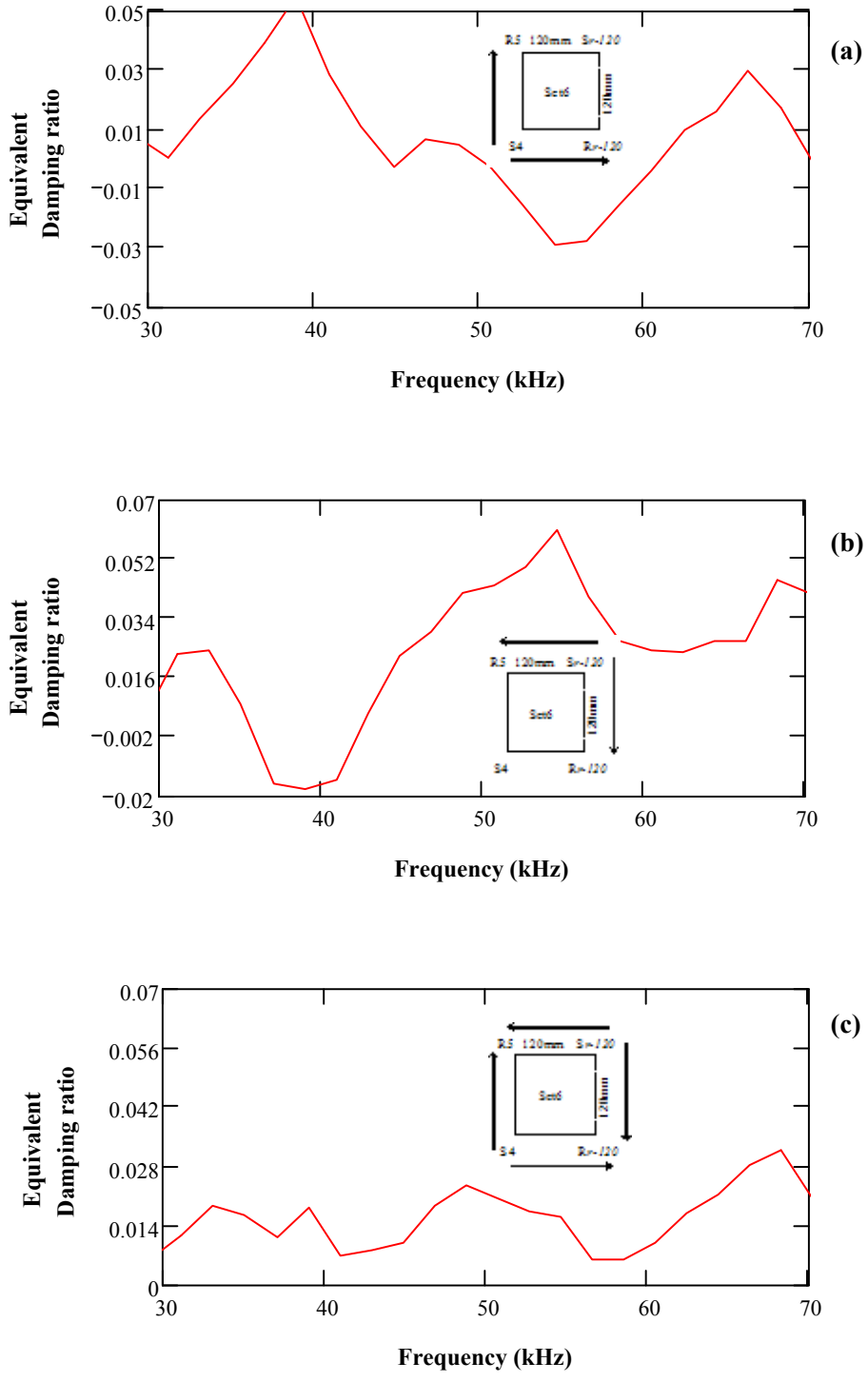

Figure U-21: Equivalent damping ratio (D) vs. frequency for full signals of set 6 measurements (120mm S-R spacing) on the joint-free surface - (a) D for Signal Pair 1 of set 6 (b) D for Signal Pair 2 of set 6 (c) D for entire set 6 measurements

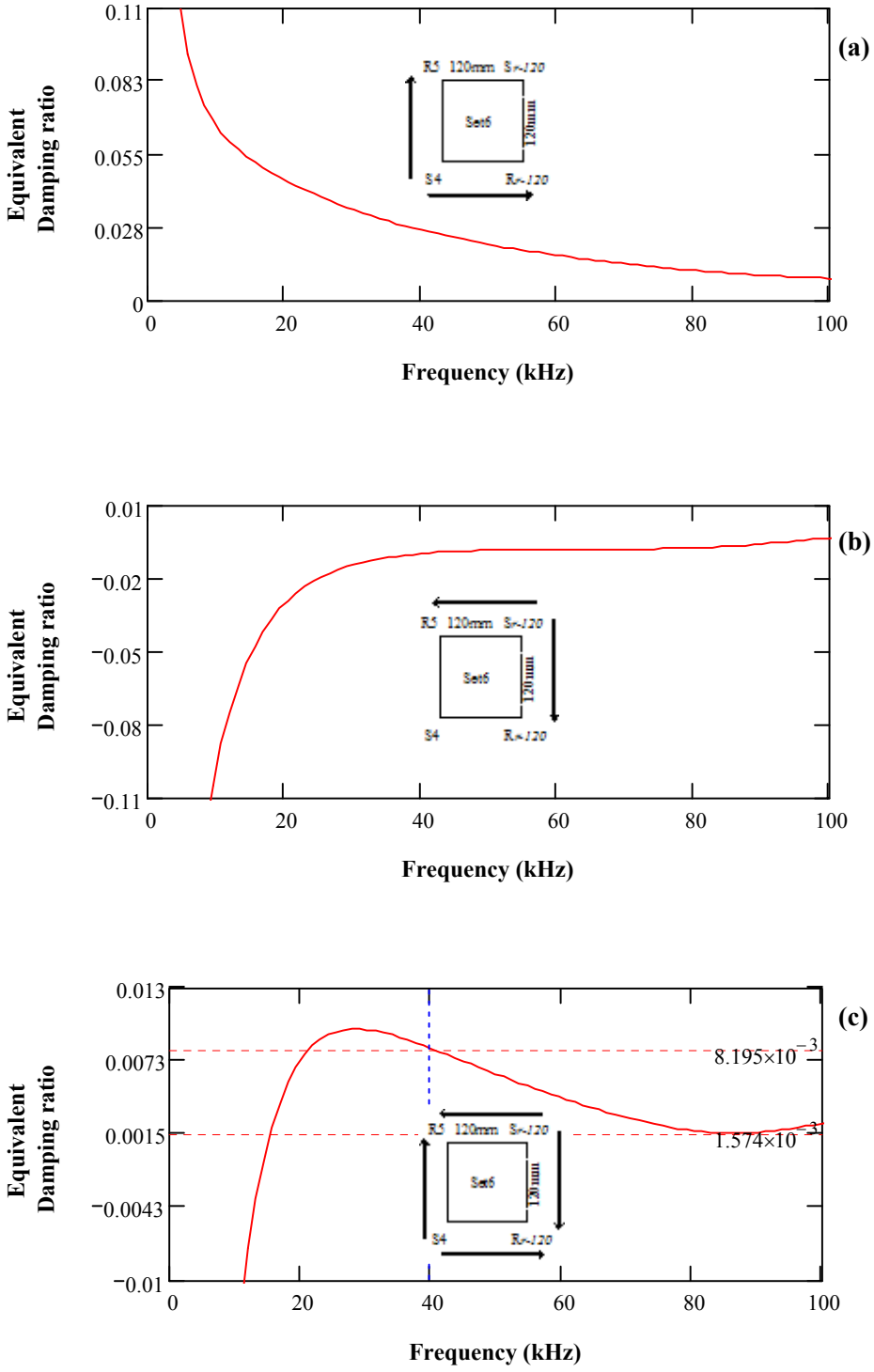

Figure U-22: Equivalent damping ratio (D) vs. frequency for P-waves for set 6 measurements (120mm S-R spacing) on the joint-free surface - (a) D for Signal Pair 1 of set 6 (b) D for Signal Pair 2 of set 6 (c) D for entire set 6 measurements

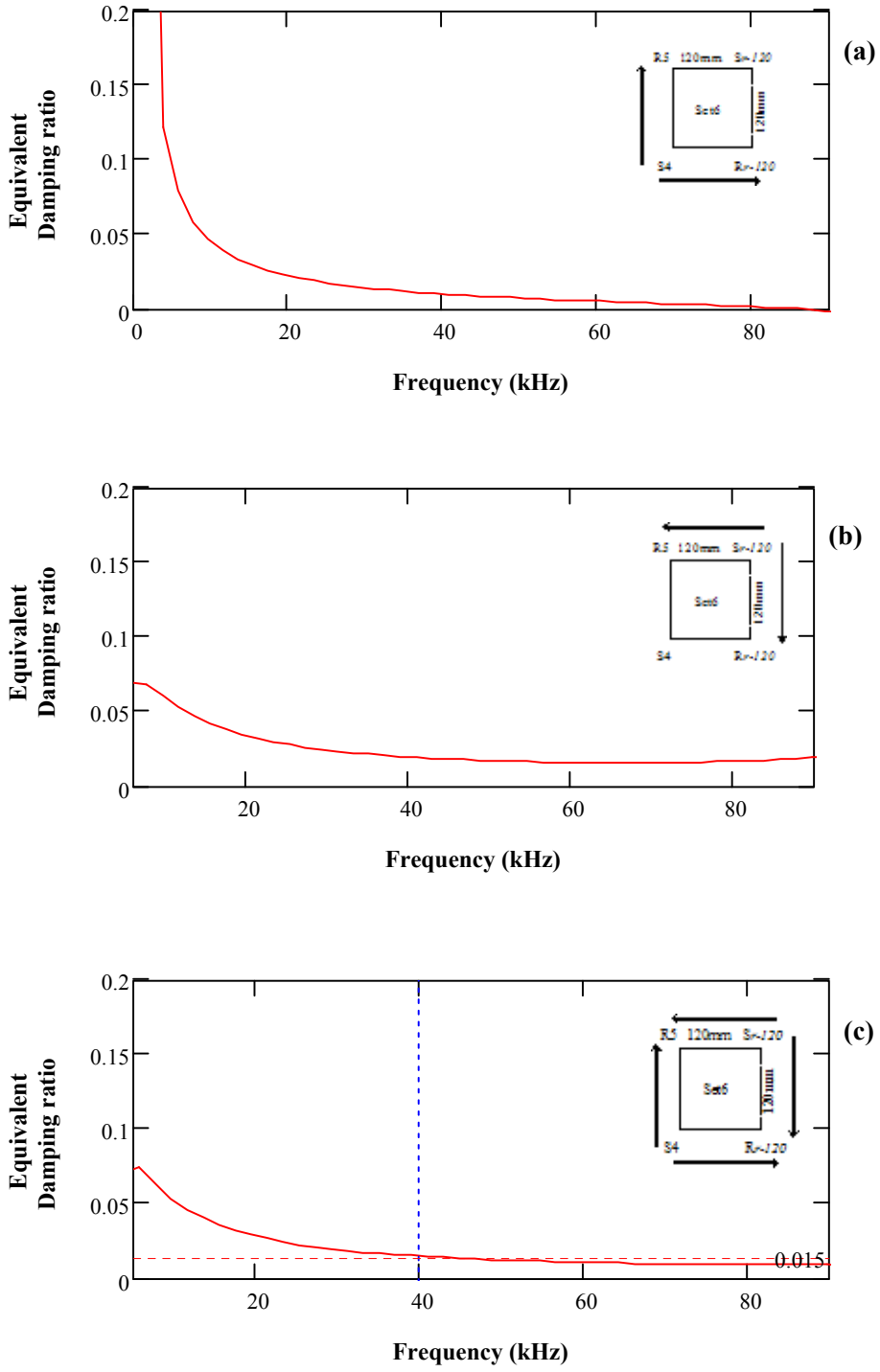

Figure U-23: Equivalent damping ratio (D) vs. frequency for R-waves for set 6 measurements (120mm S-R spacing) on the joint-free surface - (a) D for Signal Pair 1 of set 6 (b) D for Signal Pair 2 of set 6 (c) D for entire set 6 measurements

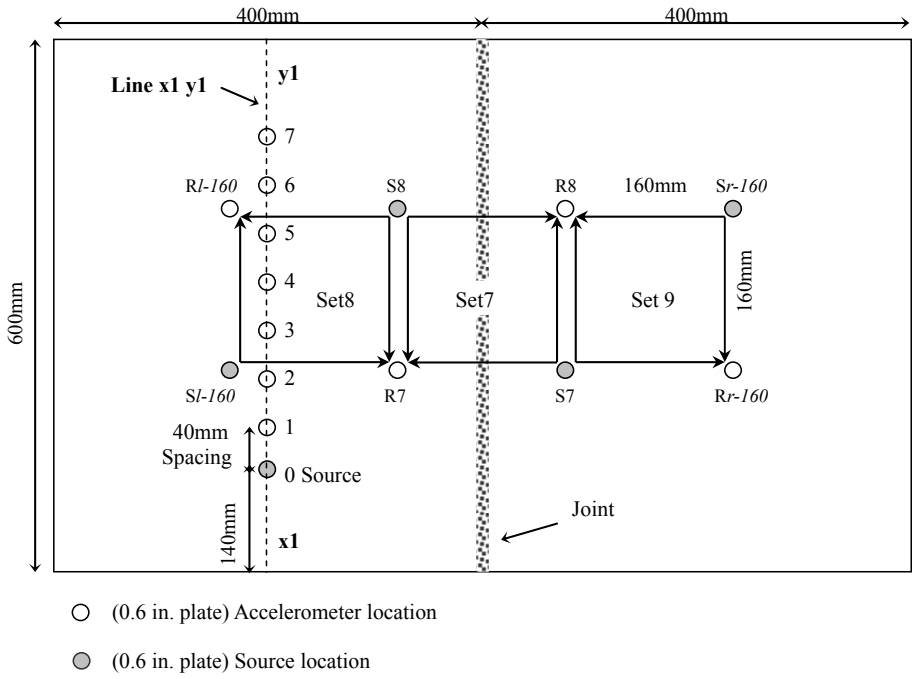

Figure U-24: 160mm S-R spacing configuration of HMA slab 3

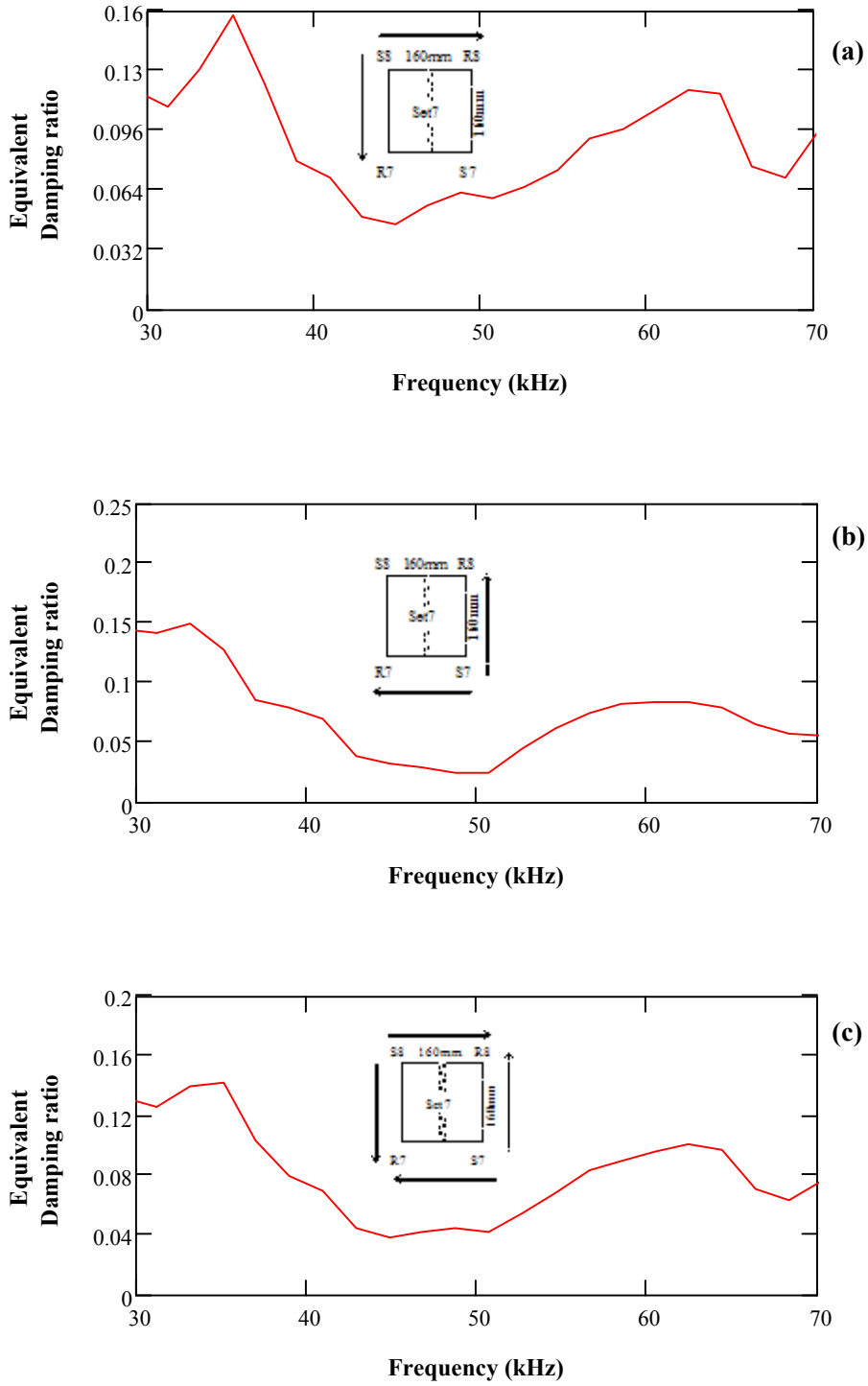

Figure U-25: Equivalent damping ratio (D) vs. frequency for full signals of set 7 measurements (160mm S-R spacing) on the jointed surface - (a) D for Signal Pair 1 of set 7 (b) D for Signal Pair 2 of set 7 (c) D for entire set 7 measurements

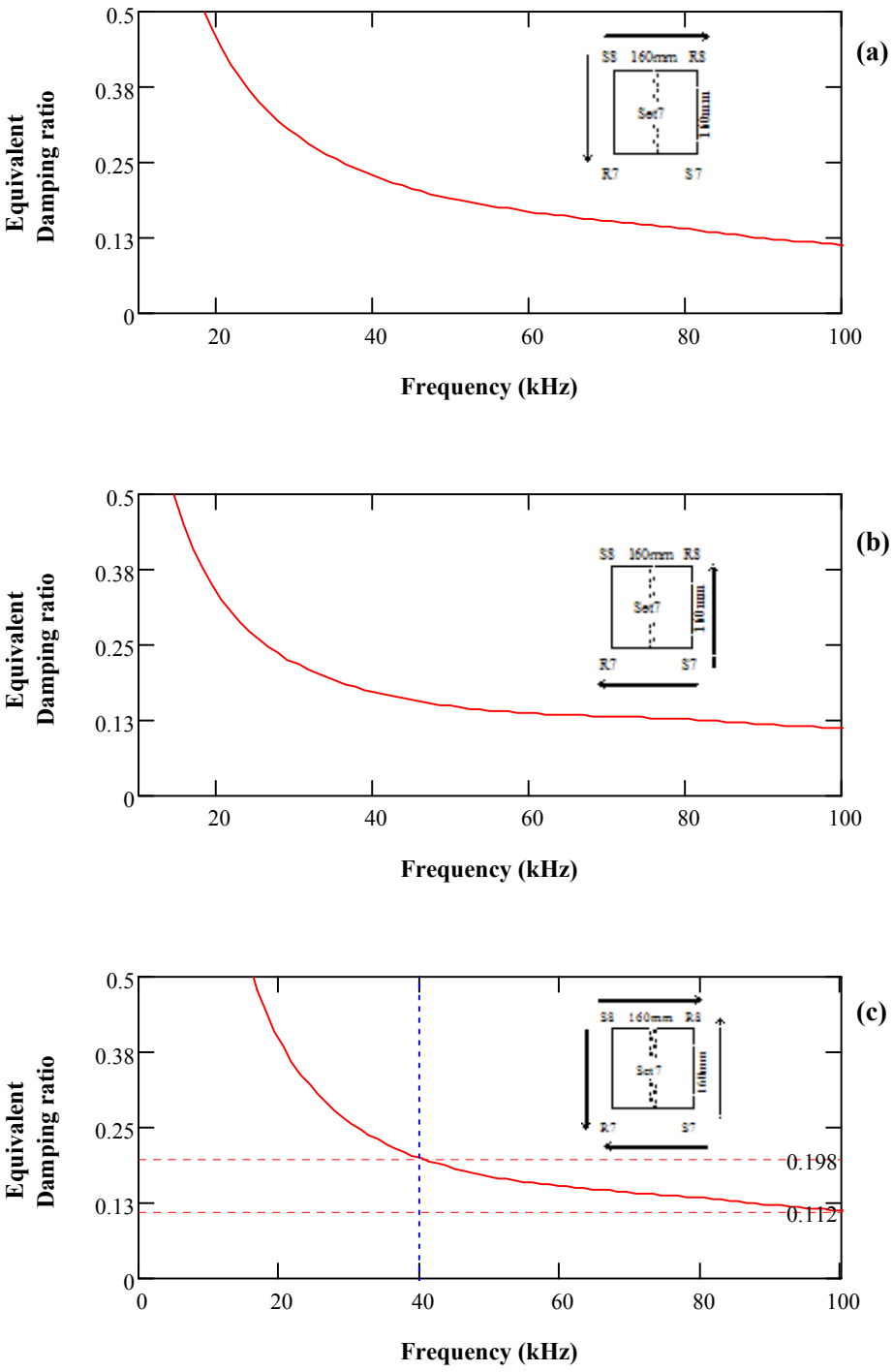

Figure U-26: Equivalent damping ratio (D) vs. frequency for P-waves for set 7 measurements (160mm S-R spacing) on the jointed surface - (a) D for Signal Pair 1 of set 7 (b) D for Signal Pair 2 of set 7 (c) D for entire set 7 measurements

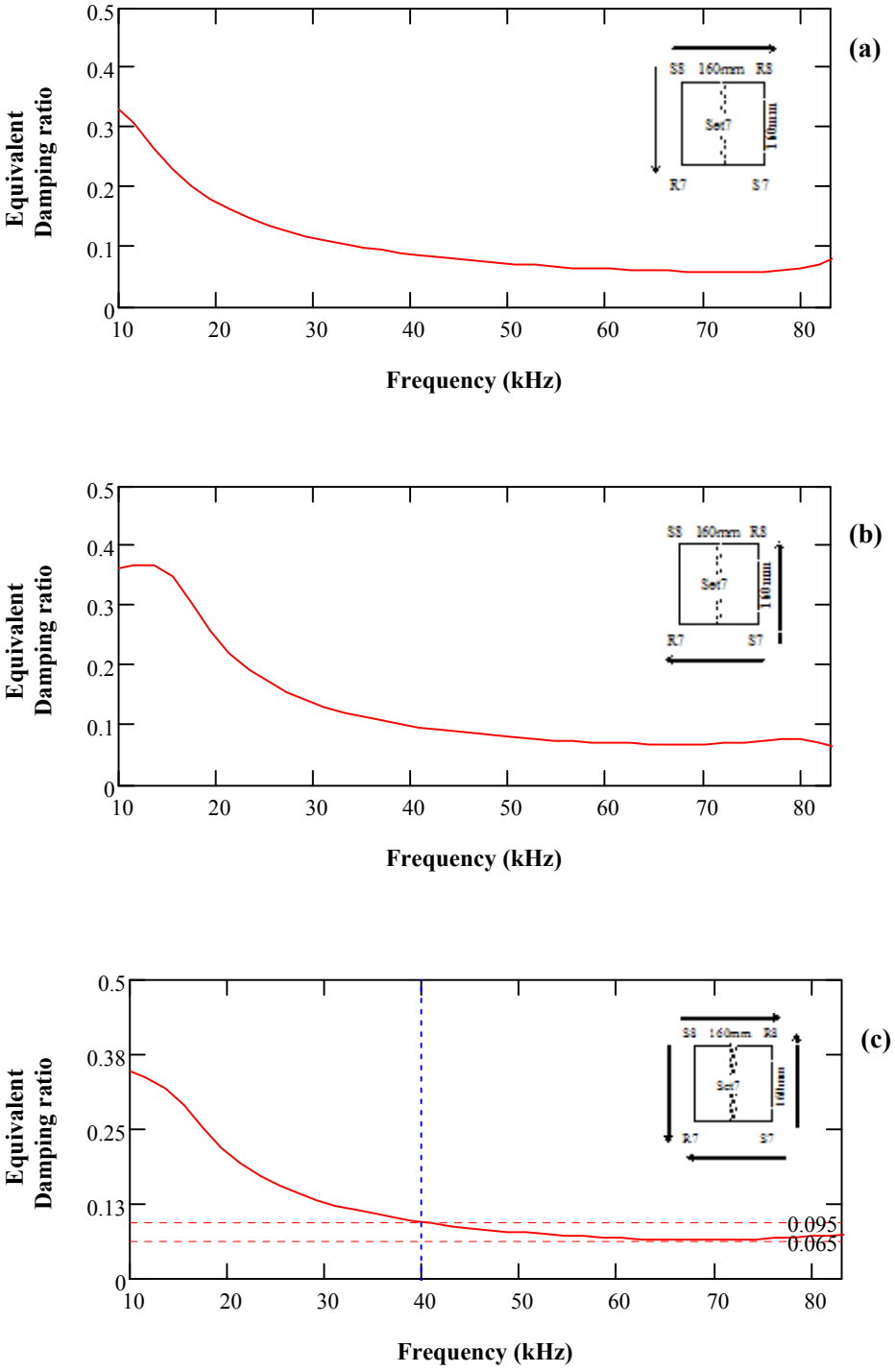

Figure U-27: Equivalent damping ratio (D) vs. frequency for R-waves for set 7 measurements (160mm S-R spacing) on the jointed surface - (a) D for Signal Pair 1 of set 7 (b) D for Signal Pair 2 of set 7 (c) D for entire set 7 measurements

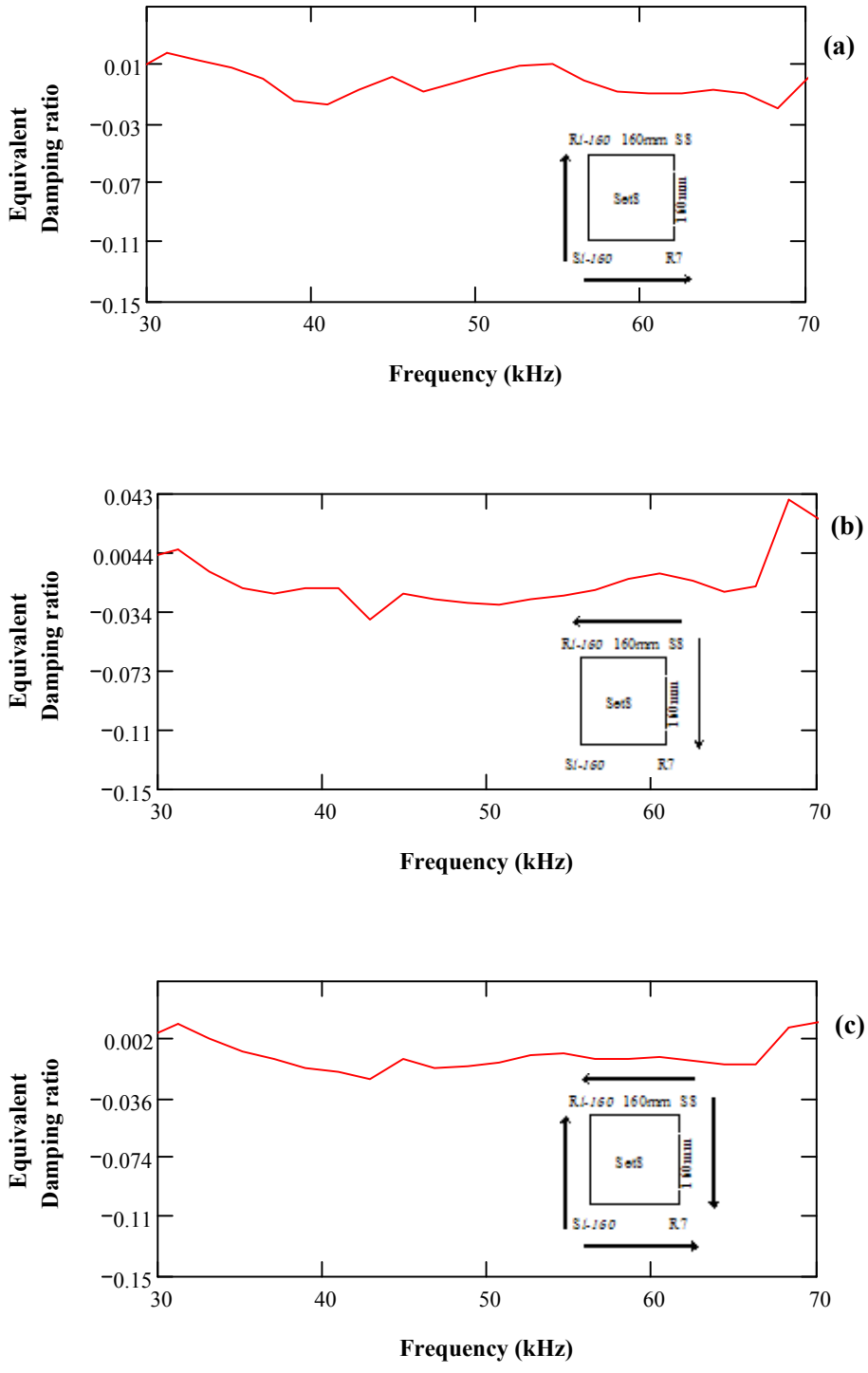

Figure U-28: Equivalent damping ratio (D) vs. frequency for full signals of set 8 measurements (160mm S-R spacing) on the joint-free surface - (a) D for Signal Pair 1 of set 8 (b) D for Signal Pair 2 of set 8 (c) D for entire set 8 measurements

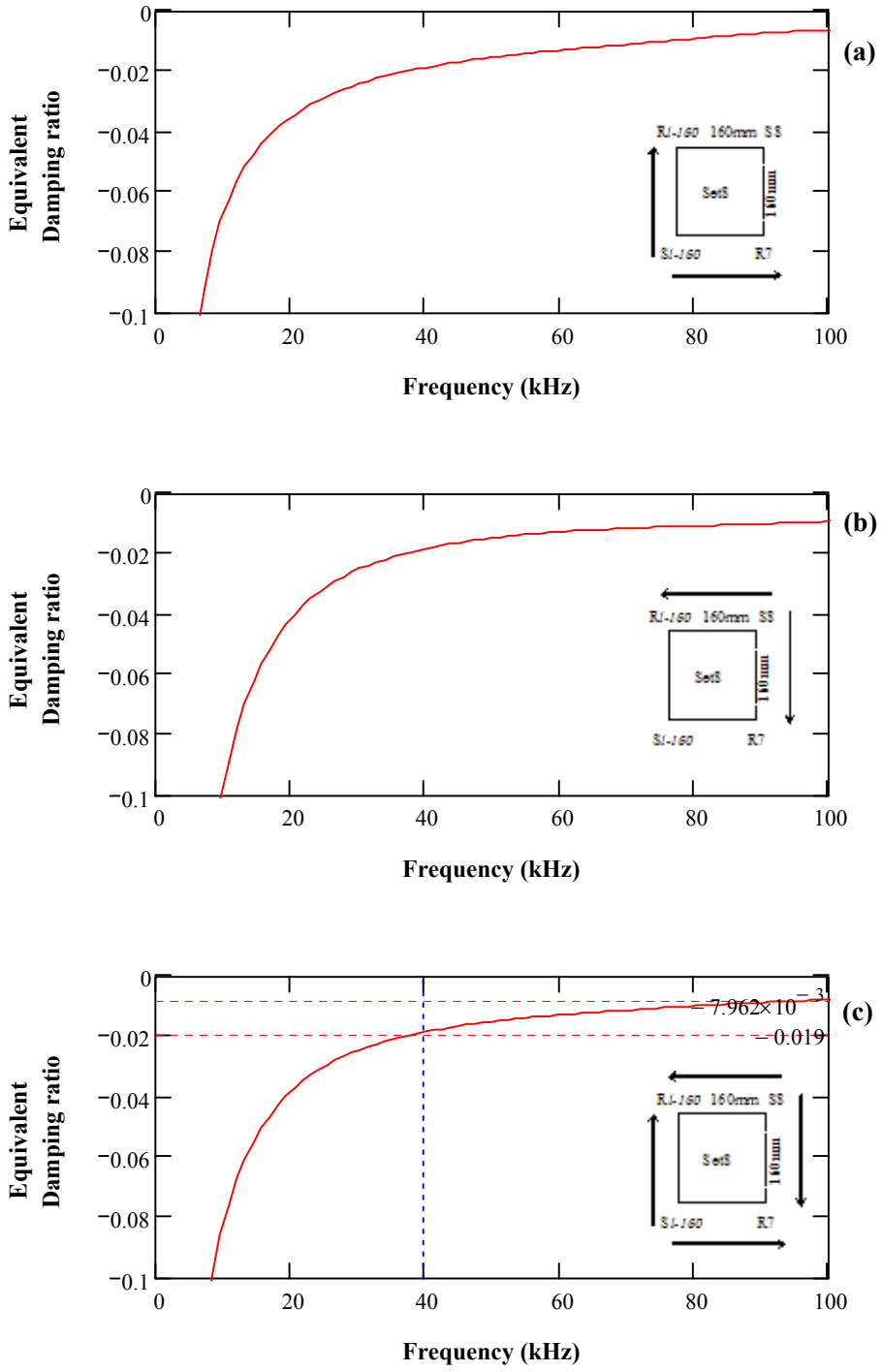

Figure U-29: Equivalent damping ratio (D) vs. frequency for P-waves for set 8 measurements (160mm S-R spacing) on the joint-free surface - (a) D for Signal Pair 1 of set 8 (b) D for Signal Pair 2 of set 8 (c) D for entire set 8 measurements

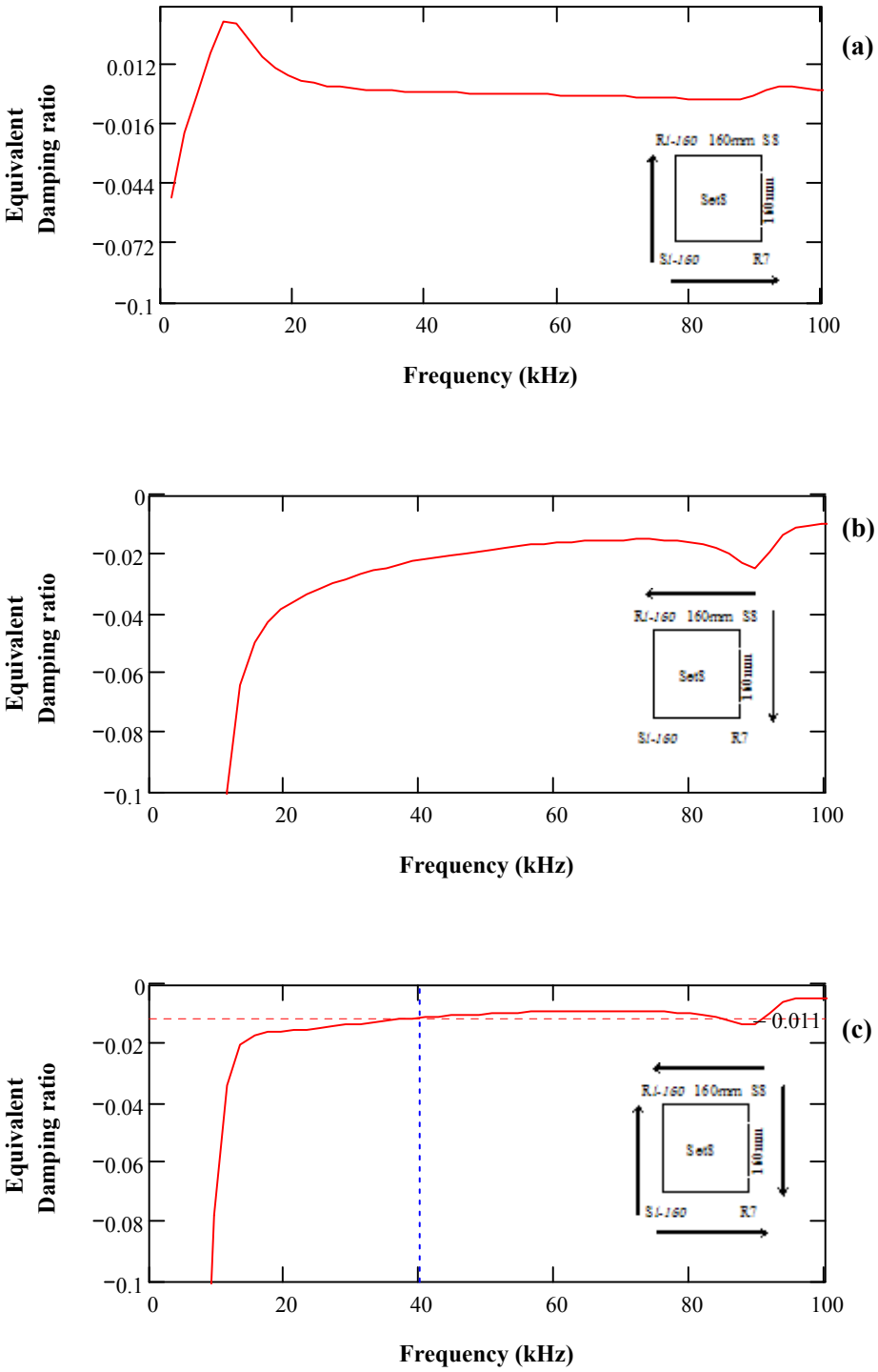

Figure U-30: Equivalent damping ratio (D) vs. frequency for R-waves for set 8 measurements (160mm S-R spacing) on the joint-free surface - (a) D for Signal Pair 1 of set 8 (b) D for Signal Pair 2 of set 8 (c) D for entire set 8 measurements

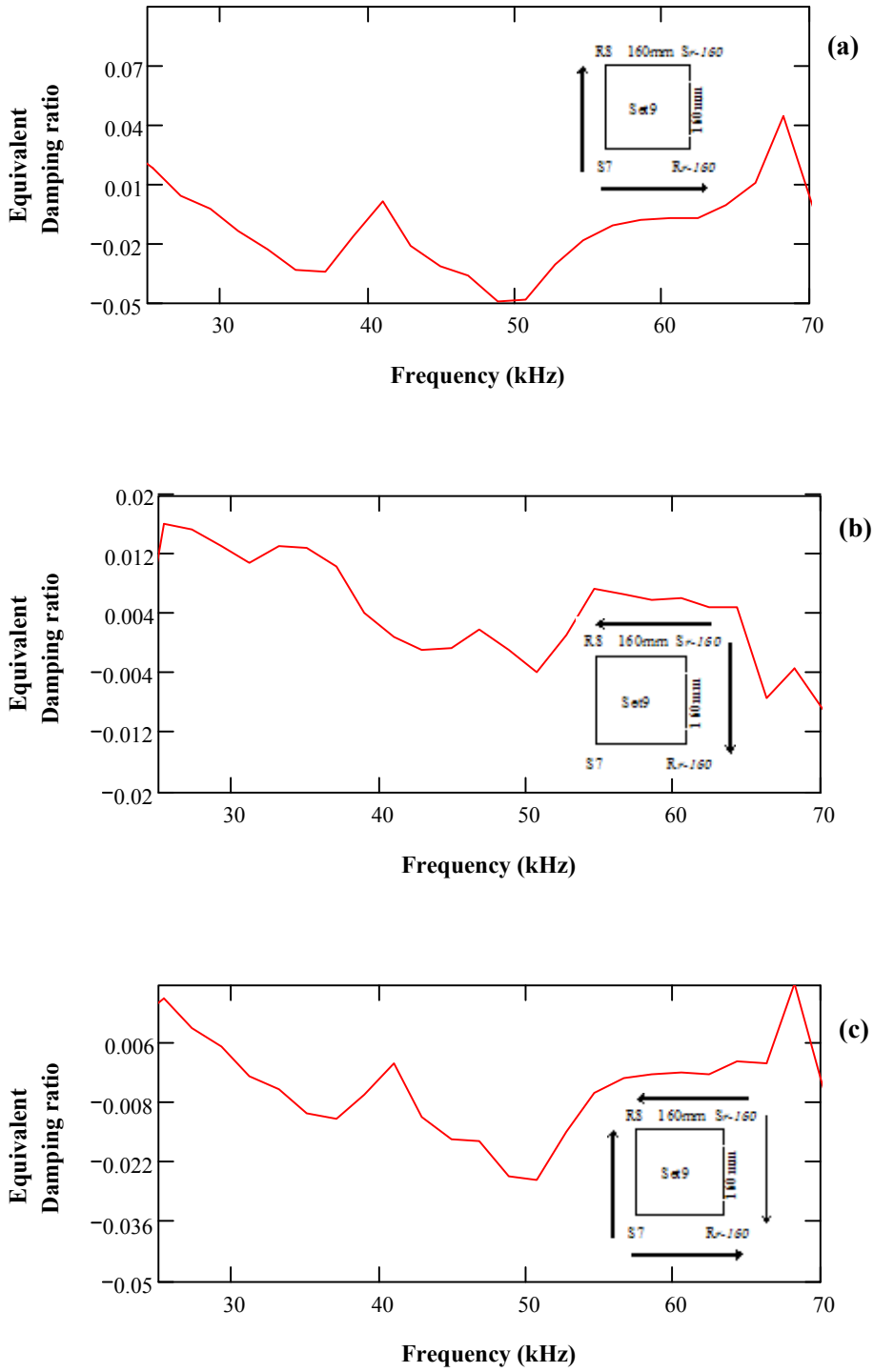

Figure U-31: Equivalent damping ratio (D) vs. frequency for full signals of set 9 measurements (160mm S-R spacing) on the joint-free surface - (a) D for Signal Pair 1 of set 9 (b) D for Signal Pair 2 of set 9 (c) D for entire set 9 measurements

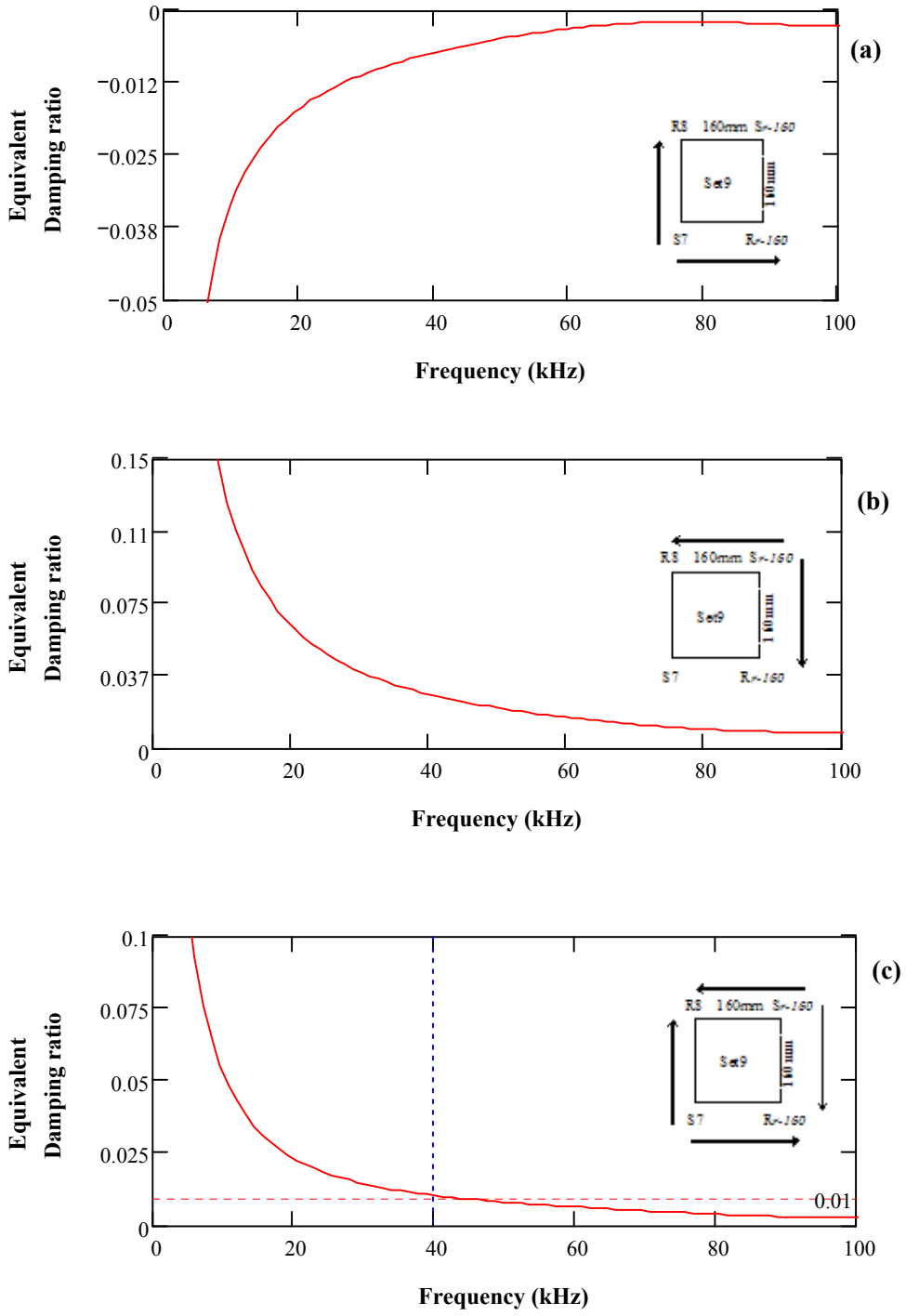

Figure U-32: Equivalent damping ratio (D) vs. frequency for P-waves for set 9 measurements (160mm S-R spacing) on the joint-free surface - (a) D for Signal Pair 1 of set 9 (b) D for Signal Pair 2 of set 9 (c) D for entire set 9 measurements

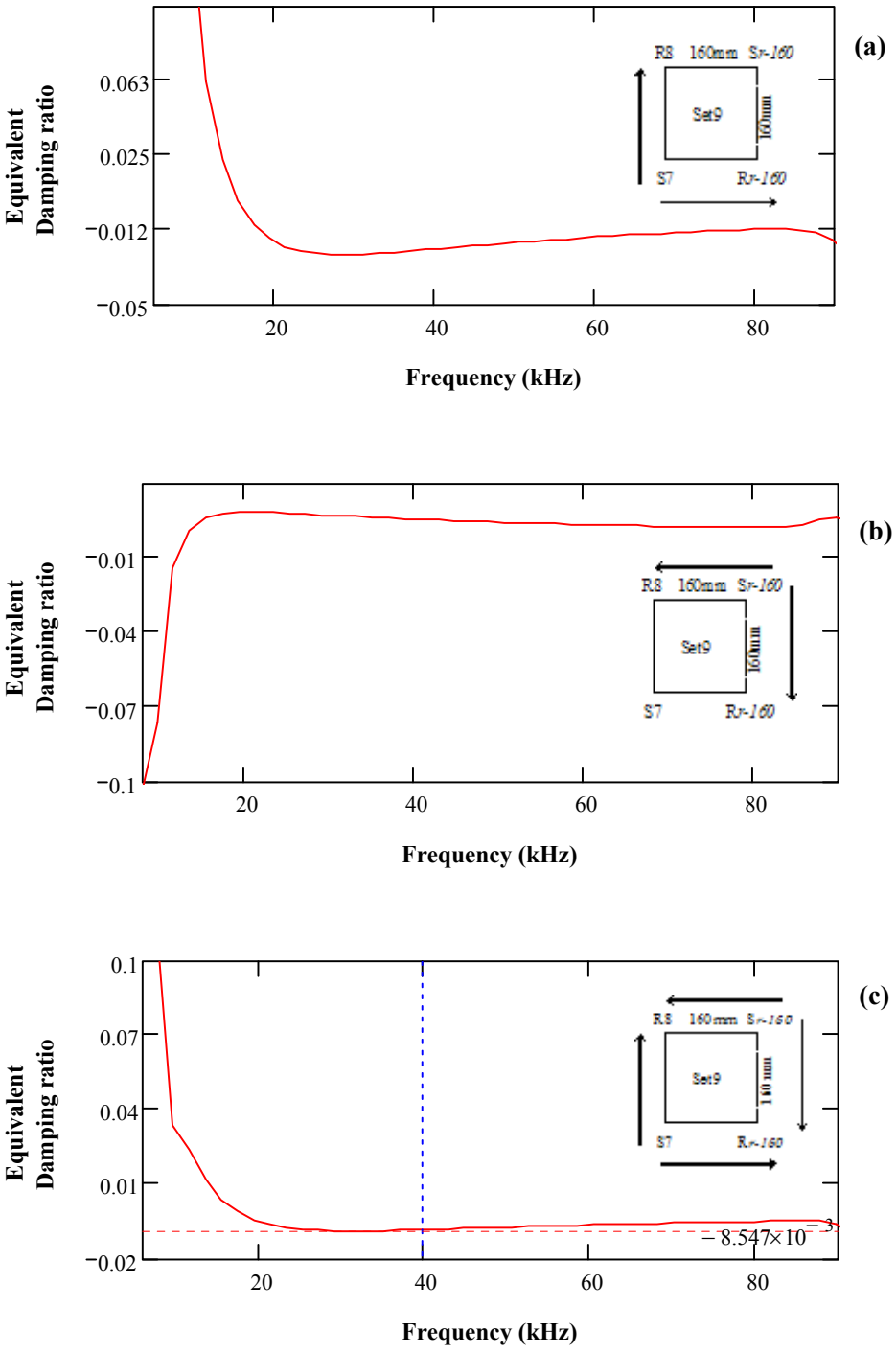

Figure U-33: Equivalent damping ratio (D) vs. frequency for R-waves for set 9 measurements (160mm S-R spacing) on the joint-free surface - (a) D for Signal Pair 1 of set 9 (b) D for Signal Pair 2 of set 9 (c) D for entire set 9 measurements

Appendix V

Signal Processing for Slab 3

- Measurements along Line x1-y1

This appendix is a PDF file available in the Appendix CD.

The file name of this PDF file is “Appendix V – Signal processing for Line x1-y1.pdf”.

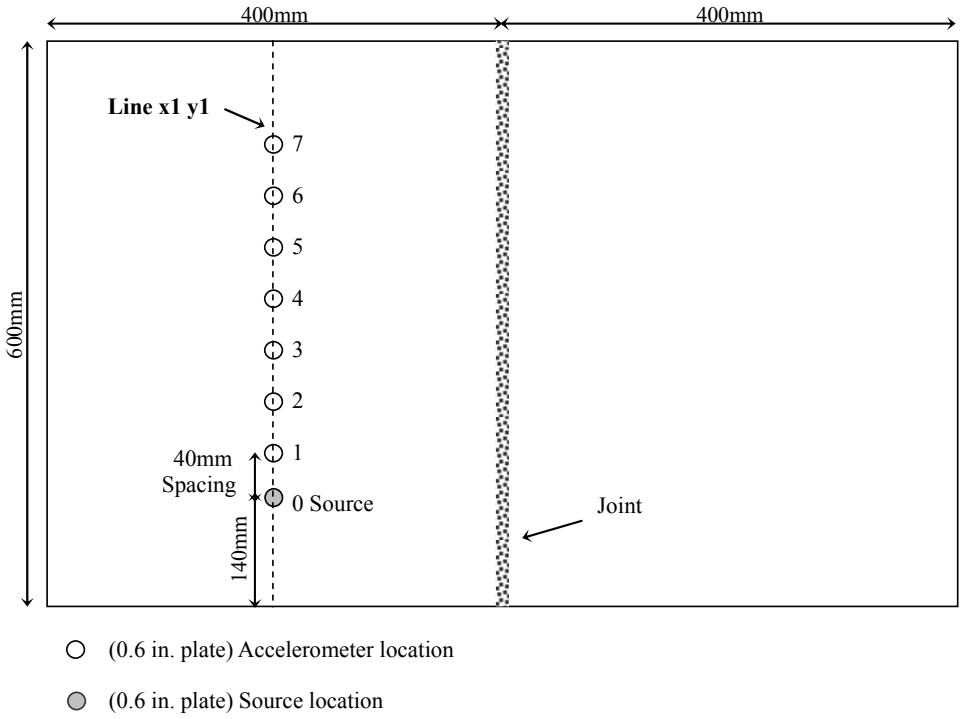

Figure V-1: Testing configuration of Line x1 y1 in HMA slab 3

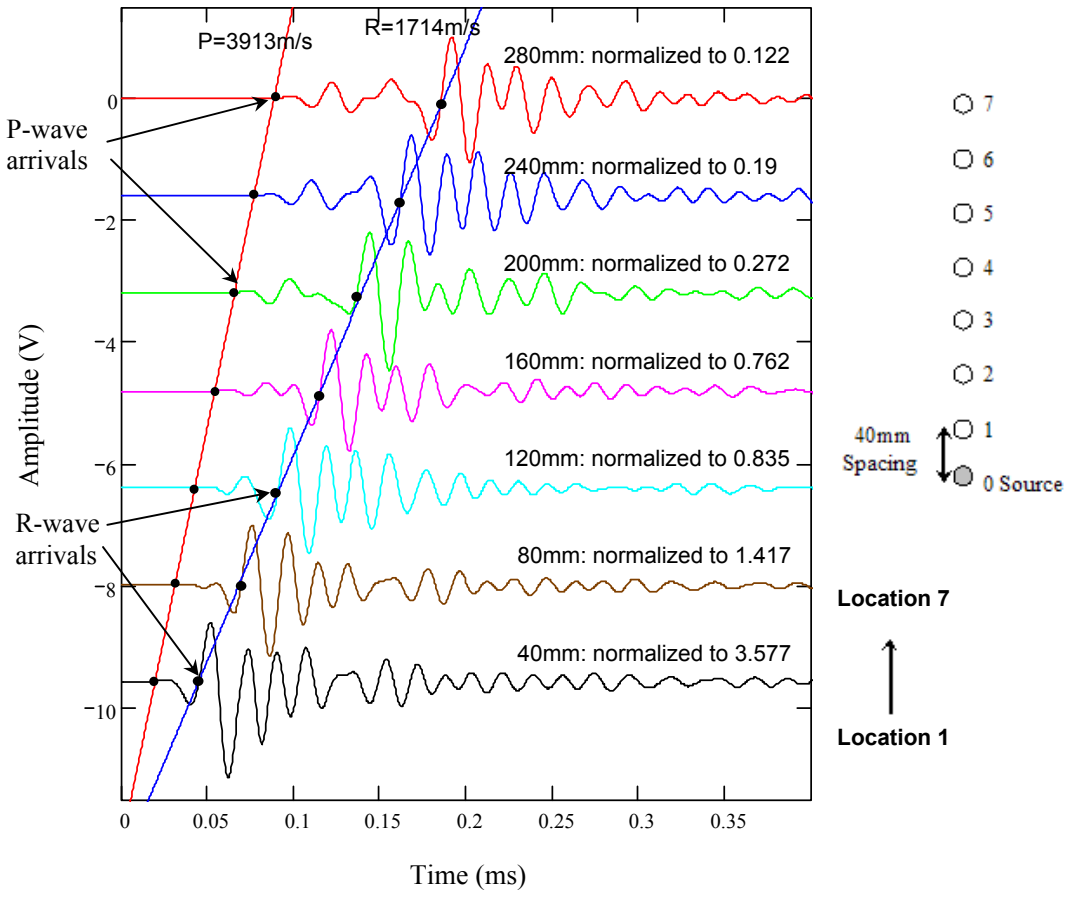

Figure V-2: Signals received using 50 kHz accelerometer along Line x1 y1

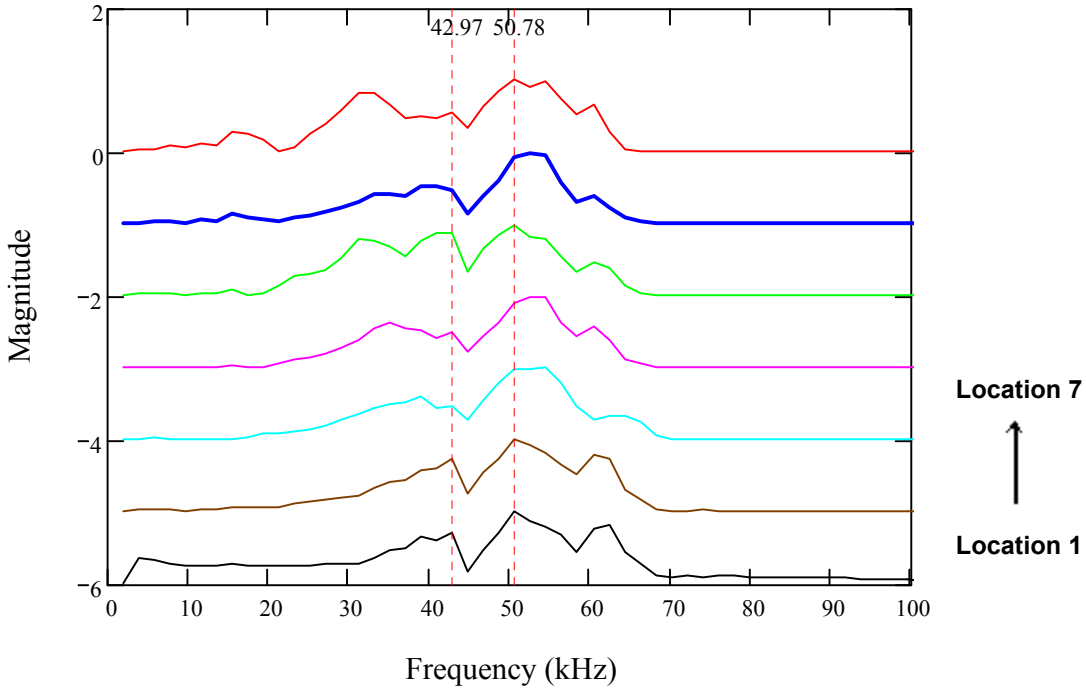

Figure V-3: Frequency spectra of signals received using 50 kHz accelerometer along Line x1 y1

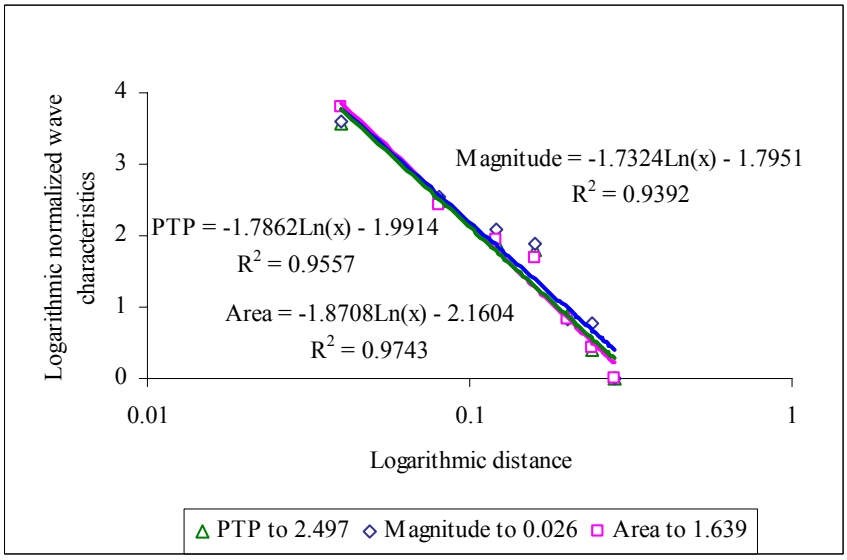

Figure V-4: Geometric attenuation evaluation based on full signals

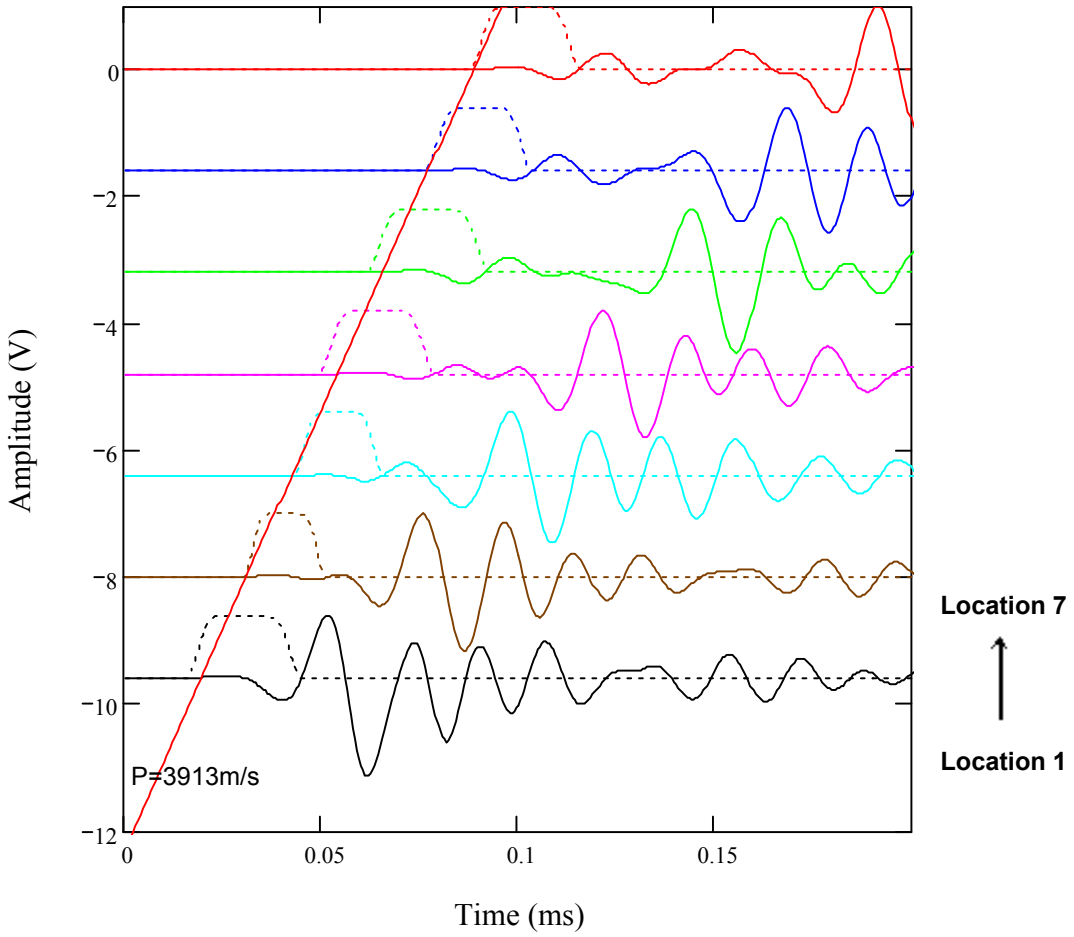

Figure V-5: Windowing P-waves of the signals received using 50 kHz accelerometer along Line x1 y1

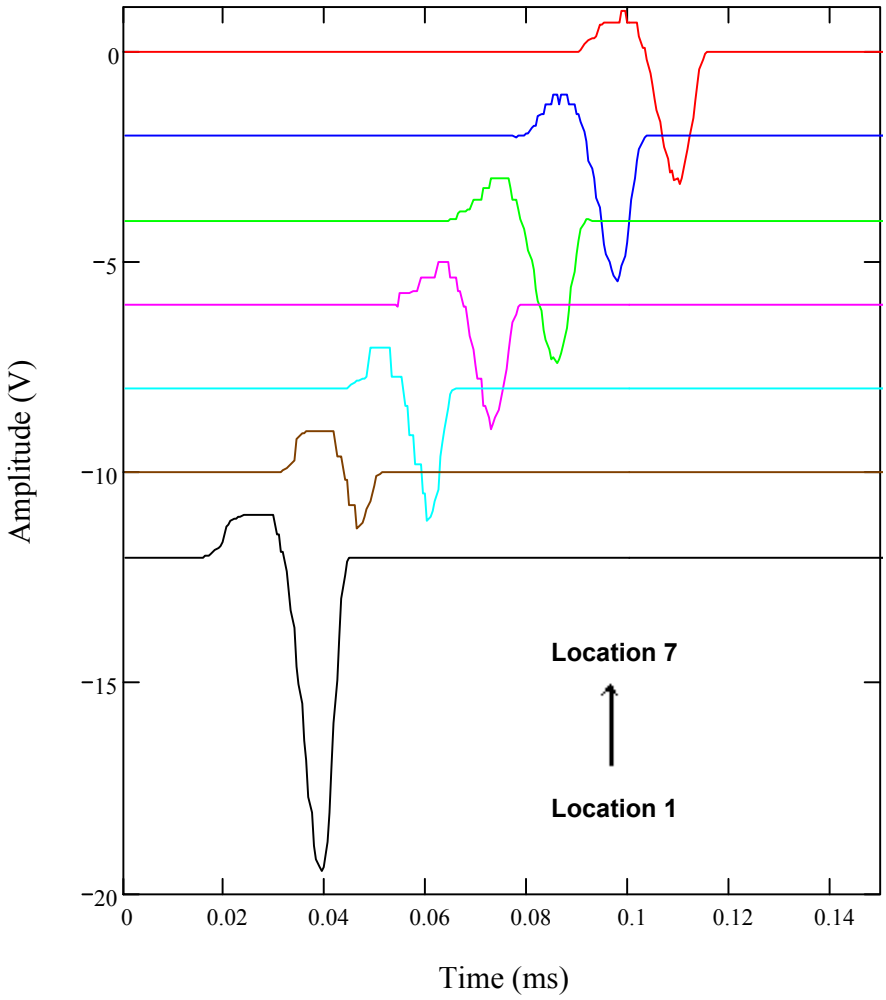

Figure V-6: Windowed P-wave portions of the signals received using 100 kHz accelerometer along Line x1 y1

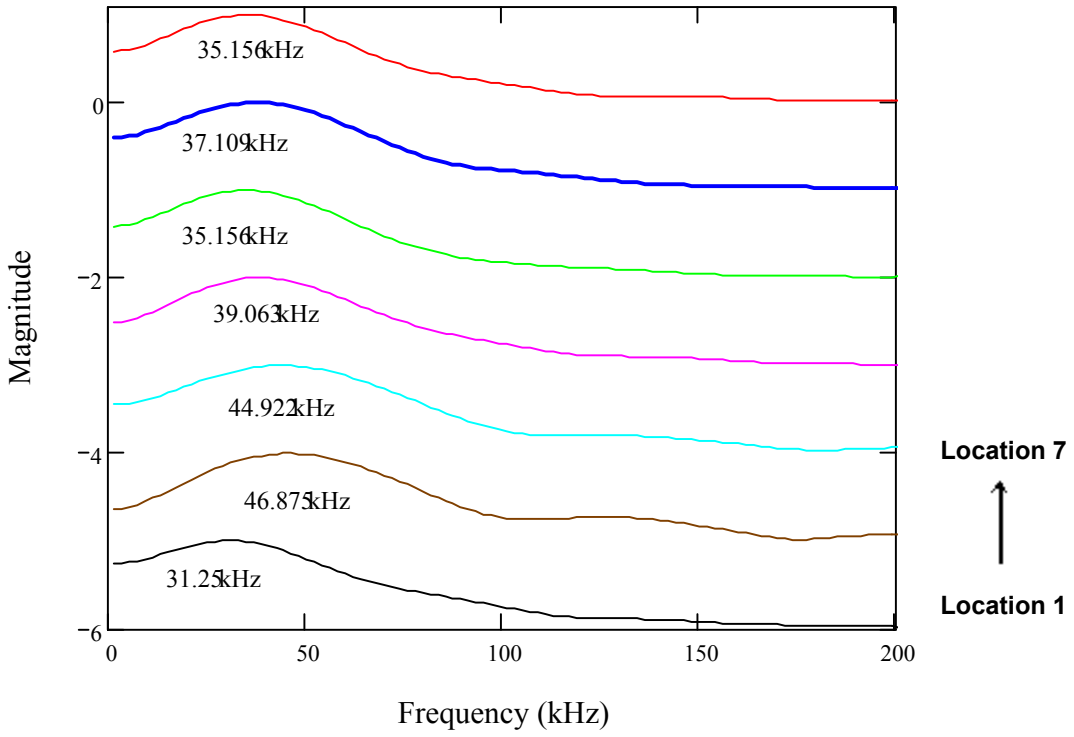

Figure V-7: Frequency spectra of the windowed P-wave portions of the signals received using 50 kHz accelerometer along Line x1 y1

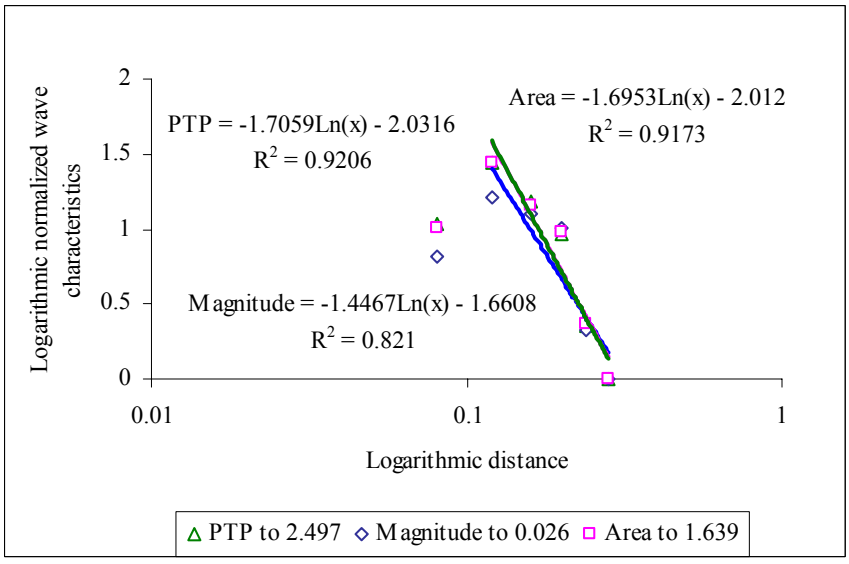

Figure V-8: Geometric attenuation evaluation based on P-waves

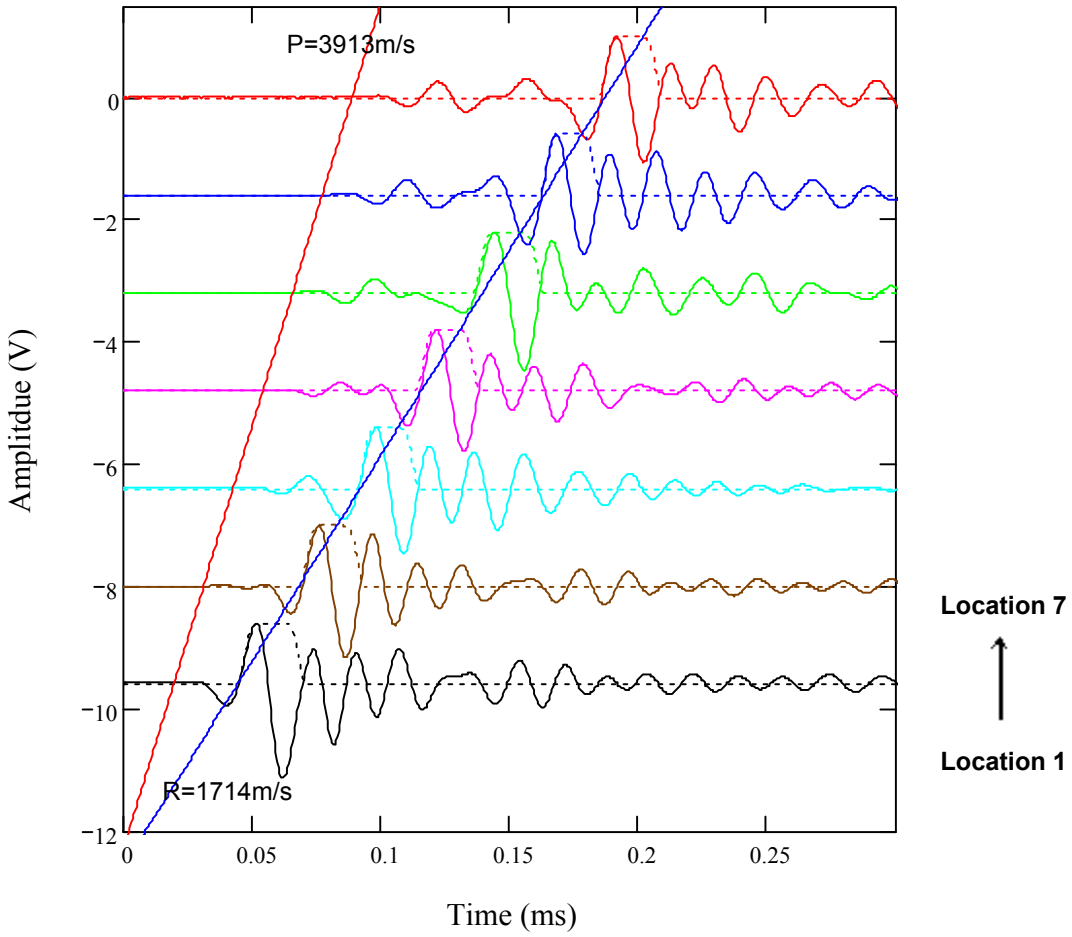

Figure V-9: Windowing R-waves of the signals received using 50 kHz accelerometer along Line x1 y1

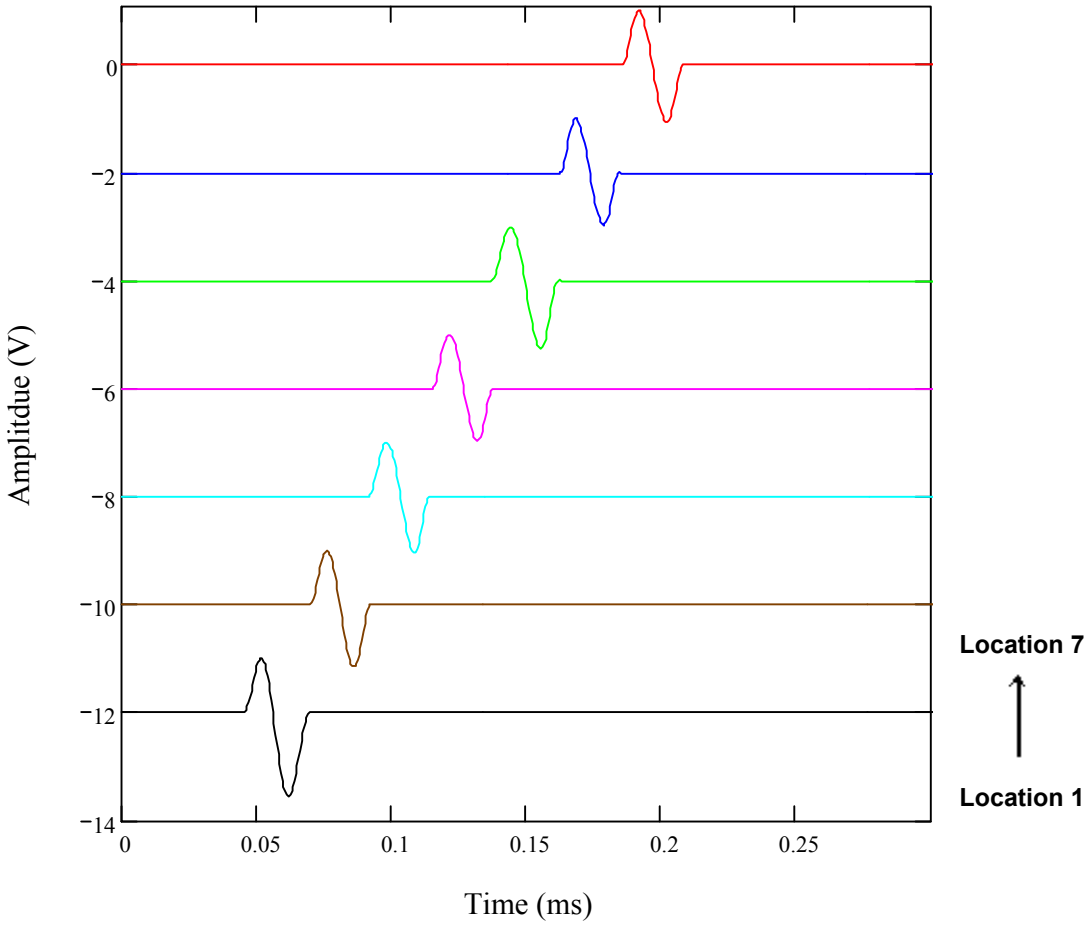

Figure V-10: Windowed R-waves of the signals received using 100 kHz accelerometer along Line x1 y1

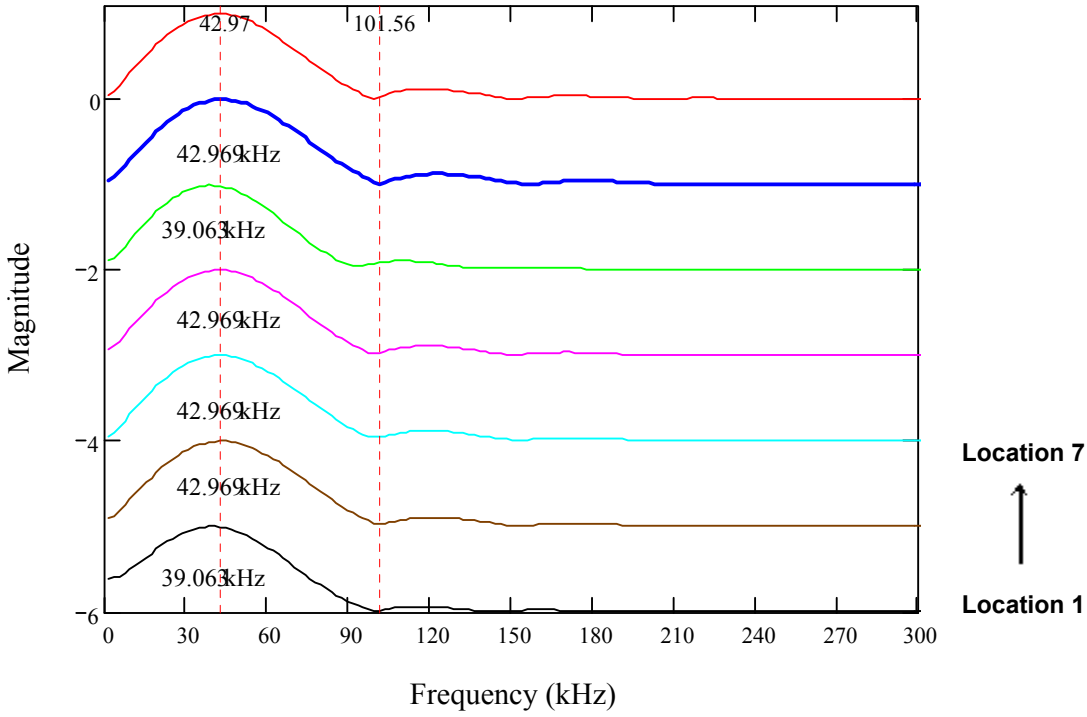

Figure V-11: Frequency spectra of the windowed R-wave portions of the signals received using 50 kHz accelerometer along Line x1 y1

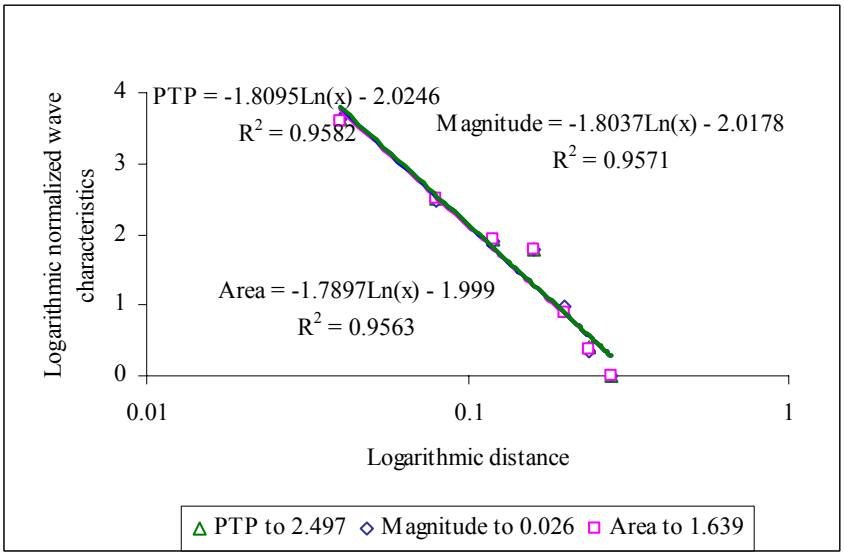

Figure V-12: Geometric attenuation evaluation based on R-waves

Appendix W

Signal Processing for Slab 3

– Measurements on the Jointed and the Joint-free Surfaces

This appendix is a PDF file available in the Appendix CD.

The file name of this PDF file is “Appendix W – Signal processing for jointed and joint-free surfaces.pdf”.

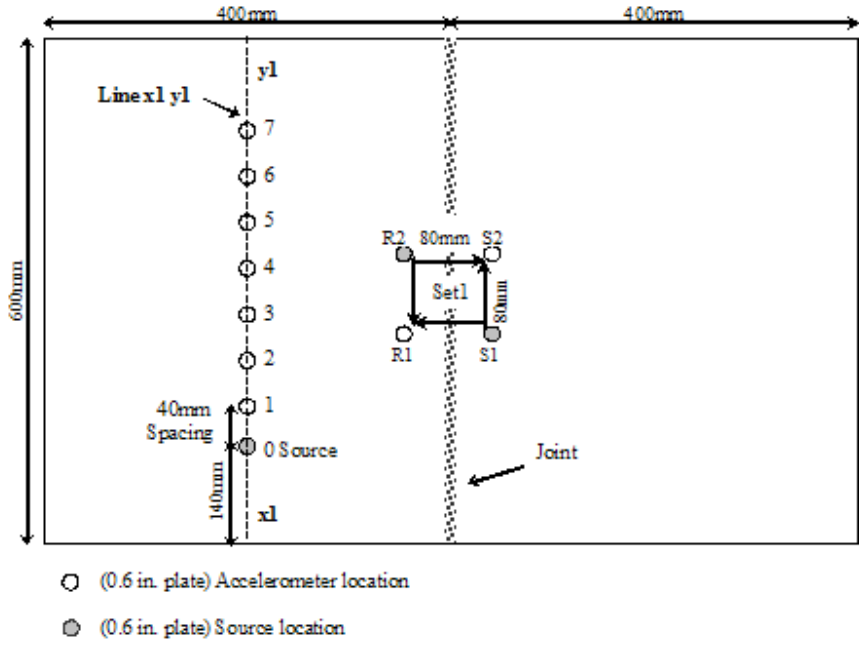

Figure W-1: Ultrasonic testing configuration of 80mm S-R spacing in slab 3

Measure Slab 3 80MM S-R spacing using 50kHz P-Wave Transducer as the transmitter and 50kHz accelerometer as the reveiver:

Pulse receiver and filter parameter setting			
Pulse receiver setting:	Pundit	**Filter setting:**	No amplification
			100kHz cutoff frequency
		Transducers setting:	Transmitter: Resonant frequency = 50kHz
			Accelerometer (PCB353B65): Resonant frequency = 50kHz

Oscilloscope setting: **Sampling Rate Δt:** $full\_signal\frac{50\mu s}{100}$ **1000 Points in Total**

Index $N := 2^{10}$ $ORIGIN \equiv 1$ $P - wave\_portion \cdot \frac{10\mu s}{100}$

$i := 1 .. N$ $u := 1 .. \frac{N}{2}$ $f_u := \frac{u}{N \cdot 5 \cdot 10^{-4}}$ $fl_u := \frac{u}{N \cdot 1 \cdot 10^{-4}}$

$all :=$ Reading data $J := 1 .. 9$ $avg_J := mean\left(all^{\langle J \rangle}\right)$ $signal^{\langle J \rangle} := all^{\langle J \rangle} - avg_J$

1. Definition of full signals for Set 1 at 80mm S-R spacing:

$S1\_R2 := signal^{\langle 1 \rangle}$ $S1\_R1 := signal^{\langle 2 \rangle}$ $S2\_R1 := signal^{\langle 3 \rangle}$ $S2\_R2 := signal^{\langle 4 \rangle}$

Analyses of full time signals:

Parameter $p := 1 .. 4$ $\omega o_p := 2\pi \cdot 1.08$

Arrival Time (AT) of the signal: $AT := 0.035$

$tp := ceil\left(\left(\frac{AT}{0.0005}\right)\right) \cdot 0.0005$ $wp(t, \omega o) := \begin{cases} 10\left|\cos(\omega o \cdot t)^{5000} - 1\right| & \text{if } 0 \le t \le \frac{\pi}{\omega o} \\ 0 & \text{otherwise} \end{cases}$

Define **Time Window** (Twind) to amplify the arrival of the signals:

$Twind :=$ for $p \in 1 .. 4$
  for $i \in 1 .. N$
    $ampl_{i,p} \leftarrow wp(i \cdot 0.0005 - tp, \omega o_p)$
  $ampl$

Fourier Transform of the Windowed Signals: $FTW^{\langle p \rangle} := CFFT\left(\overrightarrow{\left(Twind^{\langle p \rangle} \cdot signal^{\langle p \rangle}\right)}\right)$

Windowed Signals: $P_{i,p} := Twind_{i,p} \cdot signal_{i,p}$

f_{S1_R2} (joint-free) & f_{S1_R1} (joint)

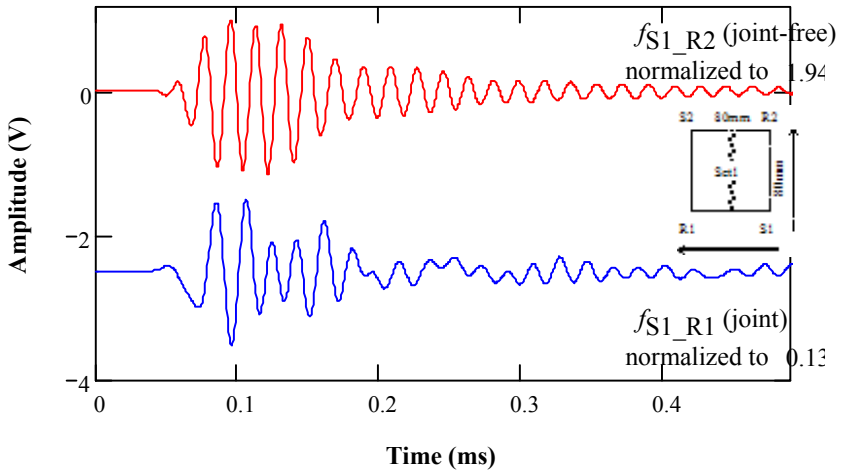

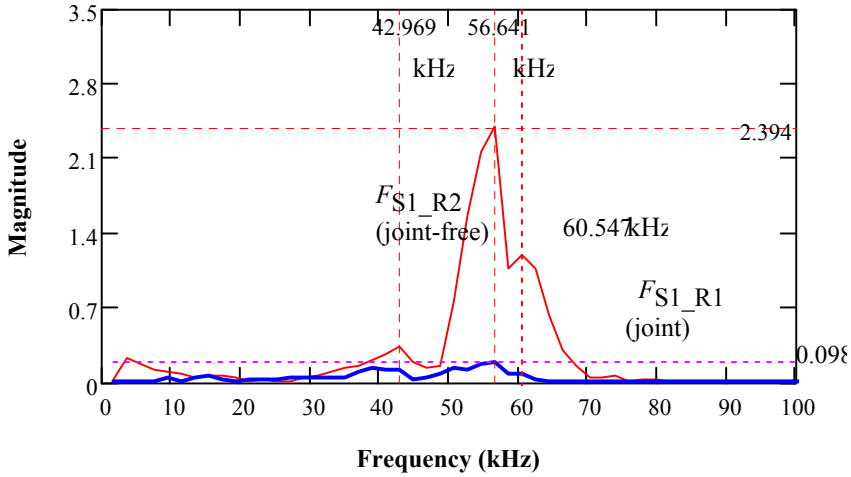

PTP ratio: $\frac{\text{joint}}{\text{joint} - \text{free}} \quad \frac{\max\left(P^{\langle 2 \rangle}\right) - \min\left(P^{\langle 2 \rangle}\right)}{\max\left(P^{\langle 1 \rangle}\right) - \min\left(P^{\langle 1 \rangle}\right)} = 0.063$

Maximum Area in Frequency Domain for the Windowed Signal

$\frac{\text{joint}}{\text{joint} - \text{free}} \quad \frac{MA_{100,2}}{MA_{100,1}} = 0.071$

$MM1 := \frac{0.293}{2.394 \cdot 3}$ $MM1 = 0.041$

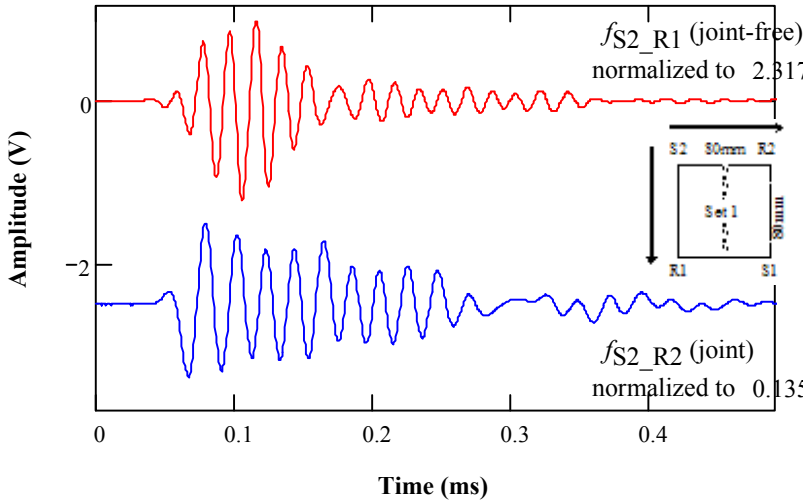

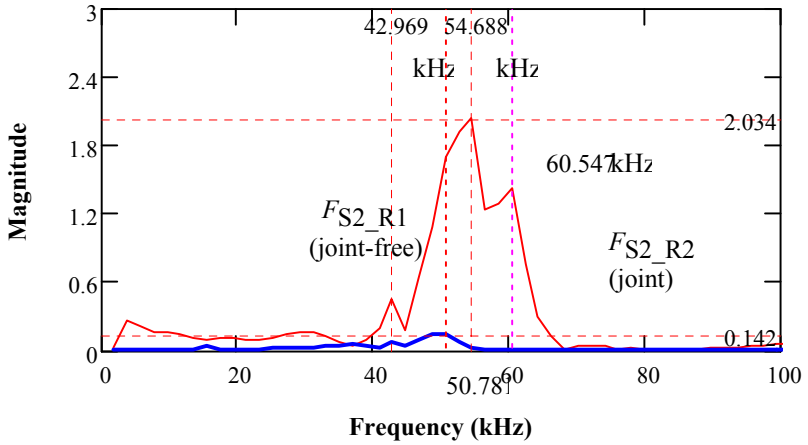

PTP ratio: $\frac{\text{joint}}{\text{joint} - \text{free}} \quad \frac{\max\left(P^{\langle 4 \rangle}\right) - \min\left(P^{\langle 4 \rangle}\right)}{\max\left(P^{\langle 3 \rangle}\right) - \min\left(P^{\langle 3 \rangle}\right)} = 0.05$

Maximum Area in Frequency Domain for the Windowed Signal

$\frac{\text{joint}}{\text{joint} - \text{free}} \quad \frac{MA_{100,4}}{MA_{100,3}} = 0.066$

Maximum Magnitude in Frequency Domain (MM):

$\frac{\text{joint}}{\text{joint} - \text{free}} \quad MM2 := \frac{0.44}{2.034 \cdot 3} \quad MM2 = 0.072$

Transmission Coefficient (TC) =

$$TC_u := \sqrt{\frac{|FTW_{u,2}| \cdot |FTW_{u,4}|}{|FTW_{u,1}| \cdot |FTW_{u,3}|}}$$

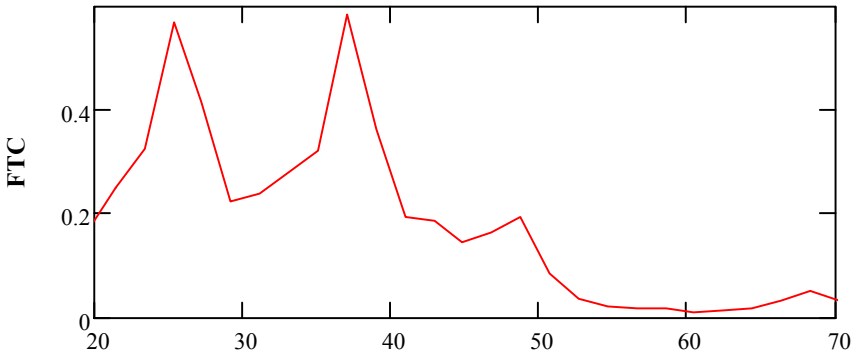

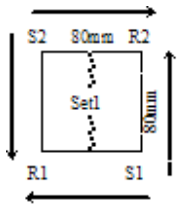

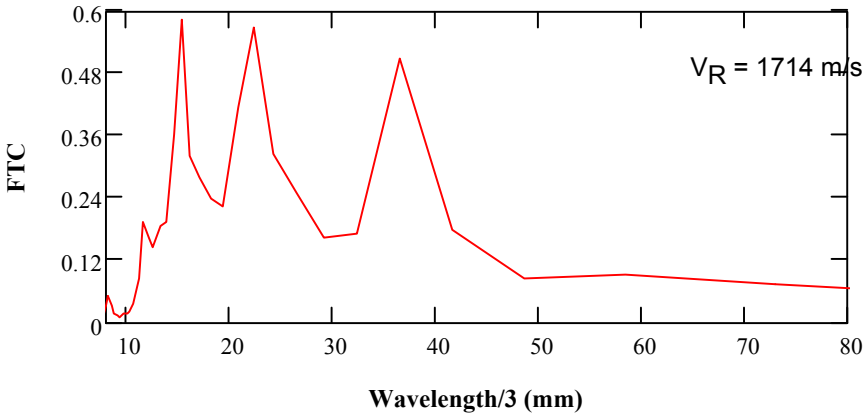

Damping ratio @ 54kHz

fre := 54.2

f_{S1_R2} (joint-free) & f_{S1_R1} (joint) $\left(\frac{2\pi fre \cdot 80}{1.714 \times 10^3}\right)^{-1} \cdot \ln\left(\frac{1}{MM1}\right) = 0.201$

f_{S2_R1} (joint-free) & f_{S2_R2} (joint) $\left(\frac{2\pi fre \cdot 80}{1.714 \times 10^3}\right)^{-1} \cdot \ln\left(\frac{1}{MM2}\right) = 0.165$

Damping analysis for full signals:

$$\Delta\Phi 1_u := \left(\frac{2\pi f_u \cdot 80}{1.714 \times 10^3} \right)^{-1}$$

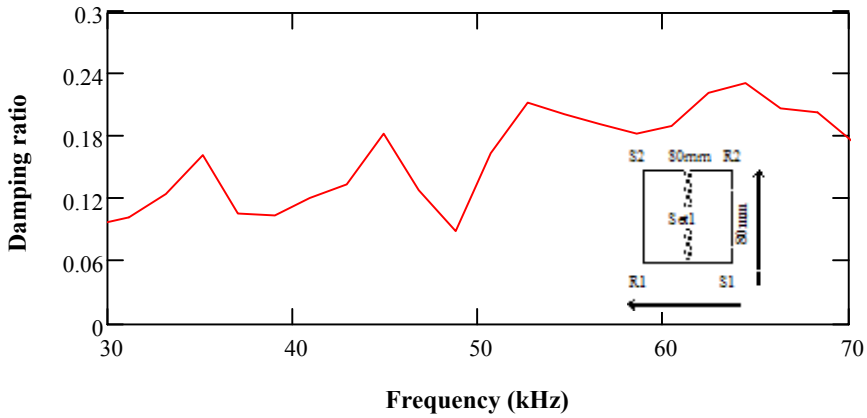

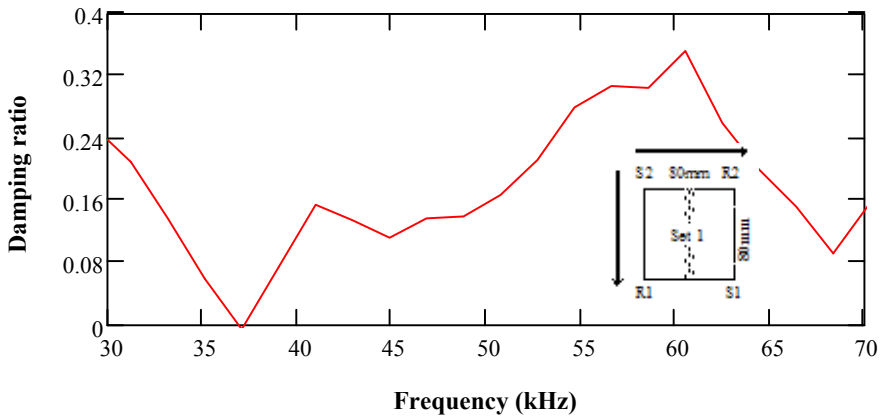

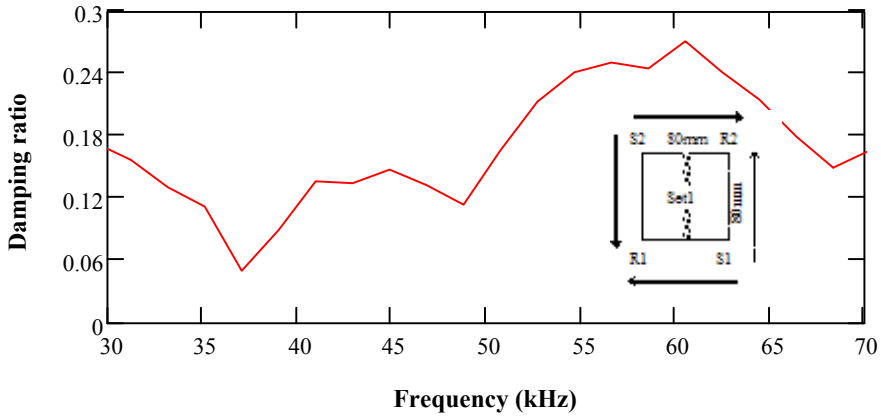

Damping analysis for full signals - using spectrum area:

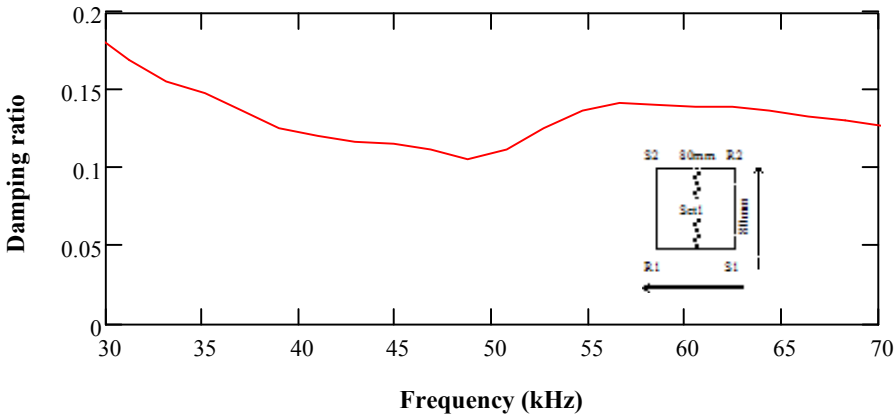

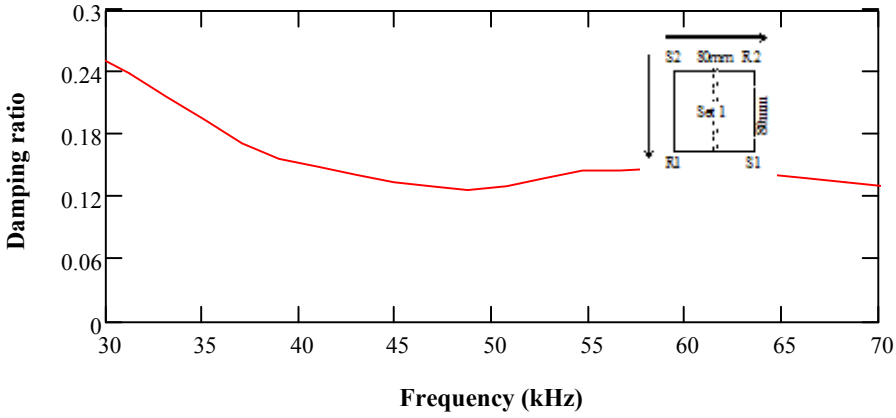

Definition of P-wave portions for the above full signals:

$S1\_R2\_F := all^{\langle 5 \rangle} - 1 \cdot 0.029$ $S1\_R1\_F := all^{\langle 6 \rangle} - 1 \cdot 0.027$

$S2\_R1\_F := all^{\langle 7 \rangle} - 1 \cdot 0.072$ $S2\_R2\_F := all^{\langle 8 \rangle} - 1 \cdot 0.045$

$Front := (\, S1\_R2\_F \quad S1\_R1\_F \quad S2\_R1\_F \quad S2\_R2\_F \,)^T$

Window the P-wave of the time signals - window 1:

Parameter $p := 1 .. 4$ $\omega o_p := 2\pi \cdot 20$

$\omega o_2 := 2\pi \cdot 16$ $\omega o_3 := 2\pi \cdot 18$ $\omega o_4 := 2\pi \cdot 18$

Arrival Time (AT) of the signal: $AT := (\, 0.0286 \quad 0.0376 \quad 0.027 \quad 0.039 \quad 0.04 \quad 0.04 \quad 0.044 \,)^T$

$$tp_p := ceil\left(\left(\frac{AT_p}{0.0001}\right)\right) \cdot 0.0001$$

$$wp(t, \omega o) := \begin{cases} 10\left|\cos(\omega o \cdot t)^{10} - 1\right| & \text{if } 0 \le t \le \frac{\pi}{\omega o} \\ 0 & \text{otherwise} \end{cases}$$

Define **Time Window** (Twind) to amplify the arrival of the signals:

$$Twind := \left| \begin{array}{l} \text{for } p \in 1 .. 4 \\ \quad \text{for } i \in 1 .. N \\ \quad\quad ampl_{i,p} \leftarrow wp\left(i \cdot 0.0001 - tp_p, \omega o_p\right) \\ ampl \end{array} \right.$$

Zero-padding

$k := 1 .. 8N$ $f1_k := \frac{k}{N \cdot 1 \cdot 10^{-4}}$ $signal\_F_{k,p} := 0$

$signal\_F_{i,1} := \left(Twind^{\langle 1 \rangle}\right)_i \cdot S1\_R2\_F_i$ $signal\_F_{i,3} := \left(Twind^{\langle 3 \rangle}\right)_i \cdot S2\_R1\_F_i$

$signal\_F_{i,2} := \left(Twind^{\langle 2 \rangle}\right)_i \cdot S1\_R1\_F_i$ $signal\_F_{i,4} := \left(Twind^{\langle 4 \rangle}\right)_i \cdot S2\_R2\_F_i$

Fourier Transform of the Windowed Signals: $FTTW^{\langle p \rangle} := CFFT\left(signal\_F^{\langle p \rangle}\right)$

Spectral Area $$MA_{u,p} := \sum_{u=1}^{u} \frac{\left|FTTW_{u,p}\right|}{N \cdot 0.001}$$

f_{S1_R2} (joint-free)& f_{S1_R1} (joint)

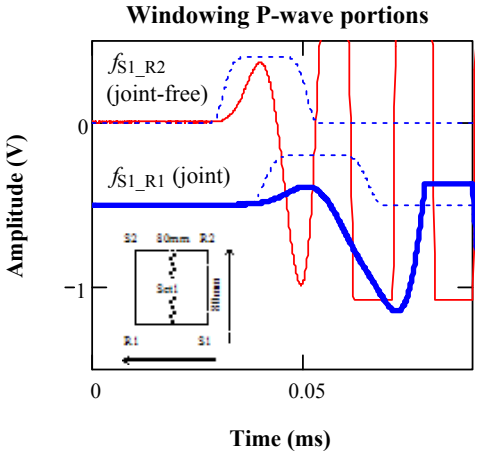

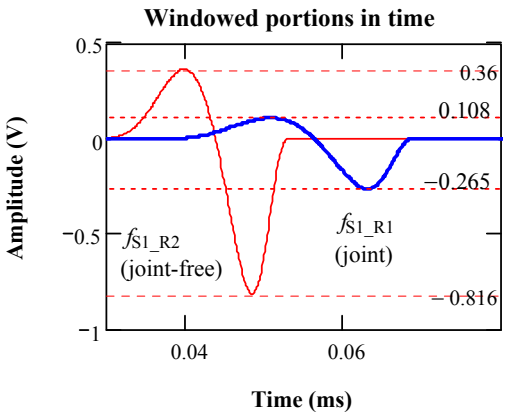

f_{S2_R1} (joint-free)& f_{S2_R2} (joint)

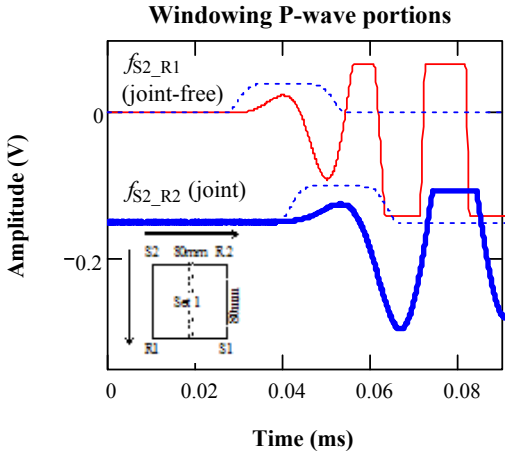

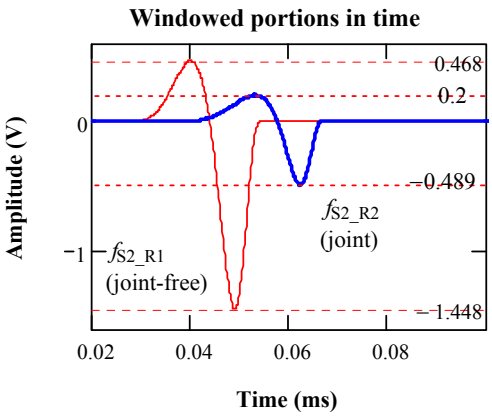

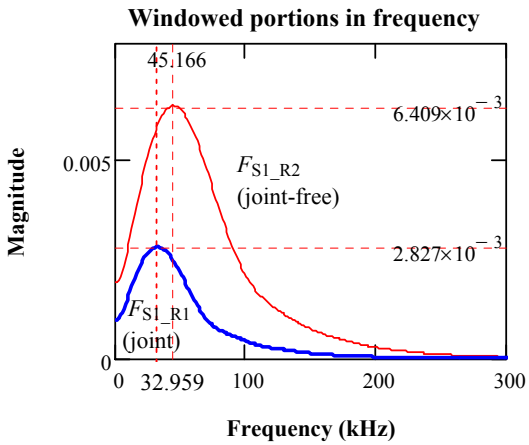

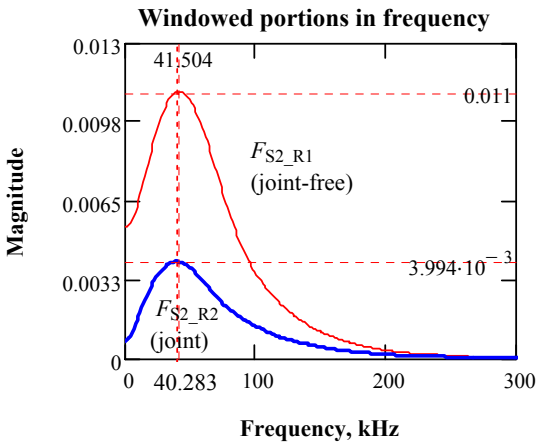

PTP ratio: $\frac{\text{Joint}}{\text{no}-\text{Joint}}\ \frac{\text{PTP}^{\langle 2\rangle}}{\text{PTP}^{\langle 1\rangle}} = 0.317$ $\frac{\text{PTP}^{\langle 4\rangle}}{\text{PTP}^{\langle 3\rangle}} = 0.363$

Maximum Area in Frequency Domain for the Windowed Signal (MA):

$\frac{\text{Joint}}{\text{no}-\text{Joint}}\ \frac{\text{MA}_{300,2}}{\text{MA}_{300,1}} = 0.329$ $\frac{\text{MA}_{300,4}}{\text{MA}_{300,3}} = 0.352$

Maximum Magnitude in Frequency Domain (MM):

$\frac{\text{Joint}}{\text{no}-\text{Joint}}\ \text{MM1} := \frac{2.827\times 10^{-3}}{6.409\times 10^{-3}}$ $\text{MM1} = 0.441$ $\text{MM2} := \frac{3.994\times 10^{-3}}{0.011}$ $\text{MM2} = 0.363$

Transmission Coefficient (TC)

$$TC_u := \sqrt{\frac{|FTTW_{u,2}| \cdot |FTTW_{u,4}|}{|FTTW_{u,1}| \cdot |FTTW_{u,3}|}}$$

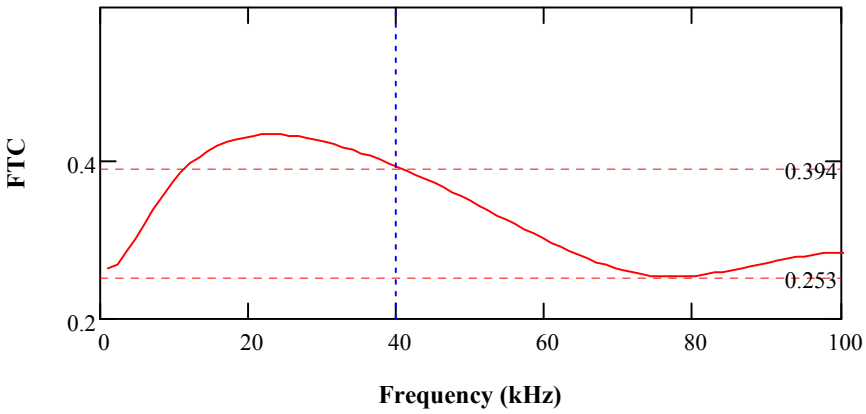

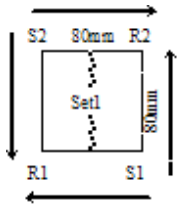

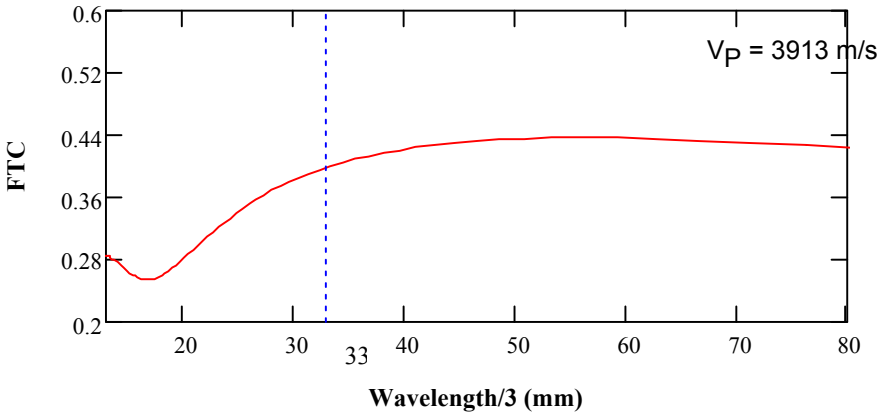

Damping ratio @ 39kHz

fre := 40

f_{S1_R2} (joint-free) & f_{S1_R1} (joint) $\left(\frac{2\pi fre \cdot 80}{3.913\times 10^3}\right)^{-1} \cdot \ln\left(\frac{1}{MM1}\right) = 0.159$

f_{S2_R1} (joint-free) & f_{S2_R2} (joint) $\left(\frac{2\pi fre \cdot 80}{3.913\times 10^3}\right)^{-1} \cdot \ln\left(\frac{1}{MM2}\right) = 0.197$

For the set $\left(\frac{2\pi fre \cdot 80}{3.913\times 10^3}\right)^{-1} \cdot \ln\left(\sqrt{\frac{1}{MM2 \cdot MM1}}\right) = 0.178$

Damping analysis for P-wave signals:

$$\Delta\Phi 1_u := \left(\frac{2\pi\, 0.125 f1_u \cdot 80}{3.913 \times 10^3} \right)^{-1}$$

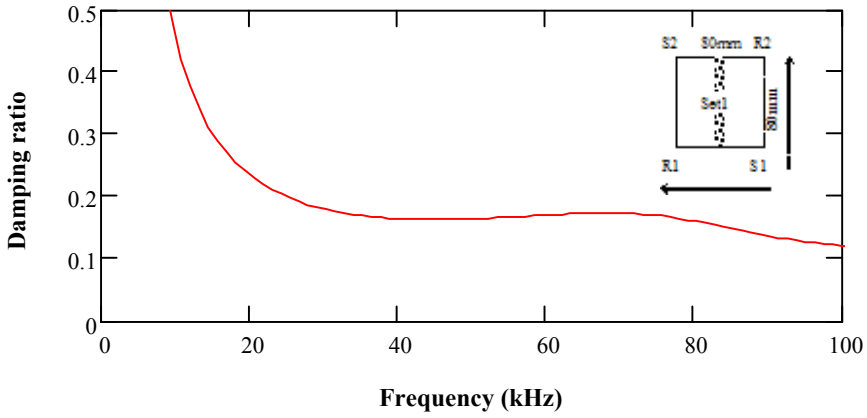

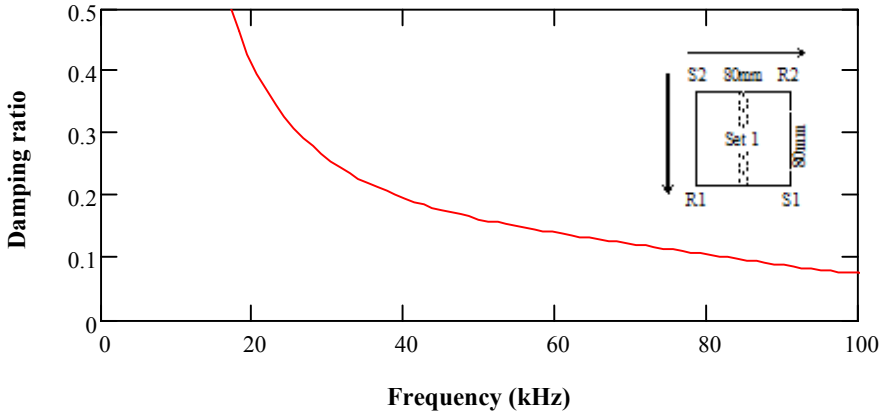

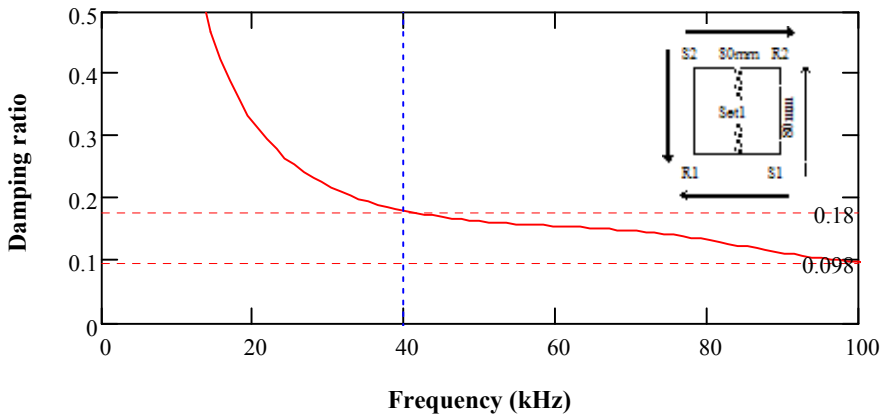

Damping analysis for full signals - using spectrum area:

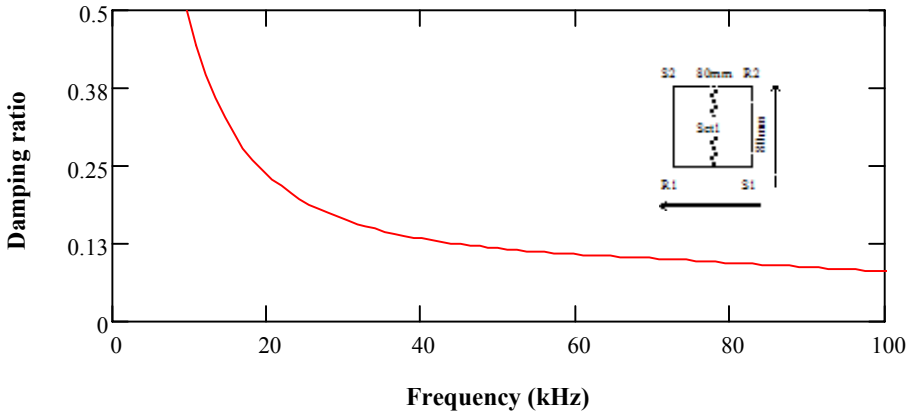

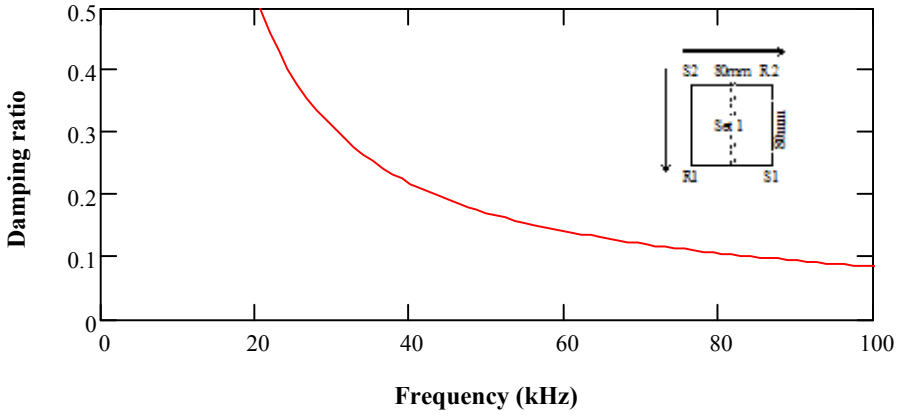

Window the R-wave arrival of time signals - window 2:

Parameter $p := 1..4$ $\omega o_p := 2\pi \cdot 26$

$\omega o_2 := 2\pi \cdot 21.5$ $\omega o_3 := 2\pi \cdot 23.5$ $\omega o_4 := 2\pi \cdot 20.5$

Arrival Time (AT) of the signal: $AT := (0.072 \quad 0.079 \quad 0.072 \quad 0.073 \quad 0.0915 \quad 0.0675 \quad 0.104)^T$

$tp_p := ceil\left(\left(\frac{AT_p}{0.0005}\right)\right) \cdot 0.0005$

$$wp(t, \omega o) := \begin{cases} 10\left|\cos(\omega o \cdot t)^{10} - 1\right| & \text{if } 0 \le t \le \frac{\pi}{\omega o} \\ 0 & \text{otherwise} \end{cases}$$

Define **Time Window** (Twind) to amplify the arrival of the signals:

$$Twind := \left| \begin{array}{l} \text{for } p \in 1..4 \\ \quad \text{for } i \in 1..N \\ \quad\quad ampl_{i,p} \leftarrow wp\left(i \cdot 0.0005 - tp_p, \omega o_p\right) \\ ampl \end{array} \right.$$

Fourier Transform of the Windowed Signals: $FTW^{\langle p \rangle} := CFFT\left(\overrightarrow{\left(Twind^{\langle p \rangle} \cdot signal^{\langle p \rangle}\right)}\right)$

Windowed Signals: $P_{i,p} := Twind_{i,p} \cdot signal_{i,p}$

Spectrum area $MA_{u,p} := \sum_{u=1}^{u} \frac{\left|FTW_{u,p}\right|}{N \cdot 0.001}$

f_{S1_R2} (joint-free)& f_{S1_R1} (joint)

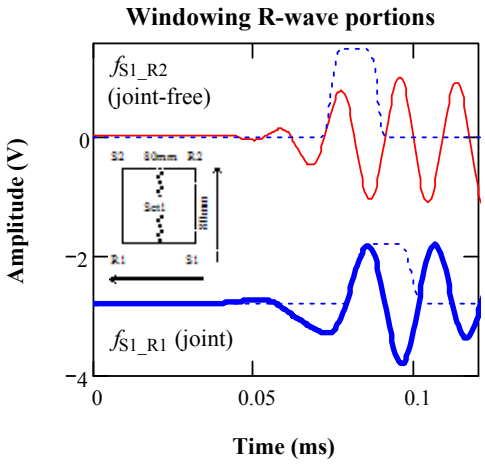

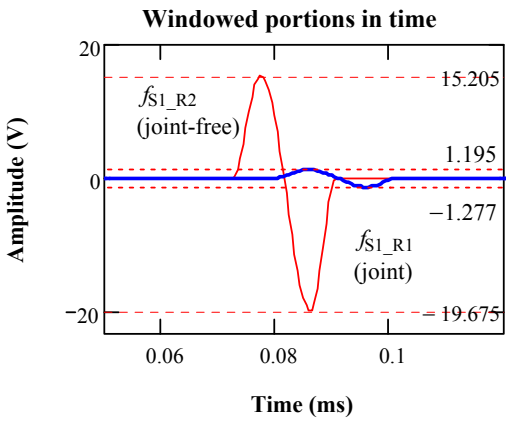

f_{S2_R1} (joint-free)& f_{S2_R2} (joint)

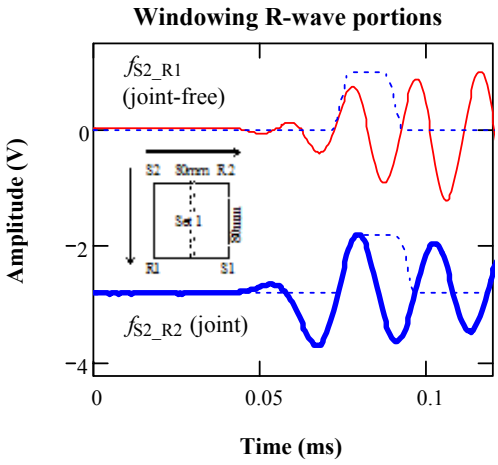

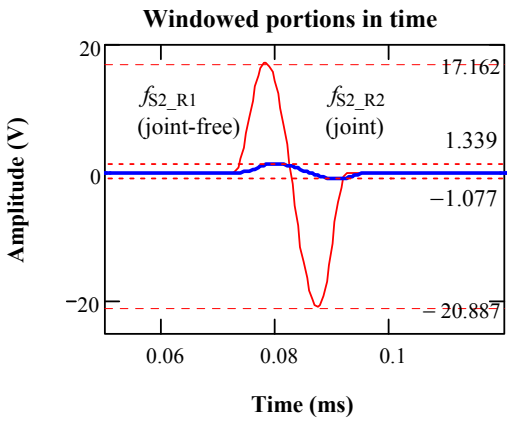

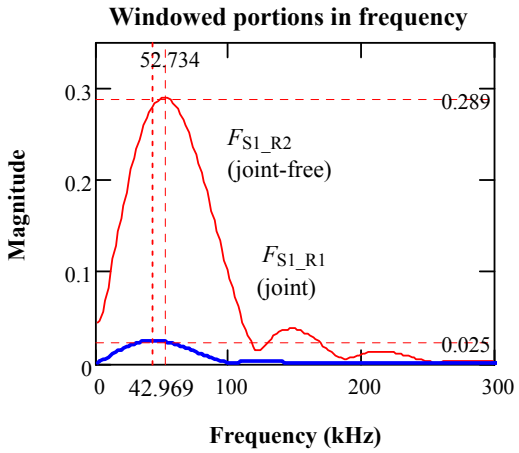

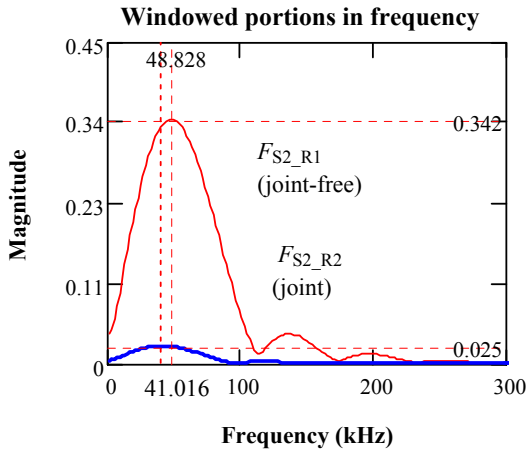

PTP ratio: $\frac{\text{Joint}}{\text{no}-\text{Joint}}$ $\frac{\max\left(P^{\langle 2\rangle}\right)-\min\left(P^{\langle 2\rangle}\right)}{\max\left(P^{\langle 1\rangle}\right)-\min\left(P^{\langle 1\rangle}\right)}=0.073$ $\frac{\max\left(P^{\langle 4\rangle}\right)-\min\left(P^{\langle 4\rangle}\right)}{\max\left(P^{\langle 3\rangle}\right)-\min\left(P^{\langle 3\rangle}\right)}=0.064$

Maximum Area in Frequency Domain for the Windowed Signal (MA):

$\frac{\text{Joint}}{\text{no}-\text{Joint}}$ $\frac{MA_{100,2}}{MA_{100,1}}=0.073$ $\frac{MA_{100,4}}{MA_{100,3}}=0.065$

Maximum Magnitude in Frequency Domain (MM):

$\frac{\text{Joint}}{\text{no}-\text{Joint}}$ $MM1:=\frac{0.025}{0.289}$ $MM1=0.087$ $MM2:=\frac{0.025}{0.342}$ $MM2=0.073$

Transmission Coefficient (TC) = $\frac{\text{Joint}}{\text{no}-\text{Joint}}$ $TC_u := \sqrt{\frac{|FTW_{u,2}| \cdot |FTW_{u,4}|}{|FTW_{u,1}| \cdot |FTW_{u,3}|}}$

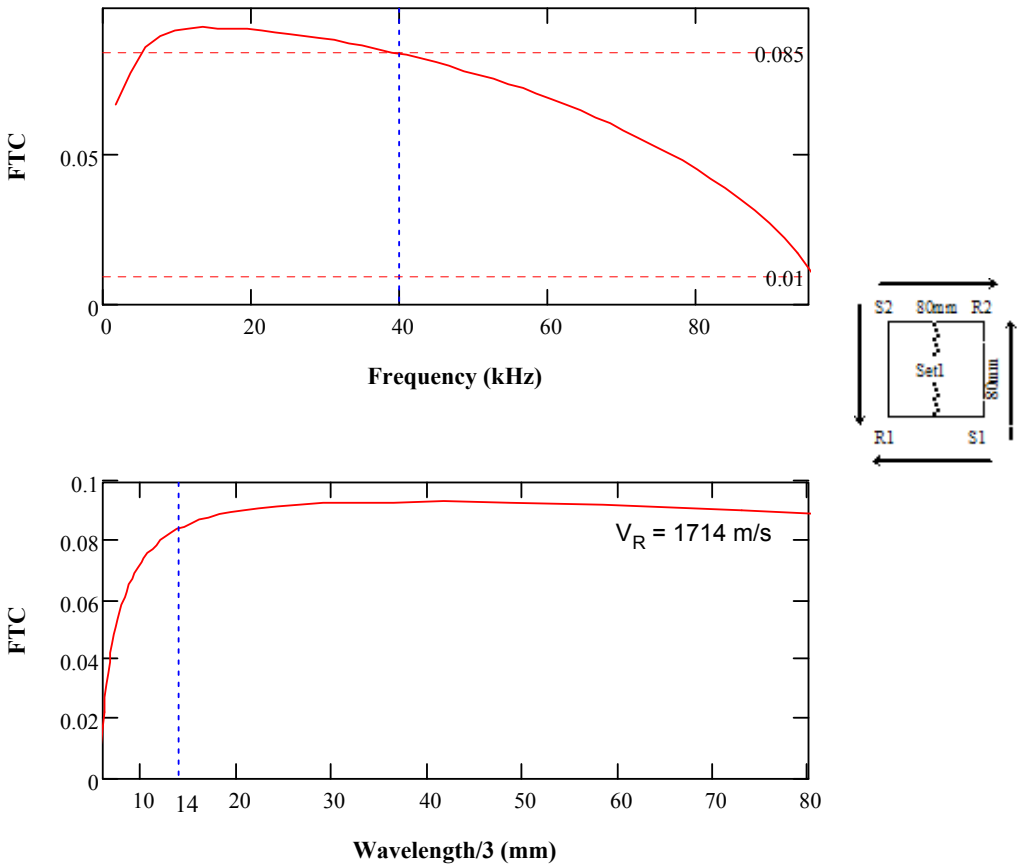

Damping ratio @ 47kHz

$fre := 46.875$

Damping ratio Based on Spetrum Area

For JL & JI

$$\left(\frac{2\pi fre \cdot 80}{1.714\times 10^3}\right)^{-1} \cdot \ln\left(\frac{1}{MM1}\right) = 0.178 \qquad \left(\frac{2\pi fre \cdot 80}{1.714\times 10^3}\right)^{-1} \cdot \ln\left(\frac{MA_{100,1}}{MA_{100,2}}\right) = 0.19$$

For KI & KL

$$\left(\frac{2\pi fre \cdot 80}{1.714\times 10^3}\right)^{-1} \cdot \ln\left(\frac{1}{MM2}\right) = 0.19 \qquad \left(\frac{2\pi fre \cdot 80}{1.714\times 10^3}\right)^{-1} \cdot \ln\left(\frac{MA_{100,3}}{MA_{100,4}}\right) = 0.199$$

For the sqaure

$$\left(\frac{2\pi fre \cdot 80}{1.714\times 10^3}\right)^{-1} \cdot \ln\left(\sqrt{\frac{1}{MM2 \cdot MM1}}\right) = 0.184 \qquad \sqrt{MM2 \cdot MM1} = 0.08$$

Damping analysis for R-wave signals:

$$\Delta\Phi 1_u := \left(\frac{2\pi f_u \cdot 80}{1.714 \times 10^3} \right)^{-1}$$

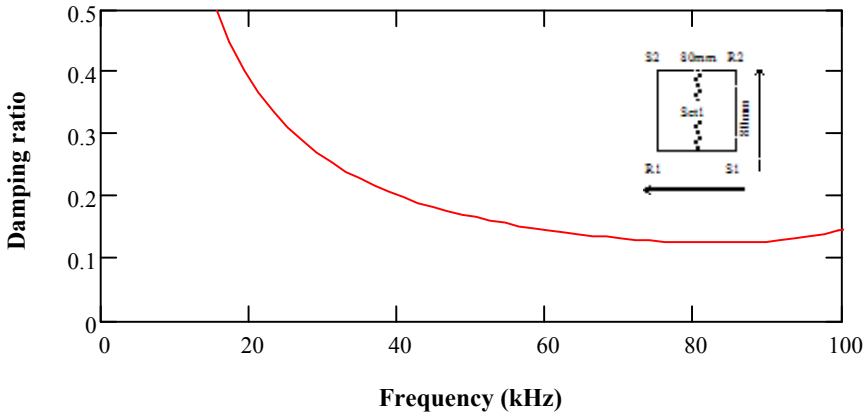

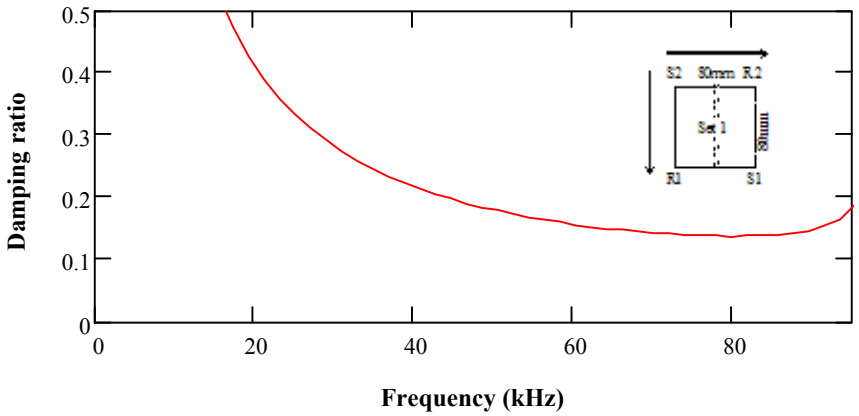

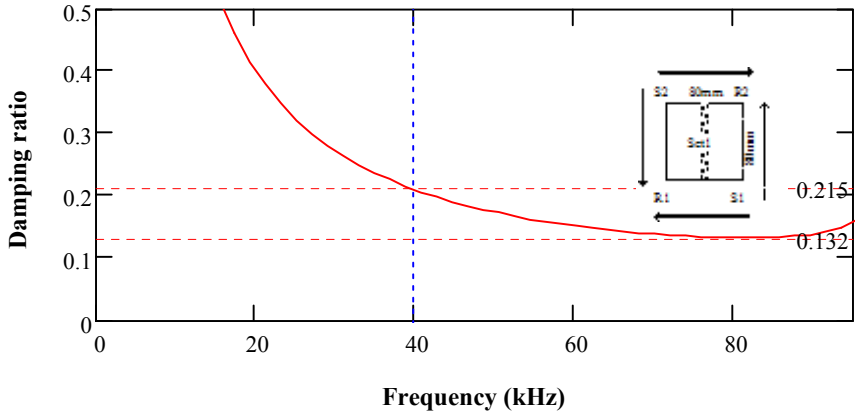

Damping analysis for full signals - using spectrum area:

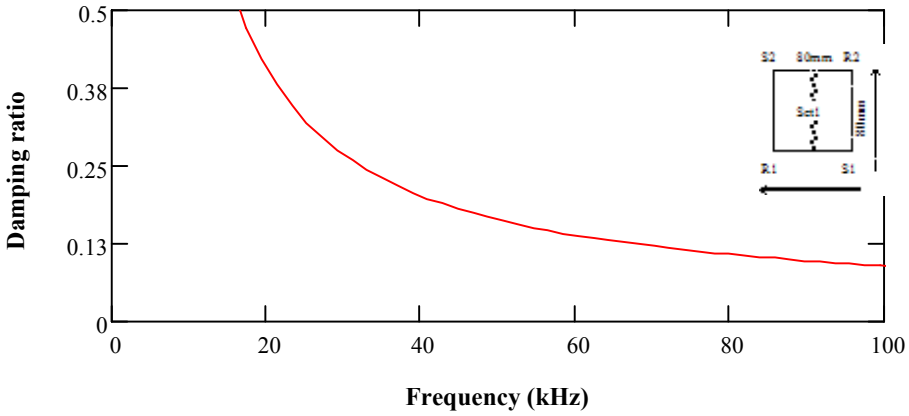

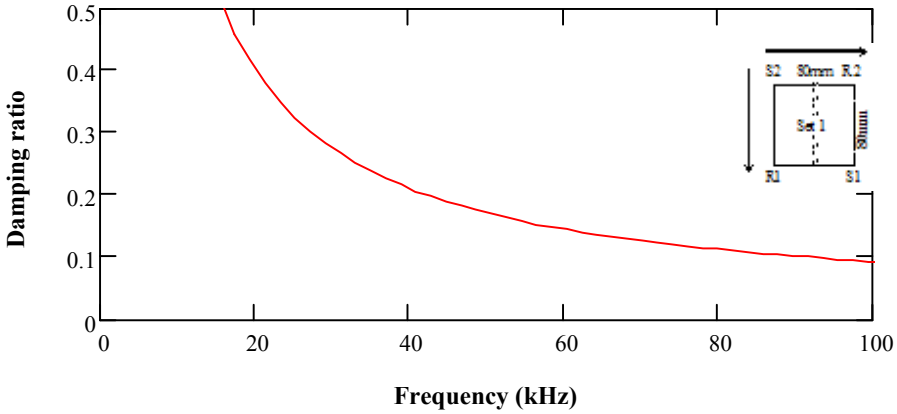

Wavelet transform - for dominant frequency in full sinnals, deifferent center frequency for 4 signals defined by "aX"; Time shift by "τ".

$aJL := 17.6$ $\frac{1}{2 \cdot aJL \cdot 5 \cdot 10^{-4}} = 56.625$ kHz $aKI := 18.28$ $\frac{1}{2 \cdot aKI \cdot 5 \cdot 10^{-4}} = 54.687$ kHz

$aJI := 17.6$ $\frac{1}{2 \cdot aJL \cdot 5 \cdot 10^{-4}} = 56.625$ kHz $aKL := 20.4$ $\frac{1}{2 \cdot aKL \cdot 5 \cdot 10^{-4}} = 48.828$ kHz

Definition of Morlet wavelet $\tau := 1 .. N$

f_{S1_R2} (joint-free) $w\_JL_{i,\tau} := aJL^{-\frac{1}{2}} \cdot \left[e^{j \cdot \frac{-\pi}{aJL} \cdot (\tau - i)} \cdot e^{-1 \cdot \left(\frac{\tau - i}{aJL} \right)^2} \right]$

f_{S1_R1} (joint) $w\_JI_{i,\tau} := aJI^{-\frac{1}{2}} \cdot \left[e^{j \cdot \frac{-\pi}{aJI} \cdot (\tau - i)} \cdot e^{-1 \cdot \left(\frac{\tau - i}{aJI} \right)^2} \right]$

f_{S2_R1} (joint-free) $w\_KI_{i,\tau} := aKI^{-\frac{1}{2}} \cdot \left[e^{j \cdot \frac{-\pi}{aKI} \cdot (\tau - i)} \cdot e^{-1 \cdot \left(\frac{\tau - i}{aKI} \right)^2} \right]$

f_{S2_R2} (joint) $w\_KL_{i,\tau} := aKI^{-\frac{1}{2}} \cdot \left[e^{j \cdot \frac{-\pi}{aKL} \cdot (\tau - i)} \cdot e^{-1 \cdot \left(\frac{\tau - i}{aKL} \right)^2} \right]$

Wavelet transform

f_{S1_R2} (joint-free) $WJL_\tau := \sum_i \left(w\_JL_{i,\tau} \cdot JL_i \right)$ f_{S1_R1} (joint) $WJI_\tau := \sum_i \left(w\_JI_{i,\tau} \cdot JI_i \right)$

$WJL_\tau := \left| WJL_\tau \right|$ $WJI_\tau := \left| WJI_\tau \right|$

f_{S2_R1} (joint-free) $WKI_\tau := \sum_i \left(w\_KI_{i,\tau} \cdot KI_i \right)$ f_{S2_R2} (joint) $WKL_\tau := \sum_i \left(w\_KL_{i,\tau} \cdot KL_i \right)$

f_{S1_R2} (joint-free) & f_{S1_R1} (joint)

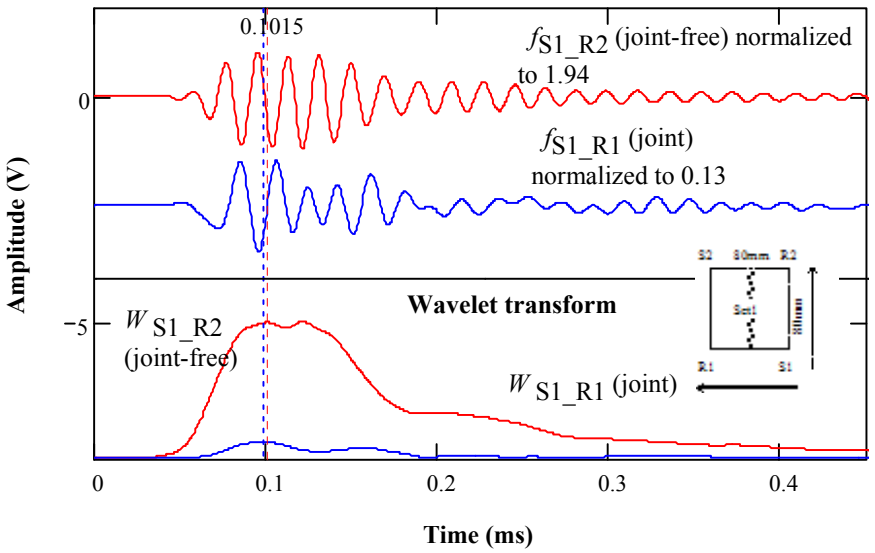

f_{S2_R1} (joint-free) & f_{S2_R2} (joint)

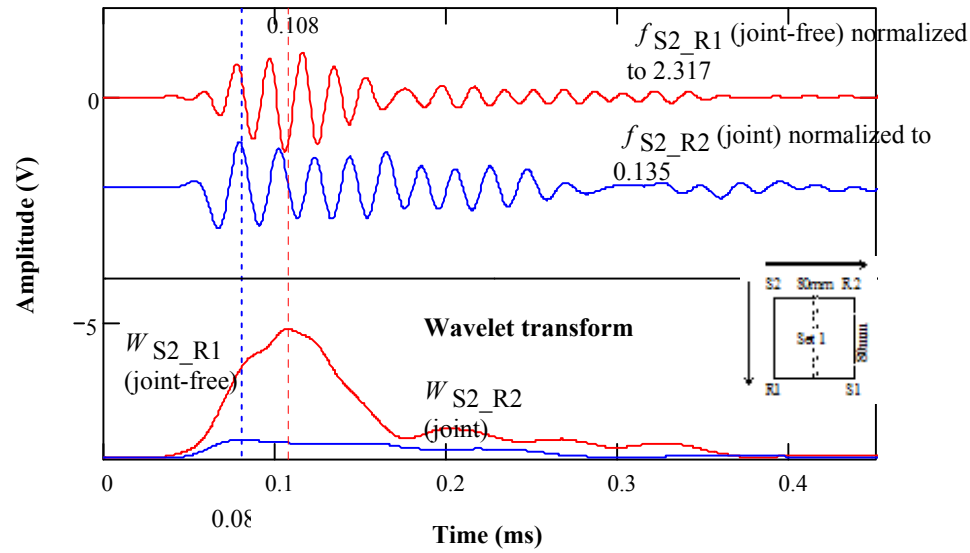

Amplitude ratio

$$\frac{\max(WJI)}{\max(WJL)} = 0.06 \qquad \frac{\max(WKL)}{\max(WKI)} = 0.054 \qquad \sqrt{\frac{\max(WJI)}{\max(WJL)}\frac{\max(WKL)}{\max(WKI)}} = 0.057$$

Wavelet transform - for P-wave, deifferent center frequency for 4 signals defined by "aX"; Time shift by "τ".

$aJL := 22.1$ $\frac{1}{2 \cdot aJL \cdot 5 \cdot 10^{-4}} = 45.167$ kHz

$aKI := 24.0$ $\frac{1}{2 \cdot aKI \cdot 5 \cdot 10^{-4}} = 41.511$ kHz

$aJI := 30.3$ $\frac{1}{2 \cdot aJI \cdot 5 \cdot 10^{-4}} = 32.96$ kHz

$aKL := 24.8$ $\frac{1}{2 \cdot aKL \cdot 5 \cdot 10^{-4}} = 40.29$ kHz

Definition of Morlet wavelet

$\tau := 1 .. N$

f_{S1_R2} (joint-free) $w\_JL_{i,\tau} := aJL^{-\frac{1}{2}} \cdot \left[e^{j \cdot \frac{-\pi}{aJL} \cdot (\tau - i)} \cdot e^{-1 \cdot \left(\frac{\tau - i}{aJL} \right)^2} \right]$

f_{S1_R1} (joint) $w\_JI_{i,\tau} := aJI^{-\frac{1}{2}} \cdot \left[e^{j \cdot \frac{-\pi}{aJI} \cdot (\tau - i)} \cdot e^{-1 \cdot \left(\frac{\tau - i}{aJI} \right)^2} \right]$

f_{S2_R1} (joint-free) $w\_KI_{i,\tau} := aKI^{-\frac{1}{2}} \cdot \left[e^{j \cdot \frac{-\pi}{aKI} \cdot (\tau - i)} \cdot e^{-1 \cdot \left(\frac{\tau - i}{aKI} \right)^2} \right]$

f_{S2_R2} (joint) $w\_KL_{i,\tau} := aKI^{-\frac{1}{2}} \cdot \left[e^{j \cdot \frac{-\pi}{aKL} \cdot (\tau - i)} \cdot e^{-1 \cdot \left(\frac{\tau - i}{aKL} \right)^2} \right]$

Wavelet transform

f_{S1_R2} (joint-free) $WJL_\tau := \sum_i \left(w\_JL_{i,\tau} \cdot JL_i \right)$

$WJL_\tau := \left| WJL_\tau \right|$

f_{S1_R1} (joint) $WJI_\tau := \sum_i \left(w\_JI_{i,\tau} \cdot JI_i \right)$

$WJI_\tau := \left| WJI_\tau \right|$

f_{S2_R1} (joint-free) $WKI_\tau := \sum_i \left(w\_KI_{i,\tau} \cdot KI_i \right)$

f_{S2_R2} (joint) $WKL_\tau := \sum_i \left(w\_KL_{i,\tau} \cdot KL_i \right)$

f_{S1_R2} (joint-free)& f_{S1_R1} (joint)

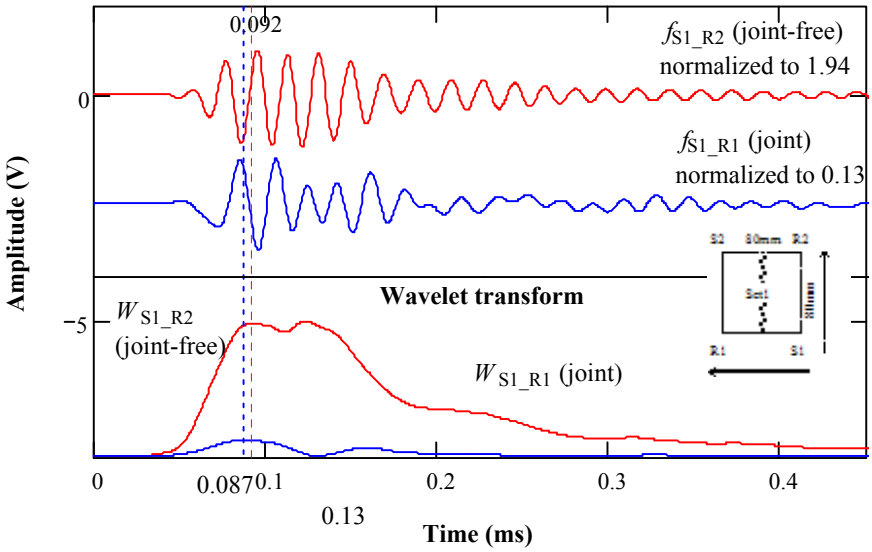

f_{S2_R1} (joint-free)& f_{S2_R2} (joint)

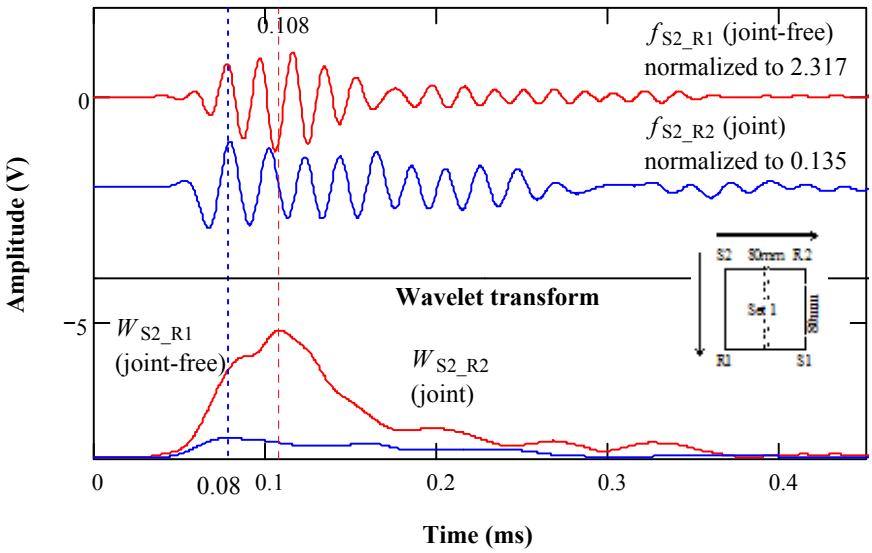

Amplitude ratio

$$\frac{\max(WJI)}{\max(WJL)} = 0.061 \qquad \frac{\max(WKL)}{\max(WKI)} = 0.059 \qquad \sqrt{\frac{\max(WJI)}{\max(WJL)}\frac{\max(WKL)}{\max(WKI)}} = 0.06$$

Wavelet transform - for R-wave, different center frequency for 4 signals defined by "aX"; Time shift by "τ".

$aJL := 18.96 \qquad \frac{1}{2 \cdot aJL \cdot 5 \cdot 10^{-4}} = 52.743\ kHz$

$aKI := 20.48 \qquad \frac{1}{2 \cdot aKI \cdot 5 \cdot 10^{-4}} = 48.828\ kHz$

$aJI := 23.27 \qquad \frac{1}{2 \cdot aJL \cdot 5 \cdot 10^{-4}} = 52.743\ kHz$

$aKL := 24.38 \qquad \frac{1}{2 \cdot aKL \cdot 5 \cdot 10^{-4}} = 41.017\ kHz$

Definition of Morlet wavelet

$\tau := 1 .. N$

f_{S1_R2} (joint-free) $\quad w\_JL_{i,\tau} := aJL \cdot e^{-\frac{1}{2} \cdot \left[j \cdot \frac{-\pi}{aJL} \cdot (\tau - i) - 1 \cdot \left(\frac{\tau - i}{aJL} \right)^2 \right]}$

f_{S1_R1} (joint) $\quad w\_JI_{i,\tau} := aJI \cdot e^{-\frac{1}{2} \cdot \left[j \cdot \frac{-\pi}{aJI} \cdot (\tau - i) - 1 \cdot \left(\frac{\tau - i}{aJI} \right)^2 \right]}$

f_{S2_R1} (joint-free) $\quad w\_KI_{i,\tau} := aKI \cdot e^{-\frac{1}{2} \cdot \left[j \cdot \frac{-\pi}{aKI} \cdot (\tau - i) - 1 \cdot \left(\frac{\tau - i}{aKI} \right)^2 \right]}$

f_{S2_R2} (joint) $\quad w\_KL_{i,\tau} := aKI \cdot e^{-\frac{1}{2} \cdot \left[j \cdot \frac{-\pi}{aKL} \cdot (\tau - i) - 1 \cdot \left(\frac{\tau - i}{aKL} \right)^2 \right]}$

Wavelet transform

f_{S1_R2} (joint-free) $\quad WJL_\tau := \sum_i \left(w\_JL_{i,\tau} \cdot JL_i \right)$

$WJL_\tau := \left| WJL_\tau \right|$

f_{S1_R1} (joint) $\quad WJI_\tau := \sum_i \left(w\_JI_{i,\tau} \cdot JI_i \right)$

$WJI_\tau := \left| WJI_\tau \right|$

f_{S2_R1} (joint-free) $\quad WKI_\tau := \sum_i \left(w\_KI_{i,\tau} \cdot KI_i \right)$

$WKI_\tau := \left| WKI_\tau \right|$

f_{S2_R2} (joint) $\quad WKL_\tau := \sum_i \left(w\_KL_{i,\tau} \cdot KL_i \right)$

$WKL_\tau := \left| WKL_\tau \right|$

f_{S1_R2} (joint-free)& f_{S1_R1} (joint)

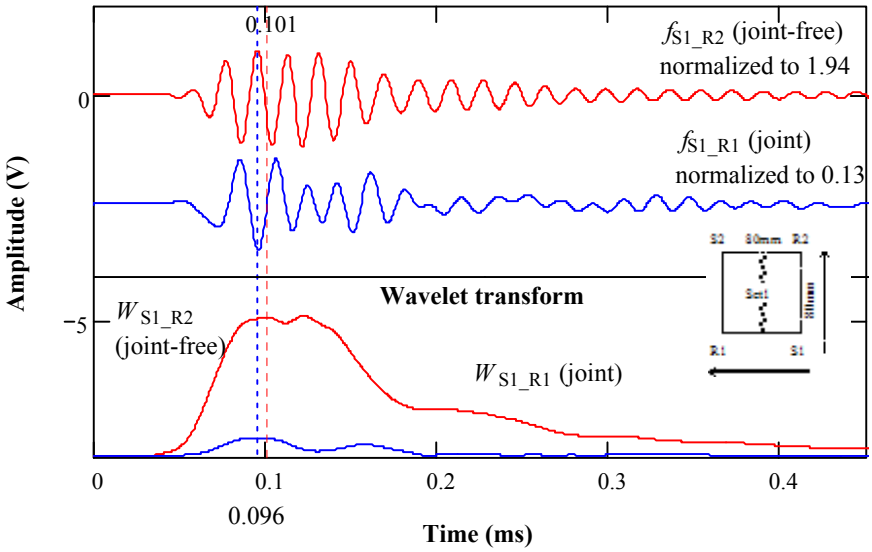

f_{S2_R1} (joint-free)& f_{S2_R2} (joint)

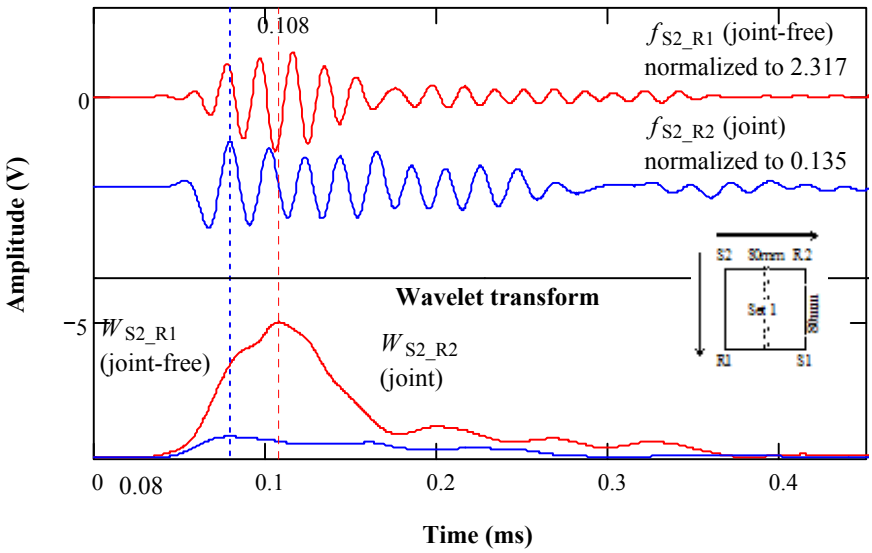

Amplitude ratio

$$\frac{\max(WJI)}{\max(WJL)} = 0.069 \qquad \frac{\max(WKL)}{\max(WKI)} = 0.06 \qquad \sqrt{\frac{\max(WJI)}{\max(WJL)}\frac{\max(WKL)}{\max(WKI)}} = 0.064$$